

Rabindranath Bera
Subir Kumar Sarkar
Swastika Chakraborty
Editors

Advances in Communication, Devices and Networking

Proceedings of ICCDN 2017

Lecture Notes in Electrical Engineering

Volume 462

Board of Series editors

Leopoldo Angrisani, Napoli, Italy
Marco Arteaga, Coyoacán, México
Bijaya Ketan Panigrahi, New Delhi, India
Samarjit Chakraborty, München, Germany
Jiming Chen, Hangzhou, P.R. China
Shanben Chen, Shanghai, China
Tan Kay Chen, Singapore, Singapore
Rüdiger Dillmann, Karlsruhe, Germany
Haibin Duan, Beijing, China
Gianluigi Ferrari, Parma, Italy
Manuel Ferre, Madrid, Spain
Sandra Hirche, München, Germany
Faryar Jabbari, Irvine, USA
Limin Jia, Beijing, China
Janusz Kacprzyk, Warsaw, Poland
Alaa Khamis, New Cairo City, Egypt
Torsten Kroeger, Stanford, USA
Qilian Liang, Arlington, USA
Tan Cher Ming, Singapore, Singapore
Wolfgang Minker, Ulm, Germany
Pradeep Misra, Dayton, USA
Sebastian Möller, Berlin, Germany
Subhas Mukhopadhyay, Palmerston North, New Zealand
Cun-Zheng Ning, Tempe, USA
Toyoaki Nishida, Kyoto, Japan
Federica Pascucci, Roma, Italy
Yong Qin, Beijing, China
Gan Woon Seng, Singapore, Singapore
Germano Veiga, Porto, Portugal
Haitao Wu, Beijing, China
Junjie James Zhang, Charlotte, USA

**** Indexing: The books of this series are submitted to ISI Proceedings, EI-Compendex, SCOPUS, MetaPress, Springerlink ****

Lecture Notes in Electrical Engineering (LNEE) is a book series which reports the latest research and developments in Electrical Engineering, namely:

- Communication, Networks, and Information Theory
- Computer Engineering
- Signal, Image, Speech and Information Processing
- Circuits and Systems
- Bioengineering
- Engineering

The audience for the books in LNEE consists of advanced level students, researchers, and industry professionals working at the forefront of their fields. Much like Springer's other Lecture Notes series, LNEE will be distributed through Springer's print and electronic publishing channels.

For general information about this series, comments or suggestions, please use the contact address under "service for this series".

To submit a proposal or request further information, please contact the appropriate Springer Publishing Editors:

Asia:

China, *Jessie Guo, Assistant Editor* (jessie.guo@springer.com) (Engineering)

India, *Swati Meherishi, Senior Editor* (swati.meherishi@springer.com) (Engineering)

Japan, *Takeyuki Yonezawa, Editorial Director* (takeyuki.yonezawa@springer.com)
(Physical Sciences & Engineering)

South Korea, *Smith (Ahram) Chae, Associate Editor* (smith.chae@springer.com)
(Physical Sciences & Engineering)

Southeast Asia, *Ramesh Premnath, Editor* (ramesh.premnath@springer.com)
(Electrical Engineering)

South Asia, *Aninda Bose, Editor* (aninda.bose@springer.com) (Electrical Engineering)

Europe:

Leontina Di Cecco, Editor (Leontina.dicecco@springer.com)
(Applied Sciences and Engineering; Bio-Inspired Robotics, Medical Robotics, Bioengineering; Computational Methods & Models in Science, Medicine and Technology; Soft Computing; Philosophy of Modern Science and Technologies; Mechanical Engineering; Ocean and Naval Engineering; Water Management & Technology)
(christoph.baumann@springer.com)

(Heat and Mass Transfer, Signal Processing and Telecommunications, and Solid and Fluid Mechanics, and Engineering Materials)

North America:

Michael Luby, Editor (michael.luby@springer.com) (Mechanics; Materials)

More information about this series at <http://www.springer.com/series/7818>

Rabindranath Bera · Subir Kumar Sarkar
Swastika Chakraborty
Editors

Advances in Communication, Devices and Networking

Proceedings of ICCDN 2017

Editors

Rabindranath Bera
Department of Electronics
and Communication Engineering
Sikkim Manipal Institute of Technology
Majitar, Rangpo, Sikkim
India

Swastika Chakraborty
Department of Electronics
and Communication Engineering
Sikkim Manipal Institute of Technology
Majitar, Rangpo, Sikkim
India

Subir Kumar Sarkar
Department of Electronics
and Telecommunication Engineering
Jadavpur University
Kolkata, West Bengal
India

ISSN 1876-1100 ISSN 1876-1119 (electronic)
Lecture Notes in Electrical Engineering
ISBN 978-981-10-7900-9 ISBN 978-981-10-7901-6 (eBook)
<https://doi.org/10.1007/978-981-10-7901-6>

Library of Congress Control Number: 2018930103

© Springer Nature Singapore Pte Ltd. 2018

This work is subject to copyright. All rights are reserved by the Publisher, whether the whole or part of the material is concerned, specifically the rights of translation, reprinting, reuse of illustrations, recitation, broadcasting, reproduction on microfilms or in any other physical way, and transmission or information storage and retrieval, electronic adaptation, computer software, or by similar or dissimilar methodology now known or hereafter developed.

The use of general descriptive names, registered names, trademarks, service marks, etc. in this publication does not imply, even in the absence of a specific statement, that such names are exempt from the relevant protective laws and regulations and therefore free for general use.

The publisher, the authors and the editors are safe to assume that the advice and information in this book are believed to be true and accurate at the date of publication. Neither the publisher nor the authors or the editors give a warranty, express or implied, with respect to the material contained herein or for any errors or omissions that may have been made. The publisher remains neutral with regard to jurisdictional claims in published maps and institutional affiliations.

Printed on acid-free paper

This Springer imprint is published by the registered company Springer Nature Singapore Pte Ltd. part of Springer Nature
The registered company address is: 152 Beach Road, #21-01/04 Gateway East, Singapore 189721, Singapore

Preface

International Conference on Communication, Devices and Networking (ICCDN 2017) is organized by the Department of Electronics and Communication Engineering, Sikkim Manipal Institute of Technology, Majitar, Sikkim, during 3–4 June 2017.

The aim of the conference is to provide a platform for researchers, engineers, academicians and industry professionals to present their recent research works and to explore future trends in various areas of engineering. The conference also brings together both novice and experienced scientists and developers, to explore newer scopes, collect new ideas, establish new cooperation between research groups and exchange ideas, information, techniques and applications in the fields of electronics, communication, devices and networking.

The ICCDN 2017 committees rigorously invited submissions for many months from researchers, scientists, engineers, students and practitioners related to the relevant themes and tracks of the conference. The call for papers of the conference was divided into six tracks as mentioned: Track-1: Electronics and Nanotechnology, Track-2: Energy and Power, Track-3: Microwave, Track-4: Wireless Communication and Digital Signal Processing, Track-5: Control and Instrumentation, and Track-6: Data Communication and Networking.

All the submissions underwent a strenuous peer review process which comprised expert reviewers. The papers were then reviewed based on their contributions, technical content, originality and clarity. The entire process, which includes the submission, review and acceptance processes, was done electronically. A total of 263 papers have been received out of which 101 papers have been accepted. All these efforts undertaken by the Organizing Committees led to a high-quality technical conference programme, which featured high-impact presentations from guest speakers and from paper presenters. All attendees appreciated and expanded their expertise in the latest developments in their relevant fields.

We would like to thank the Patrons, General Chairs, the members of the Technical Programme Committees, Advisory Committees and reviewers for their excellent and tireless work. We also want to thank Springer for the support and the authors for the success of the conference.

Majitar, Rangpo, India
Kolkata, India
Majitar, Rangpo, India

Rabindranath Bera
Subir Kumar Sarkar
Swastika Chakraborty

Organization

CHIEF PATRON

Dr. Somnath Mishra, VC, SMU

PATRON

Dr. Ashis Sharma, Registrar, SMU

Dr. Amik Garg, Director, SMIT

Dr. Sadasivan Thekkey Veetil, Addl. Director, SMIT

GENERAL CHAIR

Dr. Rabindranath Bera, ECE, SMIT

INTERNATIONAL ADVISORY COMMITTEE

Dr. Hiroshi Iwai, Tokyo Institute of Technology, Yokohama, Japan

Dr. Durgamadhab Misra, New Jersey Institute of Technology (NJIT), NJ, US

Dr. Valentina Emilia Balas, Romania

Dr. EfeFrancis Orunmwense, CRART, South Africa

Dr. Subhas Chandra Mukhopadhyay, Macquarie University, Australia

Dr. Rajeev Kumar Kanth, University of Turku, Finland

Dr. Rupesh Kumar, Technicolor, Rennes, France

Dr. BabuSena Paul, University of Johannesburg, South Africa

Dr. Sanjeevikumar Padmanaban, University of Johannesburg, South Africa

NATIONAL ADVISORY COMMITTEE

Dr. Mrinal Kanti Ghose, SMIT

Dr. Sanjay Dahal, Dean, SMIT

Dr. Rabindranath Bera, SMIT

Dr. Ajoy Kr. Ray, SMIT

Dr. Ajeya Jha, SMIT

Dr. Karma Sonam Sherpa, SMIT

Dr. Kalpana Sharma, SMIT

Dr. B. B. Pradhan, SMIT

Dr. H. K. D. Sarma, SMIT
Prof. C. J. Thomas, SMIT
Dr. Sangeeta Jha, SMIT
Dr. Vinod Kumar Sayal, SMIT
Dr. Gobinda Chandra Mishra, SMIT
Dr. D. R. Poddar, Jadavpur University, Kolkata
Dr. J. P. Banerjee, IRPEL, CU
Dr. Sayan Chatterjee, Jadavpur University
Dr. Kiran Shankar Hazra, Scientist, Institute of Nano Sci. and Tech.
Dr. Rohit Sinha, IIT Guwahati
Dr. Rajib Kumar Panigrahi, IIT Roorkee
Dr. Ratnajit Bhattacharjee, IIT Guwahati
Dr. Shaik Rafi Ahamed, IIT Guwahati
Mr. Chinmay Kumar Nayak, SC-E, DRDO, Chandipur
Dr. Singam Jayanthu, NIT Rourkela
Dr. Kanak Chandra Sarma, Gauhati University
Dr. B. K. Rai, IIT Guwahati
Dr. Subir Kumar Sarkar, Jadavpur University, Kolkata
Dr. Rowdra Ghatak, NIT Durgapur
Dr. V. Sarala, SC-F, DRDO, Hyderabad
Dr. Monojit Mitra, IEST, Shibpur
Mr. Arijit Mazumdar, SC-E, SAMEER, Kolkata
Dr. Bansibadan Maji, NIT, Durgapur
Dr. Samarjit Ghosh, Thapar University, Punjab
Dr. Debdatta Kandar, NEHU, Shillong, Meghalaya, India
Dr. RajeebDey, NIT, Silchar
Dr. Roy P. Paily, IIT, Guwahati
Dr. Abhilasha Mishra, Maharashtra Institute of Technology
Dr. Sumana Kumari, University Polytechnic, B.I.T. Mesra
Dr. Nagendra Pratap Singh, IIT-BHU
Dr. Sanjay Kumar Ghosh, Bose Institute, Kolkata
Dr. C. K. Sarkar, Jadavpur University
Dr. Sujit Kumar Biswas, Jadavpur University
Dr. P. C. Pradhan, SMIT
Dr. S. R. M. Prasanna, IIT Guwahati
Dr. P. K. Bora, IIT Guwahati
Dr. Kuntal Deka From IIT
Dr. Rahul Shrestha, IIT Mandi
Dr. Jolly Dhar, Sc – F, ISRO-SAC
Dr. Ajit Pal, IIT Kharagpur
Dr. Debadatta Pati, NIT Nagaland

TECHNICAL PROGRAMME COMMITTEE

Dr. Rabindranath Bera, SMIT
Dr. Subir Kumar Sarkar, Jadavpur University, Kolkata
Dr. Rupesh Kumar, Rennes, France
Dr. Babu Sena Paul, University of Johannesburg, South Africa
Dr. Rajeev Kumar Kanth, University of Turku
Dr. Ashik Paul, IRPEL, CU
Dr. Angsuman Sarkar, Kalyani Govt. Eng. College, Kalyani
Dr. Himadri Sekhar Dutta, Kalyani Govt. Eng. College, Kalyani
Dr. Prolay Saha, Jadavpur University, Kolkata, India
Dr. Sanatan Chattopadhyay, University of Calcutta
Dr. Kaustavl, Physics Department, Jadavpur University
Dr. Valentina Emilia Balas, Romania
Dr. Nagendra Pratap Singh, Banaras Hindu University
Dr. Rajeeb Dey, National Institute of Technology, Silchar
Dr. Roy P. Paily, IITG
Dr. Abhilasha Mishra, Maharashtra Institute of Technology
Dr. Sumana Kumari, University Polytechnic, B.I.T. Mesra
Dr. Debdatta Kandar, NEHU
Dr. P. K. Banerjee, Jadavpur University, Kolkata
Dr. Sukla Bose, Kalyani Govt. Eng. College, Kalyani
Dr. Saurabh Das, Indian Statistical Institute, Kolkata
Mrs. Barnali Dey, SMIT
Dr. L. Joyprakash Singh, NEHU
Mr. S. K. Dutta, NEHU
Dr. Sam Darshi, IIT Ropar
Mr. Pranab Kishore Dutta, NERIST
Dr. Brijesh Kumbhani, IIT Ropar
Mr. Madhusudhan Mishra, NERIST
Dr. Murli Manohar, IIIT Manipur
Dr. Anjan Kundu, IRPEL, CU
Dr. Dipanjan Bhattacharjee, SMIT
Dr. Md Ruhul Islam, SMIT
Md. Nasir Ansari, SMIT
Mr. Amit Kumar Singh, SMIT
Dr. Mousumi Gupta, SMIT
Dr. Samarjeet Borah, SMIT
Dr. Utpal Deka, SMIT
Dr. Bibhu Prasad Swain, SMIT
Dr. Somenath Chatterjee, SMIT
Dr. Sourav Dhar, SMIT
Dr. Tanushree Bose Roy, SMIT
Mr. Akash Kumar Bhoi, SMIT
Dr. Amrita Biswas, SMIT
Dr. Swastika Chakraborty, SMIT

Mr. Hemanta Saikia, SMIT
Mr. Debjyoti Ghosh, SMIT
Mr. Om Prakash Singh, SMIT
Ms. Soumyasree Bera, SMIT
Mr. Arun Kumar Singh, SMIT
Mr. Samarendra Nath Sur, SMIT
Mr. Amit Agarwal, SMIT
Dr. Swanirbhar Majumder, NERIST
Dr. Nagesh Ch, IIIT Manipur
Dr. Satyabrata Das, VSSUT, Burla
Dr. Rajib Jana, NIT AP
Dr. J. P. Singh, NIT Patna
Dr. Jitendra Mohan, IIIT Noida
Mrs. Deepika Hazarika, Tezpur University
Dr. Vijay Kumar Nath, Tezpur University
Dr. Aheibam Dinamani Singh, NERIST
Ms. Sayantani roy
Mr. Rochan banstola
Mr. Surya prakash tamang
Mr. Saumya das
Mr. Suman das
Mr. Himangshu pal
Ms. Tinku biswas
Ms. Rijhi dey

CONVENER

Mr. Samarendra Nath Sur

Co-CONVENER

Mr. Soumyasree Bera
Mr. Arun Kumar Singh
Mr. Amit Agarwal

Contents

Modelling of Thermoelectric and Conduction Mechanism of Multi-nanoribbon Matrix	1
Amit Agarwal, P. C. Pradhan and Bibhu P. Swain	
Stabilization of Pulsed IMPATT Oscillator at W Band Over Extended Ambient Temperature Range	9
Sukhendu Bhanja, Mousumi Sarkar, Tanmay Ghoshal and Arijit Majumder	
Geometrically Intricate Oxide-Based Heterostructure Over Flexible Platform: Morphology-Induced Catalytic Performance Enhancement Under UV Light	21
Subhasish Thakur, Soumen Maiti, Shreyasi Pal and Kalyan Kumar Chattopadhyay	
Investigation of Super-Gaussian Pulse Amplification in Semiconductor Optical Amplifier (SOA)	29
Mijanur Rahim and Md. Asraful Sekh	
Design of an Energy Efficient, Low Phase Noise Current-Starved VCO Using Pseudo-NMOS Logic	35
Moumita Das, Posiba Mostafa, Antardipan Pal, Debmalya Das and Sayan Chatterjee	
Performance Comparison of 1-Bit Conventional and Hybrid Full Adder Circuits	43
Inamul Hussain and Saurabh Chaudhury	
VLSI Implementation of Booth's Multiplier Using Different Adders . . .	51
Ujjaljyoti Sarkar, Rongan Nath and Suman Das	
A Density Functional Theory-Based Study of Electronic and Optical Properties of Anatase Titanium Dioxide	57
Debashish Dash, Saurabh Chaudhury and Susanta Kumar Tripathy	

Performance Analysis of a Front High-K Gate Stack Dual-Material Tri-gate SON MOSFET	69
Pritha Banerjee, Anup Sarkar, Dinesh Kumar Dash and Subir Kumar Sarkar	
Comparative Study of n-ZnO/SiO₂/p-Si and Pd/n-ZnO/SiO₂/p-Si Thin Film-Based H₂ Sensor Fabricated by Sol-gel Process	79
Sreeparna Barua, Anup Dey, Subhashis Roy and Subir Kumar Sarkar	
Complementary Energy Path Adiabatic Logic-Based Adder Design in 32 Nm FinFET Technology	87
Suresh Kumar Pittala and A. Jhansi Rani	
Analytical Modeling and Simulation of Triple Metal Front Gate Stack DG-MOSFET with Graded Channel (GC-TMDG MOSFET)	97
Priyanka Saha, Saheli Sarkhel, Dinesh Kumar Dash, Suvam Senapati and Subir Kumar Sarkar	
Integrated TTL Driver with SPDT Switch	107
Priyanka Shukla, Rakhi Kumari and Rabindranath Bera	
A 3D Analytical Modeling of Dual-Metal Tri-Gate Silicon-On-Nothing Tunneling Field Effect Transistor	115
Esita Mitra, Dinesh Kumar Dash and Subir Kumar Sarkar	
Modeling of Lead-Free CH₃NH₃SnI₃-Based Perovskite Solar Cell Using ZnO as ETL	125
Tapas Chakrabarti, Malay Saha, Ambar Khanda and Subir Kumar Sarkar	
Experimental Investigation on Mustard Oil-Based Alumina Nanofluid Under Varying Temperature and Humid Condition	133
Sachin Thakur, Jaspreet Singh Chahal and Sunny Vig	
Optimization Method for Unit Commitment in High-Level Wind Generation and Solar Power	143
Saket Saurabh and MdIrfan Ahmed	
An Implicit Approach to Minimize the Reactive Power of a 765 kV Interconnected Bus System in India	151
Rishiraj Sarker, Debaparna Sengupta, Susanta Kumar Bhattacharya and Asim Datta	
A CFS–DNN-Based Intrusion Detection System	159
Sayak Paul, Chandan Banerjee and Moinak Ghoshal	
A Compact Ku-Band Bandpass Filter with Wide Upper Stopband Using SIR	169
Atiqur Rahman, Sushanta Kabir Dutta and Pankaj Sarkar	

A Corporate Feed Network Optimization for Performance Enhancement 177
 Seyi Stephen Olokede and Babu Sena Paul

A Reconfigurable Defected Ground Structure Resonator Based on Coplanar Waveguide 183
 Amit Baran Dey, Arnab Nandi, Vinay Kumar Verma and Banani Basu

Assessment of Wind Energy Potential in Northeastern Cities of India 191
 Singh Rahul and Om Prakash

A Multifractal Detrended Fluctuation Analysis-Based Framework for Fault Diagnosis in Autonomous Microgrids 199
 S. Pratiher, M. Mukherjee and N. Haque

A Work on Grid Connected Solar Photovoltaic System Using Particle Swarm Optimization Technique 209
 Bharti and Akhil Gupta

Review of Small-Signal Analysis of Microgrid in Islanding Operation 223
 Dhanprakash Singh, Kamal Kant Sharma, Inderpreet Kaur and Balwinder Singh

Optimization of Wind Power Using Artificial Neural Network (ANN) 233
 Dinesh Chauhan and Sunny Vig

Cost Analysis of Hybrid Power System Design Using Homer 247
 Gopal Thakur, Kamal Kant Sharma, Inderpreet Kaur and Balwinder Singh

Stability Investigation for a 100 kW Solar Photovoltaic Grid-Connected System Using D-STATCOM Control 259
 Akhil Gupta and Kapil Verma

Comparative Review on Microgrid Management System 275
 Susheel Kumar and Inderpreet Kaur

Solution of Economic Load Dispatch Problems Through Moth Flame Optimization Algorithm 287
 Princi Tripathi, Upendra Tomar, Vinod Kumar Singh and Akash Kumar Bhoi

Noise Reduction in Synthetic Aperture Radar Images Using Fuzzy and Self-Organizing Map 295
 Kishore Medhi, Khwairakpam Amitab, Debdatta Kandar and Babusena Paul

Design of a Quasi-Lumped Resonator Antenna Array Based on a Novel Optimized Corporate Network Feed	303
Seyi Stephen Olokede and Babu Sena Paul	
Development of a Drowsy Driver Detection System Based on EEG and IR-based Eye Blink Detection Analysis	313
Oindrila Sinha, Soumendra Singh, A. Mitra, S. K. Ghosh and S. Raha	
Microstrip Patch Antenna with Fractal Structure Using Superstrate Operating in ISM Band	321
Shreema Manna, Tanushree Bose and Rabindranath Bera	
Assessment of Pulse-Doppler Radar and Digital Beamforming Radar	329
Nima Donka Tamang, Samarendra Nath Sur, Soumyasree Bera and Rabindranath Bera	
FMCW Waveform-Based Vehicular Radar	343
Additi Mrinal Singh and Rabindranath Bera	
Multiband Slotted Circular Microstrip Patch Antenna	351
Rajshri, Saumya Das and Tanushree Bose	
Multi Resonant Textile Antenna with Partial Ground for Multiband Applications	359
Rahul Saini, Vinod Kumar Singh, Niharika Singh, J. P. Saini and Akash Kumar Bhoi	
Microstrip Textile Antenna with Jeans Substrate with Applications in S-Band	369
Niharika Singh, Vinod Kumar Singh, Rahul Saini, J. P. Saini and Akash Kumar Bhoi	
Antenna for Wireless Area Network and Bluetooth Application	377
Manju Devi, Vinod Kumar Singh, Sanjeev Sharma and Akash Kumar Bhoi	
Estimation of Frequency Band of Microstrip Antenna (MSA) with Radial Basis Function (RBF)	385
Ashish Kumar, Archana Lala, Vinod Kumar Singh and Akash Kumar Bhoi	
Design and Analysis of Microstrip Antenna Using Multilayer Feed-Forward Back-Propagation Neural Network (MLPFFBP-ANN)	393
Poornima Singh, Vinod Kumar Singh, Archana Lala and Akash Kumar Bhoi	
Performance of SC Receiver Over OWDP Fading Channels	399
Suparna Goswami and Aheibam Dinamani Singh	

Performance Analysis of STBC-FSO Communication System in Different Turbulence Regimes 409
 Sonali Garg, Abhishek Dixit and Virander Kumar Jain

A Low-Cost Refractometer with Misaligned Optical Fibers 419
 Dipankar Chetia, Tenison Basumatary, Hidam Kumarjit Singh and Tulshi Bezboruah

Fiber Optic Sensor for Detection of Chlorine Level in Water 429
 Sebina Yesmin, Dipankar Chetia, Tenison Basumatary and Hidam Kumarjit Singh

Effect of LO Phase Noise on Front-end Receiver Performance 439
 Manish Kumar, T. K. Pal, B. S. V. Prasad, G. Arun Kumar, Sukhendu Bhanja and Arijit Majumder

Design of a Proactive Distance Handover Algorithm for WSN: A Case Study-Based Approach 447
 M. S. Saketh, N. S. Reddy and S. Dhar

Homomorphic Analysis of Vowels in Khasi Dialect 459
 Bronson Syiem, Fairriky Rynjah and L. Joyprakash Singh

Discriminant Correlation-Based Information Fusion for Real-Time Biomedical Signal Clustering 465
 Anil Hazarika, A. Sarmah, M. Boro, P. Kalita and B. K. Dev Choudhury

Development of OFDM UWB-Based RADCOMM System for Effective Utilization in Intelligent Transportation System 475
 M. Chakraborty, B. Maji, D. Kandar and S. Shome

Fixed-Point Design of 1024-Point CI-OFDM for DVB-Satellite to Handheld 485
 Rakesh Palisetty and Kailash Chandra Ray

Design of Aperture-Fed Elliptically Polarized Dielectric Resonator Antenna for WLAN IEEE 802.11 ac Applications 495
 Hashinur Islam, Saumya Das and Tanushree Bose

Broadband Glass Paperweight Dielectric Resonator Antenna for WLAN Applications 503
 Saumya Das, Hashinur Islam and Tanushree Bose

Pitch Tracking and Pitch Smoothing Methods-Based Statistical Approach to Explore Singers’ Melody of Voice on a Set of Songs of Tagore 509
 Indira Chatterjee, Priya Gupta, Parthasarathi Bera and Joy Sen

Image Contrast Enhancement Using Differential Evolution 517
 Anil Singh Parihar, Om Prakash Verma and Deepanshu Yadav

Optical Character Recognition Using Minimal Complexity Machine and Its Comparison with Existing Classifiers	527
O. P. Verma, Eshwar Agarwal, Cherry Agrawal and Avanti Gupta	
Performance Analysis of Different Models to Find Value at Risk in the Indian Market Using a Bi-Portfolio Allocation	539
Om Prakash Verma, Eshwar Agarwal, Cherry Agrawal and Avanti Gupta	
Hardware Co-simulation of Reconfigurable FIR Filters on FPGA	553
Anindita Ghosh and Debashis Chakraborty	
Ranking of Sensors for ADAS—An MCDM-Based Approach	563
Jayanta Kumar Baruah, Rabindranath Bera and Sourav Dhar	
Offline Signature Verification Using Radial Basis Function with Selected Feature Sets	573
Hemanta Saikia and Kanak Chandra Sarma	
A Study on Prosodic Feature-Based Automatic Classification of Languages from Northeastern India	583
Sushanta Kabir Dutta and Lairenlakpam Joyprakash Singh	
Introducing 5G Front-End Femtocell to Improve 4G Network Performance	591
Debasish Bhaskar, Safal Sharma, Rabindranath Bera, Ganesh Sharma, Preman Chettri and Kharka Bahadur Rai	
Narrowband Hybrid Beamformation System for Doable mmWave 5G Mobile Communication System	599
Safal Sharma, Debasish Bhaskar and Rabindranath Bera	
Accidental Event Detection Based on Optical Flow Analysis	607
Navneet Nayan, Sanjeet Kumar and Sitanshu Sekhar Sahu	
Application of 5G Waveform in Internet of Things (IoT) and Its Impact on BER in Physical Layer	615
Pallavi Neog, Rajat Paul, Shantanu Roy and Rabindranath Bera	
2D/3D Liver Segmentation from CT Datasets	625
G. K. Mourya, D. Bhatia, A. Handique, S. Warjri, A. War and S. A. Amir	
Wireless Security Over a Point-to-Point 5G Communication System	633
Rajat Paul, Pallavi Neog, Shantanu Roy and Rabindranath Bera	
An Integrated GNSS–Microcontroller–GSM System for Various Application Developments	641
Sujoy Mandal, Koushik Samanta, Basudev Das, Atanu Santra and Anindya Bose	

Finger Detection for Hand Gesture Recognition Using Circular Hough Transform	651
Amrita Biswas	
Energy Contribution of Control Packets of AODV in Various Mobility Models in MANET	661
Akash Soni, Preeti Jharia and Sonali Chouhan	
Analysis and Characterization of Spectral Signature of Soil Nitrogen Content Based on VNIR Optical Sensing for Application in Smart Farming	669
Subra Mukherjee and Shakuntala Laskar	
5G Technology Enabling the Wireless Internet of Things	679
Rabindranath Bera, Debasish Bhaskar, Samarendra Nath Sur, Soumyasree Bera, Arun Kumar Singh, Swastika Chakraborty, Amit Agarwal, Ganesh Sharma, Safal Sharma, Preman Chettri and Riwas Gurung	
Lower Facial Curves Extraction for Unconstrained Face Detection in Video	689
Dattatray D. Sawat and Ravindra S. Hegadi	
Digital Beamforming Techniques—A Comparison	701
Geheshwar Sharma Ramchurn, Sanya Dhoundiyal, Arun Kumar Singh and Bansibadan Maji	
Realization of Fractional-Order Operator in Complex Domains—A Comparative Study	711
Jaydeep Swarnakar, Prasanta Sarkar and Lairenlakpam Joyprakash Singh	
Speed Control of Single Phase Induction Motor Using Fuzzy Logic Controller	719
Kamal Sapkota, Arun Pradhan, Amit Kumar Singh and Pratiba Rai	
Speed Control of DC Motor Using Fuzzy-Based Intelligent Model Reference Adaptive Control Scheme	729
Dayarnab Baidya and Rupam Gupta Roy	
Performance Analysis of Fuzzy Logic-Based Edge Detection Technique	737
R. Lalchhanhima, D. Kandar and Babusena Paul	
Development and Performance Analysis of Stand-Alone PV-Based Induction Motor Drive	747
Sourav Ghosh and Tapas Kumar Saha	
Design of P-I Controller of Wind Turbine with Doubly Fed Induction Generator Using Flower Pollination Algorithm	755
Arnab Kumar Mondal and Parthasarathi Bera	

Dynamic Analysis of Two-Link Robot Manipulator for Control Design	767
Gourab Nandy, Basukinath Chatterjee and Amartya Mukherjee	
Design of P-I-D Based TCSC Controller for SMIB System Using Artificial Neural Network	777
Arnab Kumar Mondal, Chiborhame Suting and Parthasarathi Bera	
Nonlinear Offset Measurement and Nullification for Effective Resistive Sensor Design	789
L. Dutta, A. Hazarika, M. Boro and M. Bhuyan	
Fuzzy Rule-Based Set Point Weighting for PID Controller	797
Kausik Sen, Biswajit Chakraborty, Amit Gayen and Chanchal Dey	
RBF Neural Network-Based Wavelet Packet Energy-Aided Fault Localization on a Hybrid Transmission Line	807
Animesh Sarkar and Bikash Patel	
Design of an Adaptive Calibration Technique Using Data Fusion for Pressure Measurement	817
K. V. Santhosh and Bhagya R. Navada	
Review on Internet of Things (IoT): Making the World Smart	827
Debajyoti Misra, Gautam Das and Debaprasad Das	
Big Data and Data Science in Engineering Platform: A Techno-educational Research Study in Indian Context	837
P. K. Paul and Anubhav Kumar	
Insight into the Cloud Computing Programs at Bachelors Levels: Emphasizing International Universities and Indian Potentialities	847
P. K. Paul and M. P. Pradhan	
Approaches and Measures to Detect Wormhole Attack in Wireless Sensor Networks: A Survey	855
Diksha Giri, Samarjeet Borah and Ratika Pradhan	
Data Center Traffic Engineering: Multipath Routing with QoS Guarantee	865
Epheremika Tariang and Nabajyoti Medhi	
Two Identity-Based Aggregate Signature Schemes from Pairings	877
Subhas Chandra Sahana, Sourav Kumar Das, Sangeeta Mashahary and Bubu Bhuyan	
Real-Time Hybrid Intrusion Detection System Using Machine Learning Techniques	885
Inadyuti Dutt, Samarjeet Borah, Indra Kanta Maitra, Kuharan Bhowmik, Ayindrilla Maity and Suvosmita Das	

IoT-Based Monitoring and Smart Planning of Urban Solid Waste Management 895
 Krishangi Deka, Krishangi Goswami and Sagarika

Network Traffic Analysis and Packet Sniffing Using UDP 907
 Md Ruhul Islam, Tawal K. Koirala and Ferdousi Khatun

Strahler Order Classification and Analysis of Drainage Network by Satellite Image Processing 915
 Ferdousi Khatun and Pratikshya Sharma

Digital Pen to Convert Handwritten Trajectory to Image for Digit Recognition 923
 Debjyoti Ghosh, Sanchi Goyal and Rohit Kumar

Application of Particle Swarm Optimization-TVAC Algorithm in Power Flow Studies 933
 Poulami Ghosh and Anand Kalwar

Network-Based Digital Notice Board 943
 Saikumar Valluru, Prachi and Arun Kumar Singh

Author Index. 949

About the Editors

Prof. (Dr.) Rabindranath Bera is Head and Professor in the Department of Electronics and Communication Engineering (ECE) at SMIT and has been driving the ECE Department for 13 years. He monitors and controls academic performances of the faculty members and students of ECE Department. He also performs R&D activities including sponsored and in-house projects. He completed his B.Tech., M.Tech. and Ph.D. from Institute of Radiophysics and Electronics, University of Calcutta, Kolkata. His areas of interest are remote sensing (active and passive), communication, 4G mobile communication, integrated sensing and communication, adaptive signal processing and cognitive radio and radar systems, radio astronomy, process control instrumentation. He has won the URSI ‘International Young Scientists Award’ for the year 2005. He recently attended IEEE 5G Summit in Kolkata during 3–4 March 2017 where he has highlighted his work towards the award of ‘BOSE Fellowship’ in the year 1993 at Japan. The participation has lots of appreciation for this work. Nine Ph.D. students have already completed their PhDs under his guidance, and he is currently supervising 11 Ph.D. students. He has 3 books, 85 journal papers and 80 conference papers published to his credit.

Prof. Subir Kumar Sarkar has completed his B.Tech., M.Tech. and Ph.D. (Tech) from Institute of Radiophysics and Electronics, University of Calcutta, and Post-Doctoral from Virginia Commonwealth University (VCU), USA. He has worked around 10 years in industry like Oil and Natural Gas Corporation (ONGC) as Executive Engineer and 25 years in universities (8 years in BESU and 17 years in JU) in different capacities. He was the Head of the Department of Electronics and Telecommunication Engineering, Jadavpur University, during 2011–2013, Coordinator of the evening course of M.Tech. in ‘VLSI Design and Microelectronics Technology’ 2009–2013 and 2016–till date and Coordinator of IC Design & Fabrication Centre, Jadavpur University, from 2016 to till date. He has authored five engineering textbooks published by CRC Press, USA; Artech House, USA; Pan Stanford, USA; S. Chand & Company Pvt. Ltd., India. He has already guided 43 Ph.D. scholars (8 more registered and currently working), 15 R&D projects sponsored by different Government of India funding agencies have been

completed/ongoing, published more than 600 technical research papers in archived international/national journals and peer-reviewed conferences. His research areas include nanodevices and low-power VLSI circuits, computer networks, digital watermarking and RFID. He has visited several countries like USA, France, the UK, Switzerland, Japan, Thailand and Bangladesh as Keynote Speaker, Special Guest of Honour, Invited Speaker, for training, presenting papers and visiting sophisticated laboratories as a part of his collaborative research activities. He is a Senior Member of IEEE, IEEE EDS Distinguished Lecturer, Life Fellow of IEI (India) and IETE, Life Member of ISTE and Life Member of Indian Association for the Cultivation of Science (IACS). He has successfully organized two IEEE-sponsored International Conferences as Convener (2004) and as General Chair (2012). He has filed one Indian Patent vide file No: 669/KOL/2013 dated 5 June 2013.

Dr. Swastika Chakraborty (Mukhopadhy) is Associate Professor in the Department of Electronics and Communication Engineering, Sikkim Manipal Institute of Technology, Majitar, Rangpo, Sikkim. Previously, she was working as an Assistant Professor in the Department of Electronics and Communication Engineering, JIS College of Engineering, Kalyani, Nadia, West Bengal. She is an accomplished researcher and teaching professional with progressive experience of more than 20 years. She has a substantial number of publications in renowned international/national journals and international and national conference. She has been awarded government-sponsored research project in her capacity as a principal investigator. She is a Member of IEEE Kolkata Section and former Treasurer and present Executive Committee Member of IEEE GRSS Kolkata Chapter. She has been awarded by JIS College of Engineering for good governance for her role in teaching administration with a sponsorship of Technical Education Quality Improvement Programme (TEQIP).

Modelling of Thermoelectric and Conduction Mechanism of Multi-nanoribbon Matrix

Amit Agarwal, P. C. Pradhan and Bibhu P. Swain

Abstract In this paper, modelling of thermoelectric and conduction mechanism of multilayer graphene nanoribbon (GNR) has performed taking various temperatures. The coordination of various elements H–H–H, C–C–H was calculated using radial distribution function. The current–voltage curves GRN were estimated with variation of temperatures from 4 to 3400 K. To evaluate the conduction mechanism and conductance with different applied voltage dI/dV versus voltage has been performed with varying of temperature. Moreover, the thermoelectric coefficient of GRN with different energy at different temperature has been estimated.

Keywords Graphene · Graphene nanoribbon · Thermal coefficient Interconnects · Radial distribution function

1 Introduction

At present era, copper is used for interconnection at the BEOL instead of aluminum, as conductivity of copper is six times more than aluminum, due to which chips had smaller metal components and less energy is used to pass electricity through it which lead to better performance in signal processing from transistor to transistor with minimal heat loss. Cu is a candidate for global interconnection in the upper-level metallization in ULSI technology due to its low resistivity and high electromigration

A. Agarwal (✉) · P. C. Pradhan
Department of Electronic and Communication Engineering, Sikkim Manipal
Institute of Technology, Majitar, Rangpo 737136, Sikkim, India
e-mail: amiteng2007@gmail.com

P. C. Pradhan
e-mail: prashant.c.pradhan@gmail.com

B. P. Swain
Centre for Materials Science and Nano-Technology, Sikkim Manipal Institute
of Technology, Majitar, Rangpo 737136, Sikkim, India
e-mail: bibhuprasad.swain@gmail.com

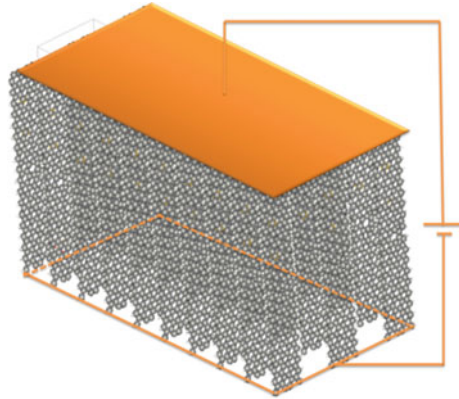
resistance however, the major obstacles to use due to stability issues like copper drift out of wiring, corrodes copper by exposure of oxygen and water, electro-migration thins copper interconnects and due to which there is increase in resistance of interconnects and break them [1]. Furthermore, the high diffusivity of copper materials is a major drawback which degrades IC performance. Graphene nanoribbon (GNR) can be a good candidate to replace Cu for interconnects at the BEOL [2]. Their 2D structure, high electrical and thermal conductivity, and low noise also make GNRs a possible alternative to copper for integrated circuit interconnects. Research is exploring the creation of quantum dots by changing the width of GNRs at select points along the ribbon, creating quantum confinement [3]. GRNs possess semiconductive properties and may be a technological alternative to silicon semiconductors [4]. GNR-FETs has capable of sustaining microprocessor clock speeds in the vicinity of 1 THz field-effect transistors dimension less than 10 nm wide with an I_{on}/I_{off} ratio $>10^6$ at room temperature. Naeemi et al. calculated conductance of GNR interconnects as a function of chirality, width, Fermi level, and the type of electron scatterings at the edges [1]. Chen et al. investigated GNR electrical properties as a function of ribbon width. The electrical current noise of GNR devices at low frequency is dominated by $1/f$ noise [5]. Hass et al. show multilayer graphene grown on carbon-terminated SiC(0001) surface which holds rotational stacking faults linked to the epitaxial state of the graphene–SiC interface, and such faults yield an electronic structure vague from an isolated graphene sheet in the zone of the Dirac point [6]. Ghosh et al. reported on investigation of the thermal conductivity of graphene suspended across trenches in Si/SiO₂ wafer. The amount of power dissipated in graphene and corresponding temperature rise were determined from the spectral position and integrated intensity of graphene’s G mode [7]. There has been no discussion on the bonding, effect of high temperature on the current, thermal coefficient, energy gap for the multi-GNR interconnects. In this paper, we modelled multi-graphene nanoribbon matrix and what is the impact of bonding on angle versus distribution, effect of temperature on $I-V$, dI/dV , energy temperature coefficient.

2 Background Theory of GNR

Figure 1 shows schematic of multi-graphene nanoribbon matrix. In this structure, there are 30 graphene nanoribbons (3×10 matrix form) used as an interconnect. Upper part of matrix is connected to one end of the transistor and lower part to the other end of the transistor, with multi-GNR in between. The transfer of current from one transistor to another transistor is done by this multi-GNR. As GNR provides high electrical, thermal conductivity, superior mobility, linear E-k relationship, width-dependent transport gap, and low noise, so due to these ballistic transport properties GNR makes most suitable candidate for interconnects.

Radial distribution function of GRN was calculated using [8, 9]

Fig. 1 Schematic of multilayer GNR as interconnects



$$g(r) = \frac{2V}{N^2} \left\langle \sum_{i < j} \partial(r - r_{ij}) \right\rangle \quad (1)$$

where N is the number of atoms, V is the volume, r_{ij} is the position vector of atom j with respect to the i th atom.

The conductance of GNR is derived using linear response of Landauer formula [10, 11]. The conductance of single GNR is given by

$$G_i = 2e^2 \int T_i(E) \left(\frac{-\partial f_0}{\partial E} \right) dE \quad (2)$$

where

$$f_0(E) = \left\{ 1 + \exp \left[\frac{(E - E_F)}{k_B T} \right] \right\}^{-1}$$

where $f_0(E)$ is the Fermi–Dirac distribution function and $T_n(E)$ is the transmission coefficient. Value of $E_0 = 0$ and $|E_i| = (|i| + 1/2) \hbar v_f / 2r$. $v_f = 106$ m/s Fermi velocity; r is width of GNR.

The total conductance of single GNR sheet is expressed as

$$G_{\text{tot}} = \sum_i G_i(e^-) + \sum_i G_i(\text{holes}) \quad (3)$$

$$G_{\text{tot}} \approx \frac{2}{\Delta E_i} \left[\int_0^{\infty} G_i(e^-) + \int_{-\infty}^0 G_i(\text{holes}) dE_i \right] \quad (4)$$

Further, we can deduce the above equation as

$$G_{\text{tot}} = \frac{8q^2 r^2 k_B T}{L h^2 v_f} \left[2 \cosh\left(\frac{E_F}{2T k_B}\right) \right] \text{func}(r, l_d) \quad (5)$$

Above equation gives us the total conductance of a GNR sheet.

3 Results and Discussion

Figure 2 shows an angle versus bonding distribution plot for multi-GNR with different bonding. From this figure, we analyze that for depending upon different bonding and different angle there is change in the distribution pattern. For H–H–H at an angle of 120, the distribution value is approximately 0.65 which is quite high as compared with other angles. Similarly, for C–H–H the distribution value is approximately 0.65 for angle of 97 and 0.3 for an angle of 175, which shows a deviation of about 50% value in distribution. The bond angle of H–H–H, H–C–H, H–C–C, C–H–H and C–C–C are of 37, 97, 175 and 120 respectively with same bond distribution value of 0.65.

Figure 3 shows the I – V characteristics of multi-GNR with varying temperature. From this figure, we analyze that with the increase of applied voltage from -1.0 to 1.0 V the current starts increasing linearly from approximately $-30,000$ to $30,000$ nA. Also with the increase of temperature from 4 to 3000 K, there is deviation of about 5% value of the current. At applied voltage of 0 V, there is no much change in current due to change of temperature from 4 to 2600 K, but there is slight deviation in current when the temperature is around 3000 K.

Figure 4 shows a dI/dV – V plot with varying temperature. From the figure, we analyze that there is a aperiodic change in dI/dV with change in applied voltage. With the change of applied voltage, there is change in dI/dV from a minimum value of $-38,000$ nA/V to a maximum value of $58,000$ nA/V. When the applied voltage is -1.0 , the dI/dV value is approximately $10,000$ nA/V, as the voltage is increased dI/dV also starts increasing from $10,000$ to $40,000$ nA/V till -0.75 applied voltages.

Fig. 2 Angle versus distribution of different bonds

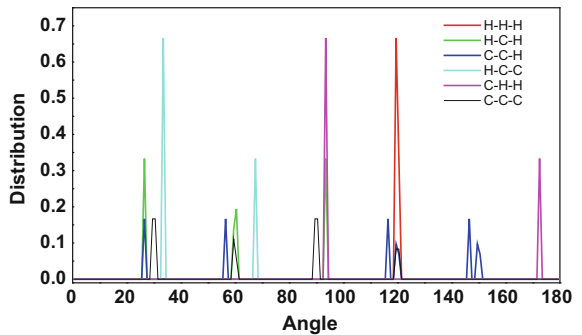


Fig. 3 Current versus voltage with varying temperature

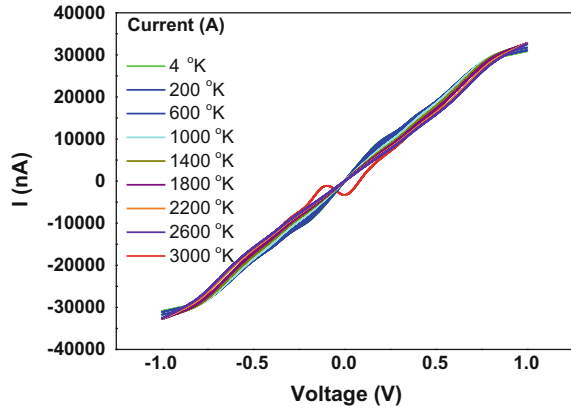
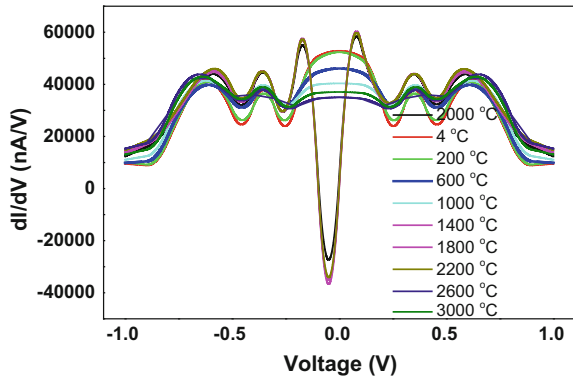


Fig. 4 dI/dV versus voltage with varying temperature

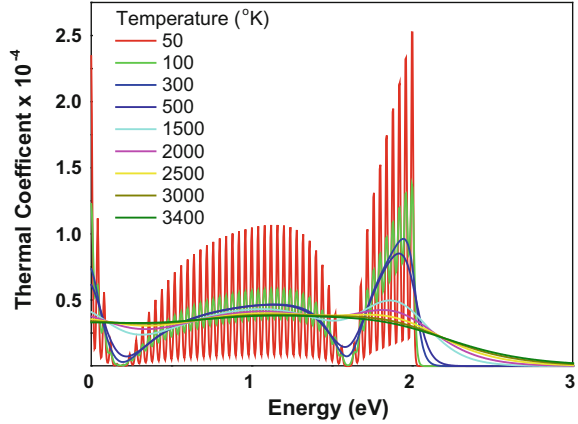


Further with the increase of voltage, the dI/dV starts decreasing from 40,000 nA/V to approximately 22,000 nA/V till -0.5 V applied voltage. This phenomenon of increasing and decreasing of dI/dV value continues till 1.0 V of applied voltage. Also with the change of temperature from 4 to 3000 K, there is deviation in the dI/dV value. At applied voltage of 0 V, the value for dI/dV at low temperature of 4 K is approximately 30,000 nA/V and at high temperature of 1800 K the dI/dV value is approximately $-30,000$ nA/V. There is quite a high deviation with the change in temperature at 0 V applied voltage. But at other values of applied voltages, the deviation of dI/dV is around 10–20% only.

Figure 5 shows a plot between thermal coefficient and energy with varying temperature. From the figure, we analyze that the value of thermal coefficient is high, i.e., 2.5×10^{-4} , for a low temperature of 50 K as compared to high temperature of 3400 K with thermal coefficient value of 0.4×10^{-4} . For a temperature of 50 K, the thermal coefficient at 0 eV is approximately 2.5×10^{-4} .

As energy is further increased, the thermal coefficient starts decreasing from 2.5×10^{-4} to 0 till 0.2 eV energy. Again, with the increase of energy the thermal coefficient starts increasing to a value of 1.0×10^{-4} . This phenomenon is

Fig. 5 Current versus voltage with varying temperature



continued till 2 eV energy. With further increase of energy, the thermal coefficient starts decreasing and finally at 3 eV the thermal coefficient approaches to zero. In case of 3400 K temperature, there is a constant value of thermal coefficient till 2 eV energy and with the further increase of energy the thermal coefficient approaches to zero.

4 Conclusion

In this paper, we experimentally modelled multi-GRN matrix and analyzed the impact of bonding on distribution and effect of temperature on current, dI/dV , temperature coefficient for multi-GRN matrix. At applied voltage of 0 V, the maximum value for dI/dV at low temperature of 4 K is approximately 30,000 nA/V and at high temperature of 1800 K the dI/dV value is approximately -30,000 nA/V. Due to this ballistic transport property, GNR makes most suitable candidate for interconnects and outperforms Cu.

References

1. A. Naeemi and J. D. Meindl, "Conductance modeling for graphene nanoribbon (GNR) interconnects," *IEEE Electron Device Lett.*, vol. 28, no. 5, pp. 428–431, May 2007.
2. M. C. Lemme, T. J. Echtermeyer, M. Baus, and H. Kurz, "A graphene field-effect device," *IEEE Electron Device Lett.*, vol. 28, no. 4, pp. 282–284, Apr. 2007.
3. Z. F. Wang, Q. W. Shi, Li, Q. Wang, X. Hou, J. G. Zheng, H. Yao, Y. Chen, J. (2007). "Z-shaped graphene nanoribbon quantum dot device". *Applied Physics Letters*. 91 (2007) (5): 053109.
4. Bullis Kevin, "Graphene Transistors". *Technology Review*. Cambridge: MIT Technology Review, Inc. Retrieved 2008-02-18.

5. Z. H. Chen, Y. M. Lin, M. J. Rooks, and P. Avouris, "Graphene nano-ribbon electronics," *Physica E-Low-Dimensional Systems & Nanostructures*, vol. 40, pp. 228–232, Dec 2007.
6. J. Hass, F. Varchon, J. E. Millan-Otoya, M. Sprinkle, N. Sharma, W. A. De Heer, C. Berger, P.N. First, L. Magaud, and E. H. Conrad, "Why multilayer graphene on 4H-SiC(0001) over-bar behaves like a single sheet of graphene," *Physical Review Letters*, vol. 100, p. 125504, Mar 2008.
7. S. Ghosh, I. Calizo, D. Teweldebrhan, E. P. Pokatilov, D. L. Nika, A. A. Balandin, W. Bao, F. Miao, and C. N. Lau, "Extremely high thermal conductivity of graphene: Prospects for thermal management applications in nanoelectronic circuits," *Applied Physics Letters*, vol. 92, p. 151911, Apr 2008.
8. D. C. Rapaport, *The Art of Molecular Dynamics Simulation*, (Cambridge University Press, New York, 1995).
9. M. R. Chavez-Castillo, M. A. Rodriguez-Mezab, and L. Meza-Montesa, "2D radial distribution function of silicene," *Revista Mexicana de Física* 58 (2012) 139–143.
10. S. Datta, *Electronic Transport in Mesoscopic Systems*. Cambridge, U.K.: Cambridge Univ. Press, 1995.
11. C. Xu, H. Li, K. Banerjee, "Modeling, Analysis, and Design of Graphene Nano-Ribbon Interconnects" *IEEE Trans. Electron Dev.*, Vol. 56, No. 8, August 2009.

Stabilization of Pulsed IMPATT Oscillator at W Band Over Extended Ambient Temperature Range

Sukhendu Bhanja, Mousumi Sarkar, Tanmay Ghoshal
and Arijit Majumder

Abstract In this paper, a technique for temperature stabilization of pulsed IMPATT oscillator has been described. The different electrical parameters of the designed oscillator at W band are studied at extended ambient temperature. Variation of oscillation frequency over extended temperature is determined by the intersection point of negative of device reactance $|X_D|$ and circuit reactance $|X_C|$. The analysis matches closely with the experimental results obtained. It is shown that the output frequency of the oscillator can be stabilized by changing the slope and amplitude of the biasing current pulse. A control circuit with integrated temperature sensor is designed for varying the current pulse amplitude dynamically over extended temperature. The designed IMPATT oscillator with integrated control circuit shows stabilization of oscillation frequency along with the considerable improvement in variation of peak power and chirp bandwidth over extended temperature.

Keywords IMPATT diode oscillator · Temperature stabilization
Bias current · Extended ambient temperature

1 Introduction

Pulsed IMPATT oscillator is one of the best high power sources for solid-state transmitter at higher frequencies. For different applications, the transmitter may be required to be operated over wide ambient temperature range. Since the junction

S. Bhanja (✉) · M. Sarkar · T. Ghoshal · A. Majumder
Circuit & System Division, SAMEER, Kolkata Centre, Kolkata, India
e-mail: Sukhendu.bhanja@mmw.sameer.gov.in

M. Sarkar
e-mail: mousumi.kundu@mmw.sameer.gov.in

T. Ghoshal
e-mail: tanmay@mmw.sameer.gov.in

A. Majumder
e-mail: arijit@mmw.sameer.gov.in

impedance of the diode is a strong function of ambient temperature, the output characteristics of the IMPATT oscillator change considerably with variation of ambient temperature.

Several techniques are reported for temperature stabilization of pulsed IMPATT oscillator with variation of ambient temperature. One common technique is the use of directly coupled stabilization cavity used for stabilization of the oscillator frequency [1, 2]. In this type of oscillator, effective output power reduces due to cavity coupling. Another reported technique is to apply constant DC current during the off period of the bias pulse so that the temperature gradient is less at elevated ambient temperature [3, 4]. This technique requires excess DC power especially when two or more oscillators are used in the same transmitter in a power combining configuration. Use of preheating pulse with the main biasing current pulse is also reported [5]. In this technique, proper synchronization of the preheating pulses and the main bias pulse becomes very critical.

In the present approach, the current density across the junction is changed which effectively maintains the oscillation frequency constant over the specified temperature range with small variation in output power. A theoretical analysis has been carried out to determine the variation of the device impedance (Z_D) over extended ambient temperature. The circuit impedance (Z_C) is determined from simulation of oscillator cavity using a full-wave 3D EM simulator. Variation of output frequency is determined by the intersection point of $|X_C|$ and $-|X_D|$ that shows negative temperature gradient of the oscillation frequency. The variation of the oscillation frequency with bias current pulse is determined experimentally that shows a positive frequency gradient with the amplitude of the bias current. It has been observed that amplitude of the biasing pulse can be adjusted to maintain a constant output frequency over extended ambient temperature. A control circuit with integrated temperature sensor has been incorporated in the biasing network of the IMPATT oscillator to stabilize the output parameters of the oscillator over the ambient temperature range from -40 to $+71$ °C. Experimental results with the designed control circuit show constant output frequency over the extended temperature range with peak output power variation of less than 6.7%. The chirp bandwidth of the oscillator is also studied that shows an improved chirp at negative temperature with the designed control circuit.

2 Scheme for Temperature Stabilization

The impedance of pulsed IMPATT diode is a strong function of the junction temperature and changes rapidly due to changes in the drift velocity and the ionization coefficient of electrons and holes. The expression for the impedance of Si-based DDR IMPATT diode is shown in (1) [6], and it decreases with increase in the junction temperature.

$$Z_D = \frac{1}{\omega C_D} \frac{1}{1 - \left[\frac{\omega}{\omega_a}\right]^2} \left\{ \frac{1 - \cos\theta_D}{\theta_D} - j \left[1 - \frac{\omega^2}{\omega_a^2} - \frac{\sin\theta_D}{\theta_D} \right] \right\} \quad (1)$$

where

ω Angular frequency

C_D Drift region capacitance

θ_D Transit angle of the drift region

ω_a RF voltage-dependent avalanche frequency given by

$$\omega_a^2 = \frac{2\bar{\alpha}_a v_D J_0}{\epsilon} \frac{2I_1(u)}{uI_0(u)}$$

where

$\bar{\alpha}_a$ Derivative of the ionization rate with respect to electric field

v_D Carrier saturation drift velocity

J_0 Current density

ϵ Dielectric permittivity and

$$u = \frac{2v_D \bar{\alpha}_a}{\omega} \hat{E}_a$$

where

E_a Electric field

The variation of the junction temperature (T_j) for different ambient temperatures can be evaluated from (2) [7] for constant voltage biasing.

$$T_j = C_2 + D_2(T - T_0) \quad (2)$$

where $\Delta T = T - T_0$ is relative ambient temperature with respect to T_0 , the ambient junction temperature.

$$C_2 = \theta_t \frac{V_0^2}{R_{sc} + \beta\theta_t V_{b0} V_0}$$

$$D_2 = 1 - \frac{\beta\theta_t V_0^2 V_{b0}}{R_{sc} + \beta\theta_t V_{b0} V_0}$$

where

β Normalized temperature coefficient of V_b , the breakdown voltage = $\frac{1}{V_{b0}} \frac{dV_b}{dT_j}$

θ_t Thermal resistance from diode junction to ambience

- V_0 Constant bias voltage
 R_{sc} Space charge resistance of the diode
 V_{bo} Breakdown voltage at reference temperature

The variation of the diode reactance at different ambient temperatures is shown in Fig. 1a. The values taken for different parameters of the millimeter-wave DDR IMPATT diode are $\theta_r \sim 37.15$ °C/W, $R_{sc} \sim 31$ Ω , $\beta \sim 5 \times 10^{-5}$ /°C, $E_a \sim 4 \times 10^7$ v/m, $J_0 \sim 5 \times 10^8$ A/m², $V_D = 24$ V, $V_{bo} = 12.5$ V [8]. The basic criteria for oscillation as given in (3) are plotted in Fig. 1a, and it shows a decrease in the oscillation frequency with increasing ambient temperature.

$$\begin{aligned}
 x_c + x_d &= 0 \\
 |r_d| &\geq r_c
 \end{aligned} \tag{3}$$

where $Z_c = r_c + jx_c$ is the circuit impedance at the device plane and $Z_d = r_d + jx_d$ is the device impedance. The values for the circuit reactance (X_c) are calculated using 3D EM solver and assumed to be constant over temperature.

The variation of output frequency with ambient temperature (both calculated and experimentally measured) is shown in Fig. 1b. The variation of the oscillation frequency with the amplitude of the biasing pulse is determined experimentally and is shown in Fig. 2a.

Schematic diagram of the test setup for temperature stabilization is shown in Fig. 2b. In this stabilization scheme, the required pulsed bias current for different temperatures is predetermined experimentally and a control circuit with integrated temperature sensor is used to stabilize the IMPATT oscillator at different temperatures.

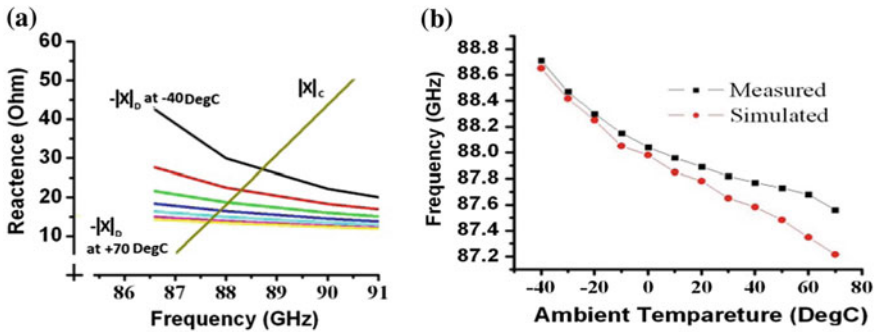


Fig. 1 a Variation of reactance with ambient temperature and determination of oscillation frequency and b variation of frequency with ambient temperature

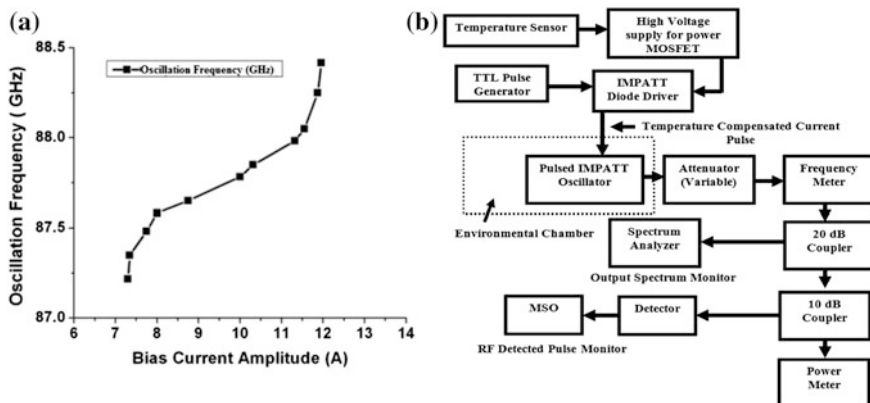


Fig. 2 a Variation of the oscillation frequency with bias current amplitude (experimental) and b schematic diagram of the test setup for temperature stabilization

3 Design and Simulation Study

To study the temperature variation of silicon-based double-drift pulsed IMPATT oscillator at W band, pulsed IMPATT cavity was designed following [9]. A driver circuit for the oscillator is used that provides a maximum 15A of peak current with duty cycle of 0.03% [10].

The design procedure of the temperature control circuit for IMPATT oscillator stabilization is described below.

3.1 Design and Simulation for Single-Diode IMPATT Oscillator

A reduced height waveguide cavity is designed with cavity height of 0.32 mm. The cavity is matched to the full height waveguide section using two quarter-wave matching sections. The bias filter for the cavity is designed using a low-pass filter structure [11]. The structure of the single-diode pulsed IMPATT oscillator is simulated in 3D EM solver. The simulated result of the structure is used to design the oscillator, where diode equivalent circuit and cavity is co-simulated using a circuit simulator. The simulation structure is shown in Fig. 3a. The fabricated cavity gives 11 W of peak power at 87.8 GHz. The fabricated cavity with the pulse driver at the top is shown in Fig. 3b.

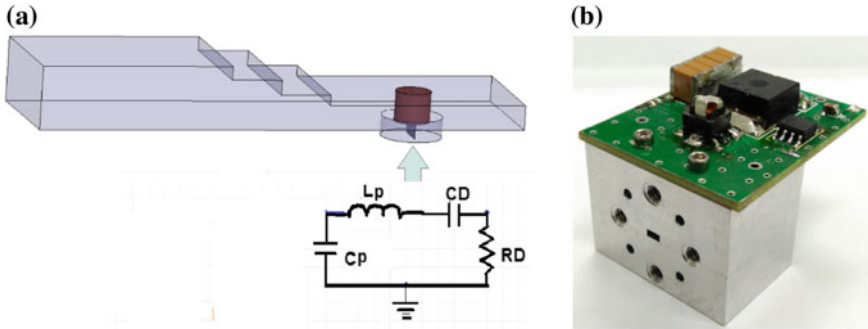


Fig. 3 **a** Simulated structure for the single-diode oscillator at W band **b** fabricated structure of the W band cavity with the bias circuit at the top

3.2 Design of Temperature-Compensated Pulsed Driver Circuit for the IMPATT Oscillator

A pulse driver circuit is designed and tested. The designed circuit is capable of driving 15A of peak current with a pulse width of 100 ns and pulse repetition frequency of 30 kHz. The driver circuit is tested with dummy load of P6KE12A which is a step recovery diode having similar DC characteristics of the IMPATT diode. The designed bias circuit has a control to change the slope and amplitude of the biasing current pulse.

For different values of the ambient temperature, the bias current amplitude is adjusted using boost converter with programmable resistor used in the feedback path. One micro-controller is used that senses the ambient temperature reading (using temperature sensor IC LM35) and reconfigures the feedback path resistor values (programmable resistor IC AD5292-EP) to change the regulated voltage of the converter IC (TPS61175). The schematic diagram for the control circuit with the fabricated PCB is shown in Fig. 4. The variation of the bias current for different ambient temperatures of the IMPATT diode is obtained experimentally. The values for the current pulse amplitude at different ambient temperatures with the corresponding bias voltage values are shown in Table 1.

4 Experimental Study

The designed oscillator at W band is tested that gives an output frequency of 87.8 GHz with a chirp bandwidth of 467 MHz at the ambient temperature. The output spectrum for the oscillator is shown in Fig. 5. The bias current pulse and the detected RF pulse (using envelop detector) for the oscillator are shown in Fig. 6. The testing is carried out at different ambient temperatures, and the variations of the

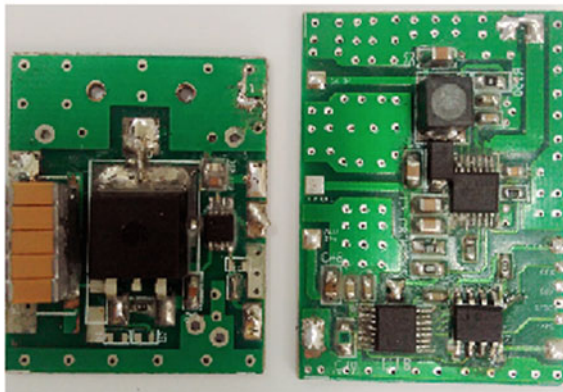
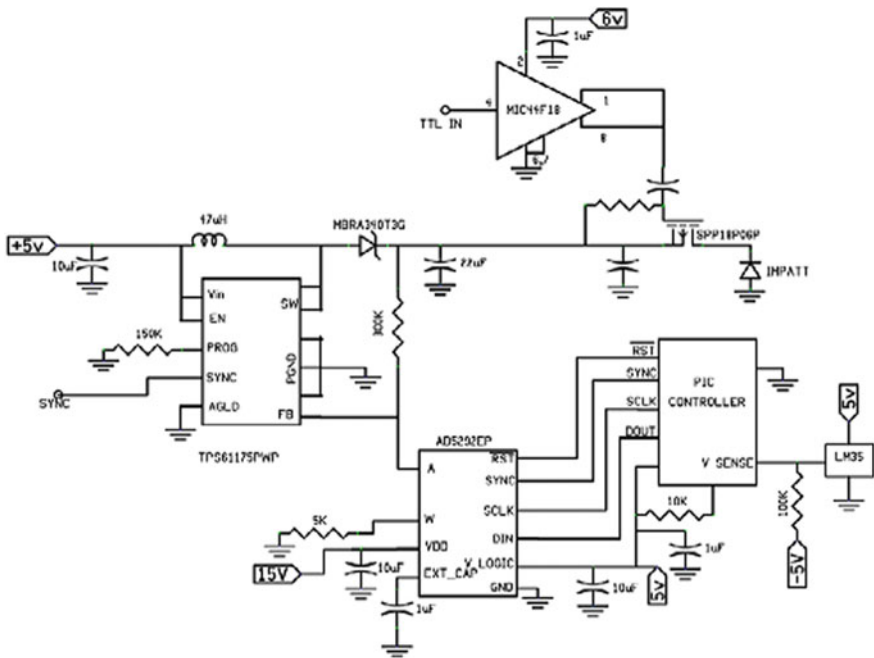


Fig. 4 Schematic diagram of the control circuit with fabricated PCB

output frequency, output power, and chirp bandwidth are studied with and without the compensation circuit.

Output frequency variation over the ambient temperature with and without the compensation circuit is shown in Fig. 7. It can be seen that the frequency variation is negligible with the compensation circuit. The variation of peak power is also reduced from ± 22 to $\pm 6.7\%$ by the compensation in the bias circuit and is shown in Fig. 8. The chirp bandwidth also reduces at negative temperature if compensation circuit is used as shown in Fig. 9.

Table 1 Values of the current pulse amplitude at different ambient temperatures to maintain the output frequency constant at 87.8 GHz

Ambient temperatures in (°C)	Values of the programmable resistor in (kΩ)	Values of the biasing voltage in (V)	Current pulse amplitude in (A)
-40	17.11	17.91	8.05
-30	16.72	18.20	8.50
-20	16.34	18.52	9.10
-10	15.71	19.00	9.61
0	15.40	19.31	10.01
10	14.64	20.02	10.81
20	14.64	20.12	10.92
30	14.23	20.40	11.14
40	13.46	21.20	11.31
50	12.92	21.80	11.68
60	12.41	22.40	12.01
70	11.93	23.11	12.31

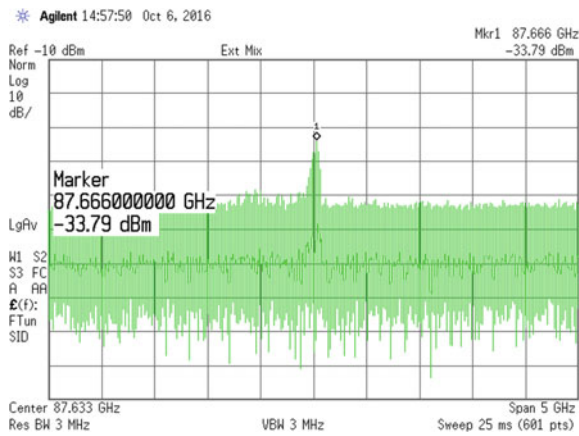


Fig. 5 Output spectrum of the designed oscillator at W band

Fig. 6 Bias current pulse (yellow) and the RF detected pulse (green) (Color online)

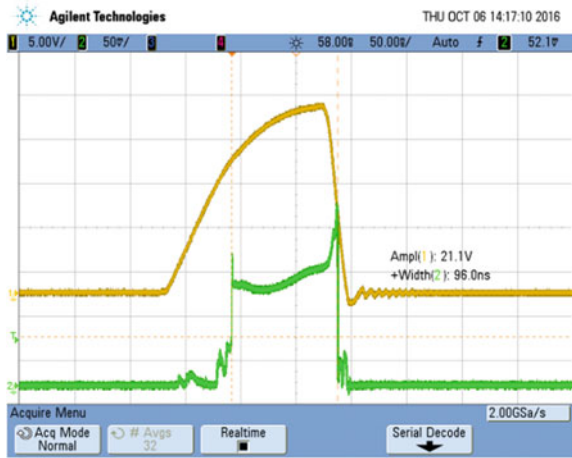


Fig. 7 Output frequency variation with and without compensation circuit

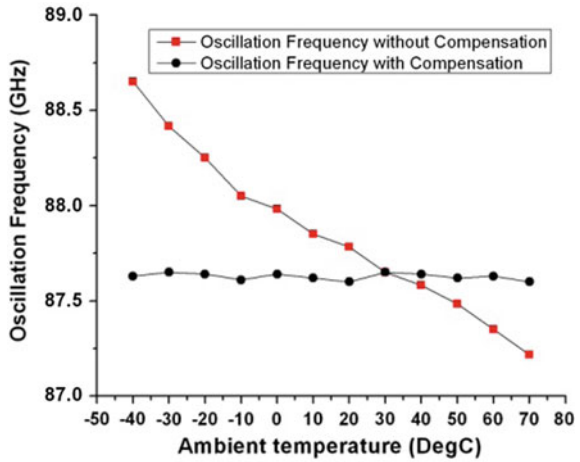


Fig. 8 Variation of peak power with and without compensation circuit

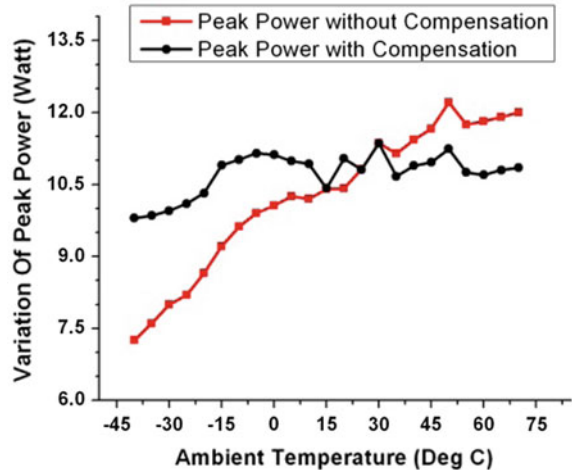
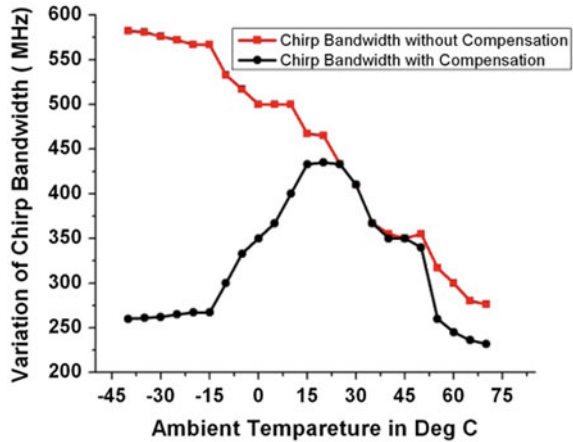


Fig. 9 Variation of chirp BW with and without compensation circuit



5 Conclusion

In this paper, a new design approach for stabilization of pulsed IMPATT oscillator at W band is described. The variation of the oscillation frequency with ambient temperature has been studied theoretically that agrees with the experimental results. The designed oscillator with the stabilization circuit shows constant output frequency with peak power variation less than $\pm 6.7\%$ at 87.8 GHz. The variation of the chirp bandwidth is also studied for the designed oscillator at different ambient temperatures.

Acknowledgements We are thankful to Director General, SAMEER, MeitY, for his help and encouragement and for allowing us to carry this work. We are also thankful to mechanical division of SAMEER, Kolkata Centre, for their mechanical support in fabricating the cavity and setting up the test arrangements.

References

1. S. Nagano, "Highly Stabilized Half-Watt IMPATT Oscillator," Microwave Symposium, G-MTT 1970 International, Newport Beach, CA, USA, 1970, pp. 170–173.
2. J. R. Ashley and C. B. Searles, "Microwave Oscillator Noise Reduction by a Transmission Stabilizing Cavity," in IEEE Transactions on Microwave Theory and Techniques, vol. 16, no. 9, pp. 743–748, Sep 1968.
3. Wronald S. Best, "VMOS FET IMPATT diode pulse bias circuit," U.S patent US4476402 A.
4. R. L. Eisenhart and R. S. Robertson, "Controlled Bias Preheating for Variable Duty Factor IMPATT Transmitter," Microwave Symposium Digest, 1985 IEEE MTT-S International, St. Louis, MO, USA, 1985, pp. 529–530.
5. M. G. Ischenko, L. V. Kasatkin, V. M. Tarasjuk and A. V. Tsvir, "Injection-locked coherent pulsed IMPATT oscillators with a high stability of RF-parameters," Physics and Engineering of Millimeter and Sub-Millimeter Waves, 2001. The Fourth International Kharkov Symposium on, Kharkov, 2001, pp. 753–755 vol. 2.

6. U.C. Ray, A.K. Gupta, and M.N. Sen, "Frequency Response Of W-Band Pulsed IMPATTS Operating Over Extended Ambient Temperature", *International Journal of Infrared and Millimeter waves*, Vol. 10, No.9, 1989.
7. J. L. Chan, "Constant Voltage Biasing of IMPATT Injection-Locked Oscillators," *Microwave Symposium Digest, 1983 IEEE MTT-S International*, Boston, MA, USA, 1983, pp. 218–220.
8. H.J. Kuno, "IMPATT Devices for Generation of Millimeter Wave", *Infrared and Millimeter Waves*, Vol.1. ISBN 0-12-147701-0.
9. T. T. Fong and H. J. Kuno, "Millimeter-Wave Pulsed IMPATT Sources," in *IEEE Transactions on Microwave Theory and Techniques*, vol. 27, no. 5, pp. 492–499, May 1979.
10. S. Bhanja, M. Sarkar, A. Majumdar and T. Ghoshal, "A compact modulator circuit with high current protection for low chirp pulsed IMPATT oscillator," *Applied Electromagnetics Conference (AEMC), 2013 IEEE, Bhubaneswar*, 2013, pp. 1–2.
11. Eric L. Holzman, "Solid-State Microwave Power Oscillator Design", 1992 Artech Housh, Inc, ISBN 0-89006-487-3.

Geometrically Intricate Oxide-Based Heterostructure Over Flexible Platform: Morphology-Induced Catalytic Performance Enhancement Under UV Light

Subhasish Thakur, Soumen Maiti, Shreyasi Pal
and Kalyan Kumar Chattopadhyay

Abstract Tailor-made heterostructural nanoform based on multiple low-dimensional frameworks not only offers manifold functionalities also bestows several novel interface phenomena. From the broad usage window of heterostructures, photocatalysis is very significant nowadays. In this work, we have realized oxide-based hybrid comprising 1D TiO₂-ZnO nanoform on flexible carbon cloth via facile chemical approach. Successful presentation of the hybrid over foldable platform was established via FESEM which discloses its typical morphology. To attain a clear insight of the elemental composition EDX analysis and elemental mapping of the hybrid was also carried out. Catalytic activity of the synthesized samples under UV light illumination was inspected taking Rhodamine B as the model contaminant where the heterostructure exhibited much-improved performance as compared to the individual structural building block. Prolonged separation time of the photogenerated charge carriers in heterostructure ensures enhanced photocatalytic activity. Such work on morphology-induced catalytic performance enhancement will inspire the researchers toward creative designing of different photocatalyst comprising other multifunctional oxides.

Subhasish Thakur and Soumen Maiti contributed equally.

S. Thakur (✉) · S. Pal · K. K. Chattopadhyay (✉)
Thin Films and Nanoscience Laboratory, Jadavpur University, Kolkata 700032, India
e-mail: subhasishgul17@gmail.com

K. K. Chattopadhyay
e-mail: kalyan_chattopadhyay@yahoo.com

S. Maiti (✉)
CENIMAT/I3N, FCT, Universidade Nova de Lisboa, Lisbon, Portugal
e-mail: sou.maiti@gmail.com

S. Pal
Surface Physics and Materials Science Division, Saha Institute
of Nuclear Physics, Kolkata, India

Keywords TiO₂ · ZnO · Nanostructure · Flexible platform · Photocatalysis

1 Introduction

Possibility of achieving manifold functionalities, coupled with various interface phenomena from singular unit has garnered an upsurge attention from the modern era researchers in realization of novel and geometrically intricate heterostructure where such presentation is mostly achieved by the integration and direct interfacing of the lower dimensional semiconductor frameworks [1, 2]. From the widespread functional window of the nanostructure, environmental remediation through photocatalytic degradation is very appealing as contemporary era faces severe pollution issues from industrial wastes and related effluent [1, 3, 4]. Titanium oxide (TiO₂) and zinc oxide (ZnO) nanostructures have showed their proficiency in this regard; however, extension of the recombination time of photogenerated carriers in these two and thereby achievement of high catalytic performance is still challenging [3, 4]. Furthermore, ZnO nanofilm has an intrinsic drawback of corrosion effect under light illumination which also imparts a negative impact on the overall efficiency [3]. To resolve all these fundamental shortcomings for different aspects of photocatalysis intense research have been proliferated among which designing of definite facet-tuned morphology, surface modification, coupling of semiconductor into a combinatorial hybrid are the most cultivated pathway [1, 3, 5–7]. Recently, several works centered on synthesis of oxide-based heterostructure are reported where the coupled system ensures an enhanced performance as compared to the single component owing to the synergic effect [1, 3, 5]. Inspired by those literatures, in this article, we have presented TiO₂–ZnO nanorod-based heterostructure over flexible carbon fiber substrate by two-step low-temperature chemical approach. Although plenty of works on the same hybrid is already documented in the literature, however complex processing, non-uniform coating of one semiconductor over the scaffold, etc., made this study highly desirable. The photocatalytic activity of the heterostructure was investigated by degradation of stable cationic dye namely Rhodamine B (RhB) under UV light and plausible mechanism for the superior photocatalytic activity system is proposed.

2 Experimental

2.1 Synthesis of TiO₂ Nanorods

Firstly, TiO₂ sol was prepared by mixing 27 mL absolute ethanol, 7 mL titanium butoxide, 2 mL di-ethanolamine, and 400 μL deionized water. Ultrasonically cleaned and dried carbon cloth was dip coated within the TiO₂ sol and annealed for 2 h. Thereafter, the seeded substrates were placed within a 100 mL Teflon tape autoclave containing a solution mixture of 30 hydrochloric acid, 35 mL water, and

1 mL titanium butoxide and kept at 180 °C for 6 h. Then the autoclave was cooled down to room temperature. Thereby the product was collected via washing the cloth with DI water and dried in ambient condition.

2.2 *Synthesis of TiO₂-ZnO Heterostructure*

For the synthesis of ZnO nanospike over TiO₂, initially, the TiO₂ coated substrate is activated in KMnO₄ solution for further use. Two separately prepared solutions of 2 M potassium hydroxide (KOH) and 0.25 M zinc nitrate hexahydrate (Zn(NO₃)₂·6H₂O) were mixed together and transferred to a borosilicate glass bottle. Thereafter, one analytical grade zinc foil rubbed with emery paper along with the activated carbon fiber substrate with TiO₂ on it were placed in the bottle and kept for 3 h in ambient conditions. Finally, the substrate was washed with an ample amount of D.I. water and dried at room temperature.

2.3 *Photocatalytic Properties*

Photocatalytic activity of the synthesized samples was observed with RhB dye as the probe molecule under UV light. One 40 W UV tube (Phillips) served as the UV source with wavelength ~254.6 nm and tube to suspension surface distance was kept at 12 cm. Carbon cloth substrates (2.5 cm × 2.5 cm) having different nanoform on it were immersed within 40 mL aqueous solution of 10⁻⁵ M RhB in 100 ml quartz beaker and stirred for 1 h in darkness to attain adsorption/desorption equilibrium between the catalyst and dye. Thereafter, it was illuminated with UV light. Small volumes of dye solution from the reactor were withdrawn after dark stirring and afterward in regular interval. Residual dye concentration in solution was measured by monitoring the absorption intensity of RhB with UV-vis spectrophotometer.

3 **Characterizations**

Morphology of the synthesized samples were examined using field emission scanning electron microscope (FESEM, HITACHI S-4800). EDX analysis was carried out by an EDS analyzer attached with FESEM.

4 **Results and Discussion**

Figure 1 displays the FESEM images of the synthesized nanoforms grown on the carbon cloth substrate. Large-scale uniformity of the TiO₂ and TiO₂-ZnO is clearly evident from the low magnification image as shown in Fig. 1a, c. Nanorods grow

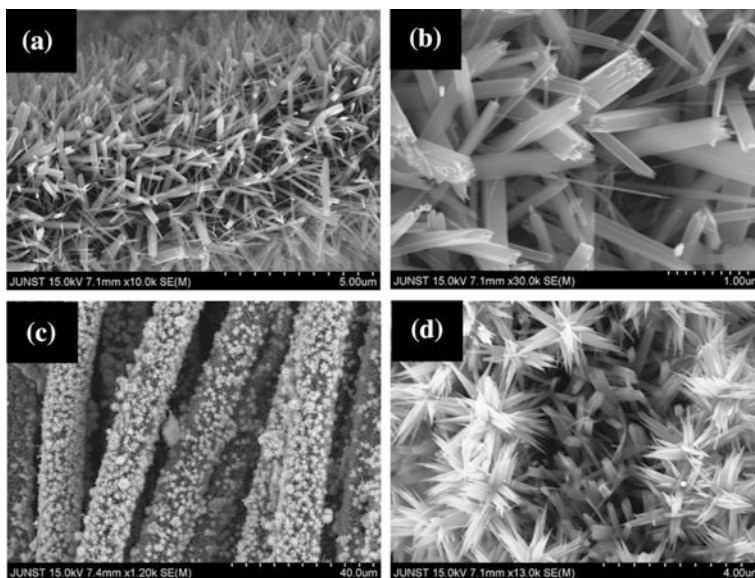


Fig. 1 FESEM images of the synthesized nanoform **a**, **b** TiO_2 and **b** $\text{TiO}_2\text{-ZnO}$

over the entire cylindrical surface of each individual fiber of the cloth with their tip radiating outward from the axis of the fiber. High magnification image in Fig. 1b discloses the actual dimension of the nanorod where the variation in diameter of the nanorods is clearly feasible. Diameter of the nanorods varies from ~ 50 to ~ 300 nm, whereas lengths remain nearly equal. Further modification of these nanorods at ambient creates a drastic change in overall morphology. Uniform coverage of ZnO nanospike growth over TiO_2 is obvious from the low magnification image (Fig. 1c). Further careful observation over of the spikes array reveals that they are not individually grown over the TiO_2 nanorods but a number of nanospikes having a common root and their outward radiating tip geometry gives rise to the beautiful spikes array. The length and the base diameter of the secondary grown spikes were estimated to be $\sim 1 \mu\text{m}$ and 200 nm, respectively.

To check the elemental composition of the heterostructure energy dispersive X-ray (EDX) analysis is carried out and depicted in Fig. 2. From the EDX scan profile (Fig. 2), appearance of the peaks related to Ti, O, Zn, and C is very obvious among which presence of extra carbon-related peak came from the underlying substrate and atmosphere as well. Further absence of other peaks related to impurity elements in EDX profile confirms the pure phase synthesis of TiO_2 and ZnO. Elemental mapping of $\text{TiO}_2\text{-ZnO}$ hybrid strand reveals regular distribution of the constituents and thereby the successful preparation of the nanoforms.

TiO_2 and ZnO both have showed good photocatalytic performance; however; they have some intrinsic bottlenecks which impart negative impact on their performance [1, 3]. By realizing heterostructure comprised of these oxides, one could expect catalytic performance enhancement by getting rid of abovementioned

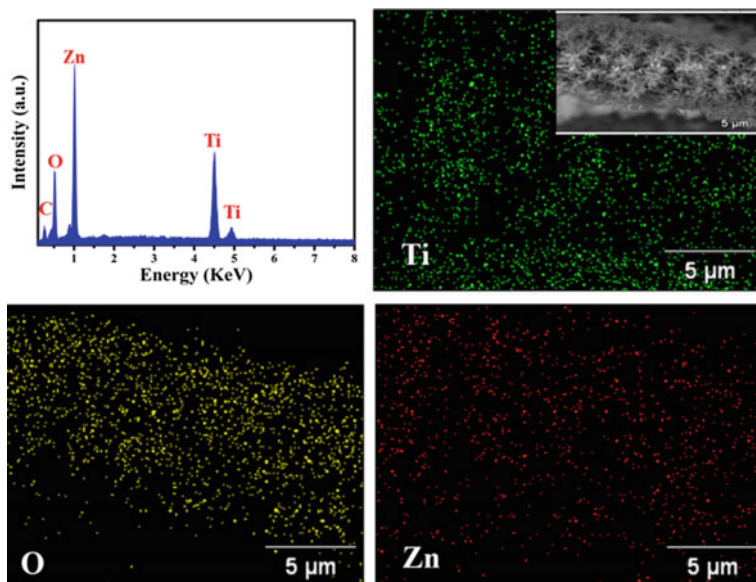


Fig. 2 EDX spectra and corresponding elemental mapping of the heterostructure

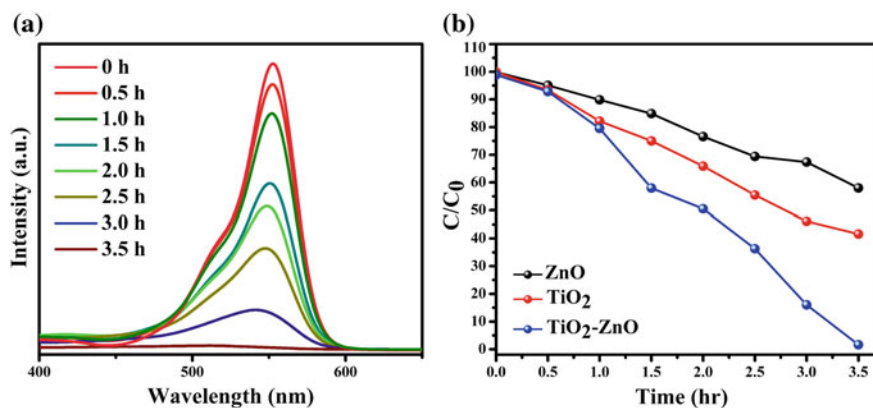


Fig. 3 Temporal evolution of UV-vis absorption spectra corresponding to RhB for TiO₂-ZnO (a); decrease in the relative concentration of dye after different exposure times

drawbacks. Temporal evaluation of the UV-vis absorption spectra of RhB under UV irradiation as a result of the catalytic activity of TiO₂-ZnO heterostructure is displayed in Fig. 3a. The intensity of the characteristic absorption peaks at ~554 nm for RhB is found to reduce gradually with time and disappear completely after 3.5 h of light exposure. For quantitative explanation of the photodegradation

behavior, decrease in dye concentration (C/C_0) as a function of time was calculated and plotted (Fig. 3b) where the symbols C_0 and C represent the initial ($t = 0$) and final (t) dye concentration in the solution, respectively. Concentration of dye is proportional to the intensity of the characteristic absorption peak; thus, ratio of C and C_0 is equal to the ratio of the intensity of the absorption peaks at time $t = 0$ and t , respectively. From the graph, high degradation ability of the $\text{TiO}_2\text{-ZnO}$ sample is prominent as compared to single component. RhB dye concentration for the hybrid sample decreases to $\sim 79.36\%$ within only 1 h of UV exposure and which was followed by a high decay rate, and finally, the concentration reduces to only to $\sim 0.49\%$ after 3.5 h.

High photocatalytic performance shown by the $\text{TiO}_2\text{-ZnO}$ hybrid can be explained on the basis of the schematic in Fig. 4. Though TiO_2 and ZnO possess almost similar bandgap (around 3.2 and 3.37 eV, respectively) yet the potentials of the valence band (VB) and conduction band (CB) of ZnO are charged slightly more negative [3]. When ZnO is illuminated by UV light, electron moves to the CB from VB leaving holes in it. Owing to the potential difference between these two oxides these electrons thereafter moved from the CB of ZnO to the CB of TiO_2 . On the other hand, the holes move in opposite direction, i.e., from VB of TiO_2 to VB of ZnO [3]. Formation of heterojunction at TiO_2 and ZnO interface ensures prolonged recombination time of electron-hole pairs [3]. Furthermore, the charge carriers (both electron and holes) on $\text{TiO}_2\text{-ZnO}$ surface rapidly goes for the redox reaction where the holes oxidize the H_2O to highly active hydroxyl ion and electrons reduce the dissolved oxygen to superoxide O_2^- ion. These highly active species oxidize the RhB to CO_2 and H_2O [3]. Additionally, presentation of the hybrid over carbon fabric having typical woven-like geometry ensures extensive surface area and sufficient spacing between individual units of the heterostructure thereby showed good catalytic behavior. Similar sort of results for different heterostructure on carbon cloth was also observed in our previous work [1].

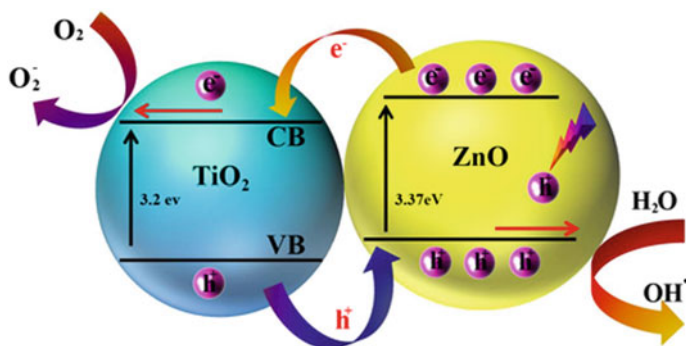


Fig. 4 Schematic diagram of the charge-transfer process in the heterostructure

5 Conclusion

In summary, we presented a two-step low-temperature synthesis protocol for the realization of TiO₂-ZnO hybrid over carbon cloth substrate. This oxide-based heterostructure showed synergy driven high photocatalytic performance under UV light irradiation which is much superior to the singular building block. Lengthening of the recombination time of photogenerated charge carriers due to heterostructure formation render improved catalytic performance. Furthermore, underlying carbon cloth having peculiar woven-like geometry promotes the mass transfer of dye and thereby boosts the performance. Not just restricted to photocatalytic study, we believe this morphology-tuned nanoform may be envisaged as a potential candidate for other application purpose also.

Acknowledgements ST thanks the DST, Department of Science & Technology Government of India, for awarding him Inspire Fellowship (JRF) during the execution of the work.

References

1. Pal S., Maiti S., Maiti U. N. and Chattopadhyay K. K.: Low temperature solution processed ZnO/CuO heterojunction photocatalyst for visible light induced photo-degradation of organic pollutants. *CrystEngComm*, vol. 17, pp. 1464–1476, (2015).
2. Maiti U. N., Maiti S., Majumder T. P. and Chattopadhyay K. K.: Ultra-thin graphene edges at the nanowire tips- a cascade cold cathode with two-stage field. *Nanotechnology*, vol. 22, pp. 505703 (8 pp), (2011).
3. Xiao F.-X., Construction of Highly Ordered ZnO-TiO₂ Nanotube Arrays (ZnO/TNTs) Heterostructure for Photocatalytic Application. *ACS Appl. Mater. Interfaces*, vol. 4, pp. 7055–7063, (2012).
4. Maiti U. N., Maiti S. and Chattopadhyay K. K.: An ambient condition, one pot route for large scale production of ultrafine (<15 nm) ZnO nanowires from commercial zinc exhibiting excellent recyclable catalytic performance: Approach extendable to CuO nanostructures. *CrystEngComm*, vol. 14, pp. 640–647, (2012).
5. Lin L., Yang Y., Men L., Wang X., He D., Chai Y., Zhao B., Ghoshroy S. and Tang Q.: A highly efficient TiO₂@ZnO n-p-n heterojunction nanorod photocatalyst. *Nanoscale*, vol. 5, pp. 588–593, (2013).
6. C. Yu, K. Yang, Y. Xie, Q. Fan, J. C. Yu, Q. Shu and C. Wang.: Novel hollow Pt-ZnO nanocomposite microspheres with hierarchical structure and enhanced photocatalytic activity and stability. *Nanoscale*, vol. 5, pp. 2142–2151, (2013).
7. Yu C., Li G., Kumar S., Yang K. and R. Jin, Phase.: Transformation Synthesis of Novel Ag₂O/Ag₂CO₃ Heterostructures with High Visible Light Efficiency in Photocatalytic Degradation of Pollutants. *Adv. Mater.*, vol. 26, pp. 892–898, (2014).

Investigation of Super-Gaussian Pulse Amplification in Semiconductor Optical Amplifier (SOA)

Mijanur Rahim and Md. Asraful Sekh

Abstract The amplification of super-Gaussian pulses in a system of bit rate 40 Gb/s with duty cycle 0.5 by traveling-wave semiconductor optical amplifier (TW-SOA) is investigated. The carrier wavelength of the super-Gaussian pulse is 1550 nm. Simulative results related to pulse broadening due to nonlinear self-phase modulation (SPM) phenomenon are analyzed and compared. This paper analyses the issues of super-Gaussian pulse and spectrum distortion in semiconductor optical amplifiers (SOA). It is shown that the amplified super-Gaussian pulse shapes and their spectra are depended on the length of SOA and compared the results with the published work.

Keywords Super-Gaussian pulse · TW-SOA · SPM

1 Introduction

Semiconductor optical amplifiers (SOA) are very important candidate in high-speed optical communication systems [1–3]. The amplifiers can amplify ultra-short optical pulses of the order of picoseconds [4, 5] as they possess very large bandwidth (~ few THz). In any amplifier, nonlinearities due to gain saturation leading to pulse distortion because the leading edge of the pulse saturates the amplifier which reduces the gain available for the trailing edge of the pulse [6, 7]. Under different operating conditions, both pulse compression and pulse broadening can be obtained in the saturation region but no such cases arise if pulse energy is a small fraction of the saturation energy and hence the input pulse can be amplified without significant distortion. Sometimes pulse shape may remain unchanged but spectrum can be

M. Rahim · Md. Asraful Sekh (✉)
Department of Electronics and Communication Engineering,
Aliah University, IIA/27, New Town, Kolkata 700156, India
e-mail: asekhh@yahoo.com

M. Rahim
e-mail: mrzeeshan.ece@gmail.com

distorted considerably which is particularly important where the changes in the carrier density occurring as a result of gain saturation and leading to large change in refractive index [8].

The spectrum shift depends on input pulse energy and the amplifier gain among other things. The physical mechanism responsible for such shift is self-phase modulation (SPM) occurring as a result of nonlinear refractive index variation induced by gain saturation. Some investigations on pulse compression [9], wavelength conversion [10], and Gaussian pulse broadening [11] by SOA have made by us. This paper, in continuation of earlier works, analyses the issues of super-Gaussian pulse and spectrum distortion in SOA.

2 Basic Equations

The material gain coefficient g per unit length depends on initial carrier density (N_i) and carrier density at transparency (N_0) [9] and is given as,

$$g = \sigma_g(N_i - N_0) \quad (1)$$

where differential gain is σ_g . Therefore, net gain coefficient per unit length will be,

$$g_T = \Gamma g - \sigma_s \quad (2)$$

where optical confinement factor is Γ , and loss is σ_s in per unit length of SOA. G_0 is the amplification factor when length is L , and therefore, $G_0 = e^{g_T L}$. Using Eqs. (1) and (2)

$$G_0 = e^{(\Gamma \sigma_g(N_i - N_0) - \sigma_s)L} \quad (3)$$

The carrier lifetime (t_c) depends on the physical parameters of SOA, namely surface and defect recombination coefficient (A), radiative recombination coefficient (B), Auger recombination coefficient (C), and initial carrier density (N_i) [10], and given as,

$$t_c = \frac{1}{A + BN_i + CN_i^2} \quad (4)$$

3 Simulation Layout

In Fig. 1, an optical signal of 1550 nm wavelength with 50 mW power is amplified by a traveling-wave SOA (TW-SOA) in a system of bit rate 40 Gb/s with duty cycle 0.5. Table 1 shows the various physical parameters used for SOA.

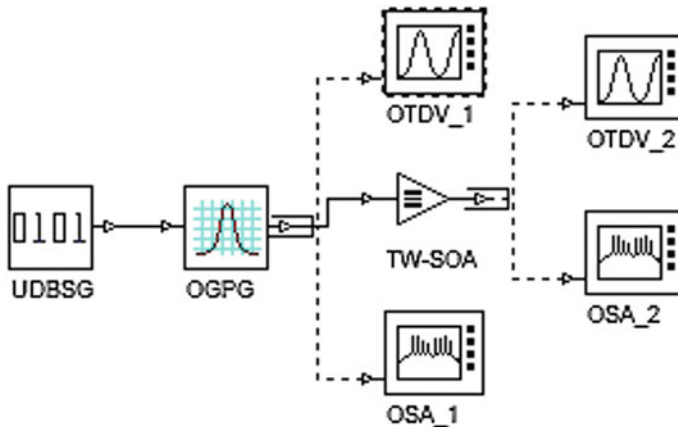


Fig. 1 Simulation layout

Table 1 Physical parameters of SOA

Parameters	Value	Units
Length (L)	0.0002, 0.0003, 0.0005	M
Width (W)	3×10^{-6}	M
Height (d)	8×10^{-8}	M
Γ	0.15	–
σ_s	0	1/m
σ_g	2.78×10^{-20}	m^2
N_0	1.4×10^{24}	m^{-3}
Line-width enhancement factor	5	–
A	143,000,000	1/s
B	1×10^{-16}	m^3/s
C	3×10^{-41}	m^6/s
N_i	3×10^{24}	m^{-3}

4 Results and Discussions

Calculated value of carrier lifetime (t_c) is 1.4 ns, bit period (T_b) is 25 ps, T_{FWHM} is 12.5 ps, and T_0 is 7.5 ps. Figure 2 shows the initial super-Gaussian pulse shape and spectra of 5, 50, and 100 mW. Figure 3 shows the shape of the amplified pulses at amplification factor of 29 dB.

In Fig. 3, the spectra of the pulses with multipeak structure and with well-expressed right shift are shown. The new spectrum and the amount of the right shift strongly depend on the initial pulse shape.

Now, the amplified super-Gaussian pulse (for same pulse and SOA parameters as above) changes as a function from the length of the TW-SOA.

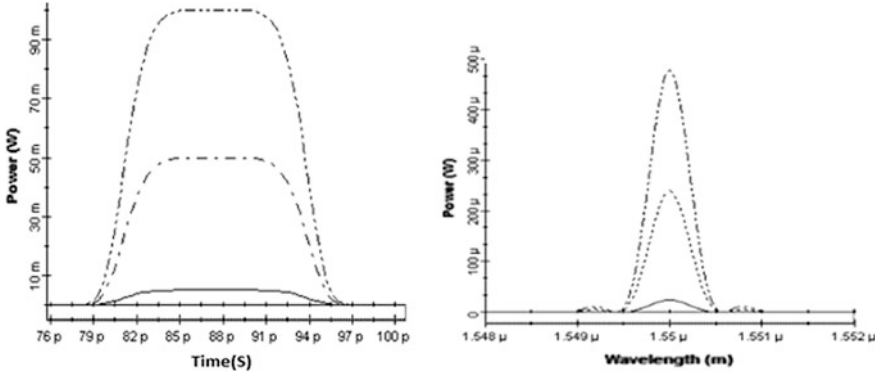


Fig. 2 Initial super-Gaussian pulses shapes and spectra

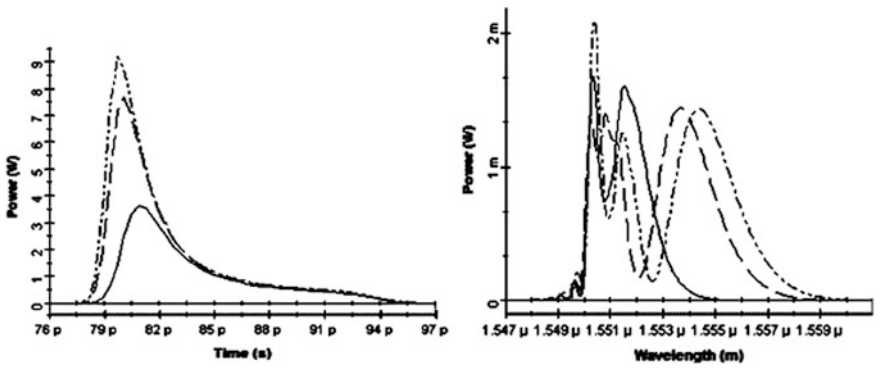


Fig. 3 Amplified super-Gaussian pulses of Fig. 2

The values of the Length of the TW-SOA are set as 0.0002, 0.0003, 0.0005 m.

Figure 4 reveals that the length factor of the TW-SOA influences the pulse shape and spectrum. For a fixed input power of 50 mW, optical confinement factor of 0.3 and zero internal losses with variable lengths (L) of 0.0002, 0.0003 m, 0.0005 leads to an increase of power of amplified super-Gaussian pulse and the more the amplification factor G_0 increases, it increases the right shift also. The spectrum develops a multi-peaks. The dominant peaks right shifted means it shifts toward longer wavelengths. Amplification factor $G_0 = e^{(\Gamma\sigma_g(N_i - N_0) - \sigma_s)L}$ and therefore increase of length leads an increase of amplification factor G_0 .

In Table 2, we can see that the amplified pulse gain will increase by increasing the length of TW-SOA [8].

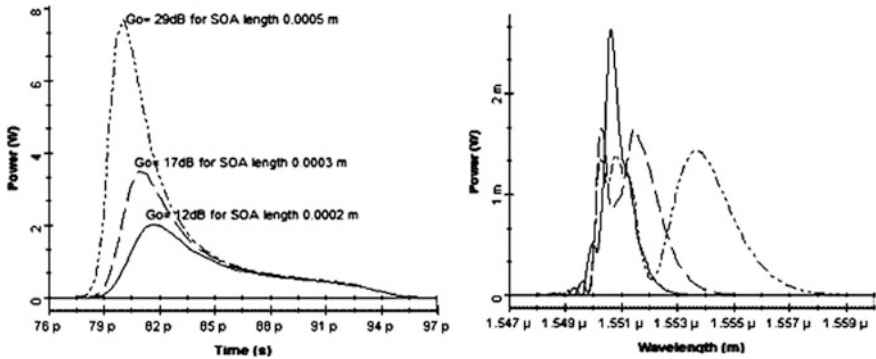


Fig. 4 Amplified super-Gaussian pulses for different length of traveling-wave SOA

Table 2 Results of amplified pulses with different length of TW-SOA

Length of TW-SOA (m)	Corresponding amplification factors (G_0) (dB)
0.0002	12
0.0003	17
0.0005	29

5 Conclusion

The amplification of super-Gaussian pulses by semiconductor optical amplifier shows pulse broadening due to SPM phenomenon. SPM induced gain saturation and hence carrier density variation in the gain medium is the basis for such broadening. Simulative results show the pulse broadening and multi-peak spectra along with the amplification of the pulse. Results also show how frequency is right shifted (so-called red shift) which is useful in group velocity dispersion compensation in optical fibers. The study can be extended for chirped pulses as well.

References

1. M. J. O'Maony, "Semiconductor laser amplifiers for use in future fiber systems", J. Lightwave Technol., Vol. 6, pp. 531-544, 1988.
2. N. A. Olsson, "Lightwave systems with optical amplifiers", J. Lightwave Tegnol., Vol. 7, pp. 1071-1092, 1989.
3. I. W. Marshall, D. M. Spirit and M. J. O'Mahony, "Picosecond pulse response of a traveling-wave semiconductor laser amplifier", Electron. Lett., Vol. 23, pp. 818-819, 1987.
4. G. Eisenstein, P. B. Hansen, J. M. Wiesenfeld R. S. Tucker and G. Raybon, "Amplification of high repetition rate picosecond pulses using an InGaAsP traveling-wave optical amplifier", Appl. Phys. Lett., Vol. 53, pp. 1539-1541, 1988.

5. N. J. Frigo, "Ultrashort pulse propagation in suitable media: A simple physical model", *IEEE J. Quantum Electron.*, Vol. QE-19, pp. 511–519, 1983.
6. A. E. Siegman, *Lasers*, Mill Valley, CA: University Science, 1986, Ch. 10.
7. G. P. Agarwal, "Self-phase modulation and spectral broadening of optical pulses in semiconductor laser amplifiers", *IEEE J. Quantum Electron.*, Vol. 25, No. 11, pp. 2297–2306, 1989.
8. A. Abd El Aziz, W. P. Ng, Z. Ghassemlooy, Moustafa H. Aly, Member, and M. F. Chiang, "Optimization of the Key SOA Parameters for Amplification and Switching", ISBN: 978-1-902560-19-9.
9. M. Rahim and Md. A. Sekh, "Pulse Compression using Semiconductor Optical Amplifier", pg. 441–446, *Conf. Proc. ICMCTI 2017*, UIT, Burdwan University, India, 23-25 March, 2017, Excel India Publishers, Page No 441–446, ISBN 9789386256607
10. M. Rahim and Md. A. Sekh, "FWM Based Wavelength Conversion Using Semiconductor Optical Amplifier (SOA)", *International Journal of Industrial Electronics and Electrical Engineering*, ISSN: 2347-6982 Volume-4, Issue-10, Oct.-2016. IJIEEE-IRAJ-DOI-6020.
11. M. Rahim and Md. A. Sekh, "Pulse Broadening in Semiconductor Optical Amplifier," in *13th International Conference on Fiber Optics and Photonics*, OSA Technical Digest (<https://doi.org/10.1364/PHOTONICS.2016.W3A.36>) (Optical Society of America, 2016), paper W3A.36.

Design of an Energy Efficient, Low Phase Noise Current-Starved VCO Using Pseudo-NMOS Logic

Moumita Das, Posiba Mostafa, Antardipan Pal, Debmalya Das and Sayan Chatterjee

Abstract This paper presents the design of a current-starved VCO using pseudo-NMOS topology. The proposed design has better phase noise, lower power consumption as compared to traditional CSVCOs and the number of components are also less (8 MOSFETs are reduced). The proposed design consists of five inverter stages, and pseudo-NMOS topology is used to replace the current sourcing PMOS blocks, thereby reducing power consumption to 155.7 μW for fundamental frequency of 1.8 GHz. The simulation results depict that the proposed CSVCO has better phase noise and lower power consumption as compared to other ring VCO topologies. The circuit performance is validated in Cadence Spectre using 180 nm CMOS technology at a supply of 1.8 V. The analysis also shows that for this CSVCO, the phase noise is (-103.73 dBc/Hz) @1 MHz offset frequency and (-124.97 dBc/Hz) @10 MHz offset frequency.

Keywords CSVCO · Phase noise · K_{vco} · CMOS · Pseudo-NMOS

M. Das (✉) · P. Mostafa · A. Pal · D. Das · S. Chatterjee
Department of E.T.C.E, Jadavpur University, Kolkata, India
e-mail: moumitad50524@gmail.com

P. Mostafa
e-mail: posiba@gmail.com

A. Pal
e-mail: ap1331@gmail.com

D. Das
e-mail: debmalya3110@gmail.com

S. Chatterjee
e-mail: sayan1234@gmail.com

1 Introduction

Voltage-Controlled Oscillator (VCO) is one of the most important blocks of the Phase-Locked Loop (PLL), which is one of the most crucial components of modern communication systems. VCO with reasonably low phase noise, high oscillation frequency [1] and low power dissipation is highly desirable for high-speed communication systems. Between the two types of VCOs, i.e. LCVCO and CSVCO, though the LCVCO has better phase noise, the presence of bulky spiral inductors and lower frequency range makes it less suitable for high frequency operation and monolithic ICs where on-chip area is constrained. So for on-chip VCOs in monolithic ICs, generally CSVCO is preferred [2].

This paper proposes the design of a five-stage current-starved VCO. Five inverter stages are cascaded to produce moderately high oscillation frequency. Since oscillation frequency is inversely proportional with number of inverter stages [2], the numbers of stages are reduced to achieve high oscillation frequency. It also requires less numbers of transistors which in turn reduces the on-chip area and reduces power consumption appreciably. The proposed work describes a current-starved VCO using pseudo-NMOS topology, and the performance has been compared with previously presented CSVCO architectures.

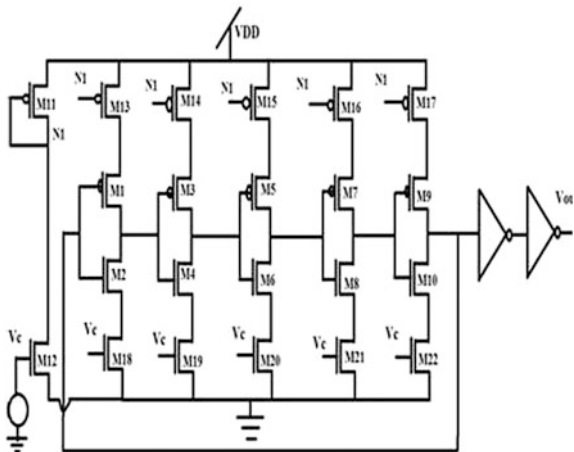
2 General CSVCO Circuit Description [2]

The operation of the current-starved VCO shown in Fig. 1 is similar to that of a ring oscillator [2]. Odd number of inverters forms a closed-looped positive feedback acting as a ring oscillator. Cascading of odd number of stages of inverter helps in fulfilment of Barkhausen criterion for oscillation [3]. The upper and lower MOSFETs source and sink the required current to drive the inverter stages. The MOS current sources limit the current available to the inverter stages. The drain currents of MOSFETs in the leftmost side of the circuit are set by the input control voltage. This current in these two MOSFETs is mirrored in each inverter/current source stage as depicted in Fig. 1 [4].

2.1 Design Equation for VCO [2]

CSVCO works on the principle of charging and discharging of the stray capacitances [5], formed by the addition of input and output capacitance of each inverter stage. The frequency of operation depends on the total charging and discharging time of the stray capacitances. The charging and discharging directly depends on the value of the current through each inverter stage. Since the current through the inverter stages is mirrored from the input source stage, which in turn is set by the

Fig. 1 Schematic of current-starved VCO



input control voltage, so indirectly the frequency of operation is controlled by the input control voltage and hence the name VCO. Mathematically, the oscillation frequency is given as follows [2]:

$$f_{\text{osc}} = \frac{1}{N \cdot (t_1 + t_2)} = \frac{I_D}{N \cdot C_{\text{total}} \cdot DD} \quad (1)$$

where I_D is the VCO bias current, N is the total number of stages, and the C_{Total} is the total oxide capacitance at low frequency. The N is selected according to the VCO operating frequency. Equation 1 shows that operating frequency depends on gate capacitance of the inverter stages. But at high frequency, the effect of parasitic capacitances generated from the source and sink transistors cannot be neglected as the total capacitance of one stage becomes:

$$C_{\text{total}} = C_{gs,p} + C_{gs,n} + C_{db,p} + C_{db,n} + C_{gd,\text{source}} + C_{gd,\text{sink}} + C_{db,\text{source}} + C_{db,\text{sink}} + C_{gs,\text{source}} + C_{gs,\text{sink}} \quad (2)$$

The current-mirroring PMOS (PM1) and control voltage should have enough capability to drive the sourcing PMOSs (M13–M17) and the sinking NMOSs (M18–M22). If this clause violates, then a huge degradation in phase noise and VCO gain may be seen. Equation 2 makes the impression of such a scenario of a CVCO operating in high frequency. Another serious issue that a VCO has to deal with is power consumption. Supply voltage of a CSVCO has to drive large number of transistor for every cycle, and all the current sourcing and sinking transistors are always drawing appreciable amount of current from the supply which leads to much power dissipation. So, it is essential to optimize the power consumption with phase noise and VCO gain.

3 Pseudo-NMOS Logic-Based CSVCO

The problems of CSVCO circuit have been overcome by proposed pseudo-NMOS logic-based CSVCO. In this architecture, all the PMOS current sources were replaced by a single PMOS. The single PMOS is sized accordingly to supply the required current to drive the inverter stages. In a similar manner, all the current-sinking NMOS are replaced using a single NMOS with proper sizing for the required current drive. These modifications show a marked improvement in the overall phase noise and reduction in the average power dissipation of the proposed circuit. As the number of transistor is reducing, it is obvious that there will be less power consumption. The number of sourcing and sinking transistor is reducing by $1/N$ factor. So, the capacitances generated from these transistors will be distributed with the inverters with the factor of $1/N$ at high frequencies.

$$C_{\text{total}} = C_{gs,p} + C_{gs,n} + C_{db,p} + C_{db,n} + (C_{gd,source} + C_{gd,sink} + C_{db,source} + C_{db,sink} + C_{gs,source} + C_{gs,sink})/N \quad (3)$$

Also, the on-chip area is reduced as lesser number of MOSFETs is used compared to traditional CSVCO designs. The schematic of the modified CSVCO is shown in Fig. 2. Here, the current-mirroring PMOS feeds the desired current to the sourcing PMOS with the help of control input voltage. Similarly, sinking NMOS draws the current from inverters using the same control input voltage.

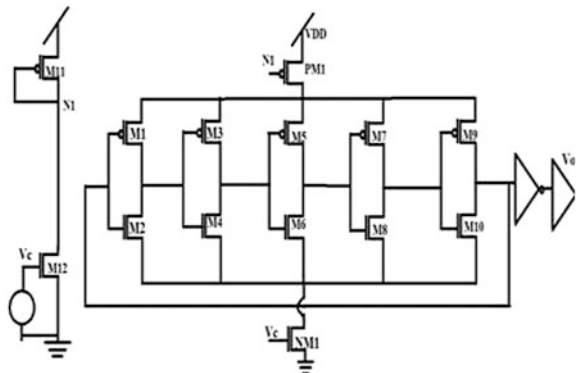
According to the current values of source and sink, the intermediate ring oscillator tunes the operating frequency.

4 Simulation Results and Discussion

For a VCO used in a PLL, the following parameters are important:

1. Tuning range: The frequency range between the minimum and maximum values of the VCO frequency.

Fig. 2 Schematic of modified current-starved VCO



2. Phase noise: Spectral purity requirements in PLL applications impose an upper bound on the VCO phase noise.
3. Input/output characteristic linearity: Variation of K_{VCO} across the tuning range is basically undesirable.
4. Settling time: The required time to generate a constant frequency at the output of the oscillator.

Here, all the above-stated parameters have been characterized for proposed architecture as well as for a general CSVCO architecture. Both are studied for the comparison proposes. Simulation has been carried out using 180 nm CMOS technology using CADENCE Spectre simulator.

The result shows that the proposed architecture is able to tune a range of frequency from 0.2 to 1.8 GHz, whereas the general architecture can produce only a range of 0.6–1.8 GHz. This outcome also says that the linearity is higher in proposed architecture.

Figure 3 shows the variation of the VCO output frequency with the input control voltage. It is seen that the curve is linear up to a control voltage of 1.0 V which corresponds to a frequency of 1.6 GHz. If the VCO is operated at higher frequencies, then the VCO gain will not be constant, which gives rise to nonlinear distortions in the VCO output signal. Calculation shows the K_{VCO} of the proposed circuit is 6.2 GHz/V, whereas the general CSVCO has K_{VCO} of 0.48 GHz/V.

Transient response of the circuits shows that proposed circuit is suitable for high-speed frequency switching PLLs since the proposed architecture has a settling time of 7 ns where the settling time of general CSVCO is 55 ns. Time domain output of the proposed circuit is shown in Fig. 4.

Phase noise occurs due to the spurious frequency component which again occurs due to static phase error. This static phase error occurs due to the current mismatch or non-idealities in the MOSFETs used in the VCO. So by changing the device dimensions, the phase noise has been changed. The phase noise plot of the

Fig. 3 Output frequency versus control input

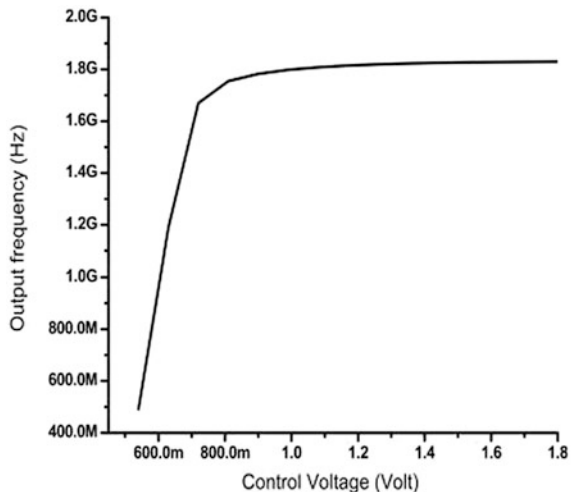


Fig. 4 Transient response for modified CSVCO

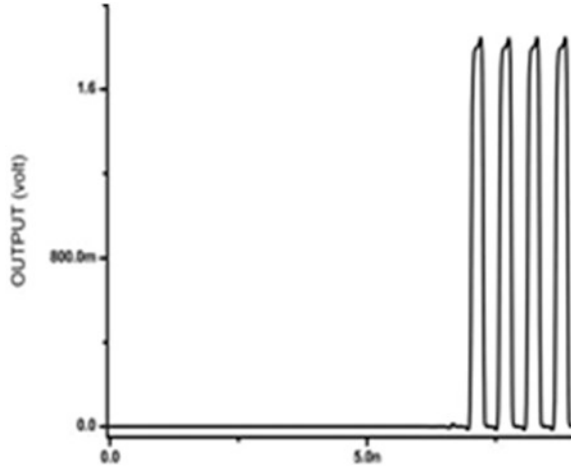
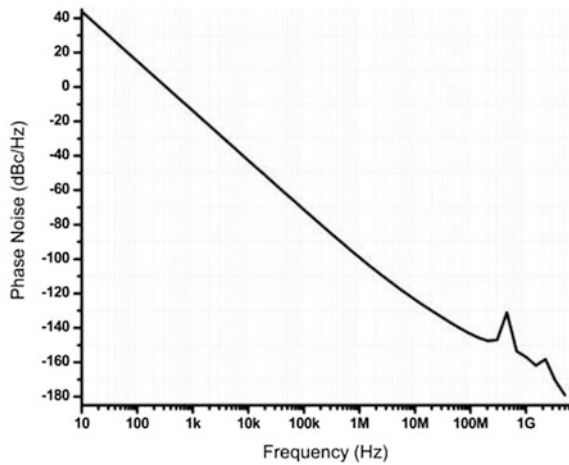


Fig. 5 Phase noise of the modified CSVCO



proposed CSVCO is shown in Fig. 5, and it comes out to be -103.73 dBc/Hz @1 MHz offset frequency and -124.97 dBc/Hz @10 MHz offset frequency. Phase noise plot is shown in Fig. 5. Phase noise of general CSVCO is improved up to -99 dBc/Hz @1 MHz by using linearization circuit but the proposed circuit almost achieves this much of phase noise without linearization. This phenomenon happens as the parasitic values have been reduced.

Dynamic power dissipation in a static CMOS is directly proportional to frequency of operation [5]. Figure 6 follows this fact for the proposed circuit as with the increment in control input, f_{osc} will increase. It has been observed that proposed circuit dissipates $155.7 \mu\text{W}$ @1.8 GHz, whereas the general CSVCO consumes $507.3 \mu\text{W}$ @1.8 GHz. This huge reduction is due to the reduction in number of transistor as well as in number of passive parasitic.

Fig. 6 Power dissipation versus input voltage CSVCO

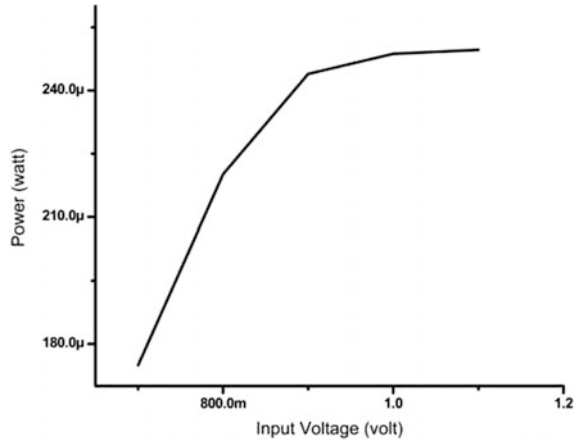


Table 1 Comparison between general CSVCO and proposed CSVCO

Architecture	Settling time (ns)	Tuning range (GHz)	KVCO (Hz/V)	Phase noise (dBc/Hz) @1 MHz	Power consumption (µw)
Proposed CSVCO	7	0.2–1.8	6.2×10^9	-103.73	155.7
General CSVCO	55	0.6–1.8	4.8×10^8	-99.46	507.3

Table 2 Comparison between different ring VCOs

Topology	Centre frequency/oscillation frequency range (GHz)	Phase noise (dB)c/Hz)	Power dissipation (mW)	Supply voltage (V)
Ring VCO [6]	3.125	-91 @1 MHz	12.6	1.8
Ring VCO [7]	5.0	-106 @1 MHz	21.0	2.5
Ring VCO [8]	5.0	-82 @1 MHz	135	1.8
Ring VCO [9]	4.3–6.1	-88 @1 MHz	80	2.5
3 stage CSVCO [10]	1.0229–3.995	-80.17 @1 MHz & -105.31 @10 MHz	7.49	1.8
Proposed work	0.2–1.8	-103.73 @1 MHz & -124.97 @10 MHz	0.155	1.8

Table 1 compares performance of the proposed circuit with the general CSVCO architecture.

Proposed circuit performance has been compared with the other presented literature also. The comparison is shown in Table 2.

5 Conclusion

The proposed circuit has been simulated in Cadence Spectre using 180 nm model and a supply of 1.8 V. VCO simulation result analysis shows that the proposed CSVCO is superior in comparison with different ring VCOs in terms of power consumption, total circuit area and phase noise.

There is also a marked improvement in the settling time as compared to general CSVCO architecture, thereby making the proposed circuit felicitous for high-speed PLLs. Layout of the proposed circuit also shows reduction in the total routing metal line length and overall area which in turn reduces the parasitic and hence improves the overall performance. The improvements in the proposed circuit will outshine various other topologies and make it a better contender to be used in monolithic integrated circuits which are used in high-speed communication systems.

Acknowledgements The authors are extremely thankful to SMDP-III(C2SD) (funded by DeitY, under Ministry of Communication and IT, Government of India) for providing them with the required laboratory facilities and software to carry on the research works, and they also extend their sincere gratitude towards Integrated Circuit Centre of Electronics & Telecommunication Engineering Department of Jadavpur University for allowing them to use the laboratory.

References

1. S.O. Mostafa and S.M. Atarodi, A High -Speed and Low-Power Voltage Controlled Oscillator in 0.18 μm CMOS- Process. IEEE International Symposium on Circuits and Systems, pp. 933–936, June 2007.
2. R. J. Baker and D. E. Boyce, CMOS circuit design, layout, and simulation, IEEE Press Series on Microelectronic Systems, 2002.
3. Bosco Leung, VLSI for Wireless Communication. Springer pp. 388–389, 404–407.
4. B. Razavi, T.C. Lee, A stabilization technique for Phase-Locked Frequency Synthesizers, IEEE J. Solid State Circuits, vol. 38, pp. 888–894, June 2003.
5. Sung-Mo Kang, yusuf Leblebici, CMOS Digital Integrated Circuits. 3rd edition, Mc Graw-Hill pp. 218–230
6. C.S. Azqueta, S. Celma and F. Aznar, A 3.125-GHz, four stage Ring VCO in 0.18 μm CMOS, In Circuits and Systems (ISCAS), vol. 44, pp. 1137–1140, May 2011.
7. F. Aznar, S. Celma and B. Calvo, Inductorless AGC amplifier for 10G Base-LX4 Ethernet in 0.18 μm CMOS, Electronics Letter, vol. 44, pp. 409–410, March 2008.
8. Y. A. Eken and J. P. Ukemura, A 5.9-GHz Voltage-Controlled Ring Oscillator in 0.18- μm CMOS, IEEE J. of Solid-State Circuits, vol. 39, Jan 2004.
9. R. Tao, M. Berroth, 5-GHz Voltage Controlled Ring Oscillator using source capacitively coupled current amplifier, Silicon Monolithic Integrated Circuits in RF Systems, pp. 45–48, April 2003.
10. Mr. Ashish Mishra and Mr. Gaurav Kumar Sharma Design of Power Optimal, Low Phase Noise Three Stage Current Starved VCO, IEEE INDICON 2015 1570184823.

Performance Comparison of 1-Bit Conventional and Hybrid Full Adder Circuits

Inamul Hussain and Saurabh Chaudhury

Abstract Adders are the integral part of arithmetic logic units in digital system. Performance of the adder circuits decides the performance of those circuit and systems. Full adders are designed either in conventional approach or hybrid approach. In conventional approach, only one logic style is used, whereas in hybrid approach, two or more logic styles are used. A performance analysis between conventional and hybrid 1-bit full adder circuits is presented in this paper. In conventional design, complementary metal–oxide–semiconductor (CMOS) full adder, complementary pass logic (CPL) full adder, and transmission gate full adder (TGA) are the most popular. In this paper, CMOS full adder and CPL full adder are reported. The hybrid adder reported in this paper is designed using CMOS logic and transmission gate (TG) logic. The circuits are implemented using Cadence virtuoso tools with 180 nm United Microelectronics Company (UMC) technology. From the pre-layout simulation, performance metrics such as power, speed, and power delay products were computed. Performance of each of the circuits in terms of power, speed, power delay product (PDP), and area requirements in terms of transistor counts for the design is then compared.

Keywords Low power · Delay · Power–delay product · CMOS
CPL · Hybrid design

1 Introduction

Adders are the main fundamental building blocks in many VLSI circuits and system such as in DSP architecture, microprocessor [1–3]. Adder is not only used in binary addition but also used in other arithmetic operations such as multiplication, division, address calculation. Performance of the overall system depends on the

I. Hussain (✉) · S. Chaudhury
Department of Electrical Engineering, National Institute of Technology,
Silchar, Assam, India
e-mail: ihinamul07@gmail.com

© Springer Nature Singapore Pte Ltd. 2018
R. Bera et al. (eds.), *Advances in Communication, Devices and Networking*,
Lecture Notes in Electrical Engineering 462,
https://doi.org/10.1007/978-981-10-7901-6_6

performance of adder circuit [1–5]. Hence, enhancing the performance of adder circuit is one of the principle goals.

Today with the increasing use of portable battery operated device, low-power design is one of major issues. To achieve a low-power design, one has to compromise with power and area [4]. So designing a low-power high speed adder is one of the most challenging issues.

Full adders are designed with different logic styles. Every design has some advantages and some disadvantages. Complementary metal oxide semiconductor (CMOS) full adder (FA) [1, 2] shows robustness against voltage scaling and transistor sizing. But it has high input capacitance and for higher bit addition when more 1bit adders are cascaded performance degrades [3]. Another type design is mirror adder [4] which consumes same power as CMOS full adder and has equal number of transistors. But it produces more delay. On the other hand, though complementary pass logic (CPL) adder shows good voltage swing, there is voltage degradation at the output [5, 6]. The voltage degradation is successfully addressed by transmission gate full adder (TGA); the disadvantage of TGA adder is that it shows high delay and consumes high power [7, 8]. To improve power and delay, Vesterbacka [9] proposed hybrid structure of full adder, but it has poor driving capability. Moreover, the performance of this adder degrades in the cascaded mode of operation. Bhattacharyya et al. [10] proposed another hybrid full adder which shows better performance. Though there is no perfect cell of full adder, hybrid full adder shows improvements in terms of power, delay, and power–delay product.

Conventionally, static CMOS, CPL, and TGA-based FAs are widely used [11–15]. However, it is seen that hybrid FA with CMOS and TGL has higher performance than conventional FAs [10]. Hence, few such adder circuits are studied from the point view of power, delay, and PDP. Among those, two conventional adders and one hybrid adder are presented in this paper. Those adder circuits are designed by using Cadence Virtuoso Tool in 180 nm UMC technology. Transient and DC analysis are performed to calculate power dissipation, delay, and power–delay products. A comparison is given to see the performance of all three adder circuits.

The remaining of this paper is arranged in the following manner. In Sect. 2, low-power design constraints for the designing of adder circuits are presented. In Sect. 3, conventional and hybrid full adder circuits are discussed. In Sect. 4, detail analysis of the circuits and performance evaluations of the adder circuit are presented. The adder circuits are compared by different performance parameter such as power, delay, power–delay product, and transistor count.

2 Power Consumption

Designing a low-power VLSI circuit is always a challenging task. For any portable device, it is necessary to design circuit which consumes less power [11]. Another important aspect of low-power design is its reliability [13]. The major components of power dissipation in CMOS design are given below.

1. **Switching Power Dissipation:** This type of power consumption occurs when there is a signal transition from 0 to 1 or vice versa in the circuit. The main reason of the dissipation is the node capacitances.
2. **Short Circuit Power Dissipation:** In CMOS design, during transistor switching, there is a moment when current flows directly from power supply to ground. The power dissipation at that moment is known as short circuit power dissipation.
3. **Static Power Dissipation:** It occurs mainly due to leakage current when the circuit is on any steady state (either ON or OFF state).

First two components are also known as dynamic power dissipation. It occurs due to the charging and discharging of the load capacitances of the circuits. The other factors that influence dynamic power are clock frequency, power supply, and switching activity [15, 16]. The average power consumed by any CMOS circuits is the summation of dynamic power dissipation and static power dissipation. In this paper, static power and average power dissipation of each adder circuits are calculated and compared. By varying the power supply from 1.0 to 1.8 V, the same is observed.

3 Full Adder Circuits

The main function of a 1-bit full adder is to add three different binary bits. Outputs of a full adder is Sum bit and Cout, where Sum is logical summation of three bits and Cout is the carry bit. The truth table of a full adder is shown in Table 1.

A , B , C_{in} are inputs. The table describes the different inputs pattern for the full adder circuits and their corresponding outputs. The expression for full adder is given in Eq. (1).

$$\begin{aligned} \text{Sum} &= A \oplus B \oplus C_{in} \\ \text{Cout} &= AB + BC_{in} + C_{in}A \end{aligned} \tag{1}$$

Based the above functional expression as shown in Eq. (1), different full adder circuits are developed.

Table 1 Truth table of 1-bit full adder

Inputs			Outputs	
A	B	C_{in}	Sum	Cout
0	0	0	0	0
0	0	1	1	0
0	1	0	1	0
0	1	1	0	1
1	0	0	1	0
1	0	1	0	1
1	1	0	0	1
1	1	1	1	1

A CMOS full adder is designed by using 28 transistors [1, 2]. The circuit shown in Fig. 1 is designed by pull-up and pull-down network. Pull-up networks are designed by using PMOS, because PMOS can provide a good logic ‘1’ and for pull-down networks NMOS is used because it can provide good logic ‘0’

The main advantage of CMOS adder is its robustness against voltage swing and transistor sizing. The disadvantage of the circuit is high input loads. This is because the size of the PMOS is larger (approximately double) than that of NMOS. Another disadvantage of CMOS full adder circuit is weak driving power, when it is used to design higher bit adder circuit. This advantage is observed because of the series transistor. It could be overcome by using buffers. The carry is produced earlier, and the signal is used for summation. So, it unnecessarily adds delay in the operation.

A CPL full adder is designed by using 32 transistors as shown in Fig. 2 [5]. CPL is one of the important styles in pass transistor logic. In pass transistor logic, instead of using pull-up or pull-down networks, either PMOS or NMOS is used. The sources of the PMOS/NMOS is connected to input signal instate of power supply (V_{dd}/gnd). Generally, NMOS is used for pass transistor style. It is because mobility of electron is higher than the mobility of holes. Since the channel width of NMOS is made smaller than PMOS, the input load of NMOS pass transistor is less.

However, there is threshold voltage drop ($V_{dd}-V_{tn}$) in the circuit; to overcome that, inverters or pull-up PMOS transistors are used [5–7]. NMOS pass transistor style is also known as CPL style. Full adders designed with CPL style are faster than that of CMOS full adders. It also uses two weak pull-up PMOS transistors for good voltage swing restoration. But it has lots of disadvantages. There is high switching activity in the intermediate nodes, and this increases switching power

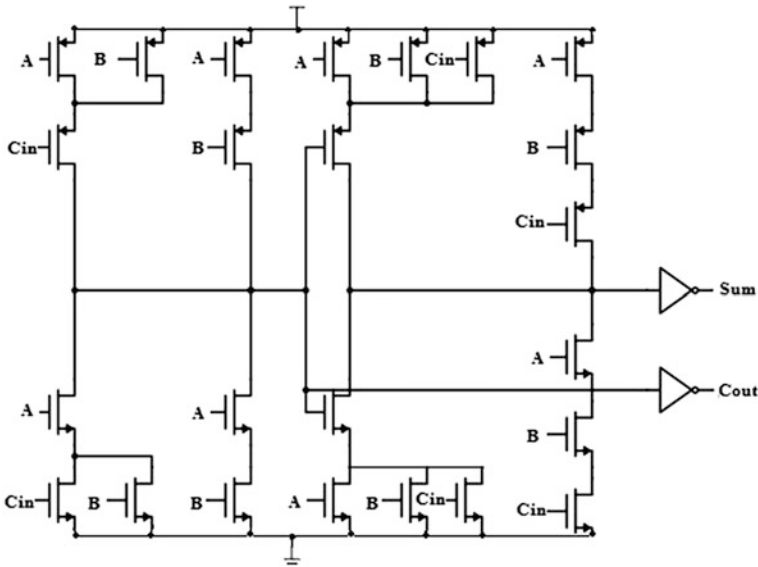


Fig. 1 CMOS full adder

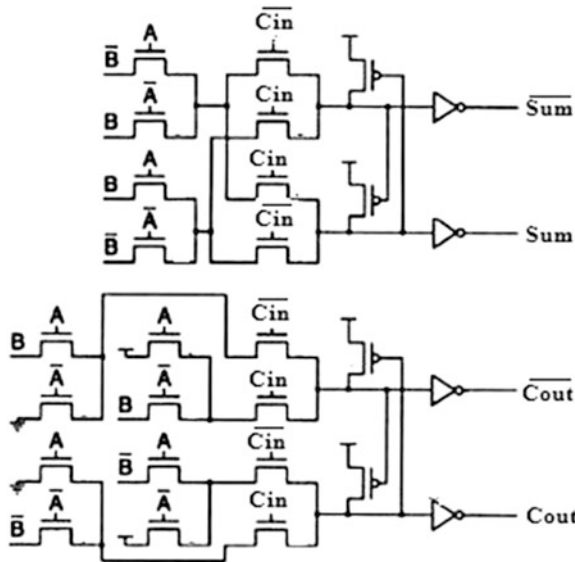


Fig. 2 CPL full adder

dissipation in the circuit. It also increases the transistor counts and also causes voltage degradation at the output.

To solve the drawbacks of conventional full adders, hybrid adders are used. Hybrid adders are designed by different logic styles. In this paper, a low-power high speed hybrid 1-bit full adder is reported [10]. The adder circuit is designed by using CMOS logic and transmission gate (TG) logic. This adder circuit as shown in Fig. 3 has improved performance in terms of power, delay, and transistor count. The adder is designed with three modules, namely XNOR module, sum module, and carry module. A modified XNOR module is designed to minimize the power. It also shows enhancement in voltage degradation. The XNOR module is designed by using six transistors. The designer introduces TG in sum module and carry module, as a result it reduces the delay. Total transistors count for the adder circuit is 16.

4 Performance Analysis

All three adder circuits are simulated with Cadence virtuoso tool by using 180 nm UMC technology. Power (static and dynamic), delay, and power–delay product are then computed with supply voltage variation from 0.8 to 1.8 V. Table 2 shows the simulation result of the adder circuits considered in this study. Though the simulation is done at the voltage range of 0.8–1.8 V, the simulation results only for the supply voltages of 1.0, 1.2, 1.5 and 1.8 V are shown in Table 2. Propagation delays between inputs and outputs of each adder are calculated, and the worst case delays

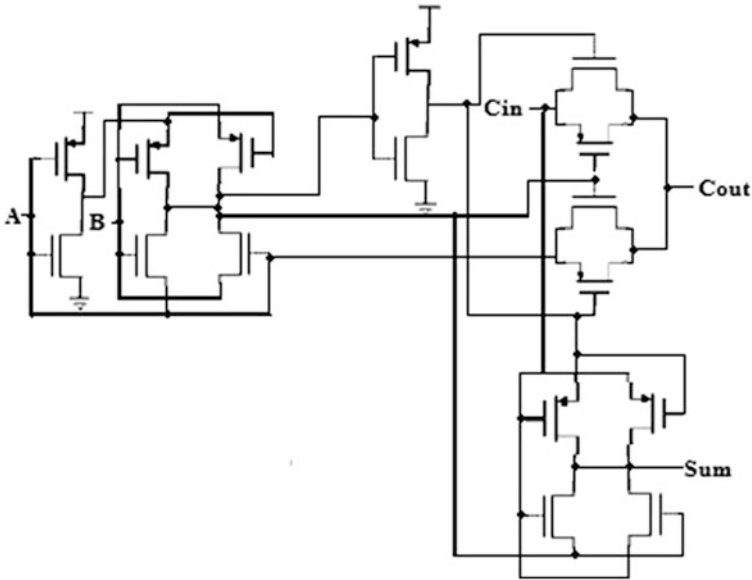


Fig. 3 Hybrid full adder

Table 2 Simulation results of adder circuits at 1.8, 1.5, 1.2, and 1 V

Power supply (V)	Adder circuit	Delay (ps)	Average power (μ W)	PDP (fJ)	Transistor count
1	CMOS	740.0	1.579	1.168	28
	CPL	476.20	1.770	8.428	32 + 6
	Hybrid	86.86	1.217	0.1057	16
1.2	CMOS	507.3	2.366	1.200	28
	CPL	337.5	2.647	0.8934	32 + 6
	Hybrid	171.18	1.782	0.3050	16
1.5	CMOS	334.8	3.978	1.332	28
	CPL	238.2	4.351	1.036	32 + 6
	Hybrid	201.65	2.854	0.5755	16
1.8	CMOS	251.7	5.542	1.395	28
	CPL	188.0	6.520	1.225	32 + 6
	Hybrid	233.64	4.189	0.9787	16

between them are considered. At 1.8 V, the delays for CMOS, CPL, and hybrid adder are found to be 251.7, 188.0, and 233.64 ps, respectively. Average power of the adder circuits is also calculated.

It is seen that at the power supply 1.8 V, average power taken by CMOS, CPL, and Hybrid adder are 5.542, 6.520, and 4.189 μ W, respectively. Again power–delay product (PDP) with different power supplies is then calculated. With a supply of 1.8 V, PDP for CMOS, CPL, and hybrid adder are found to be 1.395, 1.225, and

Table 3 Static and dynamic power consumption at 1.8 V

Adder circuit	Static power	Dynamic power
CMOS	374.0 pW	5.5416 μ W
CPL	1.383 nW	6.5186 μ W
Hybrid	233.1 pW	4.1887 μ W

0.9787 fJ, respectively. Finally, the transistor counts for CMOS, CPL, and hybrid adders are observed which are found to be 28, 32, and 16, respectively. As CPL style adder needs complementary inputs, hence it requires three more inverters to complement three inputs. It increases the overall transistor count of CPL adder by six numbers. The input supply voltage was varied from 0.8 V because the threshold voltage for MOSFET (metal–oxide–semiconductor field-effect transistor) is 0.6–0.8 V at 180 nm technology.

Static and dynamic power is also calculated separately by varying voltage supply from 0.8 to 1.8 V. Static power is calculated by replacing all the inputs by V_{dc} (power supply source in Cadence from analog library). The DC value of V_{dc} is set to 0 V, and the circuits are re-simulated. After simulation, power of each circuit is calculated; this power is considered as static power. The dynamic power of each adder circuits is calculated by subtracting static power from average power. Table 3 shows the static and dynamic power consumption of adder circuits at power supply of 1.8 V.

It is observed that with 180 nm UMC technology, dynamic power is the dominant component of power dissipation. It is because of the charging and discharging of load capacitances. Among all three adders, it seen that CPL adder has the maximum power dissipation because it has more number of transistors and it increases the switching activity of the adder. Whereas, though Hybrid adder has least dynamic power dissipation, but still it consumes little high average power as per recent trend in low power applications.

5 Conclusion

Performance parameters such as power, delay, and power–delay product (PDP) are observed for conventional adders (CMOS, CPL) and the hybrid adder. Each circuit shows its own power consumption, delay, and PDP. CMOS adder produces more delay. Though CPL shows improvements in delay, it consumes more power, as it has more switching activities in the circuit. Both CMOS and CPL adder requires large number of transistors. On the contrary, hybrid adder shows better performance in terms of power, delay, and power delay product. It also improves transistor count. Though there is no perfect adder cell, hybrid adder shows improvement in overall performance and transistor count.

Acknowledgements The authors would like to thank VLSI Laboratory, Department of Electronics and Communication Engineering, NIT Silchar, for providing the simulation facility.

References

1. D. Radhakrishnan.: Low-voltage low-power CMOS full adder. *IEEE Proc. -Circuits Devices Syst.*, vol. 148, no. 1, pp. 19–24, (2001).
2. N. H. E. Weste, D. Harris, and A. Banerjee.: *CMOS VLSI Design: A Circuits and Systems Perspective*. 3rd ed. Delhi, India: Pearson Education, (2006).
3. C. H. Chang, J. M. Gu, and M. Zhang.: A review of 0.18- μm full adder performances for tree structured arithmetic circuits. *IEEE Trans. Very Large Scale Integr. (VLSI) Syst.*, vol. 13, no. 6, pp. 686–695, (2005).
4. J. M. Rabaey, A. Chandrakasan, and B. Nikolic.: *Digital Integrated Circuits: A Design Perspective*, 2nd ed. Delhi, India: Pearson Education, (2003).
5. R. Zimmermann and W. Fichtner.: Low-power logic styles: CMOS versus pass-transistor logic. *IEEE J. Solid-State Circuits*, vol. 32, no. 7, pp. 1079–1090, (1997).
6. K. Chu and D. Pulfrey.: A comparison of CMOS circuit techniques: Differential cascode voltage switch logic versus conventional logic. *IEEE J. Solid-State Circuits*, vol. 22, pp. 528–532, (1987).
7. J. H. Pasternak and C. A. T. Salama.: Differential pass-transistor logic. *IEEE Circuits & Devices*, pp. 23–28, (1993).
8. A. M. Shams, T. K. Darwish, and M. A. Bayoumi.: Performance analysis of low-power 1-bit CMOS full adder cells. *IEEE Trans. Very Large Scale Integr. (VLSI) Syst.*, vol. 10, no. 1, pp. 20–29, (2002).
9. M. Vesterbacka.: A 14-transistor CMOS full adder with full voltage swing nodes. *Proc. IEEE Workshop Signal Process. Syst. (SiPS)*, pp. 713–722, (1999).
10. P. Bhattacharyya, B. Kundu, S. Ghosh, V. Kumar, and A. Dandapat.: Performance Analysis of a Low-Power High-Speed Hybrid 1-bit Full Adder Circuit. *IEEE Trans. Very Large Scale Integr. Syst.*, vol. 23, no. 10, pp. 2001–2008, (2015).
11. I. Hassoune, D. Flandre, I. O'Connor, and J. Legat.: ULPFA: A new efficient design of a power-aware full adder. *IEEE Trans. Circuits Syst. I, Reg. Papers*, vol. 57, no. 8, pp. 2066–2074, (2010).
12. J.-M. Wang, S.-C. Fang, and W.-S. Feng.: New efficient designs for XOR and XNOR functions on the transistor level. *IEEE J. Solid-State Circuits*, vol. 29, pp. 780–786, (1994).
13. P. Ng, P. T. Balsara, and D. Steiss.: Performance of CMOS differential circuits. *IEEE J. Solid-State Circuits*, vol. 31, pp. 841–846, (1996).
14. J.-M. Wang, S.-C. Fang, and W.-S. Feng.: New efficient designs for XOR and XNOR functions on the transistor level,” *IEEE J. Solid-State Circuits*, vol. 29, pp. 780–786, (1994).
15. H. T. Bui, Y. Wang, and Y. Jiang.: Design and analysis of low-power 10-transistor full adders using novel XOR-XNOR gates. *IEEE Trans. Circuits Syst. II, Analog Digit. Signal Process.*, vol. 49, no. 1, pp. 25–30, (2002).
16. I. Hussain and M. Kumar.: Design and performance analysis of a 3-2 compressor by using improved architecture. *Journal of Active and Passive Electronic Devices*, vol. 12, no. 3–4, pp. 173–181, (2017).

VLSI Implementation of Booth's Multiplier Using Different Adders

Ujjaljyoti Sarkar, Rongan Nath and Suman Das

Abstract Recent IC technology emphasizes on the fabrication of ICs as more area optimization and low-power practices. Among all the arithmetic operations, the most heavily used one is multiplication that measures more frequently in signal processing applications. Multiplication is a very hardware-focused subject, and we as customers are mostly worried with getting low power, smaller area, and higher speed. The most important concern in classic multiplication mostly realized by shifting and adding is to accelerate fundamental multi-operand addition of partial products. In this literature, the Booth multiplier implementation is presented with different adder architectures like ripple carry adder and carry look ahead adder and carry select adder. The time delay, area, and power have been investigated for different adders.

Keywords Ripple carry adder · Carry look ahead adder · Carry select adder
Booth's multiplier · VHDL

1 Introduction

Multipliers are significant gears of various high performances, high complex systems. In a complex system, the slowest component is multiplier and its performance is usually obtained by the performance of the multiplier. Furthermore, it is the most area consuming and complex components in a system. So the key design issue is to control the speed and to optimize the area of the multiplier [1]. However, area and

U. Sarkar · R. Nath · S. Das (✉)

ECE Department, Sikkim Manipal Institute of Technology, Sikkim Manipal University,
Gangtok 737132, Sikkim, India
e-mail: das.suman194@gmail.com

U. Sarkar
e-mail: ujjalsarkar696@gmail.com

R. Nath
e-mail: rongannath@gmail.com

speed are commonly contradictory constraints as larger area results improvement in speed. As binary adders are the backbone of different multipliers, therefore binary additions are fundamentally key component in any upgrading in the performance of computing system and, henceforth, assist in the improvement of performance of the entire system. In VLSI systems, parallel prefix adders are known as best performer. Field programmable gate arrays (FPGAs) have achieved more popularity in cutting edge technology as a reconfigurable logic because it deals with an enhanced performance in terms of speed and power over DSP-based and microprocessor-based systems for many practical designs relating mobile DSP and telecommunications uses and a substantial reduction in development time and cost over application-specific integrated circuit (ASIC) designs [2].

2 Ripple Carry Adder (RCA)

The ripple carry adder (RCA) is formed by assembling 1-bit full adders (FAs) in series. One FA adds two binary digits at any stages of the ripple carry. The carryout of one FA is fed to the carryin of the next FA. A number of 1-bit FAs can be added to the RCA adder, or RCA adders of different sizes may be added to put up binary vectors of larger sizes [3]. Figure 1 shows an example of an 8-bit RCA and its test bench waveform.

3 Carry Look Ahead Adders (CLAs)

In the RCA, its disadvantage is the time delay that an FA takes to propagate the carry. The CLA adder resolves this problem by manipulating the carry signals in advance. Carry propagation time is reduced then.

The propagation function P and generation function G in a full adder are given as follows:

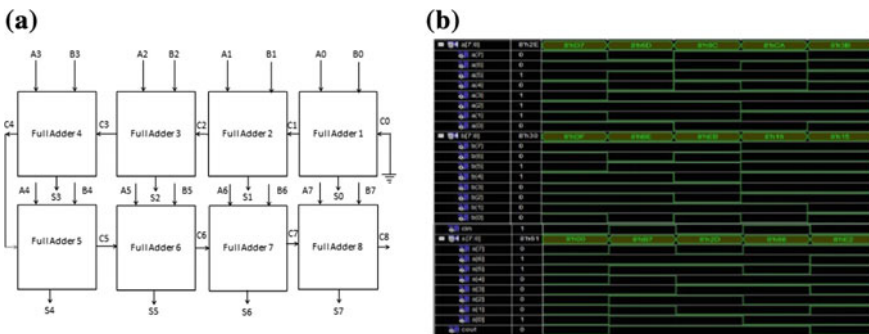


Fig. 1 a 8-bit RC adder. b Test bench waveform

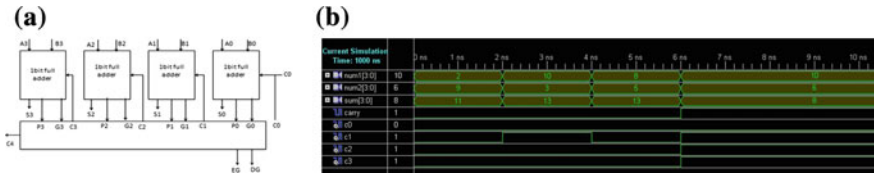


Fig. 2 a 4-bit CLA adder. b Test bench waveform

$$P_i = A_i \oplus B_i$$

$$G_i = A_i B_i$$

The new Boolean expressions for the sum are given by:

$$S_i = P_i \oplus C_{i-1} C_{i+1} = G_i + P_i C_i$$

These equations show that a carry signal will be generated in two cases:

- (1) if both bits A_i and B_i are 1.
- (2) if either A_i or B_i is 1 and the carryin C_i is 1.

Figure 2 shows a 4-bit CLA adder and its test bench waveform.

4 Carry Select Adders (CSAs)

The CSA adder is used to calculate other results in parallel and then select the precise result with single or multiple phase-ordered techniques. High-speed performance can be achieved by increasing the area requirements of CSA adder. In CSA, both sum and carry bits are designed for the two replacements: input carries “0” and “1”. Once the input carry is delivered, the exact calculation is selected (using a MUX) to create the desired output. Therefore, it is not required to wait for input carry to calculate the sum and the sum is generated as soon as the input carry gets there. The time requirement for calculating the sum is then evaded which results in a good development in speed [4–7]. A 4-bit CSA adder and its test bench waveform are shown in Fig. 3.

5 Booth’s Multiplier

Booth’s multiplier multiplies two signed or unsigned binary numbers in two’s complement notation. The algorithm and test bench waveform using carry select adder are shown in Fig. 4.

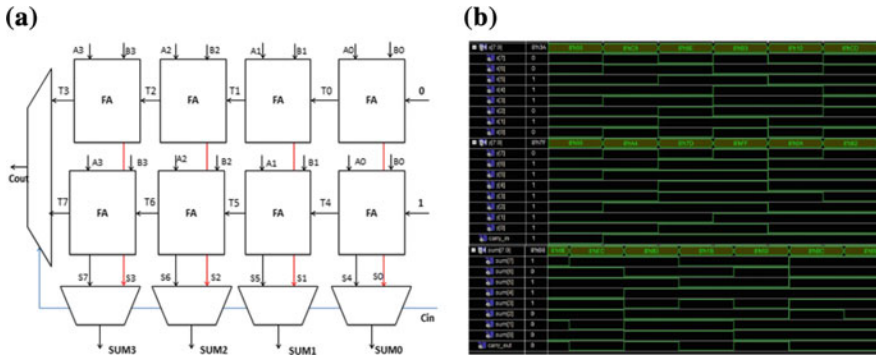


Fig. 3 a 4-bit CSA. b Test bench waveform

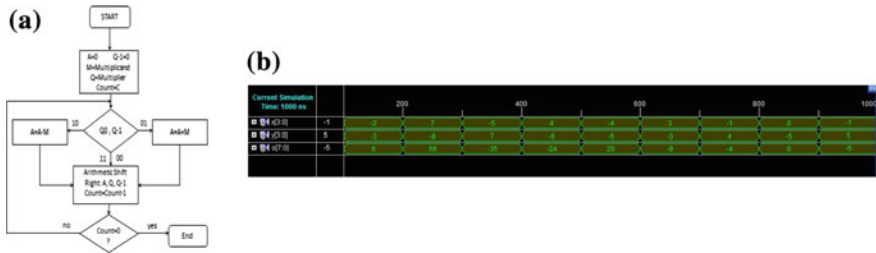


Fig. 4 a Booth's multiplication algorithm flowchart. b Test bench waveform

6 Performance Analysis of Booth's Multiplier Using Different Types of Adder

The performance in terms of power, delay, and area of Booth's multiplier using different types of adder is shown in Table 1. From table, it is clear that Booth's multiplier using carry select adder delivers good settlement of power, delay, and area than look ahead carry adder and ripple carry adder [8–10].

7 Conclusion

Design of a VHDL-based Booth's multiplier using RCA, CLA, and CSA adder was offered and implemented. CSA improves the performance of the multiplier as all types of power are increasing and cell size is decreasing to provide less area consumption. This multiplier can be further extend to any bit multiplier using proposed method.

Table 1 Performance analysis of Booth's multiplier using different adders

Design type	Cell internal power (mW)	Net switching power (mW)	Total dynamic power (mW)	Cell leakage power (mW)	Delay	Area
Booth's multiplier using RCA adder	4.6329	1.8529	6.3452	93.0186	99.5	2454 logic cells
Booth's multiplier using CLA adder	4.9865	2.2754	7.3612	108.5598	98.2	2945 logic cells
Booth's multiplier using CSA adder	5.1219	2.8564	8.2956	135.6512	85.6	2039 logic cells

References

1. J. M. Rabaey, *Digital Integrated Circuits—A Design Perspective*. Upper Saddle River, NJ: Prentice-Hall, 2001.
2. Sertbas and R.S. Ozbey, "A performance analysis of classified binary adder architectures and the VHDL simulations", *J Elect. Electron. Eng.*, Istanbul, Turkey, vol. 4, pp. 1025–1030, 2004.
3. M. Alioto, G. Palumbo, and M. Poli, "Optimized design of parallel carry-select adders," *Integration, the VLSI J.*, vol. 44, no. 1, pp. 62–74, Jan. 2011.
4. Muhammad Ali Akbar and Jeong-A Lee, Senior Member, *IEEE Comments on "Self-Checking Carry-Select Adder Design Based on Two-Rail Encoding"* *IEEE transactions on circuits and systems: regular papers*, vol. 61, no. 7, July 2014.
5. D. P. Vasudevan, P. K. Lala, and J. P. Parkerson, "Self-checking carry select adder design based on two-rail encoding," *IEEE Trans. CircuitsSyst. I, Reg. Papers*, vol. 54, no. 12, pp. 2696–2705, Dec. 2007.
6. H. Belgacem, K. Chiraz, and T. Rached, "A novel differential XOR-based self-checking adder," *Int. J. Electron.*, vol. 99, no. 9, pp. 1239–1261, Apr. 2012.
7. O. J. Bedrij, "Carry-select adder," *IRE Trans. Electron. Comput.*, pp. 340–344, 1962.
8. B. Ramkumar, H.M. Kittur, and P. M. Kannan, "ASIC implementation of modified faster carry save adder," *Eur. J. Sci. Res.*, vol. 42, no. 1, pp. 53–58, 2010.
9. T. Y. Ceiang and M. J. Hsiao, "Carry-select adder using single ripple carry adder," *Electron. Lett.*, vol. 34, no. 22, pp. 2101–2103, Oct. 1998.
10. Y. Kim and L.-S. Kim, "64-bit carry-select adder with reduced area," *Electron. Lett.*, vol. 37, no. 10, pp. 614–615, May 2001.

A Density Functional Theory-Based Study of Electronic and Optical Properties of Anatase Titanium Dioxide

Debashish Dash, Saurabh Chaudhury and Susanta Kumar Tripathy

Abstract This paper presents an analysis of structural, electronic, and optical properties of pristine anatase titanium dioxide (TiO_2) using orthogonalized linear combinations of atomic orbitals (OLCAO) basis set under the framework of density functional theory (DFT). The lattice constants such as a and c , band diagram, density of states (DOS) have also been studied. The band gap shows indirect nature around the fermi level in anatase TiO_2 . Density of states shows a contribution of Ti_{3d} and O_{2p} orbitals in conduction and valence band regions. From the analysis of optical properties, it is seen that the anatase TiO_2 supports the interband indirect transition from O_{2p} in valence region to Ti_{3d} in the conduction region. All the optical properties are discussed in detail under the energy range of 0–16 eV. Further, we have compared the results with previous works as well as with the experimental results. We found that DFT-based simulation results are approximation to the experimental results.

Keywords DFT · Anatase TiO_2 · Electronic structure · Optical properties

1 Introduction

TiO_2 is found in nature in many different structures and crystalline forms like monoclinic, orthorhombic, simple tetragonal. [1]. Interestingly, it provides many utilization ways, when it is in tetragonal form. In nature, titanium dioxide develops

D. Dash (✉) · S. Chaudhury
Department of Electrical Engineering, NIT Silchar, Silchar, India
e-mail: debashishdashnits@gmail.com

S. Chaudhury
e-mail: saurabh1971@gmail.com

S. K. Tripathy
Department of ECE, NIT Silchar, Silchar, India
e-mail: susanta96@gmail.com

tetragonal structure in two ways, namely rutile and anatase. However, they look alike, and hence a little difference exists between them. In past few years, rutile has been broadly studied both theoretically and experimentally. However due to difficulty in synthesizing better quality single crystals, anatase drew little attention [2]. In photovoltaic applications, specifically for photocatalysis with highest efficiency, long-term chemical stability and photoelectrochemical (PEC) hydrogen production through water splitting, anatase structure is preferred to other structures [3]. Anatase single crystals were first grown by Izumi and Fujiki [4]. Grunin et al. [5, 6] obtained larger TiO_2 crystals and characterized it by resistivity measurements. Forro et al. [7] investigated the transport properties of anatase TiO_2 and found a very shallow donor level and high electron mobility in anatase TiO_2 . Research works reported in [8–13] have investigated anatase structure and defined some basic properties. Although electronic structure of rutile and anatase is quite similar, experimentally they can be distinguished from other properties like magnetic, electrical, and optical. Tang et al. [2] investigated circumstantial absorption edges of both the structures and established that the nature of the exciton states of anatase is self-trapped while that of rutile is free. Lawler et al. [14] investigated the birefringence of anatase TiO_2 and investigated the excitonic effects considering Bethe–Salpeter equation (BSE). Chiodo et al. [15] developed many-body perturbation theory (MBPT) based on GW approximation and BSE.

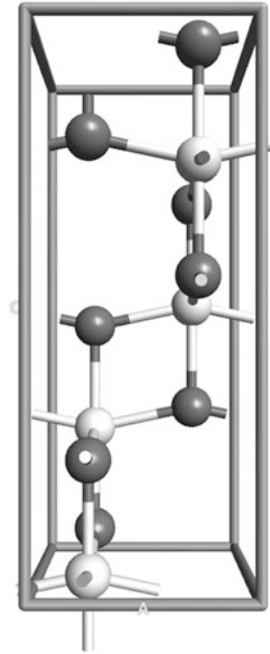
In this paper, we have presented the essential properties of anatase TiO_2 such as structural, electronic, optical property together. For this purpose, we have used orthogonalized linear combination of atomic orbitals (OLCAO) [9, 16] basis and found it suitable for finding accurate results on electronic and dielectric properties. The OLCAO method was also used to calculate band gap as well as dielectric properties. To analyze using OLCAO, first of all we have obtained the optimized structure using DFT simulator, calculating the total energy and total volume. Further, we have analyzed the band structure, density of states, optical properties like refractive index, extinction coefficient, absorption coefficient, reflectivity as well as loss function using DFT. As most of the applications of TiO_2 are for catalytic use, qualitative use of it is in paper industry for opacity increment and it is also found to be an important ingredient in cosmetic industry.

2 Computational Methods

Anatase structure of TiO_2 contains four molecules per unit cell. It is shown in Fig. 1. The structure has a lattice constant of $a = b = 3.7842 \text{ \AA}$ and $c = 9.5146 \text{ \AA}$. It is metastable having a density of 3.894 g/cm^3 [2]. It is tetragonal in nature having space group: $I4_1/amd (141)$ [17]. The lattice type of anatase structure is body-centered tetragonal. Two of its lattice constants are equal ($a = b$), whereas third one is quite longer (c) [18].

In this work, all the calculations are carried out by Quantumwise Atomistix ToolKit 2014.3 [19–21]. First of all, a basic unit cell of TiO_2 has been taken.

Fig. 1 Original TiO_2 phase of anatase. The red spheres represent the oxygen (O) atoms, while white spheres indicate the titanium (Ti) ions. The LDA structural parameters computed are:
 $a = b = 3.7842 \text{ \AA}$,
 $c = 9.5142 \text{ \AA}$



The OLCAO method is an all-electron density functional theory [22]-based method that uses local atomic orbitals in the basis expansion. OLCAO method is employed for structured optimization and for calculating the ground-state electronic properties. We have implemented limited-memory Broyden–Fletcher–Goldfarb–Shanno (LBFGS) optimization algorithm [23] which is under the family of quasi-newton methods. This algorithm is much popular for parameter estimation in machine learning. For structure optimization, we have considered a maximum force of 0.005 eV/\AA and maximum step length of 0.5 \AA . Further, we have maintained a constant (c/a) ratio with the value of 2.5143. Through an extensive simulation, we found that the lowest energy point is at the default lattice parameters. In Fig. 2, we have shown the relationship between total energy and total volume. Using these values, we have found the band diagram. Then energy–volume data is fitted to the third order Birch–Murnaghan equation of state (EOS) [24] to calculate the bulk modulus. Then we found out the total density of states (TDOS) as well as contribution of other orbitals. Finally, we have also calculated the dielectric properties and other coefficients related to dielectric property. For the calculations, we have used Perdew–Zunger [25] exchange–correlation potential for local density approximation (PZ-LDA). The grid mesh cutoff energy is set to 1633 eV (60 Hartree) [26] for the DFT calculation in room temperature. Initially, there is no charge considered and spin of electrons remained unpolarized. The Monkhorst-Pack [27] scheme is used for the k-point sampling in the first Brillouin zone. We have taken $6 \times 6 \times 3$ k-point grid [25] for DFT calculation. So the number of symmetric k-points is reduced to 54 in the first Brillouin zone for

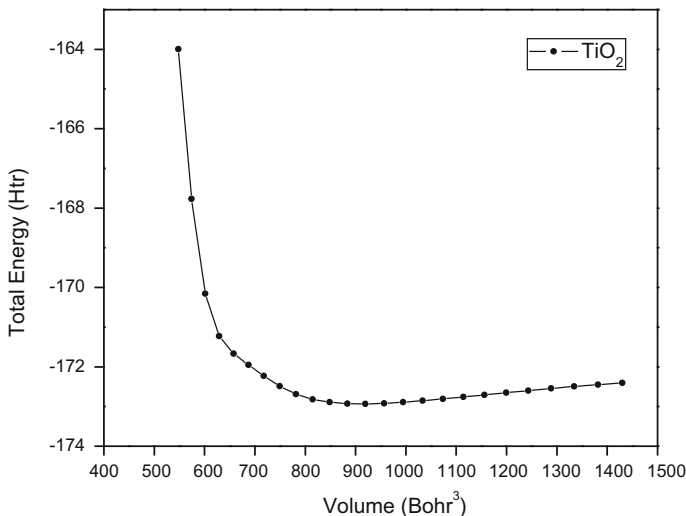


Fig. 2 Total energy versus volume of anatase TiO_2

anatase structure. For oxygen, we have used Fritz Haber Institute (FHI) [Z = 6] LDA. PZ and for titanium, FHI [Z = 4] LDA. PZ has been used.

3 Results and Discussion

3.1 Energy Band Diagram

The anatase TiO_2 is tetragonal in structure. From the simulation results, it is seen that the LDA band gap in case of anatase TiO_2 is lesser than that of experimental results. The valence band maxima lie at M and conduction band minima lie between X and Γ . From the band diagram of Fig. 3, it is apparent that an indirect transition band exists between valence band maxima and conduction band minima. This is at the symmetry point from M to lowest energy point between X and Γ as in Fig. 3. From the band diagram (Fig. 3), this energy band gap can be calculated as 1.81 eV. The structural property as calculated by LDA is a close approximation to Sai et al. [13], where they have calculated the lattice constants and interatomic positions through LDA and mBJ approximation and reported the band structure as given in Table 1.

From Table 1, column 1 represents work carried by us and other researchers. Column 2 represents exchange-correlation and technique used. It can be seen from column 3 that the considered lattice parameters (a, c) are within 1% of experimental values. However, the simulated band gap value is consistent to other researchers' work [3, 9, 11, 13, 15] and nearly 40% less than experimental value [12, 14, 19]. It may be due to discontinuity in the derivative of electron energy and ground-state

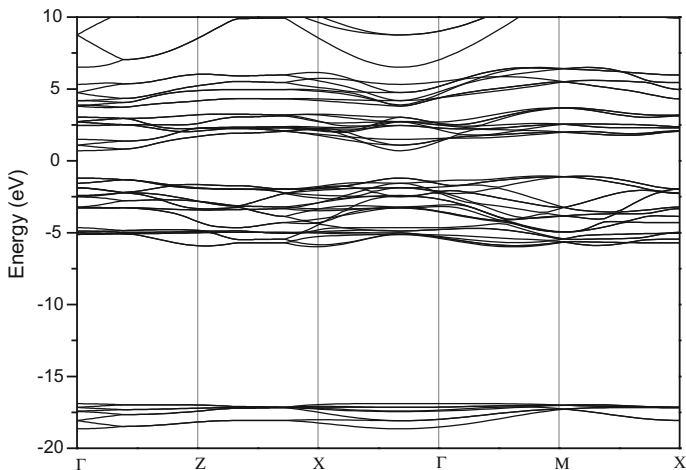


Fig. 3 Band structure of anatase TiO_2

Table 1 Comparison of band structure and optical properties with PZ-LDA-OLCAO basis set with other works

Work	Method	Lattice constants a, c (Å)	E_g (eV)	$\varepsilon_1(0)$ (eV)	η
This work	PZ-LDA	3.7842, 9.5146	1.81	4.3	2.05
Other works	LCAO/ PW	3.784, 9.515 [9]	1.88 [3], 1.98 [13], 2.04 [9, 11, 15]	6.04 [9] 4.98, [26]	2.191 [28]
Exp.	Exp.	3.782, 9.502 [18]	3.2 [12, 14, 19]	5.62 [9]	2.49 [29]

formalism of density functional theory. We also calculated plasmon energy and got an underestimated value. It may be for less grid mesh cutoff energy and less k-points symmetry. Finally, simulated dielectric constant $\varepsilon_1(0)$ and refractive index (η) are also consistent with Zhu et al. [26] and much closer to experimental value.

3.2 Density of States

One of the most important properties is the density of states (DOS) which describes the electronic property of a material. In general, it shows the energy representation for describing molecular dynamics and spectroscopy. Mathematically, it is expressed as $g(E)$ which describes the number of quantum states available within an energy range from E to $E + dE$. In other words, the density of states (DOS) is a measure of number of electron (or hole) states per unit volume at a given energy. So relations between these quantities can be created through the appropriate dispersion relationship $E(k)$.

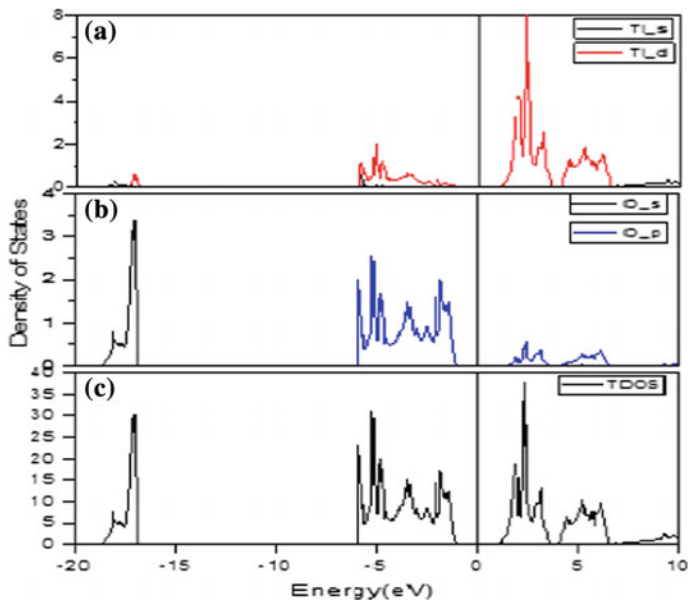


Fig. 4 a Contribution of Ti_{1s} and Ti_{3d} to, e_g , and t_{2g} conduction band states outer orbits, b contribution of O_{1s} and O_{2p} toward valence band, c total density of states of anatase TiO_2

If the eigenstates of a Hamiltonian E_n are known, then DOS is a simple count of states at any given frequency. Mathematically, it can be represented as

$$g(E) = \sum_{n=1}^{\infty} \delta(E - E_n) \quad (1)$$

where δ = probability distribution function.

So total number of states can be obtained by integrating $g(E)$ over all energies. Various bulk properties such as specific heat, paramagnetic susceptibility, and other transport properties of conductive solids depend on this function.

From Fig. 4, it is also clear that the valence band ranges from -18.62 eV to fermi level (E_F). It is subdivided into three states such as low-, intermediate-, and high-energy states. The low-energy state valence band ranges from -18.62 to 16.5 eV. It is mainly due to O_{1s} state with a mixture of Ti_{2p} and Ti_{3d} states. The intermediate energy state ranges from -6 to -2.5 eV. This is mainly formed due to O_{2p} state with a mixture of Ti_{3d} state. Finally, the higher energy state ranges from -2.5 to fermi level (E_F), which is contributed by O_{2p} and Ti_{3d} states. The conduction band ranges from 0.4 to 5.8 eV, which is mainly contributed by Ti_{2p} and Ti_{3d} energy states. After that, very little contribution is given by Ti_{1s} .

3.3 Dielectric Properties

After simulation and proper calculation of electronic properties, we further go for calculating optical properties using real dielectric constant, $\varepsilon_1(\omega)$, and complex dielectric constant, $\varepsilon_2(\omega)$, from the equation given below:

$$\varepsilon(\omega) = \varepsilon_1(\omega) + i\varepsilon_2(\omega) \quad (2)$$

As TiO₂ is considered as a super photocatalytic material, a detailed investigation is needed to know for its future applications. This can be studied if we know the dielectric properties of it. Again, the imaginary constant ε_2 of the complex dielectric constant can be of two types: one due to intraband transition of the incident electromagnetic (EM) wave and the other due to interband transition of the incident EM wave. For metals, we should go through intraband transition whereas interband is for semiconducting materials. Again, the interband transition is subdivided into two parts: direct band and indirect band transitions. Due to little contribution toward dielectric function, indirect interband transitions can be neglected, although it provides information regarding electron–phonon scattering. The direct interband transitions contribute mainly to the dielectric function (imaginary part ε_2) which can be found out from the momentum matrix elements between occupied and unoccupied wave functions. For evaluating real and imaginary parts of the dielectric function, we used Kubo–Greenwood [16, 30] formalism. Mathematically, it can be represented as

$$\chi_{ij}(\omega) = -\frac{e^2\hbar^4}{m^2\varepsilon_0V\omega^2} \sum_{nm} \frac{f(E_m) - f(E_n)}{E_{nm} - \hbar\omega - i\hbar\Gamma} \prod_{nm}^i \prod_{mn}^i \quad (3)$$

where

\prod_{nm}^i is the i th component of the dipole matrix element between state n , m , V is the volume, Γ is the broadening, and f is the fermi function. The dielectric response coefficients such as the relative dielectric constant (ε_r), polarizability (α), and optical conductivity (σ) are related to susceptibility as

$$\left. \begin{aligned} \varepsilon_r(\omega) &= (1 + \chi(\omega)), \\ \alpha(\omega) &= V\varepsilon_0\chi(\omega), \\ \sigma(\omega) &= -i\omega\varepsilon_0\chi(\omega) \end{aligned} \right\} \quad (4)$$

The real part of dielectric function (ε_1) shows how much a material becomes polarized when an electric field is applied due to creation of electric dipoles in the material, whereas the imaginary part (ε_2) shows the absorption property of a material. If this value is 0, then the material is transparent. When absorption begins, this value becomes nonzero. We have also calculated dielectric constant using LDA which has resulted in a value of 4.3 eV along the zz -axis.

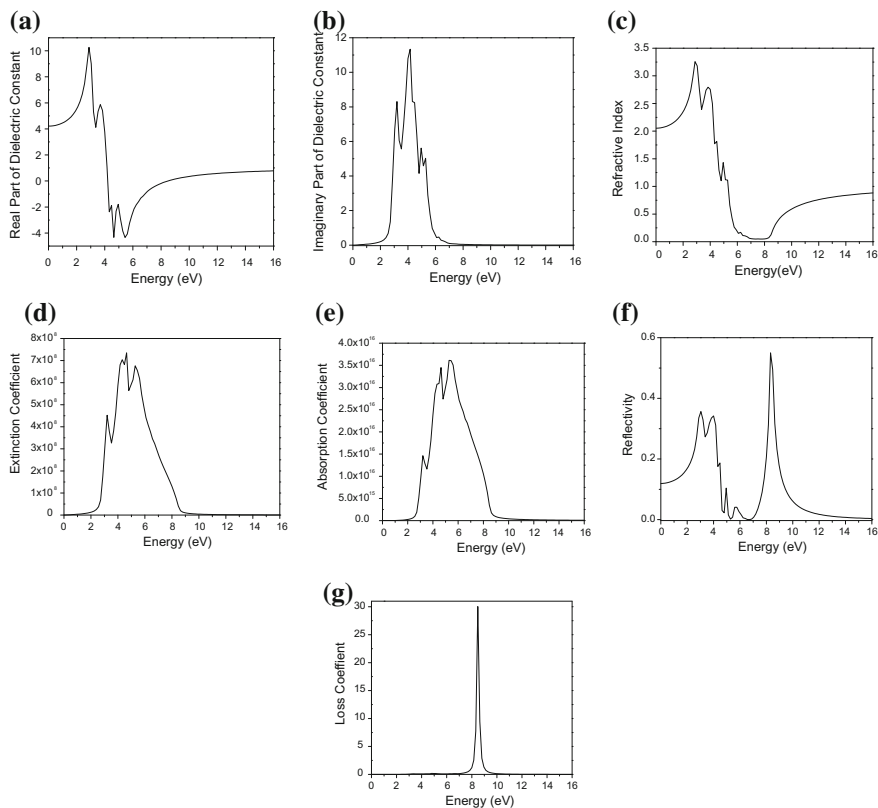


Fig. 5 **a** Calculated real part of dielectric constant of anatase TiO_2 , **b** calculated imaginary part of the dielectric constant of anatase TiO_2 , **c** refractive index curve of anatase TiO_2 , **d** extinction coefficient spectra of anatase TiO_2 , **e** calculated absorption spectra of anatase TiO_2 compound, **f** reflectivity curve of anatase TiO_2 , **g** calculated loss function of anatase TiO_2

From Fig. 5a, we can observe two major peaks. First one which is at 3.05 eV is due to transitions between the O_{2p} orbitals and the t_{2g} conduction band states, whereas the second peak is at 3.5 eV which is due to transitions between the O_{2p} orbitals and the E_g of conduction band states. Due to trapping of charge carrier in a TiO_2 and interstitial states due to presence of oxygen vacancies, both dielectric constants (ϵ_1, ϵ_2) are decreased. In Fig. 5b, we can observe that ϵ_2 has got two peaks. The first peak belongs to the transition between the valence band and 3d orbital (metal states). This peak value is mainly due to excitons or electron-hole pairs and occurs at 3.5 eV. The second or highest peak occurs at 4.5 eV which is due to direct interband transitions as well as direct excitons. This study is also validated by comparing these two peak values with the experimental ones as shown by Chiodo et al. [15]. The calculated values of dielectric constants as obtained from Eqs. (3) and (4) also validate the equation,

$$\varepsilon = \eta^2 \quad (5)$$

where η is the refractive index.

Refractive index (η) is a dimensionless quantity, which describes how light propagates through that medium. It is a function of photon energy, and it can be given as

$$\eta + ik = \sqrt{\varepsilon_r} \quad (6)$$

where k is the extinction coefficient.

From Fig. 5c, it can be seen that the calculated value of refractive index η is 2.05. Also, refractive index lies in the region of the near to infrared region (NIR) which is under the visible region in the optical theory. It can be seen that the η value increases in a nonlinear fashion and reaches to its maximum value in the visible region, then it gradually reduces to a minimum value and finally maintains a reasonable value with the increasing energy. Reported experimental value for η is in Table 1. ($E||_{zz}$), which indicates that the calculated value is approximately 17.67% lower than the experimental value. As per our calculation, light travels much faster than traditional experimental ones and also light absorption increases for lower refractive indices, which indirectly depends on solar energy conversion efficiency.

The extinction coefficient (k) is displayed in Fig. 5d. In physical meaning, the k tells about how various substances absorb the light wavelength. So, we will get similar characteristics for k and absorption coefficient (α). It is found that the value is less than 1.5 eV for zero oscillation when the value of k is very small, the material is considered to be transparent. Above 1.5 eV, k rises to its global maximum value at 4.9 eV and then gradually falls to its minimum value at around 10 eV. So for $1.5 \text{ eV} < k < 10 \text{ eV}$, material is behaving as transparent.

The absorption coefficient (α) provides important information regarding maximum solar energy conversion efficiency. It also describes how far a light with a specific energy or wavelength can travel before being absorbed. For anatase TiO_2 , the absorption coefficient starts rising from 2.5 eV up to a value at 5.5 eV approximately and then decreases gradually to a value near to 11.8 eV and after 12 eV no absorption happens as shown in Fig. 5e. As we know that the more absorption value more is the electrons penetrated into TiO_2 by capturing large number of electrons fall on it. So, for any semiconductor, it is advantageous to have more absorption coefficient.

Figure 5f shows the characteristic plot of reflectivity $R(\omega)$ versus energy. The reflectivity of anatase TiO_2 is calculated using real and imaginary part of dielectric tensor using the formula as given in Jana et al. [31]. As it is apparent from the Fig. 4f, it is seen that $R(\omega)$ increase as the energy increases in the region from 0 to 4 eV and then gradually reduces to 0 eV at about 7 eV which is coming under near to ultraviolet region (visible region). Again it sharply increases to its peak value at around 8.2 eV and then sharply falls to its minimum value at around 10 eV. The reason may be due to the inaccuracy of real dielectric constant $\varepsilon_1(\omega)$ curve in this range by Kramers–Kronig [30] conversion.

Figure 5g shows the energy loss function for a pristine a-TiO₂. It explains how much energy loss occurs when a fast electron traverses through the material. In quantum physics, it can be defined as the bulk plasma frequency ω_p , which occurs when the imaginary dielectric constant $\varepsilon_2 < 1$ and real dielectric constant $\varepsilon_1 = 0$ [23]. The loss spectra are much weaker in the lower energy regime; however, it becomes significant at around 7 eV and continues up to 11 eV. The instant at which maximum loss occur is at around 8.5 eV, which corresponds to plasmon energy ($\hbar\omega_p$) of the TiO₂ semiconductor. The characteristics observed below 8 eV are due to interband transitions, whereas the peak in the characteristics plot after 8 eV corresponds to bulk plasmon peaks associated with collective charge excitons. Thus, we can say that oscillations are formed due to valence electrons linked with plasmon peaks [32].

4 Summary

In summary, we performed calculations on structural, electronic, and dielectric properties of a-TiO₂ material using OLCAO basis sets under the framework of DFT. We compared all the results with previously calculated LDA works as well as plane wave results and found a very close result. The calculated lattice parameters of this binary compound are in good agreement with experimental data with error of <1%. Moreover, we have investigated the band structure which is closer to the experimental value of LDA. We have also studied DOS in detail to understand the anatase TiO₂. Further, we have performed the calculations of the frequency-dependent optical properties within the dipole approximation. It has been observed that the dielectric functions agree with experimental values in case of anatase-TiO₂ with a minimal error. This error will further decrease if better optimization algorithm is used.

References

1. M Landmann, E Rauls and W G Schmidt, The electronic structure and optical response of rutile, anatase and brookite TiO₂, *J. Phys.: Condens. Matter* 24 195503, pp. 1–6, 2012.
2. H Tang, F Levy, H Berger, and P E Schmid, Urbach tail of anatase TiO₂, *Phys. Rev. B*, vol. 52, no- 11, pp. 7771 – 7774, 1995.
3. Wan-Jian Yin, Shiyong Chen, Ji Hui Yang, Xin-Gao Gong, Yanfa Yan, and Su-Huai Wei, Effective band gap narrowing of anatase TiO₂ by strain along a soft crystal direction, *Appl. Phys. Lett.*, vol. 96, issue- 22, pp. 1–3, 221901.
4. F Izumi and Y Fujiki, *Bull. Chem. Soc. Jpn.* Vol. 49, 709, 1976.
5. G. D. Davtyan, *Sov. Phys. Crystallogr.*, vol. 21, 499, 1976.
6. G. D. Davtyan, V. S. Grunin, and V. A. Ioffe, *Sov. Phys. Semicond.*, Vol. 11, 1299, 1977.
7. L. Forro, O. Chauvet, D. Emin, L. Zuppiroli, H. Berger, and F. Levy, High mobility n-type charge carriers in large single crystals of anatase (TiO₂), *J. Appl. Phys.*, vol.- 75 (1), pp. 633–635, 1994.
8. Mazmira Mohamad, Bakhtiar Ul Haq, R. Ahmed, A. Shaari, N. Ali, R. Hussain, A density functional study of structural, electronic and optical properties of titanium dioxide:

- Characterization of rutile, anatase and brookite polymorphs, *Materials Science in Semiconductor Processing*, vol. 31, pp. 405–414, 2014.
9. Shang-Di Mo and W Y Ching, Electronic and optical properties of three phases of titanium dioxide: Rutile, anatase, and brookite, *Phys. Rev. B*, vol. 51, issue. 19, pp. 13023 – 13032, 1995.
 10. V P Zhukov and E V Chulkov., Ab initio approach to the excited electron dynamics in rutile and anatase TiO₂, *J. Phys.: Condens. Matter*, vol. 22, number- 43, 435802, pp. 1–8, 2010.
 11. A. Thilagam, D. J. Simpson, and A. R. Gerson, A first- principles study of the dielectric properties of TiO₂ polymorphs, *J. Phys.: Condens. Matter*, vol. 23, no. -2, 025901, pp. 1–13, 2011.
 12. R. Asahi, Y. Taga, W Mannstadt and A J Freeman, Electronic and optical properties of anatase TiO₂, *Phys. Rev. B* 61, pp. 7459–7465, 2000.
 13. Gong Sai and Liu Bang-Gui, Electronic structures and optical properties of TiO₂: Improved density-functional-theory investigation, *Chin. Phys. B*, vol. 21, no. 5, 057104, pp. 1–7, 2012.
 14. H M Lawler, J. J. Rehr, F. Vila, S. D. Dalosto, E. L. Shirley and Z. H. Levine, Optical to UV spectra and birefringence of SiO₂ and TiO₂: First- principles calculations with excitonic effects, *Phys. Rev. B* 78, 205108, pp. 1–8, 2008.
 15. Letizia Chiodo, Juan Maria Garcia- Lastra, Amilcare Iacomino, Stefano Ossicini, Jin Zhao, Hrvoje Petek and Angel Rubio, Self- energy and excitonic effects in the electronic and optical properties of TiO₂ crystalline phases, *Phys. Rev. B*, vol. 82, issue – 4, 045207, pp.- 1–12, 2010.
 16. W. Y. Ching and Yong-Nian Xu, R. H. French, First-principles investigation of the optical properties of crystalline poly (di-n-hexylsilane), *Phys. Rev. B*, vol. 54, no. – 19, pp. 13546–13550, (1996).
 17. Qi-Jun Liu, Ning-Chao Zhang, Fu-Sheng Liu, and Zheng-Tang Liu, Structural, elastic, electronic and optical properties of various mineral phases of TiO₂ from first-principles calculations, *Phys. Scr.*, vol. 89, no. – 7, 075703, pp. 1–14, 2014.
 18. Lukas Thulin and John Guerra, Calculations of strain-modified anatase TiO₂ band structures, *Phys. Rev B* 77, 195112, pp. 1–5, 2008.
 19. J. David Griffiths, “Introduction to Electrodynamics”, 3rd ed., Prentice Hall, Upper Saddle River, New Jersey, 1999.
 20. Walter A. Harrison, Bond-orbital model and the properties of Tetrahedrally coordinated solids, *Phys. Rev. B*, vol. 8, no. 10, pp. 4487–4498, 1973.
 21. Richard M Martin, “Electronic structure: Basic theory and practical methods”. Cambridge University Press, New York, 2004.
 22. T. Ozaki, Variationally optimized atomic orbitals for large- scale electronic structures, *Phys. Rev. B*, vol. 67, issue- 15, 155108, pp. 1–5, 2003.
 23. Uttam Kumar Chowdhury, Md. Atikur Rahman, Md. Afjalur Rahman, M. T. H. Bhuiyan and Md. Lokman Ali, Ab initio study on structural, elastic, electronic and optical properties of cuprate based superconductor, *Cogent Phys.*, vol. 3:1231361, pp. 1–10, 2016.
 24. F. Birch, *Phys. Rev. B*, vol. 71, pp. 809–824, 1947.
 25. J. P. Perdew & Zunger, *Physical Review B*, vol. 23, pp. 5048–5079, 1981.
 26. T. Zhu and Shang-Peng Gao, The stability, Electronic Structure, and Optical Property of TiO₂ Polymorphs, *J. Phys. Chem. C*, vol. 118, pp. 11385–11396, 2014.
 27. H. J. Monkhorst, J. D. Pack, *Phys. Rev. B*, vol. 13, pp. 5188–5192, 1976.
 28. S. Y. Kim, Simultaneous determination of refractive index, extinction coefficient, and void distribution of titanium dioxide thin film by optical methods, *Appl. Optics*, Vol. 35, No. 34, pp. 6703–6707, 1996.
 29. R. J. Gonzalez and R. Zallen, Infrared reflectivity and lattice fundamentals in anatase TiO₂, *Phys. Rev. B*, vol. 55, no.- 11, pp. 7014–7017, 1997.
 30. M. P. Desjarlais, *Contrib. Plasma Phys.*, vol. 45(3–4), pp. 300–304, 2005.
 31. Debanarayan Jana, Anirban Chakraborti, Li- Chyong Chen, Chun Wei Chen and Kuei-Hsien Chen, First principles calculations of the optical properties of C_xN_y single walled nanotubes, *Nanotechnology*, IOP publishing, vol. 20 175701, pp. 1–12, 2009.
 32. F. Wooten, “Optical Properties of Solids” (Academic Press, New York and London, 1972).

Performance Analysis of a Front High-K Gate Stack Dual-Material Tri-gate SON MOSFET

Pritha Banerjee, Anup Sarkar, Dinesh Kumar Dash
and Subir Kumar Sarkar

Abstract This present work encompasses the analytical modeling of a front high-K gate stack dual-material tri-gate SON MOSFET. By solving the three-dimensional Poisson's equation, the expression for surface potential of the proposed device is obtained. In addition, the electric field of the device is also calculated. The results obtained are compared with the model's single-metal counterpart. The extent of agreement between the analytical results and simulated results obtained from a 3-D device simulator, namely Atlas, Silvaco, is quite good that validates our proposed model.

Keywords Short-channel effects · Tri-gate MOSFET · Gate work function engineering · Hot carrier effect (HCE) · Silicon-on-insulator (SOI) · Silicon-on-nothing (SON)

1 Introduction

Researchers have always aimed at achieving cost-effective, miniaturized, high-speed and low-power-consuming devices for VLSI circuit design. Thus, innovative as well as renovative technologies are adopted to achieve devices with

P. Banerjee (✉) · D. K. Dash · S. K. Sarkar
Department of Electronics and Telecommunication Engineering,
Jadavpur University, 700032 Kolkata, India
e-mail: prithaedu7@gmail.com

D. K. Dash
e-mail: dineshdash123@gmail.com

S. K. Sarkar
e-mail: sksarkar@etce.jdvu.ac.in

A. Sarkar
Women's Polytechnic, Kolkata, India
e-mail: anupsarkar10@rediffmail.com

upgraded performance. In this context, gate work function engineering has always remained a highlighted topic to the researchers as the gate-work-function-engineered structures possess excellent immunity to the major short-channel effects [1]. Many researches on 2-D planar MOSFETs by incorporating the above technology have been published [2]. But it has always been a prime objective to achieve more and more control of the channel by the gate which could no longer be achieved with the planar MOSFETs.

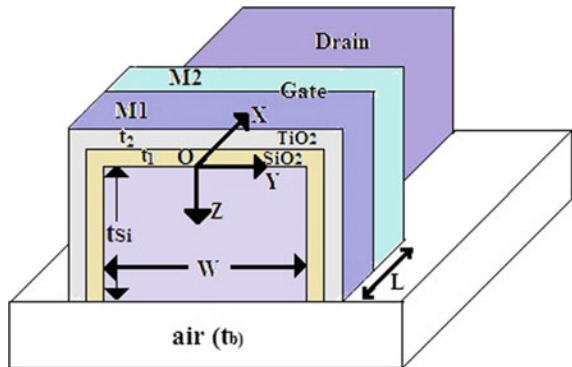
Intel's recently introduced tri-gate MOSFETs show a much better control over the channel by the gate. Tri-gate structures come with 37% speed enhancement, and their power consumption is below 50% as compared to the planar MOSFETs [3].

We have considered a dual-material tri-gate MOSFET in the current research so as to incorporate gate work function engineering to achieve better capability of suppressing the SCEs. We have also incorporated the SON technology to achieve an upgraded circuit speed [4] and a front high-k gate stack structure that improves carrier mobility. The results obtained from analytical modeling are verified using simulation data obtained from Atlas.

2 Proposed Structure

In Fig. 1, the 3-D view of the proposed model has been shown. The channel length is L . Channel width and thicknesses are, respectively, w and t_{Si} . t_2 is the thickness of the high-k dielectric, and thickness of the interfacial SiO_2 layer is t_1 . The effective oxide thickness is t_f . Thickness of the buried air layer is t_b . The uniform channel doping considered is N_a , and the source/drain doping concentration considered is N_d . The work functions of the metals M_1 and M_2 are ϕ_{M1} and ϕ_{M2} , respectively. Parameters used for calculation and simulation are given in Table 1.

Fig. 1 3-D cross-sectional view of a front high-K gate stack dual-material tri-gate SON MOSFET



2.1 Analytical Modeling

We need to consider 3-D Poisson's equation in order to obtain an expression for surface potential of the device. It is assumed that under zero bias, the channel is fully depleted, influence of the charge carriers and that of the impurity density are uniform on the electrostatics of the channel [5].

The channel is divided into two regions, region 1 and region 2 for the ease of calculation.

$$\frac{\partial^2 \phi_j(x, y, z)}{\partial x^2} + \frac{\partial^2 \phi_j(x, y, z)}{\partial y^2} + \frac{\partial^2 \phi_j(x, y, z)}{\partial z^2} = \frac{qN_a}{\epsilon_{Si}} \quad (1)$$

where $j = 1$ for region 1 defined by the boundaries ($0 \leq x \leq L_1$, $0 \leq z \leq t_{Si}$, $-w/2 \leq y \leq w/2$) and $j = 2$ for region 2 defined by the boundaries ($L_1 \leq x \leq L$, $0 \leq z \leq t_{Si}$, $-w/2 \leq y \leq w/2$). Here, ϵ_{Si} is the permittivity of silicon channel, and q is the electronic charge. The axis considered along the channel length is x -axis, the axis considered along the channel width is y -axis, and the axis considered along the channel thickness is the z -axis.

As we have considered a short-channel MOSFET, we require to take into account the parabolic potential approximation [6] between the lateral gates which is as follows:

$$\phi_j(x, y, z) \approx a_{0j}(x, z) + a_{1j}(x, z)y + a_{2j}(x, z)y^2 \quad (2)$$

$j = 1, 2$ for region 1 and 2, respectively.

The potential distribution is parabolic in the z -direction for low drain voltages, [7]. At $y = 0$, we have

$$\phi_j(x, 0, z) = a_{0j}(x, z) = \phi_{Sj}(x) + C_{1j}(x)z + C_{2j}(x)z^2 \quad (3)$$

$\phi_{Sj}(x)$ being the surface potential for regions 1 and 2. Because of the symmetry in y -direction we have,

$$a_{1j}(x, z) = 0 \quad (4)$$

Therefore,

$$a_{2j}(x, z) = (4/w^2)(\phi_{Sj}(x) - a_{0j}(x, z)) \quad (5)$$

In order to solve Eq. 1, we need to take into consideration the boundary conditions mentioned below,

$$\phi_{s1}(0) = V_{bi} \quad (6)$$

$$\phi_{s2}(L) = V_{bi} + V_{ds} \quad (7)$$

Here toward the source side, the built-in potential is V_{bi} and V_{ds} is the drain-to-source voltage.

$$\left. \frac{d\phi_j(x, y, z)}{dz} \right|_{y=0, z=0} = \frac{\epsilon_{Ox}}{\epsilon_{Si} t_f} \left(\phi_{Sj}(x) - V'_{gsj} \right) \quad (8)$$

$$t_f = t_1 + t_2(e_1/e_2);$$

where the dielectric constant of SiO_2 layer is e_1 and e_2 is the dielectric constant of the oxide placed above SiO_2 .

Here, $V'_{gsj} = V_{gsj} - V_{fbj}$, V_{fbj} is the front interface flat-band voltage of region j under M_j , $V_{fbj} = \phi_{Mj} - \phi_{Si}$, ϕ_{Si} is the work function of Si.

$$\left. \frac{d\phi_j(x, y, z)}{dz} \right|_{y=0, z=t_{si}} = \frac{\epsilon_{air}}{\epsilon_{Si} t_b} (V'_{sub} - \phi_{Sbj}(x)) \quad (9)$$

ϕ_{Sbj} is the potential at the back interface. $j = 1, 2$.

$V'_{sub} = V_{sub} - V_{fbb}$, where V_{sub} is the substrate bias voltage and is kept fixed at 0 V, V_{fbb} is the channel-back interface flat-band voltage.

Using Eqs. (2) and (8),

$$C1j(x) = \frac{\epsilon_{Ox}}{\epsilon_{Si} t_f} \left(\phi_{Sj}(x) - V'_{gsj} \right) \quad (10)$$

Using Eqs. (2), (9), and (10) we get,

$$C2j(x) = \frac{V'_{sub} - \phi_{S1}(x) \left(1 + \frac{C_{Ox}}{C_{Si}} + \frac{C_{Ox}}{C_{air}} \right) + V'_{gs1} \left(\frac{C_{Ox}}{C_{Si}} + \frac{C_{Ox}}{C_{air}} \right)}{t_{Si}^2 \left(1 + 2 \frac{C_{Si}}{C_{air}} \right)} \quad (11)$$

C_{Ox} is the oxide capacitance, C_{Si} is the Si channel capacitance, and C_{air} is the buried air layer capacitance.

Now, for region 1, the 3-D potential distribution is

$$\phi_1(x, y, z) = \phi_{S1}(x)C + D \quad (12)$$

where

$$C = 1 + g_1z - g_2z^2 - g_3zy^2 + g_4z^2y^2 D = -g_5z + g_6z^2 + g_7zy^2 - g_8z^2y^2$$

Now, for region 2, the 3-D potential distribution is

$$\phi_2(x, y, z) = \phi_{S2}(x)E + F \quad (13)$$

By calculation, $E = C$,

$$F = -g'_5z + g'_6z^2 + g'_7zy^2 - g'_8z^2y^2 \quad (14)$$

Constants g'_5 , g'_6 , g'_7 , and g'_8 are given in Appendix. Using Eqs. (12) and (13) in Eq. 1,

$$\frac{d^2\phi_{Sj}(x)}{dx^2} - \alpha\phi_{Sj}(x) = \beta_j \quad (15)$$

$$\alpha = \frac{2g_2 + 2g_3z - 2g_4z^2 - 2g_4y^2}{C},$$

$$\beta_1 = \frac{qN_a}{C\epsilon_{Si}} + \frac{-2g_6 - 2g_7z + 2g_8z^2 + 2g_8y^2}{C}$$

$$\beta_2 = \frac{qN_a}{C\epsilon_{Si}} + \frac{-2g'_6 - 2g'_7z + 2g'_8z^2 + 2g'_8y^2}{C}$$

Considering Eq. (15), the general solutions found are given by

$$\phi_{S1}(x) = M_1e^{\eta x} + M_2e^{-\eta x} - \sigma_1 \text{ for region 1}$$

Here, $\sigma_1 = \frac{\beta_1}{\alpha}$. The general solution to Eq. (15) is given by

$$\phi_{S2}(x) = M_3e^{\eta(x-L_1)} + M_4e^{-\eta(x-L_1)} - \sigma_2 \text{ for region 2}$$

$$\text{Here, } \sigma_2 = \frac{\beta_2}{\alpha}$$

Constants M_1 , M_2 , M_3 , and M_4 can be evaluated using the following boundary conditions. Surface potentials and electric flux at the interface of the two different materials M1 and M2 must be continuous [8].

Hence, $\phi_{S1}(L1) = \phi_{S2}(L1)$ and

$$\left. \frac{\partial\phi_{S1}(x)}{\partial x} \right|_{x=L1} = \left. \frac{\partial\phi_{S2}(x)}{\partial x} \right|_{x=L1}$$

The electric field which is calculated for the entire channel is expressed as

$$E = -\frac{d\phi_S(x)}{dx}$$

Table 1 Value of the parameters used in analytical modeling and simulation

Parameter	t_1	t_2	t_{Si}	t_b	N_a
Values	1 nm	2 nm	10 nm	50 nm	$1 \times 10^{20} \text{m}^{-3}$
Parameter	N_d		ϕ_{M1}	ϕ_{M2}	w
Values	$5 \times 10^{27} \text{m}^{-3}$		4.8 eV	4.6 eV	5 nm

The subthreshold swing [9] (in mV/decade) is

$$S = 2.3 V_t \left[\frac{d\phi_{Smin}}{dV_{GS}} \right]^{-1} \tag{16}$$

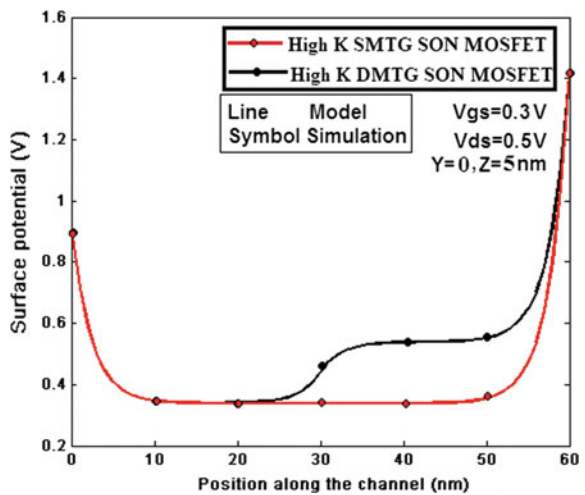
where ϕ_{Smin} is the minimum surface potential.

3 Results and Discussions

The total channel length considered is 60 nm. The ratio of L1:L2 as considered in calculation and simulation is 1:1.

Figure 2 presents the surface potential variation along the channel length for a front high-K gate stack single-material tri-gate SON MOSFET and front high-K gate stack double-material tri-gate silicon-on-nothing MOSFET. It can be observed that our proposed model possesses a single step profile which allows a high immunity toward the drain-induced barrier lowering (DIBL) but the single-metal structure does not possess any such step profile and hence it cannot battle the major

Fig. 2 Variation of surface potential along the position of the entire channel for a front high-K gate stack single-metal tri-gate and a front high-K gate stack double-metal tri-gate silicon-on-nothing MOSFETs



SCEs. A drain voltage fluctuation can affect the potential minimum of the single-metal structure and makes it highly prone to DIBL.

Figure 3 presents the variation of electric field along the channel length for front high-K gate stack single-material tri-gate SON MOSFET and front high-K gate stack double-material tri-gate SON MOSFET. The comparative study between the two structures shows that at the drain side the electric field is much diminished for our proposed model compared to its single-metal counterpart. This results in reduced hot carrier effect (HCE) in our proposed model. Figure 4 presents the subthreshold swing variation of our proposed model along the position of the channel for different oxides placed above the interfacial layer of SiO₂. It is clearly evident that our proposed model with highest dielectric value of 40ε₀ (i.e., TiO₂) has the best

Fig. 3 Variation of electric field along the position of the channel for front high-K gate stack single-metal tri-gate and front high-K gate stack double-metal tri-gate SON MOSFETs

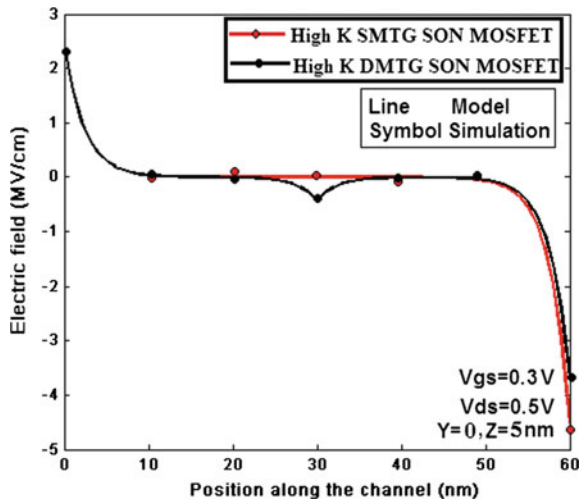
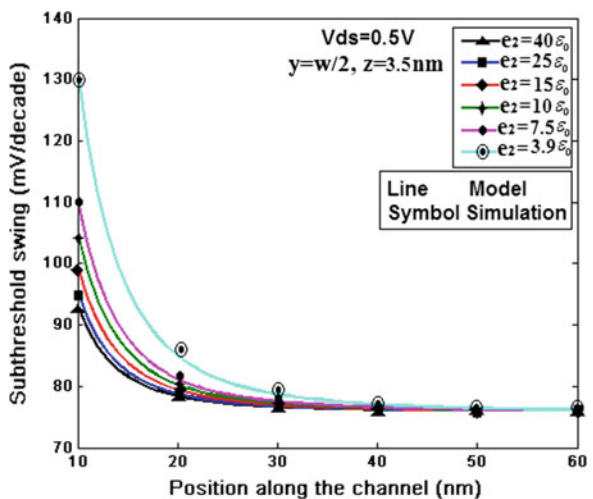


Fig. 4 Variation of subthreshold swing along the position of the channel for the proposed model for different oxides placed above interfacial SiO₂ layer



characteristic of subthreshold swing compared to the lower k-value oxides. The analytical results of this section match well with the simulated data [10].

4 Summary/Conclusion

The present work highlights the effect of gate work function engineering and high-k incorporation in a tri-gate SON MOSFET. The proposed model is found to exhibit an upgraded immunity toward the various short-channel effects like DIBL, HCE, and subthreshold slope characteristics. Also a comparative study of the different device features like surface potential and electric field has been carried out in both front high-K gate stack DMTG SON MOSFET and front high-K gate stack SMTG SON MOSFET. Our proposed model is found to possess an upgraded performance compared to its SMTG counterpart. An appreciable agreement between the analytical and simulated values evident the validity and superiority of our proposed model.

Acknowledgements Pritha Banerjee thankfully acknowledges the financial support obtained from UGC vide file no. 43-293/2014 (SR) dated 29.12.2015.

Appendix

$$g_1 = \frac{\epsilon_{Ox}}{\epsilon_{Si} t_f}, g_2 = \frac{\left(1 + \frac{C_{Ox}}{C_{Si}} + \frac{C_{Ox}}{C_{air}}\right)}{t_{Si}^2 \left(1 + \frac{2C_{Si}}{C_{air}}\right)}, g_3 = \frac{4}{w^2} g_1, g_4 = \frac{4}{w^2} g_2$$

$$g_5 = \frac{\epsilon_{Ox} V'_{gs1}}{\epsilon_{Si} t_f}, g_7 = \frac{4}{w^2} g_5, g_8 = \frac{4}{w^2} g_6, g'_5 = \frac{\epsilon_{Ox} V'_{gs2}}{\epsilon_{Si} t_f}, g'_7 = \frac{4}{w^2} g'_5$$

$$g_6 = \frac{V'_{Sub} + V'_{gs1} \left(\frac{C_{Ox}}{C_{Si}} + \frac{C_{Ox}}{C_{air}}\right)}{t_{Si}^2 \left(1 + \frac{2C_{Si}}{C_{air}}\right)}, g'_6 = \frac{V'_{Sub} + V'_{gs2} \left(\frac{C_{Ox}}{C_{Si}} + \frac{C_{Ox}}{C_{air}}\right)}{t_{Si}^2 \left(1 + \frac{2C_{Si}}{C_{air}}\right)}$$

References

1. Sourav Naskar and Subir Kumar Sarkar, "Quantum Analytical Model for Inversion Charge and Threshold Voltage of Short-Channel Dual-Material Double-Gate SON MOSFET", IEEE Trans. Electron Devices, Vol. 60, NO. 9, September 2013, Pages: 2734–2740.
2. Sanjoy Deb, N. Basanta Singh, Nurul Islam, and Subir Kumar Sarkar, "Work Function Engineering With Linearly Graded Binary Metal Alloy Gate Electrode for Short-Channel SOI MOSFET, IEEE Trans. Nanotech., VOL. 11, NO. 3, MAY 2012

3. Mayur Bhole, Aditya Kurude, Sagar Pawar, "International Journal Of Engineering Sciences & Researchtechnology", Vol.2, No.10, pp-2670–2675, October, 2013
4. Ekta Goel, Sanjay Kumar, Kunal Singh, Balraj Singh, Mirgender Kumar, and Satyabrata Jit, "2-D Analytical Modeling of Threshold Voltage for Graded-Channel Dual-Material Double-Gate MOSFETs", IEEE Trans. Electron Devices, VOL. 63, Issue: 3, Pages: 966–973, March 2016.
5. Bibhas Manna; Saheli Sarkhel; Nurul Islam; S. Sarkar; Subir Kumar Sarkar, "Spatial Composition Grading of Binary Metal Alloy Gate Electrode for Short-Channel SOI/SON MOSFET Application", IEEE Trans. on Electron Devices, Volume: 59, Issue: 12, Pages: 3280–3287, Year: December 2012
6. K. K. Young, "Short-channel effect in fully depleted SOI MOSFETs", IEEE Trans. on Electron Devices, Volume: 36, Issue: 2, Pages: 399–402, Year: 1989.
7. Hamdam Ghanatian, Seyed Ebrahim Hosseini, "Analytical modeling of subthreshold swing in undoped trigate SOI MOSFETs", J Comput Electron, pp. 508–515, April 2016.
8. [8] G. V. Reddy and M. J. Kumar, —A new dual-material double-gate (DMDG) nanoscale SOI MOSFET "Two dimensional analytical modeling and simulation", IEEE Trans. Electron Devices, vol. 4, no. 2, pp. 260–268, Mar. 2005.
9. Te-Kuang Chiang, "A Quasi-Two-Dimensional Threshold Voltage Model for Short-Channel Junctionless Double Gate MOSFETs", IEEE Trans. on Electron Devices, vol. 59, no. 9, pp. 2284–2289, Sept. 2012.
10. ATLAS User Manual: Silvaco International, Santa Clara, CA (2015)

Comparative Study of n-ZnO/SiO₂/p-Si and Pd/n-ZnO/SiO₂/p-Si Thin Film-Based H₂ Sensor Fabricated by Sol-gel Process

Sreeparna Barua, Anup Dey, Subhashis Roy
and Subir Kumar Sarkar

Abstract In this paper, Pd modified and unmodified ZnO thin film sensors were prepared by sol-gel process for detection of hydrogen (H₂) gas. Spin-coating (1200 rpm, duration 10 s) method was used to deposit the sol on above the SiO₂/p-Si substrate. The surface morphology was analyzed by field emission scanning electron microscopy (FESEM). The gas sensing characteristic was measured by 50–250 °C operating temperature and 100–3000 ppm H₂ gas concentration. Maximum sensitivity was found 74% at operating temperature 150 °C for 1000 ppm of H₂ gas concentration. Stability of Pd modified and unmodified ZnO thin film sensors has been measured at operating temperature 150 °C. Pd modified ZnO thin film sensor with Ag contact was found highest sensitivity compared to the unmodified ZnO thin film sensor with Ag contact.

Keywords Sol-gel · Spin coating · ZnO thin film · Pd modified H₂ sensor

1 Introduction

Hydrogen (H₂) is expected to supplant hydrocarbons and also becomes “the common renewable energy source of the future.” Hydrogen is an odorless, colorless, invisible, and flammable gas. It is light and has a large diffusion coefficient of

S. Barua (✉) · A. Dey · S. Roy · S. K. Sarkar
Department of Electronics and Telecommunication Engineering,
Jadavpur University, 188, Raja S. C. Mallick Road, Kolkata 700032, India
e-mail: sreeparna.ba@gmail.com

A. Dey
e-mail: anupetce@gmail.com

S. Roy
e-mail: subhashisaec@gmail.com

S. K. Sarkar
e-mail: su_sircir@yahoo.co.in

0.61 cm²/s in air. It has a wide flammable range, which is 4–75% by volume and the lowest limit of H₂ in air that causes explosion is ~5%. Therefore, to avoid the risk, there is a need for highly sensitive, selective, and fast H₂ sensor. To control the energy conversion process, different types of hydrogen sensor for each processing unit will be required. Hydrogen is a potential source of energy of future and is used in fuel cell, petroleum, H₂ engine cars, chemical, and semiconductor industries. Zinc oxide (ZnO) is n-type semiconducting oxides with a hexagonal wurtzite crystal structure related to space group P63mc and wide direct band gap (3.37 eV at room temperature) and high exaction binding energy (60 m eV). ZnO is one of the most widely used materials due to its fast response with high sensitivity toward different gases [1–4]. ZnO nanostructures are used as gas sensors and biosensors in different genomics, proteomics, diagnosis, and pharmaceuticals applications due to the possibility of integration in biochips. ZnO has higher breakdown voltage, so ability to sustain large electrical field. In the hydrogen sensing case, modifying metal oxides especially ZnO by metal additives such as Pt, Pd, Ag, or Au via different techniques are under intensive investigations [5, 6]. It is recognized that gas sensitivity depends on the high surface area and porosity which are both affected by preparation method. Earlier different various ZnO nanostructures growth techniques have been reported in literature, such as chemical vapor deposition (CVD), wet chemical process, metal-organic vapor phase epitaxy, pulsed laser deposition, molecular beam epitaxy, electrochemical deposition, thermal evaporation, spray pyrolysis, sol-gel, and sputtering. Among various techniques, sol-gel is a suitable method for preparing nanoparticles, and it is suitable for room temperature, and the cost is very low [7, 8]. High-quality metal oxide films grown and deposited on Si substrate, and it has great importance for integration of metal oxide-based devices with current Si-based IC technology. Hydrogen gas is reducing agent for an n-type ZnO layer and increasing its conductivity on interaction. As the hydrogen dissociates on the surface of the sensor, it injects electrons in the ZnO selective layer. As an outcome, the conductivity between the electrodes increase with increase in sensitivity as hydrogen is exposed to the device. Sensors based on resistivity change of palladium upon hydrogen attract a wide interest, due to their potential high sensitivity and selectivity to the gas. In this paper, Pd modified and unmodified ZnO thin film sensors were prepared by sol-gel process for detection of hydrogen (H₂) gas. Spin-coating method was used to deposit the sol on above the SiO₂/p-Si substrate. Different sensitivity has been measured for different hydrogen gas concentrations at operated temperature between 50 to 250 °C.

2 Thin Film Preparation

ZnO thin film was prepared by simple and low-cost deposition sol-gel process by using zinc acetate dehydrate and isopropyl alcohol at the ratio of 6 gm/50 cc. Then, the mixture was placed in dry for next 2 days. After that, prepared sol was

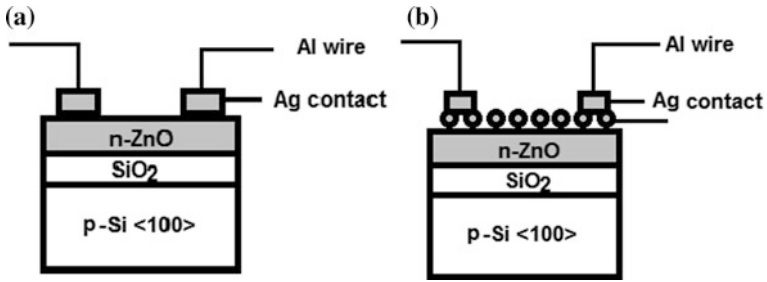


Fig. 1 Ag/n-ZnO/SiO₂/p-Si and Ag/Pd/n-ZnO/SiO₂/p-Si thin film devices **a** unmodified and **b** modified

transferred on oxidized Si substrate by spin-coating method (1200 rpm, duration 10 s) and dried at 150 °C for 30 min. To get the ZnO nanocrystalline thin film, the film was again annealed at 350 °C for 1 h. The proposed device structures are shown in the Fig. 1.

3 Experimental Results

Figure 2 shows the experimental setup used for gas sensing measurement of n-ZnO and Pd/n-ZnO thin film sensors. We used N₂ as a reference gas which directly flows to the mixing chamber at certain percentage of concentration. The proposed sensor device was placed at sensing chamber, and the temperature was varied from 50 to 250 °C. Without gas and with gas resistance value was measured by using PC interface.

Fig. 2 Experimental setup for ZnO-based thin film gas sensor for detection of H₂ gas



4 Result and Discussion

The sensitivity of the ZnO thin films for detection of H₂ gas was measured by

$$\frac{I_g - I_a}{I_a} \times 100\%$$

where I_a is sample current in air (i.e., at 0% hydrogen gas concentration), and I_g is sample current at hydrogen gas concentration.

Figure 3 shows relationship between sensitivity and operating temperature of unmodified and Pd modified ZnO thin film sensors with Ag contact for detection of H₂ gas. The sensitivity reaches the highest peak (74%) at operating temperature 150 °C, and after further increasing the temperature, the sensitivity decreases due to mechanism of gas adsorption and desorption process.

Figure 4 shows sensitivity versus hydrogen gas concentration plot at operating temperature 150 °C. It was shown that the sensitivity increased with the increased of hydrogen gas concentration. The sensitivity peak reached maximum (74%) with 1% hydrogen gas concentration; after that, the sensitivity was saturated with increased the gas concentration.

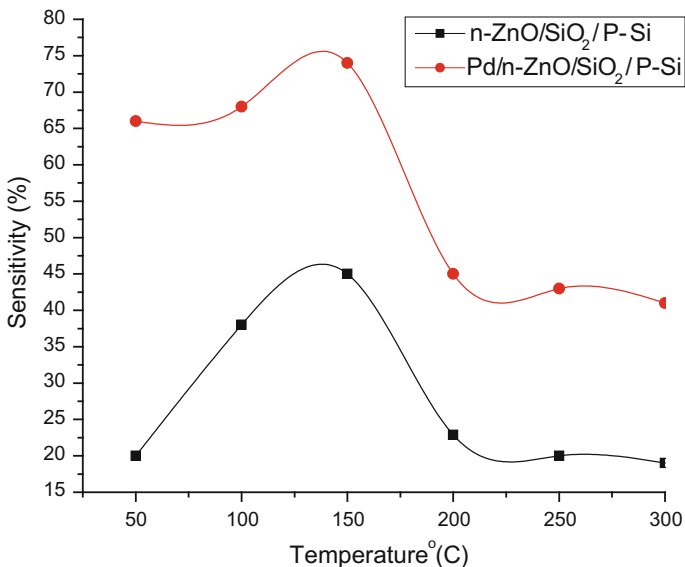
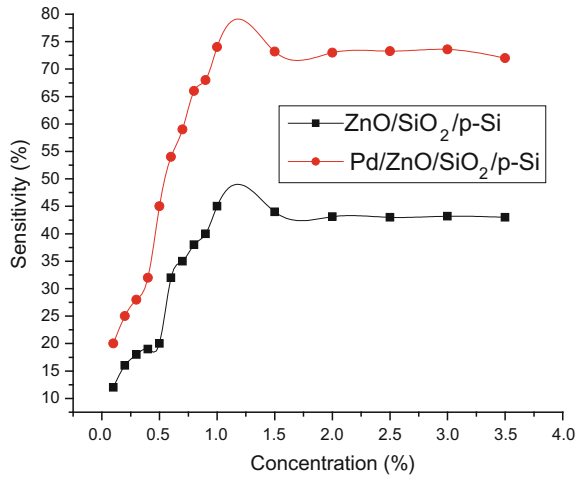


Fig. 3 Sensitivity versus operating temperature plot for unmodified and Pd modified ZnO thin film sensors at 1% hydrogen gas

Fig. 4 Sensitivity versus hydrogen gas concentration plot for unmodified and Pd modified ZnO thin film sensors



5 Surface Morphology

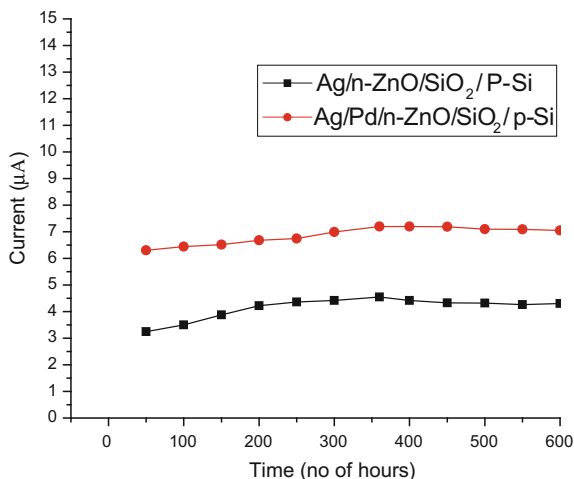
Figure 5 shows the field emission scanning electron microscopy picture of Pd modified ZnO-based thin film sensor at the annealed temperature 350 °C. FESEM picture suggests that sol-gel grown Pd modified ZnO thin films are deposited on oxidized Si substrate with different nanocrystalline grain size (uscale 500 nm).

Figure 6 shows stability plot of Ag/n-ZnO/SiO₂/p-Si and Ag/Pd/n-ZnO/SiO₂/p-Si sensor at operating temperature 150 °C. The stability has been measured up to 600 h (25 days), and it measured that Pd modified ZnO thin film sensor shown that stable current with compared to the unmodified ZnO thin film sensor.



Fig. 5 FESEM picture of Pd/n-ZnO thin film sensor at operating temperature 350 °C

Fig. 6 Stability plot of n-ZnO and pd/n-ZnO thin film sensors for detection of H₂ at operating temperature 150 °C



6 Conclusion

n-ZnO and Pd modified n-ZnO-based thin film gas sensors were fabricated for hydrogen gas sensing application. Sol-gel process is used to prepare the nanocrystalline thin film ZnO by using zinc acetate dehydrate and isopropyl alcohol at the ratio of 6 gm/50 cc. Prepared sol was deposited on above the oxidized Si substrate by spin-coating method at 1200 rpm, and the duration of time is 10 s. Hydrogen gas sensitivity was measured at the temperature range of 50–250 °C and 100–3000 ppm gas concentration. It was found that at operating temperature 150 °C, the prepared Pd modified n-ZnO thin film sensor has the highest sensitivity (74%) as compared to the unmodified n-ZnO thin film sensor.

Acknowledgements One of the authors thankfully acknowledges the financial support for this research work obtained from UGC UPE Phase II (Device and System Ref. No.-R-11/108/16) sponsored project. The authors would like to thank prof. Kalyan Kumar Chattopadhyay (Director, School of Material Science and Nanotechnology, Jadavpur University, India) for FESEM facility.

References

1. Higuchi T, Nakagomi Sh, Kokubun Y. Field effect hydrogen sensor device with simple structure based on GaN. *Sens Actuators B Chem* 2009; **140**:79–85.
2. Tsai TH, Chen HI, Lin KW, Hung CW, Hsu CH, Chen LY, et al. Comprehensive study on hydrogen sensing properties of a Pd–AlGaN based Schottky diode. *Int J Hydrogen Energy* 2008; **33**:2986–92.
3. X. L. Cheng, H. Zhao, L.H. Huo, S. Gao, J.G. Zhao “ZnO nanoparticulate thin film: preparation, characterization and gas-sensing property”, *Sensors Actuators B*, **102**, 248–252 (2004).

4. A. Dey, B. Kantha, S.K. Sarkar “Sol–gel grown Pd modified WO₃ thin film based methanol sensor and the effect of Annealing temperatures”. *Microsystem Technologies* <https://doi.org/10.1007/s00542-016-2841> (2016).
5. Tong Maosong, Dai Guorui, Gao Dingsan. WO₃ thin film sensor prepared by sol-gel technique and its low-temperature sensing properties to trimethylamine. *Materials Chemistry and Physics* **69** (2001) 176–179.
6. Ippolito SJ, Kandasamy S, Kalantarzadeh K, Wlodarski W. Hydrogen sensing characteristics of WO₃ thin film conductometric activated by Pt and Au catalysts. *Sens Actuators B Chem* 2005b; **108**:154–8.
7. B.P.J.D. Costello, R. J. Ewen, N. Guernion, N. M. Ratcliffe “Highly sensitive mixed oxide sensors for the detection of ethanol”, *Sensor Actuators*, **87**, 207–210 (2002).
8. D. F. Paraguay, M. Miki-Yoshida, J. Morales, J. Solis, L. W. Estrada “Influence of Al, In, Cu, Fe and Sn dopants on the response of thin film ZnO gas sensor to ethanol vapor”, *Thin Solid Films*, **373**, 137–140 (2000).

Complementary Energy Path Adiabatic Logic-Based Adder Design in 32 Nm FinFET Technology

Suresh Kumar Pittala and A. Jhansi Rani

Abstract In most of digital signal processing application, processing elements like adders form the basic building blocks of filtering and analysis of signals. CMOS-based adder circuits suffer from several problems like leakage current and threshold voltage variations. In this paper, a novel design of an adiabatic FinFET-based low-power processing element using complementary energy path adiabatic logic (CEPAL) in 32 nm technology is proposed. The proposed processing elements are CEPAL–FinFET-based adiabatic half adder and full adder. FinFET-based circuits are designed for deep submicron VLSI designs in signal and image applications. The FinFET design has low power consumption when combined with adiabatic design which improves scalability and design flexibility. The proposed FinFET–CEPAL-based adders show a considerable power reduction and low energy consumption with favorable performance improvement. Extensive circuit simulation has been carried out with HSPICE using predictive technology model in 32 nm FinFET technology. The analytical results validate that the proposed design exhibits the energy saving compared to standard bulk CMOS design.

Keywords Low power · Energy efficient · FinFET · Processing elements
Adiabatic · CEPAL

S. K. Pittala (✉)
Acharya Nagarjuna University, Nagarjuna Nagar,
Guntur 522 510, Andhra Pradesh, India
e-mail: dr.sureshkumarpittala@gmail.com

A. Jhansi Rani
Department of ECE, Velagapudi Ramakrishna Siddhartha Engineering College,
Vijayawada, India
e-mail: jhansi9rani@gmail.com

1 Introduction

Tremendous improvement of technology helped new handheld devices to emerge in the market as huge volumes and with advanced features. The operating frequency of these devices increased few orders of magnitude when compared to bulk devices. Even though bulk CMOS technologies have been the major centerpiece for decades, it suffers from short channel effects (SCEs), random dopant fluctuation (RDF), and undeniable loss of energy. FinFET reduces the SCEs and RDF effects. The depleted channel is advantages to remove these issues. In the literature, several techniques like super-thresholding [1], multi-thresholding [2], power gating [3], self-controllable voltage level (SVL) [4], and adiabatic logic [5–16] circuits have been proposed in the past. This research paper has been articulated with six sections. Section 1 is introduction part, while Sects. 2 and 3 present CEPAL- and FinFET-based circuits and design approach of CEPAL-based FinFET processing elements. The proposed processing elements are described in Sect. 4, followed by results and discussion and conclusion in Sects. 5 and 6, respectively.

2 Literature Review

In recent years, partially adiabatic circuits like 2 N-2P and 2 N-2N2P were presented. In [7], a bulk CMOS-based energy-efficient Vedic multiplier structure using energy-efficient adiabatic logic (EEAL) was presented. The presented design reported low energy consumption. Low-power CMOS adders utilizing ten transistors and six transistors were presented in the literature [8, 9], respectively. In [10], Cihun Siyong et al. presented an irreversible energy recovery logic (ERL) based on quasi-static ERL (QSERL) family in 180 nm technology. Emerging FinFET designs almost replaced the CMOS [11] due to the quasi-planar dual-gated device. Rudenko et al. [12] reported the efficiency of FinFET channel mobility and intrinsic gate leakage current. Power–delay product (PDP) and energy–delay product (EDP) for FinFET-based circuits were presented by Mishra and Akashe [13]. FinFET-based adiabatic circuit is designed for logic gate and one-bit adder implementation [14–16]. This work focuses on the CEPAL which uses the single-phase clock for power [16]. As of now, there is no research available on a FinFET adiabatic-based low-power processing element. This paper describes the design and experimental evaluation of FinFET adiabatic-based low-power processing element. The processing elements such as CMOS CEPAL-based half adder and full adder have been restructured by short-gate mode FinFET.

3 Background

3.1 Adiabatic Logic

Electronically adiabatic circuits operate with zero power consumption due to the retrieve of charge stored in the load capacitances. The minimization of energy dissipation is done by maintaining a low voltage drop across the load. The recycling of un-dissipated energy or charge stored on load capacitance reduces the energy dissipated as heat energy. Time-varying ramp voltage as power supply is to be designed for the adiabatic circuits. Adiabatic circuits are classified based on amount of energy retrieved into fully adiabatic circuit and partially or quasi-adiabatic circuit. Fully adiabatic circuits transfer the charge fully from load capacitances back to the power supply. In partially adiabatic circuits or quasi-adiabatic circuits, recovering is partial. The rest of charge is transferred to the ground. CEPAL inherits the family of single-phase adiabatic circuits which has minimum control overhead and robust to high-speed applications.

The basic structure of a CEPAL circuit shown in Fig. 1a is composed of a pair of charging and discharging diodes; in between these diodes, the necessary logic is implemented. The charging diodes are M2 and M4, and the discharging diodes are M1 and M3. The PC and PC bar are the power supply to the circuits. The output waveform of CEPAL inverter circuit is shown in Fig. 1b. When the output becomes high, the power clock 'PC' swings and makes the output node floating. This situation is avoided since at the same time the complement of the power clock 'PC bar' makes it swing up again. Thereby, the weak high state in the output node is eliminated. Similarly, the weak low state is eliminated with the help of the complementary energy paths created by the diodes in the CEPAL architecture. The power dissipation due to these additional diodes is negligible as there is only one charging or discharging transistor turned on at a single time instant.

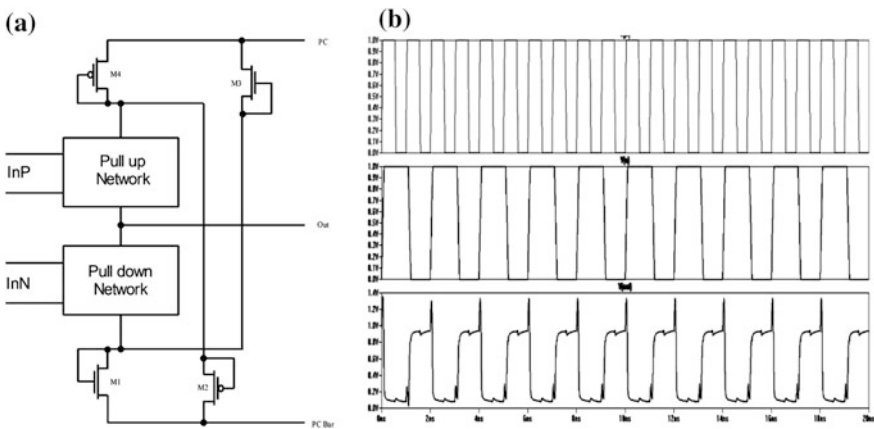


Fig. 1 a Basic structure of CEPAL circuit and b waveforms of CEPAL inverter

3.2 FinFET Device

The structure of FinFET is three-dimensional as shown in Fig. 2. In FinFET, the second gate (back gate) has been the prime factor in eliminating the SCEs as well as minimizing the leakage current. FinFET has perpendicular thin silicon body to the plane of the wafer. The flow of current is parallel to the wafer plane, and the gate electrodes wrap the entire channel in three dimensions.

It also provides high switching activity, low leakage current, and high on-state current by suppressing the SCEs by having a stronger control over the channel. The electrical characteristics of 32-nm FinFETs and 32-nm bulk CMOS device are taken form PTM.

The primary parameters obtained from the PTM are given in Table 1 Likewise, all the Double gated devices, FinFET provides more flexibility in design. FinFET basically offers three modes of operations namely short-gate mode, independent-gate

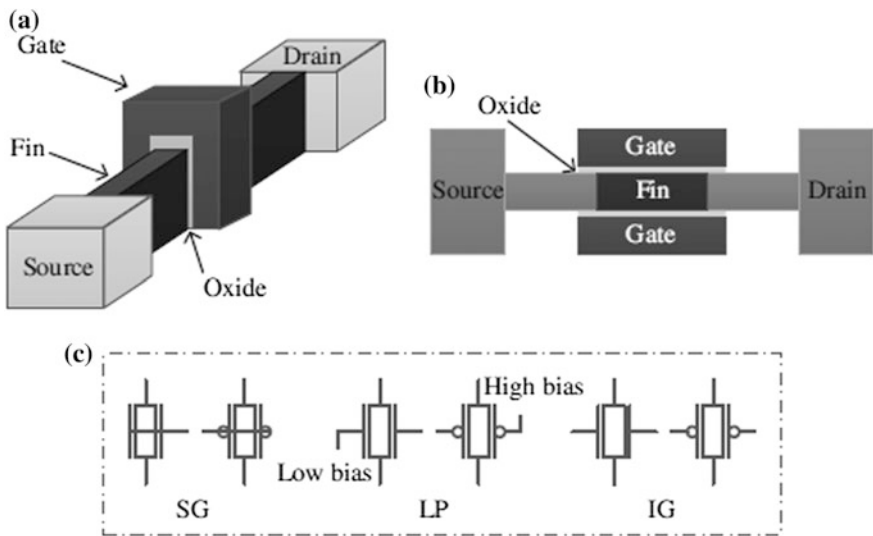


Fig. 2 a Three-dimensional structure, b cross-sectional diagram, and c symbol of short-gate (SG) mode, low-power (LP) mode, and independent-gate (IG) mode of a FinFET device

Table 1 Primary parameters in PTM

Primary parameters in PTM					
n-type FinFET	$L_{gate} = 32 \text{ nm}$	$H_{fin} = 40 \text{ nm}$	$W_{fin} = 8.6 \text{ nm}$	$T_{ox} = 1.4 \text{ nm}$	$V_{DD} = 1 \text{ V}$
p-type FinFET	$L_{gate} = 32 \text{ nm}$	$H_{fin} = 50 \text{ nm}$	$W_{fin} = 8.6 \text{ nm}$	$T_{ox} = 1.4 \text{ nm}$	$V_{DD} = 1 \text{ V}$
NMOS	$L_{eff} = 32 \text{ nm}$	$T_{oxe} = 1.4 \text{ nm}$	$V_{th0} = 0.42 \text{ V}$		$V_{DD} = 1 \text{ V}$
PMOS	$L_{eff} = 32 \text{ nm}$	$T_{oxe} = 1.5 \text{ nm}$	$V_{th0} = -0.41 \text{ V}$		$V_{DD} = 1 \text{ V}$

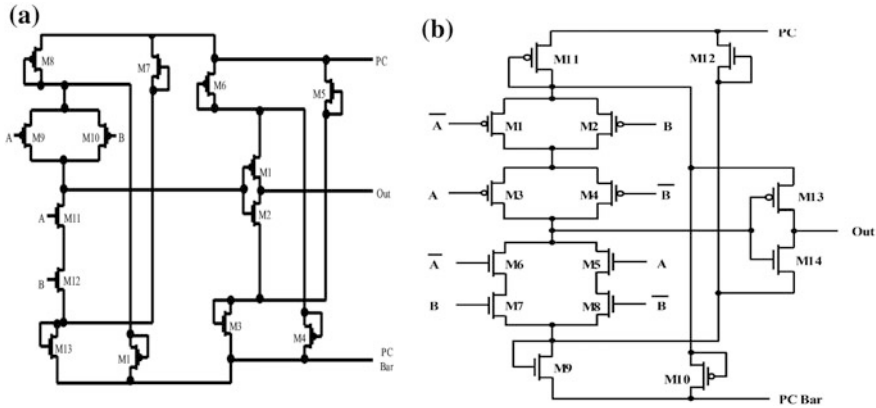


Fig. 3 a CEPAL-CMOS AND gate and b CEPAL-CMOS XOR gate

mode, and low-power mode. Symbol of short-gate (SG) mode, low-power (LP) mode, and independent-gate (IG) mode of a FinFET device is shown in Fig. 2c.

3.3 Design Approach of CEPAL-CMOS-Based Processing Elements

The conventional irreversible ERL adiabatic logics due to their dynamic characteristics suffer from high switching activity, interlaced circuit configuration, differential signaling, and output floating. Multi-phase and multiple clock operations or a trapezoid or triangular power clocks are to be designed. The design of CEPAL-based adiabatic gates will eliminate these issues. The CEPAL-CMOS AND and CEPAL-CMOS XOR gates are shown in Fig. 3a, b, respectively. The proposed CEPAL-CMOS adders are shown in Fig. 4a, b. The half adder and full adder circuits use 10 and 14 transistors with smaller area and lower power utilization.

4 Proposed Technique

Design Approach of CEPAL-FinFET-Based Processing Elements

The proposed adiabatic circuit uses only two clock signals with four phases namely Wait, Evaluate, Hold, and Recover. The phase difference between any two adjacent phases is a quarter of a period. The proposed CEPAL-based processing element inherits three advantages when compared to all the previous circuits proposed earlier. The circuit operation eliminates the Hold phase by which the throughput is increased. This feature is similar to QSERL, where the complexity is reduced.

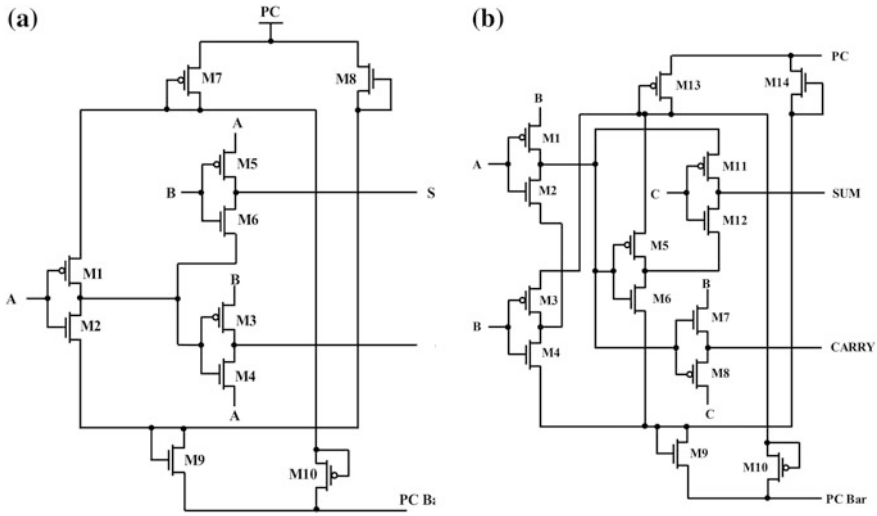


Fig. 4 a Proposed CMOS-CEPAL half adder and b proposed CMOS-CEPAL full adder

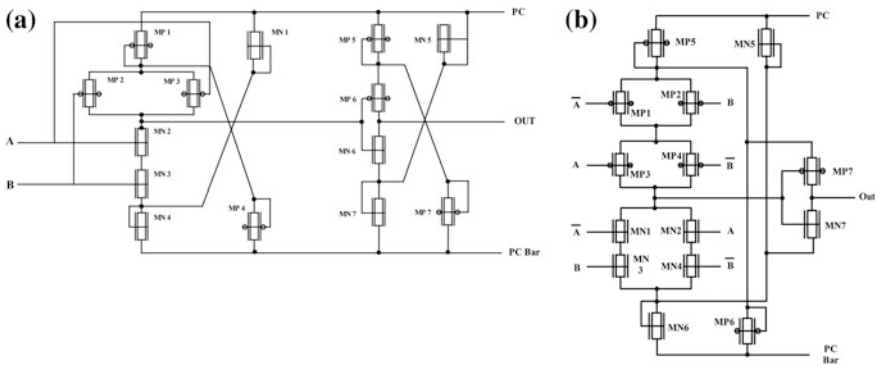


Fig. 5 a Proposed FinFET-CEPAL AND gate and b proposed FinFET-CEPAL XOR gate

The CEPAL has two paths apart from the charging and discharging paths. The number of devices is more, so implementation cost is higher. The adiabatic logic operating speed depends on the pull-up transistors since the charging and discharging operation is done through those transistors. The pull-down transistors maintain the voltage at certain nodes for operation. The leakage current and power consumption are controlled by the pull-down transistors. The AND and XOR gates of the CEPAL-FinFET are shown in Fig. 5a, b, respectively. The proposed FinFET SG Mode based half adder and full adder is presented in the Fig. 6a, b respectively.

5 Results and Discussion

FinFET-based adiabatic CEPAL processing element implementation for half adder and full adder in shorted gate mode is shown in Fig. 6a, b, respectively. For the implementation, predictive technology model for 32 nm is used. The supply voltage is 1 V; for CMOS implementation, the predictive technology model for 32 nm is used. The half adder is designed using XOR and AND gates having 14 transistors and 6 transistors, respectively. The power consumption and energy of half adder implementation using CMOS and FinFET are given in Table 2. The results show that the power dissipation in FinFET is low when compared to CMOS. The average current is also compared. The average power consumption of different device full adders for different circuits is given in Table 3. The FinFET dominates and outperforms the CMOS in its consumption of power. The measure of average power consumed is measured for a one-bit adder in 32 nm technology. Even though the existing adders in the literature show decreasing average power consumption as the process length is decreased, the proposed FinFET-based adder consumes least power among the other adders. The power consumption is reduced by nearly 65% when compared to the CMOS design. The circuit is further analyzed by executing the circuit using different supply voltage, and the leakage power is observed.

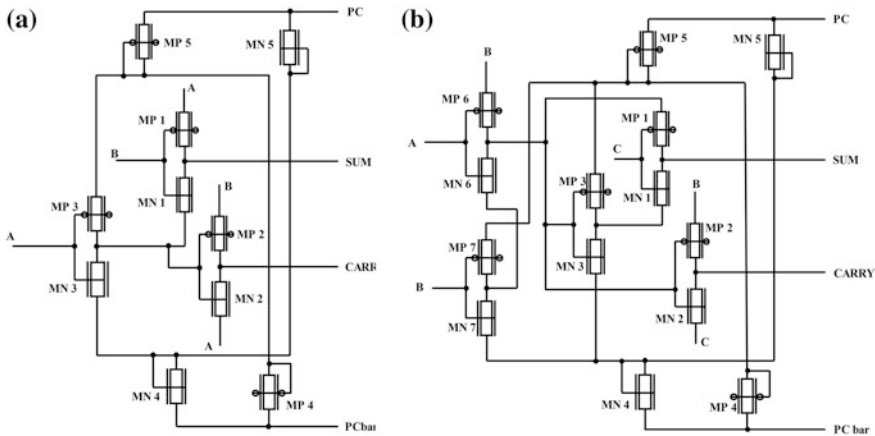


Fig. 6 a Proposed FinFET-CEPAL half adder and b proposed FinFET-CEPAL full adder

Table 2 Performance comparison of half adder using CMOS and FinFET

Circuit	CMOS			FinFET		
	P_{avg} μ W	I_{avg} μ A	E fJ	P_{avg} μ W	I_{avg} μ A	E fJ
Conventional half adder	22.9	14.5	14,500	2.41	1.0045	999.54
CEPAL half adder type	12.3	6.72	6720	0.35	0.125	125

Table 3 Performance comparison of full adder using CMOS and FinFET

Circuit	CMOS			FinFET		
	P_{avg} μ W	I_{avg} μ A	E fJ	P_{avg} μ W	I_{avg} μ A	E fJ
Conventional full adder	81.2	17.7	17,600	2.55	2.55	2550
CEPAL full adder type	80.92	2.49	2480	0.52	0.256	256

6 Conclusion

A novel design of a FinFET-based low-power processing element using complementary energy path adiabatic logic in 32 nm technology is presented in this paper. The proposed half adder and full adder contain less number of transistors and are free from leakage current. As bulk CMOS circuits are not suitable for deep sub-micron VLSI designs, FinFETs are suitable due to its high immunity to short channel effects, low leakage power consumption, higher on-state current, scalability, and design flexibility. The proposed FinFET–CEPAL-based processing elements show a considerable power reduction, low energy consumption with favorable performance improvement, and reduced number of transistors. The average power improvement is 80%. The reduction in leakage current improves by about 98.65%. The energy efficiency is also improved by 99.741%. Simulation has been carried out with HSPICE using predictive technology model in 32 nm FinFET technology.

References

1. Jianping Hu., Chenghao Han., Yuejie Zhang., Beibei Qi., and Haiyan Ni.: Super-Threshold Adiabatic FinFET Circuits Based on PAL-2 N Operating in Medium Strong Inversion Regions. *The Open Electrical & Electronic Engineering Journal*, vol. 8, pp. 263–272, (2014).
2. Liaqat Moideen Parakundil., and N. Saraswathi.: Low power pulse triggered D-flip flops using MTCMOS and Self-controllable voltage level circuit. *International Conference on Advanced Communication Control and Computing Technologies (ICACCCT)*, pp. 517–521, (2014).
3. Ehsan Pakbaznia., Farzan Fallah., and Massoud Pedram.: Charge Recycling in Power-Gated CMOS Circuits. *IEEE Transactions on Computer-Aided Design of Integrated Circuits and Systems*, vol. 27(10), pp. 1798–1811, (2008).
4. Tadayoshi Enomoto., Yoshinori Oka., and Hiroaki Shikano.: A self-controllable voltage level (SVL) circuit and its low-power high-speed CMOS circuit applications. *IEEE Journal of Solid-State Circuits*, vol. 38(7), pp. 1220–1226, (2003).
5. Antonio Blotti and Roberto Saletti.: Ultralow-Power Adiabatic Circuit Semi-Custom Design. *IEEE Transactions on Very Large Scale Integration (VLSI) Systems*, vol. 12(11), pp. 1063–8210, (2004).
6. Massimo Alioto and Gaetano Palumbo.: Performance Evaluation of Adiabatic Gates. *IEEE Transactions on Circuits and Systems—I: Fundamental Theory and Applications*, vol. 47(9), pp. 1297–1308, (2000).

7. Chanda M., Banerjee S., Saha D., and Jain S.: Novel transistor level realization of ultra low power high-speed adiabatic Vedic multiplier. *International Multi-Conference on Automation, Computing, Communication, Control and Compressed Sensing (iMac4 s)*, pp. 801–806, (2013).
8. Raju Gupta., Satya Prakash Pandey., Shyam Akashe., and Abhay Vidyarthi.: Analysis and optimization of Active Power and Delay of 10T Full Adder using Power Gating Technique at 45 nm Technology. *IOSR Journal of VLSI and Signal Processing*, vol. 2(1), pp. 51–57, (2013).
9. [9] Radhika P and Vigneswaran T.: Design Of Low Power Reduced Wallace Multiplier With Compact Carry Select Adder, Half Adder & Full Adder Using Cmos Technology. *Journal of Theoretical and Applied Information Technology*, vol. 74(2), pp. 262–268, (2015).
10. Cihun-Siyong Alex Gong., Muh-Tian Shiue., Ci-Tong Hong., Kai-Wen Yao.: Analysis and Design of an Efficient Irreversible Energy Recovery Logic in 0.18-um CMOS. *IEEE Transactions On Circuits And Systems—I*, vol. 55(9), pp. 2595–2607, (2008).
11. Prateek Mishra., Anish Muttreja., Niraj K. Jha.: FinFET Circuit Design, *Nanoelectronic Circuit Design*, pp. 23–54, (2010).
12. Rudenko T., Valeria Kilchytska., Collaert N., Alexei N. Nazarov., Jurczak M., and Denis Flandre.: *Electrical Characterization and Special Properties of FINFET Structures, Nanoscaled Semiconductor-on-Insulator Structures and Devices*. Springer Netherlands, pp. 199–220, (2007).
13. Vishwas Mishra and Shyam Akashe.: Calculation of Power Delay Product and Energy Delay Product in 4-Bit FinFET Based Priority Encoder. *Advances in Optical Science and Engineering -Springer India*, pp. 283–289, (2015).
14. Yogita Bansal and Charu Madhu A., Pardeep Kaur.: High Speed Vedic Multiplier Designs A Review. *Recent Advances in Engineering and Computational Sciences (RAECS)*, pp. 1–6, (2014).
15. Nan Liao., XiaoXin Cui., Kai Liao., KaiSheng Ma., Di Wu., Wei Wei., Rui Li., and Dun Shan Yu.: Low power adiabatic logic based on FinFETs. *Science China Information Sciences*, vol. 57(2), pp. 1–13, (2014).
16. Shipra Upadhyay., R. K. Nagaria., and R. A. Mishra.: Complementary Energy Path Adiabatic Logic based Full Adder Circuit. *International Journal of Electrical, Computer, Energetic, Electronic and Communication Engineering*, vol. 6(6), pp. 542–547, (2012).

Analytical Modeling and Simulation of Triple Metal Front Gate Stack DG-MOSFET with Graded Channel (GC-TMDG MOSFET)

Priyanka Saha, Saheli Sarkhel, Dinesh Kumar Dash, Suvam Senapati and Subir Kumar Sarkar

Abstract This paper presents an explicit 2D analytical surface potential modeling of Triple Metal Front Gate Stack DG MOSFET with Graded Channel (GC-TMDG MOSFET) to explore the dual benefits of gate and channel engineering techniques. The surface potential profile of the proposed model is derived by solving 2D Poisson's equation with suitable boundary conditions and also compared with graded channel DG MOSFET and Triple Material DG MOSFET to establish the superiority of our structure. In addition to this, lateral electric field closer to drain end is examined to substantiate the immunity of the device to hot carrier effect. For validation of analytical model, all the results are compared with 2D ATLAS device simulator data.

Keywords Graded channel · Triple material · Double-Gate MOSFET High-k · Poisson's equation · Hot carrier effect

P. Saha (✉) · D. K. Dash · S. K. Sarkar
Department of Electronics and Telecommunication Engineering,
Jadavpur University, Kolkata 700032, India
e-mail: priorient06@gmail.com

D. K. Dash
e-mail: dineshdash123@gmail.com

S. K. Sarkar
e-mail: su_sircir@yahoo.co.in

S. Sarkhel · S. Senapati
Department of Electronics and Communication Engineering,
Netaji Subhash Engineering College, Kolkata 700152, India
e-mail: saheli.sarkhel@gmail.com

S. Senapati
e-mail: suvamsenapati2@gmail.com

1 Introduction

The present VLSI era is dominated by the basic need for developing ultra-low-power low-dimensional devices to achieve higher package density with improved performance. Following Moore's law, this trend of continuous device downscaling has, however, led to device performance degradation; due to several unwanted short channel effects (SCEs) like drain-induced barrier lowering (DIBL), source/drain parasitic capacitances, impurity-induced carrier mobility reduction, increased gate tunneling effect and p-n junction leakage current [1, 2]. In order to overcome these shortcomings of a planar conventional device, several nonconventional MOSFET structures have been studied widely, of which, Double-Gate (DG) MOSFET has received significant research limelight due to its superior scalability, excellent SCE reduction, ideal subthreshold swing, double on current, and excellent gate control over the channel [3–5]. However, sub-50-nm MOS devices are still affected by hot carrier effects (HCEs) and subthreshold slope degradation. These associated problems can be mitigated by adopting alternative options of channel engineering or gate engineering [6, 7]. In lateral graded channel, a higher doping concentration is maintained near the source end and a lower doping is maintained near the drain end which reduces the drain side electric field thereby effectively reducing the possibility of impact ionization-induced HCEs at the drain side [6]. Gate engineering technique primarily involves hetero-material gate electrode where more than one metal (dual material gate (DMG), triple material gate (TMG)) with different work functions are placed side by side and act as a single gate electrode [7–9]. The subthreshold characteristics of the devices are characterized by the source side control gate, while the screen gate having lower value of work function reduces drain side peak electric field, thereby suppressing the HCEs. Moreover, the ongoing trend of device miniaturization necessitates the proportional downscaling of gate oxide thickness too making the effective oxide thickness (EOT) of conventional SiO_2 gate oxide around 1 nm for sub-45-nm conventional MOSFETs. This in turn is associated with the possible problems of direct tunneling of carriers through the dielectric thereby threatening device reliability. Thus, high-k dielectrics are now being popularly used as an alternative gate oxide of nano-dimensions offering devices with superior performance with relatively thick gate oxides. Hafnium oxide (HfO_2) is now being anticipated as a suitable alternative for low voltage, low-power nano-dimensional devices due to its higher dielectric constant value, superior thermal stability, and lower bulk trap density [10].

We have combined the recently emerging concept of channel engineering by considering a silicon channel with graded doping profile from source to drain end along with the popular scheme of gate engineering by using three metals with different work functions as gate electrode in a conventional Double-Gate (DG) MOSFET structure to develop a new Graded Channel Triple Material Double-Gate MOSFET (GC-TMDG MOSFET) with stacked front gate oxide ($\text{HfO}_2/\text{SiO}_2$ stack). This work presents a detailed two-dimensional analytical surface potential modeling of the proposed structure to establish the superiority of the

proposed GC-TMDG MOS structure over its GC DG and TMDG counterparts in terms of immunity to unwanted hot carrier effect and hence offering higher resistance to SCEs.

2 Analytical Modeling

Schematic cross-sectional diagram of the proposed Triple Material Double-Gate (TMDG) MOSFET with channel doping concentration continuously graded from source side to drain side is depicted in Fig. 1.

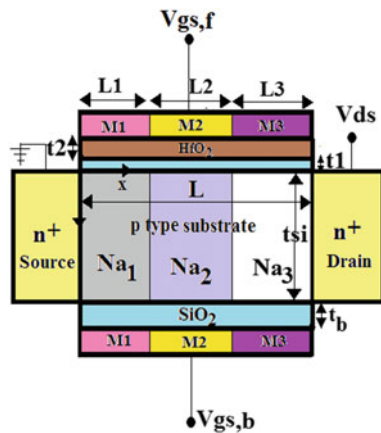
Both front and back gate electrodes consist of three metals M1, M2, and M3 having different work functions (with $\phi_{M1} > \phi_{M2} > \phi_{M3}$) of lengths $L1$, $L2$, and $L3$, respectively, over the channel region, thus effectively dividing the channel into three regions R1, R2, and R3 of lengths $L1$, $L2$, and $L3$ such that the total length of the channel is $L = L1 + L2 + L3$ with doping concentrations of Na_1 , Na_2 , and Na_3 , respectively. t_{eff} , t_b , and t_{si} are the thicknesses of stacked front gate oxide (HfO₂/SiO₂), back gate oxide (SiO₂), and channel, respectively. The effective thickness of the stacked front gate oxide can be expressed as:

$t_{eff} = t_1 + \frac{\epsilon_1}{\epsilon_2} t_2$ where t_1 is the thickness of the SiO₂ layer, t_2 is the thickness of the HfO₂ layer, ϵ_1 is the permittivity of the SiO₂ layer, and ϵ_2 is the high- k dielectric constant of HfO₂.

In the subthreshold regime, the channel is considered to be fully depleted and the 2D Poisson's equation along the channel is given by:

$$\frac{\partial^2 \psi_k(x, y)}{\partial x^2} + \frac{\partial^2 \psi_k(x, y)}{\partial y^2} = \frac{qN_{ak}}{\epsilon_{si}} \tag{1}$$

Fig. 1 Schematic diagram of triple material front gate stack DG MOSFET with graded channel



where $k = 1, 2,$ and 3 and $\psi_k(x, y)$ is the 2D electrostatic potential for regions R1, R2, and R3, respectively. N_{ak} denotes the doping concentration of the different regions of the channel; ϵ_{si} is the dielectric constant of silicon. Considering Young's parabolic potential approximation (PPA), the surface potentials under three different metals are given by:

$$\psi_k(x, y) = \psi_{sk}(x) + a_{k1}(x)y + a_{k2}(x)y^2 \quad \text{for } L_{k-1} \leq x \leq L_k, 0 \leq y \leq t_{si} \quad (2)$$

$\psi_{sk}(x)$ is the surface potential in the channel region R_k . Here, L_0 is considered as the starting point of the channel, i.e., $L_0 = 0$, and a_{k1} and a_{k2} are arbitrary constants and functions of x only.

Poisson's equation can be solved under different channel regions by using the following boundary conditions:

I. Electric field at the front gate–oxide interface is continuous for the triple metal gate. Therefore, we have

$\left. \frac{d\psi_k(x, y)}{dy} \right|_{y=0} = \frac{\epsilon_1}{\epsilon_{si}} \frac{(\psi_{sk}(x) - V'_{GSk})}{t_{eff}}$ where $V'_{GSk} = V_{gsf} - V_{FB,Lk}$, V_{gsf} is gate to source applied voltage at the front gate.

II. Electric field at the back gate oxide and the channel interface is continuous for three of the metals:

$\left. \frac{d\psi_k(x, y)}{dy} \right|_{y=t_{si}} = \frac{\epsilon_1}{\epsilon_{si}} \frac{V'_{GS,bk} - \psi_{Bk}(x)}{t_b}$ where $V'_{GS,bk} = V_{gsb} - V_{FB,Lk}$, V_{gsb} is gate to source applied voltage at the back gate. Here, $\psi_{Bk}(x)$ and $V_{FB,Lk}$ are the back surface potentials and flat band voltages in the three regions, respectively.

III. At the interface of two dissimilar metals, the surface potential is continuous:

$$[\psi_1(L1, 0) = \psi_2(L1, 0)] \quad \text{and} \quad [\psi_2(L1 + L2, 0) = \psi_3(L1 + L2, 0)]$$

IV. Electric flux at the interface of two dissimilar metals is continuous:

$$\left(\left. \frac{d\psi_1(x, y)}{dx} \right|_{x=L1} = \left. \frac{d\psi_2(x, y)}{dx} \right|_{x=L1} \right) \quad \text{and} \quad \left(\left. \frac{d\psi_2(x, y)}{dx} \right|_{x=L1+L2} = \left. \frac{d\psi_3(x, y)}{dx} \right|_{x=L1+L2} \right)$$

V. The source and drain end potentials are given by:

$\psi_{s1}(0, 0) = V_{biS}$ and $\psi_3(L1 + L2 + L3, 0) = V_{biD} + V_{DS}$ where V_{biS} and V_{biD} denote the built-in potentials at the source/channel and channel/drain interface, respectively.

Applying the boundary conditions I and II, the constants a_{k1} and a_{k2} are calculated, and putting the constants in “Eq. (2)” and also using “Eq. (1),” we get the solution of the surface potential for three different channel regions as given below:

For $0 \leq x \leq L1$ under M1

$$\Psi_{s1}(x) = A_1 \exp(\eta x) + B_1 \exp(-\eta x) - \beta_1/\alpha \quad (3)$$

For $L1 \leq x \leq (L1 + L2)$ under M2

$$\Psi_{s2}(x) = A_2 \exp(\eta(x - L1)) + B_2 \exp(-\eta(x - L1)) - \beta_2/\alpha \quad (4)$$

For $(L1 + L2) \leq x \leq (L1 + L2 + L3)$ under M3

$$\Psi_{s3}(x) = A_3 \exp(\eta(x - L1 - L2)) + B_3 \exp(-\eta(x - L1 - L2)) - \beta_3/\alpha \quad (5)$$

where $\eta = \sqrt{\alpha}$. Values of α and β_k are provided in Appendix.

Again, by using boundary conditions (III–V) the value of the constants $A1$, $B1$, $A2$, $B2$, $A3$, and $B3$ are also derived.

The lateral electric field, along the channel length, can be found by simply differentiating the surface potentials of (4), (5), and (6) with respect to x .

3 Results and Discussions

In this section, an overall performance analysis of the proposed GC-TMDG MOSFET structure based on our derived analytical results is demonstrated and compared with 2D ATLAS device simulator [11] results for validation of our analytical model. All the device parameters and biasing voltages are listed in Table 1.

Figure 2 shows the comparative analysis of the surface potential profiles of proposed GC-TMDG MOSFET with two different structures of TMDG and GC DG MOSFET. The dual step profiles existing in surface potential distribution of GC-TMDG MOSFET is responsible for screening the channel length from influence of V_{ds} fluctuations which is missing in a simple graded channel Double-Gate MOSFET. In addition to this, position of surface potential minimum plays a significant role to establish the superiority of the presented model. The position of surface potential minima of both TMDG and GC-TMDG MOSFET being closer to the source side in comparison to GC DG MOSFET structure contributes to higher immunity to DIBL. Again by exhibiting highest source/channel potential barrier

Table 1 Device parameter table

Parameters	$t1$	$t2$	tb	tsi
Value (nm)	1	2	3	10
Parameters	L	Na_1	Na_2	Na_3
Value	60 nm	$10^{24}/m^3$	$10^{23}/m^3$	$10^{22}/m^3$
Parameters	V_{ds}	$V_{gs,f}$	$V_{gs,b}$	M1, M2, M3
Value	1 V	0.5 V	0.5 V	4.8, 4.6, 4.4 eV

Fig. 2 Surface potential variation along position of channel for three different structures with $L = 60$ nm

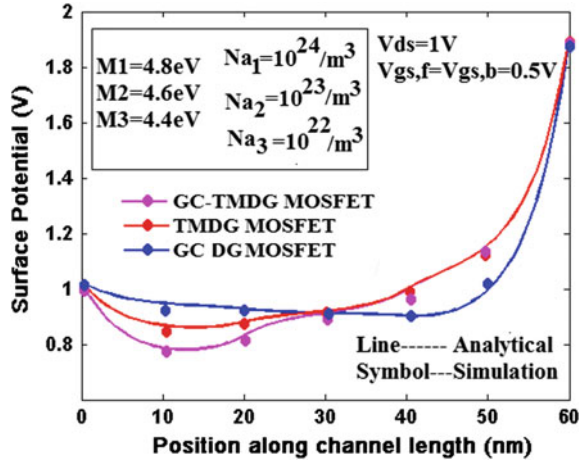
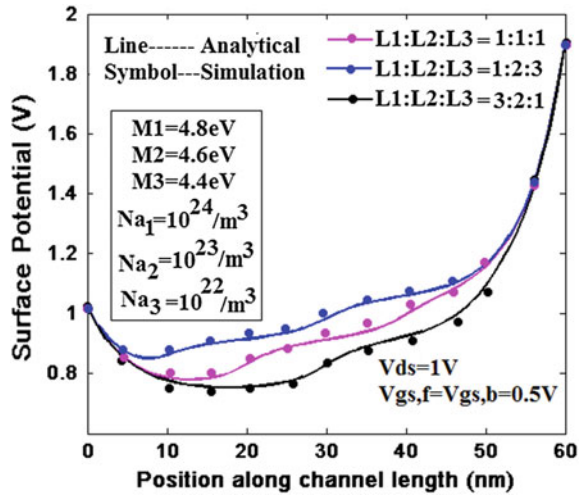


Fig. 3 Surface potential variation along position of channel varying $L1:L2:L3$ of GC-TMDG MOSFET with $L = 60$ nm



among all the three different structures, proposed model also shows suppressed SCEs in nanometer regime. Thus, GC-TMDG MOSFET reaps the dual benefits of graded channel and triple material gate electrode to bring significant improvement in device performance. Figure 3 shows variation of surface potential as function of channel position of proposed GC-TMDG MOSFET with varying ratios of $L1:L2:L3$. It is clearly evident from the figure that for $L1:L2:L3 = 1:2:3$, the minima being closer to the source end will also contribute to higher immunity to unwanted DIBL effect and can be accepted as optimized length ratio. Figure 4 plots the surface potential profile along channel position of GC-TMDG MOSFET with different drain-to-source biases. For channel length of $L = 60$ nm, increment in V_{ds} value leads to increase in surface potential. Moreover, the variation of V_{ds} only influences

Fig. 4 Surface potential variation along position of channel for different values of V_{ds} of GC-TMDG MOSFET with channel length $L = 30 \text{ nm}$ and $L = 60 \text{ nm}$

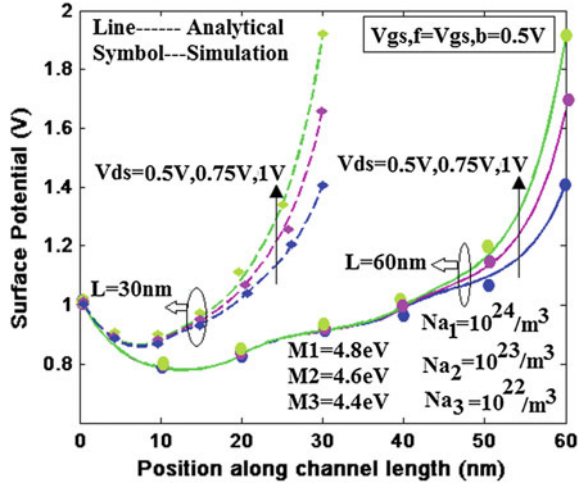
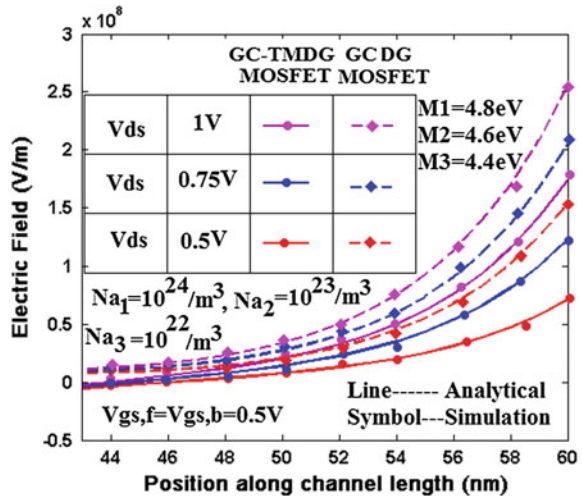


Fig. 5 Lateral electric field variation along position of channel (closer to drain end) for different values of V_{ds} of GC-TMDG MOSFET with $L = 60 \text{ nm}$



the channel potential at the drain end with almost unchanged potential throughout the major portion of the channel. Hence, it shows that the effect of DIBL is appreciably reduced in the proposed structure. As the channel length is shrunk to 30 nm, decrease in potential step is observed leading to DIBL effect significant in reduced channel lengths. In Fig. 5, lateral electric field variation along the position of the channel of GC-TMDG MOSFET is compared with GC DG MOSFET structure for different values of V_{ds} with channel length of $L = 60 \text{ nm}$. Since the electric field at the drain end is mainly responsible for the hot carrier effect, we have investigated the electric field profile closer to the drain side. The notable reduction of electric field of the proposed structure at the drain end even for high value of

$V_{ds} = 1$ V implies lower hot carrier effect as compared to GC DG MOSFET and hence reduced SCE. A close agreement between analytical and simulated results validates the accuracy of our derived model.

4 Conclusion

In this paper, performance analysis of the proposed GC-TMDG MOSFET structure based on surface potential derivation is demonstrated in terms of position of potential minima and dual step profiles. The nature of surface potential distribution for different ratio of the lengths of the triple gate electrode material regions, and by varying drain to source biases, is shown to study the benefits of GC-TMDG MOSFET. In addition to this, comparison of potential profile of proposed model is presented to check its figure of merit over GC DG MOSFET and TMDG MOSFET structures. Furthermore, lateral electric field analysis closer to the drain end of the device proves its immunity to unwanted hot carrier effect and hence reduces short channel effects. The derived analytical results are found to be in good agreement with 2D ATLAS device simulator data verifying the accuracy of our model.

Acknowledgements Priyanka Saha thankfully acknowledges the financial support as Ph.D. Fellow under “Visvesvaraya Ph.D. Scheme,” DEITY, Government of India.

Appendix

$$\alpha = \frac{2(1 + C_{\text{eff}}/C_{\text{si}} + C_{\text{eff}}/C_b)}{t_{\text{si}}^2(1 + 2C_{\text{si}}/C_b)}$$

$$\beta_k = \frac{qN_{\text{ak}}}{\varepsilon_{\text{si}}} - \frac{2V'_{\text{GS,bk}}}{t_{\text{si}}^2(1 + 2C_{\text{si}}/C_b)} - \frac{2V'_{\text{GSk}}(C_{\text{eff}}/C_b + C_{\text{eff}}/C_{\text{si}})}{t_{\text{si}}^2(1 + 2C_{\text{si}}/C_b)} \quad \text{with } C_{\text{si}} = \varepsilon_{\text{si}}/t_{\text{si}} \quad C_{\text{eff}} = \frac{\varepsilon_1}{t_{\text{eff}}} \quad \text{and } C_b = \varepsilon_1/t_b.$$

References

1. E. Weste, “Principles of CMOS VLSI Design, A System Perspective. Upper Saddle River,” NJ: Pearson Education, 2003, ch. 2.
2. M. I. Current, S. W. Bedell, I. J. Malik, L. M. Feng, and F. J. Henley, “What is the future of sub-100 nm CMOS: Ultra shallow junctions or ultrathin SOI?,” *Solid State Technol.*, vol. 43, pp. 66–77, 2000.
3. Balestra, M. Benachir, J. Brini, and G. Ghibaudo, “Analytical models of subthreshold swing and threshold voltage for thin- and ultrathin-film SOI MOSFETs,” *IEEE Trans. Electron Devices*, vol. 37, pp. 2303–2311, 1990.

4. Y. Taur, "Analytical solutions of charge and capacitance in symmetric and asymmetric double-gate MOSFETs," *IEEE Trans. Electron Devices*, vol. 48, no. 12, pp. 2861–2869, 2001.
5. S. Spedo and C. Fiegna, "Comparison of and asymmetric double-gate MOSFETs-tunneling currents and hot electrons," in *Proc. IEEE semiconductor device Res. Symp*, pp. 601–604, 2002.
6. H. Kaur, S. Kabra, S. Haldar, and R. S. Gupta, "An analytical drain current model for graded channel cylindrical/surrounding gate MOSFET," *Microelectron. J.*, vol. 38, no. 3, pp. 352–359, 2007.
7. W. Long, H. Ou, J.-M. Kuo, and K. K. Chin, "Dual-material gate (DMG) field effect transistor," *IEEE Trans. Electron Devices*, vol. 46, no. 5, pp. 865–870, 1999.
8. G. V. Reddy and M. J. Kumar, "A new dual-material double gate (DMDG) nanoscale SOI MOSFET—Two-dimensional analytical modeling and simulation," *IEEE Trans. Nanotechnol.*, vol. 4, no. 2, pp. 260–268, 2005.
9. P. K. Tiwari, S. Dubey, M. Singh, and S. Jit, "A two-dimensional analytical model for threshold voltage of short-channel triple-material double-gate metal-oxide-semiconductor field-effect transistors," *J. Appl. Phys.*, vol. 108, no. 7, pp. 074508-1–074508-8, 2010.
10. R. Kaur, R. Chaujar, M. Saxena and R. S. Gupta, "Two dimensional simulation and analytical modeling of a novel ISE MOSFET with gate stack configuration," *Microelectronic Engineering*, vol. 86, pp. 2005–2014, 2009.
11. ATLAS User's Manual: Silvaco Inc. Santa Clara, CA (2010).

Integrated TTL Driver with SPDT Switch

Priyanka Shukla, Rakhi Kumari and Rabindranath Bera

Abstract This paper describes the GaAs MESFET-based S-band (2–3 GHz) SPDT switch with TTL driver (TTL control). TTL control voltage is needed to select the RF path. At 2–3 GHz, simulated insertion loss is lower than 0.8 dB and isolation is better than 36 dB. Simulated input return loss is better than 17.5 dB and output return loss is better than 18 dB. For improvement of isolation, extra path is added. When we add extra path then isolation is increased. Simulated improved isolation is better than 43 dB and insertion loss is lower than 0.98 dB. Simulated input and output return losses are better than 14 dB.

Keywords SPDT · Switch · TTL · RF switches · S-band

1 Introduction

RF switches are important elements for any transceiver system. RF and microwave switches are extensively used in wireless communication system and defense application for the RF signals routing along different direction at different time instant. The SPDT (single pole and double through) switches receive single RF input signal and choose one RF routing path from two RF paths [1]. Selection of routing path depends upon TTL control voltages. GaAs MESFET RF SPDT switch is ON when gate voltage of MESFET is 0 V and OFF when gate voltage of MESFET is -5 V [2]. These control voltages are driven by TTL driver. TTL driver receives (TTL logic values) 0 and 5 V and gives control voltages 0 and -5 V [2] (Fig. 1).

P. Shukla (✉) · R. Bera

Department of Electronics and Communication Engineering, Sikkim Manipal University (SMIT), Rangpo, Majhitar 737136, Sikkim, India
e-mail: priyankashukla245@gmail.com

R. Kumari

Solid State Physics Laboratory, Defence Research and Development Organization, Timarpur, Delhi, India

© Springer Nature Singapore Pte Ltd. 2018

R. Bera et al. (eds.), *Advances in Communication, Devices and Networking*,
Lecture Notes in Electrical Engineering 462,
https://doi.org/10.1007/978-981-10-7901-6_13

107

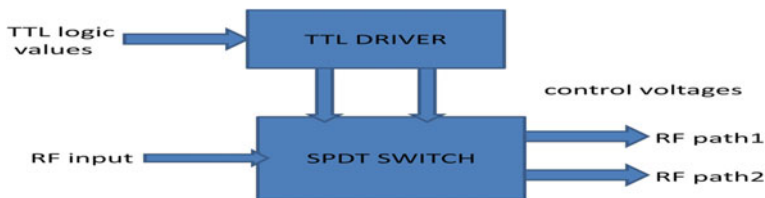


Fig. 1 Block diagram of TTL driver with SPDT switch

This SPDT switch is used in low power applications. GaAs MESFET SPDT switch provides high isolation, low insertion loss, and good input and output return losses across broad operating frequency [3]. GaAs MESFET switches [4] are mainly used in communication and in radar (for defense application) for band selection and signal routing between different RF paths. Applications of SPDT switches are in T/R module, in phased array radar, in phase shift antenna, and in space.

2 Circuit Design of S-Band SPDT Switch

For designing SPDT switch, series–shunt combination of depletion mode MESFET are taken [5]. Depletion mode MESFET is switched ON at 0 V and OFF at -5 V (negative voltage). For connecting elements, micro-strip transmission line is used. Matched line (50Ω) is used at input and output port. TTL driver is used to convert

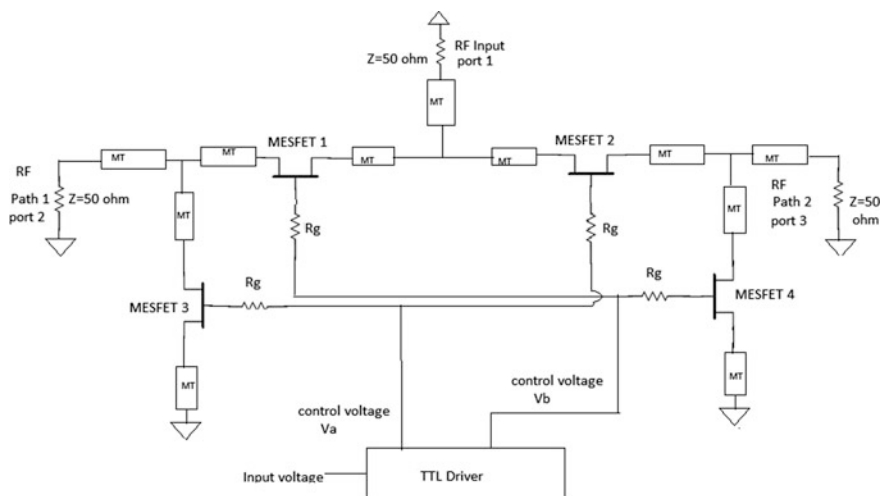


Fig. 2 Circuit of S-band SPDT switch

TTL logic values (0 and 5 V) to control voltages (0 and -5 V) [6]. Width of MESFET is 600 μm, and channel length is 0.7 μm (Fig. 2).

TTL driver receives input voltage values 0 and 5 V and converts these voltages into control voltages 0 and -5 V. When control voltage V_a is 0 V then MESFET 1 and MESFET 4 are ON, so signal is routing through RF path 1 (port 2). When control voltage V_b is 0 V then MESFET 2 and MESFET 3 are ON, so signal is routing through RF path 2 (port 3). The control voltages are brought to the device through 3111 kΩ resistor R_g to maintain an RF open circuit at the gates and to provide a good isolation.

3 Truth Table for the Control Voltages and Path Selection

Depletion mode MESFET is ON when 0 V is applied at gate and OFF when -5 V is applied at gate (Fig. 3).

4 Circuit of S-Band SPDT Switch When Extra Path Added

For improvement of isolation, extra path (MESFET 5 and MESFET 6) is added [7]. When extra path is added, isolation is increased but insertion loss is also increased and input and output return losses are decreased. So, where low insertion loss is needed, there is no need to add extra path and where high isolation is needed, add extra path. Isolation is increased approximately 6–10 dB when extra path is added (Fig. 4).

5 Simulated Result

For the above circuit, input return loss is denoted as dB(S(1,1)), output return loss is denoted as dB(S(2,2)), insertion loss is denoted as dB(S(2,1)), and isolation is denoted as dB(S(3,1)). Insertion loss is measured from ON path, and isolation is measured from OFF path. Input signal arrived at port 1 and going from path 1 (port 2) and path 2 (port 3) is OFF (Figs. 5, 6, 7 and 8).

Input voltage (TTL logic values)	Control voltages		RF input to	
	V_a	V_b	RF path 1	RF path 2
0 volt	-5 volt	0 volt	ON	OFF
5 volt	0 volt	-5 volt	OFF	ON

Fig. 3 Table of control voltages and path selection

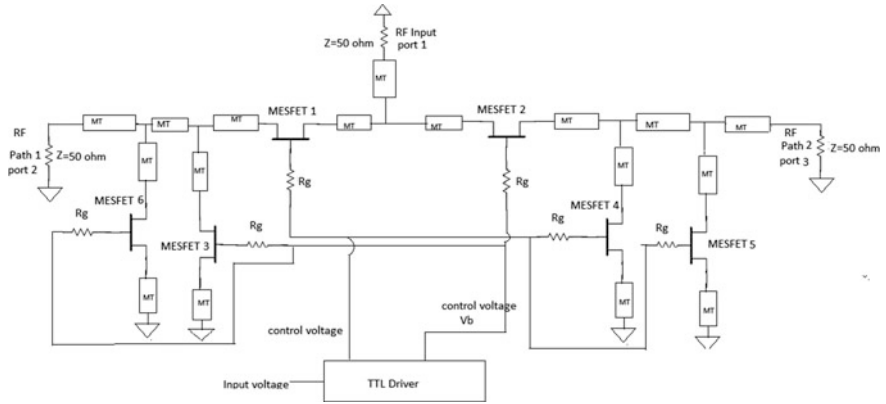


Fig. 4 Circuit of S-band SPDT switch when extra path added

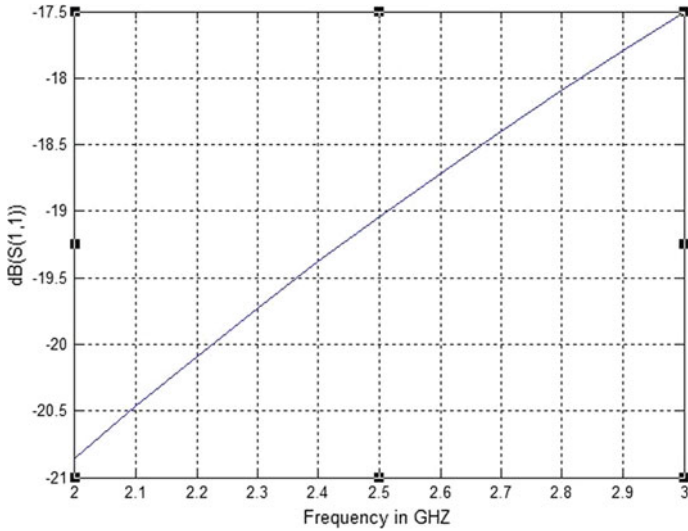


Fig. 5 Simulated input return loss

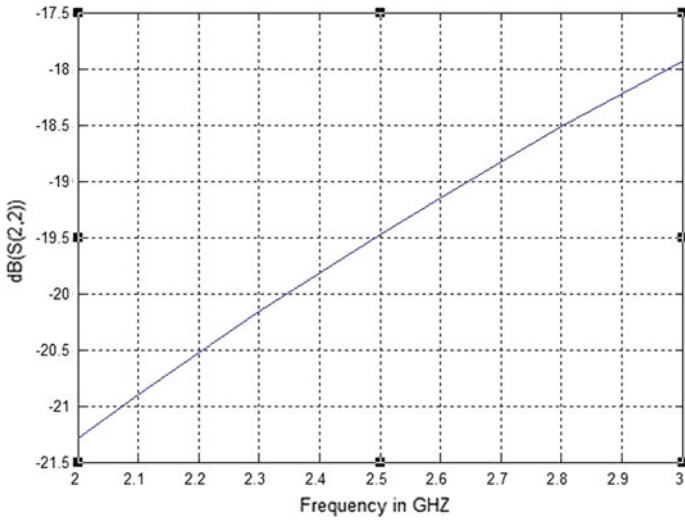


Fig. 6 Simulated output return loss

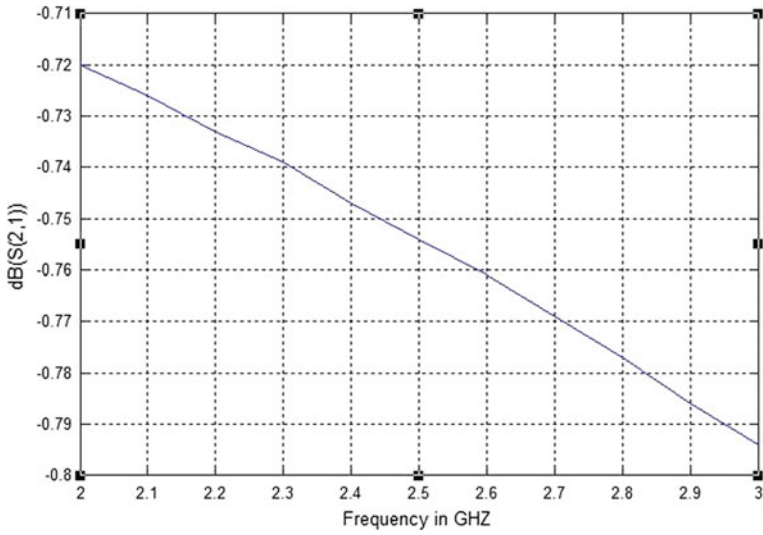


Fig. 7 Simulated insertion loss

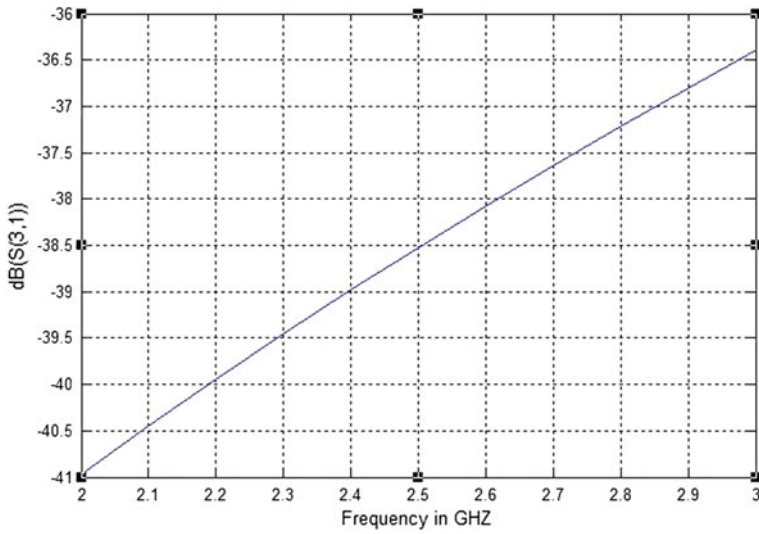


Fig. 8 Simulated isolation

6 Comparison Between Normal SPDT Switch Versus High Isolation SPDT Switch

See Figs. 9, 10, 11 and 12

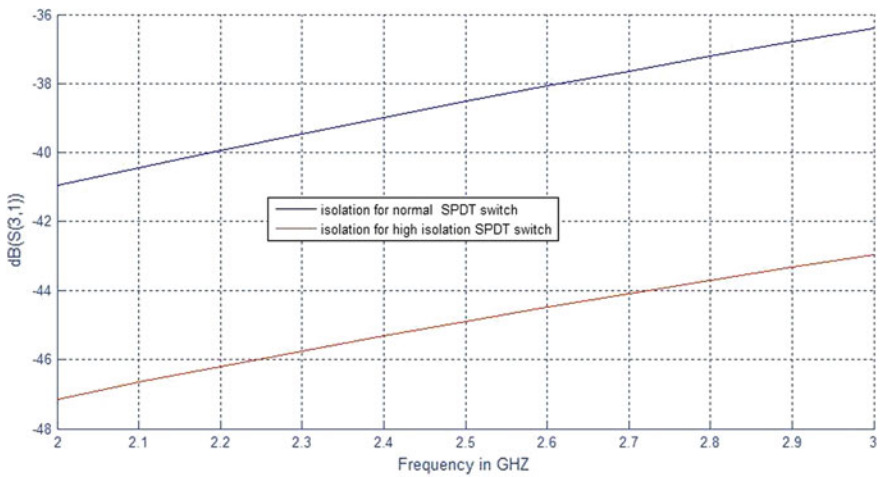


Fig. 9 Simulated isolation of normal SPDT switch versus high isolation SPDT switch

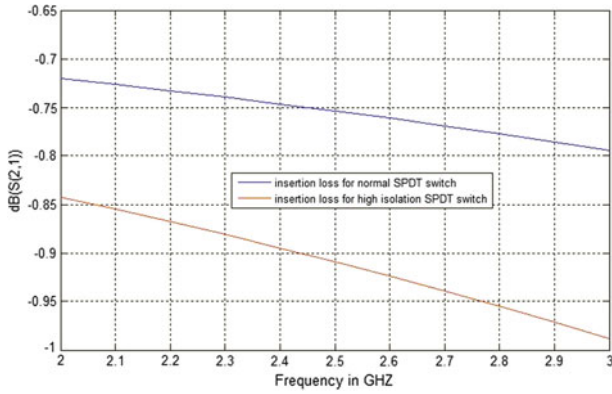


Fig. 10 Simulated insertion loss of normal SPDT switch versus high isolation SPDT switch insertion loss

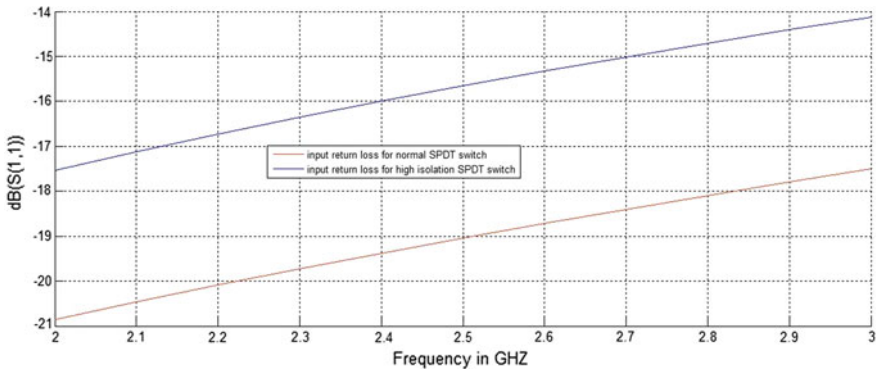


Fig. 11 Simulated input return loss of normal SPDT switch versus high isolation SPDT switch input return loss

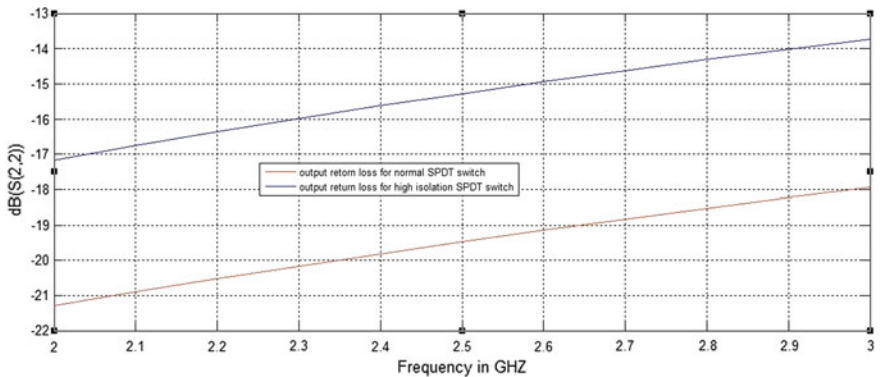


Fig. 12 Simulated output return loss of normal SPDT switch versus high isolation SPDT switch output return loss

7 Conclusion

Series/shunt topology provides improved switch performance at S-band. For switch designing, we use microstrip transmission line [8] in micrometer length and 0.7 μm gate length depletion mode GaAs MESFET device. This switch shows 36–41 dB isolation and 0.7–0.79 dB insertion loss. Input and output return losses are 17–21 dB. Isolation is also improved, when extra path is added. Isolation is increased from 41 to 47 dB (approximately 6 dB). This circuit shows good performance over 2–3 GHz for S-band SPDT switch.

References

1. <http://literature.cdn.keysight.com/litweb/pdf>, “FET solid state switches (SPDT), technical overview”, 5989–6088EN, July 2014.
2. Tyco electronics, white paper, “Driver for GaAs FET Switches”, swd 109 vol. 5, February 2006.
3. G. Wang, Ch. Liu “Wideband SPDT Switch With TTL Control”, Applied Mechanics and Materials, Vol. 599–601, Switzerland, August 2014, pp 1820–1823.
4. Zhurbenko, Vitaliy, “A high isolation switch based on a standard GaAs process”, Microwave & Optical Technology Letters, Vol. 53, May 2011, pp 984–987.
5. Pat Hindle, “The State of RF/microwave Switch Devices”, microwave journal, vol. 53, November 2010.
6. W. L. Seely, et al., “A TTL COMPATIBLE RF SWITCH TOPOLOGY FOR GaAs MMIC APPLICATIONS”, IP.com Electronic Publication, vol. 17, 2002.
7. M. H. Abdul Hadi, B. H. Ahmad, Peng Wen Wong and N. A. Shairi, “An overview of Isolation Improvement Techniques in RF Switch”, ARPJ Journal of Engineering and Applied Sciences, vol. 9, March 2014.
8. A. F. Berezniak and A. S. Korotkov, “Solid-State Microwave Switches: Circuitry, Manufacturing Technologies and Development”, Radioelectronics and Communications Systems, Vol. 56, March 2013, pp 3–20.

A 3D Analytical Modeling of Dual-Metal Tri-Gate Silicon-On-Nothing Tunneling Field Effect Transistor

Esita Mitra, Dinesh Kumar Dash and Subir Kumar Sarkar

Abstract In this paper, first time a three-dimensional analytical model of dual-metal triple-gate silicon-on-nothing tunneling field effect transistor (DMTG SON TFET) is presented. This model is derived by solving the 3D Poisson's equation. Simulation of 3D device lowered the need of parameter fittings. In addition, two different metals form a barrier over the channel region, which restricts reverse tunneling of carrier from drain to source. Choice of two different metals increases the on current and decreases the off current, thus improving the on-off current ratio of this proposed device. The electric field and the surface potential are obtained by solving the 3D Poisson's equation with proper boundary condition and the drain current is modeled by using the Kane's model also. The performance comparison of the proposed structure is done with the single-metal SON TFET and double-metal SOI TFET. The 3D analytical results are simulated using SILVACO ATLAS for this structure.

Keywords Triple gate · Three dimensional (3D) · Analytical modeling Silicon-On-Nothing (SON) · Dual metal · Band to band tunneling 3D Poisson's equation

E. Mitra (✉) · D. K. Dash (✉) · S. K. Sarkar
Department of Electronics and Telecommunication Engineering,
Jadavpur University, 188, Raja S. C. Mallick Road, Kolkata 700032, India
e-mail: brishti.mitra26@gmail.com

D. K. Dash
e-mail: dineshdash123@gmail.com

S. K. Sarkar
e-mail: su_sircir@yahoo.co.in

1 Introduction

The fundamental problem of the nanoscale circuit is the power dissipation [1]. The present trend of minimizing the size of the MOSFET faces several problems like high power consumption, stopping the leakage current that degrades the ‘on’ and ‘off’ current ratio, short-channel effects that are DIBL and so on [2]. The current switching process in the MOSFET involves the thermionic injection of electron over the energy barrier, which limits the subthreshold slope to 60 mV/decade at room temperature [3]. So, the tunnel field effect transistor meets the need for new device which can replace the CMOS technology by its low power application capability [4], low subthreshold slope <60 mv/decade, and low off-state leakage current [5].

TFET is also suffered from various drawbacks, like small on current, ambipolarity. Different methods are adopted such as heterostructures, bandgap engineering, work function engineered double gate to improve the on current. The triple-metal double-gate SOI TFET were found that exhibits better results [4, 5], but those analytical models were based on 2D Poisson’s equation and the width variation is not incorporated in that model. The triple-gate structure increases the gate control over the channel region than double gate. Till now a tri-gate tunneling field effect transistor is observed [6]. But in this device SON and dual metal is incorporated with TG TFET. This model shows the effect of structure variation rather than fitting parameters. A 3D analytical model is derived for different electrical parameters such as surface potential, electric field, drain current of dual-metal triple-gate SON TFET. In this paper, Sect. 2 explains the proposed structure. The analytical model of surface potential, electric field, and drain current is derived in Sect. 3. The Sect. 4 includes the result and discussion. Finally, the paper concludes in Sect. 5.

2 Device Structure

The proposed model of DMTG SON TFET in 3D representation is shown in Fig. 1. The proposed device has a channel length, $L = 30$ nm, where $L = L1 + L2$. The gate electrode of two sidewalls and top surface consists of two different metal M1 and M2. The work function of two metals is denoted by Φ_{M1} and Φ_{M2} .

$L1$ is the channel length under M1 and $L2$ is the channel length under M2. The on-state is denoted by ($V_{GS} = 0.7$ V and $V_{DS} = 0.01$ V) and off-state is denoted as ($V_{gs} = 0$ V and $V_{ds} = 0.01$ V). Required values of parameters used for calculation and simulation are shown in Table 1.

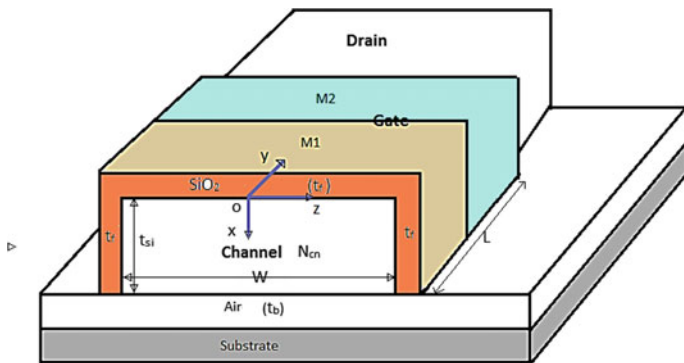


Fig. 1 3D schematic representation of DMTG SON TFET

Table 1 Parameter table

Parameters	Values
t_f	1 nm
t_{si}	10 nm
t_b	1 nm
W	10 nm
N_a	$1 \times 10^{23} \text{ m}^{-3}$
N_{cn}	$1 \times 10^{21} \text{ m}^{-3}$
N_d	$1 \times 10^{22} \text{ m}^{-3}$
Φ_{M1}	4.2 eV
Φ_{M2}	4.25 eV

3 Analytical Model

3.1 Expression of the Surface Potential

The surface potential for this model is obtained as follows where the region 1 is considered as area under metal M1 and region 2 is considered an area under metal M2.

The 3D Poisson's [7] equation is,

$$\frac{\partial^2 \phi(x, y, z)}{\partial x^2} + \frac{\partial^2 \phi(x, y, z)}{\partial y^2} + \frac{\partial^2 \phi(x, y, z)}{\partial z^2} = - \frac{qN_{CN}}{\epsilon_{si}} \tag{1}$$

For $(0 \leq y \leq L, 0 \leq x \leq t_{si}, -\frac{W}{2} \leq z \leq \frac{W}{2})$

where silicon dielectric constant is denoted by ϵ_{si} , N_{CN} is the uniform doping concentration in the channel region, and q is the electronic charge. Using Young's approximation, the potential distribution profile is considered as parabolic [7].

$$\phi_j(x, y, z) = C'_{0j}(y, x) + C'_{1j}(y, x)z + C'_{2j}(y, x)z^2 \quad (2)$$

($j = 1$ for Region 1 and $j = 2$ for Region 2)

For low drain voltage, the potential distribution is parabolic in the x direction. At $z = 0$, the potential distribution for region 1 and 2 is,

$$\phi_j(x, y, 0) = C'_{0j}(y, x) = \phi_{sj}(y) + C_{1j}(y)x + C_{2j}(y)x^2 \quad (3)$$

where $\phi_{s1}(y)$ and $\phi_{s2}(y)$ are the surface potential in region 1 and region 2. $C_{11}(y)$, $C_{21}(y)$, $C_{12}(y)$, $C_{22}(y)$ are the arbitrary constant. Due to using two different metals with different work function, makes their flat band voltages different, $V_{FB1} = \phi_{M1} - \phi_{si}$ and $V_{FB2} = \phi_{M2} - \phi_{si}$.

Where ϕ_{M1} , ϕ_{M2} are work functions of first and second metal, respectively. V_{FB1} and V_{FB2} are flat band voltages under metal M1 and M2, and ϕ_{si} is the work function of silicon.

$$\phi_{si} = x + \frac{E_g}{2q} - \phi_B \quad (4)$$

$$\phi_B = V_T \ln\left(\frac{N_{CN}}{n_i}\right) \quad (5)$$

where x is the electron affinity, E_g is the bandgap of silicon at 300 K, and ϕ_B is the built-in potential. Here V_T is the thermal voltage and n_i is the silicon's intrinsic carrier concentration.

The potential at the front and lateral interface under M1 and M2 is,

$$\phi_j(0, y, 0) = C'_{0j}(y) = \phi_{sj}(y) \quad (6)$$

So due to symmetry in z direction,

$$C'_{1j}(y, x) = 0 \quad (7)$$

Using Eq. (3) we get,

$$C'_{2j}(y, x) = -\frac{4}{W^2} \left(C'_{0j}(y, x) - \phi_{sj}(y) \right) \quad (8)$$

(1) The electric field is continuous at the front-gate oxide interface for this structure.

$$\left. \frac{d\phi_j(x, y, z)}{dx} \right|_{x=0, z=0} = \frac{\epsilon_{ox}}{\epsilon_{si}} \left(\frac{\phi_{sj}(y) - V'_{GSj}}{t_f} \right) \quad (9)$$

$j = 1$ for region 1 and for region 2, $j = 2$ where $V'_{GSj} = V_{GS} - V_{FBj}$

The electric field is continuous at the back-gate oxide and the channel interface.

$$\left. \frac{d\phi_j(x, y, z)}{dx} \right|_{x=t_{si}, z=0} = \frac{\epsilon_{air}}{\epsilon_{si}} \left(\frac{V'_{SUBj} - \phi_{Bj}(y)}{t_b} \right) \quad (10)$$

$j = 1$ for region 1 and for region 2, $j = 2$ where $V'_{SUBj} = V_{SUB} - V_{FBj}$.

- (2) At the interface of two different metals, the surface potential and electric field are continuous. So,

$$\phi_1(0, y, 0)|_{y=L1} = \phi_2(0, y, 0)|_{y=L1} \quad (11)$$

$$\left. \frac{d\phi_1(x, y, z)}{dy} \right|_{y=L1} = \left. \frac{d\phi_2(x, y, z)}{dy} \right|_{y=L1} \quad (12)$$

- (3) The source end potential is given by,

$$\phi_1(x, 0, z) = V_{bip} \quad (13)$$

where V_{bip} is the built-in potential at the source-channel interface and $V_{bip} = -V_T \ln\left(\frac{N_a}{N_{cn}}\right)$. N_a is the source doping concentration.

- (4) The potential at the drain end is given by

$$\phi_2(x, L, z) = V_{bin} + V_{DS} \quad (14)$$

where V_{bin} is the built-in potential at the drain-channel interface and $V_{bin} = V_T \ln\left(\frac{N_d N_{cn}}{n_i^2}\right)$. N_d is the doping concentration at the drain region. n_i is the silicon's intrinsic carrier concentration.

Using the boundary condition (1) and (2), the constants $C_{11}(y)$, $C_{12}(y)$, $C_{21}(y)$, and $C_{22}(y)$ are $C_{1j}(y) = \frac{\epsilon_{ox}}{\epsilon_{si}} \left(\frac{\phi_{Sj}(y) - V'_{GSj}}{t_f} \right)$;

$$C_{2j}(y) = \frac{V'_{SUBj} - \phi_{Sj}(y) \left[1 + \frac{C_f}{C_{si}} + \frac{C_f}{C_b} \right] + V'_{GSj} \left[\frac{C_f}{C_{si}} + \frac{C_f}{C_b} \right]}{t_{si}^2 \left[1 + \frac{2C_{si}}{C_b} \right]}$$

where $C_f = \frac{\epsilon_{ox}}{t_f}$, $C_{si} = \frac{\epsilon_{si}}{t_{si}}$, and $C_b = \frac{\epsilon_{air}}{t_b}$.

Now, using the boundary conditions (1)–(6) and using the value of different constant the surface potential.

$$\text{Under M1 is } \phi_{S1}(y) = Ae^{\eta y} + Be^{-\eta y} + \sigma_1 \quad (15)$$

$$\text{Under M2 is } \phi_{S2}(y) = Me^{\eta(y-L1)} + Ne^{-\eta(y-L1)} + \sigma_2 \quad (16)$$

where $\sigma_1 = -\frac{\beta_1}{\alpha}$, $\sigma_2 = -\frac{\beta_2}{\alpha}$, and $\eta = \sqrt{\alpha}$. A , B , M , N calculated using boundary conditions are,

$$A = \frac{V_{\text{bip}} - D}{C} - B - \sigma_1 \quad (17)$$

$$B = \frac{\left(\frac{V_{\text{bin}} - V_{\text{ds}} - F}{C} - \sigma_2 - \left(\frac{V_{\text{bip}} - D}{C} \right) e^{\eta L} + \sigma_1 e^{\eta L} - (\sigma_1 - \sigma_2) \cos(\eta L_2) \right) e^{\eta L}}{(1 - e^{2\eta L})}; \quad (18)$$

$$M = Ae^{\eta L1} + \frac{(\sigma_1 - \sigma_2)}{2}; \quad (19)$$

$$N = Be^{-\eta L1} + \frac{(\sigma_1 - \sigma_2)}{2}; \quad (20)$$

3.2 Expression for Electric Field

At the tunneling junction, the total electric field is,

$$E_T = \sqrt{(E_x^2 + E_y^2 + E_z^2)} \quad (21)$$

3.3 The Expression for Drain Current

The drain current

$$I_{\text{DS}} = q \iiint G_{\text{BT}} dx dy dz \quad (22)$$

and

$$G_{\text{BT}} = A1E^{d1} \exp\left(-\frac{B1}{E}\right)$$

where $A1$ and $B1$ are the Kane's parameter [8], which are material dependent, i.e., depends on the effective mass of holes and electrons. $A1 = 4 \times 10^{19} \text{ eV}^{0.5}/\text{cm-s-V}^2$

and $B1 = 41 \text{ MV/cm-eV}^{1.5}$. For indirect tunneling, the value of $d1$ is taken as 2, and for direct tunneling, it is 2.5. G_{BT} is the tunneling generation rate.

4 Result and Discussion

This section describes the overall performance of our proposed DMTG SON TFET structure using SILVACO ATLAS simulator data [9]. When operating in the off-state, the TFET has no tunneling of carriers as there is no overlap between occupied band of source and channel unoccupied band. Less reverse tunneling current flows for this reason in the proposed structure. But in the on-state, the barrier height gets reduced, which increases carrier In Fig. 2, this barrier height can be varied with changing of gate bias which increases carrier tunneling from source to drain.

Figure 3 shows the different surface potential results along the channel length for variation of V_{DS} . Figure 3 shows that the surface potential undergoes changes near the channel drain interface only. This illustrates that at the source side tunneling junction has the less effect on the variation of V_{DS} . Figure 4 shows the comparative results of the electric field of DMTG SON TFET and, SMTG SON TFET. Fig. 4 shows that close to the drain region the electric field profile is low. The high electric field near the source channel interface increases the overall drain current I_{DS} in the proposed structure. Figure 5 shows the drain current modeling of our proposed structure w.r.t the gate voltage V_{GS} for different values of work function combination. The high electric field at the source side increases the on current for this structure. The simulation is performed using Silvaco ATLAS simulator.

Fig. 2 Distribution of surface potential along the length of the channel ($L = 30 \text{ nm}$) for different values of V_{GS} . Here, $L1: L2 = 1:1$. $z = W/2$ and $x = 5 \text{ nm}$. The symbol represents the ATLAS simulated values by taking into consideration parameters of Table 1

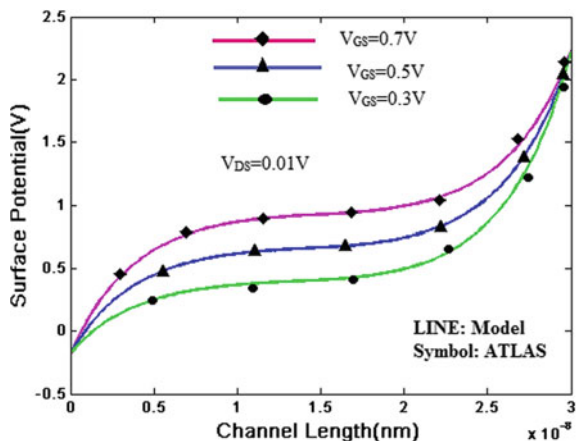


Fig. 3 Distribution of surface potential along the length of the channel ($L = 30 \text{ nm}$) for different values of V_{DS} . Here, $L1:L2 = 1:1$. $z = W/2$ and $x = 5 \text{ nm}$. The symbol represents the ATLAS simulated values by taking into consideration parameters of Table 1

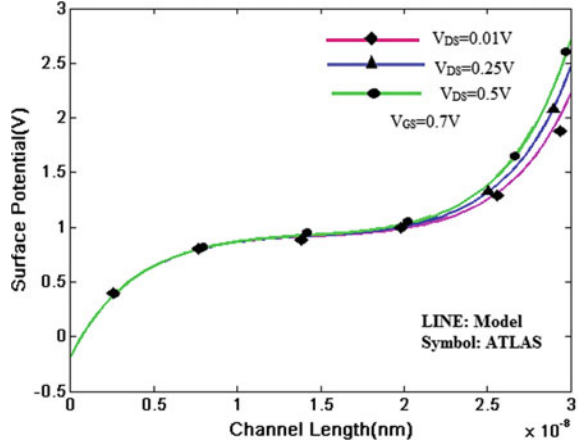


Fig. 4 Comparative analysis of electric field profile along the length of the channel ($L = 30 \text{ nm}$) for DMTG SON TFET, SMTGSON TFET. Symbol represents the ATLAS simulated values by taking into consideration parameters of Table 1

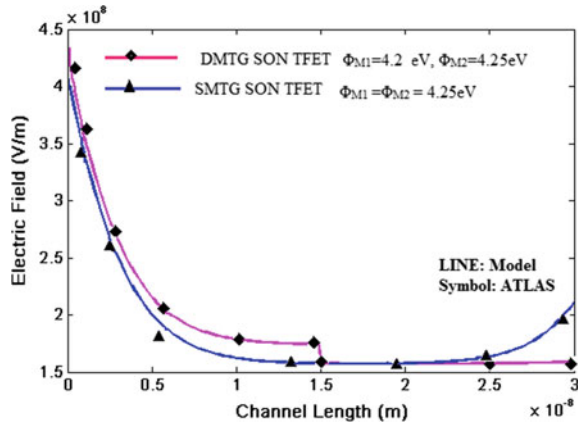
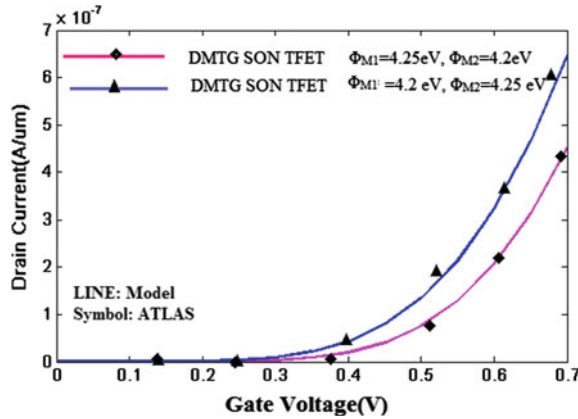


Fig. 5 Analysis of drain current w.r.t the gate voltage variation for DMTG SON TFET. Here, $L1:L2 = 1:1$. $z = W/2$ and $x = 5 \text{ nm}$. The symbol represents the ATLAS simulated values by taking into consideration parameters of Table 1. The plotting is done in a linear scale



5 Conclusion

In this paper, a 3D analytical model of DMTG SON TFET has been presented. TFET is a device which can replace the conventional MOSFET due to its most promising behavior and low power application. The modeling of dual metal reduces the reverse tunneling, increases the on-off current ratio, etc., than the SMTG SON TFET structure. The result of the proposed DMTG SON TFET is quite close of the Silvaco ATLAS simulated data.

In this paper, a 3D analytical model of DMTG SON TFET has been presented. TFET is a device which can replace the conventional MOSFET due to its most promising behavior and low power application. The modeling of dual metal reduces the reverse tunneling, increases the on-off current ratio, etc., than the SMTG SON TFET structure. The result of the proposed DMTG SON TFET is quite close of the SILVACO ATLAS simulated data.

References

1. Emerging Research Devices, Int. Technol. Roadmap Semicond., 2009.
2. A. Mallik A. Chattopadhyay “The impact of fringing field on the device performance of a p-channel tunnel field-effect transistor with a high-gate dielectric” *IEEE Trans. Electron Devices* vol. 59 no. 2 pp. 277–282 Feb. 2012.
3. R. S. Muller T. I. Kamins M. Chan *Device Electronics for Integrated Circuits* New York NY USA: Wiley pp. 443–445 2003.
4. N. Bagga S. K. Sarkar, “Analytical model for tunnel barrier modulation in triple metal double gate TFET” *IEEE Trans. Electron Devices* vol. 62 no. 7 pp. 2136–2142 July. 2015.
5. E. Gnani A. Gnudi S. Reggiani G. Bacarani “Drain-conductance optimization in nanowire TFETs by means of a physics-based analytical model” *Solid-State Electron.* vol. 84 pp. 96–102 Jun. 2013.
6. Marjani, S., Hosseini, S.E.: A 3D analytical modeling of tri-gate tunneling field-effect transistors. *J Comput Electron* **15**, 820–833 (2016).
7. K. K. Young “Short-channel effect in fully depleted SOI MOSFETs” *IEEE Trans. Electron Devices*, vol. 36 no. 2 pp. 399–402 Feb. 1989.
8. A. S. Verhulst D. Leonelli R. Rooyackers G. Groesenke “Drain voltage dependent analytical model of tunnel field-effect transistors” *J. Appl. Phys.* vol. 110 no. 2 pp. 024510 Jul. 2011.
9. ATLAS User’s Manual Santa Clara CA USA: 2010.

Modeling of Lead-Free $CH_3NH_3SnI_3$ -Based Perovskite Solar Cell Using ZnO as ETL

Tapas Chakrabarti, Malay Saha, Ambar Khanda
and Subir Kumar Sarkar

Abstract Over the last few decades, researchers have invested enormous research effort into inorganic/organic solar cells like dye-sensitized solar cells (DSSCs) due to its cost-effectiveness and simple fabrication process, over the conventional photovoltaic solar cells made of different materials like Si, Ge, GaAs, GaInP. In 2012, the solid-state perovskite materials are organic–inorganic metal trihalide materials, having chemical formula ABX_3 and having specific crystal structure as calcium titanium oxide ($CaTiO_3$) revolutionized as the light-harvesting, absorbing materials. In past couple of years, perovskite solar cells have shown significant improvement in terms of efficiency and crossed the 20% efficiency level. There has been a consistent approach among researchers to explore different materials as electron transport layer of the perovskite solar cells to improve the performance of the solar cells. The most common perovskite material used in solar cell is methyl ammonium lead iodide ($CH_3NH_3PbI_3$) along with top and bottom layer of HTO and ETO. In this work, the toxic material lead iodide (PbI_3) is replaced with tin oxide (SnI_3), and this perovskite material $CH_3NH_3SnI_3$ introduced with an ETO layer of ZnO has achieved a significant efficiency of 22.90%. In this work, zinc oxide (ZnO) layer is proposed as the electron transport layer for lead-free $CH_3NH_3SnI_3$ -based perovskite solar cells. The proposed structure is “metal contact/*spiro-MeOTAD/CH₃NH₃SnI₃/ZnO/TCO/metal contact,*” and the structure is modeled using SCAPS simulating tool.

T. Chakrabarti (✉) · M. Saha · A. Khanda
Department of ECE, Heritage Institute of Technology, Kolkata, India
e-mail: ctapash@gmail.com

M. Saha
e-mail: malaysaha7227@gmail.com

A. Khanda
e-mail: ambar.khanda@gmail.com

S. K. Sarkar
ETCE Department, Jadavpur University, Kolkata, India
e-mail: su_sircir@yahoo.co.in

Keywords Perovskite · $CH_3NH_3SnI_3$ · ETL (electron transport layer) HTL (hole transport layer) · ZnO · SCAPS · Lower unoccupied molecular orbit (LUMO) · Highest occupied molecular orbit (HOMO)

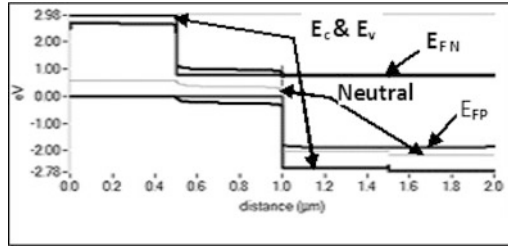
1 Introduction

In the modern world, energy has become one of the basic needs for life. With the increase in world population, the energy demand is also increasing. There is a growing concern about the energy generated from fossil fuels due to its impact on the nature. Solar energy has become one of the most focused sources of obtaining “green” energy in last few decades. Photovoltaic cells directly convert solar radiation into electricity without affecting the environment. In recent times, there has been a constant focus to find alternatives of Si-based solar cells for cheap and simple manufacturing process-based solar cells. In recent couple of years, perovskite solar cells have shown significant improvement in the efficiency and crossed the 20% efficiency level [1]. Organic–inorganic metal trihalide materials, having chemical formula ABX_3 , are called perovskite materials. Perovskite solar cells have the advantage of being able to be manufactured by cost-effective simple solution-based processing or by vapor phase deposition of cost-effective materials. A perovskite solar cell is mainly comprised of a perovskite material sandwiched between an electron transport layer (ETL) and a hole transport layer (HTL), on the top of TCO. $CH_3NH_3PbI_3$ is the most used perovskite material in the perovskite solar cells as the active layer. But due to toxicity of lead (Pb) to the human health, a suitable alternative of $CH_3NH_3PbI_3$ is being researched across the world in recent times [2–5]. $CH_3NH_3SnI_3$ has emerged as a viable alternative of $CH_3NH_3PbI_3$ in last couple of years due to its low band gap (almost 1.3 eV) and high absorption coefficient. In this work, n-doped zinc oxide (ZnO) is proposed as the electron transport layer for lead-free $CH_3NH_3SnI_3$ -based perovskite solar cells [6]. The proposed structure is “metal contact/spiro-MeOTAD(p)/ $CH_3NH_3SnI_3$ /ZnO(n)/TCO/metal contact,” and the structure is modeled using SCAPS simulating tool [7].

2 ZnO as Electron Transport Layer

Electron and hole pairs are generated in the active region (perovskite material) of the perovskite solar cells. After that the electrons and the holes need to be separated to collect the carriers at the front and back electrodes to get a net current at the outer circuit. Hole and electron transport layers are deposited to collect and transport the holes and the electrons to the electrodes efficiently and to block the other type of carriers to minimize the recombination; so that we can collect maximum number of carriers at the respective electrodes.

Fig. 1 Band diagram of the ZnO in proposed solar cell



For any material to be employed as electron transport layer (ETL) in perovskite solar cells, the material must satisfy few important properties. Those properties are: (i) Conduction band of the ETL material should be less than the LUMO level of the perovskite material (ii) high electron mobility (iii) higher band gap [8]. Now as far as the ZnO is concerned, ZnO is a wide band gap (~ 3.4 eV) material. The band structure of ZnO satisfies the necessary condition to be employed as electron transport layer, which is shown in the band diagram of the structure, Fig. 1. The most important reason behind the success of ZnO as ETL is its very high electron mobility. The electron mobility of the n-doped ZnO is almost $200 \text{ cm}^2/\text{Vs}$ [8]. The relation between current density, J_{sc} , and mobility is:

$$J_{sc} = qG \left(\sqrt{\mu_p} + \sqrt{\mu_n} \right) \left(\sqrt{\frac{KT}{q}} \tau \right)$$

From the above equation, it is very clear that the high mobility of the carriers will lead to improvement in the current density which leads to the performance of solar cell. This is our motivation behind the study of ZnO as electron transport layer for $CH_3NH_3SnI_3$ -based perovskite solar cells.

3 Proposed Device Structure

The proposed perovskite solar cell structure is “metal contact/TCO/ZnO(n)/ $CH_3NH_3SnI_3$ /spiro-MeOTAD(p)/metal contact.” In this solar cell, a planer p-i-n heterojunction architecture with the layer configuration of n-doped ZnO and p-doped spiro-MeOTAD layers are used as electron transport layer and hole transport layer, respectively, [9, 10]. The modeled, simulated perovskite solar cell schematic diagram is illustrated in the Fig. 2. Effective conduction band and valence band densities of spiro-MeOTAD are $1.176 \times 10^{18} \text{ cm}^{-3}$ and $1.166 \times 10^{19} \text{ cm}^{-3}$, respectively, and are considered in this proposed structure [11]. The parameter values of all layers are shown in Table 1 [2, 8].

Thermal velocities of the electron and hole of ZnO are both set to be equal to 10^7 cm/s for this structure. The defects are set to be single and neutral defect with a total density of $1 \times 10^{17} \text{ cm}^{-3}$, located at 0.6 eV above the top of valence band, E_v .

The parameter setting of the defects in the simulation is shown in Table 2. The constant, A_a , is assumed to be as 10^5 to obtain the absorption coefficient, alpha (α), where $\alpha = A_a * (\hbar\omega E_g)^{1/2}$ [2].

Fig. 2 Schematic diagram of the proposed cell

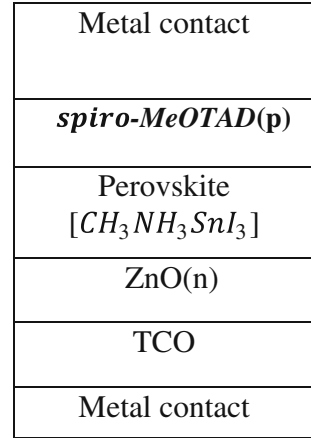


Table 1 Defect values assumed for the simulation

Parameters and units	Value
Defect type	Neutral
Capture cross-section for	1.0×10^{-15}
Electrons and holes/cm ²	1.0×10^{-15}
Energetic distribution	Single
Energy level with respect to Ev (above Ev, eV)	0.6
Total density/cm ³	1.0×10^{14}

Table 2 Layer parameters used for the simulation

Parameters	Spiro-MeOTAD (HTL)	Perovskite (CH ₃ NH ₃ SnI ₃)	ZnO (ETL)	TCO
Band gap	2.25	1.23	3.4	3.5
Dielectric constant	7.3	8.2	8.12	9
Electron affinity	3.73	4.17	4.29	4.4
Electron mobility	300	1.6	200	20
Hole mobility	100	1.6	5	10
Acceptor doping concentration (N_A)	2×10^{18}	Self doped	0	0
Donor doping concentration (N_D)	0	0	1×10^{19}	2×10^{19}
Layer thickness	0.25 μ m	0.40 μ m	0.5 μ m	0.5 μ m

4 Result and Discussion

The proposed structure is simulated in SCAPS simulating software tool, considering all the parameters of defect states to make the structure more realistic in physical environment. The efficiency of this perovskite solar cell is achieved 22.90% of efficiency, along with the short-circuit current density (J_{sc}) of 34.23 mA/cm² and the open circuit voltage (V_{oc}) of 0.87 V. The fill factor of this solar cell is observed as 76.68%. The J–V curve of this solar cell is shown in Fig. 3. The doping level of the ZnO varied and optimized the performance of the proposed solar cell. Figure 4 shows the relation between the doping level of ZnO and the efficiency of the cell.

From the Fig. 4, it is observed that the efficiency of the cell is increased with increasing doping level and the optimum level of donor doping concentration $1 \times 10^{19} \text{ cm}^{-3}$ is considered for ZnO layer.

Fig. 3 J–V curve of the proposed cell

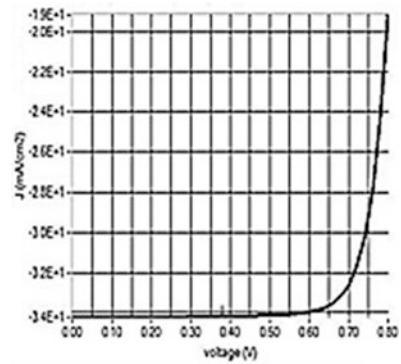
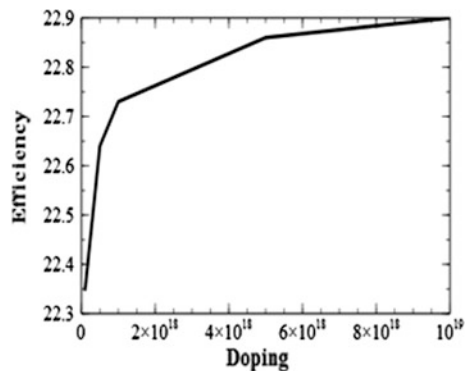


Fig. 4 Doping of ZnO versus efficiency



5 Conclusion

In this work, zinc oxide (ZnO) is proposed as the electron transport layer (ETL) for lead-free $CH_3NH_3SnI_3$ -based perovskite solar cells and the performance of the cell is also studied. The thickness and doping level of the spiro-MeOTAD layer are varied to study the optimized performance. Using ZnO as electron transport layer for the lead-free $CH_3NH_3SnI_3$ -based perovskite solar cells is a novel idea, and simulated result reveals that the efficiency of this solar cell is 22.90%. In future, the results of this proposed structure need to be validated through physical fabrication and further study

Acknowledgements The authors wish to thank Marc Burgelman and Koen Decock, ELIS, University of Gent, for providing the SCAPS simulation software.

References

1. Xuejie Zhu, Dong Yang, Ruixia Yang, Bin Yang, Zhou Yang, Xiaodong Ren, Jian Zhang, Jinzhi Niu, Jiangshan Feng and Shengzhong (Frank) Liu, "Superior stability for perovskite solar cells with 20% efficiency using vacuum co-evaporation", *rsc.li/nanoscale*, <https://doi.org/10.1039/x0xx00000x>
2. Hui-Jing Du, Wei-Chao Wang, and Jian-Zhuo Zhu, "Device simulation of lead-free $CH_3NH_3SnI_3$ Perovskite solar cells with high efficiency", *Chin. Phys. B*, Vol. 25, No. 10 (2016) 108803
3. Nakita K. Noel, Samuel D. Stranks, Antonio Abate, Christian Wehrenfennig, Simone Guarnera, Amir-Abbas Haghighirad, Aditya Sadhanala, Giles E. Eperon, Sandeep K. Pathak, Michael B. Johnston, Annamaria Petrozza, Laura M. Herza and Henry J. Snaith, "Lead-free organic-inorganic tin halide Perovskite for photovoltaic applications", *Energy Environ. Sci.*, 2014, 7, <https://doi.org/10.1039/c4ee01076k>
4. Anastasiia Iefanova, Nirmal Adhikari, Ashish Dubey, Devendra Khatiwada, and Qiquan Qiao, "Lead free $CH_3NH_3SnI_3$ perovskite thin-film with p-type semiconducting nature and metal-like conductivity", *AIP Advances* 6, 085312 (2016); <https://doi.org/10.1063/1.4961463>
5. Chong Liu, Jiandong Fan, Hongliang Li, Cuiling Zhang & Yaohua Mai, "Highly Efficient Perovskite Solar Cells with Substantial Reduction of Lead Content", *Scientific Reports*, 6:35705, <https://doi.org/10.1038/srep35705>
6. Lung-Chien Chen* and Zong-Liang Tseng, "ZnO-Based Electron Transporting Layer for Perovskite Solar Cells", *Nanostructured Solar Cells*, Intech open access book, page-203-2015, <https://dx.doi.org/10.5772/65056>
7. SCAPS Manual: http://download.scaps.com/downloads/manuals/sc_manual_sl_English.pdf
8. E. Constable and R. A. Lewis, "Optical parameters of Spiro-MeOTAD determined using continuous-wave terahertz radiation", *JOURNAL OF APPLIED PHYSICS* 112, 063104 (2012)
9. Wonchai Promnopas, Titipun Thongtem, and Somchai Thongtem, "Spiro-MeOTAD Semiconductor-Polymer Gel Compositated Electrolyte for Conversion of Solar Energy", *Journal of Nanomaterials*, Volume 2014, Article ID 529629

10. Othmane Skhouni, Ahmed El Manouni¹, Bernabe Mari, and Hanif Ullah, "Numerical study of the influence of Spiro-MeOTAD thickness on CdS/Spiro-MeOTAD solar cell performance", *Eur. Phys. J. Appl. Phys.* (2016) 74: 24602, <https://doi.org/10.1051/epjap/2015150365>
11. Ming-Hsien Li, Jun-Ho Yum, Soo-Jin Moon, Peter Chen, "Inorganic p-Type Semiconductors: Their Applications and Progress in Dye-Sensitized Solar Cells and Perovskite Solar Cells", *Energies* 2016, 9, 331; <https://doi.org/10.3390/en9050331>

Experimental Investigation on Mustard Oil-Based Alumina Nanofluid Under Varying Temperature and Humid Condition

Sachin Thakur, Jaspreet Singh Chahal and Sunny Vig

Abstract Most desirable part of the electrical machines is insulation. This paper exploits properties of mustard oil which could be the better solution in oil-cooled transformer than traditional petroleum-based mineral oils, as it exhibits better properties of flash point, fire point, and breakdown voltage. Moreover, mustard oil is non-inflammable and non-toxic in nature. Since last century, petroleum-based mineral oil is used as liquid insulating and cooling medium. Besides their good insulating and cooling properties, some environmental factors are also related to them. With the consideration of environmental factors, many researchers are intending to evolve new insulating medium having better properties to replace these presently used mineral oils. This paper mainly emphasizes on the investigation of breakdown strength of mustard oil. The breakdown test is conducted based on Indian standard (IS 6792:1992).

Keywords Breakdown voltage · Mustard oil · Fire point · Flash point
Mineral oil

S. Thakur (✉)

Electrical Department, Chandigarh University, Mohali, India
e-mail: thakurs0648@gmail.com

J. S. Chahal

Department of Electrical & Electronics Engineering,
Faculty of Electrical Engineering, I.K.G.T. University, Kapurthala, India
e-mail: jaspreet84@gmail.com

S. Vig

Department of Electrical & Electronics Engineering,
Faculty of Electrical Engineering, Chandigarh University, Mohali, India
e-mail: sunnyleo14@gmail.com

1 Introduction

In transmission and distribution setup, transformer plays very significant role as it steps up and steps down the voltage at necessary levels. Failure of transformer definitely leads to complete interruption of supply in the system. Insulation of power transformer is a very critical element, i.e., oil, paper, and pressboard insulation which directly affect the operation and life of the transformer as well. Presently, petroleum-based mineral oils (paraffin-based and naphtha-based) are in use, to insulate, to suppress corona and arcing, and to use as a coolant in power transformers.

Dielectric properties of transformer affect its service life and insulation. During service, insulation gets affected by applied stress such as electrical, thermal, and mechanical. So majority of failures may be caused due to insulation failure [1]. Petroleum-based mineral oils such as synthetic oil, silicon oil are used as insulation in oil-filled transformer. But due to their different chemical properties and high cost results to curb in specific utilization application only. On the other hand, mineral oil has good chemical properties and low cost, but their non-biodegradable, toxic, non-environmental-friendly nature makes them hard to dispose off. In view of above, researches are in progress for an environmental-friendly and easily available resources like coconut oil, vegetable oil, and palm kernel oil as alternative of these mineral oils [2]. Instead of these oils, mustard oil could also be the substitute of mineral oil because of its easy handiness. Mainly, mustard oil is used for cooking, health, skin, and hair. Mustard oil consists of a mixture of chemically modified mustard oil and alkyl esters of mustard oil fatty acids in the ratio 70:30 to 100:00 along with additives. Mustard oil is the vegetable extraction and is obtained from the seeds of black and white mustard plants. Mustard oil is used as alternating insulating fluid which is easily available and accessible in the nature.

2 Problem Overview

2.1 *Liquid Dielectrics Breakdown*

Breakdown in liquid dielectrics is a fact which linking the distance of separation between the electrodes, which resulting, the decrease of voltage and increase of current electrode. Failure of the insulating properties of liquid dielectric is non-permanent. The main purpose of the liquid dielectric is to avert electric discharge. Liquid dielectric finds application in high voltage, i.e., transformer, capacitors, high-voltage cables, switchgear, and used as electrical insulator.

2.2 Breakdown Voltage

Breakdown voltage is defined as degree of capability of oil withstands an electric stress. It is a minimum voltage which causes a breakdown due to rise of electrical conductivity. A large value of current through the breakdown region changes the characteristics of oil and causes mechanical, thermal, and chemical operation. Breakdown voltage is an indicator of oil pollution.

2.3 Electric Breakdown Strength

Besides polarization and dielectric loss, electric breakdown strength is most important quality of dielectrics. When an electric field is applied to dielectric substance or electric insulator, there is an extensive decrease in resistance of an electric insulator and outcome in insulator which becomes electrically conductive. The conduction created in dielectric substance is very outrageous which can also outcome in melting, burning, or vaporization of dielectric substance which forever spoiled the dielectric substance. This process is called the electric breakdown of the dielectric.

Electric breakdown is not controlled by voltage alone, but it is also being dependent on the electric field [3]. Consequently, electric breakdown strength can be computed using the formula

$$E_b = \frac{V_b}{D} \quad (1)$$

E_b is electric breakdown strength in [kVmm⁻¹]
 V_b is breakdown voltage in [kV]
 D is interelectrode distance.

3 Experimental

3.1 Oil Purification

It is the most important part of dielectrics to avoid discharge. Mustard oil is filtered over a 5-micron sintered glass filter with the impact of vacuum, degaussed for superior than 0.2 Torr, and then permitted to get saturated with dry air for 8–10 h. The overhead stated techniques are appropriate to filter the oil in all the experiment.

3.2 *Cleaning and Polishing of Brass Electrodes*

Brass electrode was polished on the lathe machine utilizing 600 grades, and Brasso liquid polish was used. After attentive scrubbing with cotton, they were washed with alcoholic solution to eliminate traces of brass. The polished brass electrodes are shown in Fig. 1.

3.3 *Test Cell and Electrodes*

The cubical-shaped test cell with 15 cm edge was forged using 1.0-cm-thick Polymethyl-Metha Acrylate (PMMA) sheet. It had the settlement of holding the shanks and electrodes in the vertical plane. The test cell was cleaned with soap and water, then it again cleaned with alcoholic solution and then dried, after that the processed oil is dipped into it. Protection should be taken when cleaned and polished electrodes were fixed on the shanks of the cell to circumvent any scratches on their surface and initiation of fibers or dust particles into the cell [4]. Figure 2 shows test cell with electrodes and mustard oil.

4 **Experimental Setup and Procedure**

4.1 *Test Material and Selection*

The mustard oil and nanoparticles with an average size of $d < 50$ nm (which were bought from a reputable company) were used in the tests. In this test, the specific



Fig. 1 Polished brass electrodes

Fig. 2 Test cell with electrodes and mustard oil



Table 1 Basic properties of alumina nanoparticles [6]

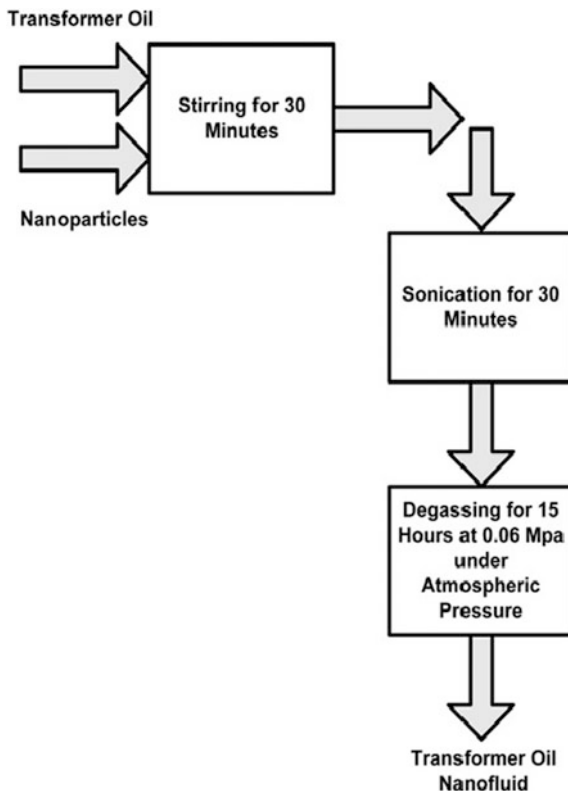
Properties	Al ₂ O ₃ nanoparticles
Conductivity, (S/m) [7, 8]	10 ⁻¹²
Relaxation time, (s) [7, 8]	42.2
Relative permittivity [7, 8]	9.9
Density, (g/cm ³)	3.97
Material type	Insulator

concentration of single nanofluid 0.1% was selected. The basic properties of the selected nanoparticle are also summarized in Table 1.

4.2 Preparation of Nanofluid

The nanofluids were prepared by mixing Al₂O₃ (size 50 nm) nanoparticles with mustard oil samples. For preparation of nanofluid, 0.1% Al₂O₃ nanoparticle volume fraction was mixed with mustard oil. The nanofluids were dispersed for 30 min by using a magnetic stirrer. Finally, to get a well-dispersed nanofluid, the ultrasonic dispersion technique was done in 2 h and was applied to the prepared nanofluids to make sure the similarity of such liquid. The magnetic stirring is very helpful to dissolve the nanopowders consistently in the base fluid, but this energy is not sufficient to break agglomeration of nanoparticles. Therefore, to break the agglomerations of nanoparticles, ultrasonic mixing device was used [5]. The nanofluid preparation process is depicted in Fig. 3.

Fig. 3 Transformer oil nanofluid preparation method



4.3 Breakdown Voltage Test of Mustard Oil

The AC breakdown voltages of the fresh mustard oil and nanofluid-based mustard oil are measured using the breakdown test. Before the breakdown test, prepared mustard oil-based nanofluid was heated at temperature 40 °C to remove the moisture content in the oil for 24 h. The basic objective of breakdown test is to examine the effect of Al₂O₃ nanoparticle on the breakdown voltage of fresh mustard oil. The liquid dielectric test kit is used to measure the breakdown voltage of fresh and nanofluid-based mustard oil. The gap spacing between the two brass electrodes is 1 mm. The rate of rise of voltage is 1 kV/Sec, and frequency is 50 Hz. The measurements observed from the test are carried out at room and different temperature condition. It is mentioned that the concentration of 0.95 gm Al₂O₃ and average nanoparticle size 50 nm to indicate insulative nanoparticles are weighed.

Furthermore, the breakdown tests are executed on 950 gm oil using 0.1% white Al₂O₃ (0.95 gm). To check the attained results, each breakdown test is carried out by taking single oil sample, and individually sample is tested four times with two-minute delay and half an hour for different temperature condition. The results obtained from the breakdown test are carried out based on average values [9]. The

measuring breakdown voltage test setup is same for simple mustard oil and nanofluid-based mustard oil. Tables 2 and 3 show the average breakdown results of simple mustard oil and nanofluid-based mustard oil. Figure 4 represents the creation of soot after breakdown in mustard oil.

Table 2 Average breakdown result of simple mustard oil

Average breakdown voltage (kV)		Temperature (°C)
1	17.61	30
2	15.02	40
3	18.85	50
4	17.27	60
5	17.80	70
6	17.11	80

Table 3 Average breakdown result of nanofluid-based mustard oil

Average breakdown voltage (kV)		Temperature (°C)
1	11.98	30
2	14.97	40
3	17.68	50
4	20.78	60
5	23.32	70
6	25.44	80

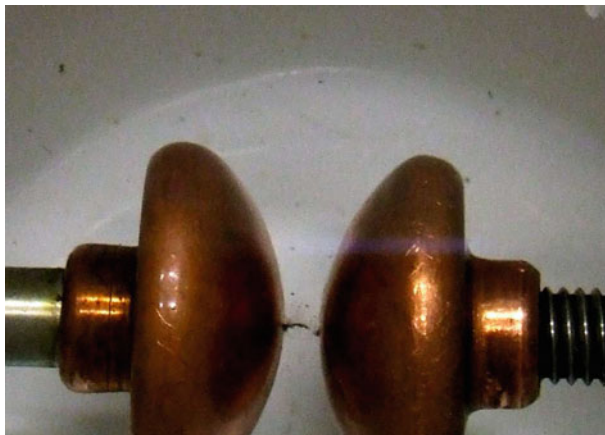


Fig. 4 Creation of soot after breakdown in mustard oil

5 Result and Discussion

The AC breakdown strength of the nanofluid as a function of the temperature is shown in Figs. 5 and 6. The AC breakdown voltages obtained during the test are measured in rms. The AC breakdown strength increases with the increase in temperature. The value of the breakdown strength increases significantly in the mass fraction of 0.1% and shown the improved dielectric strength of mustard oil. Nanofluid-based mustard oil shows greater dielectric strength at a particular temperature and lower dielectric strength at lower temperatures as compared to simple mustard oil as shown in Fig. 7.

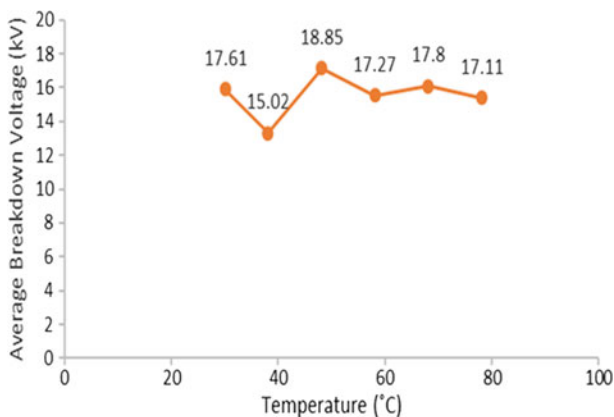
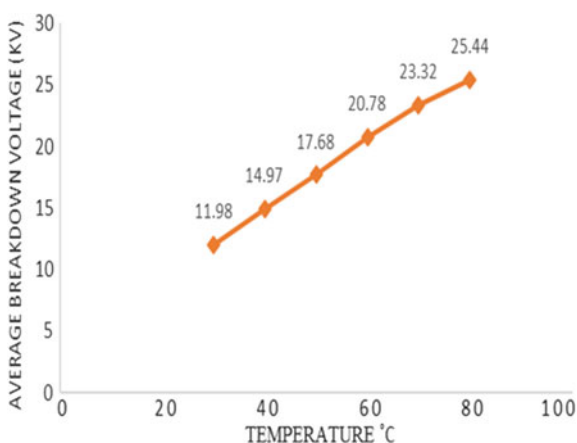


Fig. 5 Average breakdown voltage of simple mustard oil versus temperature

Fig. 6 Average breakdown voltage of nanofluid-based mustard oil versus temperature



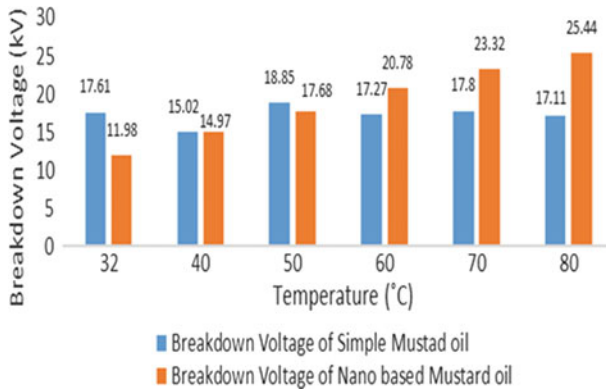


Fig. 7 Comparison of simple mustard oil versus nanofluid-based mustard oil

6 Conclusion

In this paper, initially the simple mustard oil was selected and their breakdown voltage was investigated. Furthermore, Al_2O_3 nanoparticle was selected, and transformer oil-based nanofluids were prepared with particular nanoparticle volume concentration. The AC breakdown strength of prepared nanofluids was tested and investigated. This work confers the effect Al_2O_3 nanoparticle on mustard oil. The investigation results show improvement in breakdown strength due to the addition of Al_2O_3 nanoparticle. The breakdown strength shows improvement with different temperature due to the reduction of moisture content. Additionally, the breakdown strength increases with a single mass fraction of Al_2O_3 nanoparticles, which concludes that Al_2O_3 nanoparticle shows inhibitory effect on the breakdown process. Nanofluid-based mustard oil shows greater dielectric strength than simple mustard oil at higher temperature. From the experimental results, it was observed that the nanoparticles used in the experimentation were good aspirants to improve mustard oil for dielectric applications.

References

1. B.S.H.M.S.Y. Matharage, M.A.R.M. Fernando, M.A.A.P. Bandara, G.A. Jayantha. Kalpage, "Performance of Coconut oil as an alternative transformer liquid insulation", IEEE Trans. on Dielectr. and Elect. Insul., Vol. 20 No. 3, pp. 887–898, 2013.
2. L. Syed Mohammed, Mazood, M. Bakruthen, M. Willijuice, Iruthayarajan, M. Karthik, "Studies on critical properties of vegetables oil based insulating fluids", IEEE India Conference (INDICON), pp. 1–4, 2015.
3. M. Marci, E. Csányi, "Electric breakdown strength measurement of liquid dielectric samples exposed to the weather effect", in Proc.10th Sci. Conf. of Young Researchers—FEI TU of Kosice, 2010.

4. M. M. Mohsin; M. Rehman; R. S. Nema; M. N. Narayanachar, "Measurement of transformer oil dielectric strength", IEEE Region 10 Conference TENCN, Vol. 3, pp. 436–439, 2004.
5. P. Muangpratoom, N. Pattanadech, "Dielectric Breakdown Strength Mineral Oil Based Nanofluids", in Proc. International Conference on Condition Monitoring and Diagnosis, pp. 266–269, 2016.
6. M. Rafiq, C. Li, I. Khan, H. Zhifeng, Y. Lv, K. Yi, "Preparation and breakdown properties of mineral oil based alumina nanofluids", in Proc. IEEE Int. Conf. on Emerging Technologies (ICET), pp- 1–3, Dec. 19–20, 2015.
7. J. G. Huang, M. Zahn, and F. O'Sullivan, J Appl. Phys. 107, 014310 (2010).
8. Y. F. Du and Y. Z. Lv, Effect of TiO₂ Nanoparticles on the Breakdown Strength of Transformer Oil, IEEE, San Diego, CA (2010), pp. 1–3.
9. Mohamed E. Ibrahim; Amr M. Abd-Elhady; Mohamed Izzularab, "Effect of nanoparticles on transformer oil breakdown strength: experiment and theory", IET Science, Measurement & Technology, Vol. 10, pp. 839–845, 2016.

Optimization Method for Unit Commitment in High-Level Wind Generation and Solar Power

Saket Saurabh and MdIrfan Ahmed

Abstract One of the serious challenges that the power sector is experiencing today is unit commitment. The problem becomes more severe when renewable energy is integrated with the convention power station. In the present scenario, renewable energy alone is inadequate to achieve the demand for power. Thus, operating renewable energy coherently with the conventional power station is a major complication. The demanded power must be fulfilled by the generation scheduling under the constraint of irregularities of renewable energy that can be economically availed. Application of GA can be an important tool for solving the problems of unit commitment. Like quadratic programming which is a conventional tool for mathematical optimization, the solution of GA can be reformed by applying its output as initial feasible. With the application of GA, the solution is improved under the constraint of integrating renewable energy with conventional resources.

Keywords Unit commitment problems (UCPs) • Unit commitment (UC) Genetic algorithm (GA)

1 Introduction

The total load demanded in an electric power system is not constant throughout the day. The demand as a function of time is nonlinear and dynamic, exhibits calendar effect and seasonality, and depends on weather-related effects as well as historical data. The domestic load mainly consists of lights, fans, and appliances such as

S. Saurabh (✉)

Electrical Engineering, Amity University, Ranchi, Jharkhand, India
e-mail: saket.srb@gmail.com

M. Ahmed

Electrical Engineering, Career Point University, Kota, Rajasthan, India
e-mail: irfannitp.ahmed@gmail.com

refrigerators, heater, television, and air-conditioners which has a high peak during the evening and a low peak during the remaining hours of the day. The commercial load which covers mainly shops, malls, offices, hospitals, theaters, clubs, hotels, etc., is characterized by two peaks—mornings and evenings. So, load forecasting is done for daily, weekly, and seasonal demands in advance. The load forecasting is followed by election of units which will supply the estimated load for the required period of time at minimum cost. All the available units cannot be run all the time as it is not economical. “Determining the units of a plant that should operate for a particular load is unit commitment problem.” Here, we have used economic-emission unit commitment schedule. In recent researches, renewable energy sources have been given importance along with the lower cost of electricity generation without causing adverse effects on surroundings. Along these energy sources, investigating solar and wind power and integrating them with the thermal power systems could be a suitable option. In the first stage, economic load dispatch is done, and in the second stage, UCP is implemented in wind and solar power using GA.

2 UC Problems

In order to achieve and supply the estimated power demand, UCPs include a schedule for starting up and shutting down. While solving the UCP, there are two elemental decisions. These comprise finding the UC and determining economic dispatch. The UC selection includes allotment to the yielding units. These units while taking into consideration the system capacity requirements run all along the planning perspective. It also includes sufficiency and the restrictions on starting up and shutting down of units. In determining economic dispatch, allocation of power requirement by the system and spinning reserve capacity during the explicit hour of service are involved. Though these two selections are interdependent, the UCPs generally hold one and the other decisions into the calculation. Its objective is to achieve a comprehensive minimum cost option for running the power system during the scheduled bounds. The economic dispatch and the UC selections are clashing, whereas the achievement of one restriction leads to contravention in the other.

The UC method can be categorized as follows:

- Priority list,
- Dynamic programming,
- Lagrangian relaxation,
- Branch and bound, and
- Benders decomposition.

3 Genetic Algorithm

GAs are adjusted quest procedure established on the regulation and working of “survival of the fittest” from natural evolution. GA serves as a repetitious proceeding on a hard and fast range of population. The contender solutions exhibit encoding of the matter to a type that can be compared to the chromosomes of biological systems. A potential answer for given objectives that perform once associated with everybody may be fitness price that interprets capability to sustain. GA belongs to the category of probabilistic algorithms as it mixes components of directed search as well as random search. To attribute this, GA is stronger than the existing guided search strategies [2].

3.1 Problem Formulation

The basic purpose of the UCPs is to reduce the total cost of manufacturing over the scheduling horizon. The overall costs comprise the following:

- (i) Cost of fuel: Fuel costs are computed by feeding fuel price and unit heat rate data.
- (ii) Cost of starting up: Cost of starting up can be illustrated as a function of duration in hours the unit has been down.
- (iii) Cost of shutting down: It may be defined as the constant amount in dollar per unit for every shutdown.

The constraints which must be satisfied during the optimization process are:

- (a) System power balance (demand + losses + exports),
- (b) System reserve requirements,
- (c) Unit fundamental conditions,
- (d) Unit low and high MW limits,
- (e) Unit minimum up- and downtime,
- (f) Unit status constraints (requisite run, fixed MW, unavailability, availability),
- (g) Unit price limits,
- (h) Unit starting-up and shutting-down ramps,
- (i) Unit flame stabilization fuel mix,
- (j) Unit dual or alternate fuel usage,
- (k) Unit or plant fuel availability, and
- (l) Plant crew constraints.

Restrictions (a) and (b) involve all the units of the system and are known as coupling or system constraints. The system constraints must be customized to take into consideration the exchange of schedules for multiarea unit commitment and the tie-line limitations. In general, in the allotment of the demand and the reserves to

the generating units, constraints of the system must take into account possible transmission bottlenecks. Constraints from (c) to (k) are related to particular units and are called local constraints.

3.2 Objective Function

The objective function of the thermal UC problem is comprised of fuel and start-up costs of generating units, and we can express it as

$$FC(P(t)) = \sum_{h=1}^{24} \sum_{i=1}^{10} (a_i + b_i P_{i,h}(t) + c_i P_{i,h}^2(t)) U_{i,h} + \text{start - up cost}$$

Such that

$$P_i^{\min} \leq P_i(t) \leq P_i^{\max}$$

$$\sum_{i=1}^{10} P_{i,h}(t) U_{i,h} + \text{wind}_h + \text{solar}_h = \text{Demand}_h$$

where a_i , b_i , c_i are the positive fuel cost coefficients of unit i .

U = binary operator 0 or 1 for uncommitted and committed unit, respectively.

The output power of the PV panel is

$$P_{\text{pv}}(t) = A\beta\mu(t)$$

where

A = Area of PV panel

$\mu(t)$ = Solar insolation

β = Efficiency of PV panel.

Usually, the output power of wind turbine is proportional to kinetic energy, air density, etc.

$$P_{\text{wind}}(t) = 0.5\alpha\rho(t)Av(t)^3$$

where

α = Albert Betz constant

$\rho(t)$ = air density

A = Area swept by the turbine rotor

$v(t)$ = wind speed

Fuel emission of the power plant is considered as quadratic in nature as given by

$$\varepsilon C_i(P_i(t)) = \alpha_i + \beta_i P_i(t) + \gamma_i P_i^2(t)$$

where $\alpha_i, \beta_i, \gamma_i$ are the emission coefficients of unit i .

4 Results

In this paper, three cases of UC problem and ten generator unit systems with maximum and minimum generating capacity are considered. Generation cost is reduced when we have used renewable energy sources so GENCO Company gets the profit by the use of combination of both wind and solar power system. Total execution time for the calculation of fuel cost and fuel emission is reduced by using GA (Table 1).

Case1: Only conventional units are considered for schedule demand of 24 h as given in Table 2. The cost of generation is found to be 585,288.980700 \$/24 h, and

Table 1 Generator data

	U-1	U-2	U-3	U-4	U-5	U-6	U-7	U-8	U-9	U-10
Pg (max)	455	455	130	130	162	80	85	55	55	55
Pg (min)	150	150	130	130	25	20	25	10	10	10
Uptime	8	8	5	5	6	3	3	1	1	1
Downtime	8	8	5	5	6	3	3	1	1	1
Initial status	8	8	-5	-5	-6	-3	-3	-1	-1	-1

Table 2 Load demand and renewable energy schedule

Hour (MW)	1	2	3	4	5	6
Power demand	700	750	850	950	1000	1100
Wind generation	10.54	22.27	25.5	25.5	25.5	25.5
Solar generation	0	0	0	0	0	0
Hour	7	8	9	10	11	12
Power demand	1150	1200	1300	1400	1450	1500
Wind generation	25.5	25.5	25.5	25.5	25.5	25.5
Solar generation	0.09	17.46	31.45	36.01	38.06	35.93
Hour	13	14	15	16	17	18
Power demand	1400	1300	1200	1050	1000	1100
Wind generation	25.5	24.52	20.74	14.62	25.5	19.04
Solar generation	36.78	31.59	9.7	12.92	0	0
Hour	19	20	21	22	23	24
Power demand	1200	1400	1300	1100	900	800
Wind generation	25.5	18.02	25.5	21.42	0	2.55
Solar generation	0	0	0	0	0	0

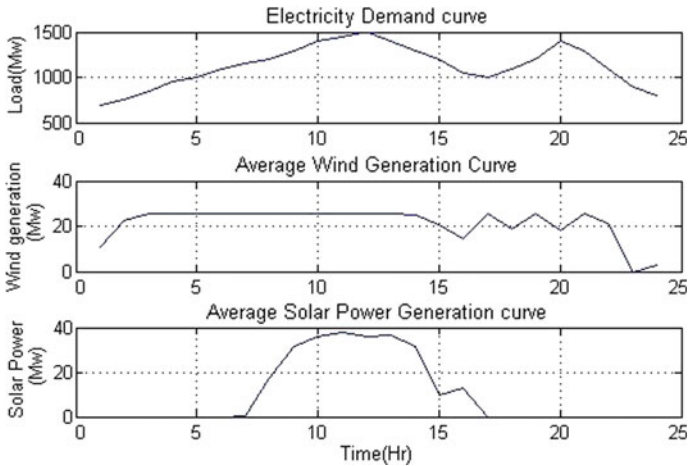


Fig. 1 Demand, wind power, and solar power curve

the fuel emission for this conventional source is found to be 26,062.283000 ton/24 h.

Case 2: Same 10 units as in case 1 are integrated with wind power generator. Average wind generation schedule as given in Table 2 is considered. The cost of generation is found to be 576,988.040184 \$/24 h, and the fuel emission for this conventional source is 26,120.473170 \$/24 h.

Case 3: Here, conventional units are integrated with both solar and wind power generator average generation schedules as given in Table 2. The cost of generation is found to be 569,958.200281 \$/24 h, and the fuel emission for this conventional source is 25,459.813462 \$/24 h (Fig. 1).

5 Conclusion

The test of UC on all the three cases shows that integration of wind and solar effectively reduces the cost of production and emission. The objective is to reduce the cost only so case 3 shows that emission and cost simultaneously decrease for green power generation. The complexity of the problem to find the optimal commitment schedule for three cases was solved within 400 s. It shows the potential of genetic algorithm to find the nearest global minima of the constraint fitness function.

Further works can be done to find the optimum UC schedule by considering both objectives of lowest cost and lowest emission with integration of renewable energy resources by multiobjective genetic algorithm.

References

1. Dasgupta, D. and McGregor, D.R.: Thermal unit commitment using genetic algorithms, IEE Proc., United Kingdom, Vol. 141, No. 5, Page No. 459–465, (1994).
2. Kazarlis, S.A. and Bakirtzis, A.G. and Petridis V.: A Genetic Algorithm Solution to the Unit Commitment Problem, IEEE Transactions on Power Systems, Greece, Vol. 11, No. 1, Page No. 83–92, (1996).
3. Swarup, K.S. and Yamashiro, S.: Unit Commitment Solution Methodology Using Genetic Algorithm, IEEE Transactions on Power Systems, Japan, Vol. 17, No. 1, Page No. 87–91, (2002).
4. Senjyu, Tomonobu and Chakraborty, Shantanu and Ahmed, Yousuf Saber and Toyama, Hirofumi and Yona, Atsushi and Funabashi, Toshihisa: Thermal Unit Commitment Strategy with Solar and Wind Energy Systems Using Genetic Algorithm Operated Particle Swarm Optimization, IEEE International Conference on Power and Energy, Page No. 876–871, (2008).

An Implicit Approach to Minimize the Reactive Power of a 765 kV Interconnected Bus System in India

Rishiraj Sarker, Debaparna Sengupta, Susanta Kumar Bhattacharya and Asim Datta

Abstract There has been phenomenal expansion in Indian power sector since independence. The first 765 kV transmission line was commissioned in 2007 in the Western part of India. It is expected that in coming years, India will be requiring a huge demand of large power stations for bulk power flow. Keeping that in mind, large substations are designed for further augmentation. This paper provides a comprehensive power flow study of a 765 kV interconnected bus system based on the standard parameters of the 800 kV (with 765 kV as the nominal voltage) class transmission system of India. This type of analysis is very useful for solving different power flow problems of an extra high-voltage (EHV) transmission system. The scope of the work is limited to air-insulated substations only. The software analysis is done on MiPower environment for real-time analysis.

Keywords MiPower · Load flow · 765 kV transmission line · Interconnected bus Gauss–Seidel

R. Sarker (✉) · A. Datta
Mizoram University, Aizawl, India
e-mail: sarker.rishiraj88@gmail.com

A. Datta
e-mail: asimdatta2012@gmail.com

D. Sengupta
Techno India College of Technology, Kolkata, India
e-mail: imdebaparna@gmail.com

S. K. Bhattacharya
Netaji Subhash Engineering College, Kolkata, India
e-mail: skbhatta1957@gmail.com

1 Introduction

Earlier in the year 1990, Central Electricity Authority (CEA) of India published a technical report detailing parameters of the 800 kV (with 765 kV as the nominal voltage) class transmission line equipment based on the recommendations of various organizations [1]. Following this, a good number of transmission lines were identified at this voltage level. Though some of these lines were installed to maintain 800 kV class parameters, they were being operated at 400 kV level due to unavailability of adequate power. With the initiative taken by the government to have 'electricity for all' in the year 2012, suddenly it came to near-reality to augment the above-mentioned lines to 765 kV. It is also expected to construct a few more intra-regional and inter-regional lines based on the EHV substation parameters of India [2, 3]. Keeping that in mind, a suitable load flow analysis is done based on the standard 765 kV substation. The design is based on the basic parameters of the equipment used in an EHV substation [4, 5]. As Newton–Raphson power flow is basically dependent on its initial values, a convergence problem has been observed in simulations due to such initialization [6]. Thus, Gauss–Seidel method of power flow is taken into consideration in this work. The program has been developed assuming loads as constant power. Different types of loads need to be considered for accurate representation of system loads [7].

Load flow or power flow study has a significant importance in power system. It deals with various quantities of the power system such as real power, reactive power, and magnitude of voltage and phase angle of voltage. Load flow studies are made to plan the best operation and control of the existing system as well as to plan for the future expansion to keep pace with the load growth. Such studies help in ascertaining the effects of new loads, new generating stations, new lines, and new interconnection before they were installed. The prior information serves to minimize the system losses and to provide a check on the system stability [8].

Load flow analysis using MiPower software is accurate and gives highly reliable results. This research makes effective use of MiPower to carry out load flow analysis of a 765 kV interconnected system. The actual ratings of power transformers, circuit breakers, current transformers, potential transformers, and isolating switches are taken [1] and modeled accordingly in MiPower. The major problem of almost all EHV transmission system is under voltage. Reactive power (VAR) cannot be transmitted over long transmission line, especially under heavy load conditions. Therefore, it is to be generated close to the point of power consumption. Due to the effect of this phenomenon, a difference between the voltages will be created, which causes reactive power (VAR) to flow, and the voltage of a power system is only $\pm 5\%$ of the nominal voltage. This small voltage difference does not ensure substantial reactive power (VAR) flow over long distances. So if that reactive power (VAR) is not available at the load center, the voltage level goes down. Chronic under voltages cause excessive wear and tear on certain devices like motor. This kind of problems can be predetermined by load flow study, and suitable precaution can be taken. Recently, reactive power compensation approach was proposed by Rajasthan

(India) Electricity EHV transmission system [9]. The analysis is very useful for mitigating reactive power problems in high-voltage transmission line.

The analysis of a high-voltage transmission noise has been shown in [10]. 765 kV single-phase switching compensation techniques were presented by American Electric Power Service Corporation in 1981 [11]. Different ground fault mitigation schemes were proposed in this paper. A novel approach for interconnecting the existing grid system of the northeastern part of India was modeled in real-time software environment [12]. Such studies are very helpful for implementing a new EHV substation or augmenting an existing one to the grid. Thukaram et al. (2006) published a paper which shows a comparative study between transient and steady-state analysis for a 765/400 kV EHV transmission substation based on Indian Power System [13]. A number of researches have been done on 765 kV interconnected bus system across the world till now, though no work related to load flow study of 765 kV interconnected bus system of India has been found till date.

2 Power Flow Analysis Using Gauss–Seidel Method

Load flow solution gives initial condition of a system when transient behavior of the system is to be studied. The solution can be done for balanced as well as unbalanced condition. The load flow solution of a system involves mainly three steps. They are drawing of single-line diagram of network, formulation of network equations, and suitable mathematical solution for the equations. The mathematical techniques include Gauss–Seidel method, Newton–Raphson method, advanced Newton–Raphson method, fast decoupled method. In this paper, load flow problem is solved by Gauss–Seidel method.

$$P = \sum_{q=1}^n (e_p(e_p G_{pq} + f_q B_{pq}) + f_p(f_q G_{pq} - e_q B_{pq})) \quad (1)$$

$$Q = \sum_{q=1}^n (e_p(e_p G_{pq} + f_q B_{pq}) + f_p(f_q G_{pq} - e_q B_{pq})) \quad (2)$$

$$|V_p^2| = e_p^2 + f_p^2 \quad (3)$$

These three sets of nonlinear load flow Eqs. (1), (2), and (3) are presented in terms of real and imaginary components of nodal voltages. Here, real power (P) and reactive power (Q) for a load bus and the real power (P) and voltage (V) for a generator bus are specified, and e_p and f_p are taken as unknown quantities, whereas G and B are conductance and susceptance, respectively. For n -bus system, the number of unknowns is $2(n-1)$ as the voltage at slack bus is known. Gauss–Seidel method is the earliest devised method which shows slower rates of convergence

compared to other iterative methods. The main advantage of using Gauss–Seidel method is its ease in programming and most efficient use of core memory.

3 Simulated System

The system under study is a five bus, 765 kV interconnected transmission system. It consists of two generators (each rated at 1500 MW), four different loads connected to the individual buses, and connecting transmission lines.

Figure 1 shows the simulated diagram to analyze the aforesaid system. Generator 1 and 2 will supply power to the 765 kV rated bus ‘North’ and ‘South,’ respectively. Base MVA is taken as 100 MVA, and frequency is 50 Hz. Each and every bus is rated at 765 kV. Minimum voltage (V_{min}) and maximum voltage (V_{max}) are 0.95 and 1.05 pu, respectively. Loss load factor is taken as 0.3. Total line charging susceptance (B) is 0.00002, and line charging MVAR at 1 pu voltage is 0.002. Tables 1, 2, and 3 show data sheet of connected loads, transmission lines, and the real and reactive power, respectively. For calculation, acceleration factor and slack bus angle (degrees) are taken as 1.4 and 0.00, respectively.

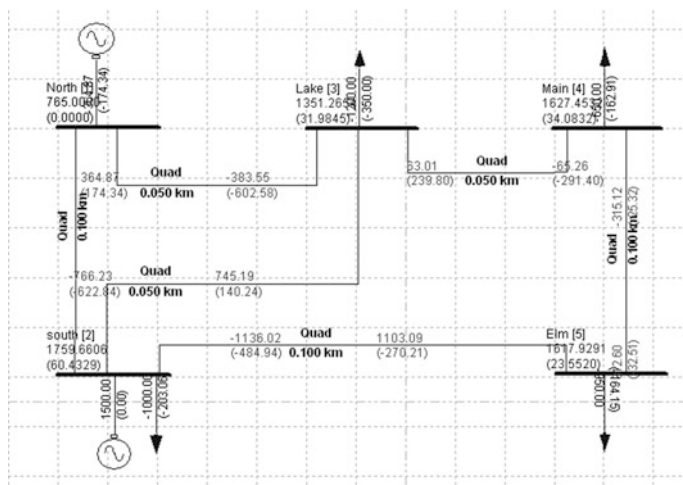


Fig. 1 Simulated diagram of 765-kV interconnected system

Table 1 Real and reactive power rating of different loads connected to the buses

	Real power (MW)	Reactive power (MVAR)	Power factor
South	300	84.209	0.963
Lake	450	127.658	0.962
Main	500	164.342	0.950
Elm	250	71.071	0.961

Table 2 Transmission line data

From node	To node	Line parameter		
		R_{pu}	X_{pu}	$B/2_{pu}$
Main (4)	Elm (5)	0.01142	0.26188	0.0000
North (1)	Lake (3)	0.01142	0.26188	0.0000
South (2)	Lake (3)	0.01142	0.26188	0.0000
South (2)	Elm (5)	0.01142	0.26188	0.0000
Lake (3)	Main (4)	0.01142	0.26188	0.0000
Main (4)	Elm (5)	0.01142	0.26188	

Table 3 Total real and reactive power

1. Total specified MW generation	3000
2. Total maximum MVAR limit of generator	1450
3. Total specified MW load	1500
4. Total specified MVAR load	447.28

4 Results and Analysis

In the system, five buses, four loads, six transmission lines, and two sources (generator) are taken. Number of iteration is taken 15 for solving the model, Q check limit is 4, P and Q tolerance is 0.001 for the system under study. Transformer R/X ratio is 0.05000, and circuit breaker X_{pu} is 0.00010 for system convenience. The iteration details are shown in Table 4. Generated P , Q , V and angle details are shown in Tables 5 and 6, respectively.

Table 4 Iteration details

Iteration count	Errors	Bus no.
1	0.453913	3
2	1.043300	5
3	1.045086	4
4	1.488521	5
5	2.856061	5
6	1.792361	4
7	0.867430	2
8	0.840217	4
9	0.458659	2
10	0.412392	5
11	0.528005	5
12	0.499622	3
13	1.802873	5
14	0.850644	2
15	1.501615	2

Table 5 Bus voltage magnitude, angle, and power

From bus	Voltage magnitude (p.u.)	Angle (°)	MW generated	MVAR generated	MW load	MVAR load
North (1)	1.0000	0.00	831.576	203.845	0.000	0.000
South (2)	1.3528	158.13	600.000	250.000	300.000	84.209
Lake (3)	1.1764	90.40	0.000	0.000	500.000	164.342
Main (4)	1.4013	131.20	0.000	0.000	250.000	71.071
Elm (5)	1.0175	120.83	0.000	0.000	450.000	127.658

Table 6 Line losses

From node	To node	Forward		Loss		MVAR loading (%)
		MW	MVAR	MW	MVAR	
Main (4)	Elm (5)	107.133	89.589	3.2219	73.8869	4.0
North (1)	Lake (3)	-431.576	43.845	9.8935	14.8740	14.1
South (2)	Lake (3)	581.648	43.121	3.3650	65.1554	12.9
South (2)	Elm (5)	330.133	66.270	11.2255	57.4326	7.5
Lake (3)	Main (4)	-408.246	69.685	14.1541	24.5941	8.4

Table 7 Power distribution

Description	Zone-1
1. MW generation	1431.576
2. MVAR generation	453.85
3. MW load	1500.0000
4. MVAR load	447.2800
5. MVAR compensation	0.0000
6. MW loss	41.86
7. MVAR loss	235.943

The following analyses are made from the above simulation (Table 7).

- The total number of buses exceeding the maximum voltage limit: 3
- Number of lines loaded between 1 and 25%: 6
- Total real power generation: 2731.576
- Total reactive power generation: 235.943
- Generation power factor: 0.793
- Total real power loss (AC + DC): 41.86 MW (41.86 + 0.000000)
- Percentage of real power loss (AC + DC): 2.79.

5 Conclusion

The principal information obtained from power flow study is the magnitude and phase angle of the voltage at each bus and the real and reactive power in each line. The voltage magnitude (pu) and the phase angle ($^{\circ}$) should be coordinated correctly with the bus switching scheme. The reactive power compensation problems can be mitigated by using VAR compensator or different FACTS controller. The loss percentage of real power is very low in our analysis, which shows the reliability of designing this kind of interconnecting EHV substations. The approach used in this paper will help to design a 1200 kV interconnecting substation in future. Hope this analysis will usher a new era in the power sector of India.

Acknowledgements The authors would like to show their sincere gratitude to Netaji Subhash Engineering College, Kolkata, India, for providing their laboratory to carry this research work.

References

1. Mukhopadhyay S.: Standard Parameter of 800 kV Class Transmission System in India. CEA., (1990).
2. Pioneer Transmission.: Advantages of 765 kV Technology.
3. CIGRE Working Group.: Technical requirements for Substation equipment exceeding 800 kV AC., Draft Chapter 1 and 3.3.6 Rev. E1., (2008).
4. AEP Interstate Project: Technologies for 21st Century Transmission., American Electric Power, (2006).
5. Sakhavati A., Mostafa Y., ShirinSaleh A. and MahaeiS. M.: 765 kV Transmission Line Design (Electrical Section)., International Journal of Electrical and Computer Engineering., vol. 2, pp. 698–707, (2012).
6. Tzerhuang W. and Taichen S.: sequential three phase power flow calculation for radial distribution system via three phase Z-bus distribution factor., Fourth International Conference on Innovative Computing, Information and Control, pp. 647–651, (2009).
7. Mohamed nor mamdouhabdel S. K.: Grid connected photovoltaic models for three phase load flow analysis, IEEE Conference, (2011).
8. Raj P.: Load Flow and Short Circuit Analysis of 400/220 kV substation., International Journal of Creative Research Thoughts., vol. 1, (2013).
9. PanwarR., Sharma V., Sharma M. P. and Vyas B.: Circulating MVAR control in Rajasthan (India) transmission system, IEEE 1st International Conference on Power Electronics, Intelligent Control and Energy Systems (ICPEICES)., pp. 1–6, (2016).
10. Richard A. P. and Knapp R. F.: Measurement and Analysis of Audible Noise From Operating 765 kV Transmission Lines., IEEE Power Engineering Review., vol. 1, pp. 78–79, (1981).
11. Shperling B. R., Fakheria. J., ShihC. H. and Ware B. J.: Analysis of Single Phase Switching Field Tests on the AEP 765 KV System., IEEE Power Engineering Review., vol. 1, pp. 44–44, (1981).
12. MaitiT., GogoiK., Chatterjee S.: Modelling and study of Indian Eastern Regional Grid analysis using PSS@E., Annual IEEE India Conference (INDICON)., pp. 1–5, (2015).
13. Thukaram D., Khincha H. P. and Shyamala P.: Comparative Studies of Transient and Steady State Analysis for a Typical 765 kV/400 kV EHV Transmission System in Indian Power System., International Conference on Power Electronic, Drives and Energy Systems (PEDES)., pp. 1–6, (2006).

A CFS–DNN-Based Intrusion Detection System

Sayak Paul, Chandan Banerjee and Moinak Ghoshal

Abstract The Internet communications are being developed to a great extent. With this development, an enormous amount of data is being generated. However, this data is not always secured. Intruders are always trying to misuse this data and gain unauthorized access, and hence, network security is also being compromised. An Intrusion Detection System (IDS) provides an efficient way to handle this. In this paper, an efficient IDS has been proposed which uses the NSL-KDD dataset which is a high-dimensional dataset. The dataset contains a large number of records, labeled as attack or normal. Correlation-based Feature Selection (CFS) method is chosen to select relevant and important features from the dataset for reducing the overall runtime of the proposed model, and a Deep Neural Network (DNN) classifier is used to examine if a record is normal or an attack. We tested our model using model validation and also compared the results with other existing models.

Keywords Feature selection • IDS • CFS • DNN • Model validation

1 Introduction

Presently, the Internet has become one of the necessities in our day-to-day lives. In many of the cases, the corresponding data is private and its security needs to be assured. But, to secure this data the network through the data is being managed also needs to be secured. Intrusion Detection Systems help in maintaining the network security [1]. IDS provides a security mechanism used to monitor the behavior of the

S. Paul · C. Banerjee (✉) · M. Ghoshal
Netaji Subhash Engineering College, Kolkata 700152, India
e-mail: chandanbanerjee1@gmail.com

S. Paul
e-mail: spsayakpaul@gmail.com

M. Ghoshal
e-mail: moinakghoshal1@gmail.com

network. To do this, the IDS compares a new user activity with already stored user activities in the IDS and gives the result. There are mainly two approaches being used in Intrusion Detection System. One is Anomaly-based Intrusion Detection and the other is misuse-based Intrusion Detection. Anomaly-based Intrusion Detection Systems are more accurate than misuse-based Intrusion Detection Systems as they cannot detect unknown attacks, whereas Anomaly-based Intrusion Detection Systems construct a general behavior of the network system using some algorithm [2, 3]. The approaches of IDS on the basis of location of monitoring can also be classified as Host-based Intrusion Detection System (HIDS) and Network-based Intrusion Detection System [4]. In this paper, we have proposed an efficient IDS which can detect whether a user activity is normal or attack. The user activities in a network are quantified in NSL-KDD dataset, and it is being used for our experimental purpose. As the dataset contains a large number of features and user records, we applied Correlation-based Feature Selection method to choose a set of important features which can be used in building our IDS. After that, we trained a Deep Neural Network and optimized it to classify if the user records are normal or not. Model validation is used to test our model. We have also compared our model with the existing models.

2 Related Work

In 2004, J. G. Dy and C. E. Brodley proposed a method of feature selection for unsupervised learning where they tackled the issues of automated feature subset selection algorithm for unlabeled data through feature subset selection using expectation maximization (EM) clustering (FSSEM) and two different performance criteria for evaluating candidate feature subsets [5]. In 2004, L. Yu and H. Liu proposed an efficient feature selection method on the basis of redundancy and relevance [6]. Feature selection is also explored in the context of intrusion detection. In 2010, R. Datti and B. Verma proposed linear discriminant analysis (LDA) algorithm to extract features for detecting intrusions. The method was able to reduce the 41 features of the dataset into 4 features [7]. In 2016, M. H. Aghdam and P. Kabiri proposed ant colony optimization-based features for Intrusion Detection System which was able to select 24 features from 41 features [8].

Combinations of feature selection methods and machine learning algorithms have also been proposed by researchers over the years. In 2013, J. Jha and L. Ragma proposed support vector machine-based Intrusion Detection System where they incorporated information gain ratio and k-means for feature selection and support vector machine for classifying if a record is attacked or not [9].

3 NSL-KDD Dataset

NSL-KDD dataset is a refinement of old KDD Cup'99 dataset which has some inherent problems. NSL-KDD dataset is comprised of four separate datasets. They are "KDDTrain+," "KDDTest+," "KDDTest-21," and "20%KDDTraining+." For our experiments, KDDTrain + has been used which 41 features with 125,973 records labeled as normal or attack [10].

Forty-one features are divided into four groups as basic features, content features, time-based traffic features, and host-based traffic features [11].

The attacks are categorized into four groups. They are denial of service attack (DoS), user-to-root attack (U2R), remote to local attack (R2L), and probing attack [12].

4 Proposed Model

We have presented an efficient IDS model which can classify an user activity (a record) either as normal or attack. NSL-KDD dataset (KDDTrain+) is used in our experiments. As discussed in the NSL-KDD dataset section, it contains a large number of features. So to reduce the number of features and thereby reducing the runtime of the classifier (which decides if a record is normal or attack) that we have used, we applied feature selection on the dataset incorporating Correlation-based Feature Selection (CFS). After that, we used the features that were selected by CFS method to train our classifier (Deep Neural Network in this case). Further, we optimized it by using Adam optimizer. We tested our model by means of model validation. Below algorithm shows the steps that were used to design our model:

Input: NSL-KDD dataset.

Output: NSL-KDD dataset classified.

Step 1: Preprocess NSL-KDD dataset.

Step 2: Normalize the dataset.

Step 3: Apply Correlation-based Feature Selection (CFS) for the task of feature selection.

Step 4: Construct a Deep Neural Network classifier with the features generated by CFS for the task of classification, i.e., to examine the records of the NSL-KDD dataset to be either normal or attack.

Step 5: Optimize the classifier using Adam optimizer.

Step 6: Train the classifier.

Step 7: Evaluate the performance of the classifier using model validation.

Step 8: Calculate the classification accuracy.

4.1 Data Preprocessing

The NSL-KDD dataset consists of 41 features and a class variable as discussed in the NSL-KDD dataset section. The features include both numeric and categorical values. For the experiments, the categorical values are converted to numeric values based on their occurrence frequencies. The attack classes were divided into four different classes. To make the dataset simple, we grouped them into one class, i.e., the attack classes were assigned the value of 2 and the normal classes were assigned the value of 1.

4.2 Data Normalization

The features of the NSL-KDD contain both discrete and continuous values. When the discrete and continuous values of these features are combined, it makes the range of the feature values different. To solve the issue, after preprocessing, we normalized the dataset using min–max technique to fit our calculations. As a result, the range of all features became same which helped our model train well.

4.3 Feature Selection

Higher dimensional data results in longer training and testing time, more usage of computer memory resources, longer processing time. More efficient model can be constructed by reducing the dimensionality of the dataset without having to compromise with the performance. This can be achieved by features selection technique in which the relevant and important features are selected using some measures [13]. We incorporated Correlation-based Feature Selection method to achieve this.

The CFS algorithm works by ranking the feature subsets based on a correlation-based heuristic evaluation function. The evaluation function selects the subsets that contain features that are highly correlated with the class variable and uncorrelated with each other. Features having low correlation with class and redundancy are ignored and considered as irrelevant. Equation (1) shows the equation that is used in the evaluation function.

$$r_{zc} = \frac{k\bar{r}_{zi}}{\sqrt{k + k(k-1)r_{ii}}}, \quad (1)$$

where r_{zc} is the correlation between the summed components and the outside variable, k is the number of components, r_{zi} is the average of the correlations between the components and the outside variable, and r_{ii} is the average inter-correlation between components [14].

4.4 Classification

After getting the feature set, a Deep Neural Network is trained with these features and their respective values. Deep Neural Network uses a simulation of computing that is very much inspired by the structure of the brain. That is why the term Neural Network. The fundamental foundational unit of a Neural Network is the neuron. Each neuron takes a set of inputs, with which a particular weight is assigned. The neuron executes some function on these weighted inputs. A linear neuron is fed with a linear combination of the weighted inputs, whereas a sigmoidal neuron is more complicated. In most of the cases, sigmoidal neurons are used much more often than linear neurons because they allow the use of more versatile algorithms as compared to linear neurons. A Neural Network comes into play when the neurons are connected to each other, i.e., to the input data and to the outputs which are essentially the network's answer to the learning problem. Figure 1 shows a general structure of a Deep Neural Network with three layers.

Neural Networks having multiple hidden layers and having connection to all the neurons at each layer are called Deep Neural Networks (DNNs). During training, the Neural Network is shown a large number of training examples and iteratively modifies the weights to minimize the errors we make on the training examples. The training is affected by the learning rate and backpropagation which is used to connect the output of each layer to its previous layer [15]. We used four layers of DNN (one input layer, two hidden layers, and one output layer) for our proposed model.

4.5 Optimization

Choosing Neural Network model architecture and parameters has a direct effect on the training accuracy. We used Adam optimization for choosing the learning rate that makes the model to generalize well to out-of-sample data [16].

4.6 Training Our Model and Testing Using Model Validation

During the model contraction, the dataset is split into training and testing set. About 70% of the dataset is used as the training set and rest is used as the testing set. Our goal is to achieve the maximum validation score based on accuracy. Accuracy is the percentage of the correctly classified instances [17].

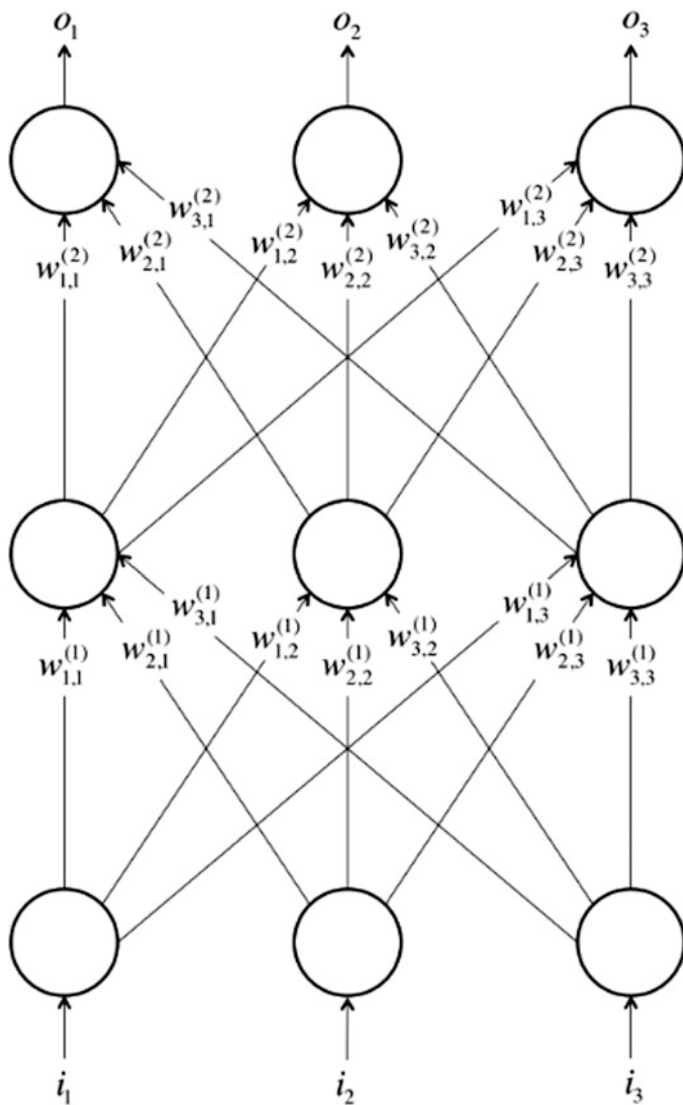


Fig. 1 A Neural Network with three layers and three neurons per layer

5 Experimental Results

Figure 2 shows a graph that compares between CFS and other feature selection methods (lasso regression, random forest) on the basis of number of features each method generated.

Fig. 2 Bar graph showing different feature selection methods, and the number of features generated by them

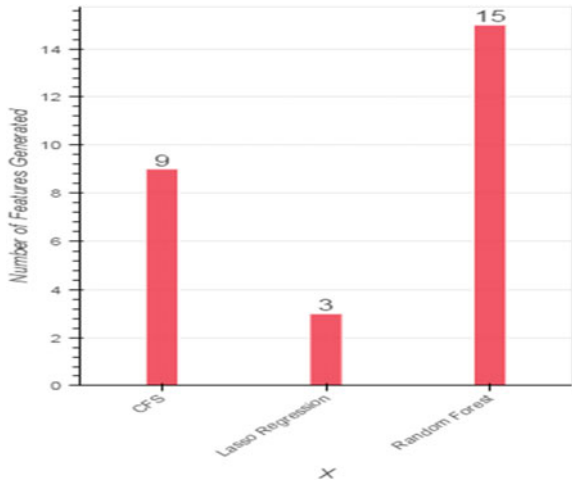


Fig. 3 Graph showing the runtimes for training the DNN with different number of features including all the features

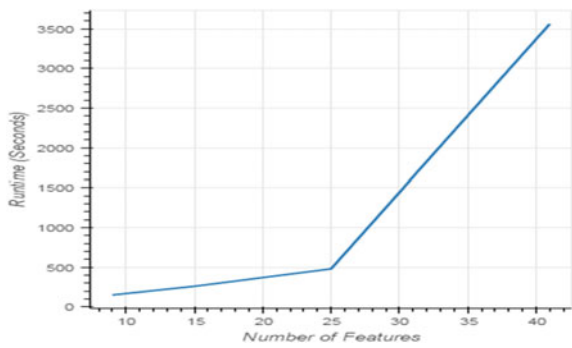


Fig. 4 Bar graph showing accuracy scores obtained by combining the above-mentioned feature selection methods with DNN

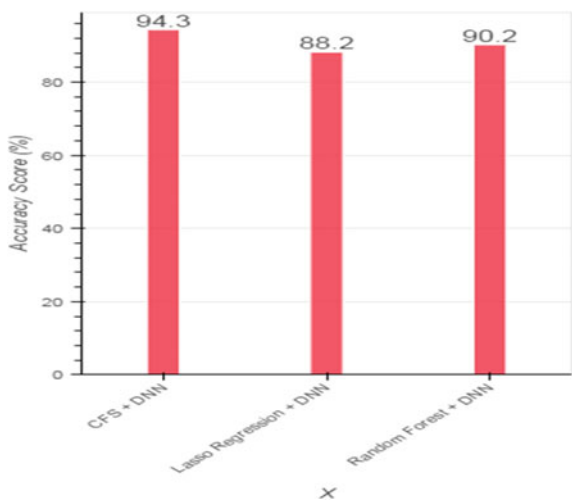
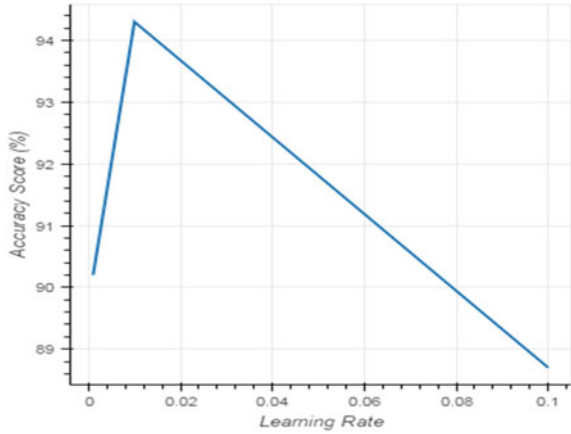


Fig. 5 Graph showing the change in accuracy scores with respect to different learning rates



In Fig. 3, different runtimes for training the DNN with different number of features including all the features have been shown.

In Fig. 4, a graph is presented to compare the accuracy scores of the above-mentioned feature selection methods paired with DNN.

Adam optimizer chooses the optimal learning rate, and it affects the training accuracy also. In Fig. 5, we show how the accuracy score changes with different learning rates.

In our case, with a learning rate of 0.01, the highest accuracy score is achieved. Figure 6 shows the accuracy scores of different classifiers including DNN coupled with CFS.

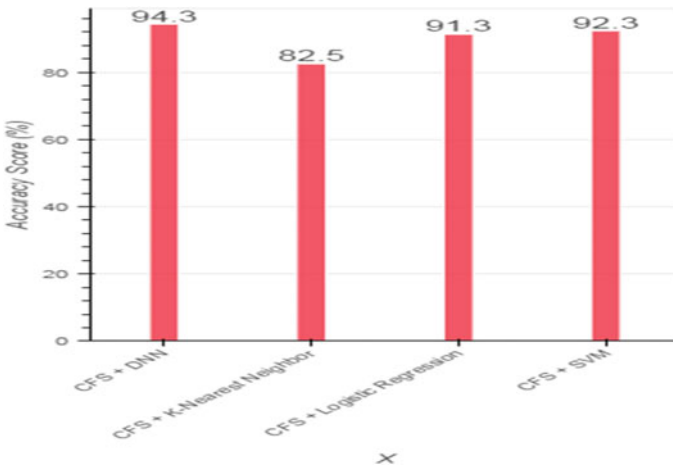


Fig. 6 Bar graph showing the accuracy scores of different classifiers including DNN with CFS

So from Fig. 3, 4, and 6, it can be seen that the proposed model produces better results (with efficient runtime) than the existing models.

6 Conclusion

In this paper, we aimed to build an efficient IDS. We have shown how CFS stands out of the other feature selection methods and how it selects important features which resulted in a much lesser run tome. Further, the features generated by it are used to train a DNN classifier for the task of classification. Our model is tested using model validation, and a comparison is also shown from which it can be seen that our model performs better than the other models.

References

1. Belavagi C. M., and Muniyal B.: Performance Evaluation of Supervised Machine Learning Algorithms for Intrusion Detection. Twelfth International Multi-Conference on Information Processing-2016 (IMCIP-2016), pp. 117–123, (2016).
2. Denning., and D. E.: An intrusion detection model. *IEEE Transaction on Software Engineering*. Software Engineering 13(2), pp. 222–232, (1987).
3. Singh S. K., Chaurasia N., and Sharma P.: Concept and proposed architecture of Hybrid Intrusion Detection System using data mining. *International Journal of Engineering and Advanced Technology (IJEAT)*., vol. 2, pp. 274–276, (2013).
4. Ubhale P. R., and Sahu A. M.: Securing Cloud Computing Environment by means of Intrusion Detection and Prevention Systems (IDPS). *International Journal of Computer Science and Management Research*., vol. 2, pp. 2430–2435, (2013).
5. Jennifer G. D., and Carla E. B.: Feature Selection for Unsupervised Learning, *Journal of Machine Learning Research* 5, pp. 845–889, (2004).
6. Yu L., and Liu H.: Efficient Feature Selection via Analysis of Relevance and Redundancy. *Journal of Machine Learning Research* 5., pp. 1205–1224, (2004).
7. Datti R., and Verma B.: Feature Reduction for Intrusion Detection Using Linear Discriminant Analysis. *International Journal on Computer Science and Engineering (IJCSSE)*., vol. 2, pp. 1072–1078, (2010).
8. Aghdam M. H., and Kabiri P.: Feature selection for intrusion detection system using ant colony optimization. *International Journal of Network Security*., pp. 420–432, (2016).
9. Jha J., and Ragha L.: Intrusion Detection System using Support Vector Machine, *International Journal of Applied Information Systems*., pp. 25–30, (2103).
10. NSL-KDD dataset for network-based intrusion detection system. Available on: <http://nsl.cs.unb.ca/NSL-KDD/>, (2009).
11. Tavallaee M., Bagheri E., Lu W., and Ali A. G.: A Detailed Analysis of the KDD CUP 99 Data Set. *IEEE Symposium on Computational Intelligence for Security and Defense Applications, CISDA 2009*., pp. 53–58, (2009).
12. MIT Lincoln Labs, 1998 DARPA Intrusion Detection Evaluation. Available on: <http://www.ll.mit.edu/mission/communications/ist/corpora/ideval/index.html>, February 2008.
13. Battiti R.: Using Mutual Information for selecting features in Supervised Neural Net Learning. *IEEE Transactions on Neural Networks*., vol. 5, pp. 537–550, (1994).

14. Hall M. A.: Correlation-based Feature Selection for Machine Learning, Department of Computer Science, The University of Waikato, New Zealand, (1999).
15. Goodfellow I., Bengio Y., and Courville A.: Deep Learning, MIT Press (2016) available on <http://www.deeplearningbook.org>.
16. Adam Optimizer (Keras official documentation) available on: <https://keras.io/optimizers/>.
17. Han J., Kamber M., and Pei J.: Data Mining: Concepts and Techniques (3rd Edition). USA, MA: Morgan Kaufmann Publishers, pp. 359–360, (2012).

A Compact Ku-Band Bandpass Filter with Wide Upper Stopband Using SIR

Atiqur Rahman, Sushanta Kabir Dutta and Pankaj Sarkar

Abstract In this paper, a Ku-band bandpass filter with wide upper stopband characteristics is presented. The bandpass filter is implemented with a stub-loaded resonator (SLR). The resonator is designed to incorporate two resonating modes in the passband. Due to the presence of higher-order harmonics, the stopband is restricted to 25 GHz. To extend the stopband, the stepped-impedance stub (SIS) is connected at the input and output port. The proposed SIS stub has broad stopband characteristics, which extend the stopband up to 40.0 GHz. The proposed filter is analysed and simulated using a 3D EM solver. Simulated response agrees well with the analytical procedures.

Keywords Ku-band bandpass filter · Stub-loaded resonator · Stepped-impedance stub · Wide upper stopband · Harmonic suppression

1 Introduction

Recently, the research to develop broadband systems for the application in medical imaging systems, pulse communication, surveillance systems and ground penetration radar has initiated tremendous interest among the researcher. A broadband system is highly essential to satisfy the demand of modern day's high data rate transmission. One of the indispensable components in microwave subsystem is the bandpass filter. A farrago of design topologies to realize the broadband bandpass filter has been reported in recent decades [1–10]. In [1], the SIR is used to implement UWB bandpass filter (3.1–10.6 GHz) by incorporating three resonating modes in passband. Fork-form resonator is used to realize broadband bandpass filter, which is presented in [3]. In [4], cross-shaped resonator and its application in UWB filter design domain are discussed. It can be seen that mostly multiple-mode

A. Rahman (✉) · S. K. Dutta · P. Sarkar (✉)

Electronics & Communication Engineering Department, School of Technology,
North Eastern Hill University, Shillong 793022, Meghalaya, India
e-mail: pankajsarkar111@gmail.com

© Springer Nature Singapore Pte Ltd. 2018

R. Bera et al. (eds.), *Advances in Communication, Devices and Networking*,
Lecture Notes in Electrical Engineering 462,
https://doi.org/10.1007/978-981-10-7901-6_20

169

resonator (MMR) is the suitable choice for broadband filter design. But the drawback of MMR-based bandpass filter is the restricted upper stopband characteristics due to higher-order harmonics. Eliminating the higher-order harmonics, the EBG-embedded MMR band broadband filter is presented in [5, 6] with wide upper stopband characteristics. Cascaded lowpass and highpass filter can also be implemented to achieve broad passband characteristics with wide upper passband response [7, 8]. A compact microstrip resonator-based Ku-band bandpass filter is presented in [9], where the upper stopband characteristic is achieved up to 25 GHz. The substrate integrated waveguide technology is explored in [10] to implement Ku-band filter.

In this paper, a Ku-band bandpass filter is implemented using a stub-loaded resonator (SLR). The proposed resonator utilized two resonating modes to generate the desired passband. The higher-order harmonics produced by the SLR is suppressed by the stepped-impedance stubs. The stubs are embedded at the input and output transmission line to achieve improved upper stopband response.

2 Filter Design

The layout of the proposed filter is shown in Fig. 1. The filter is implemented on FR4 substrate of height 0.8 mm. The proposed resonator is consisting of a stub-loaded resonator which is coupled using a coupled line. The equivalent circuit model is deduced in Fig. 2, to extract the even and odd mode resonating frequencies of the resonator. The resonator is realized on a uniform impedance resonator of electrical length $2\theta_{\text{UIR}}$ and admittance Y_1 . A T-shaped stub is loaded at the middle of the resonator of electrical length θ_s . The odd and even mode excitation is shown in Fig. 2b, c, respectively. For even and odd mode case, the input admittance is derived as follows.

$$Y_{\text{in,odd}} = -jY_1 \cot(\theta_{\text{UIR}}) \quad (1)$$

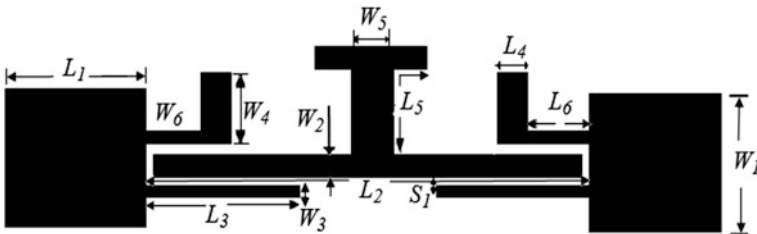


Fig. 1 Layout of the proposed filter with $L_1 = 2.0$, $L_2 = 6.4$, $L_3 = 2.6$, $L_4 = 0.3$, $L_5 = 2.0$, $L_6 = 0.6$, $W_1 = 1.5$, $W_2 = 0.2$, $W_3 = 0.1$, $W_4 = 0.6$, $W_5 = 0.4$, $W_6 = 0.1$, $S_1 = 0.15$ (All dimensions are in mm.)

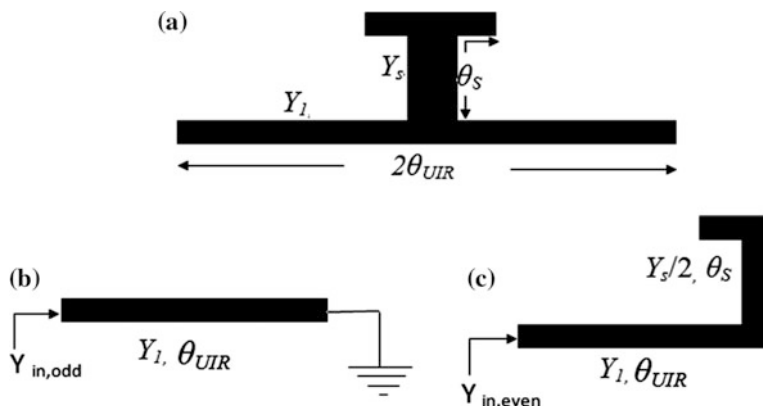


Fig. 2 a Equivalent circuit model of the proposed resonator. b Odd mode equivalent circuit. c Even mode equivalent circuit

$$Y_{in,even} = jY_l \frac{Y_s \tan(\theta_s) + 2Y_l \tan(\theta_{UIR})}{2Y_l - Y_s \tan(\theta_s) \tan(\theta_{UIR})} \tag{2}$$

The condition of resonance can be determined for the case $Y_l = Y_s/2$, by putting $Y_{ino} = 0$ and $Y_{inc} = 0$. The odd and even mode resonating frequencies can be deduced as

$$f_{odd} = \frac{(2n - 1)c}{2L_{UIR} \sqrt{\epsilon_{eff}}} \tag{3}$$

$$f_{even} = \frac{nc}{2(L_{UIR} + L_s) \sqrt{\epsilon_{eff}}} \tag{4}$$

Two resonating modes are excited in the desired passband. The normalized ($f_0 = 15.0$ GHz) odd and even mode resonating frequencies are plotted in Fig. 3a for different L_{UIR} and L_s . The SLR is designed to form the odd and even mode resonating frequencies at 13.5 and 16.5 GHz, respectively. From Fig. 3a, it can be seen that the odd mode resonating frequency depends on L_1 . The even mode resonating frequency is depending on both L_{UIR} and L_s . So the changes over the stub length will not reflect on the odd mode resonating frequency.

To study further the resonance characteristics of the proposed resonator, the resonator is simulated under weak coupling. The extracted S21 parameter is plotted in Fig. 3b. Two modes (f_{o1}, f_{o2}) are visible within the passband. To utilize the resonator as a bandpass filter, the resonator is coupled using input–output coupled line. The filter is simulated in CST Microwave Studio, and the S-parameters are illustrated in Fig. 4. It can be seen that the passband is generated from 10.0 to 20.0 GHz. The S11 parameter is below -12 dB and the S21 parameter is less than -0.2 dB at the desired band. The upper stopband performance of the filter is not satisfactory due to presence of a passband centred at 37.0 GHz.

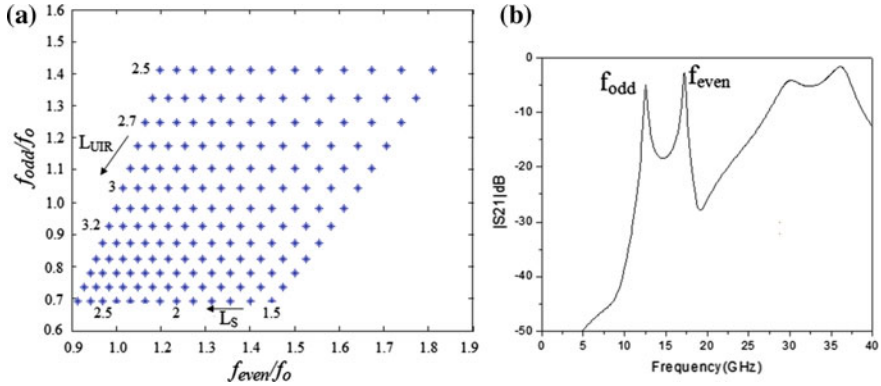
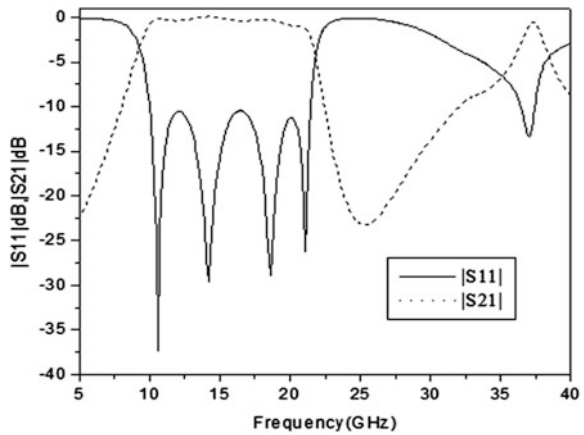


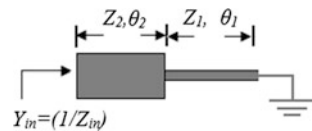
Fig. 3 a Normalized odd and even mode resonant frequency for various L_{UR} and L_S indicated in the inset. b Resonating modes of the proposed resonator under weak coupling scheme

Fig. 4 Frequency response of the proposed filter without stepped-impedance stub



In order to suppress the spurious band, the stepped-impedance resonator (SIR)-based stub is introduced at the input and output port. Figure 5 shows the configuration of a short-ended SIR. The SIR consists of a high and a low impedance section of impedance Z_1 and Z_2 with corresponding electrical length θ_1 and θ_2 , respectively. $R_Z = (Z_2/Z_1)$ is the important parameter in changing the properties of the SIR.

Fig. 5 Short-ended stepped-impedance resonator



The input admittance of the SIR is derived below

$$Y_{\text{in}} = -jY_2 \frac{Z_2 - Z_1 \tan \theta_1 \tan \theta_2}{Z_1 \tan \theta_1 + Z_2 \tan \theta_2} \quad (5)$$

The condition of resonance is determined by considering $Y_{\text{in}} = 0$. The fundamental frequency of resonance is deduced as

$$f_0 = \frac{v_p \tan^{-1} \sqrt{R_Z}}{l \times 2\pi} \quad (6)$$

The relation between the fundamental frequency (f_0), first spurious (f_{SA}) and the second spurious (f_{SB}) can be obtained from the following equation.

$$\frac{f_{\text{SA}}}{f_0} = \frac{\pi}{2 \tan^{-1} \sqrt{R_Z}} \quad (7)$$

$$\frac{f_{\text{SB}}}{f_0} = 2 \left(\frac{f_{\text{SA}}}{f_0} \right) - 1 \quad (8)$$

So, from the above equation, it can be observed that the spurious frequencies of the SIR can be controlled by changing the value of R_z . The SIR is utilized to suppress the spurious band at 37.0 GHz. The impedance ratio is selected to be 0.57 which accommodates the first two resonating frequencies at 35.0 and 40.0 GHz, respectively. The SIR is connected at the input and output transmission line such that it can introduce a virtual ground at the connecting point. The location of the stub is tuned to achieve satisfactory frequency response.

3 Results and Discussions

The proposed filter is implemented on FR4 substrate of height 0.8 mm. The simulated S-parameter is illustrated in Fig. 6. It can be seen that the proposed filter generates a passband from 10.2 to 19.8 GHz. Throughout the passband, the S11 parameter is below -12.0 dB and the S21 parameter is better than -0.3 dB. It can also be observed that the spurious band is suppressed due to the presence of stepped-impedance stub. The stopband is extended up to 40 GHz with attenuation loss more than 10 dB. The overall size of the proposed prototype is 9.8×2.1 mm².

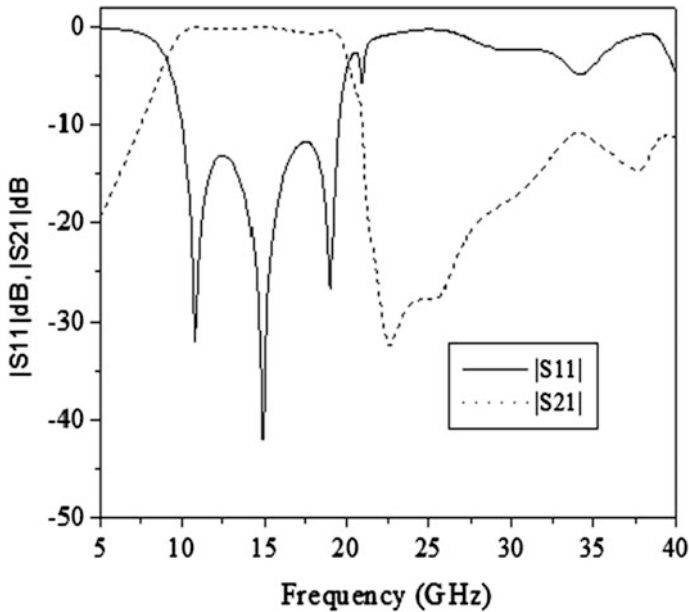


Fig. 6 Simulated S-parameters of the proposed bandpass filter

4 Conclusion

In this paper, a compact Ku-band bandpass filter is designed by incorporating two resonating modes in the passband. A stub-loaded resonator is implemented to generate the passband. Wide upper stopband characteristic is achieved by designing stepped-impedance stub. The selectivity of the passband is high. The proposed bandpass filter can be utilized for the designing Ku-band transceiver system where higher-order harmonics suppression is essential.

References

1. L. Zhu, S. Sun, and W. Menzel, "Ultra-Wideband (UWB) bandpass filters using multiple-mode resonator," *IEEE Microwave and Wireless Components Letters*, vol. 15, no. 11, pp. 796–798, Nov. 2005.
2. K. Song and Q. Xue, "Inductance-loaded Y-shaped resonators and their applications to filters," *IEEE Transaction on Microwave Theory and Techniques*, vol. 58, no. 4, pp. 978–984, Apr. 2010.
3. Chen, H.; Zhang, Y.-X.: A novel and compact UWB bandpass filter using microstrip fork-form resonators. *Progress in Electromagnetics Research*, 77 pp. 273–280, 2007.

4. Wang, H.; Yang, G.; Kang, W.; Miao, C.; Wu, W.: Application of cross-shaped resonator to the ultra wideband bandpass filter design. *IEEE Microwave and Wireless Components Letters*, Vol. 21, no. 12, pp. 667–669, 2011.
5. SaiWai Wong and Lei Zhu, “EBG-Embedded Multiple-Mode Resonator for UWB Band pass Filter With Improved Upper-Stopband Performance” *IEEE Microwave and Wireless Components Letters*, vol. 17, no. 6, pp. 421–423, June 2007.
6. Joan Garcia-Garcia, Jordi Bonache and Ferran Martin, “Application of Electromagnetic Bandgap to the Design of Ultra-Wide Bandpass Filters with Good Out of Band Performance,” *IEEE Transaction on Microwave Theory and Techniques*, vol. 54, no. 12, pp. 4136–4140, December 2006.
7. Rowdra Ghatak, Pankaj Sarkar, R. K. Mishra and D. R. Poddar, “A Compact UWB Bandpass Filter With Embedded SIR as Band Notch Structure” *IEEE Microwave and Wireless Components Letters*, vol. 21, no. 5, pp. 261–263, May. 2011.
8. Pankaj Sarkar, Rowdra Ghatak, Manimala Pal, and D. R. Poddar, “Compact UWB Bandpass Filter With Dual Notch Bands Using Open Circuited Stubs” *IEEE Microwave and Wireless Components Letters*, vol. 22, no. 9, pp. 453–455, September-2012.
9. Yi-Chyun Chiang, Wei-Lin Hsieh and Ming-An Chung, “A Method of Synthesizing Microwave Bandpass Filters Constructed With Symmetrical or Asymmetrical Compact Microstrip Resonators”, *IEEE Transaction on Microwave Theory and Techniques*, vol. 54, no. 11, pp. 3947–3953, Nov-2006.
10. D.L. Diedhiou, E. Rius, J.-F. Favennec and A.E. Mostrah, “Ku-band Cross-Coupled Ceramic SIW filter Using a Novel Electric Cross-Coupling” *IEEE Microwave and Wireless Components Letters*, Vol. 25, no. 2, pp. 109–111, Feb-2015.

A Corporate Feed Network Optimization for Performance Enhancement

Seyi Stephen Olokede and Babu Sena Paul

Abstract Big data technology sustainability is contingent on the availability of interconnections of large-scale, ultra-high-speed, densely integrated big data heterogeneous server platforms. For highly densified servers to be attainable, semiconductor technologies upon which these servers are predicated must further be miniaturized. It is recently not uncommon to implement band gap reduction engineering of SiGe HBT in a bid to attain highly densified integrated circuit for large-scale servers. Unfortunately, the parasitic effects become significant, in particular as these integrated circuits are targeted for high frequency of operations due to the interconnection links between the chip and the transceivers. Insertion loss $|S_{21}|$ becomes considerable, and both the signal level as well as noise figure depreciate substantially as a result. In this work, therefore, we investigate the extent of parasitic effect to wit performance degradation, and further to optimize the parasitics for performance enhancement.

Keywords Big data · Insertion loss · Integrated circuit · Latency
Parasitic effect · System-on-chip

1 Introduction

The system requirements for big data communication in particular with regard to hardware demands are very stringent. The interconnections of highly densified chips to meet the resource requirements of massive data communications create more rooms for densified fine wire lines with serious challenges between the chip/transceivers, signal traces, and interconnections. Unfortunately, the side effect of

S. S. Olokede (✉) · B. S. Paul
Department of Electrical and Electronic Engineering Technology,
University of Johannesburg, Johannesburg, South Africa
e-mail: solokede@gmail.com

B. S. Paul
e-mail: bspaul@gmail.com

compromising these requirements could result to substantial performance degradation, signal distortion, low speed, and, inability to recover clock signal components correctly. Transmission losses along the signal traces as well as interconnections are considerable due to discontinuities as a result of bends and junctions along the transmission lines. The parasitic effects of these interconnections cause significant propagation delay as the length and frequency increase with attendant impedance bandwidth degradation. The increase in effect of mutual coupling initiates and propagates surface waves, and thus limits the system efficiency in particular low speed, signal distortion, and inability to recover clock signal correctly.

This challenge is becoming exacerbated due to increasing need for more highly integrated SoC. The reduced chip size to meet systemic integration capability requirements put more stringent constraints on other ancillary associated circuits. For instance, the bond wire or flip chip needed to interconnect the chip to AoC/AiP is expected to be longer to be effective. Interestingly, longer length of interconnect—in order to accommodate more increasingly densified heterogeneous circuits in a chip—leads to more interconnect delay [1–5]. Unfortunately, the present deep submicron is dominated by increasing die size with decreasing wire pitch. The pressure for highly integrated single chip becomes more severe as the need for interconnections of heterogeneous integration of various technologies into one single chip increases. Research efforts have been ongoing in order to mitigate the SoC delay latency. In 1990, copper-low dielectric interconnects were propounded. However, the overtly longer interconnect delay with attendant systemic performance degradation of the SoC disqualifies the technology. The interconnect scaling is subsequently proposed. The intent of this work, however, is in first instance to empirically confirm that delay does exist in SoC due to interconnections, and the delay could cause signal distortion and inability to recover the clock signal. Second is to assess the extent of this delay, and specifically, we intend to characterize a typical interconnect in order to proffer an approximate estimate for the signal distortion and subsequent optimization.

2 Theoretical Framework

The corporate feed network (CFN) based on Wilkinson power divider is no doubt bedeviled with considerable losses owing to longer line lengths and too many discontinuities. These losses if not attended to with the view to ameliorating their effects on signal propagation may jeopardize the existing gains of the proposed feed. In this work, we intend to estimate theoretically and in concrete terms the values of these losses along the corporate feed line, and summarily determine to what extent an optimization procedure would be necessary to deliver substantial performance enhancement in order to forestall high roundtrip latency due to signal delay along the feed line. There are essentially four categories of losses along the CFN. While the losses in transmission lines include surface wave losses,

radiation energy losses, and ohmic (conductor) losses, the substrate-based losses include dielectric losses. Thus, if a current source $I = I_0 \exp(j\beta t)$ is applied to the terminal of a CFN at the application of voltage $V = V_0 \exp(j\beta t)$, the EM signal will propagate through the CFN transmission line where $I_0 = V_0/Z_c$, $\beta = k_0(\epsilon_{\text{eff}})^{-0.5}$ —the propagation constant—and Z_c is the characteristic impedance. The losses in particular ohmic losses depend on the CFN width w , and the extent can be measured by the reflection coefficient (Γ) seeing $= (Z - Z_c) \times (Z - Z_c)^{-1}$ where Z_c is contingent on the width (w) of the CFN transmission line.

Thus, the percentage of input power radiated into free space is proportional to $(h(\epsilon_{\text{eff}})^{-0.5} \lambda^{-1})^2$ for every h/λ , whereas the amount lost to surface waves depend on $(h(\epsilon_{\text{eff}})^{-0.5} \lambda^{-1})^3$ where h is the substrate thickness. To therefore optimize in order to mitigate surface wave losses, it is thus imperative to keep $(h(\epsilon_{\text{eff}})^{-0.5} \lambda^{-1})$ low. A slim microwave laminate of thin thickness and low dielectric permittivity will be ideal to achieve this. The power lost into surface wave can be determined using Eq. (6) of [6], whereas the power radiated into free space is stated in Eq. (5). Interestingly, two factors, namely characteristic impedance (Z_c) and metallization thickness, of the CFN transmission line critically influence the radiation losses with respect to the line length. Alternatively, the radiation losses increase with $(L/\lambda)^2$ in a neighborhood of $0 < L < \lambda$ where L is line length. To reduce radiation losses, it is required that the line length be reduced though within the limit of the design constraints. Summarily, both the surface wave power (P_S) and the radiated power (P_R) depend to certain extent on the Z_c , seeing both losses directly commensurate to $1/Z_c$. While the radiation losses in a straight line are marginal though contingent on the length of the line, the radiation losses become considerable at T junctions and 90° bends with attendant high voltage standing wave ratio owing to increasing inductance. The input reflection coefficient could be modified for improved performance through reduced capacitance and increases of inductance through the mitered of the square bends.

The dominant microstrip mode demonstrates substantial dielectric and ohmic losses. The equations to determine the respective ohmic and dielectric losses are stated in Eqs. (1)–(5) as reported in [7], where P_d is the average dielectric losses, P_c is the average ohmic losses, α_d is the attenuation factor due to dielectric losses, α_c is the attenuation factor due to ohmic losses, and $P(z)$ is the transmitted power by virtues of excitation of the CFN transmission line based on a current source $I = I_0 \exp(j\beta t)$.

$$\alpha_d \approx \frac{P_d}{2P(z)} \quad (1)$$

$$\alpha_d \approx 4.34 \left(\frac{q\sigma}{k_e} \left(\frac{\mu_0}{\epsilon_0} \right)^{0.5} \right) \text{ dB/cm} \quad (2)$$

$$\alpha_c \approx \frac{P_c}{2P(z)} \tag{3}$$

$$\alpha_c \approx \frac{8.68R_S}{Z_0w} \text{ dB/cm} \tag{4}$$

$$\alpha = \frac{P_c}{2P(z)} + \frac{P_d}{2P(z)} \tag{5}$$

Essentially, Eq. (5) is the total attenuation factor, where $\alpha = \alpha_c + \alpha_d$. By implication, the total attenuation is the cumulative sum of the dielectric attenuation factor plus the ohmic attenuation factor.

3 Optimization Implementation

Figure 1 demonstrates a hypothetical CFN to validate the optimization potential proposed in this work, with their respective line widths and lengths. Widths: $w_1 = 50 \Omega$, $w_2 = 70.7 \Omega$, and $w_3 = 100 \Omega$. Impedance calculator available in numerical commercial solver is used to determine the equivalent values of these impedances in mm such that $w_1 = 1.9 \text{ mm}$, $w_2 = 1.1 \text{ mm}$, and $w_3 = 0.46 \text{ mm}$, whereas, $w_4 = 0.6 \text{ mm}$. Their respective lengths are as stated in [8].

The design parameters required for the optimization is shown in Table 1. Respective attenuation factors owing to dielectric and ohmic losses are stated. The systemic dielectric losses are determined by calculating the attenuation factor-respect line lengths product function. Table 2 depicts the optimization calculation of the attenuation factors that are responsible for the losses due to different widths that invariably introduce discontinuities causing certain degree of losses. The systemic dielectric losses (P_d) as shown in Table 3 are estimated to be less than 0.005 dB. More importantly, it is observed that the dielectric loss is independent of transmission line topology. Thus, a substrate loss tangent ($\tan \delta$) of less than 0.003 is very beneficial to reduce the loss as applicable in this case.

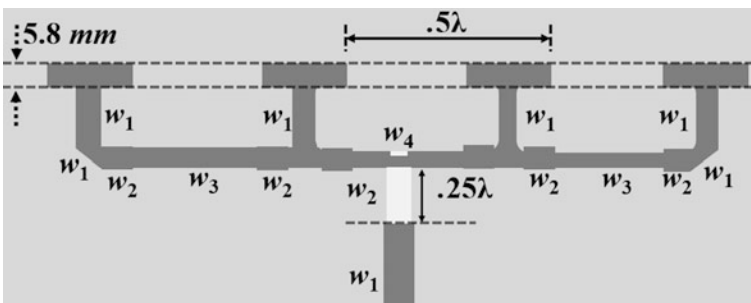


Fig. 1 A typical CFN for optimization

Table 1 Optimization design parameters

w (mm)	w/h (mm)	$10 \times w/h$ (mm)	ϵ_{eff}	$\alpha_d \times 10^{-3}$ (dB/mm)	α_c (dB/mm)
1.9	2.33	4.30	2.710	1.515	0.779
1.1	1.29	7.75	2.592	1.350	0.957
0.5	0.60	17.75	2.465	1.184	1.093
0.3	0.40	27.15	2.415	1.121	1.276

Table 2 Attenuation factor computation optimization

	w (cm)	No. of lines	Line lengths (cm)	$\alpha_d \times 10^{-3}$ (dB/mm)	α_c (dB/mm)
w_1	0.19	1	0.40	0.1515	0.0779
w_1	0.11	1	0.70	0.1350	0.0957
w_1	0.19	2	0.60	0.1515	0.0779
w_1	0.19	4	0.19	0.1515	0.0779
w_1	0.11	6	0.90	0.1515	0.0957
w_1	0.05	2	0.14	0.1182	0.1009

Table 3 Losses computation due to optimization

	w (cm)	$P_d \times 10^{-3}$ (dB)	P_o (dB)	$P_R \times 10^{-3}$ (dB)	$P_S \times 10^{-3}$ (dB)
w_1	0.19	0.060	0.0312	3.34	0.495
w_1	0.11	0.014	0.0957	5.85	0.866
w_1	0.19	0.1515	0.0779	10.02	1.867
w_1	0.19	0.1515	0.0779	6.34	0.940
w_1	0.11	0.1515	0.0957	34.21	7.462
w_1	0.05	0.1182	0.1009	2.27	0.977

Applying the same procedure, the systemic ohmic loss (P_c) across the line lengths also shown in Table 3 is determined to be less than marginal 3 dB. The narrow width transmission line feed does demonstrate relatively substantial impedance with attendant increase of ohmic loss. As such, the ohmic losses are contingent on the skin depth (δ) of the passive line traces, the effect of which increases with the square root of frequency. A passive trace of less than 0.004 cm, a metallization equivalent of three times that skin depth will sufficiently reduce the ohmic losses.

Discontinuities such as square bends, junctions, or short circuits along the transmission line often are the causes of radiation losses. Findings indicate that junctions and square bends contribute substantial radiation losses in transmission lines. To therefore implement the optimization of transmission lines, it is either the use of such discontinuities are removed, reduced or metered such that the bends become large to ensure that the metallization thickness of the ground plane and also

the transmission feed line are three-to-four skin depth thick. A microwave laminate with dielectric permittivity of less than 4, a substrate height of less than 0.01 mm, and a $\tan \delta$ of less than 0.0003 at λ of around 5 GHz to mitigate the radiation losses will be more efficient. High characteristic impedance is able to minimize the excitation of surface waves which is directly dependent on Z_c . The inverse of this high impedance mitigates the excitation of the surface waves. Impedances such as 100 and 70 Ω are high enough to mitigate the surface wave.

4 Conclusion

This work examines the feasibility of optimizing the CFN for enhanced performance profile as a priority. Four obvious findings are eminent. First is that high impedance passive reduces the surface wave excitation. The second is that the radiation losses can be minimized by the minimal use of discontinuities or when used, they are chamfered to a radius sufficient enough to be about three or four skin depth thick. The third higher impedance is due to narrow line widths. Finally, the dielectric losses are dependent on the loss tangent of the microwave laminate and not on the line geometry.

References

1. Yoon H., Kim K., and O K. K.; "Interference effects on integrated dipole antennas by a metal cover for an integrated circuit package," in Proc. IEEE AP-S Int. Symp. USNC/URSI National Radio Science Meeting, Salt Lake City, UT, (2000).
2. Wheeler H. A., "Fundamental limitations of small antennas," Proc. IRE, vol. 35, no. 12, pp. 1479–1484, (1947).
3. Kenneth K. O., Kim K., Floyd B. A., Mehta J. L., Yoon H., Hung C.-M., Bravo D., Dickson T. O., Guo X., Li R., Trichy N., Caserta J., Bomstad W. R., Branch J., Yang D.-J., Bohorquez J., Seok E., Gao L., Sugavanam A., Lin J.-J., Chen J., and Brewer J. E., "On-chip antennas in silicon ICs and their application," IEEE Transactions on Electronic Devices, vol. 52, no. 7, pp. 1312–1323, (2005).
4. Harun-our Rashid A. B. M., Watanabe S., Kikkawa T., Guo X., and O K. K.; "Interference suppression of wireless interconnection in Si integrated antenna," in Proc. of the IEEE Int. Interconnect Technology Conf., San Francisco, CA, (2002).
5. Guo X., Li R., and O K. K.; "Design guidelines for reducing the impact of metal interference structures on the performance of on-chip antennas," in Proc. IEEE AP-S Int. Symp. USNC/URSI National Radio Science Meeting, Columbus, OH, (2003).
6. Levine E., Malamud G., Shtrikman S., Treves D., "A Study of Microstrip Array Antennas with the Feed Network," IEEE Transactions on Antennas and Propagation, vol. 31, no. 4, pp. 422–434, (1989).
7. Pucel R. A., Masse D. J., Hartwig, C. P., "Losses in Microstrip," IEEE Transactions on Microwave Theory And Techniques, vol. Mtt-16, no. 6, pp. 342–350, (1968).
8. Olokede S.S., and Ain M.F., "A Linear Array Quasi-Lumped Element Resonator Antenna with A Corporate-Feed Network," Journal of Electromagnetic Waves and Applications, vol. 28, no. 1, pp. 1–12, (2014).

A Reconfigurable Defected Ground Structure Resonator Based on Coplanar Waveguide

Amit Baran Dey, Arnab Nandi, Vinay Kumar Verma
and Banani Basu

Abstract A reconfigurable defected ground structure (DGS) resonator based on coplanar waveguide (CPW) technology is being proposed. The reconfigurable resonator leads to generate multiple stopbands at arbitrary frequencies. Basically, the design is based on slot defect which is thereby created on the ground plane. Here, two different states of diode configuration are being proposed, and in particular state, multiple transmission zeros are achieved in the 0–12 GHz frequency range. To identify the transmission zeros, the slotline design equations are used. Moreover, the conventional circuit parameter extraction method is used to extract the equivalent circuit diagram of each state.

Keywords Transmission zero · Coplanar waveguide (CPW) · Electromagnetic bandgap (EBG) · Defected ground structure (DGS)

1 Introduction

During the later part of the 1980s, many EBG and defected ground structures (DGS) [1–8] and EBG structures [1, 9–14] are in interest due to their available arbitrary stopbands and suppression properties for surface waves. Henceforth, since that period, these structures are used in several applications such as band-pass filter [3, 4, 14], low-pass filters [2], waveguides [11], antennas [1], and others. A great move for configuration of reconfigurable DGS is proposed where the transmission zero can be controlled as seen from many of the recent publications [5–7]. But still, a considerable amount of work is not being published in this respect. Moreover,

A. B. Dey (✉) · A. Nandi (✉) · B. Basu
Department of ECE, NIT Silchar, Silchar, Assam, India
e-mail: amitnitsece@gmail.com

A. Nandi
e-mail: nandi_arnab@ieee.org

V. K. Verma
Department of ECE, NIT Meghalaya, Shillong, India

the work that has been published till now have considered the structures of parallel RLC equivalent circuit for representing the transmission zeros [2, 5], but not providing any design rules thus no insight into the underlying principle of electromagnetic wave propagation. Moreover, many attempts for investigating these very structures are being made by using methods such as the Linpar method [4], the Block Floquet's Theorem [15], or neural networks [6]. The disadvantage of the methods mentioned above is their limits in providing initial design rules and their mathematical complexity. Here, a reconfigurable DGS unit cell which is based on coplanar waveguide technology is proposed. The proposed unit cell might be considered to be developed version to that of [7]. Here, an additional square resonator structure is added to the initial design. Furthermore, the cell presented here provides good control over the number of transmission zeros and their resonant frequencies by using a number of PIN diodes on each side of the CPW ground plane. Two different states of diode operation are presented here. The RLC equivalent circuit using the slotline waveguide design equations of Janaswamy and Schaubert [8] and electromagnetic structure explanation is hereby presented. The simulations are being performed by using commercial software Ansoft HFSS [17]. The HFSS software helps in realizing the transmission and reflection characteristics over finite element method. The conventional circuit parameter method is used for extraction of equivalent circuit model of each state [5].

The paper is organized in the following manner: Section 2 presents briefly the description of the reconfigurable DGS. Section 3 addresses the design, and modeling of the reconfigurable DGS with the different configurations.

2 Design Configuration of the Reconfigurable DGS Resonator Structure

The structure shows the configuration of a DGS resonator which is fed by a coplanar waveguide (CPW). The DGS lattice unit is shown in Fig. 1. The cell of DGS resonator is made up of two different sized resonators in the shape of a square. The small shaped square resonator is also connected to the coplanar waveguide (CPW) by using a transverse gap. The proposed structure consists of two diodes (marked as S1 and S2) in each of the sides of the ground plane. The larger square resonator is disconnected from the smaller square resonator by using diode S1.

The smaller square resonator is divided into two halves having different size of lengths by using diode S2. The structure that is designed on dielectric substrate Rogers RO 3010 which has a relative permittivity of 10.2, loss tangent of 0.0035, and the thickness of 0.635 mm. The overall antenna dimension is 50 mm \times 50 mm \times 0.635 mm, as shown in Fig. 1. The dimension of antenna parameters for 50 Ω input impedance is $a = 3$ mm, $b = 6$ mm, $t = 0.25$ mm, $w = 2.5$ mm, and the coplanar waveguide parameters are $G = 0.715$ mm and $W = 4$ mm.

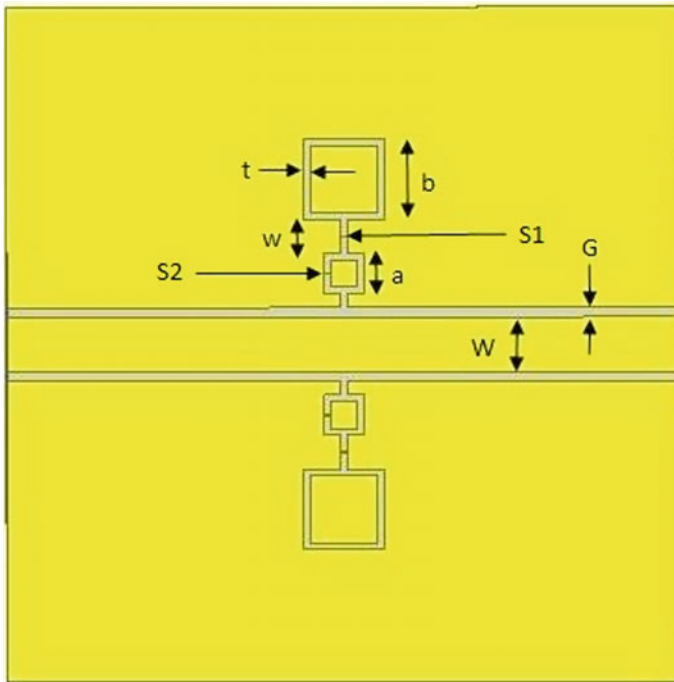


Fig. 1 Front view of the proposed reconfigurable DGS resonator (full view)

2.1 Operation of the Proposed DGS Resonator

The DGS resonator structure with overall dimensions is mentioned in the last section. Since, two diodes are in each side of the ground plane, henceforth different responses will be considered as per different diode configurations. The EM simulated results along with the DGS equivalent circuit model are discussed when the diodes have been configured as either open or short circuits.

2.1.1 First Configuration: When Diode S1 Is ON and S2 Is OFF

In the first configuration mentioned here, the upper resonator is isolated from rest part of the structure which is shown in Fig. 2a. Here, the proposed structure has a transmission zero at 5.4 GHz which is shown in Fig. 2b. The structure provides a single transmission zero so it can be represented by a parallel resonator as shown in Fig. 2c. The numerical extraction method for the calculation of the capacitance, inductance, and resistance has been explained in [5].

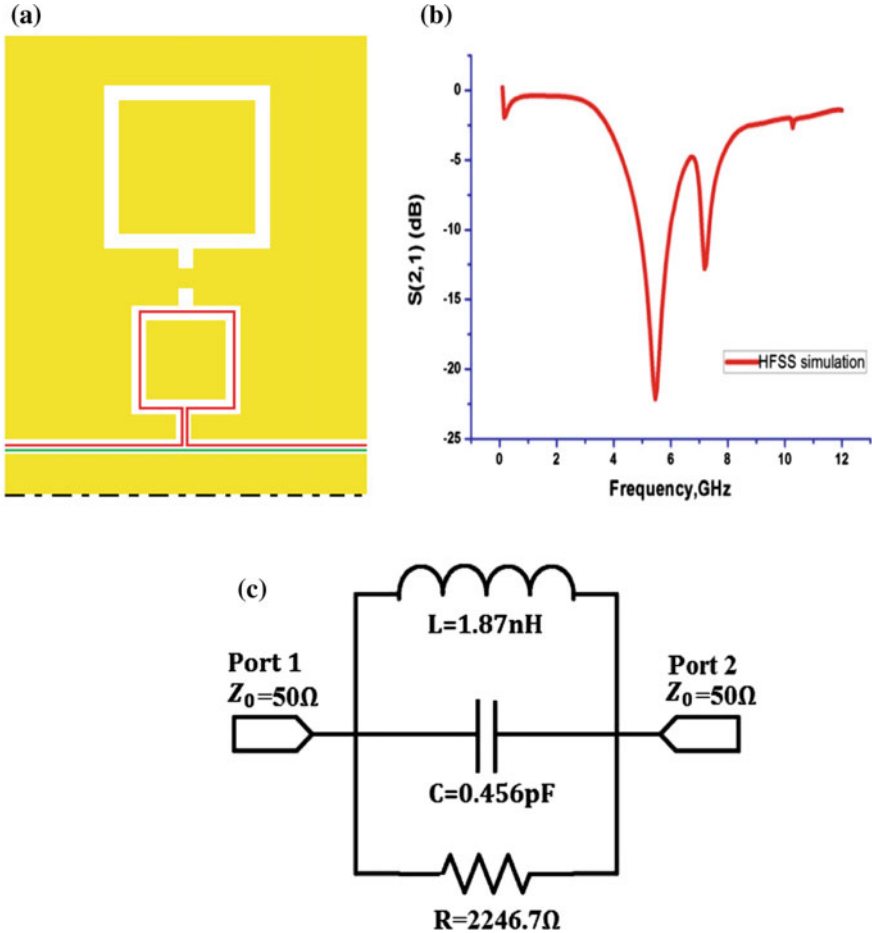


Fig. 2 **a** The configuration of the DGS resonator (when S1 is ON and S2 is OFF). **b** The simulated return loss plot of the DGS resonator (when S1 is ON and S2 is OFF). **c** The equivalent circuit model of the DGS resonator (when S1 is ON and S2 is OFF)

2.1.2 Second Configuration: When Diode S1 Is ON and S2 Is ON

In the second configuration, the upper resonator is isolated as shown in the last configuration, but here the small square resonator is again divided into two unequal resonators as shown in the Fig. 3a. The simulated response curve is shown in Fig. 3b. The structure leads to give rise to two transmission zeros at 4.36 and 9.19 GHz, which is represented by the two parallel resonators as shown in Fig. 3c.

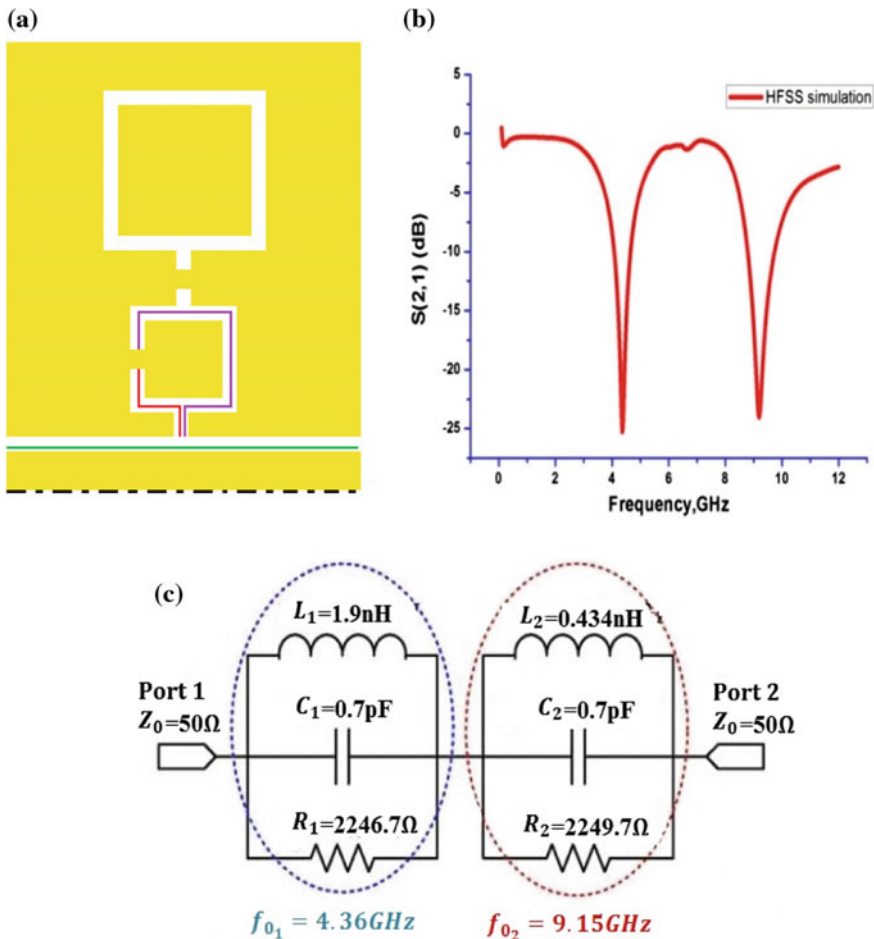


Fig. 3 a The configuration of the DGS resonator (when S1 is ON and S2 is ON). b The simulated return loss plot of the DGS resonator (when S1 is ON and S2 is ON). c The equivalent circuit model of the DGS resonator (when S1 is ON and S2 is ON)

3 Results

The simulated S-parameter results for both the diodes S1 and S2 are shown in Figs. 2b and 3b. In the first configuration, where the diode S1 is ON and S2 is OFF, a transmission zero is obtained at 5.45 GHz of -22.16 dB and a bandwidth of 1.07 GHz is obtained. In the second configuration, we have two transmission zeros at 4.36 and 9.19 GHz of -25.3 and -24.4 dB, and bandwidth of 0.58 and 0.95 GHz, respectively, is achieved. From the parameters, expected results are seen as adding a diode tends to shift the result of the resonant frequencies which is due to

the intrinsic inductance and capacitance introduced as a result of these constraints. The shift thus observed is not same in all the cases because it depends on the working condition of the diode.

4 Conclusion

A reconfigurable DGS resonator which is capable of yielding multiple arbitrary transmission zeros over the band ranging between 0 and 12 GHz is proposed. Basically, the slotline design equations are used to study the proposed structure which provides a direct insight into the electromagnetic propagation that takes place within the structure, which provides a straightforward design rule for the resonator. The reconfigurability of the structure presented here is achieved by switches. The proposed reconfigurable DGS resonator is therefore a good choice where reconfigurability and suppression of passbands are required. The proposed DGS resonator cell can be combined with a multiband antenna after a band-pass filter to suppress higher order harmonics or allow or suppress one of the bands according to the need.

References

1. H. Liu, Z. Li, X. Sun, and J. Mao, "Harmonic suppression with photonic band gap and defected ground structure for a microstrip patch antenna," *IEEE Microw. Wireless Comp. Lett.*, vol. 15, pp. 55–56, Feb. 2005.
2. J. Lim, C. Kim, D. Ahn, Y. Jeong, and S. Nam, "Design of low-pass filters using defected ground structure," *IEEE Trans. Microw. TheoryTech.*, vol. 53, no. 8, pp. 2539–2545, Jan. 2005.
3. H. B. El-Shaarawy, F. Coccetti, R. Plana, M. El-Said, and E. A. Hashish, "Compact bandpass ring resonator filter with enhanced wide-band rejection characteristics using defected ground structures," *IEEE Microw. Wireless Comp. Lett.*, vol. 18, no. 8, pp. 500–503, Aug. 2008.
4. M. Abdelaziz, A. M. E. Safwat, F. Podevin, and A. Vilcot, "Narrow bandpass filter based on the modified DGS," in *Proc. 37th Eur. Microw. Conf.*, Oct. 2007, pp. 75–78.
5. E. K. I. Hamad, A. M. E. Safwat, and A. S. Omar, "A MEMS reconfigurable DGS resonator for K-band applications," *IEEE J. Microelectromech. Syst.*, vol. 15, no. 4, pp. 756–762, Aug. 2006.
6. M. F. Karim, A. Q. Liu, A. Alphones, and A. B. Yu, "A reconfigurable micromachined switching filter using periodic structures," *IEEE Trans. Microw. Theory Tech.*, vol. 55, no. 6, pp. 1154–1162, June 2007, Part 1.
7. A. M. E. Safwat, F. Podevin, P. Ferrari, and A. Vilcot, "Tunable bandstop defected ground structure resonator using reconfigurable dumbbell-shaped coplanar waveguide," *IEEE Trans. Microw. Theory Tech.*, vol. 54, no. 9, pp. 3559–3564, Sept. 2006.
8. L. Yuan, L. Jiao, and Y. Chunhui, "The back propagation neural network model of non-periodic defected ground structure," in *Proc. Global Symp. Millimeter Waves (GSMM)*, Apr. 2008, pp. 29–32.
9. E. Yablonovitch, "Photonic band-gap structures," *J. Opt. Soc. Amer. B*, vol. 10, pp. 283–295, Feb. 1993.

10. F. Yang, K. Ma, Y. Qian, and T. Itoh, "A uniplanar compact photonic bandgap (UC-EBG) structure and its applications for microwave circuits," *IEEE Trans. Microw. Theory Tech.*, vol. 47, no. 8, pp. 1509–1514, Aug. 1999.
11. F. R. Yang, K. P. Ma, Y. Qian, and T. Itoh, "A novel TEM waveguide using uniplanar compact photonic-bandgap (UC-PBG) structure," *IEEE Trans. Microw. Theory Tech.*, vol. 47, no. 11, pp. 2092–2098, Nov. 1999.
12. T.-Y. Yun and K. Chang, "Uniplanar one-dimensional photonic- bandgap structures and resonators," *IEEE Trans. Microw. Theory Tech.*, vol. MTT-49, pp. 549–553, Mar. 2001.
13. C. Caloz and T. Itoh, "Multilayer and anisotropic planar compact PBG structures for microstrip applications," *IEEE Trans. Microw. TheoryTech.*, vol. MTT-50, pp. 2206–2208, Sep. 2002.
14. S.-G. Mao and Y. Zhi, "Coplanar waveguide BPF with compact size and wide spurious free stopband using electromagnetic bandgap resonators," *IEEE Microw. Wireless Comp. Lett.*, vol. 7, no. 3, pp. 181–183, Mar. 2007.
15. R. Janaswamy and D. H. Shaubert, "Characteristic impedance of a wide slot line on low permittivity substrates," *IEEE Trans. Microw. Theory Tech.*, vol. 34, no. 6, pp. 900–902, Jun. 1986, Part 1.

Assessment of Wind Energy Potential in Northeastern Cities of India

Singh Rahul and Om Prakash

Abstract Environmental pollution and scarce resources have led us to think of new alternatives. Even though we have plenty of alternatives like solar energy, hydro energy, bio gas, still wind energy plays an important role. It is said that if all the places in the world with wind energy potential is utilized, it will fulfill the total energy requirements of the world. Keeping it in mind, we focused on the wind energy potential for power generation in the Northeastern cities of India such as Gangtok, Tarey Bhir, Zunheboto, Bomdila, Dibrugarh, Udaipur, Ukhrul, Serchhip, and William Nagar. The wind speed data were collected over the period of 22 years (January 1983 to December 2004) from the RETScreen climate database at an altitude of 10 m from the ground. The wind speed data were subjected to two parameters: Weibull distribution with the scale (c) and shape (k) being the parameters along with other statistical techniques for assessment of wind energy potential. We found that wind speed varies between 1.94 and 7.15 m/s at different places in northeastern cities. The Weibull parameters k and c lie between 4.81–11.95 and 2.53–6.12. Also, the wind power density which is the quantitative measure of the wind energy available at any location varies from 10.2 to 186.76 W/m². The result based on the Weibull analysis indicates that only Gangtok, Tarey Bhir, Bomdila, and Dibrugarh can be used for electricity generation on a large scale at 10 m height above the ground, whereas other places can be used to extract energy from low-speed wind at a height greater than 10 m.

Keywords Wind energy · Mean wind speed · Weibull parameters
Wind power density

S. Rahul (✉) · O. Prakash
Department of Mechanical Engineering, NIT Patna, Patna, Bihar, India
e-mail: rahul282828@gmail.com

O. Prakash
e-mail: dromprakash67@gmail.com

© Springer Nature Singapore Pte Ltd. 2018
R. Bera et al. (eds.), *Advances in Communication, Devices and Networking*,
Lecture Notes in Electrical Engineering 462,
https://doi.org/10.1007/978-981-10-7901-6_23

Nomenclature

$f(v)$	Probability density function
k	Weibull shape parameter (dimensionless)
c	Weibull scale parameter (m/s)
$F(v)$	Cumulative density function
v	Wind speed (m/s)
v_m	Mean wind speed (m/s)
σ	Standard deviation
Γ	Gamma function
n	Total number of data
v_{mp}	Most probable wind speed (m/s)
$v_{E_{max}}$	Maximum energy carrying wind speed (m/s)
$p(v)$	Wind power density (W/m^2)
ρ	Air density (kg/m^3)

1 Introduction

In the current scenario, the need of energy is increasing day by day. Energy need of the world is increasing at 4–5% every year [1–3]. In a developing country like India for each activity, we need energy. Today most of our energy requirements are being fulfilled by non-renewable sources of energy, and it will not last for too long. Power generation based on burning of fossil fuels causes air, water, and land pollution. Due to limited availability of fossil fuel and its adverse effect on surroundings, the use of environment friendly renewable energy-based power generation has gained wide acceptance across the globe [4–6]. We are bound to look for new alternatives of energy and harness them to their full potential. The various alternatives include solar, wind, hydro, geothermal, biomass, and ocean thermal energy. Wind energy is the fastest emerging and most commonly used among non-renewable energy source. The key objective of this study is wind energy resource assessment for power generation at different locations of northeast India. This will not only cut the pollution level but also reduce the gap between demand and supply of energy requirement in northeastern cities of India. The wind energy resource is not evenly distributed throughout the northeastern cities of India. Therefore, a site-by-site assessment is necessary to have better idea about the wind energy distribution across the northeastern cities of India.

India has been one of those countries who have kept themselves focused in this sector. Today, India is ranked fourth in estimated wind energy potential [7, 8]. So far, wind energy utilization is mainly focused in the coastal areas of India. It is the 7500-km coastline of India that is being utilized for this purpose, whereas the rest of the part of India has been left untouched. We took into consideration nine places in the northeast region of India.

2 Methodology

The wind energy potential of nine northeastern cities of India such as Gangtok, Tarey Bhir, Udaipur, Ukhrul, Zunheboto, Serchhip, William Nagar, Bomdila, and Dibrugarh is investigated using the mean wind speed data of 22 years period (January 1983 to December 2004) from the RETScreen climate database at an altitude of 10 m from ground [9]. Table 1 illustrates the information like latitude and longitude of the selected cities for assessment of wind energy potential.

2.1 Weibull Distribution

Among the several statistical distributions available, the Weibull distribution [10–14] has been found to be most adequate and hence employed for analyzing wind energy potential of nine northeastern cities of India such as Gangtok, Tarey Bhir, Udaipur, Ukhrul, Zunheboto, Serchhip, William Nagar, Bomdila, and Dibrugarh. We used Weibull distribution with two parameters, namely shape parameter (k) and scale parameter (c). Also, the two-parameter Weibull statistical distribution is found to be more precise and accurate than corresponding three-parameter Weibull distribution [15–17]. In recent years, most attention has been focused on this method for wind energy potential assessment not only due to its greater flexibility and simplicity but also because it can give a good fit to experimental data [18]. The two-parameter Weibull distribution function is described mathematically as follows:

$$f(v) = \left(\frac{k}{c}\right) \left(\frac{v}{c}\right)^{k-1} \exp\left(-\left(\frac{v}{c}\right)^k\right) \tag{1}$$

Table 1 Location of selected cities

City	Latitude (N)	Longitude (E)
Gangtok (Sikkim)	27.34	88.61
Tarey Bhir (Sikkim)	27.22	88.64
Udaipur (Tripura)	23.54	91.49
Ukhrul (Manipur)	25.09	94.36
Zunheboto (Nagaland)	26.01	94.52
Serchhip (Mizoram)	23.34	92.85
William Nagar (Meghalaya)	25.43	90.59
Bomdila (Arunachal Pradesh)	27.26	92.41
Dibrugarh (Assam)	27.47	94.91

And the cumulative distribution function is

$$F(v) = 1 - \exp\left(-\left(\frac{v}{c}\right)^k\right) \quad (2)$$

where v is the wind speed, k is the shape parameter, and c is the scale parameter.

The mean (v_m) and variances (σ^2) of wind speed data of nine cities are calculated from the equations given below:

$$v_m = \frac{1}{n} \sum_{i=1}^n v_i \quad (3)$$

$$\sigma^2 = \frac{1}{n-1} \sum_{i=1}^n (v_i - v_m)^2 \quad (4)$$

where i is the monthly wind speed data and n is the total number of data used for each year.

The two Weibull parameters can be calculated from mean and variance as follows:

$$k = \left(\frac{\sigma}{v_m}\right)^{-1.086} \quad (5)$$

$$c = \frac{v_m}{\Gamma\left(1 + \frac{1}{k}\right)} \quad (6)$$

where v_m is mean wind speed, σ is standard deviation of wind speed data, and Γ is the gamma function.

For assessing the wind energy potential of any region, the calculation of most probable and maximum energy carrying wind speed is essential. These can be evaluated in the terms of two Weibull parameters k and c from equation given below:

$$v_{mp} = c \left(\frac{k-1}{k}\right)^{1/k} \quad (7)$$

where v_{mp} is most probable wind speed (m/s)

$$v_{E_{max}} = c \left(\frac{k+2}{k}\right)^{1/k} \quad (8)$$

where $v_{E_{max}}$ is maximum energy carrying wind speed (m/s).

The value of wind power density at any location estimates the availability of wind energy. The wind power density can be calculated as following equation:

$$p(v) = \frac{1}{2} \rho c^3 \left(1 + \frac{3}{k} \right) \tag{9}$$

where $p(v)$ is wind power density (W/m^2) and ρ is air density (kg/m^3).

3 Result and Discussions

Table 2 shows the monthly mean wind speed data of 22 years period (January 1983 to December 2004) from the RETScreen climate database at an altitude of 10 m from ground for nine northeastern cities of India.

From the above wind speed data, we have calculated the values of shape factor, scale factor, most probable wind speed, maximum energy carrying wind speed, and the wind power density for different cities under investigation.

From the data, we found that the monthly mean wind speed lies between 3.99 and 7.15 m/s for Gangtok; 3.63 and 7.1 m/s for Tarey Bhir; 1.94 and 2.9 m/s for Udaipur; 2.2 and 3.24 m/s for Ukhrul; 3.84 and 6.76 m/s for Bomdila; 2.3 and 3.47 m/s for Zunheboto; 2.02 and 2.72 m/s for Serchhip; 2.49 and 3.32 m/s for William Nagar, and 2.63 and 3.92 m/s for Dibrugarh.

Also, the cities like Udaipur, Ukhrul, Zunheboto, William Nagar, and Serchhip have very low wind speed throughout the year, whereas cities like Gangtok, Tarey Bhir, Bomdila, and Dibrugarh have wind speed above 3 m/s throughout the year. Figure 1 shows the monthly variation of wind speed of nine northeastern cities under investigation. It shows the wind energy potential of any city is not same throughout the year.

The various statistical and Weibull parameters for different cities are calculated to assess the wind energy potential of selected nine cities. The two parameters of Weibull distribution are found to lie between $4.81 \leq k \leq 11.95$ and $2.53 \leq c \leq 6.12$.

Table 2 Monthly mean wind speed data of selected cities

Sites	Months											
	Jan	Feb	Mar	Apr	May	Jun	Jul	Aug	Sep	Oct	Nov	Dec
Gangtok	6.76	6.91	7.15	6.6	5.75	4.93	4.57	4.44	3.99	5.85	7	6.55
Tarey Bhir	3.72	4.6	7.1	6.4	6.31	4.16	3.63	5.06	4.2	4.71	4.03	4.3
Udaipur	2.42	2.64	2.79	2.86	2.79	2.9	2.71	2.44	2.15	1.94	2.11	2.23
Ukhrul	2.96	3.24	3.07	2.7	2.5	2.4	2.42	2.2	2.13	2.37	2.44	2.51
Zunheboto	3.28	3.47	3.35	2.91	2.63	2.52	2.55	2.33	2.3	2.54	2.73	2.8
Serchhip	2.48	2.62	2.76	2.53	2.38	2.72	2.68	2.47	2.14	2.02	2.14	2.26
William Nagar	2.98	3.18	3.32	3.07	2.84	2.7	2.56	2.48	2.38	2.49	2.8	2.82
Bomdila	6.76	6.21	6.18	5.38	4.43	4.37	4.28	3.92	3.84	4.34	5.97	6.67
Dibrugarh	3.92	3.88	3.81	3.28	2.8	2.87	2.89	2.67	2.63	2.87	3.35	3.52

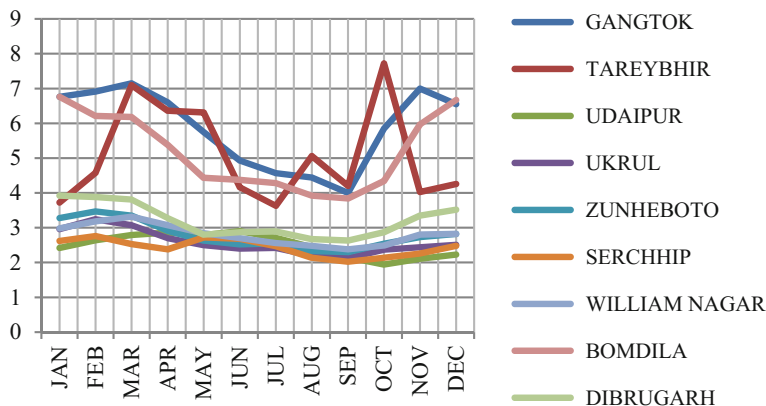


Fig. 1 Monthly variation of wind speed

Table 3 Result of Weibull statistical analysis

	Shape factor (<i>k</i>)	Scale factor (<i>c</i>)	Most probable wind speed v_{mp} (m/s)	Max energy carrying wind speed $v_{E_{max}}$ (m/s)	Wind power density $P(v)$ (W/m^2)
Gangtok	5.33	6.2	5.95	6.58	186.76
Tarey Bhir	4.81	5.3	5	5.68	120.7
Udaipur	9.04	2.64	2.6	2.7	12.31
Ukhrul	8.87	2.8	2.76	2.86	14.76
Bomdila	5.35	5.64	5.43	5.76	140.78
Zunheboto	8.4	2.96	2.91	3.036	17.69
Serchhip	11.95	2.53	2.52	2.57	10.25
William Nagar	11.47	2.92	2.90	2.96	15.78
Dibrugarh	7.83	3.41	3.35	3.51	27.56

Also, the wind power density available at these locations varies from 10.2 to 186.76 W/m^2 . The results obtained are summarized in Table 3.

4 Conclusion

The monthly mean wind speed data over the year obtained from RETScreen climate database at 10 m height are analyzed for nine northeastern cities of India for assessment of wind energy potential for power generation. The data are also subjected to two-parameter Weibull distribution and other statistical analysis. The most important outcomes of the study can be summarized as follows:

- (1) The annual mean wind speed for Gangtok, Tarey Bhir, Bomdila, and Dibrugarh are 5.71, 4.84, 5.2, and 3.21 m/s, respectively. So, we can say that wind power generation for commercial is feasible only at these places where the mean speed is above 3 m/s.
- (2) The wind speed carrying maximum energy and most probable speed for these location are 5.95, 5, 2.6, 2.76, 2.9, 2.52, 2.9, 5.43, 3.35, 6.57 and 5.7, 2.7, 2.87, 3.03, 2.57, 2.96, 5.7, 3.5. The wind carrying maximum energy can be used to determine the rated wind speed, while most probable wind speed indicates the peak of the probability function.
- (3) The wind power density varies from 10.25 to 186.76 W/m². Higher the wind power density, the higher is the electric power generating capacity of the location. Therefore, the wind energy potential for power generation is greater in Gangtok, Tarey Bhir, Bomdila, and Dibrugarh than in Udaipur, Ukhrul, William Nagar, Serchhip, and Zunheboto. So, we can say that it is feasible to set up a wind power generation in Gangtok, Tarey Bhir, Bomdila, and Dibrugarh, but it would not be of any use to set up wind power generation farm at Udaipur, Tarey Bhir, Bomdila, Zunheboto, and Ukhrul as the amount of production will not be able to overcome the expenses.
- (4) The mean annual value of Weibull shape parameter k is between 4.81 and 11.95, while the annual value of scale parameter c is between 2.53 and 6.12. The dimensionless shape parameter k indicates how peaked the wind distribution is, whereas the scale parameter c gives an idea about how windy is a location.

The result based on the Weibull analysis indicates that only Gangtok, Tarey Bhir, Bomdila, and Dibrugarh can be used for electricity generation on a large scale at 10 m height above the ground, whereas the other places can be used to extract energy from low-speed wind at a height greater than 10 m.

References

1. Ajayi, O.O., Fagbenle, R.O. and Katende, J. Assessment of Wind Power Potential and Wind Electricity Generation Using WECS of Two Sites in South West, Nigeria. *International Journal of Energy Science*, 1, 78–92. (2011).
2. Oztopal, A. Sahin, A.D. Akgun, N. and Sen, Z. On the Regional Wind Energy Potential of Turkey. *Energy*, 25, 189–200 (2000).
3. Feretic, D., Tomsic, Z. and Cavlina, N., Feasibility Analysis of Wind-Energy Utilization in Croatia. *Energy*, 24, 239–246 (1999).
4. Sulaiman, M.Y., Akaak, A.M., Abd. Wahab, M., Zakaria, A., Sulaiman, Z.A. and Suradi, J. Wind Characteristic of Oman. *Energy*, 27, 35–46 (2002).
5. Rehman, S. and Ahmed, A. Assessment of Wind Energy Potential for Coastal Locations of the Kingdom of Saudi Arabia. *Energy*, 29, 1105–1115 (2005).
6. Ahmed Shata, A.S. and Hanitsch, R. Evaluation of Wind Energy Potential and Electricity Generation in Egypt. *Renewable Energy*, 31, 1183–1202 (2006).
7. Ahmed, S.A. Wind Energy as a Potential Generation Source at Ras Benas, Egypt. *Renewable and Sustainable Energy Reviews*, 14, 2167–217 (2010).

8. Albadi, M.H., El-Saadany, E.F. and Albadi, H.A. Wind to Power a New City in Oman. *Energy*, 34, 1579–1586 (2009).
9. RETScreen Database, www.etscreen.net.
10. Mathew, S., Pandey, K.P. and Kumar, A.V. Analysis of Wind Regimes for Energy Estimation. *Renewable Energy*, 25, 381–399 (2002).
11. Seguro JV, Lambert TW. Modern estimation of the parameters of the Weibull wind speed distribution for wind energy analysis. *J Wind Eng Ind Aerodyn*; 85:75–84 (2000).
12. Pashardes S, Christofides C. Statistical analysis of wind speed and direction in Cyprus. *Sol Energy*; 55(5):405–14 (1995).
13. Ilinca, A., McCarthy, E., Chaumel, J.-L. and Retiveau, J.-L. Wind Potential Assessment of Quebec Province. *Renewable Energy*, 28, 1881–1897 (2003).
14. Argungu, G.M., Bala, E.J., Momoh, M., Musa, M., Dabai, K.A., Zangina, U. and Maiyama, B.A. Statistical Analysis of Wind Energy Resource Potentials For Power Generation In Jos, Nigeria, Based on Weibull Distribution Function. *The International Journal Of Engineering And Science (IJES)*, 2, 22–31 (2013).
15. Lipson, C. and Sheth, N.J. *Statistical Design and Analysis of Engineering Experiments*. McGraw-Hill, New York (1973).
16. Keyhani, A., Ghasemi-Varnamkhasti, M., An Assessment of Wind Energy Potential as a Power Generation Source in the Capital of Iran, Tehran. *Energy*, 35, 188–201 (2010).
17. Samuel Perkin, Deon Garrett, and Pall Jensson, “Optimal wind turbine selection methodology: A case-study for Búrfell, Iceland”. *Renewable Energy* 75, pp. 165–172 (2015).
18. Wei zhou, Hongxing Yang, Zhaohong Fang, “Wind Power Potential and Characteristic Analysis of the Pearl River Delta Region, China” *Renewable Energy* Vol. 31, pp 739–753 (2006).

A Multifractal Detrended Fluctuation Analysis-Based Framework for Fault Diagnosis in Autonomous Microgrids

S. Pratiher, M. Mukherjee and N. Haque

Abstract The time series obtained during different fault events in an inverter-based microgrid are known to be inherently nonlinear, non-stationary and exhibits multifractal, chaotic behavior. This paper proposes a novel feature extraction and fault detection methodology based on multifractal detrended fluctuation analysis (MFDFA). The limitations of single-scale detrended fluctuation analysis and its susceptibility to interfere with the background noises are overcome in MFDFA which characterizes the multi-scaling nonlinear behavior of load signals during faults. The shape and distribution of the multifractal spectrum along with Hurst exponent are extracted from MFDFA analysis for pattern recognition and classification of different fault events. The efficacy of multifractal features in fault detection and localization with artificial neural network (ANN)-based classifier validates the adequacy of the proposed model.

Keywords Detrended fluctuation analysis · Multifractal spectrum
Microgrids · Power system faults · ANN

S. Pratiher (✉)

Department of Electrical Engineering, Indian Institute of Technology,
Kanpur, Uttar Pradesh, India
e-mail: sawon1234@gmail.com

S. Pratiher

Department of Mathematics, Indian Institute of Technology, Kharagpur,
West Bengal, India

M. Mukherjee · N. Haque

Department of Electrical Engineering, Jadavpur University, Kolkata,
West Bengal, India

M. Mukherjee

School of Electrical Engineering & Computer Science,
Washington State University, Pullman, USA

© Springer Nature Singapore Pte Ltd. 2018

R. Bera et al. (eds.), *Advances in Communication, Devices and Networking*,
Lecture Notes in Electrical Engineering 462,
https://doi.org/10.1007/978-981-10-7901-6_24

1 Introduction

The rapid progress in the distributed power generation sector has led to the establishment of microgrids, which in turn has accelerated the feasibility of power supply to locally spaced loads by distributed means. These microgrids are formed by clustering a number of power electronic devices that converts the dc power generated by photo voltaic cells, fuel cells, etc., to ac power for local utilization, thereby unleashing autonomous power systems. Overall, these microgrids provide substantial reliability and efficiency to the underlying power system but these are prone to power system transients like faults and voltage dips due to their inherent negligible physical inertia. So, a proper fault detection and protection mechanism is a crucial aspect for autonomous microgrid operation [1, 2].

Now, a microgrid can operate in a grid connected mode or an islanded mode. For a grid connected mode, voltage and frequency of the microgrid are primarily determined by the main grid [3]. Whereas, in case of a microgrid operating in an islanded mode, majority of the faults arises from within the microgrid arises, and hence, fault detection becomes difficult. In a larger network of interconnections, the magnitude of fault current is very high and so, faults are easily detectable [4]. Whereas in an inverter-based microgrid operating in an islanded mode fault detection is difficult as the inverters are only able to supply fault currents that are only twice of the rated value [5]. Thus, traditional over current relay-based protection systems are inadequate for fault detection. To overcome this difficulty, different solutions were proposed. This can be solved by enhancing the fault current by increasing the inverter capacity or by incorporating energy storage elements [6]. Also suitable feature vectors can be determined and trained with machine learning tools for identifying fault conditions. Statistical machine learning tools like support vector machines (SVMs) and principal component analysis (PCA) have shown competence as fault localization [7, 8]. In this paper, we have utilized an artificial neural network-based learning model using multifractal features of fault events for fault segregation.

The paper is organized in the following sections. Section 2 provides a dynamic model for an inverter-based microgrid. An autonomous microgrid model comprising of three inverters and domestic loads interconnected by a network has been developed. In Sect. 3, the underlying theory for the non-stationary fault events, their fractal parameter extraction and classification using neural network is discussed. Results obtained from different kinds of simulated faults are discussed in Sect. 4. Finally, the possibility of integration of the suggested analysis to real-time systems is discussed in Sect. 5.

2 Dynamic Model of the Inverter-Based Microgrid

The microgrid system considered in this work for fault prediction consists of three distributed generation system (DG). Each DG is operated based on the droop-based power sharing that consists of a VSI on common reference frame [9]. The detailed

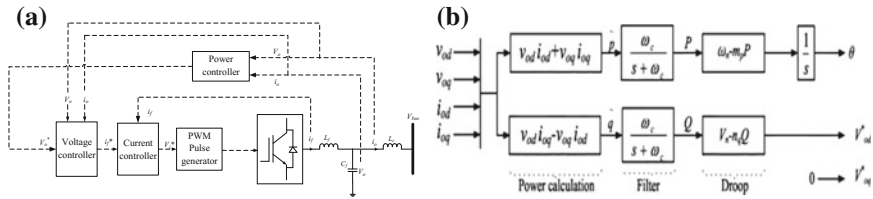


Fig. 1 Block diagram of **a** voltage source inverter model and **b** power controller

model of a single VSI is shown in Fig. 1a which mainly consists of the inverter, output filter, power-sharing controllers, voltage and current controllers. The power-sharing controllers control both the real and imaginary power using droop control of frequency and voltage, respectively, as shown in Fig. 1b. They mainly replicate the governor action as in the case of a synchronous generator. The active power droop control works with the main principle of decreasing active power with the increase in frequency and vice versa [5]. Also, the reactive power droop control works with a similar principle of decreasing reactive power with the increase in the voltage. The conventional controller used is a linear PI controller. The voltage controller along with all its feedback and feed-forward elements with its control action conventionally achieved using PI controllers can be traced from [9].

2.1 Output LC Filter Coupling Inductance Model

The main purpose of the LC filter is that it can remove the high frequency harmonics. Also the LC filter prevents the chance of resonance with the network and load side if chosen according to the system [5]. The coupling inductance mainly reduces the coupling between the active and reactive power components. A single inverter is thus a combination of the DG, power controllers, current and voltage controllers and output LC filter and coupling inductances. The inverter model simulated includes three voltage source inverter of same rating. The three inverters are interconnected through the two transmission lines which are considered as network. The transmission lines are considered to be short transmission lines and are emulated using suitable R-L branch. The inverters are connected to three loads as shown in Fig. 2 with the help of the network. The load considered in this work is resistive load. The inverter parameters are used for the simulation as given in Table 1 and have been adopted from [4, 10].

2.2 Methodology and Simulated Faults

Different fault conditions for the microgrid model are simulated and are shown in Table 2. The output current of the three inverters is recorded in dq reference frame

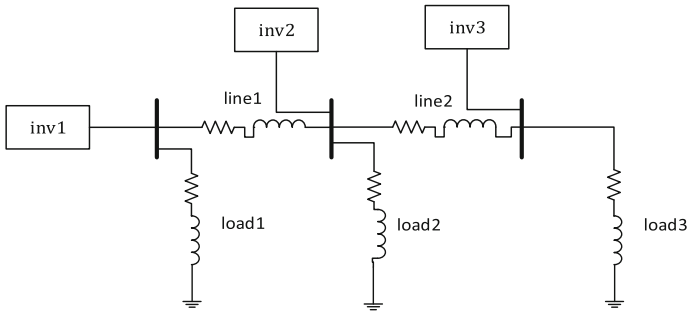


Fig. 2 Complete test system used

Table 1 Inverter parameters used for simulation [10]

Inverter	Parameter	Value
<i>Inverter parameters</i>		
1,2,3	mp, nq	1.57×10^{-6} , 0.002
1,2,3	K_{vi} , K_{vp}	390, 0.05
1,2,3	K_{ci} , K_{cp}	16×10^3 , 10.5
1,2,3	R_n	1000 Ω
<i>Line parameters & load parameters</i>		
Line 1	R_{line1} & X_{line1}	0.23 & 0.1 Ω
Line 2	R_{line2} & X_{line2}	0.35 & 0.58 Ω
Inverter 1	Active power	5.8 kW
Inverter 2	Active power	6.5 kW
Inverter 3	Active power	7.3 kW

Table 2 Different fault conditions simulated

Fault simulated			
Inverter	Type of faults	Fault instant (for training)	Fault instant (for testing)
1,2,3	Line-to-ground (A)	0.3	0.5
1,2,3	Line-to-ground (B)	0.3	0.5
1,2,3	Line-to-ground (C)	0.3	0.5
1,2,3	Line–line–ground (AB)	0.3	0.5
1,2,3	Line–line–ground (BC)	0.3	0.5
1,2,3	Line–line–ground (AC)	0.3	0.5
1,2,3	Line–line–line–ground (ABC)	0.3	0.5
1,2,3	Line–line–line–ground (ABC)	0.3	0.5
1	Line–line–line–ground (ABC)	0.3	0.5
2	Line–line–line–ground (ABC)	0.3	0.5
3	Line–line–line–ground (ABC)	0.3	0.5

and have been used for MF DFA analysis for multifractal feature extraction and fault localization and detection using neural networks. The time series generated by the load currents during normal operation and during different fault conditions and are obtained by the taking the cumulative sum of fluctuations. The time series is analyzed by MF DFA for extracting the multifractal features. The singularity spectrum width of the multifractal spectrum and the Hurst exponent quantifying the long-run correlations are the extracted features of the time series which is tested with analysis of variance (ANOVA) validating the efficacy of the features' and fed to artificial neural network (ANN) model for fault detection.

3 Theory

3.1 Multifractal Detrended Fluctuation Analysis (MF DFA)

The time series generated by the load events are analyzed using MF DFA. The steps involved in MF DFA are summarized as follows. Let us consider $y(n)$ to be a non-stationary, nonlinear time series of length N [11]. The mean value of the time series is given by Eq. (2).

$$\bar{y} = \frac{1}{N} \sum_{n=1}^N y(n) \tag{1}$$

The integrated time series is computed by subtracting the mean value from the signal as shown in Eq. (2).

$$X(i) = \sum_{n=1}^i [y(n) - \bar{y}] \forall i \in 1, 2, \dots, N \tag{2}$$

The next step consists in dividing the time series into N_s non-overlapping segments, where s denotes the segment length and $N_s = \text{int}(N/s)$. For N not divisible by s , a section of data sequence is left out. For including the left out data, the procedure is reiterated from the reverse end and thus rendering $2N_s$ number of segments. Using least square polynomial approximation, the variation in local trends for each of the $2N_s$ is computed for each sequence fragments as shown in Eq. (3).

$$F^2(s, v) = \frac{1}{s} \sum_{i=1}^s \{X[(v-1)s + i] - x_v(i)\}^2 \text{ where } v = 1, 2, \dots, N_s \tag{3}$$

where $x_v(i)$ signifies the least square fitted value in the v th segment. By taking the average of $2N_s$ segments the q th order fluctuation function, $Fq(s)$ is computed, where q is the scaling index as given by Eq. (4).

$$F_q(s) = \left\{ \frac{1}{2Ns} \sum_{v=1}^{2Ns} [F^2(s, v)]^{0.5q} \right\}^{1/q} \quad (4)$$

Since, $F_q(s)$ depends on both the values of q and time scale s , its variation is analyzed using a log–log plot. It is computed for all time-scale range [10]. When the $y(n)$ is long-range power-law correlated, then $F_q(s)$ versus s shows a power-law variation with a slope as function of $H(q)$ as shown in Eq. (6). For $H(q)$ being the generalized Hurst exponent

$$F_q(s) \propto s^{H(q)} \quad (5)$$

For monofractal time series, the scaling behavior of $F_2(s, v)$ is similar for all segments and for all values of q which means that $H(q)$ is independent of q . But, for a multifractal time series, $H(q)$ is a function of q and the Hurst exponent is taken for $q = 2$, and the scaling characteristics of segmental fluctuation is described by $H(q)$ for all values of q .

3.2 Multifractal Spectrum

The long-range correlations of a monofractal time series are characterized by a single Hurst exponent with the multifractal scaling exponent $\tau(q)$ showing linear dependency on the scaling exponent q . The multifractal scaling exponent $\tau(q)$ is related with the generalized Hurst exponent $H(q)$ by the relation shown in Eq. (6).

$$\tau(q) = qH(q) - 1 \quad (6)$$

While a multifractal time series is a set comprising of multiple Hurst exponents and there is nonlinear dependency of $\tau(q)$ on q as reported in [11]. With the help of Legendre transform, the relationship between singularity spectrum $f(\alpha)$ and scaling exponent $\tau(q)$ is obtained as given in Eq. (8).

$$\alpha = d\tau/dq \ \& \ f(\alpha) = q\alpha - \tau(q) \quad (7)$$

where α is the singularity exponent and $f(\alpha)$ signifies the fractal dimension of series subset characterized by α . Mathematically, α and $f(\alpha)$ can be expressed in terms of $H(q)$ as given by Eq. (8)

$$\begin{aligned} \alpha &= H(q) + q(q) \\ f(\alpha) &= q[\alpha - H(q)] + 1 \end{aligned} \quad (8)$$

The singularity spectrum $f(\alpha)$ of the multifractal spectrum determines the long-range correlation property of a time series. The width of the multifractal

spectrum quantifies the multifractality of the spectrum. A large spectral width is associated with a high degree of multifractality and vice versa. Since $H(q)$ is independent of q for a monofractal time series; hence, the multifractal spectrum width will be zero [12].

3.3 Artificial Neural Network (ANN)

ANN inspired from biological computations consists of a multilayered weighted combination of signals coming from a cluster of neural units called neurons. The self-learning tuning of the weights of the network paths with different activation functions coupled with a threshold function limit false triggers before propagating to other neurons provides an excellent nonlinear feature learning methodology where traditional learning fails. Mathematically, it is expressed as Eq. (10).

$$y_i = \sum_{m=1}^{L_i} \left[\omega_{ij} \sigma \left(\sum_{k=1}^n h_{jk} i_{ok} + \varphi_{vj} \right) + \theta_{wi} \right] \text{ where } i = 1, 2, \dots, n \quad (10)$$

where i_{ok} and y_i are the output currents and output of the ANN and h_{jk} and w_{ij} are hidden and output layer weights. The weights of these interconnections are updated in the learning process. Details about the application of ANN to microgrid fault prediction can be found in [8, 13, 14].

4 Observations

4.1 Line Faults in Inverters

Line faults in an inverter are marked by increase in output current to the saturation level. Faults occurring for a very short duration are difficult to detect with an ANN. Number of inputs and outputs of the ANN is 6 which is same as that of the number of output currents (I_{od1} , I_{oq1} , I_{od2} , I_{oq2} , I_{od3} , I_{oq3}) while the optimum number of hidden layers is determined by prior iterations and maximizing the accuracy. More details can be found in [8].

4.2 MF DFA Features

During normal operation of a microgrid, all the load currents exhibit anti-persistent ($H(q=2) < 0.5$) and similar generalized Hurst exponent scaling behavior and multifractal spectrum characteristics. But when fault occurs in any inverter, the load

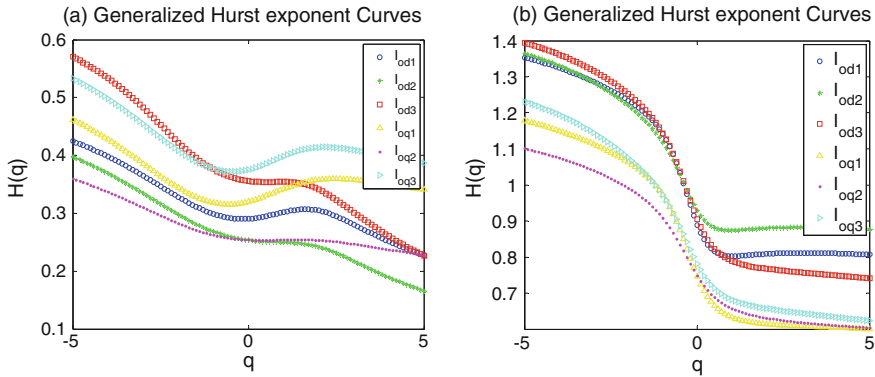


Fig. 3 Generalized Hurst exponent curves of the Iod’s a normal operation b line fault at DG3

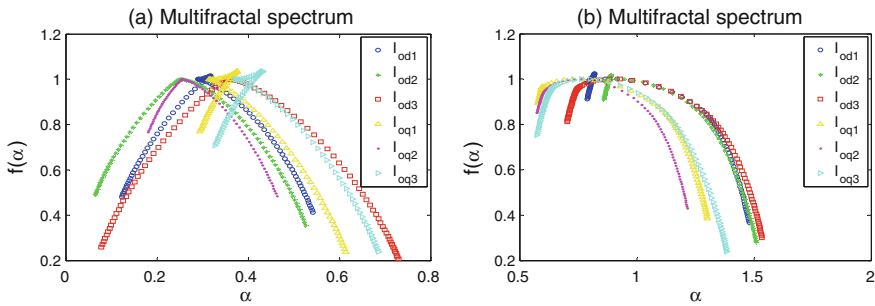


Fig. 4 Multifractal spectrum of the Iod’s a normal operation b line fault at DG3

lines supplying current to the fault areas gets interrupted and as such their fractal nature changes. These changes are manifested in the Hurst exponent and spectrum width values. Analyzing these changes in multifractal features of the load currents and fault localization is done in the microgrid by a neural network model. The generalized Hurst exponent curves and the multifractal spectrum of the normal and fault load currents are shown in Figs. 3 and 4, respectively.

5 Conclusions

The inherent fractal nature of the time series generated during normal operation and fault events of a microgrid has been characterized by MFDFA analysis. The Hurst exponent and the multifractal spectrum parameters are trained with ANN for fault detection in microgrids. Also, the extreme behavior of windowed fractal analysis

for finding the exact instant of fault localization is being studied for autonomous operation and integration to real systems.

References

1. Jayawarna, Nilanga, et al. "Safety analysis of a microgrid", 2005 International Conference on Future Power Systems, IEEE (2005).
2. Bo, Z. Q., et al. "Transient based protection for power transmission systems", Power Engineering Society Winter Meeting, 2000, Vol. 3 (2000).
3. Maria, Tim C. Green, and John DF McDonald, "Modeling and analysis of fault behavior of inverter microgrids to aid future fault detection", IEEE International Conference on System of Systems Engineering (2007).
4. Nagaraju Pogaku, Milan Prodanovic and Timothy C. Green, "Modeling, Analysis and Testing of Autonomous Operation of an Inverter-Based Microgrid", IEEE Transactions on Power Electronics, Vol. 22, No. 2, March (2007).
5. SalomonssonDaniel, LennartSoder, and AmbraSannino, "Protection of low-voltage DC microgrids", IEEE Transactions on Power Delivery, Vol. 24, no. 3, pp. 1045–1053 (2009).
6. DewadasaManjula, Arindam Ghosh, and Gerard Ledwich, "Line protection in inverter supplied networks", Power Engineering Conference, AUPEC'08, Australasian Universities (2008).
7. J. Chen, and J. Hou. "SVM and PCA based fault classification approaches for complicated industrial process", Neurocomputing 167, pp. 636–642 (2015).
8. A. Shankar, "Toward intelligent fault classification in autonomous microgrids", Industry Applications Society Annual Meeting, IEEE (2015).
9. D. Pullaguram, M. Mukherjee, S. Mishra, N. Senroy, "Non-linear fractional order controllers for autonomous microgrid system", IEEE 6th International Conference on Power Systems (ICPS), India, March (2016).
10. M. Mukherjee, D. Pullaguram, S. Mishra, "Dynamic droop based inverter control for autonomous microgrid", Biennial International Conference on Power and Energy Systems: Towards Sustainable Energy (PESTSE), India, January (2016).
11. Kantelhardt, Jan W., et al. "Multifractal detrended fluctuation analysis of nonstationary time series", Physica A: Statistical Mechanics and its Applications, Vol. 316, no. 1, pp. 87–114 (2002).
12. E. A. F. Ihlen. "Introduction to multifractal detrended fluctuation analysis in Matlab", Fractal Analyses: Statistical and Methodological Innovations and Best Practices, pp. 97 (2012).
13. Hopfield, John J., "Artificial neural networks", IEEE Circuits and Devices Magazine, Vol. 4, no. 5, pp. 3–10 (1988).
14. Mitchell, Tom M. "Artificial neural networks", Machine learning 45, pp. 81–127 (1997).

A Work on Grid Connected Solar Photovoltaic System Using Particle Swarm Optimization Technique

Bharti and Akhil Gupta

Abstract Nowadays, solar photovoltaic (PV) systems are rapid growing energy resources in the world. Solar PV system depends upon the solar irradiation and temperature. Number of maximum power point tracking (MPPT) techniques can be used to extract the maximum power. During bad weather condition or partial shading condition, conventional MPPTs are unable to recognize the maximum power point (MPP). Consequently, these algorithms cannot be utilized as a part of PV framework to concentrate maximum accessible power. For this, particle swarm optimization (PSO) is utilized to reinstate particles to scan for the new maximum power point (MPP). A detailed simulation is done in the MATLAB/Simulink. PSO system gives various focal points, it has a speedier following velocity, it can likewise build up the MPP for any ecological varieties including partial shading condition, and also it is easy to develop.

Keywords PSO · MPPT · PV system · Partial shading · MPPT technique

1 Introduction

Photovoltaic (PV) energy is one of the well-known wellsprings of non-conventional energy because of many advantages such as less pollution and low operational cost. PV sources are very important for mitigating global warming. Also, use of grid-connected solar PV systems is increasing due to development in technology, reduced rate in power electronic devices, a variety of incentive programs introduced by government, and also advances similar to environment friendly and low maintenance cost. Large grid-connected PV systems show sign of improvement in

Bharti (✉) · A. Gupta (✉)

Department of Electrical Engineering, Chandigarh University, Mohali, Punjab, India
e-mail: bhartithakur009@gmail.com

A. Gupta
e-mail: akhilgupta1977@gmail.com

productivity and dependability of both the PV boards and converters and to decrease overall cost [1–5].

The output power of PV module specifically relies on the atmospheric conditions like temperature and sunlight. As these amounts shift with time, in this manner, effectiveness of sun-powered cell is low that is around 20%. Along these lines, a control rationale is required that can monitor the terminal voltage and current and furthermore refreshes the signal as needs be. Terminal voltage ought to be proportionate to the comparing MPP esteem. To attain these goals, and to track the time-varying MPPT of solar PV array depending on its operating conditions of insolation and temperature, numbers of conventional MPPT algorithms [6–23] have been introduced. Most popular conventional MPPT methods used in PV system are perturb and observe (P & O), hill climbing (HC), and incremental conductance (INC), and these are used due to their simple structure. But responses of these methods are a bit slow and difficulty of steady-state oscillations is there. In addition to the varying environment, the performances of these methods are not satisfactory for all time. Comparisons of various MPPT techniques used in the PV systems are discussed in [13]. To get better the MPPT performance, the conventional perturb and observe (P & O) method based on fuzzy logic (FL) is used in [24]. But with fuzzy logic controller, the adequacy depends a ton on the certainties of the control build in picking the exact mistake calculation and upcoming by means of the rule base table. The neural system (NN)-based strategies have additionally been actualized for MPPT, yet immense measure of information is desirable for preparing the system. Moreover, through change of PV array with time, the NN techniques should be occasionally prepared to ensure adjust MPPT [24]. Another and effective arrangement is given by particle swarm optimization (PSO)-based strategy which has fast computational capacity and easy to actualize because of its basic and simple structure.

In the event that a PV exhibit is mostly shaded by a structure like a building, a tree, as well as mists, it ends up plainly complex for ordinary MPPT plans to concentrate greatest power. In the event that modules with various ideal streams, brought about by irregular insolation, are associated in arrangement parallel, MPPs frequently come into view in the power versus voltage trademark. This is on the grounds that the ideal current of each PV module is practically corresponding to the insolation on it. In such circumstances, traditional MPPT controller for the most part discovers nearby MPP as an option of search the local MPP. Henceforth, the created PV power, and the general module effectiveness is little. CSS-MPPT strategies generally depend upon P and O steps and utilize the HC thought in taking after accentuations. In the meantime, these procedures take a gander at prior and the present power values constantly, and the moment when they get the basic neighborhood most extraordinary, the computation halt forward direction processing. Besides, these ordinary techniques separate most extreme power just while the global MPP is the main utmost control peak. On the off chance that the global MPP seems later than the nearby MPP all through the inquiry procedure, the CSS techniques hit the local peak of the neighborhood MPP and after that settle or swing around this point figuratively speaking. These calculations are not equipped for

recognize the local and global MPPs. Of course, they are absolutely talented to catch single MPP that may be local or global, which is based on the condition of the power versus voltage curves. On the basis of partial shading condition, its position with respect to the PV module, initialization of shading, and its direction of exploration PV power and voltage curve can be drawn. In [25, 26], a specification of different PV modules which are used to track the global MPP has done and an effort has been done to make it more efficient. PSO calculation-based MPPT system has been discussed in this paper where the duty cycle of boost converter is changed with one MPPT controller to track the global most extreme power purpose of the framework.

2 About Photovoltaic Systems and MPPT Algorithm

2.1 PV Array Model

As given in Fig. 1, the solar cell is essentially a *p-n* junction diode. Henceforth, I_{ph} is the photo current specifically relative to the insolation E (Kw/m^2). Here, I_D is the diode current, I_p is parallel current, R_s and R_p are arrangement resistor and parallel resistors separately, V_D is the voltage of diode, and V_C is the solar cell voltage. Output current I_C can be given by condition (1) [27].

$$I_c = I_{ph} - I_D - I_p \tag{1}$$

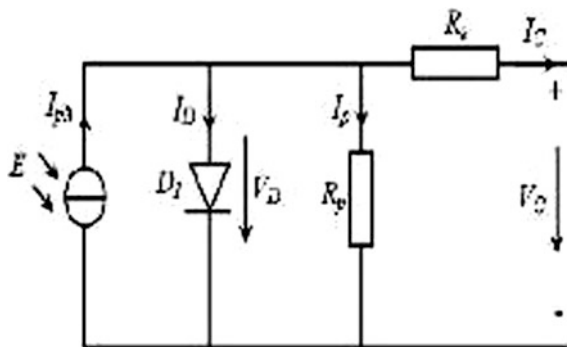
where;

$$I_D = I_s \{ \exp (V_D / m . V_T) - 1 \}$$

$$V_D = V_C + I_C . R_s$$

$$V_T = k . T / e$$

Fig. 1 Proportional circuit of a PV array [27]



$$I_P = V_D/R_P$$

Furthermore, I_s is diode immersion current, V_T is warm voltage, m is diode calculate, k is Boltzmann steady (1.38×10^{-23} J/K), T is absolute temperature, and e is electron charge (1.6×10^{-19}) in Coulombs. In this manner, the output energy of a PV exhibit relies on upon the quantity of cells associated in arrangement (N_s) and parallel (N_p) with a specific end goal to meet the essential evaluated control. The aggregate voltage and current can be communicated as taking after conditions 2 and 3, separately:

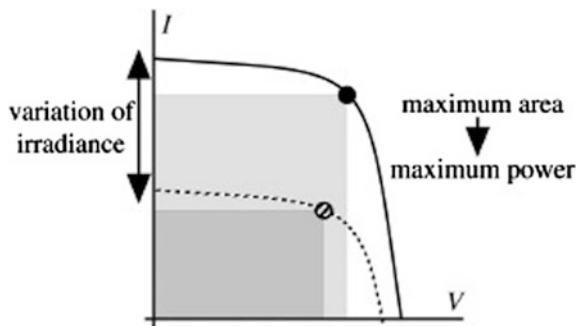
$$V_{dc} = N_S(V_D - I_C R_S) \tag{2}$$

$$I_{dc} = N_p I_C \tag{3}$$

2.2 Characteristics of Photovoltaic Array

A PV module is made up of series combination of solar cells which are connected in parallel arrangement. A glass is used to protect it against natural changes and falling of trees, raining, dust and many more. Its $V-I$ characteristics are appeared in Fig. 2. Where in the current is almost relative to sunlight based insolation. The dominant part of PV modules additionally has a bypass diode and an invert blocking diode. A standard PV era framework is comprised of various such module to get together to meet up demand on load side. Here, a PV framework has two modules, coupled through bypass diodes, participated in arrangement are measured for global power point tracking examinations. Imagine that solitary module is completely lit up, at the same time as another is in part in the shade. In this circumstance, the present going throughout the two modules is comparative as the modules are associated in arrangement, yet the current produced by the second module is a lesser measure of than that of the completely lit up module. Subsequently, the surplus current goes through the bypass diode.

Fig. 2 $V-I$ characteristics of solar cell [27]



The $V-I$ characteristics of a single PV module under shaded and non-shaded condition and also total PV module are appeared in Fig. 3.

On the off chance that there are more modules, the qualities of irregular radiations are complex, and may potentially show at least two MPPs. It becomes obviously confused to comprehend the MPPT utilizing traditional strategies. Regardless of the possibility that it is achievable to observe the global MPP, every module cannot be worked at the most ideal condition, as their ideal current is characteristically extraordinary at various insulations. On the off chance that the PV module can be isolated into smaller sub-types called sub-modules. Each module is controlled by MPPT controller. Due to which the power loss because of partial shading can be decreased. More voltage and current are required by this technique as appeared in Fig. 4.

Keeping in mind to reduce the cost and also the inconveniences related with the following plan, the control scheme must be basic and simple to execute with a most minimal number of sensors. So, another control scheme is appeared in Fig. 5, and in this method, a single sensor can be adopted to get the MPPT of PV module. This sensor is made up of single match of voltage and current.

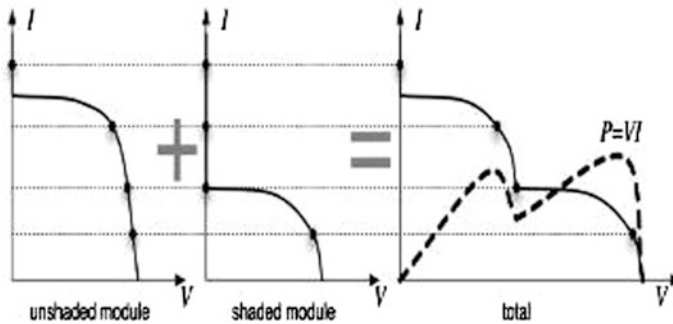


Fig. 3 Characteristics of PV modules connected in series [28]

Fig. 4 Various arrays controlled by different MPPT controllers [28]

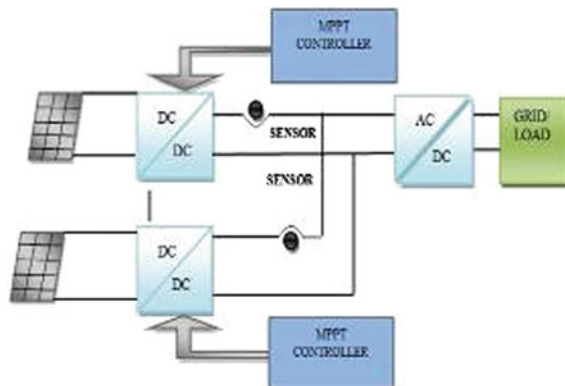
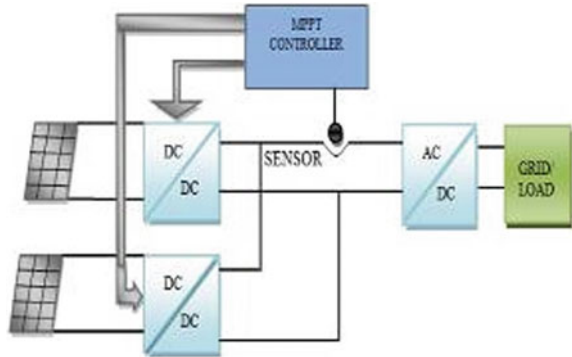


Fig. 5 Multiple arrays controlled by single centralized MPPT controller [28]



2.3 Particle Swarm Optimization (PSO) Algorithm

It is an Evolutionary Computation (EC) technique that reproduces the social lead of the swarm in nature, for example, schools of fish and rushes of winged creatures where they discover food normally in a particular zone. More especially, PSO is an iterative estimation that relies on upon finding the space and choosing the perfect plan of a goal work or objective (fitness function). Assessment of algorithm depends on the development of each molecule and additionally joint effort of the swarm. Every particle begins to move about unevenly in light of its own best data and the swarm's involvement. It is likewise pulled in toward the area of current global best position X_{gbest} and its own best position X_{pbest} . Particle swarm optimization (PSO) is a stochastic, populace-based search strategy, displayed after the execution of flying creature runs. A PSO calculation keeps up a swarm of individual (called particles), where every last one particle represents an applicant arrangement or solution. Particles seek after a simple conduct: imitate the accomplishment of adjacent particles, and its own victories accomplished. The place of a particle is so affected by the most fabulous particle in an environment, and additionally the best arrangement found by the particle. Molecule position, X_i , is balanced utilizing condition 4.

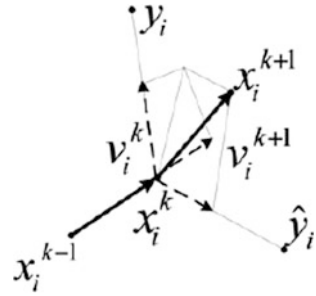
$$X_i(j+1) = X_i(j) + v_i(j+1) \quad (4)$$

where the velocity component, v_i , represents the step size. The velocity is calculated by Eq. (5).

$$v_i(j+1) = w v_i(j) + c_1 r_1 \{y_i(t) - x_i(t)\} + c_2 r_2 \{\hat{y}_i(t) - x_i(t)\} \quad (5)$$

where w = inertia weight, c_1 and c_2 = acceleration coefficients, $r_1, r_2 \in U(0, 1)$, y_i is the personal best position of particle i , and \hat{y}_i is the neighborhood best position of particle i . Development of PSO agent is shown in Fig. 6 [28].

Fig. 6 Development of PSO agent [28]



2.4 PSO-Based MPPT

A PSO calculation is connected to track the most extreme power of the PV exhibit utilizing the $P-I$ characteristics with a specific end goal to begin the advancement, and response vector of global current with N_p particle can be characterized as condition 6.

$$X_i^k = I_g = [I_{g1}, I_{g2}, I_{g3}, \dots, I_{gj}] \tag{6}$$

$$j = 1, 2, 3, \dots, N_p$$

The objective function is defined as:

$$f(x_i^k) > f(y_i) \tag{7}$$

where f is representation of the operating power of solar PV module. Normally, control from PV array frequently changes because of partial shading. Subsequently, in such cases, the particles must be reinitialized to look for the new global point (MPP). In this manner, taking after condition 8 is utilized to reinitialize the particles.

$$|P(x_{i+1} + 1) - P(x_i)/P(x_i)| > \Delta P \tag{8}$$

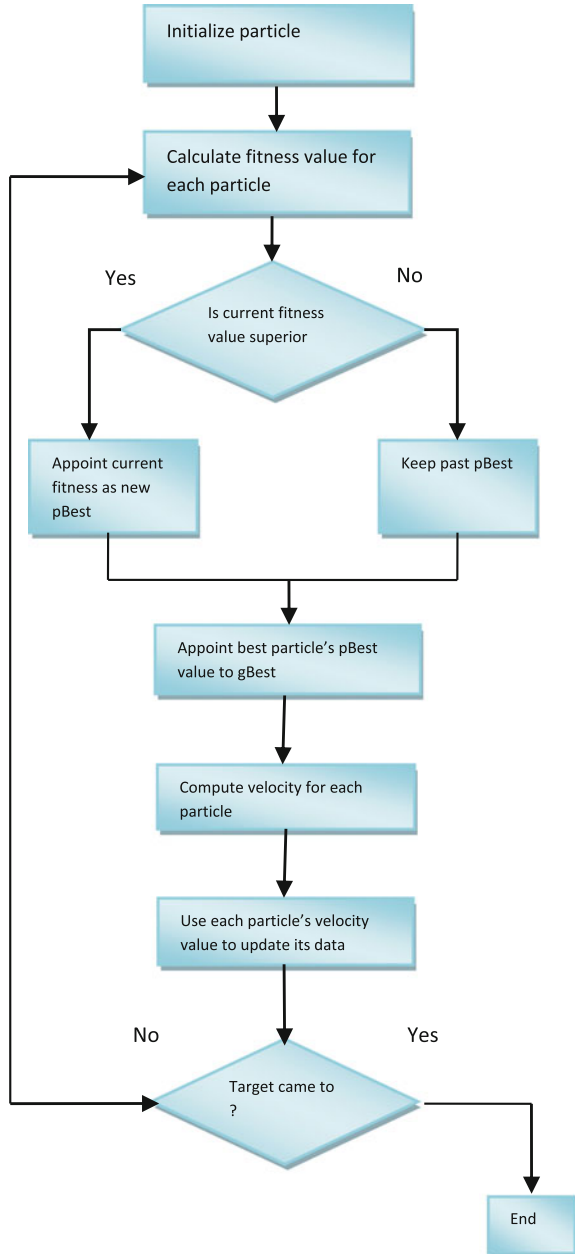
2.5 Implementation of PSO Algorithm

- (1) After particles and parameters are established then speed and the position values are decided.
- (2) For each and every particle, present speed as well as position are started unevenly.
- (3) Estimation has been computed for pbest for every particle also the value of each particle has been computed.
- (4) When the particle's best value is there, then the value of gbest has been set.
- (5) Repeat method 3 and method 4 again and again until ideal arrangement is achieved.

- (6) Repeat the means 3 and 4 until the ideal arrangement is achieved.
- (7) Enhanced optimized value has been resolved at the end of iteration on the basis of global best value.

PSO algorithm flowchart of the proposed PV system is illustrated in Fig. 7 [26, 29].

Fig. 7 PSO method flowchart [26]



3 Simulation Results

Simulink model consists of solar photovoltaic module which is connected to a grid through boost converter and three-level multilevel inverter. PSO technique is used in the boost converter. Simulink model of photovoltaic system is shown in Fig. 8.

Proposed system has two inputs as shown in Fig. 9a, b that permit you fluctuating sun irradiance (in W/m^2) and temperature (in $^{\circ}C$). The photovoltaic array

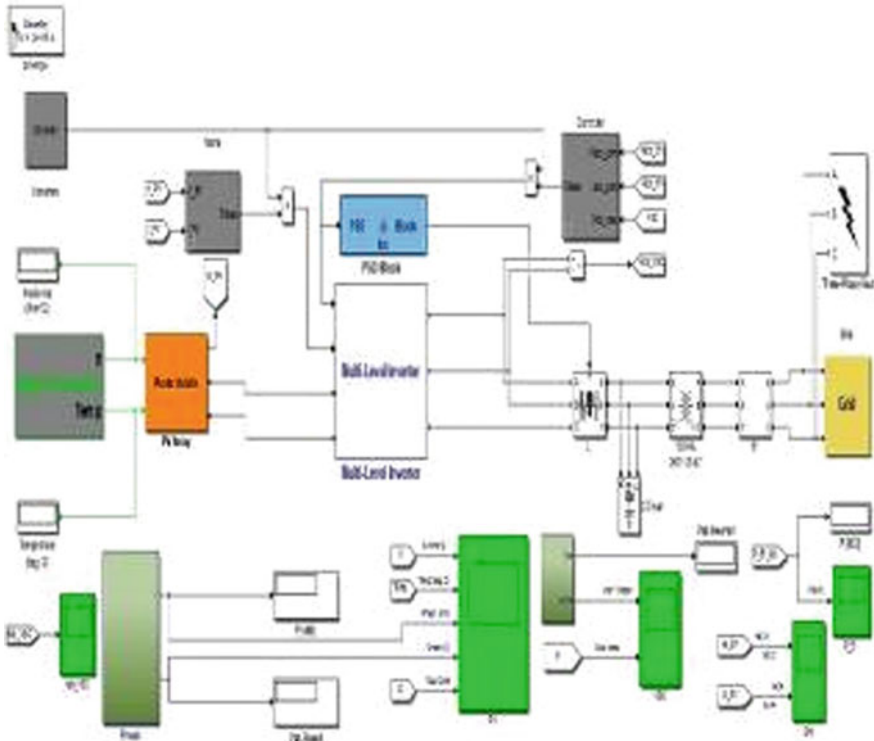


Fig. 8 Simulink model of a PV system using PSO

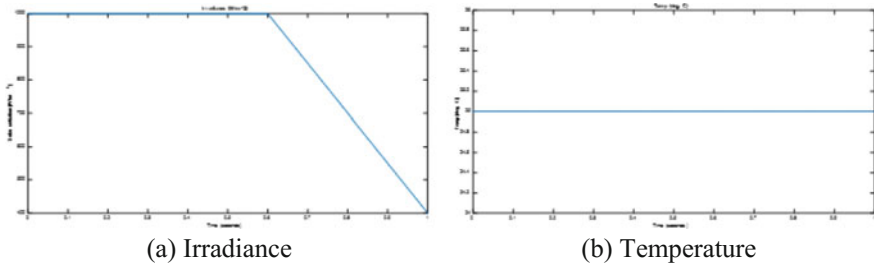


Fig. 9 (a), (b) input irradiance and temperature

exhibit utilizes 330 sun control modules, and it comprises of 66 strings of five arrangement-associated modules associated in parallel.

Output voltage and current of photovoltaic array are appeared in Fig. 10a, b. Additionally, DC-to-DC boost converter expands voltage from normal photovoltaic 273 V DC at most extreme energy to 500 V DC at appeared in Fig. 11. Voltage and current buses are of 25 kV ratings, and it is observed from the output obtained at grid at phase-A that there is unity power factor.

At time $t = 0.4$ s, MPPT is empowered. The MPPT controller begins directing PV voltage by differing duty cycle with a specific end goal to concentrate maximum power. What is more, most extreme power is gotten when the duty cycle is 0.454. From time $t = 0.6$ s to $t = 1.1$ s, sun irradiance is inclined down from 1000 to 400 W/m². MPPT keeps on following most extreme power. At $t = 1.2$ s, when irradiance has diminished to 400 W/m² obligation cycle is 1 relating PV voltage and power are 259.9 and 29.57 kW. Take note of that MPPT continual following maximum power along with this quick irradiance change. Figures 12, 13, and 14 show the simulation results of voltage, current, and power, respectively, tracked at phase-A of grid.

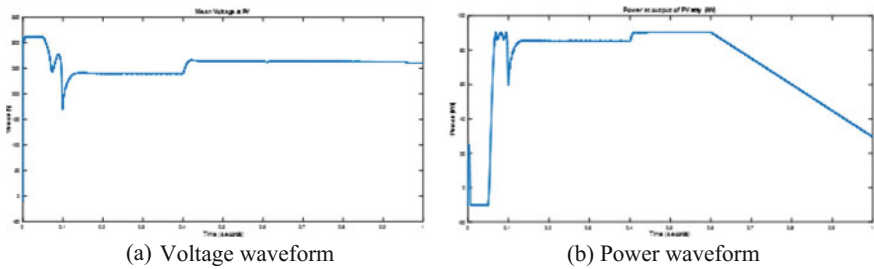


Fig. 10 (a), (b) voltage and current waveform at the output of PV array

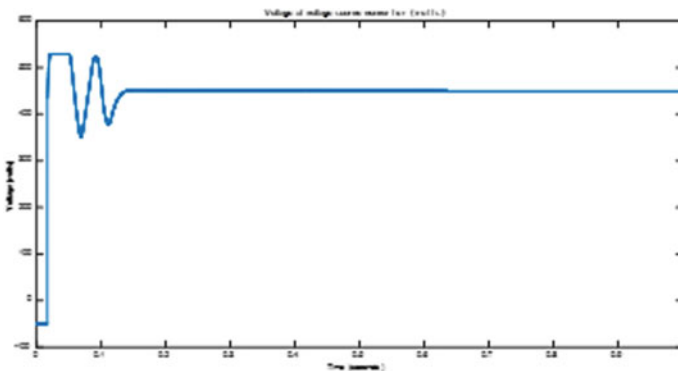


Fig. 11 Voltage waveform at voltage source converter

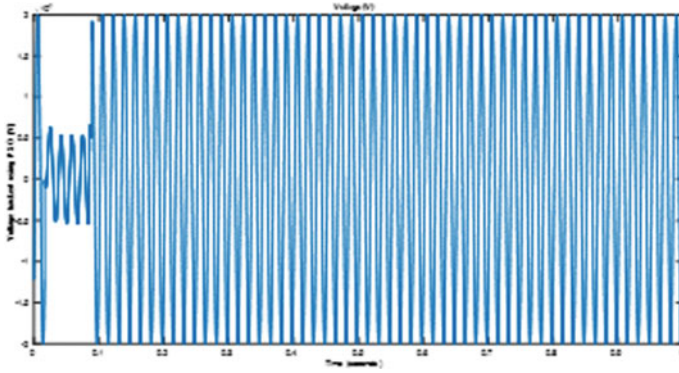


Fig. 12 Simulation results of voltage, tracked at grid

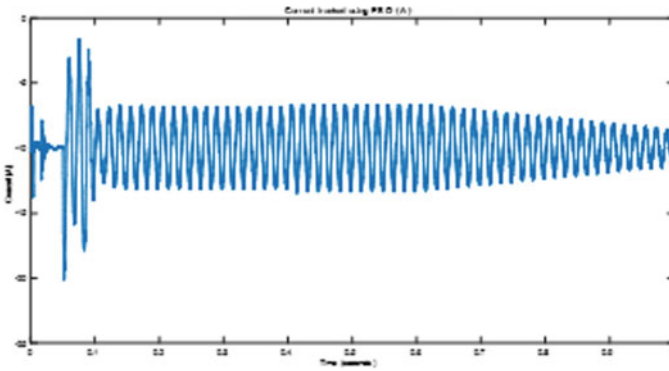


Fig. 13 Simulation results of current, tracked at grid

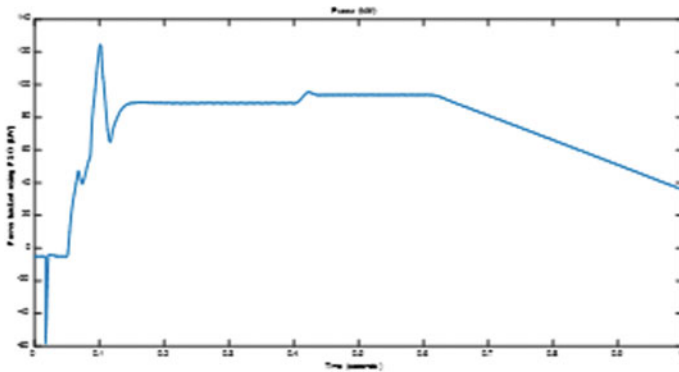


Fig. 14 Simulation results of power, tracked at grid

4 Conclusion

Voltage–current characteristics for PV show that in partial shading condition or bad weather condition and it is difficult to locate global MPPs at the season of incomplete shading or partial shading, making it hard to locate the global MPP utilizing conventional techniques. To beat this trouble, MPPT calculation utilizing a PSO strategy is presented. This proposed calculation utilizes just a single combine of sensors for controlling number of PV exhibits, subsequently bringing about lower cost, effortlessness, higher overall efficiency.

References

1. Oprism M. and pneumaticos S.: Potential for electricity generation from emerging renewable sources in Canada, in Proc. IEEE EIC. Climate Change technology conf., pp. 1–9, (2006).
2. Bo Y., Wuhua L., Yi Z. and Xiangning H.: design and analysis of a grid connected photovoltaic power system, IEEE Transaction on Power electronics. vol. 25, no. 4, pp. 992–1000, (2010).
3. Femia N., Granozio D., spagnuolo G. and vitelli M.: optimized one-cycle control in photovoltaic grid connected applications, IEEE Transaction on Aerospace and Electronic System, vol. 42, no. 3, pp. 954–972, (2006).
4. Petrone G., Spagnuolo G., Teodorescu R., Veerachary M. and Viteli M.: reliability issues in photovoltaic power processing systems, IEEE Transaction on Industrial electronics, vol. 55, no. 7, pp. 2569–2580.
5. Katiraei F. and Aguero J.: Solar integration challenges, IEEE power Energy Mag., vol. 9, no. 3, pp. 62–71, (2011).
6. Enslin J. H. R., Wolf M.S., Snyman D.B. and Swiegers W.: Integrated photovoltaic maximum power point tracking converter, IEEE Transaction on Industrial electron., vol. 44, pp. 769–773, (1997).
7. Hua C., Lin J. and Shen C.: Implementation of a DSP-controlled photovoltaic system with peak power tracking, IEEE Transaction on Industrial Electron., vol. 45, pp. 99–107, (1998).
8. Veerachary M., Senjyu T., and Uezato K.: Neural-Network based maximum power point tracking of coupled-inductor interleaved boost converter supplied PV system using fuzzy controller, IEEE Transaction on Industrial Electronics, vol. 50, pp. 749–758, (2003).
9. Veerachary M., Senjyu T. and Uezato K.: Feedforward maximum power point tracking of PV system using fuzzy controller, IEEE Transactions on Aerospace and Electronic System, vol. 38, pp. 969–981, (2002).
10. Kasa N., Iida T. and Chen I.: Flyback inverter controlled by sensor less current MPPT for photovoltaic power system, IEEE Transaction on Industrial Electronics, vol. 52, pp. 1145–1152, (2005).
11. ESRAM T. and Chapman P. L.: Comparison of photovoltaic array maximum power point tracking technique, IEEE Transaction on Energy Conversion, vol. 22, pp. 439–449, (2007).
12. Sun X., Wu W. and Zhao Q.: A research on photovoltaic energy controlling system with maximum power point tracking, In Proceeding of PCC-OSAKA, vol. II, pp. 822–826, (2003).
13. Kasa N., Iida T. and Majumdar G.: Robust control for maximum power point tracking in photovoltaic system, In Proceeding of PCC-OSAKA, vol. II, D6–4, pp. 827–832, (2002).
14. Shraif M. F., Alons C. and Martinez A.: A simple and robust maximum power point control for ground photovoltaic generators, In proceedings of IPEC-Tokyo, vol. I, pp. 158–163, (2000).

15. Veerachary M.: Power tracking for non-linear PV sources with coupled inductor SEPIC converter, *IEEE Transactions on Aerospace and Electronic System*, vol. 41, 1019–1029, (2005).
16. Matsui M.: New MPPT control scheme utilizing power balance at DC link instead of array power detection, In *Proceedings of IPEC-Tokyo*, vol. 1, pp. 164–169, (2000).
17. Kuo Y.: Novel maximum power point tracking controller for photovoltaic energy conversion system, *IEEE Transaction on Industrial electronics*, vol. 48, 594–601, (2001).
18. Kobayashi K., Matsuo H. and Sekine Y.: “An excellent operating point tracker of the solar cell power supply system,” *IEEE Transaction on Industrial Electronics*, vol. 53, pp. 495–499, Feb. 2006.
19. Kim I. S., Kim M. B. and Youn M. J.: New maximum power point tracker using sliding mode observer for estimation of solar array current in the grid connected photovoltaic system, *IEEE transaction on industrial electronics*, vol. 53, pp. 1027–1035, (2006).
20. Mutoh N., Ohno M. and Inoue T.: A method for MPPT control while searching for parameters corresponding to weather conditions for PV generation systems, *IEEE Transaction on Industrial Electronics*, vol. 53, pp. 1055–1065, (2006).
21. Kim I. S., Kim M. B. and Youn M.J.: New Maximum power point tracker using sliding mode observer for estimation of solar array current in grid connected photo voltaic system, *IEEE Transaction on Industrial Electronics*, vol. 53, pp. 1027–1035, (2006).
22. Mutoh N., Ohno M. and Inoue T.: A method for MPPT control while searching for parameters corresponding to weather conditions for PV generation systems, *IEEE Transaction in Industrial Electronics*, vol. 53, pp. 1055–1065, (2006).
23. Kajihara A. and Harakawa T.: On consideration of equivalent model about PV cell under partial shading, In *Proceeding of Japan Industry Application Society Conference*, vol. 1, pp. 289–292, (2005).
24. Zhang L., Bai Y. and Amoudi A.: GA-RBF neural network based maximum power point tracking for grid connected photovoltaic systems, In *Proceeding of IEEE International Conference on Power Electronics, Machines and Drives*, pp. 18–23, (2002).
25. Kennedy J. and Eberhart R.: Particle swarm optimization, In *Proceeding of IEEE International Conference on Neural Networks*, vol. IV, pp. 1942–1948, (1995).
26. Kadiramanathan V., Selvarajah K. and Fleming P. J.: Stability analysis of the particle dynamics in particle swarm optimizer, *IEEE Transaction on Evolutionary Computation*, vol. 10, pp. 245–255, (2006).
27. Manohar K. and Rani P. S.: MPPT and simulation for a grid connected photovoltaic system and fault analysis, *The International Journal of Engineering and Science*, vol. 1, pp. 158–166, (2012).
28. Miyatake M., Veerachary M., Fujii F., Ko H.: Maximum power point tracking of multiple photovoltaic arrays- A PSO approach, *IEEE Transaction on Aerospace and Electronic Systems*, vol. 47, no. 1, (2011).
29. Valle Y. D., Vanayagamoorthy G.K., Mohagheghi S., Hernandez J.C. and Harley R. G.: Particle swarm optimization -Basic concepts, variants and applications in power systems, *IEEE Transaction on Evolutionary Computation*, vol. 12, no. 2, pp. 171–195, (2008).

Review of Small-Signal Analysis of Microgrid in Islanding Operation

Dhanprakash Singh, Kamal Kant Sharma, Inderpreet Kaur and Balwinder Singh

Abstract This paper presents autonomous operation of microgrid by using modeling and small-signal analysis. State space technique is very good for finding the system small-signal stability. When microgrid having a number of generating units then it is very simple and time saving technique for solving system stability. In my microgrid model there are two micro generating sources and for checking System stability we are using the state space matrix and calculate the Eigen values and find the individual and combined DGs stability. These analyses Eigen values define the system stability and dynamics under the variation of controller and system parameters. And also verify the results with time domain simulation in MATLAB.

Keywords Small-signal analysis · Distributed sources · Micro-source interface

1 Introduction

Nowadays, microgrid is very popular. It is a type of grid where micro-generating sources (synchronous generators, induction generators, and voltage regulators) are connected very easily to feed power to the utility grid. As the population is increasing day by day, electric power demand (EPD) also increases. To fulfill this

D. Singh (✉) · K. K. Sharma · I. Kaur
Department of Electrical Engineering, Chandigarh University,
Mohali, India
e-mail: Dhanprakash412@gmail.com

K. K. Sharma
e-mail: sharmakamal2002@gmail.com

I. Kaur
e-mail: inder_preet74@yahoo.com

B. Singh
Department of Electrical Engineering, PEC University of Technology,
Chandigarh, India
e-mail: balwindersingh658@yahoo.com

EPD, we required to generate more electric power, so we are moving toward distributed generation (DG). Distribution systems have distribution energy resources, storage devices, and controlling devices operated on the utility grid under connected or islanding operation conditions. Microgrid gives a novel distribution system which is based on smart grid concept. Source generating the power less than 1 MW is called as micro-generating source.

A fault is occurring on the transmission line between utility grid and microgrid, due to the fault microgrid is disconnected from utility grid. This term is called islanding of an electrical system. Now, DGs are the only source of supplying electrical power to the electrical load which is isolated from the whole system.

We take the model reference which is given in [6]. Model consists of a micro-asynchronous generating unit and a micro-PV generating unit with voltage source converter (VSC) interfacing unit which are connected with microgrid.

Small-Signal Analysis Basics

Small signal has different-different uses like:

- Find out the exact common operating point of generating units.
- Helpful in designing the controlling parameters.
- Optimize the full system to increase all the stability of the system.

The behavior of the autonomous system is given by

$$\dot{X} = f(x, u) \quad (1)$$

The mathematical model of linearized equations of microgrid is given in the form of,

$$\Delta\dot{X} = A \Delta X + B \Delta u \quad (2)$$

Section 2 describes the test system. Section 3 consists of DG unit equations. Section 4 consists of calculations. Section 5 concludes the results.

2 Test System Representation

2.1 System Study

There are two types of micro-generating sources. As DG1 is asynchronous generator and DG2 is PV generator with VSC respectively. Which are connected with the microgrid is shown in Fig. 1 microgrid is connected with the utility grid via a transformer and transmission lines.

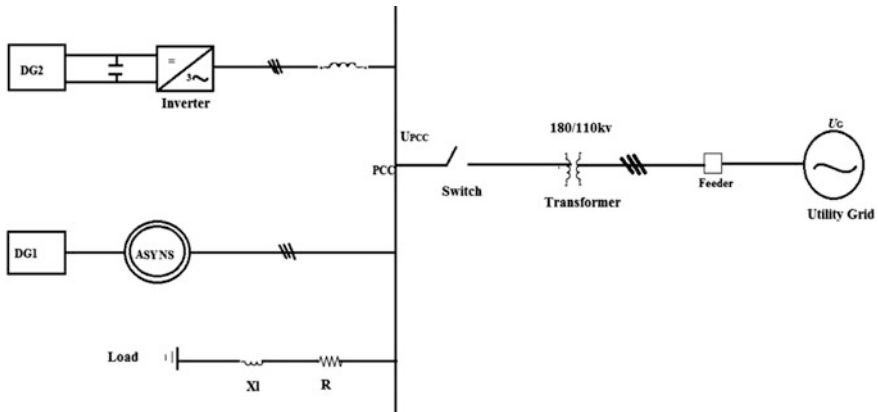


Fig. 1 Distributed generation in islanding mode

2.2 Single Line Diagram

Figure 2 is single line diagram of microgrid whose voltage level is 380 V where n is the number of DGs units.

3 Equations of DGs Used in Microgrid

3.1 Reference Frame Transformation

Because both DGs are different types, they require a common reference so that they convert very easily into the common linear equation form. So transformation is done on one single point which is called point of common coupling (PCC).

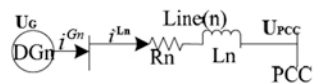
Transformation equation is written as,

$$f^g = T_n f^n \tag{3}$$

where

$f^g = [f_d^g f_q^g]^T$ is the vector of f in d - q frame and $f^n = [f_d^n f_q^n]^T$; if δ_n is the angle between d -axis and rotating reference planes, then transformation matrix is given by,

Fig. 2 Micro-source interface with system



$$T_n = \begin{bmatrix} \cos \delta n & -\sin \delta n \\ \sin \delta n & \cos \delta n \end{bmatrix} \tag{4}$$

All the equations coming after the transformation are linear at common operating point which are used in state space technique for finding out the small-signal analysis.

3.2 Dynamic Model of DG1

Basically asynchronous type of DGs like wind generators, whose stator is connected with microgrid directly. During its operation, two types of power flow are observed (Fig. 3);

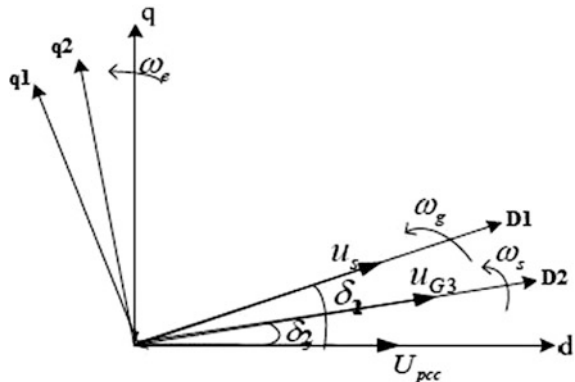
- (a) Active power flow from DGs to microgrid and
- (b) Reactive power flow from grid to the DGs, which is used for DGs excitation.

$$\begin{cases} u_{ds} = -R_s i_{qs} + X'_s i_{qs} + u'_d \\ u_{qs} = -R_s i_{qs} - X'_s i_{ds} + u_q \\ \dot{u}'_d = -\frac{1}{T'_0} [u'_d - (X_s - X'_s) i_{qs}] + p u'_q \theta_g \\ \dot{u}'_q = -\frac{1}{T'_0} [u'_q - (X_s - X'_s) i_{ds}] - p \theta_g u'_d \\ \frac{d\omega_g}{dt} = \frac{1}{2H} (T_m - T_e) \end{cases} \tag{5}$$

Equation 5 is linear about operating point and represents the small-signal model given in Eq. (6)

$$\Delta \dot{X}_{G1} = A_{G1} \Delta X_{G1} + B_{G1} \Delta u_{G1} + C_{G1} \Delta u_{pcc} \tag{6}$$

Fig. 3 Global and local rotating references frames of the system of Fig. 1



where

$\Delta X_{G1} = [\Delta u'_d \Delta u'_q \Delta \omega_g]^T$ and $\Delta u_{G1} = \Delta T_m$ are the state variables and input variables of DG1

3.3 Dynamic Model of DG2

In this type of power plant, VSC is interfacing between PV and DG

$$P \begin{bmatrix} x_p \\ x_q \end{bmatrix} = -I_{2 \times 2} \begin{bmatrix} P_{\text{inv}} \\ Q_{\text{inv}} \end{bmatrix} + I_{2 \times 2} \begin{bmatrix} P_{\text{inv}}^* \\ Q_{\text{inv}}^* \end{bmatrix} \quad (7)$$

The VSC output power in Eq. (7) can be expressed as:

$$\begin{cases} P_{\text{inv}} = u_{\text{ds}}^{G2} i_{d_ \text{inv}}^{G2} \\ Q_{\text{inv}} = u_{\text{ds}}^{G2} i_{q_ \text{inv}}^{G2} \end{cases} \quad (8)$$

$$\Delta \dot{X}_{G2} = A_{G2} \Delta X_{G2} + B_{G2} \Delta u_{G2} + C_{G2} \Delta u_{\text{pcc}} \quad (9)$$

where

$\Delta X_{G2} = [\Delta x_p \ \Delta x_q]^T$ and $\Delta u_{G2} = [\Delta P_{\text{inv}}^* \ \Delta Q_{\text{inv}}^*]^T$ are the state and input variables of VSC.

3.4 Dynamic Model of Microgrid

Under microgrid autonomous operation mode, Δu_{pcc} is determined by the combination of both microgrid and DG units. From Fig. 1

$$\begin{bmatrix} U_{\text{pcc}} \\ 0 \end{bmatrix} = \begin{bmatrix} R_L & -X_L \\ X_L & R_L \end{bmatrix} \begin{bmatrix} i_{dL} \\ i_{qL} \end{bmatrix} \quad (10)$$

where R_L, X_L are the load resistance and inductive reactance, while i_{dL}, i_{qL} are the load current along d and q axis represented by state space method. In Eqs. 11 and 12,

$$\begin{bmatrix} i_{dL} \\ i_{qL} \end{bmatrix} = \begin{bmatrix} i_{d_ind}^G \\ i_{q_ind}^G \end{bmatrix} + \begin{bmatrix} i_{d_inv}^G \\ i_{q_inv}^G \end{bmatrix} \tag{11}$$

$$\begin{cases} A = \begin{bmatrix} A_{G1} + C_{G1}H_1 & C_{G1}H_2 \\ C_{G2} & A_{G2} + H_2C_{G2} \end{bmatrix} \\ B = \begin{bmatrix} B_{G1} & 0 \\ 0 & B_{G2} \end{bmatrix} \end{cases} \tag{12}$$

4 Calculation for Small-Signal Analysis

The linearized mathematical model of the microgrid helps to calculate the system small-signal dynamic behavior and other parameters for optimum performance.

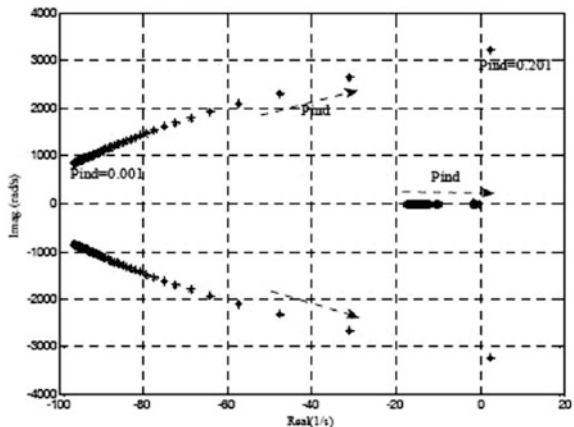
Line parameters of DG1 and DG2 are given as: $Z_1 = R_1 + jX_1 = (0.05 + j0.00157) \Omega$ and $Z_2 = R_2 + jX_2 = (0.0298 + j0.005) \Omega$; microgrid rated voltage and frequency are 380 V and 50 Hz; VSC active power reference P_{inv}^* is 100 kW; reactive power reference Q_{inv}^* is 0 kVar (Fig. 4).

Power angle curve shown in Fig. 5 as the power of the Asynchronous generator is increase to the value more then 0.201 the system became unstable because with increase in active power Eigen values moves toward right hand side of the plane and making system unstable.

Figure 6a shows that when proportional gain increases then the more dominant roots were not very much affected as compared to the less dominant roots affected, which makes our system stable. Figure 6b shows the converter operation mode when it works in inversion mode, and its roots move toward imaginary axis, which increase its transient time.

We also study results in MATLAB simulation shown in Fig. 7a, b. When small disturbance occurs then what is the response of all the DGS. Figure 7a shows the

Fig. 4 Trace of Eigen values when the active power of DG2 increases



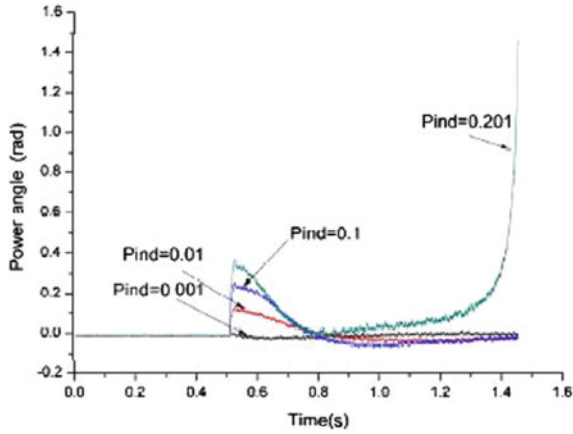


Fig. 5 Power angle of asynchronous generator to PCC response when active power of asynchronous generator changes

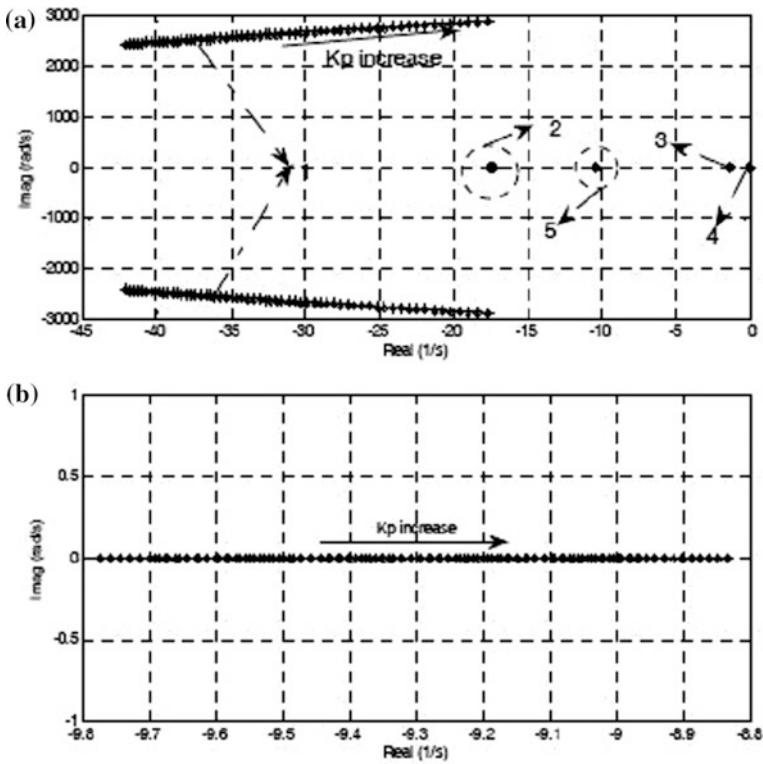


Fig. 6 Trace of Eigen values when the proportional gain of power loop changes, **a** with asynchronous generator **b** with VSC

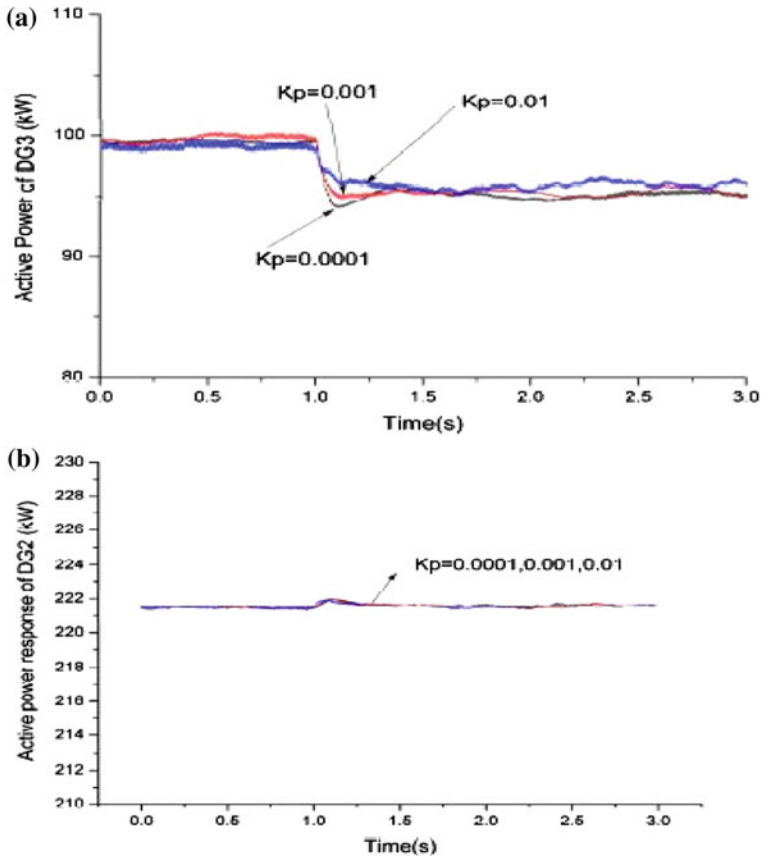


Fig. 7 Active power response of different micro-sources when proportional gain of VSC power loop changes, **a** asynchronous generator **b** VSC

asynchronous generator response variation, and Fig. 7b shows the VSC output variation of power when a step changes in the load power.

Response time of asynchronous generator with active power is shown in Fig. 7a, and we can see that as the proportional gains increase the output of the VSC decreases in Fig. 7b. The simulation results in MATLAB also show this result analysis.

5 Conclusion

This paper describes the microgrid model with reduced order having asynchronous generator and PV generator with electronically interfaced DGs unit. It represents a linear model of microgrid, in which all the DGs are connected linearized around

PCC operating, So We define a matrix which is basically a system matrix and is used to find out the Eigen value. The Eigen value comes are used to find out the system stability and system dynamics which is affected by the variation of the output of the asynchronous system and the result which had come and checked by the simulation.

Which shows the parameters of the controller's loop are not affected very much but affecting the output power of the VSC but not affecting the stability of the system to a very much.

References

1. LU Zong-xiang, WANG Cai-xia, MIN Yong, et al. "Overview on microgrid research," *Automation of Electric Power Systems*, 31(19): 25–34, (2007).
2. Chris Marnay. "Distribution systems and dispersed generation", (2010).
3. Venkataramanan G., Marnay C., "A larger role for microgrids," *Power and Energy Magazine, IEEE*, 6(3): 78–82, (2008).
4. Xu Xialing, Zha Xiaoming. "Overview of the researches on Distributed Generation and microgrid," *IPEC 2007 8th International Power Engineering Conference*, (2007).
5. Fang Z. Peng, Yun Wei Li, Leon M. Tolbert. "Control and protection of power electronics interfaced distributed generation systems in a customer-driven microgrid," *PES General Meeting*, (2009).
6. F. Katiraei, M. R. Iravani, P. W. Lehn. "Small-signal dynamic model of a micro-grid including conventional and electronically interfaced distributed resources," *IET Generation, Transmission and Distribution*, 1 (3): 369–378, (2007).
7. Nagaraju Pogaku, Milan Prodanovic, Timothy C. Green. "Modeling, analysis and testing of autonomous operation of an inverter-based microgrid," *IEEE Transactions on Power Electronics*, 22 (2): 613–625, (2007).
8. Charles K. Sao, Peter W. Lehn. "Control and power management of converter fed microgrids," *IEEE Transactions on Power Systems*. 23 (3): 1088–1098, (2008).
9. Prabha Kundur. "Power system stability and control," US: Mc Grew Hill, 1994.
10. Katiraei, F., M.R. Iravani. "Power management strategies for a microgrid with multiple distributed generation units," *IEEE Transactions on Power Systems*, 21(4): 1821–1831, (2006).
11. Vladislav Akhmatov. "Induction generators for wind power," Independent Pub Group, 2005.
12. L. Meegahapola, T. Littler, B. Fox, et al. "Voltage and power quality improvement strategy for a DFIG wind farm during variable wind conditions," Eds. 2010.
13. A. Petersson. "Analysis, modeling and control of doubly-fed induction generators for wind turbines," Ph.D., dissertation, Chalmers University of Technology. Sweden, (2005).
14. F. Katiraei, M. R. Iravani, and P. W. Lehn, "Small-signal dynamic model of a micro-grid including conventional and electronically-interfaced distributed resources," *Proc. Inst. Elect. Eng., Gen., Transm., Distrib.*, accepted for publication.
15. F. Katiraei, M. R. Iravani, and P. W. Lehn, "Micro-grid autonomous operation during and subsequent to islanding process," *IEEE Trans. Power Del.*, vol. 20, no. 1, pp. 248–257, (2005).
16. J. V. Milanovic and T. M. David, "Stability of distributed networks with embedded generators and induction motors," in *Proc. IEEE Power Eng. Soc. Winter Meeting*, New York, vol. 2, pp. 1023–1028, (2002).
17. C. L. Smallwood, "Distributed generation in autonomous and non-autonomous micro grids," in *Proc. IEEE Rural Electric Power Conf.*, pp. D1/1–D1/6, (2002).

18. E. A. A. Coelho, P. C. Cortizo, and P. F. D. Garcia, "Small-signal stability for parallel-connected inverters in stand-alone AC supply systems," *IEEE Trans. Ind. Appl.*, vol. 38, no. 2, pp. 533–542, (2002).
19. J. Ma, X. Wang, and X. Lan "Small-Signal Stability Analysis of Microgrid Based on Perturbation Theory," in *Proc. The 4th IEEE Asia-Pacific Power and Energy Engineering Conference (APPEEC)*, (2012).
20. R. H. Lasseter, "Microgrids and Distributed Generation," *Journal of Energy Engineering*, vol. 133, no. 3, pp. 144–149, (2007).
21. Joselin Herbert GM, Iniyas S, Sreevalsan E, "A review of Wind Energy Technologies", *Syst Energy Rev* 11, No. 6, pp 1117–1145.
22. J. G. Slootweg and W.L. Kling, "The Impact of Wind Power Generation on Power System Oscillations", *Electric Power System Research*, vol. 67, pp. 9–20, (2003).
23. L. B. Shi. Et al. "Analysis of Impacts of Grid Connected Wind Power on Small Signal Stability", *Wind Energy* 2010.
24. Martinez, C. Joos G. and Ooi B.T. "Power System Stabilizers in Variable Speed Wind Farms", *Power and Energy Society General Meeting*, (2009).
25. A. Tapia, G. Tapia, J. Ostolaza, and J. Saenz, "Modeling and control of A Wind turbine driven doubly fed induction generator," *IEEE Trans. Energy Converse*, vol. 18, no. 2, pp. 194–204, (2003).
26. M. Klein, G.J. Roger, S. Moorthy, P. Kundur, "Analytical Investigation of Factors Influencing Power System Stabilizers Performance", *IEEE Transactions on Energy Conversion*, vol. 7, No. 3, (1992).
27. K. Rudion, A. Orths, Z. Styczynski, and K. Strunz, "Design of Benchmark of medium voltage distribution network for investigation of DG integration," in *Proc. IEEE/Power Eng. Soc. General Meeting*, (2006).
28. R. H. Lasseter, "Microgrids and Distributed Generation," *Journal of Energy Engineering*, vol. 133, no. 3, pp. 144–149, Sep. (2007).
29. R. H. Salim, R. Kuiava, R. A. Ramos and N. G. Bretas, "Impact of power factor regulation on small-signal stability of power Distribution systems with distributed synchronous generators", *European Transactions on Electrical Power*, v. 21, n. 7, p. 1923–1940, (2011).
30. N. Pogaku, M. Prodanovic, and T. C. Green, "Modeling, analysis and Testing of autonomous operation of an inverter-based microgrid," *IEEE Trans. Power Electron.* vol. 22, no. 2, pp. 613–625, (2007).
31. M. Schweizer and J.W. Kolar, "Shifting input filter resonances – an Intelligent converter behavior for maintaining system stability," in *2010 International Power Electronics Conference (IPEC)*, pp. 906–913, (2010).
32. J. Sun, "Small-signal methods for AC distributed power systems—A review," *IEEE Trans. Power Electron.*, vol. 24, no. 11, pp. 2545–2554, (2009).
33. M. A. Pai, D. P. Sen Gupta and K. R. Padiyar, *Small Signal Analysis of Power Systems*. Harrow: Alpha Science International Ltd., (2004).
34. Q. Jiang, M. Xue, and G. Geng, "Energy management of microgrid in grid-connected and stand-alone modes," *Power Systems, IEEE Transactions on*, vol. 28, no. 3, pp. 3380–3389, (2013).
35. N. Hatziaziyriou, H. Asano, R. Iravani, and C. Marnay, "Microgrids," *Power and Energy Magazine, IEEE*, vol. 5, no. 4, pp. 78–94, (2007).
36. A. Chaouachi, R. Kamel, R. Andoulsi, and K. Nagasaka, "Multiobjective intelligent energy management for a microgrid," *Industrial Electronics, IEEE Transactions on*, vol. 60, no. 4, pp. 1688–1699, (2013).

Optimization of Wind Power Using Artificial Neural Network (ANN)

Dinesh Chauhan and Sunny Vig

Abstract Wind energy is one of the best alternatives for the fossil fuels in the field of electricity generation. They have many advantages, when compared to the fossil fuels, such as it is available naturally, does not have harmful effect on the environment and will not be get depleted with the passage of time. Besides all these advantages of the wind energy, when the wind is used for the generation of electrical energy, there are lot of issues related to wind like fluctuations in wind speed which cause major problems in power generation. Variation in wind speed can also cause power fluctuation, which will cause discomfort at the consumer level. Many developing nations have now moved towards wind energy to meet their growing energy demands. The problem of power output variation of wind farms can be optimized by various optimization techniques like particle swarm optimization, genetic algorithm and artificial neural network. In this study, the technique of artificial neural network is being used for the optimization of wind power. In the neural network toolbox, the optimum value for wind power is first determined individually for three different input variables (wind speed, tip-to-speed ratio and coefficient of power) and then the final optimum values are determined by using all these parameters as input variables at the same time.

Keywords Fossil fuels · Wind power · Tip-to-speed ratio · Coefficient of power Artificial neural network · MATLAB toolbox

1 Introduction

Since its invention in the nineteenth century, electrical energy has changed the world for good. The human race has become so dependent on electrical energy that today it is not possible to survive without electrical energy. All the luxuries,

D. Chauhan (✉) · S. Vig
Chandigarh University, Mohali, India
e-mail: dineshchauhan0915@rediffmail.com

S. Vig
e-mail: sunnyleo14@gmail.com

comfort and easiness in our life are mainly due to electrical energy. The working of a normal house to a large industry cannot be possible without electrical energy. After realizing the benefits, we get from electrical energy, and we simply kept our focus on the maximum generation of electrical energy. The major part of today's energy generation is done by coal and other fossil fuels. The unprecedented use of fossil fuels has resulted in many environmental issues like global warming, climate change and the increase in the quantity of greenhouse gases [1]. After realizing the harmful effects of fossil fuels, the government of each country is shifting its focus to renewable sources of energy. These renewable sources of energy have many advantages like they did not have any harmful effect on the environment and also, they are free of cost. Among these renewable sources of energy, wind energy is the important one as it will remain till the sun is there. Basically, wind is caused by the uneven heating of the earth surface by the sun. Throughout the world, wind energy has a huge potential which can be harnessed for the generation of electrical power. In India as on February 2017, the installed capacity for wind power is 28 GW [2]. This will further increase in the coming years as Indian Government is encouraging private partners to be associated in the field of power generation with renewable sources. But besides all these advantages, wind power with certain limitations like its generation is mainly dependent on the availability of the wind. If the wind is available, then the next issue is the speed of the wind. In large wind farms, multiple wind turbines are connected in parallel to get the maximum output. But with multiple wind turbines connected together, the speed with which wind hits the turbines is not the same for each turbine. So, we can optimize the wind power of each turbine. There are many optimization techniques available like particle swarm optimization, genetic algorithm and artificial neural network. In this study, artificial neural networks technique is being implied for the optimization of wind power.

2 Artificial Neural Networks (ANN)

In the field of artificial intelligence, there are two main branches: one is expert system and other is the artificial neural network [4]. Over a period of last decade, there has been the great development in the field of artificial neural network. In the recent years, ANN has been applied successfully for image recognition, sound, speech pattern identification and much more. Artificial neural networks are very much similar to the biological neural network and follow the same principle of learning of past experiences. The artificial neural network gives the best optimum value after training it multiple times. Figure 1 shows the diagram for a biological neuron.

It is estimated that human brain has billions of neurons connected together for the flow of information. Each neuron in the brain has the same four basic elements known by their biological names—dendrites, soma, axon and synapses [4]. The diagram showing the simplified model of the artificial neuron is shown in Fig. 2. ANN is basically formed by the interconnection of these artificial neurons. In such a system, excitation is applied to the input of the network. At the synapses, there is a

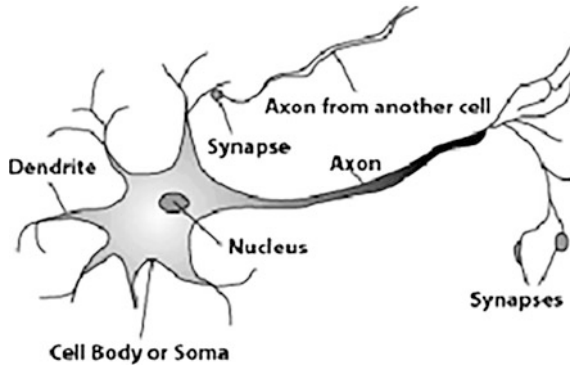


Fig. 1 Basic biological neuron

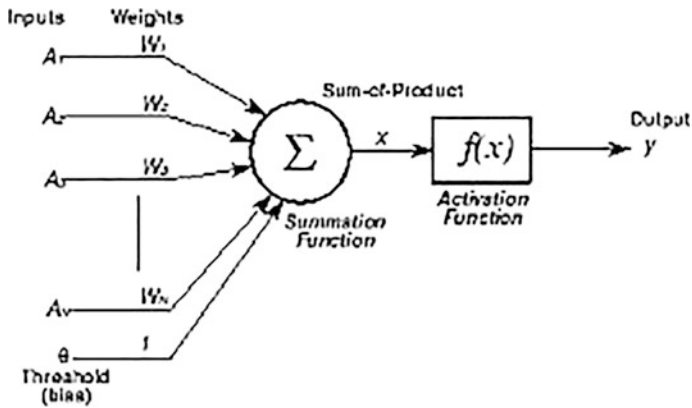


Fig. 2 Artificial neuron model

compilation of some potential which, in the case of the artificial neurons, is represented as a connection weight [4, 5]. These connection weights are modified continuously, based on the learning rules. When compared to biological neuron, the wires will replace the axon, the weight function will replace synapses and activity in soma is replaced by the activation function.

3 Data Used and Calculations

The maximum power that can be extracted from the wind turbine is given the mathematical formula described by Eq. (1) below

$$P = \frac{1}{2} \rho A C_p v^3 \tag{1}$$

In Eq. (1)

- P Power that can be extracted from the wind.
- ρ Air density.
- A Area swept by the turbine blades.
- C_p Coefficient of power.
- V Velocity of the wind or simply wind speed.

For the calculation of wind power, the values for wind speed are taken from a report. Wind speed data for a place are taken on the monthly basis for a whole year. Average wind speed for each month of the year is shown in tabular form in Table 1. Air density is constant and its value is 1.23 kg/m^3 . The most general rotor blade used in wind power plant has a radius of 52 m. Thus, the area swept by the blade will be calculated from the formula $A = \pi r^2$. The coefficient of power has a maximum value of 0.59, but its value varies with tip-to-speed ratio (λ). Tip-to-speed ratio is defined as the ratio of the blade tip speed and wind speed. Blade tip speed is defined by Eq. (2) shown below

$$\text{Blade tip speed} = \frac{\text{Rotational speed} * \pi * D}{60} \tag{2}$$

where D is the diameter of the rotor blade. Generally, the rotational speed of the turbine is between 15 and 20 rpm for the generation of power. For the calculation purpose, here, it is being taken as 15 rpm. The value of the coefficient of power is calculated manually for different tip-to-speed ratio value. The graph showing the variation of coefficient of power with the tip-to-speed ratio is shown in Fig. 3.

Table 1 Wind speed data on monthly basis over the year [6]

Sr. No	Month	Wind speed
1	January	5.0
2	February	5.6
3	March	6.3
4	April	8.3
5	May	10.1
6	June	12.1
7	July	13.9
8	August	12.5
9	September	9.8
10	October	5.9
11	November	5.8
12	December	6.5

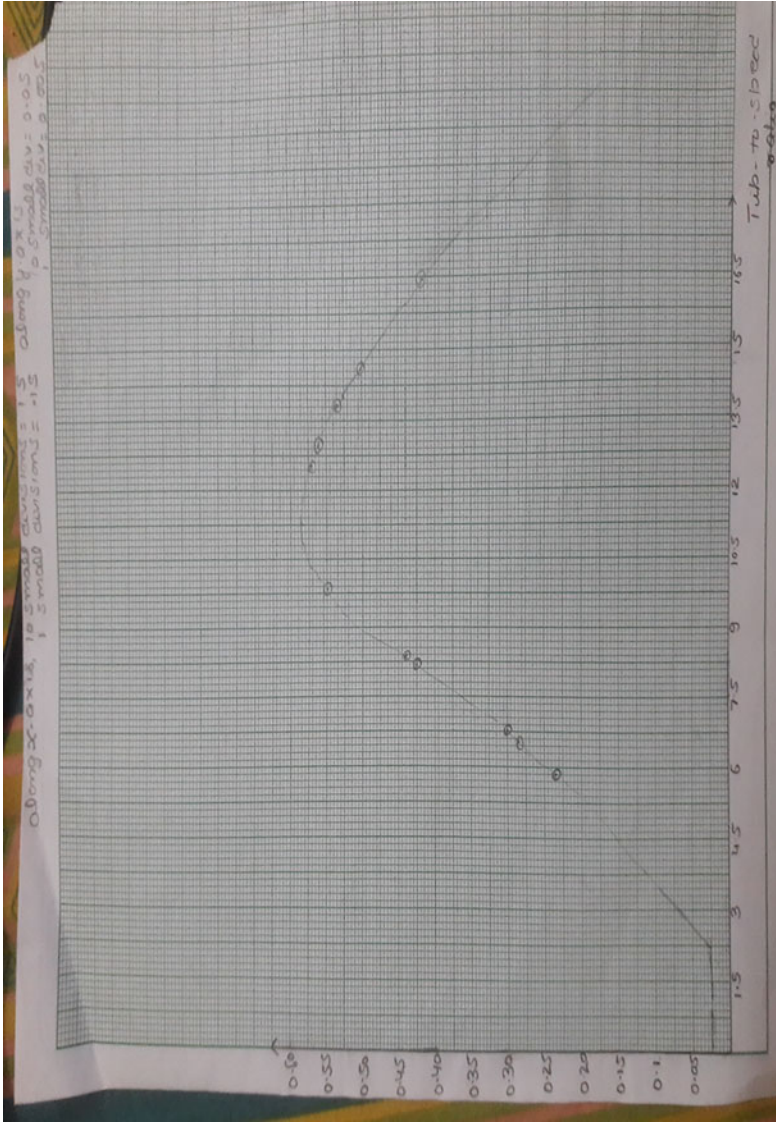


Fig. 3 Values of coefficient of power corresponding to the values of tip-to-speed ratio

Table 2 All calculated parameters (tip-to-speed ratio, coefficient of power and power output)

Sr. No	Wind speed (m/s)	Tip-to-speed ratio (λ)	Coefficient of power (C_p)	Power output (MW)
1	5.0	16.32	0.415	0.27
2	5.6	14.57	0.503	0.46
3	6.3	12.95	0.560	0.73
4	8.3	9.83	0.550	1.64
5	10.1	8.08	0.425	2.29
6	12.1	6.74	0.300	2.27
7	13.9	5.87	0.235	3.29
8	12.5	6.53	0.285	2.90
9	9.8	8.33	0.440	2.16
10	5.9	13.83	0.535	0.57
11	5.8	14.07	0.525	0.53
12	6.5	12.56	0.570	0.81

Thus, by knowing each parameter, the value of wind power is calculated by using Eq. (1) corresponding to each wind speed. Every calculated value in the tabular form is shown in Table 2.

4 System Modelling and Observations

After calculation of the parameters, the optimum values for power output are obtained by neural network toolbox in MATLAB. In neural network toolbox, the optimum values for power output are calculated by using wind speed, tip-to-speed ratio and coefficient of power as input variables individually and output power as output variable for each one of them. In this study, back proportion feed-forward algorithm is used for the calculation of optimum values. The mean square error curves for each case are shown in Figs. 4, 5, and 6, respectively.

The mean square error curves shown above are obtained after retraining the network multiple times. The network is retrained till the time the validation data curve becomes constant. These curves show the best validation performance of the data. The best performance is obtained after 19 iterations when wind speed is used as the input variable, after 30 iterations when the tip-to-speed ratio is used as the input variable and after 4 iterations when the coefficient of power is used as the input variable. The regression curves showing the relationship between the output and target for each case are shown in Figs. 7, 8, and 9.

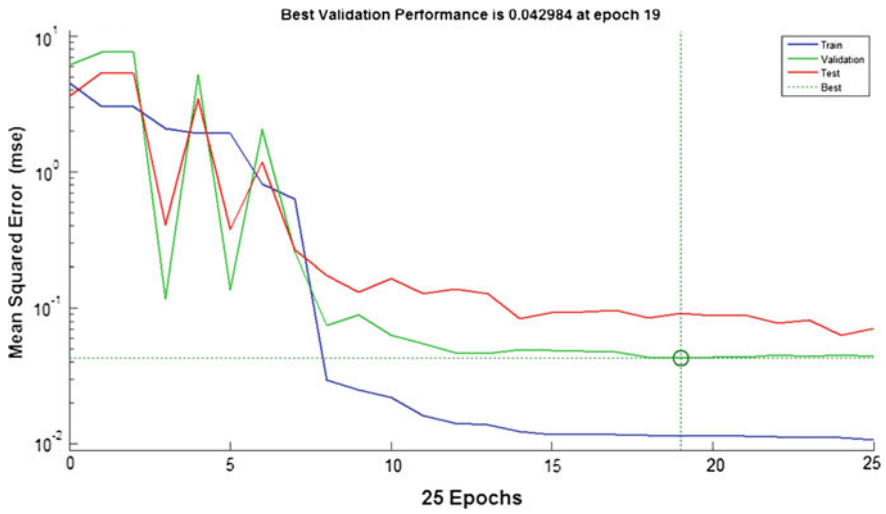


Fig. 4 Mean square error curve when only wind speed is used as an input variable

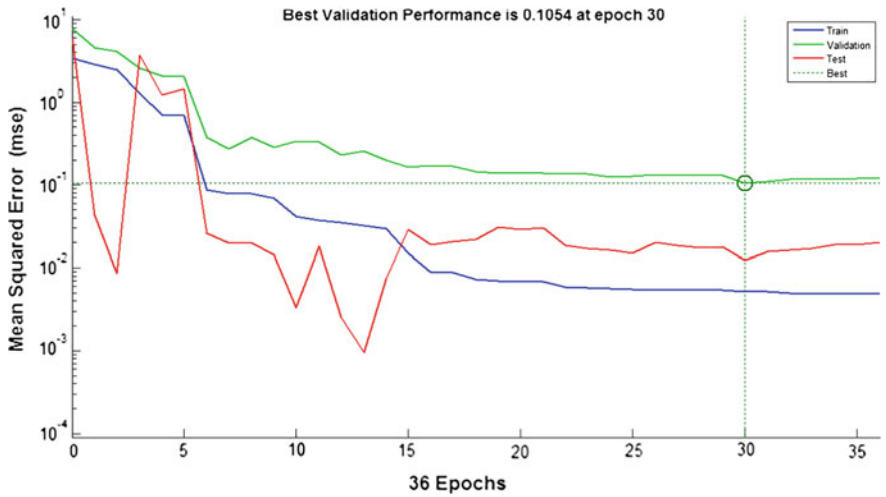


Fig. 5 Mean square error curve when only tip-to-speed ratio is used as an input variable

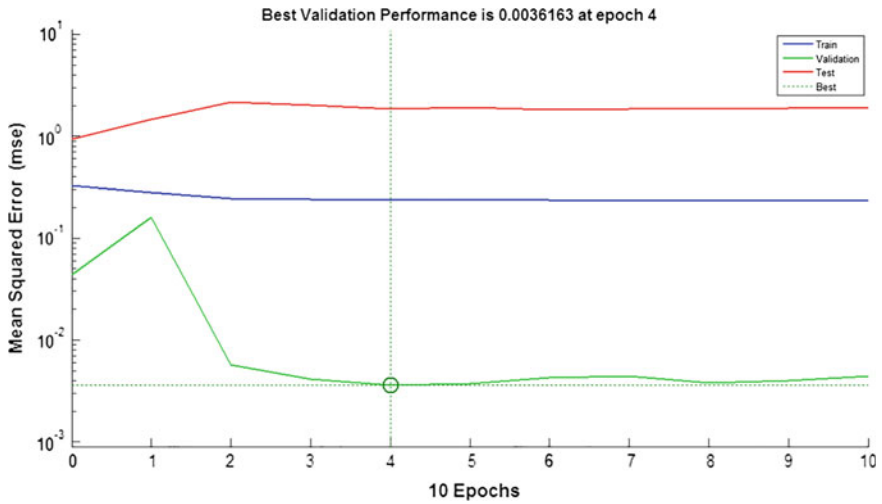


Fig. 6 Mean square error curve when only coefficient of power is used as input variable

The optimum values obtained for each of these cases are shown in Fig. 10.

Above values and curves are obtained when these input parameters are used individually. The best optimum value of the wind power can be obtained from neural network toolbox by using all these parameters as input variables together and power output as output variable because power depends upon these input variables. The mean square error curve, regression curve and the optimum values for this case are shown in Figs. 11, 12, and 13, respectively.

5 Results and Conclusions

The optimum values obtained from the whole data for each case are put in the tabular form in Table 3. From this research paper, it can be concluded that the artificial neural network (ANN) optimization technique can be helpful in finding the best optimum value of wind power by using multiple values of the wind. In this paper, monthly based data are used for different values of wind. For future work, data can be taken on yearly basis.

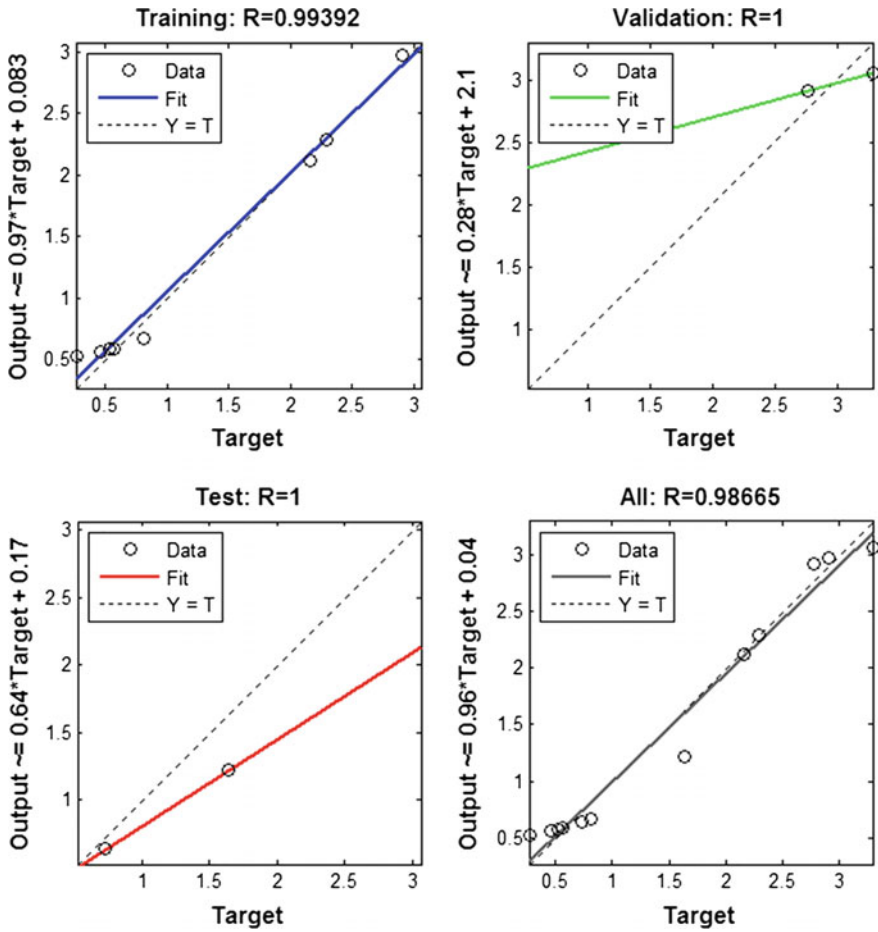


Fig. 7 Regression curve when wind speed is used as input variable

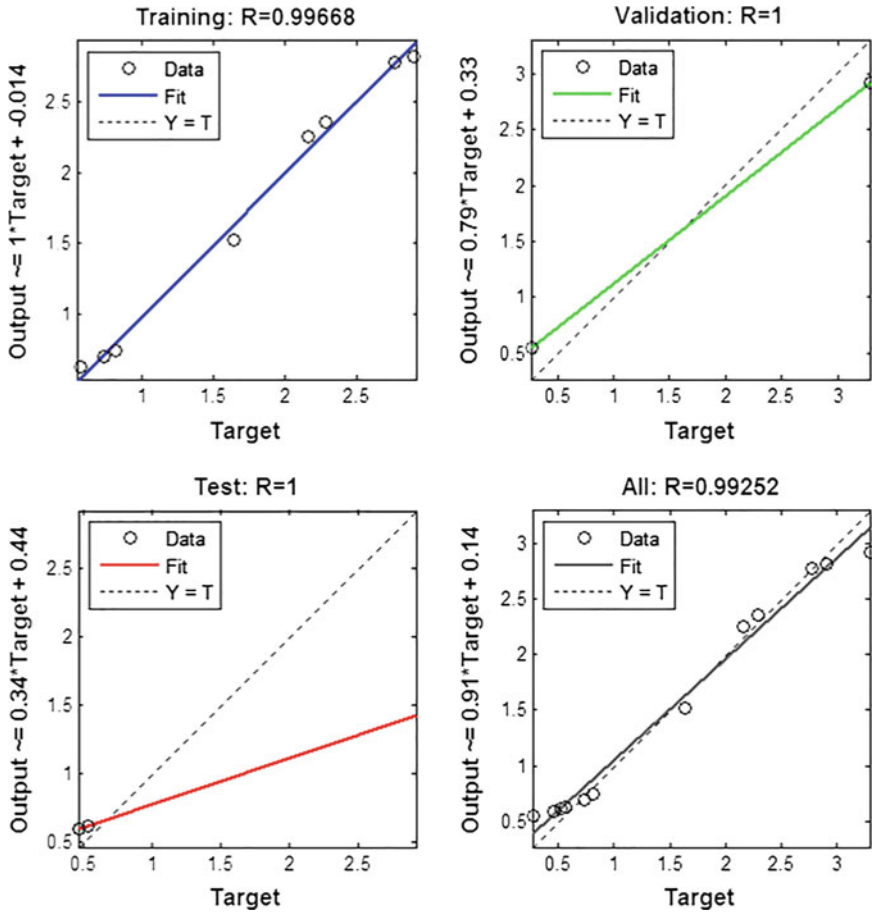


Fig. 8 Regression curve when tip-to-speed ratio is used as input variable

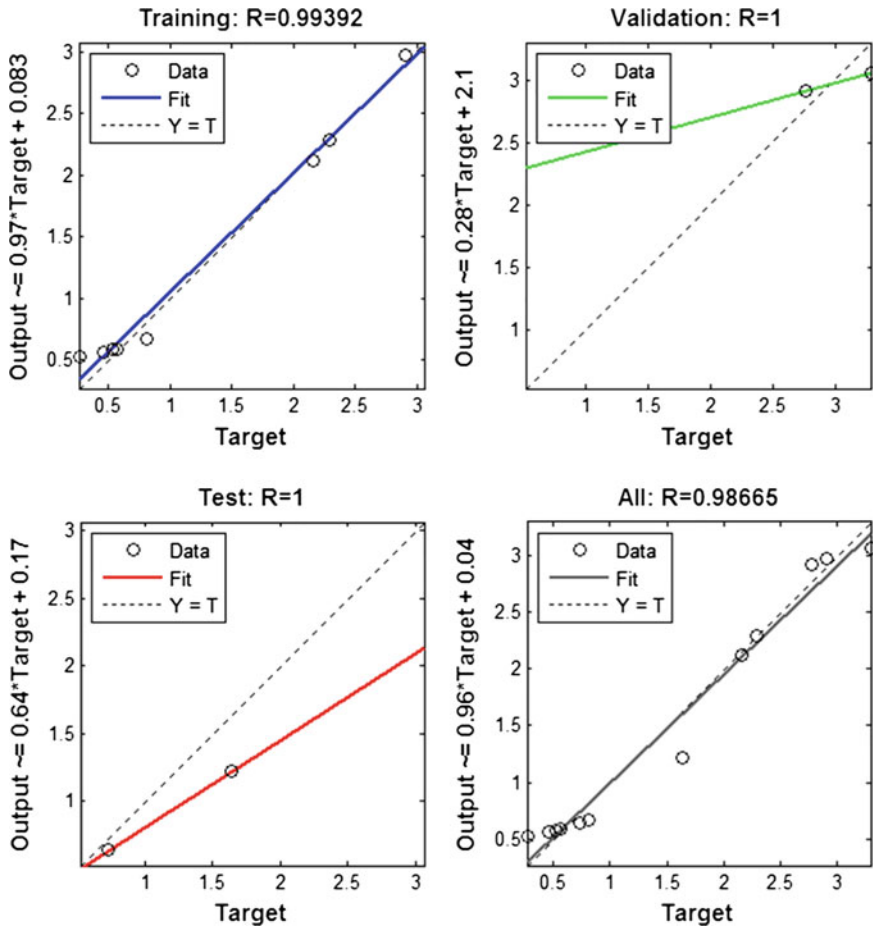


Fig. 9 Regression curve when coefficient of power is used as input variable

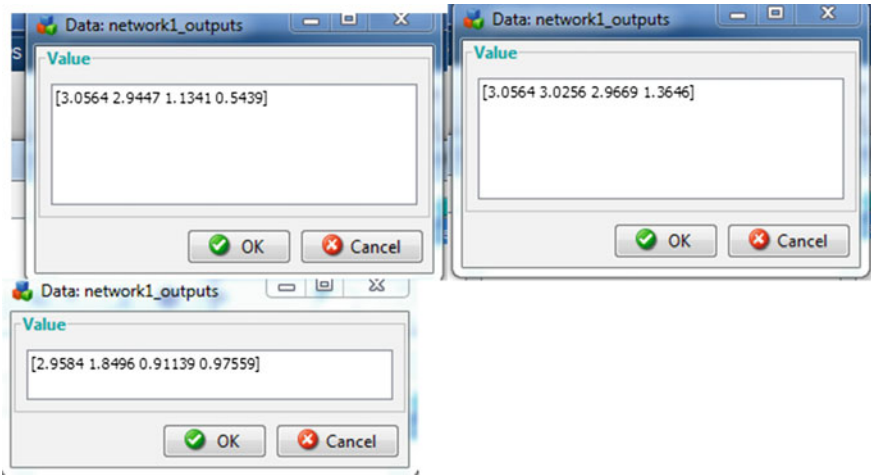


Fig. 10 Optimum values of the power obtained for the different cases

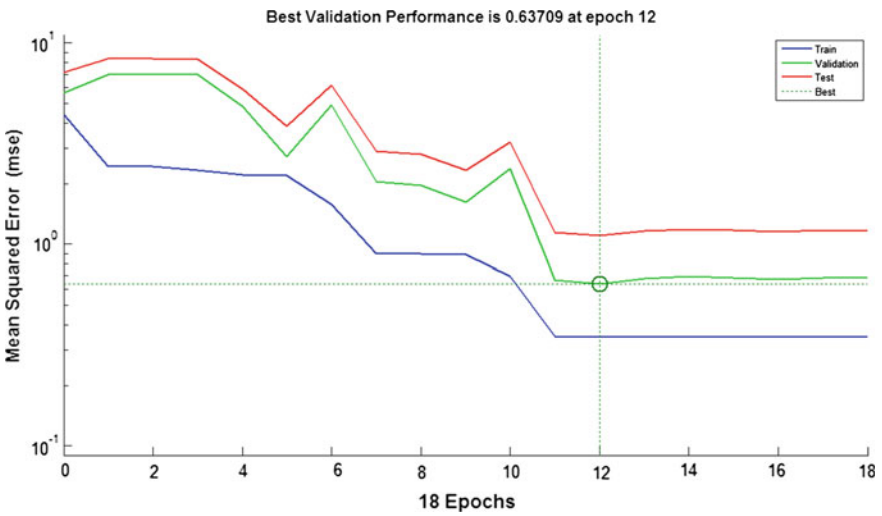


Fig. 11 Mean square error curve when all three are used as input variables

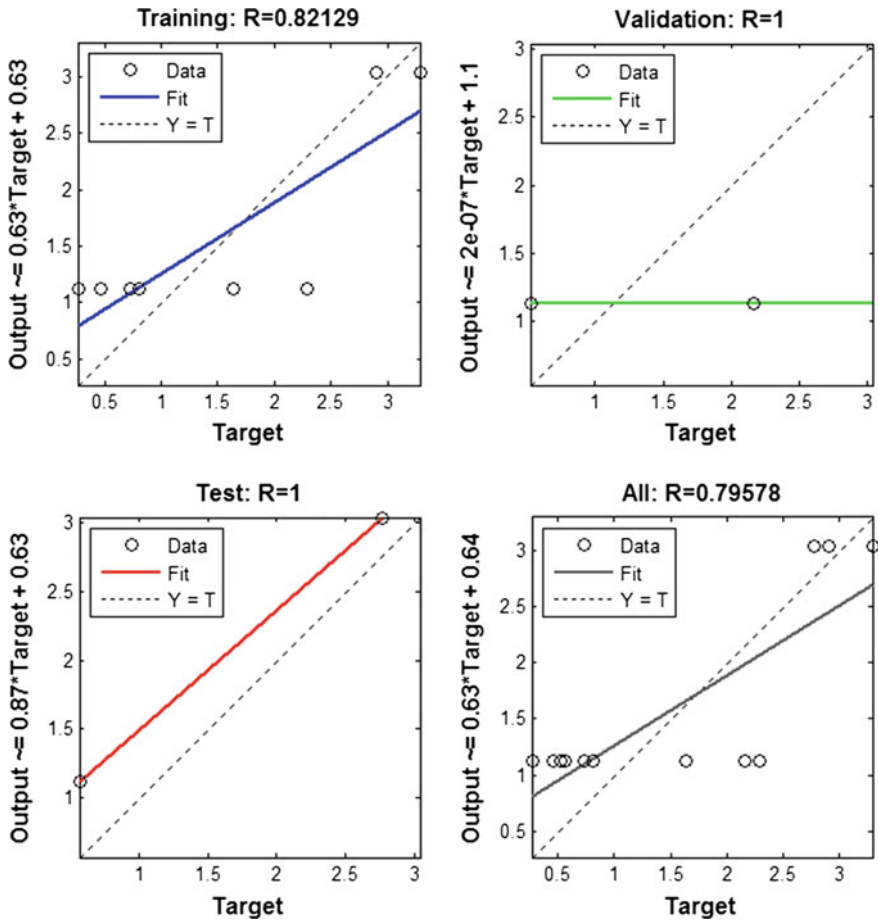


Fig. 12 Regression curve when all three are used as input variables

Fig. 13 Optimum value when all three are used as input variables

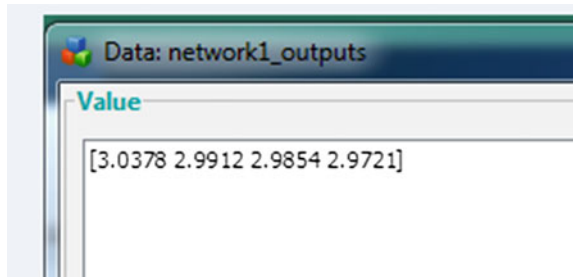


Table 3 Optimum values for all the different cases

Sr. No	For wind speed as input variable (MW)	For tip-to-speed ratio as input variable (MW)	For coefficient of power as input variable (MW)	When all are used as input variables (MW)
1	3.05	3.05	2.95	3.03
2	3.02	2.94	1.84	2.99
3	2.96	1.13	0.91	2.98
4	1.36	0.54	0.97	2.97

References

1. A. Sharma, J. Srivastava, S.K. Kar, A. Kumar, "Wind energy status in India: a short review" *Renewable and Sustainable Energy Reviews*, volume 16, issue 2, page 1157–1164, February 2012.
2. http://www.cea.nic.in/reports/monthly/installedcapacity/2017/installed_capacity-02.pdf.
3. G. M. J. Herbert, S. Iniyan, E. Sreevalasan, S. Rajapandian, "A Review of wind energy technologies" *Renewable and Sustainable Energy Reviews*, volume 11 issue 6, page, August 2007.
4. S.A. Kalogirou, "Artificial neural networks in renewable energy systems applications: a review." *Renewable and Sustainable Energy Reviews*, volume 5, page 373–401, 2001.
5. R. Ata, "Artificial neural network applications in wind energy systems: a review" *Renewable and Sustainable Energy Reviews*, volume 49, page 534–562, September 2015.
6. http://www.pmd.gov.pk/wind/wind_project_files/sindh_wind-03year.pdf.
7. S.K. Kar, A. Kumar, "Wind power developments in India" *Renewable and Sustainable Energy Reviews*, volume 48, Page 264–275, August 2015.

Cost Analysis of Hybrid Power System Design Using Homer

Gopal Thakur, Kamal Kant Sharma, Inderpreet Kaur
and Balwinder Singh

Abstract The paper proposes cost analysis of hybrid power system design using homer both grid-tied and off-grid mode of hydropower plant operative everywhere in the nation. Wind power systems are used to make system efficient and reliable. Hybrid energy system is used to decrease dependency on convention or renewable energy sources. Models of electric non-conventional (HOMER) are equated along with the operative and economical parameter with hydropower system parameter, and wind parameter with cost-effective approach is presented.

Keywords Wind–hydro hybrid · Homer · Cost optimization · Renewable energy resources · Power management

1 Introduction

Since Distribution generation (DG) very popular now in these days with this types of DG provide improve reliability of power and integrated resources. Distributed generation is the small-scale generation. Distributed generation term involves combination of small hydro, small gas, small solar and diesel, and small fuel sources of power generation [1]. Distribution generation is AC and DC types. AC generation is easily connected to existing AC power system, while DC microgrid

G. Thakur (✉) · K. K. Sharma · I. Kaur
Department of Electrical Engineering, Chandigarh University, Mohali, India
e-mail: gopalthakurmanali@gmail.com

K. K. Sharma
e-mail: sharmakamal2002@gmail.com

I. Kaur
e-mail: inder_preet74@yahoo.com

B. Singh
Department of Electrical Engineering, PEC University of Technology,
Chandigarh, India
e-mail: balwindersingh658@yahoo.com

has the ability to connect load very easily because the nature of the load is similar to DC microgrid [2]. Wind energy has been noted as the most clean, cost-effective, ecofriendly source of energy, among all other sources of energy. Non-conventional demand increases day by day due to increasing price of fossil fuel [3]. Non-conventional source is natural resources of energy, e.g., wind, hydro, geothermal, solar [4]. Optimization of hybrid energy system is cost-effective and reliable [5]. In this paper, hybrid energy system is used to make system cost-effective. Economic operation is done by (HOMER) software (hybrid optimization renewable energy resources) [6]. With the advancement of technology, renewable energy cost is very less as compared to capital cost of hydro plant which is very high [7]. To make a system ecofriendly, a wind turbine system is therefore added to conventional stand-alone system [8]. The issue related to hybrid system fault occurs on the system so we increase or decrease the value of circuit breaker, when network is in islanding mode or out of synchronism [9–11]. Overcurrent relay (OC) is used for major protection in distribution generation system. OC resolves all faults in the system [8].

The main objective of this paper to make an analysis of hybrid power system consisting of wind and hydro system to meet the load demand and compare with hydropower system to make a system cost-effective. In order to meet objective, economical parameter of hybrid system with the (HOMER) software (hybrid optimization renewable energy resource) is equated.

2 Wind and Hydro System Modeling

Wind and hydro hybrid system is used to make system efficient and reliable. In this paper, we analyze cost of hybrid system before we analyze cost we know about data of wind speed, water flow, and load demand [7, 12].

2.1 Wind Speed Data

Wind source data are taken from NASA for Jabalpur India (longitude $79^{\circ}59'$ and latitude $23^{\circ}10'$). The average wind speed is 4.001 m/s. Also, we find out the initial cost, operating cost, NPC (net present cost), O&M (\$/year) with the help of HOMER software.

2.2 Mini- and Microhydro Plant Data

Hydro sources data are taken from Bharmour, Himachal Pradesh, India (latitude $32^{\circ}36'$ and longitude $76^{\circ}32'$); the average water flow rate is 27.32 cumecs.

Figure shows monthly average water flow rate l/s. Also, we find out the initial cost, operating cost, and NPC which are shown in tabular or graphical forms [7, 12].

2.3 Load/Demand Data

Electrical load consists of more than one apparatus which perish more electrical power. Load demand contain from NASA; Jabalpur India and residential block of Chamba district. Daily load consumption 675 kw/day and perish by consumer and where peak load is found 1500 k/w. Load perished by consumer is shown in Fig. 4 [13, 14].

2.4 Battery Storage Data

Distributed generation consisting of wind and hydro equivalent have changeable nature as input are not keep up continuous power supply. In order to maintain continuous supply, we are using battery storage devices. Battery storage are used smoothness or if load is not matching in wind and hydro system equipment maintenance. The cost of grid takes account of battery. In hybrid system, battery is 6 V, 360, and 12 V D.C bus.

2.5 Hybrid System Modeling

See Figs. 1, 2, 3, 4, 5 and Tables 1, 2.

3 Methodology

The proposed hybrid non-conventional energy system consists of wind and hydro hybrid system, cost analysis, and economic analysis; we are using homer software hybrid optimization renewable energy resources.

HOMER software is very useful for designing off-grid and connected grid of renewable energy system in countless application of renewable energy system. It is also used for cost analysis of hybrid energy system, and design of equipment analyzes cost of hybrid power (wind, hydro) system to meet the load demand and compare with hydropower system, can equate economical parameter of hybrid system with the help of (HOMER) software (Hybrid Optimization renewable energy resource. For designing any electrical power system, we need know about specification of apparatus and structure of system to be analyzed like (element, component). Availability of renewable energy sources, cost of each obtainable technology [7, 14, 15].

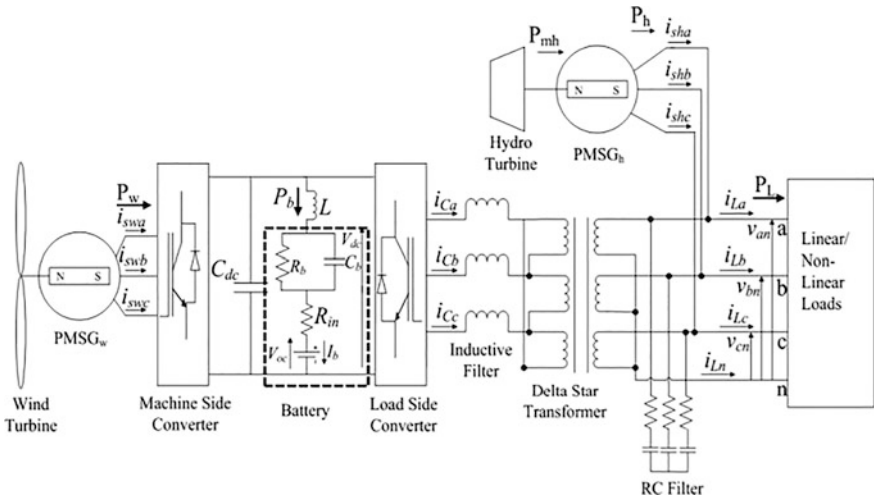


Fig. 1 Schematic diagram of wind and hydro system

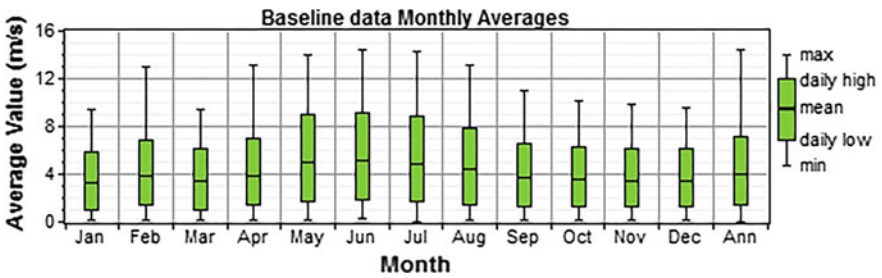


Fig. 2 Baseline data monthly averages

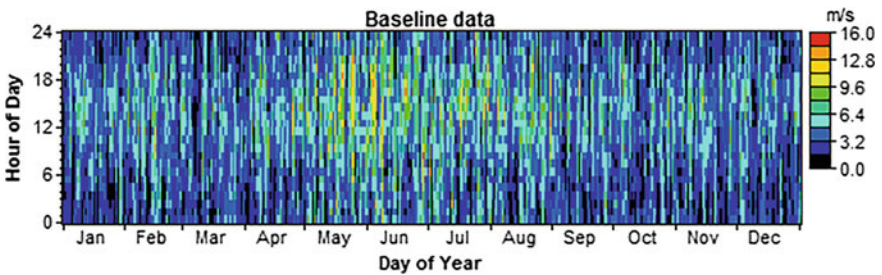


Fig. 3 Wind speed probability distribution, average wind speed, average data hour of day

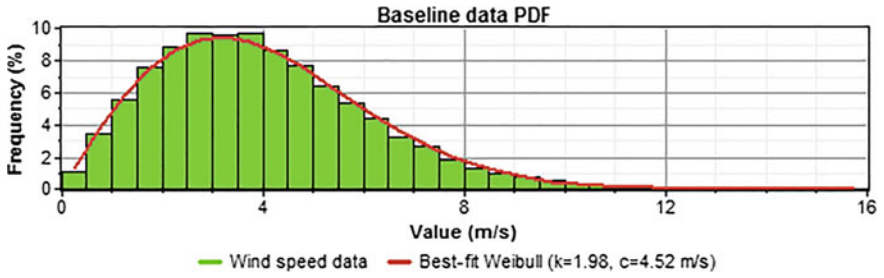


Fig. 4 Baseline data in maximum ranges

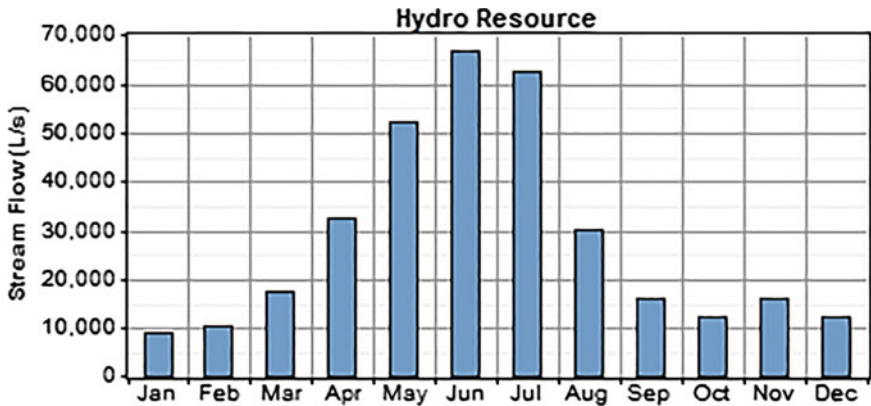


Fig. 5 Average speed of water stream flow l/s

Table 1 Monthly average wind speed [5]

Month	Wind speed (m/s)
January	3.350
February	3.890
March	3.395
April	3.885
May	4.956
June	5.176
July	4.796
August	4.376
September	3.666
October	3.600
November	3.600
December	3.420
Average	4.001

Table 2 Monthly average hydro stream flow [5, 13]

Month	Water flow (l/s)
January	8850
February	10,040
March	10,983
April	17,130
May	32,400
June	52,143
July	66,590
August	62,277
September	30,087
October	15,903
November	12,090
December	9433
Average	27,323

3.1 Simulation

Simulation of wind and hydro hybrid system is conducted with the help of homer equipment elected by end user. Homer will calculate energy that depends upon configuration of component and size of equipment or specification of design apparatus [4]. In this paper, we study about hydro and wind turbine with convertor or battery component analysis. So we can make system reliable, feasible, or accurate. So we can serve good load demand. HOMER will find out the initial cost, replacement cost, NPC (net present cost) of the hybrid system.

3.2 Optimization

Optimization process is used after simulation result. Optimization is used to find out the net present cost values compared from lower to higher (TNPC). We can compare TNPC from lower to higher values. We can find these results with variable sensitivity result that is used by designer.

4 Simulation and Results

Wind turbine is 65 Kw having a following speed with power characteristics as shown (Figs. 6, 7, 8, 9 and 10).

Simulation and optimization of hybrid energy sources are conducted. Homer will calculate energy and find total net present cost of hybrid system with the help of portable graph or tabular form of the system (Fig. 11).

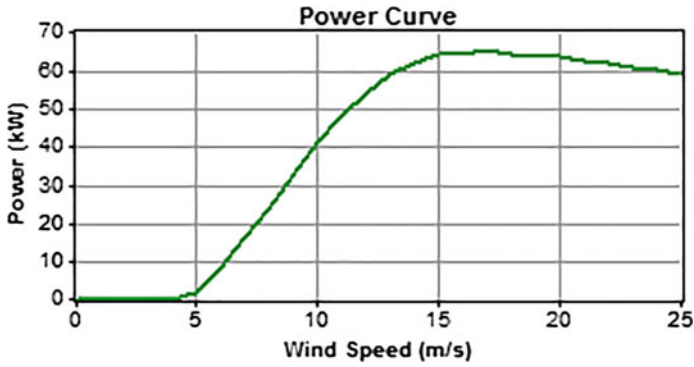


Fig. 6 Power versus speed curve

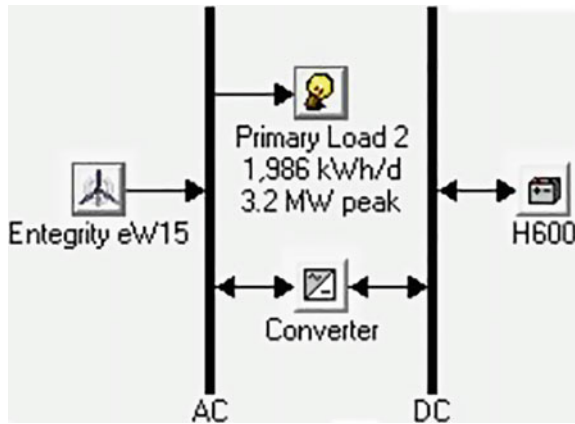


Fig. 7 Wind energy stand-alone system

Sensitivity variables

Wind Speed (m/s) 4

Double click on a system below for simulation results.

	eW15	H600	Conv. (kW)	Initial Capital	Operating Cost (\$/yr)	Total NPC	COE (\$/kWh)	Ren. Frac.	Capacity Shortage
	3	1	30	\$ 83,450	569,615,936	\$ 6,638,150...	2457...	1.00	1.00

Fig. 8 Sensitivity parameter of wind turbine

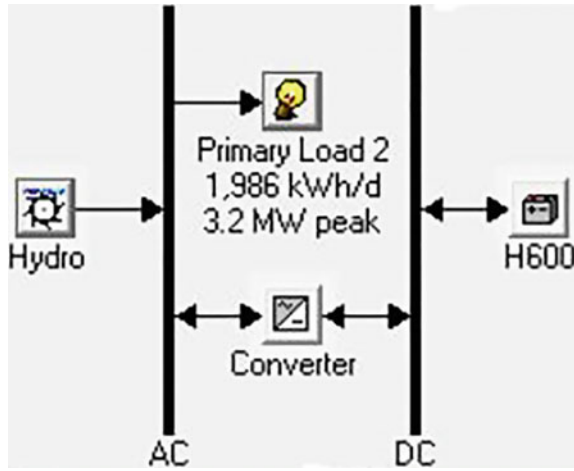


Fig. 9 Stand-alone hydro system

Double click on a system below for optimization results.

Stream Flow (L/s)			Hydro (kW)	H600	Conv. (kW)	Initial Capital	Operating Cost (\$/yr)	Total NPC	COE (\$/kWh)	Ren. Frac.	Capacity Shortage
28086.0			6402	1	30	\$ 323,450	1,874,675	\$ 22,170,132	2.624	1.00	0.26
20000.0			6402	1	30	\$ 323,450	1,874,675	\$ 22,170,132	2.624	1.00	0.26
21000.0			6402	1	30	\$ 323,450	1,874,675	\$ 22,170,132	2.624	1.00	0.26
22000.0			6402	1	30	\$ 323,450	1,874,675	\$ 22,170,132	2.624	1.00	0.26
23000.0			6402	1	30	\$ 323,450	1,874,675	\$ 22,170,132	2.624	1.00	0.26
24000.0			6402	1	30	\$ 323,450	1,874,675	\$ 22,170,132	2.624	1.00	0.26
25000.0			6402	1	30	\$ 323,450	1,874,675	\$ 22,170,132	2.624	1.00	0.26
30000.0			6402	1	30	\$ 323,450	1,874,675	\$ 22,170,132	2.624	1.00	0.26

Fig. 10 Sensitivity result of hydro energy resources

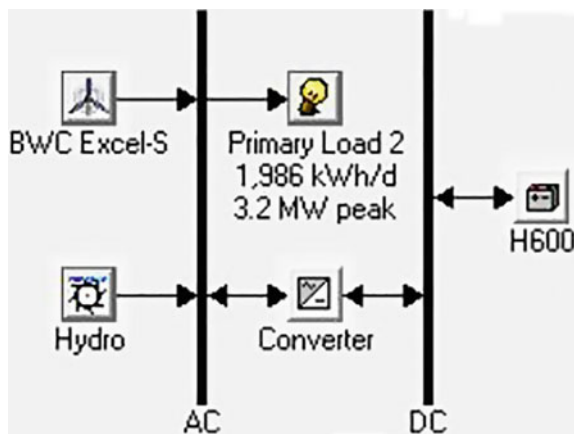


Fig. 11 Wind and hydro hybrid system

5 Optimization Results

See Figs. 12, 13, and 14.

Sensitivity Results		Optimization Results									
Sensitivity variables											
Wind Speed (m/s)		12		Stream Flow (L/s)		30,000					
Double click on a system below for simulation results.											
System	XLS	Hydro (kW)	H600	Conv. (kW)	Initial Capital	Operating Cost (\$/yr)	Total NPC	COE (\$/kWh)	Ren. Frac.	Capacity Shortage	
System 1	<input checked="" type="checkbox"/>	3	6402	1	30	\$ 383,450	1,857,241	\$ 22,026,964	2.607	1.00	0.26
System 2	<input checked="" type="checkbox"/>		6402	1	30	\$ 323,450	1,874,675	\$ 22,170,132	2.624	1.00	0.26

Fig. 12 Hybrid simulation results

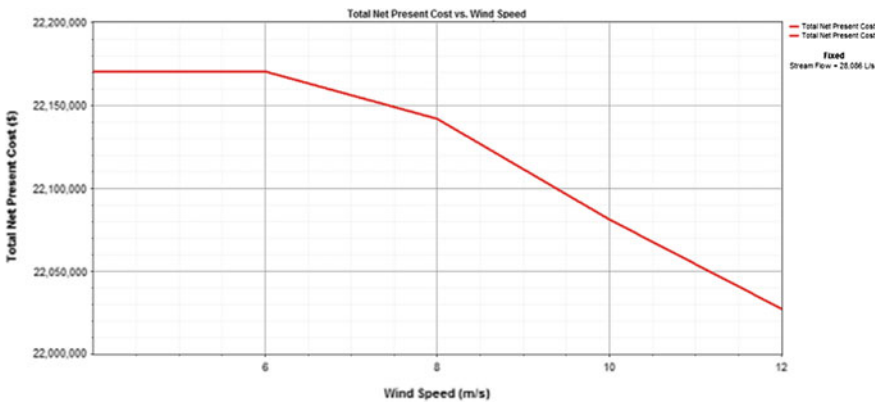


Fig. 13 NPC of wind turbine

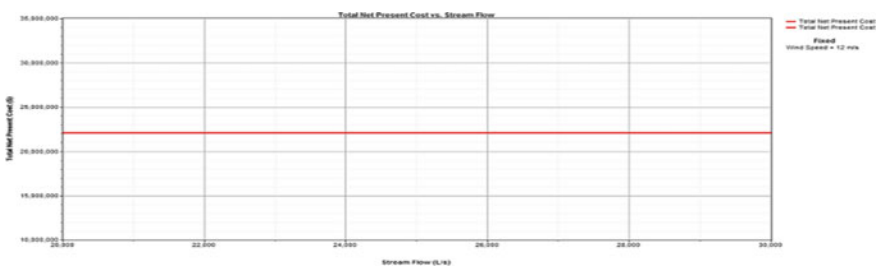


Fig. 14 NPC of hydro system

6 Conclusion

By this analysis, it is proved that hydro is more efficient and reliable than wind because cost of hydro is more than that of wind. Hydro net present cost is 22,170\$, and wind net present cost is 22,000\$; hydro is more stable or economical than wind so we prefer hydro because it is more reliable and efficient than wind.

References

1. Puneet K. Goel, Bhim Singh, and Navin Kishore, S. S. Murthy, “ Isolated Wind–Hydro Hybrid System Using Cage Generators and Battery Storage, IEEE transactions on industrial electronics, vol. 58, no. 4, APRIL 2011.
2. R. Uhumwangho, Ph.D. and E.K. Okedu, “Small Hydropower for Sustainable Development” The Pacific Journal of Science and Technology, Vol 10, no 2, November 2009.
3. Barsoum, N.N., Yong, H.H., Chang, H.M.A. and Goh, W.C. Modeling and Cost Effective Simulation of Stand-Alone Solar and Micro-Hydro Energy. Proceeding of PSACO 2008 Conference, Vishakhapatnam, 13–15 March, 809–814.
4. L. Deepak, B. Bhushan and A. K. Akella (2011, Sep.). Optimization of PV/Wind/ Micro-hydro/Diesel hybrid power system in HOMER for the study area. Int. Jour. on Elect. Eng. and Informatics (IJEEI’11), vol. 3, no. 3, pp. 307–325.
5. Negi, Swati, and Lini Mathew. “Optimization and Comparative analysis of non-renewable and renewable system.” International Journal of Advances in Engineering & Technology, vol. 7, no. 3 (2014).
6. Lambert, Tom, Paul Gilman, and Peter Lilienthal. “Micropower system modeling with HOMER.” Integration of PV Wind-Diesel-Battery Microgrid”, IEEE Powertech, Eindhoven, pp. 1–6, 2015. alternative sources of energy 1.15 (2006): 379–418.
7. P. C. Loh, D. Li, Y. K. Chai, and F. Blaabjerg, “Autonomous operation of AC-DC Microgrid with minimized interlinking energy flow,” IET Power Electron., vol. 6, no. 8, pp. 1650–1657, 2013.
8. C. So and K. Li, “Overcurrent relay coordination by evolutionary programming,” Electric Power Systems Research, vol. 53, pp. 83–90, 2000.23] Y.S. Foo Eddy, H.B. Gooi, S.X. Chen, “Multi-Agent System for Distributed Management of Microgrids,” IEEE Transactions on Power System, Vol. 30, no. 1, pp. 24–34, 2014.
9. C. Wang, M. H. Nehrir, “Power Management of a Stand-alone Wind/Photovoltaic/Fuel Cell Energy System,” Energy Conversion, IEEE Transactions on, Vol. 23, pp. 957–967.
10. Kamal Kant Sharma, Kruti Gupta “Stability Analysis of Hybrid Power Systems with BESS” International Journal of Control Theory and Applications, vol. 9, issue 14, pp. 6519–6529, 2016.
11. Kamal Kant Sharma, Samia, Balwinder Singh, Inderpreet Kaur, Samia “Power System Stability for the Islanding Operation of Micro Grids” Indian Journal of Science and Technology vol. 9, issue 38, pp. 1–5, 2016.
12. S. M. Islam, M. T. Iqbal, and J. E. Quaicoe, “Voltage Fluctuations in a Remote Wind-Diesel Hybrid Power System”, ICECE 2008, International Conference on Electrical and Computer Engineering, pp. 699–705, 2008.
13. K. Kauhaniemi and L. Kumpulainen, “Impact of distributed generation on the protection of distribution networks,” in Eighth IEEE International Conference on Developments in Power System Protection, pp. 315–318, Vol. 1, 2004.

14. A. Fazanehrafat, S. A. M. Javadian, S. M. T. Bathaee, and M. R. Haghifam, "Maintaining The Recloser-Fuse Coordination in Distribution Systems in Presence of DG by Determining DG's Size," in IET 9th International Conference on Developments in Power System Protection, (DPSP) pp. 132–137, 2008.
15. J. M. Guerrero, P. C. Loh, T.-L. Lee, and M. Chandorkar, "Advanced control architecture for intelligent Microgrid – part II: power quality, energy storage, and AC/DC Microgrid," IEEE Trans. Ind. Eletron., vol. 60, no. 4, pp. 1263–1270.

Stability Investigation for a 100 kW Solar Photovoltaic Grid-Connected System Using D-STATCOM Control

Akhil Gupta and Kapil Verma

Abstract This paper investigates the study of stability for a 100 kW solar photovoltaic (SPV) grid-connected system using distributed static compensator (D-STATCOM) control. The proposed D-STATCOM control works as compensating reactive power source, which decreases the voltage variation on the distribution side of the proposed system. In addition, an isolated DC–DC converter has been implemented in conjunction with three-phase DC–AC voltage source converter (VSC) in double-stage grid-connected system operating at unity power factor. Especially, an integral regulator (IR) type of incremental conductance (IC)–maximum power point tracking (MPPT) technique has been applied, which controls the output voltage of SPV array and derives the maximum power from SPV array under changing atmospheric circumstances. Furthermore, the proposed MPPT technique has been proven highly converging in tracking of maximum power and keeps a steady DC link supply by altering the index of the converter. For the duration of the faulted conditions at grid side, the resulting balanced waveforms at point of common coupling (PCC) have been obtained. Additionally, harmonic study carried demonstrates the role of D-STATCOM in the reduction of harmonics and DC offset at utility side providing a stable steady state and transient response. In order to authorize the proposed system, the MATLAB simulations have been performed to show the usefulness of D-STATCOM control in proposed double-stage SPV grid-connected system.

Keywords Solar photovoltaic • Control, stable • Power • D-STATCOM
Maximum power point tracking

A. Gupta (✉) · K. Verma
Electrical Engineering Department-UIE, Chandigarh University,
Mohali, Punjab, India
e-mail: akhilgupta1977@gmail.com

K. Verma
e-mail: kapilverma.eee1@gmail.com

1 Introduction

In India, the increasing demand of renewable energy production through solar photovoltaic (SPV) plants operating in distribution generation (DG) is causing serious stability and power quality problems such as flow of transients, voltage imbalance, and fluctuations. In order to address these problems, a model for SPV grid-connected system is developed in which distributed static compensator (D-STATCOM) control is build to investigate stability of the system. The maximum power point tracking (MPPT) device has been linked to capitalize the usefulness of a SPV cell, which shows dynamic performance of a SPV generator [1]. The simulation of elevated performance-type power conditioning system (PCS) of grid-connected SPV system with their control schemes in DG systems is illustrated in [2]. Here, the proposed PCS system employs a two-stage power alteration topology composed of a three-level voltage source converter (VSC) and DC–DC converter. A three-level control scheme has been considered to contain a full decoupled current control policy, which is independently exchanging reactive powers as well as active power with the distribution system [3]. The proposed designed system is beneficial for power electronics based designers, which requires an accurate, fast, simple, and easy to use modeling scheme for using in Simulink of SPV systems [4]. The SPV generator is an electrical device that changes the power that comes from the sun into electrical energy. A set of connected SPV cells forms a SPV panel, which is normally connected in series to get large output energy. The energy obtained at the output of generator can be increased by increasing the surface area of a SPV cell [5]. It has been reported in [6–8] that the mitigation of voltage swell and sag can be done by using DVR controller. It has provided an effective solution by setting up the appropriate voltage quality level. To make input voltage of DC–DC converters a stable waveform, the SPV applications are frequently required with sophisticated controlling techniques. In this case, conventional converters, the V_{in} is controlled and V_{out} is constant [9]. To defend sensitive loads from disturbances in voltage of the DG system, dynamic voltage restorer (DVR) is linked [10]. The VSC works on a reactive power production mode in the lack of active power on input side, the powers which maintain a DC voltage. MPPT schemes control power superiority at a peak point due to sinking of total harmonic distortion (THD) as per IEEE-519/1547 [11–13]. The MPPT algorithm is based on single-phase arrangements in which the power oscillation is instantaneous at twice the line frequency. These oscillations also cause a ripple on the DC power and DC voltage of the SPV array. MPPT algorithm controls V_{out} of SPV array during quickly changing climate conditions [14–16].

This paper analyzes and addresses the steady-state and transient-state stability using a D-STATCOM control for 100 kW SPV grid-connected system during abnormal conditions. In order to reduce voltage variations under both the conditions, the control scheme of VSC generates a controlled modulating signal for insulated gate bipolar transistor (IGBT)-based VSC. An integral regulator (IR) with incremental conductance (IC)–MPPT technique has been implemented which can

control the oscillations at MPP and derives maximum power from SPV array. The performance of this scheme has been found to be satisfactory as compared to conventional MPPT techniques. The role of D-STATCOM is highlighted in maintaining stable waveforms during the faulted period and the simulation study. D-STATCOM has been able to mitigate transients occurring during periods of high-frequency switching of IGBT-based VSC. Additionally, reactive power compensation is shown by controlling the voltage at busbar at grid side and VSC. Especially, the results obtained in harmonics and DC offset clearly prove that the proposed system has been able to supply a stable electric power through SPV grid-connected system in accordance with the IEEE-1547 standard.

2 SPV Grid-Connected System MPPT Control

The block figure of SPV grid interfacing structure is shown in Fig. 1 having interconnected reactor capacitor and IGBT-based VSC as an LCL-filter. The proposed model has been developed as double-stage grid interfacing system. The control side of DC–DC converter boosts the DC supply, which is produced from SPV array. The output of DC–DC converter has been fed to three-phase IGBT inverter for AC inversion. The regulated output voltage from VSC control and MPPT controller is used to provide continuous supply to the hybrid loads. MPPT control has been introduced to provide the maximum output energy from SPV array during the sunshine hours.

Figure 5 represents the Simulink diagram of the proposed system, which consists of 100 kW SPV cells arrangement connected in parallel and series to generate maximum energy from sun radiations. The output current and voltage of SPV system depends upon changing solar radiation and ambient temperature levels. A MPPT controller is used to optimize the performance and effectiveness of the SPV power alteration from solar light.

To determine the characteristics of the SPV unit, the P - V and I - V curves have been derived at three parameters, namely MPP (V_{mp} , I_{mp}), short circuit current (I_{sc}),

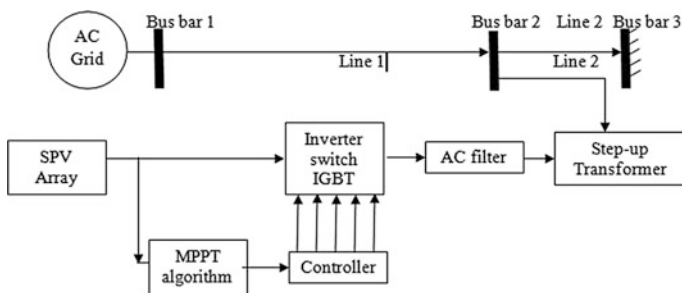


Fig. 1 Block figure of SPV grid interfacing structure

and open circuit voltage (V_{oc}). The I - V and P - V characteristics curves of a SPV array are nonlinear due to availability of solar energy because the SPV array sends energy directly to the converter. In order to validate the performance of SPV system, manufacturer data sheets have been used at maximum power points. There is an exclusive MPP on the P - V curve, where the SPV unit generates the highest energy. This point is acknowledged as the MPP (V_{mpp} , I_{mpp}). The value of maximum powers depends on the environmental factors, such as ambient temperature and changing solar radiation levels. The condition for highest energy arises at knee of the P - V characteristic curvature. The variations in irradiance have a good impact on the I_{sc} and resulted power of the unit but slight impact on the V_{oc} . Fig. 2 depicts the I - V and P - V characteristics arcs which have been attained at different solar radiation stages and a constant temperature ($25\text{ }^{\circ}\text{C}$) condition. Figure 3 depicts the P - V and I - V characteristics curves at ambient temperature and a constant solar radiance. It is evident that there is a strong impact of change in V_{oc} and output energy of a SPV cell, but slight impact on the I_{sc} .

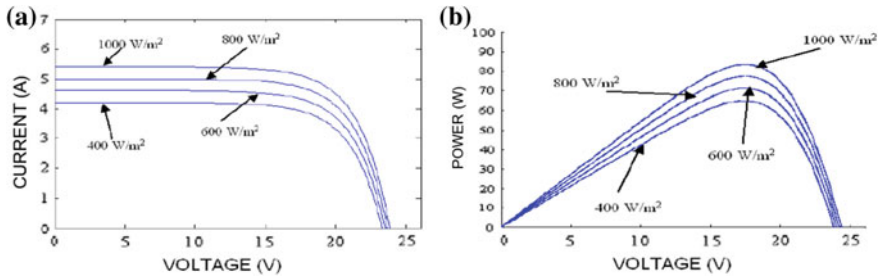


Fig. 2 P - V and I - V characteristics of a SPV arrangement in a constant temperature and varying solar power

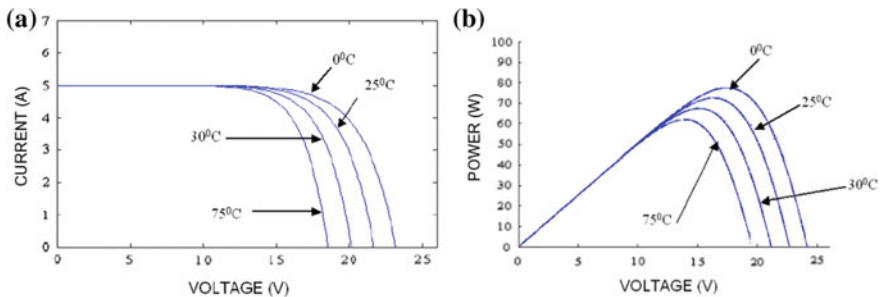


Fig. 3 P - V and I - V characteristics of a SPV unit in fixed solar radiation and varying temperatures level

2.1 Modeling of a SPV Array

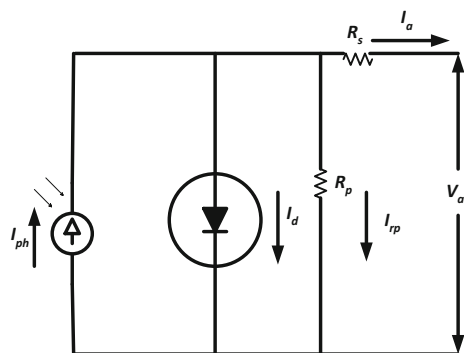
SPV cell’s equivalent basic circuit is shown in Fig. 4 which collects light from the sun and generates the output current flowing in the load circuit. Diode is presenting $p-n$ junction’s nonlinear impedance with R_p and R_s . The series resistance R_s accounts the resistance through semiconductor objects, current collecting bus, contact, and metal grid. The individual value of R_s is multiplied by the number of cells connected in series. The shunt resistance R_p is a loss coupled with a minor leakage current by a parallel resistive path to the apparatus.

In this paper, D-STATCOM device has been used with a 100 kW SPV grid-connected systems to investigate stability of the system. In DG schemes, all available electric energy is distributed to the network. The point, where SPV array delivers the maximum power is called MPP, which is obtained by MPPT control. MPPT method efficiently generates SPV power even under changing climate conditions. With function of fault on network side, the proposed MPPT method with D-STATCOM manage gives alteration less active power from SPV array, with tiny fluctuations during the presence of faults.

2.2 Basic MPPT Technique

To effectively generate the pure energy by a SPV array, the modified form of IC-based MPPT technique has been implemented in this study. This technique is based on DC–DC converter that optimizes the combination between SPV array, utility grid, and load connected. The most modern MPPT’ controller gives up to 99% efficiency in the conversion. The IC method, the open circuit voltage scheme, the perturbation and observation (P&O) technique, and ripple-based methods are the common MPPT techniques. A better MPPT technique should construct a well-organized and efficient system at a cheap price because SPV systems will have to be bulk produced. By combination of IR and IC–MPPT method, the array

Fig. 4 Electric equivalent circuit of a practical SPV cell



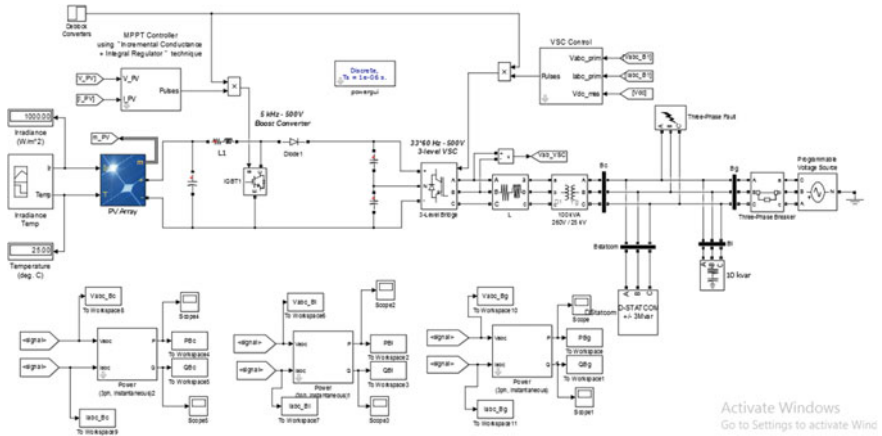


Fig. 5 MATLAB/Simulink model for SPV grid-connected system with D-STATCOM control

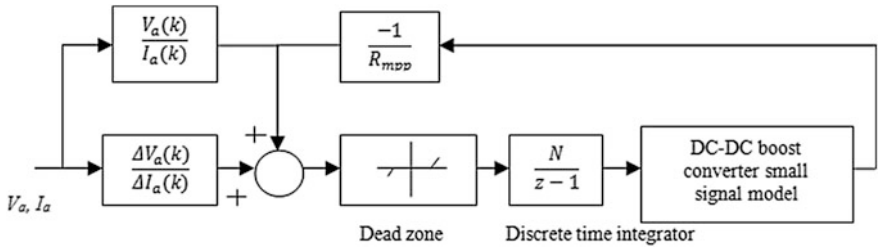


Fig. 6 Schematic diagram of a SPV system with modified incremental conductance MPPT control

terminal voltage is constantly attuned due to the MPP voltage. It depends upon the instant conductance of the SPV element (Fig. 5).

As depicted in Fig. 6, incremental conductance MPPT technique has been modified by discrete integral or accumulation regulator technique (with forward Euler integration method) of unity gain which minimizes error between both sides of equation resulting Eq. (1) from Eq. (2). The scaling factor N is chosen as ($N = 7$) which makes sure superior steady state and dynamic work. The scaling factor regulates the incoming signal to a magnitude prior to appraise the subsequent step dimension. A changeable step dimension MPPT is implemented to the trade-off in the steady state and dynamics oscillations at MPP. Based on various literature surveys, traditional incremental conductance MPPT technique is introduced briefly here. The principle of IC algorithm flowchart is given by differentiating SPV array power P_a (W) with respect to its voltage V_a (V) and equating output equal to 0 as per Eq. (1)

$$\frac{dP_a}{dV_a} = \frac{dV_a I_a}{dV_a} = I_a + V_a \frac{dI_a}{dV_a} = 0 \quad (\text{at MPP}) \tag{1}$$

Rearranging the above equation gives

$$\frac{-I_a}{V_a} = \frac{dI_a}{dV_a} \tag{2}$$

Hence one side, Eq. (2) shows the reverse of SPV immediate supply, while other side represents its IC, where (A) is solar PV array current. Both measurements must be equivalent in magnitude but reverse in symbol at MPP.

3 Computational Scheme for D-STATCOM Control

Out of all custom power devices, D-STATCOM is a quick compensating reactive power device, which can be connected on distribution side of any system to decrease current variations such as surges, sags, flicker, and fluctuations caused by quickly varying reactive power requirement. In the present work, D-STATCOM control has been designed as a VSC linked with the power network through PCC. The phase angle of the VSC voltage has been proscribed for synchronization with utility grid at PCC, so that the reactive power and real power flow can take place. The MATLAB/Simulink electric circuit of D-STATCOM has been depicted in Fig. 7 together with capacitor, filter, and converter. The filter consists of an inductance L_s and resistance R_s , whereas the voltage across the capacitor is variable in nature due to varying nature of solar radiation levels. The reference value of DC link voltage has been maintained constant at 500 V.

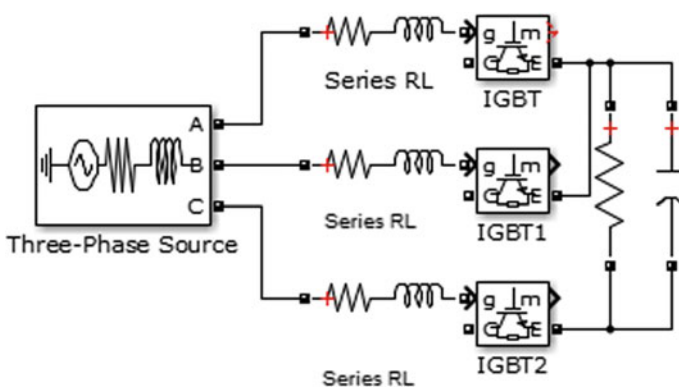
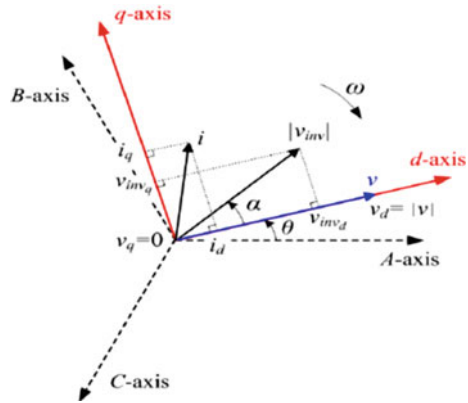


Fig. 7 Basic MATLAB/Simulink electric circuit for D-STATCOM

Fig. 8 Space phasor diagram of D-STATCOM in d - q form [5]



According to Park’s transformation, the d - q transformation technique has been performed for the analysis of D-STATCOM control. Figure 8 depicts the phasor diagram for d - q transformation in clockwise direction

where $\theta = \omega t$, and it is the revolving phase angle of E . The E is represented by Eq. (3) as

$$E \begin{bmatrix} E_a \\ E_b \\ E_c \end{bmatrix} = E \begin{bmatrix} \sin \theta \\ \sin \left(\theta - \frac{2\pi}{3} \right) \\ \sin \left(\theta + \frac{2\pi}{3} \right) \end{bmatrix} \tag{3}$$

The park transformation equations depend upon d - q -axis, where q -axis is in quadrature and d -axis is associated with the E vector at common coupling point with it. By altering the system to this frame, the equation can be given as:

$$\begin{bmatrix} E_d \\ E_q \\ 0 \end{bmatrix} = K_\theta \begin{bmatrix} E_a \\ E_b \\ E_c \end{bmatrix} \tag{4}$$

$$K_\theta = \frac{2}{3} \begin{bmatrix} \sin \theta & \sin \left(\theta - \frac{2\pi}{3} \right) & \sin \left(\theta + \frac{2\pi}{3} \right) \\ \cos \theta & \cos \left(\theta - \frac{2\pi}{3} \right) & \cos \left(\theta + \frac{2\pi}{3} \right) \\ \frac{1}{\sqrt{2}} & \frac{1}{\sqrt{2}} & \frac{1}{\sqrt{2}} \end{bmatrix} \tag{5}$$

By replacing Eq. (5) in Eq. (4), the q -axis and d -axis component of voltage will be as:

$$\begin{bmatrix} E_d \\ E_q \end{bmatrix} = \sqrt{\frac{2}{3}} \begin{bmatrix} \cos \theta & \cos \left(\theta - \frac{2\pi}{3} \right) & \cos \left(\theta + \frac{2\pi}{3} \right) \\ -\sin \theta & \sin \left(\theta - \frac{2\pi}{3} \right) & \sin \left(\theta + \frac{2\pi}{3} \right) \end{bmatrix} \begin{bmatrix} E_a \\ E_b \\ E_c \end{bmatrix} \tag{6}$$

By applying KVL in the circuit of Fig. 7, the D-STATCOM is written as:

$$\begin{bmatrix} E_d \\ E_q \end{bmatrix} = R_s \begin{bmatrix} i_d \\ i_q \end{bmatrix} + L_s \frac{d}{dt} \begin{bmatrix} i_d \\ i_q \end{bmatrix} + \omega_s L_s \begin{bmatrix} i_d \\ i_q \end{bmatrix} + \begin{bmatrix} V_d \\ V_q \end{bmatrix} \tag{7}$$

The derivative division can be detached in steady-state order, so the d -axis and q -axis equation can be written as:

$$\vec{E}_{dq} = R_s \vec{I}_{dq} + J \omega_s L_s \vec{I}_{dq} + \vec{V}_{dq} \tag{8}$$

Therefore, the D-STATCOM has been alienated into I_q and I_d by using d - q transformation. Hence, the active power and reactive power organize loops are resulted in order to examine the behavior of D-STATCOM in system.

4 Results and Discussion

In this paper, the data sheets of SPV array identified by the manufacturer have been tested by its interfacing with double-stage converter system and a utility grid [17–22]. At the same time, the developed system has been integrated with D-STATCOM control in MATLAB/Simulink environment [23–25]. The chosen specifications for a SPV array and controllers implemented are given in Tables 1, 2 whereas Table 3 represents the total harmonic distortion analysis using IC–MPPT. The investigation carried focuses on steady-state and transient-state stability by introducing a single line to ground fault at load side. It is important to note that the impact of the fault has also been studied at VSC and load side during abnormal conditions. The study made in this paper has been presented and discussed under two case studies: case 1 includes the study for an uncompensated system, whereas case 2 highlights the impact of D-STATCOM control for proposed system. The complete study also highlights real and reactive power graphs which indicate the stability of three-phase grid-associated SPV system using D-STATCOM control. A line to ground fault with phase A is connected before load during the fault time period from $t = 4$ s to $t = 6$ s.

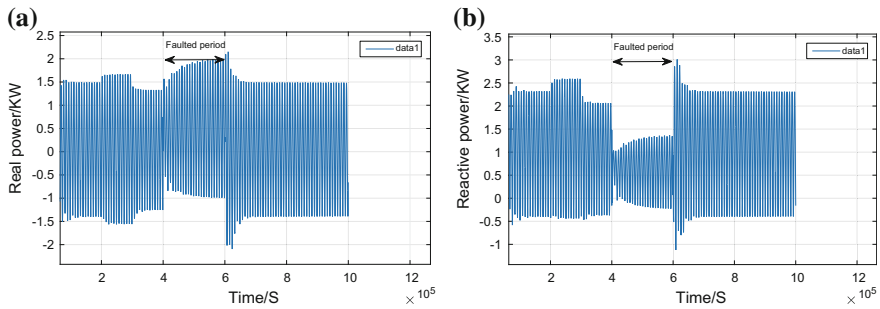
Case A: *Steady state and transient behavior during the presence of fault on SPV grid-connected system*

Table 1 Specifications taken for SPV array

System name with components and symbol	Values
DC nominal voltage	500 V
Nominal frequency and power	[50 Hz, 100 KW]
DC voltage regulator gains [K_i K_p]	[800, 7]
Current regulator gains [K_i K_p]	[20, 0.3]
Load [V_n P $-Q_c$]	[440 V, 10 kW, -10 kVAR]

Table 2 Specifications adopted for IGBT-based VSC control

System name	Rating values
Number of solar cells per module	96
Number of series-connected modules per string	5
Number of parallel strings	66
Module specifications under STC [V_{oc} , I_{sc} , V_{mp} , I_{mp}]	[64.2 V, 5.96 A, 54.7 V, 5.58 A]
Model parameters for one module [R_s , R_p , I_{sat} , I_{ph} , Q_d]	[0.038 Ω , 993.5 Ω , 1.1753e-008 A, 5.9602 A, 1.3]
Maximum power P_{mp}	$66 \times 5 \times 54.7 \times 5.58 = 100.7$ KW

**Fig. 9** Uncompensated **a** real power and **b** reactive power on grid side

Without D-STATCOM, simulation results are presented in case A in which single phase to ground fault is applied, via a fault resistance of 0.055 Ω and ground resistance of 0.001 Ω . Figure 9a, b depicts the Simulink results of real power and reactive power without D-STATCOM on grid side. A three-phase grid network has been developed for the present study. As shown, there has been unbalanced sinusoidal waveform of real power being generated by grid. However, as evident from Fig. 9b, the reactive power generated by grid has been reduced during the faulted period. Peak value of real and reactive power has been found to be 2.1 kW and 2.6 kVAR, respectively. A sharp transient in reactive power is also evident at $t = 6$ s which is controllable by varying the gain of voltage and current controllers. From Fig. 10b, it has been observed that real power is not being consumed, whereas the reactive power is not being generated. A small disturbance is also evident during the faulted period. Figure 11a, b depicts the real power- and reactive power-generated waveforms of SPV array through VSC converter system, respectively (Figs. 12, 13, and 14).

Case B: Steady state and transient behavior during the presence of fault during D-STATCOM control on SPV grid-connected system

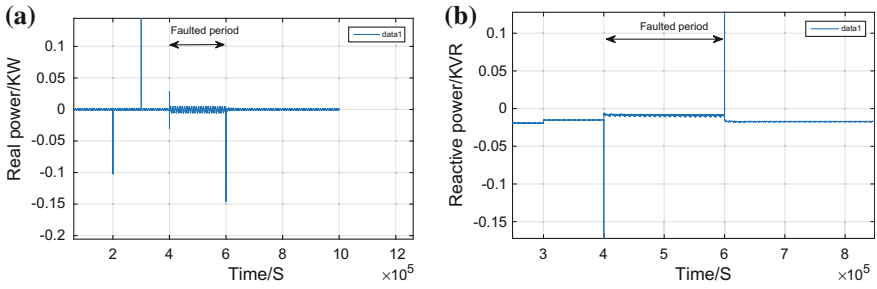


Fig. 10 Uncompensated **a** real power and **b** reactive power on load side

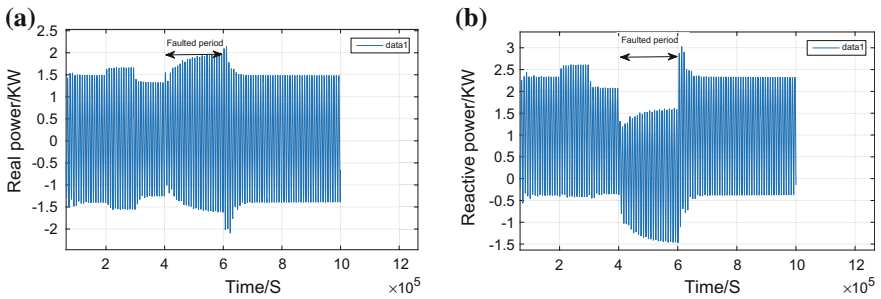


Fig. 11 Uncompensated **a** real power and **b** reactive power from VSC

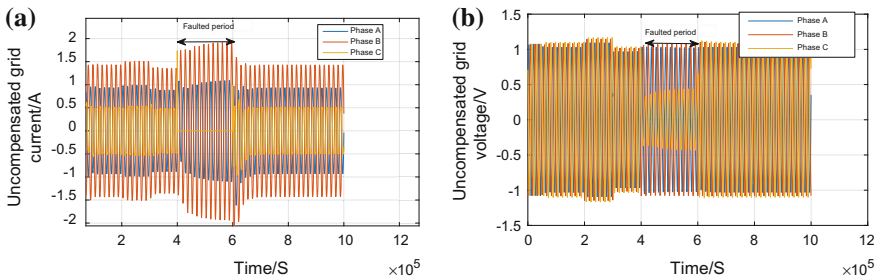


Fig. 12 Uncompensated **a** grid current and **b** grid voltage

In case B, simulation is conceded using the similar circumstances as above but now using D-STATCOM in system. Figures 15, 16, and 17 depict the Simulink results of real power and reactive power using D-STATCOM. Figs. 18, 19, 20 depict the voltage and current waveforms with D-STATCOM. A line to ground fault (on phase A) has been introduced on load side. The fault timing is $t = 4$ s to

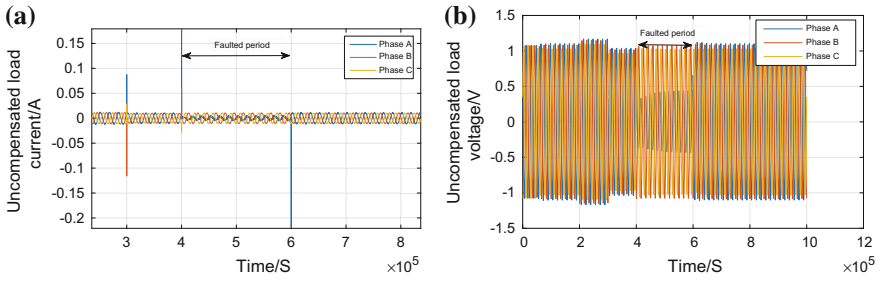


Fig. 13 Uncompensated a load current and b load voltage

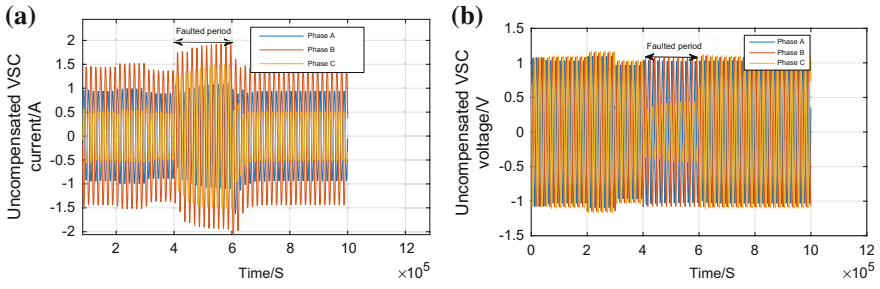


Fig. 14 Uncompensated a VSC current and b VSC voltage

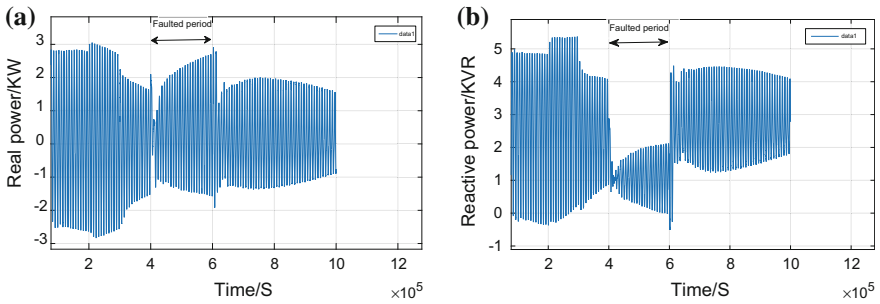


Fig. 15 Compensated a real power and b reactive power on grid side

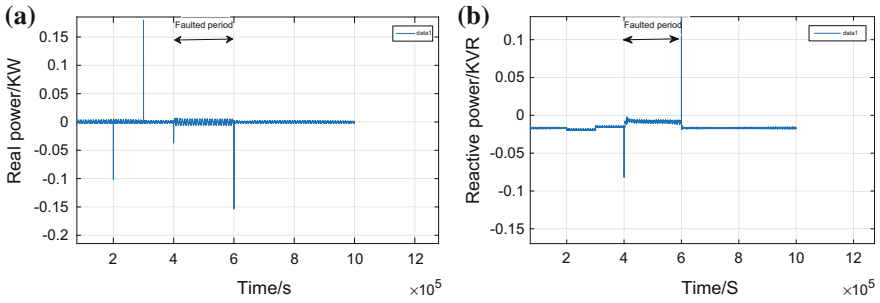


Fig. 16 Compensated **a** real power and **b** reactive power from load

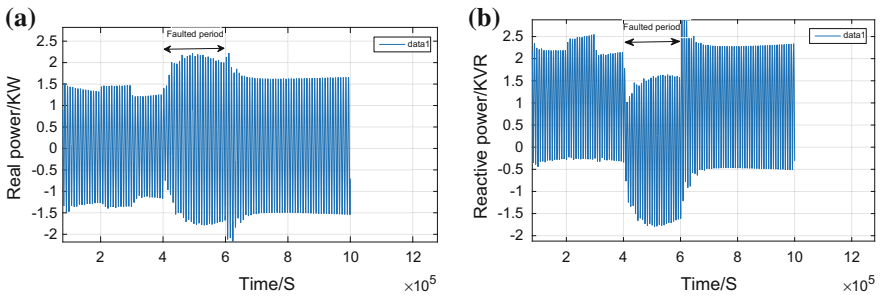


Fig. 17 Compensated **a** real power and **b** reactive power from VSC

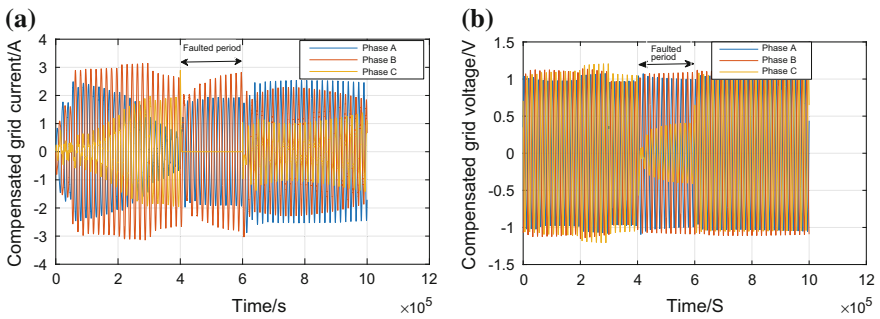


Fig. 18 Compensated **a** grid current and **b** grid voltage

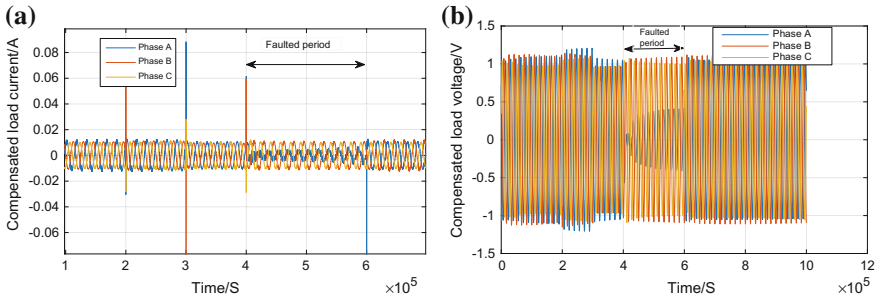


Fig. 19 Compensated **a** load current and **b** load voltage

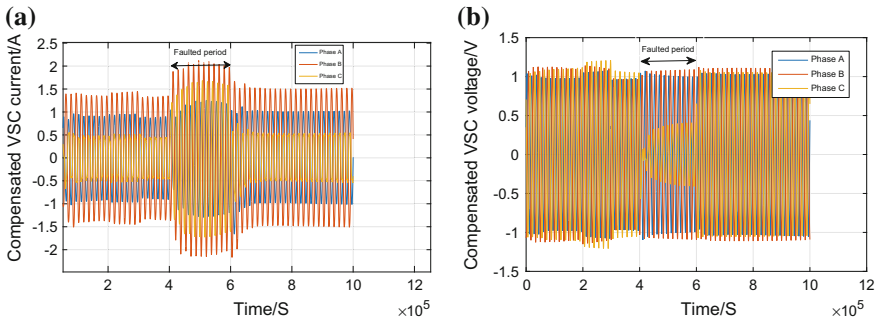


Fig. 20 Compensated **a** VSC current and **b** VSC voltage

Table 3 Total harmonic distortion analysis using IC-MPPT

Parameter	THD (%)	DC current component (A)
DC-AC converter voltage	6.60	2.3
DC-AC converter current	85.77	0.9547
linear load voltage	6.60	1.358
linear load current	0.93	0.654
Utility grid voltage	0.22	1.543
Utility grid current	28.94	0.5239

$t = 6$ s. During fault time, the results demonstrate unbalanced sag/swell in VSC, load, and grid. The real power is near to 0 to keep the DC bus voltage constant. It can also be recognized that the inserted reactive power to PCC is rising when the fault occurs. The D-STATCOM is inserting additional reactive current to the system, and the current is near to 0 under ordinary circumstances. Table 3 illustrates the analysis of THD and DC offset current.

5 Conclusion

This paper has investigated the stability of DG network by using D-STATCOM control in double-stage SPV grid-interfaced systems. The performance of the implemented schemes has been validated by demonstrating the stability achieved in steady state and transient state in the output waveforms. It has been verified that D-STATCOM control has been able to mitigate the unbalanced response during the faulted conditions at the grid side. In addition, the compensation is also achieved in voltage and current waveforms at PCC of load and IGBT-based VSC. Apart from this, the reactive power compensation required by load connected has been demonstrated. Harmonic and DC offset values have been derived using fast Fourier transform. Satisfactory level in the level of harmonics and DC offset has been obtained at PCC of load, grid, and IGBT-based VSC. The D-STATCOM has been established to be a useful way to recover the stability during the abnormal conditions, which may be useful in large power scale quantities of DG powers sources. It is clear that the projected system has proven its efficacy in faster convergence toward achieving the stable response output in steady state and transient behavior responses at all points of common couplings.

Acknowledgements The study stability has been completed by implementing D-STATCOM control on grid side for a SPV grid-interfaced system. Authors are keen to develop a prototype model for the proposed work in future with the inclusion of digital signal processing controlling techniques.

References

1. Tan Y. T., Kirschen D. S. and Jenkins N.: A model of PV generation suitable for stability analysis. *IEEE Transactions on Energy Conversion*, vol. 19, pp. 748–755, (2004).
2. Molina M. G. and Juanico L. E.: Dynamic Modeling and Control Design of Advanced Photovoltaic Solar System for Distributed Generation Applications. *Journal of Electrical Engineering: Theory and Application*, vol. 1, pp. 141–150, (2010).
3. Villalva M. G., Gazoli J. R. and Filho E. R.: Analysis and simulation of the P&O MPPT algorithm using a linearized PV array model. *Power Electronics Conference, COBEP '09, Brazilian*, vol. 1, pp. 189–195, (2009).
4. Villalva M. G., Gazoli J. R. and Filho E. R.: Comprehensive Approach to Modeling and Simulation of Photovoltaic Arrays. *IEEE Transactions on Power Electronics*, vol. 24, pp. 1198–1208, (2009).
5. Moghbe G. and Masoum M. A. S.: D-STATCOM Based on Hysteresis Current Control to Improve Voltage Profile of Distribution Systems with PV Solar Power. *Australasian Universities Power Engineering Conference (AUPEC2016)*, vol. 1, pp. 1–5, (2016).
6. Wasynczuk O.: Modeling and dynamic performance of a line-commutated photovoltaic inverter system. *IEEE Transactions on Energy Conversion*, vol. 4, pp. 337–343, (2002).
7. Wang L. and Lin Y. H.: Dynamic stability analysis of a photovoltaic array connected to a large utility grid. *IEEE PES Winter Meeting*, vol. 1, pp. 476–480, (2000).

8. Villalva M. G., De Siqueira T. G., Espindola M. F. and Ruppert E.: Modeling And Control Of A Three-Phase Isolated Grid-Connected Converter For Photovoltaic Applications,” *Revista Controle & Automação*, vol. 10, pp. 215–228, (2009).
9. Villalva M. G. and Filho E. R.: Dynamic analysis of the input controlled buck converter fed by a photovoltaic array. *Revista Controle automação*, vol. 19, pp. 463–475, (2008).
10. Gupta A., Chanana S. and Thakur T.: THD reduction with reactive power compensation for fuzzy logic DVR based SPV grid connected system. *Frontiers in Energy*, vol. 8, pp. 464–479, (2014).
11. Gupta A., Chanana S. and Thakur T.: Power quality improvement of solar photovoltaic transformer-less grid-connected system with maximum power point tracking control. *International Journal of Sustainable Energy*, vol. 33, pp. 921–936, (2014).
12. Gupta A., Chanana S. and Thakur T.: Grid connected photovoltaic system with data-based MPPT and fuzzy controlled DVR. *Power Electronics (ICPE), 2014 IEEE 6th India International Conference*, vol. 1, pp. 1–6, (2014).
13. Gupta A., Chanana S. and Thakur T.: Power quality assessment of a solar photovoltaic two-stage grid connected system: Using fuzzy and proportional integral controlled dynamic voltage restorer approach. *Journal of Renewable and Sustainable Energy*, vol. 7, pp. 013113 (7–18), (2015).
14. Calais M. and Hinz H.: A ripple-based maximum power point tracking algorithm for a single-phase grid connected photovoltaic system. *Solar Energy*, vol. 63, pp. 277–282, (1998).
15. Hussein K. H., Muta L., Hoshino T. and Osakada M.: Maximum photovoltaic power tracking: An algorithm for rapidly changing atmospheric conditions. *Proc. Inst. Elect. Eng. Gen., Transm. Distrib.*, vol. 142, pp. 59, (1995).
16. Enslin J. H. R., Wolf M. S., Snyman D. B. and Swiegers W.: Integrated photovoltaic maximum power point tracking converter. *IEEE Trans. Ind. Electron.*, vol. 44, pp. 769–773, (1997).
17. Kasa N., Iida T. and Majumdar G.: Robust control for maximum power point tracking in photovoltaic power system. *Proceedings of Power Conversion Conference*, vol. 1, pp. 827–832, (2002).
18. Femia N., Petrone G., Spagnuolo G. and Vitelli M.: Optimization of perturb and observe maximum power point tracking method. *IEEE Transactions on Power Electronics*, vol. 20, pp. 963–973, (2005).
19. Gow J. A. and Manning C. D.: Development of a photovoltaic array model for use in power-electronics simulation studies. *Proceedings of IEE Electronics Power Applications*, vol. 146, pp. 193–200, (1999).
20. Xiao W., Dunford W. G. and Capel A.: A novel modeling method for photovoltaic cells. *Proceedings of IEEE Power Electronics Specialists Conference*, vol. 3, pp. 1950–1956, (2004).
21. Matagne E., Chenni R. and Bachtiri R. E.: A photovoltaic cell model based on nominal data only. *Proceedings of International Conference on Power Engineering, Energy and Electrical Drives*, vol. 1, pp. 562–565, (2007).
22. Yu G. J., Jung Y. S., Choi J. Y., Choi I., Song J. H. and Kim G. S.: A novel two-mode MPPT control algorithm based on comparative study of existing algorithms. *Proceedings of IEEE Photovoltaic Specialists Conference*, vol. 1, pp. 1531–1534, (2002).
23. Liu S., Dougal R. A.: Dynamic multiphysics model for solar array. *IEEE Transactions on Energy Conversion*, vol. 17, pp. 285–294, (2002).
24. Esram T. and Chapman P. L.: Comparison of photovoltaic array maximum power point tracking techniques. *IEEE Transactions on Energy Conversion*, vol. 22, pp. 439–449, (2007).
25. Menniti D. and Pinnarelli.: “A novel compensation approach for dc current component in a grid-connected photovoltaic generation system,” In: *IEEE Proceedings of International Conference on Power and Energy Society General Meeting, San Diego, CA*, (2012).

Comparative Review on Microgrid Management System

Susheel Kumar and Inderpreet Kaur

Abstract Energy supply should be diverse and sustainable, and it needs to be utilized more effectively. It is necessary for promoting human's quality of life with the economic development of energy resources. Microgrid works with renewable energy sources such as biomass, solar, wind and waste-to-energy. The microgrid can be disconnected from the main supply itself and connected to the load in order to supply power to the load when power failures occur. The goal of this paper is to provide a review on microgrid management system using technologies and its applications. Paper also includes different techniques like optimal control technique, best power management using optimization technique and function of battery-based energy storage element in microgrid for power management system.

Keywords Microgrid control • Energy storage elements • Optimal control technique • Distributed generation • Multi-agent

1 Introduction

Energy [1] supply should be diverse and sustainable, and it needs to be utilized more effectively. It is necessary for promoting human's quality of life with the economic growth of energy resources. The term microgrid (PG) refers to the concept of small amount of distributed energy (DER) using single power subsystem related to the renewable energy source which comprises a distributed and/or

S. Kumar (✉)

Department of Electrical Engineering, Chandigarh University, Gharauran, Mohali, India
e-mail: Kumarsushee90@gmail.com

I. Kaur

Faculty of Electrical Engineering, Chandigarh University, Gharauran, Mohali, India
e-mail: hod.eee@cumail.in

© Springer Nature Singapore Pte Ltd. 2018

R. Bera et al. (eds.), *Advances in Communication, Devices and Networking*,
Lecture Notes in Electrical Engineering 462,
https://doi.org/10.1007/978-981-10-7901-6_30

275

conventional sources, including solar, wind, hydro, internal combustion engines, gas turbines, microturbines along with a load group [2]. Applying single distributed energy resources can lead to local voltage increases, the potential for exceeding the thermal limits of certain lines and transformers and the problem of the high capital costs; so microgrid may be a better solution for this problem. In microgrid system, DER should be equipped with suitable (power electronic interface) PEI and controlled to ensure that the flexibility of the system polymerization as a single operation, to retain the quality of power and energy output [3]. Microgrid works with renewable energy sources such as biomass, solar, wind and waste-to-energy. The microgrid can be disconnected from the main supply itself and connected to the load in order to supply power to the load when power failures occur.

Architecture of microgrid is shown in Fig. 1. It mainly consists of two distributed generation sources, which are energy storage and both are AC and DC loads and a plug-in hybrid electric vehicle (PHEV). The microgrid [4] has two buses which are DC bus and AC bus. DC bus is used to connect the DG sources, storage device and the DC loads, whereas in AC bus, AC loads and the utility grid are connected as shown in Fig. 1. This intelligent building consists of utility grid, wind turbines and PV arrays, controllable loads (CLs). In case when the supply cut off, storage battery is used to provide power on that time. Wind turbine as it is the source of renewable energy is used to convert mechanical energy into electrical energy. As the air strike on the wings of wind turbine starts rotating, thus the mechanical energy is converted into electrical energy. Photovoltaic array is used to generate electrical power which consists many PV modules and panels. The solar panel observes solar light and converts that into electrical signals.

Fig. 1 Microgrid architecture [1]

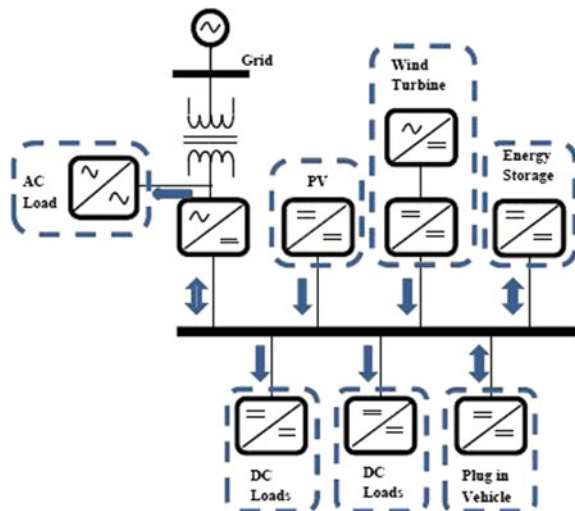


Table 1 Overview of distributed generation technologies

	Size range (KW)	Efficiency (%)		Footprint (Sqrft/KW)	Installation cost (\$/KW)	Electric cost to generate (cents/KWh)	Maintenance cost (Cents/Kwh)
		Electric	Overall				
<i>Reciprocating Engines</i>							
Spark ignition	30-5.0	31-42	80-89	0.28-37	150-600	7.6-13	0.7-2.0
Diesel	30-5.0	26-43	85-90	0.22-0.31	150-600	7.1-14.2	0.5-1.5
Dual fuel	100-5.0	37-42	80-85	0.15-0.25	150-450	7.4-10.7	
<i>Fuel cell</i>							
PEM	5-10	36-50	50-75	0.9	400-1.00	21.9-33.3	0.19-1.53
Phosphoric acid	200	40	84	0.9	360	18.6-22.8	
<i>Renewable</i>							
PV	5-5.0	NA	NA	NA	150-300	18.0-36.3	0.3-0.7
Wind	5-1.0	NA	NA	NA	500-4K	6.2-28.5	1.5-2.0

Table 2 Construction period and economic lifetime

Technology	Construction period (year)	Economic lifetime (year)
Solar PV	1	30
Wind	2	30
Solar thermal	2	30

2 Distributed Generators

Distributed generators are of two types [5] such as renewable and non-renewable distribution energy sources. Renewable distribution generations consist of renewable energy sources such as solar, thermal, photovoltaic, wind, hydro and biomass. Non-renewable distribution generation consists of non-renewable energy sources such as diesel engine, steam engine, gas engine. Renewable energy generation is challenging because they repeated power sources. Output power depends largely on solar energy; almost all types of renewable energy have some significance to the solar system. Thus, the construction of power systems without any kind of non-renewable DGs is risky in terms of reliability.

In Table 1, a review of distributed generation technologies has been [5] provided from a component which depends on design of plant and system requirements, whereas the cost analysis information is provided in Table 2. The power generation from renewable distribution generation becomes a challenge, because they are not regular power sources. The output power mainly depends on solar system because the sun emits about 3.86×10^{26} W of energy. Most of this energy goes into space, but 1.74×10^{17} W of energy strikes on the earth surface. (i.e. 174,000,000,000,000,000, or 174 quadrillion watts). This energy can be used for generating electric power. Thus, making a power system without any sort of non-renewable distributed generators is risky in terms of reliability.

3 Cost Analysis

This section describes the various methods of cost analysis:

The levelized cost of energy:

It can be written as levelized cost of energy (LCOE). It is used to measure the cost of generated electric power from different sources. It is also used to [6] compare the generated power with different generated sources. It is the average of electricity cost needed for a net present value of zero when performing a discounted cash flow analysis.

Construction period and Economic lifetime:

Construction period is the time in which the system has to be installed [7], and it is in working condition. Based on AEMO data set, construction period and economic lifetime has been presented in Table 2.

Capacity factor:

The capacity factor of renewable [7] energy sources will depend upon the quality of the renewable energy sources from which the energy is generated. In countries with competitive wholesale electricity market, slow growth in demand, renewable energy generation capacity increases and low natural gas prices tend to reduce conventional base load power generation technologies (such as coal-fired and nuclear power plants) wholesale price. In some cases, especially in areas with a large number of countries, wind power, electricity rates may be lower or even during the off-peak period is negative, because there is no fuel cost of air, and the wind turbine owners to sell electricity per kilowatt get a tax credit. These factors make it profitable because the wind turbines are obtained at very low or even negative prices to market. The increase of surplus-generating capacity, ability to pay competitive area, is identified capacity auction can be reduced. Some of the existing coal and nuclear power plant operators face the challenge of a growing

Table 3 Capacity factors

Technology	Capacity factor	
Wind	30%	
Solar PV	20%	
Solar thermal	Varied by plant storage configuration	
Power conversion	Description	Application
AC-AC	These are used to convert AC power to power, i.e. adjusting the output AC power. TRIAC is used to control the output. Also known as AC voltage regulator	Voltage regulator, heating control, lightning and frequency level changer
AC-DC	These are used to convert AC voltage to DC voltage. Thyristor is used to control the output. Input may be 1Ø3 Ø	Energy storage system, DGs technologies and high-voltage DC transmission
DC-AC	DC input power is used to convert AC voltage, frequency and phase	UPS, induction heating PV or fuel cell
DC-DC	These are used to adjust DC output voltage w.r.t the DC input voltage	Power, supplies for electronic equipment, robotics, switching power amplifier, photovoltaic system
AC-DC-AC	These are the converters used to convert the AC-AC using DC link, which consists of rectifier, DC link and inverter	DG applications and in microgrid applications

number of covering their fixed costs; this situation will require new investment at its plant so that operation is continued (Table 3).

4 Microgrid Management System

A microgrid management system [8] has been developed in MICROGRIDS scheme by taking the benefit of agent technologies. Management system architecture is shown in Fig. 2. It consists of microgrid agent platform which consists of microgrid centre controller.

4.1 Microgrid Agent Platform

It provides the platform [8] in which microgrid centre controller, load controller and microsource controller are executed.

4.2 Source Controller

This mainly consists of generator agent, schedule agent and bid agent.

4.3 Load Controller

These are used to support property protocols as well as the XML-RPC standard.

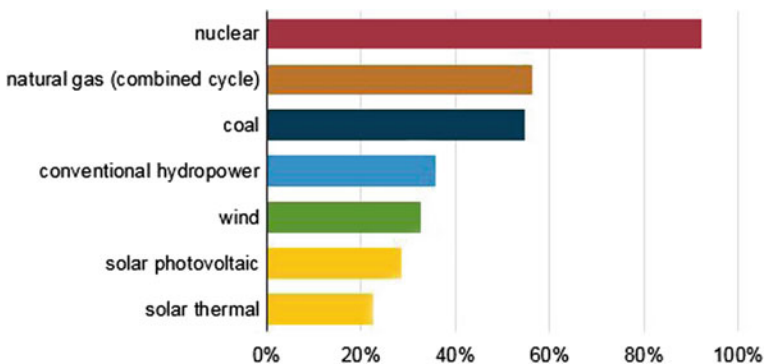


Fig. 2 Capacity factors of different energy sources

4.4 Microgrid Central Controller

Microgrid central controller mainly [9] consists of main container in which DF and AMF are found. It consists:

4.5 Pulling Agent

It is used for measuring source active and reactive power, frequency and voltage and stored their results in data base.

4.6 Database Agent

It is used for data storing and browsing.

4.7 Control Agent

It is used to control and modify the generation schedule according to the user's requirements.

4.8 Shifting Agent

It is used to shift load connection and also assign timing for the connection that is how long the connection is made.

5 Microsource Controller

MSC executes in an agent platform container. Generator agent is used by other users [9] to transmit power and receive data which is obtained by working with XML-RPC server. Schedule agent is used to obtain active power output which tracks the generation schedule. Bid agent is used to transmit active power and reference implementation read it from the system file.

5.1 Load Controller

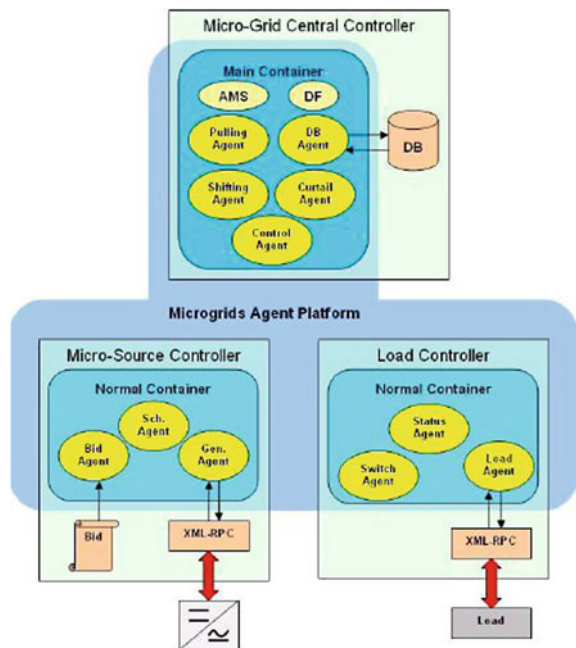
Load controller mainly consists of load agent, status agent and switch agent. Load agent shifts the load according to the demand-side management action. Status agent is used to control on and off of the load. Switch agent is used to switch between receiving, executing and curtailing commands [13].

5.2 Related Work

Bill Moran [4] has examined the method for calculating, evaluating, controlling the load in given conditions for maximizing the microgrid performance. Numbers of strategies are provided for load classification, to identify active and inactive loads for loads to generation matching. The author has discussed the requirement of active load control, high-speed control operation, load management system role, relationship among the energy storage and active load management (Fig. 3).

Bhavsar et al. [17] have developed the software with wind turbine generator, photovoltaic system, and energy and grid management controller with the battery storage system. The outcome is given in the variable generation conditions with the variable load. Static switches are utilized with the control of gate signals produced by system of energy management for each load and source. The system is

Fig. 3 Management system architecture [8]



developed with DC microgrid with PM DC generator (photovoltaic array and wind turbine generator), load, and grid and battery storage system.

Oyarzabal [8] has described a microgrid management system using agent-based technologies and its application. The present structure of microgrid has been examined in laboratory under various microgrid configurations. The effectiveness and suitability of the used software was assessed by dual strategy; on the one hand, the system is tested in a laboratory environment; in the laboratory environment, real-time power generation, storage and loading facilities are being monitored and controlled, and on the other hand, authors examined the agents in connection with framework performance and scalability issues.

Shi [20] has proposed a microgrid EMS called MP, considering the functional requirements and engineering challenges. MP in the sense of using ROA DER support device insertion and playback, and load functions are flexible and scalable. MP by ESI achieves interoperability. The author has tested bench development and deployment of prototype systems and conducted experiments to study the micronetwork management and control in real-world settings SMERC of UCLA. MP will be able to manage a variety of test equipment Taichung, interact with external systems, and implement the optimal scheduling of energy and DR.

6 EXISTING Techniques Used in Microgrid

Following are the techniques being utilized the last years and are defined below:

6.1 Function of Battery-Based Energy Storage Element in Microgrid for Power Management

In this section, the use of batteries for power management systems in microgrid management is used. Energy element such as composite energy storage system, super energy storage system and wireless power management with battery has been discussed. Important functions are stored separately to avoid changing load, uninterruptible power supply and power Ping Heng. Since the goal could not be obtained by a single type of battery, a photovoltaic array having a composite paper develops energy storage. The system consists of a battery and a super capacitor having a high energy and power density of the composition, for storage. The modular power converter design is the best way to connect the battery and supercapacitor with a DC link.

6.2 *Best Power Management by Using Optimization Techniques*

Power management-based [11] optimization approach uses the cooling heat and power jointly also known as combined cooling heat power (CCHP). Using this technique, it increases the output power and decreases the operating cost. It includes two parts: electrical and heat. The electrical power consists of biogas that uses animal waste to obtain electrical energy. To improve the reliability of systems, cooling water and exhaust gas are used in a system based on thermal design. This can be done with the help of the refrigerator and heat exchanger constituting the heat part.

6.3 *Optimal Control Techniques*

In the structure [12] of environmental and economic issues and microgrid stability, optimal control technique is used to minimize the consumption of fossil fuel. This will also optimize the storage management and loads. Optimal control technique is used to find the minimum value of the function in order to define the linear and nonlinear constraints in the continuous and discrete space.

7 Conclusion

Almost every microgrid is highly dependent on communication and control operations to meet their needs and optimization constraints. In recent years, research has turned to the distributed microgrid control to reduce computation and communication load caused by the increased number of distributed generators. Microgrid reduces dependence on fossil fuels and improves the overall efficiency of the power grid reliability and power quality. This is an important aspect of the future smart grid. Important aspect is the grid integration and energy management programs to microgrid proper operation. Overview of the control and microgrid management has different energy management programme that will be reviewed to improve and stabilize the operation of microgrid and optimize the use of renewable energy sources.

References

1. S. Monisha, S. G. Kumar and M. Rivera, "Microgrid energy management and control: Technical review", IEEE International Conference on Automatica (ICA-ACCA), Curico, 2016, pp. 1–7.

2. Wu, Xing, "Research on Microgrid and its Application in China", *Energy and Power Engineering* 2013, pp. 171–176. S.A. Kalogirou, "Artificial neural networks in renewable energy systems applications: a review." *Renewable and Sustainable Energy Reviews*, volume 5, page 373–401, 2001.
3. Mariam, Lubna, Malabika Basu, and Michael F. Conlon, "A review of existing microgrid architectures," *Journal of Engineering* 2013, pp. 1–8.
4. B. Moran, "Microgrid load management and control strategies," *IEEE/PES Transmission and Distribution Conference and Exposition (T&D)*, Dallas, TX, 2016, pp. 1–4.
5. Bayindir, Ramazan, "A comprehensive study on microgrid technology," *International Journal of Renewable Energy Research* 4.4 (2014): 1094–1107.
6. Resnick Institute Report "Grid 2020 Towards a Policy of Renewable and Distributed Energy Resources", September 2012.
7. Eklas Hossain, Ersan Kabalci, Ramazan Bayindir, Ronald Perez, "A Comprehensive Study on Microgrid Technology", *International Journal Of Renewable Energy Research*, 2014, pp. 1094–1107.
8. J. Oyarzabal, J. Jimeno, J. Ruela, A. Engler and C. Hardt, "Agent based micro grid management system", *International Conference on Future Power Systems*, Amsterdam, 2005, pp. 6–10.
9. Veeramani, M., C. K. Sundarabalan, and J. Sanjeevikumar, "An Efficient Microgrid Management System for Rural Area using Arduino", *International Journal of Engineering Trends and Technology (IJETT)*, 2016, pp. 335–341.
10. A. A. A. Moussavou, M. Adonis and A. Raji, "Microgrid energy management system control strategy", *International Conference on the Industrial and Commercial Use of Energy (ICUE)*, Cape Town, 2015, pp. 147–154.
11. Jingwei, Hu, Zhang Teyan, and Zhao Yan Du Shipeng, "Research on Micro-grid Control and Management System", *Advance science and technology letters*, 2014, pp. 36–43.
12. Tazvinga, Henerica, Xiaohua Xia, and Bing Zhu, "Optimal energy management strategy for distributed energy resources," *2014 Energy Procedia*, 2014, pp. 1331–1334.
13. Mariam, Lubna, Malabika Basu, and Michael F. Conlon, "A review of existing microgrid architectures," *2013 Journal of Engineering* 2013.
14. Natesan, Chitra, "Power Management Strategies In Microgrid: A Survey", *International Journal of Renewable Energy Research (IJRER)* 2015, pp. 334–340.
15. Minchala-Avila, Luis I, "A review of optimal control techniques applied to the energy management and control of microgrid," *2015 Procedia Computer Science*, 2015, pp. 780–787.
16. S. Parhizi, H. Lotfi, A. Khodaei and S. Bahramirad, "State of the Art in Research on Microgrids: A Review", *IEEE Access*, 2015, pp. 890–925.
17. Y. S. Bhavsar, P. V. Joshi and S. M. Akolkar, "Simulation of Microgrid with energy management system", *International Conference on Energy Systems and Applications*, Pune, 2015, pp. 592–596.
18. M. Yazdani and A. Mehrizi-Sani, "Distributed Control Techniques in Microgrids", *IEEE Transactions on Smart Grid*, 2014, pp. 2901–2909.
19. P. Borazjani, N. I. A. Wahab, H. B. Hizam and A. B. C. Soh, "A review on microgrid control techniques", *IEEE Innovative Smart Grid Technologies - Asia (ISGT ASIA)*, Kuala Lumpur, 2014, pp. 749–753.
20. W. Shi, E. K. Lee, D. Yao, R. Huang, C. C. Chu and R. Gadh, "Evaluating microgrid management and control with an implementable energy management system", *IEEE International Conference on Smart Grid Communications (SmartGridComm)*, Venice, 2014, pp. 272–277.
21. T. E. Del Carpio Huayllas, D. S. Ramos and R. L. Vasquez-Arnez, "Microgrid systems: Current status and challenges", *IEEE/PES Transmission and Distribution Conference and Exposition: Latin America (T&D-LA)*, Sao Paulo, 2010, pp. 7–12.

Solution of Economic Load Dispatch Problems Through Moth Flame Optimization Algorithm

Princi Tripathi, Upendra Tomar, Vinod Kumar Singh
and Akash Kumar Bhoi

Abstract This paper presents a significantly efficient nature-motivated moth flame optimization (MFO) algorithm to solve the convex economic load dispatch (ELD) problems of the power system. The ELD focuses on the effective scheduling of the power-generating units so as to fulfil the total load demand and to satisfy the various constraints of the generating units as well as power network limitations. The aim of the proposed work is to reduce the quadratic cost function of the generating unit and hence obtain the minimum cost of generation so as to maintain the economy of the generation plant. The obtained better positions of moths around the flames describe about the best solutions obtained as so far for the proposed work of the ELD problems. This paper performs test on convex cost function of 18 unit system so as to validate the efficiency, reliability and robustness of the proposed methodology.

Keywords Economic load dispatch • Moth flame optimization algorithm

P. Tripathi · U. Tomar
Department of Electrical Engineering,
Vikrant Institute of Technology and Management, Gwalior, India
e-mail: princi1991@gmail.com

V. K. Singh (✉)
Department of Electrical Engineering,
SR Group of Institutions, Jhansi, UP, India
e-mail: singhvinod34@gmail.com

A. K. Bhoi
Department of Electrical and Electronics Engineering,
Sikkim Manipal Institute of Technology (SMIT), Majitar,
Rangpo 737136, Sikkim, India
e-mail: akash730@gmail.com

1 Introduction

The economic load dispatch has grown to be an essential function in process and controlling action of power system. Here, we schedule the generators that provide power by satisfying or meeting the total load demand of the system and at the same instance minimizing the cost function that is considered to be the main object function. Improvement in the economic load dispatch analysis is done in two parts.

In economic load dispatch, the cost function of various generators is in a quadratic equation form and it ignores the transmission network limitations [1]. There are basically two constraints in economic load dispatch problem. First one is equality constraint, and second is inequality constraint. The real and reactive power of generator limits is also varied in the specified limits to minimize the fuel cost. Equality constraint is basically used for load generation balance [2]. Inequality constraint consists of voltage constraint and generator constraint. Voltage constraint describes about the voltage limits within which we need to transfer the power, and generator constraint describes the KVA loading of generator should not exceed the prescribed limits. In power system, all the various power plants including the generating units are located at a very large distance from the load demand centres, and huge amount of economy gets varied due to the losses, generation cost, fuel cost, maintenance cost, transmission cost, etc., and therefore, to maintain the stability of the system, proper scheduling of the generating units is very essential part of power system.

The various nature-inspired optimization techniques are real-coded genetic algorithm [3], genetic algorithm [4] particle swarm optimization [5], new particle swarm optimization [6], differential evolution [7], recent advances in economic dispatch [8], quantum-inspired particle swarm optimization [9], simulated annealing [10], biogeography-based optimization [11], artificial immune system [12], evolutionary programming optimization for solving economic load dispatch problems of power system [13], artificial bee colony algorithm [14] and improved differential evolution [15].

The modern optimization technique used in this paper is the moth flame optimization algorithm. This algorithm is used to minimize the objective function by satisfying various constraints of the system so as to provide the effective results. It is a novel nature-inspired optimization paradigm. The most effective technique or the methodology of this optimization is the tendency of the navigation of the fanciest insects called moths in nature. This navigation tendency is referred as the transverse orientation. By keeping this methodology, various results have been calculated to make the system more efficient.

2 Problem Formulation

The primary objective of economic load dispatch problem is to meet the load demand of power system by minimizing the objective function which is the cost function equation of various generating units. This cost function is represented mathematically in quadratic form having various cost coefficients and variables. The amount of power generated from these generating units is shown by P_i MW. Where:

i = number of generating units of the power system network whose values are ranging from 1 to n .

F_i = fuel cost of i th generating unit.

P_i = power generated from the i th generating unit.

$F_i(P_i)$ = cost function of i th generating unit in power system.

a_i , b_i and c_i are the fuel cost coefficients of the i th generating unit.

P_D = total power demand of the system.

P_L = total power loss occurred in the system.

V_{\min} = minimum value of the voltage.

V_{\max} = maximum value of the voltage.

P_i^{\min} = minimum value of the power generated by the i th generating unit.

P_i^{\max} = maximum value of the power generated by the i th generating unit.

The objective function which is a cost function equation is represented as follows:

$$\text{Min } F_i(P_i) = \min \sum_{i=1}^n [(a_i \times P_i^2 + b_i \times P_i + c_i)]$$

This equation is a convex type economic load dispatch problem formulation. The economic dispatch for a certain load demand should also satisfy the following constraints.

(A) Equality Constraint:

(1) Power Balance Constraint:

If the losses are considered, the equation is:

$$\sum_{i=1}^n P_i = P_D + P_L$$

In this system, the losses are zero; therefore, the power balance constraint equation becomes as follows:

$$\sum_{i=1}^n P_i = P_D$$

(B) Inequality constraints:

- (1) Voltage Constraint: It describes about the voltage limits within which we need to transfer our power to the load.

$$V_{\min} \leq V \leq V_{\max}$$

2. Generator Constraint: It describes the KVA loading of the generator should not exceed the limits.

$$P_i^{\min} \leq P \leq P_i^{\max}$$

3 Moth Flame Optimization Algorithm

This algorithm has completely adopted a special way of navigational technique adopted by the insects called as moths, and hence, this enhances its feature in this modern research system.

The moths have a tendency of flying in night by maintaining a constant angle with respect to moon. This makes them to travel in a straight line. If there is any artificial light, then they move spirally. Hence, this special movement technique is used in the optimization process.

Steps for the proposed algorithm are as follows:

1. Initially, we assume the total population of moths. We randomly generate the initial positions of moths in the space. The moths have a tendency of moving around the flame in a specific manner.

$$A(k, l) = (\text{popmax}(k) - \text{popmin}(k)) * \text{rand}() + \text{popmin}(k);$$

Here, popmax is the maximum limit of the power generated by the generator, and popmin is the minimum limit of the power generated by the generator.

2. After the generation of initial positions of moths, this function runs till this condition is satisfied.

3. After every iteration, the sorting of flames is done. Therefore, we update the number of flames by using formula as:

$$\text{flame number} = \text{round}\left(S - R * \frac{S - 1}{V}\right)$$

where S is the maximum number of flames, R is the number of iterations, and V is the maximum number of iterations. After each execution of the iterations, the sequence of the flames changes and moths update their position with respect to the flame.

4. The condition is checked whether the moths are within the searching area or not. If the moths are within the searching area, it is called as exploitation, and if the moths are outside the range of searching area, it is called as exploration. If moths are not within the area, then they are needed to bring back.
5. Now, the iteration condition is satisfied. If the condition gets satisfied, the sorting of the population of moths is done. It updates the new position of moths in the searching area.
6. For every iteration, the condition is checked that whether the moths are lesser than or equal to the flame number, and if the condition is satisfied, then the flames are sorted according to their fitness values. Then, we update the new positions of moths with respect to the corresponding flame.
7. Now, the process of updating a new positions of moths with respect to the flames after every iteration is done by following a special function called as spiral function. In this algorithm, this spiral movement is considered as very essential function which also gives about the assurance of the exploitation concept which means that moth always lies within the searching area of the region. The equation for spiral function is defined as

$$P(A_k, B_l) = H_k \cdot e^{gt} \cos(2\pi \cdot t) + B_l$$

where H_k represents the distance of k th moth from the l th flame, g is defined as the constant for the shape of the spiral function, and t is the random number in $[1, -1]$.

8. After assigning moths to new position, we need to calculate the distance of moth from the flame using the following equation:

$$H_k = |B_l - A_k|$$

where H_k is the distance of k th moth, B_l indicates the l th flame, and A_k is the k th moth.

9. Now to calculate t , we are considering a constant q called as the convergence constant whose value decreases from -1 to -2 over the entire process of iteration. Here, the convergence curve defines the best flame score. This factor results a fast convergence of moths around the flame during the entire iteration process.

The proposed nature-inspired moth flame optimization technique has been worked in the MATLAB software. The accuracy and the efficiency of the algorithm have been tested in two systems to resolve the economic load dispatch dilemma by optimizing the object function. The optimization is made without bearing in mind the power losses.

4 Results Discussion

This case studies an 18 unit thermal generating system for optimization process. The input information for standard 18 unit system is occupied from the reference [3]. The system data includes the values of the constant coefficients in the total fuel cost equation of the generating units without any power losses. The maximum power demand for this system is 365 MW, and the various percentages factor considered are 80 and 70% of the maximum power demand. The obtained results are shown in the Table 1 which validates and proves the effective performance and accuracy of the MFO algorithm, and its results are compared with those obtained from the biogeography-based optimization (BBO) [11], real genetic algorithm (RGA) and lambda iteration. Figs. 1 and 2 shows the power generated by all the 18 generating units whose summation of the values becomes equal to the power demanded.

Table 1 Comparison results for 18 unit system (maximum power $P = 365$ MW)

Demand	λ -iteration	GA	Real GA	BBO	MFO
80%P	23861.58	23980.24	23861.58	22648.0008	19537.7533
70%P	20393.43	20444.68	20396.39	19278.2320	16921.6825

Fig. 1 Cost convergence characteristics curve for power demand $P_D = 255.5$ MW

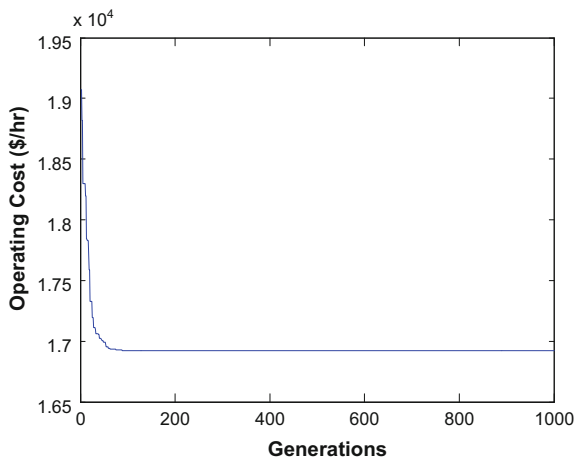


Fig. 2 Cost convergence characteristics for power demand $P_D = 292$ MW

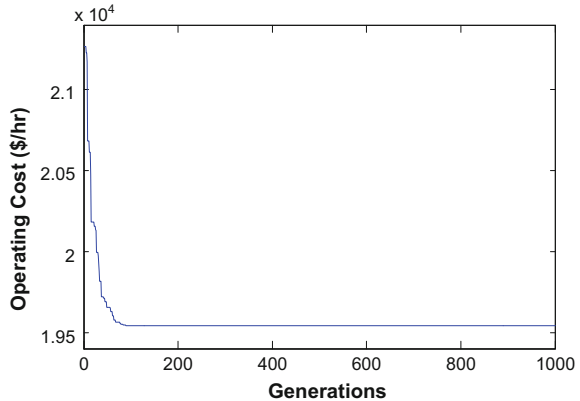


Table 1 gives us a brief description about the comparison results obtained from the proposed moth flame optimization technique with those of earlier results obtained from the biogeography-based optimization algorithm, real genetic algorithm, genetic algorithm and λ iterations. The new results gained have much more accuracy and effectiveness in solving the problems of economic load dispatch concept.

5 Conclusion

This paper effectively validates the proposed MFO algorithm to solve ELD problems of power system by obtaining the better results as compared to other implemented techniques in previous analysis. The main purpose of optimizing the ELD problems has been done to minimize the cost function of the generating units, and hence, lesser value of cost is obtained with the proposed technique as nowadays the cost reduction has become a vast area of interest in solving the ELD problems. Therefore, this concept extremely requires a very effective strategy in proper planning and controlling of the generating units in the power plant. Comparing and considering the various previous obtained results, various convergence characteristics, demands and with the new obtained results, it can be inferred that the proposed methodology performs very effectively, having great potential in solving the problems, having faster solution obtaining capability and has feasibility in nature, and hence, it can be concluded that the proposed methodology can be applied for optimizing the ELD problems in the power system.

References

1. Sadat Hadi: *Power System Analysis*, McGraw-Hill (1999).
2. Wood A.J and B.F Wallenberg: *Power Generation, Operation and Control*, 2nd edition, John Wiley Sons, New York, USA, (1996).
3. Dokopoulos Petros S., Damousis G. Ioannis, and Bakirtzis G. Anastasias: Network-Constrained Economic Dispatch Using Real-Coded Genetic Algorithm, *IEEE Transactions on Power System*, Vol. 18, No. 1, February (2003).
4. Chen P.H. and Chang C.H: Large Scale Economic Dispatch by Genetic Algorithm, *IEEE Transactions on Power System*, Vol. 10, No. 4, pp. 1919–1926, (1995).
5. L. Srivastava, Chaturvedi K.T, and Pandit M.: Self-Organizing Hierarchical Particle Swarm Optimization for Nonconvex Economic Dispatch, *IEEE Transactions on Power System*, Vol. 23, No. 3, pp. 1079–1087, (2008).
6. K. Thanushkodi, A Immanuel, and Selva Kumar: A New Particle Swarm Optimization solution to nonconvex economic dispatch problem, Vol. 22, No. 1, pp. 42–51, (2007).
7. H. Iba, and Noman N: Differential Evolution for economic load dispatch problems, *Electric Power System Research*, Vol. 78, No. 8, pp. 1322–1331, August (2003).
8. S. Rahman and B.H Choudhary: A review of recent advances in economic dispatch, *IEEE Transactions on Power System*, Vol. 5, No. 4, pp. 1248–1259 (1990).
9. K.P Wong, Z. Dong, H.G Wang and K. Meng: Quantum-Inspired Particle Swarm Optimization for Value-Point Economic loads dispatch, *IEEE Transactions on Power System*, Vol. 25, No. 1, pp. 215–222 (2010).
10. Panigrahi B.K, Pandit Manjaree, Dubey Hari Mohan, and Vishvakarma Kumar Kamlesh: Simulated Annealing Approach for Solving Economic Load Dispatch Problems with Value Point Loading Effects, *International Journal of Engineering, Science and Technology*, Vol. 4, No. 4, pp. 60–72, (2012).
11. A.K Wadhvani, Wadhvani S., Agrawal Neetu, Agrawal Shilpy and K.K Swarnkar: Economic Load Dispatch Problem With Ramp Rate Limit Using BBO, *International Journal of Information and Education Technology*, Vol. 2, No. 5, October (2012).
12. Jonathan Timmis, De Castro and Leandro N: *Artificial Immune System: A New Computational Intelligence Approach*, Springer, UK, (2002).
13. Huang C.L, Yang P.C and Yang H.T: Evolutionary Programming Based Economic Dispatch for Units with Non-Smooth Fuel Cost Function, *IEEE Transactions on Power Systems*, Vol. 11, No. 1, pp. 112–118 (1996).
14. Dixit Prasad Gaurav, B.K Panigrahi, Pandit Manjaree and Dubey Hari Mohan: Economic Load Dispatch Using Artificial Bee Colony Optimization, *International Journal of Advances in Electronics Engineering*, Vol. 1, Issue. 1, pp. 119–124, (2011).
15. Basu M: Improved Differential Evolution for Economic Dispatch, *Electrical Power and Energy Systems*, Vol. 63, pp. 855–861, (2014).

Noise Reduction in Synthetic Aperture Radar Images Using Fuzzy and Self-Organizing Map

Kishore Medhi, Khwairakpam Amitab, Debdatta Kandar
and Babusena Paul

Abstract Images captured by synthetic aperture radar (SAR) are generally corrupted with noises. SAR images are commonly affected by speckle noise and impulse noise. Noise filtering techniques must remove noises and simultaneously preserve valuable information present in the images. This article presents a noise filtering techniques based on soft computing. The proposed filters are implemented in two phases: In the first phase, the presence of noise in a particular pixel is detected by using fuzzy logic, and in the second phase, noisy pixels are filtered by using Self-Organizing Map (SOM). From our experiment, it is found that the proposed SOM filter reduces both speckle and impulse noise and also preserves the information present in the image. The proposed SOM filter is comparatively evaluated with various filters based on peak signal-to-noise ratio and edge-preserving factor.

Keywords Fuzzy logic · Impulse · Neural network · Self-Organizing Map
Speckle · Synthetic Aperture Radar

1 Introduction

SAR is imaging RADAR system [1]. SAR images are useful in many applications including monitoring natural resources, geographical mapping, urban growth, and weather forecasting [2]. However, the presence of noises in SAR images degrades

K. Medhi (✉) · K. Amitab
Department of Information Technology, North Eastern Hill University,
Shillong, India
e-mail: kishoremedhi2015@gmail.com

K. Amitab
e-mail: khamitab@gmail.com

D. Kandar · B. Paul
Department of Electrical and Electronic Engineering, University of Johannesburg,
Johannesburg, South Africa

the quality of image and causes difficulty in interpreting the images. Noise removal techniques must be carefully designed to reduce noise significantly, and at the same time, vital information present in the images must be retained [3]. Speckle noise and impulse noise are the most common types of noise that are present in the SAR images. The distribution of noise and amount of noise present in the SAR images are unpredictable, soft computing are capable of approximate reasoning and can handle uncertainty [4], this indicates that soft computing based noise filters may give good result. This article presents a novel noise filter which exploits the advantages of two soft computing techniques, namely fuzzy logic and SOM.

2 Proposed Noise Filter

The proposed filtering technique filters noises in two phases: In the first phase, it detects noise using fuzzy rules, and in the second phase, it removes noise using SOM techniques.

2.1 Fuzzy Noise Detection Phase

The main objective of this phase is to determine whether a pixel is affected by noise or not. To detect noisy pixels, a moving window of size 3×3 is used as shown in Fig. 1 [5].

Let the difference between the central pixel $X(i, j)$ and neighboring pixels is denoted by Δi , where $i \in \{1, 2, 3, 4, 6, 7, 8, 9\}$, and the two smallest value in Δi is represented by $\Delta s1$ and $\Delta s2$. Compute the average of them as $\Delta s = (\Delta s1 + \Delta s2)/2$.

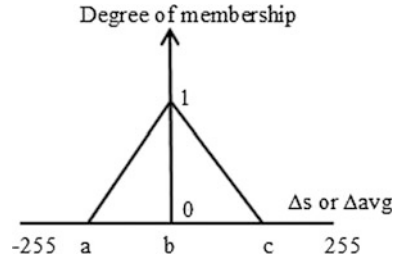
Rule 1.1: *If the value of Δs is LARGE then noise is present in $X(i, j)$.*

The value of Δs will be very small, if the neighboring pixels have similar intensity, and Δs will have large value if $X(i, j)$ is noisy. However, this condition may fail if neighboring pixels are noisy but central pixel is not noisy. To solve this problem, we calculate the average of all eight difference Δi , i.e., $\Delta_{avg} = \frac{\sum \Delta i}{8}$.

Fig. 1 Pixels under 3×3 window

1	2	3
$X(i-1,j-1)$	$X(i-1,j)$	$X(i-1,j+1)$
4	5	6
$X(i,j-1)$	$X(i,j)$	$X(i,j+1)$
7	8	9
$X(i+1,j-1)$	$X(i+1,j)$	$X(i+1,j+1)$

Fig. 2 Fuzzy membership function SMALL



Rule 1.2: *If the Δ_{avg} value is LARGE then $X(i, j)$ is affected by noise.*

Rule 1.3: *If Δ_s and Δ_{avg} is LARGE then noise is present in $X(i, j)$.*

Rule 1.1 and Rule 1.2 are combined in Rule 1.3. LARGE is a fuzzy membership function, and it is defined as $LARGE = 1 - SMALL$. And SMALL is defined by using triangular shaped membership function as shown in Fig. 2.

2.2 Noise Reduction Using Unsupervised Self-Organizing Map

Self-Organizing Map is an unsupervised artificial neural network (ANN) technique and training of the network is entirely data-driven and no target results for the input data vectors are provided. The SOM network as shown in Fig. 3 consists of input and output layer and they are connected by the weight. If noise is detected, an input is supplied to the network and the algorithm run until termination condition is met. After termination condition is met, the affected pixel value is replaced by the output of the network. During computation, network learns the input parameter and accordingly updates the value of weights. The output is computed by taking mean of the final weights [6].

The steps involve in SOM are as follows [6]:

- (a) Select output layer network topology.
- (b) Initialize current neighborhood distance $D(0)$, to a positive value.

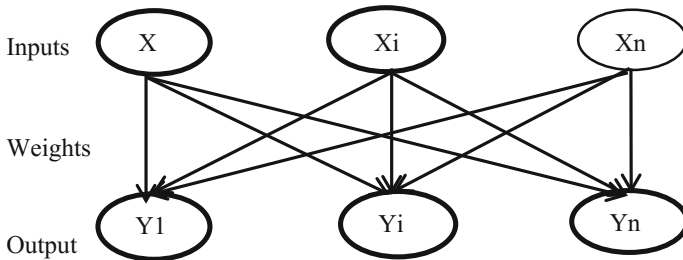


Fig. 3 SOM network architecture

- (c) Initialize weights from inputs to outputs to small random values.
- (d) While computational bounds are not exceeded do
- (1) Select an input sample
 - (2) Compute the square of the Euclidean distance from weight vectors (w_j) associated with each output node $\sum_{k=1}^n (i_{l,k} - w_{j,k}(t))^2$
 - (3) Select output node j^* that has weight vector with minimum value from step 2.
 - (4) Update weights of all nodes within a topological distance given by $D(t)$ from j^* , using the weight update rule: $w_j(t+1) = w_j(t) + \eta(t) (i_l - w_j(t))$
 - (5) Learning rate " $\eta(t)$ " generally decreases with time and it lies between 0 and 1.
 - (6) End

Here, " $W(i)$ " represents the weight connecting between input and output neurons, " η " is the learning rate, j^* represents the winning neuron, $D(t)$ represents the neighborhood distance, and " i " represents the input.

3 Experimental and Results

Fuzzy membership function SMALL is used to derive LARGE in noise detection phase of the proposed method and it is associated with three parameter a , b , and c . The parameters value for Rule 1.3 are $a = -20$, $b = 0$, $c = 20$. The output of noise detection gives noise level " L " affecting the pixels in the range $[0 \ 1]$, if $L \leq 0.3$ it is assumed that no noise is present, if $0.3 < L \leq 0.5$ then a 3×3 window is used for filtering assuming that the image is affected by less amount of noise, if $0.5 < L \leq 0.9$ then 5×5 window is used assuming that the image is affected by moderate amount of noise and for $L > 0.9$ we have used 7×7 window assuming that the image is highly corrupted by noise. In case of SOM, the termination condition is set to 150 iterations, the learning rate " η " is taken as 0.7, and initially the number of neighbors is taken as 7. A grayscale SAR image shown in Fig. 4a added with different percentage of speckle, fixed and random impulse noises are used to evaluate the accuracy of the proposed filter. Peak signal-to-noise ratio (PSNR) and edge-preserving factor (EPF) are used for evaluating. PSNR is defined as the ratio between the maximum gray intensity ($MAX = 255$) and the intensity of noises.

$$PSNR = 10 \text{Log} \left(\frac{MAX^2}{MSE} \right) \quad (1)$$

where mean square error (MSE) is the average of square difference between the filtered image and the desired target image.

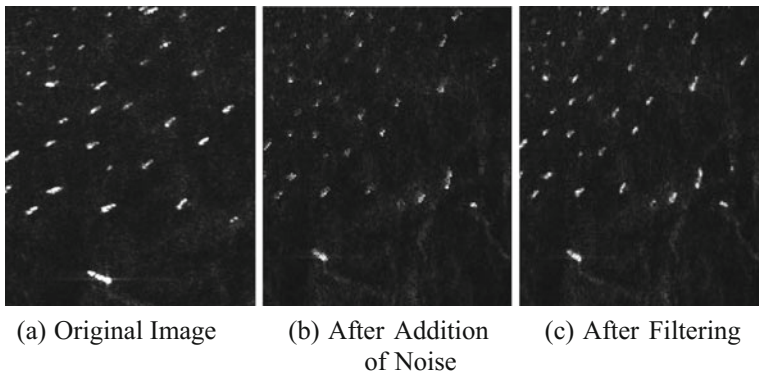


Fig. 4 Sample images used for filtering

$$MSE = \frac{1}{MN} \sum_{i=1}^N \sum_{j=1}^M (I(i,j) - I(i,j)')^2 \tag{2}$$

where M and N are number of rows and columns, $I(i, j)$ represent the filtered pixel intensity, and $I(i, j)'$ represent the desired pixel intensity. The edge-preserving factor (EPF) is computed using the formula [7, 8].

$$EPF = \frac{\sum (\Delta x - \Delta x')(\Delta y - \Delta y')}{\sqrt{\sum (\Delta x - \Delta x')^2 (\Delta y - \Delta y')^2}} \tag{3}$$

where Δy and Δx represent the edges present in the filtered image y and original image x , $\Delta y'$ and $\Delta x'$ are the mean value of Δy and Δx . Laplacian operator is used for extracting the edges [9]. To evaluate the performance of filter, we have used mean, median, and multilayer perceptron (MLP) filter [10].

From the experimental result shown in Tables 1, 2, and 3, it is clear that the proposed SOM filter has the highest PSNR and EPF value on average, compared to other filters on images affected with speckle and impulse noise. The PSNR value gives us the amount of noise suppressed by the filter, and the EPF value gives us the amount of edges preserved or recovered after filtering.

Figure 4a shows a SAR image of sea near a busy port [11] and it is used for our experimentation, Fig. 4b shows the image after adding 20% speckle noise, and Fig. 4c shows the image after filtering using proposed method.

Table 1 PSNR performance of filters on image affected by different percentage of random and fixed impulse noise

% of noise	Proposed SOM filter		MLP filter		Mean filter		Median filter	
	Random impulse noise	Fixed impulse noise	Random impulse noise	Fixed impulse noise	Random impulse noise	Fixed impulse noise	Random impulse noise	Fixed impulse noise
40	19	18	18	15.5	19	17.3	19	17.8
20	23.5	18.5	19.5	18.13	22	20	25	23
10	27.2	24	21.7	20.5	23.3	21.8	25.2	25
9	28	25	22	21.4	23.6	22	25.5	25.5
7	28.50	26.16	22.5	21.37	24	22.8	26	25.5
5	31.5	29	23.6	23.5	24.5	23.8	26	26
2	33	32	24.5	25	24.8	24	26.4	26.3

Table 2 EPF performance of filters on image affected by different percentage of random and fixed impulse noise

% of noise	Proposed SOM filter		MLP filter		Mean filter		Median filter	
	Random impulse noise	Fixed impulse noise	Random impulse noise	Fixed impulse noise	Random impulse noise	Fixed impulse noise	Random impulse noise	Fixed impulse noise
40	2.9	1.29	2.5	1.7	2	1.3	2.9	0.6
20	4.5	3.7	3.2	2.9	3	2	4.8	3
10	5.8	4.55	4.14	3.7	3.5	2	5.5	5
9	5.9	4.43	4.06	4.2	3.7	2.8	5.5	5.8
7	6	5.24	4.4	4	4	3	5.7	5.8
5	6.33	5.73	4.6	4.65	4.3	3.9	5.8	5.7
2	6.54	6.27	4.65	5	4.7	4	5.8	5.9

Table 3 PSNR and EPF performance of filters on image affected by different percentage of speckle noise

% of noise	Proposed SOM filter		MLP filter		Mean filter		Median filter	
	PSNR value	EPF value	PSNR value	EPF value	PSNR value	EPF value	PSNR value	EPF value
40	17	3.03	11	1.7	19.11	1.69	15.5	0.46
20	19	3.8	13.5	2.5	20.9	2.23	18.2	1.22
10	21	4.57	17	3	22	2.99	2.05	2.5
9	21	4.82	17	3	22.7	3.19	20	2.73
7	22	5.16	18	3.2	23	3.6	21	3.36
4	24	5.70	20.3	3.77	23.9	4	23.16	4.5
2	26	6	23.8	4.5	24.6	4.5	24.5	5

4 Conclusion

This paper presents a soft computing-based noise removal filter. The filter is implemented in two phases, noise detection and reduction. Fuzzy rules are used for detecting the noisy pixel, and SOM is used for reducing the noise. The accuracy of the proposed SOM filter is comparatively evaluated with mean, median, and MLP filter based on PSNR and EPF value. We have tested on the radar images affected by different percentage of speckle, fixed, and random impulse noise. Amongst the implemented filters, the proposed SOM filter has highest PSNR and EPF value in the image is affected by impulse and speckle noise.

References

1. Moreira, A., Prats-Iraola, P., Younis, M., Krieger, G., Hajnsek, I., & Papathanassiou, K. P. A tutorial on synthetic aperture radar. *IEEE Geoscience and Remote Sensing Magazine*, vol. 1(1), pp. 6–43, (2013).
2. Al-amri, Salem Saleh, Namdeo V. Kalyankar, and Santosh D. Khamitkar. A comparative study of removal noise from remote sensing image. *arXiv preprint arXiv*: pp. 1002–1148, (2010).
3. Argenti, F., Lapini, A., Bianchi, T., & Alparone, L. A tutorial on speckle reduction in synthetic aperture radar images. *IEEE Geoscience and remote sensing magazine*, vol. 1(3), pp. 6–35, (2013).
4. Pal, Sankar K., Ashish Ghosh, and Malay K. Kundu, eds. *Soft computing for image processing*. Physica, Vol. 42, (2013).
5. Kwan HK. Fuzzy filters for noise reduction in images. In: Nachtegael M, Van der Weken D, Kerre EE, Van De Ville D, editors. *Fuzzy Filters for Image Processing*. Berlin Heidelberg, Springer. pp. 24–53, (2003).
6. Haritopoulos, Michel, Hujun Yin, and Nigel M. Allinson. Image denoising using self-organizing map-based nonlinear independent component analysis. *Neural Networks*, vol. 15(8), pp. 1085–1098, (2002).
7. Wang, Guobao, and Jinyi Qi. Penalized likelihood PET image reconstruction using patch-based edge-preserving regularization. *IEEE transactions on medical imaging*, vol. 31(12), pp. 2194–2204, (2012).
8. Umamaheswari, G., & Vanithamani, R., An adaptive window hybrid median filter for despeckling of medical ultrasound images. *International journal of scientific and industrial research*, vol. 73(1), pp. 100–102, (2014).
9. Gonzalez, R. C. *Digital image processing*. Pearson Education, India, Third Edition, (2009).
10. Ghosh, A., & Chakraborty, M. Hybrid Optimized Back propagation Learning Algorithm for Multi-layer Perceptron. *International Journal of Computer Applications*, vol. 57(1), pp. 1–6, (2012).
11. S. C. Liew, *Principles of remote sensing*, Centre for Remote Imaging, Sensing and Processing, Available at: http://www.crisp.nus.edu.sg/~research/tutorial/sar_int.htm.

Design of a Quasi-Lumped Resonator Antenna Array Based on a Novel Optimized Corporate Network Feed

Seyi Stephen Olokede and Babu Sena Paul

Abstract A corporate network-fed quasi-lumped resonator antenna array is presented. A new class of patch antennas comprising of an interdigital capacitor in parallel with a straight strip inductor is employed as radiators, whereas an optimized corporate feed network is designed to couple excitation power to the radiating elements. The proposed radiating elements rely on the long but folded capacitance occurring between the interdigit gap, thus ensuring the miniaturization of the passives. The feed network has also been optimized for compactness and power propagation efficiency with minimum transmission losses. An 8×1 and an 8×2 are prototyped and investigated using the finite integration technique numerical code. The resulting design is lithographically etched on a Roger duroid microwave laminate and subsequently measured. Findings indicate that the resulting design is compact in terms of estate area occupancy and demonstrates reasonable radiation efficiency.

Keywords Corporate feed network · Directive characteristics · Quasi-lumped Slim antenna · Size occupancy

1 Introduction

In spite of the many advantages of corporate feed networks (such as a relatively wide frequency pattern owing to mismatch loss reduction, control flexibility of individual radiators with respect to phase and amplitude, good design suppleness, even excitation capabilities of the radiators, ease and flexibility of splitting power

S. S. Olokede (✉) · B. S. Paul
Department of Electrical and Electronic Engineering Technology,
University of Johannesburg, Johannesburg, South Africa
e-mail: solokede@gmail.com

B. S. Paul
e-mail: bspaul@uj.ac.za

with desired phase and magnitude), they are hampered by expansive estate occupancy, poor mechanical simplicity, and lossy feed lines owing to bends, discontinuities, junctions, and joints along the feed line. Different alternative solutions to achieve compactness in terms of estate occupancy and efficient feed lines have been reported in the literature [1–4]. Unfortunately, these alternatives are bedeviled by large radiators (though with optimized feed networks) or other problems. In this work, we present a simple optimized corporate feed network with highly compact radiators. We anticipate substantial estate utilization efficiency if both the aperture sizes of the radiators and the optimized feed lines are compact. We introduce a new antenna element, whose target frequency is independent of the radiation wavelength. Instead, its resonance is dependent on the quasi-lumped element equivalence. As a result, the usual electrical length limitation often holding sway on small antennas is avoided. Moreover, the proposed radiating element's intrinsic passive capacitive and inductive constructs allow the addition of both capacitive and inductive contributions that eventually contribute to the proposed passive performance profile. Ordinarily, it is expected that small antennas will demonstrate inferior radiation resistance owing to a small form factor, poor directive characteristics, and a meager frequency pattern. The capacitive and inductive construct of the new radiator circumvents these challenges to a reasonable extent. The various digit conductors sum up as inductance including the center-shortened inductor (L), and as such, the magnetic fields from each turn of the resonator add up, whereas the gaps that form the interdigit capacitor (C) from each turn account for the electric fields in order to build up the inductance/capacitance associated with the magnetic/electric fields. The capacitors from the edge of each conductor form the capacitance to ground (otherwise called pad capacitances), the effect of which is not particularly significant except for tuning. The cumulative summation of various inductances, along with the center inductor plus that of the capacitance, particularly the long but folded interdigit capacitance that occurs across the narrow gap with implicit fringing capacitance between the long common edge areas of the metal fingers, separated by very small spacing depending on the minimum gap permitted by the foundry, causes the antennas to outperform their contemporaries. As a result, both the impedance bandwidth (of 79.73%) and the directive characteristics (54.66%) are significant, as demonstrated in Figs. 4 and 6 of [5], whereas Table 4 similarly demonstrates the robustness of the proposed resonator over a typical traditional microstrip patch antenna at the same resonance frequency.

In addition, an aperture size reduction of $5.8 \times 5.6 \text{ mm}^2$ at 5.8 GHz achieved with the above average antenna efficiency has been reported in [6]. Further flexibility of the proposed passive vis-à-vis its size dimension with respect to other frequency bands, design equations, and its aspect ratio diversity is reported in the same publication. Figure 1a shows the geometry of the proposed new antenna element, and Fig. 1b describes its quasi-lumped perspective.

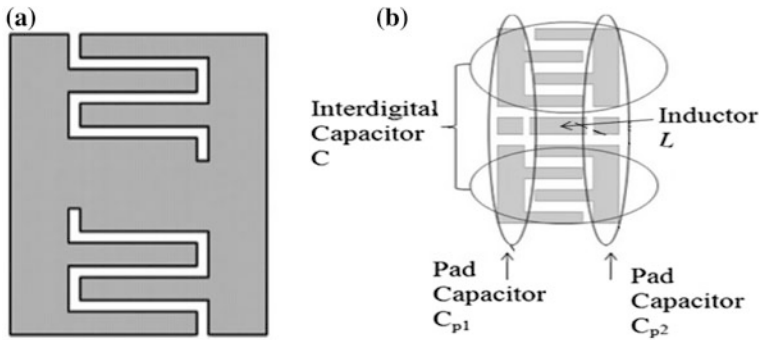


Fig. 1 Proposed quasi-lumped element resonator. **a** The resonator, **b** resonator components

2 Theoretical Framework

2.1 Proposed Resonator

The term interdigital refers to a digit-like or finger-like periodic pattern of parallel in-plane electrodes used to build up the capacitance associated with electric fields [5]. The proposed resonator shown in Fig. 1 basically consists of microstrip lines and shorts with their corresponding inductances and capacitances. The capacitance occurs across a narrow gap between the conductors. These gaps are essentially very long and folded in order to use a small area. Reducing the width of the fingers reduces the required area, but increases the characteristic impedance of the line and in general lowers the effective capacitance. Because they consist of a microwave-lumped element capacitor and inductor, their resonance frequency does not depend on their electrical dimension as does that of the other microstrip patch antennas, but rather on some lumped component, as stated in Eq. 7 of [5]. This is the reason for their compact capability. Not only that; there are assumptions about constant voltage–current across the sections, insignificant phase shift, and no propagation delay. Essentially, this is responsible for the efficiency of the antenna irrespective of its compact structure.

When an external voltage is applied across the proposed resonator, as shown in Fig. 1 of [5], the voltage and current allocations are as reported in Fig. 6 of [6, 7]. To this effect, there is a capacitance effect among the parallel conductors and also between the conductors and the ground. The capacitance can be increased by increasing the number of fingers, the length of the resonator, using a thin layer of high dielectric material between the conductors and the substrate or using an overlay high- k dielectric layer, which acts as a protective shield. The capacitance increases as the gaps are decreased as well. On the other hand, the inductance of the structure is dominated by the magnetic field close to the central strip that produces the magnetic energy. The inductance is dependent on the length of the center

inductor and its line width. While narrow strips inductor is more inductive owing to reduced width, such strip inductor is not expedient as the current becomes less. A trade-off will be reasonable to achieve an optimal achievable inductance.

2.2 Corporate Feed Network

Surface waves are essentially electromagnetic phenomena occurring between the dielectric interfaces of the metallic patch. They are often generated at the bends, T-junctions, cross-junctions, step discontinuity, open ends, and other discontinuities. When an excitation signal propagates along a transmission line with the presence of these discontinuities, surface waves are generated, travel and subsequently attenuate the excitation signal. This phenomenon becomes more precarious when an excitation signal propagates through a conventional corporate feed network owing to the presence of a sizeable amount of discontinuity along the signal path. A typical quarter-wave transformer stub owing to its configuration generates not only surface waves, but also substantial insertion loss. A high voltage standing wave ratio of 90 degree bends, its low impedance value of square bends, and high input reflection coefficient are reasons for the lossy nature of this type of transmission line and inadvertently compromise its efficiency. Compensation modalities such as mitered square bends decrease capacitance and also increase inductive contribution; tampering with the step discontinuity of the quarter-wave transformer mitigates the effect of parasitics by adjusting the lengths of the line, thus creating a very small offset on T-junctions. If the corporate feed line is optimized based on these identified compensation techniques, the resulting feed line will be efficient, as demonstrated in this work. Figure 2a shows the implementation of a one-stage Wilkinson power divider with nominal port impedance. The matrix of scattering parameters of the quarter-wave transmission line of length $\lambda/4$ is [8]

$$S = \begin{bmatrix} 0 & j \\ -j & 0 \end{bmatrix} \quad (1)$$

where the characteristic impedance of the line is equal to Z_0 , and Z_0 is the port nominal impedance.

3 Proposed Antenna Array Design

3.1 8×1 Corporate-Fed Array

Figure 3a shows a prototype of an 8×1 array with an optimized corporate feed network where all the discontinuities have been optimized as demonstrated in Sect. 2.2 for optimal performance. Power splits into two sub-arrays, each of four

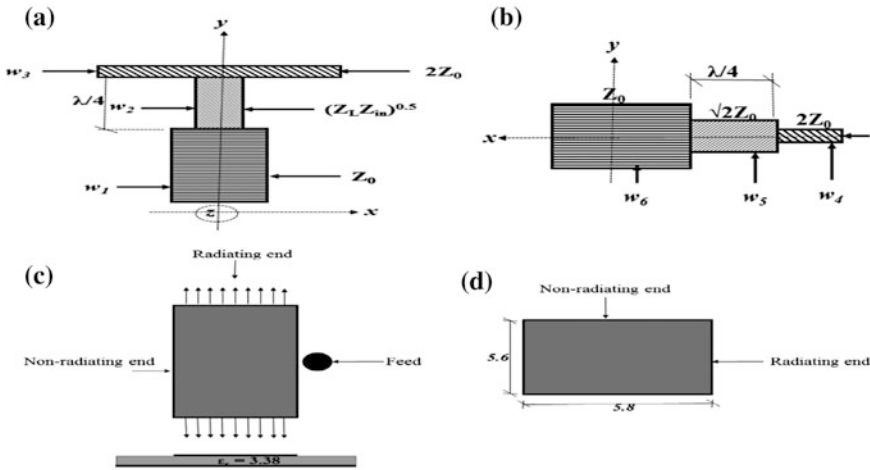


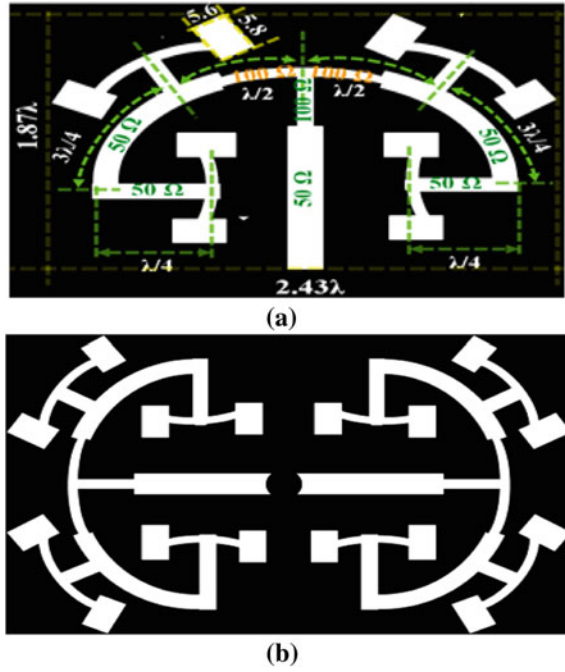
Fig. 2 Radiating element excitation mechanism. **a** Wilkinson power divider, **b** quarter-wave transformer, **c** feed location, **d** non-radiating edge

elements. The equal length splits result in equal power and equal phase to all of the feed points. The number of feeds and power divisions required is dictated by the number of microstrip radiators, as demonstrated in [9]. Each resonator is fed at the non-radiating edge as shown in Fig. 2d. It is anticipated that the non-radiating edge-fed corporate network will yield enhanced gain, higher efficiency, a wider frequency pattern, etc. [10]. This technique ensures lower insertion loss. The inter-element spacing is set at $1.3\lambda_g/2$ with approximate width of 18.2 mm. This spacing is sufficiently large to accommodate the trailing edges of the radiating elements such that the internal mutual coupling effect between neighboring junctions is avoided. The entire arrangement is fed by the proposed optimized Wilkinson power divider. The power divider denoted by the T-junction splits the 50 Ω line into two ($2 \times 100 \Omega$) as shown in Fig. 2a. The transformation from 50 to 100 Ω and vice versa is implemented as depicted by T (Fig. 2a) using the transmission line quarter-wavelength transformer shown in Fig. 2b.

The transformation is determined by the equation $\sqrt{2}Z_0$ and estimated as 70.7 Ω. The transmission line widths labeled w_1 , w_2 , and w_3 as shown in Fig. 2a, b are dependent on the characteristic impedance at each location and are determined by Eq. (2) for $w/h \geq 1$. Using the said equation, w_1 is calculated to be equal to 1.898 mm, w_2 is 1.05 mm, and w_3 is 0.46 mm with corresponding impedances of 50, 70.7, and 100 Ω, respectively.

$$Z_0 = \frac{120\pi}{\sqrt{\epsilon_{\text{eff}}} \left[\frac{w}{h} + 1.393 + \frac{2}{3} \ln \left[\frac{w}{h} + 1.444 \right] \right]} \tag{2}$$

Fig. 3 Proposed array. **a** The 8×1 , **b** the 8×2



where

$$\epsilon_0 = \frac{\epsilon_r + 1}{2} + \frac{\epsilon_r - 1}{2} \left[1 + 12 \left(\frac{h}{w} \right)^{-0.5} \right]. \tag{3}$$

3.2 8×2 Corporate-Fed Array

In Fig. 3b, the proposed antenna configuration is presented. It is a direct reflection of the 8×1 elements with two of them combined to form the 8×2 parallel array network with a common corporate feed. In order to understand the performance characteristics and the radiation pattern of the proposed antenna better, an analytical CST microwave studio employing the finite integration technique was used for full-wave analysis.

4 Experimental Results and Discussions

4.1 8×1 Corporate-Fed Array

Both antenna structures were built on Roger RO4003C microwave laminate substrate with ϵ_s of 3.38 and a thickness of 0.813 mm. The measurements of the proposed antennas were done using HP 8720B network analyzer to observe the reflection and radiation characteristics (this time along with the spectrum analyzer). Figure 4a shows the simulation and measured return loss results of the proposed antenna. For the 8×1 -element configurations, the simulated reflection coefficient was -41 dB with a bandwidth patter of 6.10–5.60 GHz at about 5.8 GHz. The measured reflection coefficient was -42 dB and an impedance bandwidth pattern of 610–5.49 GHz at 5.81 GHz. Both reflection coefficients indicate a significant matching level and good agreement. Figure 5a, b shows the simulated and measured radiation patterns of the 8×1 quasi-lumped element resonator sub-array in E - and H -planes, respectively. Two reasonable side lobe levels of about -15 dB were seen. The level of side lobes was more visible in the H -plane polar plot shown in Fig. 5a, b. The measured E -plane agreed reasonably with the simulated result but differed slightly because of a noticeable sidelobe differential of negligible magnitude.

4.2 8×2 Corporate-Fed Array

The simulated and measured return loss results of the 8×2 configuration of the proposed antenna were given in Fig. 4b. The simulated input reflection coefficient was substantial and concisely put at -49 dB, indicating a very good impedance match. The bandwidth was 6.15–5.49 GHz. The measured return impedance bandwidth loss at about 5.81 GHz was 6.01–5.61 GHz. The simulated and measured radiation pattern of the 8×1 array antenna is depicted in Fig. 5a, b, whereas Fig. 5c, d gives the simulated and measured radiation pattern of the 8×2 quasi-lumped element resonator array configuration of both the E - and H -planes. The patterns are taken at the resonant frequency for which maximum power is the highest. The simulated and measured patterns of both planes agree significantly. The radiations are inclined upward at the principal axis ($\theta = 0$) with a measured gain advantage of 19.06 dBi, as shown in Fig. 5e. A slight sidelobe level due to surrounding radiations was also noticed at the right hemisphere of the E -plane plot.

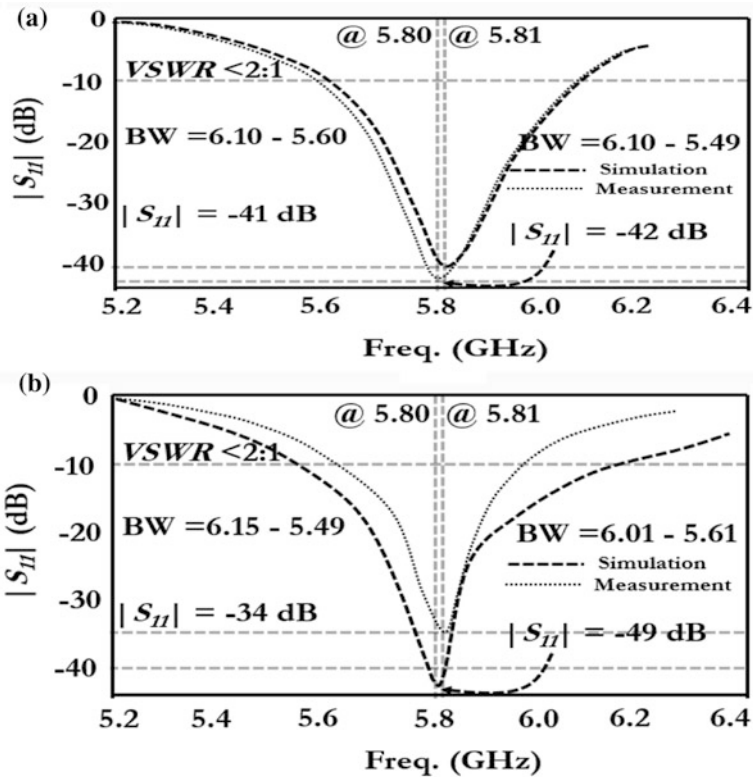


Fig. 4 Reflection coefficient of the array. a 8×1 , b 8×2

4.3 Comparison Between 8×1 and 8×2 Corporate-Fed Array

For the purpose of comparison, it was noted that a measured excess bandwidth difference of 160 MHz constituting about 32% impedance bandwidth differential was obtained in the case of the 8×2 -element array compared to the 8×1 -element array configuration. A similarly larger gain by an amount of about 36.44% was achieved in the 8×2 -element array. Another observation was the reduced side lobe level difference of about -7 dB for the E -plane and -2.13 for the H -plane over the 8×2 -element array. It was therefore obvious that the 8×2 -element array exhibited better bandwidth, an enhanced directional characteristic and a lower sidelobe level with a reasonable gain excess of 5.09 dBi.

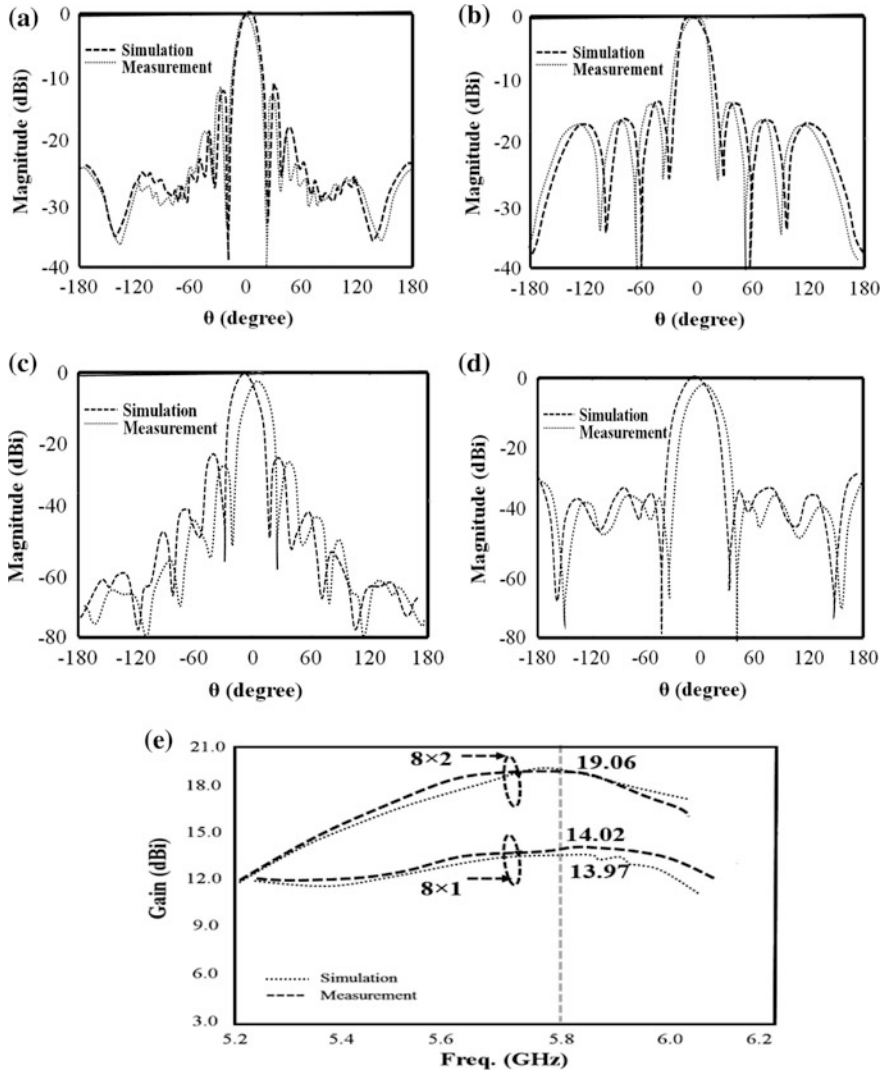


Fig. 5 Directive characteristics. **a** E-plane of 8×1 , **b** H-plane of 8×1 , **c** E-plane of 8×2 , **d** H-plane of 8×2 , **e** gain

5 Conclusion

Experimental study on the design of a quasi-lumped element resonator antenna array with corporate feed was carried out, both for 8×1 - and 8×2 -element arrays. All the designs demonstrated brilliant impedance match. The simulated and measured results were in good agreement. It was found that a quasi-lumped element

resonator was not only suitable for antenna design but had a compact size advantage. The 8×1 configuration demonstrated real estate of $1.87\lambda \times 2.43\lambda \text{ mm}^2$, while the 8×2 configuration indicated a size of twice the 8×2 array. Comparative analysis carried out between the 8×1 - and 8×2 -element sub-arrays showed that the 8×2 -element array had a better performance profile with a reasonable gain advantage of 5.09 dBi.

References

1. Lu K. H., and Chang T.-N., "Circularly polarized array antenna with corporate-feed network and series-feed elements," *IEEE Transactions on Antennas and Propagation*, vol. 53, no. 10, pp. 3288–3292, (2005).
2. Olokede S. S., Adamariko C. A., Almohammad T. A., Jiya E. A., "A novel t-fed 4-element quasi-lumped resonator antenna array," *Radioengineering*, vol. 23, no. 2, pp. 717–723, (2014).
3. Joubert J., and Odendaal J.W., "2×2 etched slot array with corporate slotline feed network," *Electr. Letts.*, vol. 44, no. 14, pp. 833–834, (2008).
4. A. Chen, Y.-J Zhang, and Z.-H Chen, "A Ka-band high-gain circularly polarized microstrip antenna array," *IEEE Antennas and Wireless Propagation Letters*, vol. 9, pp. 1115–1118, (2010).
5. Hong J. S., and Lancaster M. J., *Microstrip filters for RF/microwave applications*. John Wiley & Sons Inc., Hoboken, N.J., (2001).
6. Ain M. F., Olokede S. S., Qasaymeh Y. M., Marzuki A., Mohammed J. J., Sreekantan S., Hutagalung S. D., Ahmad Z. A., Abdullah M. Z., "A novel 5.8 GHz quasi-lumped element resonator antenna," *Int. J. Electron. Commun. (AEU)*, vol. 67, no. 7, pp. 557–563, (2013).
7. Hung F., Avenhaus B., Lancaster M.J., 'Lumped element switchable superconducting filters', *IEE Proceeding of Microwave and Antenna Propagations*, vol. 145, no. 3, pp. 229–233, (1999).
8. Djordjevic A. R., Bazdar M.B., Harrington R.F., Sakar T.K., *Scattering parameters of microwave networks with multi-conductor transmission lines, versions 2.0*, (Software and user's manual). Boston: Artech house, (1999).
9. Muson R. E., "Conformal microstrip antenna and microstrip phased arrays," *IEEE Trans. on Antennas and Propagation*, vol. 22, no. 1, pp. 74–78, (1974).
10. Gray D. P., Ravipati C. B., Shafai, L., "Corporate fed microstrip arrays with non radiating edge fed microstrip patches," *IEEE Antennas and Propagation Society International Symposium*, vol. 2, pp. 1130–1133, (1998).

Development of a Drowsy Driver Detection System Based on EEG and IR-based Eye Blink Detection Analysis

Oindrila Sinha, Soumendra Singh, A. Mitra, S. K. Ghosh and S. Raha

Abstract Driver fatigue leading to drowsy driving is a severe traffic safety problem and is widely believed to be one of the largest contributors to fatalities and severe injuries on the road at present. Nodding off for just three seconds or less while driving can prove fatal. Drowsy driving slows reaction times, reduces vigilance, impairs information processing and creates un-mindfulness. We have developed a detection system for drivers under drowsiness, using non-invasive sensors. The system uses brain-computer interface (BCI) to determine the mental attention level of the driver following a complex recursive algorithm. In order to reduce false alarms in such detection system, we have incorporated two additional sensors in it. Infrared (IR) trans-receiver system emits an infrared signal to the eyes and another infrared photoresistor measures the reflected wave. The reflectivity of the open eye is grossly different from closed eye owing to the structure and presence of tear film in the eye. The microcontroller continuously compares and detects the difference in eye-blinking patterns of a normal person and that of a driver under drowsiness. The sleeping driver has certainly less or no eye blinking, which will be detected online and immediately without any time lag to prevent accident. Finally, a 3-axis compass sensor placed on the steering wheel will detect further the angular movement of the steering wheel of the vehicle. The driver under drowsiness will show an irregularity in eye-blinking pattern together with an abnormality in steering movement. On coincidence of all the three sensors, in order to reduce any false alarm, the driver will be alerted with a blinking LED placed within his/her view angle. If the driver does not respond and the statistics do not come back to normal, the software would prompt to apply emergency brakes automatically and simultaneously it would send SMS/email to the concerned authorities. The vehicle may also be fitted with additional blinking lights visible to other drivers too, to alert them on the road.

S. Singh (✉) · A. Mitra · S. K. Ghosh · S. Raha
Department of Physics, Centre for Astroparticle Physics and Space Science,
Bose Institute, Block - EN, Sector - V, Salt Lake City, Kolkata 700091, India
e-mail: soumendras@gmail.com

O. Sinha
Presidency University, 86/1 College Street, Kolkata 700073, India

© Springer Nature Singapore Pte Ltd. 2018
R. Bera et al. (eds.), *Advances in Communication, Devices and Networking*,
Lecture Notes in Electrical Engineering 462,
https://doi.org/10.1007/978-981-10-7901-6_34

Keywords Drowsy driver · EEG sensor · Blink sensor · Arduino
LabVIEW · Data acquisition

1 Introduction

In recent years, drowsiness or sleepiness has been attributed as a major contributory factor to all the major traffic accidents. The American National Highway Traffic Safety Administration (NHTSA) estimates that drowsy driving was responsible for 72,000 crashes, 44,000 injuries, and 800 deaths in 2013 [1]. However, these numbers are underestimated and up to 6000 fatal crashes each year may be caused by drowsy drivers [2–4]. The statistics are really alarming. With our stressed lifestyle where sleep deprivation is a common problem of the masses, accidents related to drowsiness should really be answered. Sleep deprivation increases the risk of sleep-related crashes; less the people sleep, the greater is the risk of an accident on wheels.

Sleep-related crashes are most common in young people, especially men, adults with children and shift workers. According to the NSF's 2002 poll, adults belonging to the age group of 18–29 are more likely to drive, while drowsy, compared to other age groups. Men are more likely than women to drive while drowsy (56 vs. 45%) and are almost twice as likely as women to fall asleep while driving (22 vs. 12%). Shift workers are more likely to fall asleep at wheels than those who work a regular daytime as it interrupts the circadian cycle of the body. According to a study by the AAA Foundation for Traffic Safety, people who sleep six to seven hours a night are twice as likely to be involved in such a crash as those sleeping 8 h or more, while people sleeping less than 5 h increased their risk four to five times [4]. A study by researchers in Australia showed that being awake for 18 h produced an impairment equal to a blood alcohol concentration (BAC) of 0.05, and 0.10 after 24 h; when 0.08 is considered legally drunk. Many other researches indicate that commercial drivers as well as people suffering from undiagnosed sleep disorders such as sleep apnea and acute insomnia are also at greater risk in fall asleep road crashes.

According to a recent report of NHTSA, driver performance-related factor, falling asleep on the wheels, is the most significant factor in the occurrence of fatal road crashes. This is followed by other factors including alcohol use and unmanageable vehicle speed. It is reported that driver's drowsiness and fatigue lead to 3.6% of fatal crashes. In 2002, the National Sleep Foundation (NSF) also reported that 51% of adult drivers kept driving even under the drowsy condition, and it is shocking to learn that 17% of which had actually fallen asleep on a moving vehicle.

Recently, researchers have tried to develop different techniques of fatigue detection and countermeasure technologies, in which electroencephalography (EEG) is a substantial contributor. However, EEG techniques have been found to be much more reliable, as the reproducibility of data was found to be more accurate than other biomedical techniques which seem to be in its infancy. Many other works on this field have been based on EOG (Electrooculogram) as well as the

facial muscle change detection system. Recently a drowsy driver detection system was developed using non-intrusive machine vision-based concept. The system uses a small monochrome security camera that points directly toward the driver's face and monitors the driver's eyes in order to detect fatigue. In such a case when fatigue is detected, a warning signal is issued to alert the driver [5, 6]. The problem with such system is that the photograph quality of the camera used should be very high, which largely increases the cost of the production therefore decreasing the chance of its use in real-time product due to cost ineffectiveness. Another system for detecting impairment of a driver of a vehicle was made with a sensor for sensing a position of the driver's head at a plurality of time points, an alarm for alerting the driver and a microprocessor. The microprocessor is configured to determine changes in the position of the driver's head between the plurality of time points and evaluate whether the changes in the position of the driver's head between the plurality of time points exhibit at least one of a periodic and a quasiperiodic pattern and determine whether the driver is impaired based on the pattern of the changes in the position of the driver's head and, if the driver is impaired, it alerts the driver using the alarm [7]. The drawback of such a system includes the lack of similarity in the head position of all the drivers.

However, the society is still waiting for a reliable product which could detect as well as set countermeasures for drivers under drowsiness to save lives and resources.

Although a lot of work in this field aims to cater to the complex problem of drowsy driver syndrome and falling asleep at the wheels, a flawless system answering all the parts of complexities have still not been invented. With this project, we aim to integrate all the different parts of this problem in a single product and increase its efficiency and as well as to make it a real-time product, which can actually be used to solve this acute problem and save lives.

2 Materials and Methods

Materials: All the materials used in the prototype design have been purchased from the local market. To the extent of our knowledge and capacity, the materials used were of not only highest purity but also keeping in mind the cost feasibility of the crude materials.

Figure 1 shows the sensor arrangement and dataflow diagram and connection flow. Figure 2 shows a real photograph of hardware integrated drowsy driver alert system.

EEG detection Sensor: The electrodes (microwave mobile headset) used to measure EEG are purchased from NeuroSky and have been hardware integrated to the cap of the prototype to ease the process of data acquisition. We use the physiological signals acquired by the electrodes to detect drowsiness by using mathematically derived attention level curve. The values of the attention level are continuously acquired by the sensor and are stored to the system computer via

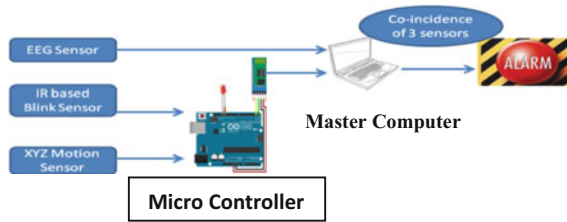


Fig. 1 Schematic diagram of the designed setup. Figure shows the dataflow from all the three sensors to the microcontroller and the master computer

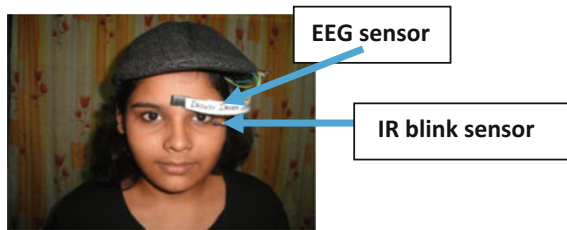


Fig. 2 Photograph to show the placement of sensors and hardware integration of the sensor in the cap. The sensor is to be placed on the forehead and the IR led and photodetector pair assembly are to be placed in front of eyes to measurement reflectivity data

Bluetooth. Mindwave mobile is a wireless device, which records the EEG signal with the help of a single electrode placed on the forehead using wireless bluetooth technology. The received signals are then evaluated using software developed on LabVIEW platform and the alarm is generated as and when a drowsy state is detected. The mindwave mobile is preferred over conventional wet electrodes because of its basic advantages like the absence of conductive gel for long time EEG measurement, the need of a single sensor on FP1. The reference electrode present in the ear clip thus removes ambient noise and provides less erroneous data. It also has the property of signal amplification as well as noise cancellation.

Commercial grade **infrared LED and photodetector pair** is purchased from local market. The pair is powered using ARDUINO UNO microcontroller. The analog output pin was then connected to the analog input pin of the microcontroller. A Bluetooth breakout board HC-05 was connected to the arduino for wireless data transfer to the computer. The IR from the led is designed to be incident on the eyes if the driver the reflected signal back to the photodetector. The reflected signal is collected and passed on to the microcontroller which transfers it back to the master computer for analysis.

The connected master computer runs on the software developed on LabVIEW platform which checks for incoming data from EEG and counts for pulse owing to the blink related difference of reflectivity in the photodetector.

Software: The programming code has been developed on the LabVIEW platform. As shown in Fig. 3, the flowchart clearly shows that the software checks for EEG data converted to attention level via a for loop thus guaranteeing 10 number of input data from the sensor. The master computer collects data in parallel with the other two sensors. The collected data is then analyzed online for determination of the drowsy state of the driver. The software also caters for an alarm sounding if such state is detected. Figure 4 shows the screenshot of the developed software and its indicators and controls.

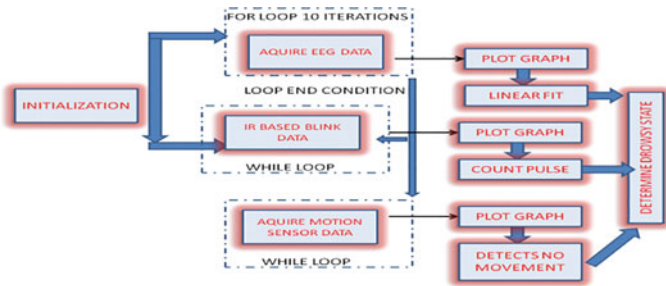


Fig. 3 Flow chart of the developed software in the LabVIEW platform for the data acquisition and online monitoring/alarm sounding

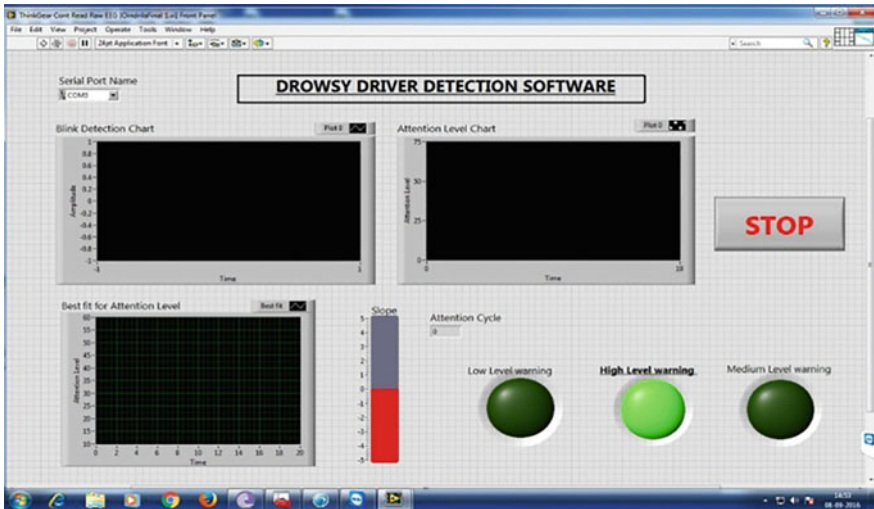


Fig. 4 Screenshot of the developed software

3 Results and Discussion

The data from the EEG sensor is received by the computer and is plotted in real time. After successful acquisition for 10 signals in an un-calibrated scale of 0–100, a liner fit is applied on the acquired data. The real-time results of the liner fit are displayed on the screen and the slope of the data becomes a marker of the attention state of an individual. A negative slope is an indicator of a person’s losing attention level. We have concluded by repeated experimentation that a slope value to -2 might be an ambiguous indicator of a sleeping human. Figure 5 shows the falling attention level curve and can be one of the precursors of sleep condition. All measurements are relative to a particular individual and thus can be applied to everybody without worry about the case to case-specific problems.

The blink sensor data is actually a measure of the difference between the IR reflectivity of the open and closed eyes. An IR trans-receiver has been designed and the arduino is set to read the analog values of the photodetector. With every eyeblink the sensor records a pulse and the pulse count after a fixed interval of time. The pulse count becomes the marker of a number of eyeblinks of a person. A sleeping human being will always record a different number of pulses than a fully aware person. With repeated experimentation we have determined that less than eight blinks in 10 s (which is our deterministic interval) is the reference marker of a sleeping individual. Figure 6 shows a sample data of the eye blink patterns recorded with our setup. It is to be mentioned that the amplitudes of the peak are not relevant to the conclusion and hence this can also be applied to various human beings.

The third sensor is a 3-axis compass which is attached to the steering to record movement by assessing the peak to peak values within a fixed threshold.

The coincidence of all the alarm condition of three sensors will conclusively decide the drowsy driver and hence can raise the alarm. However, EEG sensor and eye blink sensor individual alarm condition will produce a low-level and a medium-level warning respectively. The warning condition is manifested by the blinking lights for the safety of other drivers and by application of emergency brakes followed by sending email and SMS to pre-defined numbers via a GSM module.

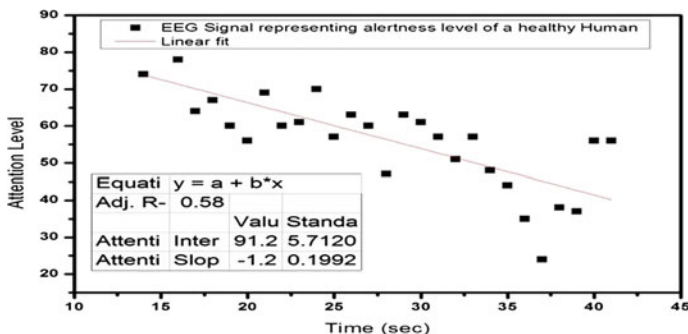
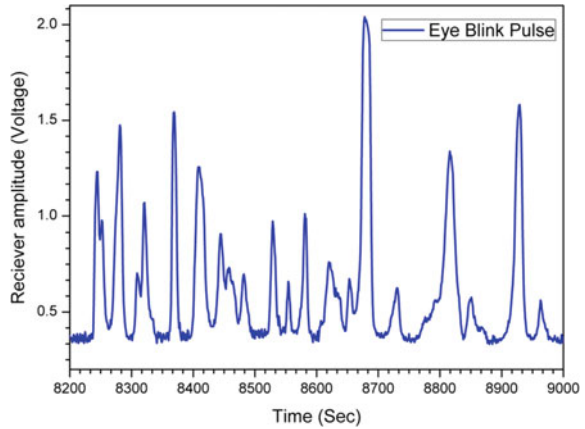


Fig. 5 Falling attention of a sleeping individual

Fig. 6 Pulse pattern attributed to eye blinking of human subjects in the IR-based system. The developed software intelligently understands the blink pattern difference between an alert and a drowsy individual



4 Conclusion

We present design and construction at a low cost (25,000 INR with master computer and 15,000 INR with only the software) sensor-based driver-monitoring system to effectively decide the sleep condition to avoid fatal road accidents. The advantage over other existing systems has been discussed and possible remedies are also suggested. The simplicity of the design is shown and the “cap” is made ready for the use of non-trained labor.

Acknowledgments We wish to thank Dr. Sanat Kr. Das and Dr. Abhijit Chatterjee for their constant valuable inputs throughout the work.

References

1. National Highway Traffic Safety Administration. Research on Drowsy Driving. Accessed October 20, 2015.
2. Masten SV, Stutts JC, Martell CA. Predicting daytime and nighttime drowsy driving crashes based on crash characteristic models. 50th Annual Proceedings, Association for the Advancement of Automotive Medicine; October 2006; Chicago, IL.
3. Klauer SG, Dingus TA, Neale VL, Sudweeks JD, Ramsey DJ. The Impact of Driver Inattention on Near-Crash/Crash Risk: An Analysis Using the 100-Car Naturalistic Study Data, 2006. Springfield, VA: DOT; year. DOT HS 810 594.
4. Tefft BC, AAA Foundation for Traffic Safety. Prevalence of Motor Vehicle Crashes Involving Drowsy Drivers, United States, 2009–2013 [457 KB]. Washington, DC: AAA Foundation for Traffic Safety; 2014. October 19, 2015.
5. TENGshe, V. V. and V. G. TENGshe (2007). Drowsy driving alarm system, Google Patents.
6. Parmar, N. (2002). “Drowsy driver detection system.” Engineering Design Project Thesis, Ryerson University.
7. Wu, R., et al. (2016). Drowsy driver detection system, Google Patents.

Microstrip Patch Antenna with Fractal Structure Using Superstrate Operating in ISM Band

Shreema Manna, Tanushree Bose and Rabindranath Bera

Abstract The designed microstrip patch antenna has a planner structure and operates in industrial, scientific and medical (ISM) band. The operating centre frequency of ISM band is 2.45 GHz. The final structure has been achieved after three iterations. Cross-type fractal with a superstrate layer is introduced here. The superstrate layer is used in all the iterations. When a superstrate is used on a microstrip antenna, the antenna properties like its radiation efficiency, gain, return loss, VSWR, resonant frequency and bandwidth are changed which may alter the antenna performance. The antenna structures are simulated in IE3D platform. A comparison of return loss, bandwidth, gain, directivity, VSWR, radiation pattern and overall area of the patch is also presented in this paper.

Keywords Patch antenna · ISM band · Fractal design · Superstrate

1 Introduction

Nowadays, the interest is growing rapidly in the domain of wearable technology, especially wearable devices for medical, military and security applications. A wearable medical device helps in monitoring the patients' health condition from a distant place. The antenna within the wearable device is the main component which helps in sending the biological signal to a distant place. Proper antenna must be designed for such devices. The size and structure of the antenna, which is mainly

S. Manna (✉) · T. Bose · R. Bera
Sikkim Manipal Institute of Technology, Majitar, Rangpo, Sikkim, India
e-mail: shreema123@gmail.com

T. Bose
e-mail: tanushree.contact@gmail.com

R. Bera
e-mail: rbera50@gmail.com

the structure of the radiating patch, are very much crucial for such devices as the device is wearable. Mechanical structure of such antenna is provided by the substrate which is the intermediate layer between patch and the ground plane. The most antenna parameters such as radiation pattern, efficiency, gain, bandwidth, resonant frequency depend on the permittivity of the dielectric used. In this proposed work, the substrate material used is Roger 5880 having dielectric constant 10.2. Industrial, scientific and medical band (ISM band) of frequency 2.4–2.5 GHz with centre frequency 2.45 GHz are recommended by Federal Commission Communication (FCC) for wearable medical devices. Several studies are going on around the globe on the design of different off-body wearable communication system. From [1–6], the research work was on the design of wearable antenna operating both as on-body and off-body communication system operating in ISM band.

2 Antenna Designs

The proposed antenna structures are designed and simulated in IE3D platform. The final antenna structure is achieved in three iterations and is simulated using IE3D. S parameter display illustrates that the final antenna covers ISM band from 2.37 to 2.47 GHz with centre frequency of 2.42 GHz. The antennas are simulated using dielectric having permittivity 10.2 and thickness of 1.6 mm. Copper is used as metal layer of the patch and the ground plane. All the three iterations are further simulated using a superstrate layer of copper of thickness 1.9 mm. The metal layer for ground plane and the patch has thickness of 0.002 mm. The structure is assembled as patch on one side and ground plane on the other side of the substrate. Microstrip line feed has been used in all the iterations.

The width of the microstrip patch antenna is calculated using the following standard formula,

$$W = \frac{1}{2f_r \sqrt{\mu_0 \epsilon_0}} \sqrt{\frac{2}{\epsilon_r + 1}} = \frac{v_0}{2f_r} \sqrt{\frac{2}{\epsilon_r + 1}}$$

The effective length of the microstrip patch is calculated as,

$$\Delta L_{\text{eff}} = 0.412h \frac{(\epsilon_{\text{reff}} + 3) \left(\frac{w}{h} + 0.264\right)}{(\epsilon_{\text{reff}} - 0.258) \left(\frac{w}{h} + 0.8\right)}$$

$$L_{\text{eff}} = L + 2\Delta L_{\text{eff}}$$

where effective permittivity is given as

$$\epsilon_{\text{reff}} = \frac{\epsilon_r + 1}{2} + \frac{1}{2} \frac{\epsilon_r - 1}{\sqrt{1 + \frac{12h}{w}}}$$

The resonant frequency

$$f_r = \frac{v_0}{2\sqrt{\epsilon_{\text{reff}}}} \frac{1}{(L + 2\Delta L_{\text{eff}})}$$

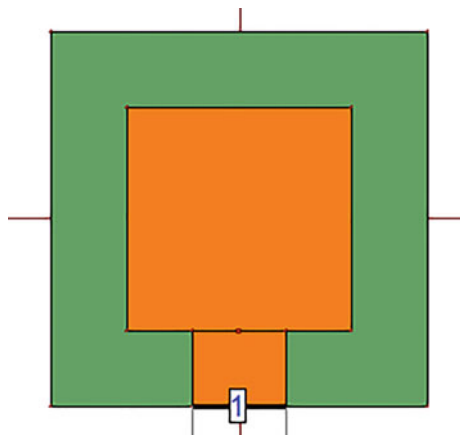
In this case of antenna design, the values considered for calculations are: resonant frequency (f_r) of 2.45 GHz and permittivity (ϵ_r) of the dielectric material is of 10.2 with substrate height (h) 1.9 mm. By substituting these values in the above formulas, we get the dimension of patch as $24 \times 24 \text{ mm}^2$. Hence, the simulation has been started using patch having this dimension.

3 Results and Discussion

Initially in the zeroth iteration, a $24 \times 24 \text{ mm}^2$ square copper plate is used as radiating patch and $40 \times 40 \text{ mm}^2$ square copper plate is used as ground plane as shown in Fig. 1. The S parameter display of zeroth iteration is shown in Fig. 2. It shows that the antenna covers the bandwidth 2.40–2.54 GHz with centre frequency of 2.47 GHz and return loss of -26.9 dB . The centre frequency is shifted by 0.02 GHz from the target frequency of 2.45 GHz, but the bandwidth covers the whole ISM band.

Figure 3 shows a structure with first iteration. A fractal design of cross-structure has been introduced. The ground is cut accordingly to provide size reduction and

Fig. 1 Iteration 0 radiating patch



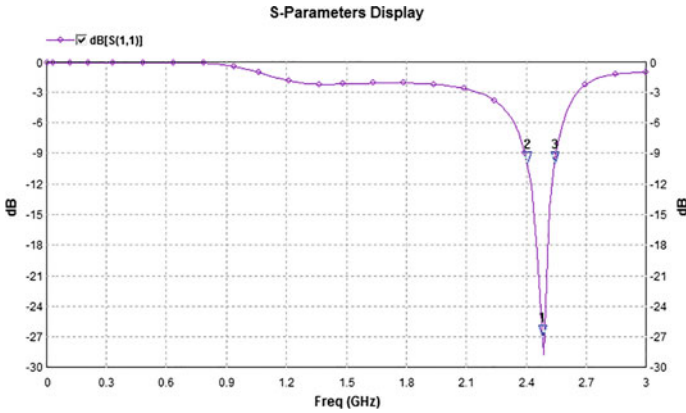
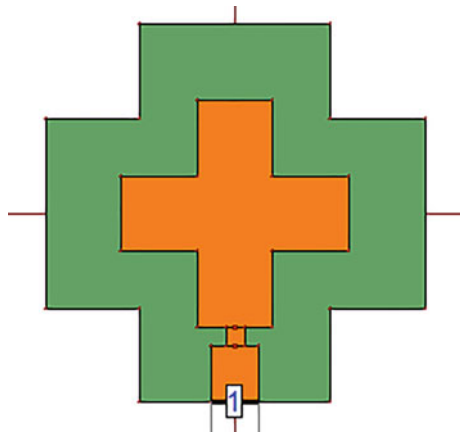


Fig. 2 S_{11} display of iteration 0

Fig. 3 Iteration 1 patch



compactness to the antenna without compromising much with its efficiency. The following Fig. 4 depicts its corresponding S parameter. The simulation result shows that the antenna of iteration 1 covers the bandwidth from 2.43 to 2.58 GHz with centre frequency 2.51 GHz and return loss of -12.6 dB.

In the second iteration, a second level of fractal of cross-structure has been introduced. As an effect, the dimension of the patch is much reduced but the overall structure is not reduced. Figures 5 and 6 show the structure of the antenna and S_{11} parameter, respectively. From the S parameter display, it is clear that the antenna covers the band of 0.1 GHz ranging from 2.32 to 2.43 GHz with centre frequency 2.38 GHz. The return loss achieved is -21.9 dB. This shows much improvement in return loss than the first iteration.

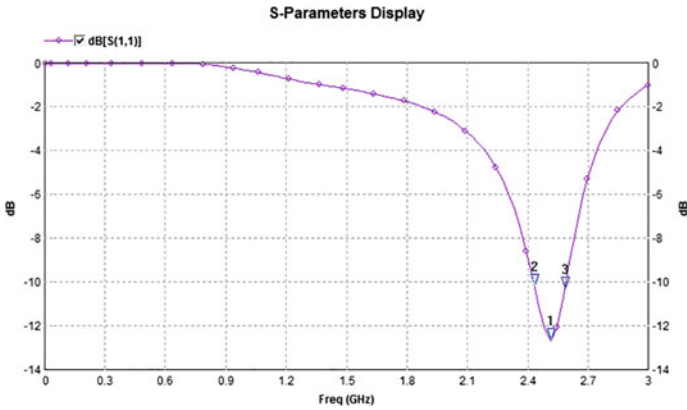
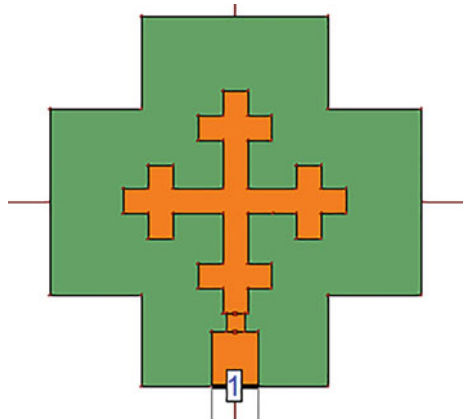


Fig. 4 S_{11} display of iteration 1

Fig. 5 Iteration 2 patch



The result is slightly shifted from that of the ISM band, which ranges between 2.4 and 2.5 GHz. Figure 7 shows the final structure with superstrate. Figure 8 displays its corresponding S parameter.

From the simulation, result shows that the designed antenna covers the band from 2.35 to 2.47 GHz with centre frequency 2.42 GHz and return loss of -36.37 dB.

Table 1 provides the comparison of different parameters of the different iterations of the designed antenna. From the table, it is clear that there substantial improvement in the resonant frequency and return loss when we incorporate superstrate. A complete omnidirectional radiation pattern is achieved in all the

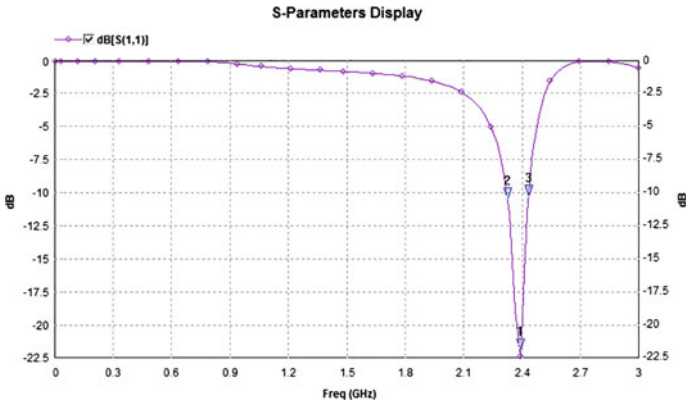
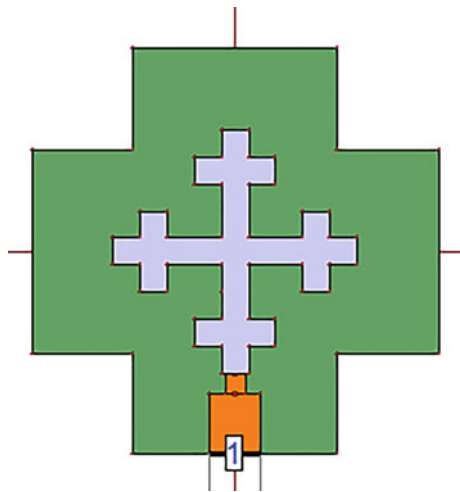


Fig. 6 S_{11} display of iteration 2

Fig. 7 Second iteration patch with superstrate



iterations. The first iteration is very inefficient since the centre frequency is much shifted from the target frequency of 2.45 GHz, also the return loss is very poor (only -12.6 dB) and VSWR is 4.13 which is not acceptable. The VSWR is improved in different iterations. In the final structure, a VSWR of 0.52 is achieved at the resonant frequency of 2.42 GHz and bandwidth of 12 MHz. Also, the return loss is very good in the final structure.

Table 2 shows the same comparison of different parameters of the different iterations with superstrate of the designed antenna. The copper is used as the

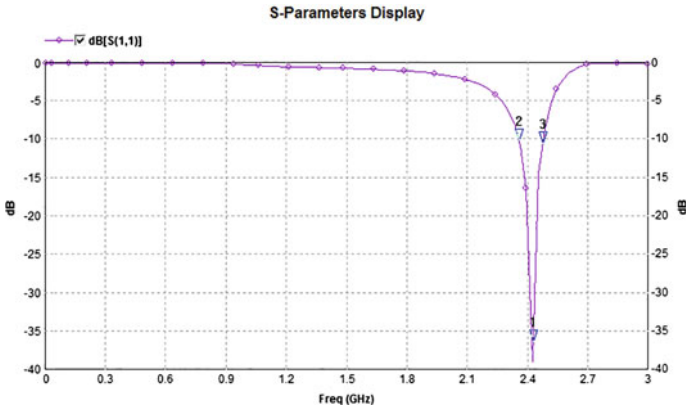


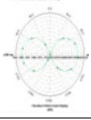
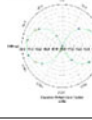
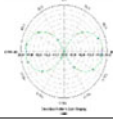
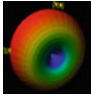
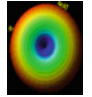
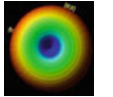
Fig. 8 S_{11} display

Table 1 Comparison of different parameters of the designed antenna **without superstrate**

Parameters	Iteration 0	Iteration 1	Iteration 2
Frequency band (GHz)	2.40–2.54	2.43–2.58	2.32–2.43
Band width (GHz)	0.14	0.15	0.11
Centre frequency (GHz)	2.47	2.51	2.38
Return loss (dB)	-26.9	-12.6	-21.9
Gain	3.02	2.53	2.46
Directivity	3.56	2.9	2.94
2D pattern			
3D pattern			
VSWR (dB)	1.3	4.13	1.62
Overall area of the patch	576 mm ²	323.208 mm ²	179.56 mm ²

radiating element, and dielectric having permittivity 10.2 is used as the substrate in between. In Table 2, the improvement of the parameters over Table 1 is highlighted by bold. From both the comparison table, it is clear that the return loss, gain, directivity, VSWR are significantly improved after incorporating superstrate.

Table 2 Comparison of different parameters of the designed antenna with superstrate of height 1.9 mm

Parameters	Iteration 0	Iteration 1	Iteration 2
Frequency band (GHz)	2.40–2.54	2.40–2.52	2.37–2.49
Band width (GHz)	0.14	0.12	0.12
Centre frequency (GHz)	2.47	2.47	2.42
Return loss (dB)	−27.15	−14.10	−21.1
Gain	3.32	2.36	2.46
Directivity	4.99	2.9	2.97
2D pattern			
3D pattern			
VSWR (dB)	0.87	3.53	1.62
Overall area of the patch	576 mm ²	323.208 mm ²	179.56 m ²

4 Conclusion

This paper presented an antenna structure incorporating fractal and groove structure. The final antenna design is achieved after successive iterations. A comparison table of all the structures is also presented in this paper. From the table, it is clear that the final structure proved the best result in terms of resonating frequency, VSWR, return loss, radiation pattern and patch dimension.

References

1. Koichi Ito, Chia – Hsien Lin, “Dual mode wearable antenna for medical applications”, Antenna Technology (IWAT) International Workshop, IEEE 2013.
2. Gareth A Conway, William G. Scanlon, “Antennas for over-body-surface communication at 2.45 GHz”, IEEE Transaction on Antennas and Propagation, 2009.
3. Asimina Kiourti, Konstantina S. Nikita, “Miniature scalp implantable antennas for telemetry in the ISM and MICS bands: design, safety considerations and link budget analysis”, IEEE Transaction on Antennas and Propagation, 2012.
4. Md. Masudur Rahman, Md. Mozaffor Hossain, Kallol Krishna Karmakar, “II shaped microstrip antenna design for WiMAX, WiFi and biomedical application at 2.45 GHz”, IEEE International Advanced Computing Conference, 2013.
5. Haroon, S. Ullah, J. A. Flint, “Electro-textile based wearable patch antenna on biodegradable poly lactic acid (PLA) plastic substrate for 2.45 GHz, ISM band applications”, IEEE 2014.
6. Sen Yan, Gui A. E. Vandenbosch, “Radiation pattern-reconfigurable wearable antenna based on metamaterial structure”, IEEE Antennas and Wireless Propagation Letters, Vol. 15, 2016.

Assessment of Pulse-Doppler Radar and Digital Beamforming Radar

Nima Donka Tamang, Samarendra Nath Sur, Soumyasree Bera and Rabindranath Bera

Abstract In radar domain, digital beamforming radar is evolving as a promising radar technology as compared to conventional pulse-Doppler radar. The design of PD radar and DBF radar is done by keeping all the design parameters same, and its performance is compared in this work. Needless to say that PD radar uses only analog systems but DBF radar uses digital systems. DBF radar's performance is high, as compared to PD radar because of the use of digital techniques and MIMO antennas. The difference in signal to clutter ratio is 5.23 dB, i.e., SNR of DBF radar is three times greater than PD radar. The only limitation of DBF radar is being the hardware complexity, due to the use of multiple transceivers at each element of an antenna array, resulting in increased cost, size, weight, and power of the overall system.

Keywords Pulse-Doppler radar · Digital beamforming radar · Multiple-input multiple-output · Constant false alarm rate · Spread spectrum digital beamforming

1 Introduction

Starting from identifying the enemy planes to announcing early warning of a tornado or tsunami, the radar technology has been extensively used and is one of the most vital technologies in the current world. Pulse-Doppler radar can measure

N. D. Tamang (✉) · S. N. Sur · S. Bera · R. Bera
Department of Electronics and Communication Engineering,
Sikkim Manipal University, Rangpo, Sikkim, India
e-mail: nimadonka18@gmail.com

S. N. Sur
e-mail: samar.sur@gmail.com

S. Bera
e-mail: soumyasree.bera@gmail.com

R. Bera
e-mail: rbera50@gmail.com

target range and velocity of both immobile and moving target almost accurately after the pulse compression. Velocity is found out by sending the successive pulses toward the target and measuring the in-between phase difference of the returned signal from the target [1–3]. In PD, radar target will be detected along with strong unwanted peaks or clutter since it does not use any digital techniques to increase SNR at the receiver. It is also susceptible to jamming since no anti-jamming measures are taken.

In order to enhance the features, such as increased SNR at the receiver contemporary radar, use multiple-input and multiple-output (MIMO) antennas along with digital beamforming techniques. The use of manifold antennas at the transmitter and receiver will result in an array gain as well as multiplexing gain. An area for fresh research MIMO technology increases the performance of wireless communication systems at no extra cost of spectrum, only hardware complexity proliferates [4].

With DBF, techniques in radar result in target detection with suppressed unwanted peaks or clutter after PC and an increased SNR. But the main constraint toward implementation of DBF in radar, radio frequency sensing systems, and communication systems is its requirement of manifold transceiver modules for each antenna element. This leads to an increment in weight, size, power, and cost of the overall system [5].

Some works have been done to eradicate the problem of using manifold transceiver elements by merging the features of spread spectrum techniques with DBF resulting in SSDBF in [6–8].

A platform for learning TDM MIMO DBF concept where a single transceiver element is used which is presented in this paper. With mathematical examination and experiment results indicating this idea can reduce the number of transceiver elements and reduce budget, also it can gain greater angular resolution as compared to conventional DBF radar [9].

SMILE, a new technique with one RF channel and DBF skills, based on smart antenna receiver array is projected by Fredrick et al. in [10] which shrink the necessity of bulk RF hardware for most smart antenna systems. It also decreases power dissipation as well as circuit size. This is achieved by sampling the envelope of received signal at each antenna element, followed by multiplexing, down-converting, de-multiplexing, filtering, and then finally digitizing to be processed under lesser speeds.

2 Mathematical Model for DBF RADAR

2.1 For Transmitter

Phased array antenna is used to transmit $x[m]$ the information signal that signifies data, into a specific region in space [11–13]. The complex weight multiplication stage is the primary stage of DBF transmitter where multiplication of information

signal $i[m]$ with the real part and the imaginary part of the complex weight takes place subsequently we get two signals $i_n[m]$ and $q_n[m]$ from individual antenna channel which is given as follows:

$$i_n[m] = x[m] \operatorname{Re}\{w * n\}, \quad (1)$$

$$q_n[m] = x[m] \operatorname{Im}\{w * n\}, \quad (2)$$

where $\{w * n\}$ is the complex weight and θ_n is the phase delay

$$w * n = e^{j\theta_n} = \operatorname{Cos} \theta_n + j \operatorname{Sin} \theta_n, \quad n = 0, 1, 2, \dots, N \quad (3)$$

$$\text{where } \operatorname{Re}\{w * n\} = A_n \operatorname{Cos} [\theta_n] \quad (4)$$

$$\operatorname{Im}\{w * n\} = A_n \operatorname{Sin} [\theta_n] \quad (5)$$

The digital up-conversion stage is the second stage of the DBF transmitter. Here a digital local oscillator generates a sinusoidal signal and its 90° phase-shifted version; these signals are multiplied with $i_n[m]$ and $q_n[m]$. The result of this multiplication is:

$$f i_n[m] = i_n[m] \operatorname{Cos} [w_{IF}m] = A_n x[m] \operatorname{Cos} [\theta_n] \operatorname{Cos} [w_{IF}m], \quad (6)$$

$$f q_n[m] = i_n[m] \operatorname{Sin} [w_{IF}m] = A_n x[m] \operatorname{Sin} [\theta_n] \operatorname{Sin} [w_{IF}m], \quad (7)$$

Now, the signals $f i_n[m]$ and $f q_n[m]$ are denoted using trigonometric identities in the following form:

$$f i_n[m] = \frac{A_n \cdot x[m]}{2} \operatorname{Cos} [w_{IF}m + \theta_n] + 2 \operatorname{Cos} [w_{IF}m - \theta_n], \quad (8)$$

$$f q_n[m] = \frac{A_n \cdot x[m]}{2} \operatorname{Cos} [w_{IF}m - \theta_n] - 2 \operatorname{Cos} [w_{IF}m + \theta_n], \quad (9)$$

Conversion of digital signal into analog domain is the last stage of DBF transmitter. If DAC having a sampling frequency f_s is used, then result of DAC is denoted as follows:

$$f_n(t) = f[m]_{m=fs} = A_n \cdot x(fs) \operatorname{Cos} (w_{IF}fst - \theta_n), \quad (10)$$

where A_n is the complex weight's magnitude and $f[m]$ is the band-pass signal.

To simplify $f_n(t)$, the constant f_S in the signal $x(t f_S)$ will be deleted and the variable $w_{IF} = \omega_{IF} f_S$ will be used to differentiate the cosine component in the analog domain from its digital representation. Finally, the output of DBF transmitter is

$$f_n(t) = A_n x(t) \cos(w_{IF} t - \theta_n). \quad (11)$$

2.2 For Receiver

The incident plane wave on an antenna array's receiver can be modeled by the following equation:

$$\begin{aligned} f(t, p_n) &= x(t - \tau_n) (\cos w_{RF}(t - \tau_n)), \quad n = 0 \dots N - 1 \\ &\approx x t \cos w_{RF} t - \theta_n, \end{aligned} \quad (12)$$

where θ_n is given by $\theta_n = w_{RF} \tau_n$.

RF modulation stage has an LO with frequency w_{LO} , and modulation is done as follows:

$$g'_n(t) = x(t) \cos(w_{RF} t - \theta_n) \cos(w_{LO} t) \quad (13)$$

Using trigonometric identities, the signal $g(t)$ can be represented as a sum of two cosines:

$$g'_n(t) = \frac{x(t)}{2} [\cos(\omega_{IF} t - \theta_n)], \quad (14)$$

$$\text{where, } w_{IF} \triangleq w_{RF} - w_{LO}, w_{IM} \triangleq w_{RF} + w_{LO}, \quad (15)$$

If passband filters with gain $G = 2$ are used centered at the signal's component with ω_{IF} as its center frequency, the output signal obtained as:

$$g_n(t) = x(t) \cos(w_{IF} t - \theta_n). \quad (16)$$

The ADCs with a sampling rate T_S can be used to transform the signal into a digital representation:

$$g(m) = g_n(t) = x[mT_S] \cos[w_{IF} mT_S - \theta_n] \quad (17)$$

The digital signal observed in each DBF receiver channel n of the phased array antenna PAA is:

$$g[m] = x[m] \cos[\omega_{IF}m - \theta_n] \quad (18)$$

The digital down-conversion is performed by multiplying the digital signal with a sinusoidal signal and a 90° phase-shifted version of the sinusoidal signal both generated by digital local oscillator. Both mathematical operations can be represented in the following form

$$i'_n[m] = g_n[m] \cos[\omega_{DLO}m] = x[m] \cos[\omega_{IF}m - \theta_n] \cos[\omega_{DLO}m] \quad (19)$$

$$q'_n[m] = g_n[m] \sin[\omega_{DLO}m] = x[m] \cos[\omega_{IF}m - \theta_n] \sin[\omega_{DLO}m] \quad (20)$$

$$i_n'[m] = \frac{x(m)}{2} (\cos[2\omega_{IF}m] + \cos[\]), \quad (21)$$

$$q_n'[\] = \frac{x(m)}{2} (\sin[2\omega_{IF}m] + \sin[\theta_n]) \quad (22)$$

$$i[m] = [m] \cos[\theta_n] \quad (23)$$

$$q[m] = [m] \cos[\theta_n] \quad (24)$$

The second stage of the DBF receiver is the complex weight multiplication (CWM) stage. To represent this complex multiplication operation, a signal $[m]$ will be defined which is composed of the signals $i_n'[m]$ and $q_n'[m]$:

$$[m] = [m] - jq_n[m] = x[m] (\cos[\theta_n] - j \sin[\theta_n]) = x[m] e^{-j\theta_n} \quad (25)$$

The last stage of the DBF receiver involves the addition of all the resulting signals,

$$y_n[m] : y[m] = \frac{1}{N} \sum_{n=0}^{N-1} y_n[m] = \frac{1}{N} \sum_{n=0}^{N-1} r_n[m] + j \frac{1}{N} \sum_{n=0}^{N-1} s_n[m] = r[m] + js[m] \quad (26)$$

3 Pulsed-Doppler Radar

3.1 Block Diagram of Pulse-Doppler Radar System

Linear frequency modulated (LFM) waveform is used as input waveform [14]. In LFM, the frequency is swept linearly across the pulse width, either upward (up-chirp) or downward (down-chirp) or in other words, frequency of input signal varies linearly with time over its pulse duration. The waveform includes the real part and the imaginary part (Fig. 1).

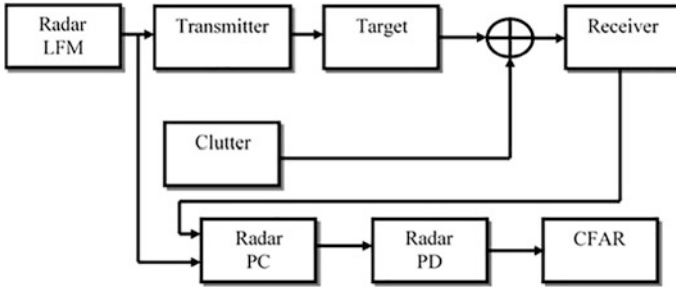


Fig. 1 Block diagram of pulse-Doppler radar system

The equation for LFM chirp signal is as follows:

$$s(t) = \exp(j\phi(t)) \tag{27}$$

where $\phi(t) = 2\pi(f_0 + kt^2)$ is the instantaneous phase

A linear function of time of the instantaneous frequency is articulated as:

$$\frac{1}{2}\pi\left(\frac{d\phi}{dt}\right), f_i = f_0 + kt. \tag{28}$$

where k is the slope and f_0 is the fundamental frequency.

We have designed a pulse-Doppler radar, and the input waveform used is LFM signal. The block diagram consists of the input waveform block, transmitter, target, clutter, receiver, and various signal processing blocks. Inside the transmitter block, it consists of the input waveform, oscillators, amplifiers, filters, and modulators. The input source is sampled, and it is up-converted to RF by a power amplifier and is transmitted toward the target. The ECHO and clutter are added and sent toward the receiver.

At the receiver, the RF signal is demodulated and the carrier is detached; hence, we get the baseband signal which is transformed into complex form and further sent for signal processing. The PC block, PD, and CFAR blocks are used for signal processing. After the PC, the output signal level is at 23.96 dB, clutter level is at 21.552 dB, signal to clutter ratio (SCR) = 2.43 dB.

3.2 Results and Plots

(I) Radar Linear Frequency Modulated Waveform (Fig. 2)

Here red colored signal is the real part and blue is the imaginary part.

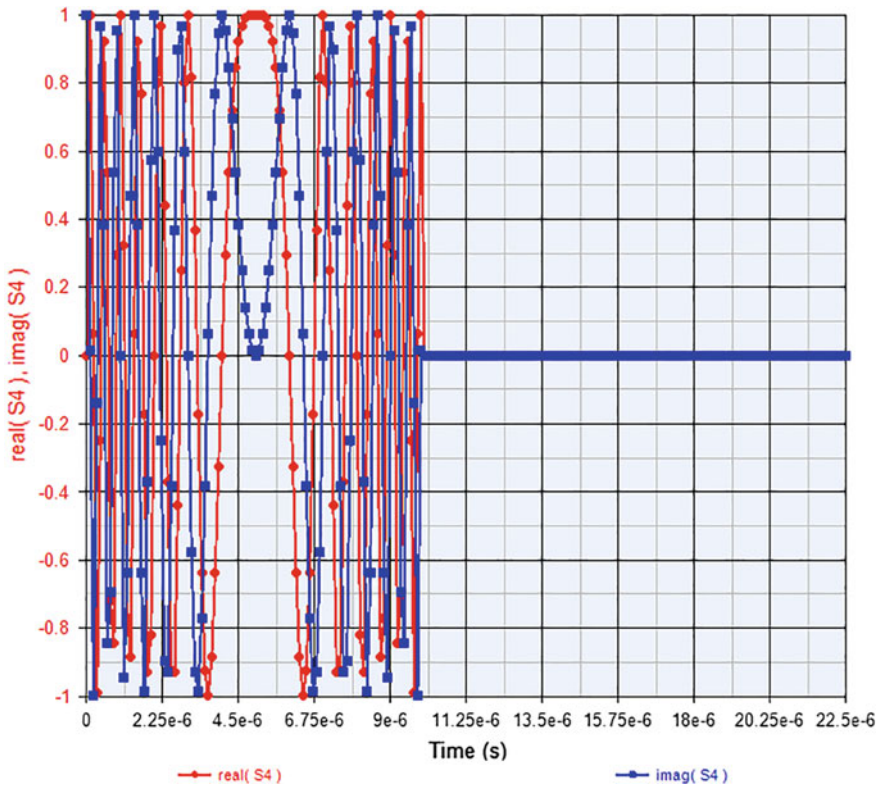


Fig. 2 Radar LFM signal [15]

- (II) **Radar Pulse Compression Output at $v_t = 80$ m/s distance = 100 km**
(Fig. 3)
- (III) **Constant False Alarm Rate Output at $v_t = 80$ m/s distance = 100 km**
(Fig. 4)

4 Digital Beamforming Radar

4.1 Basics of Beamforming

To generate the desired beam pattern in the same path as that of the target with an antenna array, beamforming techniques are used. It is a method where individual radiation from each antenna will be superimposed or added up in one preferred direction of interest to give higher directivity or gain. It is advantageous in

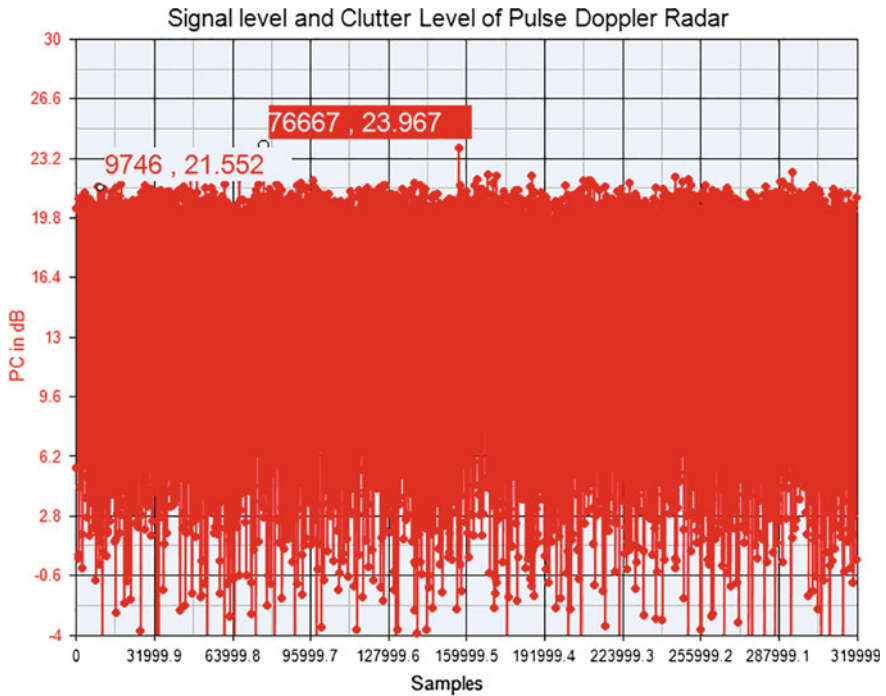


Fig. 3 Target detection after PC [15]

improving SNR at the receiver. Different types of beamforming techniques are analog beamforming and digital beamforming. In this paper, we discuss only DBF.

4.2 Block Diagram DBF

(I) DBF

DBF is a signal processing method applied in the sensor arrays for directional signal transmissions or reception. It is done in baseband. Using DBF, all functions are executed in digital, and dedicated DSP chips are used for this. The DBF techniques require multiple transceiver elements for each antenna in an array. This results in hardware complexity, thereby increasing the cost, size, weight, and power of the overall system. The advantage being the increased SNR at the receiver. After PC with the signal level at -6.478 dB, and the clutter level is at -14.139 dB, we are getting signal to clutter (SCR) = 7.66 dB which is much greater than the PD radar keeping same design specifications as PD radar. The radar signal processing blocks are same as PD radar, and other blocks are explained in details below (Fig. 5).

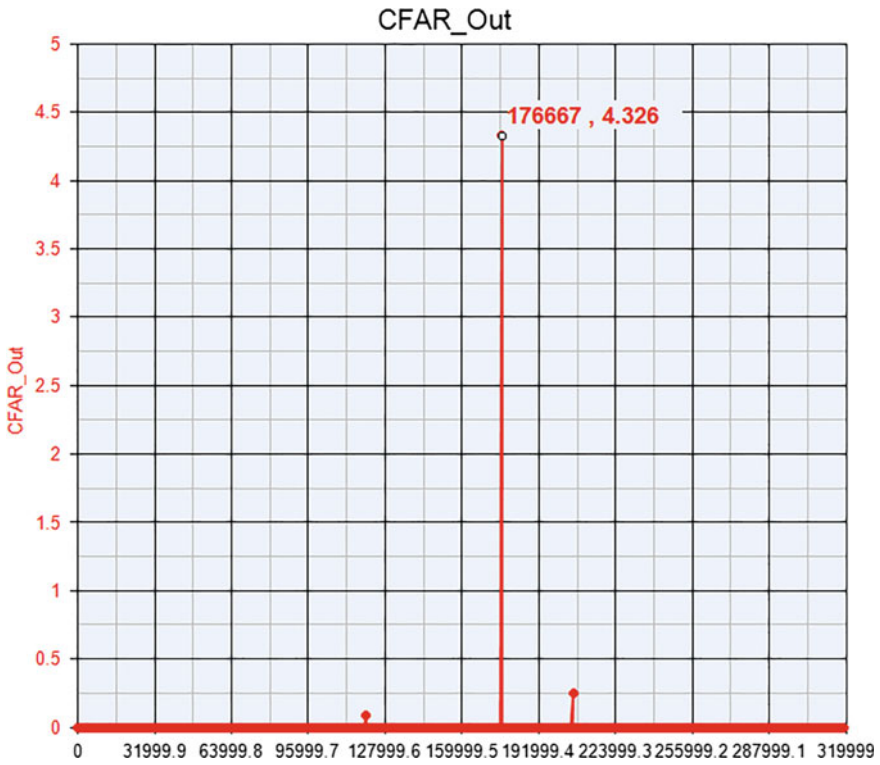


Fig. 4 Target detection after CFAR [15]

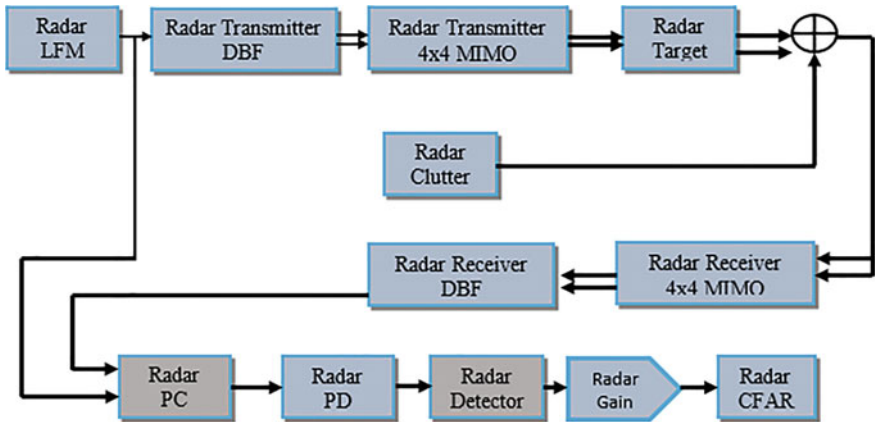


Fig. 5 Block diagram of digital beamforming radar

(II) Radar Transmitter DBF Block

This model is used for transmitting signal digital beam synthesis. It is used to synthesize the main lobe along the direction determined by theta and phi. Only linear array and rectangular planar array are supported. In this model, the number of antennas in the x -axis is 4 and in the y -axis is 4. Hence, the total number of antenna is 16. The separation is $\lambda/2$ for two adjacent antennas. If the separation is $\lambda/2$ for two antennas, then the signal can be added constructively.

(III) Radar Transmitter Block (4×4 MIMO)

This model is a conceptual multi-channel digital up-converter and RF transmitter model. A total of 16 such channels of this model are there inside radar transmitter 4×4 block. The amplifier, mixer, and analog BPF models are used to simulate the RF sub-system. The DUC block is used to simulate the DUC and D/A functions. It is used for the up-conversion of the signal received from radar Tx_DBS_2D block. There are two stages of up-conversion process in this block. In the first stage, the signal is up-converted to IF of 70 MHz and then again to 1GHz. After this block, the signal is ready to be transmitted using antenna array (Fig. 6).

(IV) Radar Receiver Block (4×4 MIMO)

This model is a conceptual multi-channels RF receiver and digital down-converter model. A total of 16 such channels of this model are there inside radar receiver 4×4 block. The amplifier, mixer, LO, delay line, and analog BPF models are used to simulate the RF receiver sub-system. The digital down-converter block (DDC) is used to simulate the A/D functions and digital down-converter functions (Fig. 7).

It is basically the receiver block which is responsible for the reception of signals transmitted by the antenna array. This block can be considered as the receiver front end. Here the signals from 16 different antennas are processed separately. First, the signal is passed through the amplifier block. If the RF signal is converted into IF of 70 MHz, then the IF signal is processed through the radar DDC block which will convert the IF signal into baseband signal for 16 different antennas.

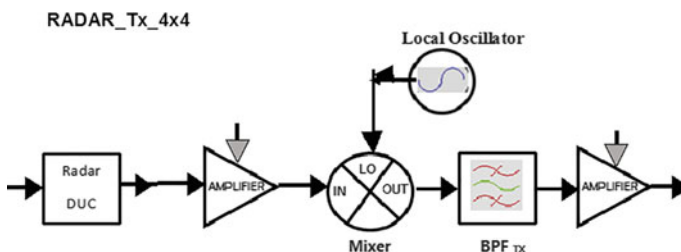


Fig. 6 Radar transmitter block (4×4) [15]

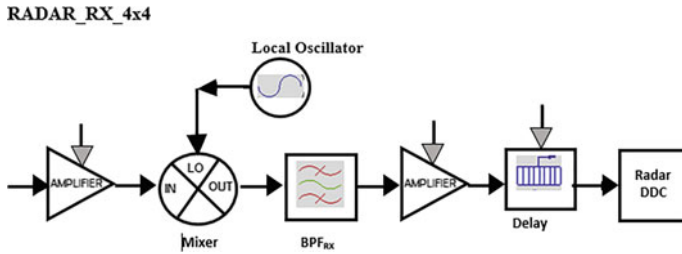


Fig. 7 Radar receiver block (4 × 4) [15]

(V) **RADAR RX-DBS-2D**

This model is used for digital beamforming. This block is responsible for the addition of same signal from 16 different antennas to make the resultant pattern determined by theta and phi in order to extract the information.

4.3 Results and Plots

- (I) **Radar Pulse Compression Output at $V_t = 80$ m/s distance = 100 km**
(Fig. 8)
- (II) **Constant False Alarm Rate Output at $V_t = 80$ m/s distance = 100 km**
(Fig. 9)

5 Comparison of Pulse-Doppler Radar and SSDBF Radar

See Table 1.

6 Conclusion

The assessment is done to verify the performance of PD radar and DBF radar. In doing so, we found out that PD radar can find target range and velocity almost accurately.

Keeping all the system specifications same of both PD radar and DBF radar and with target power at 0.029 W and clutter power 6.911×10^{-21} W, there was a difference in SCR at the output of PC. The difference in SCR is 5.23 dB, i.e., SNR of DBF radar is three times greater than PD radar. This difference is the result of use of digital techniques and MIMO antenna system. The only drawback of DBF radar

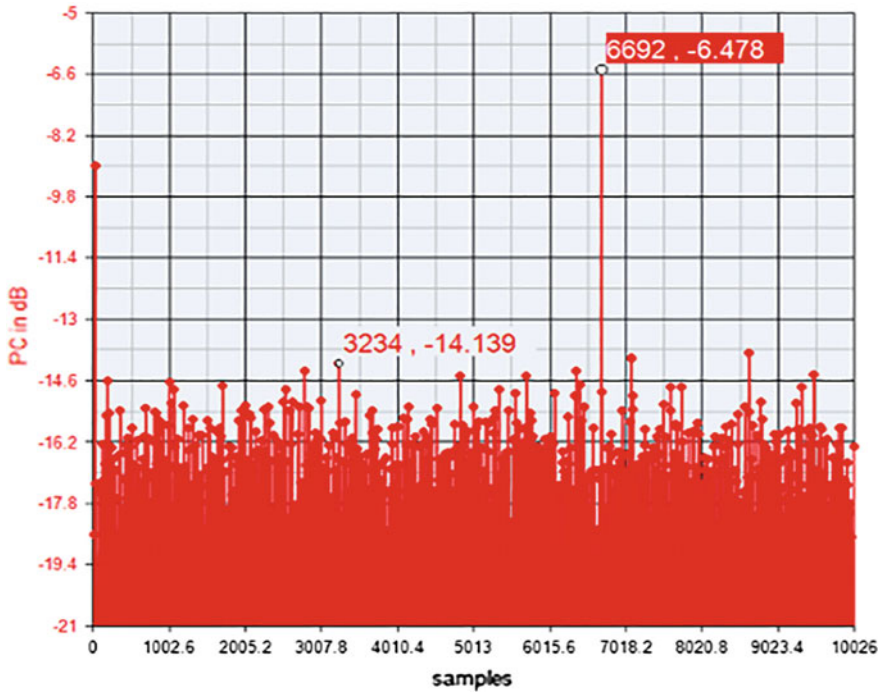


Fig. 8 Target detection after PC [15]

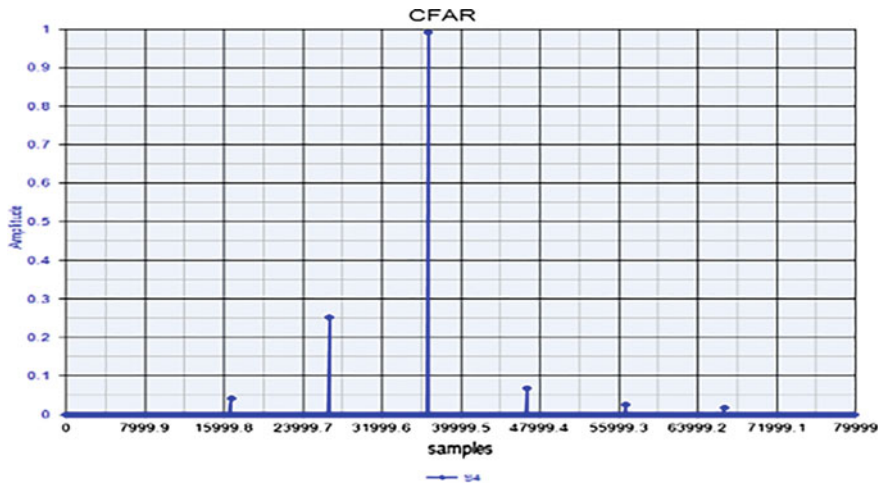


Fig. 9 Target detection after CFAR [15]

Table 1 Comparison of pulse-Doppler radar and SSDBF radar

Sl. no.	Pulse-Doppler radar	DBF
1	Single antenna system	Multiple antenna systems (4×4 MIMO)
2	After pulse compression, the target is being detected along with strong unwanted peaks, i.e., clutter	After pulse compression, the target is being detected with suppressed clutter
3	Signal level is at 23.96 dB. Clutter level is at 21.552 dB. Signal to clutter difference (SCR) = 2.43 dB (from Fig. 3)	Signal level is at -6.478 dB. Clutter level is at -14.139 dB. Signal to clutter difference (SCR) = 7.66 dB (from Fig. 8)

is the use of multiple transceiver elements which makes it not CSWAP empowered system. Therefore in future, we can move toward design of systems which are CSWAP-enabled system. With the use of TDM, CDMA, etc., techniques with DBF, we can eliminate the drawback of the use of multiple transceiver elements.

References

1. Skolnik: Radar Handbook, 2nd ed. McGraw-Hill, Inc., pp 22–24, (1990).
2. Mahafza, Bassem R.: Radar Systems Analysis and Design Using MATLAB, *Third Edition*. CRC press, pp. 282–283, (2013).
3. Richards, M. A.: Fundamentals of radar signal processing. Tata McGraw-Hill Education. (2005).
4. X Gu, X-H Peng and G C Zhang.: MIMO systems for broadband wireless communications, BT Technology Journal, Vol. 24, pp-90–96, April 2006.
5. Haynes, T.: A Primer on Digital Beamforming, Spectrum Signal Processing vol. 11, pp-1–15, (1998).
6. Bergamo M. A., and Weedon W. H.: Spread spectrum digital beamforming virtual array and scalability to millimeter wavelength frequencies MMW-SSDBF virtual array, In Phased Array Systems and Technology, IEEE International Symposium on, pp. 649–652, (2013).
7. Bergamo M. A.: Spread Spectrum Digital Beamforming, In Phased Array Systems and Technology (ARRAY), IEEE International Symposium, vol. 7, pp. 651–657, (2010).
8. Bera S., Sur S. N., and Bera R.: Spread Spectrum-Digital Beam Forming Radar with Single RF Channel for Automotive Application, 9th International Radar symposium, pp. 1–5, (2013).
9. Tang, Y., & Lu, Y.: Single transceiver-based time division multiplexing multiple-input–multiple-output digital beamforming radar system concepts and experiments, IET Radar, Sonar & Navigation, vol. 8(4), pp. 368–375, (2013).
10. Fredrick, J. D., Wang, Y., Itoh, T.: A smart antenna receiver array using a single RF channel and digital beamforming. IEEE Transactions on Microwave Theory and Techniques, vol-50 (12), pp-3052–3058, (2002).
11. Okorogu, V. N., Nwalozie, G. C., Okoli, K. C., & Okoye. E. D.: Design and simulation of a low cost digital beamforming (DBF) receiver for wireless communication, International Journal of Innovative Technology, pp 1–17, (2013).

12. Juan A. Torres-Rosario.: Implementation of a Phased Array Antenna Using Digital Beamforming, Master of Sciences. In Electrical Engineering, University Of Puerto Rico, Mayagüez Campus, pp 1–233, (2005).
13. Haynes, T.: A Primer on Digital Beamforming, Spectrum Signal Processing vol. 11, pp-1–15, (1998).
14. Parwana, S., Kumar, S.: Analysis of LFM and NLFM radar waveforms and their performance analysis, International Research Journal of Engineering and Technology, pp-1–6, (2015).
15. Agilent SystemVue 2013.01.

FMCW Waveform-Based Vehicular Radar

Additi Mrinal Singh and Rabindranath Bera

Abstract Millimeter wave frequency modulation continuous wave (FMCW) waveform is very popular for its range and velocity detection for vehicular applications. However, it has false target detection problem in multiple target scenarios. This paper presents a double FMCW waveform for target detection in multi-target situations. This approach is considered to reduce the false target detection and to solve the ambiguity problem. Then Range–Doppler under different conditions is tested and shown in this paper.

Keywords Frequency modulation continuous wave · Double frequency modulation continuous wave · Multiple targets

1 Introduction

Radar is a target detection system that is in use since 1930 for the detection and estimation of target-related information such as range, angle, velocity, and direction [1]. Sensors such as radar-, lidar-, and UWB-based driver safety system are in use to enhance road and driving safety [2]. Among this, radar is the most popular sensor used for vehicular safety due to its working capability in dark, rain and foggy conditions. Functions of vehicular radar are adaptive cruise control, blind spot monitoring, crash mitigation, and collision warning system. Today vehicular radar uses millimeter wave as an active safety system to improve driving efficiency and improve safety on road due to its small size, such that it can be fitted in vehicles without taking much space. Automotive long-range radar system works on frequency of 76–77 GHz, and most commonly used LRR is FMCW. FMCW is a

A. M. Singh (✉) · R. Bera
Department of Electronics and Communication Engineering,
Sikkim Manipal Institute of Technology, Majitar, Rangpo 737136, Sikkim, India
e-mail: adittimrinal18@gmail.com

R. Bera
e-mail: rbera50@gmail.com

special type of radar sensor which radiates continuous transmission power like simple continuous wave radar [3–6]. To avoid accidents, the most important requirement is to detect the target and other objects in its surroundings. So, in this paper, target detection capability of FMCW radar under different conditions is tested using MATLAB and is shown in Sect. 4.

2 Related Works

The multiple target detection and the problem of mutual interference have been addressed by several authors. In this section, an overview over multiple target detection using FMCW and mutual interference problem reasons is discussed. In [1], a new waveform design was proposed, and a 2D-FFT was considered to estimate the velocity and range information. The principle used in this paper allows the use of very broadband sweeps. The main aim of FMCW vehicular radars is to obtain the velocity and range information from the beat frequency, which has propagation delay and Doppler frequency [5]. However, in multiple target detection scenario, FMCW radar suffers from ambiguity problem of the range–velocity [6], which causes false target detection and target miss.

3 FMCW Design and Multi-target Algorithm

FMCW radar is a system in which an electromagnetic signal is transmitted continuously [1]. For measuring the range and velocity simultaneously for single and multiple targets, FMCW radar is used. It is also used due to its high resolution, low-power transmission, and low cost.

FMCW has a transmitter, receiver, and mixer [2]. A modulated signal is passed through transmitter and receives a reflected echo from target (Fig. 1). The difference between the transmitted and received signal is known as the beat frequency, and it

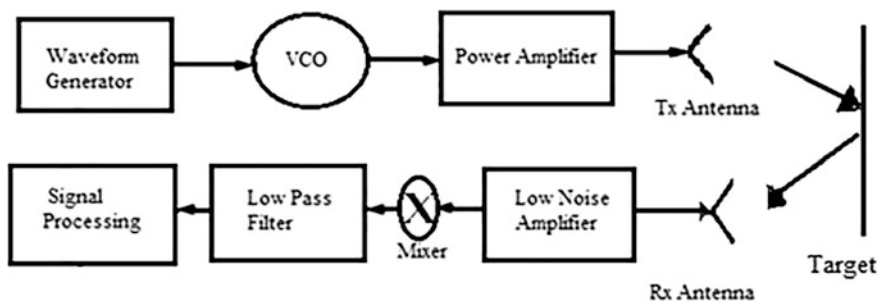


Fig. 1 Block diagram of a FMCW radar system

is used to solve R and V estimation [3]. But it is suitable for single target only; in case of multiple target, we get ghost target and false target detection. Therefore, dual FMCW modulation technique is approached in this paper for more accurate range and velocity detection, without ghost target interruption even in the case of multiple target detection scenario.

3.1 Waveform Design

The maximum range, the range resolution, and velocity resolution are main requirements for automotive radar systems. The maximum target distance that any radar can measure is called as radar range and is 250 m for long-range automotive radar.

$$R = \frac{c \tau}{2} \quad (1)$$

$$\tau = \frac{2R}{c} \quad (2)$$

$$\vartheta = \frac{c f_d}{2 f_c} \quad (3)$$

$$f_d = \frac{2\vartheta}{\lambda} \quad (4)$$

where τ is time delay, V is radial velocity, f_d is Doppler frequency, c is propagation constant, f_c is carrier frequency, λ is c/f_c . Range resolution is the ability of the radar to detect two or more objects in close proximity as different target with the same velocity. If there is two or more objects, it is needed to be separated by radar to get two distinct echo signals. Similarly, velocity resolution (Δv) is the minimum distinguishable velocity with the same range [7]. The range resolution of the radar is 1 m, and the velocity resolution is 1.3 km/h calculated by performing MATLAB operation. Therefore,

$$\Delta R = \frac{c}{2B} \quad (5)$$

$$\Delta \vartheta = \frac{c}{2f_c T} \quad (6)$$

$$f_s \geq \frac{2B R_{\max}}{cT} + \frac{2f_c \vartheta}{c} \quad (7)$$

$$f_b = \frac{2RB}{Tc} \quad (8)$$

$$\left. \begin{aligned} f_{b_u} &= f_b + f_d \\ f_{b_d} &= f_b - f_d \end{aligned} \right\} \tag{9}$$

$$\left. \begin{aligned} R_{est} &= \frac{cT}{8B}(f_{b_u} + f_{b_d}) \\ V_{est} &= \frac{c}{4f_c}(f_{b_u} - f_{b_d}) \end{aligned} \right\} \tag{10}$$

The sampling frequency is denoted by f_s , f_b is the beat frequency, f_{b_u} and f_{b_d} are the beat frequencies for up and down chirp, and B is bandwidth. For double FMCW [8], two FMCW waveforms are considered with slightly different slopes and same bandwidth as given in Fig. 2. Considering the maximum range and velocity, the beat frequency of the waveforms are determined using the formula:

$$\left. \begin{aligned} f_{b_u1} &= f_b + f_d \\ f_{b_d1} &= f_b - f_d \end{aligned} \right\} \tag{11}$$

$$\left. \begin{aligned} f_{b_u2} &= f_b + f_d \\ f_{b_d2} &= f_b - f_d \end{aligned} \right\} \tag{12}$$

By pairing the up and down beat frequencies of both the waveforms, the estimated range and velocity will be determined [8] using:

$$\left. \begin{aligned} R_{est,i} &= \left(\frac{cT}{8B}\right)(f_{b_ui} + f_{b_di}) \\ V_{est,i} &= \frac{c}{4f_c}(f_{b_ui} - f_{b_di}) \end{aligned} \right\} \tag{13}$$

where $R_{est,i}$ and $V_{est,i}$ are estimated range and velocity of target ($i = 1, 2$) for both the waveforms. The system specification for dual FMCW waveform is given below in Table 1.

Fig. 2 Proposed double FMCW waveform

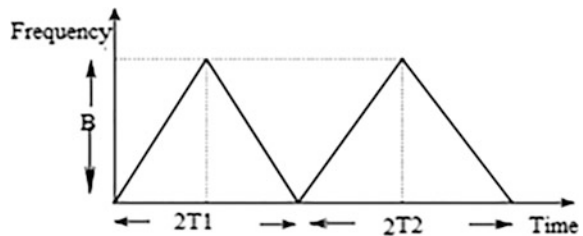


Table 1 Design specification

Parameter	Value
Range	250 m
Max. radial velocity	230 kmph
Range resolution	1 m
Velocity resolution	1 km/h
Bandwidth	150 m
Ramp duration	7e-06s, 7.7e-06s

4 Simulation Result

In this section, multiple target detection under different scenario is considered, and its range–Doppler response is presented using MATLAB Simulink. The working model of FMCW waveform-based vehicular radar system is given in Fig. 3. Two targets are considered here; first target is a car and second target is a heavy-load vehicle. The modulated signal is transmitted by the transmitter, and the reflected echo signal is received by the receiving antenna. The signal is then passed through the mixer, and signal processing of the signal is done; then the range and velocity are calculated. The targets moving at 19.445 and 18.889 m/s are at the range of 70 and 90 m, respectively. The maximum range considered for 77 GHz FMCW radar is 250 m, and maximum velocity is ± 180 km/h. The range and velocity resolution for this operating frequency are 1 m and 1.3 km/h, respectively.

The range–Doppler graph in Fig. 4 represents a Doppler versus range graph of multiple targets detected under different scenario. The top-left Doppler–range response is a situation when radar is constant and both targets are approaching toward it. The middle graph represents the situation when radar is constant and both the targets are approaching toward it. The top-right graph represents the radar moving at certain speed; the first target is approaching toward radar, and second target is receding away from it. The left bottom figure represents that both the targets are approaching toward the radar when radar is moving. The middle graph represents that radar is moving and both the targets are receding. The last figure in right is the output graph of radar moving at 100 km/h, and the targets are moving at same speed as radar.

The velocity and range under different condition are analyzed, and the actual and estimated range and velocity calculated when radar is moving at the rate of 27.77 m/s are given in Table 2. Here we observe that the target range and velocity are detected correctly without ghost target interference.

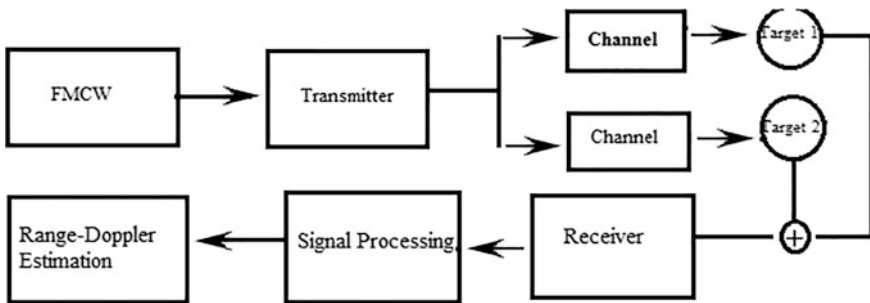


Fig. 3 FMCW waveform-based vehicular radar

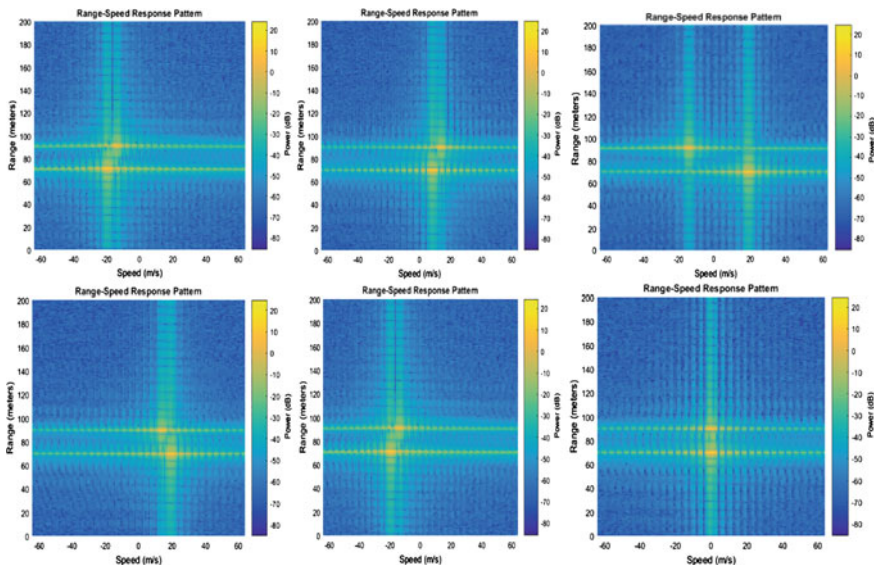


Fig. 4 Range–Doppler response of multiple targets under different conditions

Table 2 Actual and estimated range and velocity

S. No.	Target range (T1, T2) m		Target velocity (V1, V2) m/s		Radar velocity (m/s)	Est. range (in m)		Est. velocity (in m/s)	
I	70	90	19.445	18.88	0	70.23	90.20	-20.14	-18.07
II	70	90	-19.445	-18.88	27.778	69.99	90.20	18.33	18.49
III	70	90	-19.445	18.88	0	70.02	90.23	-20.04	16.42
IV	70	90	19.445	18.88	0	69.92	90.21	20.73	19
V	70	90	-19.445	-18.33	27.778	70.20	90.23	-19.72	-15.57
VI	70	90	27.77	27.77	27.778	70.15	90.20	0.49	2.11

5 Conclusion

In this paper, multiple target detection using dual FMCW waveform is approached to reduce false target detection. By comparing the results obtained from two waveforms, the nearest range and velocity are considered. The R and V estimation under different conditions is tested and shown. The minimum detectable velocity resolution calculated from this experiment is 1.3 km/h.

References

1. Minki Song, et al.: The Velocity And Range Detection Using The 2D-FFT Scheme For Automotive Radars, Department of Electronics and Computer Engineering Hanyang University, Seoul, Korea, IEEE, pp. 507–510, (2014).
2. J. Dickmann, et al.: Automotive Radar the Key Technology For Autonomous Driving - From Detection and Ranging to Environmental Understanding, IEEE Radar Conference, pp. 1–6, (2016).
3. Winkler, V.: Range Doppler detection for automotive FMCW radar, Proceedings of the 4th IEEE European Radar Conference, pp. 166–169, (2007).
4. Rohling H, Moller C.: Radar waveform for automotive radar systems and applications, IEEE Radar Conference, pp. 1–4, (2008).
5. Rohling H, Meinecke: Waveform design principles for automotive radar systems, CIE International Conference on Radar, pp. 1–4, (2001).
6. Folster F, Rohling H.: An automotive radar network based on 77 GHz FMCW sensors, International Radar Conference, IEEE, pp. 1–6, (2005).
7. Jau-Jr Lin, et al.: Design of an FMCW radar baseband signal processing system for automotive application, National Chunghua University of Education, Taiwan, Springer Plus, pp. 1–16, (2016).
8. Ali Bazzi, Camilla Krnfeldt, et al.: Estimation Techniques and Simulation Platforms for 77 GHz FMCW ACC Radars, European Physical Journal, EDP Sciences, 57 (1), pp. 1–16, (2012).

Multiband Slotted Circular Microstrip Patch Antenna

Rajshri, Saumya Das and Tanushree Bose

Abstract Design and analysis of Circular Microstrip Patch Antenna (CMPA) using slots etched on patch for multiband applications is presented in this paper. Lightweight, low cost, plain configuration, and multiband functionality are the advantages and serve many applications like satellite communication, air traffic control, and radar communications. The substrate used is FR4 epoxy which has relative permittivity of 4.4. Introduction of slots increases resonant frequencies and bandwidth which make antenna serve multiple applications. The design is simulated using Ansoft HFSS software, and return loss, gain, VSWR, radiation pattern, and field distributions are studied.

Keywords Microstrip · Circular patch antenna · Multiband · Slot antenna

1 Introduction

Antenna is an electrical device that transmits the signals such as microwave, radio, or satellite signals at the input and the transmitted signal is sent and received at the output. Microstrip patch antennas are relatively easy to manufacture and simple to configure. Common microstrip patch antenna shapes are rectangular, circular, square, and elliptical. With the development of wireless communication systems, the requirement of lightweight, high gain, and minimum return loss antennas which ensure high efficiency, mobility, and wide coverage has increased. Narrow bandwidth is one of the major drawbacks of microstrip patch antenna which is due to the

Rajshri (✉) · S. Das · T. Bose (✉)

Department of Electronics and Communications Engineering (ECE),
Sikkim Manipal Institute of Technology, Majitar, Rangpo, Sikkim, India
e-mail: 511rajshrisuman@gmail.com

T. Bose
e-mail: tanushree.contact@gmail.com

S. Das
e-mail: saumya.das.1976@gmail.com

surface wave losses and large size of patch. A high demand is increasing for wideband application along with multiband for multifrequency operation by a single antenna. So, there was a requirement for designing multiband microstrip patch antenna [1, 2]. Probe compensation (L-shaped probe, capacitive “top hat” on probe), parasitic patches, direct-coupled patches, slot- and slit-loaded patches (U- or V-shaped slots and E patch, U-shaped slit), stacked patches, patch with parasitic strip, and the use of electromagnetic band gap (EBG) structures [3] are some techniques which can be applied to design wideband and multiband microstrip patch antennas.

In this paper, slotted CMPA is chosen for the design because of its simplicity in designing. Moreover for such antennas, production cost is low. Shape of the patch is chosen to be circular as they are omnidirectional in the horizontal plane and have maximum radiation oriented at the certain angle to the azimuth. This property leads it to be widely used as antenna array elements in microwave communications, radars, as well as cellular and automobile antennas [4].

Microstrip slot antenna was invented in 1938 by Alan Blumlein. Slot radiator or slot antennas are antennas that are used in frequency range from about 300 MHz to 25 GHz. The slot behaves as resonant radiator as per Babinet’s principle. The theorem of similar diffraction patterns produced by two complementary screens was given by Jacques Babinet (1794–1872) who was a French physicist and mathematician. Moreover, the advantages like low profile, low cost, small size, easier integration with other circuits, and conformability to a shaped surface of microstrip patch antenna are the motivation of this work [5].

2 Antenna Designs

Here, a multiband circular patch antenna of radius 8 mm is designed and simulated on an FR4 epoxy substrate with a dielectric constant $\epsilon_r = 4.4$ and thickness as $h = 0.5$ mm. Further two different slots are cut on the patch, and the performance of the circular patch antenna is analyzed and discussed. The operating bands are evaluated by Ansoft HFSS with the criterion of return loss less than -10 dB.

2.1 Design 1: Simple Circular Microstrip Patch Antenna (CMPA)

A CMPA of radius 8 mm is designed on a FR4 epoxy substrate of thickness $h = 0.5$ mm and dielectric constant $\epsilon_r = 4.4$, and the performance is analyzed. All other design specifications are given in Table 1 (Fig. 1).

Parameters Considerations:

See Table 1.

2.2 Slotted CMPA

A slotted CMPA of radius 8 mm is designed on a FR4 epoxy substrate of thickness $h = 0.5$ mm; slots of different dimensions and shapes have been created and other parameters are constant and dielectric constant $\epsilon_r = 4.4$; and the performance is analyzed. All other design specifications are given in Tables 2 and 3.

These parameters are constant for all the slotted antennas in this work.

These are the parameters of slots of different slotted antennas.

Design 2: One Slotted Circular Microstrip Patch Antenna (CMPA): (Fig. 2)

Design 3: Three Slotted Circular Microstrip Patch Antenna (CMPA): (Fig. 3)

Design 4: One Slotted Circular Microstrip Patch Antenna (CMPA): (Fig. 4)

3 Results and Analysis

3.1 Design 1: Simple Circular Microstrip Patch Antenna (CMPA)

In this design of CMPA, two bands are obtained; return loss (dB) is -39.5 and -23 , bandwidth (GHz) obtained is 0.28 and 0.81, and resonant frequency (dB) is 10.7 and 19.2. This type of antenna design is applicable for X-band and K-band. Gain of the antenna is 1 dB (Fig. 5).

Table 1 Design specifications of the antenna Simple Circular Microstrip Patch Antenna (CMPA)

Parameters	Dimensions
Patch (circular)	Radius = 8 mm
Ground	30 mm × 30 mm
Substrate	30 mm × 30 mm
Feed (rectangular)	15 mm × 2 mm
Feed pin	0.12 mm

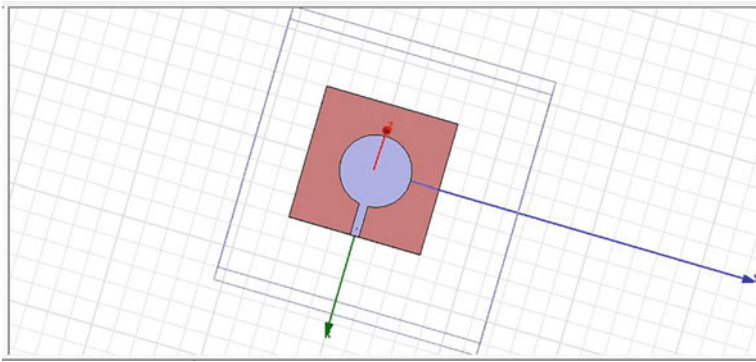


Fig. 1 Circular Microstrip Patch Antenna

Table 2 Design specifications of the Slotted Circular Microstrip Patch Antenna (CMPA)

Parameters	Dimensions
Patch (circular)	Radius = 8 mm
Ground	30 mm × 30 mm
Substrate	30 mm × 30 mm
Feed (rectangular)	15 mm × 2 mm
Feed pin	0.12 mm

Table 3 Design specifications of the slots of different Slotted Circular Microstrip Patch Antenna

Antenna design	Slot dimensions
Design 2	Rectangle 1 = 2 mm × 5 mm Rectangle 2 = 5 mm × 2 mm
Design 3	Rectangle = 4 mm × 1 mm Circle 1 = 1.5 mm Circle 2 = 1.5 mm
Design 4	Rectangle 1 = 5 mm × 1 mm Rectangle 2 = 1 mm × 5 mm

3.2 Design 2: One Slotted Circular Microstrip Patch Antenna (CMPA)

In this design of CMPA, four bands are obtained; return loss (dB) is -14.5, -26, -26, and -12, bandwidth (GHz) obtained is 0.12, 0.15, 0.57, and 0.27 and resonant frequency (GHz) is 7.9, 8.8, 18.2, and 19. This type of antenna design is applicable for C-band, X-band, and K-band. Gain of the antenna is 1 dB (Fig. 6).

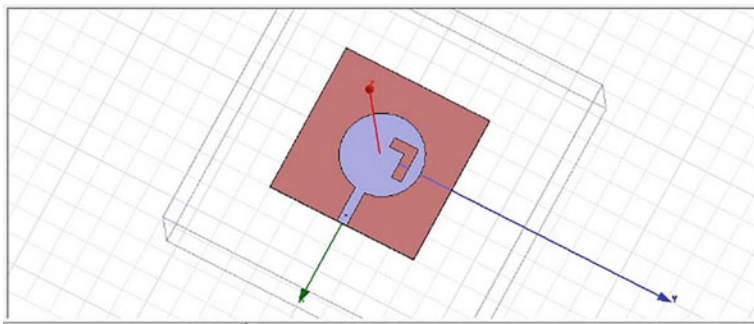


Fig. 2 Top view

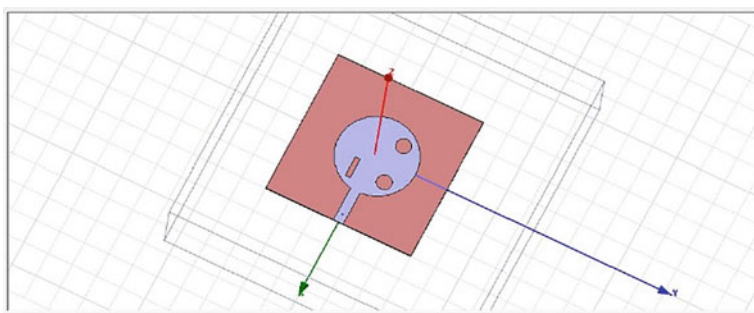


Fig. 3 Top view

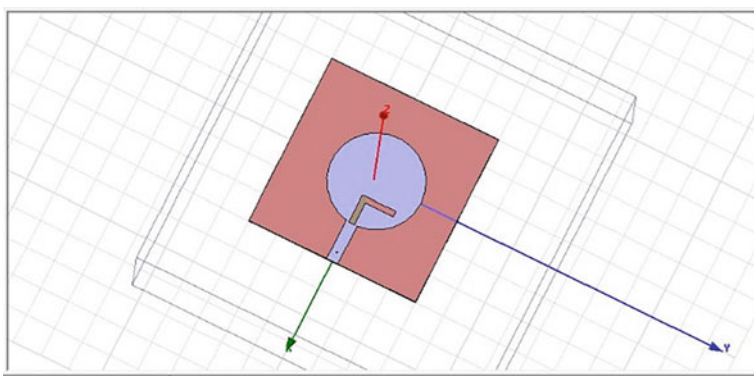


Fig. 4 Top view

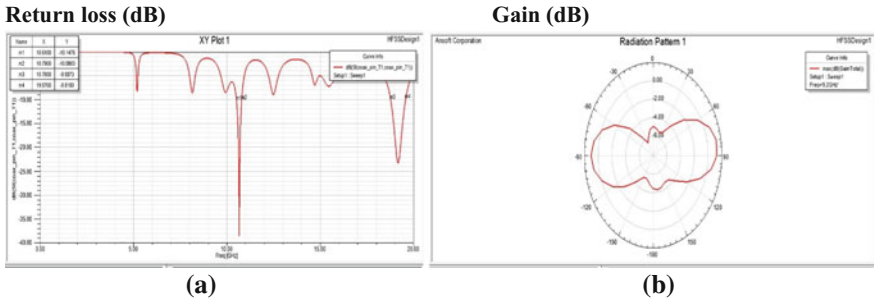


Fig. 5 a Return Loss of Design 1. b Gain of Design 1

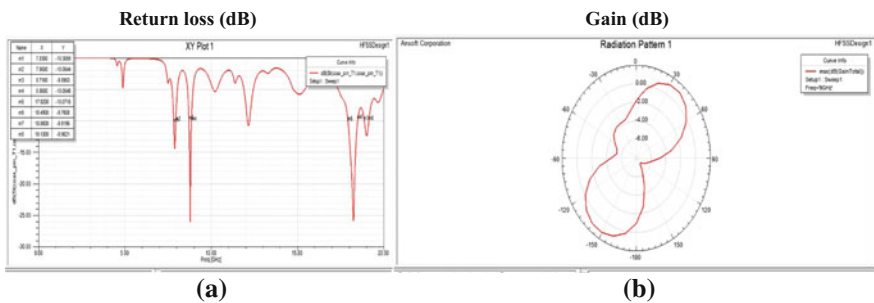


Fig. 6 a Return Loss of Design 2. b Gain of Design 2

3.3 Design 3: Three Slotted Circular Microstrip Patch Antenna (CMPA)

In this design of CMPA, four bands are obtained; return loss (dB) is -14 , -17.5 , -17 , and -30 , bandwidth (GHz) obtained is 0.11 , 0.28 , 0.51 , and 1.55 , and resonant frequency (dB) is 7.8 , 9.8 , 11.7 and 19.3 . This type of antenna design is applicable for C-band, X-band, and K-band. Gain of the antenna is 1 dB (Fig. 7).

3.4 Design 4: One Slotted Circular Microstrip Patch Antenna (CMPA)

In this design of CMPA, five bands are obtained; return loss (dB) is -17.2 , -14.9 , -17.6 , -16 and -13.8 , bandwidth (GHz) obtained is 0.14 , 0.2 , 0.35 , 0.33 and 0.55 , resonant frequency (dB) is 8 , 12.1 , 15.2 , 16.4 and 19.2 . This type of antenna design is applicable for C-band, Ku-band, and K-band. Gain of the antenna is 1 dB (Fig. 8; Table 4).

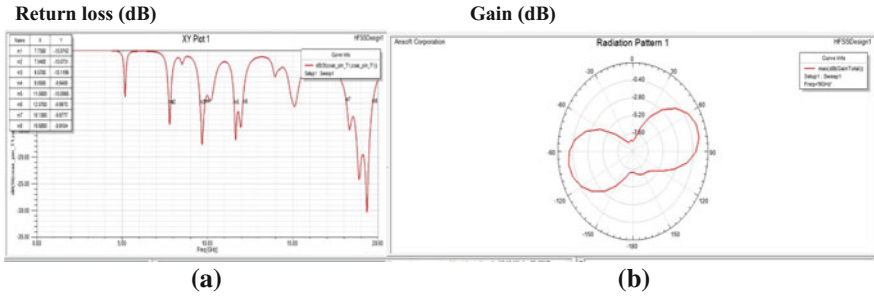


Fig. 7 a Return Loss of Design 3. b Gain of Design 3

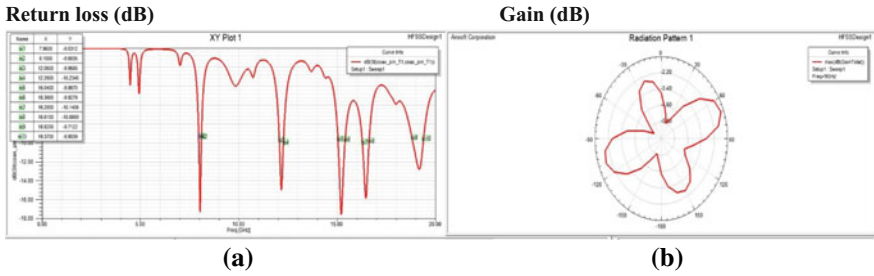


Fig. 8 a Return Loss of Design 4. b Gain of Design 4

Table 4 Input and output parameter of the CMPA

Antenna design	Input	Output					
	Radius (mm)	No. of bands	Resonant frequency (GHz)	Return loss (dB)	Bandwidth (GHz)	Gain (dB)	Type of band
Design 1	8	2	10.7	-39.5	0.28	1	X-band
			19.2	-23	0.81		K-band
Design 2	8	4	7.9	-14.5	0.12	1	C-band
			8.8	-26	0.15		X-band
			18.2	-26	0.57		K-band
			19	-12	0.27		K-band
Design 3	8	4	7.8	-14	0.11	1	C-band
			9.8	-17.5	0.28		X-band
			11.7	-17	0.51		X-band
			19.3	-30	1.55		K-band
Design 4	8	5	8	-17.2	0.14		C-band
			12.1	-14.9	0.2		Ku-band
			15.2	-17.6	0.35		Ku-band
			16.4	-16	0.33		Ku-band
			19.2	-13.8	0.55		K-band

4 Conclusion

From the project, it is concluded that the antenna designed without slots have less bands, whereas the antennas designed with slots have more number of bands. Slotted antennas can be used to embed more number of applications in a single antenna. Some of the applications are satellite communications, weather monitoring, etc. Return loss and bandwidth have also shown good response in the slotted antennas.

5 Future Scope

1. More shapes and dimensions of slotted antenna can be designed to get the more satisfactory and optimized results.
2. Different types of substrate material can be used to design antennas to get more satisfactory results.
3. Design of antennas employing foam substrates to improve the bandwidth.
4. Array investigation on circularly polarized antennas.
5. Broadbanding techniques can be used like broadbanding using coplanar parasitic elements.

References

1. Jeevani W. Jayasinghe, Jaume Anguera, and Disala N. Uduwawala, "A simple design of multi band microstrip patch antennas robust to fabrication tolerances for gsm, umts, lte, and bluetooth applications by using genetic algorithm optimization", *International Journal of Communication and Computer Technologies* Volume 02 – No. 1 Issue: 04 April 2014.
2. Radouane KARLI, Hassan AMMOR, "A SIMPLE AND ORIGINAL DESIGN OF MULTI-BAND MICROSTRIP PATCH ANTENNA FOR WIRELESS COMMUNICATION", *International Journal of Microwaves Applications*, Volume 2, No. 2, March–April 2013.
3. S. Atchaya, N. Dhanalakshmi, R. Veeramani, "A Compact Design of Multiband Microstrip Patch Antenna for GSM, Bluetooth and WiMAX Applications", *International Journal of Communication and Computer Technologies* Volume 02 – No. 1 Issue: 04 April 2014.
4. Andrey S. Andrenko, Senior Member, IEEE, Igor V. Ivanchenko, Senior Member, IEEE, Denis I. Ivanchenko, Sergey Y. Karelin, Alexey M. Korolev, Evgeniy P. Laz'ko, and Nina A. Popenko, Senior Member, IEEE, "Active Broad X-Band Circular Patch Antenna", *IEEE ANTENNAS AND WIRELESS PROPAGATION LETTERS*, VOL. 5, 2006.
5. NEHA GUPTA, "EFFECTS OF SLOTS ON MICROSTRIP PATCH ANTENNA", *International Research Journal of Engineering and Technology (IRJET)* e-ISSN: 2395-0056, Volume: 04 Issue: 02 | Feb-2017.

Multi Resonant Textile Antenna with Partial Ground for Multiband Applications

Rahul Saini, Vinod Kumar Singh, Niharika Singh, J. P. Saini and Akash Kumar Bhoi

Abstract The proposed design of antenna is the powerful textile antenna used to increase bandwidth efficiently. The proposed antenna has various applications like satellite communication, defense system, medical applications, and air traffic control. The proposed antenna acquires multiple frequency bands with bandwidth coverage percentage, first band from 2.81 to 3.692 GHz with 27.44%, second band from 4.556 to 5.618 GHz with 20.88%, third band with from 6.446 to 7.67 GHz with 17.35%, fourth band from 8.948 to 11.288 GHz with 23.13%, and lastly, fifth band from 12.134 to 17.606 GHz with 36.80%. The textile as the dielectric has many advantages as easy to wear, low material cost, easy availability, and high flexibility. The studied results of the proposed antenna show highly negative return loss, high directivity, radiation pattern, gain, and high efficiency.

Keywords Jeans • Self-adhesive copper tape • Return loss • CST studio software

J. P. Saini

Department of Electronics and Communication Engineering,
Bundelkhand Institute of Technology, Jhansi, UP, India
e-mail: jps_uptu@rediffmail.com

V. K. Singh (✉)

Department of Electrical Engineering, SR Group of Institution,
Jhansi, UP, India
e-mail: singhvinod34@gmail.com

R. Saini • N. Singh

Department of Electronics and Communication Engineering,
SR Group of Institution, Jhansi, UP, India
e-mail: rahulsainiec052@gmail.com

N. Singh

e-mail: niharikasinghec2010@gmail.com

A. K. Bhoi

Department of Electrical and Electronics Engineering,
Sikkim Manipal Institute of Technology (SMIT), Majitar, Rangpo 737136, Sikkim, India
e-mail: akash730@gmail.com

© Springer Nature Singapore Pte Ltd. 2018

R. Bera et al. (eds.), *Advances in Communication, Devices and Networking*,
Lecture Notes in Electrical Engineering 462,
https://doi.org/10.1007/978-981-10-7901-6_39

359

1 Introduction

In the present day scenario, the wireless communication has made demand of the small sized, highly directive, and most importantly the wearable antennas. The material like textile is in demand due to their high flexibility, low cost, lightweight, low profile, and due to their simple realization process. The textile materials like jean have a lower value of dielectric constant which lowers the value of dielectric constant of the material and also improves the bandwidth of impedance [1–9]. The value of the dielectric constant of the material is proportional to the antenna size; hence with the textile materials, compact antennas are easy to be made. The properties of the antenna such as the return loss, voltage standing wave ratio, antenna gain, and antenna radiation pattern are studied and analyzed for antenna designing [10–13]. The proposed antenna has an advantage due to its wearable property and ease of integration on clothes or body. The proposed antenna has been designed using computer simulation tool software and fabricated with the loss tangent value 0.025 and the dielectric value of textile material jean as 1.7. The wearable antenna can be used as clothing used for communication purpose, like tracking and navigation, satellite communication, and public safety. The basic requirements of the textile antenna are a planar structure, high flexibility of the substrate material [14–18], robustness, less power consumption, and highly comfortable [16–19]. The paper discusses the textile antenna designing, antenna fabrication with substrate material jeans fabric and the partial ground and the patch consists of an adhesive thin copper tape, and also the study of antenna properties like reflection coefficient, antenna gain, and antenna efficiency.

2 Antenna Designing

In this paper, the proposed antenna substrate is fabricated with the jean having low dielectric value as 1.7, and the partial ground and patch comprise of very thin adhesive copper tape with the thickness 0.03 mm. The proposed antenna is suitable for multiband communication systems and wireless communications as the antenna acquires multiple frequency bands for operations. The geometrical representation of the proposed antenna is shown in Fig. 1, with the dimension of partial ground 28 mm × 32 mm, diameter of the patch 24 mm, and substrate with dimension 60 mm × 60 mm. The design parameters obtained by calculations are described in Table 1.

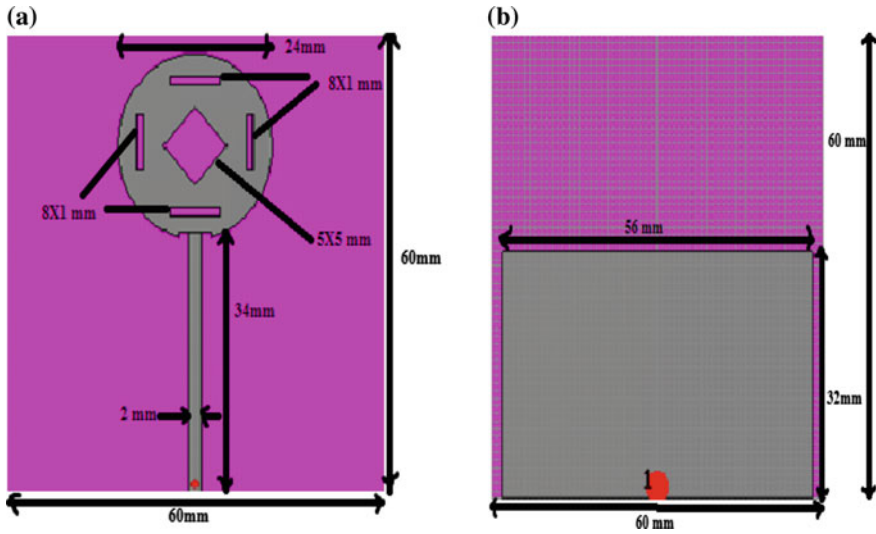


Fig. 1 Antenna dimensions a patch view b partial ground plane view

Table 1 Dimension of proposed textile antenna

S. NO.	Antenna parameter	Values
1	Substrate thickness, h (mm)	1
2	Relative permittivity (ϵ_r)	1.7
3	Loss tangent	0.025
4	Partial ground dimension (mm)	56×32
5	Substrate dimension (mm)	60×60
6	Patch radius (mm)	12
7	Center square slot (mm)	5×5
8	Microstrip feed line dimension (mm)	34×2
9	Four rectangular slots dimension (mm)	8×1

3 Optimization of Antenna Geometries

The geometrical representation of the antenna designing with three different designs antenna1, antenna2, and antenna3 is represented in Fig. 2. The comparison of the simulated plot of return loss versus frequency between the three antennas is shown in Fig. 3, which clearly explains the increase in the negative value of the return loss and finalizing the antenna design of antenna3 with better results.

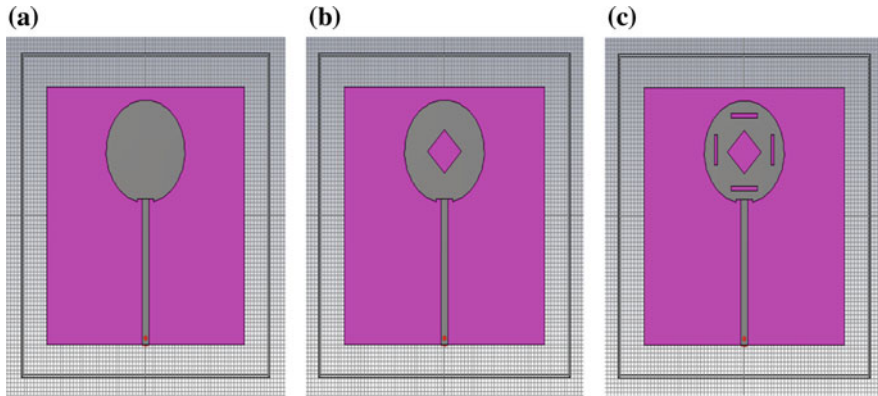


Fig. 2 Antenna's geometry a antenna1 b antenna2 c proposed antenna3

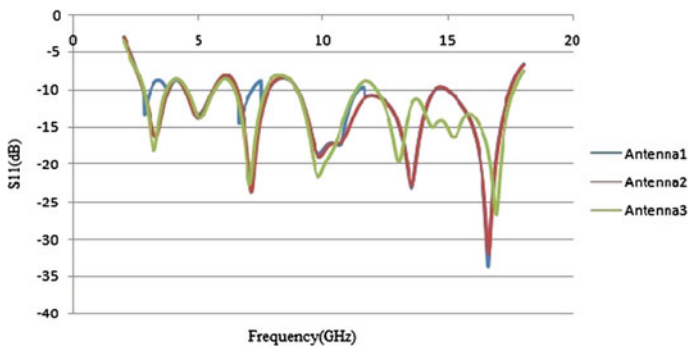


Fig. 3 Return loss versus frequency of antenna1, antenna2, and proposed antenna3

4 Fabricated Proposed Antenna and Experimental Results

The simulation of the proposed antenna is done by using computer simulation tool (CST) microwave studio 2010 software. Figure 4 shows the front view and the partial ground plane of the proposed antenna. The antenna is fabricated by using the jeans as substrate and copper as the conductive patch of the antenna. The fabricated antenna is tested in IIT Kanpur Lab, and the results are recorded. The recorded results are plotted on the graph which shows quite compromising measured results with the simulated results. The comparison of the return loss of both the measured and the simulated antenna3 is in Fig. 5. In Table 2, it can be easily judged that the

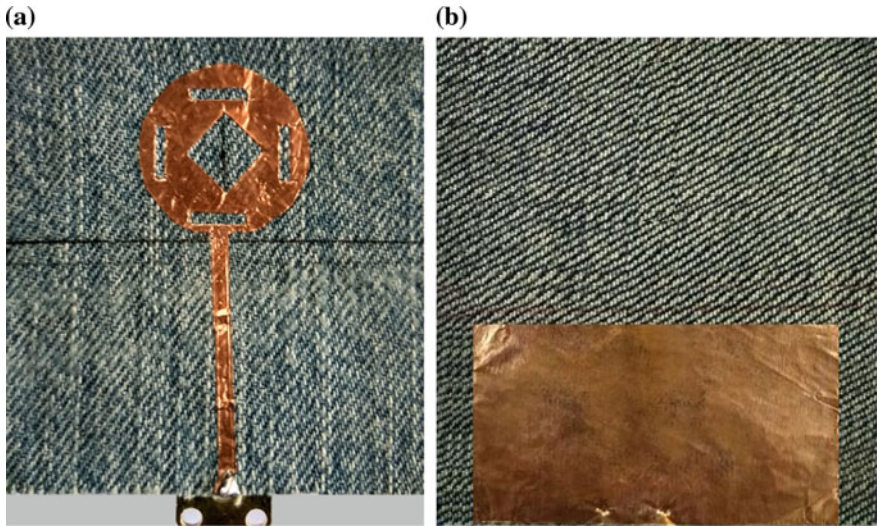


Fig. 4 Hardware of the proposed antenna a patch view b partial ground plane view

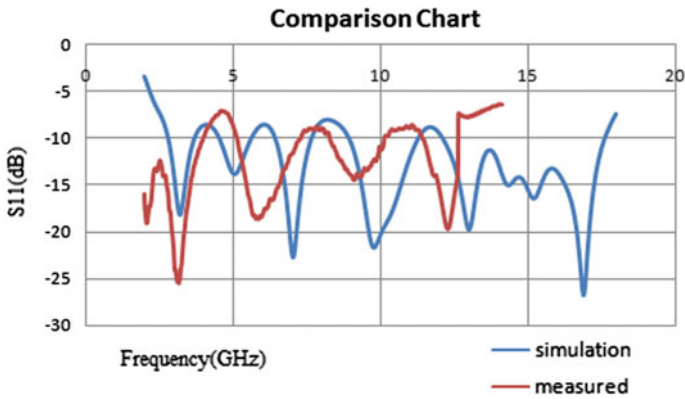


Fig. 5 Comparison shows S11 (dB) versus frequency (GHz) plot of the simulation result and measured result of the proposed antenna (antenna3)

Table 2 Comparison of the antenna simulated and measured results

Bands	Simulated result		Measured result	
	Frequency range (GHz)	Band width (%)	Frequency range (GHz)	Band width (%)
First	2.81–3.692	27.44	2–4.2	70.92
Second	4.556–5.618	20.88	5.5–7.88	35.57
Third	6.446–7.67	17.35	8.98–11.02	20.45
Fourth	8.948–11.288	23.13	11.432–13.25	13.78
Fifth	12.13–17.606	36.80	–	–

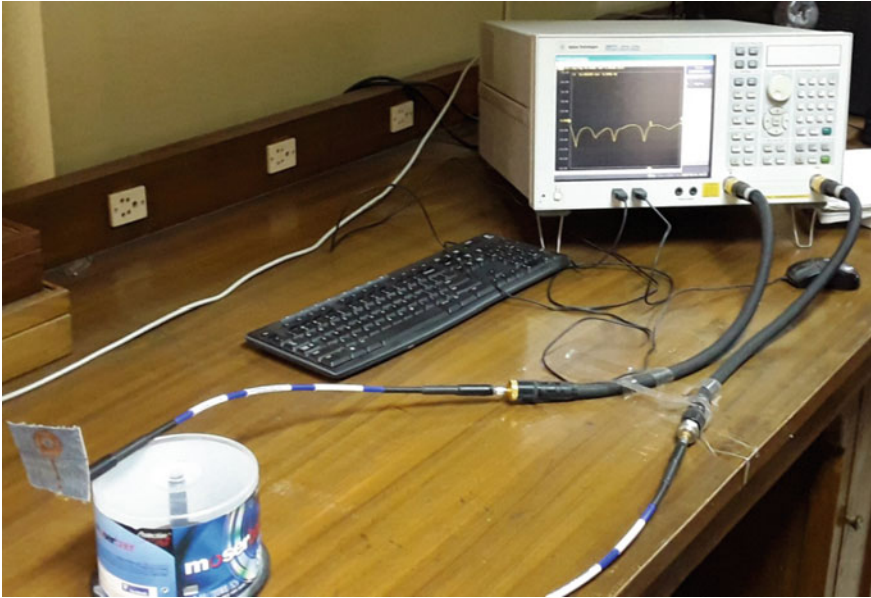


Fig. 6 Practical setup to measure returns loss of proposed antenna at IIT Kanpur Laboratory

bandwidth percentage of the simulation results and measured results. The bandwidth percentage of measured results is better than the simulation results. In Fig. 6, practical setup to measure returns loss of proposed antenna at IIT Kanpur Laboratory gives a final output of the proposed antenna. Figure 7 shows 3D radiation pattern at different resonant frequency 3.206, 5.078, 7.058, 9.7951, and 13.016 GHz.

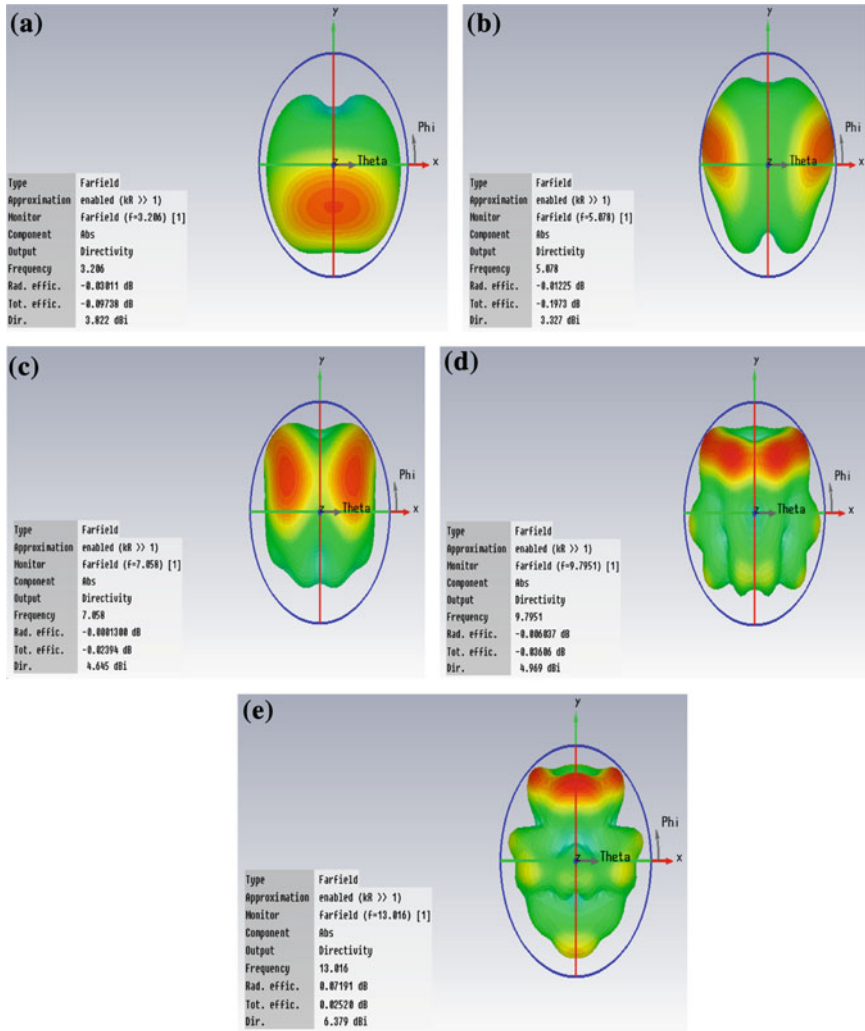


Fig. 7 3D radiation pattern at resonant frequency **a** 3.206 GHz, **b** 5.078 GHz, **c** 7.058 GHz, **d** 9.7951 GHz, **e** 13.016 GHz

5 Conclusion

The designed textile antenna can be used for body-centric wireless and satellite communication because it is directional in nature. The major applications of the antenna achieved by the use of jean as the substrate are monitoring of human body or object. The design of the antenna consists of a partial ground plane, jean substrate, and circular patch design modified with center square-shaped tilted slot

surrounded by four rectangular slots. The antenna covers different frequency ranges. The antenna covers five frequency bands between 2 and 18 GHz with impedance bandwidth percentages 27.44, 20.88, 17.35, 23.13, and 36.80%, and hence can be used for multiband applications.

References

1. Raghupatruni V., Ram Krishna, and Raj Kumar: Design of Temple Shape Slot Antenna for Ultra Wideband Applications, *Progress In Electromagnetic Research B*, vol. 47, pp. 405–421, (2013).
2. Balanis CA: *Antenna Theory: Analysis and Design*, John Wiley and Sons, New York, 2004.
3. Vinod Kumar Singh, Zakir Ali, Shahanaz Ayub, and Ashutosh Kumar Singh: A wide band Compact Microstrip Antenna for GPS/DCS/PCS/WLAN Applications, *Intelligent Computing, Networking, and Informatics*, (ISBN: 978-81-322-1664-3), Springer, vol. 243, pp. 1107–1113, (2014).
4. Rajat Srivastava, Vinod Kumar Singh, and Shahanaz Ayub: Comparative Analysis and Bandwidth Enhancement with Direct Coupled C Slotted Microstrip Antenna for Dual Wide Band Applications, *Frontiers of Intelligent Computing: Theory and Applications*, (ISBN: 978-3-319-12011-9), Springer, vol. 328, pp. 449–455, (2015).
5. Vinod Kumar Singh, Zakir Ali, Shahanaz Ayub, and Ashutosh Kumar Singh: Bandwidth Optimization of Compact Microstrip Antenna for PCS/DCS/Bluetooth Application, *Central European Journal of Engineering*, Springer, vol. 4, no. 3, pp. 281–286, (2014).
6. Nikhil Singh, Ashutosh Kumar Singh, and Vinod Kumar Singh: Design Performance of Wearable Ultra Wide Band Textile Antenna for Medical Applications, *Microwave and Optical Technology Letters*, vol. 57, no. 7, pp-1553–1557, (2015).
7. Stuti Srivastava, Vinod Kumar Singh, Zakir Ali, and Ashutosh Kumar Singh: Duo Triangle Shaped Microstrip Patch Antenna Analysis for WiMAX lower band Application, *International Conference on Computational Intelligence: Modelling Techniques and Applications (CIMTA-2013)*, *Procedia Technology Elsevier* 10, pp. 554–563, (2013).
8. Nikhil Kumar Singh, Vinod Kumar Singh, and Naresh. B: Textile Antenna for Microwave Wireless Power Transmission, *International Conference on Computational Modelling and Security (CMS 2016)*, *Procedia Computer Science*, vol. 85, pp. 856–861, (2016).
9. Neha Gupta, Vinod Kumar Singh, Zakir Ali, and Jitendra Ahirwar: Stacked Textile Antenna for Multi Band Application Using Foam Substrate, *International Conference on Computational Modelling and Security (CMS 2016)*, *Procedia Computer Science*, vol. 85, pp. 871–877, (2016).
10. Amit Kumar Rawat, Vinod Kumar Singh, and Shahanaz Ayub: Compact Wide band Microstrip Antenna for GPS/WLAN/WiMax Applications, *International Journal of Emerging Trends in Engineering and Development*, no. 2 vol. 7, pp. 140–145, (2012).
11. Rishabh Kumar Baudh, Ranjan Kumar, and Vinod Kumar Singh: Arrow Shape Microstrip Patch Antenna for WiMax Application, *Journal of Environmental Science, Computer Science and Engineering & Technology*, vol. 3, no.1, pp. 269–274, (2013).
12. Janabeg Loni, Shahanaz Ayub, and Vinod Kumar Singh: Performance analysis of Microstrip Patch Antenna by varying slot size for UMTS application, *IEEE Conference on Communication Systems and Network Technologies (CSNT-2014)*, pp. 01–05, (2014).
13. Rajat Srivastava, Shahanaz Ayub, and V. K. Singh: Dual Band Rectangular and Circular Slot Loaded Microstrip Antenna for WLAN/GPS/WiMax Applications, *IEEE Conference on Communication Systems and Network Technologies (CSNT-2014)*, pp. 45–48, (2014).

14. Seema Dhupkariya, and Vinod Kumar Singh: Textile Antenna for C-Band Satellite Communication Application, *Journal of Telecommunication, Switching Systems and Networks*, vol. 2, no. 2, pp. 20–25, (2015).
15. Janabeg Loni, and Vinod Kumar Singh: Development of Bandwidth Enhanced Microstrip Patch Antenna for UMTS Application, *Journal of Microwave Engineering & Technologies*, vol. 2, no. 1, pp. 01–07, (2015).
16. Vinod Kumar Singh, and B. Naresh: Multi Resonant Microstrip Antenna with Partial Ground for Radar Application, *Journal of Telecommunication, Switching Systems and Networks*, vol. 2, no. 1, pp. 01–05, (2015).
17. Manvendra Singh, Vinod Kumar Singh, and B. Naresh: Rectangular Slot Loaded Circular Patch Antenna for WLAN Application, *Journal of Telecommunication, Switching Systems and Networks*, vol. 2, no. 1, pp. 07–10, (2015).
18. Mai A. R. Osman, M. K. A. Rahim, M. Azfar N. A. Samsuri, F. Zubir, and K. Kamardin: Design, implementation and performance of Ultra-Wideband Textile Antenna, *Progress In Electromagnetics Research B*, vol. 27, pp. 307–325, (2011).
19. Vinod Kumar Singh, and Nikhil Kumar Singh: Compact Circular Slotted Microstrip Antenna for Wireless Communication Systems, *Journal of Microwave Engineering & Technologies*, vol. 1, no. 1, pp. 07–14, (2015).

Microstrip Textile Antenna with Jeans Substrate with Applications in S-Band

Niharika Singh, Vinod Kumar Singh, Rahul Saini, J. P. Saini and Akash Kumar Bhoi

Abstract In this article, the proposed textile antenna has been studied with better results, high directivity, high gain, good return loss and multiple bands are obtained for wide range of applications in S-band with multiple bands. The substrate material of the proposed antenna is a jean which is a flexible material, the patch and partial ground plane are of copper. There is a modification in proposed textile antenna design with the same size but better return loss and multiple bands. The simulations of the proposed antenna were carried using CST Microwave Studio software.

Keywords Jeans • Self-adhesive copper tape • Return loss • CST studio software

N. Singh (✉)

Department of Electronics and Communication Engineering,
SR Group of Institution, Jhansi, UP, India
e-mail: niharikasinghec2010@gmail.com

V. K. Singh (✉)

Department of Electrical Engineering, SR Group of Institutions,
Jhansi, UP, India
e-mail: singhviod34@gmail.com

R. Saini

Department of Electronics and Communication Engineering,
SR Group of Institution, Jhansi, UP, India
e-mail: rahulsainiec052@gmail.com

J. P. Saini

Department of Electronics and Communication Engineering,
Bundelkhand Institute of Technology, Jhansi, UP, India
e-mail: jps_uptu@rediffmail.com

A. K. Bhoi

Department of Electrical and Electronics Engineering,
Sikkim Manipal Institute of Technology (SMIT), Majitar,
Rangpo 737136, Sikkim, India
e-mail: akash730@gmail.com

© Springer Nature Singapore Pte Ltd. 2018

R. Bera et al. (eds.), *Advances in Communication, Devices and Networking*,
Lecture Notes in Electrical Engineering 462,
https://doi.org/10.1007/978-981-10-7901-6_40

1 Introduction

Microstrip patch antennas have been an interested topic for study due to its low profile structure, compact size, and lightweight, and more economical. The microstrip patch antenna with substrate material as fabric has made it possible to be used as wearable antennas which are being used for various applications such as military purpose, tracking and navigation, mobile computing, biomedical, radar, and aircraft applications [1–11]. The proposed antenna has been aimed to be used for wide frequency range in the ultra wide band. The modification has been carried out in the antenna design to gain better results with compact size, low cost, and ease of integration on device [12–15]. The wearable textile antennas can be easily integrated into clothes or body. We are using computer simulation tool (CST studio 2010) for antenna virtual designing, the loss tangent being 0.025 and experimented with the substrate material as textile material jean. The CST studio is helped in the simulation of antenna and also calculating antenna parameters. The requisite for the working of the wearable antenna is a planar structure with high flexibility of the substrate material [16–18], along with electronic devices being robust, low power consumption, and comfortable. This makes wearable antenna to be easily used for the purposes like tracking and navigation, satellite communication, and public safety [16–21].

This paper describes the modified design of textile antenna with jeans fabric as the substrate. The simulated antenna design has been given in section 2 and hardware design has been given in section 4. The section 3 describes the simulated results of the proposed antenna which includes gain, return loss versus frequency, and 3D radiation pattern of multiple resonating frequencies. Section 5 includes the conclusion.

2 Antenna Designing

In this paper, the antenna consists of the substrate material as a textile material jean with the dielectric value 1.7, and the radiating plane (patch) and the partial ground plane are made of adhesive copper tape with the thickness of 0.03 mm. The substrate can be of any material like textile, cotton, flannel, and glass epoxy, with low dielectric value, as the size of antenna is proportional to dielectric value of substrate. The proposed antenna design is suitable for wireless communication with multiple frequency bands for operation. The geometrical representation of the antenna along with the dimensions is been shown in Fig. 1, with partial ground 50 mm × 27 mm, patch diameter of 32 mm, and substrate with 60 mm × 60 mm. The antenna simulation and analysis of the antenna have been carried on the computer simulation tool (CST) Microwave Studio 2010 software. Table 1 describes the design parameters of the antenna with the values.

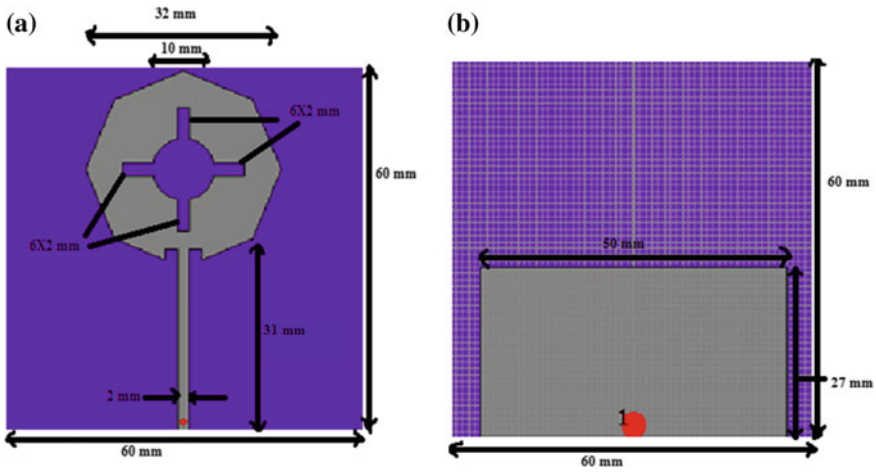


Fig. 1 Antenna dimensions with a front view and b back view

Table 1 Dimension of proposed textile antenna

S. No.	Antenna parameter	Values
1	Substrate thickness	1
2	Relative permittivity	1.7
3	Loss tangent	0.025
4	Partial ground dimension (mm)	50 × 27
5	Substrate dimension (mm)	60 × 60
6	Patch radius (mm)	16
7	Patch inner circle radius (mm)	5 × 5
8	Microstrip feed line dimension (mm)	31 × 2
9	Four rectangular slots dimension (mm)	6 × 2

3 Optimization of Antenna Geometries

This paper describes the analysis of the modification of the proposed textile antenna design to obtain better results and multiple bands for applications. Figure 2 shows the different designing steps of the proposed textile antenna with modification in each step. Figure 2a shows the basic design, and then Fig. 2b shows the design with a circular slot on the patch. Figure 2c shows the final design of the proposed antenna with the substrate dimension 60 × 60 (mm × mm), patch radius 16 mm with the inner circular slot of radius 5 mm, and the four rectangular slots in the patch of antenna with the dimension 6 mm × 2 mm, and the microstrip feed line of 31 mm × 2 mm. Figure 3 plots the graph between the simulated return loss and frequency of presented antenna1, antenna2, and proposed antenna (antenna3).

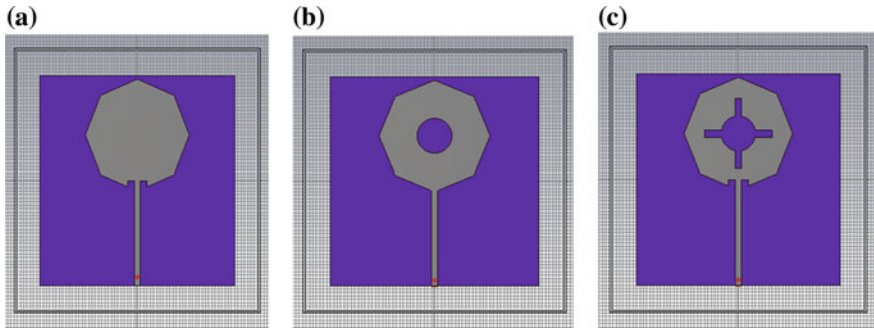


Fig. 2 Structures of presenter antennas **a** antenna1, **b** antenna2, and **c** proposed antenna3

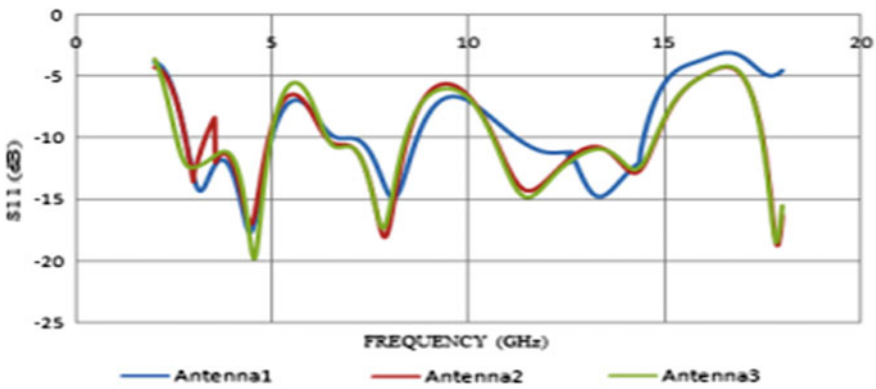


Fig. 3 Reflection coefficient versus frequency of antenna1, antenna2, and proposed antenna3

4 Fabricated Proposed Antenna and Experimental Results

The hardware design of the fabricated antenna (antenna3) with its front view and partial ground view (back view) is been shown in Fig. 4. The proposed antenna is fabricated by using the jeans as substrate and copper as the conductive patch of the antenna. The fabricated antenna is tested in IIT Kanpur Lab, and the results were recorded. The recorded results are plotted on the graph which shows quite compromising measured results with the simulated results. The comparison of the return loss of both the measured and the simulated antenna3 is in Fig. 5. Table 2 shows that the bandwidth percentage of the simulation results and measured results. In Fig. 6, practical setup to measure returns loss of proposed antenna at IIT Kanpur Lab which gives final output of the fabricated antenna. Figure 7 shows 3D Radiation pattern at different resonant frequencies (a) 4.538 GHz, (b) 7.832 GHz, and (c) 11.486 GHz.

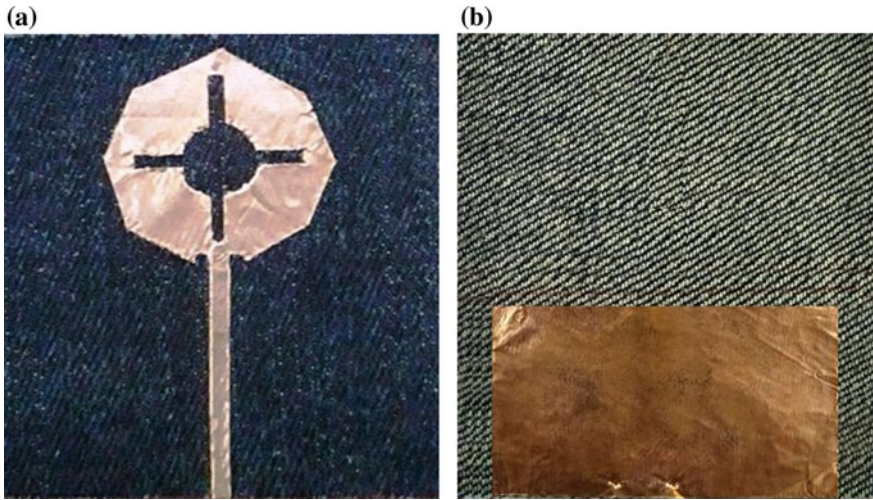


Fig. 4 Hardware of proposed antenna a front view and b partial ground plane

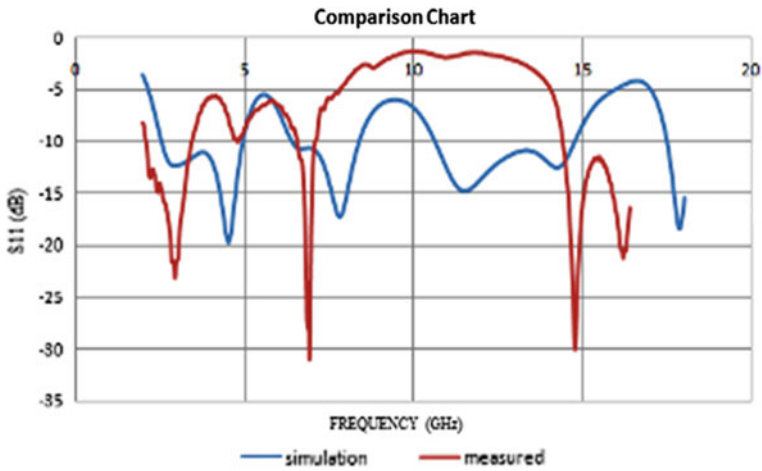


Fig. 5 Comparison of return loss versus frequency plot of simulated results and measured result of proposed antenna

Table 2 Comparison of simulated result and measured result of antenna

Bands	Simulated		Measured	
	Frequency range (GHz)	Band width (%)	Frequency range (GHz)	Band width (%)
First	2.558–4.88	62.44	2.12–3.62	52.27
Second	6.32–8.174	25.59	6.6–7.9	20.45
Third	10.46–12.296	16.14	15.8–18	13.02

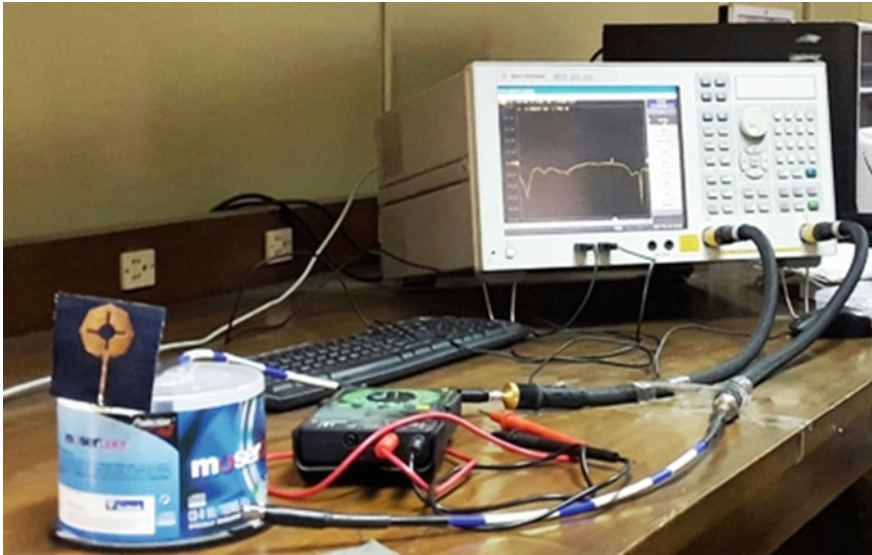


Fig. 6 Practical setup to measure returns loss of proposed antenna at IIT Kanpur lab

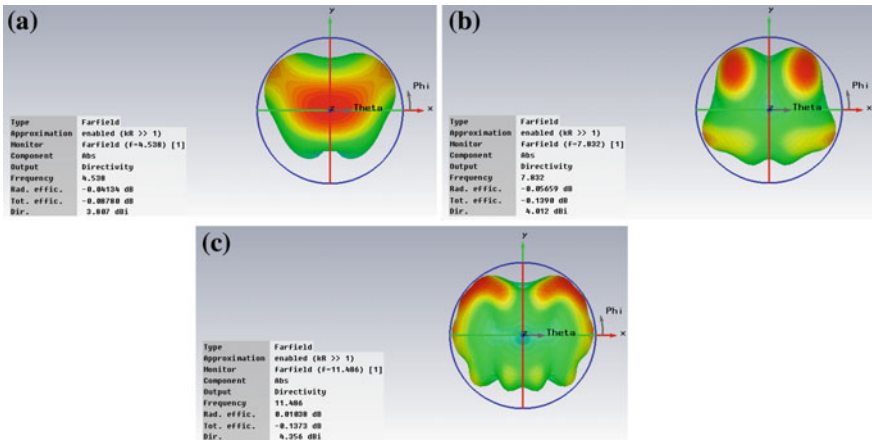


Fig. 7 Three-dimensional radiation patterns at frequencies a 4.538 GHz, b 7.832 GHz, and c 11.486 GHz

5 Conclusion

The advantage of the textile material (jeans) used as the substrate makes it applicable for monitoring human body or object, with easiness of integration on body without being noticed and, also easily manageable and portable as it is integrated

not carried in hands. The design of the proposed antenna is been finalized after modification in designs, studying and analyzing the results. The proposed antenna design comprises of partial ground plane which minimizes the cost and weight of antenna, a polygon-shaped radiating plane (patch) along with circular and rectangular slots over the patch. The antenna has wide frequency band coverage with a compact size and large value of bandwidth percentage for S-band. Hence, the proposed antenna works efficiently.

References

1. Jamshed A. Ansari, Sapna Verma, Mahesh K. Verma, and Neelesh Agrawal: Wide Band Microstrip-Line-Fed Antenna with Defected Ground for CP Operation, *Progress In Electromagnetic Research C*, vol. 58, pp. 169–181, (2015).
2. Raghupatruni V., Ram Krishna, and Raj Kumar: Design of Temple Shape Slot Antenna for Ultra Wideband Applications, *Progress In Electromagnetic Research B*, vol. 47, pp. 405–421, (2013).
3. Balanis CA: *Antenna Theory: Analysis and Design*, John Wiley and Sons, New York, 2004.
4. Vinod Kumar Singh, Zakir Ali, Shahanaz Ayub, and Ashutosh Kumar Singh: A wide band Compact Microstrip Antenna for GPS/DCS/PCS/WLAN Applications, *Intelligent Computing, Networking, and Informatics*, (ISBN: 978-81-322-1664-3), Springer, vol. 243, pp. 1107–1113, (2014).
5. Rajat Srivastava, Vinod Kumar Singh, and Shahanaz Ayub: Comparative Analysis and Bandwidth Enhancement with Direct Coupled C Slotted Microstrip Antenna for Dual Wide Band Applications, *Frontiers of Intelligent Computing: Theory and Applications*, (ISBN: 978-3-319-12011-9), Springer, vol. 328, pp. 449–455, (2015).
6. Vinod Kumar Singh, Zakir Ali, Shahanaz Ayub, and Ashutosh Kumar Singh: Bandwidth Optimization of Compact Microstrip Antenna for PCS/DCS/Bluetooth Application, *Central European Journal of Engineering*, Springer, vol. 4, no. 3, pp. 281–286, (2014).
7. Nikhil Singh, Ashutosh Kumar Singh, and Vinod Kumar Singh: Design & Performance of Wearable Ultra Wide Band Textile Antenna for Medical Applications, *Microwave and Optical Technology Letters*, vol. 57, no. 7, pp-1553–1557, (2015).
8. Stuti Srivastava, Vinod Kumar Singh, Zakir Ali, and Ashutosh Kumar Singh: Duo Triangle Shaped Microstrip Patch Antenna Analysis for WiMAX lower band Application, *International Conference on Computational Intelligence: Modelling Techniques and Applications (CIMTA-2013)*, *Procedia Technology Elsevier* 10, pp. 554–563, (2013).
9. Nikhil Kumar Singh, Vinod Kumar Singh, and Naresh. B: Textile Antenna for Microwave Wireless Power Transmission, *International Conference on Computational Modelling and Security (CMS 2016)*, *Procedia Computer Science*, vol. 85, pp. 856–861, (2016).
10. Neha Gupta, Vinod Kumar Singh, Zakir Ali, and Jitendra Ahirwar: Stacked Textile Antenna for Multi Band Application Using Foam Substrate, *International Conference on Computational Modelling and Security (CMS 2016)*, *Procedia Computer Science*, vol. 85, pp. 871–877, (2016).
11. Amit Kumar Rawat, Vinod Kumar Singh, and Shahanaz Ayub: Compact Wide band Microstrip Antenna for GPS/WLAN/WiMax Applications, *International Journal of Emerging Trends in Engineering and Development*, no. 2 vol. 7, pp. 140–145, (2012).
12. Rishabh Kumar Baudh, Ranjan Kumar, and Vinod Kumar Singh: Arrow Shape Microstrip Patch Antenna for WiMax Application, *Journal of Environmental Science, Computer Science and Engineering & Technology*, vol. 3, no. 1, pp. 269–274, (2013).

13. Janabeg Loni, Shahanaz Ayub, and Vinod Kumar Singh: Performance analysis of Microstrip Patch Antenna by varying slot size for UMTS application, IEEE Conference on Communication Systems and Network Technologies (CSNT-2014), pp. 01–05, (2014).
14. Rajat Srivastava, Shahanaz Ayub, and V. K. Singh: Dual Band Rectangular and Circular Slot Loaded Microstrip Antenna for WLAN/GPS/WiMax Applications, IEEE Conference on Communication Systems and Network Technologies (CSNT-2014), pp. 45–48, (2014).
15. Seema Dhupkariya, and Vinod Kumar Singh: Textile Antenna for C-Band Satellite Communication Application, Journal of Telecommunication, Switching Systems and Networks, vol. 2, no. 2, pp. 20–25, (2015).
16. Manvendra Singh, Vinod Kumar Singh, and B. Naresh: Rectangular Slot Loaded Circular Patch Antenna for WLAN Application, Journal of Telecommunication, Switching Systems and Networks, vol. 2, no. 1, pp. 07–10, (2015).
17. N. M. Din, C. K. Chakrabarty, A. Bin Ismail, K. K. A. Devi, and W.Y. Chen: Design of RF Energy Harvesting System For Energizing Low Power Devices, Progress In Electromagnetics Research, vol. 132, pp. 49–69, (2012).
18. Mai A. R. Osman, M. K. A. Rahim, M. Azfar N. A. Samsuri, F. Zubir, and K. Kamardin: Design, implementation and performance of Ultra-Wideband Textile Antenna, Progress In Electromagnetics Research B, vol. 27, pp. 307–325, (2011).
19. Janabeg Loni, and Vinod Kumar Singh: Development of Bandwidth Enhanced Microstrip Patch Antenna for UMTS Application, Journal of Microwave Engineering & Technologies, vol. 2, no. 1, pp. 01–07, (2015).
20. Vinod Kumar Singh, and B. Naresh: Multi Resonant Microstrip Antenna with Partial Ground for Radar Application, Journal of Telecommunication, Switching Systems and Networks, vol. 2, no. 1, pp. 01–05, (2015).
21. Vinod Kumar Singh, and Nikhil Kumar Singh: Compact Circular Slotted Microstrip Antenna for Wireless Communication Systems, Journal of Microwave Engineering & Technologies, vol. 1, no. 1, pp. 07–14, (2015).

Antenna for Wireless Area Network and Bluetooth Application

Manju Devi, Vinod Kumar Singh, Sanjeev Sharma
and Akash Kumar Bhoi

Abstract This chapter presents a dumb-bell shape microstrip patch antenna mainly used for wireless local area network application. The simulated result shows that the presented antenna has dual bandwidth of 49.60 and 10.05% covering the frequency range from 1.629 to 2.705 GHz and 3.411 to 3.772 GHz. In the end, the general investigation of the reflection coefficient, gain and efficiency of the anticipated antenna has been studied.

Keywords Microstrip antenna · Broadband · Efficiency · Bandwidth

1 Introduction

The mobile phones free the human being from the handset cords in many home, institutions and offices. Now we can speak with each other at any place with the help of cell phones without disturbance. Wireless technology provides more

M. Devi
Department of Electronics and Communication Engineering,
Uttar Pradesh Technical University, Lucknow, UP, India
e-mail: manavya36@gmail.com

V. K. Singh (✉)
Department of Electrical Engineering, SR Group of Institutions, Jhansi, UP, India
e-mail: singhvinod34@gmail.com

S. Sharma
Department of Electronics and Tele Communication,
Sandeep Institute of Technology and Research, Nashik, India
e-mail: sanjeevietb@rediffmail.com

A. K. Bhoi
Department of Electrical and Electronics Engineering,
Sikkim Manipal Institute of Technology (SMIT), Sikkim, India
e-mail: akash730@gmail.com

independence to us to access to the Internet without suffering from running yards of unsightly and costly cable. The trend of these applications and technology has drastically decreased the weight and volume. Therefore, there is requirement for antennas of small-sized, lightweighted, low profile with good directivity and radiation pattern in the horizontal plane [1–5]. The fringing field at the patch periphery can be increased by low value of dielectric constant. This is resulted that the radiated power of the antenna will be also increased. An increase in the substrate thickness has altered the antenna nature. A high substrate loss tangent increases the dielectric loss of the antenna which results in reducing the antenna efficiency [6–10].

2 Design of Proposed Antenna

The design of dumb-bell shape has cut on the patch antenna that is shown in Fig. 1. An antenna has 38.40 mm \times 46.80 mm ground plane and 28.80 mm \times 37.20 mm of patch dimensions. The dielectric material of the substrate (ϵ_r) chosen for this design is glass epoxy that has a dielectric constant of 4.4. The design specifications of the proposed antenna are given in Table 1 [10–15].

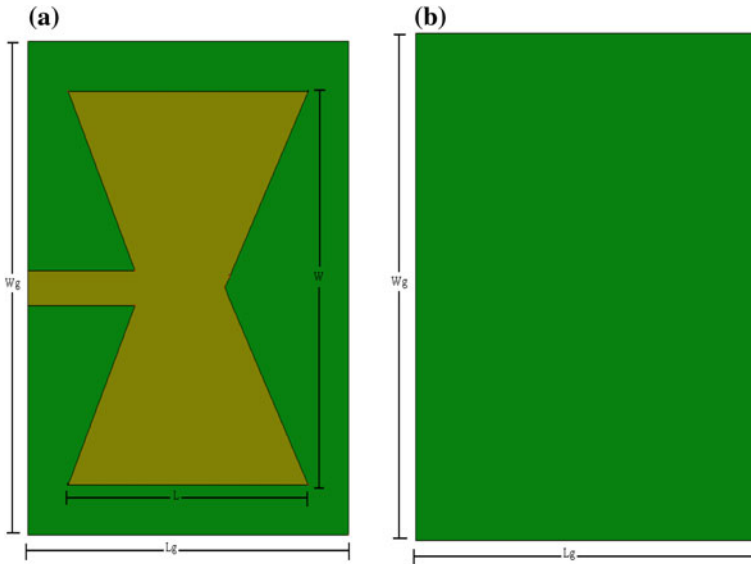


Fig. 1 Structure of presented antenna **a** front view and **b** back view

Table 1 Dimension of proposed textile antenna

S. No	Antenna parameter	Values
1.	Substrate thickness, $h(\text{mm})$	1.6
2.	Relative permittivity (ϵ_r)	4.4
4.	Width of ground dimension (mm)	46.8
5.	Length of ground plane (mm)	38.4
6.	Width of patch (mm)	37.2
7.	Length of patch (mm)	28.8

3 Results and Discussion

The simulated reflection coefficient versus frequency plot is presented in Fig. 2. The anticipated antenna is resonating at 2.45 GHz frequency and has frequency range from 1.629 to 2.705 GHz and 3.411 to 3.772 GHz giving a dual wide-bandwidth of 49.60 and 10.05%. Figure 3 shows the VSWR versus frequency plot of planned microstrip antenna. The efficiency versus frequency plot has been described in Fig. 4 and Fig. 5 shows the directivity versus frequency plot of anticipated antenna. The comparison of measured and simulated results is shown in Table 2.

4 Fabricated Antenna and Experimental Results

A compact dumb-bell shape microstrip antenna has been tested in microwave laboratory at IIT Kanpur which has provided measured bandwidth of 41.54 and 8.38% [16–19]. The prototype of presented antenna is shown in Fig. 6, and the comparative study of simulated and experimental results is shown in Fig. 7. The experimental results are in fine conformity with the simulation results. Figure 8 depicts the practical setup to measure return loss of proposed antenna at IIT Kanpur.

Fig. 2 Reflection coefficient versus frequency of plot

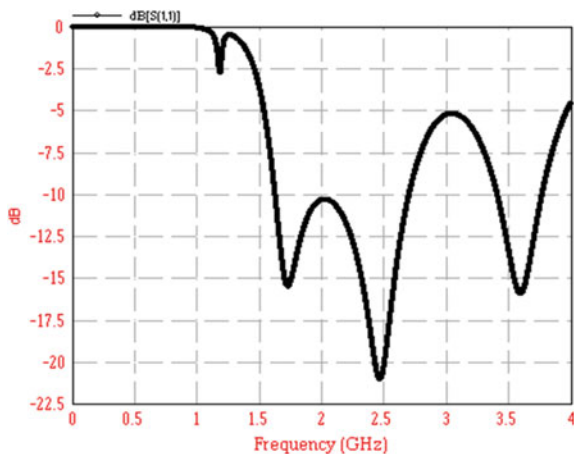


Fig. 3 VSWR versus frequency plot of anticipated antenna

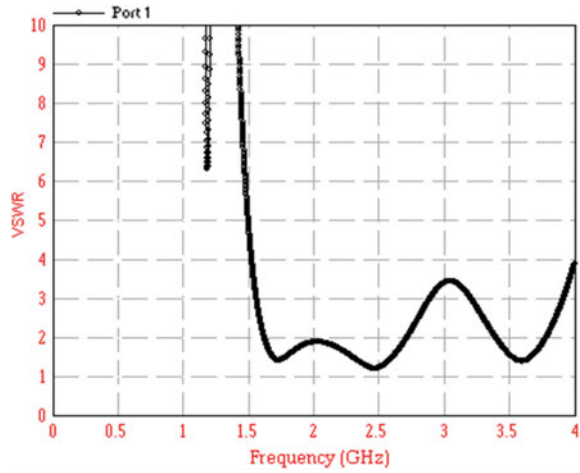


Fig. 4 Efficiency versus frequency plot of anticipated antenna

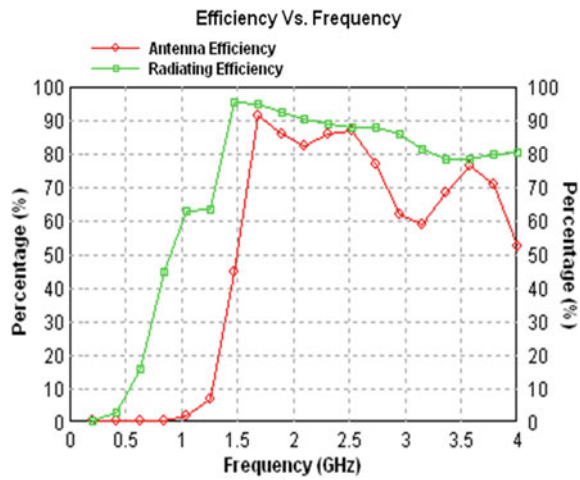


Table 2 Simulated and measured results of proposed antenna

Bands	Simulated		Experimental	
	Frequency range (GHz)	Bandwidth (%)	Frequency range (GHz)	Bandwidth (%)
First	1.629–2.705	49.60	1.697–2.586	41.54
Second	3.411–3.772	10.05	3.475–3.879	10.98

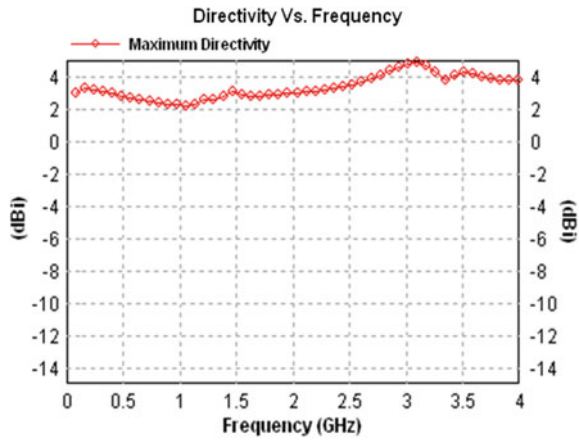


Fig. 5 Directivity versus frequency plot of anticipated antenna

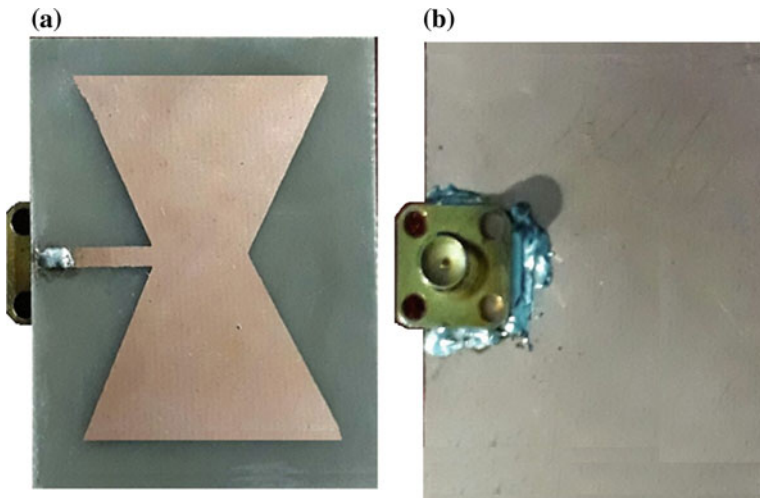


Fig. 6 Hardware of proposed antenna a top view and b bottom view

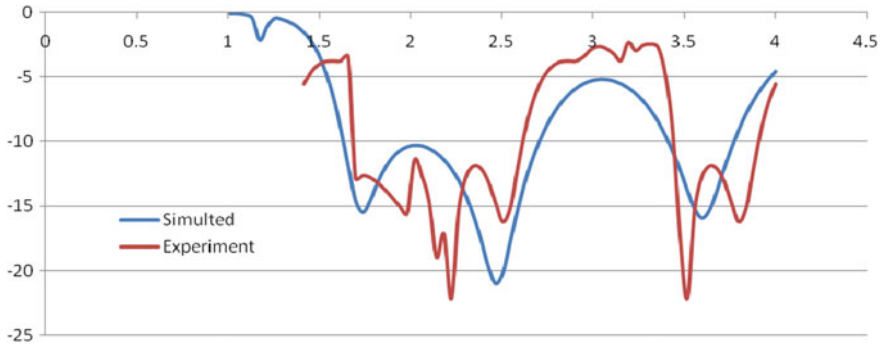


Fig. 7 Comparative study of simulated and measured results



Fig. 8 Practical setup to measure return loss of proposed antenna at IIT Kanpur

5 Conclusion

This antenna presents an excellent candidate for emerging wireless communications at 2.4 GHz frequency and suitable for WLAN applications. The simulated result shows that dual bandwidth of 49.60 and 10.05% are obtained that covers the frequency band from 1.629 to 2.705 GHz and 3.411 to 3.772 GHz.

References

1. Raghupatruni V., Ram Krishna, and Raj Kumar.; Design of Temple Shape Slot Antenna for Ultra Wideband Applications, Progress In Electromagnetic Research B, vol. 47, pp. 405–421, (2013).
2. Balanis CA.; Antenna Theory: Analysis and Design, John Wiley and Sons, New York, 2004.
3. Vinod Kumar Singh, Zakir Ali, Shahanaz Ayub, and Ashutosh Kumar Singh.; A wide band Compact Microstrip Antenna for GPS/DCS/PCS/WLAN Applications, Intelligent Computing, Networking, and Informatics, (ISBN: 978–81-322-1664-3), Springer, vol. 243, pp. 1107–1113, (2014).
4. Rajat Srivastava, Vinod Kumar Singh, and Shahanaz Ayub.; Comparative Analysis and Bandwidth Enhancement with Direct Coupled C Slotted Microstrip Antenna for Dual Wide Band Applications, Frontiers of Intelligent Computing: Theory and Applications, (ISBN: 978-3-319-12011-9), Springer, vol. 328, pp. 449–455, (2015).
5. Vinod Kumar Singh, Zakir Ali, Shahanaz Ayub, and Ashutosh Kumar Singh.; Bandwidth Optimization of Compact Microstrip Antenna for PCS/DCS/Bluetooth Application, Central European Journal of Engineering, Springer, vol. 4, no. 3, pp. 281–286, (2014).
6. Nikhil Singh, Ashutosh Kumar Singh, and Vinod Kumar Singh.; Design-Performance of Wearable Ultra Wide Band Textile Antenna for Medical Applications, Microwave and Optical Technology Letters, vol. 57, no. 7, pp. 1553–1557, (2015).
7. Stuti Srivastava, Vinod Kumar Singh, Zakir Ali, and Ashutosh Kumar Singh.; Duo Triangle Shaped Microstrip Patch Antenna Analysis for WiMAX lower band Application, International Conference on Computational Intelligence: Modelling Techniques and Applications (CIMTA-2013), Procedia Technology Elsevier 10, pp. 554–563, (2013).
8. Nikhil Kumar Singh, Vinod Kumar Singh, and Naresh. B.; Textile Antenna for Microwave Wireless Power Transmission, International Conference on Computational Modelling and Security (CMS 2016), Procedia Computer Science, vol. 85, pp. 856–861, (2016).
9. Neha Gupta, Vinod Kumar Singh, Zakir Ali, and Jitendra Ahirwar.; Stacked Textile Antenna for Multi Band Application Using Foam Substrate, International Conference on Computational Modelling and Security (CMS 2016), Procedia Computer Science, vol. 85, pp. 871–877, (2016).
10. Amit Kumar Rawat, Vinod Kumar Singh, and Shahanaz Ayub, Compact Wide band Microstrip Antenna for GPS/WLAN/WiMax Applications, International Journal of Emerging Trends in Engineering and Development, no. 2 vol. 7, pp. 140–145, (2012).
11. Rishabh Kumar Baudh, Ranjan Kumar, and Vinod Kumar Singh.; Arrow Shape Microstrip Patch Antenna for WiMax Application, Journal of Environmental Science, Computer Science and Engineering & Technology, vol. 3, no.1, pp. 269–274, (2013).
12. Janabeg Loni, Shahanaz Ayub, and Vinod Kumar Singh.; Performance analysis of Microstrip Patch Antenna by varying slot size for UMTS application, IEEE Conference on Communication Systems and Network Technologies (CSNT-2014), pp. 01–05, (2014).
13. Rajat Srivastava, Shahanaz Ayub, and V. K. Singh.; Dual Band Rectangular and Circular Slot Loaded Microstrip Antenna for WLAN/GPS/WiMax Applications, IEEE Conference on Communication Systems and Network Technologies (CSNT-2014), pp. 45–48, (2014).
14. Seema Dhupkariya, and Vinod Kumar Singh.; Textile Antenna for C-Band Satellite Communication Application, Journal of Telecommunication, Switching Systems and Networks, vol. 2, no. 2, pp. 20–25, (2015).
15. Janabeg Loni, and Vinod Kumar Singh.; Development of Bandwidth Enhanced Microstrip Patch Antenna for UMTS Application, Journal of Microwave Engineering & Technologies, vol. 2, no. 1, pp. 01–07, (2015).
16. Vinod Kumar Singh, and B. Naresh.; Multi Resonant Microstrip Antenna with Partial Ground for Radar Application, Journal of Telecommunication, Switching Systems and Networks, vol. 2, no. 1, pp. 01–05, (2015).

17. Manvendra Singh, Vinod Kumar Singh, and B. Naresh,: Rectangular Slot Loaded Circular Patch Antenna for WLAN Application, *Journal of Telecommunication, Switching Systems and Networks*, vol. 2, no. 1, pp. 07–10, (2015).
18. Mai A. R. Osman, M. K. A. Rahim, M. Azfar N. A. Samsuri, F. Zubir, and K. Kamardin,: Design, implementation and performance of Ultra-Wideband Textile Antenna, *Progress In Electromagnetics Research B*, vol. 27, pp. 307–325, (2011).
19. Vinod Kumar Singh, and Nikhil Kumar Singh,: Compact Circular Slotted Microstrip Antenna for Wireless Communication Systems, *Journal of Microwave Engineering & Technologies*, vol. 1, no. 1, pp. 07–14, (2015).

Estimation of Frequency Band of Microstrip Antenna (MSA) with Radial Basis Function (RBF)

Ashish Kumar, Archana Lala, Vinod Kumar Singh
and Akash Kumar Bhoi

Abstract This article explains the application of artificial neural network for the judgment of bandwidth of microstrip antenna. The algorithms of radial basis function (RBF) are used to make the neural network model. The training and testing data of the neural network are procured by analyzing the microstrip patch antenna by IE3D software. The results procured from ANN are tallied with IE3D and are quite reasonable. The operating frequency range of the antenna varies from 1.879 to 2.896 GHz. The results acquired from IE3D and those acquired from ANN are highly correlated.

Keywords Antenna · Bandwidth · Artificial neural network · RBF

1 Introduction

The patch antennas are being normally used in wireless communication because of its low weights, low price, and directive with high transmission efficiency, compatibility with microwave circuit and wireless communication equipment; therefore, it is commonly used in different wireless communication systems. However, rectangular microstrip antennas have few drawbacks such as narrow bandwidth, low gain, restricted power handling capacity and poor polarization. In the current paper, an artificial neural network is expanded to analyze the frequency

A. Kumar · A. Lala

Department of Computer Science Engineering, SR Group of Institution, Jhansi, India
e-mail: ashishyadav.510@gmail.com

V. K. Singh (✉)

Department of Electrical Engineering, SR Group of Institution, Jhansi, India
e-mail: singhvinod34@gmail.com

A. K. Bhoi

Department of Electrical and Electronics Engineering,
Sikkim Manipal Institute of Technology (SMIT), Rangpo, Sikkim, India
e-mail: akash730@gmail.com

© Springer Nature Singapore Pte Ltd. 2018

R. Bera et al. (eds.), *Advances in Communication, Devices and Networking*,
Lecture Notes in Electrical Engineering 462,
https://doi.org/10.1007/978-981-10-7901-6_42

band and bandwidth of microstrip antenna [1–5]. Application of neuro models is well suited for efficient and precise designing of MSA. The IE3D software has been put to produce the data related to training and test for artificial neural network which is a computational EM simulator based on technique of moments mathematical methods.

It is analyzed that in 3D and multi-layer structure of common shapes, feed point must be placed to get different results. The return loss is obtained and that feed point is chosen as the finest one where the reflection coefficient is most negative. The optimum feed point that produced return loss is the point that yields most negative return loss. It is simple to shape and straightforward to match by controlling the probe feed coordinates [6–13]. The anticipated antenna has been intended to provide a broad bandwidth, i.e. 42.60%, encompassing the frequency varying from 1.879 to 2.896 GHz which is most appropriate for WLAN system.

2 Designing and Data Generation of the Planned Antenna

The configuration of the planned antenna is depicted in Fig. 1. An antenna has $33.0 \text{ mm} \times 40.0 \text{ mm}$ modified ground plane and $23.4 \text{ mm} \times 30.4 \text{ mm}$ of rectangular patch dimensions. The patch length L and the patch width W of the proposed antenna, having thickness h , are shown in Fig. 1. The operating frequency (f_o),

Fig. 1 Configuration of proposed microstrip antenna

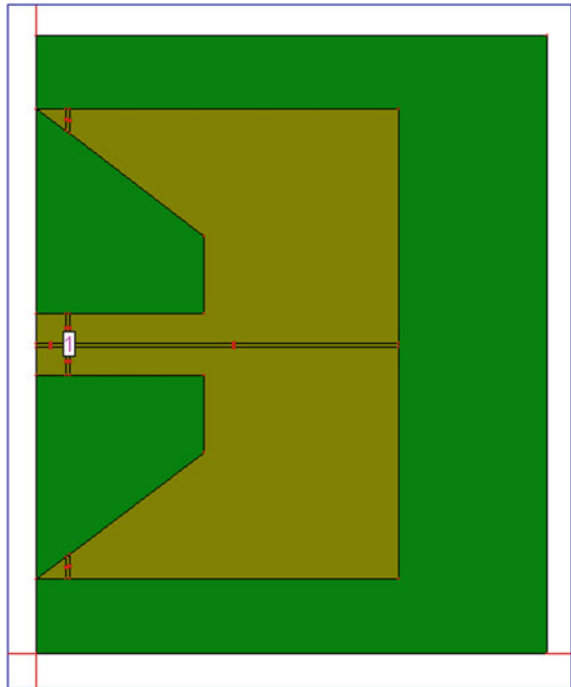


Fig. 2 Radial basis function model

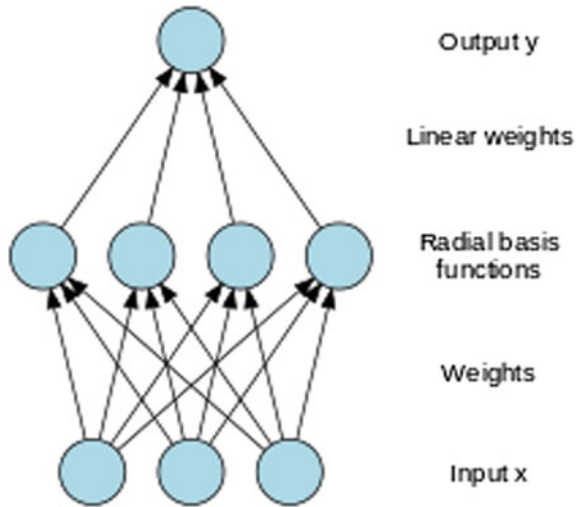


Table 1 Parameters used for designing the antenna

Parameters	Figures
f	3.0 GHz
h	1.6 mm
Wg	40.0 mm
Lg	33.0 mm
L	23.40 mm
W	30.40 mm

dielectric constant (ϵ_r) and height of the substrate (h) are the three vital parameters for designing antenna [14–18]. The glass epoxy is the dielectric material of the substance, having a dielectric constant of 4.4, and is preferred for designing antenna. Figure 2 shows the radial basis function artificial neural network model (Table 1).

3 Introduction to RBF Network

This paper reveals that radial basis function neural network is utilized to analyze rectangular patch antenna. Radial basis function network is a feed-forward neural network with a concealed layer which uses radial basis activation function for hidden neurons. RBF network is implemented for numerous microwave modelling functions. It consists of three layers in which the second layer shows a sequence of

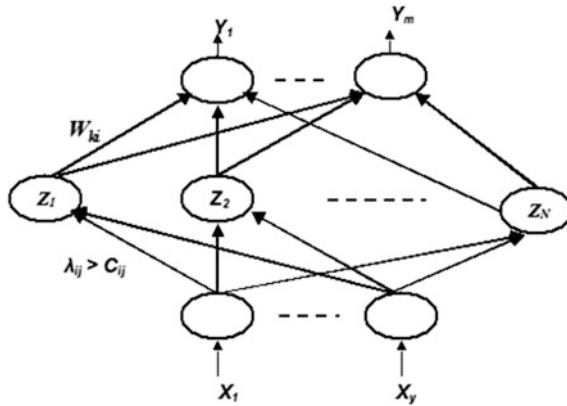


Fig. 3 Typical radial basis function network

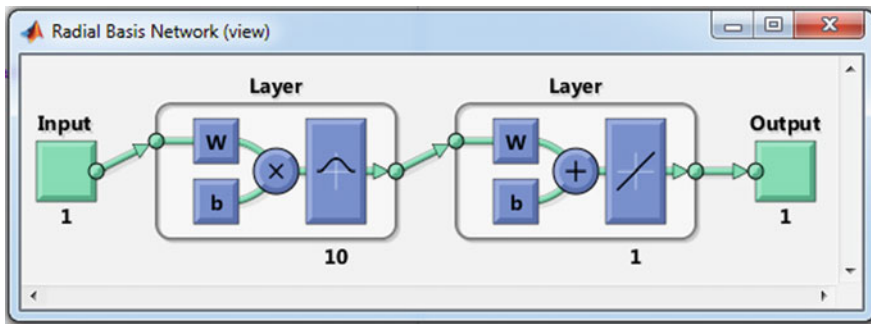


Fig. 4 Radial basis function network depicting the three prominent layers

centres in the input data space. The centres and the widths formed by these algorithms then form the weight of device of the concealed layer that remains unaffected after the clustering has been finished. An RBF network is shown in Fig. 3. In the arrangement, one input and one output are used for the analysis of ANN as shown in Fig. 4, and RBF networks are quicker and successful in comparison with MLPFFBP for the anticipated antenna. Figure 5 represents the application of RBF network for training performance of developed neural model. Bandwidth procurable via IE3D with the use of RBF network for various test patterns is compared in the following table (Table 2).

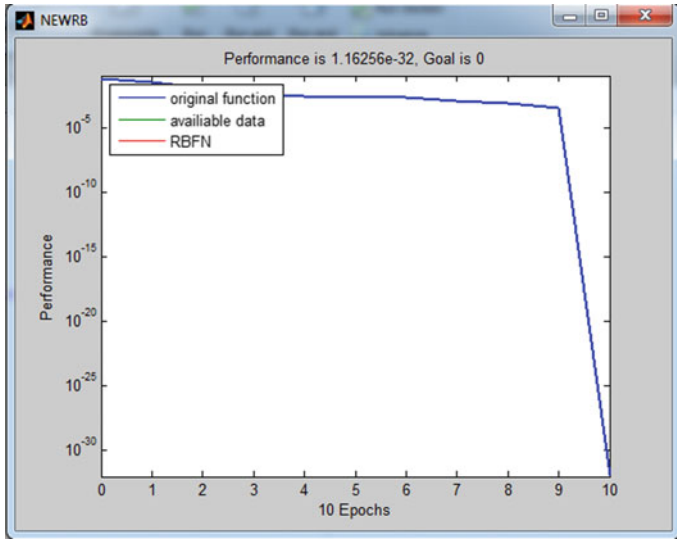


Fig. 5 Application of RBF network for highlighting training performance of developed neural model

Table 2 Return loss obtained using IE3D by varying probes

Length	Width	Probe(x, y)	f ₁	f ₂	Frequency band IE3D GHz	Frequency band RBF GHz
23.40	30.40	0.3, 19.9	2.308	2.629	0.321	0.3210
23.40	30.40	0.5, 19.9	2.278	2.669	0.391	0.3910
23.40	30.40	0.8, 19.9	2.237	2.709	0.472	0.4720
23.40	30.40	1.0, 19.9	2.193	2.735	0.542	0.5420
23.40	30.40	1.3, 19.9	2.067	2.769	0.702	0.7020
23.40	30.40	1.5, 19.9	1.930	2.807	0.877	0.8770
23.40	30.40	1.8, 19.9	1.886	2.849	0.963	0.9630
23.40	30.40	2.0, 19.9	1.879	2.896	1.017	1.0170
23.40	30.40	2.3, 19.9	2.619	2.950	0.331	0.3310
23.40	30.40	2.5, 19.9	1.924	2.143	0.219	0.2190
23.40	304.	2.8, 19.9	2.729	2.990	0.261	1.2610

4 Result and Discussion

Figure 6 shows the reflection coefficient (S_{11}) versus frequency plot of anticipated microstrip antenna which possesses frequency ranging from 1.879 to 2.896 GHz results in a broad bandwidth of 42.60%. It is apparent that the results procured from IE3D and ANN tools have good conformity and hence give accurate result after numerous trainings (Table 3).

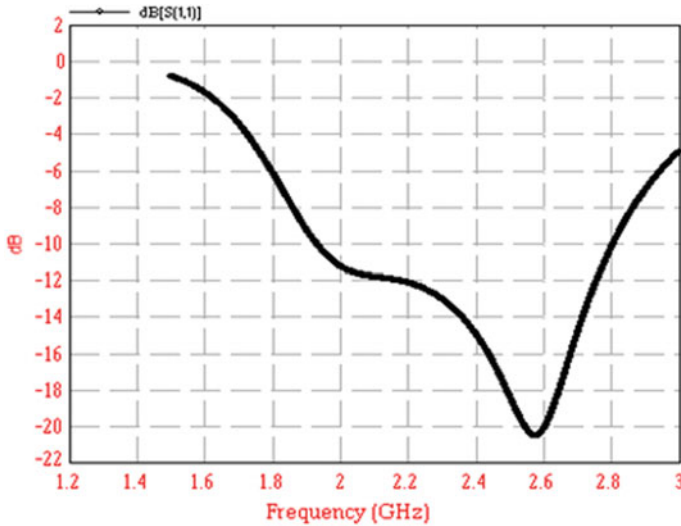


Fig. 6 Reflection coefficient (S_{11}) versus frequency

Table 3 Comparisons of IE3D results and RBFANN results

Parameters	Simulated result (IE3D)	Simulated result (RBF ANN)
Frequency range	1.879–2.896 GHz	1.879–2.896 GHz
Bandwidth	42.60%	42.48%

5 Conclusions

This paper reveals a design of an anticipated antenna for HYPERLAN, WiMAX and WLAN purposes. A broad bandwidth of 42.60% is procurable with the use of glass epoxy substrate of dielectric constant of 4.4. The readings obtained from IE3D and ANN are well correlated. Besides being accurate, the result is quick which is evident from Table 2. The performance training as shown by RBF system is completed in lesser epochs than MLPFFBP, and hence, it is accomplished that RBF is superior to MLPFFBP.

References

1. J.R. James and P.S. Hall: Handbook of microstrip antennas, London, peter Peregrinus Ltd., (1989).
2. Girish Kumar and K.P. Ray: Broadband Microstrip antennas, Norwood: Artech House, (2003).

3. Zakir Ali, Vinod Kumar Singh, Ashutosh Kumar Singh, Shahanaz Ayub: E shaped Microstrip Antenna on Rogers substrate for WLAN applications, Proc. IEEE, pp. 342–345, Oct. (2011).
4. Ang, B. K. and B. K. Chung: A wideband E-shaped microstrip patch antenna for 5–6 GHz wireless communications, Progress in Electromagnetics Research, PIER 75, 397–407, (2007).
5. Zealand software inc. IE3D: MoM-based EM simulator. Web: <http://www.zealand.com>.
6. Y. X. Guo, L. Bian and X. Q. Shi: Broadband Circularly Polarized Annular-Ring Microstrip Antenna, IEEE Transactions on Antennas and Propagation, AP-57, 8, pp. 2474–2477, (2008).
7. Islam M.T., M.N. Shakib and N. Misran: Multi-Slotted Microstrip Patch Antenna for Wireless Communication, Progress In Electromagnetics Research Letters, Vol.10, pp. 11–18, (2009).
8. Ramu Pillalamani, G Sasi Bhusana Rao, S. Srinivasa Kumar: Novel printed rectangular patch monopole antennas with slit ground plane for UWB applications, The NEHU Journal, Vol 7, no. 1, (2010).
9. Islam M.T., Shakib M.N., Misran N.: Design Analysis of High Gain Wideband L-Probe Fed Microstrip Patch Antenna, Progress In Electromagnetics Research, PIER 95, 397–407, (2009).
10. V.V. Thakre, P.K. Singhal: Band width analysis by introducing slots in microstrip antenna design using ANN, Progress in electromagnetic research M, Vol.9, pp. 107–122, (2009).
11. B. K. Ang and B. K. Chung: A Wideband E-shaped microstrip patch antenna for 5–6 GHz wireless Communications, Progress in Electromagnetic Research, PIER75, pp. 397–407, (2007).
12. Hassoun, M. H: Fundamentals of Artificial Neural Network, chapter 8, New Delhi, Prantice Hall of India (1999).
13. MATLAB software version R (2013).
14. IE3D simulation software version 12.0.
15. Ali, Z.; Singh, V.K.; Singh, A.K.; Ayub, S.: Wide Band Inset Feed Microstrip Patch Antenna for Mobile Communication, Communication Systems and Network Technologies, vol., no., pp. 51–54, (2013).
16. Ashutosh Kumar Singh, R. A. Kabeer, M. Shukla, Z. Ali, V. K. Singh, Shahanaz Ayub: Performance analysis of first iteration Koch curve fractal log periodic antenna of varying flare angles, Central European Journal of Engineering (CEJE), Springer, Volume 3, Issue 1, pp. 51–57, (2013).
17. C. A. Balanis: Antenna Theory, Analysis and Design, John Wiley & Sons, New York, (1997).
18. Singh, V.K.; Ali, Z.; Singh, A.K.; Ayub, S.: Dual Band Microstrip Antenna for UMTS/WLAN/WIMAX Applications, Communication Systems and Network Technologies, vol., no., pp. 47–50, (2013).

Design and Analysis of Microstrip Antenna Using Multilayer Feed-Forward Back-Propagation Neural Network (MLPFFBP-ANN)

Poornima Singh, Vinod Kumar Singh, Archana Lala and Akash Kumar Bhoi

Abstract In this article, the algorithms of MLPFFBP-ANN are used to make the neural network model and for the judgment of bandwidth of microstrip antenna. The training and testing data of the neural network are procured by analyzing the microstrip patch antenna by IE3D software. The results obtained by using MLPFFBP-ANN are tallied with IE3D and are quite reasonable. The operating frequency range of the antenna varies from 1.66 to 2.53 GHz. The results acquired from IE3D and ANN are highly correlated.

Keywords Antenna · Bandwidth · Artificial Neural Network · MLPFFBP-ANN

1 Introduction

Rectangular microstrip antennas have few drawbacks such as narrow bandwidth, low gain, restricted power handling capacity, and poor polarization; however, these are usually used in wireless communication because of its low weights, low price, and directive with high transmission efficiency, compatibility with microwave circuit, and wireless communication equipment; therefore, it is commonly used in different wireless communication systems. In the current paper, an artificial neural network is expanded to analyze the frequency band and bandwidth of microstrip

P. Singh · A. Lala

Department of Computer Science Engineering, S. R. G. I., Jhansi, India
e-mail: singh.poornima55@gmail.com

V. K. Singh (✉)

Department of Electrical Engineering, S. R. G. I., Jhansi, India
e-mail: singhvinod34@gmail.com

A. K. Bhoi

Department of Electrical and Electronics Engineering,
Sikkim Manipal Institute of Technology (SMIT), Sikkim, India
e-mail: akash730@gmail.com

© Springer Nature Singapore Pte Ltd. 2018

R. Bera et al. (eds.), *Advances in Communication, Devices and Networking*,
Lecture Notes in Electrical Engineering 462,
https://doi.org/10.1007/978-981-10-7901-6_43

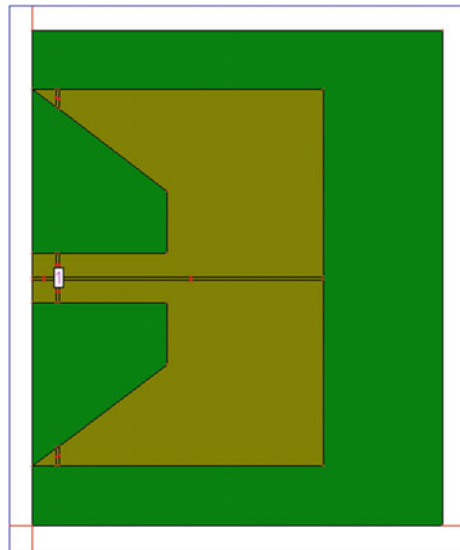
393

antenna [1–6]. Neuro-models are mathematically more efficient than EM models. Application of neuro-models is well suited for efficient precise optimization and designed within the range of training. The IE3D software has been put to produce the data related to training and test for an artificial neural network which is a computational EM simulator based on technique of moments mathematical methods. It is analyzed that the optimum feed point produced return loss is the point that yields most negative return loss. It is simple to shape and straightforward to match by controlling the probe feed coordinates [7–15]. The anticipated antenna has been intended to provide a broad bandwidth, i.e., 41.52%, encompassing the frequency varying from 1.66 to 2.53 GHz which is most appropriate for WLAN system.

2 Designing and Data Generation of the Planned Antenna

The configuration of the planned antenna is depicted in Fig. 1. An antenna has $33.0 \text{ mm} \times 40.0 \text{ mm}$ modified ground plane and $23.4 \text{ mm} \times 30.4 \text{ mm}$ of rectangular patch dimensions. The patch length L and the patch width W of the proposed antenna, having thickness h , are shown in Fig. 1. The operating frequency (f_o), dielectric constant (ϵ_r), and height of the substrate (h) are the three vital parameters for designing antenna [16–18]. The glass epoxy is the dielectric material of the substance, having a dielectric constant of 4.4, which is preferred for designing antenna. Figure 2 shows MLFFBP artificial neural network model and Fig. 3 describes MLFFBP network depicting the three prominent layers. The Parameters used for designing the antenna is shown in Table 1.

Fig. 1 Configuration of proposed microstrip antenna



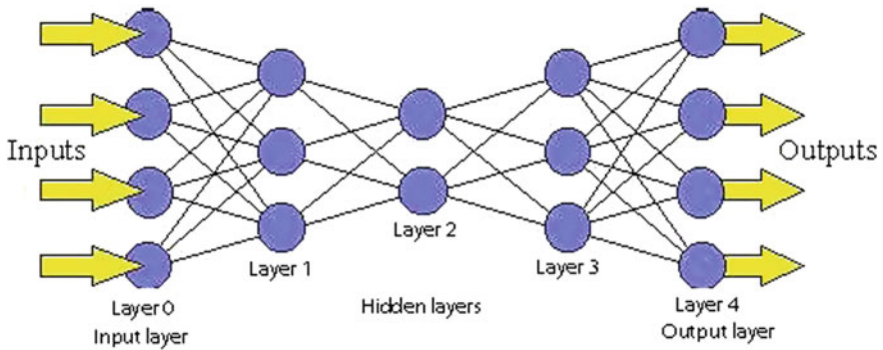


Fig. 2 MLPFFBP artificial neural network model

Table 1 Parameters used for designing the antenna

Parameters	Data
f	2.45 GHz
h	1.6 mm
Wg	46.80 mm
Lg	38.40 mm
L	28.80 mm
W	37.20 mm

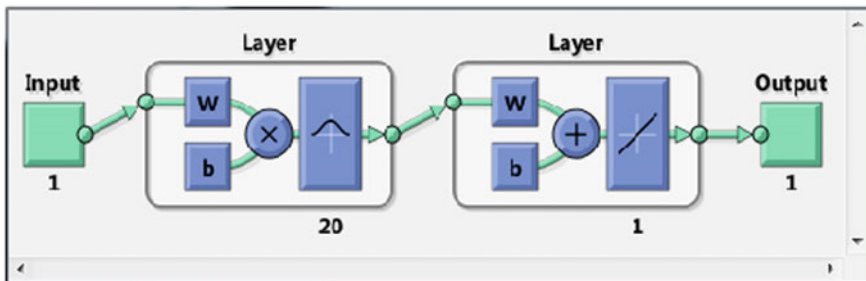


Fig. 3 MLPFFBP network depicting the three prominent layers

3 Result and Discussion

This paper reveals that MLPFFBP is utilized to analyze rectangular patch antenna. Multilayer perceptron feed-forward network is implemented for numerous microwave modeling functions. Multilayer perceptron feed-forward network is shown in Fig. 4. Figure 4 represents the application of MLPFFBP network for training performance of developed neural model. Bandwidth procurable via IE3D with the

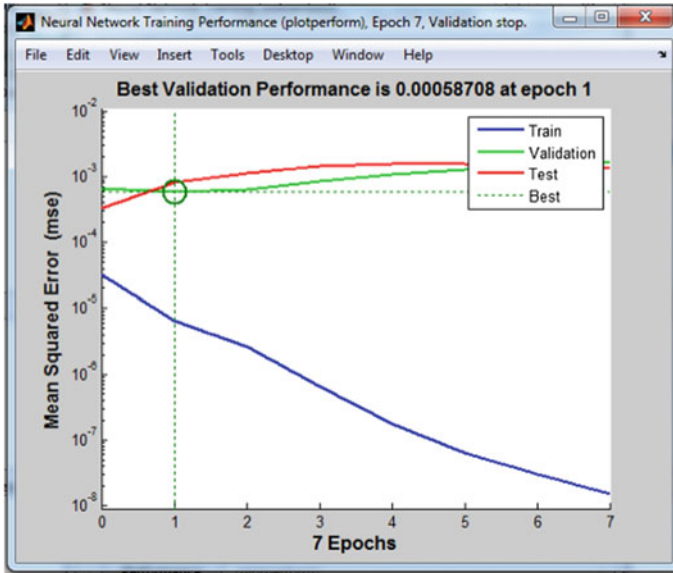


Fig. 4 Application of MLPFFBP network for highlighting training performance of developed neural model

Table 2 Return loss obtained using IE3D by varying probes

Length	Width	Probe(x, y)	f ₁	f ₂	Frequency band IE3D GHz	Frequency band MLPFFBP GHz
28.80	37.20	0.0,22.4	1.65	2.53	0.88	0.8754
28.80	37.20	0.3,22.4	1.67	2.51	0.84	0.8400
28.80	37.20	0.5,22.4	1.67	2.49	0.82	0.7804
28.80	37.20	0.8,22.4	1.69	2.47	0.78	0.7857
28.80	37.20	1.0,22.4	1.70	2.46	0.76	0.7588
28.80	37.20	1.3,22.4	1.71	2.43	0.72	0.7204
28.80	37.20	1.5,22.4	1.72	2.43	0.71	0.7952
28.80	37.20	2.0,22.4	1.75	2.40	0.65	0.6504
28.80	37.20	2.5,22.4	1.80	2.36	0.56	0.5250
28.80	37.20	3.0,22.4	1.83	2.32	0.49	0.4920

use of RBF network for various test patterns is compared in the following Table 2. Figure 5 shows the reflection coefficient (S_{11}) versus frequency plot of anticipated microstrip antenna which possesses frequency ranging from 1.66 to 2.53 GHz results in a broad bandwidth of 41.52%. It is apparent that the results procured from IE3D and MLPFFBP-ANN tools have good conformity and hence give accurate result after numerous training (Table 3).

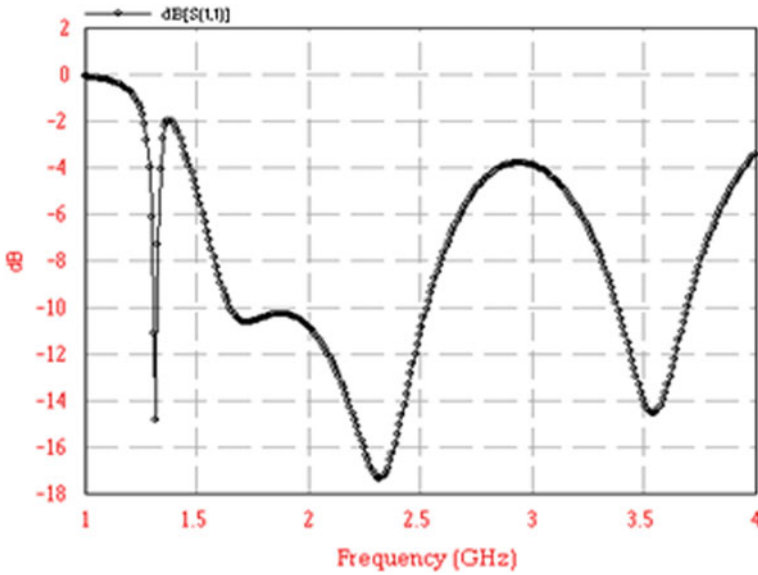


Fig. 5 Reflection coefficient (S_{11}) versus frequency

Table 3 Comparisons of IE3D results and RBF-ANN results

Parameters	Simulated result (IE3D)	Simulated result (MLPFFBP-ANN)
Frequency band	1.66–2.53	1.66–2.53
Bandwidth	41.52%	40.98%

4 Conclusions

This paper reveals a design of an anticipated antenna for HYPERLAN, WiMAX, and WLAN purposes. A broad bandwidth of 41.52% is procurable with the use of glass epoxy substrate of the dielectric constant of 4.4. The readings obtained from IE3D and ANN are well correlated. Besides being accurate, the result is quick which is evident from Table 2.

References

1. J.R. James and P.S. Hall: Handbook of microstrip antennas, London, peter Peregrinus Ltd., (1989).
2. Girish Kumar and K.P. Ray: Broadband Microstrip antennas, Norwood: Artech House, (2003).

3. Zakir Ali, Vinod Kumar Singh, Ashutosh Kumar Singh, Shahanaz Ayub: E shaped Microstrip Antenna on Rogers substrate for WLAN applications, Proc. IEEE, pp. 342–345, Oct. (2011).
4. Ang, B. K. and B. K. Chung: A wideband E-shaped microstrip patch antenna for 5–6 GHz wireless communications, Progress in Electromagnetics Research, PIER 75, 397–407, (2007).
5. Zealand software inc. IE3D: MoM-based EM simulator. Web: <http://www.zealand.com>.
6. Y. X. Guo, L. Bian and X. Q. Shi: Broadband Circularly Polarized Annular-Ring Microstrip Antenna, IEEE Transactions on Antennas and Propagation, AP-57, 8, pp. 2474–2477, (2008).
7. Islam M.T., M.N. Shakib and N. Misran: Multi-Slotted Microstrip Patch Antenna for Wireless Communication, Progress In Electromagnetics Research Letters, Vol.10, pp. 11–18, (2009).
8. Ramu Pillalamani, G Sasi Bhusana Rao, S. Srinivasa Kumar: Novel printed rectangular patch monopole antennas with slit ground plane for UWB applications, The NEHU Journal, Vol 7, no. 1, (2010).
9. Islam M.T., Shakib M.N., Misran N.: Design Analysis of High Gain Wideband L-Probe Fed Microstrip Patch Antenna, Progress In Electromagnetics Research, PIER 95, 397–407, (2009).
10. V.V. Thakre, P.K. Singhal: Band width analysis by introducing slots in microstrip antenna design using ANN, Progress in electromagnetic research M, Vol.9, pp. 107–122, (2009).
11. B. K. Ang and B. K. Chung: A Wideband E-shaped microstrip patch antenna for 5–6 GHz wireless Communications, Progress in Electromagnetic Research, PIER75, pp. 397–407, (2007).
12. Hassoun, M. H: Fundamentals of Artificial Neural Network, chapter 8, New Delhi, Prantice Hall of India (1999).
13. MATLAB software version R (2013).
14. IE3D simulation software version 12.0.
15. Singh, V.K.; Ali, Z.; Singh, A.K.; Ayub, S.: Dual Band Microstrip Antenna for UMTS/WLAN/WIMAX Applications, Communication Systems and Network Technologies, vol., no., pp. 47,50, (2013).
16. Ali, Z.; Singh, V.K.; Singh, A.K.; Ayub, S.: Wide Band Inset Feed Microstrip Patch Antenna for Mobile Communication, Communication Systems and Network Technologies, vol., no., pp. 51,54, (2013).
17. Ashutosh Kumar Singh, R. A. Kabeer, M. Shukla, Z. Ali, V. K. Singh, Shahanaz Ayub: Performance analysis of first iteration Koch curve fractal log periodic antenna of varying flare angles, Central European Journal of Engineering (CEJE), Springer, Volume 3, Issue 1, pp. 51–57, (2013).
18. C. A. Balanis: Antenna Theory, Analysis and Design, John Wiley & Sons, New York, (1997).

Performance of SC Receiver Over OWDP Fading Channels

Suparna Goswami and Aheibam Dinamani Singh

Abstract The expressions for performance parameters of selection combining (SC) diversity receiver with L -branch over one wave diffused wave (OWDP) fading channel has been found out. The cumulative distribution function (cdf) of the signal-to-noise ratio (SNR) output has been obtained. Using the obtained cdf equation, the probability distribution function (pdf) of received SNR of the system over OWDP fading channel has been evaluated. The pdf obtained has been employed to evaluate the performance measurement namely for different coherent and non-coherent modulations. The outcomes obtained for the fading parameter K and the total number of branch L have been analyzed. The obtained outcomes are verified through Monte Carlo Simulation.

Keywords ABER · Diversity receiver · Outage probability · OWDP Selection combining

1 Introduction

The existence of fading in the channel deteriorates the execution of wireless networks. To reduce the bad influence of the fading in wireless medium, the diversity technique is employed. In a diversity receiver, several replicas of same information are gathered at the receiver from distinct fading channels. The signals are then added up to give the improved signal-to-noise ratio (SNR). The selection combining (SC) technique is the simplest one among all diversity combining technique. Hence, this technique is essential for execution. The one wave diffused power (OWDP) fading is composed of one specular component and many diffused propagating waves. The OWDP fading channel is effective in wireless network

S. Goswami (✉) · A. D. Singh
Department of ECE, NERIST, Nirjuli, Arunachal Pradesh, India
e-mail: suparnanerist@gmail.com

A. D. Singh
e-mail: ads@nerist.ac.in

those are framed inside an aperture such as tunnel, aircraft, buses, trains. OWDP is a particular case of two wave diffuse power (TWDP) fading channels [1]. The analysis on bit error rate (BER) performance of binary phase shift keying (BPSK) system in TWDP fading is done in [2]. The execution of BPSK scheme by using pre-detection maximal ratio combining (MRC) technique has been analyzed over N TWDP channels [3]. The expression for average bit error rate (ABER) of quadrature amplitude modulation (QAM) using cumulative distribution function (cdf) is expressed over TWDP fading channel [4]. The performance analysis of L -branch SC receiver in κ - μ and η - μ fading channel has been presented in [5]. The symbol error rate (SER) of the SC receiver with M -ary Phase Shift Keying (MPSK) and MQAM has been evaluated for TWDP fading channel in [6]. The expression for symbol error probability (SEP) of M -ary rectangular QAM using moment generating function (mgf) over TWDP fading channel is expressed in [7]. In [8], the evaluation of capacity of various adaptive transmission techniques over TWDP fading is done. The outage probability and ABER expressions for SC over TWDP fading are obtained in [9]. The capacity of adaptive techniques of MRC receiver over TWDP fading channel is done in [10]. In [11], the capacity expression of adaptive receiver for MRC system with dual branch over unequal TWDP fading channel has been obtained. Performance analysis of system over TWDP fading channel is done in [12]. From the literature study, it can be observed that no work on performance evaluation for SC scheme is being presented in regard to OWDP fading channel. This extends the idea and motivation to work on the execution of the parameters for SC technique on OWDP fading channels.

The paper is arranged in the following manner. Sect. 2 contains the discussion about the OWDP model. In Sect. 3, the SNR pdf of SC receiver is derived. Section 4 gives the derived expressions of performance parameters for SC technique on OWDP model. In Sect. 5, the discussion on obtained results is presented. Finally, the paper is concluded in the last part, i.e., Sect. 6.

2 Channel and System

The OWDP fading channel contains only one wave with constant amplitude. The medium is being considered to be slow, flat, with OWDP fading data. The envelope pdf of OWDP fading from [1] can be written as

$$P_R(r) = \sum_{i=1}^M a_i \frac{r}{\sigma^2} e^{-\left\{\frac{r^2 + 2\sigma^2 K}{2\sigma^2}\right\}} I_0\left(\frac{r}{\sigma^2} \sqrt{2\sigma^2 K}\right), \quad (1)$$

where r is the fading amplitude, σ^2 is the variance, $I_0(\cdot)$ is defined as first kind Bessel function with zeroth order, K is the fraction of total specular power to diffused power. The order of approximation is represented by i . After the square and random variable transformation is performed, the SNR pdf of OWDP model can be obtained as

$$f_{\gamma}(\gamma) = \eta \sum_{i=1}^M a_i e^{-\{\eta\gamma + K\}} I_0\left(2\sqrt{K\eta\gamma}\right), \quad (2)$$

where $\eta = \frac{K+1}{\bar{\gamma}}$.

3 Selection Combiner Output SNR Pdf

In SC combining technique, the receiver with strongest SNR is being chosen. The received output SNR is given in [13] as

$$\gamma_{SC} = \max(\gamma_1, \gamma_2, \dots, \gamma_N) \quad (3)$$

where $\gamma_t = \frac{E_b}{N_0} r_t^2$ and $t = 1, 2, \dots, N$ is the input instantaneous SNR of SC receiver.

The SNR pdf at m th branch is obtained as

$$f_{\gamma_m}(\gamma_m) = \eta_m \sum_{i=1}^M a_i e^{-\{\eta_m\gamma_m + K\}} I_0\left(2\sqrt{K\eta_m\gamma_m}\right). \quad (4)$$

where $\eta_m = \frac{K+1}{\bar{\gamma}_m}$. $\bar{\gamma}_m$ is the average branch SNR.

The cdf at m th input is obtained as

$$\begin{aligned} F_{\Gamma_m}(\Gamma_m) &= \int_0^{\Gamma_m} f_{\gamma_m}(\gamma_m) d\gamma_m \\ &= 1 - \eta \sum_{i=1}^M a_i e^{-K} \int_{\Gamma_m}^{\infty} e^{-\eta\gamma_m} I_0\left(2\sqrt{K\eta\gamma_m}\right) d\gamma_m \\ &= 1 - \eta \sum_{i=1}^M a_i e^{-K} \times \int_{\Gamma_m}^{\infty} e^{-\eta_m\gamma_m} I_0\left(2\sqrt{K\eta_m\gamma_m}\right) d\gamma_m. \end{aligned} \quad (5)$$

The integral in (5) can be solved using [14, (1)]. The final expression for the cdf is expressed as

$$F_{\Gamma_m}(\Gamma_m) = 1 - \sum_{i=1}^M a_i Q_1\left(\sqrt{2K}, \sqrt{2\eta_m\Gamma_m}\right), \quad (6)$$

where $Q_M(\alpha, \beta)$ is Marcum Q function and can be written as $Q_M(\alpha, \beta) = \frac{1}{\alpha^{M-1}} \int_{\beta}^{\infty} x^M e^{-\frac{x^2 + \alpha^2}{2}} I_{M-1}(\alpha x) dx$ [14]. The cdf of the SNR with L-SC receiver is obtained by multiplying L cdfs in (6). The expression can be written as

$$F_{\gamma_{sc}}(\gamma_{sc}) = \prod_{l=1}^L \left\{ 1 - \sum_{i=1}^M a_i Q_1(\sqrt{2K}, \sqrt{2\eta_l \gamma_{sc}}) \right\}, \tag{7}$$

where $\gamma_m = \gamma_{sc}, \forall m$. Considering same parameter of fading and $\overline{\gamma}_m$, the cdf for SC receiver is obtained as

$$F_{\gamma_{sc}}(\gamma_{sc}) = \left[1 - \sum_{i=1}^M a_i Q_1(\sqrt{2K}, \sqrt{2\eta \gamma_{sc}}) \right]^L. \tag{8}$$

The pdf expression of output SNR for same fading parameter can be obtained by differentiating (8) with respect to γ_{sc}

$$\frac{dF_{\gamma_{sc}}(\gamma_{sc})}{d\gamma_{sc}} = \frac{d}{d\gamma_{sc}} \left(\left[1 - \sum_{i=1}^M a_i Q_1(\sqrt{2K}, \sqrt{2\eta \gamma_{sc}}) \right]^L \right). \tag{9}$$

The final expression is

$$f_{\gamma_{sc}}(\gamma_{sc}) = L\eta \left[1 - \sum_{i=1}^M a_i Q_1(\sqrt{2K}, \sqrt{2\eta \gamma_{sc}}) \right]^{L-1} \times \sum_{i=1}^M a_i e^{-(K + \eta \gamma_{sc})} I_0(2\sqrt{K\eta \gamma_{sc}}). \tag{10}$$

Similarly, by differentiating (7) with respect to γ_{sc} , the pdf expression of output SNR for unequal fading parameter is

$$\frac{dF_{\gamma_{sc}}(\gamma_{sc})}{d\gamma_{sc}} = \frac{d}{d\gamma_{sc}} \left(\prod_{l=1}^L \left\{ 1 - \sum_{i=1}^M a_i Q_1(\sqrt{2K}, \sqrt{2\eta_l \gamma_{sc}}) \right\} \right). \tag{11}$$

The final expression of pdf for unequal fading parameter is expressed as

$$f_{\gamma_{sc}}(\gamma_{sc}) = \sum_{l=1}^L \sum_{i=1}^M a_i \eta_l e^{-(K + \eta_l \gamma_{sc})} I_0 \left(2\sqrt{K \eta_l \gamma_{sc}} \right) \times \prod_{j=1}^L \left\{ 1 - \sum_{i=1}^M a_i Q_1 \left(\sqrt{2K}, \sqrt{2\eta_j \gamma_{sc}} \right) \right\} \quad (12)$$

$(j \neq l)$

4 Performance of SC Receiver

4.1 Outage Probability

Outage probability (P_{out}) measures the performance of the system. P_{out} is the probability that the rate of information is less than a required threshold γ_{th} . The P_{out} is being evaluated by computing $\gamma_{SC} = \gamma_{th}$ [13]. For same fading variable, the equation for outage probability can be written as

$$P_{out}(\gamma_{th}) = \left[1 - \sum_{i=1}^M a_i Q_1 \left(\sqrt{2K}, \sqrt{2\eta_i \gamma_{th}} \right) \right]^L \quad (13)$$

The expression of outage probability for unequal fading parameter can be written as

$$P_{out}(\gamma_{th}) = \prod_{l=1}^L \left\{ 1 - \sum_{i=1}^M a_i Q_1 \left(\sqrt{2K}, \sqrt{2\eta_l \gamma_{th}} \right) \right\} \quad (14)$$

4.2 ABER

The ABER is the average of conditional BER and the pdf SNR. The expression of ABER is written from [13] as

$$P_E = \int_0^{\infty} p_e(\varepsilon/\gamma_{SC}) f_{\gamma_{SC}}(\gamma_{SC}) d\gamma, \quad (15)$$

where $p_e(\varepsilon/\gamma_{SC})$ is termed as conditional BER as per the incorporated modulation scheme.

4.2.1 Coherent Modulation

The conditional BER for coherent modulation is expressed as $p_e(\varepsilon/\gamma_{SC}) = aQ(\sqrt{b\gamma})$, where the values of the modulation parameters a and b are taken from Table I used in [12]. Substituting $p_e(\varepsilon/\gamma_{SC})$ and $f_{\gamma_{SC}}(\gamma_{SC})$ from (9) in (13), the expression for same fading variable for coherent modulation is obtained as

$$P_{e,coh}(\bar{\gamma}) = L\eta a \int_0^{\infty} \left[1 - \sum_{i=1}^M a_i Q_1\left(\sqrt{2K}, \sqrt{2\eta\gamma_{sc}}\right) \right]^{L-1} Q\left(\sqrt{b\gamma_{sc}}\right) \times \sum_{i=1}^M a_i e^{-(K+\eta\gamma_{sc})} I_0\left(2\sqrt{K\eta\gamma_{sc}}\right) d\gamma_{sc}. \quad (16)$$

Similarly, for unequal fading, the ABER for coherent modulation can be obtained through substituting $p_e(\varepsilon/\gamma_{SC})$ and $f_{\gamma_{SC}}(\gamma_{SC})$ from (10) in (13). The expression can be written as

$$P_{e,coh}(\bar{\gamma}) = a \sum_{l=1}^L \sum_{i=1}^M a_i \eta_l \int_0^{\infty} Q\left(\sqrt{b\gamma_{sc}}\right) I_0\left(2\sqrt{K\eta_l\gamma_{sc}}\right) e^{-(K+\eta_l\gamma_{sc})} \times \prod_{\substack{j=1 \\ (j \neq l)}}^L \left\{ 1 - \sum_{i=1}^M a_i Q_1\left(\sqrt{2K}, \sqrt{2\eta_j\gamma_{sc}}\right) \right\} d\gamma_{sc}. \quad (17)$$

4.2.2 Non-coherent Modulation

For non-coherent modulation, $p_e(\varepsilon/\gamma_{SC}) = ae^{-b\gamma_{sc}}$, where the values of the modulation parameters a and b are taken from Table II used in [12]. Substituting $p_e(\varepsilon/\gamma_{SC})$ and $f_{\gamma_{SC}}(\gamma_{SC})$ from (9) in (13), the expression for equal fading is evaluated as

$$P_{e,ncoh}(\bar{\gamma}) = \frac{L\eta a}{2} \int_0^{\infty} \left[1 - \sum_{i=1}^M a_i Q_1\left(\sqrt{2K}, \sqrt{2\eta\gamma}\right) \right]^{L-1} \times \sum_{i=1}^M a_i e^{-[K+(b+\eta)\gamma_{sc}]} I_0\left(2\sqrt{K\eta\gamma_{sc}}\right) d\gamma_{sc}. \quad (18)$$

Similarly, for unequal fading, the ABER for coherent modulation can be obtained by putting $p_e(\varepsilon/\gamma_{SC})$ and $f_{\gamma_{SC}}(\gamma_{SC})$ from (10) in (13). The expression can be written as

$$\begin{aligned}
 P_{e,ncoh}(\bar{\gamma}) = & \frac{a}{2} \sum_{l=1}^L \sum_{i=1}^M a_i \eta_l \int_0^{\infty} e^{-(b\gamma_{sc} + K + \eta_l \gamma_{sc})} I_0\left(2\sqrt{K\eta_l \gamma_{sc}}\right) \\
 & \times \prod_{\substack{j=1 \\ (j \neq l)}}^M \left\{ 1 - \sum_{i=1}^L a_i Q_1\left(\sqrt{2K}, \sqrt{2\eta_j \gamma_{sc}}\right) \right\} d\gamma_{sc}.
 \end{aligned}
 \tag{19}$$

5 Results and Discussion

Mathematical evaluation of the equation derived for outage probability and ABER performance of different coherent and non-coherent modulation methods is being done in previous section. The obtained graphs are numerically analyzed and are validated in Monte Carlo Simulation. In Fig. 1, the outage probability versus received SNR in dB for equal fading parameter has been plotted. From the plot, it can be observed that when the number of diversity branch L increases, the system gives better performance. This is for the reason that decrease in the total probability will lead to deep fade in fading channels. Since K signifies direct wave power is more. Hence if K increases, the channel is more effective. In Fig. 2, the outage

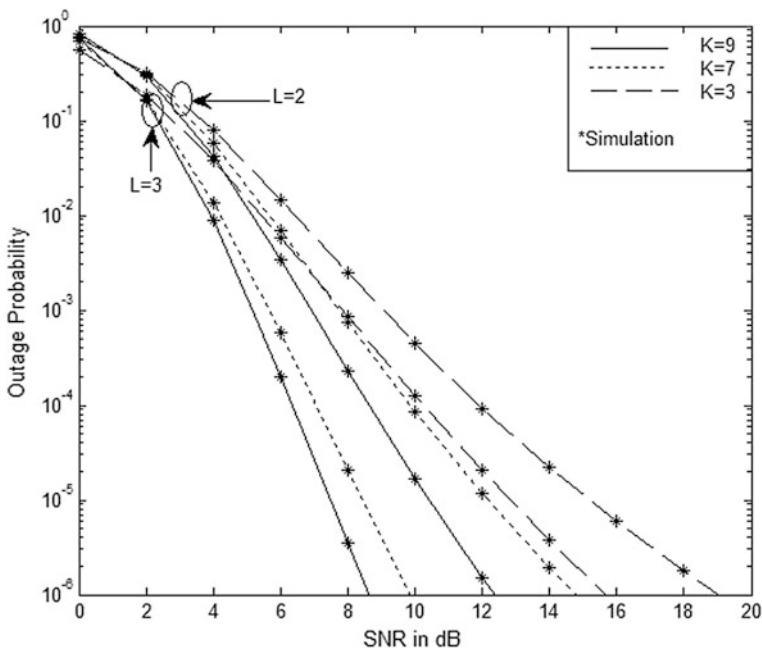


Fig. 1 L-SC receiver with identical fading for outage probability

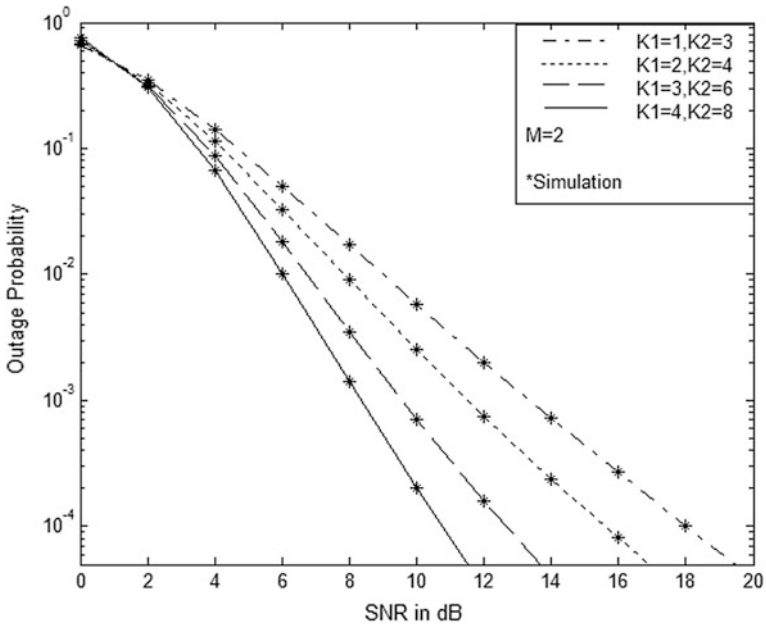


Fig. 2 L-SC receiver with non-identical fading for outage probability

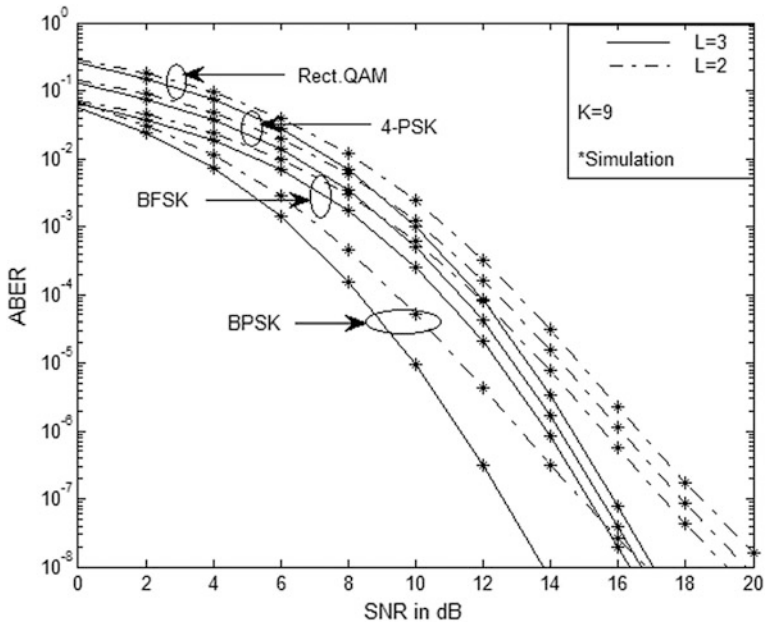


Fig. 3 ABER of L-SC receiver coherent modulation

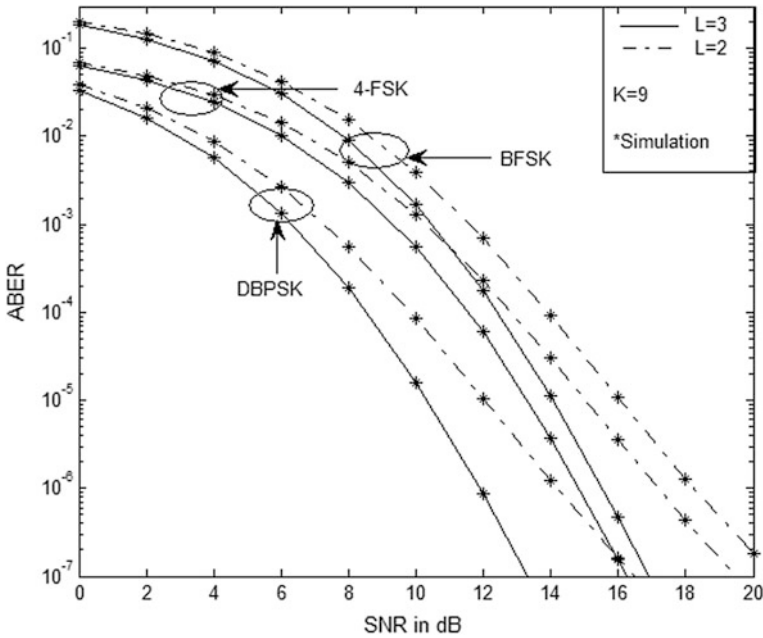


Fig. 4 ABER of L-SC receiver non-coherent modulation

probability versus received SNR in dB for unequal fading parameter has been represented. The graph is obtained for $L = 2$ and number of K_1 and K_2 variables. It can be understood that the system performs better when the value of parameter K_1 and K_2 increases. The reason for this is increased value of K_1 and K_2 specifies higher power of direct waves. In Fig. 3, the ABER versus received SNR in dB for different coherent modulation scheme has been plotted. If parameter K is constant, then ABER performance improves with higher number of branch L . Furthermore, it can be observed that the performance of coherent BPSK is effective than coherent BFSK. This is in view of the fact that the message in BPSK is stored in phase variation. The noise cannot affect the phase variation of the signal easily. Therefore, the ABER performance of BPSK is better. At the same time, the plot is obtained for other coherent modulation schemes. It can be seen that the behaviour of the system using Rect.QAM modulation is inferior to all coherent modulation schemes used. This is because amplitude of the carrier signal of QAM contains the message. The information is then affected by deep fading. In Fig. 4, the ABER versus received SNR in dB for different non-coherent modulation scheme has been represented. From the graph, it is observed that the ABER response of differential binary phase shift keying (DBPSK) is better than non-coherent BFSK and 4-FSK. The reason for this is stated above.

6 Conclusions

In this paper, the analysis of the performance parameters for L-SC system on OWDP fading channel is been presented. The expressions are obtained employing the equation obtained for the SNR pdf of the system and Marcum Q function. The expressions are obtained for both equal and unequal fading parameter. The results are verified and ensured to be correct.

References

1. Durgin G. D., Rappaport T. S., and Wolf D. A. de.: New analytical models and probability density functions for fading in wireless communication, *IEEE Trans. Commun.* vol. 50, no. 6, pp. 1005–1015, (Jun. 2002).
2. Oh Soon H., and Li Kwok H.: BER performance of BPSK receivers over two-wave with diffuse power fading channels, *IEEE Trans. Wireless Commun.*, vol. 4, no. 4 pp. 1448–1454, (Jul. 2005).
3. Oh S. H., Li K. H., and Lee W. S.: Performance of BPSK pre-detection MRC systems over two-wave with diffuse power fading channels, *IEEE Trans. Wireless Commun.* vol.6, no. 8, pp. 2772–2775, (Aug. 2007).
4. Suraweera Himal A., Lee Wee. S., and Oh Soon H.: Performance analysis of QAM in a Two-Wave with Diffuse Power fading environment, *IEEE Commun. Letters*, vol. 12, no. 2 pp. 109–111, (Feb. 2008).
5. Subadar Rupaban, Reddy T. Siva Bhaskar, Sahu P. R.: Performance of an L-SC Receiver over κ - μ and η - μ Fading Channels, *IEEE ICC proceedings*, (2010).
6. Tan Beng Soon, Li Kwok Hung and The Kah Chan.: Symbol Error Rate of Selection Combining over Two Wave with Diffuse Power Fading, *IEEE ICSPCS Honolulu, Hawaii*, (Dec. 2011).
7. Lu Yao and Yang Nan.: Symbol error probability of QAM with MRC diversity in two wave with diffuse power fading channels, *IEEE Commun. Lett.* vol. 15, no. 1, pp. 10–12, (Jan. 2011).
8. Saikia Bhargabjyoti and Dr. Subadar Rupaban.: Capacity Analysis of Adaptive Transmission Techniques over TWDP Fading Channel, *IJEEEE*, vol. 2, Issue. 4, pp. 1–11, (April 2012).
9. Subadar R., and Singh A. D.: Performance of SC receiver over TWDP fading channels, *IEEE Wire. Commun. Lett.*, vol.2, no. 3, pp. 267–270, (June. 2013).
10. Singh Aheibam Dinamani, and Subadar Rupaban.: Capacity Analysis of MRC receiver with adaptive transmitters over TWDP Fading Channels, *International Symposium on Advanced Computing and Communication (ISACC)*, (2015).
11. Singh Aheibam Dinamani, and Subadar Rupaban.: Capacity of DualMRC receiver with adaptive transmitters over non identical TWDP Fading Channels, *International Conference on Advances in Computer Engineering and Applications (ICACEA) IMS Engineering College Ghaziabad India*, (2015).
12. Singh Aheibam Dinamani, and Goswami Suparna.: Performance of Digital Modulations over TWDP Fading Channel, *International Conference on Electronic Design, Computer Networks and Automated Verification (EDCAV)* pp. 135–138, (2015).
13. Simon M. K., and Alouini M. -S.: *Digital Communications Over Fading Channels: A Unified Approach to Performance Analysis*. New York: Wiley (2000).
14. Weisstein E. W.: Marcum Q-Function from MathWorld-A Wolfram Web Resource. <http://mathworld.wolfram.com/MarcumQFunction.html>.

Performance Analysis of STBC-FSO Communication System in Different Turbulence Regimes

Sonali Garg, Abhishek Dixit and Virander Kumar Jain

Abstract The major concern in free-space optical communication is atmospheric turbulence which may significantly degrade the performance depending upon the level of turbulence. The use of spatial time diversity can mitigate the effects of fading caused by atmospheric turbulence. The simulation results show the application of space-time block coding in intensity modulation and direct detection system to improve the bit error rate performance. The improvement in terms of coding gain is maximum when the turbulence level is high.

Keywords Free-space optical communications · Space-time block coding Lognormal · Negative exponential · Gamma-gamma

1 Introduction

Free-space optical (FSO) communication is an age long technology which transmits information content from one point to another in free-space using optical wavelengths. Its advantages include the use of unlicensed spectrum, large bandwidth, low power requirement, and low-cost deployment [1]. The various applications of FSO include providing high-speed space communication and last-mile access (which implies connectivity between the end users and the edge router), and providing protection or backup links when the working communication links break down. The FSO communication systems are classified into terrestrial links like

S. Garg (✉) · A. Dixit · V. K. Jain
Department of Electrical Engineering, IIT Delhi, New Delhi 110075, India
e-mail: sonali@ee.iitd.ac.in; eez168075@iitd.ac.in

A. Dixit
e-mail: abhishek.dixit@iitd.ac.in

V. K. Jain
e-mail: vkjain@ee.iitd.ac.in

building-to-building, and space optical links like satellite-to-satellite communications [1, 2].

Although there are many advantages of using FSO system, the link is affected by weather and atmospheric conditions in the propagation path [1, 2]. In the atmosphere, many air pockets are randomly formed due to the refractive index variation with temperature. These air pockets produce random fluctuations in the irradiance of the transmitted optical beam, which is known as atmospheric scintillation, and severely degrade the link performance. To mitigate such effects, various approaches have been proposed in the literature, like the use of space-time block coding (STBC) [3]. STBC uses both spatial and temporal diversities, and thus reduces the probability of error in FSO communication system by reducing scintillation/turbulence effects. In this paper, we analyze the performance of Alamouti space-time coding in three turbulence regimes, i.e., low, moderate, and high turbulence. Alamouti space-time coding is a multiple-input single-output (MISO) system which uses multiple antennas at the transmitter side and helps in the reliable reception of all expected forms of information signal and thus resulting in a higher reliability of information transfer. In this paper, we study the bit error rate (BER) performance of single-input single-output (SISO)-FSO and multi-input single-output (MISO)-FSO systems under three different turbulence regimes—lognormal, negative exponential, and gamma-gamma. We found that the STBC improves the performance of the link in all three regimes significantly—between 13 and 24 dB depending upon the turbulence levels.

The organization of the paper is as follows: Section 2 describes the atmospheric turbulence and fading. Section 3 discusses the system model. In Sects. 4 and 5, simulation results for the BER performance of STBC-FSO system are presented. For comparative study, simulation results without coding scheme are also presented. Finally, conclusions of the study are given in Sect. 6.

2 Description of Atmospheric Turbulence and Fading

Turbulence is the result of variation in the refractive index of air with the temperature. It is a random phenomenon caused by the heated air rising from the earth's surface, which creates random air pockets. Turbulence is characterized in terms of refractive index structure coefficient, C_n^2 [2]. The variation of C_n^2 with height h is often described by the Hufnagel—Valley formula as given below:

$$C_n^2(h) = 0.00594 \left(\frac{V}{27} \right)^2 (10^{-5}h)^{10} \exp\left(\frac{-h}{1000} \right) + 2.7 \times 10^{-16} \exp\left(\frac{-h}{1500} \right) + A \exp\left(\frac{-h}{100} \right) \quad (1.1)$$

where h is the altitude in meters, V the rms wind speed in meters per second, and A the value of $C_n^2(0)$ at ground level in $m^{-2/3}$. Atmospheric turbulence results in scintillation, beam wander, and beam spreading of a propagating beam. Scintillation is defined as the fluctuations of the laser beam in space and time domains [2]. Scintillation for the small fluctuations follows a lognormal distribution, whereas for larger fluctuations distribution tends to be negative exponential. Beam wander is the result of turbulent eddies becoming larger in size than the beam size and thus deflecting the direction of propagation. Beam spreading is the natural phenomena and is always present. This represents the spread of the beam as it passes through the atmosphere.

Atmospheric turbulence-induced fading is modeled by different distributions based on the level of turbulence. Three commonly used distributions are briefly discussed below [1, 2]

1. Lognormal distribution: The optical turbulence can be modeled as a lognormal distribution for a weak turbulence regime [4]. The probability density function (pdf) of the received intensity and I with low turbulence is given as

$$f_I(I) = \frac{1}{2I} \frac{1}{(2\pi\sigma_x^2)^{1/2}} \exp\left\{-\frac{[\ln(I) - \ln(I_o)]^2}{8\sigma_x^2}\right\} \quad (1.2)$$

where σ_x^2 represents the mean square amplitude fluctuations, I the irradiance, I_o the mean irradiance, and $f_I(I)$ the pdf of I .

2. Negative exponential distribution: In this model, scattering field is considered to be the result of large number of non-dominant scatterers, where each scatterer contributes a random optical phase at the detector. This model is applicable to moderate turbulence regime [5]. The intensity statistics for the negative exponential is given as

$$f_I(I) = \frac{1}{I_o} \exp\left\{-\frac{I}{I_o}\right\}, I \geq 0 \quad (1.3)$$

3. Gamma-gamma distribution: In this model, irradiance of optical field is taken as the product of two random processes arising from larger and smaller turbulent eddies. Thus, gamma distribution is used to model both weak and high turbulence regimes [6]. Gamma-gamma pdf in terms of irradiance I is given as

$$f_I(I) = \frac{2(\alpha\beta)^{(\alpha+\beta)/2}}{\Gamma(\alpha)\Gamma(\beta)} I^{(\alpha+\beta)/2} K_{\alpha-\beta}(2\alpha\beta I) \quad (1.4)$$

where α and β are the effective number of small-scale and large-scale eddies of the scattering environment, Γ represents the gamma function and $K_{\alpha-\beta}$ the modified Bessel function of the second kind and of order, $\alpha-\beta$.

3 System Model

To combat the effects of fading, the use of multiple transmitters and single receiver is explored in [7]. We have made use of two transmitters, i.e., two lasers and one receiver for the same. This system of transmitting a signal through multiple antennas (lasers) and receiving by one antenna (photodetector) in our case is referred to as MISO system. The separation between the two lasers should not exceed θL , where θ represents receiver field of view (assumed very small here) and L the link length. In this paper, intensity modulation and direct detection (IM/DD) links are considered for investigation. The fading channel between two sources and detector pair is considered to be uncorrelated. The channel is also assumed to be flat and non-frequency selective [3, 7]. The input data are mapped on to the STBC signal vector and then transmitted. For the link, the received optical power at the detector is given by

$$Y_i(t) = H_{1i}(t)X_i(t) + N_i(t) \tag{1.5}$$

Where $X_i(t)$ represents the input optical power from source i , and $H_{1i}(t)$ the channel gain for the optical path $1i$. The channel is considered to be time invariant during a code word transmission. The random process $N(t)$ includes the thermal noise as well as the noise caused by the ambient light sources (Fig. 1).

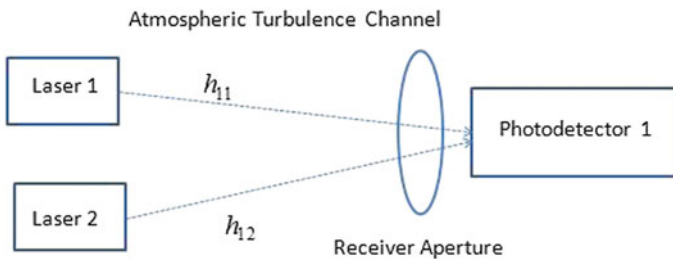


Fig. 1 Block diagram of 2×1 STBC-FSO system

4 Performance Evaluation with STBC

We have implemented the conventional STBC scheme with two transmit apertures and one receiver aperture employing on-off keying (OOK) considering lognormal, negative exponential, and gamma-gamma fading channels in MATLAB. In the first symbol period, x_1 and x_2 signals are transmitted from laser 1 and laser 2, respectively, and during the second symbol period, \bar{x}_2 and x_1 signals are transmitted from laser 1 and laser 2, respectively. Here, overbar denotes the complement of the signal obtained by reversing the roles of “on” and “off.” Here, we need to emphasize that in the case of OOK, we deal with real signals. Thus, it is not necessary to take the complex conjugate notation as done in conventional STBC scheme [8]. We have done a comparative study of the simulation results obtained by employing this technique. The received signals in the first and second bit intervals are given by

$$y_1 = h_{11}x_1 + h_{12}x_2 + n_1 \quad (1.6)$$

$$y_2 = h_{11}\bar{x}_2 + h_{12}x_1 + n_2 \quad (1.7)$$

Further these equations can be written in the vector form as

$$\bar{Y} = \bar{H} \times \bar{X} + \bar{N} \quad (1.8)$$

where \bar{H} represents the channel matrix, \bar{X} and \bar{N} the signal and noise vector, respectively. We have evaluated the performance results of this scheme under the perfect channel state information (CSI). The channel information may be derived by pilot symbol insertion and extraction [3]. The average energy transmitted per symbol by an antenna is taken to be halved. The decoding process involves multiplication of received vector with optical to electrical conversion coefficient because we are working in optical domain. The decoded vector \bar{W} is therefore given by

$$\bar{W} = R \times \bar{H}_m \times \bar{Y} \quad (1.9)$$

where R represents the optical to electrical conversion coefficient ($\mu A/\mu W$), H_m is the transpose of the channel matrix. From Eqs. (1.8) and (1.9), decoded vector \bar{W} can be written as

$$\bar{W} = R \times |\bar{H}|^2 \times \bar{X} + \bar{H}_m \times \bar{N} \quad (1.10)$$

Substitution of Eqs. (1.6) and (1.7) in the above equation lead to

$$\hat{x}_1 = (h_{11}^2 + h_{12}^2)x_1 + h_{11}n_1 + h_{12}n_2 \quad (1.11)$$

$$\hat{x}_2 = (h_{11}^2 + h_{12}^2)x_2 + h_{12}n_1 - h_{11}n_2 \quad (1.12)$$

where \hat{x}_1 and \hat{x}_2 represent the combined received signal when passed through two different channels. The demodulation of OOK-based STBC-FSO is feasible during atmospheric turbulence because of coherence time of channel, which is of the order of milliseconds and is much longer than the typical duration of two consecutive data symbols ($\cong \mu s$). This implies that the channel properties are time invariant during a minimum of two symbol duration. Decoding process involves a sampler, correlator, and a threshold detector. The detector threshold is set midway between expected signal levels corresponding to bits “1” and “0.”

5 Simulation Results

The three cases of turbulence regimes, i.e., low, moderate, and high turbulence modeled as lognormal, negative exponential, and gamma-gamma model, respectively, are considered in simulation. The aperture of receiver lens is less than the fading correlation length, and consequently, the effect of aperture averaging is negligibly small [9]. It is considered that the total power is equally divided among the number of transmit antennas and flat-fading channel tap coefficients remains unaltered over two consecutive symbol period. For the simulation purpose, operating wavelength is taken to be 800 nm and data rate to be 10 Mbps. For high turbulence, α and β are taken as 4.2 and 1.4, respectively, which leads to a Rytov variance of 3.5 (strong turbulence). The remaining simulation parameters are given in Table 1, and simulation results are given in Figs. 2, 3, 4, 5, 6, and 7.

It is clear from the Fig. 2 that the level of turbulence increases, and BER increases. At $E_b/N_o = 12$ dB, the resulting BER is 10^{-3} for lognormal, $10^{-1.06}$ for negative exponential, and $10^{-0.82}$ for gamma-gamma models.

A comparison of three cases of turbulence regimes (low, moderate, and high) in STBC-FSO system is given in Fig. 3. It shows that at a practical value of E_b/N_o , strong turbulence, i.e., gamma-gamma distribution leads to maximum error and weak turbulence, i.e., lognormal leads to minimum error.

It is clear from the Fig. 4 that at low E_b/N_o , using STBC leads to increase in BER for lognormal fading channel. However, at high E_b/N_o , performance is enhanced by the application of STBC. For the lognormal model, at the BER of 10^{-1} , coding gain is 13 dB. However, for negative exponential and gamma-gamma models at the same BER, coding gain is much higher which is about 15 (Fig. 5) and 24 dB (Fig. 6), respectively.

Table 1 Simulation parameters

Turbulence regime	Rytov variance (σ_R^2)	C_n^2 (in $m^{-2/3}$)	Link length (in km)
Low	0.7	1.2×10^{-17}	50
Moderate	1.0	1.2×10^{-15}	5
High	3.5	0.8×10^{-13}	1

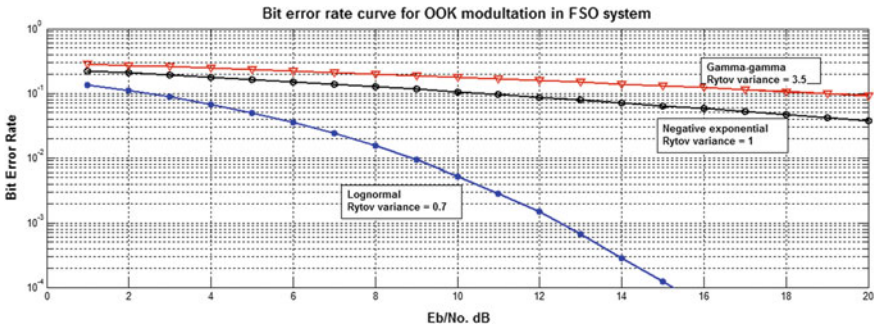


Fig. 2 BER in FSO system in different turbulence regimes

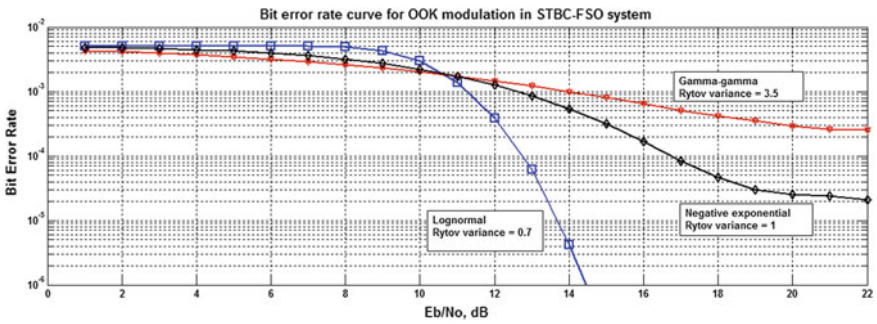


Fig. 3 BER in STBC-FSO system in different turbulence regimes

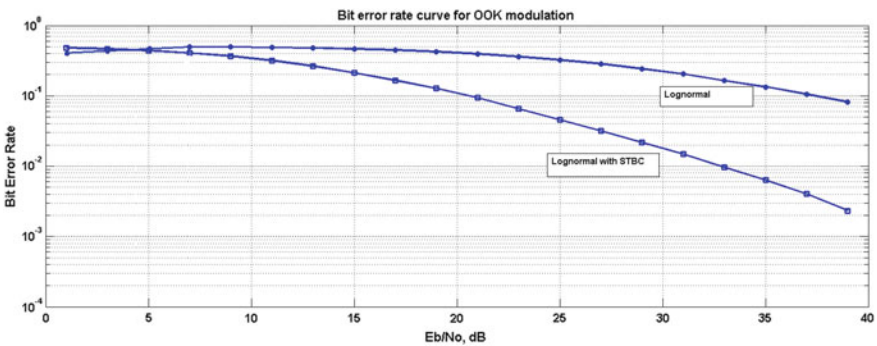


Fig. 4 Comparison of BER versus E_b/N_o with and without STBC for lognormal fading channel

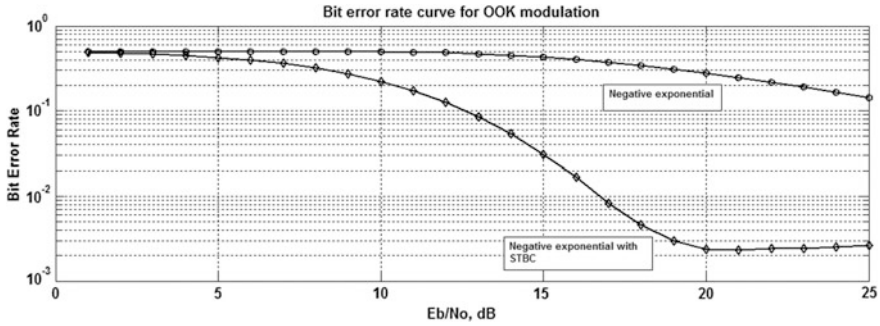


Fig. 5 Comparison of BER versus E_b/N_o with and without STBC for negative exponential fading channel

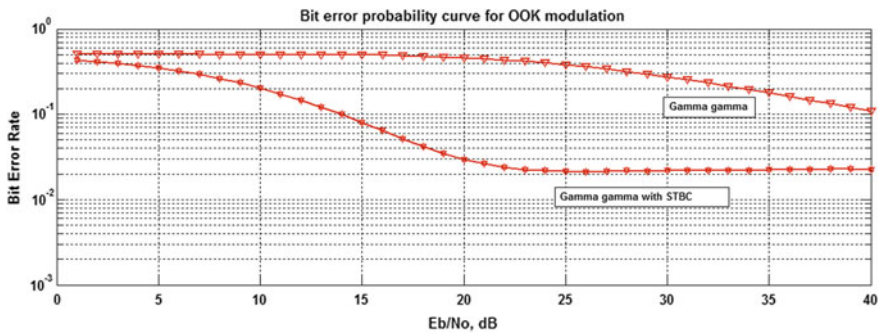


Fig. 6 Comparison of BER versus E_b/N_o with and without STBC for gamma-gamma fading channel

Table 2 Summary of simulation results

Turbulence regime	Rytov variance (σ_R^2)	BER	E_b/N_o Gain (in dB)
Low	0.7	10^{-1}	13
Moderate	1.0	10^{-1}	15
High	3.5	10^{-1}	24

6 Conclusions

In this paper, average BER of OOK modulated STBC-FSO scheme has been plotted. The atmospheric channel is modeled using lognormal, negative exponential, and gamma-gamma distributions. Simulation results show that the usage of 2×1 STBC scheme gives significant coding gain. The coding gain is more when the turbulence level is high.

The numerical results are summarized in Table 2 which also gives a comparative performance of the coding scheme in different turbulence regimes.

References

1. Z. Ghassemlooy and W. O. Popoola, *Terrestrial Free-Space Optical Communications*, InTech, 2010.
2. D. Chadha, *Terrestrial Wireless Optical Communication*, McGraw-Hill, 2013.
3. S. M. Alamouti, "A simple transmit diversity technique for wireless communications." *IEEE Journal on Selected Areas in Communications*, vol. 16, no. 8, pp. 1451–1458, Oct. 1998.
4. M. S. Islam, and S. P. Majumder, "Performance analysis of a free space optical link using Alamouti type Space Time Block Code with the weak turbulent condition," *IEEE, 7th International Conference on Electrical & Computer Engineering (ICECE)*, pp. 287–290, Dec. 2012.
5. O. W. Popoola, and Z. Ghassemlooy, "BPSK subcarrier intensity modulated free-space optical communications in atmospheric turbulence," *Journal of Lightwave Technology*, vol. 27, no. 8, pp. 967–973, Apr. 2009.
6. J. Park, E. Lee, and G. Yoon, "Average bit-error rate of the Alamouti scheme in Gamma-Gamma fading channels," *IEEE Photonics Technology Letters*, vol. 23, no. 4, pp. 269–271, Feb. 2011.
7. A. Garcia-Zambrana, "Error rate performance for STBC in free-space optical communications through strong atmospheric turbulence," *IEEE Communications Letters*, vol. 11, no. 5, pp. 390–392, May 2007.
8. M. K. Simon, and V. Vlnrotter, "Alamouti-type space-time coding for free-space optical communication with direct detection," *IEEE Transactions on Wireless Communications*, vol. 4, no. 1, pp. 35–39, Jan. 2005.
9. P. Kaur, V. K. Jain, and S. Kar, "BER performance improvement of FSO links with aperture averaging and receiver diversity technique under various atmospheric conditions," *IEEE, 9th International Conference on Industrial and Information Systems (ICIS)*, pp. 1–6, Dec. 2014.

A Low-Cost Refractometer with Misaligned Optical Fibers

Dipankar Chetia, Tenison Basumatary, Hidam Kumarjit Singh and Tulshi Bezboruah

Abstract A fiber optic sensor has been reported for use in measurement of refractive index (RI) of transparent liquids. The sensing principle of the sensor is based on the effect of the RI of the liquid present between two misaligned optical fibers on coupling of light between them. In the proposed sensor, the displaced fiber ends are suitably intruded inside a liquid chamber, and optical power coupled from input fiber to the output fiber is observed w.r.t. change in RI of liquid sample, that is, introduced inside the liquid chamber. From experimental observations, the sensor can detect RI change up to resolution of 10^{-4} .

Keywords Optical fiber · Refractometer · Sensor · Light coupling
Refractive index

1 Introduction

Determination of refractive index (RI) for liquid has got immense importance in different chemical, pharmaceutical, and beverage industries. Classical methods of measuring RI include measurement using critical angle, Brewster angle, angular and lateral deviation of light [1–4]. Modern fiber optic refractometers have several advantages over refractometers using classical methods [5]. Several fiber optic refractometers involving different sensing techniques have been proposed in the

D. Chetia (✉) · T. Basumatary · H. K. Singh · T. Bezboruah
Department of Electronics and Communication Technology,
Gauhati University, Guwahati, India
e-mail: deep.jeet333@hotmail.com

T. Basumatary
e-mail: tenibas143@gmail.com

H. K. Singh
e-mail: kumarjit_hidam@yahoo.com

T. Bezboruah
e-mail: zbt_gu@yahoo.co.in

past two decades. Common techniques include surface plasmon resonance (SPR) effect, optical evanescent waves, total internal reflection (TIR) etc. Special kind of fibers like Bragg grating (FBG) and photonic crystal are also used to design refractometers. Kim K. T. et al. proposed a RI sensor [6], in which a fiber is side polished and is used where the surrounding liquid medium is acting like a waveguide. Two adjacent resonance wavelengths of the coupler are used to capture the RI of the liquids. Several TIR-based refractometers have also been reported by many researchers. M. H. Shiu et al. reported a sensor based on the total internal reflection heterodyne interferometry [7], and they try to calculate the RI of liquid sample from the phase shift difference due to the TIR effect between the S and P polarizations. P. Nath et al. reported a refractometer based on frustrated total internal reflection (TIR) [8], Banerjee A. et al. described that cladding modes are mainly responsible for sensing the RI of the liquid, they have used a U-shaped fiber probe for sensing, and RI of the liquid was sensed by allowing liquid to interact with evanescent wave of a partially de-cladded region of an optical fiber [9]. Bergmen et al. reported another sensor based on evanescent wave [10]. Sensors based on the angular deviation of the light in the liquid medium are also reported as in [11–13]. In [14], Chetia D. et al. reported a longitudinally displaced optical fiber sensor for determination of the RI, and a hollow glass chamber is used to make coupling of light between two multimode fibers having a certain longitudinal gap in-between them. They found that for a longitudinal gap the light power coupled to the receiving fiber varies with the RI of the poured sample.

Several sensors based on FBG sensor for measuring the RI of the liquid solution, including sensors using periodically tapered fiber, are reported as in [15, 16]. P. Wang et al. reported a RI sensor [17] which consists of a small core fiber sandwiched between two standard single mode fibers, with tapers periodically fabricated along the small core fiber. Dip wavelength shift of the multimode interference within the small core fiber cladding is used to sense the RI. While SPR-based techniques are used in the designing of the fiber optic refractometer as in [18, 19], Z. Q. Tou et al. demonstrated a sensor [20] where a photonic crystal fiber which is spliced between the multimode fibers. In this, evanescent field of cladding modes excite gold nanoparticles immobilized on the PCF surface. In [21–23] Jha R. et al., Wang et al. and Banerjee et al. reported optical fiber sensor based on the fiber optic crystal. Banerjee demonstrates the one-dimensional ternary photonic crystals as the RI sensing element.

Those refractometers based on the FBG, SPR effect, and the photonic crystals are highly sensitive but the design and characterization processes are expensive. In this paper, we report a simple refractometer designed with misaligned multimode plastic optical fiber (POF) separated by a longitudinal and lateral.

2 The Sensor

2.1 Sensing Principle of the Proposed Sensor

The sensing principle of the sensor is based on the effect of the RI of the liquid present between two displaced optical fibers on coupling of light between them. In the proposed sensor, the displaced fiber ends are suitably intruded inside a liquid chamber, and optical power coupled from input fiber to the output fiber is observed w.r.t. change in RI of liquid sample, that is, introduced inside the liquid chamber. Two identical optical fibers with lateral displacement d are shown in Fig. 1a. Due to the displacement, the overlapped area between the core of the two fibers gets decreased as shown in Fig. 1b. If $2a$ is the diameter of the fiber cores, then overlapped area A can be determined by considering the area under the arc LM and area of the right-angle triangle LOM . LOM has a base $d/2$ and hypotenuse a [24].

$$A = 4 \left\{ \frac{\theta}{2\pi} \pi a^2 - \frac{1}{2} \frac{d}{2} \left[a^2 - \left(\frac{d}{2} \right)^2 \right]^{1/2} \right\} \tag{1}$$

where

$$\cos \theta = \left(\frac{d}{2a} \right) \tag{2}$$

Now, if we introduce an axial gap x , the light coming out of the first fiber will be intercepted by the core of the second fiber. Here, divergence of the light cone will increase as the axial gap ‘ x ’ increases as shown in Fig. 2a. Hence, the overlapped area A' between light cone and core of the second fiber will be in the form of (3)

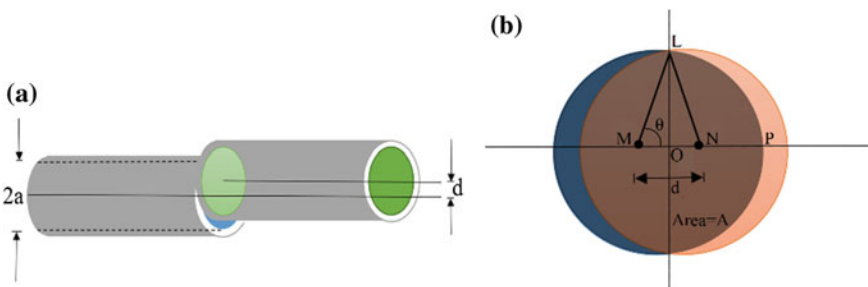


Fig. 1 Schematic of **a** laterally misaligned fibers and **b** geometrical view of the opposite fiber ends

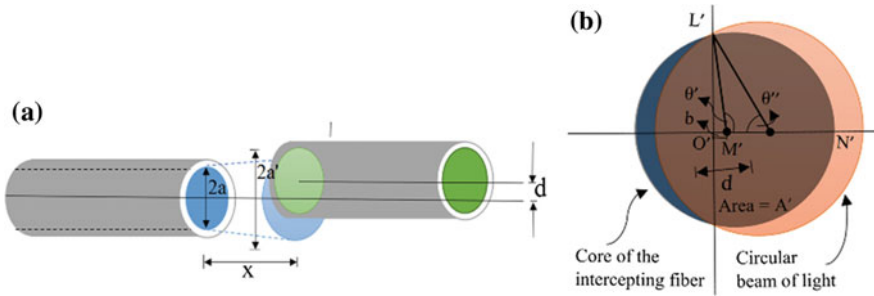


Fig. 2 Schematic of **a** longitudinally and laterally misaligned fibers and **b** geometrical view of circular light spot and intercepting fiber end

$$A' = 2 \left\{ \frac{\theta''}{2\pi} \pi a'^2 - \frac{1}{2} (d \pm b) \left[a'^2 - (d \pm b)^2 \right]^{1/2} \right\} + 2 \left\{ \frac{\theta'}{2\pi} \pi a^2 \pm \frac{1}{2} b \left[a^2 - b^2 \right]^{1/2} \right\} \tag{3}$$

where a' is the radius of the circular light spot falling onto the core of second fiber and b is the length of $M'O'$, which can be measured practically. Further, in Fig. 2b, θ' and θ'' are given by (4).

$$\theta' = \cos^{-1} \left(\frac{b}{a} \right) \text{ and } \theta'' = \cos^{-1} \left(\frac{d \pm b}{a'} \right) \tag{4}$$

We found the light coupling efficiency η of the displaced fibers in the form (5), as in [24].

$$\eta = \frac{1}{\pi} \left\{ \cos^{-1} \left(\frac{d \pm b}{2a'} \right) - \left(\frac{d \pm b}{2a'} \right) \left[1 - \left(\frac{d \pm b}{2a'} \right)^2 \right]^{1/2} \right\} + \frac{1}{\pi} \left\{ \cos^{-1} \left(\frac{b}{2a} \right) - \left(\frac{b}{2a} \right) \left[1 - \left(\frac{b}{2a} \right)^2 \right]^{1/2} \right\} \tag{5}$$

In (5), a' and b are the parameters that vary with RI of liquid [25], whereas ' a ' and ' d ' are constant parameters. So, η will vary when RI of liquid changes in the gap. Hence, optical power output of second fiber will vary with RI of liquid.

2.2 Sensor Fabrication and Sample Preparation

The proposed sensor is designed with two customized glass chambers (dimension: $20\text{ mm} \times 30\text{ mm} \times 50\text{ mm}$). The chambers have inlet and outlet ports for liquid filling and draining purposes. They have two capillary tubes fitted at both ends, through which optical fiber is inside them. With the help of the capillary tubes, lateral and longitudinal displacements can be adjusted in-between the opposite fiber ends intruded inside the chamber. Arrangements are made so that the light is allowed to couple from one fiber to another through refraction only. A simple functional block diagram of the proposed sensor setup is shown in Fig. 3.

As shown in Fig. 3, we use a laser diode (LD) having peak wavelength 650 nm and 0.5 mW optical power output. The optical beam is divided into 50:50 parts, and they are coupled into the light transmitting optical fibers (LTF_S and LTF_R). The light receiving optical fibers (LRF_S and LRF_R) obtain optical power from the LTF fibers via displaced fiber gaps. At the outer end of the LRF, photodiodes (PD_S and PD_R) convert coupled optical power into proportional voltage levels. The response of PD_S and PD_R is processed by a customized data acquisition system, which is interfaced to a personal computer.

The samples are prepared by mixing different amount of the glycerol with the plain water. This is done to tune the RI of the samples. The glycerol is completely miscible in water and hence can be diluted to different concentration easily. The RI of glycerol can also be tuned by dilution as various experiment suggest. A plot between glycerol concentration (in % v/v) in glycerol-water solutions and refractive indices is shown in the Fig. 4. For the experiment, we prepared six no. of water-glycerol solutions of different concentrations.

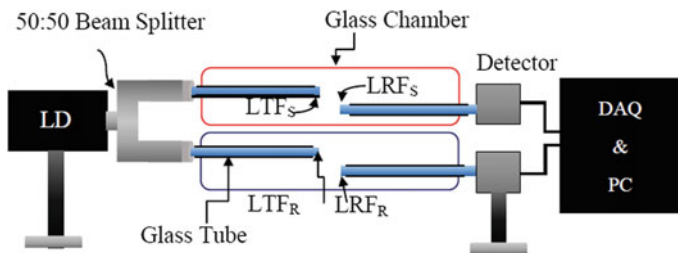
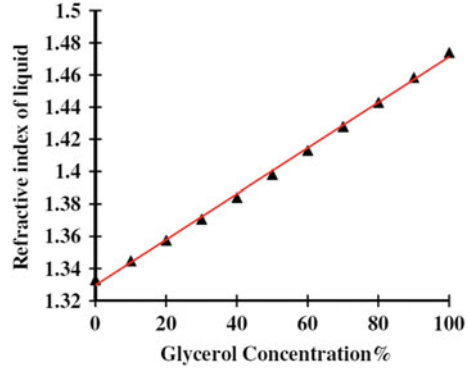


Fig. 3 Experimental arrangement of the proposed sensor

Fig. 4 Refractive index of liquid sample versus concentration of glycerol



3 Experimental Observations

The reference chamber is filled with water during the time of the experiment. While the sensing chamber is filled with different previously prepared liquid samples one after another, for the observation of sensor response. Every time a new liquid solution is introduced in the sensing chamber that the DAQ system records the sensor output. We do this for all the liquid solutions, keeping the values of longitudinal and later gap same in both the chambers. When these values, viz. longitudinal and later gap are changed, they are changed equally in both the chambers. Here, in our experiments we have used the value of gap ‘x’ which is considerably larger than core radius ‘a’. After changing these values, the sensor outputs are again observed for all the liquid solutions one after another as mentioned above. In this manner, we take to record all the sensor outputs for different liquid solutions at different longitudinal and later gap.

Liquids were injected the glass chambers through the inlet of the chambers and taken out through the outlet after taking readings, and the chamber is cleaned with water and dried up using a dryer before inserting a new sample every time.

We then plot the normalized sensor response versus glycerol concentration for different lateral and different longitudinal gap values Fig. 5, and also plot the amplified sensor response versus RI Fig. 6.

Next, from amplified sensor response, we determine the sensitivity of the sensor by calculating the ratio of voltage change versus the RI change, considering 5% of uncertainty error during the measurement of the output voltage (V_O) and the RI. Then, there will be total 10% of uncertainty for both, is included in the measurement of the sensitivity. We add a term 10^3 , in the equation of sensitivity, to convert

Fig. 5 Normalized sensor responses versus glycerol concentration for fixed lateral gap of 0.5 mm and different longitudinal gap (magnified responses for 6 and 7 mm longitudinal can be seen in the inset)

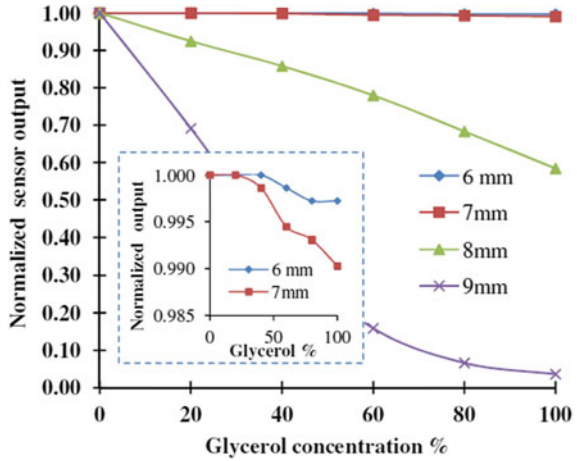
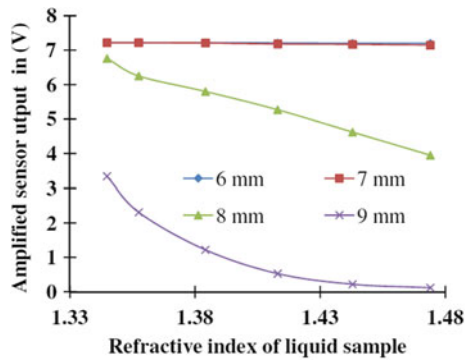


Fig. 6 Amplified sensor responses versus refractive index for fixed lateral gap of 0.5 mm and different longitudinal gap



the units into millivolts. The term 10^{-2} signifies that the proposed sensor is designed to detect the change of the RI in the order of 0.0001.

$$\text{Sensitivity} = \frac{\Delta V_0 \pm 10\%}{\Delta RI \pm 10\%} \times 10^{-4} \times 10^3 \tag{6}$$

Finally, we keep the longitudinal and lateral displacement values fixed at some certain values and observe sensor response for two liquid solutions by inserting them alternatively and repeatedly into the chamber for the duration of one hour. The chamber cleaning time in-between two observations is also noted.

4 Results and Discussions

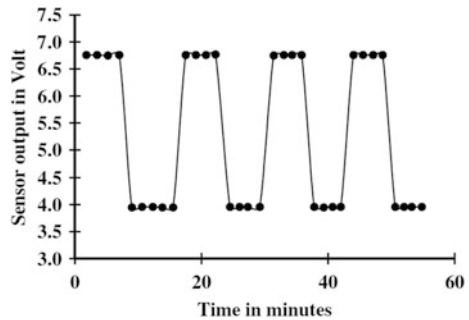
Experimentally, obtained sensor responses agree with (5). Figure 5 shows that sensor response decreases with increasing concentration of glycerol in liquid sample. Further, Fig. 6 shows that sensor response decreases with increasing RI. Since RI of liquid sample is directly proportional to glycerol concentration as shown in Fig. 4, we can conclude that Figs. 5 and 6 convey the same information. This goes well with equation (5), however it is also notable that for small value of d and x when the values of d and x are close to the value of $2a$ the sensor response should increase with an increase in RI unlike in this case. These response plots have also shown that sensor response becomes more sensitive when longitudinal misalignment is greater. It is also evident from smaller slopes of the curves as longitudinal misalignment decreases. For longitudinal misalignment 6 and 7 mm, the response curves have very small slopes, and they are almost indistinguishable in Figs. 5 and 6.

From Table 1, we can see that the sensitivity value changes with different values of longitudinal gap. It is highest for 9 mm longitudinal gap for the proposed sensor but not uniform for all the RI range; the sensitivities for 6 and 7 mm are uniform but very less while for 8 mm sensitivity is slightly less than the sensitivity of 9 mm but is uniform throughout the RI range. During our experiment, it was very difficult to vary lateral misalignment due to design-related issues of the glass chamber and capillary pipe fitting. So, we kept lateral misalignment fixed at 0.5 mm. We have calculated the stability and repeatability (Fig. 7) of the sensor from the above data, and the resolution is found to be $\sim 10^{-4}$ which is comparable to other reported refractometers. Being an intrusive type of sensor, it will not be suitable to work with highly acidic and alkaline liquids.

Table 1 Sensitivity of the sensor with a 20% possible error

Longitudinal gap	6 mm	7 mm	8 mm	9 mm
Sensitivity in (mV)	(0.50 ± 0.12) mV	(0.55 ± 0.12) mV	(2.65 ± 0.66) mV	(5.45 ± 1.36) mV (at max)

Fig. 7 Time response of the sensor



5 Conclusion

A low-cost refractometer design has been proposed, which uses coupling between two optical fibers as sensing mechanism for liquid RI measurement. The sensor can detect RI change up to a resolution of 10^{-4} . The sensitivity of the sensor varies with the longitudinal gap for a fixed lateral gap. The sensor has good resolution and repeatable response.

References

1. Brief History of Refractometers. accessed on Apr. 12, 2015. [Online]. Available: <http://www.refractometer.pl/refractometer-history>
2. Pulfrich refractometer, available online at <http://www.refractometer.pl/Pulfrich-refractometer> (accessed date: 12.04.2015).
3. History of refractometer, [Online]. Available: <http://www.refractometer.pl/refractometer-history> (accessed date: 12.04.2015).
4. G. H. Meeteen, "Refractive Index Measurement." Copyright 2000 CRC Press LLC., [Online]. Available: <http://dsp-book.narod.ru/MISH/CH61.PDF> (accessed date: 12.04.2015).
5. M.H. Chiu, J.Y. Lee and D.C.Su, "Refractive index measurement based on total internal reflection and heterodyne interferometry," *Appl. Opt.*, vol. 36, no.13, pp. 2936–2939, 1997.
6. K.T. Kim, K.H. Lee, S. Hwangbo, K.R. Sohn, "A refractometer based on fiber-to-liquid planer waveguide coupler," *Sens. Actuators A*, vol. 126, no. 2, pp. 335–339, Elsevier, 2006.
7. M.-H. Chiu, Sh.-N. Hsu, and Hs. Yang, "D-type fiber optic sensor used as a refractometer based on total-internal reflection heterodyne interferometry," *Sensors and Actuators B*, 101 pp. 322–327, Elsevier, 2004.
8. P. Nath, H.K. Singh, P. Datta and K.C. Sarma, "All-fiber optic sensor for measurement of liquid refractive index," *Sens. Actuators A*, vol. 148 no. 01, pp. 16–18, Elsevier, 2008
9. A. Banerjee *et al.*, "Fiber optic sensing of liquid refractive index," *Sens. Actuators B: Chem*, vol. 123, no. 1, pp. 594–506, Elsevier, 2007.
10. T.L. Bergman, F.P. Incropera and W.H. Stevenson, "Miniature fiber-optic refractometer for measurement of salinity in double- diffusive thermohaline systems," *Rev. Sci. Instrum.*, vol. 56, no. 2, pp. 291–296, 1985.
11. A.L. Chaudhari and A.D. Shaligram, "Multi-wavelength optical fiber liquid refractometry based on intensity modulation," *Sens. Actuators A*, vol. 100 no. 2–3, pp. 160–164, Elsevier, 2002.
12. G. Govindan, S. G. Raj and D. Sastikumar, "Measurement of refractive index of liquids using fiber optic displacement sensors," *Jour. American Sci.*, vol. 5 no. 2, pp. 13–17, 2009.
13. A. Suhadolnik and J. B. Mozina, "Optical fiber reflection refractometer," *Sens. and Actuators B*, vol. 29, pp. 428–432, 1995.
14. D. Chetia. T. Basumatary, H.K. Singh, T. Bezbaruah, "Low cost refractometer with longitudinally displaced optical fibers" *IEEE Sensors Journal*, Volume: PP, Issue: 99. 07 June 2016.
15. T. Zhu, Y. Song, Y. J. Rao and Yong Zhu, "Highly Sensitive Optical Refractometer Based on Edge-Written Ultra-Long-Period Fiber Grating Formed by Periodic Grooves," *IEEE Sensors J.*, vol. 9 no. 6, pp. 678–681, 2009. A. Banerjee *et al.*, "Fiber optic sensing of liquid refractive index," *Sens. Actuators B: Chem*, vol. 123, no. 1, pp. 594–506, Elsevier, 2007.
16. A. Asseh *et al.*, "Fiber optical Bragg grating refractometer," *J. of Fiber and Integrated Optics*, vol. 17, no.1, pp. 51–62, Taylor and Francis, 1998. A. Suhadolnik and J. B. Mozina, "Optical fiber reflection refractometer," *Sens. and Actuators B*, vol. 29, pp. 428–432, 1995.

17. P. Wang *et. al.*, “Enhanced Refractometer Based on Periodically Tapered Small Core Singlemode Fiber”, *IEEE Sensors Journal*, vol. 13, no. 1, 2013.
18. A. K. Sharma, R. Jha, and B. D. Gupta, “Fiber-Optic Sensors Based on Surface Plasmon Resonance: A Comprehensive Review,” *IEEE Sensors Journal*, vol. 7, no. 8, 2007.
19. J. Cao, E. K. Galbraith, T. Sun and K. T. V. Grattan, “Comparison of Surface Plasmon Resonance and Localized Surface Plasmon Resonance-based optical fibre sensors,” *Journal of Physics: Conference Series* 307, 012050, IOP Publishing, 2011.
20. Zh. Q. Tou, Ch. Ch. Chan, W. Ch. Wong, and L. H. Chen, “Fiber Optic Refractometer Based on Cladding Excitation of Localized Surface Plasmon Resonance,” *IEEE Photonics Technology Letters*, vol. 25, no. 6, 2013.
21. R. Jha, J. Villatoro, G. Badenes, and V. Pruneri, “Refractometry based on a photonic crystal fiber interferometer,” vol. 34, no. 5, *Optics Letters*, OSA, 2009.
22. Pengfei Wang *et. al.*, “A photonic crystal fiber half taper probe based refractometer,” *Optical Society of America*, 2013, [Online], Available: <http://www.orc.soton.ac.uk/publications/66xx/6694.pdf> (accessed date: 04.05.2015).
23. A. Banerjee, “Enhanced refractometric optical sensing by using one-dimensional ternary photonic crystals,” *Proc. of Progress in Electromagnetics Research*, PIER 89, pp. 11–22, 2009, [Online], Available: <http://jpieer.org/PIER/pier89/02.08112105.pdf> (accessed date: 04.05.2015).
24. Rajpal S. Sirohi, “Fiber Optic- and MEM-Based Measurements,” in *Introduction to Optical Metrology*, Special Indian ed., CRC Press. Boca Raton, FL, 2016, pp. 335–366.
25. W. van Etten, W. Lambo, and P. Simons, “Loss in multimode fiber connections with a gape,” *Appl. Opt.*, vol. 24, no. 7, pp. 970–976, 1985.

Fiber Optic Sensor for Detection of Chlorine Level in Water

Sebina Yesmin, Dipankar Chetia, Tenison Basumatary and Hidam Kumarjit Singh

Abstract We report a fiber optic sensor to measure the level of free chlorine present in chlorinated water. The sensor is made of an optical fiber that has been suitably bent in the form of U-shape. The sensor produces its sensing action when the U-shape probe is dipped inside liquid samples. Sensing principle of the sensor is based on absorption of fiber optic evanescent light wave by surrounding liquid medium. Experimental observations have shown that sensitivity increases with decrease in wavelength of excitation light source. We found that resolution of the sensor varies from 2.7 to 5.5 mg/L at 430 nm wavelength. The proposed sensor has the potential to be a low-cost alternative device for measuring free chlorine level of chlorinated drinking water very precisely and accurately.

Keywords Liquid · Multimode optical fiber · Sensor · Viscosity

1 Introduction

Chlorination is commonly done to disinfect drinking water. During chlorination process, chlorine is introduced into water in the form of gas or bleaching powder salts, as in [1]. During the chemical reactions, hypochlorous acid is formed. Further,

S. Yesmin (✉)

Department of Electrical and Electronics Engineering,
Assam Don Bosco University, Guwahati, India
e-mail: yashmin.nik08@gmail.com

D. Chetia · T. Basumatary · H. K. Singh

Department of Electronics and Communication Technology,
Gauhati University, Guwahati, India
e-mail: deep.jeet333@hotmail.com

T. Basumatary

e-mail: tenibas143@gmail.com

H. K. Singh

e-mail: kumarjit_hidam@yahoo.com

© Springer Nature Singapore Pte Ltd. 2018

R. Bera et al. (eds.), *Advances in Communication, Devices and Networking*,
Lecture Notes in Electrical Engineering 462,
https://doi.org/10.1007/978-981-10-7901-6_47

hypochlorous acid dissociates into hypochlorite ion, which is known as free chlorine [1]. Presence of excessive amount of free chlorine in disinfected water leads to health hazards and complications to human beings and other living creatures [2]. The acceptable level of free chlorine in water should be in the range 0.2–0.5 mg/L as per technical guidelines of World Health Organization [3]. Several analytical, electrochemical, chromatographic, and spectroscopic methods have already existed for determination of free chlorine level in disinfected water, as in [4]. At the same time, many researchers have been reporting new sensors for determining free chlorine level with better precision and accuracy. These sensors are based on iodometry, spectrophotometry, ion chromatography, chemiluminescence, etc. as in [5]. Light absorbance (at 437 nm wavelength)-based measurement of residual chlorine level in gray water treated with o-tolidine reagent was reported in [6]. Refractive index change of cyanuric acid-based polymer coating caused by reaction with free chlorine was exploited for chlorine sensing with the help of an interferometric optical waveguide, as in [7]. Colorimetric sensor based on chemical reaction between potassium–starch solution and free chlorine dissolved in water was reported in [8]. R. B. R. Mesquita et al. reported a spectrophotometric method for measurement of free chlorine level of tap water by using tetramethylbenzidine as chemical reagent, as in [9]. Graphite electrode-based chlorine sensor based on chronoamperometry-based was reported in [10]. In [11], o-phenylenediamine was electrochemically immobilized on an optical fiber, which was already coated with indium tin oxide film. The sensor was used for the detection of free chlorine level based on light absorbance principle. Surface plasmon resonance (SPR)-based fiber optic chlorine gas sensor was reported in [12, 13]. In recent time, zinc oxide and graphene quantum dot-based nano-sensors were also reported for chlorine detection in [14, 15]. The above reported sensing methods are quite good with sensitivity ranging from 0.02 $\mu\text{g/L}$ to 50 mg/L . Choudhury et al. proposed a method based on evanescence wave, using a U-shaped probe [16], and in this model, diethyl phenylenediamine is mixed in the water solution for better color development .

As the reported sensors need several chemical processes and coating materials, they may contaminate liquid samples and their reliability is expected to be poor. Quantum dot sensors are quite sensitive and selective as compared with other types. However, fiber optic sensors have several advantages compared with other types of sensor regarding remote interrogation options and noise immunity. As such, we proposed a novel fiber optic sensor for chlorine level detection of water. The proposed sensor is an intrusive sensor type, but it does not use any kind of material coating in the sensing probe. The sensing principle of the sensor is based on absorption of fiber optic evanescent light wave by surrounding liquid medium containing free chlorine. In this paper, we compare the experimentally recorded responses of the sensor at four different colors of light source, and finally, the sensitivity of the sensor is determined by using the data obtained with blue color light. Theory of the proposed sensor and experimental details is described in Sects. 2 and 3, while results and discussion are given in Sect. 4.

2 Basic Theory of the Proposed Sensor

Fiber optic evanescent wave is basically portion of electric field and magnetic field intensity components of light wave guided inside an optical fiber. This wave penetrates through cladding region of the fiber, and its amplitude decays exponentially into surrounding medium of cladding. Penetration depth d_p of the evanescent wave is measured along the direction normal to fiber axis, and it is the distance at which electric field amplitude decays to 37% of its value at core-cladding interface. Mathematical expression for penetration depth is given by (1), as in [17].

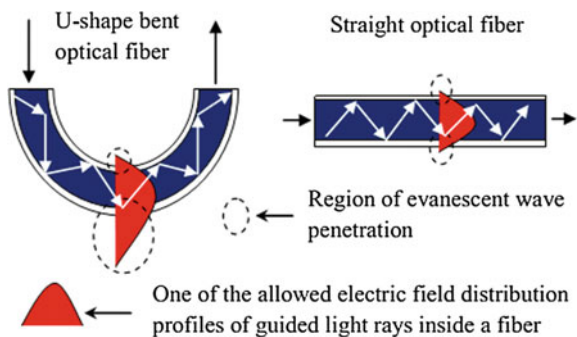
$$d_p = \frac{\lambda}{4\pi [n_1^2 \sin^2 \theta - n_2^2]^{1/2}} \tag{1}$$

where λ = wavelength of light propagating inside the fiber, n_1 = core refractive index, n_2 = cladding refractive index, and θ = angle of incidence of light at core-cladding interface. The extent of penetration becomes greater at the region where fiber bending occurs, as in [18]. Figure 1 shows pictorial illustration of evanescent wave in U-shaped bent fiber and straight optical fiber, as in [18]. Hence, a U-shaped bent fiber has been used in the proposed sensor to allow the evanescent wave to interact significantly with surrounding liquid medium. During the interaction, absorption of evanescent light wave occurs due to the presence of free chlorine inside the samples. The intensity of light transmitted I_{TR} through the other end of the optical fiber can be expressed in the form of (2) with the help of Lambert-Beer law.

$$I_{TR} = I_{IN} \exp(-\varepsilon \cdot C \cdot x) \tag{2}$$

where x is the length of the fiber around which light absorption occurs, ε is molar absorption coefficient, C is molar concentration of free chlorine in the sample, and I_{IN} is incident light intensity. Equation (2) shows that I_{TR} decreases with increase in C when I_{IN} , x , and ε are held constant. Figure 2 shows simplified schematic of the

Fig. 1 Evanescent wave penetration through cladding region of optical fiber



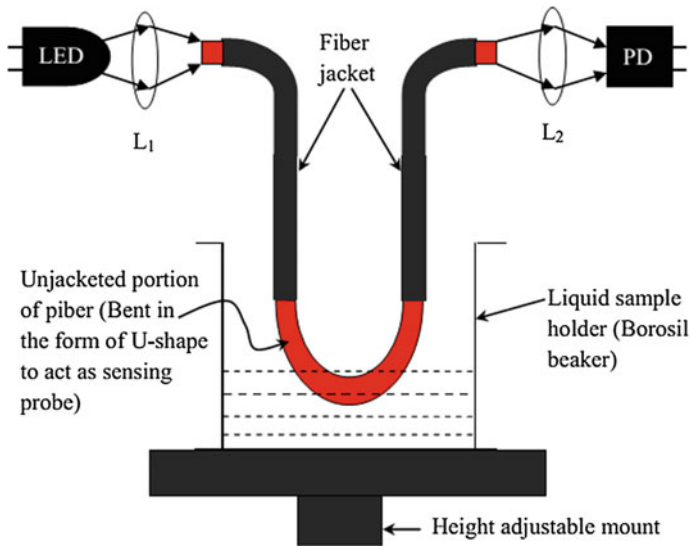


Fig. 2 Simplified schematic of the proposed sensor

proposed sensor. In this sensor, the transmitted light is detected by a photodetector (PD). So, open-circuit voltage V_{PD} of the PD in photovoltaic mode can be expressed in terms of I_{TR} by (3) as in [17].

$$V_{PD} = \frac{k_B T}{q} \ln \left(\frac{\eta A q \lambda}{h c I_0} \cdot I_{TR} \right) \quad (3)$$

where k_B = Boltzmann constant, T = temperature in Kelvin, q = magnitude of electronic charge, η = quantum efficiency of PD, A = active area of PD exposed to light, h = plank constant, c = velocity of light, and I_0 = reverse saturation current of PD. Since I_{TR} decreases with increase in C in (2), we can say that V_{PD} of (3) will decrease with increase in C when other parameters are held constant. Thus, V_{PD} can be calibrated in terms of free chlorine concentration to get overall response of the proposed fiber optic sensor.

3 Experimental Details

A simplified experimental arrangement of the proposed sensor is shown in Fig. 3. This arrangement basically comprises of fabricated fiber optic sensors and electronic amplifiers A_1 and A_2 (A_1 acts as voltage follower, while A_2 acts as differential amplifier). Light is coupled from a light-emitting diode (LED) into the fibers, and transmitted light beams are detected by PD. A_2 amplifies the difference of PD

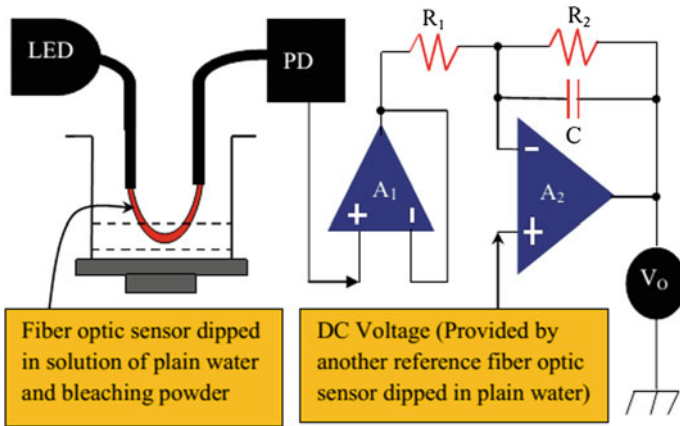


Fig. 3 Experimental arrangement of the proposed sensor

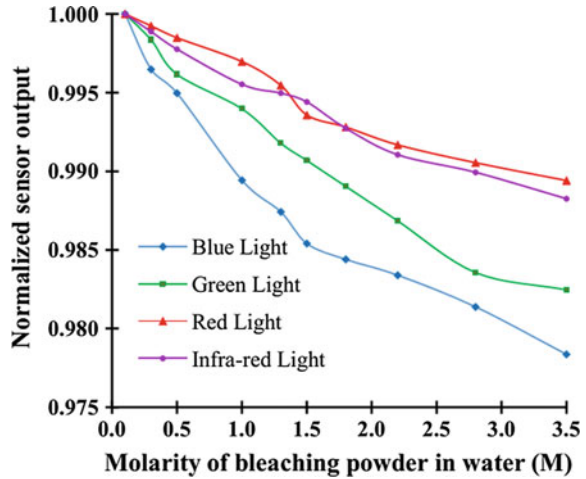
Table 1 Details of the liquid samples used in the experiment

Sample number	Molar concentration of bleaching powder in (M)	Corresponding weight of bleaching powder in (g) (measured with digital balance)	Corresponding weight of chlorine calculated theoretically by considering 40% active chlorine content in bleaching powder in (g)
S0	0	0	0
S1	0.1	0.28	0.11
S2	0.3	0.86	0.34
S3	0.5	1.43	0.57
S4	1.0	2.86	1.14
S5	1.3	3.72	1.49
S6	1.5	4.29	1.72
S7	2.0	5.15	2.06
S8	2.5	6.29	2.52
S9	3.0	8.00	3.20
S10	3.5	10.01	4.00

open-circuit voltages obtained from the reference fiber and sensing fibers. We have shown a DC voltage source in place of the reference fiber to simplify the schematic diagram.

Table 1 shows the liquid samples prepared and used in the experiment. These samples (20 mL in quantity) are kept separately in separate beakers, and these samples are to be kept in sealed condition in dark room if not used. This is necessary because chlorine concentration of the sample decreases with time and usage, as in [6] Experimental observations are taken by dipping the sensing fiber

Fig. 4 Unamplified response curves of the proposed sensor with change in molar concentration of bleaching powder in water (influence of light color is also illustrated in this plot)



probe in different liquid samples, while the reference fiber remains dipped inside plain water.

The sensing fiber probe is cleansed properly and dried before dipping in the new liquid sample. We use an adjustable mount to maintain equal immersion depth of fiber probe in all the samples. Influence of the wavelength of light source is also investigated by using blue, green, red, and infrared LED. The LED is driven by regulated DC power supply, and the whole experimental observations are carried out in dark room. Besides, vibration isolation optical bench has been used all throughout. Finally, we have drawn scattered plots of the sensor responses by using the experimentally recorded data. Figure 4 shows a normalized plot of unamplified PD response obtained from sensing fiber. This plot also shows the influence of the wavelength of light on sensor response. Figure 5 shows the scattered plot drawn by using amplified sensor output voltage V_0 obtained with blue LED. Figure 6 shows the response curve of the sensor with change in the amount of chlorine present in liquid samples.

4 Results and Discussions

Experimental observations have shown that response of the sensor varies with molar concentration of bleaching powder in water. Figure 4 shows normalized sensor response obtained with different wavelengths of light. The data of the normalized plot are obtained by dividing all the unamplified voltage outputs of sensing PD by its maximum value. The normalized plot shows that unamplified sensor response decreases with increase in bleaching powder concentration. Further, slopes of the curves show that sensitivity increases with decrease in wavelength of light source. However, influence of wavelength seems to be less significant beyond

Fig. 5 Amplified response curves of the proposed sensor (plotted with $\pm 5\%$ error bars) with change in molar concentration of bleaching powder in water (blue-colored light source is used since it shows the greatest influence on sensor response)

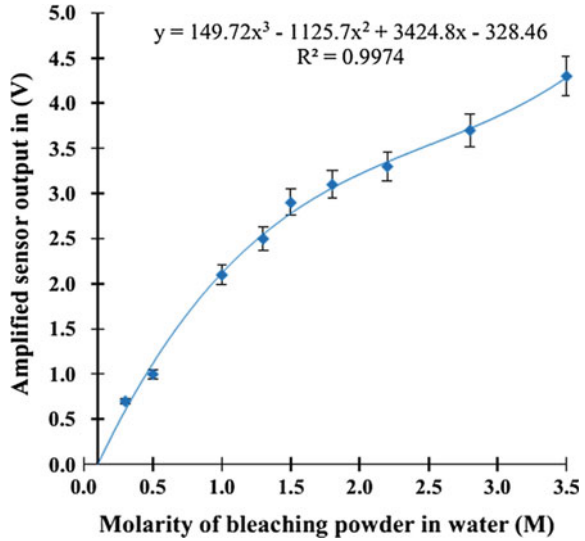
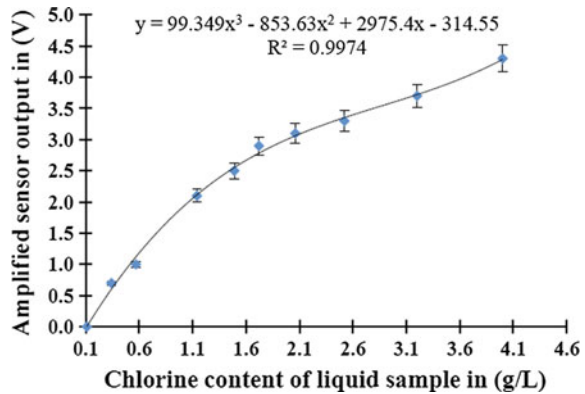


Fig. 6 Amplified response curves of the proposed sensor (plotted with $\pm 5\%$ error bars) with change in amount of chlorine in water samples (weight of the chlorine is 40% of the weight of bleaching powder as shown in Table 1)



visible wavelength of light, which is evident from the closeness of normalized sensor responses obtained at red and infrared colors of light.

The amplified sensor response of Fig. 5 has been obtained by amplifying difference of the voltage outputs of sensing PD and reference PD. Hence, the amplified response curve has positive slope as compared with the normalized plot of Fig. 4. We use blue-colored light source in the experiment to obtain data of Figs. 5 and 6, because sensor response has greatest sensitivity with blue-colored light source, which is evident from Fig. 4. We have determined sensitivity of the sensor from Fig. 6 as our purpose is to determine chlorine level. Sensitivity is obtained by calculating the ratio of the change in amplified sensor output voltage to the change in amount of chlorine. Resolution of the sensor is further obtained by finding reciprocal of sensitivity and multiplied it by full-scale voltage span of the sensor

output. Thus, calculated resolution of the sensor varies from 2.7 to 5.5 mg/L. This means that the chlorine detection limit of the proposed sensor is 2.7 mg/L.

The present sensor has some advantages. The proposed sensor does not contaminate liquid samples, because no extra chemical reagents are needed to test chlorinated liquid sample, unlike [16]. Besides, the sensing fiber probes do not have any kind of material coating. So, the sensor can be used in both laboratory and field testing applications.

Over and above, the sensor design methodology is very simple, which reduces its development cost. Sensitivity of the sensor is a bit lesser than the reported sensor. However, it can be optimized for further improvement. Disadvantages of the sensor may include possible deterioration of sensing fiber probe due to aging effect. So, replacement of the fiber probe and its recalibration will have to be done at regular intervals. In future direction of the work, we will interface digital read-out electronics with the sensor, and calibration will be done with the help of standard sensors commercially available in the market.

5 Results and Discussions

A novel fiber sensor has been reported for use in detection of chlorine level in chlorinated water. The sensor has promising scope for use in both laboratory and field testing of chlorinated water due to its low-cost and non-contaminating nature.

Acknowledgements The authors express their sincere thanks to Prof. T. Bezboruah, Head of the Department of ECT, Gauhati University, for providing infrastructure support and encouragement to this work. And, they are also thankful to Prof. Shakuntala Laskar and Asst. Prof. Bikamrjit Goswami of EEE Department, Assam Don Bosco University, Assam, India, for providing valuable suggestions during the work.

References

1. D.L. Harp, *Current technology of chlorine analysis for water and wastewater*, Technical information series-Booklet no. 17, Hach Company, USA, 2002.
2. *Chlorine in drinking water*, Published in Guidelines for drinking-water quality, 2nd ed. Vol.2. Health criteria and other supporting information, World Health Organization, Geneva, 1996.
3. *Measuring chlorine levels in water supplies*, Technical notes in drinking water, hygiene and sanitary in emergencies, World Health Organization, WEDC Loughborough University, Leicestershire LE11 3TU UK.
4. T. L. Engelhardt, V. B. Malkov and Hach®, *Chlorination, chloramination and chlorine measurement*, Hach Company, USA, 2015.
5. Cai-Yan Kang, Dan-Li Xi, Su-Mei Zhou, and Zhi-Liang Jiang, "A novel and selective spectral method for the determination of trace chlorine in water basing on the resonance scattering effect of rhodamine B-I3 association nanoparticles," *Talanta* 68, pp. 974–978, Elsevier B.V., 2006.

6. J.G. March, M. Gual and B.M. Simonet, Determination of residual chlorine in greywater using *o*-tolidine,” *Talanta* 58, pp. 995–1001, Elsevier B.V., 2002.
7. Jie Xu, Ke Feng, and Marcus Weck, “Free chlorine sensing using an interferometric sensor,” *Sensors and actuator-B*, 156, pp. 812–819, Elsevier B.V., 2011.
8. S. Sumriddetchkajorn, K. Chaitavon, Y. Intaravanne, “Mobile device-based self-referencing colorimeter for monitoring chlorine concentration in water,” *Sensors and actuator-B*, 182, pp. 592–597, Elsevier B.V., 2013.
9. R. B.R. Mesquita *et. al.*, “Use of tetramethylbenzidine for the spectrophotometric sequential Injection determination of free chlorine in waters,” *Talanta* 72, Issue 3, pp. 1186–1191, Elsevier B.V, 2007.
10. Si Pan, M. J. Deen, and R. Ghosh, “Low-Cost Graphite-Based Free Chlorine Sensor,” *Anal. Chem.* 87, pp. 10734–10737, American Chemical Society, 2015.
11. Ivan Kashi *et.al.*, “Fiber-optic detection of chlorine in water,” *Sensors and Actuators B*, 139, pp. 139–142, Elsevier B.V., 2009.
12. S. P. Usha, S. K. Mishra and B. D. Gupta, “Fabrication and Characterization of a SPR Based Fiber Optic Sensor for the Detection of Chlorine Gas Using Silver and Zinc Oxide,” *Materials* 8, pp. 2204–2216; (<https://doi.org/10.3390/ma8052204>), 2015.
13. Rana Tabassum and Banshi D. Gupta, “Surface plasmon resonance based fiber optic detection of chlorine utilizing polyvinylpyrrolidone supported zinc oxide thinfilms.” *Analyst* 140, pp. 1863–1870, Royal Society of Chemistry, 2015.
14. Kulvinder Singh and S. K. Mehta, “Luminescent ZnO quantum dots as an efficient sensor for free chlorine detection in water” *Analyst*, 141,2487–2492, Royal Society of Chemistry, 2016.
15. Y. Dong, G. Li, N. Zhou, R. Wang, Y. Chi, and G. Chen., “Graphene Quantum Dot as a Green and Facile Sensor for Free Chlorine in Drinking Water” *Anal. Chem.*, 84, pp. 8378–8382, American Chemical Society, 2012.
16. P. K. Choudhury, T. Yoshino, “On the evanescent field fiber-optic sensor for the detection of chlorine in drinking water”, *Proc. of SPIE* Vol. 5634, pp. 136–139, 2005.
17. A.B. Maity, *Optoelectronics and optical fiber sensors*, PHI Learning Private Ltd., New Delhi, India, 2013.
18. S.O. Kasap, *Optoelectronics and photonics –principles and practices*, Pearson Education Inc., New Delhi, India, 2009.

Effect of LO Phase Noise on Front-end Receiver Performance

Manish Kumar, T. K. Pal, B. S. V. Prasad, G. Arun Kumar, Sukhendu Bhanja and Arijit Majumder

Abstract Low phase noise is an important parameter, which determines the overall performance of the pulsed radar receivers in terms of range, Doppler and also operational robustness. Poor local oscillator (LO) phase noise causes reduction in the IF signal power as well as deterioration in phase noise. Considerable efforts are made to improve the LO phase noise. However, there is always an uncertainty as to how much phase noise should be tolerable and at the cost of what amount of performance. In this paper, a method is being proposed to ascertain the minimum tolerable phase noise or threshold LO phase noise and the impairments in performance thereof. It has also been shown that beyond a certain value, the improvement in performance vis-a-vis the cost and complexity is negligible.

Keywords Local oscillator · Phase noise · Radar · Receiver · Sensitivity

M. Kumar (✉) · T. K. Pal · B. S. V. Prasad
Research Centre Imarat, DRDO, Kurmalguda, Hyderabad, India
e-mail: manish.kumar23@rcilab.in

T. K. Pal
e-mail: tkp_007@rcilab.in

B. S. V. Prasad
e-mail: prasad.bsv@rcilab.in

G. Arun Kumar · S. Bhanja · A. Majumder
SAMEER Kolkata Centre, Kolkata, India
e-mail: g.arun@mmw.sameer.gov.in

S. Bhanja
e-mail: sukhendu.bhanja@mmw.sameer.gov.in

A. Majumder
e-mail: arijit@mmw.sameer.gov.in

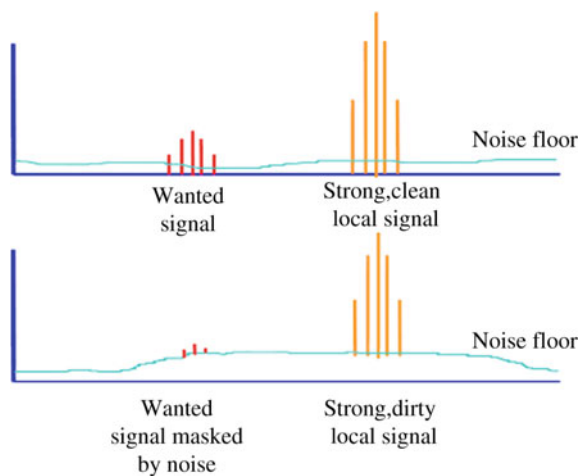
1 Introduction

In the real world, there would be no signal without noise in any application. We know intuitively that low noise in a system is always better than high noise. Depending upon requirements, a typical radar receiver may have one or more signal sources, all in coherence, to generate various signals. Phase noise of different signals has their bearing by different mechanisms, for example poor phase noise of the received signal results in spillage of power from carrier into the sidebands whereas the poor phase noise of the local oscillator (LO) signal deteriorates the overall noise floor of the receiver, reducing the signal-to-noise ratio (SNR) finally. The effect of phase noise on overall receiver performance can be summarized as follows [1–5]:

- (a) The energy from the centre/carrier is spread into the adjacent frequencies.
- (b) The overall noise floor of the receiver is increased.
- (c) It results in detection of unwanted signals adjacent to the desired signal.
- (d) The problem is even more critical in CW systems such as FMCW-based radar altimeters, wherein the poor phase noise of the transmitted signal, which leaks into the receiver, masks the weaker echo signal from closer ranges. The energy from the centre/carrier is spread into the adjacent frequencies.
- (e) The overall noise floor of the receiver is increased.
- (f) It results in detection of unwanted signals adjacent to the desired signal.

The local oscillator phase noise characteristics will dominate the entire system performance. A typical transmitter spectrum for a clean and noisy local source is shown in Fig. 1. The lower diagram shows how a noisy local oscillator can raise the noise floor, swamping low power signals close to carrier.

Fig. 1 A typical transmitter spectrum



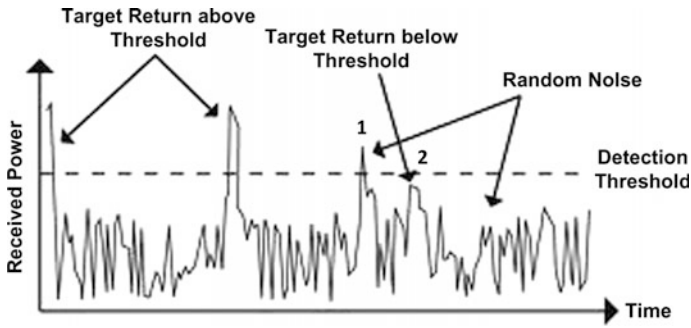


Fig. 2 A typical radar detection scenario [2]

A lot of studies have been carried out on the various effects and characteristics of phase noise by earlier researchers [6–16], though a rational basis to quantify the effects of phase noise on the overall receiver performance has not been elucidated.

In this paper, a methodology has been devised to ascertain the minimum phase noise that can be termed as threshold LO phase noise, up to which the desired system performance in terms of range and Doppler determination is achieved reliably.

A typical radar detection scenario is shown in Fig. 2 [2]. As per the study, it will be shown in subsequent sections that the phase noise of LO reduces IF signal power thereby decreasing the detectable range. It also increases the power level between the discrete FFT spectral lines, thereby impeding the quality of detection in terms of target Doppler.

2 Phase Noise

Phase noise is basically a frequency domain representation of the time domain jitters in a signal. It may also be defined as the short-term random fluctuations in the frequency or phase of an oscillator signal [1–4]. The spectrum of an ideal single tone signal consists of a single spectral line as shown in Fig. 3a. However, practically the spectrum is never a single spectral line, and it is rather as shown in Fig. 3b.

The phase noise is defined for the certain offset frequency from the nominal frequency as shown in Fig. 4. It is a rate of the noise power P_{noise} in 1 Hz bandwidth at the offset frequency to the signal power P_{sig} . Phase noise is expressed in a logarithmic scale and its unit is dBc/Hz, thus the power in decibels related to the carrier power [6, 7].

$$L_m(\omega_m) = 10 \log\left(\frac{P_{noise}(\omega_m)}{P_{sig}}\right) \quad [\text{dBc/Hz}]$$

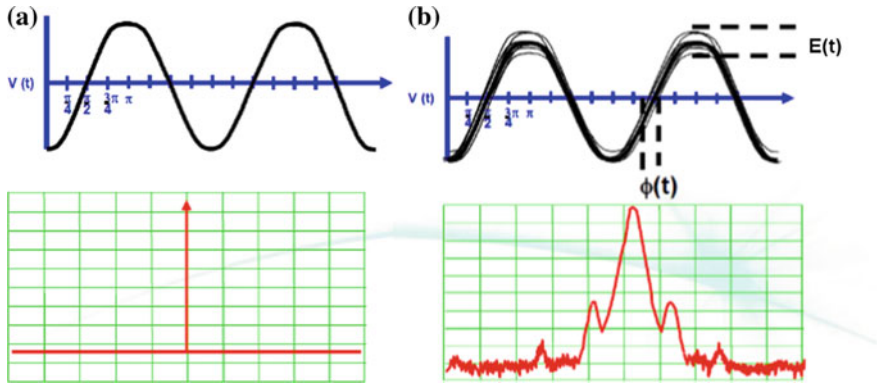
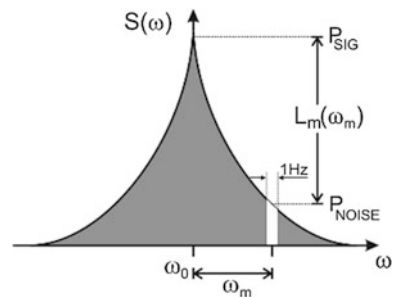


Fig. 3 Spectrum of an a ideal b practical single tone signal

Fig. 4 Spectrum of a practical single tone signal [6, 7]



3 Modelling and Simulation

A typical radar receiver for monopulse-based operation has been designed for the study. It is a single-stage down-conversion super-heterodyne receiver which works at W-band frequencies and has an IF at L-band. In actual scenario, the IF signal is further down-converted to a VHF signal, amplified and then filtered. This VHF signal is then sampled by a high-speed ADC, and the samples are then processed in analytic domain to extract desired information finally. The schematic of the receiver is as shown in Fig. 5. For the sake of simplicity and without loss of generality, only the front-end part of the receiver has been simulated. The results and conclusion equally hold for further down-conversion and so on. Specifications of the receiver are given in Table 1. The simulation has been carried out using an EDA tool Advanced Design System-2015.

For the simulations, the phase noise of the LO signal is varied as per the profile given in Fig. 6, whereas keeping other parameters constant. The power of the LO signal is kept at +10 dBm. The input to the receiver is a pulsed RF signal having peak power of -110 dBm as expected in real scenario. The gain of the receiver is 25 dB, which corresponds IF signal power of -85 dBm. In the first case, when the

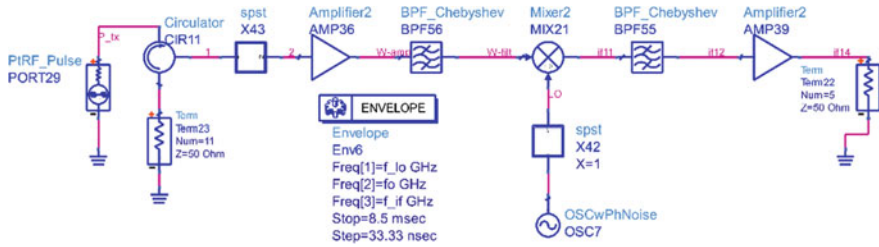


Fig. 5 Schematic of a receiver chain

Table 1 Specifications of the receiver

Sl. No.	Parameters	Specification
1	Gain	25 dB
2	Signal bandwidth	10 MHz
3	P1 dB (input)	-15 dBm
4	Sensitivity	-115 dBm
5	Noise figure	10 dB

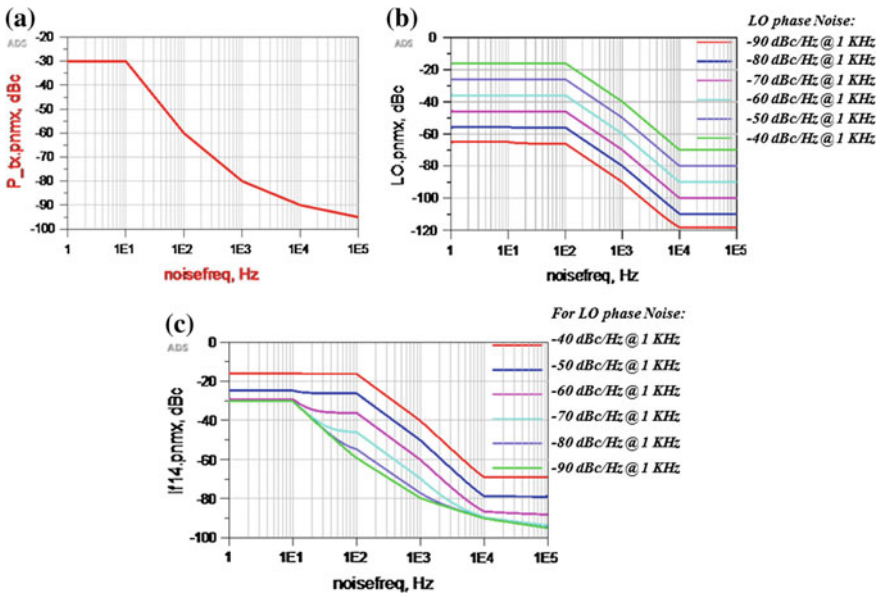


Fig. 6 Phase noise plots of a input CW RF signal b LO signal c IF signal

phase noise of the LO signal is -90 dBc/Hz @ 1 kHz the IF signal power is around -85 dBm as depicted in Fig. 7. Similarly, the phase noise of the LO is varied from -90 to -60 dBc/Hz @ 1 kHz as per the given profile, and no substantial reduction in the IF power is observed. As the phase noise is further increased to -50 and

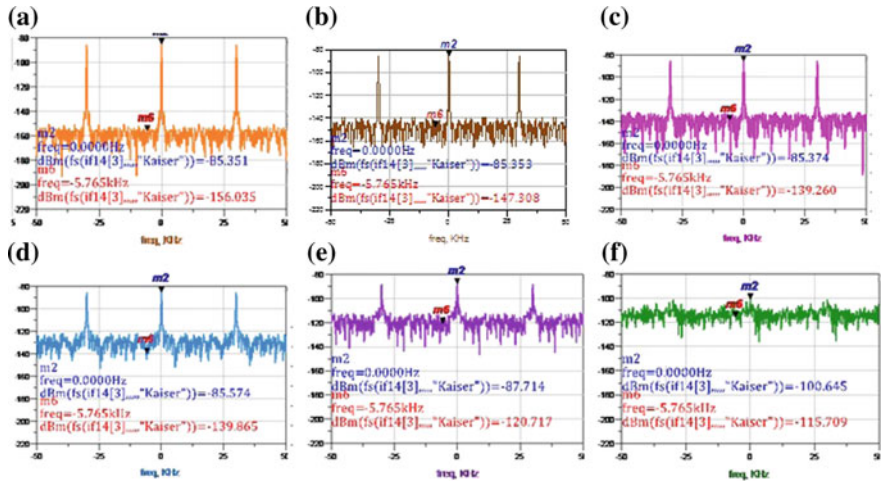


Fig. 7 Simulated FFT spectral lines of IF output for LO phase noise of **a** -90 dBc/Hz **b** -80 dBc/Hz **c** -70 dBc/Hz **d** -60 dBc/Hz **e** -50 dBc/Hz **f** -40 dBc/Hz at 1 kHz

Table 2 Results

Sl. No.	LO phase noise versus IF signal power and phase noise (LO power = + 10 dBm, RF input power = -110 dBm)		
	LO phase noise at 1 kHz (dBc/Hz)	IF power (dBm)	IF phase noise (at 1 kHz) (dBc/Hz)
1	-90	-85.351	-80
2	-80	-85.353	-78
3	-70	-85.374	-70
4	-60	-85.574	-58
5	-50	-87.714	-50
6	-40	-100.645	-40

-40 dBc/Hz @ 1 kHz, the IF power reduces substantially to -87.7 dBm and -100.65 dBm, respectively.

The phase noise of the IF signal has also been studied with respect to the phase noise of the LO signals. For this study, a CW RF signal at W-band having phase noise profile as shown in Fig. 6 has been given to the input and the effects of variation in the LO phase noise has been summarized in Table 2.

4 Conclusion

The following major conclusions can be drawn from this study to judiciously select the LO phase noise parameter for designing a radar front-end receiver:

- (a) The power and phase noise of IF signal decreases substantially as the phase noise of the LO signal deteriorates below the threshold LO phase noise (-50 dBc/Hz @ 1 kHz). Thereby, causing a corresponding decrease in the SNR and hence the detectable range.
- (b) The phase noise of the signal deteriorates under vibration. Therefore, the necessary margin should be kept wherever applicable, while designing the LO signal, such that even under vibration it should not go below threshold LO phase Noise, thereby ensuring no substantial reduction in SNR and hence the range performance.
- (c) Improvement in phase noise of the LO signal can be accomplished only with considerable cost and complication; however, beyond a certain point, the improvement in receiver performance is negligible.

Acknowledgements The authors extend their deep gratitude to Shri BHVSN Murthy, Outstanding Scientist and Director, RCI, DRDO for his continuous guidance and support. The authors are also thankful to Dr S. B. Gadgil, Outstanding Scientist, Associate Director and Shri BRK Reddy, Technology Director, RCI, DRDO for their constant encouragement during the study.

References

1. David M. Pozar, Microwave Engineering 2nd ed, John Wiley & Sons Inc.
2. Merrill I. Skolnik, Radar Handbook 2nd ed, McGraw Hill.
3. Raoul Pettai, Noise in Receiving Systems, John Wiley & Sons.
4. James A. Scheer and James L. Kurtz, Coherent Radar Performance Estimation, Artech House.
5. William F. Egan, Lecturer in Electrical Engineering, Practical RF System Design, IEEE.
6. Thomas H. Lee, Oscillator Phase Noise: A Tutorial (Invited), Custom Integrated Circuits Conference, 1999, IEEE Page No: 373–380.
7. Thomas H. Lee, Member, IEEE, and Ali Hajimiri, Member, IEEE, Oscillator Phase Noise: A Tutorial, 2000, IEEE. Page No: 326–336.
8. Ondrej BARAN, Miroslav KASAL, Oscillator Phase Noise Models, 978-1-4244-2088-9/08 (c) 2008, IEEE.
9. Xiangdong Zhang and Brian J. Rizzi, A New Measurement Approach for Phase Noise at Close-in Offset Frequencies of Free-running Oscillators, 1996 IEEE MTT-S Digest. Page No: 1679–1682.
10. Manish Kumar, Nilang Trivedi, BSV Prasad, JV Prasad, A W-B and Target echo simulator (W-TES) for Radar Application, ICCSPCIT-2014, Pg.01–08, ISBN: 978-93-83.038-27-5.
11. Kaneyuki Kurokawa, Member, IEEE, Noise in Synchronized Oscillators, Page No: 234–240.
12. www.agilent.com.
13. Rodolphe boudot and Enrico Rubiola, Phase Noise in RF and Microwave Amplifiers, 2012, IEEE, Page No: 2613–2624.
14. Jerry L. Eaves and Edward K. Reedy, Principles of Modern Radar, Van Nostrand Reinhold Company, New York.
15. D.B. Leeson, “A simple model of feed back oscillator noise spectrum”, Proc. IEEE, vol. 54, Page No: 329–330, Feb. 1966.
16. E. Rubiola, Phase Noise and Frequency Stability in Oscillators. Cambridge, UK: Cambridge University Press, 2008.

Design of a Proactive Distance Handover Algorithm for WSN: A Case Study-Based Approach

M. S. Saketh, N. S. Reddy and S. Dhar

Abstract Mobile applications are gaining substantial interests in recent years in large-scale wireless sensor networks (WSN). To achieve uninterrupted functioning of WSN, it is essential to initiate handover from current wireless node to another suitable node. A proactive distance handover algorithm for WSN is presented in this work. The algorithm is successfully validated considering the case studies of different mobility pattern.

Keywords WSN · Handover · Mobility · Sensor node

1 Introduction

Wireless sensor network (WSN) is a combination of sensor nodes that are capable of sensing various physical parameters, raw data processing within the network, and delivering the processed results over the wireless ad hoc/multi-hop link [1]. Sensor nodes, in a WSN, are capable of self-organizing themselves to maintain a network without any manual intrusion. The nodes smaller in size and their ability to communicate wirelessly provide WSN the strategic advantage in scenarios when nodes are to be deployed in inaccessible places or when wired systems are simply too expensive. Similarly, deployment and maintenance of such networks may be possible without upsetting the normal operation of the structure or process they are monitoring. Depending on the type of deployment, WSN applications are broadly classified in two major categories (Fig. 1).

M. S. Saketh · N. S. Reddy · S. Dhar (✉)

Electronics and Communication Engineering Department of Sikkim Manipal Institute Technology, Sikkim Manipal University, Majitar, Rangpo, East Sikkim 737136, India
e-mail: sourav.dhar80@gmail.com

© Springer Nature Singapore Pte Ltd. 2018

R. Bera et al. (eds.), *Advances in Communication, Devices and Networking*,
Lecture Notes in Electrical Engineering 462,
https://doi.org/10.1007/978-981-10-7901-6_49

447

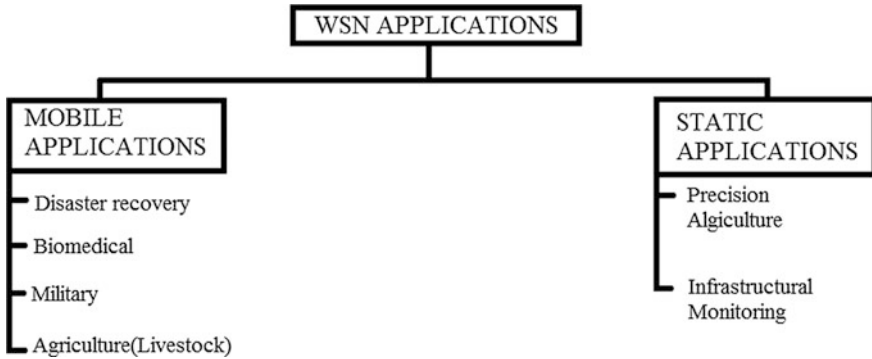


Fig. 1 Classification of WSN applications based on mobility

1.1 *Static Applications*

This class of applications either does not require nodes to move or does have occasional/minor modifications in the network topology. A WSN developed by Mainwaring et al. [2] to collect information from temperature, barometric pressure, humidity, and light sensors to monitor the actions of seabirds. Deployments of sensors to monitor the structural integrity of infrastructures [3] and active volcanoes by means of seismic and infrasonic sensors are examples of static deployment [4]. Some other popular applications include precision agriculture [5, 6] and mine safety monitoring [7, 15].

1.2 *Mobile Applications*

Wireless sensor nodes are too deployed in scenarios which demand nodes to be mobile; for example, biomedical sensor nodes that are put on to the body of a patient [8] or nurses [9] for monitoring their activities. Workers can avoid dangerous situations during disaster management [10] and oil extraction and refinery plants [11] by carrying appropriate sensors. Sensor nodes are also employed for reporting on events occurring during a mission [12]. Animal health and behavior in outdoor environments being monitored is yet another well-known application of sensor nodes [13]. The necessity of individual and herd-wide monitoring of cattle arises due to the level of complications involved in the management of large farms.

Handover is essential in mobile WSN applications for seamless operation [14], and hence, this issue is considered in this paper. The paper is organized as follows: Sect. 2 details the need for handover in WSN, problem scenario and algorithm design are discussed in Sect. 3, validation of algorithm is done with help of four case studies in Sect. 4, and finally, the work has been concluded in Sect. 5.

2 Mobility: The Need for Handover

2.1 Weak Mobility

Depending on the application requirements, there are two types of nodes, static and mobile, available in WSN. Any type of hardware failure or battery exhaustion can cause nodes to leave a network. Similarly, fresh nodes may get added to the network to compensate for the non-functional nodes. Such consistent changes in network topology are referred as weak mobility [16].

2.2 Strong Mobility

On the contrary, the physical mobility of sensor nodes may be due to the intentional movement of objects/persons or by external forces, is the primary characteristics of strong mobility [16]. The repercussions of strong mobility are challenging to deal with since they involve facing some tough challenges in design of protocols, principally, at the network layer and at the link layer. The mobility of nodes may cause worsening in the quality of an established connection, and hence to disrupt the data transmission. Thus, the probability of packet retransmission as well as the total energy consumption will be increased. Mobility may also cause recurrent route changes those results in a substantial delay in delivery of packets and the enhanced design complexity of protocols in the network layer. Nodes joining a certain network need to wait for a specified time period since only specific time slots are intended to accommodate mobility in MAC protocols based on scheduling. Similarly, in contention-oriented MAC protocols, a mobile sensor node is authorized to enter a network only after it receives a synchronization packet from a sensor node which already exists in the network. Therefore, the mobile node has to be idly listening in the network until the synchronization packet is received. In contention-based MAC protocols, packet collision rate may also increase while in schedule-based MAC protocols, schedule inconsistencies may arise due to inconsistencies in two-hop neighborhood once nodes enter or leave the network.

3 Problem Scenario

3.1 Mobility Scenario

Figure 2 shows a simple mobility scenario in a WSN, where two relay nodes (RN) are linked with two sinks. A mobile node (MN) moving in a random path sends information to the sinks through the RNs. Due to the random motion of MN, the time-varying distances between MN and RNs are denoted by $X_1(t)$ and $X_2(t)$

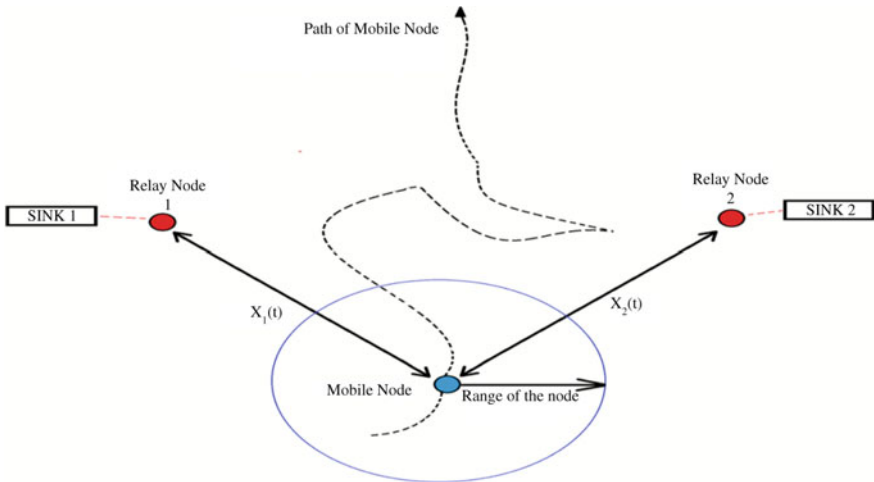


Fig. 2 Mobility scenario

Also, the MN has a fixed range or a threshold distance up to which it can communicate. Beyond the threshold distance, a link cannot be established.

3.2 Initial Link Establishment

Figure 3 shows that a link is established between MN and RN1 when RN1 is within the communication range of MN. During this period, sensor data can be forwarded from MN to RN1, which then forwards the data directly to sink1. As long as RN1 is within the range of MN, they can communicate with each other, even in mobility conditions. However, when RN1 is out of MN’s range, handover must be initiated. When handover is initiated MN searches for other RNs in the vicinity. If there are any, handover can be implemented successfully; else, there will be a link failure.

3.3 Link Handover

It can be seen from Fig. 4 that handover is initiated as MN moved away from RN1. As RN2 is in the vicinity, i.e., $X_2(t) < (\text{threshold distance})$, connection is handed over from RN1 to RN2. When MN travels away from both RN1 and RN2 since both the relay nodes are out of MN’s range, handover cannot be accomplished and the link fails, as shown in Fig. 5.

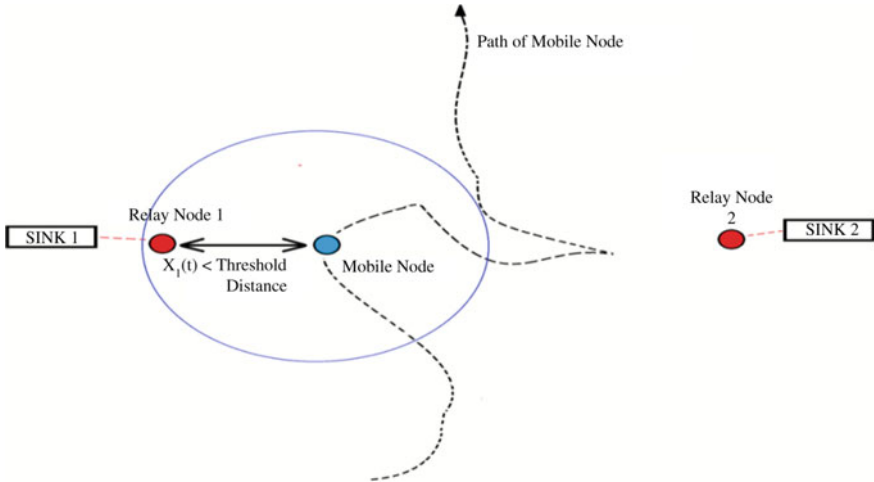


Fig. 3 Link between MN and RN

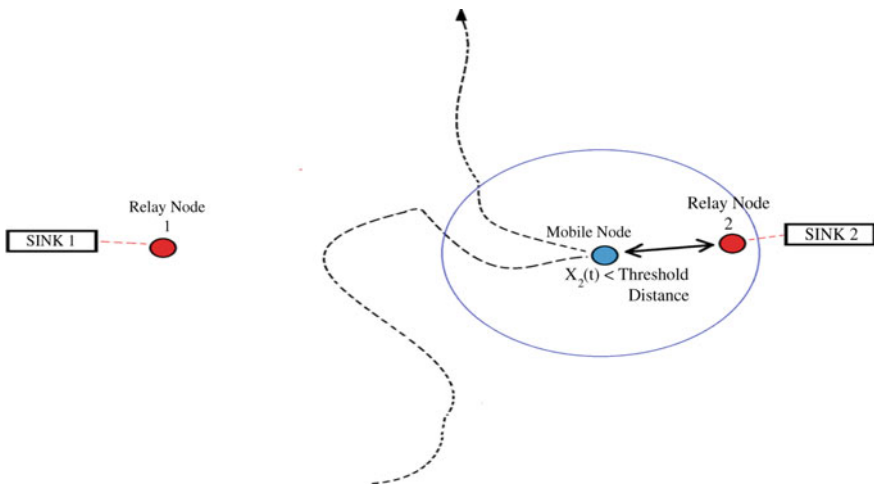


Fig. 4 Link handover to RN2

3.4 Handover Algorithm Design

To handle the variations that are caused due to mobility, an algorithm that can proficiently switch a node into and out of a network is essential. In view of distance as the main factor impelling handover, a proactive distance handover algorithm has been developed (Fig. 6) for a typical mobility scenario. An MN will initiate a link establishment with an RN within the threshold distance. As the MN moves,

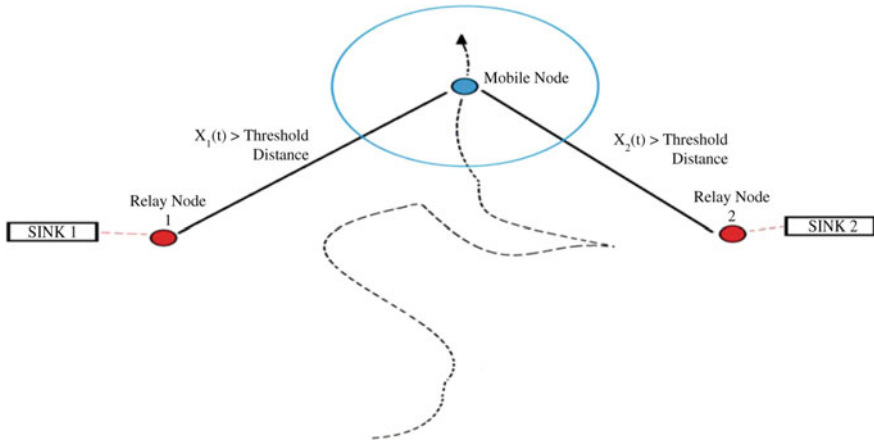


Fig. 5 Link failure

whenever the distance among communicating nodes goes beyond the threshold distance, handover is initiated, depending upon availability of relay nodes.

4 Validation

4.1 Case Study I

Considering the mobility scenarios described in the previous section, four case studies are done with specific fixed parameters and rules:

Threshold distance was chosen to be 25 m.

A handover index (*HO*) variable was assumed such that:

When MN is linked with RN1, $HO = 10$;

When MN is linked with RN2, $HO = 20$;

When there is a link failure, $HO = 0$;

In each case study, a different mobility pattern was tested for handover. For the first case study, $X_1(t)$ and $X_2(t)$ were defined as follows:

$$X_1(t) = t^2 \tag{1}$$

$$X_2(t) = \sin(t) * t^2 \tag{2}$$

In Fig. 7, the orange curve represents $X_1(t)$, yellow curve represents $X_2(t)$, and black curve represents handover index (*HO*). When RN1 is within range, i.e., $X_1(t) < 25$, $HO = 10$, when RN1 is out of range and RN2 is within range, i.e., $X_1(t) > 25$ and $X_2(t) < 25$, $HO = 20$, when both RN1 and RN2 are out of range, i.e., $X_1(t) > 25$ and $X_2(t) > 25$, $HO = 0$.

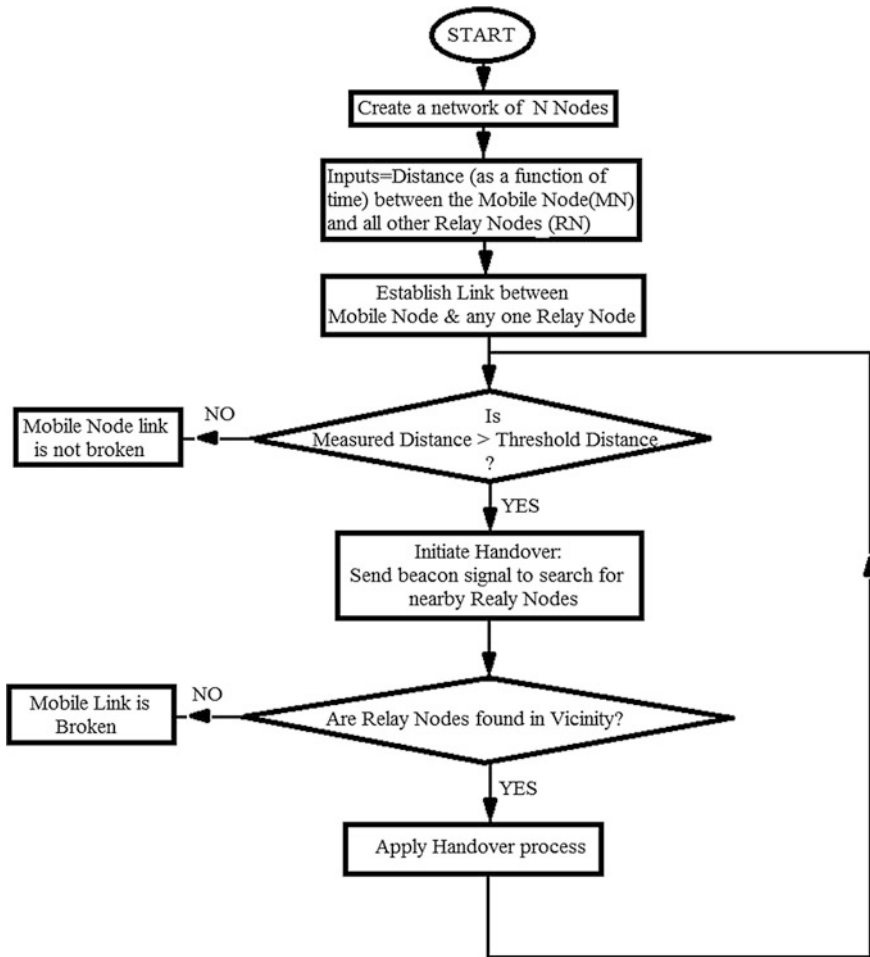


Fig. 6 Distance handover algorithm in a WSN

4.2 Case Study II

For the second case study, $X_1(t)$ and $X_2(t)$ were defined as follows:

$$X_1(t) = t^2 - (t * \sin(t)) \tag{3}$$

$$X_2(t) = \text{abs}((\tan(t))^2) \tag{4}$$

We can infer from Fig. 8 that whenever RN1 is within range, i.e., $X_1(t) < 25$ $HO = 10$, when RN1 is out of range and RN2 is within range, i.e., $X_1(t) > 25$ and $X_2(t) < 25$, $HO = 20$, when both RN1 and RN2 are out of range, i.e., $X_1(t) > 25$ and $X_2(t) > 25$, $HO = 0$.

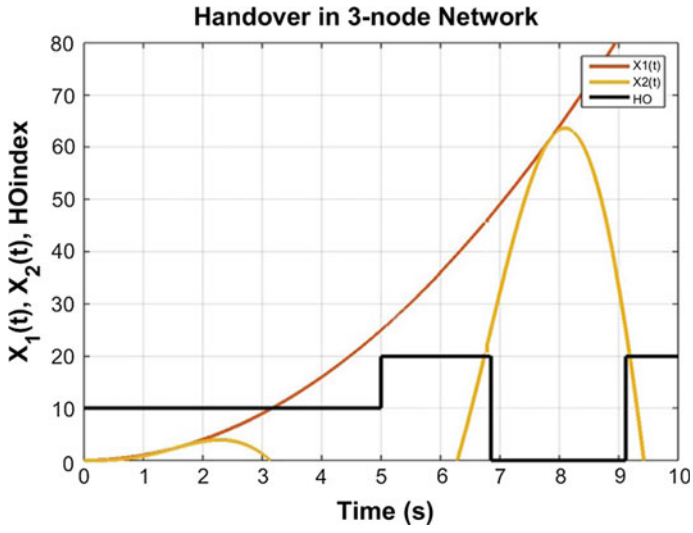


Fig. 7 Handover in case I

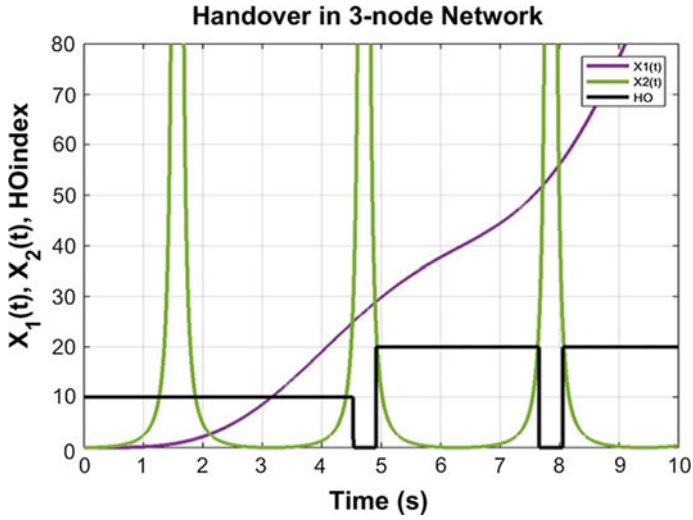


Fig. 8 Handover in case II

4.3 Case Study III

For the third case study, $X_1(t)$ and $X_2(t)$ were defined as follows:

$$X_1(t) = \left(\frac{2}{t-1}\right) + 18 * t \tag{5}$$

$$X_2(t) = (t^2 - (t * \sin(t))) * \sin(t) \tag{6}$$

We can see in Fig. 9 that and in the previous case studies that irrespective of the mobility pattern, handover is being implemented successfully.

4.4 Case Study IV

For the fourth case study, $X_1(t)$ and $X_2(t)$ were defined as follows:

$$X_1(t) = \sqrt{\left(\frac{10}{\sin c(t)}\right)} \tag{7}$$

$$X_2(t) = t^2 - (t * \sin(t)) \tag{8}$$

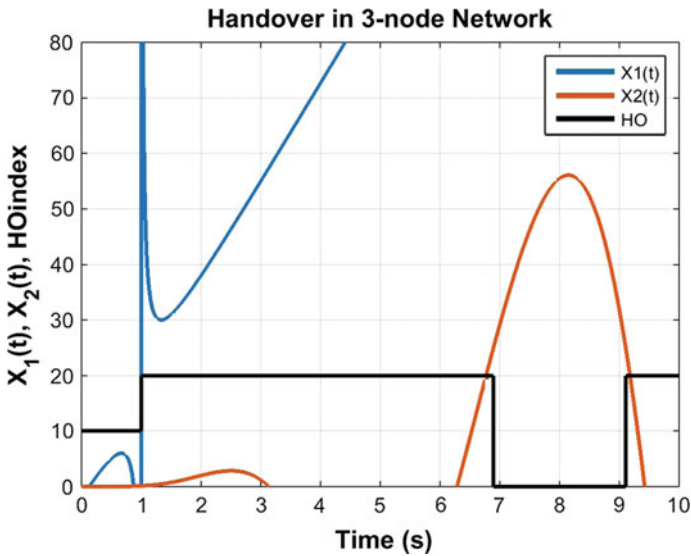


Fig. 9 Handover in case III

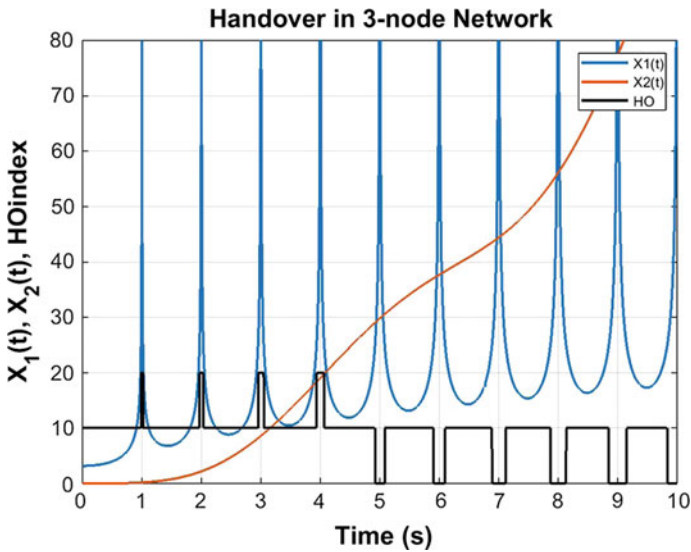


Fig. 10 Handover in case IV

We can see in Fig. 10 that and in the previous case studies that irrespective of the mobility pattern, handover is being implemented successfully.

5 Conclusion

The algorithm is simple, yet highly efficient and proactive for initiating distance handover. However, the algorithm considers scenarios wherein a single or two relay nodes are put into use. Furthermore, the algorithm can be improved by considering a more complex network and applying optimization techniques to obtain a faster and more efficient response.

References

1. Walteneug Dargie and Christian Poellabauer. Fundamentals of Wireless Sensor Networks: Theory and Practice. Wiley Publishing, 2010.
2. Alan Mainwaring, David Culler, Joseph Polastre, Robert Szewczyk, and John Anderson. Wireless sensor networks for habitat monitoring. Proceedings of the 1st ACM international workshop on Wireless sensor networks and applications, pages 88–97. ACM, 2002.
3. Sukun Kim, S. Pakzad, D. Culler, J. Demmel, G. Fennes, S. Glaser, and M. Turon. Health monitoring of civil infrastructures using wireless sensor networks. 6th International Symposium on Information Processing in Sensor Networks, pages 254–263, April 2007.

4. G. Werner-Allen, K. Lorincz, M. Ruiz, O. Marcillo, J. Johnson, J. Lees, and M. Welsh. Deploying a wireless sensor network on an active volcano. *IEEE Internet Computing*, 10:18–25, March 2006.
5. J. Burrell, T. Brooke, and R. Beckwith. Vineyard computing: sensor networks in agricultural production. *IEEE Pervasive Computing*, 3:38–45, March 2004. 1.
6. Alberto Camilli, Carlos E., Antonio M. Saraiva, Andr R. Hirakawa, and Pedro L.P. Corra. From wireless sensors to field mapping: Anatomy of an application for precision agriculture. *Computers and Electronics in Agriculture*, pages 25–36, August 2007.
7. Chehri, A., Farjow, W., Mouftah, H. T., & Fernando, X. (2011, May). Design of wireless sensor network for mine safety monitoring. In *Electrical and Computer Engineering (CCECE), 2011 24th Canadian Conference on* (pp. 001532–001535). IEEE.
8. S. Dagtas, Y. Natchetoi, and H. Wu. An integrated wireless sensing and mobile processing architecture for assisted living and healthcare applications. Proceedings of the 1st ACM SIGMOBILE international workshop on Systems and networking support for healthcare and assisted living environments, pages 70–72, 2007.
9. Mingang Cheng, Masako Kanai-Pak, Noriaki Kuwahara, Hiromi Itoh Ozaku, Kiyoshi Kogure, and Jun Ota. Dynamic scheduling based inpatient nursing support: applicability evaluation by laboratory experiments. Proceedings of the 3rd ACM International Workshop on Context-Awareness for Self-Managing Systems, pages 48–54, 2009.
10. Konrad Lorincz, David J. Malan, Thaddeus R. F. Fulford-Jones, Alan Nawoj, Antony Clavel, Victor Shnayder, Geoffery Mainland, Matt Welsh, and Steve Moulton. Sensor networks for emergency response: challenges and opportunities. *IEEE Pervasive Computing*, 3:16–23, October 2004.
11. Xiaojuan Chao, Walteneus Dargie, and Guan Lin. Energy model for H2S monitoring wireless sensor network. Proceedings of the 2008 11th IEEE International Conference on Computational Science and Engineering, pages 402–409, 2008.
12. Sang Hyuk Lee, Soobin Lee, Heecheol Song, and Hwang Soo Lee. Wireless sensor network design for tactical military applications: remote large-scale environments. Proceedings of the 28th IEEE conference on Military communications, pages 911–917, 2009.
13. E. S. Nadimi, H. T. Sogaard, T. Bak, and F. W. Oudshoorn. Zigbee-based wireless sensor networks for monitoring animal presence and pasture time in a strip of new grass. *Comput. Electron. Agric.*, 61(2):79–87, May 2008.
14. S. Dhar, A. Ray, R. Bera, “Cognitive vertical handover engine for vehicular communication”, *Peer-to-Peer Netw. Appl.*, Springer, 2013, Volume 6, Issue 3, pp 305–324.; <https://doi.org/10.1007/s12083-012-0171-5>.
15. N. S. Reddy, M.S. Saketh, S. Dhar, “Review of sensor technology for mine safety monitoring systems: A holistic approach”, *IEEE First International Conference on Control, Measurement and Instrumentation (CMI)*, 8–10 Jan. 2016, Kolkata, pp (429–434), <https://doi.org/10.1109/cmi.2016.7413784>.
16. Muneeb Ali, Tashfeen Suleman, and Zartash Afzal Uzmi. MMAC: a mobility-adaptive, collision-free MAC protocol for wireless sensor networks. 24th IEEE International Performance, Computing, and Communications Conference, pages 401–407, April 2005.

Homomorphic Analysis of Vowels in Khasi Dialect

Bronson Syiem, Fairriky Rynjah and L. Joyprakash Singh

Abstract A few researches have been conducted in the past decades for analyzing speech signal. For efficient study on the nature of the actual production of speech, the effect of vocal tract response and excitation source should be taken separately. However, this task is practically problematic since the components forming speech are not linearly combined. This paper presents homomorphic analysis and a method for nonlinear filtering of vowels in Khasi dialect has been proposed. A log-spectrum of each of the eight vowels was obtained. The first three formants frequencies of each vowel from four different Khasi speaking speakers were calculated.

Keywords Cepstrum · Formant frequency · Homomorphic · Log-spectrum
Quefrency · Vocal tract response · Vowel

1 Introduction

Northeast India is known for its richness in tribal and cultural diversity. Each tribe from all the states has its own unique language. Khasi is an Austroasiatic language spoken by Khasi speakers of Meghalaya, a state of northeast India. Depending on the geographical region, Khasi language has been sub-categorized into different dialects. The Bhoi Khasi of the East Khasi Hills and Khasi dialects spoken by Khasis from Nongpoh to Umsning region is very different from the Khasi dialect of Cherrapunji (Sohra). Khasi dialect from Sohra (Cherrapunji) is considered as the standard Khasi dialect. In spite of some degrees of variance among different Khasi dialects, they all share a common script (Khasi alphabet). Khasi language did not

B. Syiem (✉) · F. Rynjah · L. Joyprakash Singh
Speech and Image Processing Lab Department of ECE, NEHU, Shillong 793022, India
e-mail: bronzoe12@gmail.com

F. Rynjah
e-mail: phemaky.rynjah@gmail.com

L. Joyprakash Singh
e-mail: jplairen@gmail.com

have its own script until Thomas Jones initiated the process of writing Khasi language in Roman script. Bareh [1] described some phonemic vowels that can be found in Khasi dialects such as /a/, /e/, /ɪ/, /ɛ/, /ʌ/, /o/, /ɔ/, and /u/. A vowel is the unit of the sound system of a language and it represents a speech sound produced by the open vocal tract in such a way that the tongue does not touch the lips, teeth, or roof of the mouth. Representation of vowel can be used to obtain accent-adapted features and therefore suitable to identify accents [2]. In this paper, an approach to nonlinear filtering of vowels found in Khasi dialect has been presented.

2 Data Collection

Currently, there is no standard database for Khasi dialect in speech processing research. For this paper, data were collected from four native Khasi speakers. Two were female and two were male. Each speaker is given a script and as they read, the speeches were recorded using Zoom H4n handy portable digital recorder. The time frame for recording is 10 min each for every speaker. From the collected data, the vowels were extracted for analysis.

3 Homomorphic Analysis

Speech is a fast time-varying signal produced due to acoustical excitation of the vocal tract when air is expelled from the lungs. Speech signal waveforms can be taken into different segments called frames for analysis. Each short segment or frame of speech signals can be viewed as it has been generated by exciting a linear time-varying (LTV) system either by a quasi-periodic impulse or random noise. This technique of analyzing the speech signal is called homomorphic analysis. Homomorphic analysis is also called cepstral analysis and is based on the principle of superposition. A reasonable model for the speech waveforms consists of the convolution of components representing the contributions of pitch, glottal pulse, and impulse due to vocal tract and for speech bandwidth compression and to study the nature of the speech wave, it is necessary to isolate the effects of each of these components. Basically, homomorphic analysis is a procedure for deconvolution or nonlinear filtering of the signal which has been non-additively combined [3]. In other word, homomorphic analysis is designed to separate convolved signal components by transforming the signal to a domain where components are added in a distinct region. It is accepted that linear prediction is a method for obtaining all-pole speech representations but it has

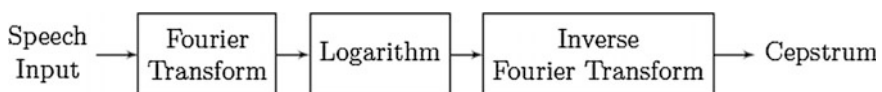


Fig. 1 Block diagram of homomorphic analysis

some limitation for pitch synchronization. This can be overcome by homomorphic analysis [4]. Similarly, homomorphic deconvolution can be used for spectral smoothing interpretation [5]. In this paper, we used homomorphic analysis to extract vocal tract impulse response of each of the eight vowels in Khasi dialect.

The output speech signal (vowel) $s(n)$ can be considered as a resultant of convolution of two components, i.e., vocal pulse $g(n)$ and the impulse response due to vocal tract $h(n)$. Since these components cannot be separated by linear filtering, we transform this signal into a domain where the components are additively combined. Figure 1 shows the homomorphic analysis of speech signal. The speech signal is converted to frequency domain by applying Fourier transform. The logarithm of the transformed signal is then applied, which is then sent to the inverse Fourier transform block to obtain the cepstrum.

$$s(n) = g(n) * h(n) \tag{1}$$

$$S(W) = G(W) \cdot H(W) \tag{2}$$

$$\text{Log } |S(W)| = \text{Log } |G(W)| + \text{Log } |H(W)| \tag{3}$$

$$\text{IFFT} [\text{Log } |S(W)|] = \text{IFFT} [\text{Log } |G(W)| + \text{Log } |H(W)|] \tag{4}$$

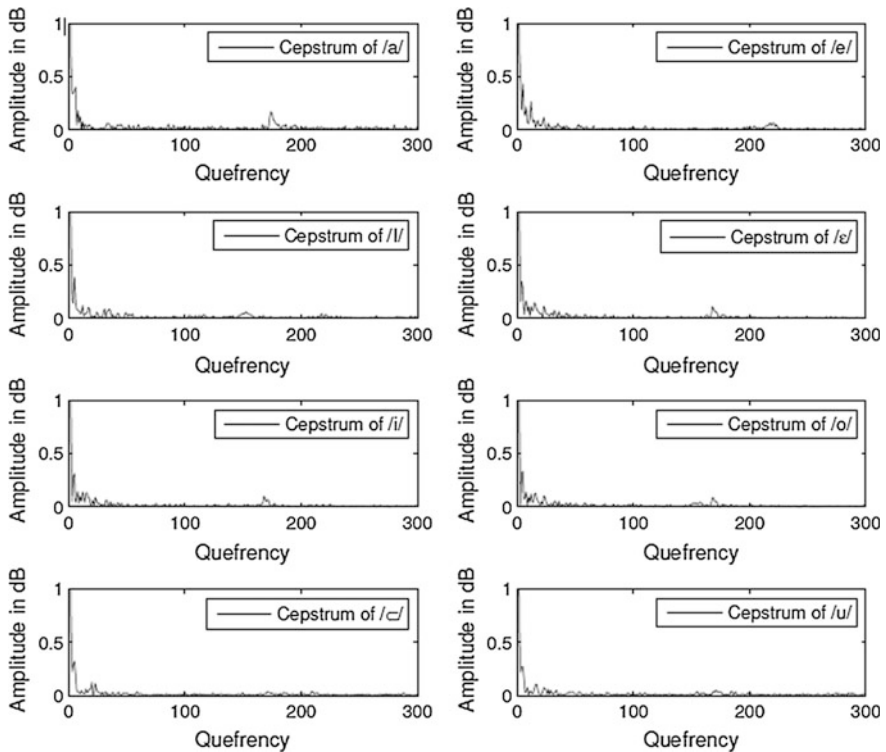


Fig. 2 Cepstrum of the vowels /a/, /e/, /ɪ/, /ɛ/, /i/, /o/, /ɔ/, and /u/

The slow-varying envelope in the cepstrum, close to the origin, corresponds to the vocal tract parameters [6]. This was extracted by using low-time liftering window. The window length ranging from 20 to 80 samples in the quefrequency domain is usually taken. In our experiment, we took a window length of 40 samples. Obtaining log-spectrum of vocal tract was done by Fourier transform of the windowed cepstrum. Formant frequency estimation was carried out by finding the first three peaks from the log-spectrum of low-time liftered cepstrum.

4 Experimental Results

The present investigation represents a nonlinear filtering of vowels in Khasi dialect. The cepstrum of eight vowels in Khasi dialect is shown in Fig. 2. The peak in the higher quefrequencies indicates that there is some periodicity in the signal. Log-spectrum of vocal tract parameters was obtained for each of the eight vowels and is shown in Figs. 3 and 4. The first three formant frequencies (F_1 , F_2 , and F_3) obtained from the four different speakers were calculated and the resultant values are given in Table 1.

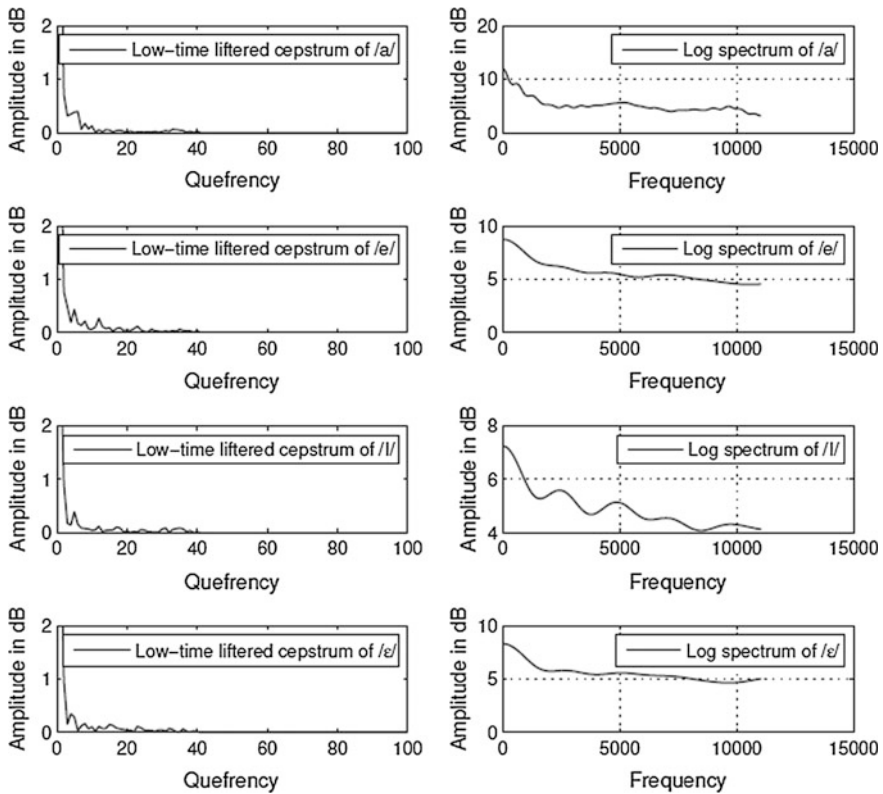


Fig. 3 Low-time liftered cepstrum and their corresponding log-spectrum of the vowels /a/, /e/, /I/, /ɛ/

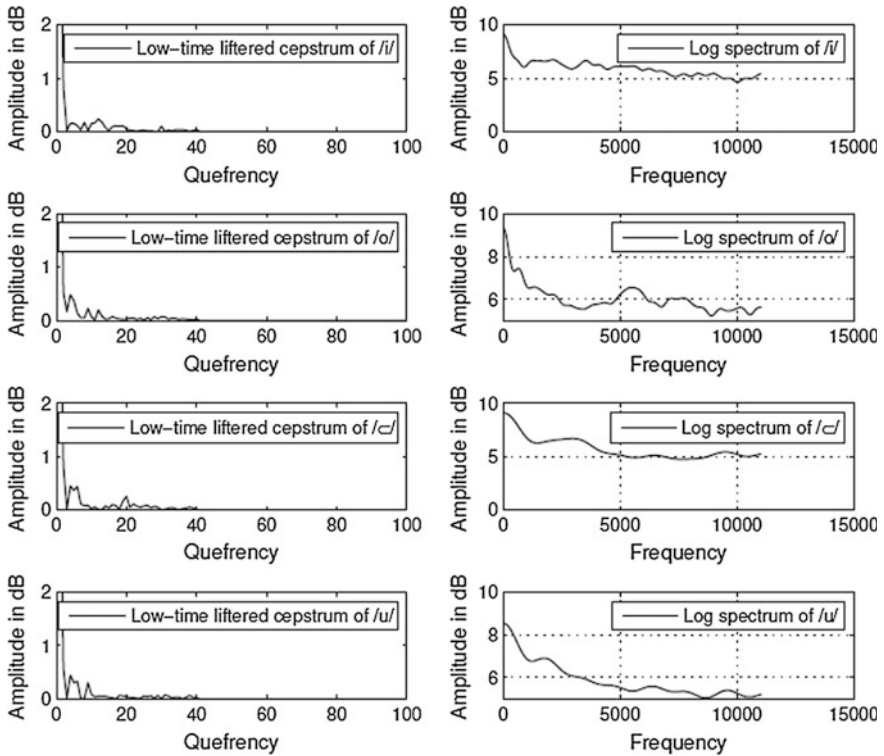


Fig. 4 Low-time filtered cepstrum and their corresponding log-spectrum of the vowels /i/, /o/, /ɔ/, and /u/

Table 1 Formant frequencies

Vowel		/a/	/e/	/ɪ/	/ɛ/	/ʌ/	/o/	/ɔ/	/u/
Female	F ₁ in Hz	580	2390	2440	550	1300	650	2950	1750
	F ₂ in Hz	1230	4400	4860	1230	2120	1320	6500	3300
	F ₃ in Hz	1980	6950	7000	1770	3540	2120	9500	4700
Female	F ₁ in Hz	580	2250	3000	630	830	1350	3200	3100
	F ₂ in Hz	1190	4330	6400	1330	1650	2700	6600	6400
	F ₃ in Hz	1730	7900	10,200	2350	2180	3800	11,000	10,900
Male	F ₁ in Hz	720	2400	4000	740	2200	800	1700	2200
	F ₂ in Hz	1160	6000	7200	1160	4600	1560	3400	4800
	F ₃ in Hz	1780	8600	11,000	1800	6400	2260	5500	6600
Male	F ₁ in Hz	600	2400	3400	1200	1400	1900	2000	1800
	F ₂ in Hz	1200	3700	5800	2900	2200	3800	3800	3600
	F ₃ in Hz	1650	5700	8800	4000	3300	7000	5000	5200

5 Conclusion

Homomorphic analysis of vowels in Khasi dialect was done using nonlinear filtering of the speech signal. This experiment and the information obtained can be useful for future studies particularly related to speech processing and to obtain synthetic vowels in Khasi dialect.

References

1. S.Bareh: Khasi proverbs: Analysing the ethnography of speaking folklore. Ph.D. thesis (2004).
2. Z.Ge, *at el.*: Accent classification with phonetic vowel representation. Pp. 529–533 (2015).
3. A.V. Oppenheim, R.Schafer: Homomorphic analysis of speech. *IEEE transactions on Audio and Electroacoustics* AU-16(2), Pp. 221–226 (1968).
4. G.Kopec, *at el.*: Speech analysis Homomorphic prediction. *IEEE transaction on Acoustics, speech and Signal processing*. 25(1), Pp. 40–49 (1977).
5. T.Quatieri: Minimum and mixed phase analysis-synthesis by addaptive homomor-phic deconvolution. *IEEE transaction on Acoustics, speech and Signal processing*. 27(4), Pp. 328–335 (1979).
6. S.D.Shaila: *Speech and Audio processing*, vol. 1. Wiley India Pvt Ltd (2012).

Discriminant Correlation-Based Information Fusion for Real-Time Biomedical Signal Clustering

Anil Hazarika, A. Sarmah, M. Boro, P. Kalita
and B. K. Dev Choudhury

Abstract Increasing availability of multiple responses and requirement of thorough analysis demand efficient modeling to derive a feasible support system which can make the analysis less-onerous, time-consuming, error-prone. Further, it is an indispensable provision to develop compact health monitoring devices, utility, and reliability of which rely on efficiency of program embedded that can manage the jobs without intervention of clinicians. In this article, a feature-level fusion framework is addressed using discriminant correlation analysis to effectively classify electroencephalogram (EEG) templates. Experiment on EEG data set shows that proposed method is efficacious and promising in terms of accuracy in comparison to the state-of-the-art methods.

Keywords Feature-level fusion · Discriminant correlation · And electroencephalogram (EEG)

A. Hazarika (✉) · M. Boro
Department of Electronics and Communication Engineering,
Tezpur University, Assam, India
e-mail: anilh@tezu.ernet.in

M. Boro
e-mail: minu@tezu.ernet.in

A. Sarmah · P. Kalita · B. K. Dev Choudhury
Pub Kamrup College, Guahati University, Guahati, India
e-mail: arupsarmah21@gmail.com

P. Kalita
e-mail: kalita.pankaj9@gmail.com

B. K. Dev Choudhury
e-mail: bdevchoudhury@yahoo.com

1 Introduction

Increasing availability of multiple measurements and studies tremendously grows data traffic in medical professions. Efficient modeling with well-adapted feature from available information helps promoting to derive a feasible support system. In deriving such system, information fusion, specifically feature-level fusion (FLF) plays significant role [1–4]. In real world, it is often generated multiple views of same or different types, e.g., EEG templates or of different types. Albeit different views reflect their typical behavior, learning from such views helps promoting to efficiently characterize the object than from single view and shows promising results [4, 6, 7]. Further input space may contain many redundant and irrelevant information which degrades the quality of model outputs. FLF helps eliciting the most energy contents from underlying views in terms of compact view through dimension reduction strategy.

Recently, canonical correlation analysis (CCA) [8] is popular and widespread used in pattern recognition applications [5–7]. It finds inherent representation of information based on the degree of proximity between two views of multidimensional vectors. Thus, it is a promising strategy for better insights and finer details of problems at hand. Nonetheless, CCA does not include the class structure which results close separation margin among various feature groups in the decision surface. Consequently, from time-to-time generalized versions of CCA, e.g., sparse CCA, multi-CCA [4], are reported. In this article, a generalized version, namely discriminant correlation analysis (DCA), is addressed to cluster EEG patterns. The major challenge is how the learning compact distribution of information can enhance the performance of models.

2 Literature Review

Quantitative methods (QMs) are more instructive and attract the eye of researchers. Electroencephalogram (EEG) is complex pattern that provides electrical potentials produced by the brain. Over the decades, a large number of QM with various feature extraction methods are reported. Even though considerable challenges still exist due to nonstationary and complex pattern of EEG. For example, Hassanpour et al. [9] develop time-frequency-based seizure detection technique. In [10], the author develops a versatile DWT-based technique. Hassan et al. [11] adopt a linear programming boosting. First, use ensemble empirical mode decomposition to decompose EEG and spectral moments are used for classification. Additionally, bootstrap aggregating in [12], tunable-Q factor wavelet transforms (TQWT) [13], adaptive boosting, and decision trees [14] are also reported. Orhan et al. [15] introduce a neural network using DWT coefficients for epilepsy diagnosis. Soomro et al. [16] adopt the combination of canonical correlation (CCA) analysis and neural network for epileptic seizures prediction. Kiymik et al. [17] use power spectral density-based approach to study alert, drowsy, and sleep.

Despite being success, they pose certain limitations due to aforementioned reasons and use of DWT that requires manual intervention [18]. Further, the choice of coefficients varies with problems, which may amount to result diversity. Thus, there dire need of viable supportive system that effectively explore class patterns.

3 Method

3.1 Data Sets

This study includes EEG data collected from benchmark online available database. EEG data includes 150 recordings (50 A, 50 B, and 50 C) [19]. Five sets of data are encoded from A to E, each of which contains 100 single-channel EEG recordings and each collected for 23.6 s duration. The data sets were recorded at the University Hospital Bonn, Germany, with inbuilt amplifier and 12 ADC at sampling rate of 173.61 Hz (i.e., $n = f_s t = 173.6 \times 23.6 = 4097$ samples). Further, band setting of filter was 060 Hz. During data collection, the healthy volunteers were relaxed in an awake state with eyes open (A) and eyes closed (B), respectively. Sets C, D, and E originated from our EEG archive of pre-surgical diagnosis. Sets C and D were measured during seizure-free interval. Set E only contained seizure activity (Figs. 1 and 2).

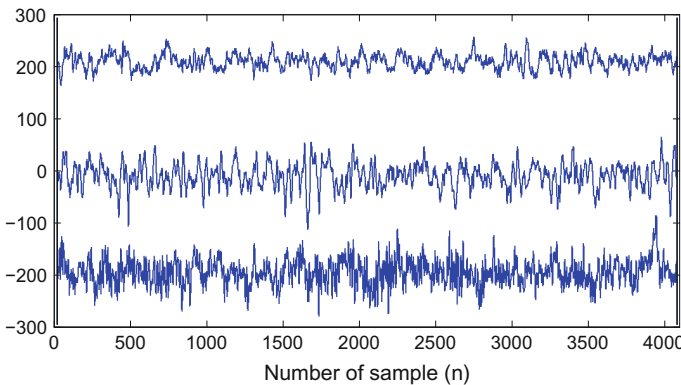


Fig. 1 Three typical EEG patterns A, B, and C (top to bottom)

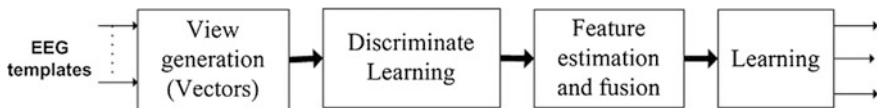


Fig. 2 Schematic diagram of proposed learning model

3.2 Discriminant Model

View or vectors are generated for all studied groups by registering q templates associated with the class in sequential order onto $X_c(n) = [X_1(p), \dots, X_q(p)]^T$, with $p = 2n$ samples and $c = 1, \dots, 3$, followed by view decomposition to create multiple views for each class group. Next, performing discrete wavelet transformation (DWT) on input patterns and considering only low frequency components [i.e., coarse approximations (A2)] same way, second set of views is generated for each group. Afterward, DCA is performed over two statistically independent space to evaluate class-specific feature vectors (FVs).

Let $X_1 \in R^{q \times p}$ and $X_2 \in R^{q \times p}$ be two views of same class and $\sum_{11} \in R^{q \times q}$ and $\sum_{22} \in R^{q \times q}$ denote the within-sets covariance matrices of X_1 and X_2 and $\sum_{12} \in R^{q \times q}$ denote the between-set covariance matrix (note that $\sum_{12} \sum_{21} = \sum^T$). CCA seeks linear combinations. $X_2 = W_z^* X_1, X_2 = W_y^*$, by solving the following equation:

$$\sum_{11}^{-1} \sum_{12} \sum_{22}^{-1} \sum_{21} \hat{A} = \alpha^2 \hat{W}_x, \tag{1}$$

where \hat{w}_x and $\hat{w}_y = 1/\alpha \sum_{11}^{-1/2} \sum_{21} \sum_{22}^{-1/2} W_x$ are two eigenvectors and α_2 is the diagonal matrix or square of canonical correlation with $d = \text{rank}(X_1, X_2) \leq \min(p, q)$ nonzero elements such that $\alpha_1 \geq \alpha_2, \dots$ which indicate nonzero correlation between same indice pairs of FV. It is worth mentioning that principle component analysis (PCA) is incorporated over inputs space to avoid dimensionality issue before CCA. As in [20], the estimated FVs are fused via parallel strategy as below:

$$Z2 = X_1^* + \dots + X_{22}^* = \begin{bmatrix} W_x \\ W_y \end{bmatrix}^T \begin{bmatrix} X_1 \\ X_2 \end{bmatrix} \tag{2}$$

where $Z2$ is canonical correlation discriminant features (CCDFs). Further, to avoid FB DWT with prototype Daubechies wavelet, i.e., db2 is used on views and subsequently, same way taking low frequency components, A_{2s} , $Z2$ with matrices \overline{W}_x and \overline{W}_y are estimated. For DCA, assume that data matrix composed of C separate classes and n_i ($n = \sum_i n_i$) columns corresponds to i th class and represents FV corresponding to j th sample in i th class. The sample and global mean are $x_1 = \frac{1}{n_1} \sum_{j=1}^{n_1} x_{1j}$ and $\mu = \sum_{i=0}^c n_i x_i$, respectively.

The between scatter matrix is defined as

$$S_B = \sum_c n_i (\nabla_i)(\nabla_i)^T = \Phi_{bx} \Phi_{bx}^T \tag{3}$$

where $\nabla_i = \bar{x}_i - \mu$, $\Phi_{bx(p \times C)} = [\sqrt{n_1}(\bar{x}_1 - \mu), \dots, \sqrt{n_C}(\bar{x}_C - \mu)]$. As FVs are larger than classes, i.e., $p \gg C$, it is relevant to solve $(\Phi_{bx}^T \Phi_{bx})_{C \times C}$ rather than Eq. (3),

by mapping the eigenvectors of $(\Phi_{bx}^T \Phi_{bx})$, which requires to solve $C \times C$ covariance matrix [20]. To ensure well-class separation, $(\Phi_{bx}^T \Phi_{bx})$ is diagonalized, i.e.,

$$P^T (\Phi_{bx}^T \Phi_{bx}) P = \bar{A} \tag{4}$$

where P is the orthogonal eigenvector and \bar{A} is the diagonal matrix having real nonnegative eigenvalues in descending order. Let $Q_{C \times r}$ matrix contain first r eigenvectors of P .

$$Q^T (\Phi_{bx}^T \Phi_{bx}) Q = A_{r \times r} \tag{5}$$

The most significant eigenvectors of S_B can be found by mapping: $Q \rightarrow \Phi_{bx} Q$. That is $(\Phi_{bx} Q)^T S_B (\Phi_{bx} Q) = A_{r \times r} \cdot W_{bx} = \Phi_{bx} Q A^{1/2}$ transformation utilizes S_B to make reduce X , from p to r , i.e.,

$$W_{bx}^T S_B W_{bx} = I, \hat{X}_{r \times n} = W_{bx(r \times n)}^T X_{p \times n}. \tag{6}$$

\hat{X} is the transformed pattern of X , where classes are well separated. Similarly, second data matrix, X_2 or Y , can be reduced. It is necessary to ensure that FV in one set have nonzero correlation only with their corresponding FV s in the other set for which the between-set covariance matrix of the mapped FV sets is diagonalized using singular value decomposition (SVD):

$$\sum_{12(r \times r)} = U \sum V^T \Rightarrow U^T \sum_{12} V = \sum. \tag{7}$$

The \sum is a diagonal matrix whose main diagonal elements are nonzero. Let $W_{cx} = U \sum^{-1/2}$ and $W_{cy} = V \sum^{-1/2}$ so that $W_{cx}^T \sum_{12}^- W_{cy} = I$ which unitizes the between-set covariance matrix. Now the newly transformed FV sets are as below, which are later fused via Eq. (2)

$$\bar{X} = W_{cx}^T \bar{X} = \underbrace{W_{cx}^T W_{bx}^T}_{\text{}} X = W_x X, \tag{8}$$

$$\bar{Y} = W_{cy}^T \bar{Y} = \underbrace{W_{cy}^T W_{by}^T}_{\text{}} Y = W_y Y. \tag{9}$$

4 Results and Discussion

Following the idea presented in Sect. 3.2, DWT views depicted in Fig. 3, where approximate and detail coefficients are compared for each group to enable the understanding of feature extraction mechanism. Next using equation in (9), two sets of estimated FV are fused [i.e., via Eq. (2)] and summed to a single pattern vectors (PVs). Finally, estimated PVs from all sub-views are concentrated to effectively explore the class information. Afterward, PVs are fed to LDA from where the best features corresponding to the higher eigenvalues of LDA matrix are estimated and applied to ensemble classifier. The promising performance of classifier is outlined in Table 1 in terms of sensitivity (S_n), specificity (S_p), and accuracy (A_c) [21–24]. Thus, effectiveness of discriminant FLF is apparent from the significant parameter values. It is to be mentioned that LDA helps finding the optimum decision surface

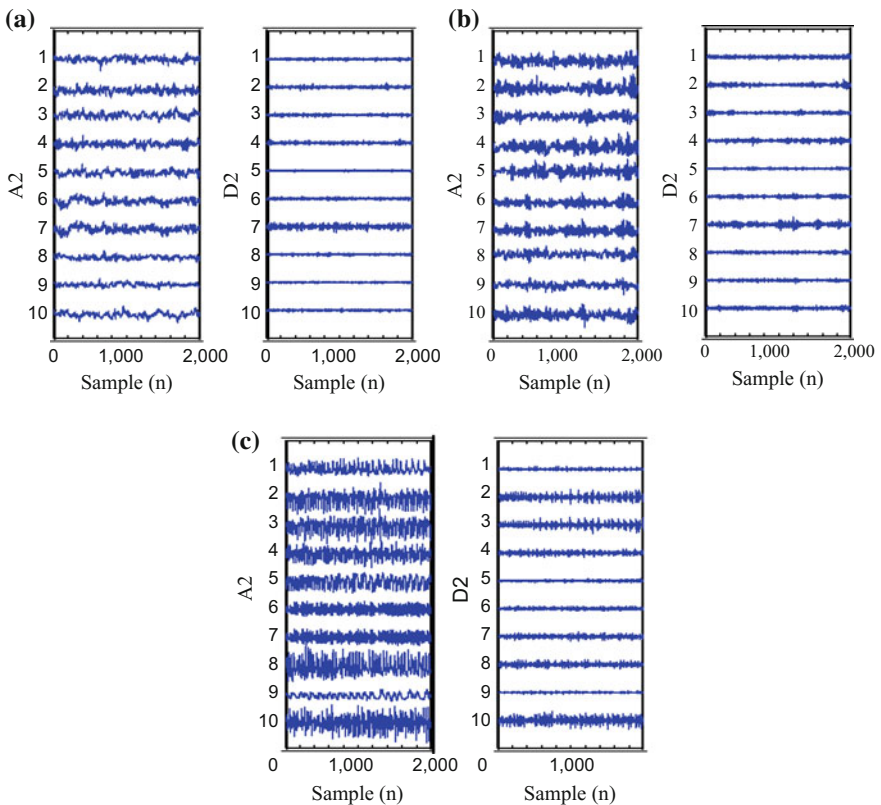


Fig. 3 DWT coefficient, approximation coefficients (A2s) (left), and details (D2s) of A (top), B (middle), and E (bottom) subject

Table 1 Mean performance (μ in %) with various combinations of classifiers [normal densities-based linear classifier (LDC), quadratic classifier (QDC)]

Models	SnE $_{\mu}$ (%)	SpA $_{\mu}$ (%)	SpE $_{\mu}$ (%)	Ac $_{\mu}$ (%)
PCA + DCA + LDA + LDC	99.43	98.09	98.57	98.70
PCA + DCA + LDA + QDC	98.00	98.00	100.0	99.33

by enhancing the separation margin among multigroup features exploiting the class information [25, 26]. That is if S_W and S_B are within-class and between-class variance matrices, it maximizes S_B and minimizes S_W , which are given as follows:

$$S_W = \sum_c N_c (\mu_c - \mu)(\mu_c - \mu)^T \quad (10)$$

$$S_B = \sum_{x \in C_c} (x - \mu_c)(x - \mu_c)^T \quad (11)$$

where μ_c , μ , and N_c stand for class mean, overall mean of the entire sample set, and number of samples in class C respectively. The learned low-dimensional pattern with significant t-test values ($\alpha \leq 0.5$) is applied to the classifier. The algorithm is implemented in MATLAB (*The Math Works, Inc., Natick, United States*) on an Intel (R) Xeon (R) machine (Precision T3500, processor 2.8 GHz, RAM 8 GB).

5 Comparison with the State of the Arts

To demonstrate the efficacy of adopted FLF model, a comparison is outlined in Table 2. EEG signals (A, B, and E) were categorized using DWT-based statistical model, k-nearest neighbor (KNN) [27], artificial neural network (ANN) [28], neuro-fuzzy system (ANFIS) [29], and quadratic approach [30]. Nonetheless, use of DWT requires human intervention and sub-band statistics reduces the curse of *dimensionality* for wide variability of templates; however, it may not be feasible for the analysis. Further, inherent nonstationary nature of templates and use of DWT features lead to result diversity. Apart from reported works, this study is based on subspace learning, through which promising results are observed in comparison to results reported in the literature. The integrity of the proposed technique is due to well-defined feature extraction and fusion strategy which in turn decreases the complexity. Further, unique features can be easily captured, which plays a crucial role in multitasking learning models. Additionally, the algorithm involves a number of steps and it takes mean execution time 78.72 s approximately over three runs. However, it could vary with machine.

Table 2 Comparison of OAs with the state-of-the-art-techniques

# Classifier	Feature type	Study groups/subject	Ac_{μ}
KNN [27]	DWT	5/10	97.00
ME, ANN [28]	DWT	2/10	94.50/93.20
ANFIS [29]	DWT	5/10	92.55
Quadratic [30]	DWT-FFT	3/10	98.70
Adopted	DCA-SF^a	3/10	99.33/98.70

Boldface indicates the correct classification

Note ^astatistical feature (SF)

6 Conclusion

The article addresses a FLF model for automatic classification of various EEG pattern (A, B, and E). It achieves promising performances by reducing the dimensionality of model that is apparent from significant parameters' values. Nonetheless, to explore further it is necessary to implement the algorithm with large scale data. We thus conclude, as the experimental aftermaths and thorough analysis unequivocally suggest that the adopted strategy is e cacious and its performance makes this work an important step for a fully automated system that aids physicians, large scale diagnosis research as well as portable device implementation for detect alarming trends in the health status of users. Future works include multiple models learning to meliorate algorithmic performance.

References

1. T. Xia, D. Tao, T. Mei, and Y. Zhand, "Multiview spectral embedding," *IEEE Trans. Syst. Man, Cybern. B, Cybern.*, vol. 40, no. 6, pp. 1436–1446, Dec. 2010.
2. Hazarika, M. Barthakur, L. Dutta and M. Bhuyan, "Two-fold feature extraction technique for Biomedical signals classificatio," *IEEE conf. on Inventive Computation Technologies., IEEE press, India* (2016).
3. Hazarika, M. Barthakur, L. Dutta and M. Bhuyan, "Fusion of projected feature for classification of EMG patterns," *IEEE conf. on Recent Advances and Innovations in Engineering., IEEE press, India* (2016).
4. X. Shen and Q. Sun, "A novel semi-supervised canonical correlation analysis and extensions for multi-view dimensionality reduction," *J. Vis. Commun. and Image Represent.*, vol. 25, no. 8, pp. 1894–1904, Nov. 2014.
5. Y. Sun, X. M. Zhang, J. Li, and X. M. Mao, "Feature fusion using locally linear embedding for classification," *IEEE Trans. Neural Netw.*, vol. 21, no. 1, pp. 163–168, Jan. 2010.
6. Q. S. Sun, S. G. Zeng, Y. Liu, P. A. Heng, and D. S. Xia, "A new method of feature fusion and its application in image recognition," *Pattern Recog.*, vol. 38, no. 12, pp. 2437–2448, Dec. 2005.
7. M. E. Sargin, Y. Ycel, and E. Engin, "Audiovisual synchronization and fusion using canonical correlation analysis," *IEEE Trans. Multimedia*, vol. 9, no. 7, pp. 1396–1403, Oct. 2007.

8. Hotelling, "Relations between two sets of variates," *Biometrika*, vol. 28, no. 3/4, pp. 321–377, Dec. 1936.
9. H. Hassanpour, M. Mesbah, B. Boashash, "Time-frequency feature extraction of newborn EEG seizure using SVD-based techniques," *EURASIP J. on Applied Signal Proces.*, vol. 2004, pp. 2544–2554, 2004.
10. Subasi, M. I. Gursoy, "EEG signal classification using PCA, ICA, LDA and support vector machines," *Expert Syst. Appl.*, vol. 37, no. 12, pp. 8659–8666, 2010.
11. R. Hassan, A. Subasi, "Automatic identification of epileptic seizures from EEG signals using linear programming boosting," *Comput. Methods Programs Biomed.*, vol. 136, pp. 65–77, 2016.
12. A. R. Hassan, M. A. Haque, "Computer-aided obstructive sleep apnea screening from single-lead electrocardiogram using statistical and spectral features and bootstrap aggregating," *Biocybern. Biomed.*, vol. 36, no. 1, pp. 256–266, 2016.
13. R. Hassan, "Computer-aided obstructive sleep apnea detection using normal inverse Gaussian parameters and adaptive boosting" *Biomed Signal Proces. Control*, no. 29, pp. 22–30, 2016.
14. R. Hassan, M. I. H. Bhuiyan, "Automatic sleep scoring using statistical features in the EMD domain and ensemble methods," *Biocybern. Biomed.*, no. 36, no. 1, pp. 248–255, 2016.
15. U. M. H. Orhan, M. Ozer, "EEG signals classification using the K-means clustering and a multilayer perceptron neural network model," *Expert Syst. Appl.*, vol. 38, no. 10, pp. 13475–13481, 2011.
16. M. H. Soomro, S. H. A. Musavi, B. Pandey, "Canonical Correlation Analysis and Neural Network (CCA-NN) Based Method to Detect Epileptic Seizures from EEG Signals," *Int. Journal of Bio-Science and Bio-Tech.*, vol. 8, no. 4, pp. 11–20, 2016.
17. M. K. Kiyimik, M. Akin, A. Subasi, "Automatic recognition of alertness level by using wavelet transform and artificial neural network," *J. of neuroscience methods*, vol. 139, no. 2, pp. 231–240, 2004.
18. G. Naik, S. Selvan, and H. Nguyen, "Single-channel EMG classification with ensemble-empirical-mode-decomposition-based ICA for diagnosing neuromuscular disorders," *IEEE Trans. Neural Syst. Rehabil. Eng.*, vol. 24, no. 7, pp. 734–743, July 2016.
19. R. G. Andrzejak, K. Lehnertz, C. Rieke, F. Mormann, P. David, C. E. Elger, "Indications of nonlinear deterministic and finite dimensional structures in time series of brain electrical activity: Dependence on recording region and brain state," *Phys. Rev. E*, vol. 64, pp. 061907, 2001.
20. M. Haghghat, M. Abdel-Mottaleb, W. Alhalabi, "Discriminant correlation analysis: Real-time feature level fusion for multimodal biometric recognition," *IEEE Trans. Inform. Forensics and Security*, vol. 11, no. 9, pp. 1984–1996, 2016.
21. M. Barthakur, A. Hazarika, and M. Bhuyan, "Rule based fuzzy approach for peripheral motor neuropathy (PMN) diagnosis based on NCS data," in *proc. IEEE int. Conf. Proc. Recent Advances and Innovations in Eng.*, 2014, pp. 1–9.
22. M. Barthakur, A. Hazarika, M. Bhuyan, "Classification of Peripheral Neuropathy by using ANN based Nerve Conduction Study (NCS) Protocol," *ACEEE Int. J. on Commun.* vol. 5, no. 1, pp. 31, 2014.
23. M. B. arthakur, A. Hazarika, M. Bhuyan, "A Novel Technique of Neuropathy Detection and Classification by using Artificial Neural Network (ANN)," *Proc ACEEE int Conf Adv Signal Process Commun*, pp. 706–713, India (2013).
24. M. Barthakur, A. Hazarika, M. Bhuyan, "A Computer-assisted Technique for Nerve Conduction Study in Early Detection of Peripheral Neuropathy using ANN," *Int. j. of Electronics and Commun. Eng. Tech.*, vol. 4, no. 5, pp. 47–65, 2013.
25. Dutta, L., Hazarika, A., Bhuyan, M.: Comparison of Direct Interfacing and ADC Based System for Gas Identification using E-Nose. *Int. IEEE Conference on Inventive Computation Technologies, IEEE press*, India (2016).
26. L. Dutta, A. Hazarika, M. Bhuyan, "Microcontroller Based E-Nose for Gas Classification without Using ADC," *Sensors and Transd.*, vol. 202, no. 7, pp. 38–45, 2016.

27. U. Orhan, M. Hekim, M. Ozer, "EEG signals classification using the K-means clustering and a multilayer perceptron neural network model," *Expert Syst Appl*, vol. 38, pp. 13475, 2011.
28. Subasi, "EEG signal classification using wavelet feature extraction and a mixture of expert model," *Expert Syst Appl*, vol. 32, pp. 1084, 2007.
29. M. Hekim, "The classification of EEG signals using discretization-based entropy and the adaptive neuro-fuzzy inference system," *Turk J. Elec. Eng. Comp. Sci.*, vol. 24, pp. 285–297, 2016.
30. Gajic D. et al., "Detection of epileptiform activity in EEG signals based on time- frequency and non-linear analysis," *Frontiers in Comput. Neurosci.*, vol. 9, pp. 38, 2015.

Development of OFDM UWB-Based RADCOMM System for Effective Utilization in Intelligent Transportation System

M. Chakraborty, B. Maji, D. Kandar and S. Shome

Abstract With the advent of Internet of Things (IoT) and the advanced intelligent transportation systems (ITS), the concept of integration of data with technology and simultaneous sensing and communication is essential. These application areas would be driven by road safety and vehicular infotainment. The challenges in this regard are simultaneous vehicle-to-vehicle (V2V) sensing and communication. Here we have proposed the development of an OFDM UWB system whereby the UWB radar is sensing the object and the communication information is embedded in the transmitted UWB pulses. The radar receiver detects the target as well as estimates its range and velocity within the coherent processing interval. A realistic multipath fading channel is used with two moving targets.

Keywords ITS · UWB · RADCOMM · OFDM · V2V

M. Chakraborty (✉)
School of Engineering and Technology, ADAMAS University,
Kolkata 700126, India
e-mail: mithunchakraborty03@gmail.com

B. Maji
Department of ECE, NIT, Durgapur 713209, India
e-mail: bansibadan.maji@ece.nitdgp.ac.in

D. Kandar
Department of Information Technology, NEHU,
Shillong 793022, Meghalaya, India
e-mail: kdebdatta@gmail.com

S. Shome
Department of ECE, SIEM, Siliguri 734009, India
e-mail: subho.ddj@gmail.com

1 Introduction

Always connected vehicle [1] is a key component of advanced intelligent transportation system and Internet of Things. To manage traffic flow and improve traffic safety [2] by reducing accidents as well as human fatalities, researchers and automakers are investing more and more. Gartner predicted [3] that in the next 5 years there would be a large increase in connected cars running on road and by 2020 almost two hundred million connected vehicles would be enabled with new in-vehicle services and automated driving capabilities. Vehicles powered with intelligent sensing and communication with enhanced driver assistance system [4] in one side and intelligent traffic control and fleet management [5] on the other side can address these issues. In order to integrate the radar and communication (RADCOMM) on the same platform an integrated waveform is designed to fulfill the radar and communication functionality [6, 7]. These integrated systems have the advantage of reduced system volume, and reduced interference between the transmitter and receiver compared with the previous separated radar and communication system [8]. Researchers have also proposed the integration of radar and communication based on the orthogonal frequency division multiplexing (OFDM) technology in [9, 10]. These systems are limited by the high implementation cost due to the complex signal processing and high peak-to-average power ratio of the OFDM signals. Another approach is proposed theoretically in [11] but lacking in substantiation result. Article [12] proposes the integration by direct sequence UWB, which is limited by the imperfect autocorrelation property of the sequence used.

The UWB [13, 14] has very high frequency, wide bandwidth, very low power requirement as well as protected from interference from nearby devices. We have proposed OFDM UWB-based integrated RADCOMM system for effective utilization in intelligent transportation systems. The stress was how to hide the communication information with higher data rate on the radar pulses. While the communication information is hidden in the radar waveform, it does not anyway influence or interfere with the radar signal. The rest of the paper is organized as Sect. 2 describes the RADCOMM signals and system modeling, Sect. 3 presents results and analysis, and Sect. 4 provides the conclusion followed by references.

2 System Modeling

This section describes the general model of the integrated radar communication (RADCOMM) system, which focuses multifunctionality of RF with consideration of target range and Doppler effects.

A. Integrated RADCOMM signal model

The envelope of the OFDM baseband signal with N contiguous subcarriers with M number of symbols and symbol duration T at z^{th} time instant is

$$S_z(t) = \sum_{j=0}^{M-1} \sum_{k=0}^{N-1} X_{z,k} e^{j2\pi k T} \quad (1)$$

where $X_{z,k}$ is the symbol of the k^{th} subcarrier, $j = \sqrt{-1}$.

The frequency shifting among them is Δf . For the UWB radar system, Gaussian doublet (two Gaussian pulses) pulses are generated. A time domain Gaussian doublet pulse is

$$P_{\text{GD}}(t) = \frac{1}{\sqrt{2\pi\sigma}} \left[e^{(-\frac{1}{2})\left(\frac{(t-\mu)}{\sigma}\right)^2} - e^{(-\frac{1}{2})\left(\frac{(t-\mu-Tw)}{\sigma}\right)^2} \right] \quad (2)$$

where Tw is the time duration between two consecutive maxima of the pulses. The possible values of effective time length is $Tp = 14\sigma$ at, $Tw = 7\sigma$.

The pulse repetition frequency (PRF) is kept as

$$\text{PRF} = \frac{1}{(\text{pulse width})PW} = \frac{C}{2R_{\text{unambigu}}} \quad (3)$$

$$\text{Range resolution, } R_{\text{RES}} = c \frac{PW}{2} \quad (4)$$

The Doppler frequency shift f_D is-

$$f_D = -\frac{1}{2\pi} \frac{d}{dt} \left(\frac{4\pi r}{\lambda} \right) = -\frac{2}{\lambda} \frac{dr}{dt} = -\frac{2vf_0}{c} \quad (5)$$

'-' sign represents phase lag for increase in distance r , and λ is the operating wavelength.

The resulting time domain integrated RADCOMM signal is the modulation of OFDM signal on BPSK-modulated doublet represented as

$$y(t) = \sum_{j=0}^{M-1} \sum_{k=0}^{N-1} X_{z,k} e^{j2\pi k T} \left\{ P_{\text{GD}}(t) \exp^{(j(2\pi f_0 + \psi_0)t)} \right\} \quad (6)$$

B. RADCOMM system model

Binary data is transformed into OFDM signal, which will be modulated on the UWB radar signal. In the receiver, the multipath signal is correlated with the UWB radar receiver portion with a reference signal taken from doublet pulse generator in the transmitter, and target parameter is estimated. The receiver radio portion contains band-pass filters for detecting the carrier frequency followed by OFDM demodulator as shown in Fig. 1.

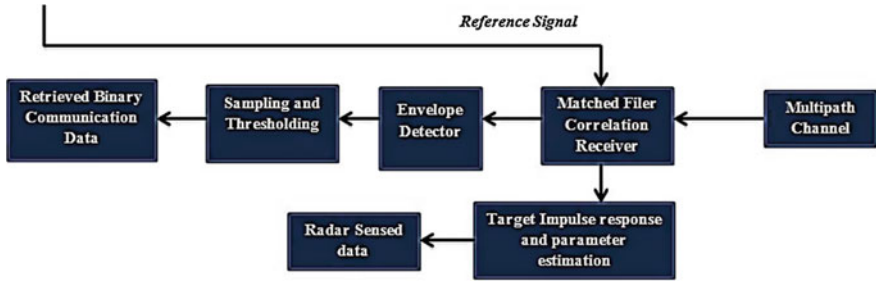


Fig. 1 Integrated RADCOMM receiver block diagram

Table 1 Multipath channel parameters

Channel model	Variable delay (τ)/phase shift	Variable gain (G)
Direct path (LOS)-CM-1	No delay	1.0000
Indirect path 1 (NLOS)-CM-2	6 nanosec	0.1743
Indirect path 2 (NLOS)-CM-3	12 nanosec	0.1399
Indirect path 3 (NLOS)-CM-4	24 nanosec	0.3972

Multipath channel considerations

The integrated RADCOMM signal is based on the ultra-wide band signal being modulated by the communication data. The transmitted signal propagates through four multipaths with variable gain and variable path delays and reflected from two target vehicles with velocities and distance apart from radar Table 1.

The signal received $r(t)$ can be expressed as:

$$r(t) = \gamma \left\{ \sum_{j=0}^{M-1} \sum_{k=0}^{N-1} X_{z,k} e^{j2\pi k_i (T-t_D)} \left\{ P_{GD}(t - t_D) \exp^{j(2\pi f_0 + \psi_0)(t-t_D)} \right\} \right\} \quad (7)$$

where γ is the target cross section.

The delayed received signal is fed simultaneously to both the radar receiver and the communication receiver portion. The receiver radar portion correlates the received pulse with a template signal generated locally in the receiver to take the decision about the target presence and estimate the target parameters. The communication portion passes the incoming signal through a matched filter matched to the signal $r(t)$. The matched filter is defined for the signaling interval of the integrated RADCOMM waveform. As the envelope of the matched filter output is unaffected by the received signal phase orientation, the output is passed through an envelope detector and then sampled at the signaling interval to make decisions about ‘1’ or ‘0’ transmission.

For the communication portion, the output of the matched filter may be expressed as

$$Y(t) = \int_0^{MT} r(t - t_D) \cos[2\pi f_o(T - t + \tau)] d\tau \tag{8}$$

$$= \left\{ \begin{aligned} &\cos(2\pi f_o(T - \tau)) \int_0^{MT} r(t - t_D) \cos(2\pi f_o \tau) d\tau \\ &\sin(2\pi f_o(T - \tau)) \int_0^{MT} r(t - t_D) \sin(2\pi f_o \tau) d\tau \end{aligned} \right\} \tag{9}$$

And the output of the envelope detector is –

$$\sqrt{\left[\int_0^{MT} r(t - t_D) \cos(2\pi f_o \tau) \right]^2 + \left[\int_0^{MT} r(t - t_D) \sin(2\pi f_o \tau) \right]^2} \tag{10}$$

This envelope is sampled by the sampler, and depending on a threshold, it takes the decision and the transmitted data is retrieved.

The receiver radar correlated signal may be represented as

$$X_{CORR}(t) = \int_0^{MT} r(t - t_D) y(t - \tau) d\tau \tag{11}$$

‘*T*’ is the pulse duration, and ‘*M*’ is the number of pulses per frame.

From Eq. (11) for peak value or maximum value of the correlation target is detected, and its range and Doppler are estimated.

3 Results and Analysis

In the configuration of communication system, the number of data bits per channel to be transmitted is 128. No of subcarrier channel used is 8; OFDM block size = 16, and length of cyclic prefix = 1. Fig. 2 shows the OFDM data to be transmitted. For the UWB radar system, the pulses used are Gaussian doublet, no of pulses = 8, pulse width = 0.2 nanosecond, sampling frequency = 100 GHz, and bit rate = 500 Mbps. BPSK-modulated UWB doublet is shown in Fig. 3.

The communication signal modulated on the radar pulses is shown in Fig. 4. As we increase the number of pulses, more nulls are produced in the transmitted spectrum, which is useful in avoiding interferences from the other systems as shown in Fig. 5.

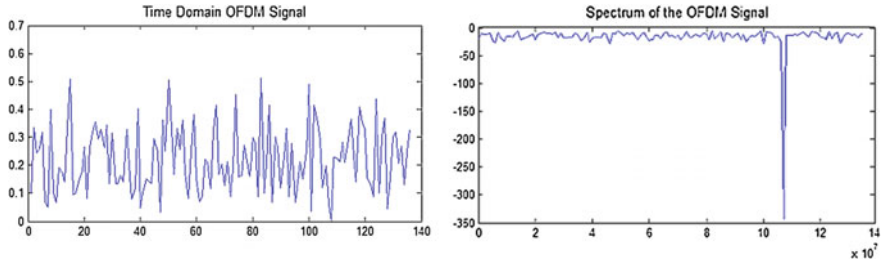


Fig. 2 OFDM signal in time and frequency domains

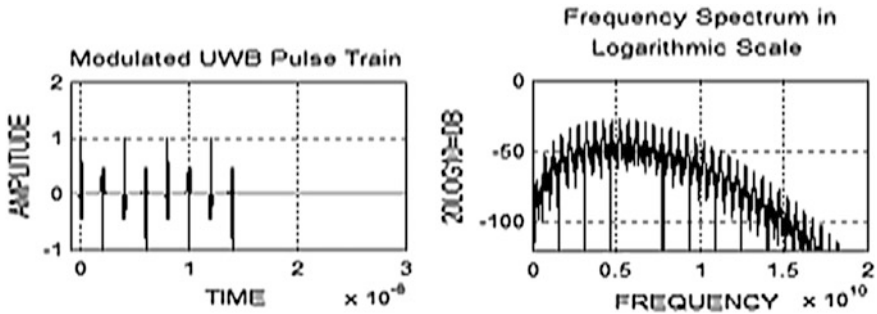
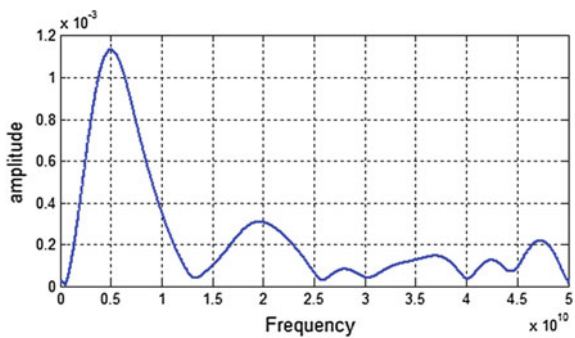


Fig. 3 BPSK-modulated UWB radar signal in time and frequency domains

Fig. 4 Integrated RADCOMM signal in frequency domain



We have used a realistic multipath (four paths) channel with variable gain, phase shift and delay. In the integrated receiver, the signal is passed through a bank of matched filter. The correlated low-pass-filtered output is shown in Fig. 6. This correlated output detects the target after passing through peak detector.

The probability of detection curves is plotted in Fig. 7 for four different signal-to-noise ratio (SNR) values. From the plot, we can observe that as we

Fig. 5 Integrated signal output after multipath channel

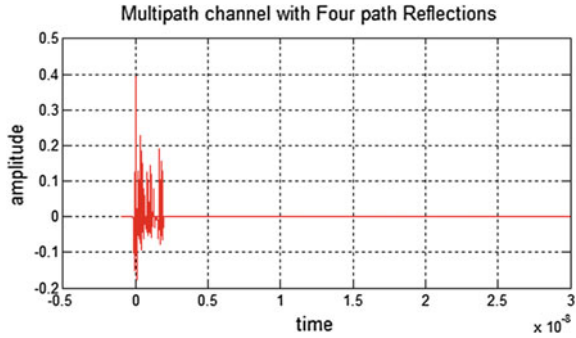


Fig. 6 Spectrum of correlated filtered (low pass) output

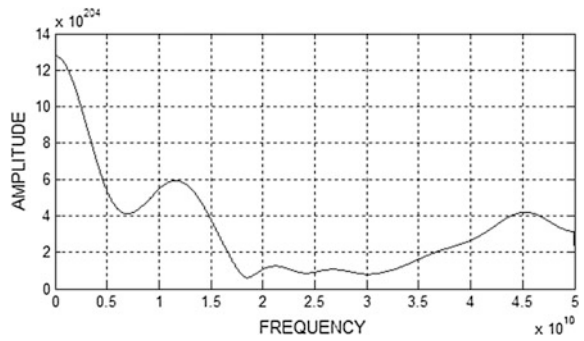


Fig. 7 Radar receiver probability of detection curve for different false alarm rate

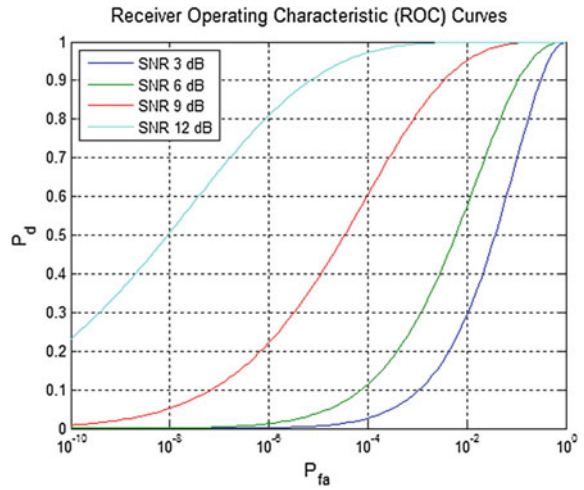


Fig. 8 Probability of detection curves for different SNR values

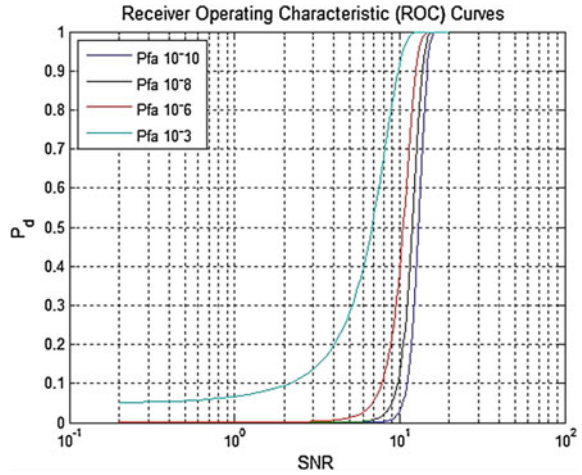
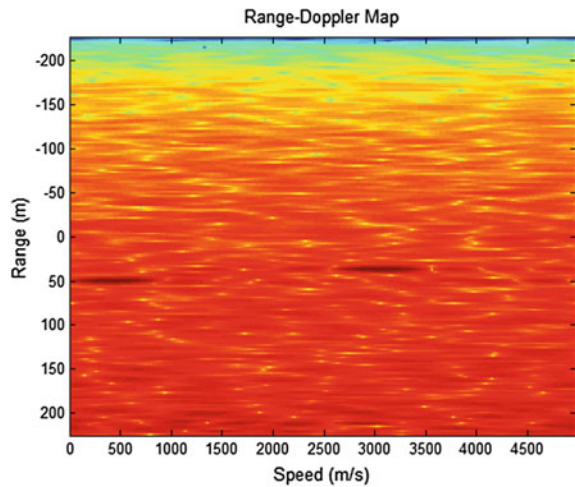
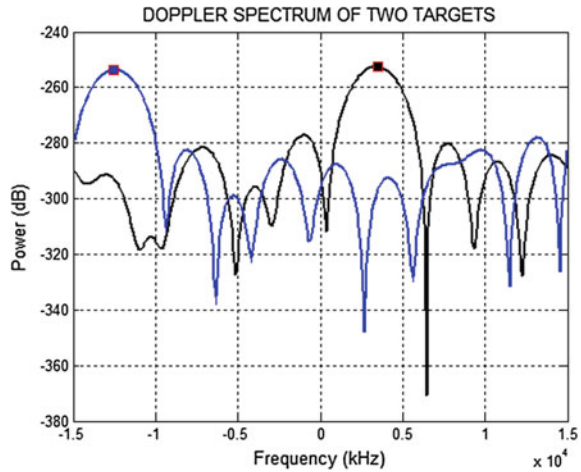


Fig. 9 Range–Doppler map of two targets



increase the SNR of the system, probability of false alarm rate decreases and the detection probability increases, and Fig. 8 states that for the same probability of detection, increased SNR decreases the probability of false alarm. Figure 9 shows the range–Doppler measurements of two vehicles detected at 30.41 m and 50.38 m apart with different relative velocities. The Doppler shifts due to the target car velocity for the received echo are plotted in Fig. 10.

Fig. 10 Doppler spectrum of two targets



4 Conclusion

In this paper, we integrated radar and communication systems based on OFDM UWB where the waveforms step by step have been analyzed. Because of the UWB pulse transmission, the system is immune to interference and noise. On the arrival of reflected echo, correlation method extracts target vehicle and after Doppler processing, high-range resolution image is created. The communication data is separated by filter and detected. This may give one new dimension to the development of next generation e-vehicle for advanced ITS.

References

1. Ning Lu, Nan Cheng, Ning Zhang, Xuemin (Sherman) Shen, Jon W. Mark "Connected Vehicles: Solutions and Challenges", IEEE Internet of Things Journal, Volume: 1, Issue: 4, (Aug. 2014).
2. P Papadimitratos, A de La Fortelle, K Evenssen, R Brignolo and S Cosenza "Vehicular Communication Systems: Enabling Technologies, Applications, and Future Outlook on Intelligent Transportation", IEEE Communications Magazine •, p-84-95, (November 2009).
3. Gartner, Musings From Def Con 23: Internet of Things Risks Are Bad and Likely to Get Worse, (25 September 2015).
4. C. Olaverri-Monreal, P. Gomes, R. Fernandes, F. Vieira, and M. Ferreira, "The see-through system: A VANET-enabled assistant for overtaking maneuvers," in Proc. IEEE Intelligent Vehicles Symposium (IV), San Diego, CA, USA, (June 2010).
5. J. Anda, J. LeBrun, D. Ghosal, C.-N. Chuah, and M. Zhang, "VGrid: vehicular adhoc networking and computing grid for intelligent traffic control," in Proc. IEEE VTC Spring, Stockholm, Sweden, (June 2005).
6. M Braun, C Sturm and F K. Jondra "On the Frame Design for Joint OFDM Radar and Communications", (2010).

7. Y Sit, L Reichardt, C Sturm, T Zwick "Extension of the OFDM Joint Radar-Communication System for a Multipath, Multiuser Scenario", 978-1-4244-8900-8/11/\$26.00 ©(2011) IEEE.
8. I. Yattoun, T. Labia, A. Peden, et al, "A millimetre communication system for IVC," Proc. Seventh Int. Conf. Intelligent Transportation Systems Telecommunications, pp. 1-6, (2007).
9. Y. L. Sit, C. Sturm, L. Reichardt, T. Zwick and W. Wiesbeck, "The OFDM Joint Radar Communication System: An Overview," The Third International Conference on Advances in Satellite and Space Communications, pp. 69-74, (2011).
10. C. Sturm, T. Zwick and W. Wiesbeck, "An OFDM System Concept for Joint Radar and Communications Operations," IEEE 69th Vehicular Technology Conference, pp. 1-5, (2009).
11. Hüseyin Arslan and Mustafa E. ,Sahin,"Cognitive UWB-OFDM: Pushing Ultrawideband Beyond Its Limit via Opportunistic Spectrum Usage", JOURNAL OF COMMUNICATIONS AND NETWORKS, VOL. 8, NO. 2, (JUNE 2006).
12. Xu S. J., Chen Y. and Zhang P, "INTEGRATED RADAR AND COMMUNICATION BASED ON DS-UWB", Ultrawideband and Ultrashort Impulse Signals, (18-22 September, 2006), Sevastopol, Ukraine.
13. S Mohammad, S SADOUGH," A Tutorial on Ultra Wideband Modulation and Detection Schemes", (April 2009).
14. Malek G M Hussain," Ultra Wide band Impulse Radar-An overview and Principles", IEEE AES system magazine, (1998).

Fixed-Point Design of 1024-Point CI-OFDM for DVB-Satellite to Handheld

Rakesh Palisetty and Kailash Chandra Ray

Abstract The Digital Video Broadcasting Satellite to handheld (DVB-SH-A) employs Orthogonal Frequency Division Multiplexing (OFDM) that suffers from high Peak to Average Power Ratio (PAPR). Carrier Interferometry (CI) spreading codes is an efficient method that reduces PAPR with less computational complexity and without degrading BER performance. Therefore, CI-OFDM is proposed in place of OFDM for the existing DVB-SH-A. The fixed-point design of 1024-point CI-OFDM baseband transceiver using QPSK scheme is designed using Xilinx System Generator (XSG) and Verilog HDL with signed representation. Oversampling method is employed to approximate the baseband PAPR. Also, the behavior of CI-OFDM is validated on fixed-point AWGN channel. The fixed-point performance parameters like BER and PAPR are compared with MATLAB simulations.

Keywords CI-OFDM · DVB-SH-A · OFDM · Oversampling
PAPR

1 Introduction

The existing mobile television broadcasting through cellular network is unable to deliver the same broadcasting content to multiple users at the same time. Also, it is operable only within the network of cellular region. To overcome the existing short comes, Digital Video Broadcasting (DVB) organization proposed an open standard for broadcasting multimedia streams for mobile devices, PDAs, and other portable gadgets with Digital Video Broadcasting through satellite to handheld devices (DVB-SH) [1] derived from DVB-Terrestrial (DVB-T) [2] and DVB-Satellite (DVB-S2) [3]. DVB-SH is a hybrid satellite/terrestrial transmission system pro-

R. Palisetty (✉) · K. C. Ray
Indian Institute Technology-Patna, Patna 801106, India
e-mail: rakeshp@iitp.ac.in; rakeshp2608@gmail.com

K. C. Ray
e-mail: kcr@iitp.ac.in

viding services directly via satellite or through satellite cum terrestrial network. The DVB-SH system has two transmission modes, i.e., DVB-SH-A and DVB-SH-B. Orthogonal Frequency Division Multiplexing (OFDM) [4] employed in DVB-SH-A system is used in both satellite and terrestrial paths, and this transmission mode is derived from DVB-T. DVB-SH-B, derived from DVB-S2, uses Time Division Multiplexing (TDM) and is used only in the direct path, i.e., satellite. DVB-SH-A outperforms DVB-SH-B transmission mode in terms of spectral efficiency due to single frequency network [1]. Since DVB-SH-A system employs OFDM, it suffers from high Peak to Average Power Ratio (PAPR) [5]. The High Power Amplifier (HPA) used in the satellite system penalizes the nonlinear characteristics due to high PAPR. Therefore, the DVB-SH-A system must operate by backing off the HPA to quasi-linear region [6] that reduces the maximum satellite transmission power in order to avoid nonlinear distortions. Also, high PAPR demands Analog to Digital Converters (ADC) with large dynamic ranges to vary with high peaks of OFDM.

Methods such as clipping and filtering [7], nonlinear companding [8], coding schemes [9], partial transmission scheme and selective mapping [10, 11], peak reduction carriers [12], tone reservation and tone injection [13] suffered from in-band distortion that degrades Bit Error Rate (BER) and out-band distortion that causes spectral re-growth, reduced transmission rate, and higher complexity. The authors in [14, 15] proposed Carrier Interferometry (CI) spreading codes that are applied to OFDM (CI-OFDM), thereby reducing the PAPR with BER performance on AWGN channel as that of OFDM, lessening computational complexity and countering the deep fades in high attenuation conditions. CI-OFDM-based multi-carrier transmission technique in nonlinear satellite channel for satellite systems was recommended in [16]. CI-OFDM is limited to theoretical studies and MATLAB simulations.

The rest of the paper is organized as follows. Section 2 describes the DVB-SH-A transmission system with CI-OFDM. Section 3 describes fixed-point design of 1024-point CI-OFDM baseband transceiver. Section 4 describes the results and its analysis, and Sect. 5 concludes the paper.

2 DVB-SH-A Transmission System with CI-OFDM

The block diagram of DVB-SH-A is shown in Fig. 1. The MPEG transport stream contains a fixed data field length of eight user packets. Each user packet length is defined by 188 bytes out of which the first byte corresponds to synchronous byte. Sixteen-bit Cyclic Redundancy Check (CRC) encoding is performed on these user packets in mode adaptation. After CRC encoding, the data field length is equal to 12,096 bits (eight user packets with each of them bearing 189 bytes, i.e., $189 \times 8 \times 8$ bits) [1]. Mode adaptation also contains Encapsulation Signalling (ESignalling) that consists 114 bits of frame header information for MPEG data packet. In stream adaptation, zero padding is performed to make the frame length

equal to 12,282 bits (this frame length is chosen to match the input of turbo encoding) followed with scrambling [17]. Turbo encoder is used as Forward Error Correction (FEC) with code lengths of 1/5, 2/9, 1/4, 2/7, and so on as mentioned in [1] followed with a defined puncturing pattern. The channel interleaver improves the error efficiency of FEC. The input to the symbol interleaver is demultiplexed into substreams depending upon the modulation schemes. The symbol interleaver therefore maps these demultiplexed substreams onto the subcarriers of OFDM. The modulation schemes defined in DVB-SH-A transmission mode are QPSK and 16-QAM.

OFDM employs 1 k (1024), 2 k (2048), 4 k (4096), and 8 k (8192) modes. In order to avoid Intersymbol Interference (ISI), cyclic prefix is added to the OFDM-based transmission system. Cyclic prefix lengths of 1/4, 1/8, 1/16, and 1/32 are defined by the DVB-SH standard. Finally, the signal is passed through DAC and carrier modulated to the Radio Frequency (RF).

As discussed, OFDM has drawback of high PAPR and therefore the existing DVB-SH-A system can be replaced by CI-OFDM (the dotted block in Fig. 1). In CI-OFDM, the information data streams are passed on all the subcarriers, thereby achieving frequency diversity. The baseband-transmitted CI-OFDM symbol is expressed as

$$c(i) = \frac{1}{N} \sum_{q=0}^{N-1} \sum_{p=0}^{N-1} a_q e^{j\frac{2\pi}{N}qp} e^{j\frac{2\pi}{N}ip} \tag{1}$$

where p is the subcarrier index, q is the data index, and $\frac{2\pi}{N}qp$ is the CI spreading code for the information data a_q . Therefore, CI-OFDM is implemented with two IDFTs, i.e., one for generating CI codes and other for OFDM system. The computational complexity can be further reduced by using IFFT. The discrete time baseband CI-OFDM PAPR is approximately estimated with oversampling method. It is mentioned in [18] that oversampling with a factor M equal to 4 gives the same PAPR as that of continuous time baseband CI-OFDM. Hence, with oversampling,

$$c'(i) = N\text{-point(IFFT)}.NM\text{-point(IFFT)}$$

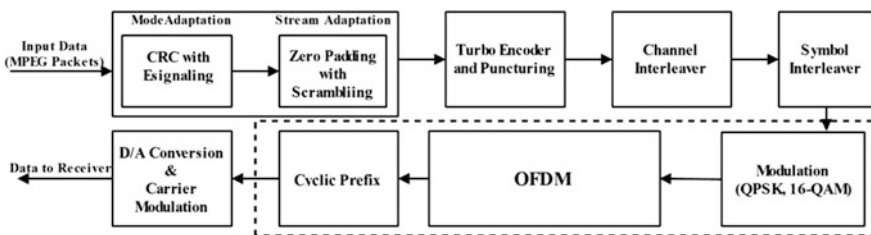


Fig. 1 DVB-SH-A transmission system

and the PAPR of the system with oversampling is

$$\text{PAPR} = \frac{\max_{m=0,1,\dots,NM-1} |c'(i)|^2}{E\{|c'(i)|^2\}} < N \tag{2}$$

3 Fixed-Point Design of 1024-Point CI-OFDM Baseband Transceiver

The block diagram of CI-OFDM baseband transceiver with QPSK modulation scheme and oversampling over AWGN channel is shown in Fig. 2. The design is implemented using XSG and Verilog HDL with signed representation. The bit width precision is chosen as fixed 25 bits with 24 bits binary point. The BER plot is degraded for a bit width precision of 16 bits and is discussed in results section. The entire design is modeled in such a way that data is processed continuously all the time by employing pipelined methodology.

The QPSK modulation scheme encodes a data bit 0 by -0.707 and data bit 1 by 0.707 [19]. The FFT in the design is Cooley–Tukey decimation in frequency with pipelined architecture. Oversampling method with a factor M equal to 4 inserts zeros in between the data subcarriers, and the size of second IFFT is therefore 4096-point as shown in Fig. 3. The N -point IFFT generates the spreading codes for the incoming data from QPSK modulation. Further, the output data from N -point IFFT is passed to oversampling block for approximating discrete time baseband PAPR. Oversampling block maps these information symbols on the NM -point IFFT with defined index location. The indexed data output from oversampling block, i.e., 0–511, is mapped onto NM -point on locations from 0 to 511, and data from 512 to 1023 is mapped onto the locations of 3584–4095. Remaining locations are padded with zeros, i.e., 512–3583, on NM -point IFFT. The oversampling method is used only for approximating the PAPR in high-level simulation, and in real-time applications it is not required.

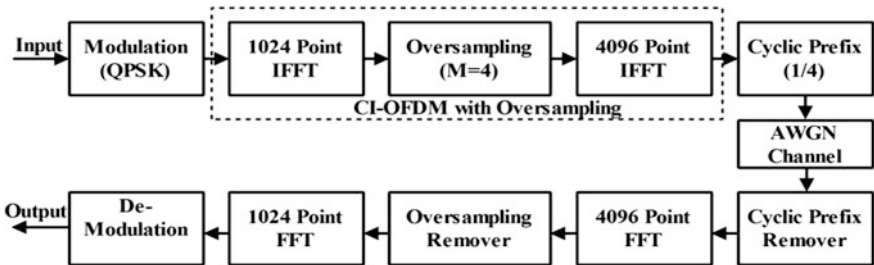


Fig. 2 Block diagram of proposed CI-OFDM baseband transceiver

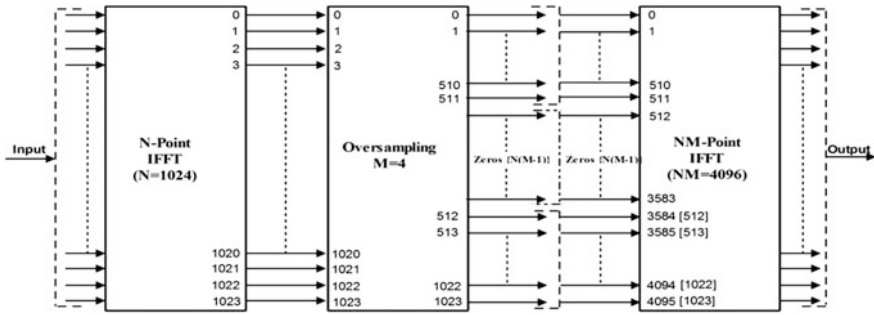


Fig. 3 Block diagram of proposed CI-OFDM with oversampling

The architecture of cyclic prefix with length $\frac{1}{4}$ th of the total symbol period is shown in Fig. 4. The data from output port in Fig. 3 is passed to the upper registers P0–P4095, with each data processed for a period of 5 clock cycles. Once the data is fully loaded into the upper registers, the load pin is enabled low and data from upper registers is mapped on to the lower registers, i.e., from Q0 to Q5119 with each data processed for a period of 4 clock cycles. It can be seen from Fig. 4 that port P0–P1023 is connected to port Q4095–Q5119 as cyclic prefix.

The fixed-point AWGN channel with mean equal to zero and standard deviation equal to one is shown in Fig. 5. Total normalized power value is obtained by multiplying normalized power of N-point IFFT, normalized power of NM-point IFFT, and the energy wasted due to the cyclic prefix. The Signal-to-Noise Ratio (SNR) from bit energy to noise power is calculated as shown in Eq. 3.

$$\left(\frac{E_s}{N_o}\right)_{dB} = \left(\frac{1024}{5120}\right)_{dB} + \left(\frac{1024}{4096}\right)_{dB} + (2)_{dB} + \left(\frac{E_b}{N_o}\right)_{dB} \quad (3)$$

Receiver modules are inverse mechanism of the transmitter modules. To determine the number of resources the design requires, it is synthesized on Xilinx Virtex xc5v1x110t-1 FPGA device. The synthesized results showed that the design requires 1,261,219 slice registers out of available 69,120 and 751,515 slice look up

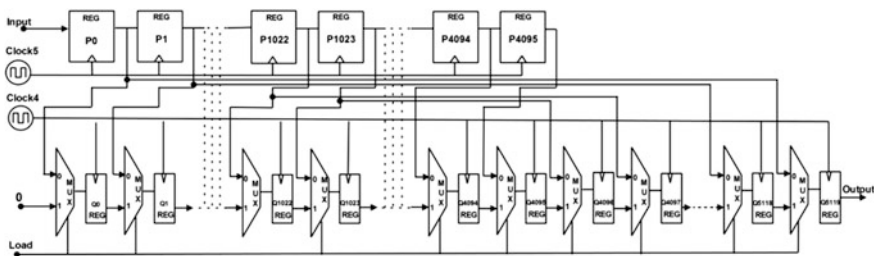


Fig. 4 Proposed cyclic prefix module

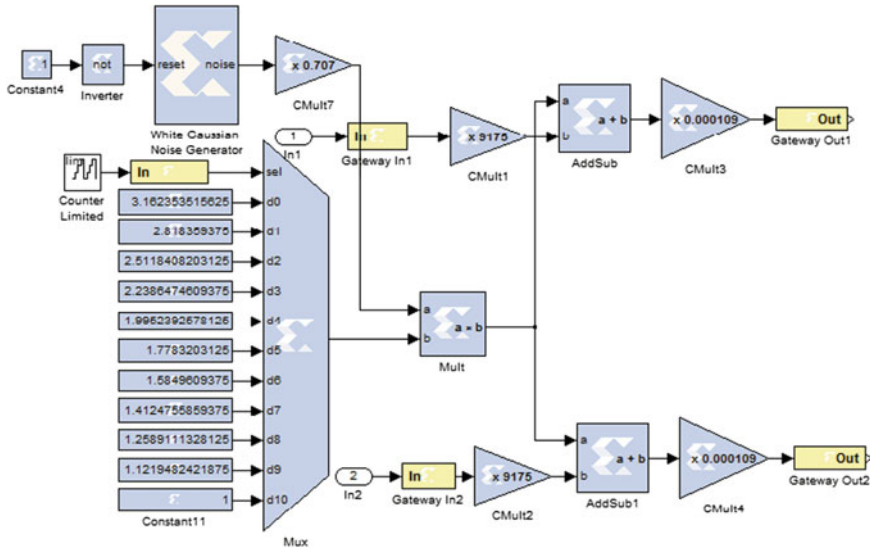


Fig. 5 Fixed-point AWGN channel using XSG

tables out of available 69,120. Also, the design required 112 DSP48Es out of available 64. Henceforth, the resources available on the commercial FPGA device are insufficient for the prototype.

4 Results and Analysis

A known sequence of input data is taken for validating the transmitted and received data over AWGN channel. The fixed-point behavioral simulation results are shown in Fig. 6 for a SNR of 0 dB and Fig. 7 for a SNR of 9 dB. The modules inside the waveform include input data, CI-OFDM signal with cyclic prefix, noise samples generated in the AWGN channel, and the received data. The received output is highly corrupted in Fig. 6 for a SNR of 0 dB. The simulation results are zoomed for



Fig. 6 Behavioral simulation of CI-OFDM baseband transceiver at 0 dB

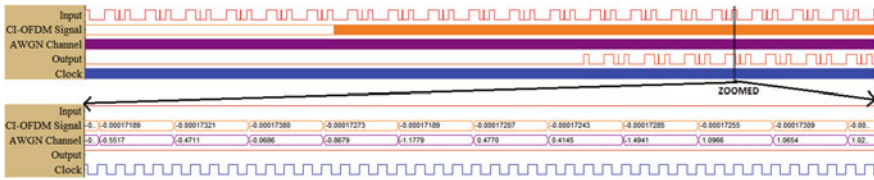


Fig. 7 Behavioral simulation of CI-OFDM baseband transceiver at 9 dB

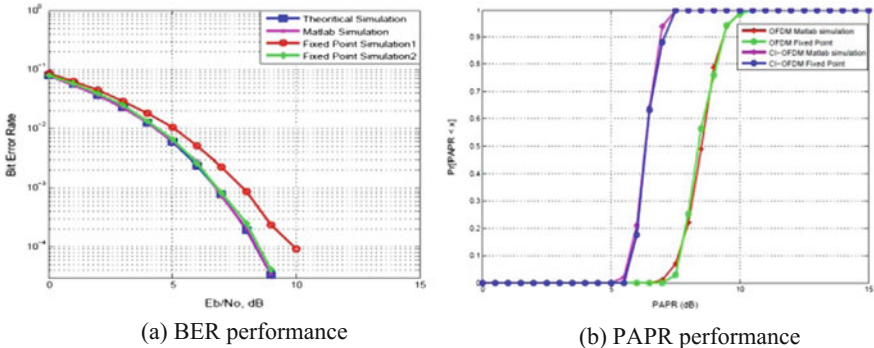


Fig. 8 a BER and b PAPR performance of 1024-point CI-OFDM

in-depth view of the signals. Figure 7 has the received data same as that of input data for a SNR of 9 dB.

The fixed-point BER plot of 1024-point CI-OFDM using QPSK modulation on AWGN channel is shown in Fig. 8a. The fixed-point simulation1 BER plot has a bit width precision of 16 bits, and fixed-point simulation2 BER plot has a bit width precision of 25 bits. These fixed-point BER plots are compared with theoretical and MATLAB simulations. It is seen that the fixed-point simulation1 plot is degraded by 1.529 dB for a BER of 10⁻⁴ with respect to theoretical plot. Fixed-point simulation2 exhibits a BER of 10⁻⁴ for a SNR of 8.4 dB that is same as obtained through theoretical and MATLAB simulations. Therefore, the BER performance is not degraded with respect to OFDM.

The Cumulative Distribution Function (CDF) of fixed-point PAPR plot along with MATLAB simulation PAPR plot is shown in Fig. 8b. It is seen that, in case of OFDM, 80% transmissions exhibit a PAPR < 9.03 dB and 100% transmissions for PAPR < 10.5 dB. In CI-OFDM, 80% of transmissions show PAPR < 6.76 dB and 100% transmissions for PAPR < 7.5 dB. There is a gain of 3 dB PAPR reduction. Both the fixed-point simulations and MATLAB simulations are approximately close and similar to each other.

5 Conclusion

In this paper, the fixed-point design of 1024-point CI-OFDM using QPSK modulation is proposed for DVB-SH-A. In order to validate the results, the behavioral simulation is shown for different SNRs. Moreover, the performance parameters like BER and PAPR are compared with MATLAB simulations. It is observed that fixed-point with bit width precision of 25 bits and MATLAB simulations are approximately equal. The PAPR performance of 1024-point CI-OFDM exhibits better than OFDM. Also, the computational complexity is reduced by employing FFT for generating CI codes and has the same spectral efficiency as of OFDM. Therefore, OFDM can be replaced with CI-OFDM in DVB-SH-A to perform better in power limited conditions. Further, for real-time implementation, the design can be carried out for ASIC implementation.

Acknowledgements The authors would like to thank MeitY, Government of India, for funding of this research under the project entitled “Design and FPGA Prototype of Multi-Carrier Multiple Access Schemes for Variable Rate Multimedia Satellite Communication,” Project Reference No. *R&D/SP/EE/DEIT/DFP/2013-14/61*.

References

1. ETSI, “Digital Video Broadcasting (DVB); framing structure, channel coding and modulation for Satellite Services to Handheld devices (SH) below 3 GHz”, 2010.
2. ETSI, “Digital video broadcasting; framing structure, channel coding and modulation for 11/12 ghz satellite services”, August 1997.
3. ETSI, “Digital video broadcasting (dvb); framing structure, channel coding and modulation for digital terrestrial television”.
4. Y. Wu and W. Zou, “Orthogonal frequency division multiplexing: a multi-carrier modulation scheme”, IEEE Transactions on Consumer Electronics, vol. 41, no. 3, pp. 392–399, Aug 1995.
5. T. Jiang and Y. Wu, “An overview: Peak-to-average power ratio reduction techniques for ofdm signals”, IEEE Transactions on Broadcasting, vol. 54, no. 2, pp. 257–268, June 2008.
6. P. Kelley and C. Rigal, “Dvb-sh: mobile digital tv in sband”, in EBU technical review, July 2007.
7. X. Li and L. Cimini, “Effects of clipping and filtering on the performance of ofdm”, in Vehicular Technology Conference, IEEE 47th, vol. 3, May 1997.
8. T. Jiang, W. Xiang, P. Richardson, D. Qu, and G. Zhu, “On the nonlinear companding transform for reduction in papr of mcm signals”, IEEE Transactions on Wireless communications, vol. 6, no. 6, pp. 2017–2021, June 2007.
9. J. Davis and J. Jedwab, “Peak-to-mean power control and error correction for ofdm transmission using golay sequences and reed-muller codes”, Electronics Letters, vol. 33, no. 4, pp. 267–268, Feb 1997.
10. S. Muller and J. Huber, “Ofdm with reduced peak-to-average power ratio by optimum combination of partial transmit sequences”, Electronics Letters, vol. 33, no. 5, pp. 368–369, Feb 1997.

11. R. Bauml, R. Fischer, and J. Huber, "Reducing the peak-to-average power ratio of multicarrier modulation by selected mapping", *Electronics Letters*, vol. 32, no. 22, pp. 2056–2057, Oct 1996.
12. E. Lawrey and C. Kikkert, "Peak to average power ratio reduction of ofdm signals using peak reduction carriers," in *Signal Processing and Its Applications*, proceedings of the Fifth International Symposium, vol. 2, 1999, pp. 737–740.
13. J. Tellado and J. Cioffi, "Efficient algorithms for reducing par in multicarrier systems," in *Information Theory*, IEEE International Symposium on, Aug 1998.
14. D. A. Wiegandt, Z. Wu, and C. R. Nassar, "High-throughput, high performance ofdm via pseudo-orthogonal carrier interferometry spreading codes", *IEEE Transactions on Communications*, vol. 51, no. 7, pp. 1123–1134, July 2003.
15. H. G. Ryu, "System design and analysis of mimo sfbc ci-ofdm system against the nonlinear distortion and narrowband interference", *IEEE Transactions on Consumer Electronics*, vol. 54, no. 2, pp. 368–375, May 2008.
16. ITU-R S.1878, "Multi-carrier based transmission techniques for satellite systems", Geneva, Dec 2015.
17. R. Palisetty, V. K. Sinha, S. Mallick, and K. C. Ray, "FPGA prototyping of energy dispersal and improved error efficiency techniques for dvb-satellite standard", in *VLSI Systems, Architecture, Technology and Applications (VLSI-SATA)*, Jan 2015, pp. 1–5.
18. Y. S. Cho, J. Kim, W. Y. Yang, and C. G. Kang, *MIMO-OFDM Wireless Communications with MATLAB*. John Wiley & Sons, 2010.
19. "IEEE standard for local and metropolitan area networks part 16: Air interface for broadband wireless access systems amendment 3: Advanced air interface", *IEEE Std 802.16 m-2011*, pp. 1–1112, May 2011.

Design of Aperture-Fed Elliptically Polarized Dielectric Resonator Antenna for WLAN IEEE 802.11 ac Applications

Hashinur Islam, Saumya Das and Tanushree Bose

Abstract In recent times, Wi-Fi (802.11 ac) is gaining popularity as it supports multistation WLAN and high throughput. Dielectric resonator antennas find many useful applications because of their low weight, low profile, low loss, conformability, and easy realization. In this paper, an aperture-coupled elliptically polarized rectangular dielectric resonator antenna is presented. Elliptical polarization is utilized to enhance the impedance bandwidth and gain in WLAN recommended band. The antenna is seen to be elliptically polarized with maximum gain of 7.50 dB and impedance bandwidth 550 MHz.

Keywords Dielectric resonator antenna (DRA) · Wireless local area network (WLAN) · Elliptically polarized

1 Introduction

Wireless communications have experienced runaway expansion in the communication field over the last two decades, and now, about 10 billion users worldwide are getting its advantages everyday.

Cellular phones, internet access, video calling, satellite communications, broadcast radio, security systems, remote control, and wireless power transfer are the most emerging applications of wireless communication in the present era.

The importance of antenna in the field of wireless communication is not at all arguable. Dielectric resonator antenna (DRA) has started playing an important role

H. Islam (✉) · S. Das · T. Bose
Department of Electronics and Communications Engineering (ECE),
Sikkim Manipal Institute of Technology, Majhitara, Sikkim, India
e-mail: hashinur0001@gmail.com

S. Das
e-mail: saumya.das.1976@gmail.com

T. Bose
e-mail: tanushree.contact@gmail.com

in antenna research as it exhibits characteristics like light weight, small dimensions, low loss, and thermal stability [1, 2]. Both microwave and millimeter wave communications find DRAs applicability in the suitable ranges [3]. DRA could give a good solution to the losses in the metallic antenna used in satellite and radar applications [1]. DRA could be excited with various feeding techniques, and the behavior of radiation strongly depends on those feeding techniques [4]. The shape of DRA also plays an important contribution on the selection of radiation frequency and desired gain [4]. Rectangular DRA is widely chosen as it offers more degree of freedom than cylindrical or spherical DRA.

In this paper, an aperture-coupled rectangular DRA is presented to establish a wireless communication for 5.21 GHz (Wi-Fi) range. Two different length cross-slots with 90° phase difference are used to generate elliptically polarized electromagnetic wave for radiation. This type of feeding technique is used to enhance bandwidth as well as gain for antenna applications [5].

2 Antenna Designing Parameters

The top view of the proposed dielectric resonator antenna (DRA) is displayed in Fig. 1. A rectangular dielectric with permittivity $\epsilon_r = 10.2$ is considered as radiator in the system. Table 1 lists detailed dimensions of the DRA design.

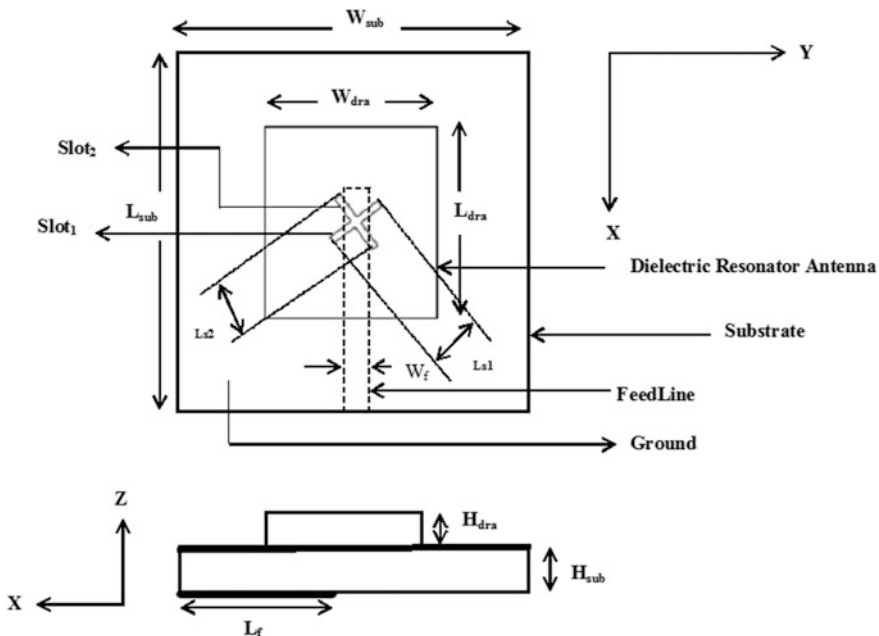


Fig. 1 Top view and side view of the presented cross-slot coupled elliptically polarized dielectric resonator antenna

Table 1 Antenna design dimensions

Parameters	Dimensions
Substrate (FR4 epoxy)	$L_{\text{sub}} = 48.27$ mm, $W_{\text{sub}} = 46.27$ mm, $H_{\text{sub}} = 1.6$ mm
Ground plane	$L_{\text{g}} = 48.27$ mm, $W_{\text{g}} = 46.27$ mm
Slot1 and slot2	$L_{\text{s1}} = 8$ mm, $L_{\text{s2}} = 8.5$ mm, $W_{\text{s1}} = W_{\text{s2}} = 1$ mm
DRA (Rogers RO3210(tm))	$L_{\text{dra}} = 21$ mm, $W_{\text{dra}} = 18$ mm, $H_{\text{dra}} = 4.8$ mm
Feed line	$L_{\text{f}} = 16.8$ mm, $W_{\text{f}} = 4.16$ mm

The substrate used is FR4 ($\epsilon_r = 4.4$), and the thickness is taken as 1.6 mm. The metallic ground plane is placed on the substrate, and the DRA is located on the top of ground plane. Two cross-slots are made on the ground plane, and the aperture is kept below the substrate. So aperture is indirectly coupling the DRA through the slots. HFSS platform has been used to carry out the simulation work.

The dimensions of different parts of the antenna are listed in Table 1.

L_{sub} : length of the substrate, W_{sub} : width of the substrate, H_{sub} : height of the substrate, L_{g} : length of the ground, W_{g} : width of the ground, $L_{\text{s1}} = L_{\text{s2}} =$ length of slot1 and slot2, $W_{\text{s1}} = W_{\text{s2}} =$ width of the slot1 and slot2, $L_{\text{dra}} =$ length of the DRA, $W_{\text{dra}} =$ width of the DRA, $H_{\text{dra}} =$ height of the DRA, $L_{\text{f}} =$ length of the feed line, $W_{\text{f}} =$ width of the feed line.

Resonating frequency for TE_{mnl} mode for DRA is given by the following formulas [6],

$$f_0 = \frac{c}{2\pi\sqrt{\epsilon_r}} \sqrt{\left(k_x^2 + k_y^2 + k_z^2\right)} \quad (1)$$

where $k_x = \frac{m\pi}{a}$, $k_y = \frac{n\pi}{b}$, $k_z = \frac{l\pi}{2d}$,

where $a = L_{\text{dra}}$, $b = W_{\text{dra}}$, $h = H_{\text{dra}}$, $m = 1$, $n = 1$, and $l = 1$

$$k_x^2 + k_y^2 + k_z^2 = \epsilon_r k_0^2 \quad (2)$$

where $k_0 = \frac{2\pi f_0}{c}$, $\epsilon_r = 10.2$.

For TE_{111} mode, by substituting the values in the Eqs. 1 and 2, the calculated resonant frequency obtained is 5.97 GHz.

3 Results and Analysis

3-D polar plot in Fig. 2 shows the broadside radiation pattern. The colored scale shows a gain variation from -20.8260 to 7.3794 dB.

The simulated return loss of the proposed antenna is shown in Fig. 3. The graph shows that the minimum S_{11} of -24.42 dB is at a resonant frequency of 5.30 GHz. So this simulated resonant frequency nearly matches the calculated resonance

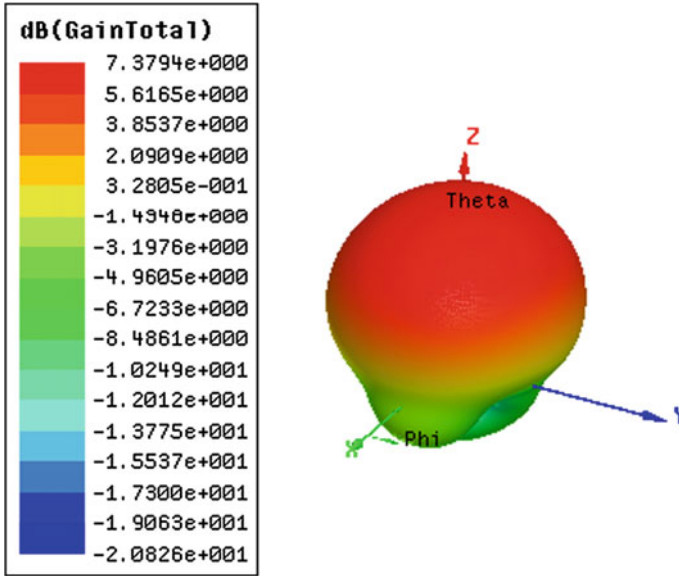


Fig. 2 3-D polar plot showing total gain (in dB)

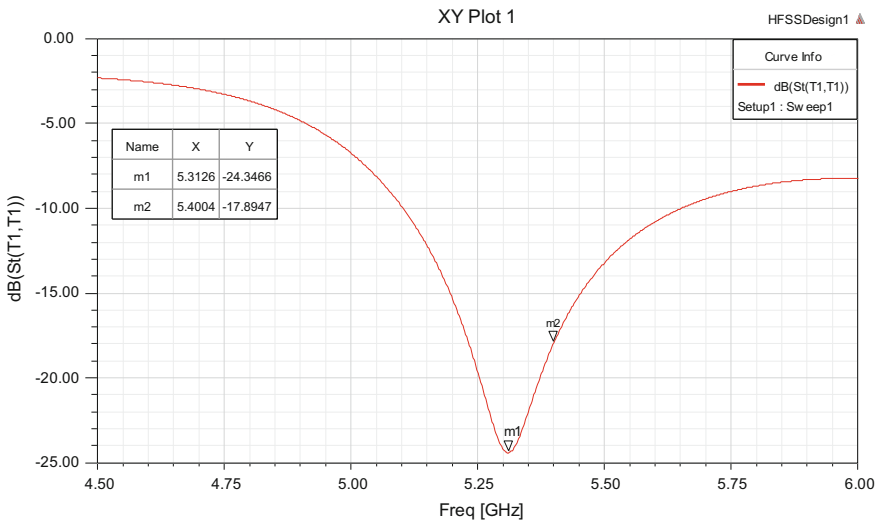


Fig. 3 Return loss of the proposed antenna

frequency from Eqs. 1 and 2. The graph also depicts the wide bandwidth of 550 MHz from 5.10 to 5.65 GHz. So the achieved bandwidth is much more than the required bandwidth of WLAN which is about 160 MHz [7].

2-D gain at $\Phi = 0^\circ$ and 90° is shown in Fig. 4. It can be seen from the graphs that gain at 0° and 90° is equal to 7.50 dB, which is sufficient for WLAN communication as it is expected to be around 5 dB [8].

S-parameter report of Z_{11} is shown in Fig. 5. The graph shows that at resonating frequency, the characteristic impedance (re) is nearly equal to 50Ω , whereas the reactance (img) value nearly touches 0Ω .

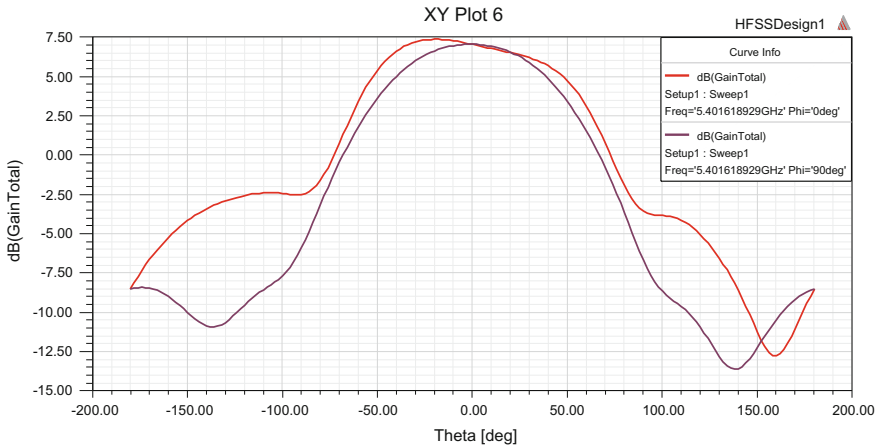


Fig. 4 2-D gain at $\Phi = 0^\circ$ and 90° at $f_0 = 5.40$ GHz

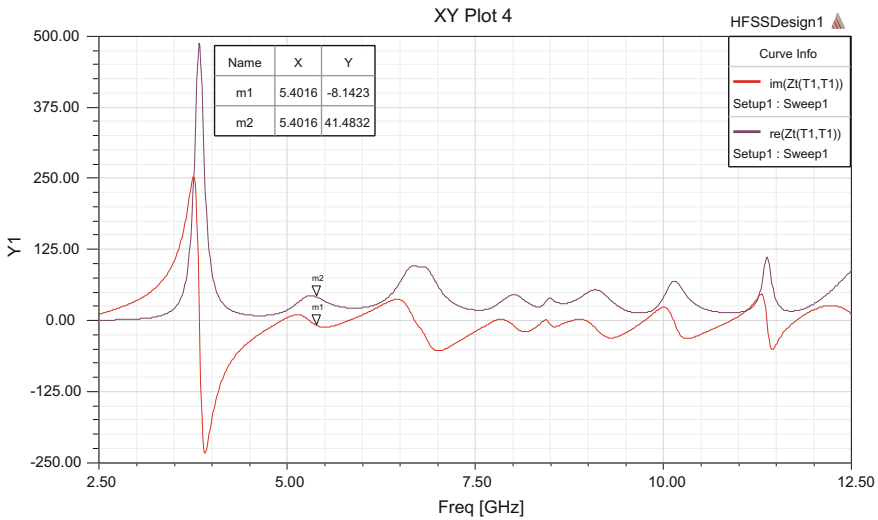


Fig. 5 S-parameter report of Z_{11} at $f_0 = 5.40$ GHz

The voltage standing wave ratio (VSWR) of the proposed antenna is 1.29 at 5.40 GHz as shown in Fig. 6. It can be concluded that the matching ability of the antenna is satisfactory over the resonating range of frequency as VSWR always maintains a value less than 2.

From the axial ratio plot, it is clearly visible that as its value is more than 1, the polarization could be considered to be elliptical. Although the DRA is fed with 90°

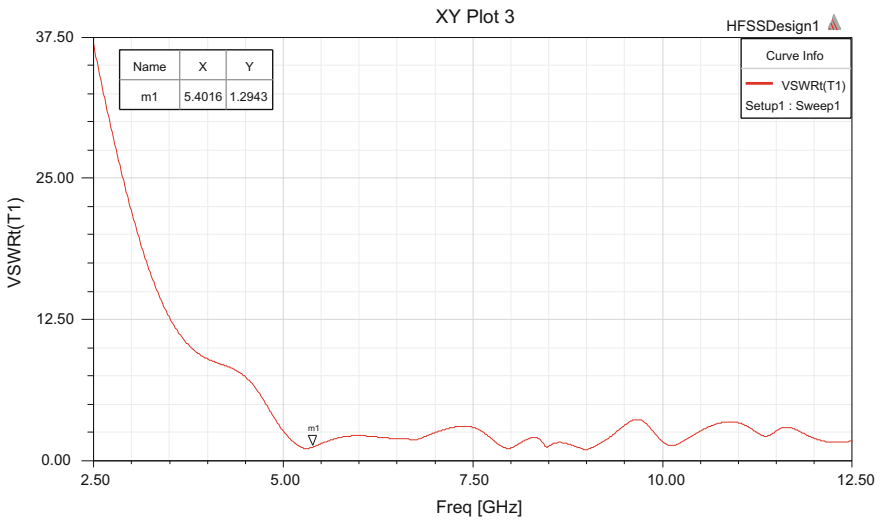


Fig. 6 VSWR of the proposed antenna design

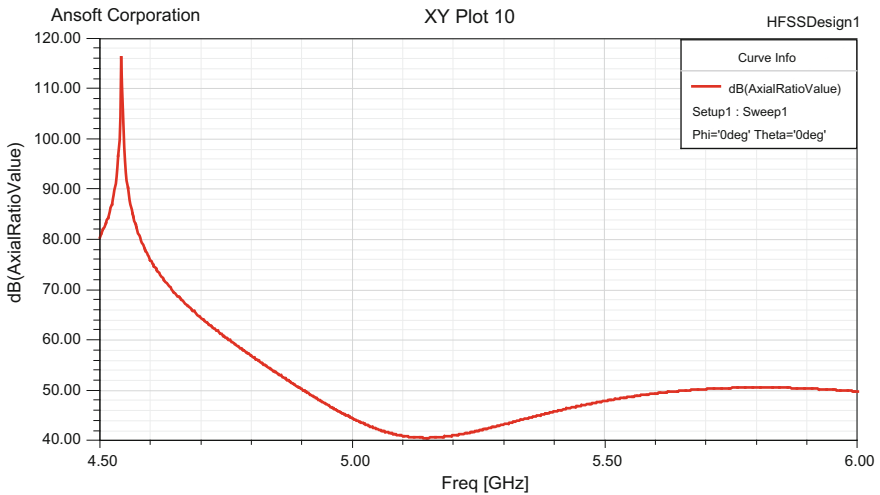


Fig. 7 Axial ration in dB

phase differed cross-slots, but because of unequal slots length, elliptical polarization is the outcome of the proposed antenna and hence, the maximum radiation is aligned with the principal axes of the field components [9, 10] (Fig. 7).

4 Conclusion

In this paper, a simple dielectric resonator antenna structure has been proposed to execute **IEEE 802.11 ac** range applications with compact size. Different length cross-slots have been placed under the DRA to achieve the elliptical polarization with considerable gain and a wide bandwidth.

References

1. Kumar, J., and Gupta, N.: Performance analysis of dielectric resonator antennas. *Wireless Pers commun.*, vol. 75, no. 2, pp. 1029–1049, (2014).
2. Kumar, J., and Gupta, N.: Bandwidth and Gain Enhancement Technique for Gammadion Cross Dielectric Resonator Antenna. *Wireless Pers Commun.*, vol. 85, no. 4, pp. 2309–2317, (2015).
3. Wahab, W. M. A., Busuioc, D., and Safavi-Naeini, S.: Low cost planar waveguide technology-based dielectric resonator antenna (DRA) for millimeter-wave applications: Analysis, design, and fabrication. *IEEE Transactions on Antennas and Propagation*, vol. 58 no. 8, 2499–2507, (2010).
4. Petosa, A.: *Dielectric resonator antenna handbook*. Artech House, (2006).
5. Pozar, D. M.: Microstrip antenna aperture-coupled to a microstripline. *Electronics letters*, vol. 21 no. 2, 49–50, (1985).
6. Luk, K. M., Leung, K. W., Luk, K. M., and Leung, K. W.: *Dielectric resonator antennas*. RESEARCH STUDIES PRESS LTD. Baldock, Hertfordshire, England, (2002).
7. Ong, E. H., Knecht, J., Alanen, O., Chang, Z., Huovinen, T., and Nihtilä, T.: IEEE 802.11 ac: Enhancements for very high throughput WLANs. In *Personal Indoor and Mobile Radio Communications (PIMRC)*, 2011 IEEE 22nd International Symposium on (pp. 849–853). IEEE, (2011, September).
8. Nasir, S. A., Mustaqim, M., and Khawaja, B. A.: Antenna array for 5 th generation 802.11 ac Wi-Fi applications. In *High-capacity Optical Networks and Emerging/Enabling Technologies (HONET)*, 2014 11th Annual (pp. 20–24). IEEE, (2014, December).
9. Balanis, C. A.: *Fundamental parameters of antennas*. *Antenna Theory Analysis and Design*, vol. 3, pp. 27–132, (2005).
10. Sinclair, G.: The transmission and reception of elliptically polarized waves. *Proceedings of the IRE*, vol. 38, no. 2, pp. 148–151, (1950).

Broadband Glass Paperweight Dielectric Resonator Antenna for WLAN Applications

Saumya Das, Hashinur Islam and Tanushree Bose

Abstract In recent times, Wi-Fi b/g (802.11 b/g) has been profoundly accepted due to the desire for increased data rates and minimal costs. It promotes the industrial, scientific, and medical (ISM) applications. Dielectric resonator antenna has been widely preferred for the various applications due to their low weight, low profile, conformability, easy and cheap realization. In this paper, an aperture-fed rectangular glass paperweight dielectric resonator antenna has been proposed. This antenna serves a great advantage because of its low cost, as glass material is utilized as radiator. The antenna seems to support near omnidirectional pattern providing a widespread impedance bandwidth of 1960 MHz.

Keywords Dielectric resonator antenna (DRA) · Glass Paperweight antenna
Wireless local area network (WLAN) · Aperture coupled

1 Introduction

A dielectric resonator antenna (DRA) is a dielectric material antenna which is useful for radiating radio waves. It is widely used in mobile phones, satellite communication, and different other electromagnetic devices [1]. Dielectric material with dielectric constant around 10 is mostly used for exploring radiating property. So commonly material company-made materials such as Rogers TMM 10, Rogers RT/duroid 6010, ECCOSTOCK HiK 500F are used for DRA fabrication. But the cost of

S. Das (✉) · H. Islam · T. Bose

Department of Electronics and Communications Engineering (ECE),
Sikkim Manipal Institute of Technology, Majhitara, Sikkim, India
e-mail: saumya.das.1976@gmail.com

H. Islam

e-mail: hashinur0001@gmail.com

T. Bose

e-mail: tanushree.contact@gmail.com

© Springer Nature Singapore Pte Ltd. 2018

R. Bera et al. (eds.), *Advances in Communication, Devices and Networking*,
Lecture Notes in Electrical Engineering 462,
https://doi.org/10.1007/978-981-10-7901-6_55

503

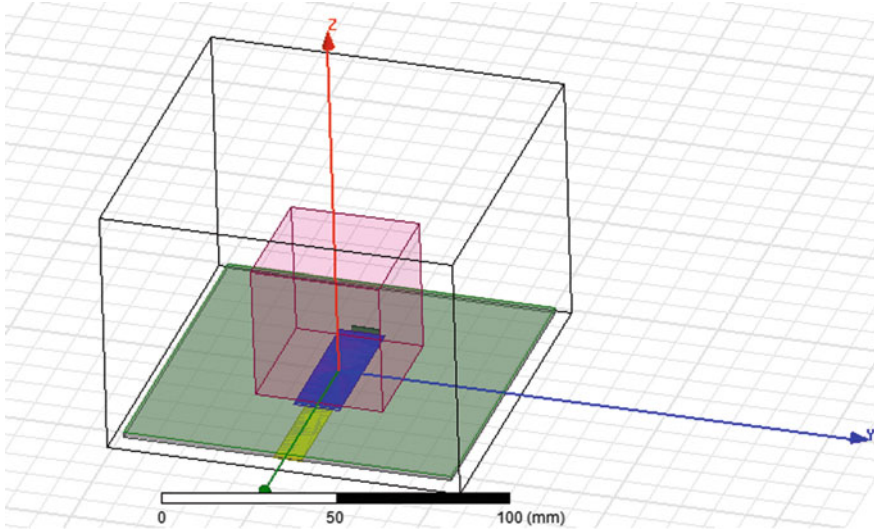


Fig. 1 3-D view of the model in HFSS

the project increases with the use of such costly materials. To reduce the cost, glass material could be used as dielectric for this type of antenna designing [2, 3].

WLAN communication at 2.4 GHz is widely used for its wide signal coverage area, better penetration through walls, and physical barriers [4, 5]. 2.4 GHz is also well known for its application in industrial, scientific, and medical (ISM) [6]. This frequency range is applicable also in Bluetooth, telecommand systems, movement detection, etc. [7, 8].

In this paper, an almost cube glass paperweight structure DRA as shown in Fig. 1 has been aperture fed to use as a radiator at 2.4 GHz. The antenna is simulated and analyzed using ANSYS HFSS CAD software which is based on finite element method (FEM) of computational electromagnetics [9].

2 Antenna Designing Parameters

The designing of the presented antenna has been done with aperture feeding technique. The dimensions of the glass DRA are 39 mm × 39 mm × 41 mm. The substrate used is FR4 epoxy. The dimensions of the substrate is 100 mm × 100 mm × 1.6 mm having $\epsilon_r = 4.4$. The DRA which is made of K9 glass material has the relative permittivity of 6.85, i.e., $\epsilon_r = 6.85$. DRA is excited through a linear slot on the ground plane of the antenna. Rectangular DRA is chosen here as it offers more degree of freedom than cylindrical or spherical DRA. The 3-D view of the model in HFSS is shown in Fig. 1.

Resonating frequency for TE_{mnl} mode for DRA is given by the following formulas [10, 11],

$$f_0 = \frac{c}{2\pi\sqrt{\epsilon_r}} \sqrt{(k_x^2 + k_y^2 + k_z^2)} \tag{1}$$

where $k_x = \frac{m\pi}{a}$, $k_y = \frac{n\pi}{b}$, $k_z = \frac{l\pi}{2d}$,

where $a = L_{DRA}$, $b = W_{DRA}$, $h = H_{DRA}$, $m = 1$, $n = 1$, and $l = 1$

$$k_x^2 + k_y^2 + k_z^2 = \epsilon_r k_0^2 \tag{2}$$

where $k_0 = \frac{2\pi f_0}{c}$, $\epsilon_r = 6.85$.

For TE_{111} mode, by substituting the values in the Eqs. 1 and 2, the resonant frequency obtained is 2.196 GHz.

The configuration of the antenna is shown in Fig. 2 with the specifying parts, and their dimensions are listed in Table 1.

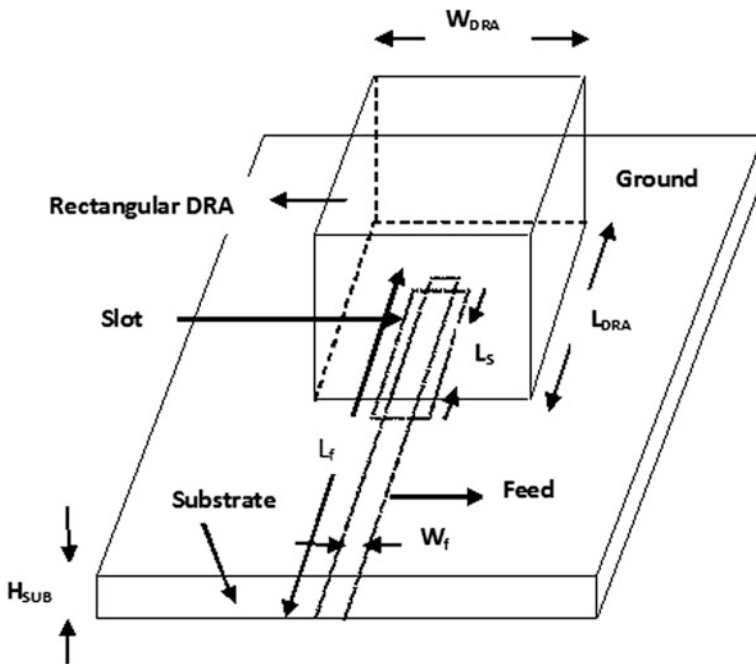


Fig. 2 3-D view of the proposed aperture-fed rectangular DRA antenna

Table 1 Antenna design dimensions

Parameters	Dimensions
Substrate (FR4 epoxy)	$L_{sub} = 100$ mm, $W_{sub} = 100$ mm, $H_{sub} = 1.6$ mm
Ground plane	$L_g = 100$ mm, $W_g = 100$ mm
Slot	$L_{slot} = 14$ mm, $W_{slot} = 44$ mm
DRA (glass)	$L_{DRA} = 39$ mm, $W_{DRA} = 39$ mm, $H_{DRA} = 41$ mm
Feed line	$L_f = 75$ mm, $W_f = 8.32$ mm

L_{SUB} = length of the substrate, W_{SUB} = width of the substrate, H_{SUB} = height of the substrate, L_G = length of the ground, W_G = width of the ground, L_S = length of the slot, W_S = width of the slot, L_{DRA} = length of the DRA, W_{DRA} = width of the DRA, H_{DRA} = height of the DRA, L_f = length of the feed, W_f = width of the feed

3 Results and Analysis

The simulated return loss of the glass antenna is 15.01 dB at the resonant frequency of 2.4 GHz which is shown in Fig. 3. The bandwidth is 1960 MHz which ranges from 1.57 to 3.53 GHz. So, calculated resonance frequency nearly matches the simulated resonating frequency.

The voltage standing wave ratio (VSWR) of the proposed antenna is shown in Fig. 4. It can be observed from the result that the VSWR value is 1.43 at the resonating frequency 2.4 GHz. This is suitable for the antenna designing as it gives VSWR less than or equal to 2 ($VSWR \leq 2$).

In Fig. 5, the radiation pattern of antenna is displayed in polar coordinate. From the plot, it can be concluded that with glass radiator, it is possible to achieve near omni-power pattern with a maximum gain of 2.32 dB.

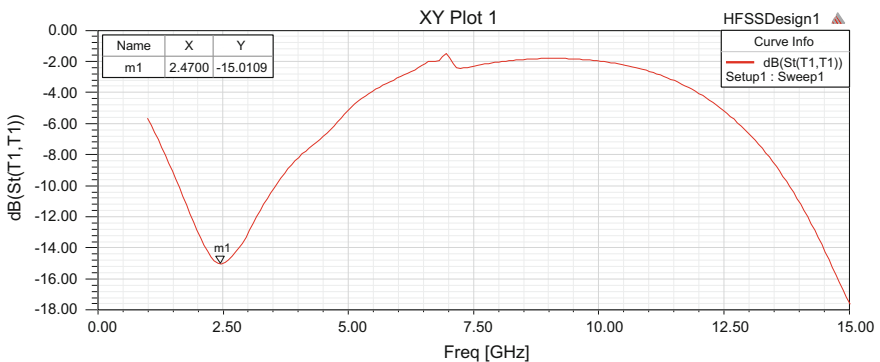


Fig. 3 Return loss of the proposed antenna

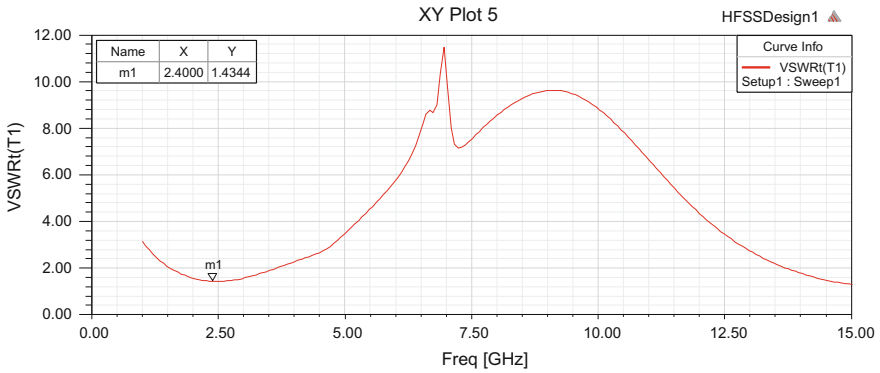


Fig. 4 VSWR of the proposed antenna design

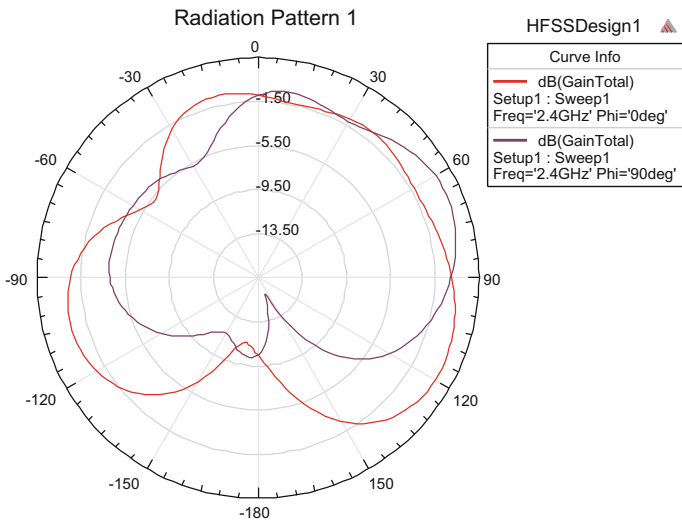


Fig. 5 Near omni-power pattern

4 Conclusion and Future Work

In this paper, a simple and cheap glass paperweight DRA antenna has been proposed to execute IEEE 802.11 b/g ISM range application. The antenna is aperture fed to achieve a broad bandwidth and reasonable gain. This proposed antenna now needs to be fabricated, and performance parameters are to be measured to verify the simulated results.

References

1. Kumar, J., and Gupta, N.: Performance analysis of dielectric resonator antennas. *Wireless Pers commun*, vol. 75, no. 2, pp. 1029–1049, (2014).
2. Leung, K. W., Pan, Y. M., Fang, X. S., Lim, E. H., Luk, K. M., & Chan, H. P.: Dual-function radiating glass for antennas and light covers—Part I: Omnidirectional glass dielectric resonator antennas. *IEEE Transactions on Antennas and Propagation*, vol. 61 no. 2, pp. 578–586, (2013).
3. Leung, K. W., Fang, X. S., Pan, Y. M., Lim, E. H., Luk, K. M., & Chan, H. P.: Dual-function radiating glass for antennas and light covers—Part II: Dual-band glass dielectric resonator antennas. *IEEE Transactions on Antennas and Propagation*, vol. 61 no. 2, pp. 587–597, (2013).
4. Zhu, H., Li, M., Chlamtac, I., and Prabhakaran, B.: A survey of quality of service in IEEE 802.11 networks. *IEEE Wireless Communications*, vol. 11, no. 4, pp. 6–14, (2004).
5. Lin, A., and Ling, H.: Through-wall measurements of a Doppler and direction-of-arrival (DDOA) radar for tracking indoor movers. In *Antennas and Propagation Society International Symposium*, Vol. 3, pp. 322–325, IEEE, (2005, July).
6. Soras, C., Karaboikis, M., Tsachtsiris, G., and Makios, V.: Analysis and design of an inverted-F antenna printed on a PCMCIA card for the 2.4 GHz ISM band. *IEEE Antennas and propagation Magazine*, vol. 44, no. 1, pp. 37–44, (2002).
7. Liu, Y. H., Huang, X., Vidojkovic, M., Ba, A., Harpe, P., Dolmans, G., and de Groot, H.: A 1.9 nJ/b 2.4 GHz multistandard (Bluetooth Low Energy/Zigbee/IEEE802. 15.6) transceiver for personal/body-area networks. In *Solid-State Circuits Conference Digest of Technical Papers (ISSCC)*, 2013 IEEE International, pp. 446–447, IEEE, (2013, February).
8. de Francisco, R., and Pandharipande, A.: Spectrum occupancy in the 2.36–2.4 GHz band: Measurements and analysis. In *Wireless Conference (EW)*, 2010 European, pp. 231–237, IEEE, (2010, April).
9. Ansoft, H. F. S. S. 14, User Manual, (2013).
10. Luk, K. M., Leung, K. W., Luk, K. M., and Leung, K. W.: *Dielectric resonator antennas*. RESEARCH STUDIES PRESS LTD. Baldock, Hertfordshire, England, (2002).
11. Petosa, A.: *Dielectric resonator antenna handbook*. Artech House, (2006).

Pitch Tracking and Pitch Smoothing Methods-Based Statistical Approach to Explore Singers' Melody of Voice on a Set of Songs of Tagore

Indira Chatterjee, Priya Gupta, Parthasarathi Bera and Joy Sen

Abstract The paper depicts a systematic procedure using pitch tracking and pitch smoothing methods-based statistical approach for exploring the singers' melody of voice for a set of songs of poet Rabindranath Tagore sung by different renowned singers. The medium category (Mudara) of songs started with vowel 'aa' has been incorporated in the data set of songs. Index of melody has been estimated numerically based on semitones of different singers for a particular duration of the first vocal phrase. The value of probability of significance calculated by one-way ANOVA has been considered for the comparative study of the index of melody of the singers of particular song, and the results show the significant difference among the singers of same song of Tagore.

Keywords Melody · Probability of significance · Song of Tagore

1 Introduction

Singing comprises of lyrics and music and lyrical song brings to light various feelings of mankind. A song draws listeners' attraction when a singer sings the song by his perceived vocal quality and melodious voice. Melody is one of the most fundamental components of a song. A note is a sound with a pitch and duration [1]. Melody of a piece

I. Chatterjee (✉) · J. Sen

The Science and Heritage Initiative, IIT Kharagpur, Kharagpur, West Bengal, India
e-mail: chaterjee.indira@gmail.com

J. Sen

e-mail: joysen@arp.iitkgp.ernet.in

P. Gupta · P. Bera

The Science and Heritage Initiative,
Kalyani Government Engineering College, Kalyani, West Bengal, India
e-mail: priyaguptaccp@gmail.com

P. Bera

e-mail: parthabera1977@gmail.com

© Springer Nature Singapore Pte Ltd. 2018

R. Bera et al. (eds.), *Advances in Communication, Devices and Networking*,
Lecture Notes in Electrical Engineering 462,
https://doi.org/10.1007/978-981-10-7901-6_56

of song is the notes that catch listeners ear as he listens. Note or semitone can be calculated from singer's pitch or fundamental frequency [2]. Pitch tracking method used to determine accurate pitch frequency from speech signal waveform [3–5]. In this paper, a systematic procedure has been proposed to make the comparative analysis of melody of voices of different singers who have sung different songs of poet Rabindranath Tagore (Rabindra Sangeet) of medium range (*Mudara*). A low-pass filter has been used on digitalized signals of songs to cut down unwanted high-frequency components [6]. In our work, pitch tracking [7–9] has been used to identify the pitch frequency with respect to time and pitch smoothing [10] has been used to eliminate undesirable pitches. One-way ANOVA has been used to calculate the probability of significance, and Tukey's test [11] has been performed to figure out significant difference between two singers to compare every mean with every other mean value.

2 Song Database

For the present work, a set of five songs of Tagore of medium category (*Mudara*) where each song started alphabetically with vowel 'AA' have been used as a song database [12] for the analysis. The songs have been sung by different singers, and the lists of songs with the name of singers are given in Table 1. Full names of each singer are given in Table 1. The total number of singer considered is nine for this work where each song has been sung by three different singers. The digitized version of these songs with duration of first eight seconds from the beginning of the vocal phrase has been segmented for the analysis.

3 Features of Melody

3.1 The Shape or Contour of a Melody [13]

The progress of melody depends on pitches either go up or down rapidly. One can draw a line going up perpendicularly if the cadence abruptly reaches to higher note

Table 1 Name of songs and singers

Song No.	Name of song	Singer's name
1	Aamar Bhanga Pather	DB, HM, PKM
2	Aamar Je Din	CC, DB, PKS
3	Aamar Jibano Patra	CC, HM, MD
4	Aamar Mon Bole	BS, MC, SaS
5	Aamar Priyar Chaya	DB, HM, PKM

BS Babul Supriyo, *CC* Chinmoy Chatterjee, *DB* Debabrata Biswas, *HM* Hemanta Mukherjee, *MC* Mrinal Chakraborty, *MD* Manna Dey, *PKM* Pankaj Kumar Mallick, *PKS* Pijush Kanti Sarkar, *SaS* Santanu Sen

Fig. 1 Shape or contour of a melody



or that goes down accordingly if melody is at low ebb, and this line is called as contour or shape of a melody. Figure 1 shows the shape or contour of melody.

3.2 *Melodic Motion [13]*

A melody that is up and down gradually sheer small pitch alters slowly between one note and the next is called conjunct. A melody that goes up and goes down rapidly with large intermissions between one note and the next is called disjunct melody. Figure 2 shows the conjunct and disjunct melody.

3.3 *Melodic Phrases [13]*

In fact, a musical phrase acts abundantly like a grammatical phrase. A phrase in a sentence is a group of words making sense together and exposes a certain notion but a melodic phrase consists of several notes making sense together and bringing to light a definite melodic notion.

4 Procedure for Acoustic Measurement

In this work, first 8 s of vocal phrase of different singers for each song has been considered for pitch extraction and overlap between neighboring frames to reduce discontinuity between them has been allowed. Since melody is the single



Fig. 2 Conjunct and disjunct melody

(monophonic) pitch sequence [14, 15] therefore pitch, i.e., fundamental frequency of segmented vocal phrase has been considered for the analysis. The segmented vocal phrase is filtered to remove as many harmonics as possible, while preserving the fundamental frequency. Before further processing, the acoustic input must go through a low-pass filter at 1047 Hz to cut down unwanted high-frequency components and then pitch tracking and pitch smoothing methods have been used on the low-pass output signal for getting the semitones of different singers for a song.

Here, the sampling frequency $f_s = 11,025$ Hz, bit resolution = 8, frame size = 512, overlap = 340 are considered. As the frame rate is $f_s/(\text{frame size} - \text{overlap})$, the value of frame rate for this work is $11025/(512 - 340) = 64$. Here, autocorrelation function [9] and average magnitude difference function (AMDF) [9] methods have been used for pitch tracking.

The autocorrelation function for a discrete time signal $x(n)$ is defined as:

$$D_{\text{ACF}}(m) = \frac{1}{N} \sum_{n=0}^{N-1} x(n) \times x(n+m) \quad (1)$$

And the short-time AMDF is defined as

$$D_{\text{AMDF}}(m) = \frac{1}{N} \sum_{n=0}^{N-1} |x(n) - x(n+m)| \quad (2)$$

In this case, $x(n)$ are the samples of speech, $m = \text{lag index}$.

For the present work, index of melody (M_L) has been estimated by the value of semitone. After obtaining the pitch frequencies, semitones have been calculated by using the following formula:

$$\text{semitone} = 12 \times \log_2 \left(\frac{\text{freq}}{440} \right) + 69 \quad (3)$$

Here, freq represents the pitch frequency and 69 represents central LA (A440, 440 Hz). Pitch smoothing has been performed by passing the pitch contour through a medium filter of size 5.

Figure 3 shows the pitch values for a song ‘Amar Bhangra Pather’ sung by DB, HM, and PKM. The pitch values for singer DB have been compared with HM and PKM to see the significant difference of melody of voice among each other. The pitch values of HM have been compared with the pitch values of PKM to see the significant difference of melody of voice between HM and PKM.

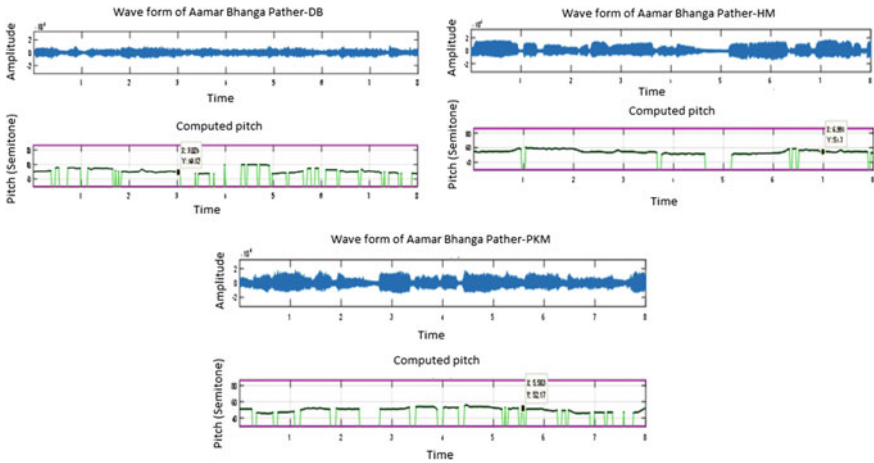


Fig. 3 Semitone values of DB, HM, and PKM for the song Amar Bhanga Pather for first eight sec vocal phrase

4.1 Algorithm

- Step-1:** The digitized version of these songs with a length of 8 s from the beginning of the vocal phrase has been taken.
- Step-2:** The acoustic input must go through a low-pass filter at 1047 Hz to cut down unwanted high-frequency components.
- Step-3:** Different notes can be obtained from the low-frequency signal of a song for a singer after using pitch tracking and pitch smoothing methods.
- Step-4:** Calculate the probability of significance (p) for M_L for pair of singers of each song for the comparative study of the melody of voice between two singers. If the value of $p < 0.05$, then there is a significant difference between the singers of that song.

5 Results and Discussions

Table 2 shows the value of probability of significance (p) as found by one-way ANOVA using SPSS software for index of melody (M_L) for pair of singers for each song as given in Table 1 for the comparative study. From this Table 2, it is seen that there is a significant difference of M_L as $p = 0$ for DB and HM, $p = 0$ for DB and PKM, $p = 0$ for HM and PKM for song no. 1 and same for song no. 2, 3, and 5. There is no significant difference of M_L between BS and SaS as $p = 0.905$ for song no. 4 but there is a significant difference of M_L as $p = 0$ for BS and MC, $p = 0$ for MC and SaS for song no. 4.

Table 2 Values of p between two singers for M_L

Song No.	Name of song	Singer's name	Singer's name	p Value
01	Aamar Bhanga Pather	DB	HM	0.000
			PKM	0.000
		HM	PKM	0.000
02	Aamar Je Din	CC	DB	0.000
			PKS	0.000
		DB	PKS	0.000
03	Aamar Jibano Patra	CC	HM	0.000
			MD	0.000
		HM	MD	0.000
04	Aamar Mon Bole	BS	MC	0.000
			SaS	0.905
		MC	SaS	0.000
05	Aamar Priyar Chaya	DB	HM	0.000
			PKM	0.000
		HM	PKM	0.000

6 Conclusion

In the present work, pitch tracking and pitch smoothing methods-based statistical analysis have been performed for exploring the singers' melody of voice for a set of songs of poet Rabindranath Tagore sung by different renowned singers. Index of melody has been estimated by the value of semitone for each song. The value of probability of significance calculated by using one-way ANOVA has been considered for the comparative study of melody of voice of the singers, and the results have been shown. It is evident from these results that there are significant differences in almost all the cases between the singers of same song by poet Rabindranath Tagore. It is also observed that the probability of significance is a reliable predictor of difference between two singers' melody of voice, and the present algorithm based on statistical analysis provides the information of differences of singer's melody of voice of the considered set of song data.

Acknowledgements The present research is a part of the Language Project ambit of the Science and Heritage Initiative (SANDHI), IIT Kharagpur (Web site: www.iitkgpsandhi.org).

References

1. Mazzoni, D. and Dannenberg, R.B., Melody Matching Directly From Audio. in 2nd Annual International Symposium on Music Information Retrieval, (2001), Indiana University, 17–18.
2. Francis Nolan, "Intonational equivalence: an experimental evaluation of pitch scales", proceedings of the 15th International Congress of Phonetic Sciences, pp 771–774, Spain 2003.

3. Rabiner L. R. "On the Use of Autocorrelation Analysis for Pitch Detection". IEEE Transactions on ASSP, vol. 25, pp. 24–33, 1977.
4. Pitton J. W. and Atlas L. E., "Discrete-Time Implementation of the Cone-Kernel Time-Frequency Representation". IEEE Transactions on Signal Processing, vol. 43, no. 8, pp. 1996–8, Aug. 1995.
5. Kunieda N., Shimamura T., and Suzuki J. "Robust Method of Measurement of Fundamental Frequency by ACOLS-autocorrelation of log Spectrum". IEEE Int. Conf. on Acoustics, Speech, and Signal Processing, vol. 1, Atlanta, GA, pp. 232–235, May 1996.
6. R. J. McNab, L. A. Smith, D. Bainbridge, and I. H. Witten, "The New Zealand digital library melody index," D-Lib Magazine, vol. 3, no. 5, pp. 4–15, 1997.
7. D. Talkin, A robust algorithm for pitch tracking (RAPT), Speech Coding and Synthesis, Elsevier Science, (1995) pp. 495–518.
8. M. J. Ross, H. L. Shaffer, A. Cohen, R. Freudberg, and H. J. Manley, IEEE Trans. on Acoustics, Speech, Signal Processing 22, 353 (1974).
9. J. R. Deller, J. G. Proakis, J. H. L. Hansen, "Discrete time processing of speech signals," New York: Macmillan Pub. Co., 1993.
10. Jyh-Shing Roger Jang, Ming-Yang Gao, "A Query-by-Singing System based on Dynamic Programming 1", International Workshop on Intelligent Systems Resolutions, PP. 85–89, Hsinchu, Taiwan, Dec 2000.
11. Sabine Landau and Brian S. Everitt, "A Handbook of Statistical Analyses Using SPSS", Chapman & Hall/CRC Press, 2004.
12. Akira Sasou, "Singing voice recognition considering high-pitched and prolonged sounds", 14th European Signal Processing Conference, 2006.
13. www.aboutmusictheory.com/melody-shape.html.
14. R. Foucard, J.-L. Durrieu, M. Lagrange, and G. Richard, "Multimodal similarity between musical streams for cover version detection," in Proc. ICASSP, Dallas, TX, Mar. 2010, pp. 5514–5517.
15. Meinard Müller, Daniel P. W. Ellis, Anssi Klapuri, and Gaël Richard, "Signal Processing for Music Analysis" IEEE Journal of Selected Topics In Signal Processing, Vol. 5, No. 6, October 2011.
16. Thomas F. Quatieri, "Discrete-Time Speech Signal Processing", Pearson, 2006.
17. L.R. Rabiner and R. W. Schafer, "Digital Processing of Speech Signals", Pearson Education, 2004.
18. Sadaoki Furui, "Digital Speech Processing, Synthesis and Recognition", Marcel Dekker Inc., 2001.

Image Contrast Enhancement Using Differential Evolution

Anil Singh Parihar, Om Prakash Verma and Deepanshu Yadav

Abstract This paper presents an optimal fuzzy system for image contrast enhancement using differential evolution. The algorithm uses different fuzzification functions for underexposed and overexposed regions of the image. After fuzzification, both of these regions namely underexposed and overexposed are modified using a fuzzy intensification (FINT) operator and power-law, respectively. The fuzzy values are defuzzified using inverse of the membership functions to get enhanced image. An objective function based on histograms of the input and enhanced image is formulated and used in differential evolution algorithm to get the optimized enhancement. The evaluation of the proposed algorithm is evaluated visually as well as quantitatively. The comparison with existing algorithms establishes the supremacy of the proposed algorithm.

Keywords Contrast enhancement · Exposure · Fuzzy · Differential evolution

1 Introduction

The most important preprocessing step in any image-based application is image contrast enhancement. Contrast enhancement brings out the otherwise hidden details of the images. A lot of contrast enhancement algorithms exist in the literature. Histogram equalization (HE) [1] one is the most popular as well as simple contrast enhancement algorithm. However, it has some serious drawbacks such as

A. S. Parihar (✉) · O. P. Verma · D. Yadav
Department of Computer Science & Engineering,
Delhi Technological University, Delhi, India
e-mail: parihar.anil@gmail.com

O. P. Verma
e-mail: opverma.dce@gmail.com

D. Yadav
e-mail: rohantheyadav@gmail.com

under-enhancement and over-enhancement, saturation effects. There have been several attempts to overcome these issues. Contrast limited adaptive histogram equalization (CLAHE) [2] proposed that the peaks of the histogram should be suppressed to avoid saturation. Chen and Ramli [3] performed recursive division of the histogram of the input image on the basis of mean intensity. The contrast enhancement can be done by equalizing each such sub-histogram separately. In dynamic histogram equalization (DHE) [4], the histogram is divided at local minima and each of the sub-histogram is allocated a new dynamic range based on the number of pixel in it. Arici et al. [5] proposed a framework for image contrast enhancement. This framework uses the fact that for a good contrast enhancement the histogram should be uniform but it should not deviate much from the input characteristics of the image. Celik et al. [6] used a two-dimensional histogram to incorporate the local characteristics of the image. Singh et al. [7] proposed a new histogram equalization approach using only texture region.

Fuzzy theory finds many applications in contrast enhancement algorithms. In brightness preserving dynamic fuzzy histogram equalization (BPDFHE), the input histogram is fuzzified to get the smoother histogram. Hanmandlu and Jha [8] proposed fuzzy measures and used these measures to get the optimal contrast enhancement. Evolutionary algorithms are used in many cases to get optimal contrast enhancement. Hanmandlu et al. [9] presented an optimal fuzzy system (OFSBA) using bacterial foraging algorithm (BFA) [10] to get the optimal contrast enhancement. Kwok et al. [11] used particle swarm optimization (PSO) [12] and preserve the intensity of a pixel which gets modified during enhancement.

In this paper, we present a new contrast enhancement algorithm using fuzzy theory differential evolution (DE) [13]. This work is a modification to OFSBA. OFSBA works well for low exposure images, but fails to give significant contrast enhancement for other low contrast images. We used a fuzzy intensification operator (FINT) and a histogram-based optimization function to improve the performance for nearly all type of images. The DE is used to get the optimal contrast enhancement. The organization of the rest of the paper is as follows: Sect. 2 presents the proposed approach, Sect. 3 presents result and analysis, and Sect. 4 presents the conclusion of the work.

2 Proposed Approach

Sometimes darker and brighter regions may be present in the same image. Thus, applying same approach to the entire image may not give the desired contrast. In underexposed and overexposed regions, most of the pixels belong to lower part and upper part of the dynamic range, respectively. The image regions may be divided into two categories by using the exposure [9] of the image. The exposure is defined as:

$$\text{exposure} = \frac{1}{L} \sum_{k=0}^{L-1} p(r_k) \cdot r_k \tag{1}$$

where r_k is the k th gray-level value of the image, $p(r_k)$ is the histogram of image, and L is the total number of gray levels. The parameter “exposure” is normalized in the range $[0, 1]$. The image regions are divided using an exposure threshold of 0.5, i.e., region with exposure value more than 0.5 is considered overexposed and below 0.5 underexposed. It is experimentally analyzed that image with pleasing visual quality has exposure value close to 0.5. Thus, the images with spatially varying exposure are divided into the underexposed and overexposed regions. The threshold for histogram division based on the exposure is given as:

$$a = L(1 - \text{exposure}) \tag{2}$$

Thus, the input image is divided into two categories: $[0, a - 1]$ for underexposed image regions and $[a, L - 1]$ for overexposed image regions.

2.1 Fuzzification

After dividing the image histogram into underexposed and overexposed regions, it is fuzzified using two different membership functions. The former region is fuzzified with a modified Gaussian membership function defined as [8]:

$$\mu_U(r_k) = \exp \left\{ - \left[\frac{(r_k - r_{k_{\max}})}{\sqrt{2}f_h} \right]^2 \right\} \tag{3}$$

where r_k is the k th the gray level of the underexposed region in the range $[0, a - 1]$, and $r_{k_{\max}}$ is the maximum intensity level present in the image. The parameter f_h is the fuzzifier, and its initial value is computed as:

$$f_h^2 = \frac{1 \sum_{k=0}^{L-1} (r_k - r_{k_{\max}})^4 p(r_k)}{2 \sum_{k=0}^{L-1} (r_k - r_{k_{\max}})^2 p(r_k)} \tag{4}$$

The latter is fuzzified using a triangular membership function defined as:

$$\mu_O(r_k) = \begin{cases} 0, & \text{if } x \leq a \\ \frac{r_k - a}{L - a}, & \text{else } x > a \end{cases} \tag{5}$$

2.2 Modification

The fuzzy membership values obtained in the previous step are modified to achieve the contrast enhanced image. A fuzzy intensifier (FINT) [14] is used for modification of fuzzy values which correspond to underexposed regions of the image. The FINT is defined as:

$$\mu'_U(r_k) \begin{cases} \alpha(\mu_U(r_k))^\beta, & \text{if } (\mu_U(r_k) < 0.5) \\ 1 - \alpha(1 - \mu_U(r_k))^\gamma, & \text{else} \end{cases} \quad (6)$$

where α , β , and γ follow the constraint as follows

$$\alpha^{-1} = 2^{-\beta} + 2^{-\gamma} \quad (7)$$

The fuzzy values corresponding to overexposed regions are modified using following power-law function to adjust the contrast in these regions

$$\mu'_O(r_k) = \max(\mu_O(r_k)) \left(\frac{\mu_O(r_k)}{\max(\mu_O(r_k))} \right)^\delta \quad (8)$$

2.3 Defuzzification and Image Enhancement

The enhanced image can be obtained by defuzzifying the modified fuzzy values. The defuzzification is performed using the inverse of the earlier equations which were used to fuzzify the image.

$$r'_{k_\mu} = \mu_U^{-1} [\mu'_U(r_k)] \quad (9)$$

$$r'_{k_o} = \mu_O^{-1} [\mu'_O(r_k)] \quad (10)$$

New modified histogram is achieved by combining values from both regions as follows

$$r'_k = \begin{cases} r'_{k_\mu}, & \text{for } 0 \text{ to } a - 1 \\ r'_{k_o}, & \text{for } a \text{ to } L - 1 \end{cases} \quad (11)$$

The modified histogram is used for mapping between low contrast image and enhanced image. The fuzzification and modification process involves many parameters, which need to be selected for each image. However, manual selection is not feasible for obtaining good contrast images each time. Thus, the DE is used to get the optimized values of these parameters.

3 Optimization

The parameters α , β , δ , and f_h control the shape of the membership function and its membership values. Thus, an optimal value of these parameters will result in optimal contrast enhancement. The DE algorithm is used for optimizing these parameters. The DE algorithm is briefly presented in Appendix A for easy reference. The values of DE parameters used in works are shown in Table 1.

The objective function for optimization using DE is formulated as follows:

$$J = \sum_{k=0}^{L-1} (h_i(k) - h_o(k))^2 + \lambda \sum_{k=0}^{L-1} (h_o(k) - g)^2 \quad (12)$$

where h_i is input histogram, h_o is histogram of the enhanced image in previous step, and g is the uniformly distributed histogram. The objective function is based on the fact that for good contrast enhancement histogram needs to be uniformly distributed, i.e., maximum contrast can be achieved if each intensity is present with equal probability. However, the originality of the histogram should not be much compromised. The first term denotes how much the new histogram is deviated from the original histogram, and the second term denotes how much the new histogram is deviated from the uniformly distributed histogram. λ functions as a trade-off between the two. Its suitable value can be found by running the algorithm various times. The values of parameters α , β , δ , and f_h can be obtained by DE algorithm which performs search in five-dimensional search space. The overall algorithm is summarized as follows:

1. Input the given image and convert RGB to HSV.
2. Calculate the input histogram $p(x)$, where $x \in V$.
3. Obtain the values of exposure as well as using (1) and (2), respectively.
4. Set the bounds on the parameters α , β , γ , f_h using the constraint given in (7).
5. Learn the value of α , β , γ , f_h using differential evolution algorithm with objective function given in (12).
6. Using above parameters, fuzzify V to get $\mu_U(r_k)$ and $\mu_O(r_k)$ using (3) and (5), respectively.
7. Modify membership values $\mu'_U(r_k)$ and $\mu'_O(r_k)$ for the underexposed region and the overexposed region using (6) and (8), respectively.
8. Defuzzify the values obtained in previous step for $\mu'_U(r_k)$ and $\mu'_O(r_k)$ by using the inverse MFs defined in (9) and (10), respectively.
9. Based on the value of a , obtain the enhanced intensity V' using (11).
10. Display the enhanced HSV image.

Table 1 Values of DE parameters

Parameter	Value
Initial population (N)	100
Crossover ratio (CR)	0.2
Maximum number of iterations	20

4 Result and Analysis

The proposed algorithm is tested on a large set of images from Berkeley [15] image database and CSIQ image database [16]. The proposed method is compared with existing contrast enhancement methods namely HE [1], CLAHE [2], BPDFHE [17], OFSBA [9]. The algorithms are implemented with default parameters as suggested by corresponding authors. The performance of the algorithms is analyzed visually and quantitatively as well.

4.1 Visual Assessment

The contrast is a subjective quality of the image. Thus, the visual analysis is performed for all the resulting images by various algorithms. The visual analysis of few sample images is presented here. In Fig. 1, the “bird” image and its enhanced images by various algorithm are shown. It may be noticed that HE, BPDFHE, and CLAHE introduce distortions especially in the sky region due to saturation. OFSBA gives slightly better color preservation, but contrast is not much improved. The proposed algorithm gives good contrast enhancement with naturally looking colors. In Fig. 2, lighthouse again HE and BPDFHE show the saturation artifacts and degrade image quality. CLAHE gives slightly better contrast, but artifacts may be noticed around cloud region. OFSBA once again gives brighter image, but slightly lesser contrast. The proposed algorithm results in good contrast image.

It may be noticed from Fig. 3 monument BPDFHE and OFSBA fail to give significant contrast and degrade the visual quality of the image. HE and CLAHE give good contrast, but artifacts may be noticed in the corner regions. The proposed algorithm once again results in good contrast natural quality image. Figure 4 named Cactus shows HE, BPDFHE show saturation artifacts and degrade the image quality. OFSBA produces extremely bright image, which results in faded looking image. CLAHE gives slightly better contrast, but few artifacts near corner may be noticed. The proposed algorithm produces good contrast image with almost no artifacts. Thus, the visual analysis shows that the proposed algorithm produces images with good contrast and also retains their natural characteristics.



Fig. 1 Contrast enhancement results of “lighthouse” image by different algorithms: **a** original, **b** HE, **c** BPDFHE, **d** CLAHE, **e** OFSBA, **f** proposed

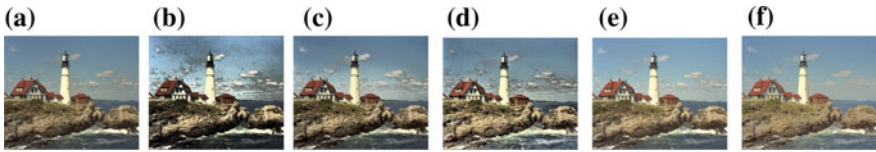


Fig. 2 Contrast enhancement results of “lighthouse” image by different algorithms: a original, b HE, c BPDFHE, d CLAHE, e OFSBA, f proposed

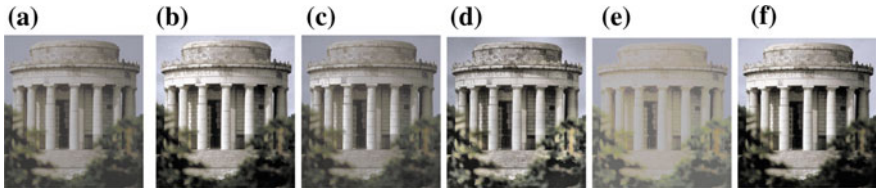


Fig. 3 Contrast enhancement results of “monument” image by different algorithms: a original, b HE, c BPDFHE, d CLAHE, e OFSBA, f proposed

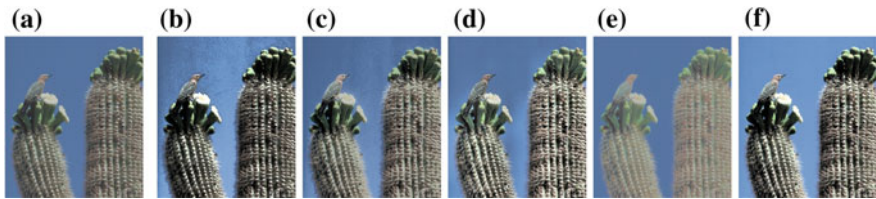


Fig. 4 Contrast enhancement results of “cactus” image by different algorithms: a original, b HE, c BPDFHE, d CLAHE, e OFSBA, f proposed

4.2 Quantitative Assessment

The contrast is a subjective quality, and it is difficult to define a parameter that determines the level of enhancement of the image. However, it is always desirable to have a quantitative measure for the validation of a scientific research. There have been various attempts such as image quality assessment [18], EME. In this work, we use a universal image quality (UIQ) index [19] which proposes a universal index for evaluating contrast enhancement. Higher value of the index corresponds to better contrast enhancement. Images which are pleasing to view have quality index greater than 0.9. The UIQ values are computed for all the images produced by various comparing algorithm and the proposed algorithm. Table 2 shows the UIQ metric for sample images using different algorithms. The highest values for each image are highlighted in bold. In most of the cases, the proposed algorithm gives highest UIQ values. Thus, the quantitative assessment of the various algorithms establishes supremacy of the proposed algorithm.

Table 2 UIQ values for various algorithms

Image	HE	BPDFHE	CLAHE	OFSBA	Proposed
Bird	0.4542	0.6391	0.6239	0.7788	0.9369
House	0.5309	0.6681	0.8196	0.7463	0.9643
Cactus	0.5162	0.6772	0.6561	0.5619	0.9685
Monu	0.7088	0.6505	0.8633	0.5966	0.9675
Statue	0.8302	0.8991	0.7458	0.9359	0.9563
Stone	0.8173	0.9235	0.7214	0.8621	0.9583
Builds	0.7365	0.9065	0.7217	0.8335	0.9058
Buffalo	0.8127	0.9256	0.7356	0.9161	0.9069
Friends	0.7539	0.9344	0.7151	0.8916	0.9646
Boat	0.9281	0.9211	0.6798	0.9030	0.9319

5 Conclusion

We presented a contrast enhancement algorithm using fuzzy theory and differential evolution. The algorithm uses histogram characteristics of input image and uniformly distributed histogram to achieve desired contrast. The proposed algorithm improves contrast as well as characteristics of the given image. The algorithm is tested on various images from Berkeley image database and CSIQ image database. The comparison with existing algorithms establishes the supremacy of the proposed algorithm.

Appendix A: Differential Evolution

It is a evolutionary algorithm which comprises of three steps

The Differential Evolution Algorithm is given as follows:

Generate the initial population of individuals.

repeat

For each individual j in the population

Choose n_1, n_2 and n_3 such that $1 \leq n_1, n_2, n_3 \leq N$ with $n_1 \neq n_2 \neq n_3 \neq j$

Generate a Random integer $j_{\text{rand}} \in (1, N)$

For each parameter i

$$y^{i,g} = x^{n_1,g} + F(x^{n_2,g} - x^{n_3,g})$$

$$z^{i,g} = \begin{cases} y^{i,g} & \text{if rand() < CR or } j = j_{\text{rand}} \\ x^{i,g} & \text{otherwise} \end{cases}$$

END FOR

Replace $x^{i,g}$ with the child $z^{i,g}$ if the child is better

END FOR

until Termination condition is reached

A.1 Mutation

This step expands the search space as follows: Choose n_1 , n_2 , and n_3 such that $1 \leq n_1, n_2, n_3 \leq N$ with $n_1 \neq n_2 \neq n_3 \neq j$.

A.2 Recombination

Recombination incorporates successful solutions from the previous generation. The details are:

$$z^{i,g} = \begin{cases} y^{i,g} & \text{if rand() < CR or } j = j_{\text{rand}} \\ x^{i,g} & \text{otherwise} \end{cases}$$

A.3 Selection

Replace $x^{i,g}$ with the child $z^{i,g}$ if the child is better. This ensures that one with lowest function value is admitted in the next generation.

References

1. R. C. Gonzalez and R. E. Woods, Digital image processing. Pearson Education India, 2009.
2. K. Zuiderveld, "Contrast limited adaptive histogram equalization," in Graphics gems IV. Academic Press Professional, Inc., 1994, pp. 474–485.
3. S.-D. Chen and A. R. Ramli, "Contrast enhancement using recursive mean-separate histogram equalization for scalable brightness preservation," IEEE Transactions on Consumer Electronics, vol. 49, no. 4, pp. 1301–1309, 2003.
4. M. Abdullah-Al-Wadud, M. H. Kabir, M. A. A. Dewan, and O. Chae, "A dynamic histogram equalization for image contrast enhancement," IEEE Transactions on Consumer Electronics, vol. 53, no. 2, pp. 593–600, 2007.
5. T. Arici, S. Dikbas, and Y. Altunbasak, "A histogram modification framework and its application for image contrast enhancement," IEEE Transactions on image processing, vol. 18, no. 9, pp. 1921–1935, 2009.
6. T. Celik, "Two-dimensional histogram equalization and contrast enhancement," Pattern Recognition, vol. 45, no. 10, pp. 3810–3824, 2012.
7. Singh, D. K. Vishwakarma, G. S. Walia, and R. Kapoor, "Contrast enhancement via texture region based histogram equalization," Journal of Modern Optics, pp. 1–7, 2016.
8. Hanmandlu and D. Jha, "An optimal fuzzy system for color image enhancement," IEEE Transactions on image processing, vol. 15, no. 10, pp. 2956–2966, 2006.
9. Hanmandlu, O. P. Verma, N. K. Kumar, and M. Kulkarni, "A novel optimal fuzzy system for color image enhancement using bacterial foraging," IEEE Transactions on Instrumentation and Measurement, vol. 58, no. 8, pp. 2867–2879, 2009.
10. K. M. Passino, "Biomimicry of bacterial foraging for distributed optimization and control," IEEE control systems, vol. 22, no. 3, pp. 52–67, 2002.

11. N. M. Kwok, Q. P. Ha, D. Liu, and G. Fang, "Contrast enhancement and intensity preservation for gray-level images using multiobjective particle swarm optimization," *IEEE Transactions on Automation Science and Engineering*, vol. 6, no. 1, pp. 145–155, 2009.
12. J. Kennedy, "Particle swarm optimization," in *Encyclopedia of machine learning*. Springer, 2011, pp. 760–766.
13. P. Civicioglu, "Transforming geocentric cartesian coordinates to geodetic coordinates by using differential search algorithm," *Computers & Geosciences*, vol. 46, pp. 229–247, 2012.
14. A. S. Parihar, O. P. Verma, and C. Khanna, "Fuzzy-contextual contrast enhancement," *IEEE transactions on image processing*, vol. Accepted for publication, 2016.
15. P. Arbelaez, M. Maire, C. Fowlkes, and J. Malik, "Contour detection and hierarchical image segmentation," *IEEE transactions on pattern analysis and machine intelligence*, vol. 33, no. 5, pp. 898–916, 2011.
16. E. C. Larson and D. M. Chandler, "Most apparent distortion: full-reference image quality assessment and the role of strategy," *Journal of Electronic Imaging*, vol. 19, no. 1, pp. 011 006–011 006, 2010.
17. D. Sheet, H. Garud, A. Suveer, M. Mahadevappa, and J. Chatterjee, "Brightness preserving dynamic fuzzy histogram equalization," *IEEE Transactions on Consumer Electronics*, vol. 56, no. 4, pp. 2475–2480, 2010.
18. Z. Wang, A. C. Bovik, H. R. Sheikh, and E. P. Simoncelli, "Image quality assessment: from error visibility to structural similarity," *IEEE transactions on image processing*, vol. 13, no. 4, pp. 600–612, 2004.
19. Z. Wang and A. C. Bovik, "A universal image quality index," *IEEE signal processing letters*, vol. 9, no. 3, pp. 81–84, 2002.

Optical Character Recognition Using Minimal Complexity Machine and Its Comparison with Existing Classifiers

O. P. Verma, Eshwar Agarwal, Cherry Agrawal and Avanti Gupta

Abstract Optical character recognition is an important field of research with widespread applications. Researchers have endeavored to replicate the human ability to read printed text, and extensive research has been carried out. In this paper, we recognize optical characters using a recently proposed classifier minimum complexity machine (MCM). To aid in performance analysis, with existing classifiers we have compared the results obtained from MCM with results from support vector machine (SVM) and k -nearest neighbor (k -NN). A common dataset for testing and training was used throughout to determine the accuracy and time taken for testing. Principal component analysis has been used to obtain a reduced set of features prior to the training and testing process. An analysis of the effect of the number of components on the accuracy of minimum complexity machine, support vector machine, and k -nearest neighbor has been provided as well. It was noted that minimum complexity machine has given accuracy comparable to that of the existing classifier though the time taken for testing was substantially reduced.

Keywords Minimal complexity machine · k -nearest neighbor · Support vector machine · Principal component analysis · Optical character recognition

O. P. Verma (✉) · E. Agarwal · C. Agrawal (✉) · A. Gupta
Delhi Technological university, Delhi, India
e-mail: opverma.dce@gmail.com

C. Agrawal
e-mail: cherryagrawal17@gmail.com

E. Agarwal
e-mail: eshwar1995@gmail.com

A. Gupta
e-mail: avanti.gupta95@gmail.com

1 Introduction

Humans are naturally wired to identify and categorize objects in different classes. Humans employ this cognition to identify various characters that occur across different languages. There has been intensive research to replicate this capability of humans in machines for a very long time now. Many commercial establishments have manufactured recognizers of varying capabilities as well [1]. This technique is commonly known as optical character recognition (OCR) and finds widespread use across various fields. Some of the commonly used applications include image-invoicing, captcha, institutional repository, scanning of paper documents, handwriting recognition, and digit recognition and optical music recognition [2]. Optical character recognition involves two steps, i.e., 1. preprocessing and feature extraction and 2. classification.

Firstly, the image is preprocessed to eliminate noise segment if necessary, and features are extracted. Segmentation and noise elimination may especially be useful when the images are obtained from real-life scenarios. Extraction of features from a dataset helps to reduce dimensionality of the database while retaining its characteristics. We have used principal component analysis [3] for the purpose of feature extraction. PCA is a statistical technique that uses the theory of linear transformations and reduces the dimensions of a vector. The eigenface approach is being employed for face recognition problem since it is computationally effective in terms of speed, accuracy, and convenience. Secondly, the preprocessed image is fed to a classifier that finds a class to which the preprocessed object belongs to.

Classifiers are supervised learners that require a training set of correctly labeled inputs. The common classifiers in use include neural networks, support vector machines, K-means [4], minimum distance classifier. Each classifier has its associated advantages and disadvantages. We have classified optical characters with the minimum complexity machines that were proposed by Jayadeva [5]. Support vector machines thus produce respectable results; however, the VC dimensions can be unbounded. Here, MCM a hyperplane classifier can be used to minimize an exact or Θ bound on its VC dimension. The implementation of the machine involves solving a simple linear programming problem.

We have implemented support vector machines [6] and k-nearest neighbors [7] for recognizing the characters also. Support vector machines create maximum margin hyperplanes for classifying whether the test image belongs to a class or not [8]. k-nearest neighbor classifies the test image on the basis of the closest sample in the training space.

All the classifiers were compared on the basis of accuracy as well as the average time taken to test each image. The variation in the results of the classifier with a change in the number of principal components was also recorded. For the purpose of uniformity, all the experiments were carried out on a standardized database that contained the multiple common ways to denote a character in different fonts and typographical emphasis.

Thus to sum up the contribution of the paper:

1. Implement optical character recognition using PCA and MCM.
2. Implement optical character recognition using SVM and k-NN.
3. Comparison of the result of SVM and k-NN with those from MCM.
4. Ascertain the effect of changes in the number of principal components on the accuracy of the classifiers.

2 Related Work

Paul and Suman have highlighted the use of PCA for face recognition [9]. In their research work, Ilin and Raiko have attributed the mathematical properties and their importance in PCA [10]. Dhanda has thrown light upon the eigenface approach of PCA and how it can be employed conveniently for face recognition [11]. Kumar, Jindal, and Sharma have used a PCA-based system for handwritten optical character system and provided results for the variation of accuracy with PCA components [3]. Bag and Harit have given a detailed survey of OCR on Indian scripts [12] (Fig. 1).

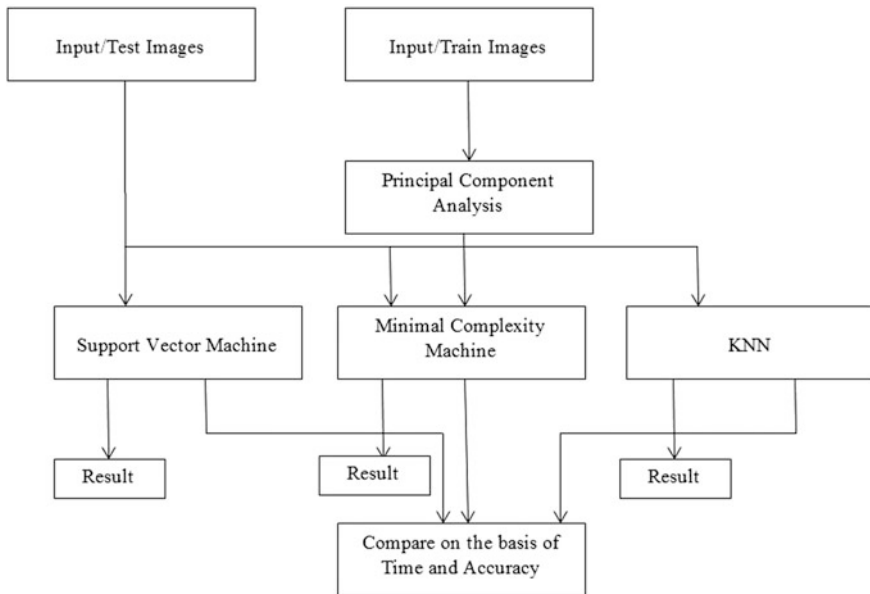


Fig. 1 Flowchart of general procedure [13]

3 Preprocessing and Principal Component Analysis

In this, we have used the Chars74K image dataset in which the images are already processed and the application of any filter like Gaussian filter, median filter, mean filter did not resulted in minor change in accuracy. However, in case of images obtained from real-life sources which have large amount of noise such filtering may be necessary, an example of such character are given in the Chars74K [14] image dataset.

We have binarized the images for the purpose of classification by using `imbinarize()` function of MATLAB. `imbinarize()` creates binary image from the original image by using a thresholding method. It sets all the values above a globally determined threshold value to 1, and all other values to 0. It is basically a step in the preprocessing of images. This process resulted in increase of accuracy of classification by 3–4% points.

Principal component analysis is a statistical [9] procedure for reducing the dimensions in a vector. In face recognition, it reduces the number of variables. It is a classical data analysis technique, employed for finding linear [10] transformations that retain the maximum variance. In the case of face recognition, we use PCA with eigenface [11] approach due to its simplicity, speed, and accuracy.

Algorithm:

1. Consider M images of $N \times N$ matrix, each representing pixel intensities in the matrix form.
2. Convert them into $N \times 1$ matrix. For converting the 2-D matrix into a 1-D row matrix, each element is column-wise inserted from the original $N \times N$ matrix to a single row matrix.
3. Find average image of all the m training images and subtract this from each image.
4. Find covariance matrix X .
5. Find eigenvectors of matrix X and find eigenfaces.
6. Take ' k ' columns from the eigenface matrix corresponding to k highest eigenvalues.
7. Now find weight matrix for each image.

Now, we get a $k \times M$ weight matrix W corresponding to M images in training sample where one column represents features of one image.

4 Support Vector Machine

The support vector machine (SVM), proposed by Cortes and Vapnik [6], is a supervised learning model that generates input–output mapping functions from a set of labeled training data. It has found wide use in varied application and has proved

to be fairly noteworthy in its performance [8]. We have used the binary variant of support vector machine. The SVM is first trained on a large dataset with varied writing styles for the same character. A one-versus-all approach has been employed to check whether the given test element belongs to this class or not. If it belongs to a particular class, it is classified else the procedure is repeated with the next class.

For the implementation of SVM, the following steps were carried out.

4.1 Training

1. The images were fed to the standard function SVM train in MATLAB.
2. As part of the one-versus-all approach for a hyperplane corresponding to a class, the training data associated with the class were located the value of 1, while the rest were given the value of 0.
3. This was repeated for one less than the total number of classes.

4.2 Testing

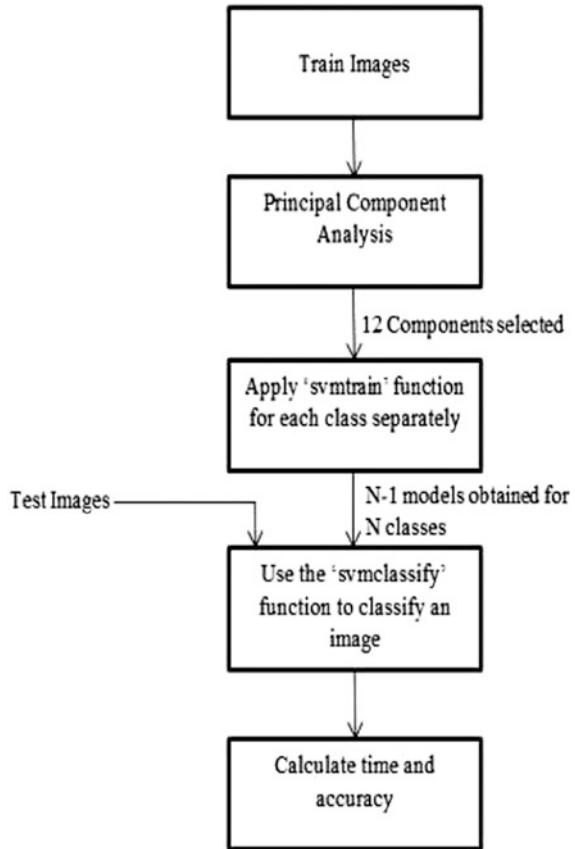
1. The representative weight for the test image is calculated.
2. It is fed to the standard function SVM classify corresponding to each hyperplane.
 - a. *If the test image is classified (i.e., 1 is returned) to a particular class, the process is terminated.*
3. In case it is classified to none of the hyperplanes, it belongs to the last class (Fig. 2).

5 k-Nearest Neighbor Algorithm

k-NN stands for k-nearest neighbor [7] and is a nonparametric method used for classification and regression algorithms. This algorithm is used to classify the object based on the closest training examples in the training space. k-NN is a lazy instance-based learning where the function is approximated early and all the computation is deferred until classification. The value of the k in k-NN is set depending upon the classification problem. If the classification of the sample is unknown, it could be predicted by the classification of its samples with k-nearest neighbors.

For the implementation of the k-NN, the following steps were carried out:

Fig. 2 Flowchart of SVM code



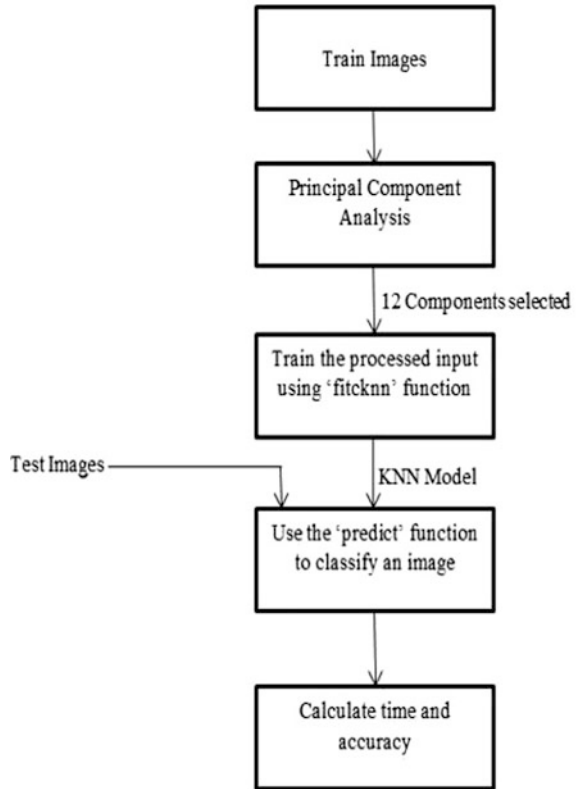
5.1 Training

1. The images were fed to the standard function fitcknn in MATLAB.
2. This function creates the k-NN model and calculates the Euclidian distance between the training images.
3. The step 2 is repeated for every other image.

5.2 Testing

1. The representative weight for the test image is calculated.
2. It is fed to the standard predict function corresponding to each test image.
3. The class of the test image is recorded (Fig. 3).

Fig. 3 Flowchart of k-NN code



6 Minimal Complexity Machine

The VC dimension measures the complexity of a learning machine, and a low VC dimension leads to good generalization. VC dimension of SVM, a hyperplane classifier, is unbounded, and there is no guarantee of good generalization. In fact, as suggested by Burges [15], presently there exists no method to advocate a good performance for the support vector machines. Here, we have implemented the minimal complexity machine (MCM) which was recently proposed.

MCM is also a linear hyperplane classifier like SVM but gives better generalization than SVM by minimizing an exact bound on VC dimension.

Jayadeva [5] has proved MCM is all about solving the following optimization problem:

$$\min_{\Theta, b} y_i [\Theta^T x^j + b]$$

$$y_i [\Theta^T x^i + b] > = 1 \quad \forall i = 1, 2, \dots, m$$

For an unknown variable x , sign of $\Theta^T x + b$ determines the output class.

An advantage of MCM being a linear classifier is that it has comparable accuracy as compared to nonlinear classifier but consumes less time in the classification process. This approach learns classifier with error rates much less than that of the SVMs while often using less support vectors which is one-tenth of that used in SVM.

It is to be noted that MCM is a binary classifier and optical character recognition happens to be a multiclass problem we have classified the characters using one-versus-all approach. Though we have explored MCM as a linear classifier, it can be extended to least square classifiers and for usage as a regression machine.

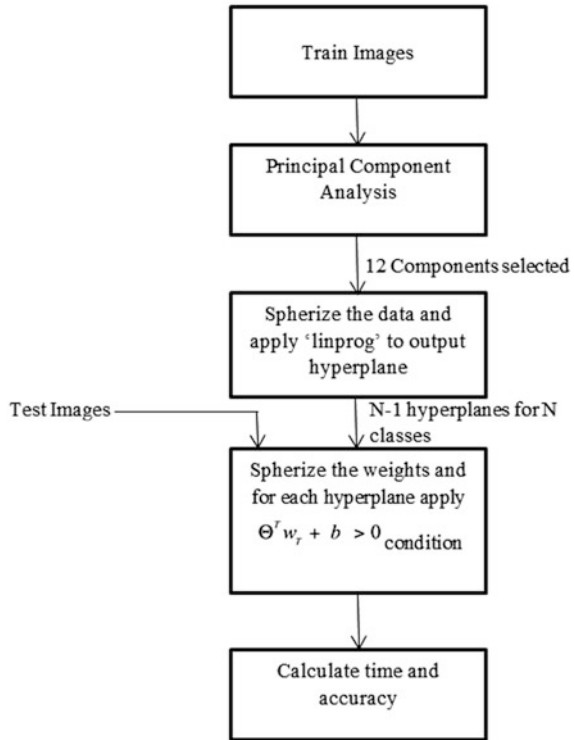
6.1 Training

1. Training inputs to MCM are just like SVM. Subtract mean and divide by variance to spherize the data.
2. In one-versus-all approach of multiclass classification, We separate a class from all other classes. For separating class 'X' from the rest, we feed output label corresponding to class 'X' as 1 and output label corresponding to all classes except class 'X' as '-1.'
3. Call 'linprog' function of MATLAB to solve the linear programming problem. 'Linprog' will output Θ vector and b . This implies linprog will output hyperplane.
4. Repeat steps 2 and 3 until we get all the hyperplanes. If we have 'Y' number of classes, we repeat step 2 'Y - 1' times.

6.2 Testing

1. Transform test images into their representative weights.
2. Subtract mean and divide by variance to spherize the weights. Say w_T is such $k \times 1$ vector.
3. For (hyperplane number = 1 to 'Y - 1')
4. If $\Theta^T x + b$, break.
 - a. Else continue checking for other hyperplanes (Fig. 4).

Fig. 4 Flowchart of MCM code



7 Dataset

The standard dataset [14] consists of 74,000 images, distributed in 64 different classes, consisting of Latin scripts and Hindu-Arabic numerals. We selected a subset of the original dataset for training and testing purpose. Each class pertains to the capitalized English alphabets. Each training class has 60 images, and each testing class has 20 images, respectively. The same dataset is being fed to different classifiers and forms the database of the complete project (Fig. 5).

Fig. 5 Dataset



8 Experimentation and Result

The project was implemented in MATLAB [16]. Initially, 60 images per class were chosen to train each of the classifiers. The chosen images reflected possible fonts available in various typographical emphases. The images were then fed to PCA for feature extraction. Various numbers of features were chosen to see its effects on the final accuracy. The extracted features of the training images were then fed to each classifier. The classifiers were trained on the training images, and the testing is performed (Table 1).

Formula

Average Testing Time = Testing time for the classifier/Total number of test images

Accuracy = Correct classification by the classifier/Total number of test images.

The program was run iteratively using different number of components for each classifier to find the associated accuracy. Same dataset was used throughout the process to maintain uniformity. It was found that the number of components chosen had substantial effects on the accuracy of the classifiers; i.e., the classifiers were sensitive to the number of components chosen (Fig. 6).

Three different datasets were prepared to compare the accuracy of the classifiers. The classifiers were then run in series on each dataset. The number of PCA components used for this classification was fifteen. The results for accuracy were noted

Table 1 Accuracy based on the number of features extracted

No. of PCA components	Accuracy of SVM	Accuracy of MCM	Accuracy of k-NN
11	96.25	68.75	97.14
12	92.5	85	97.10
13	91.25	80	95.59
14	91.25	92.5	95.52
15	91.25	95	92.42
16	91.25	93.75	92.31
17	91.25	92.5	96.88

Fig. 6 Comparison of accuracy based on the number of features extracted

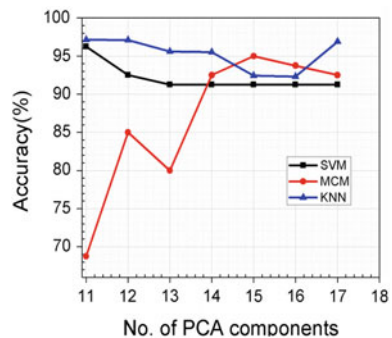


Fig. 7 Plot of time taken by different classifiers

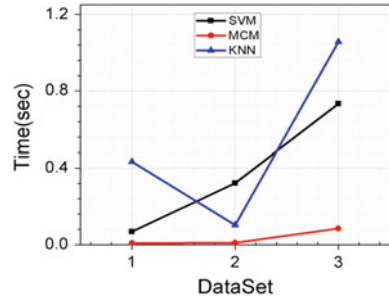


Table 2 Time and accuracy comparison of different classifiers on different datasets

	SVM		MCM		k-NN	
	Accuracy	Time	Accuracy	Time	Accuracy	Time
Dataset 1	91.25	0.069	95.00	0.009	92.42	0.433
Dataset 2	96.25	0.322	92.50	0.0095	89.39	0.102
Dataset 3	95.00	0.733	93.75	0.085	98.51	1.057

and compared. The time taken for testing by each classifier for the three cases was noted as well for comparison (Fig. 7; Table 2).

9 Conclusion

The project was carried out successfully, and desired results within permissible error limits were obtained for all the cases. The number of principal components had substantial effects on the accuracy of all the classifier. It was noted that the results around 15 components were fairly nice for all the classifiers.

The accuracy of all the classifiers on the three datasets was comparable with each classifier giving maximum accuracy for one case. On an average, the accuracy of MCM was 93.67% compared to SVMs 94.16% and k-NNs 93.44%. It is to be noted here that standard optimized functions of SVM and k-NN were used compared to line-by-line implementation of MCM.

On the other hand, the time taken to test by MCM was substantially less as compared to the other two classifiers. On an average, MCM took 0.034 ms to test one image compared to 0.374 ms of SVM and 0.530 ms of k-NN.

10 Future Work

The project can be further optimized using genetic algorithms to obtain better results. The classifiers can also be tested on real-life images like the ones given in the referenced dataset [14] and the classifiers be modified accordingly. Such images

may require more extensive preprocessing. Datasets of various other languages can be used as well. Also, more application of support vector machines can be explored using minimum complexity machines.

References

1. Govindan, V. K., and A. P. Shivaprasad. "Character recognition—a review." *Pattern recognition* 23.7(1990): 671–683.
2. Singh, Amarjot, Ketan Bacchuwar, and Akshay Bhasin. "A survey of OCR applications." *International Journal of Machine Learning and Computing* 2.3 (2012): 314.
3. Kumar, Munish, Manish Kumar Jindal, and Rajendra Kumar Sharma. "PCA-based Offline Handwritten Character Recognition System." *Smart CR* 3.5 (2013): 346–357.
4. Ayodele, Taiwo -Oladipupo. *Types of machine learning algorithms*. INTECH Open Access Publisher, 2010.
5. Jayadeva. "Learning a hyperplane classifier by minimizing an exact bound on the VC dimensions." *Neurocomputing* 149 (2015): 683–689.
6. Cortes, C. & Vapnik, V. *Mach Learn* (1995) 20: 273. <https://doi.org/10.1007/bf00994018>.
7. Imandoust, Sadeq Bafandeh, and Mohammad Bolandraftar. "Application of k nearest neighbor (knn) approach for predicting economic events: Theoretical background." *International Journal of Engineering Research and Applications* 3.5 (2013): 605–610.
8. Wang, Lipo, ed. *Support vector machines: theory and applications*. Vol. 177. Springer Science & Business Media, 2005.
9. Paul, Liton Chandra, and Abdulla Al Sumam. "Face recognition using principal component analysis method." *International Journal of Advanced Research in Computer Engineering & Technology (IJARCET)* 1.9 (2012): 135–139.
10. Ilin, Alexander, and Tapani Raiko. "Practical approaches to principal component analysis in the presence of missing values." *Journal of Machine Learning Research* 11 Jul (2010): 1957–2000.
11. Dhanda, Mamta. "Face Recognition Using Eigenvectors from Principal Component Analysis." *International Journal of Advanced Engineering Research and Studies* 1.2 (2012): 37–39.
12. Bag, Soumen, and Gaurav Harit. "A survey on optical character recognition for Bangla and Devanagari scripts." *Sadhana* 38.1 (2013): 133–168.
13. Duda, Richard O., Peter E. Hart, and David G. Stork. *Pattern classification*. John Wiley and Sons (2012): 5–9.
14. T. E. de Campos, B. R. Babu, M. Varma, "Character recognition in natural images", *Proceedings of the International Conference on Computer Vision Theory and Applications*, February 2009.
15. C. J. Burges, A tutorial on support vector machines for pattern recognition, *Data mining and knowledge discovery* 2 (2) (1998) 121–167.
16. MATLAB, version R2016b, The Math Works Inc., Natick, Massachusetts, 2016.

Performance Analysis of Different Models to Find Value at Risk in the Indian Market Using a Bi-Portfolio Allocation

Om Prakash Verma, Eshwar Agarwal, Cherry Agrawal
and Avanti Gupta

Abstract Risk analysis is one of the most important components of any financial decision and has been a subject of extensive research. We present here a comparative analysis of different methods to calculate value at risk (VaR) in the Indian Market. The models that have been explored are filtered historical simulations, Monte Carlo, historical simulation, and variance–covariance. The implementation was carried out in MATLAB, and the stock indices of NIFTY 50 and BSE SENSEX were used as a representative of the Indian Stock Market. The results obtained were first compared on the basis of time taken to calculate the risk incurred using six different datasets. They were also compared on the basis of whether the actual losses were within the calculated VaRs. A theoretical comparison on the various methods was also performed.

Keywords FHS · HS · Monte Carlo · Variance–covariance VaR
VaR in Indian Market

1 Introduction

It is ingrained in the human nature to evaluate risks that are involved in a certain proposition before reaching any decision. In case of financial dealings, it becomes even more important to weigh the risks as the consequences of an unwise decision can be monetary. Furthermore, over the last few decades, the scope of investment

O. P. Verma (✉) · E. Agarwal (✉) · C. Agrawal (✉) · A. Gupta (✉)
Delhi Technological University, Delhi, India
e-mail: opverma.dce@gmail.com

E. Agarwal
e-mail: eshwar1995@gmail.com

C. Agrawal
e-mail: cherryagrawal17@gmail.com

A. Gupta
e-mail: avanti.gupta95@gmail.com

has increased manifolds with the invention of new financial instruments requiring new objective methods to compute the incurable risks. Also, the recent crash of the financial market in 2008 has increased the importance of such risk calculations. In finance, such a risk is quantified in terms of value at risk (VaR).

Value at risk measures the potential loss in value of a risky asset or portfolio over a defined period for a given confidence interval [1]. So if we invest Rs. 1000 in the Bombay Stock Exchange with a 95% VaR of Rs. 100, then it means the chances of incurring loss of more than Rs. 100 is less than 5%. VaR can be measured using a variety of ways. However, according to a McKinsey report [2], the two of the more popular methods are Monte Carlo (employed by 15% of the banks), historical simulation (employed by 75% of the banks), and the rest (15%) using a hybrid version of the two. However, VaR has also faced criticism as the results are as good as the underlying inputs and assumptions. In fact, the calculated VaR can give a false sense of security by underestimating worst results [3].

The paper has been implemented on the Indian Stock Market characterized using the BSE SENSEX and NIFTY50 stock indices. The Indian Stock Market is one of the dominant markets of the world that attracts a lot of domestic and international investors. The origin of the Indian stock markets can be traced to the time of British, and it has recently seen exponential growth [4]. However, the Indian Market is regarded as more volatile than the markets in developed countries [4]. Bombay Stock Exchange (BSE) launched in 1875 is the first stock exchange in Asia, and its equity index BSE SENSEX (www.bseindia.com) is the most widely tracked benchmark index in India. The National Stock Exchange (NSE) launched in 1994 is the fourth largest in the world by equity trade volumes (www.nseindia.com). NIFTY50 is the popular index associated with NSE.

The paper explores and compares four methods, namely, filtered historical simulations, Monte Carlo approach, historical simulations, and variance–covariance for risk evaluation with a specific emphasis on its adaptability to Indian Market. The former two are more advanced and complex as compared to the latter two. Filtered historical simulation is semi-parametric approach for calculating VaR. It uses historical returns to predict likely incurable loss with a level of confidence. It uses bootstrapping as one of its intermediate steps to lend it a nonparametric nature, while EGARCH provides the parametric nature resulting in overall semi-parametric nature [5].

Monte Carlo simulation is parametric approach and incorporates non linearities of the portfolio values. It creates Monte Carlo simulation trials for all possible occurrences to predict likely incurable loss with a level of confidence. Extreme value theory (GPD) is then used to analyze the tails in order to find the VaR [6].

Historical simulation uses past data to simulate future returns of the given portfolio at the desired confidence levels. It does not make any assumptions about normality like the variance–covariance method does. However, Fat tails can pose a challenge here [7]. Variance–covariance assumes that the returns of a portfolio are normally distributed and exploits the properties of the normal distribution curve to find value at risk [8]. For more than one asset, the value of covariance is incorporated [9].

We have made six datasets by using the daily closing prices of NIFTY50 and BSE SENSEX. Each dataset was run separately for all the approaches and the VaR, and time elapsed to find the VaR was recorded. A graph was plotted for all the approaches to help in comparative analysis. A comparative table based on existing theory and experimentation result was also made.

Thus, the contribution of the paper can be summarized as follows:

1. Implementation of VC, HS, FHS, MC methods to calculate VaR.
2. Evaluation of VaR for NIFTY 50 and BSE SENSEX.
3. Comparison of time required for implementation of datasets of different sizes.
4. Comparison of VaR obtained for different datasets.
5. Theoretical comparison of the methods.

2 Related Work

Extensive research has been carried out in the field of VaR, and various models have been developed. Three approaches are common in finding VaR, i.e., parametric, semi-parametric, and nonparametric [10]. Some of the frequently used models, variance–covariance, historical simulations, and Monte Carlo have been compared by Ćorkalo, Šime [11]. Hull and White [12] have worked to incorporate features of FHS in HS. Barone-Adesi et al. [13] have also worked in improving the HS to take it toward FHS. Ghashang Piroozfar [14] has also published a detailed thesis on comparisons between the nonparametric historical simulations and parameterized historical simulation. Nan Zhang, Ka Lok Man and Eng Gee Lim have worked on multithread programs to find VaR [15]. Hong and Liu [16] have used Monte Carlo to calculate conditional VaR.

3 Filtered Historical Simulation

Filtered historical simulation (shortened as FHS) [5], a semi-parametric approach, i.e., combination of nonparametric and parametric approach, is an advanced version of historical simulation which is a nonparametric approach for calculating value at risk. The FHS method was evolved to overcome the deficiency of HS [14]. HS which is nonparametric method in nature is not able to incorporate and model the volatility. FHS considers the past returns for calculating the VaR. It is basically based on the belief that the past repeats itself. It analyzes the previous returns, and based upon that value, it predicts the VaR for future. It uses bootstrapping approach which is sampling with replacement to calculate the market VaR from the past particular time period. It constructs a cumulative distribution function of returns over time. FHS works on the assumption that the return vectors are independent and identically

distributed. For this, we remove serial correlations and volatility clustered from data using ARMA and EGARCH [17] models, respectively. In the simulation, we only use the historical distribution and not the theoretical distribution.

Algorithm [14, 18]:

1. The datasets consists of the daily closing prices of two separate equity indices, spanning certain trading days.
2. Consider an equiweighted portfolio and calculate the arithmetic returns by multiplying the data with the weights and then calculate the logarithmic returns.
3. To meet the requirements of approximately independent and identically distributed observations, we use the autoregressive model to compensate for the autocorrelation and the EGARCH model to compensate for the heteroscedasticity.
4. The bootstrapped standardized residuals obtained simulate 2000 different independent trials over a one-month horizon consisting of 22 trading days.
5. Reintroduce the autocorrelation and heteroscedasticity using the filter function in MATLAB and get the portfolio returns.
6. Now sum all the portfolio returns to get a cumulative returns and draw a cumulative distribution function.
7. Calculate the desired VaR values at various confidence levels over one-month horizon or as needed (Fig. 1).

4 Monte Carlo Simulation

Monte Carlo simulation is an instance of mathematical technique [19] which is used for risk analysis and decision making. It can be put to use in areas like finance, manufacturing, and engineering; it is instrumental in providing information on the possibility and likelihood of occurrence of an outcome.

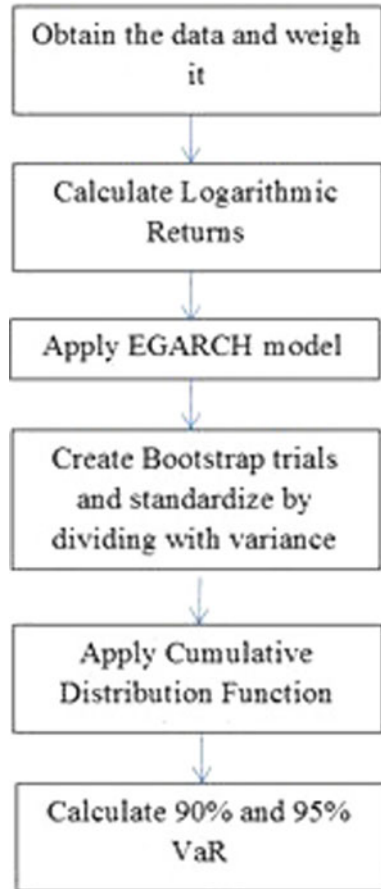
It considers a range of possible inputs and evaluates outcomes based on these inputs, henceforth, providing an option of choosing from wide range of actions. The advantage of this approach is that extreme cases can be considered too.

Here, we consider a wide range of inputs which are used to calculate randomly generated possible results [6]. These results are iteratively calculated taking different values each time. The distributions hence produced reflect the possible outcome. The technique is unique in the sense that it creates simulations for the randomly sampled outcome [20]. These simulations are run several hundreds of times, and the resultant is plotted as a probability distribution of possible outcomes.

Algorithm [21–23]:

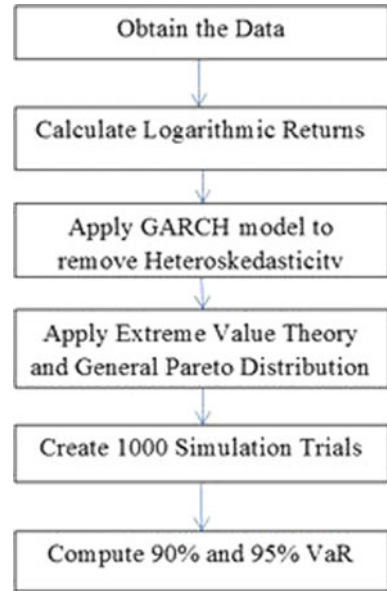
1. The datasets consist of the daily closing prices of two separate equity indices spanning certain trading days.

Fig. 1 Basic approach of FHS



2. Consider an equiweighted portfolio and calculate the arithmetic returns by multiplying the data with the weights and then calculate the logarithmic returns.
3. The Monte Carlo simulation assumes that the observations are IID. so that we use the GARCH [24] model to compensate for the heteroscedasticity [25].
4. Extreme value theory [26] is applied at tails of the curve to remove fluctuations and even out the values. These values are randomly sampled from the input probability distribution curve.
5. Note the outcome from these samples and create 1000 simulation trials. Calculate the desired VaR values at various confidence levels over one-month horizon or as needed (Fig. 2).

Fig. 2 Basic approach of MC

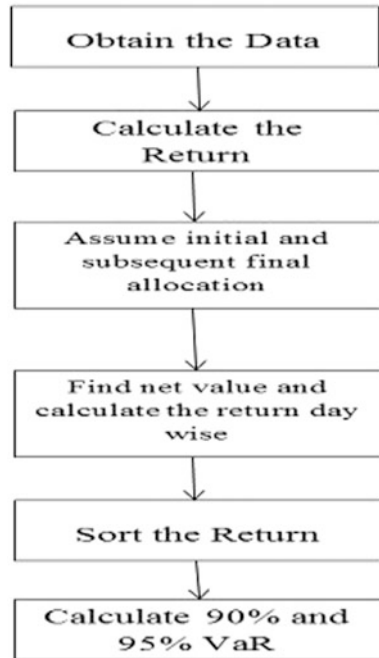


5 Historical Simulation

This is a nonparametric IID. [27] approach in nature and uses empirical distribution of past returns to derive VaR results. It is nonparametric since it does not use distributional assumptions to model VaR unlike other approaches which use models like normal distribution as an intermediate step. It is a relatively easier approach and incorporates correlations empirically. Historical simulation has the limitation [11] that it takes the assumption that history repeats itself. Another assumption is that it values recent data same as the old data, which in return becomes a cause for bad estimated for parameters like high volatility. As a trade-off, sufficiently large data are required to observe the rare events and base the results more accurately.

Algorithm [28]:

1. Load the dataset consisting of the daily value of portfolio.
2. Calculate the return incurred on each equity index.
3. Assume the initial allocation (considered equal in this case) and find the subsequent allocations of the portfolio.
4. Find the net value of portfolio for each day and calculate the return day wise.
5. Sort the returns and find data on the approximate ninety-fifth and ninetieth percentage location.
6. Adjust the VaR so obtained according to the time period required (Fig. 3).

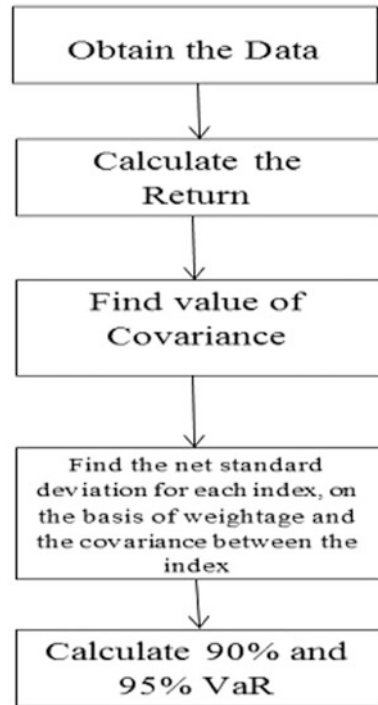
Fig. 3 Basic approach of HS

6 Variance–Covariance Approach

It is the static risk management technique for evaluating the maximum loss incurred in an investment portfolio for a specified time at a certain confidence level. It is a parametric method since it calculates mean, expected value, or standard deviation to calculate VaR. It uses the probability theory on a look-back period to calculate the maximum [29] loss. The assumption made in the technique is that price returns and volatility follow a normal distribution curve. Variance [7] follows from the principle that more the standard deviation, more the price moves, which results in higher loss or profits. For covariance, the principle being followed is that the volatility of every asset is positively correlated, negatively correlated, or not correlated at all. The advantages [30] are that the approach is easy to understand with minimum efforts in its implementation. The complex calculation methodology and need of extensive amount of data account for disadvantages.

Algorithm [8, 9, 31]:

1. Load the dataset consisting of the daily portfolio.
2. Calculate the return incurred on each index.
3. For the stock indices, find the value of covariance.

Fig. 4 Basic approach of VC

4. Find the net standard deviation on the basis of weightage, the standard deviation of each index, and the covariance value between the indexes.
5. Find the VaR using the standard normal distribution formulas (Fig. 4).

7 Dataset

We have considered the stock indices, BSE SENSEX and NSE NIFTY50, as a representative of the stock market to find VaR. The details are taken from Yahoo Finance for the specified period of time in history. A consolidated list, based on close price, is henceforth, prepared.

It is to be noted that both the indices were used simultaneously for the dataset. An equiweighted portfolio was prepared assuming equal investment in each asset of the portfolio at the beginning of time. Stock prices are taken for business days, excluding any form of holidays. The datafeed toolbox was used to import data from Yahoo Finance, and the needed postprocessing was done to align the data of the different indices according to dates from the last to the first. The above process was carried out on six different datasets. The 90 and 95% VaRs over a period of one month were calculated for all the methods, and the time was noted. For the purpose of validation, the data for month in consideration were downloaded from Yahoo Finance.

8 Experimentation and Result

The coding for all the models was carried out on MATLAB [32]. The data was imported from Yahoo Finance, and closing prices for the two portfolios were considered. This dataset was processed further to obtain the return prices.

This was done over six different datasets over different time periods ranging from one to two years over various years. The dataset is treated through all the four techniques. The VaR for 90 and 95% confidence levels was calculated. The techniques were also compared on the basis of methodology adopted, time taken to obtain the result, and whether the actual results were within the calculated values (Tables 1, 2; Fig. 5).

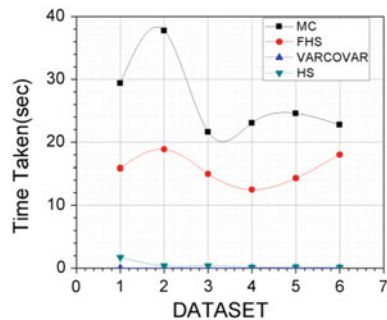
Table 1 Time taken by different techniques

Dataset	VC	HS	MC	FHS
1	0.0053	1.7150	29.4075	15.8489
2	0.0315	0.3640	37.7804	18.8381
3	0.0045	0.3698	21.6208	15.0086
4	0.0057	0.1536	23.0421	12.5042
5	0.0371	0.1749	24.5717	14.3213
6	0.0074	0.1431	22.7394	17.9902

Table 2 Value at risk calculation by different techniques

Dataset	MC		FHS		VARCOVAR		HS	
	90% VaR	95% VaR	90% VaR	95% VaR	90% VaR	95% VaR	90% VaR	95% VaR
1	5.6324	7.6189	8.5256	11.6944	5.4010	6.9303	5.1784	7.0743
2	6.5131	8.7713	8.9400	12.1124	5.6796	7.2878	5.5801	7.4862
3	7.2510	10.1342	7.4624	10.2342	5.9213	7.5980	5.5801	7.4862
4	2.7624	4.0299	2.9211	4.3486	4.4541	5.7153	3.7555	5.1786
5	4.0029	6.1739	2.8027	4.2357	7.1763	9.2083	2.5500	3.4401
6	6.1389	8.8811	6.0001	8.3863	6.4819	8.3172	3.7364	5.8703

Fig. 5 Plot of time taken by different techniques



To calculate the actual values of VaR, the data for the month in consideration were obtained. An equal investment in both the shares was initially assumed, and subsequent values were found. The returns were then calculated over the particular period. A comparison table was prepared to illustrate the difference between the four models.

To calculate the actual values of loss, the data for the month in consideration were obtained from Yahoo Finance. An equal investment in both the shares was initially assumed and subsequent values were found. The approximate values of 90% and 95% data points were then calculated over the particular period. It was then seen if the obtained values were within the risk values as predicted by each model (Tables 3 and 4).

Table 3 Validation table

	Actual loss		VC		HS		MC		FHS	
	90% Point	95% Point	90% VaR	95% VaR	90% VaR	95% VaR	90% VaR	95% VaR	90% VaR	95% VaR
Dataset 1	No loss	No loss	✓	✓	✓	✓	✓	✓	✓	✓
Dataset 2	No loss	No loss	✓	✓	✓	✓	✓	✓	✓	✓
Dataset 3	2.77%	-3.30%	✓	✓	✓	✓	✓	✓	✓	✓
Dataset 4	2.77%	-3.30%	✓	✓	✓	✓	✓	✓	✓	✓
Dataset 5	2.1%	3.25%	✓	✓	✓	✓	✓	✓	✓	✓
Dataset 6	1.95%	2.4%	✓	✓	✓	✓	✓	✓	✓	✓

Table 4 Comparison table

	Variance covariance	Historical simulation	Monte Carlo simulation	Filtered historical simulation
Nature	Parametric	Nonparametric	Parametric	Semi-parametric
Time	Least time required for computations	Takes more time than VC but lesser time than the other two approaches	Takes considerably more time than FHS	Takes lesser time than MC
Bootstrapping	Bootstrapping isn't performed	Bootstrapping is not performed	Bootstrapping is not performed	Bootstrapping is performed
Computational cost	Least expensive	More expensive than VC	Computationally very expensive	Computationally less expensive than MC

(continued)

Table 4 (continued)

	Variance covariance	Historical simulation	Monte Carlo simulation	Filtered historical simulation
Methodology	Considers the price movement over a look-back period and uses the probability theory to compute the maximum loss	The price change is applied to portfolio to generate a historical series, and this is sorted into percentiles to find VaR	Generates large number of hypothetical trials from the past data to find VaR	Uses past data of the portfolio combined with some econometric model to find VaR
Dataset requirement	Requirement is high	Requirement is high	Requirement is low	Requirement is low
Normality assumption	Assumes normal distribution	Does not assume normality	Assumes normal distribution	Does not assume normality
Advantages	Easy to understand and implement	Easy approach, incorporates correlations empirically	Helps reduce uncertainty by considering wide range of possibilities, flexible and customizable for various assets and portfolios	Less data requirement, use shocks instead of raw returns, use volatility model without distribution of the observation
Disadvantages	Complex calculations involved and high data requirement	Assumes that history repeats itself, high data requirement, values recent data same as the old data	Underestimates the probability of extreme cases, wide range of inputs can also pose problem if they are not fairly considered	Does not consider all possible scenarios like Monte Carlo Simulation

9 Conclusion

In this paper, we had aimed to implement and compare the four models variance–covariance, HS, FHS, and Monte Carlo on the Indian Market using NIFTY50 and BSE SENSEX. The project was carried out successfully and results within the desired error limits were obtained.

A detailed table of comparison was drawn on the basis of available theory and results obtained from the experimentation. It was noted that the maximum time was taken by Monte Carlo, followed by filtered historical simulation, historical simulation, and variance–covariance. On an average, Monte Carlo took 26.527 ms, FHS took 15.7519 ms; HS took 0.4867 ms, and variance–covariance tool 0.01525 ms to find both the VaRs. A decrease in the time taken was accompanied by decrease in the complexity of implementation.

10 Future Work

Value at risk models can be further improved by incorporating real-time data like news, market conditions. The methods can further be studied to ascertain their accuracy during times of high risk when the losses are extreme. Allocation to more than two components of equity can also be studied. Portfolio allocation to achieve minimum risk can also be an area of future research.

References

1. "Value at Risk (VaR)." NYU Stern. 2016 Leonard N. Stern School of Business. Web. 25 February 2017. <http://people.stern.nyu.edu/adamodar/pdfiles/papers/VAR.pdf>.
2. Mehta, Neukirchen, Pfetsch, Poppensieker. "Managing Market Risk: Today and Tomorrow." Mckinsey and Company, 2012. Web. 11 December 2016.
3. Gurrola, Pedro, and David Murphy. "Filtered historical simulation Value-at-Risk models and their competitors". (2015).
4. Mishra, Bishnupriya, and Sathya Swaroop fDebasish. Indian Stock Market. Excel Books India, Pg 3–4.
5. Adamko, Peter, Erika Spuchľáková, and Katarína Valášková. "The History and Ideas Behind VaR." *Procedia Economics and Finance* 24 (2015): 18–24.
6. "Monte Carlo Simulation." MathWorks. The MathWorks, Inc., 1994–2017. Web. 24 February 2017. <https://in.mathworks.com/discovery/monte-carlo-simulation.html>.
7. Hendricks, Darryll. "Evaluation of value-at-risk models using historical data (digest summary)." *Economic Policy Review Federal Reserve Bank of New York* 2.1 (1996): 39–67.
8. "An Introduction to Value at Risk (VaR)." Investopedia. 2017, Investopedia, LLC. Web. 22 March 2017. <http://www.investopedia.com/articles/04/092904.asp>.
9. "Value at Risk." 2017 Hong Kong Monetary Authority. Web. 27 March 2017. <http://www.hkma.gov.hk/media/eng/publication-and-research/reference-materials/banking/ch15.pdf>.
10. M Manganelli, Simone, and Robert F. Engle. "Value at risk models in finance." (2001).
11. Čorkalo, Šime. "Comparison of Value at Risk Approaches on a Stock Portfolio." *Croatian Operational Research Review* 2.1 (2011): 81–90.
12. Hull, John, and Alan White. "Incorporating volatility updating into the historical simulation method for value-at-risk." *Journal of Risk* 1.1 (1998): 5–19.
13. Barone-Adesi, G., Giannopoulos, K., Vosper, L. (1999), VaR Without Correlations for Portfolios of Derivatives Securities, *Journal of Futures Markets*, Vol. 19, pp. 583–602.
14. Piroozfar, Ghashang. "Forecasting value at risk with historical and filtered historical simulation methods." *UUDM Project Report* 15 (2009).
15. Zhang, Nan, Ka Lok Man, and Eng Gee Lim. "Parallel Computation of Value at Risk using the Delta-Gamma Monte Carlo Approach." *Proceedings of the International MultiConference of Engineers and Computer Scientists*. Vol. 2. 2014.
16. Hong, L. Jeff, and Guangwu Liu. "Simulating sensitivities of conditional value at risk." *Management Science* 55.2 (2009): 281–293.
17. Kalyanaraman, Lakshmi. "Stock Market Volatility in Saudi Arabia: An Application of Univariate GARCH Model." *Asian Social Science* 10.10 (2014): 142.
18. "Using Bootstrapping and Filtered Historical Simulation to Evaluate Market Risk." MathWorks. The MathWorks, Inc., 1994–2017. Web. 22 February 2017. <https://in.mathworks.com/help/econ/examples/using-bootstrapping-and-filtered-historical-simulation-to-evaluate-market-risk.html>.

19. "Monte Carlo Simulation." Palisade. 2017 Palisade Corporation. Web. 2 February 2017. http://www.palisade.com/risk/monte_carlo_simulation.asp.
20. Capriotti, Luca. "SJ Mason, RR Hill, L. Mönch, O. Rose, T. Jefferson, JW Fowler eds".
21. "Calculating VaR Using Monte Carlo Simulation." Finance Train. Web. 22 March 2017 <http://financetrain.com/calculating-var-using-monte-carlo-simulation/>.
22. "Using Extreme Value Theory and Copulas to evaluate Market Risk." Mathworks. The Mathworks, Inc., 1994–2017. Web. 24 February 2017. <https://in.mathworks.com/company/newsletters/articles/using-extreme-value-theory-and-copulas-to-evaluate-market-risk.html>.
23. "Modelling Market Risk using Extreme Value Theory and Copulas." Mathworks. The Mathworks, Inc., 1994–2017. Web. 24 February 2017. <https://in.mathworks.com/company/newsletters/articles/modeling-market-risk-using-extreme-value-theory-and-copulas.html>.
24. Engle, Robert. "GARCH 101: The use of ARCH/GARCH models in applied econometrics." *The Journal of Economic Perspectives* 15.4 (2001): 157–168.
25. William, Richard. "Heteroskedasticity-University of Notre Dame." University of Notre Dame, 2015. Web. 10 December 2016.
26. Gilli, Manfred. "An application of extreme value theory for measuring financial risk." *Computational Economics* 27.2–3 (2006): 207–228.
27. Sharma, Meera. "The historical simulation method for value-at-risk: A research based evaluation of the industry favorite." (2012).
28. "Calculating VaR Using Historical Simulation." Finance Train. Web. 22 March 2017 <http://financetrain.com/calculating-var-using-historical-simulation/>.
29. Toggins, W.N. (2008), *New Econometric Modelling Research*, Nova Publishers.
30. Aniūnas, Povilas, Jonas Nedzveckas, and Rytis Krušinskas. "Variance–covariance risk value model for currency market." *Engineering Economics* 61.1 (2015).
31. "Calculating Covariance For Stocks." Investopedia. 2017, Investopedia, LLC. Web. 20 March 2017. <http://www.investopedia.com/articles/financial-theory/11/calculating-covariance.asp>.
32. MATLAB, version R2016b, The MathWorks Inc., Natick, Massachusetts, 2016.0.

Hardware Co-simulation of Reconfigurable FIR Filters on FPGA

Anindita Ghosh and Debashis Chakraborty

Abstract Field programmable gate array (FPGA) provides an attractive platform for realization of different logical functions and hardware components frequently used in digital signal processing (DSP) applications. These platforms present new challenges for logic and hardware designers, particularly for the module that involves the mapping of desired functionality onto the underlying prefabricated reconfigurable hardware resources. A fundamental aspect of the DSP is filtering. Digital filters having finite duration of impulse responses are referred to as finite impulse response (FIR) filters. This paper mainly emphasizes on the design and implementation of FIR filters of different forms in FPGA. The proposed design algorithm of FIR is modeled in VHDL followed by verification and synthesis using the XST tool. The performance of FIR is analyzed using the timing diagrams, HDL synthesis report, and device utilization summary. This work also incorporates hardware co-simulation of the system with real filter analysis.

Keywords FIR · Xilinx System Generator · Simulink · FPGA
Hardware–software co-simulation · JTAG

1 Introduction

FPGAs provide an alternative approach to ASICs. Among the important advantages of FPGA are their re-configurability and on the fly design approach, large-scale integration, availability of several onboard macros, and intellectual property

A. Ghosh (✉)

Department of Electronics and Telecommunication Engineering,
Jadavpur University, Kolkata 700032, West Bengal, India
e-mail: aninditaaghosh@gmail.com

D. Chakraborty (✉)

Department of Electronics and Communication Engineering,
Future Institute of Engineering and Management, Kolkata 700150, West Bengal, India
e-mail: debashisc77@gmail.com

© Springer Nature Singapore Pte Ltd. 2018

R. Bera et al. (eds.), *Advances in Communication, Devices and Networking*,
Lecture Notes in Electrical Engineering 462,
https://doi.org/10.1007/978-981-10-7901-6_60

553

(IP) cores. Owing to these features, FPGAs are rapidly shifting from prototype designing to batch productions. Modern FPGAs have lookup tables (LUTs) [1] as the basic logic unit and also support fast carry-chains in their logic slices. The inclusion of the fast carry-chain has enabled efficient realization of arithmetic circuits since the general FPGA routing can be avoided. Apart from the general LUT-carry-chain fabric, state-of-the-art FPGAs have in-built full custom processing elements like adders, multipliers, DSP blocks, high-speed clocking, and I/O resources. However, along with the advantages of the prefabricated aspects of FPGAs it also limits the optimized synthesis of different circuits on these platforms.

Filter circuits allow electric signals at definite frequencies or frequency ranges whereas eliminating others. FIR system consists of finite-duration impulse responses and a finite count of nonzero terms. During the last few years, extensive research work has been carried out in the field of formation of FIR (finite impulse response) filter. Linear FIR filter can be designed using frequency weighting model. FIR filters are stable and insensitive to quantization effect [2], so they are useful for applications involving accurate, linear phase response. In this particular work various FIR digital filter algorithms are designed in MATLAB, which is implemented into VHDL code with the aid of Xilinx System Generator [3], the designed model is further programmed onto an FPGA. The obtained responses are analyzed and studied from the spectrum scope. The hardware–software co-simulation [4] ensures that the designed model is practically realizable onto hardware.

2 FPGA-Based FIR Filter Design

2.1 Digital Filters

A digital filter enhances or reduces certain signal characteristics by performing mathematical operations on a sampled, discrete-time signal. These are made up of an analog-to-digital converter which samples the input signal, a microprocessor, and few peripheral components like the memory for storing the data and filter coefficients. The microprocessor consists of program instruction software; this software performs necessary mathematical operations on the numbers received from the ADC [5] to implement the digital filter. To expedite the filtering operations in high-performance applications, an ASIC or FPGA is preferred over a specialized DSP with specific paralleled architecture or a general-purpose microprocessor.

2.2 FIR Filters

Digital filters having finite impulse response are termed as finite impulse response (FIR) filters. Unlike the IIR filters, these filters are non-recursive linear

time-invariant systems where the present output is independent of the previous outputs and depends only on the current input and the previous inputs.

The output of the FIR filter is calculated as a finite term, weighted sum of the past, present, and maybe the future values of the filter input. The coefficients, order, and type of the digital filter are to be determined from the given frequency response specification. Filtering operation from the designed model is implemented using suitable hardware or software. A difference equation or a system function specifies the filter characteristics. The linear constant coefficient difference equation of a $(M + 1)$ th order recursive FIR filter is given as follows which explain the relation between output $y(n)$ and input $x(n)$, where b_k are filter coefficient (here $a_k = 0$).

$$Y(n) = \sum_{k=0}^M b_k x(n - k) \quad (1)$$

Past input only $a_k = 0$

Similarly, the Z-domain representation of the system transfer function $H(z)$ is given below:

$$H(z) = \sum_{k=0}^M b_k z^{-k} \quad (2)$$

The difference equation signifies that the output response of the FIR filter is the weighted sum of current and previous M inputs. The filter has order M and has $M + 1$ taps [6]. If the length of the impulse response is $M + 1$ and $H(z)$ is a polynomial in z^{-1} of order M , then $H(z)$ has M poles at $z = 0$ and M zeros at positions in the z -plane determined by the coefficients b_k . A FIR filter of order N has $N + 1$ coefficients and requires $N + 1$ multipliers along with N two-input adders. If the filter structure implements coefficients of the transfer function as the multiplier coefficients, it is termed as a direct-form structure. These structures are efficient in terms of memory requirement since the count of delay element is reduced. Direct form is extensively used for all practical applications.

3 Methodology

3.1 Xilinx System Generator (XST)

Xilinx System Generator is used to design efficient DSP algorithm on FPGA. ‘Xilinx System Generator’ [7] is a high-level tool that aids in designing and modeling high-end DSP systems that are realized in FPGAs. XST integrates Xilinx with Simulink; it creates an *.ise* file which is used in Xilinx using the model file of Simulink.

3.2 *Hardware and Software Required*

We have used the Xilinx Spartan-3A FPGA to implement our design, and the software and hardware used in our work are:

3.3 *Spartan-3A*

The Spartan-3A FPGA platform consists of five high-performance devices having 50 K to 1.4 M system gates, density migration feature, and 108 to 502 I/Os. The main advantage of Spartan-3A is its low cost compared to its other counterparts. It supports up to 176 Kbits of distributed RAM and 576 Kbits of byte-write enable, fast-block RAM. Moreover, it has built-in multipliers for efficient DSP implementation along with digital clock managers (DCMs) for system-level clock management functions. These features remarkably reduce system cost and result in shorter design cycles (Table 1).

4 Implementation

Following are the steps for implementing the FIR/IIR filter on FPGA.

Step 1: The filter models are realized in Simulink. The in-built ‘FDA tool’ is used to provide the filter specifications. The FDA tool computes the filter coefficient with these input specifications, and this coefficient is saved in the workspace for further use. The ‘Spectrum Scope/B-FFT’ block analyzes and displays the mean-square spectrum of the response.

Step 2: In the next step, we use the Xilinx block set—‘FIR Compiler 5.0.1’, which uses the previously stored FDA filter coefficient to compute the filter characteristics. It supports direct-form-based MAC (multiply accumulate) FIR and transposed direct-form-based MACFIR. This block helps in simulating different hardware architectures of the filter specification (2).

The block set operates between the gateways—‘gateway-in’ and ‘gateway-out.’ The sampled input from the random source is fed in the ‘gateway-in’ which forms the input to the FIR Compiler; the response from the ‘gateway-out’ is analyzed in the ‘Spectrum Scope/B-FFT.’

Table 1 Hardware and software required

Requirement	Specification
Hardware/target device	xc3s700a-4fg484
Software used (versions)	MATLAB (R2010a) Xilinx 14.3 ISE

Table 2 Hardware and software specifications

Property name	Value
Top-level source type	HDL
Product category	All
Family	Spartan-3A and Spartan 3AN
Device	XC3S700A
Package	FG484
Speed	-4
Synthesis tool	XST (VHDL/Verilog)
Simulator	ISim (VHDL/Verilog)
Preferred language	VHDL
VHDL source analysis standard	VHDL-93

Step 3: Finally, a JTAG token [7] is generated from the System Generator. The corresponding VHDL code is compiled in ISE software to generate a .bit file. The .bit file is burnt into the FPGA—the synthesized spectrum from FPGA is also analyzed in the Spectrum Scope/B-FFT'. A 20-ns FPGA clock period is configured with the corresponding Simulink time period of 1/48,000 s while generating the co-simulation token. The 'Hardware Co-Simulation' [8] blocks in System Generator route the model created in Simulink into FPGA, thus giving the flexibility of simultaneously running the design in hardware and also simulating a similar model in software. Also, the generated co-simulation block ensures that the design is synthesizable on the actual hardware.

5 FIR Filter Realization

This paper explains the realization of digital filters with different windowing techniques and response types. A low-pass Hann window filter design is explained in detail.

5.1 Filter Specifications

The Filter Design and Analysis Tool (FDA Tool) generates the filter coefficient. Here, we have used the Hann window technique.

Windows are added in the design of digital filters to convert an 'ideal' impulse response of infinite duration into a finite impulse response (FIR). The FDA filter specification to design an optimized LPF with Hann window of the model for hardware–software co-simulation is listed in Table 3. The FIR Compiler [7] further uses this coefficient to analyze the filter response. The FIR specifications are listed in Table 4.

Table 3 Design properties

Filter property	Value
Response type	Low pass
Design method	FIR (window)
Specify order	25
Window method	Hann
Sampling freq. (Fs)	48,000 Hz
Cutoff freq. (Fc)	10,800 Hz

Table 4 FIR Compiler—properties

Property	Value
Coefficient type	Inferred
Quantization method	Maximize dynamic range
Coefficient width	16
Fraction length	Best precision
Number of paths	1
Filter type	Single rate
Output rounding mode	Full precision

5.2 Block Diagram to Design LPF

The system is modeled in the Simulink, and below is the block diagram of the FIR model (Fig. 1).

5.3 RTL Schematic

The actual high-level RTL schematic and low-level RTL schematic (Fig. 2) of the LPF are shown below.

Once the filter is designed in MATLAB based on their specifications, the Xilinx System Generator is then used for the appropriate FIR FPGA filter implementation. The current generations of FPGAs contain a huge number of configurable logic blocks (CLBs) and thus are becoming more feasible for implementing a wide range of complex applications. Our design is routed and programmed onto the FPGA block.

5.4 Hardware–Software Co-simulation

The software filter model is further synthesized in the hardware. This ensures that the design is configurable in the hardware. The response from the hardware is compared with the software responses. The filters coefficients are adjusted so as to

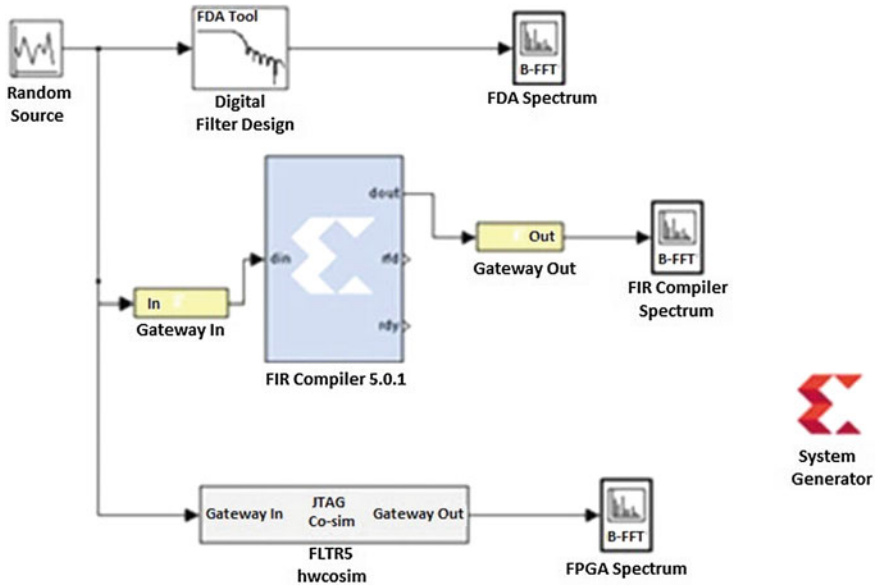


Fig. 1 Hardware–software co-simulation block

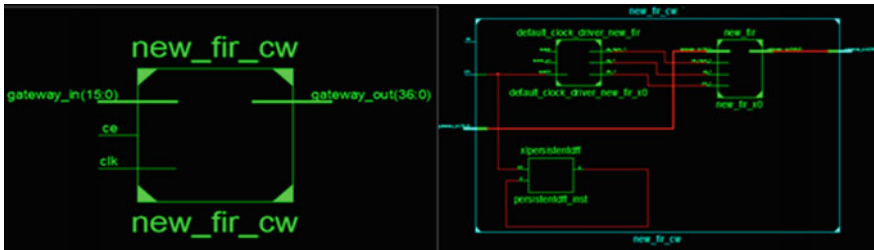


Fig. 2 Low- and high-level RTL schematic of the FIR model

minimize the difference in response characteristics of the hardware and software simulation.

6 FPGA Implementation

Recent technologies allow implementing digital filter algorithms on FPGAs. Digital filtering applications are designed with data path design approach which is well suited for FPGAs. The benefit of the FPGA approach of digital filter implementation is its higher sampling rates compared to the traditional DSP chips, lesser costs than an ASIC implementing a moderate volume applications, and finally more

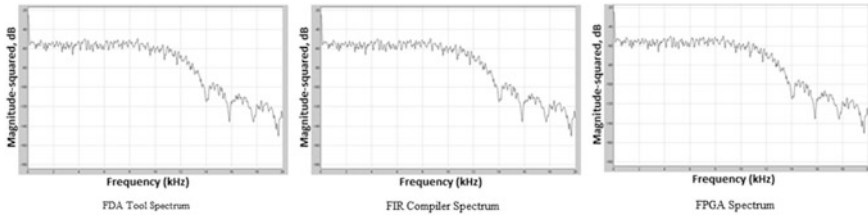


Fig. 3 Waveforms of the hardware–software co-simulation

flexibility than the alternate approaches. In particular, multiple multiply-accumulate (MAC) units [9] may be implemented on a single FPGA.

Further since many current FPGA architectures are in-system programmable, we can alter the configuration of the device to implement alternate filtering operations or an entirely different functionality.

7 Results and Simulation

The performance comparison based on spectral analysis of the FDA tool, FIR Compiler, and FPGA—all subjected to similar input is analyzed. The output response from the hardware is exactly similar to the simulated FDA response, thus validating the correctness of the designed model.

Below are the waveforms for LPF Hann window in Fig. 3.

8 Conclusion

This paper has presented a guideline to design and implement the digital filters with the help of Simulink; the design is further realized in the field programmable gate arrays (FPGA) hardware, thus making the model practically configurable. The designed filters can be used as basic blocks in systems for communication, audio synthesis, image processing, etc. According to the real-time challenges, we can customize the filter specifications to make it compatible with the systems for various applications.

9 Future Scope

Further research may be extended for designing an adaptive filter, where we can change the filter coefficient based on certain variable real-time input parameters according to an optimization algorithm. Also, we can fabricate a universal filter by partitioning the FPGA block and synthesizing different filters in different blocks.

References

1. Kumar, T. Nandha, Hsaider AF Almurib, and Fabrizio Lombardi. "A novel design of a memristor-based look-up table (LUT) for FPGA." *Circuits and Systems (APCCAS), 2014 IEEE Asia Pacific Conference on*. IEEE, 2014.
2. Martone, Michele, Benjamin Brautigam, and Gerhard Krieger. "Quantization effects in TanDEM-X data." *IEEE Transactions on Geoscience and Remote Sensing* 53.2 (2015): 583–597.
3. Prince, A. Amalin, et al. "Efficient implementation of empirical mode decomposition in FPGA Using Xilinx System Generator." *Industrial Electronics Society, IECON 2016–42nd Annual Conference of the IEEE*. IEEE, 2016.
4. Staunstrup, Jørgen, and Wayne Wolf. *Hardware/software co-design: principles and practice*. Springer Science & Business Media, 2013.
5. Oshima, Takashi. "Analog-to-digital converter." U.S. Patent No. 9,444,482. 13 Sep. 2016.
6. Ghauri, Sajjad Ahmed, et al. "Implementation of OFDM and Channel Estimation using LS and MMSE Estimators." *IJCER* 2.1 (2013): 41–46.
7. Xilinx System Generator, basic tutorial, www.xilinx.com.
8. Rotger-Griful, Sergi, et al. "Hardware-in-the-loop co-simulation of distribution grid for demand response." *Power Systems Computation Conference (PSCC), 2016*. IEEE, 2016.
9. Devi, Sarungbam Sanahanbi, Madhuparna Chakraborty, and Roshan JameerPatan. "Field programmable gate array implementation of digital filter for cochlear implant." *Communication and Signal Processing (ICCSP), 2016 International Conference on*. IEEE, 2016.

Ranking of Sensors for ADAS— An MCDM-Based Approach

Jayanta Kumar Baruah, Rabindranath Bera and Sourav Dhar

Abstract Nowadays, advanced driver assistance system (ADAS) is one of the utmost emerging matters of intelligent transportation system (ITS). Many sensors, with their own advantages and limitations, are available in market, to be implanted in the vehicle to provide guidance to the driver. Such guidance enables the action of vehicle by providing drivers advanced control and better driving experience. But the choice of sensors among the available sensors is an important issue that needs to be addressed. This paper presents a method, considering multiple constraints, to provide ranking of those sensors to be used to design a robust, reliable, and cost-effective ADAS.

Keywords ITS · ADAS · MCDM · AHP · Sensors

1 Introduction

The day-to-day problem in road transportation is now a social issue [1] because people are facing substantial losses in financial matters, health, time, and mobility in the absence of proper traffic management infrastructure. To improve traffic safety and movement, vehicles and roadways are brought under the umbrella of intelligent transportation systems (ITS). ITS is defined to be the application of progressive and incipient technologies (electronic devices, sensors, communications, and computer-based control) in conveyance to save primarily human lives and in addition to that to save time, energy, and the environment toward overall economic growth of a

J. K. Baruah (✉) · R. Bera · S. Dhar
Sikkim Manipal Institute of Technology, Majitar 737136, Sikkim, India
e-mail: jkbaruah01@yahoo.com

R. Bera
e-mail: rbera50@gmail.com

S. Dhar
e-mail: sourav.dhar80@gmail.com

Table 1 ADAS available in the market

Manufacturer	ADAS implemented
Nissan	Forward collision warning (FCW), LKS, low-speed ACC
Honda	Night visions and collision mitigation brakes
Mitsubishi	ACC
Mercedes Benz	ACC and alarm for lane passing
Fiat	Sensors for tires
Toyota	Brake assist and navigation link
BMW	Blind spot detection
Audi	ACC stop and go including traffic jam assistant

nation [2]. American ITS society (ITSA) has already considered “vision zero” as its primary objective, i.e., its principal motto is to minimize the road accidents and interruptions in transportation as less as possible [3]. The main cause of 57% of accidents is human error, whereas it acted as a catalyst in 95% of the accidents [4].

Advanced driver assistance system (ADAS), a part of ITS, provide assistance and guidance to the driver in the process of driving by introducing sensor-based electronic automation in vehicular systems. Safety features of ADAS are designed for collision avoidance by introducing technologies that alert the driver to possible threats or by implementing precautions and taking over control of the automobile. There may be several adaptive features of ADAS like adaptive cruise control (ACC), auto braking, smartphones/GPS-based traffic warnings, alerting driver about other cars or obstacles, keeping driver in right lane or show what is in blind spots [5, 6]. Hence by incorporating human-machine interface in ADAS, passenger safety and road safety can be increased to a large extent.

The use of sensor-based electronics and computation based on system on chip in modern vehicles have introduced several noteworthy active vehicle safety systems such as electronic stability program (ESP), lane departure warning (LDW), lane keeping system (LKS), and adaptive cruise control (ACC) which have contributed significantly in life saving. Several ADAS already available in market are summarized in Table 1.

This paper aims to investigate the different types of sensors which could be used to make ADAS more robust. The actual purpose of such investigation is the implementation of different types of driver assistance systems by addressing the practical problem of driving tiredness and the boring procedures of driving tasks including lane-change maneuvers, lane keeping, avoiding obstacles, or overtaking vehicles ahead [7].

2 Sensor Technologies for ADAS

Nowadays, a wide range of sensors (such as sensors for measurement of lateral and longitudinal acceleration, steering wheel angle, yaw rate, and wheel speed as well as GPS, ultrasonic sensors, infrared sensors, cameras, and humidity sensors) are

readily available. This allows combining multiple sources of information to help the driver in decision-making process.

Sensors collect information from their adjacent environment such as pedestrians and incoming vehicles. The sensors, used for ADAS to detect the neighboring road traffic atmosphere of the vehicle, may be categorized into two types, viz. passive sensors and active sensors [8]. Passive sensors (such as optical sensors/cameras) identify the naturally emitted energy by the object and collect the statistical data in a non-intrusive way. On the contrary, active sensors identify an object by analyzing the echo of incident electromagnetic energy (for example, microwave radar, laser, ultrasonic, and infrared sensors). Active sensors are capable of direct measurement of distance and velocity of the target irrespective of weather conditions. However, the drawbacks of active sensors are the low scanning speed, low spatial resolution, bigger size and higher cost. On the contrary, by using high-resolution imaging sensors (camera) the moving vehicles can be effectively tracked and the photographic information captured can be used for vehicle identification [5]. Unlike active sensors, the passive sensors are significantly sensitive to environmental and illumination conditions. Some of the sensors used in ADAS are listed in Table 2.

Table 2 Sensors used in ADAS

	Sensors	Output format	Advantages	Limitations
Active sensors	IR	Image	Accuracy is very high to measure a short distance	Small detector outputs
	Lidar	Image	More efficient and cost effective	Pulse is not reflected properly if wet, reflective objects
	Radar	Structured time series	Superior penetration capability through any type of weather condition, and can be used in the day or night time	Cannot track if deceleration is greater than one mph
	Ultrasonic	Structured time series	The response of analog ultrasonic sensors is linear with distance	Broad beam width
Passive sensors	Camera	Image	Measurements of less than one micron at reduced cost	Accuracy will be affected if it is not clean and free from dirt and other foreign materials. Sensitive to environmental and illumination variations
	Optical	Image	Sensitivity is very high	Interference from multiple effects. Sensitive to environmental and illumination variations

3 MCDM-Based Design

It is evident from Table 2 that every sensor has its own advantages and limitations. Thus, choice of proper sensor is a big challenge to design an efficient and cost-effective yet accurate ADAS. The choice of sensors cannot be made based on single criteria. There are multiple attributes that need to be considered. Here, analytic hierarchy process (AHP) which is a “multi-criteria decision-making method (MCDM)” has been explored for the sensors ranking.

3.1 Level-1 AHP

AHP is a mathematical MCDM tool developed by Satty [9] to solve critical decision-making problems. There are three principles that are to be typically followed to solve a decision problem using AHP (Table 3).

- a. Organization of the model.
- b. Comparative decision of the alternatives and the criteria.
- c. Combination of the priorities.

The step-by-step procedures of AHP-based solution are discussed in detail in co-author’s previous works [10, 11].

Initially, active sensors like radar, ultrasonic sensor, lidar, IR and passive sensors like camera are considered for ranking. The attributes that influence the decision for choice of sensor in ADAS are the performance, reliability, robustness, cost, and availability. Figure 1 shows the decision hierarchy for sensor selection specific to ADAS.

3.2 Level 2 AHP

(i) **Reliability** (Table 4)

(ii) **Robustness** (Table 5)

(iii) **Performance** (Table 6)

(iv) **Cost** (Table 7)

(v) **Availability** (Tables 8, 9, 10)

Table 3 Level-I AHP matrix for finding relative priority of sensors

Criteria	Reliability	Robustness	Performance	Cost	Availability	Priority vector	Consistency ratio (CR)
Reliability	1	3	4	6	9	0.4661	CR = 00.0832
Robustness	0.3333	1	3	5	7	0.2587	
Performance	0.2500	0.3333	1	6	7	0.1839	
Cost	0.1666	0.2000	0.1666	1	2	0.0567	
Availability	0.1111	0.1428	0.1428	0.5000	1	0.0346	

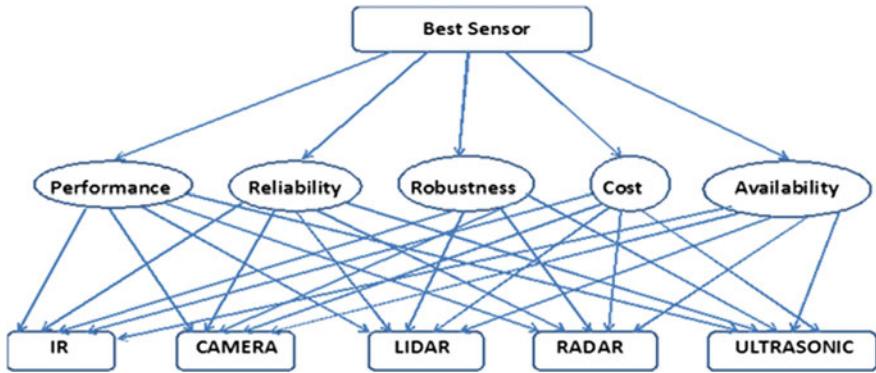


Fig. 1 Decision hierarchy for sensor selection specific to ADAS

Table 4 Level-II AHP matrix for determining relative priority of sensors for reliability

Reliability	IR	Camera	Lidar	Radar	Ultrasonic sensor	Priority vector	Consistency ratio (CR)
IR	1	0.2000	0.3333	0.1428	0.1666	0.0410	CR = 0.0518
Camera	5	1	3	0.2500	0.3333	0.1503	
Lidar	3	0.3333	1	0.1666	0.3333	0.0751	
Radar	7	4	6	1	2	0.4409	
Ultrasonic sensor	6	3	5	0.5000	1	0.2927	

Table 5 Level-II AHP matrix for determining relative priority of sensors for robustness

Robustness	IR	Camera	Lidar	Radar	Ultrasonic sensor	Priority Vector	Consistency ratio (CR)
IR	1	2	0.3333	0.1666	0.3333	0.0749	CR = 0.0763
Camera	0.5	1	0.3333	0.1428	0.2000	0.0482	
Lidar	3	3	1	0.2000	0.2000	0.1251	
Radar	6	7	5	1	3	0.4877	
Ultrasonic sensor	3	5	5	0.3333	1	0.2641	

3.3 Final Ranking

The final ranking of the five alternatives is calculated by multiplying the priority vector of the criteria’s (from article 3.1) to the matrix of individual priorities (from each of the AHP matrix of article 3.2) for five decision alternatives for five criteria.

Table 6 Level-II AHP matrix for determining relative priority of sensors for performance

Performance	IR	Camera	Lidar	Radar	Ultrasonic sensor	Priority vector	Consistency ratio (CR)
IR	1	0.1428	0.5	0.2000	0.3333	0.0515	CR = 0.0411
Camera	7	1	5	3	2	0.4346	
Lidar	2	0.2000	1	0.3333	0.2500	0.0776	
Radar	5	0.3333	3	1	2	0.2420	
Ultrasonic sensor	3	0.5000	4	0.5000	1	0.1942	

Table 7 Level-II AHP matrix for determining relative priority of sensors for cost

Cost	IR	Camera	Lidar	Radar	Ultrasonic sensor	Priority vector	Consistency ratio (CR)
IR	1	4	4	7	0.5000	0.3044	CR = 0.0512
Camera	0.2500	1	2	5	0.2000	0.1279	
Lidar	0.2500	0.5000	1	3	0.2000	0.0850	
Radar	0.1428	0.2000	0.3333	1	0.1428	0.0379	
Ultrasonic sensor	2	5	5	7	1	0.4431	

Table 8 Level-II AHP matrix for determining relative priority of sensors for availability

Availability	IR	Camera	Lidar	Radar	Ultrasonic sensor	Priority Vector	Consistency ratio (CR)
IR	1	3	3	5	1	0.3424	CR = 0.0125
Camera	0.3333	1	1	3	0.3333	0.1298	
Lidar	0.3333	1	1	3	0.3333	0.1298	
Radar	0.2000	0.3333	0.3333	1	0.2000	0.0557	
Ultrasonic sensor	1	3	3	5	1	0.3424	

4 Discussion and Conclusion

Majority of the sensors have a specified measurement range and signal bandwidth restrictions. Thus, it becomes hard to distinguish “intended signal” (such as obstacles in the road) and the system “noise.” The level of inconvenience, for the sensors to track moving objects, takes a paradigm shift during hostile environmental conditions such as rainy and foggy conditions.

Table 9 Matrix of individual priorities

Sensors/criteria	Reliability	Robustness	Performance	Cost	Availability
IR	0.0410	0.0749	0.0515	0.3044	0.3424
Camera	0.1503	0.0482	0.4346	0.1279	0.1298
Lidar	0.0751	0.1251	0.0776	0.0850	0.1298
Radar	0.4409	0.4877	0.2420	0.0379	0.0557
Ultrasonic sensor	0.2927	0.2641	0.1942	0.4431	0.3424

Table 10 Final ranking

Sensors	Final priority	Ranking
Radar	0.3803	1st
Ultrasonic sensor	0.2774	2nd
Camera	0.1741	3rd
Lidar	0.0909	4th
IR	0.0771	5th

ADAS performance can be improved by optimizing system performance through effective sensor fusion techniques which is the coherent combination of measured data from different sensors. Hence, it is important to choose proper set of sensors for enhanced ADAS performance.

In this work, a ranking of sensors is found by considering multiple constraints like reliability, robustness, performance, cost, and availability. It is found that the active sensors like radar and ultrasonic sensors are having highest priority indices, whereas passive sensor (camera) can also play an important role in the design of a reliable, robust yet cost-effective ADAS for vehicular safety application.

References

1. Jarašūnienė A., “Analysis Of Possibilities And Proposals Of Intelligent Transport System (Its) Implementation In Lithuania”, *Transport – 2006*, Vol XXI, No 4, 245–251, Taylor & Francis; <https://doi.org/10.1080/16484142.2006.9638074>.
2. H. Leung, N.E.E. Faouzi, A. Kurian, “Intelligent Transportation System (ITS)”, *Information Fusion 12* (2011) 2–3, Elsevier; <https://doi.org/10.1016/j.inffus.2010.06.003>.
3. Website: <http://www.itsa.org>.
4. Amardeep Sathyanarayana, Pinar Boyraz *, John H.L. Hansen, “Information fusion for robust ‘context and driver aware’ active vehicle safety systems”, *Information Fusion 12* (2011) 293–303; <https://doi.org/10.1016/j.inffus.2010.06.004>.
5. F. Sattar, F. Karray, M. Kamel, L. Nassar and K. Golestan, “Recent Advances on Context-Awareness and Data/Information Fusion in ITS”, *Int. J. ITS Res.* (2016) 14:1–19, Springer, <https://doi.org/10.1007/s13177-014-0097-9>.

6. R. O. Chavez-Garcia and O. Aycard, "Multiple Sensor Fusion and Classification for Moving Object Detection and Tracking", IEEE Transactions on Intelligent Transportation Systems, Vol. 17, NO. 2, February 2016, pp 525–534; <https://doi.org/10.1109/its.2015.2479925>.
7. Bera R, Dhar S, Kandar D, Sinha NB, Mitra M (2008), "Modeling and Implementation of Wireless Embedded System For Intelligent Transport System Application", IEEE Region 10 Colloquium and the Third International Conference on Industrial and Information Systems, December 8–10, 2008, Kharagpur, India; <https://doi.org/10.1109/iciinfs.2008.4798428>.
8. Tideman, M., van der Voort, M.C., van Arem, B., Tillema, F.: A review of lateral driver support systems. IEEE Intelligent Transportation Systems Conference, pp 992–999 (2007); <https://doi.org/10.1109/itsc.2007.4357753>.
9. Saaty, T.L.; (1980): "*The Analytical Hierarchy Process*". New York: McGraw-Hill, 1980.
10. S. Dhar, A. Ray and R. Bera (2010), "Design and Simulation of Vertical Handover Algorithm for Vehicular Communication", International J. of Engineering Science and Technology, vol 2, no 10, October, 2010; Link: <http://www.ijest.info/docs/IJEST10-02-10-080.pdf>.
11. S. Dhar, A. Ray and R. Bera (2013), "Cognitive vertical handover engine for vehicular communication", Peer-to-Peer Netw. Appl. (2013), Springer, 6: 305. <https://doi.org/10.1007/s12083-012-0171-5>.

Offline Signature Verification Using Radial Basis Function with Selected Feature Sets

Hemanta Saikia and Kanak Chandra Sarma

Abstract This paper presents evaluation results of support vector machine (SVM) classifiers with radial basis function (RBF) kernel in offline signature verification. We have used two data sets of offline signatures and extracted 15 (fifteen) features from each signature sample of the data sets. The best feature subsets of the data sets were selected using filter and wrapper methods. For both the data sets, SVM classifiers with RBF kernel were designed with every selected feature sets individually. Classifiers were optimized, and their performances were evaluated using 10-fold cross-validation. Another classifier was designed using both the data sets combined to test the generalizability of the classifier across two different signatures.

Keywords Support vector machine • Radial basis function • Offline signature verification • Feature selection • Filter method • Wrapper method

1 Introduction

Offline signature verification is one of the demanding pattern recognition problems. Confidentiality and legal issues are associated with handwritten signatures. So, availability of standard benchmark signature database is very limited for offline signature verification.

In offline signature verification, a signature image under inspection is matched with its known genuine signature images. Using different pattern recognition

H. Saikia (✉)

Department of Electronics & Communication Engineering,
Sikkim Manipal Institute of Technology, Majitar, Sikkim, India
e-mail: h.saikia.in@ieee.org

K. C. Sarma

Department of Instrumentation & USIC, Gauhati University,
Guwahati, Assam, India
e-mail: kanak_sarma50@rediffmail.com

© Springer Nature Singapore Pte Ltd. 2018

R. Bera et al. (eds.), *Advances in Communication, Devices and Networking*,
Lecture Notes in Electrical Engineering 462,
https://doi.org/10.1007/978-981-10-7901-6_62

573

techniques, forgery is tried to detect. There are three types of signature forgeries [1] (i) random forgery, (ii) simple forgery and (iii) skilled forgery. In random forgery, the forger does not know anything about the original genuine signature; the forger produces just a random signature. When the forger produces a signature not having access to the original signature but only knowing the name of the original signer, it is called simple forgery. In skilled forgery, the forger has access to the original signature. Thus, skilled forgery is the most difficult forgery to detect.

Being a pattern recognition problem, there are these six phases in offline signature verification: (i) data acquisition, (ii) preprocessing, (iii) feature extraction, (iv) feature selection, (v) classification and (vi) performance Evaluation.

2 Data Acquisition and Data set Preparation

For our experimentation, we have used two offline signature data sets. The first one was our own signature data set (data set 1) of 313 offline signatures. This data set comprised of 191 genuine and 122 forged signature samples.

While collecting the signature samples, following protocols were followed:

- (i) All the signature samples were collected on white A4 size papers.
- (ii) Different pens were used by the signers.
- (iii) Signature samples were collected in 7 (seven) different sessions in a span of (9) nine days. Some signatures were collected in the morning, some in the noon, some in the evening and some of them in the late night.
- (iv) Signature images were scanned by a digital scanner with 200 dpi.

For producing the forged signatures, the forgers were supplied the genuine signature. They were given enough time to practise the signature. All scanned signature images were stored in JPEG format.

The other data set that we used was the IAPR-TC data set (data set 2) [2]. Seventy-six genuine and 104 forged (skilled) signatures (total of 180 signatures) were used from this data set.

Signatures in both the data sets were with English scripts. In data set 1, signatures were skewed (signature baseline is not properly horizontal), whereas in data set 2, signatures were not skewed, but they had vertical long strokes. Visually, variations were more between the signature samples of data set 2 as compared to data set 1.

Another data set (data set 3) was also used in our experimentation which was a combined data set of data set 1 and data set 2.

After acquiring the data sets, they were prepared for next stages of classification by applying some preprocessing operations. Preprocessing helps to simplify and improve the subsequent operations in pattern recognition. The preprocessing operations applied on our signature samples were binarization, filtering and cropping.

3 Feature Extraction

Feature extraction is a process of deriving some characteristic parameters from the patterns (signature images). The extracted features should represent their parent pattern with reduced amount of data. Feature extraction helps in decreasing the computation complexities in the subsequent stages of signature verification.

Features of offline signatures are broadly classified into two main categories—(i) local features and (ii) global features [3].

Local features are extracted from a small region of the signature. These features are very much noise sensitive. Extraction of local features is computationally expensive. Global features are extracted from the complete signature image. Global features are easy to extract, and these are least sensitive to noise.

For our experimentation, we have extracted the following 15 (fifteen) features from each of the signature samples (genuine and forged) present in the data sets.

1. *Slope between corners*: It is the slope of the line joining the lower left corner and upper right corner of a cropped signature image.
2. *Aspect Ratio*: This is the ratio of signature width to signature height.
3. *Pure Height*: This is the height of the signature after removing the vertical blank spaces.
4. *Pure Width*: The width of the image after removal of horizontal blank spaces.
5. *Normalized Signature Height*: It is the ratio of maximum pure height to maximum pure width.
6. *Area of the signature Bounding Box*: It is the area of the signature bounding box after cropping of the signature image.
7. *Normalized Signature Area*: This is the ratio of the area occupied by signature pixels to the total number of pixels.
8. *Centre of Gravity (CG) in X direction*: The value of X coordinate of the CG of a signature image is its CG in X direction.
9. *CG in Y direction*: The value of Y coordinate of the CG of a signature image is its CG in Y direction.
10. *CG of the first half (H1) of the signature in X direction*: When the signature is vertically divided into two parts after cropping, the CG of the first half of a signature in X direction is the CG of the first half.
11. *CG of the first half (H1) of the signature in Y direction*
12. *CG of the second half (H2) of the signature in X direction*
13. *CG of the second half (H2) of the signature in Y direction*
14. *Baseline Shift*: It is the difference between the vertical centre of gravity of the left (H1) and right parts (H2) of the signature image. This indicates the overall orientation of the signature.
15. *Slope between H1 and H2*: It is the measure of the slope between the CG of the two vertically divided signature halves H1 and H2.

In the following sections, these features are indicated by their corresponding serial numbers as mentioned above.

4 Feature Selection

Feature selection is a process of finding out the smallest possible subset of the most important and relevant features from the complete set of extracted features so that the total number of features is reduced, but their class discriminatory information is still intact [4]. Selected features must minimize the dissimilarity between genuine signature samples and must maximize the dissimilarity between genuine and forged signatures.

In feature selection, using a comprehensive search method, the ‘best feature subset’ is tried to find that has the minimum number of features but contributes maximum towards classification accuracy. The best feature subset is evaluated with three different methods [5]: (i) filter methods, (ii) wrapper methods and (iii) embedded methods.

Filter method of feature selection uses different statistical tests to find out the features that have the highest predictive power. For a chosen statistical measure, this method calculates a score for each feature, and based on the scores, features are given a rank. This method is independent of the classifier.

Wrapper method divides the feature set into some subsets using a search procedure. It applies the classifier on them, and based on the classification accuracy, feature subset is evaluated using cross-validation [6].

Embedded methods perform selection of features during the training of a specific classifier. The criteria for feature selection are found out during training. In this method, feature selection and training of the classifier are combined together.

For our experimentation, we have used 2 (two) filter methods and a wrapper method for feature evaluation. Individual feature subsets were evaluated and selected for data set 1, data set 2 and data set 3 (the combined data set of data set 1 and data set 2).

(a) *Feature subset F1*: Feature subset F1 was selected using filter method. Here, attribute subset evaluator was correlation-based feature selection subset evaluator (CFS subset evaluator) and search method was the Best first.

CFS subset evaluator considers the individual predictive ability of each feature along with the amount of redundancy between them to assess the significance of a feature subset. Preference of selection is given to those feature subsets which are highly correlated with their native class and have low inter-correlation with the other class [7].

The best first search is basically based on greedy hill-climbing algorithm, but it is augmented with a backtracking facility. It starts with no feature and generates all possible single feature expansions. The subset with the utmost assessment is chosen and is expanded in the same way by adding the features one by one. When no improvement is resulted by addition of a subset, the search drops back to its previous node and starts searching the next best unexpanded subset from there. The best first searches the whole feature subset space till the evaluation of the subset improves due to addition of a new feature. When further addition of subsets results in no improvement, search is stopped and the best feature subset is returned [7].

(b) *Feature subset F2*: This subset was also selected by filter method. But, chi-squared ranking filter was the attribute subset evaluator, and search method was

Table 1 Evaluated features with evaluation methods

Signature set	Filter method		Wrapper method
	F1	F2	W1
Data set 1	2, 3, 4, 7, 8, 11, 12, 14, 15	8, 15, 14, 11, 3, 12, 7, 4, 10, 1, 2, 5, 13, 9, 6	3, 6, 8, 10, 14, 15
Data set 2	4, 6, 7, 10, 11, 12	10, 12, 4, 11, 6, 13, 15, 5, 7, 3, 9, 2, 8, 14, 1	3, 4, 7, 8, 9, 10, 11, 12
Data set 3	1, 3, 4, 8, 10, 11, 15	11, 8, 15, 4, 12, 14, 3, 10, 7, 13, 5, 6, 1, 2, 9	2, 3, 4, 7, 8, 10, 12, 14, 15

attribute ranking. This feature subset evaluator evaluates the significance of a feature by calculating the value of the chi-squared statistic with respect to the class. This attribute ranking search algorithm gives ranks to all the features based on their predictive powers. We selected the best 11 features from them, because the scores for the remaining four features were too low. For data set 2, their scores were 0 (zero).

(c) *Feature subset W1*: This subset was selected using wrapper method. Attribute subset evaluator was wrapper subset evaluator with support vector machine (SVM) as the classifier and search method was the best first. Wrapper subset evaluator uses the classifier (SVM in this case) to evaluate the feature sets. Cross-validation is used to estimate the accuracy of the classifier for a feature set. While selecting W1, we optimized the classifier parameters (C and γ) using all the features of the data set. In feature selection, these parameter values were used.

Table 1 shows the feature subsets F1, F2 and W1 evaluated for the three data sets—data set 1, data set 2 and data set 3.

5 Classification with SVM and Evaluation Results

Support vector machine or SVM is a supervised learning algorithm. SVM constructs a hyperplane which separates the two classes with the largest possible margin [8]. For linearly separable data of two classes, SVM finds an optimal hyperplane to separate them so that the distances of the hyperplane to the closest positive and negative training patterns (margin) are the maximum. When the data samples are not linearly separable, SVM maps the data points into a higher dimensional space called feature space using a nonlinear kernel. A separating hyperplane with maximum margin is constructed in the feature space.

For a training set of instance-label pairs (x_i, y_i) , $i = 1, 2, \dots, l$, where $x_i \in R^n$ and $y \in \{1, -1\}^l$, the SVM finds the optimum solution of the following problem [9]:

$$\min_{\mathbf{w}, b, \xi} \frac{1}{2} \mathbf{w}^T \mathbf{w} + C \sum_{i=1}^l \xi_i, \quad (1)$$

subject to

$$y_i (\mathbf{w}^T \phi(x_i) + b) \geq 1 - \xi_i, \quad \xi_i \geq 0 \quad (2)$$

Here, b is a bias term, and ξ is a nonnegative ($\xi \geq 0$) term called the slack variable. The function ϕ maps the training vectors x_i into a higher dimensional space. SVM finds a linear separating hyperplane with the maximal margin in this higher dimensional space. C is the penalty associated with the errors. Small C makes the cost of an error low, and large C makes the cost of an error high.

$K(x_i, x_j) \equiv \phi(x_i)^T \phi(x_j)$ is called the kernel function. Kernel function is used for making nonlinear feature map. Some popular kernel functions are:

Linear kernel:

$$K(x_i, x_j) = x_i^T x_j \quad (3)$$

Polynomial kernel:

$$K(x_i, x_j) = (\gamma x_i^T x_j + r)^d \quad (4)$$

where $\gamma > 0$

RBF kernel:

$$K(x_i, x_j) = \exp(-\gamma \|x_i - x_j\|^2) \quad (5)$$

where $\gamma > 0$

Here γ , r and d are kernel parameters.

With some parameter values of C and γ , RBF kernel can perform like a linear kernel [9]. Thus, RBF kernel can handle both nonlinearly separable and linearly separable data. In the literatures [10–12], it has been found that in offline signature verification, RBF kernel performs better than linear kernel and polynomial kernel. We used SVM classifier with RBF kernel for our experimentation.

In an SVM with RBF kernel, C and γ are the kernel parameters. C is the cost parameter. And the γ parameter defines the radius of influence of a single training example. For optimizing the classifier model, suitable values of C and γ are chosen which give the best recognition rate.

C and γ were optimized using grid search method. The optimized classifier models were evaluated using tenfold cross-validation. Following three parameters were considered for evaluating the classifiers:

$$\text{Recognition rate} = \frac{\text{No. of corectly classified signatures}}{\text{Total no.of signatures}} \times 100\%$$

$$\text{FRR} = \frac{\text{Total no. of genuine signatures classified as forged}}{\text{Total no. genuine signatures}} \times 100\%$$

$$\text{FAR} = \frac{\text{Total no. of forged signatures classified as genuine}}{\text{Total no. forged signatures}} \times 100\%$$

For data set 1, first we designed the classifier using all the 15 extracted features. Performance of the optimized model is shown in Table 2, column Full. Then, using the selected feature subsets F1, F2 and W1, three different classifiers were designed, optimized and evaluated (Table 2, column F1, F2 and W1). From F2, best 11 (eleven) features were used to design the classifiers.

Similarly, classifiers were modelled and evaluated for data set 2 (Table 3) and data set 3 (Table 4).

Table 2 Evaluation with Data set 1

Parameters/measures	Full	F1	F2	W1
<i>C</i>	2	3	2	2
γ	4	5	4	4
Recognition rate in %	99.36	99.36	99.36	99.68
FRR	1.05	1.05	1.05	0.52
FAR	0	0	0	0

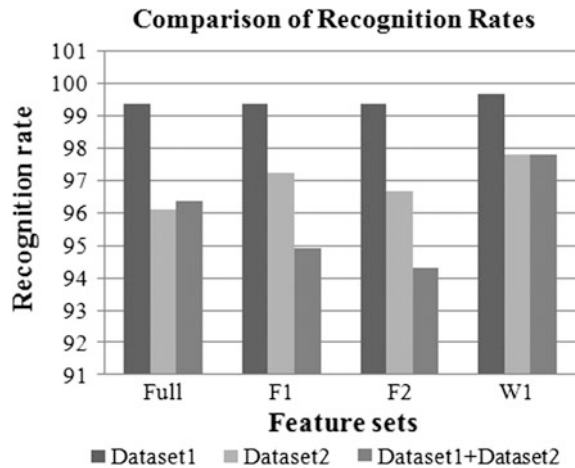
Table 3 Evaluation with Data set 2

Parameters/measures	Full	F1	F2	W1
<i>C</i>	3	2.5	3	2
γ	1	3	1	1.5
Recognition rate in %	96.11	97.22	96.67	97.78
FRR	6.58	6.58	6.58	2.63
FAR	1.92	0	0.96	1.92

Table 4 Evaluation with Data set 3

Parameters/measures	Full	F1	F2	W1
<i>C</i>	9.5	9.5	9.5	9.5
γ	4.5	4.5	4.5	4.5
Recognition rate in %	96.35	94.93	94.32	97.77
FRR	4.49	3.37	3.37	1.12
FAR	2.65	7.08	8.41	3.54

Fig. 1 Comparison of recognition rates



6 Observation

In the classifier models designed for the three data sets—data set 1, data set 2 and data set 3, feature subsets selected by wrapper method (W1) gave the highest recognition rates. The highest recognition rate achieved in our experimentation was 99.68% in data set 1 with feature subset W1. Out of 313 signature samples, in this case, there was a single misclassification (false negative). With other feature subsets—Full, F1 and F2, recognition rates for data set 1 were 99.36% (2 wrong classifications, false negatives), which were higher than data set 2 and data set 3.

Figure 1 shows the comparison of recognition rates of the three data sets with 4 (four) feature subsets—Full, F1, F2 and W1 derived from Tables 2, 3 and 4.

7 Conclusion

In our experimentation, we used two data sets with two different signatures. Both the signatures were English script based. But their styles were different. We tried to detect forgery using the same set of features and methodologies on them. It was observed that the features selected for data set 1 and data set 2 (and data set 3) were different (Table 1). Thus, it was evident that the effectiveness of the features was not same for both the data sets. The reason behind this was that the style of a signature defines its geometrical structure. Therefore, variations in the style of the signatures result variations in their geometrical measurements. The features used in our experimentation were some geometrical measurements of the signatures, and thus, their effectiveness varied with the two different styled signatures.

There are diverse styles of signatures found in existence. Some signatures are long and some are short, and some are graphical, while some of them are scripted. Some signatures have long vertical or horizontal strokes, some signatures are skewed, some are inclined, etc. Styles of the signatures based on different scripts may also be different. Some features are not equally effective for all signature styles. Depending on the style of the signature, stability of its features varies. Stability of the features influences the recognition rate. Thus, recognition rate is also affected by the style of the signature. To find a general model that will classify every style of signatures, we must find out those features which are stable across all styles of signatures. A proper combination of feature subsets and the classifier may result a good recognition rate in offline signature verification.

References

1. Batista. L, Rivard D., Sabourin R., Granger E., and Maupin P.: State of the art in off-line signature verification. *Pattern Recognition Technologies and Applications: Recent Advances*, 1st ed., B. Verma, M. Blumenstein, Eds. New York: IGI Global, pp. 39–62, (2008).
2. Liwicki M., Heuvel E. V. D., Found B., and Malik M. I.: Forensic Signature Verification Competition 4NSigComp2010 – Detection of Simulated and Disguised Signature. *IEEE Proc. - 12th International Conference on Frontiers in Handwriting Recognition*, pp. 715–720, (2010).
3. Impedovo D., and Pirlo G.: Automatic Signature Verification – The State of the Art. *IEEE Transactions on Systems, Man and Cybernetics - PART C: Applications and Reviews*, Vol. 38, No. 5, pp 609–635, (2008).
4. Theodoridis S. and Koutroumbas K.: *Pattern Recognition*, 4th ed., Elsevier, (2009).
5. Isabelle G., and Elisseff A.: An introduction to variable and feature selection. *The Journal of Machine Learning Research*, vol 3, pp. 1157–1182, (2003).
6. Kohavi R., John G. H.: Wrappers for feature subset selection. *Artificial Intelligence*, vol. 97, issue 1–2, pp 273–324, (1997).
7. Hall M. A., and Smith L. A.: Practical feature subset selection for machine learning. *Computer Science '98, Proceedings of the 21st Australasian Computer Science Conference ACSC'98*, C. McDonald, Ed., Perth, pp. 181–191, Berlin: Springer, (1998).
8. Cortes C., and Vapnik V.: Support-vector networks. *Machine learning*, vol. 20, issue 3, pp. 273–297, (1995).
9. Keerthi S. S., and Lin C. J.: Asymptotic behaviors of support vector machines with Gaussian kernel. *Neural Computation*, vol. 15, no. 7, pp 1667–1689, (2003).
10. Randhawa M. K., Sharma A. K. and Sharma R. K.: Off-line Signature Verification with concentric squares and slope based features using support vector machines. *3rd IEEE International Advance Computing Conference*, pp. 600–604, (2013).
11. Ferrer M. A., Vargas J. F., Morales A. and Ordóñez A.: Robustness of offline signature verification based on gray level features. *IEEE Transactions on Information Forensics and Security*, vol. 7, no. 3 pp 966–977, (2012).
12. Ferrer M. A., Alonso J. B. and Travieso C. M.: Offline geometric parameters for automatic signature verification using fixed-point arithmetic. *IEEE Trans. on Pattern Analysis and Machine Intelligence*, vol. 27, no. 6, pp. 993–997, (2005).

A Study on Prosodic Feature-Based Automatic Classification of Languages from Northeastern India

Sushanta Kabir Dutta and Lairenlakpam Joyprakash Singh

Abstract This paper describes a study on prosodic feature-based automatic language classification system for four Indian languages from Northeastern India. However, the number of languages may be increased. The present system can classify the selected Indian languages into two broad groups of tonal and non-tonal languages, based on the possibility of use of lexical tone in them. The lexical tonality in a language is measured by the speed and level of pitch variations in utterances. These parameters are applied as the inputs to a Naive Bayes classifier to complete the design of the system. Here three Indian languages and one dialect, namely Manipuri, Assamese, and Bengali languages and Kakching dialect of Manipuri language, have been used. All these languages are from the Northeastern part of India and are selected since no language classification or identification work is reported for these languages so far. The experimental results reveal that the present system is able to classify the Indian languages into broad groups of tonal and non-tonal languages for a relatively less amount of training data being in use.

Keywords Tonal · Non-tonal · Prosodic feature · Speed of pitch
Level of pitch · Naive Bayes classification

1 Introduction

A language is said to be a tonal language, if the pitch variation within a word changes the meaning of the word [1]. Manipuri, a scheduled Indian language spoken by the people in the state of Manipur and part of Assam, is a tonal language.

S. K. Dutta (✉) · L. J. Singh
North Eastern Hill University, Shillong 793022, Meghalaya, India
e-mail: sushantatzp@gmail.com

L. J. Singh
e-mail: jplairen@nehu.ac.in

Table 1 An example of Manipuri tone

Tone description	Level tone	Falling tone
Tone symbol	Unmarked	/˥/
Meitei Mayek	Mi	Mi
English gloss	Spider	Man

Phonemically, there are only two tones in the Manipuri language [2, 3], though there are languages around the world like Mandarin Chinese, Vietnamese, etc., having four to eight tones [4]. In Manipuri, the tones are (i) level tone and (ii) falling tone. The level tone is unmarked while the falling tone is marked as /˥/. Some of the examples of the Manipuri tones are shown in Table 1. However, in non-tonal languages like Assamese and Bengali, pitch variations are observed only in long duration of speeches.

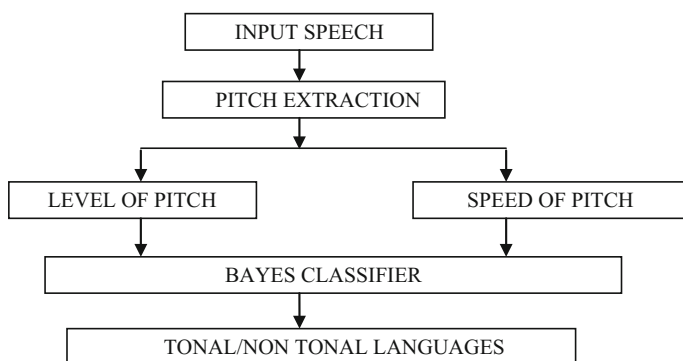
In spoken languages, pitch is as a good representative of prosodic feature that relates to phonation [5].

In order to design a tonal and non-tonal language classification system accompanying these pitch variation information, the Naive Bayes classifier has been used here.

The rest of paper is organized as follows: Sect. 2 explains the detail of classification system while Sect. 3 describes the speech corpus. Experimental results are available in Sects. 4 and 5 which also conclude the study.

2 Design of the Classification System

The details of the components used in the design of the language classification system are mentioned below. The block diagram of the proposed system is shown in Fig. 1.

**Fig. 1** Prosodic feature-based classification system

3 Pitch Estimation

Autocorrelation method is used here for pitch estimation [6]. Accordingly, a speech signal was segmented into successive frames of 20 ms each with a frame shift of 10 ms overlapping on one another. Next, the voiced frames were captured. Pitch estimation has to be done on the voiced frames only. Therefore, voiced frames were then passed through a low-pass filter having cutoff frequency at 900 Hz. Autocorrelation function was calculated for voiced each frame, and from there pitch estimation is done.

3.1 Speed of Pitch Change Module

The speed of pitch and level of pitch change were calculated after extracting the pitch information from the speech signal. The pseudocode used for calculating the speed of pitch change is mentioned as below:

1. Initialize counter $k = 1$ and $V =$ total number of voiced segment
2. Initialize i and j as beginning and endpoint of k th voiced segment
3. Assuming the k th voiced segment has N number of frames, and speed of pitch change (sp_k) for k th segment was calculated as

$$sp_k = \sum_{i=1}^{N-1} |f_{i+1} - f_i| \quad (1)$$

4. Increment k as $k = k + 1$
5. Check whether $k > V$, and if so then go to statement 6, else return to 2
6. Calculate 'speed of pitch change' (SP) for the entire utterance

$$SP = \sum_{k=1}^V sp_k \quad (2)$$

3.2 Level of Pitch Change Module

The pseudocode used for calculating the level of pitch change is stated as under:

1. Initialize counter $k = 1$ and $V =$ total number of voiced segment
2. Initialize i and j as beginning and endpoints of k th voiced segment
3. Calculate average pitch frequency f_{avg} for k th voiced segment. Assuming the k th voiced segment has N number of frames and calculate the level of pitch change (LP_k) for k th segment as

$$LP_k = \sum_{k=1}^{N-1} |f_{\text{avg}} - f_i| \quad (3)$$

where f_i is the pitch frequency of the i th frame

4. Increment $k = k + 1$
5. If $k > V$, then go to statement 6; otherwise, return to 2
6. Calculate 'level of pitch change' (LP) for the entire utterance as below

$$LP = \sum_{k=1}^V LP_k \quad (4)$$

3.3 Design of the Classifier

Naive Bayes probabilistic model is used for the design of the classifier [6, 7]. Abstractly, the probability model for a classifier is a conditional model.

$$p(C|F_1 \dots F_n)$$

Over a dependent class variable C with a small number of outcomes or classes, conditional on several feature variables F_1 through F_n . However, a more tractable model using Bayes theorem is put down as

$$p(C|F_1 \dots F_n) = \frac{p(C)}{p(F_1 \dots F_n)} \times p(F_1 \dots F_n|C)$$

The denominator in the above equation is constant, and the numerator can be broken down using class conditional probability as

$$p(C|F_1 \dots F_n) = p(C) \times p(F_1 \dots F_n|C)$$

Now using Naive conditional independence assumptions that each feature F_i is conditionally independent of every other feature F_j for i and j being different, the joint model can be expressed as

$$p(C, F_1 \dots F_n) = p(C) \prod_{i=1}^n p(F_i|C)$$

Now, when dealing with the continuous data, a typical assumption is that continuous values associated with each class are distributed according to a Gaussian distribution. Here, the attributes are the speed and the level of pitch changes being considered as belonging to Gaussian distributions.

4 Description of the Speech Database

The data were collected from the native speakers of the languages Manipuri, Assamese, Bengali, and Kakching dialect in studio. An equal ratio of male and female speakers is kept in all cases. After recording, the data are sliced up into smaller chunks of approximately 10 s duration. Only two of the languages are used for training of the classifier. In this work, a total of 90 samples of each of Manipuri and Assamese language data were used for training the classifier as tonal and non-tonal samples, respectively. Thus, the total duration of training data is around 30 min. However, during testing the data from all the four languages Manipuri, Assamese, Bengali, and Kakching were used. Around 1 hour of data were used for each of the languages during testing.

5 Experimental Setup and Results

The experimental setup consists of two phases which can be summarized as in the following sections.

5.1 Training Phase

In the training phase, the ‘speed of pitch change’ and ‘the level of pitch change’ were calculated as discussed for all voiced frames for samples of the training data. Then the means and variances of ‘the speed of pitch change’ and ‘the level of pitch change’ for tonal and non-tonal data are estimated considering them to be coming from Gaussian probability density functions. These values were later used in the testing phase for estimating the likelihood of each class.

5.2 Testing Phase

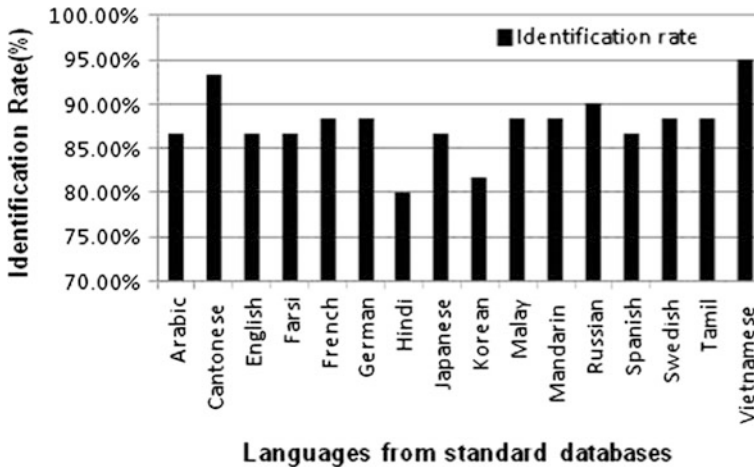
The ‘speed of pitch change’ and the ‘level of pitch change’ for the samples to be tested were estimated. The probability density values were therefore estimated as $f(\text{SP}|\text{tonal})$, $f(\text{LP}|\text{tonal})$, $f(\text{SP}|\text{non-tonal})$, $f(\text{LP}|\text{non-tonal})$. Then the likelihood scores for each class were calculated as

$$f(\text{TL}|\text{SP}, \text{LP}) = f(\text{SP}|\text{TL}) \times f(\text{LP}|\text{TL}) \quad (5)$$

$$f(\text{NTL}|\text{SP}, \text{LP}) = f(\text{SP}|\text{NTL}) \times f(\text{LP}|\text{NTL}) \quad (6)$$

Table 2 Performance of the classification system

Language	Number of samples	Correct identification	False alarm	Identified as	Accuracy in percentage (%)
Assamese	330	298	32	Non-tonal	90.30
Manipuri	330	313	17	Tonal	94.84
Bengali	293	219	74	Non-tonal	74.74
Kakching	213	129	84	Tonal	60.56

**Fig. 2** Results for classification of accuracies in standard databases

where TL stands for tonal, NTL for non-tonal SP for speed of pitch change and LP for level of pitch change. Each speech sample is therefore classified as tonal and non-tonal on the basis of whichever class has the highest likelihood score. The total number of samples used for each of the languages during testing phase along with the correct recognition and false alarm are presented in Table 2.

The above results are then compared with some similar findings for non-Indian languages using a GMM-based classification system [8] from a few standard databases, namely CALLFRIEND, OGI-TS, and OGI-22 and are found to be satisfactory. The results reported from standard databases are shown in Fig. 2.

6 Conclusion

Differences in the prosodic features among languages are not always very significant [9] in a way such that a complete languages identification system can be built using only these features. Therefore, a prosodic feature-based system described

above should only be used as a pre-classifier and must be coupled with a state-of-the-art language identification system such as the Gaussian mixture model-based universal background model (GMM-UBM) [10]. The pre-classification stage would reduce to a large extent the need of building up a comparatively larger GMM-UBM for all the languages to be identified since this would help categorize the languages into two subgroups. The task of identifying any language would then be limited to identifying within the subgroups.

References

1. Yip M.: *Tone..* University press, Cambridge: UK, (2002).
2. Arono M. (ed.): *Morphology Now.* State University of New York Press (1992).
3. Singh H. D. and Singh S. I.: *Exotic Phonemes: A Study of Manipuri Phonemes Language in India.* Languages in India, Vol 7, (2007).
4. Liu Q., Wang J., Wang M., Jiang P., Yang X. and Xu J.: A pitch smoothing method for mandarin tone recognition. *Int. J. Signal Process., Image Process. and Pattern Recog.*, Vol. 6, 245–254, (2013).
5. Roca I. and Johnson W.: *A Course in Phonology.* Oxford: Blackwell, (1999).
6. Tan L. and Karnjanadecha M.: A pitch detection algorithm: autocorrelation method and AMDF. *Proceedings of 3rd International Symposium on Communication and Information Technology*, pp. 551–556, (2003).
7. Lowd D. and Domingos P.: Naive Bayes' models for probability estimation. In *proceedings of 2nd international conference in Machine learning*, pp. 529–536, (2005).
8. Wang L., Ambikairajah E. and Choi E.: A novel method for automatic tonal and non-tonal language classification. In: *IEEE International Conference on Multimedia Expo Workshops*, pp. 352–355, (2007).
9. Mary L. and Yegnanarayana B.: Extraction and representation of prosodic features for language and speaker recognition. *Speech commun.*, pp. 782–796, (2008).
10. Kumar R. V., Vydana, H. and Vuppala, A.: Significance of GMM-UBM based modeling for Indian language identification. *Procedia Comput. Sci.*, Vol. 54, pp. 231–236, (2015).

Introducing 5G Front-End Femtocell to Improve 4G Network Performance

Debasish Bhaskar, Safal Sharma, Rabindranath Bera,
Ganesh Sharma, Preman Chettri and Kharka Bahadur Rai

Abstract The rapid pace at which data traffic is increasing day by day in wireless networks is a matter of concern. Thus, developing reliable solution that can handle this ever-growing data traffic is vital. 5G-based cellular networks have several distinct benefits. First and foremost, it will be able to deliver services similar to a fiber-based broadband network. This is a significant performance improvement over previous radio access technology. In this work, FBMC-based 5G front-end Femtocell has been introduced. This introduction has helped to improve the performance of existing LTE-based 4G JIO radio access. The designed model and proposed infrastructure help to achieve a very high data throughput of the order of 1 Gbs per second and good signal strength with reduced BER.

Keywords Data traffic · Radio access technology · 5G · FBMC
LTE · JIO · Data throughput · BER

1 Introduction

World enjoyed the flavor of most extensively sold cellular technology known as 3G. This was capable of providing multimedia communication with the usage of Wideband Code Division Multiple Access (WCDMA) and High-Speed Packet Access (HSPA) technology. With 4G coming up at a rapid pace that uses LTE network to support flexible bandwidth up to 20 MHz and Multiple Output (MIMO) antenna transmission [1]. LTE uses orthogonal frequency division multiplexing (OFDM) technology [2]. To improve the existing LTE network, the wireless technology roadmap now extends to LTE-Advanced to meet IMT-Advanced requirements that support bandwidth up to 100 MHz and is capable of providing peak throughput rates that exceed 1 Gigabit per second [3]. But with the present scenario that the world is going through in terms of data usage, these infrastructures

D. Bhaskar (✉) · S. Sharma · R. Bera · G. Sharma · P. Chettri · K. B. Rai
Sikkim Manipal University (SMIT), Majhitar, Sikkim, India
e-mail: debasishbhaskar@gmail.com

would not be sufficient to meet the consumer's demand [4]. Presently cellular networks are overloaded with huge growth in data traffic. To deal with this rapid explosion in mobile data usage, new solutions are required that can enhance the performance of existing technology. Introduction of Femtocell and heterogeneous networks with wireless fidelity are some of the solutions that can help to deal with the massive explosion in data usage [5]. There is a requirement for new network infrastructure. 5G is expected to introduce FBMC as desired waveform [6]. FBMC is an upgraded version of currently used OFDM where multiple antenna technique can be applied and MIMO technique [7] can be applied and offers higher spectral efficiency, higher immune to multipath and zero inter-carrier interference [7]. In this paper, we are interested to improve the performance of existing 4G JIO network with the introduction of FBMC-based 5G Femtocell for better user connectivity [5].

2 Problem Associated with 4G JIO

The survey report of 4G JIO done at SMIT campus is presented in Table 1. In this survey, measurements of different network parameters at different receiver height have been tabulated. We are interested to stream high multimedia video using 4G JIO enabled receiver handset. As it is clear from the table that when receiver is at greater height we are able to watch high-quality video with good receiver signal strength but as height gets decreased we observe that we are not able to watch the video due to different network-related problems [8]. We can broadly sum up these problems as a function of network congestion and signal propagation problem,

$$f(\text{congestion and propagation}), \quad (1)$$

Congestion problem arrives from higher network layer but propagation problem is associated with physical layer and it can be reduced with proper signal filtering technology at waveform level and with proper antenna beam formation [1].

The standardization process for 5G has not yet begun. A challenge of today's 5G research is in the waveform part and in the antenna part as the mobile

Table 1 4G JIO survey done at SMIT campus at different receiver height

Height (ft)	Video quality (HIGH–LOW)	Channel type (SD/HD)	RF signal level metering (bar)	Bit rate at physical layer (Kbps)	Network layer bit rate (Kbps)
60	HIGH	HD	3	1260	1670
30	HIGH	HD	2	664	1190
0	HIGH	HD	1	nil	nil
0	LOW	SD	1	443	760

communication at these mm-wave bands is far more challenging than the current frequencies that are being used around the world as signals will suffer with more noise.

3 Feasible Solution

In this proposed work, we are interested to mitigate the JIO 4G propagation problem by improving the network performance of 4G JIO system by the introduction of indoor 5G front-end Femtocell that will act as the trump card for achieving good BER performance even at indoor units where 4G system alone is not sufficient to provide required communication. A Femtocell is a cell that is located in a cellular network that provides proper signal coverage to desired users. Femtocell has been placed in an indoor unit that provides better coverage and it practically enhances the data throughput and makes signal connectivity stronger. Femtocell can provide connectivity to ten active residential users [5]. 5G Femtocell connects to standard 5G-enabled cell phones and similar devices through their wireless interfaces. Here, we are restricted to simulation platform as 5G has not yet deployed and there is no such 5G enabled device.

The block diagram depicted in Fig. 1 has two units, namely outdoor unit and indoor unit. Outdoor unit consists of 4G base station terminal, JIO-Fi modem, and WiFi to 5G modem. Indoor unit consists of 5G Femtocell of 20 m. Let us take up the system model as shown in Fig. 2. This system model has been developed with SystemVue 2016.08 simulation platform by Keysight Technologies Inc., USA. The BER metering tool has been set at outdoor JIO-Fi unit and indoor 5G unit. We have replaced 4G mobile receiver equipment terminal with JIO-FI MODEM that is placed at 10 m height above from normal 4G user mobile equipment to receive 4G signal. We have used simulation platform to show the performance of the proposed model. The simulation results that has been presented in Sect. 3 shows that that the

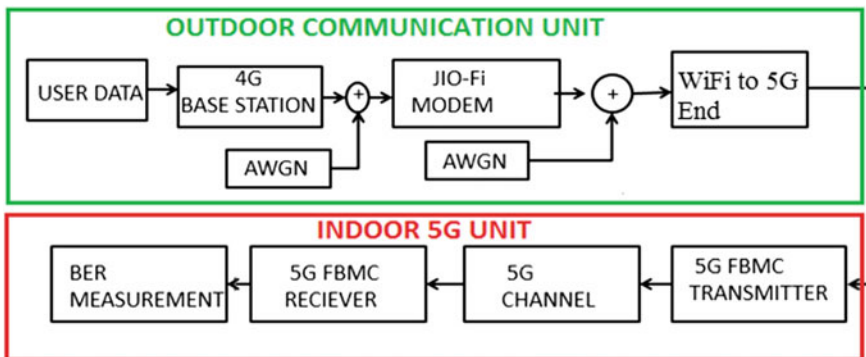


Fig. 1 Block representation of outdoor communication unit and indoor 5G unit

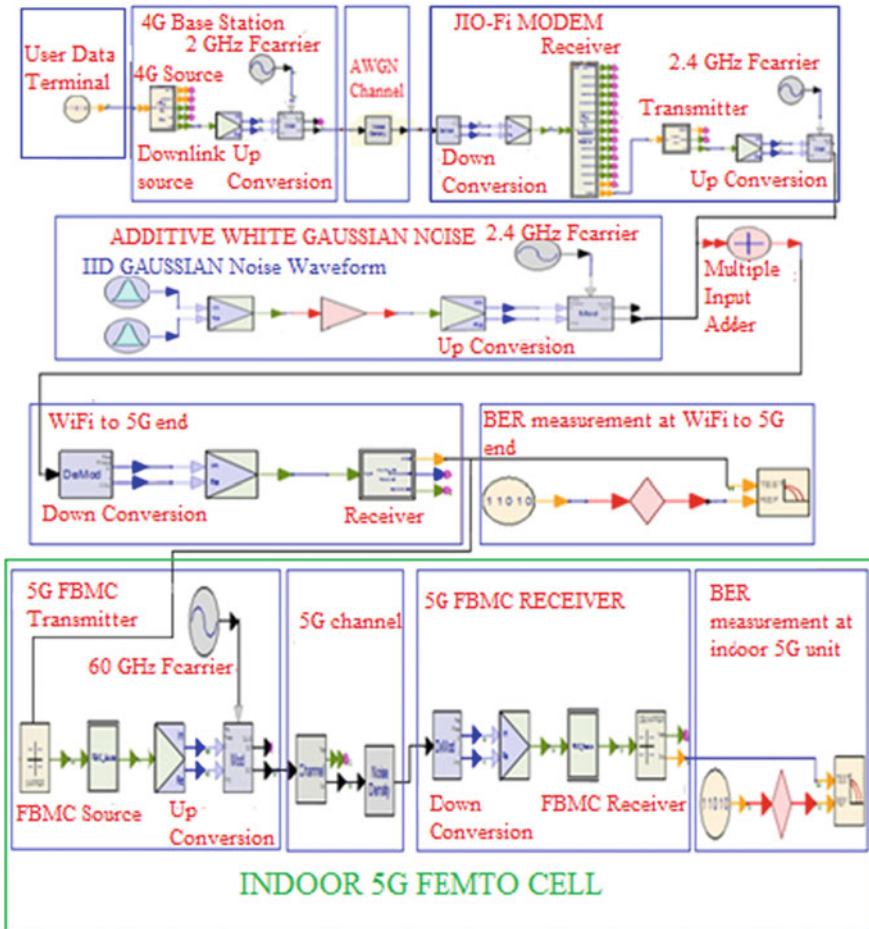


Fig. 2 System model of our proposed solution

This received signal will be directed as WiFi signal to feed it to an indoor 5G unit that contains 5G FBMC transmitter and receiver. With the aid of JIO-Fi modem, we will be able to capture RF signal that has been transmitted from 4G JIO base station antenna even at places where signal suffers from high propagation loss and has very high tendency to get fade. JIO-Fi modem will convert that signal into WiFi signal and it will be again retransmitted and it will be received by WiFi receiver and then it will be transmitted as 5G-FBMC signal.

Various data signal are given as input in Fig. 4 which can be mathematically written as,

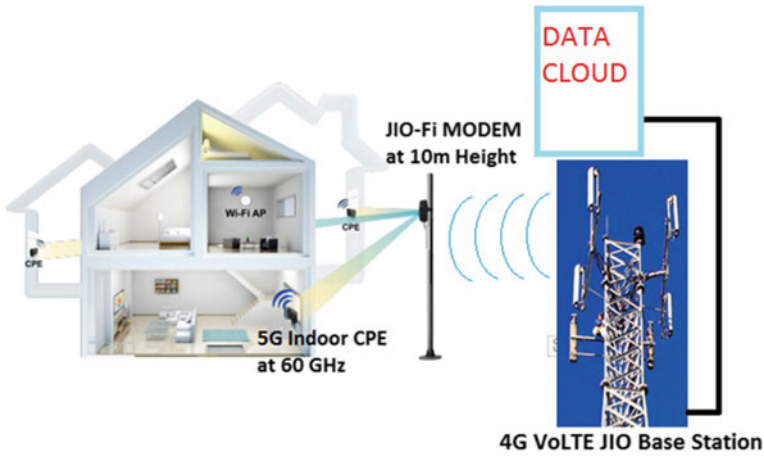


Fig. 3 Real-time deployment

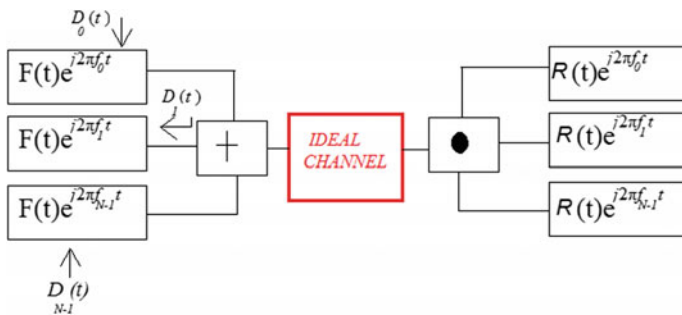


Fig. 4 Block diagram of 5G FBMC transceiver system

$$D_k(t) = \sum_n D_K[n] \delta(t - nT), \tag{2}$$

where $D_K[n]$ are the data symbols of different subcarrier with K as subcarrier index and T is the symbol time spacing. Figure 4 depicts FBMC transceiver structure for next-generation 5G system. FBMC is an upgraded version of ODFM. The major dissimilarities lie in the choice of T and the transmitter and receiver prototype filters $F(t)$ and $R(t)$.

Similarly, the transmitted signal of Fig. 4 can be mathematically acquired as,

$$T(t) = \sum_n \sum_{n \in \beta} D_K[n] F(t - nT) e^{j2\pi(t-nT)f_k} \tag{3}$$

where β denotes a various indices of active symbols. Here, in this structure, we have assumed the channel to be ideal, the received signal $R(t)$ will be same as transmitted signal $T(t)$. The diagram depicted in Fig. 3 shows the real-time deployment scenario of our proposed work. We can see from the figure that JIO-Fi modem has been placed at 10 m height that will capture the 4G base station RF signal. 5G indoor CPE unit will receive the JIO-Fi signal upon which mobile users at indoor residential units will be able to enjoy high-speed data connectivity.

4 Simulation Results

The system presented in Fig. 2 has been used as our desired model to obtain simulation results in this section. Figures 5 and 6 show the simulation results where we can observe the enhancement in performance by the introduction of FBMC-based 5G Femtocell. Figure 5 shows the plot of SNR versus BER performance at outdoor WiFi to 5G end and at indoor 5G end. We observe that there is an improvement in BER up to the order of almost zero upon good signal strength at FBMC receiver end. If we see the BER plot, then we observe that BER measured at indoor 5G end is less as compared to BER achieved at outdoor WiFi to 5G end. Figure 6 shows the data throughput that has been achieved at outdoor WiFi to 5G end and indoor 5G end. We observe enhancement in data throughput at 5G end that offers data throughput of almost gigabits per second experience to 5G residential users.

Fig. 5 BER performance of proposed model

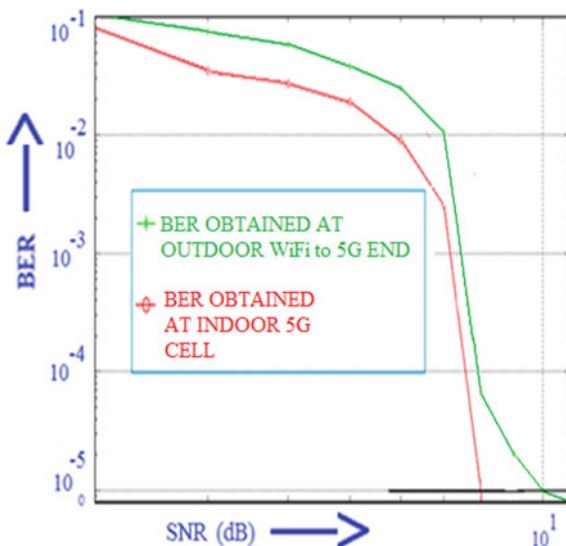
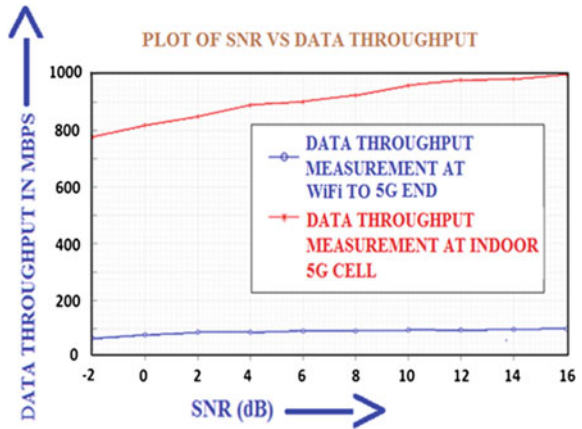


Fig. 6 Data throughput performance of proposed model



5 Conclusion

In this work, we have showed that existing 4G JIO network can be improved by using upcoming 5G technology. 5G front-end Femtocell and WiFi networks can be considered as silver lining to deal with current 4G JIO network coverage problem that has been overloaded by huge data usage. In this paper, we proposed a 5G Femtocell and JIO-Fi modem as a feasible solution for above-mentioned problems. 5G networks are in standardization stage, and there is no physical infrastructure available. Since, there is a craze going on around the globe about the launch of 5G, existing LTE 4G JIO network can be improved with the aid of 5G cell in terms of good data throughput and reduced BER. We have catered for real-time deployment of our proposed work that has been depicted in Fig. 4. We believe our obtained simulation results are highly valuable for the enhancement of current cellular infrastructure.

References

1. A. Ghosh., R. Ratasuk., B. Mondal., N. Mangalvedhe., and T. Thomas.: LTE-advanced: next-generation wireless broadband technology. *IEEE Wireless Commun.*, vol. 17, no. 3, pp. 10–22, (2010).
2. K. Kumaravel.: Comparative Study of 3G and 4G in Mobile Technology. *IJCSI International Journal of Computer Science Issues.*, vol. 8, issue 5, no. 3, (2011).
3. 3GPP TR 25.996.: spatial channel model for multiple input and multiple output (MIMO) simulations. (2012).
4. Cisco visual networking index.: Global mobile data traffic forecast update. White paper, (2012).
5. Mahmoud H. Qoutqut., Fadi M. Al-Turjman and Hossam S. Hassanein.: MFW: Mobile Femto cells utilizing WiFi. *EEE ICC.*, (2013).

6. S. Shin.: Implementing a Flexible Testbed for 5G Waveform Generation and Analysis. Keysight Technologies., (2015).
7. H. Zhang., D. L. Ruyet., D. Roviras., Y. Medjahdi and H. Sun.: Spectral efficiency comparison of OFDM/FBMC for uplink cognitive radio networks. EURASIP Journal on Advances in Signal Processing., vol. 2010, article id 621808, 14 pages, (2010).
8. A. Ghosh., R. Ratasuk., B. Mondal., N. Mangal vedhe and T. Thomas.: LTE-advanced: next-generation wireless broadband technology. IEEE Wireless commun., vol. 17, no. 3, pp. 10–22, (2010).

Narrowband Hybrid Beamformation System for Doable mmWave 5G Mobile Communication System

Safal Sharma, Debasish Bhaskar and Rabindranath Bera

Abstract This paper introduces a new high-performance narrowband Hybrid Beamformation (HBF) system for upcoming mmWave-based 5G system. HBF system overcomes the pitfall of narrowband Analog only Beamformation and narrowband Digital only Beamformation. Next-generation 5G communication system will be taking the advantage of millimeter wave (mmWave) frequencies band that inherits signal fading and immense propagation loss. The move toward the mmWave spectrum facilitates the use of shorter wavelength. This facilitation makes possible for small antennas to focus its radiated signals into narrow beam to compensate for signal fading and path loss. An enhanced version of antenna gain with much focused antenna beam with HPBW of almost 11° with gain of 23.45 dB has been obtained in this paper. Assuming that both BS and MS have prior knowledge of the narrowband mmWave channel, we were able to achieve very low BER of almost zero when good signal strength was maintained after Beamformation.

Keywords Narrowband · HBF · Analog beamforming · Digital beamforming
Antenna gain · HPBW · BER

1 Introduction

If we look globally, then cellular communication has become an everyday artifact. If we go back to past decades, then we observe a vivid transformation of this technology, from being a basic voice communication system that supported only Analog technology to today's system that facilitates advanced Digital technology. In order to master the advanced technology of today's world, it is important to credit their origination and their transformation. We can classify the roadmap of mobile communication into many versions, with 1G version being basic voice

S. Sharma (✉) · D. Bhaskar · R. Bera
Sikkim Manipal University (SMIT), Majitar, Sikkim, India
e-mail: safalmate@gmail.com

© Springer Nature Singapore Pte Ltd. 2018
R. Bera et al. (eds.), *Advances in Communication, Devices and Networking*,
Lecture Notes in Electrical Engineering 462,
https://doi.org/10.1007/978-981-10-7901-6_65

communication system that supported only analog modulation. This version was followed by second version named as 2G, which facilitated data connectivity by means of Digital technologies. This version was the pioneering version in terms of wireless data connectivity in cellular networks. The introduction of data connectivity in 2G gave word the taste of wireless data access, and it was positively welcomed by the world. This gave motivation for further enhancements in this area that credited to next 3G version. This version was equipped with high-speed data connectivity using technologies such as wideband code division multiple access (WCDMA) and high-speed packet access (HSPA) [1]. Presently, this network version is the most accepted version of cellular networks among the consumers around the globe, although next 4G network version is coming up at a rapid pace [1]. Currently, 4G is providing its essence to the world that uses orthogonal frequency division multiplexing (OFDM) technology with bandwidth of 20 MHz and multiple input and multiple output (MIMO) [2] antenna transmission. The itch of the data usage among the consumers is increasing day by day globally, and it is vital to enhance existing LTE network with LTE advanced that supports maximum bandwidth of 100 MHz [3]. With this rapid pace of increase in data usage, LTE-advanced technology would not be sufficient to satisfy this pace after few more years. World is looking into a newer version of cellular network that will act as a silver lining to this data usage problem that can occur in coming years. This newer version is termed as 5G version that is expected to introduce new technology. The problem of today's 5G research is to tackle the waveform frequencies that are being used around the world as signals will suffer from more noise at these frequencies. And these noise levels can be minimized by performing proper antenna Beamforming [4].

2 Millimeter Wave-Based 5G Communication

Presently, cellular networks have become overpopulated with huge data traffic, and in coming years, these infrastructures would not be sufficient to fulfill this overpopulation. So, the next-generation 5G network is expected to exploit Wave spectrum bands as shown in Fig. 1 that enables gigabit per second data rates and supports transmission of large amount of data known as big data. If we move to mmWave spectrum bands, we observe an increase in carrier frequency about decuple times than the current frequency bands at which current cellular infrastructure operates. In reality, the path loss and fading with the use of mmWave are bound to exist. To compensate for these aforementioned problems, mmWave spectrum facilitates the use of very short wavelengths. This gives feasibility to small antennas to concentrate signals into highly focused beams with enough gain to overcome propagation loss and fading [5]. In this process, the beam gets narrower and this narrowing of beam is called Beamforming where signals will be summed constructively at some point in space to provide good signal strength with

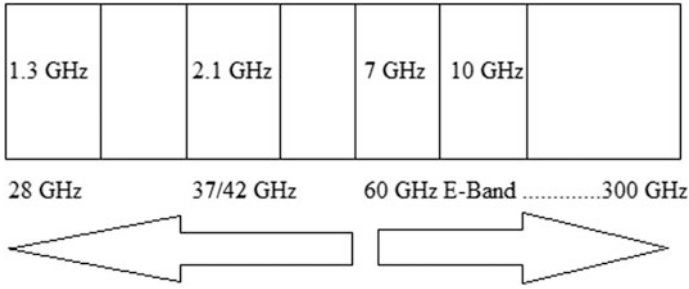


Fig. 1 Various spectrum bands at mmWave frequencies

low noise and enhanced BER. To overcome the limitations of analog only Beamformation and digital only Beamformation, newer solutions known as hybrid Beamformation were proposed [6]. Analog beamforming with narrowband mmWave signals is not capable of achieving higher gains, and performance of analog strategies was inadequate as compared with digital strategies [6]. Additionally, digital beamforming with hundreds of antennas for narrowband mmWave signals is not feasible due to hardware complexity and cost. We need a compromising solution between these two technologies that divide the precoding operations between the analog and digital domain, such that complexity and cost are reduced providing better level of performance than that of digital beamforming. This type of Beamforming technique is known as narrowband Hybrid Beamforming.

The channel estimation for propagation of narrowband mmWave signal is very challenging [7]. We consider that both base station and mobile station have perfect knowledge of the narrowband mmWave channel.

3 5G Narrowband Hybrid Beamformation System

Let us consider a single-user mmWave 5G narrowband hybrid Beamformation system as in Fig. 2. A base station (BS) transceiver and mobile station (MS) transceiver use analog and digital precoder/combiner at transmit and receive end, respectively. The number of antennas at BS and MS transceiver is nT and nR , respectively. This work emphasizes on downlink transmission. The parameter nC is the number of data creeks that are equal at MS and BS. The parameter nRF is the number of RF chains that have been considered to be equal at BS and MS. BS antenna nT establishes nC data creek communication as in [6] with MS antenna nR such that

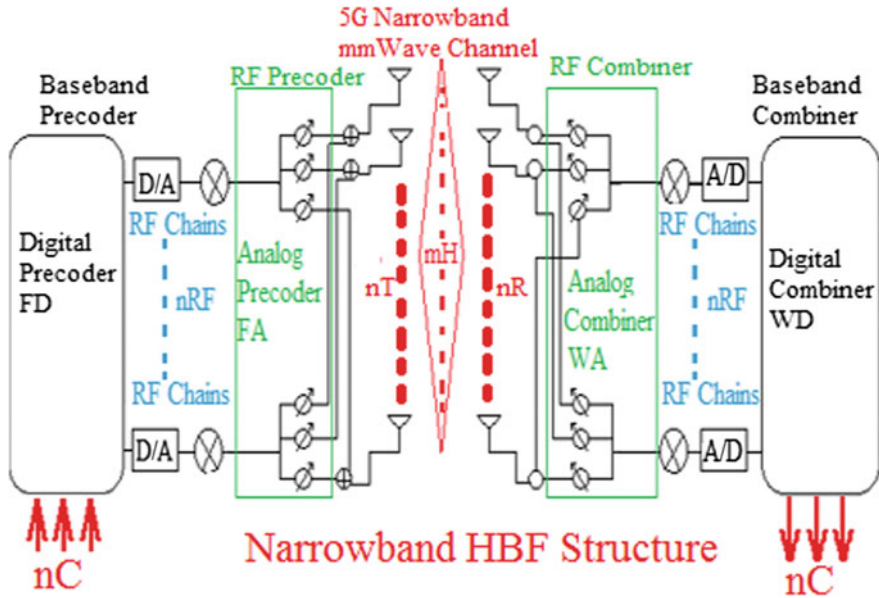


Fig. 2 5G mmWave 5G narrowband HBF system

$$(nC = nRF) < (nR) < (nT), \tag{1}$$

BS applies $(nRF \times nC)$ and $(nT \times nRF)$ digital precoder *FD* and analog precoder *FA*, respectively.

Now,

$$F_T = FDFA, \tag{2}$$

this is the $(nT \times nC)$ combined matrix that is used for precoding operations at digital and analog domain. Hence, the transmitted signal that is of discrete time in nature is given by

$$S = F_T s, \tag{3}$$

The variable *s* denotes the $nC \times 1$ transmitted symbol vectors. Similarly, the combiner at MS is composed of the analog and digital combiner *WA* and *WD* such that

$$W_T = WAWD, \tag{4}$$

The signal *R* that came from transmitter traveling through narrowband mmWave channel gets received upon processing with the combiner W_T . For sagacity, we take

up a narrowband mmWave propagation channel as in [7–9], that rewards the 5G MS receiver with the received signal,

$$R = \sqrt{\rho}mHF_T + n. \quad (5)$$

where mH is the narrowband mmWave channel that exists across transmitter at BS and receiver at MS. The parameter mH is a matrix having dimension of $nT \times nR$, and n is the noise. The noise n is of Gaussian type that attenuates the signal that is being received at MS terminal, and ρ denotes the average power at receiver side. Here, we consider that both BS and MS have perfect channel state information of the narrowband mmWave channel mH . Doing so, very high Beamforming gain and an enhanced version of BER have been achieved which are presented in Sect. 3. The channel estimation is a challenge in narrowband mmWave channel, and there are various potential ways to exploit the narrowband mmWave channel which is still a continuing topic of research. Various constrains of the propagation medium (channel) like path delay, power, angle of arrival, and angle of departure are evaluated stochastically. These stochastically collected data are based on the measurements from channel extraction parameter. Some of the channel parameters that have been defined in our model are as follows:

- BS Height = 8m and MS Height = 1.3m
- MS – BS 2D distance = 98m

4 Simulation Outcomes

The simulation results of our proposed mmWave 5G narrowband Hybrid Beamformation system has been presented in this section. SystemVue 2016.08 simulation platform by Keysight Technologies Inc., USA, have been used to develop this system. The limited scattering nature of mmWave channels has been assumed. Further, these simulation results have been used to evaluate its performance. The carrier frequency and bandwidth used were 73 GHz and 2.5 kHz, respectively. The sampling frequency is set as 5 kHz that has been oversampled to 20 kHz with oversampling ratio (OSR) four. By doing so, the narrowband mmWave signal can be perfectly reproduced with less noise and distortion. The mmWave 5G narrowband Hybrid Beamformation system discussed in Sect. 2 considers only one BS-MS link with no interfering BSs, and it has been used as our desired system model for simulation.

5 Performance Assessment in Terms of BER

QPSK modulation scheme has been applied by all three types of Beamforming strategies. The mapping of bits into symbol is such that one symbol is carrying two bits. The BER achievement of our proposed mmWave 5G narrowband Hybrid Beamformation system is depicted in Fig. 3, along with the BER performance of narrowband Digital Beamformation and narrowband Analog Beamformation. The proposed system gives reduced BER as compared to narrowband Digital and narrowband Analog Beamformation alone. This reduced BER obtained here is sufficient to support narrowband Hybrid Beamformation as an enabling technology for next-generation narrowband mmWave 5G communication system as compared to narrowband Analog Beamformation and narrowband Digital Beamformation alone.

6 Performance Assessment in Terms of Antenna Gain and HPBW

The placement of antenna arrays is uniform rectangular array (URA) at transmitter with spacing between arrays equal to $\lambda/2$. Antennas are positioned in three-dimensional rectangular geometry where the number of transmitter antennas at position $x = 1$, position $y = 8$, and position $z = 8$, such that $nT = 64$. Similarly, uniform linear array (ULA) (placement is configured at receiver with equal spacing between antenna arrays as that of transmitter. Placement of receiver antennas in three-dimensional linear geometry is such that number of receiver antennas at position $x = 1$, receiver antennas at position $y = 8$, and receiver antennas at position $z = 1$, such that $nR = 8$. We considered single BS-MS link with single RF chain at BS and MS with no other interfering BSs and MSs as in Sect. 2. The simulation results of resultant antenna beam pattern of transmitted signal in

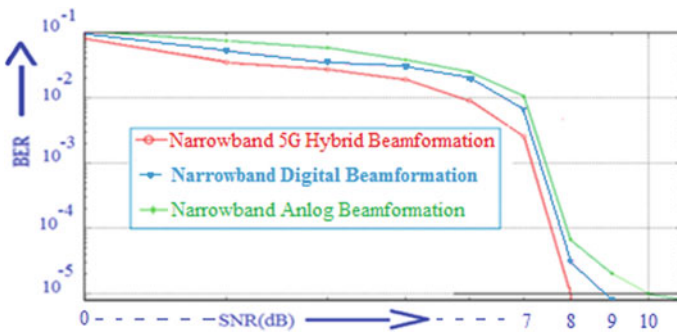


Fig. 3 Figure compares the BER achievement of narrowband Hybrid Beamformation system with that of narrowband RF and narrowband digital beamforming

three-dimensional spherical geometry with antenna pattern type as three-sector antenna elements with Y-Z uniform rectangular array configuration is presented in this section. In Fig. 5, the HPBW Beamwidth of 11.23° for phi beamwidth and 11.33° for theta beamwidth with antenna gain of 23.45 dB is observed. Whereas in Fig. 4, the HPBW beamwidth of 23.34° for phi beamwidth and 23.22° for theta beamwidth with antenna gain of 17.87 dB is observed. The measurement results obtained in Fig. 5 show that those measurements results are an enhanced version of the measurements results obtained in Fig. 4. Thanks to narrowband Hybrid Beamformation presented in Sect. 2 that helped to enhance the measurement results.

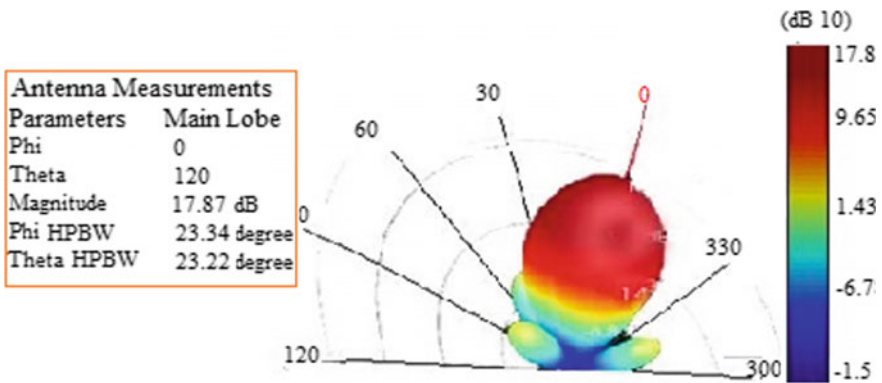


Fig. 4 Figure shows the resultant transmit antenna pattern in absence of narrowband Hybrid Beamformation

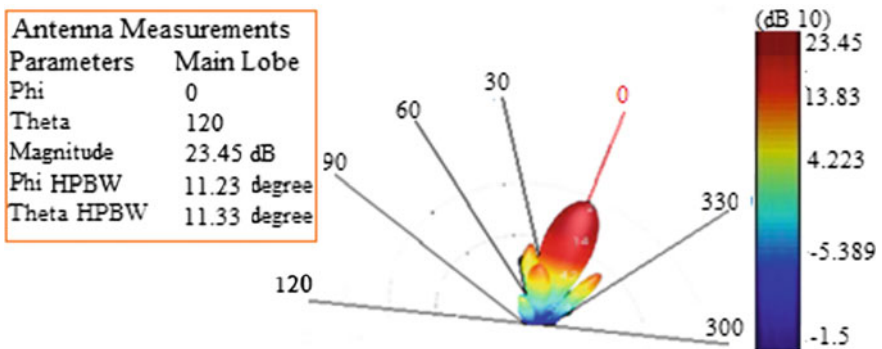


Fig. 5 Figure shows the transmit antenna pattern as a result of narrowband Hybrid Beamformation

7 Conclusion

Narrowband Hybrid Beamformation system was forward as a doable solution for next-generation mmWave-based 5G system. The simulation results presented in Sect. 3 showed that this type of system offers much focused and concentrated beams of an antenna array. The Beamforming ability presented in this paper helps to master the path loss and signal fading introduced by narrowband mmWave channel. This paper showed that successful communication can be established when mmWave narrowband signal was being used as a propagation signal. The narrowband HBF system presented in Sect. 2 maintained very low BER and high antenna gain by broadcasting very narrow beam. The authors of this work believe that the simulation outcomes that have been achieved in this paper would help for the development of 5G communication system.

References

1. T. Rappaport., et al.: Millimeter wave mobile communications for 5G cellular: It will work. *IEEE Access.*, vol. 1, pp. 335–349, (2013).
2. 3GPP TR 25.996.: spatial channel model for multiple input and multiple output (MIMO) simulations. (2012).
3. Ghosh., R. Ratasuk., B. Mondal., N. Mangalvedhe and T. Thomas.: LTE-advanced: next-generation wireless broadband technology. *IEEE Wireless Commun.*, vol. 17, no. 3, pp. 10–22, (2010).
4. W.Roh., et al.: Millimeter Wave Beam forming as an Enabling Technology for 5G Cellular Communications: Theoretical Feasibility and Prototype Results. *IEEE Commun. Mag.*, vol. 54, pp. 106–113, (2014).
5. T.Rappaport., F. Gutierrez., E. Ben-Dor., J. Murdock., Y. Qiao., and J. Tamir.: Broadband millimeter-wave propagation measurements and models using adaptive-beam antennas for outdoor urban cellular communications. *IEEE Trans. Antennas Propag.*, vol. 61, no. 4, pp. 1850–1859, (2013).
6. A.Alkhateeb., Omar El Ayach., Geert Leus and Robert W. Heath.: Channel Estimation and Hybrid Precoding for Millimeter Wave Cellular Systems. *IEEE J. Sel. Topics in Signal Processing.*, vol.8, pp. 831–846, (2014).
7. O. E. Ayach., S. Rajagopal., S. A. Surra., Z. Pi., R. W. Heath.: Spatially Sparse Precoding in Millimeter Wave MIMO Systems., *IEEE Trans. on Wireless Comm.*, vol. 13, no. 3, (2014).
8. J. Brady, N. Behdad, and A. Sayeed.: Beam space MIMO for millimeter wave communications: system architecture, modeling, analysis, and measurements. *IEEE Trans. Antennas Propag.*, vol. 61, no. 7, pp. 3814–3827, (2013).
9. Z. Pi.: Optimal transmitter beamforming with per-antenna power constraints. *Proc. 2012 IEEE International Conf. Commun.*, pp. 3779–3784, (2012).

Accidental Event Detection Based on Optical Flow Analysis

Navneet Nayan, Sanjeet Kumar and Sitanshu Sekhar Sahu

Abstract Event detection, in simple terms, means detection of the incidences occurring around us satisfying the threshold condition of some predefined criteria. In present scenario, event detection is gaining importance because of its versatility regarding predefined criteria, threshold conditions and its widespread applications. Many works have been done in this area. In the present paper, our goal is to detect the accidents occurring on the streets, roads and highways. For this, we have done the correlation analysis of optical flow and exhaustive simulation has been performed to show its effectiveness. The results based on optical flow of frames and its correlation show that the event is detected more accurately compared to the results obtained due to correlation only. Also, an exhaustive study has been performed on various accidental scenarios and it has been observed that the proposed method accurately identifies the accidental scenario in every case, be it any kind of traffic (more dense or less).

Keywords Accident detection · Optical flow · Correlation · Correlation coefficient · Frame rate

1 Introduction

Event detection in present scenario is one of the most diverse and versatile area of research. Also, event detection has widespread applications in the areas like traffic monitoring, video surveillance, environmental monitoring, remote sensing. The very first concept which should be known is “What is an event”. An event is any

N. Nayan (✉) · S. Kumar · S. S. Sahu
Department of ECE, BIT Mesra, Mesra, India
e-mail: navneetnayan543@gmail.com

S. Kumar
e-mail: sanjeet@bitmesra.ac.in

S. S. Sahu
e-mail: sssahu@bitmesra.ac.in

kind of occurrences satisfying the threshold condition of some predefined criteria. These two “the threshold condition” and “the predefined criteria” are responsible for the diverseness and versatility of this field. The various criteria decide which kind of event it is, like our event may be accident detection, crowd dispersion, traffic jam, crowd density estimation, etc. Many works have been done in all these various areas. Here, we are focused on road accident detection.

At present time, traffic on roads is growing day by day at a rapid rate and the area of highways and road is fixed. The increment in traffic capacity on the limited road area and the rough and improper driving ultimately results in fatal road accidents resulting in loss of lives. According to the reports of Association for Safe International Road Travel (ASIRT), nearly 1.3 million people die in road accidents every year and more than 50% of them are the ones having age in the range 15–44. In context of India, scenario becomes a bit more terrifying, having nearly 0.5 million deaths per year. Nearly half of these deaths result only because the accidents are not reported within the time and the victims do not reach hospitals at time. So there should be some way so that every accident occurring anywhere should be reported within time and lives should be saved. Here comes the concept of “automatic accident detection”.

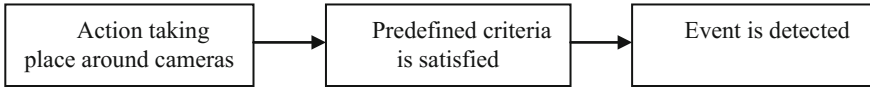
Here in this paper, we will be using the concepts of optical flow and correlation coefficient for the detection of an accident. After this brief introduction, the entire paper is documented as follows: Sect. 2 contains previous works, Sect. 3 has the methodology and its flow diagram followed by Sect. 4 having results and comparison with several other methodology, and Sect. 5 concludes the paper.

2 Previous Works

Many works have been done in the area of event detection (mainly, crowd dispersion and crowd density estimation), and optical flow has been a very important tool for it. In [1], Horn and Schunck have discussed the formation of optical flow. In [2], different optical flow methods and their performances were compared. The concept of optical flow has been widely used for crowd dispersion and crowd density estimation. In [3], the event criteria were to find crowd dispersion based on the abrupt change in the weighted velocity of the crowd. Also, concept of divergent centers has been proposed in this paper. In [4], authors have used roadside video data for learning the traffic pattern and also they have used vision-based techniques for tracking and determining the kinetic features of vehicles. An Android-based application has been developed and tested in [5]. Here, the authors have tried to minimize the delay from the detection of the accident till the victim is safely handed to the hospital or the concerned authorities. Along with it, there has been a discussion of both visual and audio surveillance of road accidents in [6, 7]. In [8], correlation of matrices has been discussed.

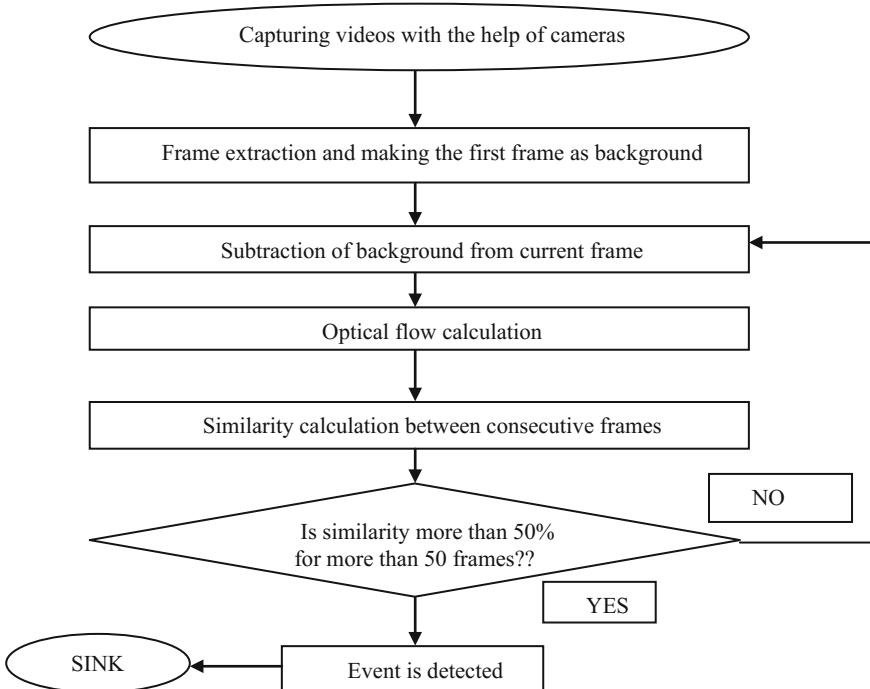
3 Methodology

The entire framework can be shown as



3.1 Idea to be Exploited for Accident Detection

In case of a normal moving traffic, the scene will keep on changing in a regular manner. Hence, the correlation between the matrices of consecutive frames will keep on changing as well as the correlation values will be less. After the accident took place, the part of the scene where the accident took place will remain static and hence the correlation values between consecutive frames will be more for longer period of time. In this paper, we have tried to find a pattern of correlation coefficient of the optical flow of consecutive frames rather than the correlation coefficient of consecutive frames, before and after the accident. The flow chart of the entire process can be described as



4 Results and Discussions

The above-mentioned methodology has been tested on the videos obtained from YouTube. We have performed the simulation on Intel(R) Core(TM) i7-6700 CPU @ 3.40 GHZ processor with 8.00 GB RAM. We have two kind of videos. The first video, i.e., video 1 has least traffic, and only two vehicles are moving which were moving and made a collision. Two frames of this video have been shown here. The second video is the CCTV footage of a very busy road of Nepal. The frames of this video are clearly indicating the density of traffic. Here in this video, a motor cyclist lost his balance and hit the bus coming toward him. The parametric description of these videos is as follows.

Video 1: The length of video is 10 s and has 242 frames. The frame size is 1280 by 720. We have extracted the frames with a gap of 8 frames, and the processing was done on these frames. In Fig. 1 first picture indicate the accident took place and second picture is the last frame of the video.

In Fig. 2, we plotted the correlation coefficient values of optical flow of consecutive frames versus frame number. Here, two regions have been highlighted. Region 1 shows the point of accident, i.e., the frame around which accident took place. As we all know, the accidental spot in the scene remains static, and region 2 describes this static behavior. In region 2, we see that the values of correlation coefficient are very high and maintaining those high values till the end of scene. This pattern shows that there is an accident and hence an event occurred. In Fig. 3, we have plotted the correlation coefficient values of consecutive frames versus frame number. Here, it is observed that the range of correlation coefficient values is between 0.97 and 1. Hence, it is a bit tedious task to make a threshold condition and to make a decision of accident in this case.

Video 2: The length of video is 3 min 22 s and has 5072 frames. The frame size is 1280 by 720. We have extracted the frames with a gap of 24 frames. Its result is shown in Fig. 4.



Fig. 1 First picture shows the frame in which the accident took place, and second picture is the last frame of video

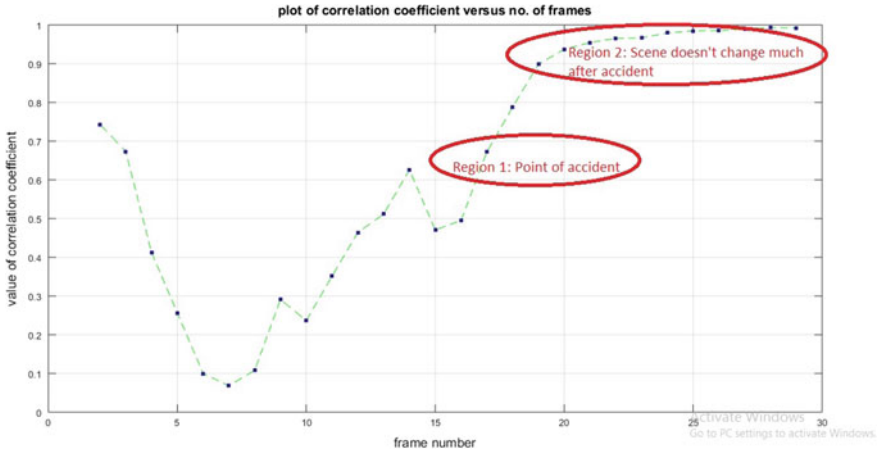


Fig. 2 Plot of correlation coefficient versus frame number when correlation analysis was done on the optical flow of consecutive frames. Here, we find an accurate detection of accident

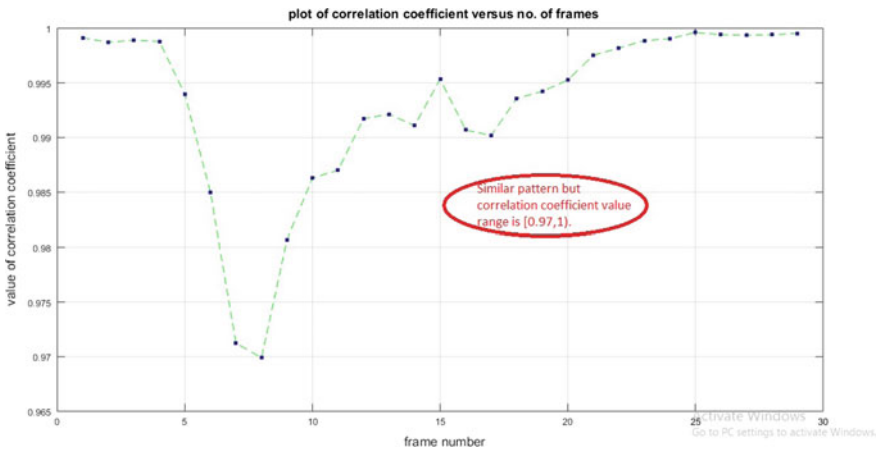


Fig. 3 Plot of correlation coefficient versus frame number when correlation analysis was done only on consecutive frames

In Fig. 5, we are clearly getting a pattern. Here also we have some regions. Region 1 is showing the point of accident, i.e., the frame number around which the accident took place, and region 2 once again showing the pattern of high correlation values after the point of accident, which signifies that there are little changes in the scene after the accident. Whereas in Fig. 6, it is tough to find any pattern or region indicating any accident or event. The entire result for detecting an event is summarized in Table 1.



Fig. 4 Two frames are showing the accidental frame and the last frame of video

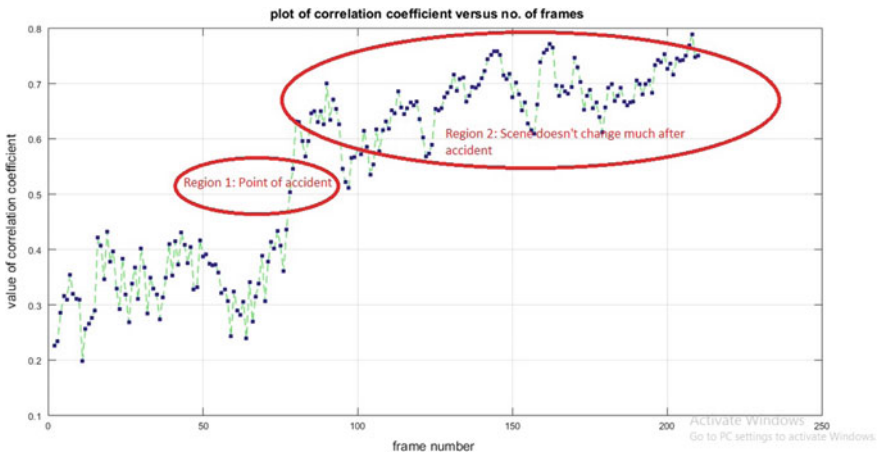


Fig. 5 Plot of correlation coefficient values of consecutive optical flow of frames against frame number

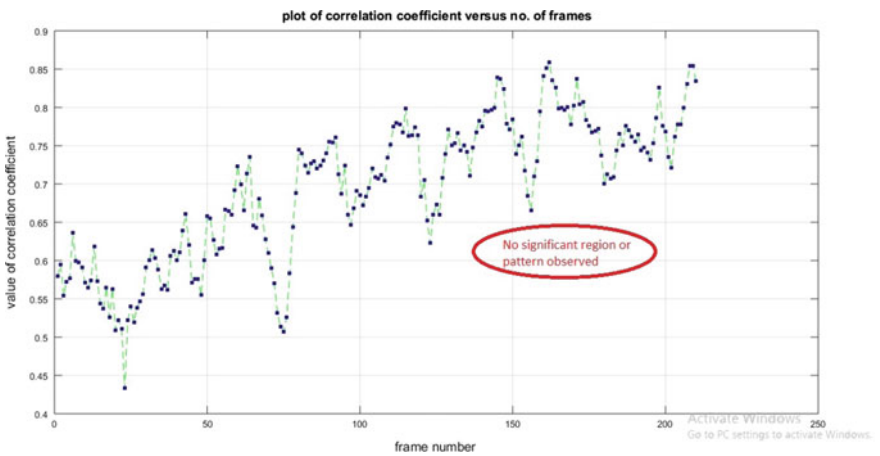


Fig. 6 Plot of correlation coefficient values of consecutive frames versus number of frames. Here, we can see that no significant region or pattern was observed which can decide the accidental scene

Table 1 Summary of the results and discussions of video 1 and video 2

Methodology	Serial number of video	Number of frames to be processed	Time taken for entire processing (in seconds)	Range of correlation coefficient	Pattern observed	Remarks regarding accident detection
Only correlation analysis	Video 1	32	24.68	0.97–0.99	Yes	Not detected
	Video 2	212	175	0.43–0.86	No	Not detected
Correlation analysis of optical flow	Video 1	32	26.12	0.09–0.99	Yes	Detected
	Video 2	212	178	0.20–0.81	Yes	Detected

5 Conclusion

In this paper, a method based on correlation analysis of optical flow has been proposed for accident detection. The proposed methodology and the tabulated results clearly explain that combining the concept of correlation and optical flow provided more accurate and perfect results as compared to the correlation alone. During the experimentation, several other factors also came into discussion. The length of videos, the gap of frames at which frames have been extracted, the area covered by vehicles in the scene, the field of view of camera and the density and movement of vehicles also put an effect on the results. For making a robust setup to detect any kind of accidental scene, it is important to make a trade-off between all these factors.

References

1. B. K. P. Horn, B. G. Schunck.: Determining Optical Flow, in *Artificial Intelligence*, Volume 17, Issues 1–3(August 1981), 185–203.
2. J.L. Barron, D.J. Fleet, S.S. Beauchemin, T.A. Burkitt.: Performance of Optical Flow Techniques, in *IEEE* (1992), 236–242.
3. C. Y. Chen, Y. Shao.: Crowd Escape Behavior Detection and Localization Based on Divergent Centers, in *IEEE Sensors Journal*, Vol. 15, No. 4 (April 2015), 2431–2439.
4. Mirza M. Lutfe Elahi, Rahat Yasir, Minhaz Ahmed Syrus, Md. S. Q. Zulkar Nine, Ishtiaque Hossain, Nova Ahmed.: Computer Vision Based Road Traffic Accident and Anomaly Detection in the Context of Bangladesh, in *3rd International conference on informatics, electronics & Vision* (2014), 1–6.
5. Hari Sankar S, Jayadev K, Suraj B and Aparna P.: a comprehensive solution to road traffic accident detection and ambulance management, in *International Conference on Advances in Electrical, Electronic and System Engineering* (November 2016), 43–47.
6. Yu Chen, Yuanlong Yu and Ting Li.: A Vision based Traffic Accident Detection Method Using Extreme Learning Machine, in *International Conference on Advanced Robotics and Mechatronics (ICARM)* (2016), 566–572.

7. Pasquale Foggia, Nicolai Petkov, Alessia Saggese, Nicola Strisciuglio, and Mario Vento: Audio Surveillance of Roads: A System for Detecting Anomalous Sounds, in *IEEE transactions on intelligent transportation systems*, vol. 17, no. 1 (January 2016), 278–288.
8. Long Bai, Alexander Velichko, and Bruce W. Drinkwater.: Ultrasonic Characterization of Crack-Like Defects Using Scattering Matrix Similarity Metrics, in *IEEE Transactions on Ultrasonics, Ferroelectrics, and Frequency Control*, vol. 62, no. 3 (March 2015), 545–559.

Application of 5G Waveform in Internet of Things (IoT) and Its Impact on BER in Physical Layer

Pallavi Neog, Rajat Paul, Shantanu Roy and Rabindranath Bera

Abstract Wireless freedom, smaller size, faster speed, smarter world: the next advancement is here, i.e., 5G. Recently, the world is going crazy over the latest technology, i.e., 4G (LTE/LTE-Advanced networks). Also in India, Reliance Jio 4G network has gained immense popularity. Already research has started in the coming next generation, i.e., 5G with an aim of increasing data rate from 10 to 100 times, reducing energy consumption by 10 times, increasing 100 times more connected devices, and also to reduce the latency. Hence, 5G network will be able to support machine to machine communication efficiently. That will make the 5G network capable of monitoring and controlling millions of devices and will provide the enormous data collection and distribution requirements of Internet of Things, i.e., IoT. Here, in this paper, a comparative analysis of BER performance of LTE-Advanced system and 5G system has been done, once with big data, i.e., wideband and then with control signals, i.e., narrowband, as for implementing IoT, big data is needed to support massive devices with high speed and narrowband is needed for controlling purpose. We are concerned about BER performance as BER is an important parameter for system performance analysis. SystemVue 2016.08 software has been used for experimental purpose. Also, MATLAB 2015 has been used.

Keywords FBMC · IoT · LTE-A · BER · SNR · OFDM

P. Neog (✉) · R. Paul · S. Roy · R. Bera
Department of Electronics and Communication Engineering,
Sikkim Manipal Institute of Technology, Majitar, Sikkim, India
e-mail: pallavineog66@gmail.com

R. Paul
e-mail: rajatpaul1992@gmail.com

S. Roy
e-mail: tubaiotubai07@gmail.com

R. Bera
e-mail: rbera50@gmail.com

1 Introduction

In today's LTE/LTE-Advanced networks, orthogonal frequency division multiplexing (OFDM) is used. To gain access to the network, two different waveforms are used: for downlink purpose, OFDM access (OFDMA) and for the uplink purpose, single carrier frequency division of multiple accesses (SC-FDMA) are being used.

1.1 Orthogonal Frequency Division Multiplexing (OFDM)

OFDM is a digital multicarrier modulation technique. It uses multiple subcarriers within the same single channel, thereby extending the concept of single carrier modulation scheme. OFDM uses orthogonal subcarriers and transmits them in parallel. OFDM uses frequency division multiplexing (FDM). Contrary to traditional FDM, in OFDM, subcarriers carry the information stream. OFDM subcarriers are orthogonal to each other. To each symbol, a guard interval is added to reduce inter-symbol interference. OFDM has the ability to cope with severe channel conditions which are not possible in case of single carrier modulation scheme. OFDM has the ability to convert frequency selective channel to flat channel.

The OFDM symbol can be mathematically expressed as

$$p(t) = \sum_{k=0}^{N-1} X_k e^{j2\pi kt/T}, 0 \leq t < T \quad (1)$$

where $\{X_k\}$ are the data symbols, N is the number of subcarriers, and

T is the OFDM symbol time. The subcarrier spacing is of $1/T$ which makes them orthogonal. The orthogonality can be expressed as

$$\frac{1}{T} \int_0^T (e^{j2\pi k_1 t/T})^* (e^{j2\pi k_2 t/T}) dt$$

$$p(t) = \frac{1}{T} \int_0^T e^{j2\pi(k_1 - k_2)t/T} dt = \delta_{k_1 k_2} \quad (2)$$

where $\{*\}$ denotes the complex conjugate operator and δ is the Kronecker delta.

A guard interval of length T_g is inserted before the OFDM block to avoid ISI. A cyclic prefix is also transmitted during this interval. The OFDM symbol with cyclic prefix can be expressed as

$$p(t) = \sum_{k=0}^{N-1} X_k e^{j2\pi kt/T}, -T_g \leq t < T \tag{3}$$

One of the applications of OFDM is LTE/LTE-A

1.2 Long-Term Evolution (LTE)

Long-term evolution (LTE), release 10, referred as LTE-Advanced, is the step toward true 4G evolution. LTE and LTE-A works under same technology with the advance signifying the difference between the release 10 and ITU/IMT-Advanced. For the multiplexing, it uses both time division multiplexing (TDM) and frequency division multiplexing (FDM). In case of LTE-A, downlink multiplexing is a combination of TDM and code division multiplexing (CDM) and for LTE, downlink multiplexing is a combination of TDM and FDM. Carrier aggregation is used in LTE-Advanced. LTE-A is one of the technologies suited for IoT. Though OFDM is currently used in 4G, it has got few significant disadvantages which need to be taken into consideration.

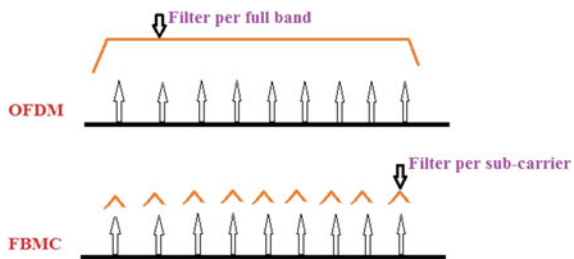
- High peak to average power ratio.
- Loss in spectral efficiency due to cyclic prefix.
- Insertion and the presence of significant out-of-band emissions.

To overcome the disadvantages of OFDM, FBMC, a new multicarrier transmission technique has been brought into the picture.

1.3 Filter Bank Multicarrier (FBMC)

FBMC is a multicarrier transmission technique which is basically an up gradation of OFDM. FBMC is suitable for new concepts, specially, cognitive radio. Unlike OFDM, where filtering is applied per full band basis, FBMC applies filtering per subcarrier basis; hence, out-of-band spectrum characteristics is improved in case of FBMC [1] (Fig. 1).

Fig. 1 Filtering methods of OFDM and FBMC



In FBMC, the neighboring subchannels are orthogonal. Offset quadrature amplitude modulation (OQAM) is used in FBMC. High bit rate is obtained due to OQAM modulation along with filter banks; hence, guard time or cyclic prefix is not needed like OFDM. First step of OQAM modulation is converting complex data to real and imaginary. And the conversion is different for even and odd subcarrier. The second step is putting the time offset of half symbol period to one of the data flow and adding the two data flow together. Real part of the complex data on the odd subcarrier multiplied with 1 will be sent to the Mux to form the second data flow.

The prototype filter of FBMC can be described by the following equation

$$p(t) = \sum_{i=0}^{L-1} h_i * x(n-1) \quad (4)$$

where L = length of filter impulse response

FBMC can be used to implement IoT.

1.4 Internet of Things (IoT)

With people craving to be surrounded by smart services and application environment, this next decade will see the development of smart city, smart wearable's with computing power, remote health care and smart education, and safety systems as a context of the former [2]. Smart agriculture will play an important role in feeding the ever-growing population with minimal harm to the environment [2]. Internet of Things (IoT) will be the fuel to avail these services. IoT will probably be the next thrilling application. By 2020, it is estimated that around trillion devices will get connected to the Internet and it will account for the maximum of the internet traffic. With devices being equipped with computational power, faster processing and battery life will be major issues. The estimated connected devices by the end of this decade will ask for massive connectivity and bandwidth. High coherence or integrity in the network will serve the massive machine to machine (M2M) traffic. The access devices in IoT will be using 5G next-generation network (NGN) for the access technology. It will serve the massive M2M traffic [3]. 5G NGN is going to be the backbone for IoT deployment process and for meeting the requirements. This next-generation network uses small cell configurations to support the high density of devices. This new generation network provides communication directly between devices, even at cell edges [3].

1.5 Review on 5G-Based IoT

IoT is expanding its reach to commercial world with its backbone as LTE/LTE-A. It is estimated that by 2020 IoT-based devices will reach over trillions. With the bandwidth of 4G (20–100 MHz), it will not be possible to accommodate this massive amount of devices. Shift to the next generation (millimeter wave), i.e., 5G will help to the cause. The European Union came up with an action plan for IoT. Internet of Things (IoT) is going to drastically reshape the way our societies function over the next decade. Internet along with wireless communication, location awareness based on users, and wireless sensor networks converts everyday objects into thinking and context-aware IoTs. Commonly known objects will be powered with Internet accessible AI. Depending on processing capabilities, the devices will offer intelligence and communication features. Over thousand devices will be used by each user by 2020, with most of them will be IoT based. With so many active devices, big data is what will describe this massive data. 5G will be used for these big data for high bandwidth, improve integrity, and lower latency. AT&T (T) already has some 8 million web-connected cars linked to its 4G network. Vodafone says it had 41 million IoT connections as of September. Cisco claims to have connected 4.9 billion devices online and will connect 12.2 billion by 2020, and few will be 5G, whereas Cisco and IBM aiming to provide low power connections to almost all IoT devices with Wi-Fi and other unlicensed spectrum.

2 System Model

With the help of SystemVue 2016.08, the bit error rate (BER) performance of 4G, i.e., LTE-A and 5G system, is analyzed. Here in case of 5G system, the waveform is chosen as FBMC. Firstly, the BER performance of LTE-A and FBMC is compared. In this case, the respective bandwidth is set to 10 MHz and the carrier frequency is set to 60 MHz. Secondly, BER comparison of narrowband IoT (NB-IoT) and FBMC-IoT is done. In these cases, the respective bandwidth is set to 180 kHz and the carrier frequency is set to 60 MHz. In the third step, the effect of widening the bandwidth of FBMC system on its BER performance is analyzed by varying the bandwidth from 10 to 100 and 1000 MHz, keeping the carrier frequency constant at 60 GHz. In all the above cases, for the FBMC system model, the antenna was not connected. So in the fourth step, omnidirectional antenna is connected in transmitter side of FBMC system by. In the receiver side of 5G system, receiving antenna is done. Same is implemented in case of FBMC-IOT system. In the fourth step, the effect of widening the bandwidth in case of FBMC system using omnidirectional antenna on its BER is analyzed by varying the bandwidth from 10 to 100 and 1000 MHz, keeping the carrier frequency constant at 60 GHz. In the fifth step, effect of narrowing the bandwidth in case of FBMC-IoT system using omnidirectional antenna on its BER is analyzed by varying the bandwidth from 10 to 1 MHz

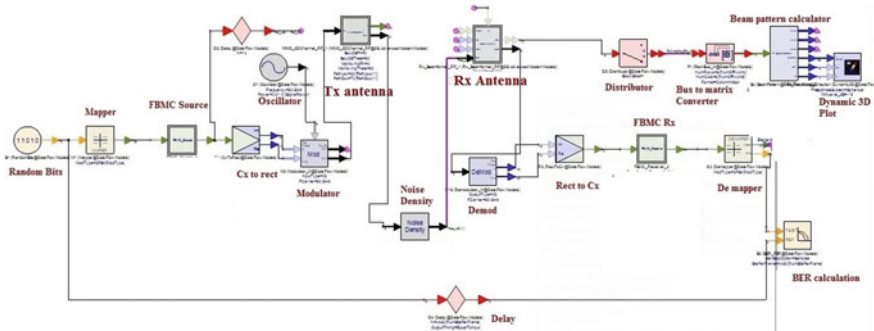


Fig. 2 System model of FBMC-based 5G system with antenna

and 100 kHz, keeping the carrier frequency constant at 60 GHz. Finally after taking all the readings from SystemVue 2016.08, the respective graphs are plotted using MATLAB 2015.

In the FBMC-based 5G system with antenna, the transmitter part consists of random bits, mapper, FBMC source, complex to rectangular converter, and modulator. Then transmit antenna is connected; after that, noise density and receiver section are connected.

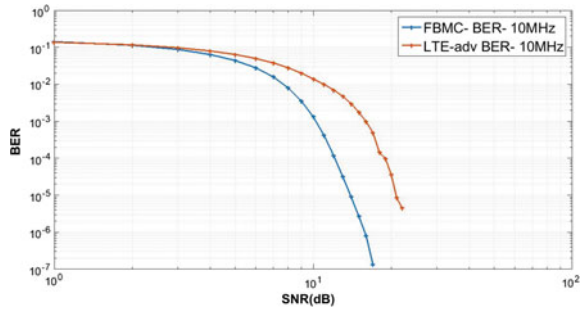
Figure 2 FBMC transmitter in which random PN sequence is the source. Followed by the mapper that is used to map the bits of the random bit sequence into the constellation. The output of the mapper is given as the input to the FBMC_Source. Then the signal is up-sampled into the RF signals which consist of the local oscillator and the modulator to simulate the effects of phase noise, IQ imbalance, and other RF impairments.

Initially, inside the FBMC source, the arbitrary waveform with explicit values is used to initiate the OFDM_SubcarrierMux. The second Block i.e., OFDM_SubcarrierMux multiplexes different Types of Signals in Frequency Domain to corresponding Subcarrier location. It consists of four/branches of input and the data input bus may be of an OFDMA user or pilot. If there is the subcarrier overlap in the input branch, then for instance, both branch i and j have allocation to the k th subcarrier, and the data in the Max (i, j)th branch will be the final value. Then OQAM modulation is done. After that polyphase network-IFFT (PPN-IFFT) is done. Then the transmitted signal passes through channel to reach the FBMC receiver. The FBMC receiver does the opposite of the source.

3 System Response

The response of the concerned models is plotted with the help of MATLAB 2015, and the response obtained is shown below.

Fig. 3 LTE-A BER v/s FBMC BER with respect to SNR at 10 MHz bandwidth



From Fig. 3, it can be concluded that at 10 MHz bandwidth, the BER response of FBMC is better than that of LTE-A. FBMC system is having a highest BER value of 10⁻⁷, whereas the LTE system is having a highest BER of 10⁻⁵.

From Fig. 4, it can be concluded that at 10 MHz bandwidth, the BER response of FBMC-IoT is better than that of NB-IoT. FBMC-IoT is having a highest BER value of 10⁻⁷, whereas the NB-IoT system is having a highest BER of 10⁻⁶. NB-IoT system is exploring OFDM.

From Fig. 5, it can be seen that with the widening of bandwidth, the BER response of FBMC system is degrading. Here in this case, the bandwidth is varied from 10 to 100 and 1000 MHz. In each case, the SNR is varied from -20 to 20. With increase in bandwidth, the BER performance is degraded. For example, in the

Fig. 4 NB-IoT BER v/s FBMC-IoT BER with respect to SNR at 10 MHz bandwidth

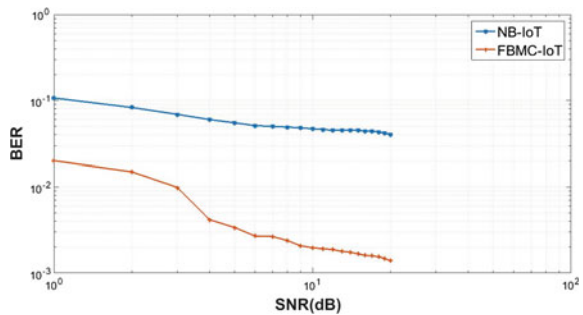
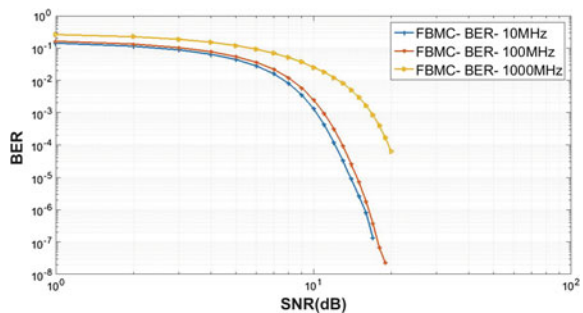


Fig. 5 BER v/s SNR response of FBMC system at 10, 100, and 1000 MHz



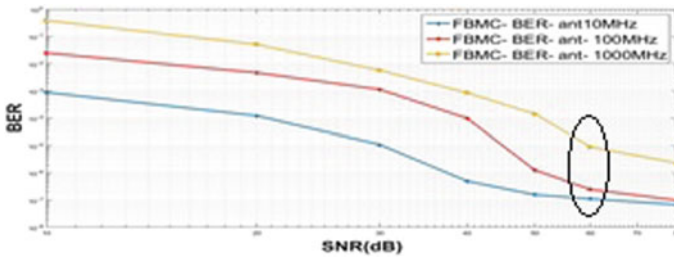


Fig. 6 4: BER v/s SNR response of FBMC with antenna at 10, 100, and 1000 MHz, respectively

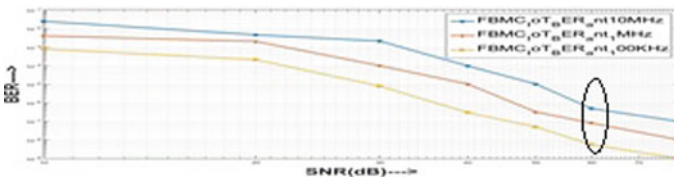


Fig. 7 BER v/s SNR response of FBMC-IoT with antenna at 10, 1, and 100 kHz, respectively

graph, it can be seen that at SNR value of 13, the BER value of FBMC with bandwidth of 10, 100, and 1000 MHz is $31.79e-6$, $92.08e-6$, and $8.073e-5$. This is happening because with increase in bandwidth, higher level of noise will be received; hence, the BER value will get enlarged.

From Fig. 6, it can be seen that when antenna is connected in the FBMC system, then after increasing the bandwidth, the BER response is getting poorer. For example, from the encircled region of the graph, it can be seen that at a SNR value of 60, the BER value of FBMC system with antenna at a bandwidth of 10, 100, and 1000 MHz is $110.9e-7$, $245.5e-6$, and $90.3e-5$, respectively.

From Fig. 7, it can be seen that when antenna is connected in the FBMC system, then after decreasing the bandwidth, the BER response is becoming better. For example, from the encircled region of the graph, it can be seen that at a SNR value of 60, the BER value of FBMC-IoT system with antenna at a bandwidth of 10, 1 MHz, and 100 kHz is $160e-6$, $319.6e-7$, and $160.3e-8$, respectively. This is because with the reduction of bandwidth, low level of noise is being received.

4 Conclusion

In this paper, the BER performance of LTE-A and FBMC system is analyzed. It has been shown that the BER performance of FBMC system is better than that of LTE-A as FBMC has highest BER in range of 10^{-7} , but LTE has highest BER up to 10^{-5} up to SNR 20. Also, BER comparison of NB-IoT and FBMC-IoT is done, and

it has been concluded that BER performance of FBMC-IoT is better than NB-IoT. Then the effect of widening the bandwidth of FBMC on its BER is analyzed. Then the effect of widening the bandwidth of FBMC system with antenna on its BER is analyzed. Then the effect of narrowing the bandwidth of FBMC-IoT system with antenna is shown. Finally, it can be concluded that the BER performance degrades with increase in bandwidth and vice versa. The reason for degradation is the introduction of noise as the channel bandwidth increases as per the formula

$$N = kTB \quad (4)$$

where N = thermal noise power, k = Boltzman's constant, T = room temperature, B = bandwidth. With the accumulation of noise number of error bits increases, i.e., the BER performance degrades. In future work, we will consider other potential waveform candidates of 5G and also will be focusing on embedding security on IoT system.

References

1. G. Jue, S. Shin.: Implementing a Flexible Testbed for 5G Waveform Generation and Analysis. Keysight Technologies, (2015).
2. Suresh Borkar, Himangi pande.: Application of 5G Next Generation Network to Internet of Things. International Conference on Internet of Things and Application(IOTA), pp. 443–447, (2016).
3. K.E Skouby.: Smart Home and Smart City Solutions enabled by5G, IoT, AAI and CoT Services. International Conference on Contemporary Computing and Informatics, pp. 874–878, (2014).
4. Maria Rita, Mischa Dohler, Alfredo Grieco, Gianluca Rizzo.: Internet of Things in the 5G Era. IEEE Journals on Selected areas of Communication, Volume 34, pp. 510–527, (2016).
5. Mamta Agiwal, Abhishek Roy, Navrati Saxena.: Next Generation 5G Wireless Networks: A Comprehensive Survey. IEEE Communications Survey, Volume 18, pp. 1617–1655, (2016).
6. Turker Yilmaz, Ozgur B. Akan.: Millimeter Wave Communication for 5G IoT Applications. Springer International Conference, Volume 8, pp. 37–53, (2016).
7. Zhiguo Ding, Yuanwei Liu, Jinho Choi.: Application of non Orthogonal Multiple Access in LTE and 5G Networks. IEEE Communications Magazine, Volume 55, pp. 185–191, (2017).
8. A. Farhangetal.: Massive MIMO and waveform design for 5th generation wireless communication systems, arXiv1501.00305v2 [cs.IT], (2016).
9. T. Fusco, et al.: *Data Aided Symbol Timing and CFO Synchronization for Filter Bank Multicarrier System*. IEEE, pp. 2705–2715, (2009)
10. J. Du, S. Signal.: Novel Preamble-Based Channel Estimation for OFDM/OQAM Systems. ACCESS Linnaeus Center, KTH - R. Inst. of Technol., Stockholm, (2009).

2D/3D Liver Segmentation from CT Datasets

G. K. Mourya, D. Bhatia, A. Handique, S. Warjri,
A. War and S. A. Amir

Abstract Imaging modalities are noninvasive, fast, and accurate in the diagnosis of different anatomical disorders. As such, there is a pertinent requirement for segmentation of the organs to give proper visual information on the morphological and pathological changes. The aim of the proposed work is to implement the automatic liver segmentation from the CT images, using active contour segmentation technique. The localization and detection of liver tumor will be easier for radiologist with the extraction of the liver from other adjoining organs. In this paper, we are discussing the different techniques employed for liver segmentation and our present ongoing study is based on 2D and 3D liver segmentation with its future implementation.

Keywords CT images · Segmentation · Image preprocessing · Image validation
Active contour

G. K. Mourya (✉) · D. Bhatia (✉) · S. Warjri (✉) · A. War (✉) · S. A. Amir (✉)
Department of Biomedical Engineering,
North Eastern Hill University, Shillong 793022, Meghalaya, India
e-mail: gajendramourya@gmail.com

D. Bhatia
e-mail: bhatiadinesh@rediffmail.com

S. Warjri
e-mail: sunitawarjri@gmail.com

A. War
e-mail: canviodle@gmail.com

S. A. Amir
e-mail: syed49400@gmail.com

A. Handique (✉)
Department of Radiology, North Eastern Indira Gandhi Regional Institute
of Health & Medical Sciences, Shillong 793018, Meghalaya, India
e-mail: drahandique@gmail.com

1 Introduction

Liver segmentation is an important prerequisite for detecting different diseases such as tumor and cancer of liver. It can be used for planning of surgical interventions such as liver tumor resections. The segmentation approach in clinical applicability must be able to cope with the high variation in shape and gray-value appearance of the liver. Several works in the past present a novel segmentation scheme based on a true 3D segmentation refinement. Liver segmentation involves abdominal images as input images from radiological sources, such as CT, MRI, for applying segmentation techniques in order to view liver segregated from other body organs in the output image. Automatic liver segmentation methods frequently fail to deliver good segmentation results, especially in case of diseased livers. For clinical application, liver segmentation must be capable of handling all possible cases in a time-efficient manner. To tackle this problem, we are using active contour technique for better and reliable segmentation of the liver.

2 Literature Review

There have been several reported works on liver segmentation by researchers worldwide, with their possible merits and demerits. Recently, methods were proposed to segment the liver efficiently and effectively and they are discussed in following sections of the paper.

Farzaneh et al. [1] proposed a hierarchical method based on probabilistic models, which are based on position and intensity of voxels for automated segmentation of the liver, and it achieves the Dice similarity coefficient of more than 89%. They employed techniques like Jaccard and Dice similarity score for validation. The paper [2] was able to conduct full vessel segmentation and recognition of multiple vasculatures effectively. The vessel context describes context information of the voxels related to the vessel properties, such as intensity, saliency, direction, and connectivity. The method was evaluated on the clinical CT datasets. In [3] by combining a spiral-scanning technique with supervised fuzzy pixel classification was employed for semi-automatic level set segmentation of liver tumors. Evaluating the algorithm on the provided test data showed an average overlap error of 32.6% and average volume difference of 17.9%. The average, the RMS, and the maximum surface distance were found to be 2.0, 2.6, and 10.1 mm, respectively. In a study [4], mean liver shape model was trained by PCA and a diffusion filter was used. The minimum description length (MDL) algorithm and Euclidean distance were used for d-dimensional images in linear time. For validation, they used average symmetric surface distance (ASD), volumetric overlap error (VOE), and also some other techniques. Another study [5] uses auto-context learning by employing 20 contrast-enhanced CT images in the training datasets, and 10 in the testing datasets. Mean shift algorithm was used for over-segmentation, for validation volumetric

overlap error, signed relative volume difference, etc. Zareei et al. [6] used active contour model incorporated with GVF and balloon energy. The balloon energy causes the contour to expand and contract depending on positive and negative value, respectively. For evaluation Dice error, volume error was used. Their method showed lower mean overlap error and volume error with average sensitivity at 0.8982.

3 Methodology

To achieve liver segmentation objective, several different methods and techniques could be employed. Basically, the main steps for image segmentation are (1) Image preprocessing; (2) Image segmentation technique; and (3) Validation.

Image preprocessing is the operation which is performed on images at the lowest level, whose main aim is improving the image data that suppresses undesired distortions or enhances the image features. There are many different types of image processing which can be used such as image cropping and filtering, intensity adjustment and histogram equalization, brightness thresholding. **Image segmentation** is often an important step in image analysis, object representation, visualization, and many other image processing tasks. The term image segmentation refers to the partition of an image into a set of regions that cover it. Some of the segmentation techniques are: threshold-based segmentations, edge-based segmentations, region-based segmentations, clustering techniques, and other techniques. **Validation** of the medical images is an important task to check the accuracy, robustness, consistency, etc. Some of the validation techniques used in several papers are Dice similarity coefficient [7–9], Jaccard index [10–12], relative volume difference [13], etc.

4 Implementation and Result

4.1 Implementation Details

In our work, we utilized 1 mm contiguous sections of CT abdomen images in DICOM 2.0 format obtained from Definition AS+ Excel 128 multi-slice CT scanner, provided by the Department of Radiology and Imaging, NEIGRIHMS Hospital, Shillong, based on mutual collaboration among departments of both institutes. The data is collected for the study based on submission of application for approval to ethical clearance committee of the host institution and its decision thereof. Ethical matter is already submitted to Institutional Ethics Committee of Human Samples and Participants (IECHSP), North Eastern Hill University, Shillong, Meghalaya, India. Before utilizing patient data, willingness and consent

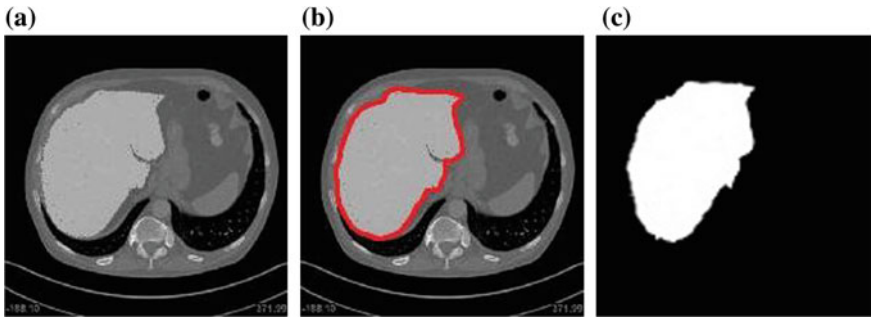


Fig. 1 **a** Gray scale of the CT image. **b** Segmentation of the liver from the input image. **c** Output is the 2D segmented liver from the rest of the organs

were obtained from each patient as well as the concerned department in the hospital. For image preprocessing gray scale, resizing, Gaussian filtering, etc. have been employed. Active contour has been used for image segmentation because outline of contour automatically converges toward borderline of liver. Converge criteria is modified to increase the accuracy of segmentation result. We have also studied some papers based on this technique and also other related works being carried out globally in this area [14–16]. We have done the segmentation of eight (8) patient datasets, and the size of each image was 512×512 pixels and the number of slices of each volume varied from 64 to 348. The figures below show the CT images after preprocessing (Fig. 1a and b), the segmented CT image of the liver (Fig. 1c), and the segmented liver in 2D binary image.

We have also projected the CT images on a 3D platform by using the 3D Visualization tool software using various tools such as Lasso, Live Wire, Thresholding, Edit Mask, and Region growing. Region growing is used to localize a certain area of interest. We have segmented the liver from various datasets, and the outputs of the segmented liver are used for correlating with the same slice of DICOM images for validation (Fig. 2).

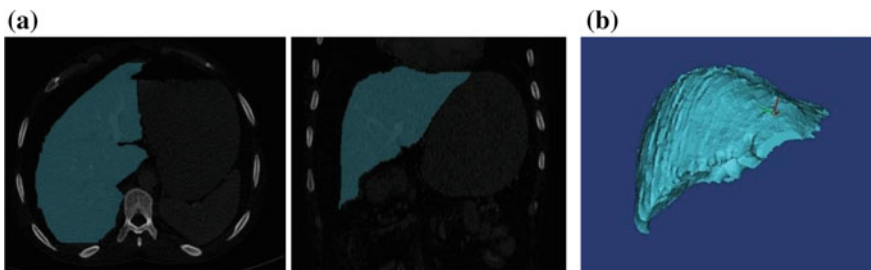


Fig. 2 **a** Segmentation of the liver in axial view and coronal view from the CT images using 3D visualization tool. **b** Output is the 3D segmented liver from the rest of the organs

4.2 Evaluation Measurement of Results

We have applied several validation techniques, viz. Dice similarity coefficient, Mean Square Error, and Average volume overlap error. The Mean Square Error (MSE) is the cumulative squared error between the compressed and the original image. The Dice similarity coefficient (DSC) between two sets of images A and B is measured by the spatial overlap between two segmentations, assuming A and B are target regions, and is defined as $DSC(A, B) = 2(A \cap B)/(A + B)$ where \cap is the intersection. Here, A is segmented image and B is reference image, as shown in Fig. 3. Jaccard index (JI) is an evaluation measurement technique by checking the similarity where it takes the ratio of lumen area in both the region R1 (the segmented image Fig. 3a) and R2 (ground truth image Fig. 3b), and then they are divided by the total size of region R1 and R2. The equation is given as: $JI(R1, R2) = |R1 \cup R2|/|R1 \cap R2|$ (Fig. 4; Table 1).

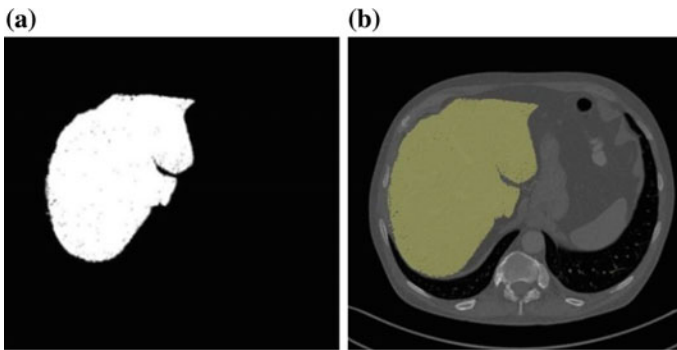


Fig. 3 Segmented image (a), reference image (b)

Fig. 4 Mean \pm standard deviation for different validation checks

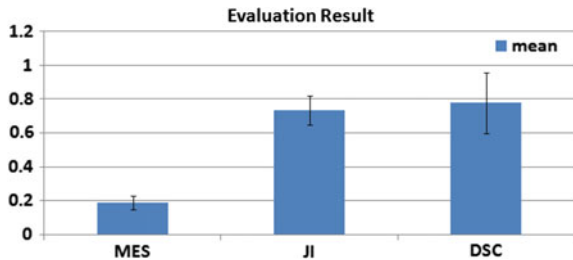


Table 1 Validation of the segmented liver image and the ground truth image

Tested subject	MES	Jl	DSC
Patient 1	0.188	0.740	0.851
Patient 2	0.196	0.693	0.701
Patient 3	0.171	0.811	0.891
Patient 4	0.169	0.791	0.887
Patient 5	0.288	0.559	0.365
Patient 6	0.177	0.693	0.851
Patient 7	0.169	0.811	0.799
Patient 8	0.184	0.791	0.891

5 Conclusion and Future Work

In this study, we presented the automatic segmentation of liver. After thorough reviewing the research done earlier, our first focus of segmentation is on the liver organ due to its important functionality, large structure, and sharp edges. As discussed, we have used the 3D Visualization tool software to segment the liver from the CT image datasets and also we are using the active contour segmentation technique. There are many approaches which are used for segmentation where we found that graph cut can also prove to be good in the segmentation of the images. In future, we would like to use different classifiers like Random Forest as it can show more accurate results in organ segmentation and also use other techniques. Our future work will be to focus on a more accurate validation of the segmented liver dataset and to employ other techniques to segment the CT images in 2D/3D with an aim to compare the results with other existing techniques.

Acknowledgements The authors of this research paper are thankful to the Department of Radiology and Imaging, North Eastern Indira Gandhi Regional Institute of Health and Medical Sciences (NEIGRIHMS), Shillong, for providing 3D medical data sets and for helping in validation of the output CT images for this study. We thank the SERB, Department of Science and Technology (DST), GOI, New Delhi, for the financial assistance (Grant: SERB/EMEQ-433/2014) during the study.

References

1. Farzaneh, N. et al.: Liver Segmentation Using Location and Intensity Probabilistic Atlases Engineering in Medicine and Biology Society (EMBC), 38th Annual International Conference of the IEEE. pp. 6453–6456 (2016).
2. Chi, Y. et al.: Segmentation of Liver Vasculature From Contrast Enhanced CT Images Using Context-Based Voting. IEEE Transactions on Biomedical Engineering vol. 58.8, pp. 2144–2153 (2011).
3. Smeets, D. et al.: Semi-automatic level set segmentation of liver tumors combining a spiral-scanning technique with supervised fuzzy pixel classification. Med. Image Anal., vol. 14, pp. 13–20 (2010).

4. Liao, M. et al.: Physica Medica Efficient liver segmentation in CT images based on graph cuts and bottleneck detection. *Phys. Medica*, vol. 32, pp. 1383–1396 (2016).
5. Ji, H. et al.: ACM-Based Automatic Liver Segmentation From 3-D CT Images by Combining Multiple Atlases and Improved Mean-Shift Techniques. *IEEE journal of biomedical and health informatics*, vol. 17.3, pp. 690–698 (2013).
6. Zareei, A. & Karimi, A.: Liver segmentation with new supervised method to create initial curve for active contour. *Comput. Biol. Med.*, vol. 75, pp. 139–150 (2016).
7. Klein, S. et al.: Segmentation of the prostate in MR images by atlas matching. 2007 4th IEEE Int. Symp. Biomed. Imaging From Nano to Macro - Proc. pp. 1300–1303 (2007).
8. Casciari, S. et al.: Fully Automatic Segmentations of Liver and Hepatic Tumors From 3-D Computed Tomography Abdominal Images : Comparative Evaluation of Two Automatic Methods., vol. 12, pp. 464–473 (2012).
9. Huynh, H. T., Karademir, I. & Oto, A.: Computerized Liver Volumetry on MRI by Using 3D Geodesic Active Contour Segmentation. *American Journal of Roentgenology*. vol. 202 no. 1 pp. 152–159 (2014).
10. Shimizu, A., Nakagomi, K., Narihira, T. & Kobatake, H.: Automated Segmentation of 3D CT Images Based on Statistical Atlas and Graph Cuts. *International MICCAI Workshop on Medical Computer Vision*. Springer Berlin Heidelberg vol. 6533. pp. 214–223 (2010).
11. Li, C. et al.: A Likelihood and Local Constraint Level Set Model for Liver Tumor Segmentation from CT Volumes. *IEEE Transactions on Biomedical Engineering*, vol. 60, pp. 2967–2977 (2013).
12. Okada, T. et al.: Multi-Organ Segmentation in Abdominal CT Images. *Engineering in Medicine and Biology Society (EMBC), Annual International Conference of the IEEE Proc.* pp. 3986–3989 (2012).
13. Chen, X. et al.: Three-dimensional segmentation of fluid-associated abnormalities in retinal OCT: Probability constrained graph-search-graph-cut. *IEEE Trans. Med. Imaging*, vol. 31, pp. 1521–1531 (2012).
14. Jiang, H. & Cheng, Q.: Automatic 3D segmentation of CT images based on active contour models. 2009 11th IEEE Int. Conf. Comput. Des. Comput. Graph. pp. 540–543 (2009).
15. Massoptier, L. & Casciari, S.: A new fully automatic and robust algorithm for fast segmentation of liver tissue and tumors from CT scans. *Eur Radiol* (2008) 18: 1658. pp. 1658–1665 (2008).
16. Li, G. et al.: Automatic Liver Segmentation Based on Shape Constraints and Deformable Graph Cut in CT Images. *IEEE Transactions on Image Processing*, vol. 24, pp. 5315–5329 (2015).

Wireless Security Over a Point-to-Point 5G Communication System

Rajat Paul, Pallavi Neog, Shantanu Roy and Rabindranath Bera

Abstract Work toward the fifth generation of mobile networks has gained a huge momentum recently. As 5G research projects have already started or are about to start, and 5G activities in standardization bodies, in particular 3GPP, have already been scheduled, it is important to start also the work on the security architecture, in order to ensure that security is built into 5G networks right from the start. Important steps will be the clarification of the security requirements, the review of existing security architectures, in particular, the LTE security architecture, and finally the selection of the 5G security measures in tight interworking with the design of the general 5G network architecture. In this paper, we go one step in this direction and hope to promote the overall work toward a sound 5G security architecture.

Keywords ECM · EMM · SK · PDK · CW · BISS

1 Introduction

Data transport is to legitimate the address issue of security, accuracy, and privacy. The purpose of security is to ensure protection of data from intentional modification, loss or damage, and fabrication of data from unauthorized individual. Once the data is captured by third person, they can modify, destroy, or move forward the data for their benefit or for entertainment. Accuracy refers to the firewall of data against

R. Paul (✉) · P. Neog · S. Roy · R. Bera
Department of Electronics and Communication Engineering,
Sikkim Manipal Institute of Technology, Majitar, Sikkim, India
e-mail: rajatpaul1992@gmail.com

P. Neog
e-mail: pallavineog66@gmail.com

S. Roy
e-mail: tubaiotubai07@gmail.com

R. Bera
e-mail: rbera50@gmail.com

loss or modification of data that may be system noise. Privacy refers to keeping data inaccessible to assailant or third person. Therefore, it is necessary to impart wireless security over a point-to-point 5G enabled IOT. VOLTE is very flourishing technology in present age for 4G mobile. It is getting extended for use in 5G [1]. Security aspects of VOLTE are only during registration process only. There is no security aspect to protect the voice conversation because if VOLTE voice is recorded on LTE mobile, it will be transferable to any other machines, whereas in DVB-S2-based DTH technology, the security is quite high because of BISS key encryption and decryption. In DTH, if we record the media files into any external media devices like pen-drive and want to play those files in another terminal like PC or laptop using any media players (like VLC), the media files cannot be played at all. Even from one commercial set up box (say Airtel DTH), it is intended to be viewed into another same branded set up box, then also the media files are not playable or viewable. So, this implies that the recorded media files are so highly secured that we are unable to decrypt it in some non-legacy media terminal. So, the inheritance of Basic Interoperable Scrambling System (BISS) key encryption and decryption in the proposed 5G model is to be inherited for enhancing wireless security which is very popular in DTH technology. The Basic Interoperable Scrambling System (BISS) is based on the DVB-S2 system, and the use of fixed keys is named as Session Words.

1.1 Conditional Access for Digital TV

“Conditional Access” refers to a technique which is used for protection a number of programs from unauthorized accessing. Its implementation requires a variety of technical and commercial system components, which has the main purpose of making the programs available only to those viewers who are authorized to receive them. Viewers have to pay a monthly or annual fee to gain access to a particular program channel and needs to pay per channel basis. In Conditional Access system, ECM denotes whether the subscriber is authorized to access the services or not. The ECM is used to inform the descrambler in the receiver how the block-wise scrambling can be revoked. The ECM performs the descrambling of the bit-by-bit scrambling. The EMMs arise from the customer administration of the CA provider, i.e., from the subscriber management system (SMS). EMM contains the information of the subscriber package which needs to activate and video on demand.

In Figs. 1 and 2, the scrambler and descrambler implement the data scrambling element, and control words are the cipher keys. CA-Host, CA-Client, and CA-Module are the three distributed components of the SAS element, and they use CA descriptors and CA messages (EMM and ECM) for communication. The data scrambling cipher is called DVB Common Scrambling Algorithm (DVB-CSA). The algorithm is a combination of 16-bit block cipher followed by a stream cipher, with a key-size of 16 bits. However, the detail is kept secret and disclosed to equipment manufacturers under nondisclosure agreement. For performance and

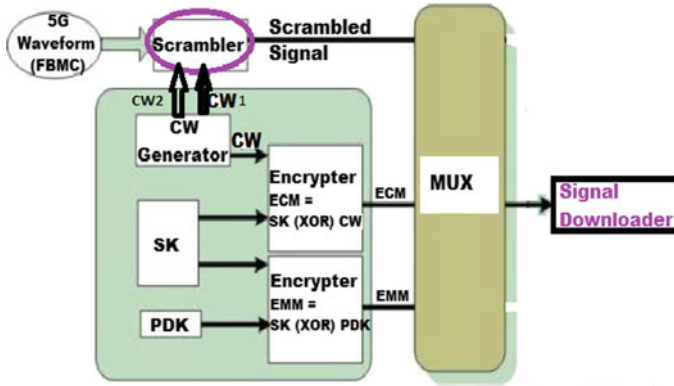


Fig. 1 Detail architecture of ‘BISS key encryption’

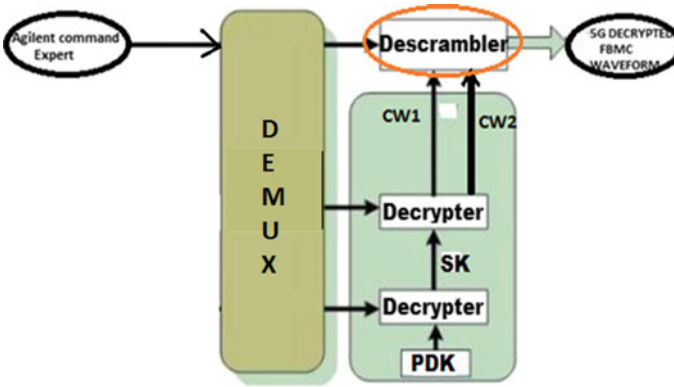


Fig. 2 Detail architecture of ‘BISS key decryption’

obscurity, the algorithm is implemented in hardware. At the broadcast center, the scrambler generates control words to scramble the contents, and it passes the control words to the CA-Host for secured distribution to descramblers via ECM CA messages. Control words change about every ten seconds, and the scrambler synchronizes the descrambler to key switching using a specific bit in data-packet headers. As a defense strategy, different TV channels are scrambled with different stream of control words. CA messages are encrypted command-and-control communications from CA-Host to CA-Modules. The DVB-CA architecture categorizes CA messages into Entitlement Control Messages (ECM) and Entitlement Management Messages (EMM). ECMs carry channel-specific access-control list and control words. EMMs deliver subscriber-specific entitlement parameters. As a strategy of defense in depth, a secret cipher different from data scrambling is used, and the details on the message formats are closely guarded secrets. CA descriptors are data records associating a protected channel to its ECMs. Since different stream

of control words are used to scramble different channels, there is no need to keep the relations secret. Thus, the CA descriptors are sent in clear via the electronic channel guide, which is transmitted continuously in the broadcast traffic.

2 System Model

In the first step, with the help of SystemVue 2016.08, the encryption and decryption of BISS Key are designed. Both in encryption and decryption part, a 16-bit input random data, i.e., (00AB) is used as BISS Key, (03AB) is used as Service Key (SK) and (03BB) is used as Personal Distribution Key (PDK). In the encryption part, two Control Words (CW)s are generated, the first control word goes to scrambler and the second control word is used for Ex-Or operation with Service Key (SK) to generate Entitled Control Message (ECM). The Entitled Management Message (EMM) is generated by the Ex-Or operation between Service Key (SK) and Personal Distribution Key (PDK). The scrambled contents, ECM and EMM, are then fed to Time Division Mux operation. In the decryption part, Control Word (CW) is encrypted by 16-bit Service Key (SK) and embedded into Entitlement Control Message (ECM). SK is encrypted by 16-bit Personal Distribution Key (PDK) of authorized users and embedded into Entitlement Management Message (EMM). In the second step, after designing the Encryption and Decryption part, the encryption part is added before the mapper and the decryption part is added after the mapper in 5G communication block. Then the input graph, encrypted graph, ECM graph, EMM graph, and decrypted graph are obtained. Finally, the graph comparison between input graph and the decrypted graph is done to validate the security.

Step 1: System model for design of encryption and decryption of BISS key involving ECM and EMM in SystemVue platform is shown in Fig. 3.

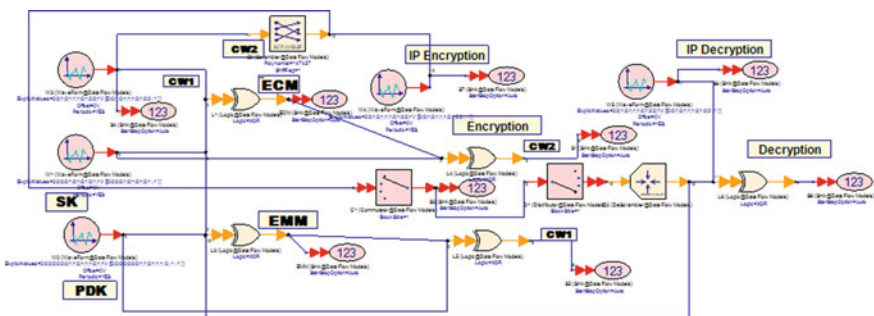


Fig. 3 Encryption and decryption of BISS key involving ECM and EMM in SystemVue platform

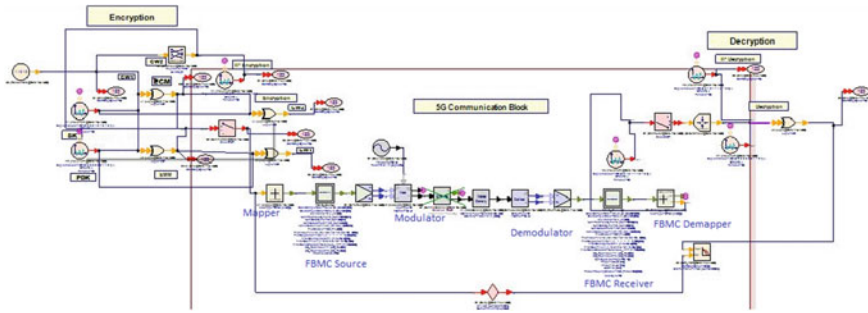


Fig. 4 5G communication block with point-to-point wireless security

Step 2: Block diagram of design of encryption and decryption of BISS KEY in 5G communication block with point-to-point wireless security in SystemVue platform is shown in Fig. 4.

3 System Response

3.1 Graphs Obtained After Simulation (For Step 1)

In Fig. 5, it is seen that the graph of encrypted data is different from the input data as the encryption of data bits is done in order to conceal the information of data bits.

In Fig. 6, the graph of ECM and EMM is shown, ECM is obtained by the Ex-Or operation between SK and CW and EMM is obtained by the Ex-Or operation between SK and PDK.

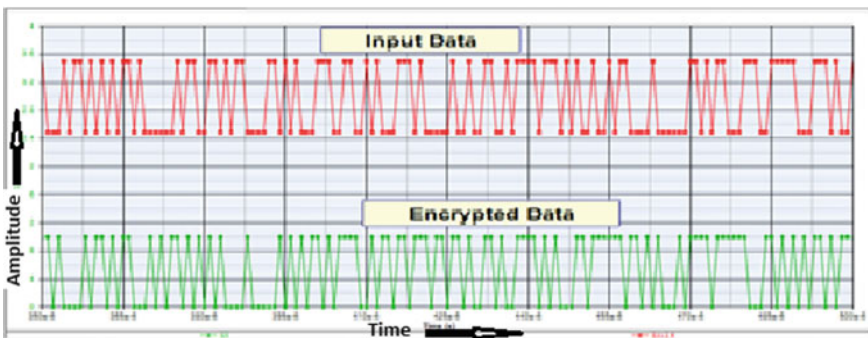


Fig. 5 Graph of input data and encrypted data

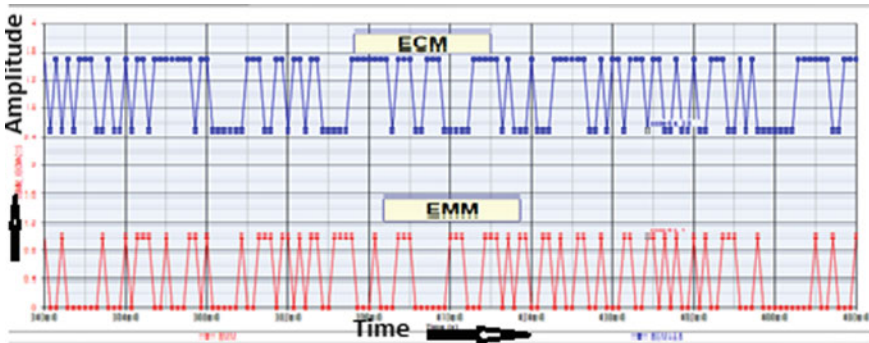


Fig. 6 Graph of Entitled Control Message (ECM) and Entitled Management Message (EMM)

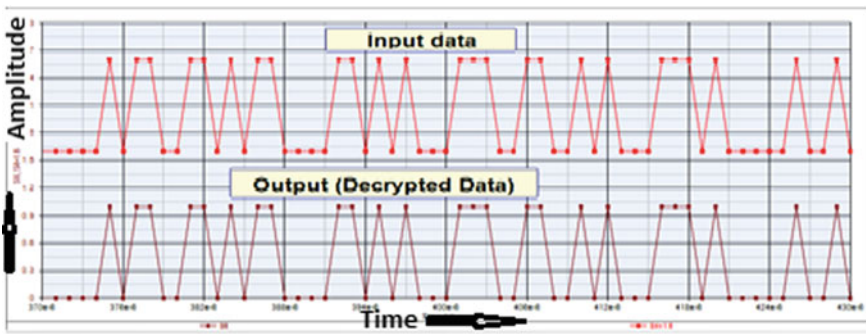


Fig. 7 Graph of input and decrypted data

In Fig. 7, it is seen that the graph of the input data bits matches with the decrypted data bits which ensures that input data bits have been retrieved successfully.

3.2 Graphs Obtained After Simulation (For Step 2)

In Fig. 8, it is seen that after inserting BISS Key encryption and decryption before and after mapper, respectively, in 5G communication block, the graph of input data bits matches with the decrypted data bits which ensures that input data bits have been retrieved successfully through 5G communication block.

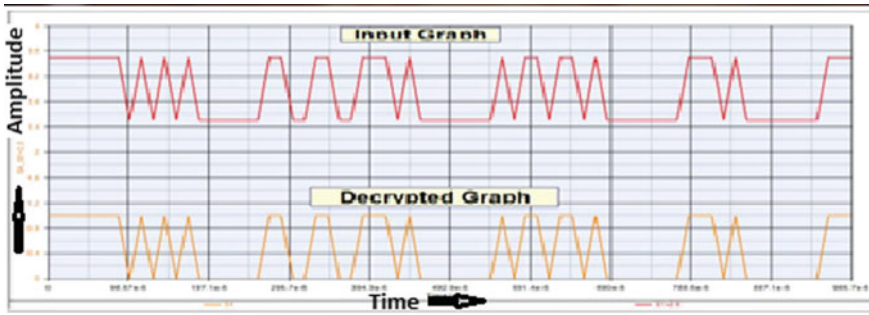


Fig. 8 Graph of fixed input data and decrypted data in 5G communication block

4 Conclusion

Security is a very challenging issue in various fields of communication. Encryption and decryption of data bits is an important topic, as secure and efficient algorithms are necessary for encryption and decryption of data bits. There are several algorithms which may be used to encode and decode the data based on the key. The proposed algorithm contains two levels of 16-bit Exclusive OR (XOR) operation. This algorithm is used for secure transmission of messages and data from one point to another. In this paper, the security involved in DVB-S2 system has been designed using SystemVue platform and inherited to 5G communication block. The input data bits are retrieved successfully through the 5G communication block as the decrypted graph obtained after simulation matches with the input graph. Security will be a key requirement of future 5G communication where embedded security will be embraced to increase the randomness among the successive keys that is the key for ensuring the greater security. As general concept, flexibility to threats in emergency conditions is to be inherited further in the architecture as future work.

References

1. 5G Security, Ericsson White Paper, pp. 1–12, June (2015).
2. G. Horn, P. Schneider: Towards 5G Security, 14th IEEE conference on trust, security and privacy in computing and communications (IEEE TrustCom-15), Helsinki, Finland, 20–22 August, (2015).
3. Kaladharan N: Unique Key Using Encryption and Decryption of Image, International Journal of Advanced Research in Computer and Communication Engineering, Vol. 3, Issue 10, pp. 8102–8104, October (2014).
4. Y.C. Zhang, et al.: Broadcast Encryption Scheme and Its Implementation on Conditional Access System, International Symposium on Web Information Systems and Applications (WISA'09), pp. 379–382, May 22–24, (2009).

5. C. Y. Sun, C. C. Chang: Cryptanalysis of a Secure and Efficient Authentication Scheme for Access Control in Mobile Pay-TV Systems, *International Journal of Network Security*, Vol. 18, No. 3, pp. 594–596, May (2016).
6. Satellite Earth Stations and Systems (SES); Broadband Satellite Multimedia (BSM); IP Interworking over satellite; Security aspects, Technical report, ETSI TR 102 287, V1.1.1, pp. 1–56, (2004–05).
7. Fu-Kuan Tu, et al., On Key Distribution Management for Conditional Access System on Pay-TV System, *IEEE Transactions on Consumer Electronics*, Vol. 45, No. 1, pp. 151–158, February (1999).
8. Digital Video Broadcasting (DVB); Implementation Guidelines of the DVB Simulcrypt Standard, technical report from ETSI TR 102 035 V1.1.1, pp. 1–35, (2004).
9. Digital Audio Broadcasting (DAB); Conditional access, technical report from ETSI TS 102 367, V1.2.1, pp. 1–24, (2006).
10. Basic Interoperable Scrambling System with Encrypted keys, technical report from Tech 3292 rev. 2, pp. 1–11, August (2002).
11. N. H. Mvungi: Conditional Access Interoperability in Digital Broadcasting, *Journal of Informatics and Virtual Education*, Vol. 1, No. 01, pp. 1–6, October (2011).
12. Voice and video calling over LTE, Ericsson white paper, 284 23–3163, Uen Rev B, pp. 1–18, November (2014).
13. Sarker, M.Z.H., Parvez, M.S.: A Cost Effective Symmetric Key Cryptographic Algorithm for Small Amount of Data, *IEEE International Conference*, pp. 1–6, (2005).

An Integrated GNSS–Microcontroller–GSM System for Various Application Developments

Sujoy Mandal, Koushik Samanta, Basudev Das, Atanu Santra
and Anindya Bose

Abstract Global Navigation Satellite System (GNSS) is used to obtain user's position, velocity and time (PVT) information. A scheme of using a low-cost, single-frequency multi-constellation GNSS hardware has been proposed here which can be used for several applications. The realization of the concept utilizes output data from a GNSS module in National Marine Electronics Association (NMEA) format that may be used by microcontroller and auxiliary hardware for location tracking, time synchronization or stamping and atmospheric monitoring purposes. The use of multi-GNSS is expected to provide enhanced capability of the generic system.

Keywords GNSS · Microcontroller · GSM · PVT · NMEA

1 Introduction

Global Navigation Satellite System (GNSS) is popular for myriads of applications. Low-cost OEM GNSS boards with small form factors are available for application development by integrating it with minimal hardware and suitable embedded software. In this paper, GNSS OEM board-based solutions are proposed using the same core hardware and different software codes that may be useful for existing and novel applications.

S. Mandal
Department of ECE, National Institute of Technology,
Durgapur 713209, India

K. Samanta · A. Santra · A. Bose (✉)
Department of Physics, The University of Burdwan,
Golapbag, Burdwan 713104, India
e-mail: abose@phys.buruniv.ac.in

B. Das
University Science Instrumentation Centre (USIC),
Golapbag, Burdwan 713104, India

Location monitoring of assets for remote tracking is an important application for location-based services (LBS) used in individual or networked services. The proposed first solution uses the system to display the position information and to send the same to a mobile by interfacing the microcontroller module with GNSS and GSM modules. Similar other solutions are available in market, but uniqueness of the proposed system lies with the use of multi-GNSS (GPS and GLONASS) instead of GPS-only for enhanced usability and effectiveness. The same setup with modified codes can be used to show time and GNSS satellites' parameters according to user needs. The system can also be used as a GNSS trainer kit for education purpose. Development of location monitoring system using microcontroller ARM7 with only GPS module has been reported by researchers [1–4]. In this paper, microcontroller of 8051 family (AT89S52) is integrated with a low-cost multi-GNSS module (GeoS-1M) which can track both GPS and GLONASS satellites. A scheme for using multi-GNSS module for such applications is proposed in [5] which is expected to provide improved precise position information [6].

The use of *L*-Band GNSS signals for atmospheric probing is a popular technique through measurement of the GNSS signal strengths [7] in terms of carrier-to-noise ratio (C/N_0). The use of more than one systems—GPS and GLONASS helps such studies offering more signals to study compared to a single-mode operation. The proposed system can be used as a device to monitor atmospheric disturbances by comparing the instantaneous signal strength with predefined values.

To summarize, this paper presents a microcontroller (μ C)-controlled, GNSS-based system that can be used for multiple applications utilizing the same basic hardware and different embedded software codes and peripherals. The presentation involves three parts—hardware design, implementation schemes and examples of successful implementation of the scheme.

2 System Architecture

This integrated system has two main parts: GNSS receiver module and the microcontroller (μ C) as shown in Fig. 1.

The GNSS module continuously transmits serial data at 1 Hz through RS232 port in the form of sentences according to the NMEA standards [8] as shown in Table 1. The \$GNRMC sentences provide latitude, longitude, altitude, velocity and UTC time information; the information of the satellites (elevation, azimuth and C/N_0 for each of the satellites) is available in the \$GPGSV and \$GLGSV sentences. Suitable NMEA message sentence can be chosen for use by the μ C for processing as per the application requirement.

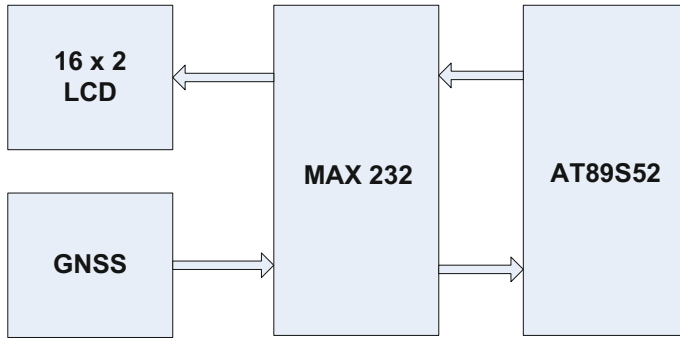


Fig. 1 Block diagram of GNSS–microcontroller integration

Table 1 NMEA sentences from GeoS-1M receiver in GPS+GLONASS mode; used NMEA sentences are shown in bold font face

\$GNGNS, 072642.00, 2315.2735340, N, 08750.8077902, E, AAA, 18, 0.71, 48.7332, 57.0382, *34
\$GNGSA, M, 3, 11, 26, 04, 08, 09, 01, 17, 28, 07, 20, 1.23, 0.71, 1.00, 1*03
\$GNGSA, M, 3, 73, 84, 85, 83, 74, 80, 1.23, 0.71, 1.00, 2*0C
\$GNGSA, M, 3, 12, 11, 1.23, 0.71, 1.00, 3*0B
\$GPGSV, 3,1, 10, 11, 26, 046, 44, 26, 23, 279, 45, 04, 13, 200, 42, 08, 85, 132, 52, 1*69
\$GPGSV, 3, 2, 10, 09, 84, 252, 51, 01, 43, 061, 46, 17, 54, 275, 48, 28, 48, 355, 46, 1*6F
\$GPGSV, 3, 3, 10, 07, 50, 151, 49, 20, 10, 120, 38, 1*64
\$GLGSV, 2, 1, 08, 73, 65, 109, 53, 84, 68, 305, 47, 85, 36, 238, 50, 83, 31, 021, 47, 1*70
\$GLGSV, 2, 2, 08, 90, 60, 266, 53, 74, 50, 348, 52, 80, 16, 139, 43, 75, 02, 330, 38, 1*7D
\$GNRMC, 072642.00, A, 2315.2735340, N, 08750.8077902, E, 0.0069, 228.840, 290713, 0.456, E, A*14
\$GNVTG, 228.840, T, 229.296, M, 0.0069, N, 0.0128, K, A*39
\$GNZDA, 072642.00, 29, 07, 2013, 00, 00*71

3 Implementation

From the comma-delimited \$GNRMC sentences, latitude and longitude values are extracted and displayed on the LCD interfaced with the AT89S52. Appropriate embedded codes may be used to extract the useful information from the NMEA sentences. Similarly, satellite information may be displayed on the LCD after extracting the values from the \$GPGSV and \$GLGSV sentences. All of this information of the satellites can be displayed sequentially on the LCD using the AT89S52. C/N₀ values for individual satellites can be monitored; any sudden and unexpected fluctuation outside a predefined value-bin may be detected and warning information may be displayed in the LCD screen. The circuit diagram of this system

24 parallel tracking channels that generate position fix data as well as extended set of auxiliary and raw measurement data in proprietary binary and standard NMEA protocols through two RS232 ports. The other modules/components for the integrated system are power supply and interface (MAX 232, an integrated circuit that converts signals from a TIA-232 (RS-232) serial port to signals suitable for use in TTL compatible digital logic circuits) for acquiring the serial data to the μC as shown in Fig. 2. In Fig. 3, the board on top is the GNSS module, on left is the LCD module, on right is the ISP programmer module that is used to load the hex file on to the target μC , and the μC board lies in the centre.

4 GNSS–Microcontroller–GSM Integration

This section focuses on transmission of position and time information to any mobile phone in form of text message (SMS) using the integrated GNSS receiver module, the μC and a GSM Module. The GNSS module continuously transmits NMEA sentences over the serial port (RS232 protocol), and the latitude and longitude values are extracted and displayed on the LCD. The μC module AT89S52 simultaneously transmits the values to the GSM module through the MAX232 module. The GSM module repeatedly sends this information to a particular fixed GSM mobile after a predefined time interval. The block diagram of this system is shown in Fig. 4, and Fig. 5 shows the complete integrated system.

A GSM modem is an ultra-compact, wireless modem that operates by inserting a valid SIM card from a mobile operator. When a GSM modem is connected to a μC , this allows the μC to use the GSM modem to communicate over the mobile network. The SIM900A module used here provides compact dual-band GSM/GPRS connectivity that can be embedded in customer applications allowing a small form factor (24 mm \times 24 mm \times 3 mm), cost and power effectiveness.

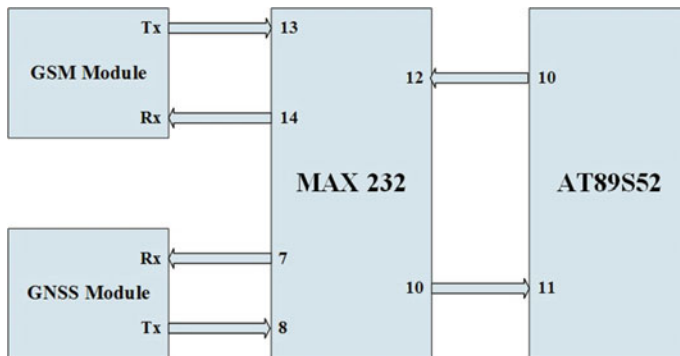


Fig. 4 Block diagram of the GNSS– μC –GSM integrated system

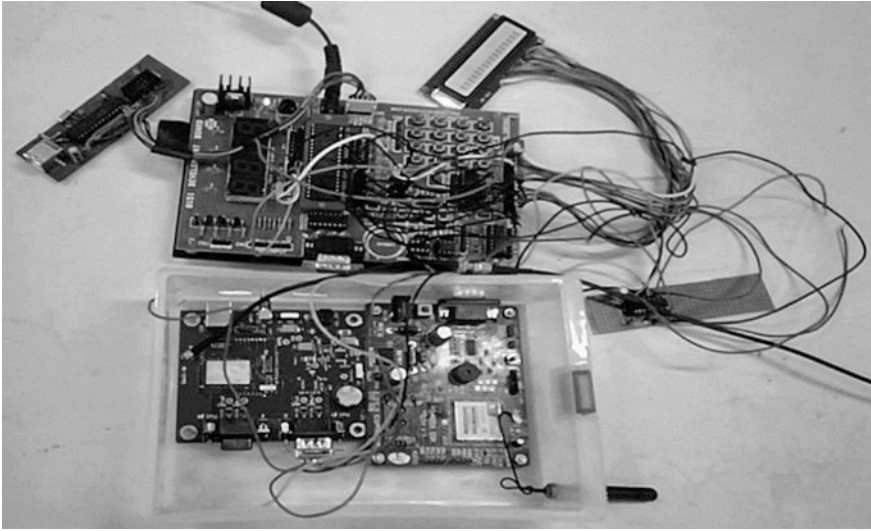


Fig. 5 Integrated GNSS, μC and GSM system

5 Results

(a) GNSS module integrated with μC and display

The integrated GNSS module with μC displays the position information (i.e. longitude and latitude), time, velocity as well as the satellite information (i.e. the total number of used satellites for providing the position information, value of the elevation, azimuth angle and C/N_0 for each of the satellites) as per user selection. These results are shown in Fig. 6.

(b) GNSS module integrated with GSM

Using the integrated GNSS- μC -GSM module, the position information (i.e. the longitude and the latitude values) is sent to a mobile phone (number is embedded in the code) through text message every 1-min interval. The mobile number and time interval may be fixed in the embedded coding. Snapshots of few consecutive SMS at every 1-min interval to a cellular phone are shown in Fig. 7.

6 Summary and Discussion

This paper focuses on the implementation of low-cost hardware-based integration of GNSS with GSM module and μC , and this will be useful for real-life applications such as vehicle tracking and asset monitoring system. The system also can be used

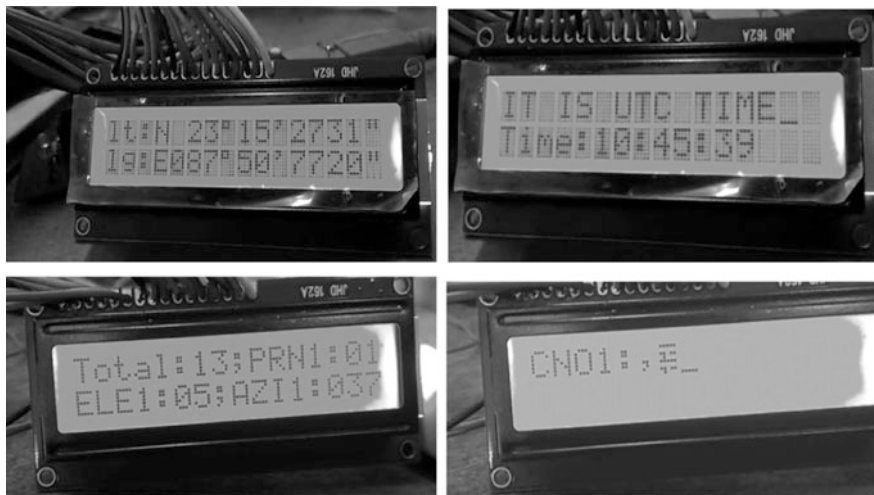


Fig. 6 Results of GNSS– μ C integration shown in LCD; the upper left figure shows position, the upper right figure shows time; lower figure shows GNSS satellite information displayed in the LCD

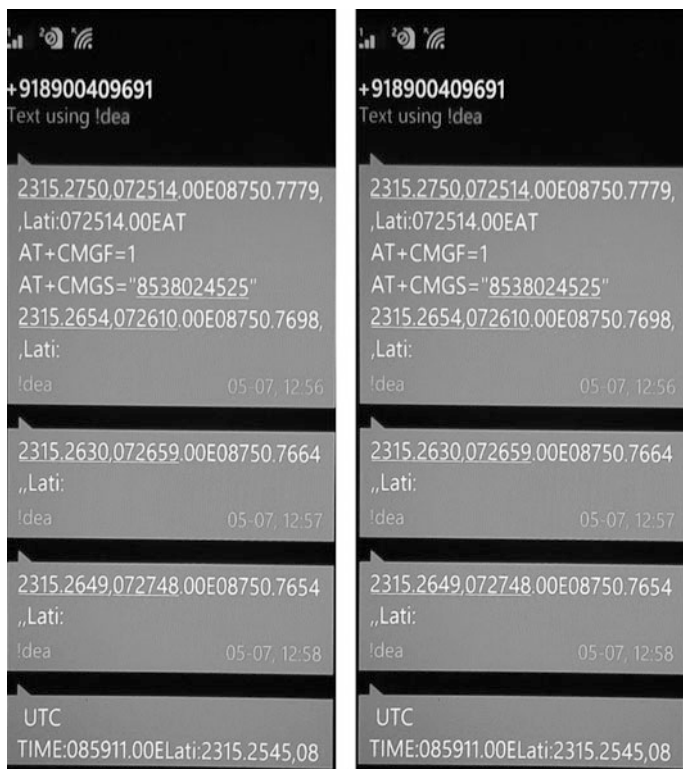


Fig. 7 Results of the GNSS– μ C–GSM integrated system; information of location and time is updated to a mobile phone once every minute

for displaying time, GNSS satellite information and also as an atmospheric disturbance monitor. The system with little modification can be used as a GNSS trainer kit. The development process discussed here is constrained by software resources (using the available free version of Keil μ Vision tool, because of coding size constraints, it is possible to display the information on up to 4 tracked satellites only) that calls for further effort towards the development of a complete generic GNSS-based system that can be used for many user-defined applications.

The integrated GNSS–Microcontroller–GSM system attached to any asset is capable of sending the positioning information of the same as an SMS to a particular mobile number at a regular interval. Implementation of a stand-alone clock providing accurate time from GNSS may be done using the system. Storing the information out of the system for post-processing towards improved position solution and embedding the algorithm in the μ C may be future scopes of work utilizing this basic system blocks and slightly modified codes.

The system may be used (with larger codes) to display all the tracked satellites' information. Integration of other sensors (such as temperature and humidity sensors) with the system would also be possible with minimal change in the embedded codes, and those systems may be efficiently used for remote monitoring of various real-life parameters needed for applications in biology, agriculture, environment.

With operation initiation of Indian Regional Navigation Satellite System (IRNSS/NavIC), in near future, it would be of interest to explore the use of IRNSS/NavIC NMEA data in stand-alone and hybrid mode for similar applications using this basic hardware configuration. IRNSS/NavIC uses geostationary satellites and signals in both *L* and *S* bands. It would be of interest to probe the atmosphere using these typical attributes of IRNSS/NavIC, and the proposed integrated system may be useful for such studies.

Acknowledgements Authors AB and AS acknowledge Space Application Centre (SAC), ISRO, Ahmedabad, for financial support through the sponsored project NGP-28.

References

1. Derekenaris G., Garofalakis J., Makris, Prentzas J., Sioutas S., and Tsakalidis A., Integrating GIS, GPS and GSM technologies for the effective management of ambulances, *Comp., Environ. Urban Sys.*, vol 25, pp. 267–278, (2001).
2. Mohammad. Al-Khedher, Hybrid GPS-GSM Localization of Automobile Tracking System, *Int. J. Comp. Sc. and Inf. Tech.*, vol 3, pp. 75–85, (2011).
3. Khan A., and Mishra R., GPS – GSM based tracking system, *Int. J. Eng. Trends and Tech.*, vol 3, pp. 161–164, (2012).
4. Maurya K., Singh M., and Jain N., Real time vehicle tracking system using GSM and GPS technology- an anti-theft tracking system, *Int. J. Elec. Comp. Sc. Eng.*, vol 3, 1103–1107, (2012).
5. Bose A., Malik R., Das S. and, Bhattacharya A., Development of a GNSS based multipurpose System, *TECHNIA – Int. J. Comp. Sc. Comm. Tech.*, vol. 8, pp. 1066–1070, (2015).

6. Sarkar S., and Bose A., Contribution of GLONASS in multi-GNSS solution accuracy, *Coordinates*, vol XI, pp. 13–16, (2015).
7. Bandyopadhyay T., Guha A., Das Gupta A., Banerjee P., and Bose A., Degradation of navigational accuracy with Global Positioning System during periods of scintillation at equatorial latitudes, *Elec. Lett.*, vol 33, pp. 1010–1011, (1997).
8. NMEA IDs, <https://github.com/mvglasow/satstat/wiki/NMEA-IDs>.

Finger Detection for Hand Gesture Recognition Using Circular Hough Transform

Amrita Biswas

Abstract This research is based on vision-based hand gesture recognition. The gesture of hands can convey important information and can be applied as a useful means for man–machine interaction. One of the primary steps of hand gesture recognition is identifying the number and coordinates of the fingers visible in the image or video frame. This work proposes a simple but effective way for locating the coordinates of the images by using Hough transform. First the prospective fingertips are detected by circular Hough transform. Next the coordinates of the fingertips are cross-verified by searching for the long Hough lines in the vicinity of the fingertip coordinates. The long Hough lines will indicate the fingers.

Keywords Gesture recognition • Image processing • Hough transform
Circular Hough transform

1 Introduction

The shape and motion of hands are often utilized to transmit the intention of the speaker. With the availability of cheap webcams, the interface between user and machine could be easily made free of touch. The images obtained from the camera could be used to track the various hand gestures made by the user, and the computer could be made to respond accordingly. Besides man–machine interfacing hand gesture recognition has several other applications in the field of sign language detection, gaming, 3D modeling, robot control, television control, etc.

However, hand gesture recognition in real time faces many challenges because of the complex nature of the human hand. Gestures could be hard to understand due to variations and flexible nature of the hand shape. The shape of gestures, real-time application issues, presence of background noise, and variations in lighting

A. Biswas (✉)

Sikkim Manipal Institute of Technology (SMIT), Majhitar,
Rangpo 737136, Sikkim, India
e-mail: amrita.a@smit.smu.edu.in

conditions are other difficulties in the field of gesture recognition. Most fingertip detection models depend on hand direction. Processing time is also a major concern in all image processing applications. The proposed algorithm is independent of hand direction and does not use any markers or data gloves.

Gestures are primarily of two types—static (fixed pose) and dynamic (set of postures). Static postures are relatively simple to analyze, while dynamic postures are more appropriate for real-time scenarios [1, 2]. Certain gesture recognition systems make use of additional hardware like data glove devices and color markers for acquisition of gesture recognition data [3]. However, methods which are based on the natural appearance of hand shape, texture, or skin color are more preferred as they tend to be more cost effective and less intrusive. Main steps involved in gesture recognition are hand detection, feature classification, and gesture recognition.

Hand detection and separation of the hand image from the rest of the background details will facilitate faster and more efficient gesture recognition. This is usually carried out by the method of segmentation for static images and by the method of tracking for dynamic images. In segmentation, the image is subdivided into several different parts. The segmentation process selected depends on the type of gesture. For dynamic gestures, the hand gesture needs to be identified and tracked. For hand tracking, either the video is divided into frames and each frame is processed alone, or some tracking details like shape or skin color using some tools such as Kalman filter are used [4]. For static gesture, the input image needs to be segmented only and can be achieved by methods like Otsu's methods, skin-color-based segmentation, transform-based segmentation, and texture-based segmentation. If the segmentation process is done correctly, features extracted are optimal and thus the classification results will be good. [2].

Feature extraction is a very important step as optimal feature selection helps in better classification and also reduces processing time and memory requirements. Different methods have been used by researchers for efficient feature extraction from the detected hand image. Various methods have been applied for representing the features that can be extracted. The method applied largely depends on application. Certain methods used the shape of the hand, for example the hand contour and silhouette, and some methods utilized fingertips position, palm center, etc. [2]. Self-Growing and Self-Organized Neural Gas (SGONG) neural algorithm [5] was used to determine the locations for the palm region, palm center, and hand slope by extracting the shape of the hand. In [6], the hand image was first segmented and then the center of gravity (COG) of the segmented hand and the distance from the COG to the farthest point in the fingers were calculated. In [7], the segmented image was divided into blocks of different sizes. Each block depicted the brightness measurements in the image. The optimal block size that will provide good recognition results was determined by conducting several experiments [8]. In [9], Gaussian probability density function was used to extract geometric central moment as local and global features.

Gesture classification method is used to recognize the gesture, after modeling and analysis of the input hand image. The performance of the gesture classification technique will largely depend on the quality of the features extracted using the

feature extraction method. A number of methods have been used by researchers for gesture classification. Researchers in [1, 7, 10] used the Euclidean distance measure for classification of hand gestures. For dynamic gesture recognition, methods like the HMM [11, 12], finite-state machines [1], and learning vector quantization methods [13] have been proposed.

Neural networks [12, 14, 15], fuzzy c-means clustering [2], and genetic algorithms [16] are the other methods that have been widely used for gesture classification.

One important step in hand gesture recognition is detecting the palm, counting the number of fingers, and determining the coordinates of the fingertips. In this research, a simple and fast technique based on circular Hough transform has been proposed for fingertip detection and counting. The proposed method is extremely simple compared to all the other methods discussed above. The rest of the paper is organized as follows:

In Sect. 2, I have described the linear Hough transform and circular Hough transform. In Sect. 3, I have discussed the proposed algorithm for finger detection and counting. In Sect. 4, the experiments performed are discussed in detail along with the results obtained. Finally, I have concluded in Sect. 5.

2 Hough Transform

Hough transform is a feature extraction technique widely used in image analysis, computer vision, and digital image processing. Hough transform groups edge points into object candidates by performing an explicit voting procedure over a set of parameterized image objects and thus facilitates in extracting the edge features of the images. Edges play an important role in object recognition [17, 21].

2.1 Linear Hough Transform

Let $(x_i, y_i) i = 1, 2, 3, \dots$ represent the i th point in the xy plane of the image space. Given an equation of a straight line $y_i = ax_i + b$, it can be observed that infinitely many lines pass through the point (x_i, y_i) satisfying the equation $y_i = ax_i + b$ for varying values of a and b . Since perpendicular lines to the x -axis can give unbounded values for parameters a and b (a and b rise to infinity), lines are parameterized in terms of theta θ and r such that

$$X \cos \theta + y \sin \theta = r \tag{1}$$

Figure 1 shows the geometrical interpretation of the parameters r and θ . Each sinusoidal curve in Fig. 2 depicts the family of lines that pass through a particular point (x_k, y_k) in the xy plane. The intersection point (r', θ') in Fig. 2 depicts the line that passes through both (x_i, y_i) and (x_j, y_j) in Fig. 1 (Fig. 3).

Fig. 1 (r, θ)
Parameterization of line in xy plane

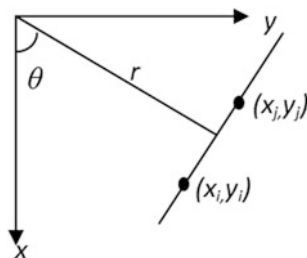


Fig. 2 Sinusoidal curves in the (r, θ) plane

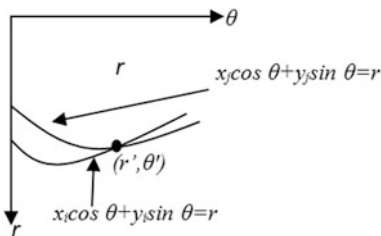
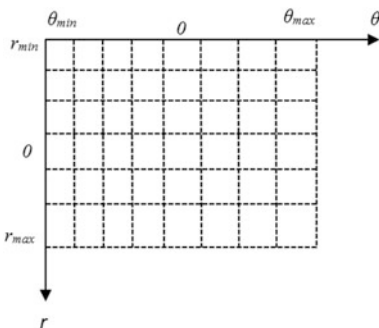


Fig. 3 Division of the (r, θ) plane into accumulator cells



An approach based on Hough transform can then be framed as follows:

Step 1: Obtain binary edge image.

Step 2: Specify subdivisions in the $r\theta$ plane, where (r_{min}, r_{max}) and $(\theta_{min}, \theta_{max})$ are expected ranges of the parameter values, $-90^\circ \leq \theta \leq 90^\circ$ and $-D \leq r \leq D$, where D is the maximum distance between opposite corners of the image.

Step 3: Initial value of cells set to zero. Cell value at coordinates (i, j) with accumulator values $A(i, j)$ indicates the square associated with parameter space coordinates (r_i, θ_j) .

Step 4: Then for every non background pixel (x_k, y_k) in the xy plane θ is equaled each of the allowed subdivision values on the θ -axis and solved for the corresponding value of r using the equation: $r = x_k \cos \theta + y_k \sin \theta$.

' r ' values obtained are rounded off to the nearest allowed cell value along the ' r ' axis. If θ_p results in r_q , then $A(p, q) = A(p, q) + 1$.

Step 5: Note the count values of the accumulator cells for high pixel concentrations.

Step 6: Find all local maxima $A(p_p, q_p)$ such that $A(p_p, q_p) > \lambda$, where λ is a user-defined threshold.

Step 7: Let ρ_d, θ_d be the arrays containing the discretized intervals of the parameter space. The output is a set of lines described by $(\rho_d(p_p), \theta_d(q_p))$.

2.2 Circular Hough Transform

The circular Hough transform depends on equations for circles. The equation of the circle is

$$r^2 = (x - a)^2 + (y - b)^2 \quad (2)$$

Here, a and b represent the coordinates for the center, and r is the radius of the circle.

The parametric representation of this circle is

$$\begin{aligned} x &= a + r^* \cos(\theta) \\ y &= b + r^* \sin(\theta) \end{aligned} \quad (3)$$

Circular Hough transform depends on three parameters that requires a longer computation time and higher memory elevating the complexity of extracting information from the image. For ease of computation, the radius is set to a constant value based on the size of the resized hand image. For every edge point, a circle is drawn with that point as origin and radius r . The circular Hough transform also uses a three-dimensional accumulator array $A(p, q, r)$. The first two variables p and q represent the coordinates of the circle, and the variable r represents the radii. The values in the accumulator (array) are incremented each time a circle is detected with the specified radii over every edge point. The accumulator keeps counts of how many circles pass through coordinates for each edge point. Finally, the highest counts in the accumulator are selected. The coordinates of the center of the circles in the images are the coordinates with the highest count.

3 Proposed Algorithm Steps

First the hand images are converted to gray scale. Preprocessing is carried out by pixel-wise adaptive Wiener filtering to estimate the local image mean and standard deviation. Filtering smoothes the image and reduces the effect of additive noise power in the images [19].

The primary steps of the proposed algorithm include the conversion of the gray-level hand image to binary edge image by using the Sobel operator for edge computation [20]. Due to low contrast and noise, the edge detection may not be satisfactory, and since the results of the Hough transform-based algorithm are mostly affected by the quality of the edge image detected, some morphological processing operations [21] are carried out on the obtained edge image. The edge image is dilated with a flat linear structuring element. The basic effect of this operator on a binary image is to slowly enlarge the boundaries of regions of foreground pixels (i.e., white pixels, typically). Thus, areas of foreground pixels grow in size, while holes within those regions become smaller.

Next the image fill operation is carried out to remove irrelevant artifacts from the images. Image fill operation works on the background pixels. It changes connected background pixels (0 s) to foreground pixels (1 s), stopping when it reaches object boundaries.

Next the circular Hough transform of the edge image is computed. The location of the peaks of the circular Hough transform is identified which denote the probable fingertip location of the image, and the number of Hough peaks identified denotes the number of probable fingertips visible.

The coordinates of the peaks thus identified are saved for further processing. Next the images are scanned to determine the longest Hough lines in the vicinity of the fingertip circles. If Hough lines are detected sufficiently close to the circle Hough transform peaks, then the corresponding set of coordinates are identified as a finger. If no significant lines are detected close to the fingertip coordinates, then those coordinates are rejected as false peaks. Finally, the number of matches are counted and the particular hand gesture image is identified as pointing zero, one, two, three, four, or five fingers.

After Hough transform computation accumulator matrix is scanned for detection of the Hough peaks. The optimal number of Hough Peaks is defined by the user. A $Q \times 2$ matrix is obtained as output. It contains the row and column coordinates of the peaks and Q ranges from 0 to number of peaks specified by the user.

Next the accumulator space is scanned to detect the extremes of the detected lines (x_0, y_0, x_1, y_1) . Coordinates of the detected lines are stored. Next the coordinates thus obtained are compared with the coordinates of the prospective fingertip coordinates. If the coordinates are in the vicinity of the circle coordinates, then those set of coordinates are finalized as a finger. The total number of finger count and their coordinates are provided as output of the algorithm. The results have been discussed in Sec. 4.

Next the accumulator array is scanned to locate the position of the peaks. A 2D Gaussian kernel is used to smooth the xy coordinates, and a 1D Gaussian kernel is used to smooth the radius column prior to peak detection. Smoothing helps to locate peaks if the accumulator array is noisy. The coordinates of the peaks are treated as prospective fingertip location and stored for further use.

4 Experiments Performed and Results Obtained

To test the proposed algorithm, a hand gesture database has been used. The database contains 100 hand images. There are 20 images showing one finger captured from different camera angles and at different inclinations, 20 images showing two fingers captured from different camera angles and at different inclinations, and so on up to five fingers. So the total number of images in the database is $20 \times 5 = 100$. Some of the sample images of the database have been shown in Fig. 4.

All the images are of size 288×352 . First the images are resized to 100×100 to ensure faster processing and lower the memory space required. Next the images are converted from color image to gray scale. Pixel-wise adaptive Wiener filtering is used with neighborhoods of size 5×5 to estimate the local image mean and standard deviation. Edges of the images are computed using Sobel Operator. Dilation and image fill operation carried out on the edge image to enlarge the boundaries and remove irrelevant artifacts from the images. The effect of dilation and image fill operation on a sample image from the database has been shown in Fig. 5.

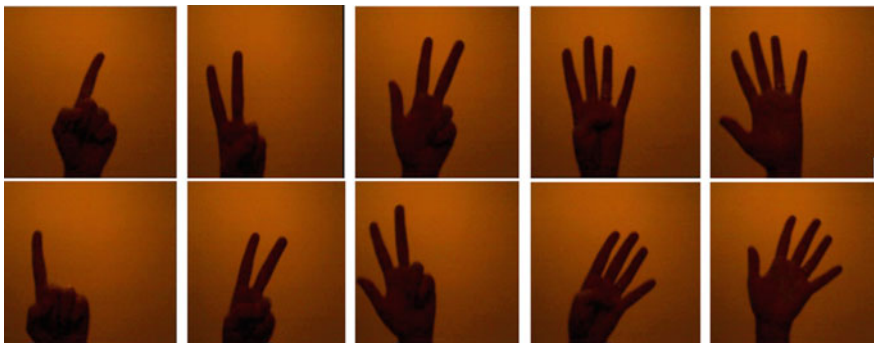


Fig. 4 Sample images of the database used

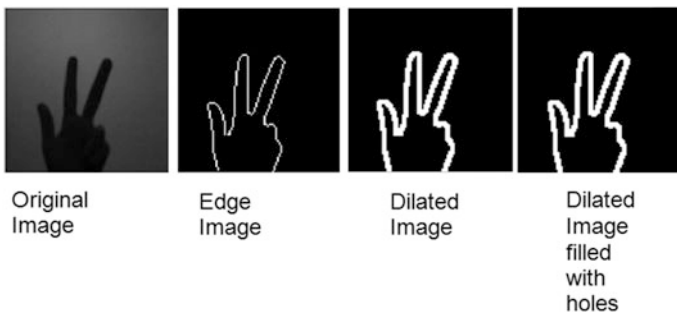


Fig. 5 Effect of dilation and image fill operation on a sample image from the database

After edge computation, the next step is to compute the circular Hough transform of the images. The accumulator matrix of the circular Hough transform is scanned to determine the significant peaks. The top five peaks are extracted provided the peak values are above a predecided threshold. Coordinates of the peaks obtained are marked on the image. A finger count counter is updated based on the number of significant peaks detected. Next linear Hough transform of the edge image is computed, and the accumulator matrix is scanned to determine the coordinates of the significant line. Next the obtained line coordinates are compared with the coordinates of the fingertips. If the end of a line originates or terminates in the vicinity of a fingertip coordinate, then the coordinates of the fingertip are finalized and the finger count counter value is retained, else the counter value is decremented (Fig. 6).

Coordinates of the fingertips for a sample image with three pointing fingers are shown in Table 1.

Among the 100 images, 95 images were correctly classified. Hence, the percentage of correctly recognized images is 95% (Table 2).

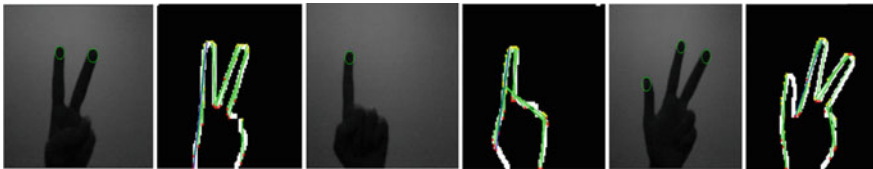


Fig. 6 Results of fingertip and finger detection for some sample images

Table 1 Coordinates of the fingertips for a sample image with three fingers pointing

Coordinates	<i>x</i>	<i>y</i>	<i>r</i>
Peak 1	280	103	11
Peak 2	210	78	11
Peak 3	121	139	11

Table 2 Result table showing the number of hand images correctly recognized

Class no.	No. of pointing fingers	Total no. of images	Correctly recognized
1	1	20	20
2	2	20	20
3	3	20	19
4	4	20	18
5	5	20	18
	Total Images =	100	95
		Correct recognition % = 95%	

5 Conclusion

In this paper, a simple and efficient method for fingertip detection has been proposed. The main advantage of this work is that the hand can be facing any direction in front of the camera, but the algorithm will still work. Also this method does not depend on detection by skin color as performance of skin-color-based methods tends to degrade with lighting conditions. However, hand image detection and extraction from a clutter background have not been implemented in this work, and in the next phase, I plan to work on that part so that a complete gesture recognition system can be developed.

References

1. S. Mitra, and T. Acharya., Gesture Recognition: A Survey, *IEEE Transactions on systems, Man and Cybernetics, Part C: Applications and reviews*, vol. 37 (3), <https://doi.org/10.1109/tsmcc.2007.893280>, 311–324, (2007).
2. Xingyan Li., Gesture Recognition Based on Fuzzy C-Means Clustering Algorithm, Department of Computer Science, The University of Tennessee Knoxville, (2003).
3. Simei G. Wyoski, Marcus V. Lamar, Susumu Kuroyanagi, Akira Iwata, A Rotation Invariant Approach On Static-Gesture Recognition Using Boundary Histograms And, Neural Networks, *IEEE Proceedings of the 9th International Conference on Neural Information Processing*, Singapore, 1–5, (2002).
4. N. Ibraheem, M. Hasan, R. Khan, P. Mishra, Comparative study of skin color based segmentation techniques, *Aligarh Muslim University, A.M.U., Aligarh, India*, 1–14, (2012).
5. Shuying Zhao, Wenjun Tan, Shiguang Wen, and Yuanyuan Liu, An Improved Algorithm of Hand Gesture Recognition under Intricate Background, *Springer the First International Conference on Intelligent Robotics and Applications (ICIRA 2008): Part I*. 2008. https://doi.org/10.1007/978-3-540-88513-9_85, 786–794 (2008).
6. Malima, A., Özgür, E., Çetin, M., A Fast Algorithm for Vision-Based Hand Gesture Recognition For Robot Control, *IEEE 14th conference on Signal Processing and Communications Applications*, <https://doi.org/10.1109/siu.2006.1659822>, 1–4, (2006).
7. M. M. Hasan, P. K. Mishra, HSV Brightness Factor Matching for Gesture Recognition System, *International Journal of Image Processing (IJIP)*, Vol. 4(5), 456–467 (2011).
8. Mokhar M. Hasan, Pramod K. Mishra, Features Fitting using Multivariate Gaussian Distribution for Hand Gesture Recognition, *International Journal of Computer Science & Emerging Technologies IJCSET*, Vol. 3(2), 73–80, (2012).
9. Mokhar M. Hasan, Pramod K. Mishra, Robust Gesture Recognition Using Gaussian Distribution for Features Fitting', *International Journal of Machine Learning and Computing*, Vol. 2(3), 266–274, (2012).
10. W. T. Freeman and Michal R., Orientation Histograms for Hand Gesture Recognition, *IEEE International Workshop on Automatic Face and Gesture Recognition*, 296–301, (1995).
11. Min B., Yoon, H., Soh, J., Yangc, Y., & Ejima, T., Hand Gesture Recognition Using Hidden Markov Models, *IEEE International Conference on computational cybernetics and simulation*. Vol. 5, <https://doi.org/10.1109/icsmc.1997.637364>, 4232–4235 (1997).
12. Minghai Y., Xinyu Q., Qinlong G., Taotao R., Zhongwang L., Online PCA with Adaptive Subspace Method for Real-Time Hand Gesture Learning and Recognition, *Journal of World Scientific and Engineering Academy and Society WSEAS*, Vol. 9(6), 583–592, (2010).

13. Luigi Lamberti, Francesco Camastra, Real-Time Hand Gesture Recognition Using a Color Glove, Springer Proceedings of the 16th international conference on Image analysis and processing: Part I ICIAP, 365–373, (2011).
14. Tin Hninn H. Maung., Real-Time Hand Tracking and Gesture Recognition System Using Neural Networks, World Academy of Science, Engineering and Technology 50, 466–470 (2009).
15. V. S. Kulkarni, S.D. Lokhande, Appearance Based Recognition of American Sign Language Using Gesture Segmentation, International Journal on Computer Science and Engineering (IJCSSE), Vol. 2(3), 560–565 (2010).
16. Verma, R., Dev A., 2009, “Vision based hand gesture recognition using finite state machines and fuzzy logic”. IEEE International Conference on Ultra-Modern Telecommunications & Workshops (ICUMT ‘09), <https://doi.org/10.1109/icumt.2009.5345425>, 1–6, (2010).
17. Shapiro, Linda and Stockman, George, Computer Vision, Edition: 1st, ISBN-13: 978-0130307965, Prentice-Hall, Inc. (2001).
18. F. Jin, P. Fieguth, L. Winger and E. Jernigan, Adaptive Wiener Filtering Of Noisy Images And Image Sequences, International Conference on Image Processing, 0-7803-7750-8/03, (2003).
19. R. C. Gonzalez and R. E. woods, Digital Image Processing, Dorling Kindersley, India, Pearson Prentice Hall, (2006).
20. <https://www.cs.auckland.ac.nz/courses/compsci773s1c/lectures/ImageProcessing-tml/topic4.htm>, 21/03/2017.
21. Amrita Biswas, M.K.Ghose, Face Recognition Algorithm based on Orientation Histogram of Hough Peaks, International Journal of Artificial Intelligence & Applications, Volume 5, No. 5, 107–114, (2014).

Energy Contribution of Control Packets of AODV in Various Mobility Models in MANET

Akash Soni, Preeti Jharia and Sonali Chouhan

Abstract In mobile ad hoc networks (MANETs), routing protocols are commonly used to manage the routes. Because of mobility of nodes, there is a need to reconfigure routes dynamically. These protocols normally suffer from various deficiencies such as high routing overhead and constrained adaptability. In MANETs, mobility pattern directly influences the performance of routing protocol because communication link failures between nodes are associated with the network topology. The performance of routing protocol depends on number of sent control packets, which in turn affects the energy consumption of whole network. This study investigates ad hoc on-demand distance vector (AODV) Perkins et al. (Ad hoc on-demand distance vector (AODV) routing, 2003 [1]) routing protocol under various network configurations and utilizing different mobility models, e.g., random waypoint (RWP), linear, Gauss–Markov, and mass mobility. All simulations have been done using OMNET++ IDE (<https://omnetpp.org/documentation/> [2]). The execution is resolved on the premise of an aggregate number of sent control packets with varying node density, mobility, and different mobility types.

Keywords Mobile ad-hoc network · Control packet · Protocols
Ad-hoc on-demand distance vector (AODV) · Mobility models

1 Introduction

Ad hoc network is a decentralized, self-determining mobile ad hoc wireless networking system consisting of independent mobile nodes that can move randomly while altering the configuration on the wireless networks. The network is ad hoc

A. Soni (✉) · P. Jharia · S. Chouhan
Indian Institute of Technology Guwahati, Guwahati 781039, Assam, India
e-mail: akash.soni@iitg.ernet.in

P. Jharia
e-mail: preeti.jharia@iitg.ernet.in

S. Chouhan
e-mail: sonali@iitg.ernet.in

because it does not depend on preexisting infrastructure such as cellular network; thus, no stationary or fixed framework exists in MANET. In an ad hoc-type network, each node is willing to forward information for different nodes; thus, the assurance of which nodes forward information is made powerfully based on the system network. The system is decentralized, as there is no fixed-point control. The configuration of the network is changing randomly and can set up whenever two or more nodes are in the vicinity because of adaptability or flexibility that a mobile ad hoc network (MANET) offers.

Since these wireless nodes are allowed to move randomly, the wireless topology of the network may progressively change in an unpredictable manner. Thus, as the nodes move, the other nodes must know the resulting change in the network topology so that previous topology information can be updated. This MANET may operate in isolation or in a stand-alone manner or may have gateways to the fixed network.

The issue of efficient routing is one of the several challenges encountered in a MANET [3, 4]. The other issue is varying the mobility patterns of different nodes; some nodes are highly mobile, while others are primarily stationary. It is difficult to predict the movement and direction of movement of nodes.

There are several studies, and improvements have been done in various routing protocols for MANETs based on its security, stability, mobility, optimality, reliability, and efficiency [5, 6]. In our paper, we have evaluated performances of most widely used MANET routing protocol, namely ad hoc on-demand distance vector (AODV) for varying mobility and number of nodes in MANET for the different types of mobility models, i.e., linear, mass, random waypoint, and Gauss–Markov mobility using OMNeT++. Our study has shown that the performance of AODV routing protocol varies with the change in mobility model. The analysis has been done using the different types of mobility with varying node density and speed in terms of sent control packets that are route request (RREQ), route reply (RREP), and route error (RERR).

In the following section, we discuss AODV routing protocol, the effect of various mobility models on the performance of routing protocol, and detail of some of the existing mobility models. Section 4 presents aspects of the followed methodology; Sect. 5 is focusing on the simulation environment and the parameters used for simulation. The obtained results are shown in Sect. 6, and we conclude the paper in Sect. 7.

2 AODV Routing Protocol

AODV is a destination-based reactive protocol. Route discovery process in AODV is derived from dynamic source routing (DSR) protocol. Main advantage of AODV over DSR is the smaller size of the header of AODV, which results in better performance especially in case of small data size. In AODV, the nodes rather than the header of data manage routing tables.

3 Mobility

The main attribute of the MANETs is the mobility of the nodes, and the execution of MANET ought to be examined in the existence of mobility. It is understood that practically it can be rely extremely upon the objectives of the mobile nodes that are the component of an independent structure. The more complicated mobility scenarios are harder to model because more purposes ought to be incorporated. The mobility patterns and test runs are used to examine the effect of mobility on MANET as practical mobility models are extremely hard to obtain. The mobility associated with node existing in MANET turns out the system configuration which should improve with time as well as system performance; hence, it should be corrected over time to incorporate the changes. In this way, the systems' administration and application protocol performance of MANETs are specially influenced by the recurrence of system topology changes.

4 System Model

Performance metric for the analysis of mobility models is the total number of control packet P_C transmitted by all the nodes in the network in order to establish the connection between transmitter–receiver pairs. We consider a network that consists of P_C mobile nodes with wireless capabilities, deployed uniformly such that the node movement is constrained in the area of observation. Each mobility model has been analyzed using different node densities. Out of N nodes, we randomly assign some of the nodes as the transmitter–receiver pair and rest of the nodes only act as a router. We increase the number of transmitter–receiver pair in the same proportion as we increase the node density. In the process of connection establishment, each node transmits RREQ, RREP, and RRER packets. Let $RREQ_i$, $RREP_i$, and $RERR_i$ denote the number of sent RREQ, RREP, and RERR packets by node i , then total number of transmitted control packet of each type in the whole network will be:

$$RREQ_T = \sum_{i=1}^N RREQ_i, \quad (1)$$

$$RREP_T = \sum_{i=1}^N RREP_i, \quad (2)$$

$$RERR_T = \sum_{i=1}^N RERR_i, \quad (3)$$

Thus, the total number of transmitted control packet P_C will be:

$$P_C = RREQ_T + RREP_T + RERR_T. \quad (4)$$

$$\text{Energy} = \text{Power} \times (\text{Transmission time}), \quad (5)$$

$$\text{Transmission time} = P_C \times \frac{\text{Packet Size (in bits)}}{\text{Bit Rate}} \quad (6)$$

From Eq. (6), it is clear that energy consumed is directly proportional to the number of sent control packets, i.e., P_C . Hence, we studied the performance of AODV protocol in terms of the total number of sent control packets in various mobility models with varying node speed from 1 to 20 m/s.

We divided our study into three different mobility regions: slow mobility region (1–8 m/s) for pedestrian environment, medium (9–15 m/s), and fast mobility (16–20 m/s) region for vehicular environment.

After this, we provide information about our simulation setup and parameter that have been used in our study.

5 Simulation Parameters

See Table 1.

Table 1 Simulation parameters

Experiment parameter	Experiment value
Simulation time	300 s
Seed	50
Terrain dimension	700 × 700 m
Number of nodes	10, 20, 30, 40, 50
Mobility speeds	1–20 m/s
Number of connections	2, 4, 6, 8, 10, respectively, with number of nodes
Mobility models	Linear, random waypoint, mass, and Gauss–Markov mobility
Routing protocol	AODV
Transmitted power	1 mW
Bit rate	2 Mbps
Size of control packets	32 Byte

6 Simulation Results and Analysis

We have studied AODV routing protocol in MANET on the OMNET++ simulation platform using the INET framework in terms of number of control packets with a variation of mobility, speed, and for different node density and found the following results:

Figures 1, 2, 3, and 4 show the effect of mobility models on varying node density. As we can see from figures, on increasing the mobility, number of sent control packets is also increasing due to the increase in the number of link breaks between nodes. In Fig. 1, in the case of 30 nodes, linear mobility shows linear behavior in slow and medium mobility region, and linearity reduces for 40 nodes and 50 nodes networks in that regions due to an approximately equal number of link establishment and link break.

There is an abrupt change in the transition from medium to fast mobility region because of a sudden increase in the number of link breaks, which requires more number of control packets.

Figure 2 shows the behavior of mass mobility model. In the slow and medium region, all node densities show approximately linear behavior, but in the transition from medium to the fast region, it does not show abrupt change due to the fact that it is a type of group mobility in which each node moves in cluster manner. In Fig. 3, it is observed that, in the medium region, the behavior of 30 and 40 nodes network is constant, but in the case of 50 nodes, random waypoint mobility shows linearly increasing zigzag behavior in entire mobility region.

In Fig. 4, In Markov model, the number of sent control packets is less as compare to random waypoint model because it is a probabilistic model in which each node can predict the path of other nodes, and hence, there are less number of link breaks. It can also be seen that as we increase network density, the rate of change of the number of sent control packets increases drastically. A similar effect of an increment in the number of nodes can be seen for different mobility models, i.e., increase in the number of nodes reduces the performance of the network. The extent of reduction in the performance of network also depends on mobility model.

Fig. 1 Effect of linear mobility on AODV routing protocol

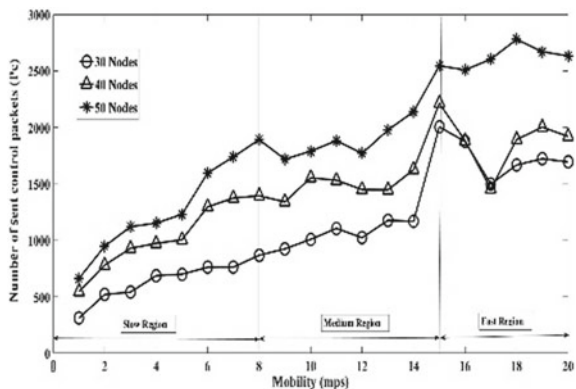


Fig. 2 Effect of mass mobility on AODV routing protocol

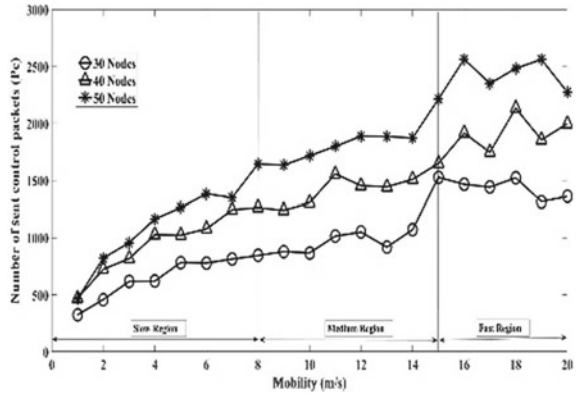


Fig. 3 Effect of random waypoint mobility on AODV routing protocol

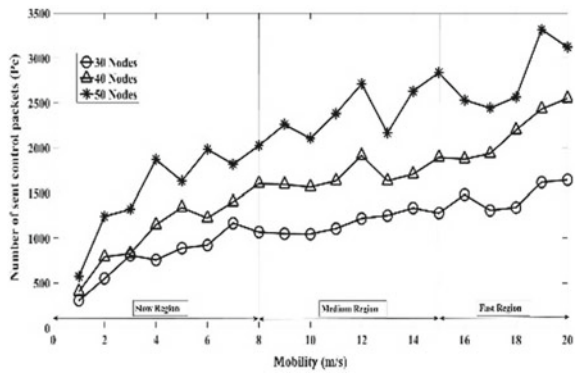


Fig. 4 Effect of markov mobility on AODV routing protocol

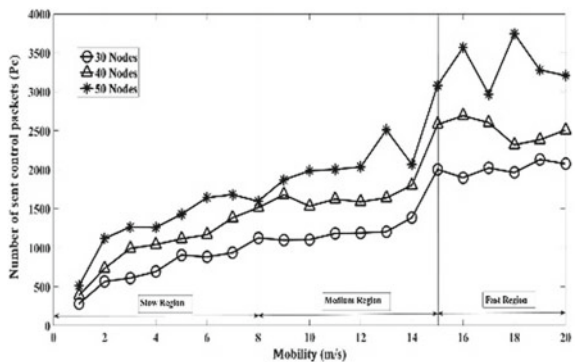


Figure 5 shows the comparison between different mobility models for 50 nodes in the network. Table 2 shows mean and variance of different mobility models in slow (1 –7 mps), moderate (8–14 mps), and fast (15–20 mps) mobility in case of Fig. 5. It is clear from the table that in slow mobility region, average number of

control packets is least in the case of mass mobility, but the variance is highest among others; hence, energy consumption is less, but it is also least stable in slow mobility region. In higher mobility region, Markov mobility shows highest energy consumption, while in this region, linear mobility is stable on increasing speed. Figure 6 Shows the contribution of RREQ, RREP, and RERR packets in P_C . In the

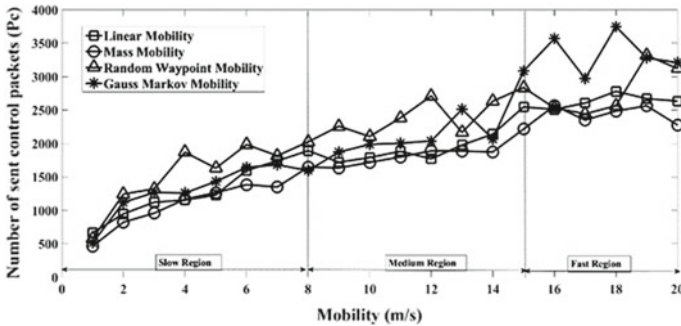
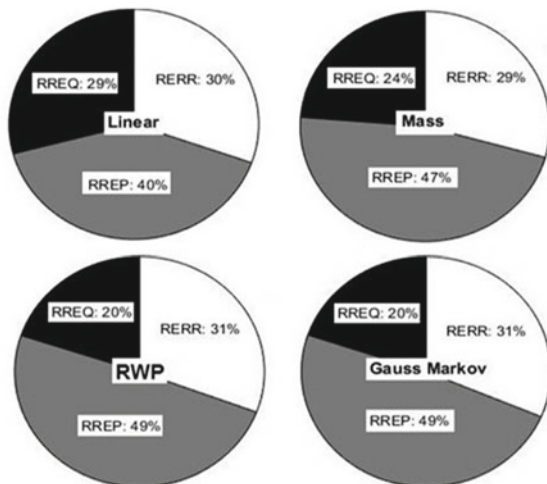


Fig. 5 Comparison of different mobility models in 50 nodes network

Table 2 Mean and variance of different mobility models for 50 nodes

Mobility	Slow		Moderate		Fast	
	Mean	Var	Mean	Var	Mean	Var
Linear	1206.4	17.45	1880.7	12.5	2623.3	9.9
Mass	1057.5	20	1776.8	10.2	2408.5	11.3
RWP	1490.4	17.4	2324.5	15.7	2801.3	19.8
Markov	1272.1	15	2010	14.8	3309	17.4

Fig. 6 Energy contribution of control packets in 50 nodes network at 20 m/s



case of mass, Gauss–Markov, and RWP mobility models, the contribution of case of mass, Gauss–Markov, and RWP mobility models, the contribution of RREP packets is high as compare to RREQ and RERR packets while in the case of linear mobility, it is approximately equal. Another interesting observation from this figure is that, in the case of Markov and RWP, the contribution of RREP packets is drastically increasing in fast mobility region.

7 Conclusion

Comparison of different mobility models for mobile ad hoc wireless networks using AODV routing protocol has been done based on the total number of sent control packets. We have classified mobility in three regions: slow, moderate, and fast. In linear mobility model, the number of control packets is less in slow mobility region. In moderate and fast mobility region, less number of control packets are required to establish connections in mass mobility model.

Random waypoint and Markov mobility model are used in most of the practical network scenario. On the comparison of these models, we found that requirement of control packets in Markov model in slow mobility region is less, while in the case of random waypoint model, it is less in fast mobility region. Furthermore, the contribution of RREP is more in control packets; hence, efforts can be made in future to decrease the number of sent RREP in AODV routing protocol.

References

1. C. Perkins, E. Belding-Royer, and S. Das, “Ad hoc on-demand distance vector (aodv) routing,” Tech. Rep., 2003.
2. “OMNeT++,” <https://omnetpp.org/documentation/>.
3. M. Das, B. Sahu, and U. Bhanja, “Mobility and its effect on the performance of manet,” in Power, Communication and Information Technology Conference (PCITC), 2015 IEEE. IEEE, 2015, pp. 871–877.
4. F. Bai and A. Helmy, “A survey of mobility models,” *Wireless Adhoc Networks*. University of Southern California, USA, vol. 206, p. 147, 2004.
5. F. Maan and N. Mazhar, “Manet routing protocols vs mobility models: A performance evaluation,” in *Ubiquitous and Future Networks (ICUFN)*, 2011 Third International Conference on. IEEE, pp. 179–184.
6. C. E. Perkins and K.-Y. Wang, “Optimized smooth handoffs in mobile ip,” in *Computers and Communications*, 1999. Proceedings. IEEE International Symposium on. IEEE, 1999, pp. 340–346.

Analysis and Characterization of Spectral Signature of Soil Nitrogen Content Based on VNIR Optical Sensing for Application in Smart Farming

Subra Mukherjee and Shakuntala Laskar

Abstract Sensing of soil nutrient content has become an integral part of soil fertility management system. Fertilizers have been in use for enhancing soil fertility since nineteenth century, but accurately applying fertilizers based on the amount required for a particular site or type of soil/crop has always remained a challenge. Moreover, standard laboratory analyses are very time-consuming and expensive. In this work, we developed a simple sensing system employing six LEDs (380, 475, 510, 570, 650, and 840 nm) and corresponding photodetector array for obtaining the diffused reflectance from five successive positions (separated by 72°). Based on this reflectance data obtained from the sensing system, unique soil spectral signatures were obtained and analyzed statistically. Two mathematical models, transformed multilinear regression model named as SSRC and exponential regression model named as ERMIR, were developed for rapid non-destructive estimation of soil nitrogen based on diffuse reflectance spectroscopy using Vis-NIR sensing. Both the models' performances were analyzed based on the three statistical parameters R^2 , RMSE, and SEE. The R^2 values obtained were almost near to 1, and the RMSE and SEE values were satisfactory. The repeatability and stability of the sensing system was also checked and found to be very satisfactory.

Keywords Total nitrogen (TN) • Soil spectral signature • Sum of square roots of reflection coefficients (SSRC) • Exponential regression model for infrared (ERMIR) Reflectance

S. Mukherjee (✉) • S. Laskar
School of Technology, Assam Don Bosco University, Guwahati, India
e-mail: subra.mukherjee@dbuniversity.ac.in

S. Laskar
e-mail: shakuntala.lashkar@dbuniversity.ac.in

1 Introduction

Nutrients present in soil play a vital role in plant growth. Deficiency as well as excess of these nutrients may impede the productivity. NPK, i.e., nitrogen (N), phosphorous (P), and potassium (K), represent the three most important nutrients in agriculture and are the prime ingredients in almost all fertilizers. Soil is the main source of nutrients for plant growth, and nitrogen is one of the most vital nutrients as it plays a fundamental role in the manufacture of chlorophyll in all plants and is an essential element of enzymatic proteins which catalyze and regulate the biological process responsible for plant growth. Soil spectral properties in the optical domain are related to soil minerals and organic compounds, water content, and soil particle size and structure [1]. Study and understanding of these relationships therefore can be of great significance for development of sensors to determine the quality of soil in terms of nutrients and other properties such as soil pH, salinity. Application of more amount of fertilizers (particularly urea) to soil in order to meet the demands of continually growing world population has led to nutrient imbalance not only in soil but has also caused air and water pollution. Nutrient management of soil is therefore a very critical part of sustainable agricultural practices [2]. Vis-NIR spectroscopy is very useful in measuring the mineral compositions of soil. Visible NIR region contains useful information about organic and inorganic materials present in the soil, and so the soil spectra obtained in this region can be used for soil mapping and monitoring and making inferences about soil quality and fertility. The soil total nitrogen (TN) content is an integral parameter that needs to be measured in precision agriculture. In [3], a portable soil TN detector was developed and a back-propagation neural network (BP-NN) estimation model was established using near-infrared reflectance spectroscopy with absorbance data at near-infrared wavelengths. The soil TN content correlation coefficient R^2 of the BP-NN estimation model was 0.88, and the validation R^2 was 0.75. In another work [4], a multispectral optical sensor was employed to measure the plant reflectance at four wavelengths, and these data were then used to develop an ANN-based model to predict the nitrogen concentration of leaves of cotton plants. Not only in agricultural fields, NIRS has been also used in dairy farming to monitor the milk quality of cow. In [5], NIRS spectroscopic sensing system has been used to monitor the three major constituents of milk, i.e., fat, protein, and lactose. The soil spectral signature method has also been employed in [6], to estimate the soil moisture content of bare soils from their spectral signatures in 400–2500 nm range. Statistical modeling such as convex envelope and ISER was used for analysis of the spectral signature. In [7], soil organic matter and available NPK were analyzed based on the near-infrared spectroscopy technology. The NIRS data were then analyzed using the least squares support vector machine model which employed the principal component analysis. Chemical fertilizer is added to soil to meet up the nutrients' requirements of plants, but the uncontrolled addition of these substances can cause severe environmental hazards such as surface and ground water pollution and also affect the quality of the crop [8–14]. Therefore, a lot of attention has been

focused in this area in the recent years, particularly in the area of precision agriculture and site-specific management procedures for obtaining localized on-the-go measurement of NPK in any soil.

2 Materials and Methods

2.1 Study Site and Sampling Design

Soil samples were collected from the turmeric and coconut fields of horticulture research center, Kamrup, on August 10, 2016 around 8:30 a.m. at temperature 23 °C and 65% humidity. Grid sampling method was used to extract the soil from a depth of 20 cm below the surface. All the samples were air-dried for about a week. The texture of the soil was found to be clay loam. The samples were then grinded and sieved through a 2-mm sieve.

2.2 Experimental Procedure

Figure 1 depicts the framework intended for the proposed work. The steps involved are as follows:

- Acquire soil samples by an appropriate soil sampling method (grid sampling)
- Illuminate the soil sample with a proper light source such that it corresponds to the vibrational frequencies of the bonds of the target ion (nitrogen)
- Measurement of diffuse reflectance from the sample under study
- Obtain spectral reflectance/absorbance data
- Statistical analysis of soil spectral signature

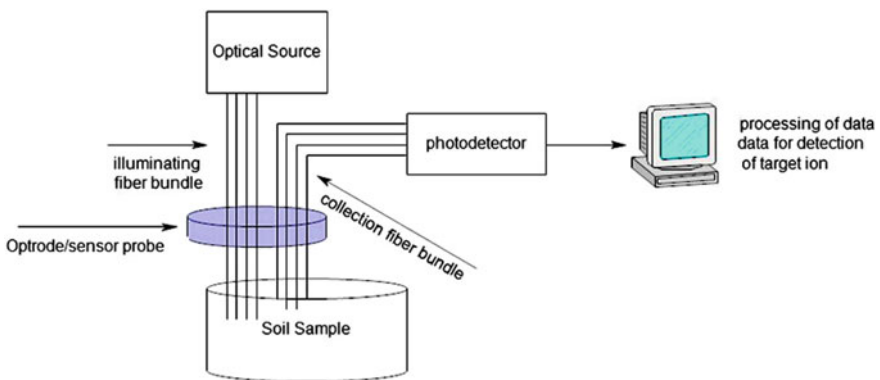


Fig. 1 Optical structure of the proposed sensing scheme for estimation of nitrogen content

- Development of prediction mathematical models for measurement of target ion concentration in the soil sample based on the unique soil spectra obtained.

As shown in Fig. 1, the optical sensor probe consisted of set 7 LEDs in the range (Vis-NIR) for illuminating the soil sample, and the reflected light from the soil is then detected by set of phototransistors and IR photodetector. Based on these data, the diffuse reflectance is then measured and spectral signature is statistically analyzed to understand the variation in the reflectance based on the amount of nitrogen present in soil.

3 Analysis of Soil Spectral Signature for Nitrogen

To characterize the soil nitrogen content and thereafter obtain a unique spectral signature, it is important to determine the most responsive wavelength. Therefore, reflectance/absorbance data were obtained for seven different wavelengths in the Vis-NIR range. The sample was illuminated with light from seven LEDs sources ranging from UV to IR (380–850 nm) containing the visible and NIR wavelengths. In addition to these, a white LED was also employed. The light was made to fall on the sample at five different positions by rotating the sample holder (petri dish) by 72° each time. The diffused reflected light was then collected at each of the angles by the array of photodetectors. Let V_i be the incident voltage and V_R the reflected voltage. Then the reflectance is given by:

$$\rho = \frac{V_R}{V_i} \quad (1)$$

For our case, the reflected voltage is the mean of the voltages collected from five different positions of the sample. Now, the reflectance for the bare soil is given by: Finally the normalized reflectance is calculated as:

$$R = \frac{\rho_{WC}}{\rho_{NC}} = \frac{V_{RWC}}{V_{RNC}} \quad (2)$$

$$\text{i.e., } R = \frac{\text{Reflected voltage from the sample with chemical}}{\text{Reflected voltage from the bare sample without chemical}} \quad (3)$$

Thus, the normalized reflectance is the ratio of the reflected output voltage obtained from the sensor for sample with the target chemical to the reflected output voltage obtained from the sensor for bare sample. After obtaining the reflectance data from the sensor, the spectral signature of soil total nitrogen content is obtained and based on the unique spectral signature obtained, regression models have been built for prediction and performance analysis of the system.

4 Mathematical Modeling of Soil Nitrogen Content

For each soil sample, several experiments were carried out to obtain the soil spectral signature of soil nitrogen content (SNC). Optimization techniques have been used to obtain the best-fit parameters for the soil nitrogen content characteristics curve. The curve fitting method determines model parameters such that the mathematical function passes through most of the experimental and gives the best fit. Based on the analyses of the soil spectral signature obtained, two models were developed: (1) *multilinear polynomial regression model—(fourth and fifth orders)* and (2) *exponential regression model*.

4.1 Soil Spectral Signature of Soil Nitrogen Content

Based on the reflectance data obtained in the region UV-Vis-NIR, the spectral signature was obtained and it was found to follow a unique pattern as shown in Fig. 2. Two multilinear regression models (of fourth and fifth orders) were estimated using curve fitting for analysis of the soil spectral signature as shown in Fig. 3. The fourth- and fifth-order estimated models obtained from the best-fitted curve are given by:

$$Y = -a_5X^5 + a_4X^4 - a_3X^3 + a_2X^2 - a_1X + \epsilon \tag{4}$$

$$Y = -a_4X^4 + a_3X^3 - a_2X^2 + a_1X - \epsilon \tag{5}$$

The magnitude of coefficients of reflection (a_5, a_4, a_3, a_2, a_1) followed a specific trend and correlation with the amount of nitrogen content in soil. So, a transformed quadratic regression model named as sum of square root of reflection coefficients (SSRC) was obtained for further statistical analysis as shown in Fig. 4. The transformed model besides reducing the complexities also aided in better analysis of the model parameters.

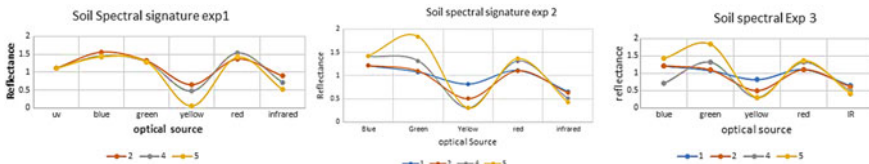


Fig. 2 Soil spectral signature for varying amount of soil nitrogen

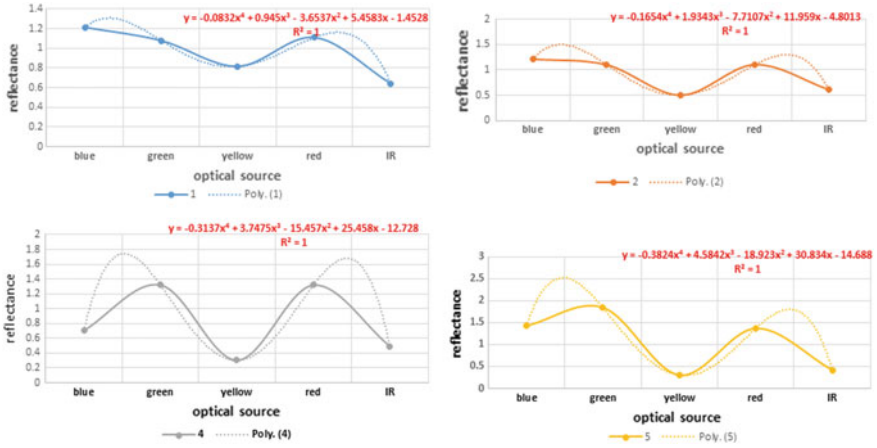


Fig. 3 Measured and fitted graphs for soil spectral signature obtained for 1, 2, 4, 5 grams of nitrogen content in 20 grams of soil (solid lines show the measured data and the dotted lines show the predicted data)

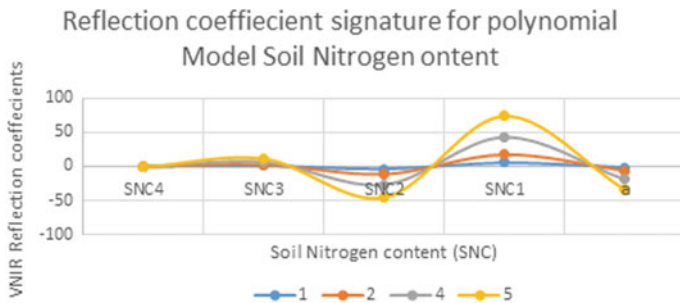


Fig. 4 Signature of the transformed model employing the reflection coefficients

4.2 Exponential Regression Model for Infrared Source

From the experimental data analysis and the graphs, it is apparent that in the entire spectrum, the infrared sensor appeared to produce the best correlation with the soil total nitrogen content. So, a separate model was developed to characterize the soil nitrogen content as shown in Fig. 5. Curve fitting was employed, and the exponential regression model that gave the best fit is given by:

$$Y = A \exp(-bX) \tag{6}$$

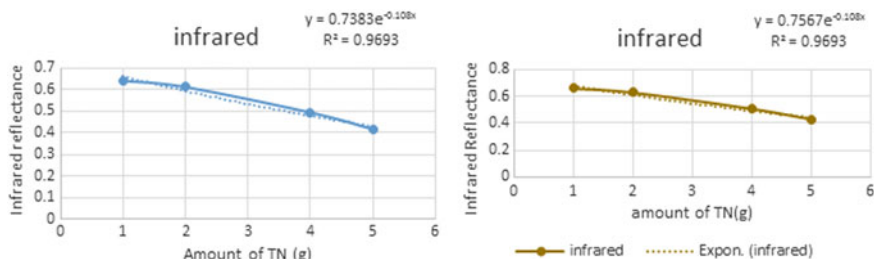


Fig. 5 Exponential model for infrared signature of soil nitrogen content (solid lines show the measured data and dotted lines show the predicted data)

5 Results and Discussions

For the quantitatively assessing the performance of the various models expressed in Eqs. (4), (5), and (6), we have employed statistical measures such as correlation coefficient (r), coefficient of determination (R^2), root mean square error (RMSE), and standard error of estimate (SEE). Moreover, each experiment was repeated under the same physical conditions several times to check the stability and reproducibility of the system. This is shown in Fig. 6.

The correlation coefficient for the various experiments was observed to be in the range of 0.95–0.99. The statistical measures of the developed models for several soil samples were calculated, a few of which is shown in the Table 1.

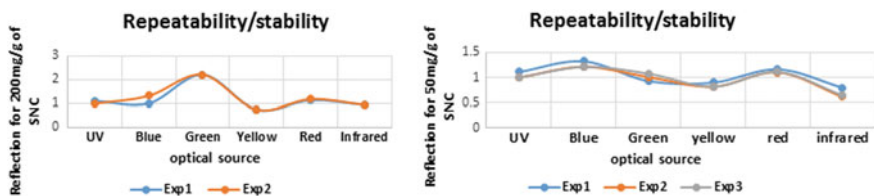


Fig. 6 Repeatability and stability of the developed sensing system for 200 and 50 mg/g of TN

Table 1 Statistical measures for performance analysis of the simulated models

Model name	R^2	RMSE	SEE
SSRC (fifth order)	1	0.001176	0.002037
SSRC (fourth order)	0.9855	0.074277	0.33
ERMIR (1)	0.9693	0.008322	0.2353
ERMIR (2)	0.9693	0.005059	0.010117

6 Conclusion

Soil samples with varying amount of nitrogen content were analyzed by the simple optical sensing system developed to obtain the reflectance measurements at six different wavelengths (380, 475, 510, 570, 650, 840 nm). The soil spectra obtained showed a unique signature, and two models SSRC and ERMIR were developed based on the experimental data obtained. The predicted/estimated data from the model were verified, and it was observed that fifth-order polynomial model (SSRC) yielded better results as the root mean square error (RMSE) and standard error of estimate (SEE) were very less and the coefficient of determination (R^2) was found to be almost 1. All these proved the efficiency of the model to predict the soil nitrogen content accurately. Also it was observed that the best correlation of the obtained reflectance with the varying amount of nitrogen was exhibited in the infrared region. So, the ERMIR model was developed for estimating the nitrogen content based on the reflectance obtained only from the NIR sensor. The obtained results validate that the developed sensing system as well as the mathematical models is capable of being employed for estimation of total soil nitrogen content and can therefore be a very useful tool in variable rate fertilizer applicator for application in smart farming.

References

1. R. Escadafal and H. A. R., "Soil optical properties and environmental applications of remote sensing," pp. 709–715, 1992.
2. K. Goulding, S. Jarvis, and A. Whitmore, "Optimizing nutrient management for farm systems," *Philos. Trans. R. Soc. London. Ser. B*, vol. 363, no. July 2007, pp. 667–680, 2008.
3. K. Wiesner, K. Fuchs, A. M. Gigler, and R. Pastusiak, "Trends in near infrared spectroscopy and multivariate data analysis from an industrial perspective," in *Procedia Engineering*, 2014, vol. 87.
4. R. Sui and J. A. Thomasson, "Ground-based sensing system for cotton nitrogen status determination," *Trans. Asabe*, vol. 49, no. 6, pp. 1983–1991, 2006.
5. "Near Infrared Spectroscopic Sensing System for online monitoring of Milk Quality during Milking," *Sens. Instrum. Food Qual. Saf.*, vol. 1, no. 1, pp. 37–43, 2007.
6. S. Fabre, X. Briottet, and A. Lesaignoux, "Estimation of soil moisture content from the spectral reflectance of bare soils in the 0.4–2.5 μm domain," *Sensors (Basel)*, vol. 15, no. 2, pp. 3262–3281, 2015.
7. Y. Qiao and S. Zhang, "Near-infrared spectroscopy technology for soil nutrients detection based on LS-SVM," *IFIP Adv. Inf. Commun. Technol.*, vol. 368 AICT, no. PART 1, pp. 325–335, 2012.
8. J Artigas, A Beltran, C Jiménez, A Baldi, R Mas, C Domínguez, J Alonso, Application of ion sensitive field effect transistor based sensors to soil analysis, *Computers and Electronics in Agriculture*, Volume 31, pp. 281–293, ISSN 0168-1699, 2001.
9. Hak Jin Kim, Kenneth A. Sudduth and John W. Hummel, Soil Macro nutrient sensing for precision agriculture, *Journal of Environmental Monitoring*, Vol. 11, pp. 1810–1824, 2009.

10. Joseph V. Sinfield, Daniel Fagerman, Oliver Colic, Evaluation of sensing technologies for on-the-go detection of macro-nutrients in cultivated soils, *Computers and Electronics in Agriculture*, Vol. 70, pp. 1–18, ISSN 0168-1699, 2010.
11. Jianhan Lin, Maohua Wang, Miao Zhang, Yane Zhang, Li Chen, Electrochemical sensors for soil nutrient detection : Opportunities and challenges, in *Proc. 12th International Conference on Computer and Computing Technologies in Agriculture (CCTA 2007)*, Wuyishan, China, pp. 1349–1353, 2007.
12. Kim, Hak-Jin, Hummel, John W, and Birrell Stuart J., Evaluation of Ion-Selective Membranes for Real-Time Soil Nutrient Sensing, in *Proc. Agricultural and Biosystems Engineering Conference*, Paper 410, 2003.
13. Ulrike Lehmann, Alain Grisel, “Miniature Multisensor Probe for Soil Nutrient Monitoring”, *Procedia Engineering*, Volume 87, pp. 1429–1432, ISSN 1877-7058, 2014.
14. Devadas R., Jones, S. D., Fitzgerald, G. J., McCauley, I., Matthews, B. A., Perry, E. M., Watt, Michelle, Ferwerda, J. G. and Kouzani, Wireless sensor networks for in-situ image validation for water and nutrient management, in *Proc. ISPRS Technical Commission VII Symposium, Institute of Photogrammetry and Remote Sensing, Vienna University of Technology*, pp. 187–192.

5G Technology Enabling the Wireless Internet of Things

Rabindranath Bera, Debasish Bhaskar, Samarendra Nath Sur, Soumyasree Bera, Arun Kumar Singh, Swastika Chakraborty, Amit Agarwal, Ganesh Sharma, Safal Sharma, Preman Chettri and Riwas Gurung

Abstract New technology trend has been initiated worldwide for the exploration of IoT using 4G and 5G mobile communications, cloud RAN, and extended coverage beyond the coverage area of mobile network. Motivated by the above trends, ECE Department, SMIT has started to build one test bed for IoT using 5G. At first, some recent papers are reviewed toward practical perspective on IoT in 5G network issues related to (i) latency critical IoT applications in 5G, (ii) efficient IoT gateway over 5G wireless, and (iii) efficient 5G small cell planning with eMBMS for optimal demand response in smart grids. This paper will discuss the detailed development efforts to achieve the IoT test bed. Efforts are rendered to make the test bed as a high-end research facility, industrial consultancy, and support toward 5G-enabled wireless IoT.

Keywords RAN · NB-IoT · LTE · CR · DR · SG · ITS · PLR
SDR · SDN · RRH · DSO · FBMC · MXG · VSA · RSMA

R. Bera (✉) · D. Bhaskar · S. N. Sur · S. Bera · A. K. Singh · S. Chakraborty
A. Agarwal · G. Sharma · S. Sharma · P. Chettri · R. Gurung
Department of Electronics and Communication Engineering,
Sikkim Manipal Institute of Technology (SMIT), Majitar,
Rangpo 737136, Sikkim, India
e-mail: rbera50@gmail.com

D. Bhaskar
e-mail: debasishbhaskar@gmail.com

S. N. Sur
e-mail: samar.sur@gmail.com

S. Bera
e-mail: soumyasree.bera@gmail.com

A. Agarwal
e-mail: amiteng2007@gmail.com

S. Sharma
e-mail: safalmate@gmail.com

1 Introduction

As an addition to the traditional communication technology, more and more professionals engaged in the communication industry pay high attention to the Internet of Things (IoT). Recently, LTE and 5G technologies are enabling the Internet of Things [1]. 3GPP has published the standards for this in release-13 in June, 2016.

The major issues in realizing IoT service using LTE/5G are as follows:

Cat-NB1 (NB-IoT) flexible deployment options: Qualcomm proposes [2] narrowband Internet of Things (NB-IoT) flexible for deployment in four ways after the amendment of LTE 4G spectrum by 3GPP. Those four ways are (a) in-band LTE/5G IoT, (b) guard-band LTE/5G IoT, and (c) stand-alone LTE/5G IoT, and (d) shared access. The options (b) and (c) are static band allocation to place the NB-IoT spectrum as it deals with the frequency band outside the 4G LTE specified spectral range. But when option (a) is to be deployed, then some of the LTE subcarriers and resource blocks have to be deactivated, and in their positions, the NB-IoT spectral components comprising of one resource block (RB) are to be accommodated. But LTE can accommodate such eight NB-IoT RBs [3] to be placed in-band of LTE spectrum. In future, the proliferation of IoT devices may reach billions. Under that scenario, the no. of NB-IoT spectral components will be huge. So, in order to accommodate them, 4G LTE spectrum will not be able to give sufficient spectral accommodation to them. As a result, the 4G LTE has to be modified to new technology, 5G. As discussed above, the in-band LTE IoT can accommodate eight RBs of NB-IoT. To do this, firstly the eight RBs of NB-IoT spectrum have to be sensed and thereby eight RBs of 4G LTE band have to be removed. In those vacant positions (white spaces) of LTE band, the incoming eight RBs of NB-IoT would have to be placed. This method needs to be done by employing cognitive radio (CR) in cloud server level. Accordingly, the enabling NB-IoT spectrum has to be controlled at IoT end node level. So, the intermediate 5G wireless gateway must have to be flexible. The same will be utilized for option shared access for IoT (d).

Enabling mission-critical control IoT services: The mission-critical applications involve the following [4]: (i) industrial automation, (ii) process automation, (iii) smart grids (SG), and (iv) intelligent transport systems (ITS). The reliability and the latency of the systems are to be typically 10^{-9} packet loss rate (PLR), and latency should vary from 250 μ s to 10 ms [5]. The improvement of physical layer and the network layer has to be done with proper protocol using software-defined radio (SDR) and software-defined network (SDN).

Extended coverage for IoT in 5G: For solving the communication problem in a hyper-remote area like Elephanta Island situated remotely in Indian Ocean and a far apart from Mumbai Harbor, it is recommended to establish a mesh hand over network among the boats running between harbor and the island. So, all the boats are needed to be IoT enabled, so that the mesh networking between the boats will be feasible.

2 A Case Study: Wireless IoT (W-IoT) Project Running at ECE Department, SMIT

Objectives: (i) Development of IoT end nodes for smart bulb to support the demand response mechanism; (ii) wireless IoT in 5G gateway development to establish a communication link at 60 GHz between the gateway and the IoT server. One resource block corresponding to NB-IoT demand is to be inserted by replacing one RB from the operational RBs within the 5G spectrum; (iii) the demand response engine is to be built in IoT server. The IoT server will receive the demand from remote IoT end nodes, and the decision toward proper response will be computed and communicated to IoT end nodes through the same communication link. Accordingly, the electrical bulb will be glowing or switched off. This technology is proposed in a smart grid (SG) system; (iv) the extension of the IoT end nodes is to be made feasible toward extended coverage through mesh network. This 4-folded objectives are depicted in Fig. 1. The highlighting features of the proposed test bed are that the above-mentioned three issues under article 1.1 have been taken care for the effective solutions.

3 Methodology and Prototyping

3.1 IoT_5G Gateway Prototyping

5G wireless network is a heterogeneous type of network where different remote radio heads (RRH) of different technology can be connected with a cloud-based

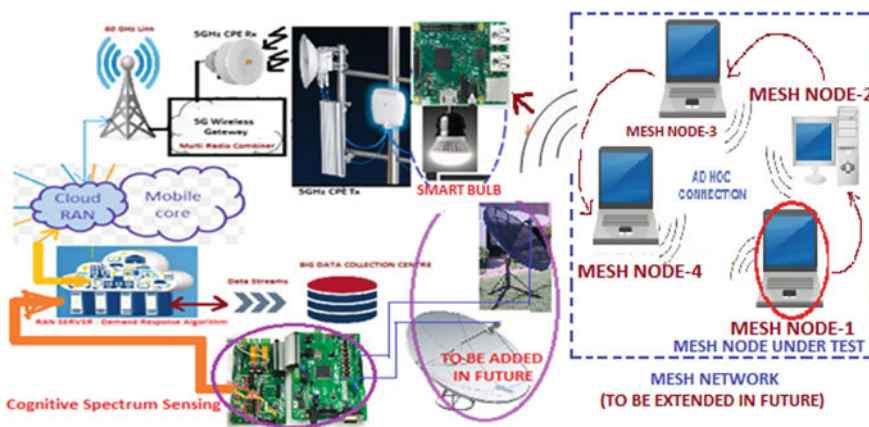


Fig. 1 A W-IoT test bed at ECE Department, SMIT, for demand response process of development of a smart bulb under smart grid application

computing server. The RRH will be connected with the cloud server using millimeter wave instead of optical front-haul cables. The low latency and higher data rate are achievable by using the 5G wireless gateway [6].

In the proposed system, the 5G wireless gateway is built out of the following ingredients:

- (i) A 5-GHz customer premises equipment (IEEE 802.11an) as the receiver for receiving the control signal from IoT device.
- (ii) The interface between the 5-GHz CPE receiver and the workstation is done by means of a digital storage oscilloscope (DSO) having a high sampling rate (~ 2 giga samples/s).
- (iii) The workstation captures the control data of IoT from the specified channel of the DSO. The captured data is taken into SystemVue software platform.
- (iv) The narrowband IoT (NB-IoT) modulation is done over the control signal. The NB-IoT signal is combined with the 5G BIGDATA. The modulation scheme used for generation of BIGDATA is filter bank multicarrier (FBMC). The multirate signal combiner is used for combining the two heterogeneous signals in SystemVue software.
- (v) The combined signal is dumped to the arbitrary waveform memory of an Agilent Mixed Signal Generator (MXG). The I & Q output of the MXG is used for mmWave upconversion.
- (vi) The I & Q output from the MXG is fed to the corresponding I & Q input of the 60-GHz transceiver board. It accepts the I & Q baseband and upconverts it to 60-GHz RF. This mmWave signal is transmitted through 60-GHz pyramidal horn antenna.
- (vii) The 60-GHz RF is propagated through a 80 m length of channel after which the 60-GHz downconverter is present at the other end of the 5G IoT wireless gateway. The retrieved narrowband control signal is directly saved in the dynamic memory of the radio access network (RAN) server.
- (viii) The decision-making algorithm exists within the RAN server. After the decision flag is generated, it is further constructed in the form of a particular signal. Here, this signal has been considered as a 1 kHz tone or 1 kHz square wave. This signal will basically signify the status of the end node device. So, this 1 kHz tone will be again retransmitted to the IoT end device through 5G wireless gateway.

3.2 IoT End Node Development

The IoT end device is considered here as an electrical lamp. The stand-alone lamp is a non-networked device. The objective is to make it a networked node for IoT compliant device. The enabling electronic part is achieved by means of a Raspberry Pi board. The smart algorithm is developed in Raspberry Pi in order to control the state of the lamp. The Raspberry Pi can control the electric lamp through a relay,

and the Raspberry Pi kit can be interfaced with a 5-GHz CPE through its LAN port. The state (the lamp is 'ON') information is transmitted from Raspberry Pi board to the 5G wireless gateway through 5-GHz transmitter CPE.

4 IoT 5G Base Station

4.1 Remote Radio Head

The remote radio head (RRH) in the above system is comprised of the MXG, 60-GHz transceiver unit, waveguide, and V-band horn antenna. This RRH is acting as the radio gateway for passing the NB-IoT signal along with the voluminous 5G-modulated data.

4.2 Base Band Unit

The base band unit (BBU) is connected to the RRH. The BBU performs the demodulation of the NB-IoT signal and FBMC waveform. The baseband equalization is done in the BBU of the receiver. IoT server is connected to BBU through proper interfacing.

5 IoT Server for Demand Response

The IoT server is connected with the receiver BBU. The state of the electrical lamp (when it is 'ON') is received through the 60-GHz wireless link and properly demodulated by the BBU. Accordingly, the demands are processed and the decision is generated within the IoT server. Finally, the response is forwarded to the IoT end node through the return path.

6 End-to-End Simulation

Figure 2 represents the 5-GHz IEEE 802.11an link between IoT end node and 5G gateway.

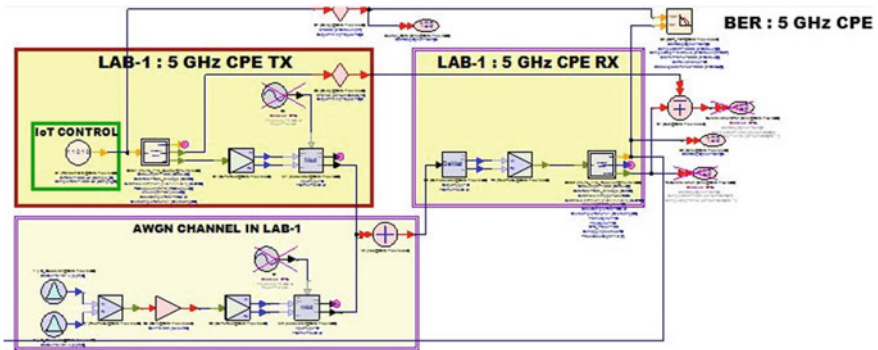


Fig. 2 5-GHz CPE link: IoT end node to 5G wireless gateway

7 Prototyping

7.1 Prototyping 1 (Guard-Band 5G IoT)

The simulated results are analyzed, and the prototyping of the above model has been initiated in the Department of Electronics and Communication Engineering, Sikkim Manipal Institute of Technology. To meet the goal of Center of Excellence, the total system is realized through a flexible 5G test bed situated at ECE research laboratory. The IoT end node to 5G gateway link is achieved by point-to-point 5-GHz Wi-fi (IEEE 802.11an) link.

The 5G modulation (FBMC waveform) part is realized in Agilent MXG. The wireless gateway link is achieved using 60-GHz transceiver unit.

Figure 3 depicts the simulation of the 5G gateway using multistandard radio (multiradio combiner). The above simulation model consists the block to retrieve the NB-IoT signal at the RAN server.

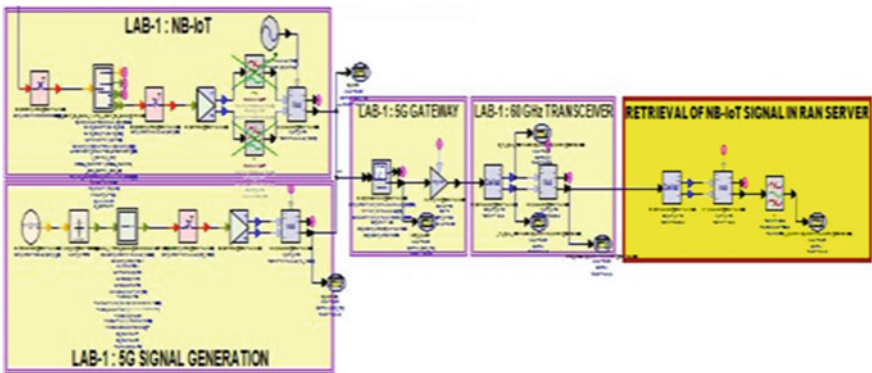


Fig. 3 Multiradio combiner and retrieval of NB-IoT signal in RAN server

Further, the design of the demand response algorithm is partially implemented in a server to control the IoT-enabled electrical lamp under consideration.

The whole system will be a miniaturized version of the above test bed as the system is to be finally delivered as an IoT product. The selection of V-band RF (60 GHz) exploits the advantage of mmWave to make the dimension of the system very small and portable.

8 Outcome and Expected Outcome

See Figs. 4 and 5.

9 Prototyping 2 (In-Band 5G IoT)

Frequency division multiplex (FDM) process is utilized for prototyping 2 with in-band 5G IoT. Both the spectrum positioning and spectrum power are flexible. The RBs for 5G and RBs for IoT can be multiplexed and placed anywhere with variable power level. The result is visualized using VSA along with Keysight 89,600 software. Further work toward this waveform design and resource spread multiple access (RSMA) is also initiated for efficient and effective coexistence of both 5G and IoT waveform.

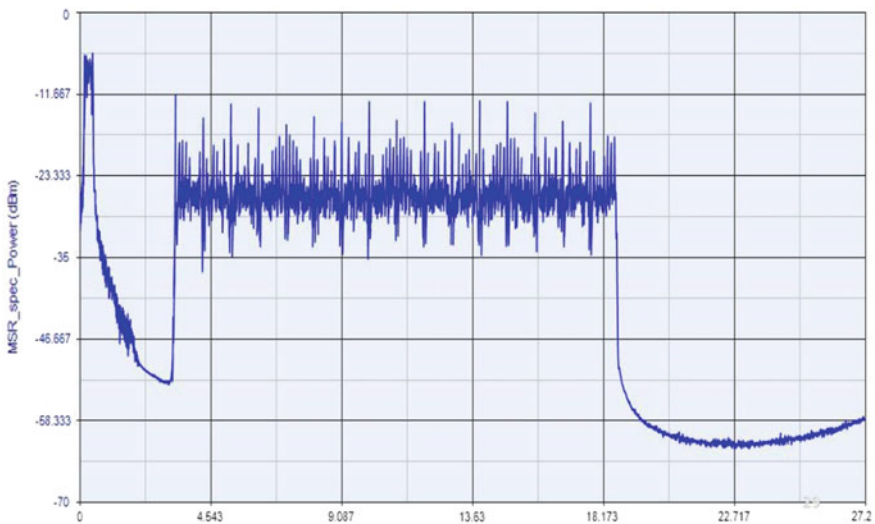


Fig. 4 NB-IoT control signal spectrum combined with wideband 5G spectrum

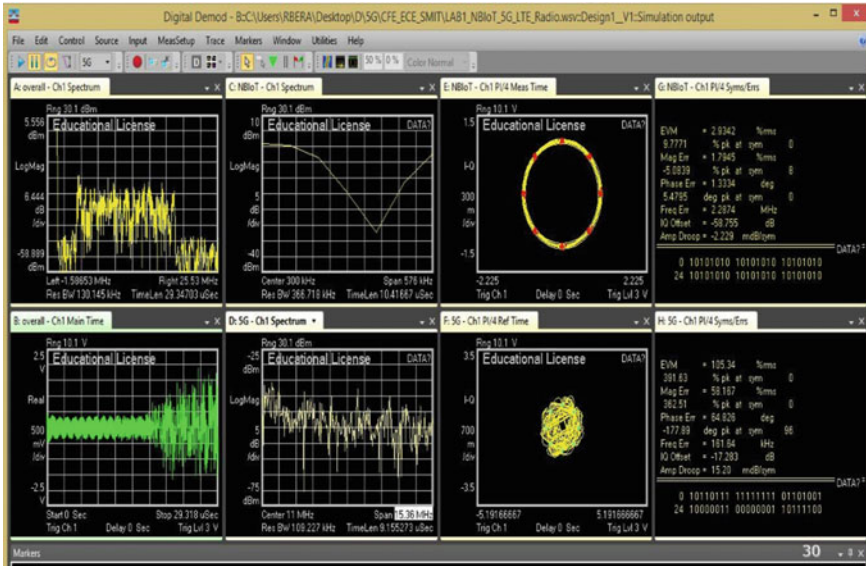


Fig. 5 NB-IoT symbol recovery through vector signal analyzer

10 Prototyping 3 (Extended Coverage)

Three laptops are configured in ad hoc mode of operation for communication and are the representative of extended coverage of the above IoT in 5G test bed. One KHz tone generated at the farthest laptop will reach to IoT end node via Laptop2 and Laptop3 using ad hoc communication. In turn, IoT end nodes will send this control signal of 1 kHz tone as demand response.

11 Summary and Conclusion

Motivated by the recent innovation of LTE and 5G technologies which are enabling the Internet of Things, one 5G-enabled IoT test bed is being established at the ECE Department, SMIT, to form the *Center of Excellence* in this technology area at the department.

The authors have highlighted some issues related to this technology realization while reviewing the recent articles. *Spectrum coexistence issues* like NB-IoT flexible deployment refer to in-band, guard-band, stand-alone, shared spectrum. The issue related to *enabling mission-critical control IoT services* dictates the redesign of the system toward a latency of the order of 1 ms or less and reliability figure 10e-9. The ad hoc mode of communication is being used worldwide to solve the issue related to extended coverage.

Based on the critical literature survey, reviews and findings, the issues and problem definitions, the authors have initiated the research work to realize ‘IoT in 5G’ test bed at ECE Department, SMIT. Objectives and the test bed configuration have been finalized. The methodology and prototyping are divided into following sublevels:

- (i) IoT_5G gateway prototyping
- (ii) IoT end node development
- (iii) IoT 5G base station
- (iv) IoT server for demand response
- (v) IoT end node extension.

Simulation and hardware testing are also initiated toward the completion of the test bed. Thus, a world-class test bed toward IoT in 5G with cloud server and extended coverage is being realized at ECE Department, SMIT.

References

1. LTE and 5G Technologies enabling the Internet of Things, www.5gamericas.org.
2. “Paving the path to Narrowband 5G with LTE Internet of Things (IoT),” Qualcomm Technologies, Inc., June, 2016.
3. Yuqing Wang, Zhanji Wu, “A Coexistence Analysis Method to Apply ACLR and ACS between NB-IoT and LTE for Stand-alone Case,” Sixth International Conference on Instrumentation & Measurement, Computer, Communication and Control (IMCCC), <https://doi.org/10.1109/imccc.2016.28>.
4. Philipp Schulz, QT et al., “Latency Critical IoT Applications in 5G: Perspective on the Design of Radio Interface and Network Architecture,” IEEE Communications Magazine, Volume: 55, Issue: 2, pp 70–78, February 2017.
5. Navrati Saxena., Abhishek Roy and HanSeok Kim, “Efficient 5G Small Cell Planning with eMBMS for Optimal Demand Response in Smart Grids,” IEEE Transactions on Industrial Informatics, <https://doi.org/10.1109/tii.2017.2681105>, 1551–3203 (c) 2016 IEEE.
6. Navrati Saxena, Abhishek Roy, Bharat J. R. Sahu, and HanSeok Kim, “Efficient IoT Gateway over 5G Wireless: A New Design with Prototype and Implementation Results,” IEEE Communications Magazine, February 2017, Digital Object Identifier: <https://doi.org/10.1109/mcom.2017.1600437cm>, 0163–6804/17/\$25.00 © 2017 IEEE.

Lower Facial Curves Extraction for Unconstrained Face Detection in Video

Dattatray D. Sawat and Ravindra S. Hegadi

Abstract Face recognition plays vital role in many of the biometric as well as other scientific applications. Face needs to be detected prior to recognition, and many researchers introduced methods for face detection along with unique features. These methods have been used in constrained and unconstrained environment. But it is difficult to tackle challenges such as occlusion, pose variation, illumination order to detect faces in unconstrained environment. Here in this paper, we are going to extract facial curves as features which will be further used for face detection. We have extracted lower facial features such as chin curves, lips curves, and ear curves by obtaining face contours using edge detection techniques in images and video frames from YouTube Faces Database. By matching majority of features, it is possible to detect face in unconstrained environment.

Keywords Unconstrained face · Face detection · Facial curves
Occlusion · Pose variation

1 Introduction

The human–computer intervention (HCI) is the most relevant area where face detection and recognition are being used for variety of applications. The face detection rate is very important in order to include all the faces that are needed to be recognized from target database containing images or videos. A recent survey by Zafeiriou et al. [1] shows that the frontal face recognition methods are being used in variety of applications, but to use face recognition techniques in challenging application like human surveillance or person identification these methods are not suitable. Most of the techniques fail due to unresolved multiple challenges.

D. D. Sawat · R. S. Hegadi (✉)
School of Computational Sciences, Solapur University, Solapur, India
e-mail: rshegadi@gmail.com

D. D. Sawat
e-mail: sawat.datta@gmail.com

In recent years, number of successful research attempts are made for the face detection and recognition of frontal faces in controlled environment. But in uncontrolled environment, these methods fail to detect faces because of unresolved challenges. Challenges such as occlusion might occur because of human activities or the accessories used by them. Occlusion hides vital features and facial organs such as eyes, nose, lips, ears. While performing daily tasks, people change their face pose from one to other that leads to partial visibility of face and detector fails to extract the key features. Many of the frontal face detectors are not able to deal with the pose variation. One more challenge which is frequently present in unconstrained faces is illumination variation, and it may vary within face or within the video frame. In such situation, it becomes necessary to build a face detector which will enhance the faces region without losing vital information. Extracting features is important step used in face detection or recognition. The rates of detection or recognition are directly proportional to how unique and robust features are extracted from given image or video.

1.1 Feature Invariance

1. Scale-Invariant Features

If the features are scale-variant, they need to be transformed. Lowe [2] transformed variant features into scale-invariant features. These scale-invariant features are then stored into database and compared them with features in target images using fast nearest neighbor method.

2. Rotation-Invariant Features

The image may contain object having rotation in degrees along with scale variation. In such case, the image features tend to be rotation-variant. To overcome this problem, many researchers have used Gabor filter along with shift variance property of discrete Fourier transform.

3. Illumination-Invariant Features

If the image is having illumination variation, then object in image may have different illumination values. In such cases, detector should match extracted features by transforming them into illumination-invariant features. Methods developed from image gradient are used to extract features from illumination-sensitive regions. Further, some researchers used subspace-based methods [3] and methods based on retinex theory to resolve illumination issue.

2 Related Works

The machine learning algorithm learns via the features extracted and builds a model to perform further classification. Viola and Jones [4] built most reliable face detector for frontal faces using rectangle-shaped Haar-like features in which they calculated sum of pixels present in that rectangle. Later, their work was extended by Lienhart et al. [5], Li et al. [6]. Mita et al. [7] also extended Viola and Jones's work by proposing similar features that finds similar joint Haar-like features. Some robust local features have been used for face detection like local binary pattern (LBP), scale-invariant feature transform (SIFT), histogram of oriented gradients (HOG), and speeded up robust features (SURF) which enhanced performance in terms of time. Ordinal features that show relationship between two pixels have been proposed and developed by Sinha [8], Sadr et al. [9].

For multi-view face detection, above-mentioned classifier needs to be trained for each view and that increases the size of feature database. Viola and Jones [10] trained classifier for each view. After their work some researcher's proposed complex face features but these features are slower than that of former features. Wu et al. [11], Li and Zang [12] proposed different approaches for multi-view face detection. Wu et al. proposed parallel cascade structure, whereas Zang proposed coarse-to-fine pyramid architecture.

All these methods discussed above require training for each view along with labeling, and their performance as well as detection rates varies from database to database according to challenges. In this paper, we propose an approach to extract lower facial features such as lips curves, chin curves, and ear curves by obtaining facial contours using edge detection techniques.

3 Database

For the experiment purpose, we used "YouTube Faces Database" built to study face recognition in unconstrained environment [13]. This database contains 3425 videos of 1595 people. The videos are downloaded from YouTube using top six links retrieved on search term. After download, videos were split into 24 separate frames. The YouTube Faces Database has separated frames for multiple videos of each subject. The authors [13] have added aligned images of faces in frames along with frame pose metadata and frame descriptors. Figure 1 shows sample image frames from YouTube database.



Fig. 1 Video frames **a–c** from YouTube Faces Database and **d** is video frame from random video downloaded from YouTube

4 Methodology

4.1 Color Space Transformation and Skin Segmentation

RGB, YCbCr, and Gaussian mixture model (GMM) color space models are primarily being used for the skin segmentation. RGB and GMM models have defined components. Based on skin color threshold values, the image pixels are classified into skin and non-skin pixels. The RGB color model uses three basic components in form of colors; those are Red, Green, and Blue. While segmenting pixel into skin and non-skin pixel, every component in RGB color space is checked for threshold values; hence, a region of image can be segmented from rest of regions. RGB color model consists of mixed chrominance and luminance information, and it is insensitive [14] to chrominance and luminance variation. Hence, if light condition varies, then it becomes difficult to segment the face regions, especially in videos.

To consider the illumination variation, the RGB color space is transformed nonlinearly into YCbCr color space consisting values of chrominance and luminance. The Y component represents luminance (luma) and calculated as

$$Y = K_R * R' + (1 - K_R - K_B) * G' + K_B * B' \quad (1)$$

where R , G' , and B' are linearly transferred to R , G , and B values, respectively. Cb is calculated as difference between two components, i.e., luma and Blue

$$Cb = Y_{ij} - B(x_{ij}, y_{ij}) \quad (2)$$

Cr is calculated as difference between luma and Red

$$Cr = Y_{ij} - R(x_{ij}, y_{ij}) \quad (3)$$

The RGB color space can be transformed into YCbCr using ITU 601 (SD) and 709–11/60 (NTSC) Standard Conversion Coefficients Matrix as follows:

$$\begin{bmatrix} Y \\ Cb \\ Cr \end{bmatrix} = \begin{bmatrix} 0 \\ 128 \\ 128 \end{bmatrix} \cdot \begin{bmatrix} 0.229 & 0.587 & 0.114 \\ -0.169 & -0.331 & 0.500 \\ 0.500 & -0.419 & -0.081 \end{bmatrix} \cdot \begin{bmatrix} R \\ G \\ B \end{bmatrix} \quad (4)$$

The YCbCr values ranges $[0.0 \ 255.0]$ $[-128 \ 127]$ $[-128 \ 127]$ respectively. Y, Cb, Cr values may be calculated in full range using Eq. (4) as follows:

$$Y_{ij} = (0.299 * R(x_{ij}, y_{ij})) + (0.587 * G(x_{ij}, y_{ij})) + (0.114 * B(x_{ij}, y_{ij})) \quad (5)$$

$$Cb_{ij} = (0.169 * R(x_{ij}, y_{ij})) - (0.331 * G(x_{ij}, y_{ij})) + (0.500 * B(x_{ij}, y_{ij})) + 128 \quad (6)$$

$$Cr_{ij} = (0.439 * R(x_{ij}, y_{ij})) - (0.368 * G(x_{ij}, y_{ij})) - (0.071 * B(x_{ij}, y_{ij})) + 128 \quad (7)$$

4.2 Threshold and Pixel Classification

We classified pixels using threshold values [15] for each component of YCbCr by the following equation:

$$s(x_{ij}, y_{ij}) = \begin{cases} 1, \forall (Cr_{ij} \geq tCr_l, Cr_{ij} \leq tCr_u, Cb_{ij} \geq tCb_l, Cb_{ij} \leq tCb_u, H_{ij} \leq tH_l, H_{ij} \geq tH_u) \\ 0, \text{otherwise} \end{cases} \quad (8)$$

where lower and upper threshold values for skin pixel in Cr component are $tCr_l = 140$, $tCr_u = 165$, for skin pixel in Cb component are $tCb_l = 140$, $tCb_u = 195$, and for skin pixel in Cr component are $tH_l = 0.01$, $tH_u = 0.1$, respectively. Figure 2 shows images after skin segmentation.

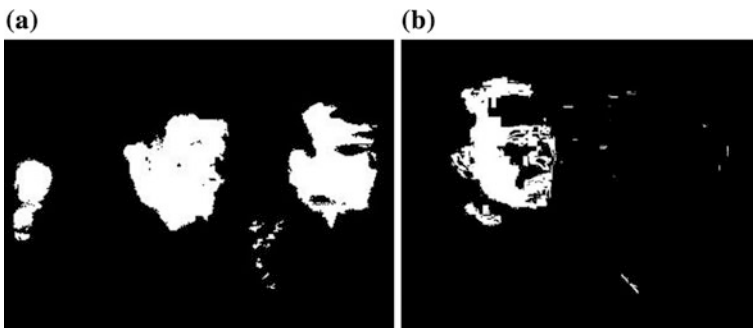


Fig. 2 a Segmented regions of Fig. 1a, b segmented regions of Fig. 1d

4.3 Closing Operation on Segmented Regions

Because of illumination variation over images, some of the segmented regions may have patches of non-skin pixels. To counter the effect of non-skin patches in segmented region and to obtain coordinates of possible face region, we performed closing operation by using structuring element with eight connected neighbors as follows. Figure 3 shows images after closing operation.

4.4 Removing Distant/Non-possible Face Regions

Once skin segmented regions are obtained, next step is to decide whether the regions are distant or non-possible face regions. We used image resolution and aspect ratio to decide whether the segmented region is distant or non-possible face region by calculating possible face area δ and compared it with area of each segmented region in image as follows:

$$\alpha = \text{size}(x) \quad (9)$$

$$\beta = \text{size}(y) \quad (10)$$

$$\delta = \begin{cases} C1, \forall (\alpha/120 == (\frac{r1}{r2}), \beta/120 == (\frac{r1}{r2})) \\ C2, \text{ otherwise} \end{cases} \quad (11)$$

Since video frames in given database are available in aspect ratio 4:3, we have used r1:r2 as aspect ratio in above equation, where α and β are number of row and column pixels in image/frame, respectively. δ is possible face area calculated by multiplying row size with constants $c1$ and $c2$, where $c1$ and $c2$ are calculated as $\alpha*4$ and $\alpha*3$, respectively, if $\alpha/120$ and $\beta/120$ have ratio $r1:r2$. By comparing segmented region size and distant/non-possible face region decision threshold

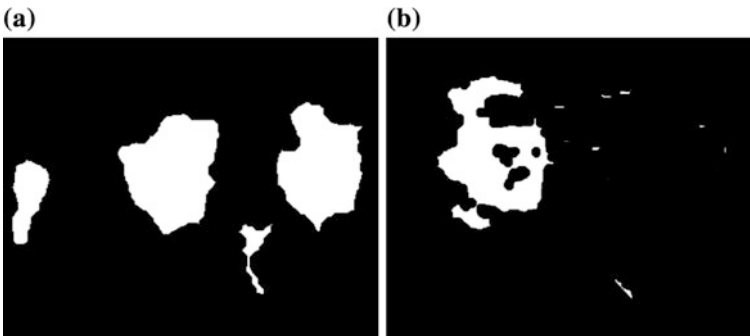


Fig. 3 Results of closing operation, a over Fig. 2a, b over Fig. 2b

$$f_p = \begin{cases} \text{no}, A_{sr} < \delta \\ \text{yes}, A_{sr} \geq \delta \end{cases} \tag{12}$$

where A_{sr} is the area of segmented region in image. Using the maximums of region coordinates, we obtained subimage from original image as shown in Fig. 4. If value of f_p is yes, then segmented region is forwarded for further processing to extract features (Fig. 5).

This step reduces the number of regions to very few, which in turn reduces total processing required for per frame as well as for video. Figs. 6 and 7 show the possible face/non-face/distant face region area against different number of regions segmented from image frames.

Fig. 4 Possible face region of Fig. 3a, b obtained by region maximums and converted to gray scale

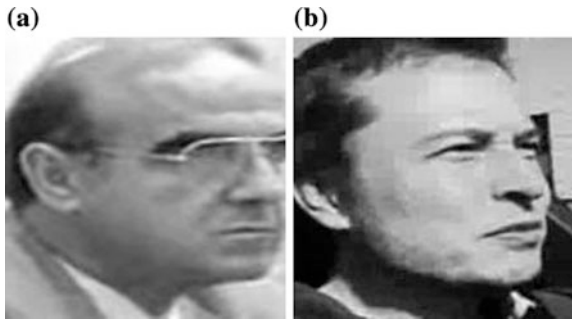
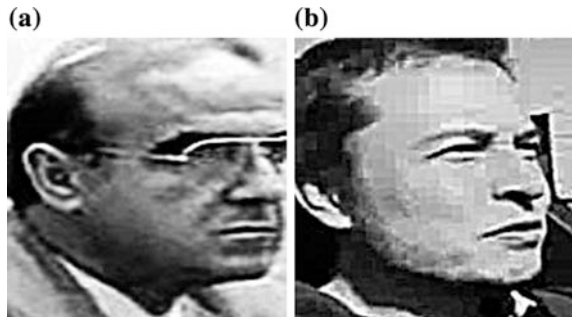


Fig. 5 a and b enhanced possible face region of Fig. 4a, b using unsharp masking



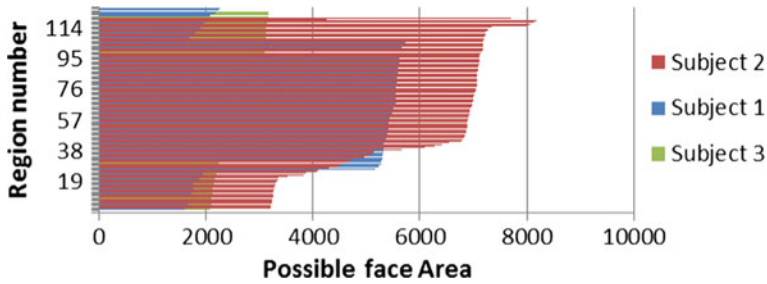


Fig. 6 Region number and area of particular region calculated for possible face area with aspect ratio 4:3

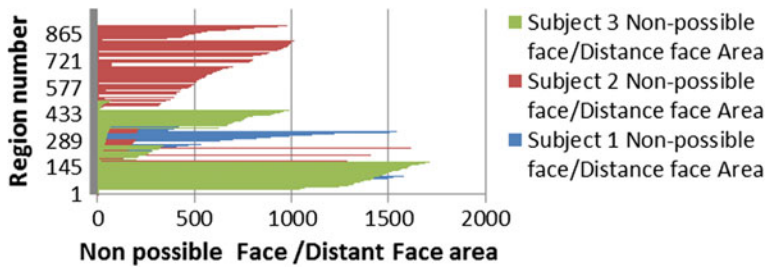


Fig. 7 Region number and area of particular region calculated for non-possible/distant face area with aspect ratio 4:3

4.5 Enhancement

The original image resized to 160×160 pixel is then enhanced by using uncap masking filter, and the operation can be defined as follows.

The blurred version of original image $f(x, y)$ can be obtained as

$$f_{sh}(x, y) = 1/2\pi\sigma^2 e^{-x^2 + y^2/2\sigma^2} \tag{13}$$

Enhanced image is obtained by subtracting blurred image from original image as

$$g(x, y) = f(x, y) - f_{sh}(x, y) \tag{14}$$

This produces image with sharp edges at the object boundaries by passing high-frequency components using above equation.

4.6 Extract Lower Facial Curves

Since our focus is for lower facial features such as lips, chin, and ears, we minimized our feature vector to lower face as shown Fig. 8. In this step, we have obtained lower facial edges by using canny edge detector along with Gabor filter and contrast enhancement. The Gabor filter considers the orientation, phase, bandwidth wavelength, etc., of frequency components. We operated Gabor filter on sharpened image with canny edge detector and Laplace of Gaussian.

The isolated points and segments of fragmented edges having pixels less than that of prime features like lips, chin, and ear curves were removed using morphological opening. That produced the resultant feature matrix containing lower facial curves like lips curve, chin curves, and ear curves as shown in Figs. 8 and 9.

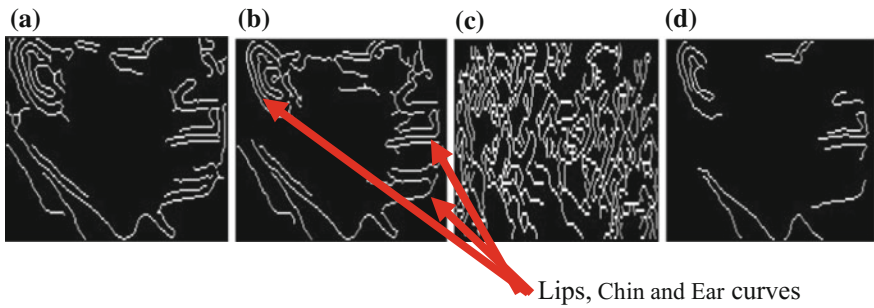


Fig. 8 Extracted lower facial curves of images from Fig. 5a. a Canny edge, b histogram equalization with canny edge, c Gabor filter with canny edge, d Laplace of Gaussian

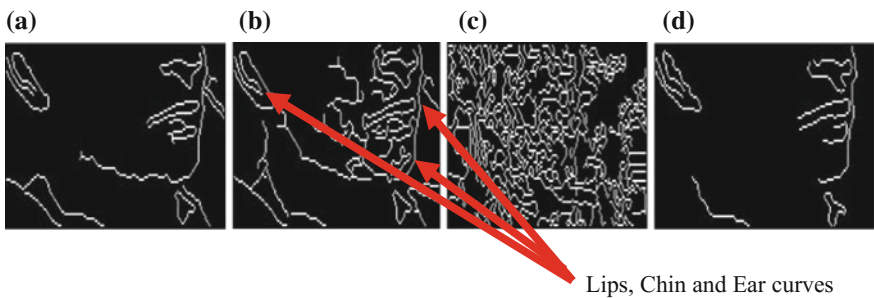


Fig. 9 Extracted lower facial curves of images from Fig. 5b. a Canny edge, b histogram equalization with canny edge, c Gabor filter with canny edge, d Laplace of Gaussian

Figure 9c shows that Gabor filter adds too much detail which would require extra processing to remove them. It is also clear that histogram equalization helps to obtain edges of toned area in region along with edge areas having sharp changes. In this experiment, we showed that a canny edge detector with simple image sharpening can give clear non-segmented edges. These lower facial curves obtained by taking skeleton of edges extracted in this section can be used as features for multi-view face detection in unconstrained images/video.

Figure 10 shows the images obtained form YouTube Faces Database having challenges like occlusion, illumination, pose variation, and unconstrained background. Figure 11 shows the extracted curves from Fig. 10.



Fig. 10 Images Fig. 10a–d from YouTube Faces Database having occlusion, illumination, pose variation, and unconstrained background

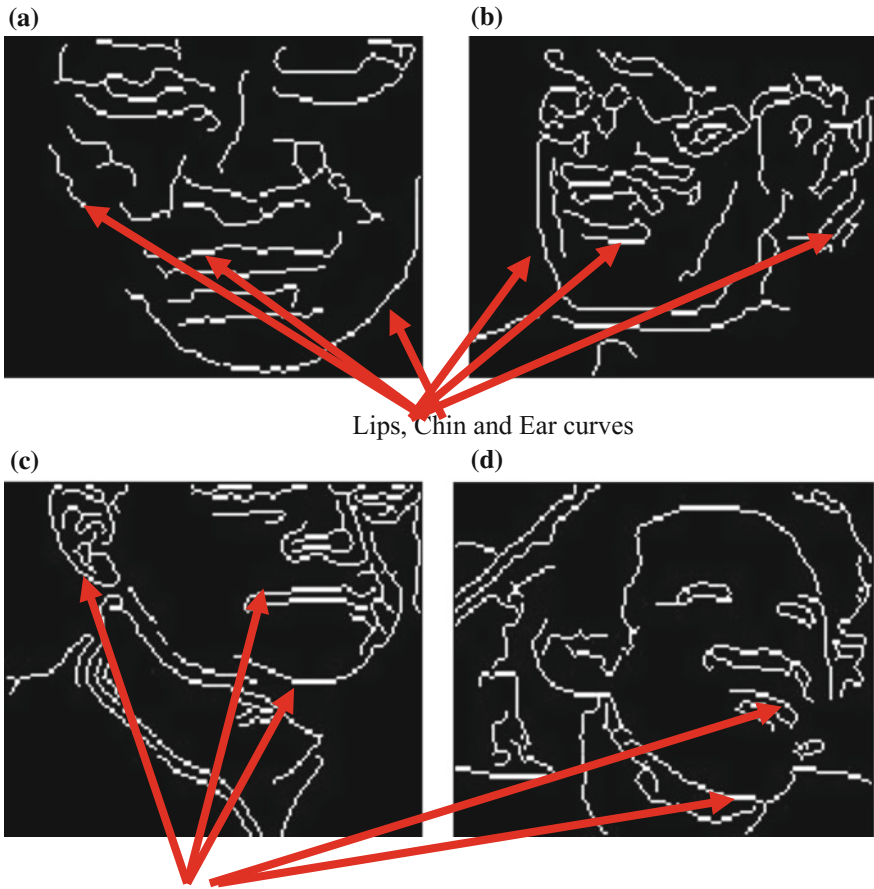


Fig. 11 Extracted lips, chin, and ear curves from Fig. 10a–d, respectively

5 Summary and Future Work

In this paper, we extracted lower facial features like lips, chin, and ear curves which can be used to detect unconstrained faces in the images or video. We performed this experiment on 500 random images/videos from database having unconstrained faces and extracted skin regions and then obtained features present in the possible face regions. We performed this experiment on random videos as well and verified the extracted features. For the samples from African region, the performance was poor as compared to rest of the regions.

In future, we look forward to employ the curve matching methods to classify the extracted features in the proposed method.

References

1. Zafeiriou S., Zhang C., and Zhang Z.: Survey on Face Detection in the wild: past, present and future. *Computer Vision and Image Understanding*, vol. 138, pp. 1–24, (2015).
2. Lowe D.: Distinctive image features from scale-invariant key points. *International journal of computer vision*, vol. 60, no. 2, pp. 91–110, (2004).
3. Viberg M.: Subspace-based methods for the identification of linear time-invariant systems. *Automatica*, vol. 31, no. 12, pp. 1835–1851, (1995).
4. Viola P., and Jones M., Rapid object detection using a boosted cascade of simple features. *IEEE Computer Society Conference on Computer Vision and Pattern Recognition*, vol. 1, pp. 511–518, (2001).
5. Lienhart R., and Maydt J.: An extended set of Haar-like features for rapid object detection. *Proceedings of the IEEE International Conference on Image Processing*, vol. 1, pp. 900–903, (2002).
6. Li S., Zhu L., Zhang Z., Blake A., Zhang H., and Shum H.: Statistical learning of multi-view face detection. *Proceedings of the 7th European Conference on Computer Vision*, vol. 2353, pp. 67–81, (2002).
7. Mita T., Kaneko T., and Hori v.: Joint Haar-like features for face detection. *Proceedings of the 10th IEEE International Conference on Computer Vision*, vol. 2, pp. 1619–1626, (2005).
8. Sinha P.: Qualitative representations for recognition. *Biologically Motivated Computer Vision Workshop*, vol. 2525, pp. 249–262, (2002).
9. Sadr J., Mukherjee S., Thoresz K., and Sinha P.: The fidelity of local ordinal encoding. *Proceedings of the Annual Conference on Neural Information Processing Systems*, vol. 1, pp. 1279–1286, (2001).
10. Jones M., and Viola P.: Fast multi-view face detection. *Mitsubishi Electric Research Lab*, TR-2003-96, (2003).
11. Wu B., Ai H., Huang C., and Lao S.: Fast rotation invariant multi-view face detection based on real AdaBoost. *Proceeding on sixth IEEE international conference on Automatic Face and Gesture Recognition*, vol. 1, pp. 79–84, (2004).
12. Li S. and Zhang Z.: Float boost learning and statistical face detection. *IEEE Transactions on Pattern Analysis and Machine Intelligence*, vol. 26, no. 9, pp. 1112–1123, (2004).
13. Wolf L., Hassner T., and Maoz I.: Face recognition in unconstrained videos with matched background similarity. *IEEE Conference on Computer Vision and Pattern Recognition*, pp. 529–534, (2011).
14. Hasan M., and Mishra P.: Superior Skin Color Model using Multiple of Gaussian Mixture Model. *British Journal of Science*, Vol. 6, no. 1, (2012).
15. Surampalli G., Dayanand J., and Dhananjay M.: An Analysis of Skin Pixel Detection using Different Skin Color Extraction Techniques. *International Journal of Computer Applications*, vol. 54, no. 17, (2012).

Digital Beamforming Techniques— A Comparison

Geheshwar Sharma Ramchurn, Sanya Dhoundiyal,
Arun Kumar Singh and Bansibadan Maji

Abstract This paper emphasizes on the beamforming techniques used in today's systems. Multiple beamforming techniques such as the Minimum Variance Distortionless Response (MVDR) and Linear Constraint Minimum Variance (LCMV), to name a few, are used to improve the capacity and data rates of various systems such as cellular system. Both mentioned techniques are based on the received weight vector of the desired signal. This paper presents the mathematical difference as well as the power difference between LCMV and MVDR beamforming techniques.

Keywords Beamforming · Digital beamforming · LCMV · MVDR
Optimum beamformer

1 Introduction

Beamforming is a signal processing technique used in sensor arrays to transmit or receive signals from defined directions. Beamforming has been studied in various areas such as radar, sonar, seismology, and wireless communications. Adopted by the audio research society for extraction of speech from a noisy environment, beamforming approaches the problem from a spatial point of view. Normally, microphone arrays are used to provide the capability of spatial filtering. These systems are designed such that they receive spatially propagating signals. At the same time, they receive many unwanted (interfering) signals. However, if the desired and interfering frequencies possess same temporal frequencies, then extraction of desired signals will not be achieved using temporal filtering. In this case, the spatial separation can be achieved using spatial filter at the receiver.

G. S. Ramchurn (✉) · S. Dhoundiyal · B. Maji
National Institute of Technology, Durgapur, West Bengal, India
e-mail: anish.2709@hotmail.com

A. K. Singh
Sikkim Manipal Institute of Technology, Majitar, Rangpo, India

Hence, the signal originating from a specific direction is extracted from all interfering signals.

With smart vehicles on the rise, beamforming is rapidly becoming a far cheaper, simpler, and more sufficient alternative to smart antennas. Beamforming can be further divided on the basis of signal processing—into analog or digital—for on the basis of the weights chosen—data independent or statistically optimum.

Analog and digital beamformings are both appropriate in different situations. However, the analog method of beamforming comes with a few problems, some of which include: the cost and its sensitivity to drifts [1]. Digital beamforming is a much more modern technology and one of the major advantages that comes with it is the fact that digital beamforming opens up the way for a multitude of digital signal processing techniques to be applied to the digital signal the antenna's data is converted to.

1.1 Types of Beamformers

Beamformers can be divided into different types, as discussed previously, on different bases.

Data-independent beamformer is designed such that a desired response is approximated independent of the array data or the data statistics.

Statistically optimum beamformer is designed such that the weights of it are chosen according to data statistics that are received at the array. It is optimized such that the output has minimal noise and interference.

Adaptive beamformer discovers the weights required for an optimum beamformer with the assumption of ergodicity of the available data. Since statistics have the potential of changing over time, the weights are determined by the use of algorithms which adapt over time.

Partially adaptive beamformer which depends vastly on the degree of freedom—i.e., the number of constrained and unconstrained weights—is implemented. As a partially adaptive beamformer has a number of constrained weights, the complexity of the system is reduced and the cost of the performance is increased as there is a reduction in freedom.

Two of the main techniques of adaptive beamforming that we have reviewed and discussed are shown below.

Linearly Constrained Minimum Variance (LCMV)

The LCMV beamformer is an adaptive beamformer that works by constraining the response of the beamformer. This assures that signals incoming from the direction of interest are passed through with a specific gain and phase. The chosen weights are picked such that the output variance is the least. This ensures that the signal has minimum interference and noise from signals coming from other directions while keeping the desired signal intact. In LCMV, there is, however, less interference

rejection than other techniques, but there is no distortion of the desired signal, unlike other methods. There is also high complexity and it can be realized as an MVDR beamformer easily [2]. It depends on weight determination and is suitable for an urban environment as it removes the multipath effect [3]. The determination of outage probability is possible. The outage performance of the wireless system with LCMV beamforming cancels a number of dominant interferers and numerical results show that the outage probability of LCMV beamforming is very sensitive to the directions of the dominant interferers [4].

Minimum Variance Distortionless Response (MVDR)

The MVDR beamformer is another type of adaptive beamformer. When a beamformer has a constant response in the direction of the useful signal, the LCMV algorithm turns into the MVDR algorithm. To reduce interference, iterative null steering has been proposed [5]. It depends on weight determination and is not suitable for an urban environment as it cannot remove the multipath effect. The output metric is power level and a study shows that it has a better response than LCMV [4].

2 Literature Review

In instances where the desired and interfering frequencies possess same temporal frequencies, then extraction of desired signals is not achieved using temporal filtering. In this case, the spatial separation is achieved using spatial filter at the receiver. The spatial filtering has two main advantages. To begin with, differentiating between signals on the spatial point of view depends on the spatial aperture. As aperture size increases, the discrimination of the signals improves. It is not the absolute aperture size that holds importance, rather its size in wavelengths is critical. Usually for high-frequency signals, a single physical antenna is enough to perform the required discrimination, since the wavelength is short. However, for low-frequency signals, the array of sensors can replace a much larger spatial aperture than that practical with a large antenna. Another notable benefit of using sensor arrays, relevant at any wavelengths, is the adaptability of spatial filtering, that discrete sampling offers. In real time, it is essential to change the spatial filtering function so that interfering signals are suppressed. This change is easily done in a discretely sampled system by altering the way in which the beamformer linearly combines sensor data. Clearly, changing the spatial filtering function of a continuous aperture antenna is not practical [6].

Moreover, beamforming techniques have been implemented in defense research. The Active Electronically Scanned Array (AESA) has been likely the best solution proposed in various department of defense. AESA can be realized using either analog beam steering or digital beam steering. When using analog beamforming, beam steering is achieved using individual transmitter–receiver modules equipped with phase shifters. This type of radar has the advantage that it possesses no moving parts which makes it more reliable than prior generations of radars that used

mechanical steering to search and track targets. Moreover, this type of radar permits tracking of multiple targets by the use of complex beamforming. However, the analog AESA has a limitation on the number of targets it can track at a time. Digital beamforming brings with it the advantage that a higher number of targets can be tracked using the AESA as compared to the analog. In this one, phase shifters are not used at each element in the phased array. Instead, the radar beam is steered digitally since digital functions are pushed forward into the system. The digital sampling takes place at the antenna element on both transmitter and receiver [7].

Furthermore, beamforming in smart antenna has been viewed as a favorable technology which enhances the capacity of users in 3G Wireless Networks, as it diminishes co-channel interference. Smart antenna increases the efficiency of digital wireless communication systems. It operates using the benefit of the diversity effect at the transceiver of the wireless system. The term diversity effect refers to the transmission and reception of multiple radio frequencies which are used to reduce errors during data communication and also to ameliorate data speed between the source and the destination. The special antenna arrays are used with signal processing algorithms to easily locate various wireless targets. They are also used to calculate the beamforming vectors and the direction of arrival [DOA] of the signal. The smart antenna technology has been applied to mobile communication systems such as GSM, CDMA, 3G, and IMT 2000, and they have produced multiple advantages. Smart antennas have provided higher network capacity, thereby increasing the revenues of network operators. Usage of smart antennas has resulted in a decreased probability of blocked or dropped calls to customers. Basically, weight adaptation is the “smart” part of the smart antenna. Every element of the antenna array has to be weighted so as to adapt to the current channel and user characteristics. The smart or adaptive arrays use advanced signal processing algorithms to continually identify the desired signals among interfering signals and also calculate their directions of arrival [3].

With the evolution of technology being as rapid as it is, the demand for higher data rates and an increase in capacity has also increased. With it, a new technology has evolved known as Long-Term Evolution or LTE and the Long-Term Evolution Advanced or LTE-A. One of the technologies used recently to improve capacity and coverage is the use of femtocells—cells that place receivers and transmitters closely together with an even spacing between them—in the vicinity of large cells. This results in increased capacity due to reused frequency and spectrum sharing. However, this results in dense networks and since femtocells share the same spectrum as large cells, there are interference issues which occur. As a solution to the problem, beamforming has been suggested [8]. 3D beamforming can be used for LTE-A, which allows the beam to be steered in both azimuth and elevation planes [9]. Other than that there are different methods of beamforming that have been suggested which include LCMV, MVDR, zero-forcing beamforming, and robust beamforming. All are variations of adaptive beamforming which is becoming more popular. There are a few challenges with LTE due to the fact that interference is a common problem; however, beamforming addresses it properly and offers a multitude of solutions that can be looked into.

3 Mathematical Difference Between LCMV and MVDR

We can show the mathematical difference between the LCMV and the MVDR beamformers below.

It is assumed that beamformer responses to a source at angle θ and with a temporal frequency of ω is given by $\omega^H d(\theta, \omega)$. Now, if we linearly constrain the weights such that they satisfy

$$\omega^H d(\theta, \omega) = g, \quad (1)$$

where g is a complex constant, then we can ensure that any signal from angle θ and frequency ω will be passed to the output with a response of g . If the LCMV problem of choosing weights is written as

$$\min_w \mathbf{w}^H \mathbf{R}_x \mathbf{w} \text{ subject to } \mathbf{d}^H(\theta, \omega) \mathbf{w} = g^* \quad (2)$$

Using the method of LaGrange multipliers, we can then write,

$$\mathbf{F}(\omega, \lambda) = \mathbf{w}^H \mathbf{R}_x \mathbf{w} \quad (3)$$

$$\mathbf{G}(\omega, \lambda) = \mathbf{d}^H \mathbf{w} - g^* \quad (4)$$

since we are given

$$\mathbf{d}^H(\theta, \omega) \mathbf{w} = g^* \quad (5)$$

For the ease of writing,

$$\mathbf{d}^H(\theta, \omega) = \mathbf{d}^H \quad (6)$$

Then,

$$L(\omega, \lambda) = \frac{1}{2} \mathbf{w}^H \mathbf{R}_x \mathbf{w} + \lambda^H (\mathbf{d}^H \mathbf{w} - g^*) \quad (7)$$

where λ^H is the Lagrangian Multiplier.

Now, we set the gradient to 0 and, as

$$\mathbf{G}(\omega, \lambda) = 0. \quad (8)$$

So,

$$\frac{\delta L(\omega, \lambda)}{\delta \mathbf{w}} = \mathbf{w}^H \mathbf{R}_x + \lambda^H \mathbf{d} \quad (9)$$

Now, if we assume that \mathbf{R}_x is in non-singular form, then we can write

$$0 = \mathbf{w}^H \mathbf{R}_x + \lambda^H \mathbf{d} \quad (10)$$

$$\mathbf{w}^H \mathbf{R}_x = -\lambda^H \mathbf{d} \quad (11)$$

$$\mathbf{w}_{opt}^H = -\lambda^H \mathbf{d} \mathbf{R}_x^{-1} \quad (12)$$

Previously, we were also given that $\mathbf{d}^H \mathbf{w} = g^*$

If we transpose and multiply the value of \mathbf{w}_{opt}^H with \mathbf{d}^H , we can get

$$\mathbf{d}^H (-\lambda \mathbf{d} \mathbf{R}_x^{-T}) = g^* \quad (13)$$

$$\mathbf{d}^H \lambda \mathbf{d} \mathbf{R}_x^{-T} = -g^* \quad (14)$$

Then, this gives us,

$$\lambda = -g^* (\mathbf{d}^{-1} \mathbf{d}^{-H} \mathbf{R}_x) \quad (15)$$

Substituting this value of the LaGrangian multiplier back into the equation for \mathbf{w}_{opt}^H , we can write,

$$\mathbf{w}_{opt}^H = -[-g^* (\mathbf{d}^{-1} \mathbf{d}^{-H} \mathbf{R}_x)] \mathbf{d} \mathbf{R}_x^{-1} \quad (16)$$

which can be further written as,

$$\mathbf{w}_{opt}^H = g^* \frac{\mathbf{d}(\theta, \omega) \mathbf{R}_x}{\mathbf{d}(\theta, \omega) \mathbf{R}_x \mathbf{d}^H(\theta, \omega)} \quad (17)$$

The above weights are the weights calculated for an LCMV beamformer. The weights of an MVDR beamformer are similar to those given above, with the only difference being that the value of $g = 1$. That is, the gain constant is unity. This kind of beamformer maximizes the likelihood function of the input signal.

4 Simulation Description

A sine wave is generated in the range of $0-4\pi$. A uniform linear array is created having two sensor elements spaced by 5 m. Random noise is generated taking into consideration the size of the incoming sine wave and the noise is added to the sine wave. The angle through which the signal is incident on the sensors is set to 45° in azimuth and 0° in elevation. Afterward, a Linear Constraint Minimum Variance (LCMV) beamformer is simulated so that the object performs a narrowband LCMV

beamforming on the received signal. Two graphs are then plotted so as to differentiate between the original signal and the beamformed. Also, the response pattern is plotted. At the angle of incidence, a normalized power of -16.55 dB is observed. The graphs below illustrate the results of the simulation (Figs. 1 and 2).

[In the simulation, the signal propagating speed is set to the speed of light (3×10^8 m/s), and the carrier frequency of the signal is set to 3×10^8 Hz.]

In order to compare the LCMV beamformer to the Minimum Variance Distortionless Response (MVDR) beamformer, another simulation has been done

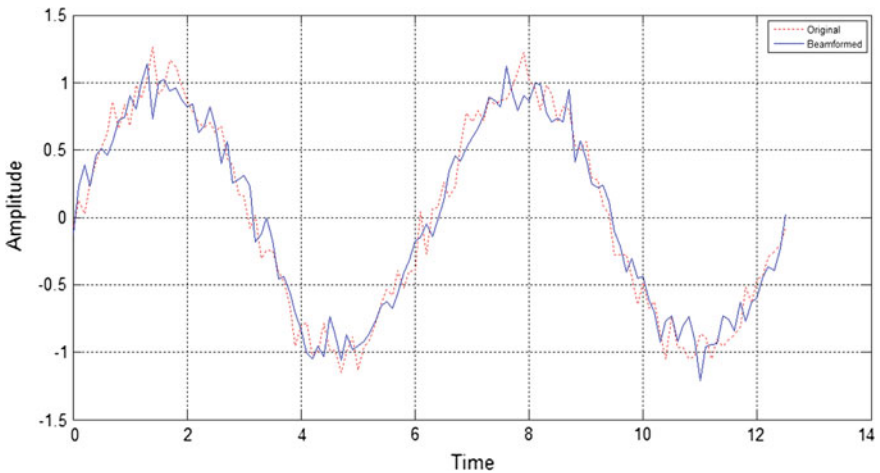


Fig. 1 Original and beamformed signal (LCMV beamformer)

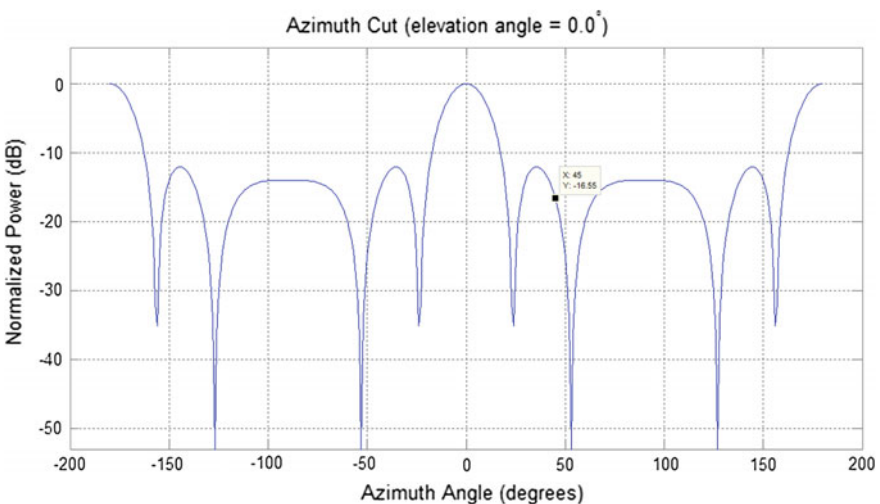


Fig. 2 Angle of arrival of incident signal (LCMV beamformer)

using the same parameters as stated earlier and applied to an MVDR beamformer. Likewise, there are two sensor elements separated by 5 m distance and the signals are incident at an azimuthal angle of 45° and 0° elevation. A MVDR beamformer is then simulated so that beamforming is performed on the incident signal. Also, the weights used in the beamformer are obtained. The difference between the original signal and the beamformed and a response pattern are plotted (Figs. 3 and 4).

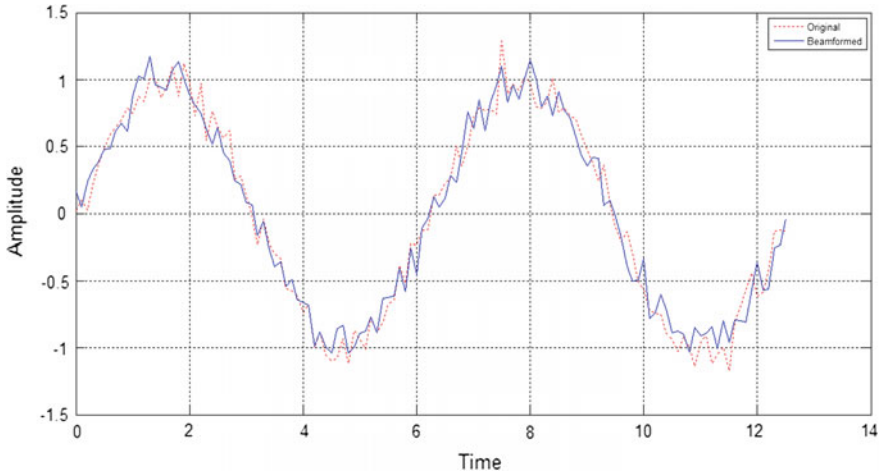


Fig. 3 Original and beamformed signal (MVDR beamformer)

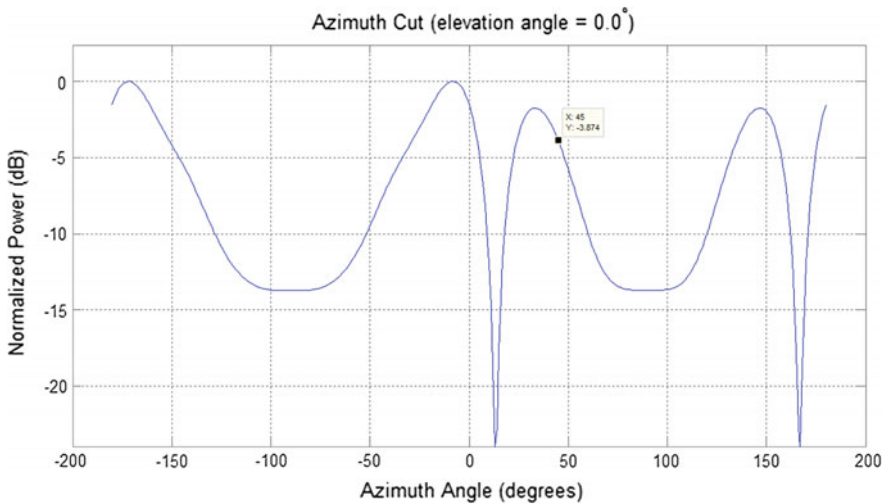


Fig. 4 Angle of arrival of incident signal (MVDR beamformer)

From the graphs obtained, it is observed that a normalized power of -3.874 dB is observed at the specified angle of incidence.

5 Conclusion

It has been seen how beamforming techniques have acquired importance in wireless mobile communication systems due to their ability to reduce co-channel and adjacent channel interferences. It has also been seen how the two techniques Linear Constraint Minimum Variance (LCMV) and Minimum Variance Distortionless Response (MVDR) depend on the received weight vector of the desired signal. In terms of power, it has been observed that with MVDR, there is better response than that of LCMV. One of the major challenges that are faced by beamforming is that while it is easy to implement in the case of singular interference sources, the complexity increases as the number of sources also increases, which is to be expected. However, MVDR beamforming technique takes care of this issue. The further work which can be carried out using these beamforming techniques is that they can be set in such a way so that focus is made directly to targets.

References

1. Cattani, A., Perini, F., Ghelfi, F., Maccaferri, A., Montebugnoli, S., Bianchi, G., Some Notes on Beamforming, <https://www.ira.inaf.it/Library/rapp-int-2004/353-04.pdf>.
2. Herbordt, W., 2005. *Sound capture for human/machine interfaces practical aspects of microphone array signal processing*, Berlin: Springer.
3. S.S. Balasem., S.K. Tiong, S. P. Koh —Beamforming Algorithms Technique by Using MVDR and LCMV World Applied Programming, Special section for proceeding of International E-Conference on Information Technology and Applications (IECITA) 2012, vol. 2, issue-5, pp. 315–324, May 2012.
4. Balasem. S.S, T. S Kiong, J. K. S Paw, G. C Hock, —Artificial Immune System Assisted Minimum Variance Distortionless Response Beamforming Technique for Adaptive Antenna System ICTC, IEEE, pp. 938–943, 2013.
5. M. Emadi, K. H. Sadeghi et al., —Co Channel Interference Cancellation by the Use of Iterative Digital Beamforming Method, Progress In Electromagnetics Research, PIER-87, pp. 89–103, 2008.
6. Barry Van Veen and Kevin M. Buckley, “Beamforming: a versatile approach to spatial filtering” IEEE Signal Processing Magazine, vol. 5, pp. 4–24, 1988.
7. Microwave Products and Technology, “Analog Versus Digital Beamforming” White Paper.
8. Chakraborty, N., Misra, A. and Sarma, K.K., 2016. Transmit Beamforming in Dense Networks-A Review. *ADBU Journal of Engineering Technology*, 4.
9. Bartoli, G., Fantacci, R., Letaief, K., Marabissi, D., Privitera, N., Pucci, M. and Zhang, J., 2014. Beamforming for small cell deployment in LTE-advanced and beyond. *IEEE Wireless Communications*, 21(2), pp. 50–56.

Realization of Fractional-Order Operator in Complex Domains—A Comparative Study

Jaydeep Swarnakar, Prasanta Sarkar
and Lairenlakpam Joyprakash Singh

Abstract The emphasis on studying fractional-order controller has gradually been increasing in the area of control theory. The elementary component of a fractional-order controller is the fractional-order operator s^β ($0 < \beta < 1$), which can either be a fractional differentiator or be a fractional integrator. The discretization of s^β is central for digital realization of the fractional-order controller. In this paper, a half-order fractional differentiator is approximated to a rational transfer function by using Oustaloup approximation. The approximated continuous-time transfer function is then discretized to obtain the corresponding transfer functions in the complex z -domain and complex delta-domain. Finally, the frequency responses obtained from two discretized transfer functions of two different complex domains are compared for simulation studies with the help of MATLAB software.

Keywords Fractional-order operator · Rational approximation of fractional-order operator · Discretization of fractional-order operator · Bilinear transformation δ -operator · Delta-domain

J. Swarnakar (✉) · L. J. Singh

Department of Electronics and Communication Engineering, School of Technology,
North Eastern Hill University, Shillong 793022, Meghalaya, India
e-mail: jaydeepswarnakar@gmail.com

L. J. Singh

e-mail: jplairen@gmail.com

P. Sarkar

Department of Electrical Engineering, National Institute of Technical Teachers'
Training and Research, Kolkata 700106, West Bengal, India
e-mail: psarkar@nittrkol.ac.in

© Springer Nature Singapore Pte Ltd. 2018

R. Bera et al. (eds.), *Advances in Communication, Devices and Networking*,
Lecture Notes in Electrical Engineering 462,
https://doi.org/10.1007/978-981-10-7901-6_77

1 Introduction

The fractional calculus is over 300-year-old theme. The first reference of fractional calculus is probably being connected by correspondence between Leibniz and L'Hospital in 1695 [1]. The theoretical development of the fractional-order derivative mostly occurred in the nineteenth century. However, application of fractional-order calculus in control theory seems to be a contemporary area of research. For pioneering works, we cite from [2–4]. The fractional-order systems are infinite-dimensional filter, i.e. contain unlimited memory, while the integer-order systems are finite-dimensional, i.e. with limited memory. So, for practical application of the fractional-order systems, it is necessary to describe the fractional-order models in terms of approximate integer-order models. To accomplish this task, rational approximations [5] are often used mainly in the continuous time domain.

In principle, the control systems can incorporate both the fractional-order plant to be controlled and the fractional-order controller (FOC). As the plant models already exist in the form of integer model in the classical sense, therefore, application of the fractional-order controller is more common in control practice. There are many fractional-order controllers found in the literature such as CRONE controller [6], TID controller [7] and $PI^\lambda D^\mu$ controller [8]. In all types of fractional-order controllers, the basic ingredient is common, i.e. fractional-order operator s^β ($0 < \beta < 1$), which can either be a fractional differentiator or be a fractional integrator depending on positive and negative values of β respectively. Discretization of s^β is essential for the digital realization of the FOC. There are two techniques for discretization in general—indirect technique and direct technique. Existing direct discretization methods include the application of the direct power series expansion (PSE) of the Euler operator [9] or the continued fraction expansion (CFE) of the Tustin or Al-Alaoui operator [10, 11]. The indirect discretization technique is performed in two steps. In the preliminary step, rational approximation of fractional-order operator is obtained in s -domain by limiting its order and then it is discretized [12–14].

The conventional modelling of discrete-time signal and systems is generally based on the forward shift operator q and associated discrete frequency variable z . However, a major development in linear system theory was brought in with the introduction of delta-operator by Richard Middleton and Graham Goodwin [15]. Contrary to common expectations, the traditional shift operator-based modelling does not converge to their continuous-time counterparts at a high sampling frequency. For this reason, a great deal of attention has been given to the alternative modelling which is based on δ -operator and associated discrete frequency variable γ . The δ -operator-based modelling is obtained by signal differencing rather than signal shifting and also converges to its continuous-time counterparts at a high sampling frequency.

In this paper, the continuous-time fractional-order operator has been discretized in complex z -domain and complex delta-domain. After that, a comparative study is

presented on the basis of frequency responses obtained from simulation results. The paper is organized as follows: Sect. 1 gives the introduction. Section 2 describes the indirect discretization of fractional-order operator s^β . Section 3 deals with the MATLAB simulation and analysis of results. Finally, conclusions are drawn in Sect. 4.

2 Indirect Discretization of Fractional-Order Operator (s^β)

Rational approximation of s^β is considered to be the first step for the indirect discretization. In our work, Oustaloup approximation technique has been used. The formula for P th-order Oustaloup approximation within a frequency range (ω_x, ω_y) can be obtained as

$$s^\beta \approx K \prod_{m=1}^P \frac{s + \omega'_m}{s + \omega_m} \tag{1}$$

where

$$\omega'_m = \omega_x \omega_a^{(2m-1-\beta)/P}, \omega_m = \omega_x \omega_a^{(2m-1+\beta)/P}, K = \omega_y^\beta \text{ and } \omega_a = \sqrt{\omega_y/\omega_x}.$$

From Eq. (1), fifth-order rational approximation of $s^{0.5}$ is obtained within the frequency range 0.01–100 rad/s. The approximated continuous-time transfer function $H(s)$ is given as follows:

$$s^{0.5} \approx H(s) = \frac{10s^5 + 298.5s^4 + 1218s^3 + 768.5s^2 + 74.97s + 1}{s^5 + 74.97s^4 + 768.5s^3 + 1218s^2 + 298.5 + 10} \tag{2}$$

Now, $H(s)$ is discretized by using two methods. The first method employs bilinear transform to obtain the discretized transfer function $H_b(z)$ in the complex z -domain, whereas the second method uses delta-transform to obtain the discretized transfer function $H_\delta(\gamma)$ in the complex δ -domain.

The bilinear transform is given as follows:

$$s = \frac{2z - 1}{Tz + 1} \tag{3}$$

The δ -operator is defined in the time domain as

$$\delta = \frac{q - 1}{T} \tag{4}$$

Table 1 Discrete-time approximation of $s^{0.5}$ in z -domain for different values of sampling periods

Sampling period (s)	$H_b(z)$
$T = 0.01$	$\frac{8.265z^5 - 39.1z^4 + 73.82z^3 - 69.54z^2 + 32.67z - 6.124}{z^5 - 4.407z^4 + 7.682z^3 - 6.607z^2 + 2.794z - 0.4621}$
$T = 0.001$	$\frac{9.781z^5 - 48.62z^4 + 96.66z^3 - 96.08z^2 + 47.75z - 9.493}{z^5 - 4.927z^4 + 9.709z^3 - 9.564z^2 + 4.71z - 0.9278}$
$T = 0.0001$	$\frac{9.978z^5 - 49.86z^4 + 99.66z^3 - 99.6z^2 + 49.77z - 9.948}{z^5 - 4.993z^4 + 9.97z^3 - 9.955z^2 + 4.97z - 0.9925}$

Table 2 Discrete-time approximation of $s^{0.5}$ in delta-domain for different values of sampling periods

Sampling period (s)	$H_\delta(\gamma)$
$T = 0.01$	$\frac{10\gamma^5 + 242.7\gamma^4 + 903.2\gamma^3 + 549.3\gamma^2 + 52.81\gamma + 0.6991}{\gamma^5 + 58.17\gamma^4 + 550.6\gamma^3 + 855.9\gamma^2 + 208.9\gamma + 6.991}$
$T = 0.001$	$\frac{10\gamma^5 + 291.9\gamma^4 + 1180\gamma^3 + 741.9\gamma^2 + 72.27\gamma + 0.9634}{\gamma^5 + 72.97\gamma^4 + 742.1\gamma^3 + 1174\gamma^2 + 287.6\gamma + 9.634}$
$T = 0.0001$	$\frac{10\gamma^5 + 297.8\gamma^4 + 1214\gamma^3 + 765.8\gamma^2 + 74.69\gamma + 0.9963}{\gamma^5 + 74.77\gamma^4 + 765.8\gamma^3 + 1214\gamma^2 + 297.4\gamma + 9.963}$

Similar relation exists in the complex domain as well. The complex δ -domain frequency variable γ can be obtained as

$$\gamma = \frac{z - 1}{T} \tag{5}$$

Substituting $z = e^{sT}$, Eq. (5) can be rearranged to obtain the mapping relation between s -domain and δ -domain as follows:

$$s = \frac{1}{T} \ln(1 + \gamma T) \tag{6}$$

$H_b(z)$ and $H_\delta(\gamma)$ are computed for three different values of sampling time, i.e. for $T = 0.01$ s, $T = 0.001$ s and $T = 0.0001$ s. The discretized transfer functions of two different complex domains are shown in Tables 1 and 2, respectively.

3 Simulation Results

As an illustrative example, the discretization of $s^{0.5}$ is studied in complex z -domain and complex delta-domain by choosing three different sampling periods. The frequency response of a half-order differentiator is shown in Figs. 1, 2 and 3 for $T = 0.01$ s, $T = 0.001$ s and $T = 0.0001$ s, respectively. Four legends indicate the bode diagram of the original fractional differentiator of order 0.5, i.e. $s^{0.5}$, the continuous-time approximation of $s^{0.5}$ in s -domain, the discrete-time approximation of $s^{0.5}$ in complex z -domain and the discrete-time approximation of $s^{0.5}$ in complex delta-domain, respectively.

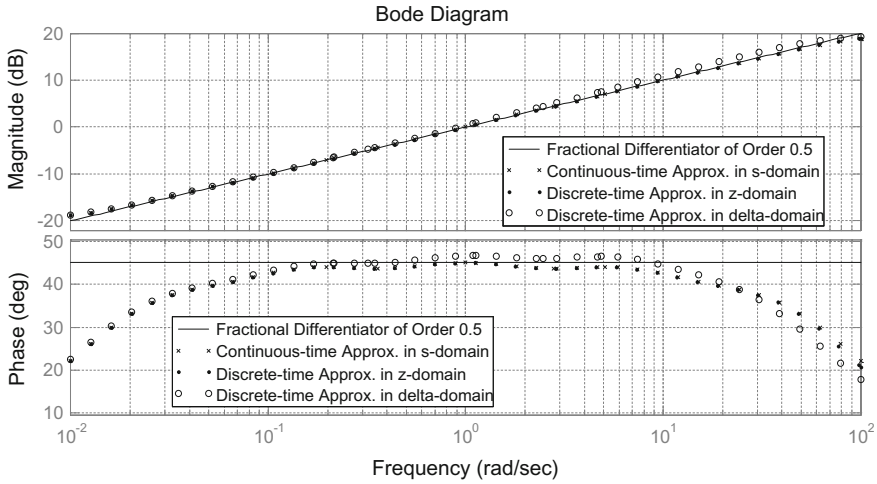


Fig. 1 Bode plot comparison of $s^{0.5}$ for $T = 0.01$ s

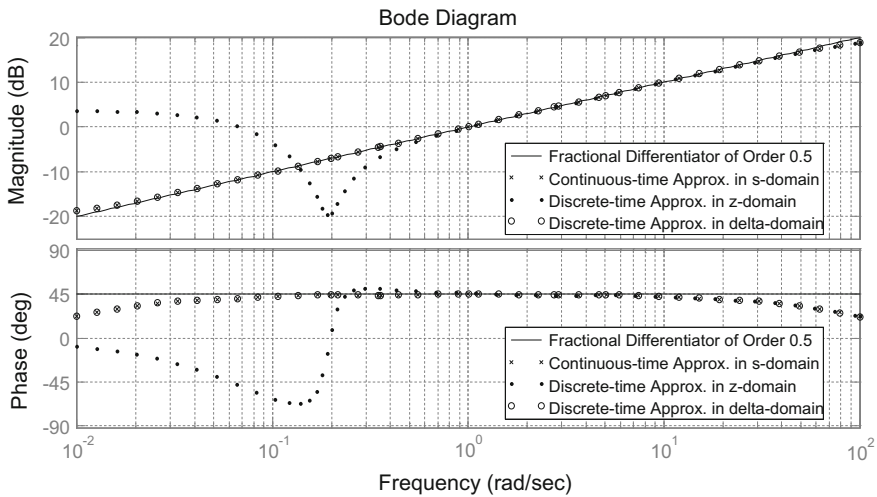


Fig. 2 Bode plot comparison of $s^{0.5}$ for $T = 0.001$ s

The comparative study in between z -domain approximation and delta-domain approximation is shown in Tables 3 and 4.

Three frequency ranges are considered in Tables 3 and 4. In the low frequency range, i.e. from 0.01 to 0.1 rad/s, delta-domain approximation seems to be closer to the frequency response of the original fractional differentiator compared to the z -domain approximation. As the sampling frequency increases, z -domain approximation becomes more vulnerable, especially to maintain the phase accuracy in the

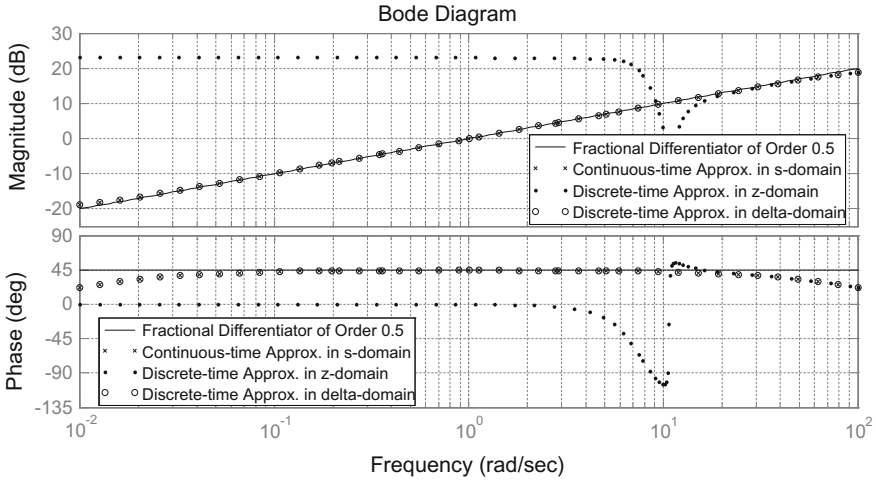


Fig. 3 Bode plot comparison of $s^{0.5}$ for $T = 0.0001$ s

Table 3 Maximum absolute error for magnitude approximation of $s^{0.5}$ in z-domain and in delta-domain for different frequency ranges and for different sampling periods

Freq. range (rad/s)	Error in z-domain (dB)			Error in delta-domain (dB)		
	$T = 0.01$ s	$T = 0.001$ s	$T = 0.0001$ s	$T = 0.01$ s	$T = 0.001$ s	$T = 0.0001$ s
0.01–0.1	1.2	23.65	43	1.2	1.2	1.2
0.1–10	0.5	13	33	0.5	0.15	0.1
10–100	1	1.23	30	0.75	1.16	1.2

Table 4 Maximum absolute error for phase approximation of $s^{0.5}$ in z-domain and in delta-domain for different frequency ranges and for different sampling periods

Freq. range (rad/s)	Error in z-domain (°)			Error in delta-domain (°)		
	$T = 0.01$ s	$T = 0.001$ s	$T = 0.0001$ s	$T = 0.01$ s	$T = 0.001$ s	$T = 0.0001$ s
0.01–0.1	22.75	100.6	45	22.5	23	23
0.1–10	2.4	112.1	150	1.7	2.1	2.33
10–100	25	23	23	27	23	23

mid-frequency range i.e. from 0.1 to 10 rad/s. In contrary, the frequency response obtained from delta-domain approximation shows significant improvement in the mid-frequency range as the sampling frequency goes high. However, both the z-domain approximation and the delta-domain approximation establish close correspondence between the continuous-time system and the discrete-time system in the high frequency range, i.e. from 10 to 100 rad/s. In the whole frequency range of

interest, i.e. from 0.01 to 100 rad/s, the maximum absolute errors in magnitude approximation and phase approximation obtained from z -domain approximation are 43 dB and 150° , respectively. On the other hand, the maximum absolute errors in magnitude approximation and phase approximation obtained from delta-domain approximation are 1.2 dB and 27° , respectively, which clearly validates the efficacy of delta-domain approximation over z -domain approximation.

4 Conclusions

The discretization of fractional operator is essential for digital implementation of a fractional-order controller. In this paper, discrete-time approximation of a half-order differentiator is obtained in complex z -domain and in complex delta-domain using the indirect discretization technique. The simulation results establish that the frequency response obtained by the delta-domain approximation is closer to the original fractional-order differentiator compared to z -domain approximation. As the sampling frequency increases, the delta-domain approximation seems to be more consistent than the z -domain approximation.

References

1. Oldham K. B., Spanier J.: The Fractional Calculus. Academic Press, New York, (1974).
2. Manabe S.: The non-integer integral and its application to control systems. English Translation Journal Japan, vol. 6, pp. 83–87, (1961).
3. Oustaloup A.: Fractional order sinusoidal oscillators: Optimization and their use in highly linear FM modulators. IEEE Transaction on Circuits and Systems, vol. 28, pp. 1007–1009, (1981).
4. Axtel M., Bise M. E.: Fractional calculus and applications in control systems. In Proceeding of the IEEE National Aerospace and Electronics Conference (NAEC), New York, pp. 563–566, (1990).
5. Vinagre B. M., Podlubny I., Hernandez, A., Feliu V.: Some approximations of fractional-order operators used in control theory and applications. Journal of Fractional Calculus and Applied Analysis, vol. 3, pp. 231–248, (2000).
6. Oustaloup A.: CRONE control: Robust control of non-integer order. Hermes, Paris, (1991).
7. Lurie B. J.: Three-Parameter Tunable Tilt-Integral-Derivative (TID) Controller. United States Patent, 5371670, (1994).
8. Podlubny I.: Fractional-order systems and $PI^{\lambda}D^{\mu}$ controllers. IEEE Transactions on Automatic Control, vol. 44, pp. 208–214, (1999).
9. Machado J. A. T.: Analysis and design of fractional-order digital control systems. Journal of Systems Analysis Modelling Simulation, vol. 27, pp. 107–122, (1997).
10. Chen Y. Q., Moore K. L.: Discretization schemes for fractional-order differentiators and Integrators. IEEE Transaction on Circuits Systems I: Fundamental Theory & Application, vol. 49, pp. 363–367, (2002).
11. Vinagre B. M., Chen Y. Q., Petras I.: Two direct Tustin discretization methods for fractional order differentiator/integrator. Journal of Franklin Institute, vol. 340, pp. 349–362, (2003).

12. Oustaloup A., Levron F., Mathieu B., Nanot F. M.: Frequency-band complex noninteger differentiator: Characterization and Synthesis. *IEEE Transaction on Circuit and Systems-I. Fundamental Theory and Application*, vol. 47, pp. 25–39, (2000).
13. Maione G.: Concerning Continued Fractions Representation of Noninteger Order Digital Differentiators. *IEEE Signal Processing Letters*, vol. 13, pp. 725–728, (2006).
14. Maione G.: High-speed digital realizations of fractional operators in the delta domain. *IEEE Transactions on Automatic Control*, vol. 56, pp. 697–702, (2011).
15. Middleton R. H., Goodwin G. C.: *Digital Control and Estimation: A Unified Approach*. Prentice Hall, Englewood Cliffs (1990).

Speed Control of Single Phase Induction Motor Using Fuzzy Logic Controller

Kamal Sapkota, Arun Pradhan, Amit Kumar Singh and Prativa Rai

Abstract This paper presents the speed control of an Induction Motor (IM) using rule-based fuzzy logic controller and simulated with the help of MATLAB Simulink and later tested with its hardware model. Because of low maintenance and robustness, IM has much application in industries. Here, the scalar control method is employed for controlling the speed of an IM where the stator voltage and the frequency to the system are changed proportionately by keeping v/f ratio constant Krishnan (Electric Motor Drives—Modeling, Analysis and Control. Prentice-Hall, Upper Saddle River, 2001 [1]). The inputs to the fuzzy logic controller (FLC) are speed error (e) and change in speed error (Δe) and output to the controller is the change of control (ω_{sl}) which is actually the frequency correction at the output. These inputs are processed according to the user-defined rule, and output is corrected and provides the required signal to control the speed of PWM inverter-fed IM. It was observed that fuzzy logic controller avoids complexity to the system design and it also avoids the mathematical computations compared to other controller design. Using fuzzy logic controller for closed loop v/f control scheme gives superior way of controlling the speed of IM by maintaining a constant maximum torque.

Keywords IM · Robustness · Fuzzy logic controller · Scalar control
Maximum torque

K. Sapkota (✉) · A. Pradhan · A. K. Singh
Department of EE, Sikkim Manipal Institute of Technology,
Majhitar, Rangpo, Sikkim, India
e-mail: kasabloggerkamal@gmail.com

A. Pradhan
e-mail: arun.pradhan81@gmail.com

A. K. Singh
e-mail: amit.s@smit.smu.edu.in

P. Rai (✉)
Department of CSE, Sikkim Manipal Institute of Technology,
Majhitar, Rangpo, Sikkim, India
e-mail: raiprativa@gmail.com

1 Introduction

1.1 Overview

Electric drives play vital role in the field of power electronics and drives system; since they are accounts for very large range of industrial applications. More than 85% of drives in industries are accounts on IM.

Synchronous speed can be controlled by varying the supply frequency. Voltage induced in the stator is

$$V \propto \Phi 2\pi f \quad (1)$$

where V is supply voltage, Φ is the air-gap flux and f is the supply frequency.

$$\Phi \propto V/f \quad (2)$$

constant = 2π

Thus, reducing the frequency without changing the supply voltage will lead to an increase in the air-gap flux which is highly undesirable. Hence, whenever frequency is varied in order to control speed of IM, the terminal voltage is also varied so as to maintain the v/f ratio constant [2].

As

$$T_m = K\Phi I_a \quad (3)$$

where

T_m maximum torque

I_a armature current

K constant

$$T_m \propto \Phi \quad (4)$$

Thus by maintaining a constant v/f ratio, the maximum torque of the motor becomes constant for changing speed. Since from the above formula, maximum torque (T_m) remains constant if the air-gap flux is constant because of constant v/f ratio [1].

IMs are most widely used motor in industrial applications due to their advantages of ruggedness, lower rotor inertia, absence of commutator and brushes, lower price and smaller size [3].

For several decades, researchers used classical method such as PI controller to control the speed of IM. Such controller requires mathematical model of the motor parameter. Nowadays, intelligence controller such as fuzzy logic controller (FLC) is widely used to control speed of IM. Since the fuzzy logic controller is more practical where we can define the operation of variable in subjective way, i.e. high,

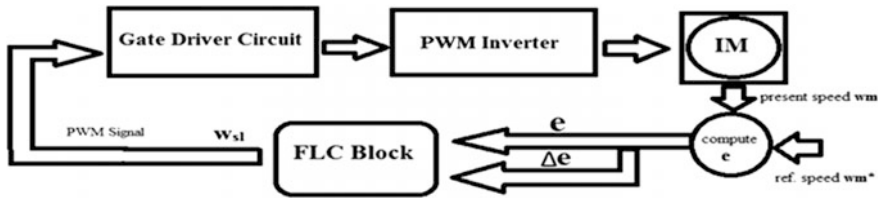


Fig. 1 Closed loop control of induction motor

low, or big, small, etc., in numeric form, they are readily available customizable in natural language terms [4]. In this thesis, speed control of IM is done using fuzzy logic controller in feedback mechanism. The following section will describe the use of FLC in electric drives and some of its related works (Fig. 1).

1.2 Scalar Control with Fuzzy Logic of the Induction Motor

In this paper, scalar control method for controlling the speed of IM is employed such that the magnitude of stator voltage and frequency are controlled in such a way that the ratio of v/f varies proportionately. Compared to conventional PI controller, fuzzy logic controller is very efficient technique since it eliminates the need of too many inputs while designing the system [5]. The current system has two inputs, namely speed error (e) and change in speed error (Δe) and output as change of control (ω_{sl}) which is actually the frequency correction. Speed error and change of speed error could be defined as follows:

$$e = V_{ref} - V_{act} \tag{5}$$

$$\Delta e = dE/dt \tag{6}$$

where

V_{ref} is the desired motor speed.

V_{act} is the measured or actual motor speed.

So these two inputs are processed according to the rule which is defined by the user while designing the system. Nowadays, fuzzy logic controller is preferred over conventional PI controller since torque ripple is high in case of PI controller; it responds slowly towards the produced error which leads to system instability. For linear system, conventional PI controller gives good result but when the system is nonlinear, it does not guarantee good performance. Also, the overshoot is more; settling time is also more so it takes more time to reach the steady-state value. Fuzzy logic controller does not require perfect mathematical model, so it uses simple mathematical calculation to simulate the expert knowledge.

2 Description of the Present Fuzzy Logic Controller

The two inputs to the controller are present speed and reference speed of motor, so by comparing these two inputs, an error signal will be generated. After generating error signal (e), a change in error (Δe) signal is also calculated and fed to the fuzzy logic controller. The controller processes these error and change in error using user-defined rule, MFs and database and gives the controlled output as change of control, which is actually the frequency correction. FLC was applied to this system to control the speed of IM.

The output from the FLC is sent to the PWM inverter to produce controlled waveform with variable voltage and variable frequency to control the speed of IM.

FLC in this system uses Mamdani-type fuzzy inference system to make relation between two inputs and the one output variable. The first input variable is the speed error (e), which is the speed difference between desired speed (set RPM) and actual speed, while the other input is the change of speed error (Δe). The output variable is the change of control which is the frequency correction at the output. The membership functions for input and output variables are shown in Figs. 2 and 3. All fuzzy rules for this proposed system are summarized in this following lookup table and are created with the help of Table 1.

Fig. 2 Membership functions for speed error (e) and change in speed error (Δe)

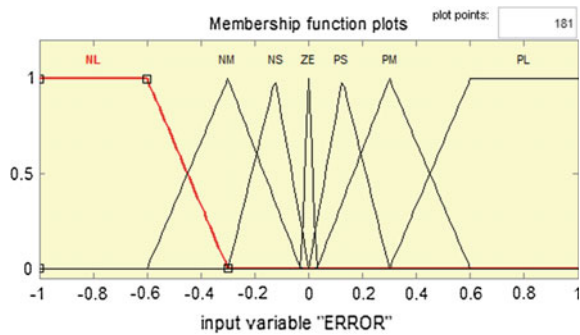


Fig. 3 Membership functions for change of control (ω_{sl})

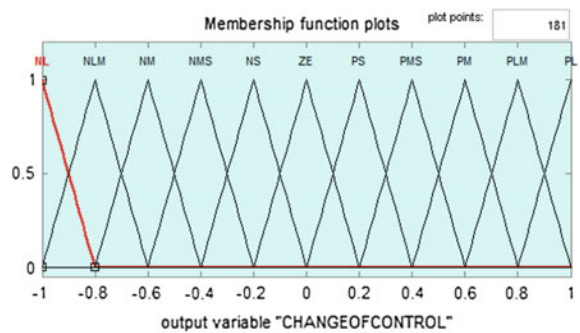


Table 1 Lookup table for fuzzy logic controller

Δe	e						
	NL	NM	NS	ZE	PS	PM	PL
NL	NL	NL	NLM	NM	NMS	NS	ZE
NM	NL	NLM	NM	NMS	NS	ZE	PS
NS	NLM	NM	NMS	NS	ZE	PS	PMS
ZE	NM	NMS	NS	ZE	PS	PMS	PM
PS	NMS	NS	ZE	PS	PMS	PM	PLM
PM	NS	ZE	PS	PMS	PM	PLM	PL
PL	ZE	PS	PMS	PM	PLM	PL	PL

3 MATLAB Simulink Model

MATLAB Simulink model for the proposed fuzzy logic controller for closed loop speed control of IM is shown (Fig. 4).

In the figure, set RPM is the desired speed of the motor set by the user, while the signal from feedback is the measured RPM of IM using speed-sensing devices. The error signal is found as the difference between motor actual speed (measure motor speed) and the desired speed of motor. This speed error and its derivative (change in error) are used as input for FLC block.

The output of FLC is the change of control which is actually the frequency control. To work the system in feedback mechanism, actual motor speed will be sent again to FLC so the closed loop control system works continuously to achieve the desired motor speed and keeps the system always in stable condition.

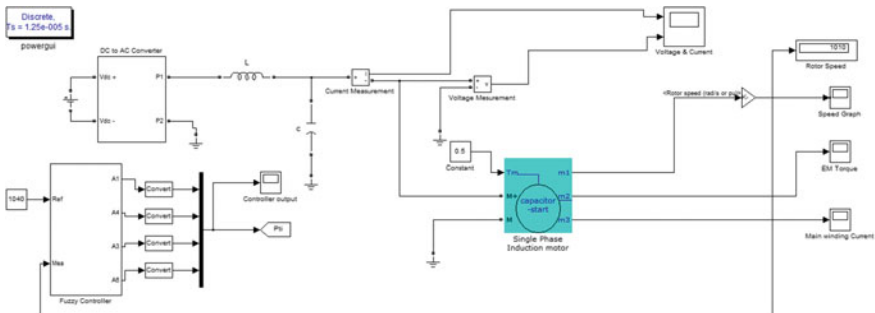


Fig. 4 Simulink model for speed control of IM using fuzzy logic in closed loop

4 Results and Discussion

Figures 5 and 6 show the performance characteristics of a 186.5 W, 200 V, 50 Hz IM, operating at no load and with 0.5 Nm load with a fuzzy logic speed controller. The reference speed for both cases is given as 1040 RPM.

Case I: For no-load condition, i.e. $T_m = 0$ Nm, it is observed that motor picks up the speed 1040 RPM at $t = 2.55$ s and also motor draws starting current up to 28 A and starting torque up to 15.97 Nm. When motor speed starts settling at 0.48 s to reference value, i.e. 1040 RPM, then the motor current settles at 1.7 A and torque also starts settling at 0.01 Nm.

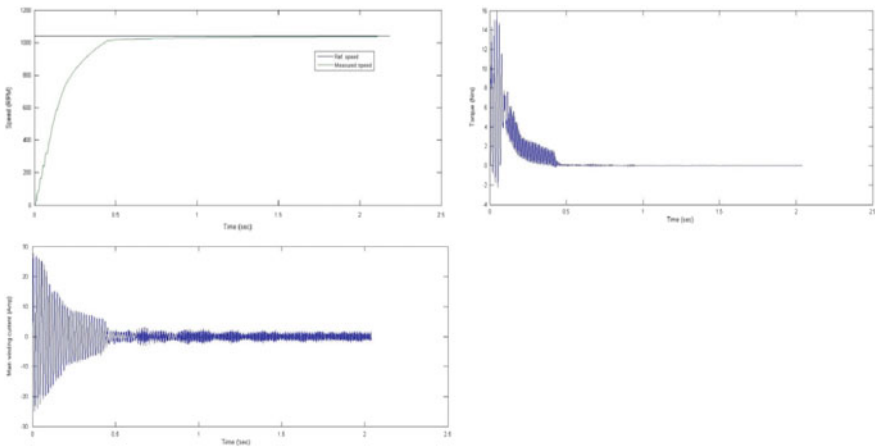


Fig. 5 Rotor speed, torque and current plot, respectively, when $T_m = 0$ Nm

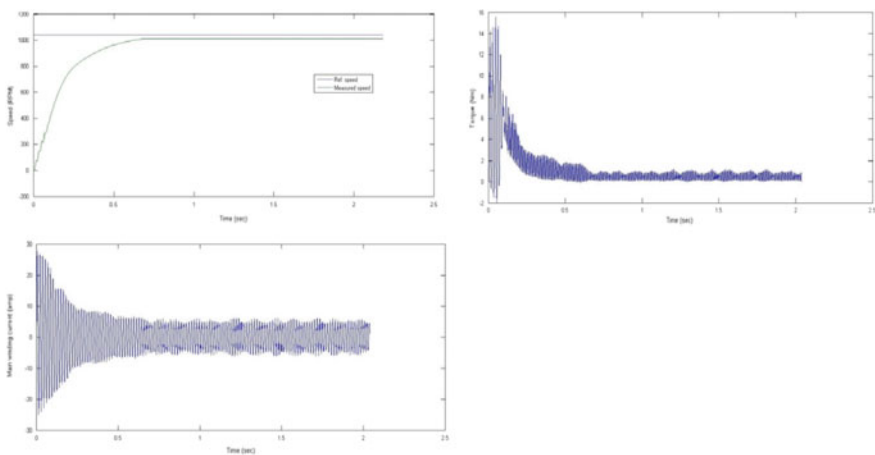


Fig. 6 Rotor speed, torque and current plot, respectively, when $T_m = 0.5$ Nm

Case II: When IM operates with small load, i.e. $T_m = 0.5 \text{ Nm}$ with a fuzzy logic speed controller, then it is observed that motor picks up the speed 1010 RPM at $t = 2.55 \text{ s}$ giving speed error value 30 RPM to the controller for its operation and also motor draws starting current up to 26.55 A and starting torque up to 15.55 Nm. When motor speed starts settling at 0.48 s to 1040 RPM, then motor current settles at 4.5 A and torque also starts settling at 0.7 Nm.

5 Hardware Implementation for Speed Control of Single Phase IM

For the Gate Driver Circuit: It consists of single phase 220 V ac supply which is step down using 220/15 V step-down transformer. This 15 V AC supply is rectified or converted into 15 V DC using bridge rectifier. A filter capacitor of 470 μF is used in order to remove the ripple of the DC output. Optocoupler is used in the gate driver circuit which requires 12 V DC. So, after getting almost 15 V DC supply, it is regulated to 12 V DC using voltage regulator IC, LM 7812. Optocoupler MCT2E is used to amplify the PWM signal as well as to isolate the Arduino UNO from rest of the circuit. The output PWM signal or pulses of the gate driver circuit is then fed to the inverter switches to drive the H-Bridge inverter (Fig. 7).

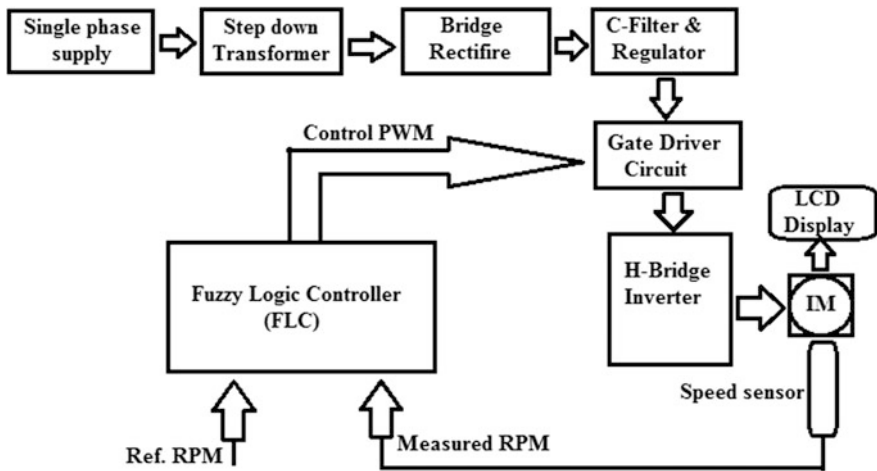


Fig. 7 General block diagram for speed control of single phase induction motor

6 Methodology

For the first time to run the motor, PWM signal is generated in ATmega328 microcontroller inside Arduino UNO and fed to H-Bridge inverter. The system has two modes of operations, i.e. manual mode and auto mode.

In manual mode, function of feedback is not included; a potentiometer is provided for user to set the motor rpm from [600, 1400]. After the set rpm (user interface) is set by the user, motor rpm (read rpm) will be sensed by the proximity speed sensor, so that this read rpm always tries to track the set rpm by correcting supply frequency and the magnitude of the stator voltage. It was observed that the difference in two speeds (speed error) is quite large in this mode of operation.

In auto mode, fuzzy logic-based program is done in ATmega328 microcontroller in such a way that the fuzzy controller always tries to keep the speed error (actual speed–set speed) within the range [–20, 20] rpm so that the user will get the desired speed more closer than in manual mode of operation (Fig. 8).

7 Conclusion

In this paper, a fuzzy logic controller is designed and is to be utilized in the speed control of an IM. The designing has been done with the help of MATLAB Simulink and microcontroller ATmega328 for designing fuzzy logic controller in hardware kit. This controller takes in crisp inputs, viz. speed error (e) and change in error (Δe), and gives an output called change in control (ω_{sl}). The output changes according to the rules designed by the user. Based on the set point and feedback signal, FLC produces the proper control signal which will be used by the inverter to control the speed of IM. Speed control is done with load and without load and outputs are analysed separately (Tables 2 and 3).

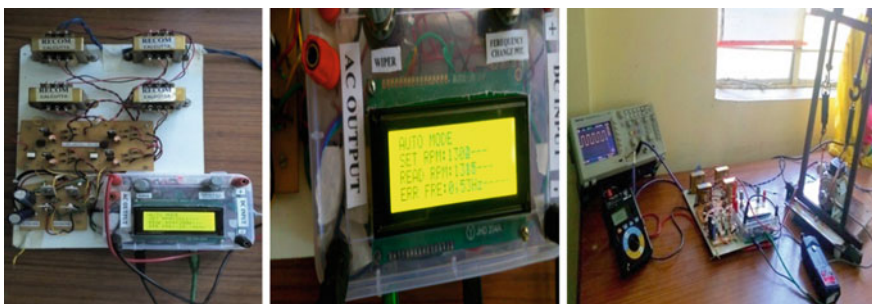


Fig. 8 Developed kit for speed control of single phase induction motor

Table 2 Data for manual mode of operation

Set RPM	Motor RPM	Speed error
900	960	60
980	1030	50
1050	1105	55
1160	1210	50
1200	1255	55
1320	1375	55
1400	1445	45

Table 3 Data for auto mode of operation

Set RPM	Motor RPM	Speed error
900	890	10
980	985	05
1050	1065	15
1160	1045	15
1200	1210	10
1320	1335	15
1400	1410	10

References

1. R. Krishnan, *Electric Motor Drives—Modeling, Analysis, and Control*. Upper Saddle River, NJ: Prentice-Hall, 2001.
2. V/F Control Of Induction Motor Drive A Thesis submitted in partial fulfillment of the requirements for the degree of Bachelor of Technology in “Electrical Engineering” By Devraj Jee, Nikhar Patel Under the guidance of Prof. M. Pattnaik Department of Electrical Engineering National Institute of Technology Rourkela-769008 (ODISHA) May-2013.
3. Novotny D.W., Lipo T.A., *Vector control and dynamics of AC drives*, Oxford University Press Inc., New York, 1996.
4. Bose B.K., “Power Electronics and Motion Control-Technology Status and Recent Trends.” *IEEE Transactions on Industry Applications*, Vol. 29, no. 5, 1993.
5. D. Asija, “Speed control of induction motor using fuzzy-pi controller,” 2010 2nd International Conference of Mechanical and Electronics Engineering (ICMEE 2010), vol. 2, pp. 460–463, 2010.

Speed Control of DC Motor Using Fuzzy-Based Intelligent Model Reference Adaptive Control Scheme

Dayarnab Baidya and Rupam Gupta Roy

Abstract This investigation deals with the introduction of a noble dynamic fuzzy model reference adaptive control scheme. In this work, we propose a new model of MRAC using fuzzy control for the speed control of DC Motor. The starting of our work is done with the general comprehensive designing of MRAC for first-order process along with the second-order process using MIT Rule. After that, the description regarding our proposed model is given. For the evaluation of the performance of the controller, fuzzy-based MRAC is applied on DC Motor. The simulation results are compared with other controllers showing that the reaching time and tracking can be extensively reduced.

Keywords Adaptive control · Dynamic fuzzy model reference adaptive control scheme · MIT rule · Model reference adaptive control · PID controllers

1 Introduction

Adaptive control system is a special type of nonlinear control system which has the ability to vary its parameters for the adjustment to the variation in dynamics of the process or characteristics change in the disturbances. MRAC is one of the adaptive strategies where a reference model is used to adjust the controller parameters. Shyu (2008) and Stefanello (2008) applied the Lyapunov theory to develop the performance of shunt active power filter [1]. Suzuki et al. [2] designed MRACS with fuzzy adaptive control rules using genetic algorithm [2]. Wong et al. [3] designed indirect fuzzy adaptive controller for the controlling of unstable inverted pendulum [3]. Hwang (2000) and Tang (2001) proposed the concept of fuzzy PID controller. Lakhekar and Roy (2014) introduce the fuzzy neural approach for the dynamic

D. Baidya (✉) · R. G. Roy

Electronics & Instrumentation Engineering, NIT Agartala, West Tripura, Tripura, India
e-mail: dayarnabbaidya@rediffmail.com

R. G. Roy

e-mail: rupamguptaroy05@gmail.com

© Springer Nature Singapore Pte Ltd. 2018

R. Bera et al. (eds.), *Advances in Communication, Devices and Networking*,

Lecture Notes in Electrical Engineering 462,

https://doi.org/10.1007/978-981-10-7901-6_79

spectrum allocation in cognitive radio networks and they contributed their efforts in developing dynamic fuzzy sliding mode control (DFSMC) for heading angle control of autonomous underwater vehicles (AUVs) in horizontal plane [4, 5].

In this article, we provide a detailed description regarding the general design procedure of the MRAC with the help of MIT Rule for the second-order process followed by our proposed model and apply it on DC motor for the control of speed. The Simulink results of different controllers are compared with the result obtained from the proposed model.

2 Design Procedure Using MIT Rule for Second-Order Process

In this case, a second-order process expressed by

$$\ddot{y} + p_1\dot{y} + p_0y = qu \quad (1)$$

is selected and the process must follow the reference model which is given by

$$\ddot{y}_m + p_{1m}\dot{y}_m + p_{0m}y_m = q_m r \quad (2)$$

A particular control law is required to vary the reference input signal so that the plant's output signal track with the reference model [6]. This control law is time dependent upon controller parameters θ_1 and θ_2 which act as the adaptation to the given plant system. This control law is given by:

$$u = r\theta_1 - y_p\theta_2 \quad (3)$$

Substituting u in (1) using (3)

$$\ddot{y} + p_1\dot{y} + p_0y = q(r\theta_1 - y\theta_2) \quad (4)$$

Taking the Laplace transform of (2) and (4) and then rearranging, we get

$$s^2Y(s) + (p_1s + p_0 + q\theta_2)Y(s) = q\theta_1R(s) \quad (5)$$

$$s^2Y(s) + p_{1m}Y_m(s) + p_{0m}Y_m(s) = q_mR(s) \quad (6)$$

The error (e) between the output of the reference model ($Y_m(s)$) and the process output (Y) is given as

$$E(s) = \frac{q\theta_1}{s^2 + p_1s + p_0s + q\theta_2} R(s) - Y_m(s) \quad (8)$$

Here, a cost function is selected as

$$\gamma(\theta) = \frac{1}{2} e^2 \quad (9)$$

From the MIT Rule, it can be written [6]

$$\frac{d\theta}{dt} = -\alpha \frac{\partial \gamma}{\partial \theta} = -\alpha e \frac{\partial e}{\partial \theta} \quad (10)$$

where $\frac{\partial e}{\partial \theta}$ is called as the sensitivity derivative of the system.

Using (11) and partially differentiating (9) with respect to θ_1 and θ_2 , we get

$$\frac{\partial E(s)}{\partial \theta_1} = \frac{q}{s^2 + p_1s + p_0 + q\theta_2} R(s) \quad (11)$$

$$\frac{\partial E(s)}{\partial \theta_2} = -\frac{q}{s^2 + p_1s + p_0 + q\theta_2} Y(s) \quad (12)$$

Now for the better performance of the plant, the reference model should be close to the plant. So (11) and (12) can be written from (8) as

$$\frac{\partial E(s)}{\partial \theta_1} = \frac{q}{s^2 + p_{1m}s + p_{0m}} R(s) \quad (13)$$

$$\frac{\partial E(s)}{\partial \theta_2} = \frac{q}{s^2 + p_{1m}s + p_{0m}} Y(s) \quad (14)$$

Inserting the following expressions of $\frac{\partial E(s)}{\partial \theta_1}$ and $\frac{\partial E(s)}{\partial \theta_2}$ in (10), it is obtained as

$$\frac{d\theta_1}{dt} = -\alpha \frac{q}{s^2 + p_{1m}s + p_{0m}} R(s) \quad (15)$$

$$\frac{d\theta_2}{dt} = \alpha \frac{q}{s^2 + p_{1m}s + p_{0m}} Y(s) \quad (16)$$

Equations (15) and (16) are the update laws for θ_1 and θ_2 .

3 Dynamic Fuzzy Model Reference Adaptive Control (DFMRAC)

The basic design of model reference adaptive control is the initiation of the design procedure and selection of the adaptive control law in such a way that the necessities of the stability criterion are fulfilled. The main scheme of our approach is fuzzification of adaptive parameters. The parameters are fuzzified corresponding to the process input, error and output of the process. In our present work, we have used fuzzy controller in place of transfer function with the fact that fuzzy will take action for the adaptation of the plant with the variations in disturbances and surrounding conditions. The block diagram of proposed control scheme is shown in Fig. 1.

3.1 Takagi–Sugeno Fuzzy Inference System (TS-FIS)

The TS-FIS is a single-stage fuzzy system. The fuzzy inference systems are composed of a set of IF–THEN rules. A TS fuzzy model has the following form of fuzzy rules [7–9]:

$$R_k : \text{If } x_1 \text{ is } A_{1k} \text{ and } x_2 \text{ is } A_{2k} \dots \text{ and } x_n \text{ is } A_{nk}$$

$$\text{Then } y = f_k(x_1, x_2, \dots, x_n), \quad (k = 1, 2, \dots, N)$$

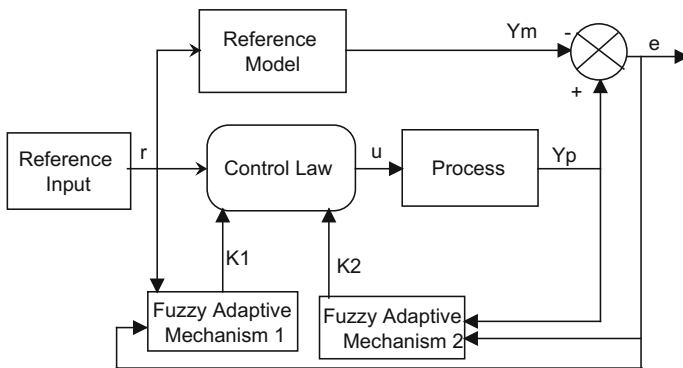


Fig. 1 Block diagram of dynamic fuzzy model reference adaptive control (DFMRAC)

where $f_k(\cdot)$ is a crisp function of x_n . Normally, $f_k(x_1, x_2, \dots, x_n) = \rho_0 + \rho_1 x_1 + \rho_2 x_2 + \dots + \rho_n x_n$. The final output of fuzzy system can be obtained as

$$y = \frac{\sum_{k=1}^N f_k(\cdot) T_{i=1}^{r_k} \mu_{ik}(x_i)}{\sum_{k=1}^N T_{i=1}^{r_k} \mu_{ik}(x_i)} \tag{18}$$

where $1 < r_k < n$ is the number of input variables in the rule premise, N is the number of fuzzy rules, n is the number of inputs, μ_{ik} is the membership function for fuzzy set, and A_{ik} and T are a T -norm for fuzzy conjunction.

4 Simulation Results

The simulation study is done for DC motor speed control. The optimal simulation result is shown in Fig. 2. Here, we have compared the simulation results of fuzzy MRAC with other controllers. Fuzzy MRAC provides a better performance in both transient and steady-state response. Fuzzy MRAC has better dynamic response curve, shorter response time.

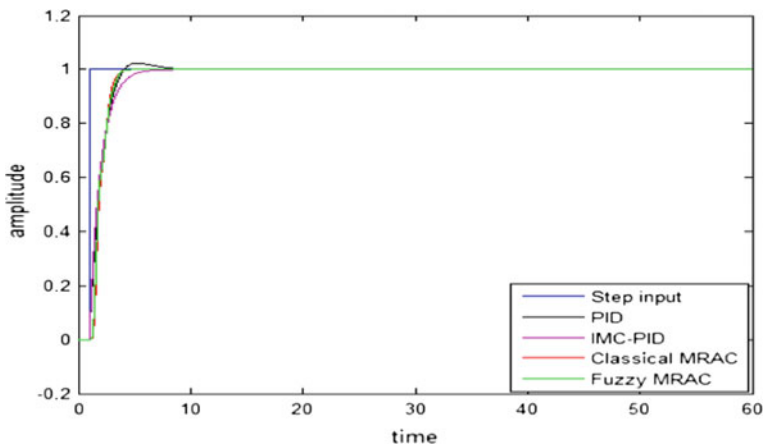


Fig. 2 Responses of DC motor under different controllers

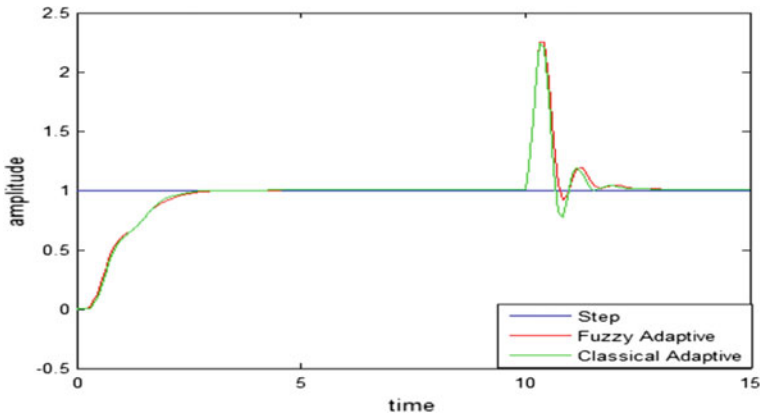


Fig. 3 Disturbance rejection response for step-type disturbance

5 Disturbance Rejection

A step-type disturbance is applied at time $t = 10$ s which is shown in Fig. 3. Oscillations of fuzzy adaptive control are less than classical adaptive control and fuzzy adaptive control settles faster. The robustness of the proposed controller is more than that of the classical adaptive control.

References

1. Swarnkar P., Jain S. and Nema R.K.: Comparative Analysis of MIT Rule and Lyapunov Rule in Model Reference Adaptive Control Scheme. *Innovative Systems Design and Engineering*, vol. 2, no. 4, (2011).
2. Suzuki T., Shida K., Fujikawa H. and Yamada S.: A design method of MRACS with fuzzy adaptive control rules using genetic algorithms. *Industrial Electronics, Control, and Instrumentation*, '93, (1993).
3. Wong C.-C., Huang B.-C. and Chen J.-Y.: Rule regulation of indirect adaptive fuzzy controller design, *IEEE Proc.-Control Theory Appl*, vol. 145, no. 6, (1998).
4. Lakhekar G.V. and Gupta Roy R.: A fuzzy neural approach for dynamic spectrum allocation in cognitive radio networks, *International Conference on Circuit, Power and Computing Technologies*, (2014).
5. Lakhekar G. V. and Gupta Roy R.: Heading control of an underwater vehicle using dynamic fuzzy sliding mode controller, *IEEE International Conference on Circuit, Power and Computing Technologies*, (2014).
6. Stellet E. J.: Influence of Adaptation Gain and Reference Model Parameters on System Performance for Model Reference Adaptive Control. *International Journal of Computer, Electrical, Automation, Control and Information Engineering* vol. 5, no. 12, (2011).

7. Chen Y., Yang B., Abraham A. and Peng L.: Automatic Design of Hierarchical Takagi–Sugeno Type Fuzzy Systems Using Evolutionary Algorithms, *IEEE Transactions On Fuzzy Systems*, vol. 15, no. 3, (2007).
8. Lee C. C.: Fuzzy logic in control systems: fuzzy logic controller-part I, *IEEE Transactions On Systems, Man, And Cybernetics*, vol. 20, no. 2, (1990).
9. Takagi T. and Sugeno M.: Fuzzy identification of systems and its applications to modeling and control, *IEEE Trans. Systems Man Cybernet*, no. 15, pp. 116–132, (1985).

Performance Analysis of Fuzzy Logic-Based Edge Detection Technique

R. Lalchhanhima, D. Kandar and Babusena Paul

Abstract Identification of objects in digital images is an important part in computer vision. Edges have high probability being the border of an object, so edge detection is very crucial in image processing. The accurate detection of edges in an image reduces the processing requirement by filtering our insignificant data, while preserving important structure in an image. In this paper, various image edge detection techniques are analyzed and presented, further the paper proposed edge detection technique based on fuzzy logic. In this paper, MATLAB software along with its pre-defined functions has been utilized for the development of such fuzzy logic-based edge detection technique, and it is compared with other existing edge detection techniques.

Keywords Edge detection · Image segmentation · Soft computing
Fuzzy logic

1 Introduction

Image edge detection and segmentation is an image processing technique whose outcome is not deterministic [1]. In image segmentation process, the image is divided into several homogeneous regions based on a particular homogeneity

R. Lalchhanhima (✉)

Department of Information Technology, Mizoram University, Aizawl, India
e-mail: chhana.mizo@gmail.com

D. Kandar · B. Paul

Department of Electrical and Electronic Engineering Technology,
University of Johannesburg, Johannesburg, South Africa
e-mail: kdebdata@gmail.com

B. Paul

e-mail: bspaul@uj.ac.za

© Springer Nature Singapore Pte Ltd. 2018

R. Bera et al. (eds.), *Advances in Communication, Devices and Networking*,
Lecture Notes in Electrical Engineering 462,
https://doi.org/10.1007/978-981-10-7901-6_80

measure. Edges have high probability being the boundary of regions while they are usually disconnected. If edges can be extracted and then connected together, then the region can be described by the edge contour. Edges are normally defined by the abrupt change in intensity which is also high-frequency component in the frequency domain.

Edge detection plays an important role in computer vision. Computer vision system is interested mainly in object detection. Different objects in an image pertain to different regions, thereby attaining boundaries between regions. So, the detected edges are likely to become the borders of objects. Therefore, accurate identification of edges in an image is one of the basic requirements in subsequent higher level of processing [2]. There are several existing segmentation methods [3–6] which are region growing based and edge detection techniques [7, 8].

2 Edge Detection Mechanism

2.1 *Traditional Edge Detection Methods*

There are different factors that the choice of edge detectors depends. Classical edge detectors operate by convolving the mask/filter with the image. The edge detector mask is designed in such a way that it is to be responsive where there is large difference in gradient and non-responsive in the smooth regions. Several edge detection operators are available, each responds differently from one another and their performance is also different with different types of images. Based on the mode of responsiveness, it is broadly divided into two types; gradient and Laplacian [9]. The gradient method works on the first derivative of the image, by finding the minima and maxima, whereas the Laplacian works on the second derivative by finding zero crossing.

In the first derivative plot of an image, the probable edge attains a shape of a ramp to highlight its location. This method includes the Sobel operator and is characterized by gradient filter family of edge detection. If the calculated gradient in a pixel exceeds some pre-defined threshold, then that location may be identified as the edge location. As edges have higher gradient value compared to the neighboring pixel, then after thresholding, it may be detected as edge pixel or not [6]. Gaussian edge detector is symmetric along the detected edge, and it reduces the noise by smoothing. The operators used here are Canny and ISEF (Shen–Castan) which convolve the image with the filter. The filters are the derivative of Gaussian for Canny and ISEF for Shen–Castan [10, 11]. In 1980, Marr and Hildreth introduced Laplacian of Gaussian (LoG) which is the combination of Gaussian filtering with the Laplacian.

2.2 The Marr–Hildreth Edge Detector

The Marr–Hildreth edge detector was well accepted till Canny proposed more optimal solution for edge detection. Marr–Hildreth proposed an operator based on gradient that utilizes Laplacian to determine the second derivative of an image. His proposed method works by first applying Gaussian filter and then detects an edge by finding zero crossing in the second derivative (Laplacian) in an image, which is determined by the presence of step difference in intensity [12].

2.3 The Canny Edge Detector

The Canny edge detector was proposed by John Canny in 1983 [13] and performed better than most existing algorithms. His method works by first filtering the noise by using Gaussian filter, then finding the intensity gradient of an image. The next step is to suppress spurious response to edge detection followed by double thresholding and tracking edges by hysteresis. The final step is to suppress all other weak edges, which are not connected by strong edges, and utilize that idea to detect the edges. The proposed method is primarily based on optimization of objective function as it pertains to signal processing optimization problem. Since the complexity of the actual solution for this problem is an exponential function, he proposed several ways to optimize the problem by approximation [14].

2.4 Soft Computing-Based Operators for Edge Detection

Image processing applications such as image enhancement, transformation, compression, extraction, classification, segmentation, edge detection, morphology retrieval, noise reduction are non-deterministic and non-trivial in nature. In order to model the uncertainties and ambiguities in the image processing, it is required to employ technique which is robust and tolerant. The answer lies on the soft computing techniques, which are able to model imprecision, and incomplete data is widely being employed in image processing. Some soft computing techniques such as fuzzy, neural, machine learning, and probabilistic reasoning differ from conventional computing by being tolerant to imprecision, incomplete data, partial truth, and approximation in order to solve real-world problems [15].

3 Proposed Fuzzy Approach for Edge Detection

Classical techniques like Sobel, Prewitt, Roberts, and Canny edge detector have their limitations primarily because they use fixed value of parameters or threshold, whereas the edges in images can be considered as dynamic in nature due to which some edges may be left undetected. Fuzzy logic, a branch of soft computing, provides us flexibility by allowing the values without any such restrictions. It is used to map an input space to an output space, and IF-THEN rules are evaluated in parallel. By using fuzzy techniques, different sizes of edges can also be detected [16, 17].

In this work, a method of 14 fuzzy rules and 2×2 mask is used for edge detection in digital images. The proposed method is implemented in MATLAB in which a fuzzy inference system (FIS) of Mamdani-type edge detection model without assigning the threshold value is designed. The method consists of convolving the 2×2 scanning mask over the image to highlight the edge pixels. The rule base then identifies the pixels whether they belong to edges. The result of detection is then compared with those traditional methods like Sobel, Robert, Prewit algorithms. Our fuzzy model considers four inputs and one output variable. The four pixels P11, P12, P21, and P22 of 2×2 mask are considered as the inputs.

Conversion of input from crisp to fuzzy set is the first step in which the two membership functions, Black and White, are defined. These two functions return a fuzzy value that determines the Black-ness and the White-ness, respectively, of that pixel. By applying these two functions to each pixel, all the image pixels (originally crisp set) are classified into Black or White fuzzy sets and thereby determining the Black-ness and White-ness of the input pixels. After fuzzification of all pixels, a rule base is then generated to get the output. A triangular membership function for the output is defined and is called as edge. In this rule base, 14 inference rules are defined and are applied on the inputs to get the output. These inference rules depend on the weights of 4 neighbors, i.e., P11, P12, P21, P22, and itself. In this inference rule base, the weights are defined as the degree of Black-ness or degree of White-ness. These weights are combined using AND operator as defined in the rule base. After applying these rules, we obtain different outputs for each of the inference rules which are again fuzzy. The output of all those rules is aggregated into a single fuzzy set by combining them with the OR (max) operation.

In the final phase, the determined output fuzzy set edge is defuzzified to get a crisp set, and it becomes the final output. In order to obtain a crisp value from the aggregated fuzzy output set, we calculate the centroid of the fuzzy area under consideration. The block diagram of designed algorithm is depicted in Fig. 1.

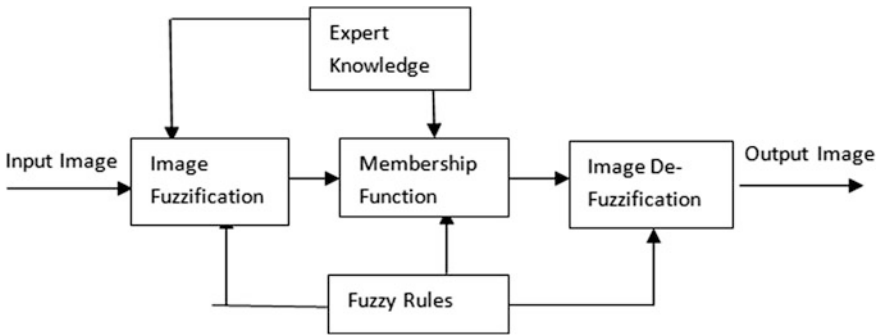


Fig. 1 Block diagram of the FIS

N edge detection results $D_1 \dots N$ are computed using N combinations of the detectors parameters. A pixel location identified as an edge by all N detector setups will have the highest correspondence (N), and a location identified as an edge by only one detector setup will have the lowest [18]. A confusion matrix is a table that supports visualization of the performance of algorithms. Each column of the matrix represents the instances in a predicted class, while each row signifies the instances in an actual class.

In predictive analytics, a confusion matrix, which is a table with two rows and two columns, reports the number of false positives (FP), false negatives (FN), true positives (TP), and true negatives (TN). The accuracy metrics are based on the relation between two regions, R1 and R2, where R1 is the reference image and R2 is the image under analysis. The pixels of both regions are classified as follows:

- NTP (true positive)—pixels present in both regions
- NTN (true negative)—pixels absent in both regions
- NFP (false positive)—pixels present in R2, absent in R1
- NFN (false negative)—pixels present in R1, absent in R2
- N—number of pixels.

Accuracy can be calculated as: $Accuracy = \frac{NTP + NTN}{NTP + NTN + NFP + NFN}$.

The results of Lena image, Coin image, Leaf image, Vegetable images are shown in Figs. 2, 3, 4, and 5, respectively. The accuracy measures as mentioned in Table 1 show that fuzzy logic-based method performs better in comparison to the other techniques.

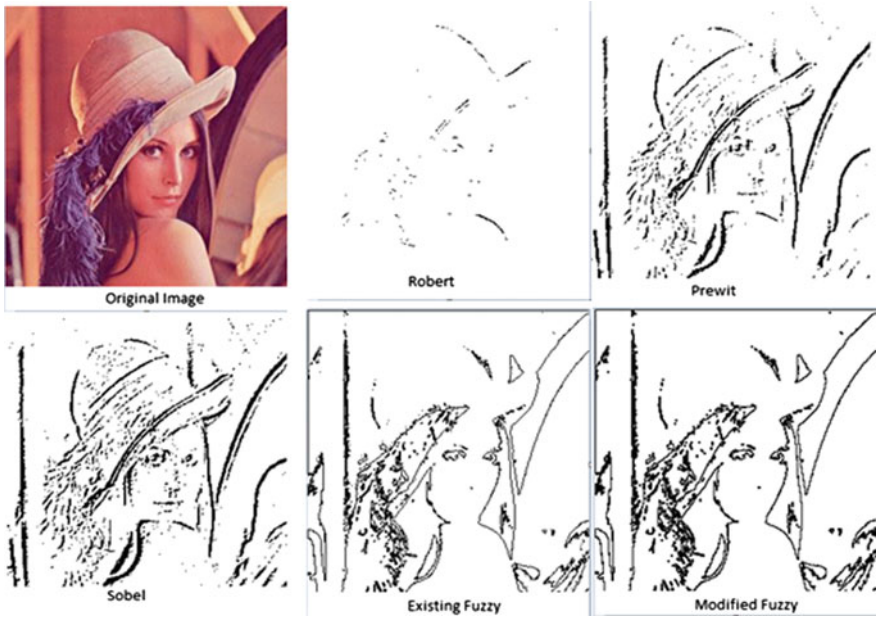


Fig. 2 Results of Lena image

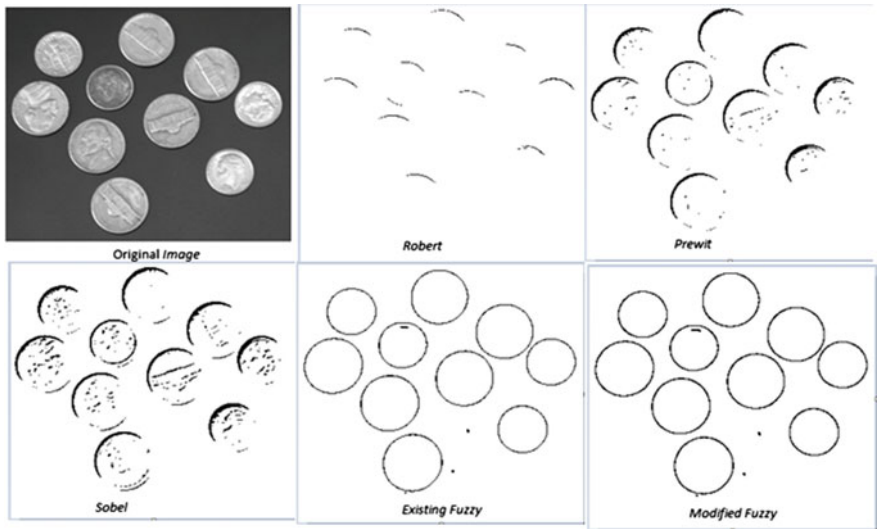


Fig. 3 Results of Coin image

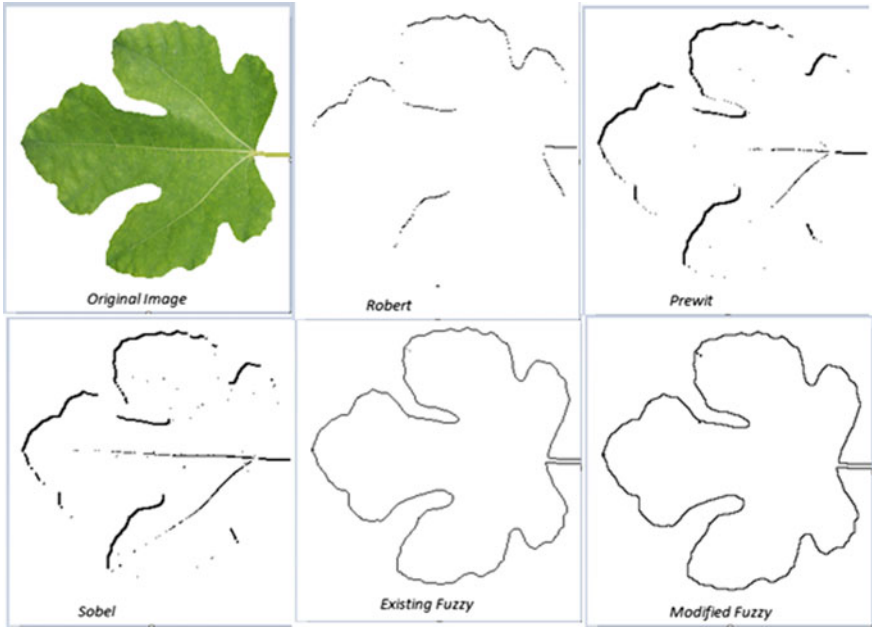


Fig. 4 Results of Leaf image

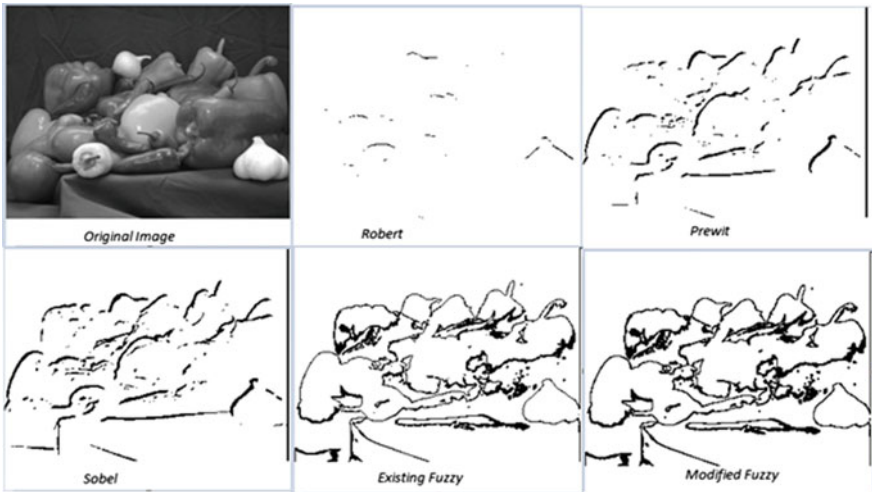


Fig. 5 Results of Vegetable image

Table 1 Accuracy value of different edge detection technique for different images

Images	Robert	Prewit	Sobel	Existing fuzzy	Fuzzy logic
Lena	0.0245	0.505	0.544	0.577	0.62
Coin	0.0824	0.539	0.594	0.608	0.685
Leaf	0.190	0.476	0.497	0.555	0.561
Veg	0.021	0.288	0.327	0.748	0.761

4 Conclusion

The field of edge detection is fast-developing field of research. In many applications like remote sensing images and medical images, the edges are vague. The fuzzy logic-based techniques have increased efficiency of the processing and the result outcomes. These approaches give flexibility in dealing with the variations in parameter value related to any application. The proposed edge detection technique is comparatively evaluated with Robert, Prewit, Sobel, and other existing techniques. For quantitative analysis of the result, we have used confusion matrix and found convincing result. The result achieved from our proposed method with the existing edge detection techniques shows that soft computing approaches perform better. Soft computing approaches help in eliminating the boundaries and restrictions of traditional fixed parameter values, which lead to give better results than the other approaches.

References

1. Chacon, Mario I., Luis Aguilar, and Abdi Delgado. "Definition and applications of a fuzzy image processing scheme." Digital Signal Processing Workshop, 2002 and the 2nd Signal Processing Education Workshop. Proceedings of 2002 IEEE 10th. IEEE, 2002.
2. M.B. Ahmad and T.S. Choi, "Local Threshold and Boolean Function Based Edge Detection", IEEE Transactions on Consumer Electronics, Vol. 45, No 3. August 1999.
3. Tou J. T. and Gonzalez R. C., Pattern Recognition Principles, Addison Wesley, USA, pp. 75–97, 1974.
4. Gary R. M. and Linde Y. "Vector Quantizers and Predicative Quantizers for Gauss-Markov Sources," IEEE Transactions on Communication, vol. 30, no. 2, pp. 381–389, 1982.
5. Thrasyvoulos N. P., "An Adaptive Clustering Algorithm for Image Segmentation." IEEE Transaction on Signal Processing, vol. 40, no. 4, pp. 901–914, 1992.
6. Yan M. X. H. and Karp J. S., "Segmentation of 3D Brain MR Using an Adaptive K-means Clustering Algorithm," in Proceedings of the 4th IEEE Conference on Nuclear Science Symposium and Medical Imaging, San Francisco, USA, vol. 4., pp. 1529–1533, 1995.
7. Yu Y. and Wang J., "Image Segmentation Based on Region Growing and Edge Detection," in Proceedings of the 6th IEEE International Conference on Systems, Man and Cybernetics, Tokyo, vol. 6., pp. 798–803, 1999.
8. Chowdhury M. I. and Robinson J. A., "Improving Image Segmentation Using Edge Information," in Proceedings of the 1st IEEE Conference on Electrical and Computer Engineering, Halifax, Canada, vol. 1, pp. 312–316, 2000.
9. R. C. Gonzalez and R. E. Woods. "Digital Image Processing". 2nd ed. Prentice Hall, 2002.

10. R.M. Haralick, L.G. Shapiro, "Computer and Robot Vision", Volume 1, Addition-Wesley Publishing Company Inc., 1992.
11. Albovik, "Handbook of Image and Video Processing", Academic Press, 2000.
12. Jean Ponce, "Lecture 26: Edge Detection II", 12/2/2004. <http://www-cvr.ai.uiuc.edu/~ponce/fall04/lect26.ppt>.
13. R. Owens, "Lecture 6", Computer Vision IT412, 10/29/1997. http://homepages.inf.ed.ac.uk/rbf/CVonline/LOCAL_COPIES/OWENS/LECT6/node2.html.
14. S. Price, "Edges: The Canny Edge Detector", July 4, 1996. http://homepages.inf.ed.ac.uk/rbf/CVonline/LOCAL_COPIES/MARBLE/low/edges/canny.htm.
15. Qinqing, Gao, et al. "Image enhancement technique based on improved PSO algorithm." Industrial Electronics and Applications (ICIEA), 2011 6th IEEE Conference on. IEEE, 2011.
16. Tyan, C.-Y. and Wang, P. P. "Image processing-enhancement, filtering and edge detection using the fuzzy logic approach." In Fuzzy Systems, 1993., Second IEEE International Conference on, 600–605. IEEE, (1993).
17. Alima DAMAK, Mohamed KRID and Dorra SELLAMI MASMOUDI, "Neural Network Based Edge Detection with Pulse Mode Operations and Floating Point Format Precision" IEEE International Conference on Design & Technology of Integrated Systems in Nanoscale Era, 2008.
18. Gasparotto Boaventura, Adilson Gonzaga. "Method to evaluate the performance of edge detector." (2009).
19. E. R. Davies. "Constraints on the design of template masks for edge detection". Pattern Recognition Lett., vol. 4, pp. 11 1–120, Apr. 1986.
20. V. Torre and T. A. Poggio. "On edge detection". IEEE Trans. Pattern Anal. Machine Intell., vol. PAMI-8, no. 2, pp. 187–163, Mar. 1986.

Development and Performance Analysis of Stand-Alone PV-Based Induction Motor Drive

Sourav Ghosh and Tapas Kumar Saha

Abstract This paper presents a three-stage control system to feed a squirrel-cage induction motor (SCIM) from stand-alone PV systems, through cascaded two-level inverters and an open-winding transformer. The main objective of this system is to extract the effective PV power, while maintaining the DC link voltage in presence of the load torque and solar irradiance variation. The DC link voltage controller is developing the reference speed for the speed controller, followed by current controller. The speed and current controllers are developed through rotor flux-oriented vector control. The SVPWM modulation technique is used to supply the desired voltage vector to the SCIM for good dynamic response. The MATLAB/Simulink simulation results are showing the worth of this proposed control strategy at considered operational conditions.

Keywords Squirrel-cage induction motor (SCIM) · Space vector pulse width modulation (SVPWM) · Standalone · PV

Nomenclature

T_e	Electromagnetic torque developed by SCIM
ω_r	Speed in rad/s
V_{dc}	DC link voltage
i	Current
V	Voltage
L_r, L_s, L_m	Rotor, stator, and mutual inductances, respectively
R_s	Stator Resistance
$\tau = \frac{L_r}{R_r}$	Time constant
$\Psi_r = \frac{L_m i_{ds}}{1 + s\tau}$	Rotor flux linkage
$\omega_{mr} = \frac{L_m i_{qs}}{\Psi_r \tau}$	Slip speed

S. Ghosh (✉) · T. K. Saha
Department of Electrical Engineering, NIT Durgapur, Durgapur 713209, India
e-mail: souravg009@gmail.com

T. K. Saha
e-mail: tapassahanit@gmail.com

$\sigma = 1 - \frac{L_m^2}{L_r L_s}$	Leakage Coefficient
p	No. of poles
$k_{pv}, k_{ps}, k_{pc}, k_{iv}, k_{is}, k_{ic}$	Proportionality and integral constants of PI controller for voltage, speed, and current, respectively

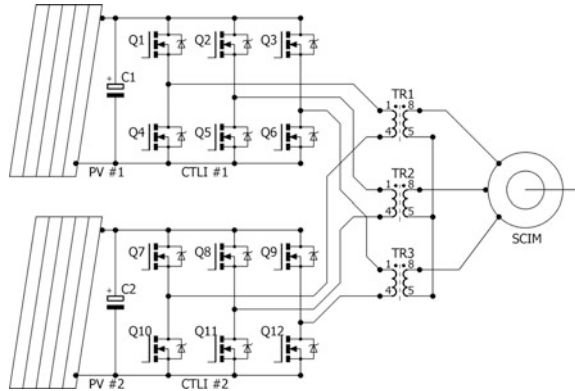
1 Introduction

Harvesting renewable energy and utilization of it is the modern trend of research and possibly the future of power sector. In order to harvest energy from solar irradiation and to convert it in standard AC source, several topologies have been adopted. Generally, two-stage converters are employed for this purpose [1]. In contrast with conventional three-phase inverters, a multilevel VSI produces lesser number of harmonics with stepped AC output voltage which in turn reduce filter circuitry thus showing improved spectral performance. Multilevel VSIs are classified by neutral point clamped (NPC), flying capacitor (FC), and cascaded H-bridge (CHB) inverter, with isolated DC source [2]. However, single-stage CTLI with NPC comprising of v/f control and MPPT can also be directly connected to PV module for driving of open-end winding induction motor [3]. Dual isolated PV source with single-stage CTLI with v/f control and dual MPPT is also very promising [4]. For higher number of multilevel operation, neutral point clamped (NPC) configuration is not preferred in three-phase application because of its increased complexity and lesser economic viability [5].

In this work, the DC link voltages are chosen to be in the order of battery voltage. In case of open circuit, short circuit, and partial shadow on PV panel, power loss is lesser in parallel combination of solar panel unit than series combination [6, 7]. Two isolated PV modules are connected at the DC links of CTLI to drive a SCIM through an open-winding step-up transformer. Different control strategies are implemented to control the VSIs for induction motor drive [8–10]. Among classical electrical drive control methods, field-oriented control (FOC) [11] and direct torque control (DTC) are dominating high-performance industrial drive application [10]. For controlling SCIM by FOC, we need current and speed feedback from SCIM to form closed-loop control. To maintain DC link, three-stage control is required. The voltage controller in the outer loop is responsible for speed reference generation [12].

For realization of PWM, several methods are there [3, 13, 14]. In this work, space vector pulse width modulation (SVPWM) is employed. The complete power circuit is described in Fig. 1. This system controller is implemented in MATLAB/Simulink domain. The simulation results show the effectiveness of the proposed control topology with considered operating conditions.

Fig. 1 Schematic block diagram of proposed SCIM drive



2 Development of Control Topology

2.1 Control System of CTLI for IM Drive

Prime objective of this topology is to maintain a DC link voltage independent of input and output disturbances. The complete control scheme is presented in Fig. 2.

The electromagnetic torque (T_e) developed inside SCIM can be stated as

$$T_e = \frac{2pL_m}{32L_r} i_{qs}^r \Psi_r \tag{1}$$

For generating q -axis voltage through equation given by

$$V_{qs}^r = \left(R_s i_{qs}^r + \sigma L_s \frac{di_{qs}^r}{dt} \right) + \frac{L_m}{L_r} \Psi_r (\omega_{mr} + \omega_e) + \sigma L_s i_{ds}^r (\omega_{mr} + \omega_e) \tag{2}$$

And fed through current controller to generate d -axis voltage by the equation described as

$$V_{ds}^r = \left(R_s i_{ds}^r + \sigma L_s \frac{di_{ds}^r}{dt} \right) + \frac{L_m}{L_r} \frac{d\Psi_r}{dt} - \sigma L_s i_{qs}^r (\omega_{mr} + \omega_e) \tag{3}$$

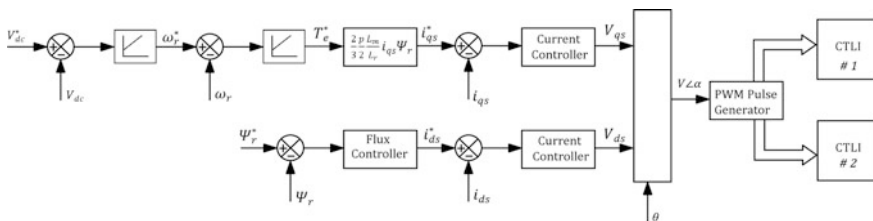


Fig. 2 Three-stage SCIM controller

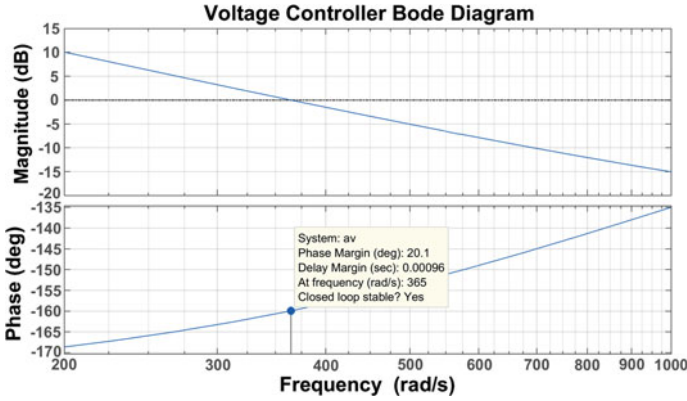


Fig. 3 Bode plot of the DC link voltage controller’s transfer function

The frequency response of the three control loops is described here. The bode plot of voltage controller is designed to have corner frequency at 365 rad/s, as shown in Fig. 3.

The bode plots of speed controller and current controller are shown in Fig. 4a, b. The controllers are designed to operate at 1000 and 3000 rad/s, respectively.

2.2 SVPWM Realization

The vector V_r in Fig. 5c represents the voltage reference vector with angle α generated from two equal magnitudes and 180° phase-shifted vectors of two CTLIs, respectively. To obtain voltage Vector V , inverter #1 the switching states performed are (0-1-2-7-2-1-0) (Fig. 5b). Simultaneously, for v' , the switching states performed are (0-4-5-7-5-4-0) (Fig. 5a).

For ON time and OFF time calculation, the angle α is equally divided into six sectors of 60° by the hexagon representation. These time values and sector number together form a value for V_a , V_b , and V_c which are then compared with a triangular wave to generate PWM signal for the inverters.

3 Simulation Result Discussion

The simulated test circuit consists of two solar PV panels of 48 V MPP, 2 nos. three-phase two-level VSI (CTLI) each having six IGBTs (900 V, 25 A), one 5 KVA, 48/230 V open terminal primary three-phase transformer and an 1 HP, 415 V, 50 Hz, 4 pole, 1.8 A SCIM. The study of the system is carried out with

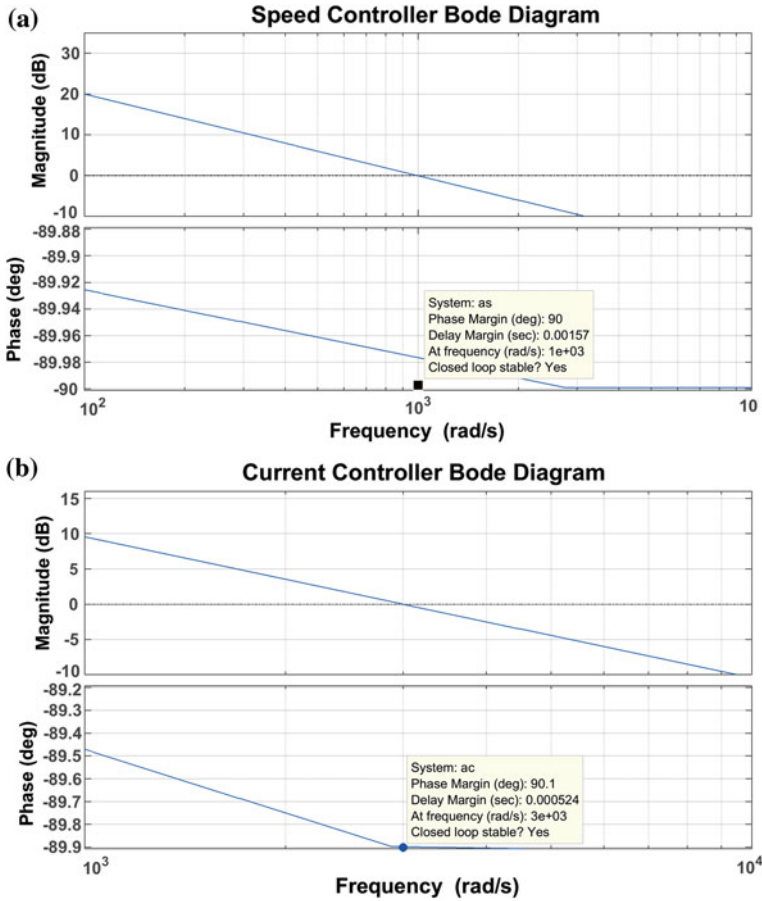
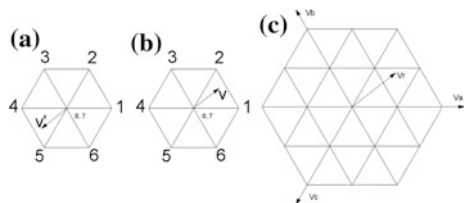


Fig. 4 Bode plot of a speed controller and b current controller's transfer function

Fig. 5 SVPWM generation



three condition variations as seen in Figs. 6a and 7a, b. The load torque is increased from 4 to 5.5 Nm at 4 s. Next the reference of DC link voltage is varied from 60 to 48 v in a slope at 7.5 s. The variation is in solar insolation input, which increases and decreases by 20% at 13 and 17 s, respectively.

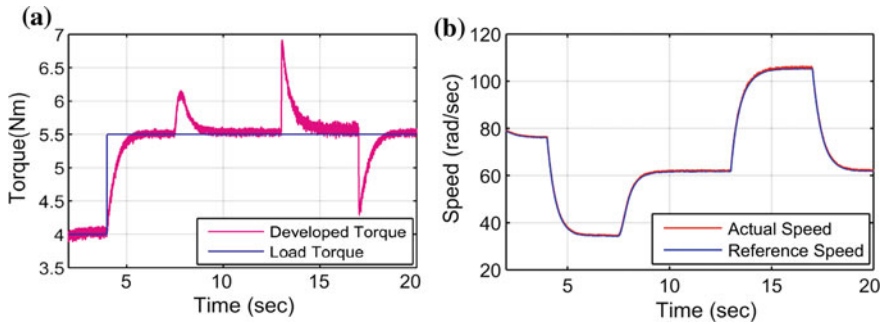


Fig. 6 a Load torque versus actual torque and b reference speed versus actual motor speed

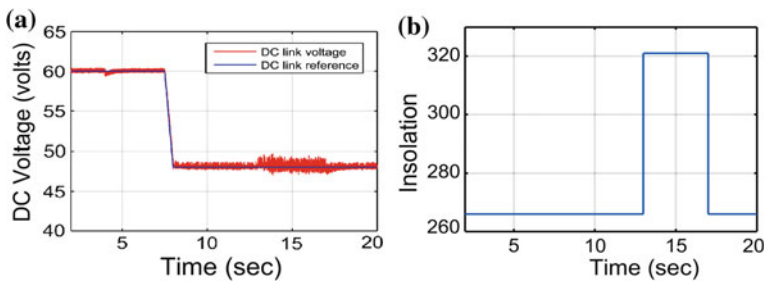


Fig. 7 a Reference DC link voltage versus actual voltage and b solar insolation variation

3.1 Increment in Load Torque

Figure 6b is showing motor speed decrement to compensate the increased load torque from 4 to 5.5 Nm, as shown in Fig. 6a, where the solar irradiation and reference DC link voltage are considered to be constant. Settling time of speed is approximately 3 s.

3.2 Alteration in DC Link Voltage Reference

The actual DC link voltage is maintained at the reference DC link voltage throughout the time of operation as shown in Fig. 7a. It is also observed that the change in DC link voltage reference was swiftly tracked by the system with 24 V/s slope. Also, the increment of motor speed due to PV panes is supplying more power because of near MPP operating voltage. In this case, settling time of speed is approximately 3 s.

3.3 Variation in Solar Irradiation

Figure 7b is showing the nature of variation in solar irradiance during $t = 13$ to $t = 17$ s. In this period, the PV panels are producing more power, thus increasing the speed which settles in approximately 3 s.

4 Conclusion

This paper developed a topology to be implemented on CTLI fed stand-alone drive for normal SCIM with isolated low voltage DC source/PV Panel with an open-winding three-phase step-up transformer. With CTLI, seven-level voltage was possible to achieve at inverter output. The proposed control system along with SVPWM successfully controlled and maintained the DC link voltage during variation in load torque, solar irradiance level, and reference value of DC link voltage. The power supplied by the PV is constant during load variations, while the power changes with solar irradiance level as well as PV output voltages successfully.

References

1. João Victor Mapurunga Caracas; Guilherme de Carvalho Farias; Luis Felipe Moreira Teixeira; Luiz Antonio de Souza Ribeiro, Implementation of a High Efficiency, High Lifetime, and Low Cost Converter for an Autonomous Photovoltaic Water Pumping System, IEEE Transactions on Industry Applications, Volume: 50, Issue: 1 Pages: 631–641.
2. Rodriguez J, Lai JS, Peng FZ. Multilevel inverters: a survey of topologies, control and applications. IEEE Trans Ind Electron 2002; 49(4):724–38.
3. Jain, S.; Thopukara, A.K.; Karampuri, R.; Somasekhar, V. T., A Single-Stage PhotoVoltaic System for a Dual Inverter fed Open-End Winding Induction Motor Drive for Pumping Applications, IEEE Transactions on Power Electronics Year: 2015, Volume: 30, Issue: 9, Pages: 4809–4818.
4. Jain, S., Ramulua, C., Padmanabanb, S., Olorunfemi Ojoc, J, Ertase, A. H., Dual MPPT algorithm for dual PV source fed Open-End Winding Induction Motor Drive for pumping application, Engineering Science and Technology, an International Journal Volume 19, Issue 4, December 2016, Pages 1771–1780.
5. Prasad, C.S.P.; Nireekshan, N.; A Higher Voltage Multilevel Inverter with Reduced Switches for Industrial Drive, International Journal of Science, Engineering and Technology Research (IJSETR), Vol. 5, Issue 1, January 2016.
6. Miiki, A. and Valkealahti, S., “Power Losses in Long String and Parallel-Connected Short Strings of Series-Connected Silicon-Based Photovoltaic Modules Due to Partial Shading Conditions,” IEEE Trans. on Energy Conversion, Vol. 27, no. 1, pp. 173–183, March 2012.
7. Vijayalekshmy, S.; Ramalyer, S.; Beevi, B., “Evaluation of power losses in a short string of series-connected and parallel-connected photovoltaic modules for low power application,” in Control Communication and Computing (ICCC), 2013 International Conference on, pp. 125–130.

8. Habibullah, M.; Dah-Chuan Lu, D; Xiao, D; Fletcher, J.E.; Rahman, M.F., Predictive Torque Control of Induction Motor Sensorless Drive Fed by a 3L-NPC Inverter, *IEEE Transactions on Industrial Informatics*, Year: 2017, Volume: 13, Issue: 1, Pages: 60–70.
9. Hannan, M. A.; Ali, J. A.; Mohamed, A; Uddin. M.N., A Random Forest Regression Based Space Vector PWM Inverter Controller for the Induction Motor Drive, *IEEE Transactions on Industrial Electronics*, Year: 2017, Volume: 64, Issue: 4, Pages: 2689–2699.
10. Lascu, C.; Jafarzadeh, S.; Fadali, M. S.; Blaabjerg, F., Direct Torque Control with Feedback Linearization for Induction Motor Drives, *IEEE Transactions on Power Electronics*, Year: 2017, Volume: 32, Issue: 3, Pages: 2072–2080.
11. Fadul, S.M.E.; Aris, I.; Misron, N.; Halin, I. A.; Parvez Iqbal, A. K. M., Modelling and Simulation of Electric Drive Vehicle Based on Space Vector Modulation Technique and Field Oriented Control Strategy, 2017 International Conference on Communication, Control, Computing and Electronics Engineering (ICCCCEE), Year: 2017, Pages: 1–7.
12. Mishra, R; Saha, T. K.; “Development of A Standalone VSCF Generation Scheme Through Three Stage Control of SCIG”, in Region 10 Conference (TENCON), 2016 IEEE, pp. 3538–354.
13. Jain, S.; Karampuri, R.; Somasekhar, V. T.; An Integrated Control Algorithm for a Single-Stage PV Pumping System Using an Open-End Winding Induction Motor, *IEEE Transactions on Industrial Electronics*, Year: 2016, Volume: 63, Issue: 2, Pages: 956–965.
14. Lakhimsetty, S.; Surulivel, N.; Somasekhar, V. T., Improvised SVPWM Strategies for an Enhanced Performance for a Four-Level Open-End Winding Induction Motor Drive, *IEEE Transactions on Industrial Electronics*, Year: 2017, Volume: 64, Issue: 4, Pages: 2750–2759.

Design of P-I Controller of Wind Turbine with Doubly Fed Induction Generator Using Flower Pollination Algorithm

Arnab Kumar Mondal and Parthasarathi Bera

Abstract In the present work, the performance of a Wind Turbine (WT) with doubly fed induction generator (DFIG) interfaced with power grid is investigated. Proportional-Integral (P-I) controllers have been considered for controlling the system, and the small signal stability model of the system has been considered for designing the controller. Gain settings of P-I controllers of WT with DFIG are optimized using Flower Pollination Algorithm (FPA). Analysis reveals that the P-I controllers with optimized gains for WT for DFIG system improve the dynamic responses significantly. Sensitivity analysis has been performed by changing WT and DFIG parameters, and results reveal that FPA-optimized P-I controller gains obtained for nominal values of these are quite robust and need not be changed.

Keywords DFIG · Wind Turbine · FPA · Sensitivity analysis

1 Introduction

For the deficiency of the conventional source of energy and for the environmental purpose, the use of wind power generation has been grown fast. The total capacity of wind power plant installed at present is approximately 432 GW [1]. So the wind power has been penetrated in grids, and the influence of WT on power system stability is rising gradually. There are several types of approach in designing WT power generation. But the recent approach of the WT with DFIG is becoming favourite among industries as it is more efficient than the other approaches. The WT

A. K. Mondal · P. Bera (✉)
Department of Electrical Engineering, Kalyani Government
Engineering College, Kalyani 741235, India
e-mail: parthabera1977@gmail.com

A. K. Mondal
e-mail: akmondal92@gmail.com

© Springer Nature Singapore Pte Ltd. 2018
R. Bera et al. (eds.), *Advances in Communication, Devices and Networking*,
Lecture Notes in Electrical Engineering 462,
https://doi.org/10.1007/978-981-10-7901-6_82

with DFIG system also has the characteristics of low investment and flexibility in control [2]. The third-order model is the most suitable among the other approaches of DFIG-based Wind Turbine for the analysis of small signal stability. The third-order model is developed by [2]. The dynamic model and state space model for the analysis of small signal stability have been illustrated in [3] without the entire design of the controllers for simplicity.

The control strategy of DFIG has been developed in [4] where the system can be controlled independently in case of controlling active or reactive power. The approach of designing a controller model for grid-connected WT with DFIG, known as Scherbius scheme, has been presented in [5] using two back-to-back PWM converter. The advantage of the control scheme is that it has smooth operation through synchronous speed, low distortion fed to supply and system power factor controlling ability. The poor selection of the proportional gain of the speed and power factor controller effects on the stability of the DFIG significantly which has been demonstrated in [6]. The decoupled control, based on the Proportional-Integral (P-I) controller, has become very popular and has been used in many research works [7–10]. Recently, Genetic Algorithm (GA) and Particle Swarm Optimization (PSO) are used to optimize the gains of the P-I controller for the optimal control of static VAR controller parameters, hydro-generator governor, and WT with DFIG [11–14]. But the limitation of GA is that it's degradation in efficiency and the premature convergence in terms of reducing the search capability [15]. On the other hand, the ease of tendency to move into local optimum in high-dimensional space, the low convergence rate in the iterative process and going to a worse position according to some probability are the limitations of PSO [16].

Flower Pollination Algorithm (FPA), a new optimization method, is an evolutionary computation technique inspired from pollination process of flower in nature. It has been found that the simulation results of the FPA are more efficient than both GA and PSO, and FPA can also solve the nonlinear design benchmark, which shows the convergence rate is almost exponential [17]. FPA has been used in structural engineering [18], and multi-objective optimization [19]. FPA also has been used in the optimal sizing of the wind/solar/hydro in an isolated power system [20] and in the optimization of Proportional-Integral Proportional-Derivative cascade controller in automatic generation control of a multi-area power system [21].

The performance of a Wind Turbine with doubly fed induction generator is investigated in the present work, and the small signal stability model has been considered for controlling DFIG system interfaced with power grid using the Proportional-Integral controller. Gains of the P-I controller of WT with DFIG are optimized using Flower Pollination Algorithm, and the dynamic responses of real and reactive power and DC link and terminal voltage have been compared considering with and without the optimized value of Proportional-Integral controller. Further, sensitivity analyses have been performed by changing the parameters of WT, DFIG system and grid-side converter.

2 DFIG System Connected with Power Grid

In general practice, there are several Wind Turbines connected to a wind power generation station. But there is no dependency between the WT if the controllers of the Wind Turbines are well designed [22]. So for simplicity, only one WT is considered in the model while designing the controller. In the present work, a WT with DFIG connected with power grid is considered and is shown in Fig. 1.

3 Modelling of the System

3.1 Model of DFIG

For DFIG system, power can be fed from both stator and rotor and the equivalent circuit of DFIG as represented in Fig. 2a [23] is similar to an induction machine.

3.2 Model of Drive Train

The drive train means the combination of mechanical parts of Wind Turbine and is imitated by a two-mass model [3]. The corresponding equations of two-mass model are given by

$$2H_t \frac{d\omega_t}{dt} = T_m - T_{sh} \tag{1}$$

$$\frac{d\theta_{tw}}{dt} = \omega_t - (1 - s_r)\omega_s \tag{2}$$

$$2H_g \frac{dS_r}{dt} = -T_{em} - T_{sh} \tag{3}$$

$$T_{sh} = K_{sh}\theta_{tw} + D_{sh} \frac{d\theta_{tw}}{dt} \tag{4}$$

Fig. 1 Wind Turbine with DFIG connected with power grid

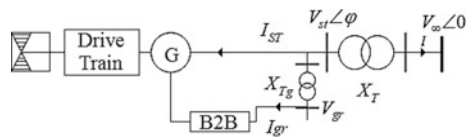
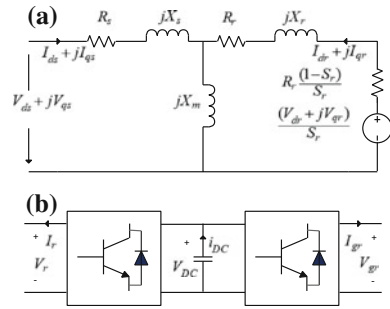


Fig. 2 Equivalent circuit:
a DFIG with respect to stator
b Back-to-back converter



3.3 Model of Converter

Figure 2b shows the configuration of the back-to-back converters with DC link capacitor and the directions of the currents in the converter. As the real power is balance, the equation of power balance is

$$P_r = P_g + P_{DC} \tag{5}$$

where

- P_r real power at the rotor-side converter end;
- P_g real power at the grid-side converter end;
- P_{DC} real power of the DC link. The corresponding equations are

$$P_r = v_{dr}i_{dr} + v_{qr}i_{qr} \tag{6}$$

$$P_g = v_{dg}i_{dg} + v_{qg}i_{qg} \tag{7}$$

$$P_{DC} = C_{vDC} \frac{dv_{DC}}{dt} \tag{8}$$

So Eq. (5) can be modified as

$$C_{vDC} \frac{dv_{DC}}{dt} = v_{dg}i_{dg} + v_{qg}i_{qg} - (v_{dr}i_{dr} + v_{qr}i_{qr}) \tag{9}$$

4 Block Diagram of Converter with Controller

4.1 Rotor-Side Converter Controller

The aim of controlling the rotor-side converter controller is to control the DFIG output active power for tracking the input of the WT torque and to maintain the

terminal voltage to a set value. The block diagram of rotor-side converter controller model is shown in Fig. 3a, and the corresponding equations are given [4] by

$$\frac{d(\Delta P^*)}{dt} = \Delta P_{ref} - \Delta P_s \tag{10}$$

$$\Delta i_{qr_ref} = K_{p1}(\Delta P_{ref} - P_s) - K_{i1}\Delta P \tag{11}$$

$$\frac{d(\Delta i_{qr}^*)}{dt} = \Delta i_{qr_ref} - \Delta i_{qr} \tag{12}$$

$$\frac{d(\Delta v^*)}{dt} = \Delta V_{s_ref} - \Delta V_s \tag{13}$$

$$\Delta i_{dr_ref} = K_{p3}(\Delta V_{s_ref} - \Delta V_s) - K_{i3}\Delta v^* \tag{14}$$

$$\frac{d(\Delta i_{dr}^*)}{dt} = \Delta i_{dr_ref} - \Delta i_{dr} \tag{15}$$

$$\Delta v_{qr} = K_{p2} \left(K_{p1} \frac{d\Delta P^*}{dt} + K_{i1}\Delta P^* - i_{qr} \right) + K_{i2}\Delta i_{qr} + s_r\omega_s L_m \Delta i_{ds} + s_r\omega_s L_{rr} \Delta i_{qr} \tag{16}$$

$$\Delta v_{dr} = K_{p2} \left(K_{p1} \frac{d\Delta v^*}{dt} + K_{i3}\Delta v^* - \Delta i_{dr} \right) - K_{i2}\Delta i_{dr} - s_r\omega_s L_m \Delta i_{qs} + s_r\omega_s L_{rr} \Delta i_{dr} \tag{17}$$

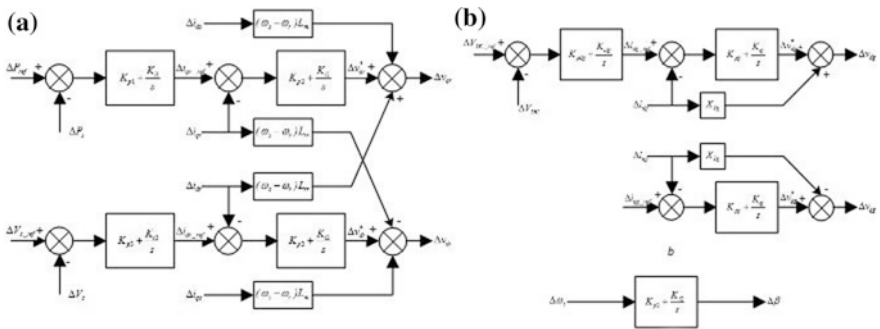


Fig. 3 Control block diagram of DFIG. **a** Block diagram of rotor-side controller **b** Block diagram of grid-side controller **c** Block diagram of pitch controller

where

ΔP_{ref} Real power control reference and

$$\Delta P_{\text{ref}} = \Delta P_B \frac{\Delta \omega_t}{\Delta \omega_{tB}} \quad (18)$$

4.2 Grid-Side Converter Controller

The aim of grid-side converter controller is to maintain the DC link voltage and control the terminal reactive power. Its block diagram is shown in Fig. 3b, and the corresponding equations are given by

$$\frac{d\Delta v_{\text{DC}}^*}{dt} = \Delta v_{\text{DC_ref}} - \Delta v_{\text{DC}} \quad (19)$$

$$\Delta i_{\text{dg_ref}} = -K_{\text{pdg}} \Delta v_{\text{DC}} + K_{\text{idg}} \Delta v_{\text{DC}}^* \quad (20)$$

$$\frac{d\Delta i_{\text{dg}}^*}{dt} = \Delta i_{\text{dg_ref}} - \Delta i_{\text{dg}} \quad (21)$$

$$\frac{d\Delta i_{\text{qg}}^*}{dt} = \Delta i_{\text{qg_ref}} - \Delta i_{\text{qg}} \quad (22)$$

$$\Delta v_{\text{dg}} = K_{\text{Pg}} \left(-K_{\text{pdg}} \frac{d\Delta v_{\text{DC}}^*}{dt} + K_{\text{idg}} \Delta v_{\text{DC}}^* - \Delta i_{\text{dg}} \right) + K_{\text{ig}} \Delta i_{\text{dg}}^* \quad (23)$$

$$\Delta v_{\text{qg}} = K_{\text{Pg}} (\Delta i_{\text{qg_ref}} - \Delta i_{\text{qg}}) + K_{\text{Iq}} \Delta i_{\text{qg}}^* \quad (24)$$

4.3 Pitch Controller

The aim of pitch controller is to control the rotating speed of the Wind Turbine to the optimal speed. The block diagram of pitch controller is shown in Fig. 3c, and the corresponding equation is given by

$$\frac{d(\Delta \beta)}{dt} = K_{p4} \frac{\Delta T_m - \Delta T_{\text{sh}}}{2H_t} + K_{i4} \Delta \omega_t \quad (25)$$

5 State Space Representation of the Small Signal Stability Analysis Model of the System

The state space representation of the model for WT with DFIG system interfaced with power grid is given below:

$$\dot{x} = Ax + Bu + Cz \tag{26}$$

where A , B and C are the system, control and input matrices.

Here, x , z and u are given by

$$x = [\Delta\omega_r, \Delta\beta, \Delta\theta_{tw}, \Delta s_r, \Delta i_{ds}, \Delta i_{qs}, \Delta E'_d, \Delta E'_q, \Delta P^*, \Delta i_{qr}^*, \Delta v^*, \Delta i_{dr}^*, v_{dc}, \Delta v_{DC}^*, \Delta i_{dg}, \Delta i_{qg}]^T$$

$$z = [\Delta v_{dr}, \Delta v_{qr}, \Delta v_{dg}, \Delta v_{qg}]^T \quad \text{and} \quad u = [\Delta v_{ds}, \Delta v_{qs}, \Delta i_{dg}, \Delta i_{qg}]^T$$

6 Objective Function

For optimizing by FPA, the objective function based on ISE criterion is used [24, 25]

$$J = \int_0^{\infty} (\Delta P_s)^2 dt \tag{27}$$

7 Flower Pollination Algorithm

Flower Pollination Algorithm (FPA) is aroused from pollination process of the flower which has been developed by Yang [18]. The following four rules are used from pollination process of the flower.

1. Cross-pollination or biotic pollination.
2. Self-pollination or local pollination.
3. Flower constancy.
4. Switch probability which is between 0 and 1.

The formula of the Global pollination is in Eq. (28)

$$x_i^{t+1} = x_i^t + L(x_i^t - g^*) \tag{28}$$

g^* is the current best solution.

L is derived from the Lévy distribution.

$$L \sim \frac{\lambda \Gamma(\lambda) \sin(\pi\lambda/2)}{\pi} \frac{1}{1 + s^{\lambda+1}} \tag{29}$$

The formula of the Local pollination is in Eq. (30)

$$x_i^{t+1} = x_i^t + \varepsilon(x_j^t - x_k^t) \tag{30}$$

where x_j^t and x_k^t are solutions of different plants. The value of ε is considered randomly between 0 and 1.

In the present work, the gains of P-I controllers are obtained by minimizing the objective function as given by Eq. (27) using FPA. The values of FPA parameters

Fig. 4 Flow chart of FPA

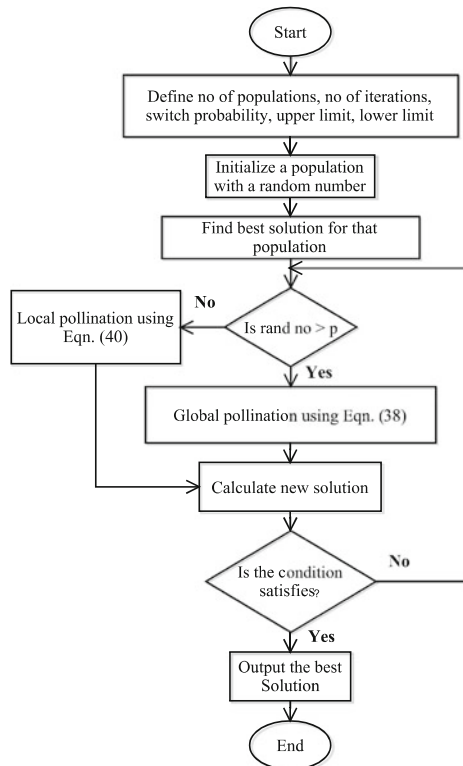
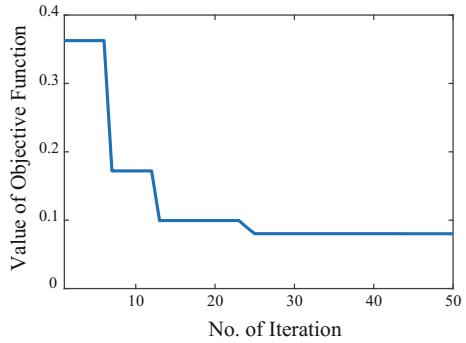


Fig. 5 Optimization of objective function by FPA



such as switch probability (p) = 0.7, strength of the pollination (λ) = 1.02 and a scaling factor (γ) = 0.15 have been considered, and the 100 number of populations and 50 number of iterations have been considered. The flow chart for FPA for the present problem is shown in Fig. 4, and the variation of values of objective function with respect to number of iteration is shown in Fig. 5.

8 Result

For verifying the enhancement in the stability by the controllers of rotor-side, grid-side and pitch controller of the DFIG with the optimized gains, simulations are performed by MATLAB programming and the step changes of 10% have been applied simultaneously to the ΔP_{ref} and ΔV_{ref} , respectively. Table 1 shows the values of gains of P-I controllers optimized using FPA based on the objective function given in Eq. (27). The comparative study of dynamic responses of the output active power, output reactive power, DC link voltage and terminal voltages is shown in Figs. 6, 7, 8 and 9, respectively, with and without FPA optimized the

Table 1 Values of gains of P-I controllers optimized by FPA

K_{p1}	K_{i1}	K_{p2}	K_{i2}	K_{p3}	K_{i3}
2.013	0.3154	0.9943	0.0500	1.9421	-0.115
K_{p4}	K_{i4}	K_{pdg}	K_{idg}	K_{pg}	K_{ig}
0.2544	0.0411	0.501	0.011	0.705	0.002

Fig. 6 Dynamic response of active power

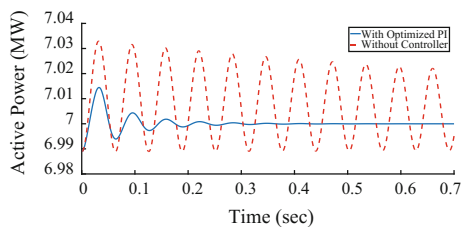


Fig. 7 Dynamic response of reactive power

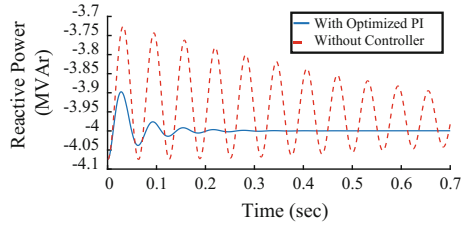


Fig. 8 Dynamic response of DC link voltage

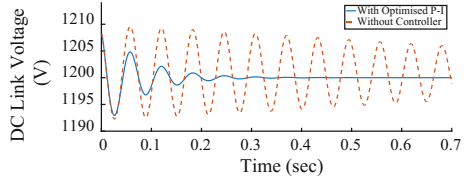
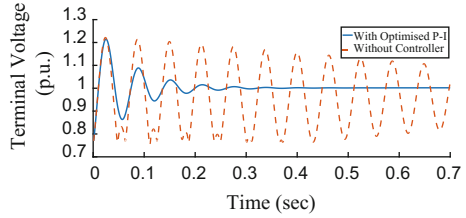


Fig. 9 Dynamic response of terminal voltage



rotor-side, grid-side and pitch controller. Table 1 shows the values of K_p and K_i for three-stage P-I controller optimized using flower flow algorithm. The effect of variation of system parameters (H_g , H_t , D_{sh} , L_s , C and X_{Tg}) has been observed by varying $\pm 40\%$ of nominal value one at a time, and the values of peak overshoot, settling time and the value of objective function J have been calculated and the results are given in Table 2. From Table 2, it is seen that the effect of change of system parameters is negligible.

Table 2 Sensitivity analysis of WT with DFIG system

Parameter variation	% change	Overshoot (M_p) in p.u.				Settling time (T_s) in sec				Objective function (J)
		ΔP	ΔQ	ΔV_{DC}	ΔV_t	ΔP	ΔQ	ΔV_{DC}	ΔV_t	
Nominal	0	0.0023	0.0255	0.0017	0.207	0.452	0.346	0.432	0.401	0.0802
H_g	+40	0.0025	0.0269	0.0021	0.205	0.462	0.351	0.453	0.432	0.0811
	-40	0.0021	0.0241	0.0013	0.186	0.441	0.334	0.422	0.389	0.0787
H_t	+40	0.0035	0.0282	0.0021	0.215	0.472	0.376	0.489	0.421	0.0815
	-40	0.0019	0.0231	0.0013	0.195	0.437	0.314	0.416	0.375	0.0764
D_{sh}	+40	0.0024	0.0254	0.0018	0.209	0.449	0.326	0.421	0.390	0.0797
	-40	0.0021	0.0257	0.0015	0.201	0.492	0.385	0.461	0.461	0.0843
L_s	+40	0.0026	0.0246	0.0014	0.194	0.453	0.347	0.432	0.401	0.0801
	-40	0.0018	0.0268	0.0027	0.219	0.451	0.346	0.431	0.402	0.0803
C	+40	0.0022	0.0255	0.0009	0.199	0.447	0.345	0.429	0.402	0.0802
	-40	0.0023	0.0256	0.0041	0.217	0.459	0.347	0.430	0.400	0.0804
X_{Tg}	+40	0.0018	0.267	0.0020	0.210	0.461	0.343	0.435	0.406	0.0795
	-40	0.0031	0.242	0.0016	0.202	0.445	0.344	0.436	0.410	0.0806

9 Conclusion

In this work, a WT with DFIG connected with power grid has been presented and the small signal stability analyses have been performed for designing the gains of P-I controllers for rotor and grid-side converter and pitch controller. The values of gains of P-I controllers have been optimized based on Flower Pollination Algorithm (FPA), and the dynamic responses of real and reactive power and DC link and terminal voltage have been compared considering with and without the controllers. Analysis reveals that the dynamic responses improve significantly with the use of P-I controller optimized by FPA for WT for DFIG system. Sensitivity analysis has been performed by varying different parameters of WT and DFIG system and results reveal that FPA-optimized P-I controller gains obtained for nominal values of these parameters are quite robust.

References

1. Global Wind Energy Council: Global Wind Report, Annual Market Update 2015.
2. Lei Y., Mullane A., Lightbody G., and Yacamini R.: ‘Modeling of the wind turbine with a doubly fed induction generator for grid integration studies’, IEEE Trans. Energy Conversion, 2006, 21, (1), pp. 257–264.
3. Mei F., and Pal B.C.: ‘Modelling and small-signal analysis of a grid connected doubly-fed induction generator’. Proc. of IEEE PES General Meeting, 2005, San Francisco, USA.
4. Yamamoto M., and Motoyoshi O.: ‘Active and reactive power control for doubly-fed wound rotor induction generator’, IEEE Transaction Power Electronics, 1991.

5. Pena R., Clare J.C., and Asher G.M.: 'Doubly fed induction generator using back-to-back PWM converters and its application to variable-speed wind-energy generation', *IEE Proc., Electr. Power Appl.*, 1996, 143, (3), pp. 231–241.
6. Ekanayake J.B., Holdsworth L., Wu X.G., and Jenkins N.: 'Dynamic modelling of doubly fed induction generator wind turbine', *IEEE Trans. Power Syst.*, 2003, 18, (2), pp. 803–809.
7. Muller B.S., Deicke M., and De Doncker R.W.: 'Doubly fed induction generator system', *IEEE Ind. Appl. Mag.*, 2002, 8, (3), pp. 26–33.
8. Mehta B., Bhatt P., Pandya V.: 'Small signal stability enhancement of DFIG based wind power system using optimized controllers' parameter', *Electrical Power and Energy Systems* 70 (2015) 70–82.
9. Mehdipour C., Hajizadeh A., Mehdipour A.: 'Dynamic modeling and control of DFIG-based wind turbines under balanced network conditions.', *Electrical Power and Energy Systems* 83 (2016) 560–569.
10. Shehata E.G., Salama G. M.: 'Direct power control of DFIGs based wind energy generation systems under distorted grid voltage conditions', *Electrical Power and Energy Systems* 53 (2013) 956–966.
11. Ju, P., Handschin, E., and Reyer, F.: 'Genetic algorithm aided controller design with application to SVC', *IEE Proc., Gener. Transm. Distrib.*, 1996, 143, (3), pp. 258–262.
12. Lansberry, J.E., and Wozniak, L.: 'Adaptive hydrogenator governor tuning with a genetic algorithm', *IEEE Trans. Power Syst.*, 1994, 9, (1), pp. 179–183.
13. Wu F., Zhang X. P., Godfrey K. and Ju P.: 'Small signal stability analysis and optimal control of a wind turbine with doubly fed induction generator', *IET Gener. Transm. Distrib.*, 2007, 1, (5), pp. 751–760.
14. Tang Y., Ju P.: 'Optimized Control of DFIG-Based Wind Generation Using Sensitivity Analysis and Particle Swarm Optimization', *IEEE Transactions On Smart Grid*, Vol. 4, No. 1, March 2013.
15. Fogel, D.B.: 'Evolutionary computation: toward a new philosophy of machine intelligence', *IEEE Press*, New York, 2000, 2nd edition.
16. S. S., Raghuvanshi M. M., Malik L.: 'A Brief Review on Particle Swarm Optimization: Limitations & Future Directions', *International Journal of Computer Science Engineering (IJCSSE)* Vol. 2 No. 05 Sep 2013 pp. 196–200.
17. Yang X.: 'Flower Pollination Algorithm for Global Optimization', *Unconventional Computation and Natural Computation 2012*, Lecture Notes in Computer Science, Vol. 7445, pp. 240–249 (2012).
18. Nigdeli S., Bekdaş G., Yang X.: 'Application of the Flower Pollination Algorithm in Structural Engineering.', X.-S. Yang et al. (eds.), *Metaheuristics and Optimization in Civil Engineering*.
19. Yang Y., He X.: 'Flower Pollination Algorithm: A Novel Approach for Multi-objective Optimization', *Engineering Optimization*, vol. 46, Issue 9, pp. 1222–1237 (2014).
20. Potli M., Damodharam Y., Balachandra J. C.: 'Optimal Sizing of Wind/Solar/Hydro in an Isolated Power System using SMUGF based FPA.' 3rd International Conference on Advanced Computing and Communication Systems (ICACCS -2016), Jan. 22 & 23, 2016, Coimbatore, INDIA.
21. Dash P., Saikia L. C., Sinha N.: 'Flower Pollination Algorithm Optimized PI-PD Cascade Controller in Automatic Generation Control of a Multi-Area Power System', *Electrical Power and Energy Systems* 82 (2016) 19–28.
22. Akhmatov V., "Analysis of dynamic behavior of electric power systems with large amount of wind power," Ph. D, Tech. Univ. Denmark, Kgs, Lyngby, Denmark, 2003.
23. Kundur, P.: 'Power system stability and control' (McGraw-Hill, Inc, New York, 1994), pp. 279–306.
24. Schultz, W.C., Rideout, V.C., Control system performance measures: past, present and future, *IRE Transactions on Automatic Control*, AC- 6,22, pp. 22–35, 1961.
25. Ogata, K., *Modern Control Engineering*, A book, Prentice-Hall, Englewood cliffs, NJ, pp. 293–313, 1970.

Dynamic Analysis of Two-Link Robot Manipulator for Control Design

Gourab Nandy, Basukinath Chatterjee and Amartya Mukherjee

Abstract Robot manipulators have become a major component in the manufacturing sectors which are utilized in several applications such as grinding, welding, assembling, and mechanical handling due to quite efficient accuracy, speed, and repeatability. These applications require proper path planning, proper generation of trajectory, and most importantly a control design. This work deals with the problem of modeling and control of a two-link robot manipulator which is a classical and simple example of robot followed in understanding the fundamentals of robotic manipulator. Since, the closed form solutions are not available so we use numerical solution. Due to these uncertainties and nonlinear behavior, it is a very difficult task to control the motion of the robotic arm at the accurate position. Here, we are focused on designing and implementation of PID controller to control the motion of the robot arm. MATLAB has been used to carry out simulation after derivation of necessary equations.

Keywords Robot manipulator · Dynamic control · PID control
Trajectory tracking · Simulation

G. Nandy (✉) · B. Chatterjee
Department of Electronics and Telecommunication Engineering,
Jadavpur University, Kolkata, India
e-mail: gnandy91@gmail.com

B. Chatterjee
e-mail: basuki.chatterjee@gmail.com

A. Mukherjee
Department of CSE, IEM Salt Lake, Kolkata, India
e-mail: mamartyacse1@gmail.com

1 Introduction

It is known to all the nature of the robot manipulators. Their nature is highly nonlinear, coupled dynamically, and time-varying system which are extensively used in industries. They are generally subjected to uncertainties because of which it is a challenging task to control the motion of robot manipulator at accurate position [1]. For accurate results, the robot has to follow predefined trajectories as close as possible. So the control of trajectory tracking is one of the most important tasks in control of robotic manipulator [2].

Dynamics of robot manipulators are described by second-order nonlinear differential equation, and the inertial parameters depend upon the payload which is often unknown and gets changed during the task. Despite long years of research, designing of control for robot manipulator has a thrust area for researchers to work upon due to the advancement of new techniques and methods [3]. Several control algorithms are utilized in position control such as PID control [4], PD control, PI control [4], feed-forward compensation control [5], adaptive control [6], and variable structure control [7]. Most of the conventional control strategies require specific mathematical modeling but it is not always possible. Proper tuning of the controller is highly required for getting the desired results. Regardless of the new advancement in the field of control theory, the PID control is still mostly preferred in the industry because of the simplicity in design and implementation [8, 9]. They have been used widely for control of diverse dynamical systems ranged from industrial processes to aircraft and ship dynamics [10].

The function of two degree of freedom robot manipulators is quite analogous to that of human arms [11]. The total energy is defined as the sum of kinetic energy and potential energy and is used to form the Lagrangian equations. Finally from these equations, we define the torque applied to each of the links. This paper presents a PID control strategy developed and applied to the problem of trajectory tracking of a two-link robot manipulator [12–14]. This mechanism is highly useful for robotic arm movement and navigation control [15–17].

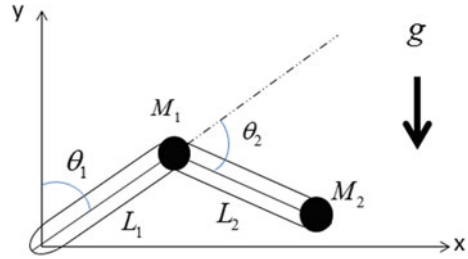
2 Dynamic Model of Two-Link Manipulators

In our paper, for study, we have used two degree of freedom planer robot manipulator as shown in Fig. 1.

We can put

$$\begin{aligned}x_1 &= L_1 \sin \theta_1 \\y_1 &= L_1 \cos \theta_1 \\x_2 &= L_1 \sin \theta_1 + L_2 \sin(\theta_1 + \theta_2) \\y_2 &= L_1 \cos \theta_1 + L_2 \cos(\theta_1 + \theta_2)\end{aligned}$$

Fig. 1 Two-DOF robot arm manipulator



So, kinetic energy could be formed as

$$KE = \frac{1}{2}M_1\dot{x}_1^2 + \frac{1}{2}M_1\dot{y}_1^2 + \frac{1}{2}M_2\dot{x}_2^2 + \frac{1}{2}M_2\dot{y}_2^2$$

By simplification,

$$KE = \frac{1}{2}(M_1 + M_2)L_1^2\dot{\Theta}_1^2 + \frac{1}{2}M_2L_2^2\dot{\Theta}_1^2 + M_2L_2^2\Theta_1\dot{\Theta}_2 + \frac{1}{2}M_2L_2^2\dot{\Theta}_2^2 + M_2L_1L_2 \cos \Theta_2 (\dot{\Theta}_1\dot{\Theta}_2 + \dot{\Theta}_1^2)$$

And potential energy is

$$PE = M_1gL_1 \cos \Theta_1 + M_2g(L_1 \cos \Theta_1 + L_2 \cos(\Theta_1 + \Theta_2))$$

So, by Lagrange Dynamics, we form the Lagrangian

$$L = KE - PE$$

$$L = \frac{1}{2}(M_1 + M_2)L_1^2\dot{\Theta}_1^2 + \frac{1}{2}M_2L_2^2\dot{\Theta}_1^2 + M_2L_2^2\Theta_1\dot{\Theta}_2 + \frac{1}{2}M_2L_2^2\dot{\Theta}_2^2 + M_2L_1L_2 \cos \Theta_2 (\dot{\Theta}_1\dot{\Theta}_2 + \dot{\Theta}_1^2) - M_1gL_1 \cos \Theta_1 - M_2g(L_1 \cos \Theta_1 + L_2 \cos(\Theta_1 + \Theta_2))$$

So, forming the dynamics equations to be

$$f_{\Theta_{1,2}} = \frac{d}{dt} \left(\frac{\partial L}{\partial \dot{\Theta}_{1,2}} \right) - \frac{\partial L}{\partial \Theta_{1,2}}$$

So, the dynamic equations after simplifications become

$$\begin{aligned}
& ((M_1 + M_2)L_1^2 + M_2L_2^2 + 2M_2L_1L_2 \cos \Theta_2)\ddot{\Theta}_1 + (M_2L_2^2 + M_2L_1L_2 \cos \Theta_2)(\ddot{\Theta}_2 \\
& - M_2L_1L_2 \sin \Theta_2(2\dot{\Theta}_1\dot{\Theta}_2 + \dot{\Theta}_2^2) - (M_1 + M_2)gL_1 \sin \Theta_1 - M_2gL_2 \sin(\Theta_1 + \Theta_2) = f_{\Theta_1} \\
& (M_2L_2^2 + M_2L_1L_2 \cos \Theta_2)\ddot{\Theta}_1 + (M_2L_2^2\ddot{\Theta}_2 - M_2L_1L_2 \sin \Theta_2\dot{\Theta}_1\dot{\Theta}_2 \\
& - M_2gL_2 \sin(\Theta_1 + \Theta_2) = f_{\Theta_2}
\end{aligned}$$

Having the system equation

$$B(q)\ddot{q} + C(\dot{q}, q) + G(q) = F$$

where $B(q)$ stands inertia matrix, C stands Coriolis matrix, and $G(q)$ stands gravity matrix.

$$q = \begin{bmatrix} \Theta_1 \\ \Theta_2 \end{bmatrix}$$

$$B(q) = \begin{bmatrix} ((M_1 + M_2)L_1^2 + M_2L_2^2 + 2M_2L_1L_2 \cos \Theta_2) & M_2L_2^2 + M_2L_1L_2 \cos \Theta_2 \\ M_2L_2^2 + M_2L_1L_2 \cos \Theta_2 & M_2L_2^2 \end{bmatrix}$$

$$C(\dot{q}, q) = \begin{bmatrix} -M_2L_1L_2 \sin \Theta_2(2\dot{\Theta}_1\dot{\Theta}_2 + \dot{\Theta}_2^2) \\ M_2L_1L_2 \sin \Theta_2\dot{\Theta}_1\dot{\Theta}_2 \end{bmatrix}$$

$$G(q) = \begin{bmatrix} -(M_1 + M_2)gL_1 \sin \Theta_1 - M_2gL_2 \sin(\Theta_1 + \Theta_2) \\ -M_2gL_2 \sin(\Theta_1 + \Theta_2) \end{bmatrix}$$

$$F = \begin{bmatrix} f_{\Theta_1} \\ f_{\Theta_2} \end{bmatrix}.$$

3 Properties of Robot Manipulator

We investigate the structure and property of each term in the robot dynamics equation.

Property 1 $B(q)$ is inertia matrix which is positive definite symmetric matrix bounded by $\mu_1 I \leq B(q) \leq \mu_2 I$, where μ_1 and μ_2 are positive constants.

$$\begin{aligned}
\mu_1 I &\leq B(q) \leq \mu_2 I \\
M_1 &\leq B(q) \leq M_2
\end{aligned}$$

Property 2 $\dot{B}(q) - 2C_m(\dot{q}, q)$ is a skew-symmetric matrix, which implies

$$\dot{B}(q) = C(\dot{q}, q) + C(\dot{q}, q)^T \quad C(\dot{q}, q) = C_m(\dot{q}, q)q$$

$C(\dot{q}, q)$ is quadratic in \dot{q}

$$\|C(\dot{q}, q)\| \leq c_b \|\dot{q}\|^2$$

Where $c_b(q)$ is a scalar function. For a robot arm, c_b is a constant independent of q .

Property 3 A bound on the gravity term can be derived for a given robot manipulator

$$\|G(q)\| \leq g_b$$

where g_b is a scalar function which can be resolved for any given robot manipulator.

Property 4 The robot dynamic equation has a property that is linear in the parameters. Here, all the parameters may be unknown; thus, the dynamics are linear in the unknown terms. It may be expressed as

$$B(q)\ddot{q} + C(\dot{q}, q) + G(q) = B(q)\ddot{q} + N(\dot{q}, q) \equiv W(q, \dot{q}, \ddot{q})\Omega$$

where Ω is a parameter vector and $W(q, \dot{q}, \ddot{q})$ is a matrix of robot function depending on the link variables, link velocities, and link accelerations. Here, the disturbance F_d is not included in the mentioned equation.

4 Design of Controller

Table 1 depicts the common parameters utilized in the simulation of control laws:

Having the system equation $B(q)\ddot{q} + C(\dot{q}, q) + G(q) = F$

We can have $\ddot{q} = B(q)^{-1}[-C(\dot{q}, q) - G(q)] + \hat{F}$

With $\hat{F} = B(q)^{-1}F \Leftrightarrow F = B(q)\hat{F}$

The system has been decoupled to have a new non-physical input

Table 1 System parameters

	Mass, M (kg)	Length, L (m)	Position (q)	q'	Desired path
Link 1	$M_1 = 1$	$L_1 = 1$	$\Theta_1 = -\pi/2$	$\Theta_1' = 0$	$\Theta_{1d} = \pi/2$
Link 2	$M_2 = 1$	$L_2 = 1$	$\Theta_2 = \pi/2$	$\Theta_2' = 0$	$\Theta_{2d} = -\pi/2$

$$\hat{F} = \begin{bmatrix} f_1 \\ f_2 \end{bmatrix}$$

Yet, the physical torque inputs to the system are

$$\begin{bmatrix} f_{\Theta_1} \\ f_{\Theta_2} \end{bmatrix} = B(q) \begin{bmatrix} f_1 \\ f_2 \end{bmatrix}$$

The error signals

$$\begin{aligned} e(\theta_1) &= \theta_{1f} - \theta_1 \\ e(\theta_2) &= \theta_{2f} - \theta_2 \end{aligned}$$

With final positions

$$\begin{bmatrix} \Theta_{1f} \\ \Theta_{2f} \end{bmatrix} = \begin{bmatrix} \pi/2 \\ -\pi/2 \end{bmatrix}$$

The system has initial positions of

$$\Theta_0 = \begin{bmatrix} -\pi/2 \\ \pi/2 \end{bmatrix}$$

With the above information, we can formulate the general structure of PID controller for any input using the classical linear law. Therefore, the entire system equations with control would be

$$\ddot{q} = B(q)^{-1}[-C(\dot{q}, q) - G(q)] + \hat{F}$$

With

$$\hat{F} = \begin{bmatrix} f_1 \\ f_2 \end{bmatrix} = \begin{bmatrix} f_1 = K_{p1}(\Theta_{1f} - \Theta_1) + K_{d1}\dot{\Theta}_1 + K_{i1} \int e(\Theta_1)dt \\ f_2 = K_{p2}(\Theta_{2f} - \Theta_2) + K_{d2}\dot{\Theta}_2 + K_{i2} \int e(\Theta_2)dt \end{bmatrix}$$

Bringing back the actual physical torques.

$$\begin{bmatrix} f_{\Theta_1} \\ f_{\Theta_2} \end{bmatrix} = B(q) \begin{bmatrix} f_1 \\ f_2 \end{bmatrix}$$

But to apply all controls of proportional–integral–derivative, an extra state is added for each angle to bear resemblance to the integration inside the computer.

So, the entire system equations are

$$\begin{aligned} \dot{x}_1 &= (\Theta_{1f} - \Theta_1) \\ \dot{x}_2 &= (\Theta_{2f} - \Theta_2) \\ \begin{bmatrix} \ddot{\Theta}_1 \\ \ddot{\Theta}_2 \end{bmatrix} &= \hat{F} = B(q)^{-1}[-C(\dot{q}, q) - G(q)] + \begin{bmatrix} f_1 = K_{p1}(\Theta_{1f} - \Theta_1) + K_{d1}\dot{\Theta}_1 + K_{i1}x_1 \\ f_2 = K_{p2}(\Theta_{2f} - \Theta_2) + K_{d2}\dot{\Theta}_2 + K_{i2}x_2 \end{bmatrix} \end{aligned}$$

5 Simulation Result

The stratagem to control the robot manipulator is done by trial and error. Parameters of the controllers are adjusted manually in order to obtain the best results. The values for the desirable performance of the controller are shown below:

$$K_{p1} = 20, K_{d1} = 10, K_{i1} = 15 \text{ and } K_{p2} = 20, K_{d2} = 15, K_{i2} = 15$$

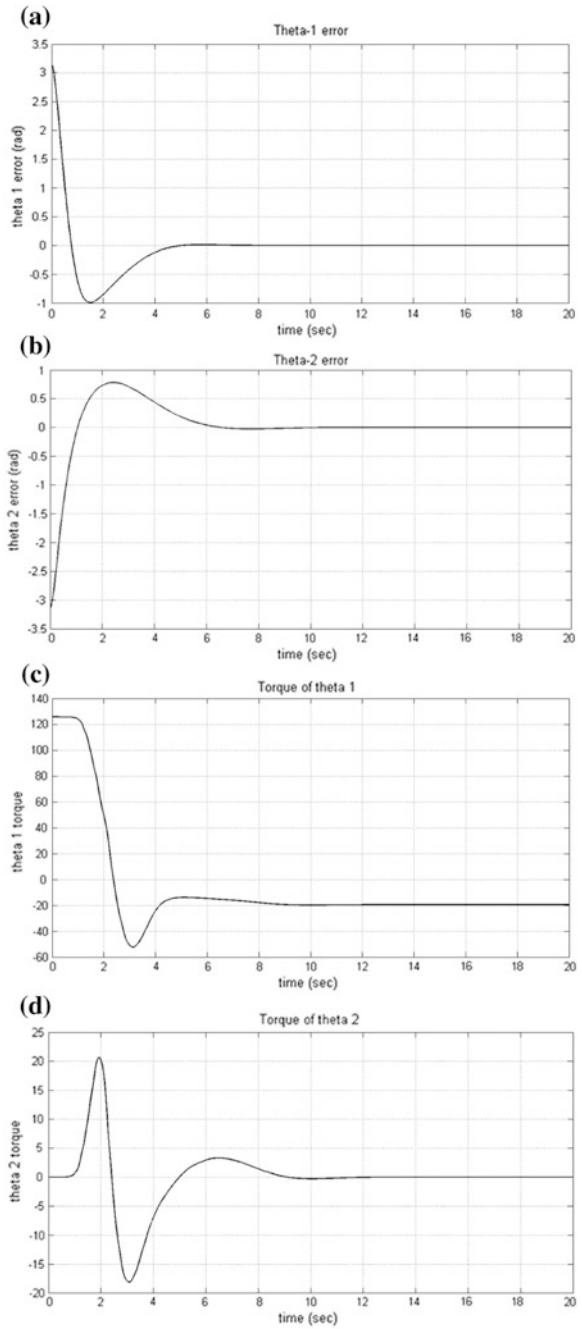
From the waveforms as shown in the Fig. 2a, b, the position error reaches zero at a considerable fast rate of time. From Fig. 2c, d, the torque applied can be observed with slight overshoot or peaks but stabilizes quickly. The same design was tested in other initial and final positions; the results were different.

6 Conclusion

In this paper, basic concepts for robot manipulator and its control methodology are discussed. We applied PID control method in a two-link robot manipulator and simulate the performance of controller using MATLAB. The simulation results show that the validity of the PID control method gives the possibility of minimizing the error for a two-link robot manipulator. Three PID control gains in K_p , K_i , and K_d are adjustable parameters. From the above observations, we can see that how K_p is associated with the tracking error and speed of evolution, K_d is associated with speed of interaction with state change, and K_i is also associated with overall error elimination. Nevertheless, if the modest alteration is made in the controller parameters, it tends to produce more overshoots and oscillations. The parameters are very sensitive to initial and final positions.

For further modification, we can propose to use other techniques, such as controllers based on fuzzy logic and sliding mode logic, that work only with angle position and torque response along with an online controller with auto-tuning of the parameters K_p , K_d , K_i . Improvements could also be made by increasing the sampling rate of the controller parameters and guarantee stability and good tracking performance.

Fig. 2 **a** error waveform of Θ_1 **b** error waveform of Θ_2 **c** actual torque on Θ_1 joint **d** actual torque on Θ_2 joint



Acknowledgements We sincerely acknowledge the support of Prof. Amitava Chatterjee and Prof. Amit Konar for their valuable suggestions.

References

1. Amol A. Khalate, Gopinathan Leena, Goshaidas Ray, 'An Adaptive Fuzzy Controller for Trajectory Tracking of Robot Manipulator', *Intelligent Control and Automation*, 2011, 364–370.
2. Koren Ward, 'Rapid Simultaneous Learning of Multiple Behaviours with a Mobile Robot' *Proc. 2001, Australian Conference on Robotics and Automation*, Sydney, 14–15 Nov 2001.
3. "Statistics, market analysis, forecasts, case studies and profitability of robot investment," in *IFR Robot. Newsletter*. Paris, France: Int. Federation of Robotics, 2001, vol. 41.
4. J.Y.S. Luh, Conventional controller design for Industrial robots-a tutorial, *IEEE Trans. Systems Man Cybernet.* 1983, 298–316.
5. Pradeep K. Khosla, Takeo Kanade, Experimental of Evaluation of Nonlinear Feedback and Feedforward Control Schemes for Manipulators, *The International Journal of Robotics Research*, Vol. 7, No. 1, February 1988.
6. J.J.E. Slotine, W. Li, Adaptive Manipulator Control: A Case Study, *IEEE Trans. Automat. Control* 33, 1988, 995–1003.
7. Mark W. Spong and M. Vidyasagar, "Robot Dynamics and control" John Wiley & Sons, 2004.
8. Jianhua Liu, Youping Gong, Guojin Chen and Huipeng Chen, "Modeling and simulation of loader working device based on SimMechanics," *IEEE International Conference on Transportation*, pp. 2054–2057, 2011.
9. Yuan Shaoqiang, Liu Zhong and Li Xingshan, "Modeling and Simulation of Robot Based on Matlab/SimMechanics," *Proceedings of the 27th Chinese Control Conference*, pp. 161–165, July 16-18, 2008.
10. Panagopoulos H, Astrom KJ, Hagglund T. Design of PID controllers based on constrained optimization. *IEE Proc Control Theory Appl* 2002; 149(1):32–40.
11. John M Hollerbach, 'Computer, Brains and the Control Movement', Manchester Institute of Technology, Artificial Intelligence Laboratory, June 1982.
12. Jolly Shah, Dr. S.S. Rattan, Prof. B. C. Nakra, 'Kinematic Analysis of a Planer Robot Using Artificial Neural Network', *International Journal of Robotics and Automation*, September 2012, 145–151.
13. Stephen Dodds, A two-link manipulator: simulation and control design Advisor: Dr. Mahboub Baccouch, University of Nebraska at Omaha, Omaha, NE, 68134, March 2012.
14. Duy Nguyen-Tuong, Jan Peters, 'Learning Robot Dynamics for Computed Torque Control using Local Gaussian Processes Regression', *ECSIS Symposium on Learning and Adaptive Behaviors for Robotic Systems*, 2008.
15. Mukherjee, Amartya, et al. "Unmanned aerial system for post disaster identification" *Circuits, Communication, Control and Computing (I4C), 2014 International Conference on.* IEEE, 2014.
16. Mukherjee, Amartya, et al. "A disaster management specific mobility model for flying ad-hoc network". *International Journal of Rough Sets and Data Analysis (IJRSDA)* 3.3 (2016): 72–103.
17. Dey, Nilanjan, and Amartya Mukherjee. *Embedded Systems and Robotics with Open Source Tools*. CRC Press, 2016.

Design of P-I-D Based TCSC Controller for SMIB System Using Artificial Neural Network

Arnab Kumar Mondal, Chiborhame Suting and Parthasarathi Bera

Abstract In the present work, the application of thyristor-controlled series capacitor (TCSC) is investigated for damping oscillation of single-machine infinite bus (SMIB) power system. The analysis is performed by considering proportional–integral–differential (P-I-D) controller for TCSC, and gain settings of the P-I-D controller of TCSC are optimized using Krill Herd Algorithm (KHA) for different values of generator active power and terminal voltage. The optimized values of gains of P-I-D controller are used for training the multilayered feedforward artificial neural network (ANN)-based controller for real-time tuning. Dynamic performances considering TCSC equipped with ANN-based P-I-D controller and the P-I-D controller optimized with KHA are compared, and it is seen that ANN-based P-I-D controller for TCSC performs well under different operating conditions.

Keywords TCSC · Krill Herd Algorithm (KHA) · Artificial neural network (ANN)

1 Introduction

Considerable research attempts have been made the dynamic stability of power systems more improved. Authors in [1] have analyzed the concept of the synchronous machine stability as affected by excitation control and have developed an understanding for stabilization of static excitation systems. Extensive works have

A. K. Mondal (✉) · C. Suting · P. Bera
Department of Electrical Engineering, Kalyani Government Engineering College,
Kalyani 741235, India
e-mail: akmondal92@gmail.com

C. Suting
e-mail: chibor915@gmail.com

P. Bera
e-mail: parthabera1977@gmail.com

presented to determine the influence of power system stabilizer (PSS) parameters on the dynamic performance of the power system [2–4]. Authors in [5–9] have presented for the parameter optimization of PSS. Also, new techniques have also been presented such as variable structure PSS [10], fuzzy logic stabilizers [11], rule-based stabilizer [12, 13], adaptive PSS [14, 15], and pole placement technique [16]. But, it is difficult for practical realization of PSS [17].

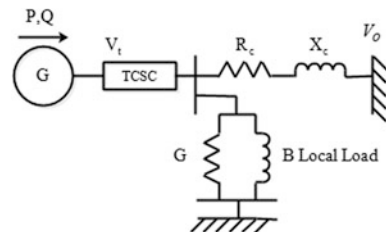
The effect of TCSC has been carried out for analyzing the dynamic stability of power system. Several modern control technologies have been applied to TCSC controller design such as the design of stabilizer for TCSC by using a pole placement technique [18]. But, for this case, all system states are required as input to the controller. Authors in [19] have presented a time-optimal control strategy for the TCSC. The adjustment of TCSC impedance has been done by deviating magnitude of speed and changing machine rotor. Authors have used genetic algorithm [20, 21] and particle swarm optimization algorithm [22, 23] for designing the lead–lag controller for TCSC. Modern control technologies such as adaptive neurofuzzy inference system (ANFIS) [24], fuzzy logic controller [25, 26], and fuzzy + PI controller [27] have been studied for TCSC to improve the power system dynamic stability.

In this paper, the investigation of TCSC is performed to damp out the power system oscillation for single-machine infinite bus (SMIB) power system and the gain settings of the P-I-D controller of TCSC are optimized using Krill Herd Algorithm (KHA) [28] for different values of generator active power, P_g , and terminal voltage, V_t . The optimized values of gains of the P-I-D controller are then used for training the multilayered feedforward artificial neural network (ANN)-based [29] controller for real-time tuning. Dynamic performances considering TCSC equipped with ANN-based P-I-D controller and P-I-D controller optimized with KHA are compared.

2 Power System Under Study

A SMIB system is considered for the present problem and is shown in Fig. 1. A TCSC is connected to the transmission network near the generator terminal. TCSC has the ability to transfer more power providing additional damping for

Fig. 1 SMIB with TCSC located near generator end



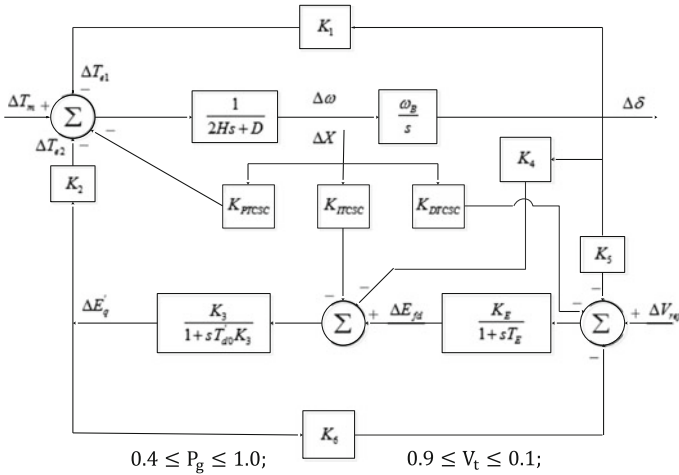


Fig. 2 Block diagram of linearized power system model with TCSC

low-frequency oscillations by modulating the reactance of one or more specific interconnecting power lines. The block diagram representation of small-signal stability model of a SMIB system with TCSC is shown in Fig. 2.

While designing the controllers for TCSC, the following assumptions have been considered:

1. The three-phase system with thyristor connected is in a balanced condition.
2. The thyristors are triggered at a continuous firing angle.
3. Filter networks made by the series capacitor is not taken in the representation.
4. The harmonics generated as for the thyristor switching are neglected.

TCSC is to be controlled by controlling its firing angle, and it is modeled by gain and time constant and is shown in Fig. 3. To verify the optimum values of the gains of P-I-D controllers, different loading conditions have been considered as given in Table 1.

The SMIB system can be operated by defining the values of the real power P_g and terminal voltage V_t , at the generator terminal. P_g and V_t have been varied over the ranges given below:

Fig. 3 Block diagram of TCSC equipped with P-I-D Controller

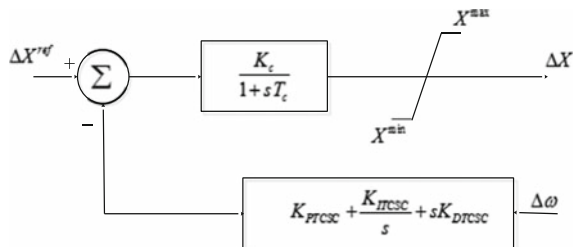


Table 1 Optimized values of gains and objective functions

Operating conditions	TCSC controller parameters using Krill Herd optimization algorithm						TCSC controller parameters computed using neural network					
	V_t	K_{prcsc}	K_{ircsc}	K_{drscsc}	Value of J		K_{prcsc}	K_{ircsc}	K_{drscsc}	Value of J		
0.40	0.90	-5.4272	-3.2611	194.7125	0.0263		-8.1644	-3.4600	199.1517	0.0281		
0.45	0.91	-1.9695	-1.2545	191.6412	0.0320		-5.4231	-1.0813	158.8173	0.0407		
0.50	0.92	0.9651	0.1043	80.3541	0.0503		1.4115	0.2052	90.5534	0.0578		
0.55	0.93	5.4177	0.5317	71.4173	0.1263		11.4471	0.6201	87.17002	0.1416		
0.60	0.94	13.9768	0.5434	41.5829	0.1927		18.7478	0.4736	52.5186	0.1816		
0.65	0.95	15.7036	0.5516	40.4951	0.0356		21.5215	0.4641	59.12174	0.0412		
0.70	0.96	19.2603	0.6018	100.8966	0.0144		26.3911	0.4577	86.3841	0.0259		
0.75	0.97	21.9719	0.6519	110.2991	0.0080		20.1488	0.5415	115.4749	0.0089		
0.80	0.98	-60.3151	0.1045	105.8697	0.0060		-51.4988	0.0914	95.4575	0.0078		
0.85	0.99	-180.0317	0.0166	115.9514	0.0043		-169.3124	0.0556	110.7251	0.0051		
0.90	1.00	-167.0894	0.0964	111.9763	0.0034		-177.4152	0.0568	94.2247	0.0041		

$$0.4 \leq P_g \leq 1.0; \quad 0.9 \leq V_t \leq 0.1;$$

3 Structure of P-I-D Based TCSC Controller

The block diagram of TCSC with P-I-D controller is shown Fig. 3. The location near the generator terminal is the best for TCSC as it gets the speed deviation $\Delta\omega$ as the input signal of its controller. Here, ΔX_{ref} is the reference angle, and the gain and time constant for TCSC are K_c and T_c , respectively.

4 State Space Representation of the System

The state space representation for the SMIB system with TCSC is:

$$\dot{X} = AX + Bp \tag{1}$$

where X and p are the state and disturbance vectors, respectively. The X and p are given as:

$$X = [\Delta\delta \ \Delta\omega \ \Delta E'_q \ \Delta E_{fd} \ \Delta V_R \ \Delta V_E \ \Delta X]^T \tag{2}$$

$$p = [\Delta T_m \ \Delta V_{ref} \ \Delta X_{ref}]^T. \tag{3}$$

5 Design of Artificial Neural Network

A multilayer feedforward neural network [29] is considered for the present analysis and is shown in Fig. 4. Here, generator real power output (P_g) and terminal voltage (V_t) are taken as the inputs of the neural network. The input signals are given to the nodes in the input layer. The output layer provides the desired TCSC parameters K_{PTCSC} , K_{ITCSC} , and K_{DTCSC} . Figure 5 shows the schematic diagram of ANN-based TCSC controller. The output layer of the artificial neural network gives the desired gains (i.e., K_{PTCSC} , K_{ITCSC} , and K_{DTCSC}) in real time.

Fig. 4 Multilayer feedforward neural network

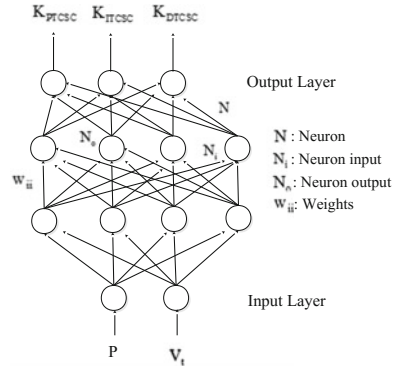
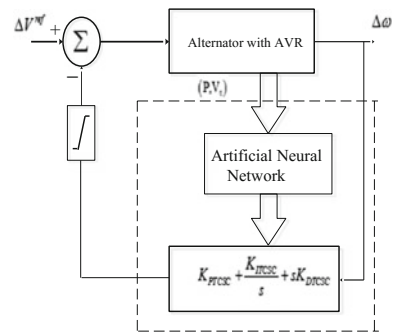


Fig. 5 Schematic diagram of ANN-based TCSC controller



6 Analysis of ANN-Based TCSC Controller

Real power (P_g) and terminal voltage (V_t) at the generator terminal define the operating condition for the considered SMIB system. P_g and V_t have been varied as mentioned in Table 1.

The value of K_{PTCSC} , K_{ITCSC} , and K_{DTCSC} is computed for each set of P_g and V_t . The input vector of the training process is now P_g and V_t , and the output vector becomes K_{PTCSC} , K_{ITCSC} , and K_{DTCSC} . Integral time-multiplied square error (ITSE) [30, 31] criteria-based objective function as given in Eq. (4) has been considered for the optimization, and it has been optimized using Krill Herd Algorithm (KHA) [28] for training the ANN-based P-I-D controller for TCSC.

$$J = \int_0^{\infty} t(\Delta\omega)^2 dt \tag{4}$$

7 Dynamic Response

Figures 6 and 7 show the comparison of dynamic responses considering gains tuned offline using KHA and with ANN-based P-I-D controller for TCSC under two different loading conditions taken from the database, i.e., from Table 1. From Figs. 6 and 7, it is observed that responses considering KHA’s optimized gains and ANN’s tuned gains are almost similar in terms of peak deviation and settling time. Figures 8 and 9 show the dynamic responses considering gains tuned with ANN-based P-I-D controller for TCSC for two different loading conditions arbitrarily and not matched with the database. Similar observations have been found for other operating conditions within the range. Therefore, it may be concluded that ANN-based P-I-D controller for TCSC is very effective for real-time control of the system.

Fig. 6 Dynamic responses of SMIB system using (i) KHA and (ii) ANN

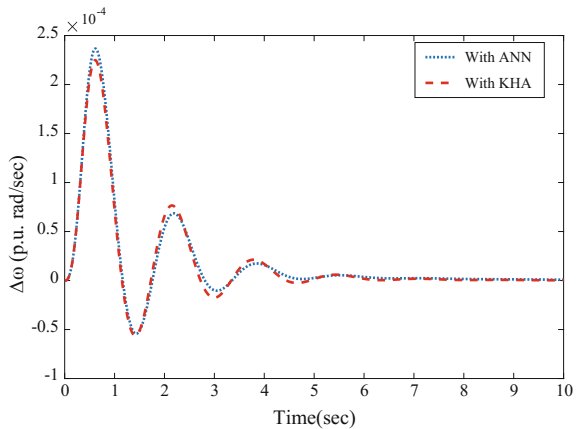


Fig. 7 Dynamic responses of SMIB system using (i) KHA and (ii) ANN

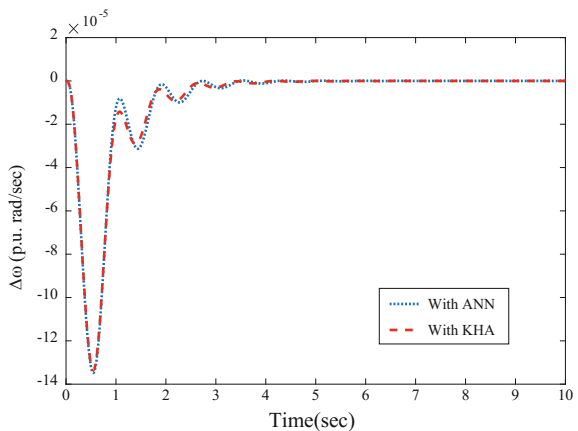


Fig. 8 Dynamic responses of SMIB system using ANN for $P_g = 0.75$ and $V_t = 0.94$

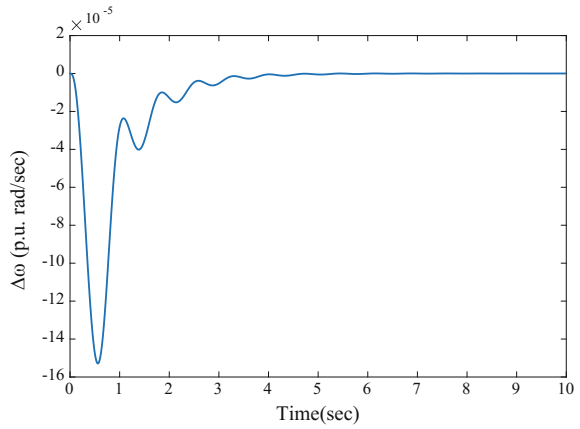
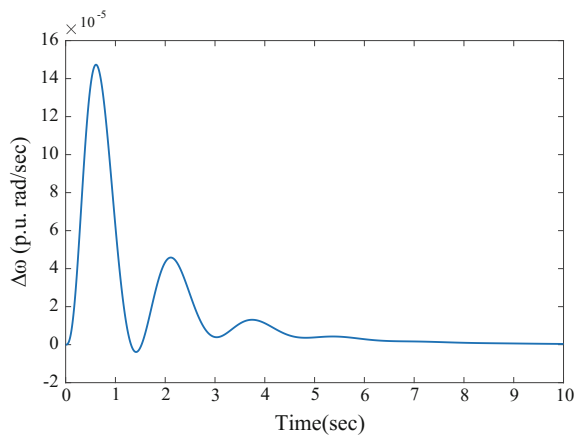


Fig. 9 Dynamic responses of SMIB system using ANN for $P_g = 0.45$ and $V_t = 0.95$



Figures 10 and 11 show the system responses to three-phase five-cycle fault at the generator ends with the two different operating conditions considering gains tuned in real time using an ANN-based P-I-D controller for TCSC. It is seen that the gains tuned for real time using ANN-based P-I-D controller for TCSC give satisfactory performances.

Fig. 10 System responses for a three-phase five-cycle fault at generator terminal $P_g = 0.9$ and $V_t = 1.0$

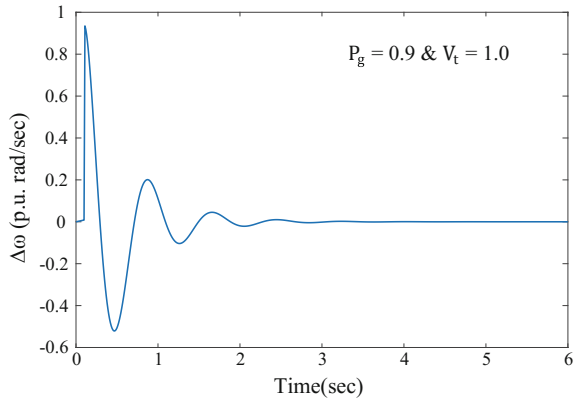
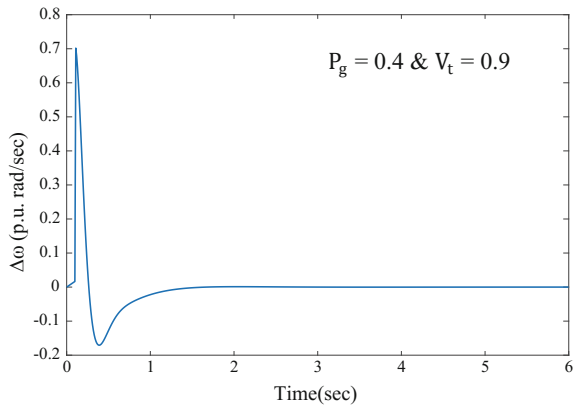


Fig. 11 System responses for a three-phase five-cycle fault at generator terminal $P_g = 0.4$ and $V_t = 0.9$



8 Conclusion

In the present work, the application of thyristor-controlled series capacitor (TCSC) in damping power system oscillation is investigated. The analysis is performed by considering proportional–integral–differential (P-I-D) controller for TCSC, and gain settings of the P-I-D controller of TCSC are optimized using Krill Herd Algorithm (KHA) for different values of generator active power and terminal voltage. The optimized values of gains of P-I-D controller are used for training the multilayered feedforward artificial neural network (ANN) for real-time tuning. Dynamic performances considering ANN-based P-I-D controller for TCSC and P-I-D controller optimized with KHA offline for different values of active power and terminal voltage are compared. The analysis reveals that ANN-based P-I-D controller for TCSC performs well for different operating conditions and also improves the transient stability.

Appendix

The values of machine parameters are given as follows:

$$H = 5 \text{ s}; f_B = 50 \text{ Hz}; T_d^0 = 6.0 \text{ p.u.}; K_E = 50; T_E = 0.05 \text{ s}; D = 0.02 \text{ p.u.} \cdot \text{rad/s}; \\ X_d = 1.6 \text{ p.u.}; X_q = 1.55 \text{ p.u.}; X'_d = 0.32 \text{ p.u.}; X'_q = 0.21 \text{ p.u.}$$

The ranges of K_{PTCSC} , K_{ITCSC} , and K_{DTCSC} for optimization using KHA are given as follows:

$$-200 \leq K_{PTCSC} \leq 30; -7 \leq K_{ITCSC} \leq 1 \text{ and } 20 \leq K_{DTCSC} \leq 200.$$

References

1. F.P. DeMello and C. Concordia, "Concepts of synchronous machine stability as affected by excitation control", IEEE Transactions on Power Apparatus and Systems, Vol. PAS-88, April 1969, pp. 316–329.
2. P. Kundur, M. Klein, G. J. Rogers, M. S. Zywno, "Application of power system stabilizers for enhancement of overall system stability", IEEE Transactions on Power Apparatus and Systems, Vol. 4, No. 2, May 1989, pp. 614–626.
3. N. Daratha, B. Das, J. Sharma, "Coordination between OLTC and SVC for voltage regulation in unbalanced distribution system distributed generation", IEEE Trans. on Pow. Sys., Vol. 29, pp. 289–299, Jan. 2014.
4. Gh. Shahgholian, A. Movahedi, "Power system stabiliser and flexible alternating current transmission systems controller coordinated design using adaptive velocity update relaxation particle swarm optimisation algorithm in multi-machine power system", IET Gener. Transm. Distrib., Vol. 10, No. 8, pp. 1860–1868, May 2016.
5. H.E. Mostafa, M.A. El-Sharkawy, A.A. Emary, K. Yassin "Design and allocation of power system stabilizers using the particle swarm optimization technique for an interconnected power system" International Journal of Electrical Power & Energy Systems, Volume 34, Issue 1, January 2012, Pages 57–65.
6. M. A. Abido, "Parameter optimization of multimachine power system stabilizers using genetic local search", Electrical Power & Energy Systems Vol. 23, 2001, pp. 785–794.
7. Y. L. Abdel-Magid, M. A. Abido and A. H. Mantawy, "Robust tuning of power system stabilizers in multimachine power systems", IEEE Transactions on Power Systems, Vol. 15, No. 2, May 2000, pp. 735–740.
8. P. Zhang and A. H. Coonick, "Coordinated synthesis of PSS parameters in multi-machine power systems using the method of inequalities applied to genetic algorithms." IEEE Transactions on Power Systems, Vol. 15, No. 2, May 2000, pp. 811–816.
9. X. Lei, H. Huang, S.L. Zheng, D.Z. Jiang, Z.W. Sun "Global tuning of power system stabilizers in multi-machine systems", Electrical Power System Research, Vol. 58, 2001 pp. 103–110.
10. S. S. Lee; J. K. Park "Design of reduced-order observer-based variable structure power system stabiliser for unmeasurable state variables" IEE Proceedings - Generation, Transmission and Distribution, Year: 1998, Volume: 145, Issue: 5, Pages: 525–530.
11. B. Shaw, A. Banerjee, S.P. Ghoshal, V. Mukherjee, "Comparative seeker and bio-inspired fuzzy logic controllers for power system stabilizers", Elec. Pow. and Energy Sys., Vol. 33, pp. 1728–1738, 2011.

12. H. F. Wang; F. J. Swift; B. W. Hogg; H. Chen; G. Tang, "Rule-based variable-gain power system stabiliser", IEE Proceedings - Generation, Transmission and Distribution, Year: 1995, Volume: 142, Issue: 1, Pages: 29–32.
13. M. A. Abido; Y. L. Abdel-Magid, "Hybridizing rule-based power system stabilizers with genetic algorithms", IEEE Transactions on Power Systems, Year: 1999, Volume: 14, Issue: 2, Pages: 600–607.
14. P. Hoang; K. Tomsovic, "Design and analysis of an adaptive fuzzy power system stabilizer", IEEE Transactions on Energy Conversion, Year: 1996, Volume: 11, Issue: 2, Pages: 455–461.
15. L. Cheng; G. Chen; W. Gao; F. Zhang; G. Li, "Adaptive Time Delay Compensator (ATDC) Design for Wide-Area Power System Stabilizer", IEEE Transactions on Smart Grid, Year: 2014, Volume: 5, Issue: 6, Pages: 2957–2966.
16. M.A. Furini, A.L.S. Pereira, P.B. Araujo, "Pole placement by coordinated tuning of Power System Stabilizers and FACTS-POD stabilizers", International Journal of Electrical Power & Energy Systems, Volume 33, Issue 3, March 2011, Pages 615–622.
17. Gh. Shahgholian, J. Faiz, "The effect of power system stabilizer on small signal stability in single-machine infinite-bus", Int. J. of Elec. And Eng., Vol. 4, No. 2, pp. 45–53, 2010.
18. M.A. Abido, "Pole placement technique for PSS and TCSC-based stabilizer design using simulated annealing", International Journal of Electrical Power & Energy Systems, Volume 22, Issue 8, 1 November 2000, Pages 543–554.
19. J. Chang, J. Chow, Time optimal series capacitor control for damping inter-area modes in interconnected power systems, IEEE Trans. PWRS 12 (1) (1997) 215–221.
20. Y.L. Abdel-Magid, M.A. Abido, "Robust coordinated design of excitation and TCSC-based stabilizers using genetic algorithms", Electric Power Systems Research, Volume 69, Issues 2–3, May 2004, Pages 129–141.
21. Gh. Shahgholian, A. Movahedi, J. Faiz, "Coordinated design of TCSC and PSS controllers using VURPSO and genetic algorithms for multimachine power system stability", Int. J. of Control, Automation, and Sys., Vol. 13, No. 2, pp. 398–409, April 2015.
22. H. Shayeghi, A. Safari, H.A. Shayanfar, "PSS and TCSC damping controller coordinated design using PSO in multi-machine power system", Energy Conversion and Management, Volume 51, Issue 12, December 2010, Pages 2930–2937.
23. Gh. Shahgholian, A. Movahedi, "Coordinated design of thyristor controlled series capacitor and power system stabilizer controllers using velocity update relaxation particle swarm optimization for two-machine power system stability", Revue Roumaine Des Sciences Techniques, Vol. 59, No. 3, pp. 291–301, 2014.
24. Gh. Shahgholian, A. Movahedi, "Coordinated control of TCSC and SVC for system stability enhancement using ANFIS method", Int. Review on Modelling and Simulations, Vol. 4, No. 5, pp. 2367–2375, Oct. 2011.
25. V.K. Tayal, J.S. Lather, "Reduced order H_{∞} TCSC controller & PSO optimized fuzzy PSS design in mitigating small signal oscillations in a wide range", International Journal of Electrical Power & Energy Systems, Volume 68, June 2015, Pages 123–131.
26. M.K. Panda, G. Pillai, V. Kumar, "An interval type-2 fuzzy logic controller for TCSC to improve the damping of power system oscillations", Frontiers in Energy, Vol. 7, No. 3, pp. 307–316, Sep. 2013.
27. G. Shahgholian, M. Maghsoodi, M. Mahdavian, S. Farazpey, M. Janghorbani, M. Azadeh, "Design of Fuzzy + PI Controller in Application of TCSC and PSS for Power System Stability Improvement", 2016 13th International Conference on Electrical Engineering/Electronics, Computer, Telecommunications and Information Technology (ECTI-CON), Year: 2016, Pages: 1–6.
28. A.H. Gandomi, A.H. Alavi, "Krill herd: A new bio-inspired optimization algorithm", Communications in Nonlinear Science and Numerical Simulation, Volume 17, Issue 12, December 2012, Pages 4831–4845.

29. R. Chakraborty and P. Bera, "Artificial Neural Network (ANN) Based Adaptive Power System Stabilizer Considering Governor Turbine Dynamics", Michael Faraday IET India Summit, Kolkata, India, November 25, 2012.
30. Schultz, W.C., Rideout, V.C., Control system performance measures: past, present and future, IRE Transactions on Automatic Control, AC- 6, 22, pp. 22–35, 1961.
31. Ogata, K., Modern Control Engineering, A book, Prentice-Hall, Englewood cliffs, NJ, pp. 293–313, 1970.

Nonlinear Offset Measurement and Nullification for Effective Resistive Sensor Design

L. Dutta, A. Hazarika, M. Boro and M. Bhuyan

Abstract Over the decades, a number of methodologies have been introduced to meliorate the resistive sensor measurement protocol for complete knowledge of the phenomenon of interest. Nonetheless, such setting requires high degree of circuit components that result high level of errors (i.e., nonlinear) and thereby, its minimization for effective design is an open question. This article presents a technique that utilizes direct resistive circuit with microcontroller (μC), followed by subsequent estimation of curve-fitting models (CFMs) to curtail the errors involved and implementation in μC to update real-time data. Further, the study exploited the effectiveness of various employed CFMs in this context. The significant aftermaths with suitable choice of CFM and subsequent comparison with the state-of-the-art approaches manifest the efficacy of the adopted scheme.

Keywords Nonlinearity · Resistive sensor · Curve-fitting model (CFM) Microcontroller

1 Introduction

Analysis with proper setting of resistive sensor circuits that have high impact on wide-scale engineering applications and research community, due to its capability of sensing various physical phenomena, has garnered attention at real-world

L. Dutta · A. Hazarika (✉) · M. Boro · M. Bhuyan
Department of Electronics and Communication Engineering,
Tezpur University, Sonitpur, Assam, India
e-mail: anilh@tezu.ernet.in

L. Dutta
e-mail: lachit@tezu.ernet.in

M. Boro
e-mail: minu@tezu.ernet.in

M. Bhuyan
e-mail: manab@tezu.ernet.in

scenario [1]. Consequently, from time to time, various read-out circuits (ROCs) have been initiated to overcome the limitations, specifically errors due to nonlinearities, by modeling circuits, such as Wheatstone bridge-based schemes [2, 3] and resistance-to-digital converters. Some ROCs are based on RC circuits and timer, counter [3–5], while others rely on resistance to various parameter conversion, e.g., time, pulse-width, and frequency. Even though considerable challenges still exist, due to which research pursuits are going on.

For example, Borchardt et al. in [2] introduced pseudo-bridge scheme with an operational amplifier for measurement of unknown impedances, wherein impedance residuals are the inherent limitations, which is later improved by Torrents et al. [3]. In [4], a new approach is implicated to measure high value resistance that varies over a wide range, while the authors report sigma-delta [5], dual slope [6], and relaxation oscillator [8]. A linear combination of resistance and capacitor circuit is developed in [7] that accept the analog voltage output from a single element resistive sensor as an input, which is converted into corresponding digital output similar to 12-bit ADC-based analysis. More recently, implementing the design setting, many improved versions such as opamp-based bridge connected resistive sensor measurement that automatically converts the offset and mismatch in the input [9], direct resistance measurement embedding microcontroller (μC) [10], and opamp-based insensitive to non-ideal parameters are reported [11]. Importantly, involvement of operational amplifier, counter, timer etc., circuits and subsequent use of advance features using μC increase the complexity that makes the system costly.

Despite being advantages of aforementioned approaches, appropriate choice of model parameters and derivation of highly simplified versions, which can minimize the bridge between measured and actual responses, are often preferred in real-time applications. Such a straightforward exploratory approach with suitable mathematical guidelines helps making the system cost-effective and reliable for practical values. The article addresses a strategy that involves two stages; in the first stage, direct resistance measurement circuit has been implemented by setting R and C parameter values, and in second stage, measuring the output response of former circuit and subsequently estimating errors by CFMs, errors have been updated with efficient CFM for real-time data in μC . Extensive experimental verification affirms the suitability of the proposed technique. Thus, it could promote analyzing large volume of data and expedite research toward future directions.

$$ae^{bx}; \quad (1)$$

$$ae^{bx} + ce^{dx}; \quad (2)$$

$$a_0 + a_1 \cos(Xw) + b_1 \sin(Xw); \quad (3)$$

$$E1 + a_2 \cos(2Xw) + b_2 \sin(2Xw); \tag{4}$$

$$a_1 e^{-((X-b_1)/c_1)^2} (G1); \tag{5}$$

$$G1 + a_2 e^{-((X-b_2)/c_2)^2}; \tag{6}$$

$$aX^b; \tag{7}$$

$$aX^b + C; \tag{8}$$

$$p_1X + p_2; \tag{9}$$

$$p_1X + p_2X + p_3. \tag{10}$$

2 Method

Figure 1 depicts the basic circuit design for measurement of sensor response in which accurate measurement of charging/discharging cycle of the capacitor via μC determines the output response of resistive sensor [7, 12]. Initially, parameter values, i.e., resistors and capacitor, are measured by using a high-resolution Keithley-2111 digital multimeter and then connected to the μC having tristate capability. The output response (i.e., voltage V_{in}) across the resistance is used to charge the capacitor, and its voltage (V_c) is compared with that of high input μC . At the same instance, a count value is assigned based on maximum duration of charging and discharging of the capacitor to operate the RC-network similar to that of a 12-bit ADC. Now the capacitor is being charged or discharged through R_1 depending on the voltage level of V_c , i.e., low or high, and accordingly, the count value is incremented or decremented.

The analog output of the sensor is measured by connecting a precision power supply in the range of maximum voltage level of μC , $0-V_{DD}$. Further, the count values are measured at increment of 0.1 V/division. Nonetheless, the estimated

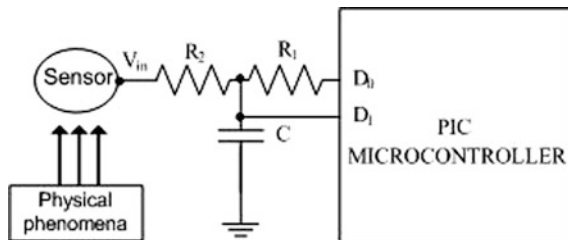


Fig. 1 Basic direct interfacing circuit. Note $R_1 = 3.1979 \text{ K}\Omega$, $R_2 = 9.861 \text{ K}\Omega$, $C = 2.255 \text{ }\mu\text{F}$, $V_{IH} = 1.962 \text{ V}$, $V_{ILow} = 1.880 \text{ V}$, and $V_{DD} = 4.65 \text{ V}$

count values are found to be nonlinear that yield error in measurements which make difficulty in correctly interpreting the outputs. Thereby, it is direly need to nullify the offsetting the error level either by soft-computing or hardware implementation instantaneously. Intending to such design focus, the errors are compensated based on the level of nonlinearity by formulation pursuit of models and subsequently estimated best-approximated one for possible implementation via μC . The algorithm is implemented in MATLAB (The MathWorks, Inc., Natick, United States) on an Intel (R) Core (TM) i3-3210 CPU with processor 3.20 GHz and 2 GB of RAM and μC mikroC PRO for PIC v.6.6.3.

3 Results and Discussion

Measurements are made under two settings: (i) $V_{in} < V_{IH}$, and (ii) $V_{in} \geq V_{IH}$, and specifically, multiple error compensating models (ECMs) are adopted for subsequent analysis. It is seen that nonlinear characteristics for two cases significantly differ from the actual values that are 301 in former case and 833 counts in later. As a result, the slopes that characterize the nonlinear behavior are quite dissimilar as depicted in Fig. 2. Therefore, deploying various ECMs and subsequent evaluation of suitable parameters helps finding the best approximation model, which is later simulated in the PIC μC to calibrate the errors. For profound understanding and thorough comparison that yield complete knowledge of wide-scale applicability of ECMs in augmented setup, it is concreted herein (Table 1). Table 1 outlines various parameters such as order of fitting functions (FFs), model equations, various type of errors, no. of coefficients involved, and memory cost. Fourier FF of second order provides optimal level of performance in terms of error; however, higher number of coefficients associated with function demands larger memory as compared to others and filtered out for further analysis. To meet the objective of finding the optimal parameters power, FF of order two is selected for analysis as follows:

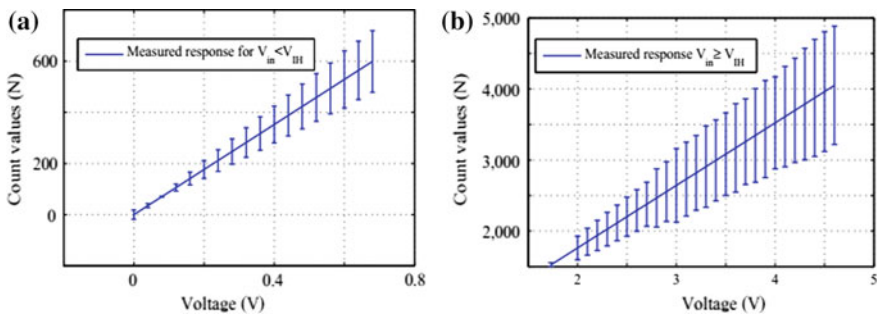


Fig. 2 Actual responses for **a** $V_{in} < V_{IH}$, and **b** $V_{in} \geq V_{IH}$

Table 1 Fitting function with order, generalized equation, sum-squared error (SSE), root-mean-squared error (RMSE), no of coefficients and memory level

# FF-order	Model	SSE		RMSE		Coeff. #n	Memory level
		$V_{in} < V_{IH}$	$V_{in} \geq V_{IH}$	$V_{in} < V_{IH}$	$V_{in} \geq V_{IH}$		
Exponential-1	Equation (1)	2.65e5	1.44e5	128.2	74.57	2	Low
Exponential-2	Equation (2)	365.6	1.49e4	5.11	24.92	4	High
Fourier-1	Equation (3)	571.8	1.37e4	6.391	23.93	4	High
Fourier-2	Equation (4)	255.5	1.09e4	4.615	22.3	6	Very high
Gaussian-1	Equation (5)	4.19e4	1.41e4	57.25	23.77	3	High
Gaussian-2	Equation (6)	9140	1.25e4	27.6	23.86	6	Very high
Power-1	Equation (7)	6321	4.07e4	19.88	39.6	2	Low
Power-2	Equation (8)	411.5	1.43e4	5.238	23.97	3	Low
Polynomial-1	Equation (9)	2761	2.40e4	13.14	30.38	2	Low
Polynomial-2	Equation (10)	571.8	1.48e4	6.174	24.35	3	High

Note that effective FF and its significant parameters' values are indicated by boldface

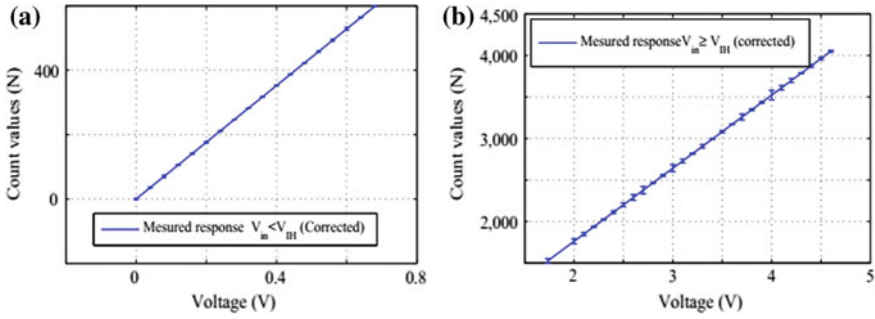


Fig. 3 Measured responses after compensation (corrected) for **a** $V_{in} < V_{IH}$, and **b** $V_{in} \geq V_{IH}$ in reference to Fig. 2

$$Y = aX^b + c; \tag{11a}$$

$$Y_i = 2.238 X_i^{0.9233} - 79.69; \tag{11b}$$

$$Y_i = 0.1526 X_i^{1.178} + 660.4. \tag{11c}$$

where a , b , and c coefficients that are computed for two cases separately and derived two models as in Eq. (11b)–(11c). Further, Y_i denotes measured response for corresponding X_i . In the next step, models are implemented in PIC μC from which the ideal counter values were elicited for various input voltage as depicted in Fig. 3. It is observed that for both cases of V_{in} , the errors have been curtailed to optimal level (i.e., 5.23 and 23.9 counts) so as to get close ideal design. Additionally, a comparison with recently reported state-of-the-art techniques is summarized in Table 2 to highlight the effectiveness of the proposed framework. It specifically outlines their measurement complexity, performance, and number of

Table 2 Comparison of performance of the state-of-the-art techniques

# Method	# Complexity	Error in %	Component Involved
[2, 3]	Low	NA	Impedances and an opamp
[4]	Low	<1	Resistance, capacitance, and opamps
[5]	Medium	<0.15	Switches, resistance, capacitance, D-flip-flop
[6]	Medium	<0.2	Switches, resistance, capacitance, opamps
[7, 12]	Low	<0.2	Two resistances, capacitor
[8]	High	<1	Bridges, opamps, resistances, capacitor
[9]	High	<0.2	Switches, resistance, capacitance, opamps
[10]	Low	NA	Resistance, capacitance, timers, etc.
[11]	Low	<0.05	Switches, resistance, capacitance, and opamps
Proposed	Low	<0.02	Two resistances, capacitor

Boldface indicates significant parameters of proposed scheme

components involved. Most importantly, it evinces two facts: First, the proposed scheme obviates the need of complex circuitry and expensive C , and second, it achieves higher accuracy with worst-case error of $<0.02\%$.

We thus conclude, as the experimental outcomes and analysis unequivocally suggest, that the adopted methodology is efficacious and its performance makes this work an important step for an accurate resistive sensor measurement design that promotes further future endeavor in this direction.

4 Conclusion

In this article, we have presented an efficient nonlinear offset measurement and nullification approach which is found to be effective based on experimental validation. Further, multiple CFMs are deployed and inspected for finding the suitable model for specific task. The significant aftermaths mark this work an important step toward accurate design setup for reliable interpretations. Future works attempt to expedite its application for multisensor array.

References

1. E. O. Doebelin, *Measurement Systems-Application and Design*, 5th ed. New York, NY, USA: McGraw-Hill, 2004.
2. G. I. Borchardt, and L. R. Holland, Pseudo bridge: a different way to compare resistances *Review of Scientific Instruments*, vol. 46, no. 1, pp. 67–70, 1975.
3. J. M. Torrents, and R. Palls-Areny, R. Compensation of impedance meters, when using an external front-end amplifier, *IEEE Transactions on Instrumentation and Measurement*, vol. 51, no. 2, pp. 310–313, 2002.
4. A. Flammini, D. Marioli, and A. Taroni, A low-cost interface to high-value resistive sensors varying over a wide range, *IEEE Transactions on Instrumentation and Measurement*, vol. 53 no. 4, pp. 1052–1056, 2004.
5. N.M. Mohan, B. George, and V.J. Kumar, Analysis of a sigmadelta resistance-to-digital converter for differential resistive sensors, *IEEE Transactions on Instrumentation and Measurement*, vol. 58, no. 5, pp. 1617–1622, 2009.
6. N.M. Mohan, B. George, and V.J. Kumar, A novel dual-slope resistance-to-digital converter, *IEEE Transactions on Instrumentation and Measurement*, vol. 59, no. 5, pp. 1013–1018, 2010.
7. T. Islam, L. Kumar, Z. Uddin, and A. Ganguly, Relaxation oscillator-based active bridge circuit for linearly converting resistance to frequency of resistive sensor, *IEEE Sensors Journal*, vol. 13, no. 5, pp. 1507–1513, 2013.
8. L. Bengtsson, “Direct analog-to-microcontroller interfacing.” *Sensors and Actuators A: Physical*, vol. 179, pp. 105–113, 2012.
9. P.R. Nagarajan, B. George, and V.J. Kumar, An Improved Direct Digital Converter for Bridge-Connected Resistive Sensors, *IEEE Sensors Journal*, vol. 16, no. 10, pp. 3679–3688, 2016.

10. O. Lopez-Lapea, E. Serrano-Finetti, and O. Casas, Low-Power Direct Resistive Sensor-to-Microcontroller Interfaces, *IEEE Transactions on Instrumentation and Measurement*, vol. 65, no. 1, pp. 222–230, 2016.
11. V. Sreenath, S. Koniya and B. George, A Resistive Sensor Readout Circuit With Intrinsic Insensitivity to Circuit Parameters and Its Evaluation, *IEEE Transactions on Instrumentation and Measurement*, vol. 99, pp. 1–9, 2017.
12. L. Dutta, A. Hazarika and M. Bhuyan, Microcontroller Based E-Nose for Gas Classification without Using ADC, *Sensors Transducers*, vol. 202, no. 7, pp. 38–45, July 2016.

Fuzzy Rule-Based Set Point Weighting for PID Controller

Kausik Sen, Biswajit Chakraborty, Amit Gayen and Chanchal Dey

Abstract PID controllers are still very popular in process industries due to their simple design and easy tuning. Model-free tuning relations are relatively preferred compared to model-based tuning relations as identification of the true model for industrial processes is not an easy task. Ziegler-Nichols (ZN) setting is one of the most widely accepted model-free tuning guidelines. However, for higher-order processes, it provides undesired oscillations during set point change and load variation. Fixed set point weighting (FSPW) and variable set point weighting (VSPW) techniques are reported to restrict the oscillations during set point tracking only. Recently, reported dynamic set point weighting (DSPW) is capable to provide an overall improvement during set point change as well as load varying conditions. But to achieve further performance enhancement of a PID controller, a simple fuzzy rule-based set point weighting (FRSPW) technique is reported here for under-damped second-order processes. Superiority of the proposed FRSPW-based PID controller is established through quantitative estimation of various performance indices and, moreover, its adequate robustness is also observed in presence of considerable perturbation of process parameters.

Keywords PID controller · Fuzzy rule-based set point weighting
Fixed set point weighting · Variable set point weighting · Dynamic set point weighting

K. Sen (✉) · B. Chakraborty · A. Gayen · C. Dey
Instrumentation Engineering, Department of Applied Physics, University of Calcutta,
Kolkata, India
e-mail: kausiksen1993@gmail.com

B. Chakraborty
e-mail: biswajit.chakraborty1991@gmail.com

A. Gayen
e-mail: gayenamit10@gmail.com

C. Dey
e-mail: cdaphy@caluniv.ac.in

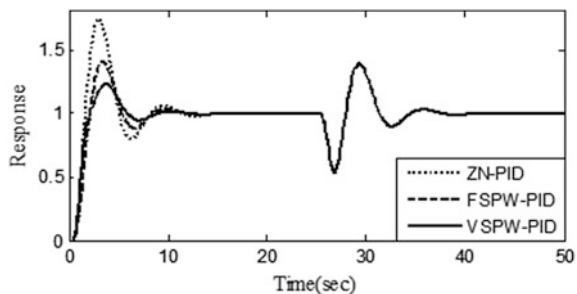
1 Introduction

PID controllers are still widely accepted in process industries for their simple design and easy tuning methodologies [1]. Due to lack of availability of exact process model usually model-free tuning techniques are relatively preferred compared to model-based tuning schemes. Ziegler-Nichols (ZN) setting [2] is one of the most widely accepted model-free tuning guidelines since from its inception. However, during closed-loop control for higher-order processes, ZN tuned PID controller (ZN-PID) is found to provide undesired oscillations during set point change and load varying phases [1]. To reduce process oscillations during set point tracking, set point weighting, and set point filtering [3–5] methods are widely used at the cost of increased rise time. But the reported filtering and fixed set point weighting (FSPW) mechanisms fail to offer any improvement during load rejection phases. In FSPW-based PID controller (FSPW-PID), a fixed weighting factor ($\beta = 0.5\text{--}0.7$) is multiplied to the set value. Variable set point weighting (VSPW) technique is suggested in [6] to restrict process oscillations during set point response without compromising in rise time value.

In VSPW, instead of a fixed weighting factor, three different values are provided as the set point weight depending on the process operating conditions during set point tracking phase. Notably, VSPW still fails to offer any improvement during load variation. The responses of ZN-PID, FSPW-PID ($\beta = 0.6$), and VSPW-PID are depicted in Fig. 1 where hardly any improvement is observed for VSPW-PID in comparison with FSPW-PID and ZN-PID during load rejection phase. To achieve an optimal response during set point change and load variation, separate set point weighting factors for proportional and derivative terms are derived in [7] using heuristic algorithms. Toward achieving improved responses during set point change as well as load variation simultaneously, an online dynamic set point weighting (DSPW) technique is reported in [8, 9]. In DSPW, the dynamic set point weighting factor β_d is heuristically derived from the instantaneous process states such as error $e(k)$ and change of error $\Delta e(k)$.

To further enhance the overall performance of a PID controller during transient as well as steady-state operating phases; here, we propose a fuzzy rule-based set point weighting mechanism (FRSPW) for conventional PID controller and the

Fig. 1 Responses of ZN-PID, FSPW-PID, and VSPW-PID for second-order process



resulting controller is named as FRSPW-PID. In the proposed FRSPW, instantaneous value of the weighting factor is obtained from a fuzzy rule base consisting of twenty-five rules only. Here, the rule base is designed based on sliding mode principle. Input variables of the fuzzy rules are considered to be error $e(k)$ and change of error $\Delta e(k)$, whereas the output is defined as the set point weighting factor β . Hence, the value of set point weighting factor varies depending on the process operating conditions in such a manner that an overall improved process response can be obtained from a conventional PID controller. To substantiate the efficacy of the proposed scheme, performance of FRSPW-PID controller is evaluated on under-damped second-order processes in comparison with variable set point weighting-based PID (VSPW-PID) and dynamic set point weighting-based PID (DSPW-PID) controllers. Designing steps of the proposed FRSPW-PID are discussed in Sect. 2, and its performance evaluation is made in Sect. 3. Considerable overall improvement is obtained during simulation study for the proposed scheme as estimated through a number of performance indices. At the end conclusion is provided in Sect. 4.

2 Controller Design

Block schematic of the proposed controller under closed-loop operation is shown in Fig. 2a. Here, the instantaneous value of the set point weighting factor is calculated from a pre-defined fuzzy rule base consisting twenty-five rules as shown in Table 1. This rule base is designed based on sliding mode principle; hence, no prior knowledge about the process is necessary for its designing. Input variables of the fuzzy rules are process error $e(k)$ and change of error $\Delta e(k)$ which are defined over the common normalized domain -1 to $+1$ with five triangular membership functions (MFs) as shown in Fig. 2b. The output variable β (weighting factor, normalized) is also denoted by five MFs defined over -1 to $+1$ as shown in Fig. 2b. All the triangular MFs are identical in shape having 50% overlap with their neighboring MFs. Input scaling factors are denoted as $G_e = 1$ and $G_{\Delta e} = 20$ and the output scaling factor is considered to be $G_\beta = 1$ for de-normalization of the weighting factor β_N as given by Eqs. (1)–(3). The blocks F and DF of Fig. 2a represent *fuzzification* and *defuzzification* modules, respectively. Nature of the weighting surface as depicted in Fig. 2c is found to be quite nonlinear in nature.

$$e_N = G_e e \tag{1}$$

$$\Delta e_N = G_{\Delta e} \Delta e \tag{2}$$

$$\beta = G_\beta \beta_N \tag{3}$$

Discrete form of fixed set point weighted PID controller at k th sampling instant is given by

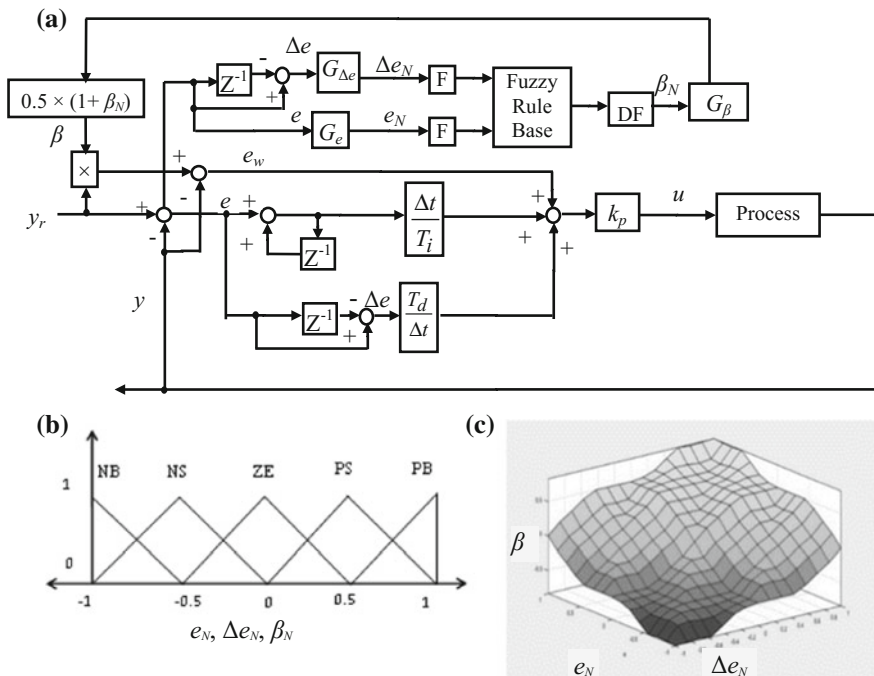


Fig. 2 a Block diagram of the proposed FRSPW-PID controller. b MFs for input and output variables. c Surface of weighting factor

Table 1 Fuzzy rule base for β

$\Delta e/e$	NB	NS	ZE	PS	PB
NB	NB	NB	NS	NS	ZE
NS	NB	NS	NS	ZE	PS
ZE	NS	NS	ZE	PS	PS
PS	NS	ZE	PS	PS	PB
PB	ZE	PS	PS	PB	PB

NB negative big, NS negative small, ZE zero, PS positive small, PB positive big

$$u(k) = k_p \left[\beta \times y_r - y(k) \right] + \frac{\Delta t}{T_i} \sum_{i=0}^k e(i) + T_d \left\{ \frac{e(k) - e(k-1)}{\Delta t} \right\} \quad (4)$$

Here, β represents the fixed weighting factor, $y(k)$ is the process output at k th instant, k_p denotes the proportional gain, T_i is the integral time, T_d is the derivative time, and Δt is the sampling interval.

In the reported dynamic set point mechanism [9], the weighting factor β_d is dynamic in nature and it is defined by the Eq. 5.

$$\beta_d(k) = [1 + \gamma \times \theta \times \Delta e_N(k)] \tag{5}$$

In Eq. (5), γ is an adjustable tuning parameter and θ is the normalized dead time of the process, and $\Delta e_N(k)$ is the normalized change of error at k th instant. But in our proposed FRSPW-PID scheme, the weighting factor β is continuously updated at every sample instant by the following relation

$$\beta(k) = 0.5 \times (1 + \beta_N) \tag{6}$$

where the instantaneous value of β_N is directly obtained from a fuzzy rule base as defined in Table 1. Here, it is to mention that in contrary to the dynamic set point weighting, process knowledge is not required for our proposed FRSPW-PID in calculating the value of the weighting factor. Moreover, the rule base for obtaining the weighting factor is designed based on sliding mode principle depending on the process error $e(k)$ and change of error $\Delta e(k)$ which can be calculated by the following relations

$$e(k) = y_r(k) - y(k) \tag{7}$$

$$\Delta e(k) = e(k) - e(k - 1). \tag{8}$$

The resultant weighting factor β is multiplied with the set point toward obtaining the weighted set point for proportional action only. This rule base (Table 1) is so designed which provides suitable weighting factor during both the transient and steady-state operating conditions in such a manner that process oscillations can be restricted within the acceptable limit. Here, it is to note that for designing the fuzzy rule base it doesn't require any prior knowledge about the concerned process. Moreover, in case of our proposed FRSPW-PID, no additional parameter (γ, θ) is required for computation of the dynamic weighting factor. The overall control strategy for the proposed FRSPW-PID is described as follows-

- When the output is diverging in nature or in other words the process response is moving away from the set point, both $e(k)$ and $\Delta e(k)$ are of similar sign, i.e., either negative or positive. During such circumstances, strong proportional action is required to bring the response back to the desired value and to restrict the further divergence of the response. Hence, the weighting factor value is so adjusted that the magnitude of effective error gets increased under such operating conditions.
- In contrary, when the response converges toward the set point (where the sign of $e(k)$ and $\Delta e(k)$ is opposite), there is a possibility of larger undershoot or overshoot in subsequent phases. Under such circumstances, the value of the weighting factor is so adjusted that the proportional control action gets reduced to restrict the probable undesired oscillation.

3 Results

Performance of the proposed FRSPW-PID is compared with variable set point weighting-based PID (VSPW-PID) and dynamic set point weighted PID (DSPW-PID) controllers through simulation study for second-order linear and second-order marginally stable processes with dead time. To have a clear comparison among the reported controllers, a number of performance indices—%OS (percentage overshoot), T_p (peak time), T_r (rise time), T_s (settling time), IAE (integral absolute error), and $ITAE$ (integral time absolute error) are evaluated for each case separately. Mamdani-type inferencing is used with centroid method for defuzzification. The general expression of a second-order process with dead time can be given by

$$G_p(s) = \frac{k e^{-Ls}}{as^2 + bs + c} \quad (9)$$

where k is the open-loop process gain and L is the dead time.

3.1 Second-Order Linear Process

A second-order linear process can be realized by considering $a = 1$, $b = 1$ and $c = 0.2$. Transfer function for the second-order linear process with open-loop gain $k = 1$ and dead time $L = 0.4$ s is given by

$$G_p(s) = \frac{e^{-0.4s}}{s^2 + s + 0.2}. \quad (10)$$

Unit step input is applied as set point change and once the process reaches the steady state, a load disturbance is applied. The overall performance indices for all the reported controllers are listed in Table 2a. To verify the robustness of the proposed FRSPW-PID along with VSPW-PID and DSPW-PID, process model parameters are perturbed by a considerable amount (20%). The perturbed model is given by Eq. (11), and corresponding performance indices are depicted in Table 2b. Responses for both the nominal and perturbed models are shown in Fig. 3a, b, respectively.

$$G_p(s) = \frac{1.2e^{-0.4s}}{1.2s^2 + 0.8s + 0.24} \quad (11)$$

Table 2 a Performance analysis for nominal model given by Eq. (10). **b** Performance analysis for perturbed model given by Eq. (11)

	VSPW-PID	DSPW-PID	FRSPW-PID
<i>a</i>			
OS%	13.10	34.80	7.30
T _p (s)	3.60	4.70	5.20
T _r (s)	2.35	2.42	2.90
T _s (s)	5.30	12.2	4.60
IAE	3.77	4.41	3.09
ITAE	66.62	53.70	40.55
<i>b</i>			
OS%	30.20	34.60	15.30
T _p (s)	3.00	4.70	2.90
T _r (s)	2.00	2.10	2.30
T _s (s)	11.70	8.20	5.70
IAE	6.13	4.22	3.31
ITAE	130.50	53.63	48.94

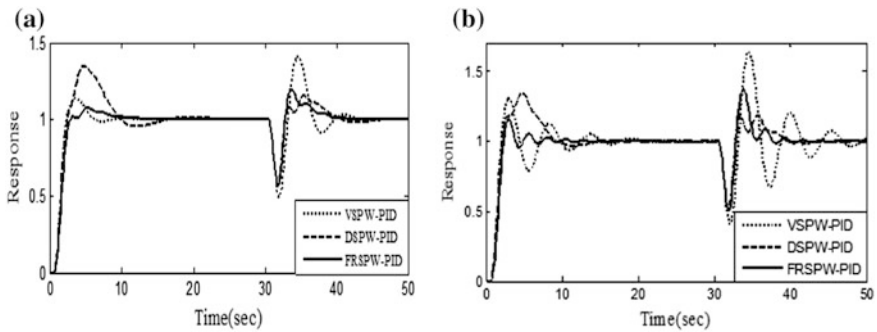


Fig. 3 a Responses of nominal model given by Eq. (10). **b** Responses for perturbed model given by Eq. (11)

3.2 Second-Order Marginally Stable Process

A second-order marginally stable process can be realized from Eq. (12) by considering $a = 1$, $b = 1$ and $c = 0$. The open-loop gain is considered to be $k = 1$ and dead time $L = 0.3$ s.

$$G_p(s) = \frac{e^{-0.3s}}{s^2 + s} \tag{12}$$

This particular model as given by Eq. (12) is very important for industrial automation processes as it represents the servo position control system. Due to location of one pole at origin, it provides highly oscillatory responses. Performance of our proposed FRSPW-PID controller is evaluated along with the VSPW-PID and DSPW-PID controllers under both set point change and load variation. Robustness feature of the reported controllers are also verified with considerable perturbation in process parameters as given by Eq. (13). Responses as shown in Fig. 4a, b along with performance indices as listed in Table 3a, b for the nominal and perturbed models clearly substantiate the superiority of the proposed FRSPW-PID in comparison with VSPW-PID and DSPW-PID.

$$G_p(s) = \frac{1.2e^{-0.3s}}{1.2s^2 + 0.8s} \tag{13}$$

Based on the simulation study, we can find that our proposed fuzzy rule-based set point weighting mechanism is quite effective in providing the desired set point response with smaller overshoot and faster settling. In addition, during load variation, it is capable to provide early recovery to regain the desired steady-state behavior. The most important feature of this proposed weighting scheme is that it does not require any prior knowledge about the process to be controlled. Hence, this technique can be used for any type of closed-loop control applications toward performance enhancement of conventional PID controllers. Number of rules in the fuzzy rule base may be increased for achieving more smooth and preferred variation of the weighting factor so that closed-loop responses can be further enhanced and all such possibilities are there in the future scope.

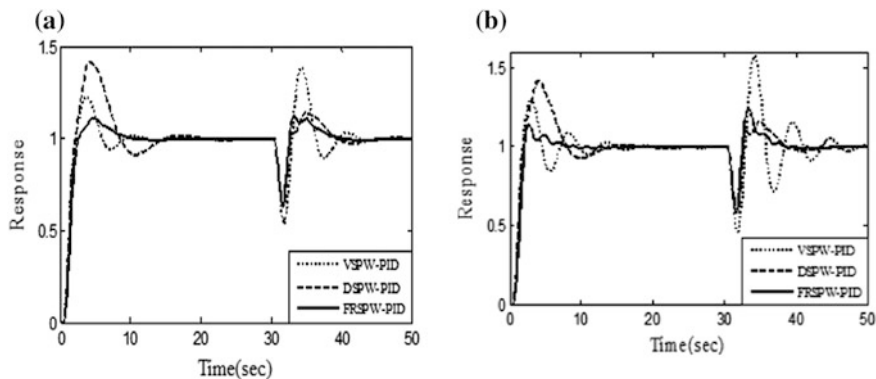


Fig. 4 a Responses of nominal model given by Eq. (12). b Responses of perturbed model given by Eq. (13)

Table 3 a Performance analysis for nominal model given by Eq. (12).

b Performance analysis for perturbed model given by Eq. (13)

	VSPW-PID	DSPW-PID	FRSPW-PID
<i>a</i>			
OS%	22.90	41.50	11.40
T _p (s)	3.70	4.13	4.61
T _r (s)	2.17	2.09	2.52
T _s (s)	7.66	12.67	7.14
IAE	3.70	4.31	2.76
ITAE	63.63	50.40	33.57
<i>b</i>			
OS%	30.40	41.9	14.00
T _p (s)	2.92	3.94	2.63
T _r (s)	1.76	1.79	2.01
T _s (s)	9.08	11.43	5.34
IAE	5.10	4.09	2.70
ITAE	106.70	49.23	36.39

4 Conclusion

Fuzzy rule-based set point weighting scheme for PID controller is proposed here. The instantaneous value of the set point weighting factor is provided from a fuzzy rule base depending on the latest process operating conditions in terms of process error and change of error. Enhancement in process response is obtained during both the set point tracking and load rejection phases. The rule base is designed here is based on sliding mode technique without any prior knowledge about the concerned process. Hence, this scheme is quite effective for achieving improved responses for any conventional PID controller employed in closed-loop control applications.

References

1. Dey, C., Mudi, R. K., An improved auto-tuning scheme for PID controllers, ISA Transactions, 48(3), pp. 396–409 (2009).
2. Ziegler, J. G., Nichols, N. B. Rochester, Y. B., Optimum settings for automatic controllers, Transaction of ASME 759–765 (1942).
3. Khan, B. Z., Lehman, B., Set-point PI controllers for systems with large normalized dead-time. IEEE Trans. Control Sys. Tech. 4(4), pp. 459–466 (1996).
4. Hang, C. C., Astrom, K. J., Ho, W. K., Refinements of Zeigler-Nichols tuning formula. IEE Proc.-D. 138(2), pp. 111–118 (1991).
5. Rangaiah, G. P., Krishnaswamy, P. R., Set-point weighting for simplified model predictive control. Chem. Eng. J. 50(3), pp. 159–163 (1992).
6. Hang, C. C., Cao, L., Improvement of transient response by means of variable set-point weighting. IEEE Trans. Ind. Elect. 43(4), pp. 477–484 (1996).

7. Prashanti, G., Chidambaram, M., Set-point weighted PID controllers for unstable systems. *J. Franklin Institute.* 337(2–3), pp. 201–215 (2000).
8. Mudi, R. K., Dey, C., Performance improvement of PI controllers through dynamic set-point weighting. *ISA Trans.* 50(2), pp. 220–230 (2011).
9. Dey, C., Mudi, R. K., Lee, T. T., Dynamic set-point weighted PID controller. *Cont. Int. Sys.* 37 (4), pp. 212–219 (2010).

RBF Neural Network-Based Wavelet Packet Energy-Aided Fault Localization on a Hybrid Transmission Line

Animesh Sarkar and Bikash Patel

Abstract This paper presents a fault localization technique based on wavelet packet decomposition (WPD) and radial basis function neural network (RBFNN) for a hybrid transmission line consisting of an overhead line and an underground cable fed from both ends. The transmission line is simulated in Electromagnetic transients program (EMTP) and only fault currents are recorded at local end of the transmission line. Third-level WPD with mother wavelet db1 is utilized to calculate wavelet packet energies of fault current at each node. The normalized values of these features are fed to the RBF neural network to estimate fault location on both overhead section and an underground cable. The algorithm is fast as only half cycle post-fault data are sufficient and need not identify the fault sections (overhead line or underground cable) for estimating fault location. The accuracy of fault localization is very high irrespective of fault resistances, fault inception angles (FIA), and fault types at different locations on the hybrid transmission line.

Keywords Hybrid transmission line · Feature extraction · Wavelet packet decomposition (WPD) · Fault inception angle (FIA) · Radial basis function neural network (RBFNN)

1 Introduction

A transmission line is an important component of electric power system, and its protection is necessary for ensuring power system stability and minimization of damage to the equipment due to short circuits that may occur on transmission lines. Fast detection of faults on a transmission line enables quick isolation of the faulty

A. Sarkar (✉) · B. Patel
Department of Electrical Engineering, Kalyani Government Engineering College,
Nadia, West Bengal, India
e-mail: animesh.6796@gmail.com

B. Patel
e-mail: biks.ee@gmail.com

line from service and hence protecting it from the harmful effects of faults. Accuracy in fault localization is important for quick repair of the faulty line to restore power supply and enhances reliability. A fault analysis technique on a transmission line based on discrete wavelet transform (DWT) and Karen Bell transformation (KBT) is presented in [1]. A combination of DWT and artificial neural network (ANN) is used for detection and classification of faults on transmission line [2, 3]. The authors in [4] introduce a fault analysis technique on a UPFC compensated double circuit transmission line using wavelet transform and fuzzy logic. Fuzzy logic-based methods require large training set for better accuracy in fault localization if the system condition is varied widely. Support vector machines (SVM)-based fault classification and localization techniques are presented in [5, 6]. Wavelet transform-aided SVM-based methods for fault localization are applied in a distribution system [7] and a transmission line [8]. Article [9] proposes a discrete orthogonal S transform (DOST) and SVM-based transmission line protection scheme. Wavelet packet decomposition-based transmission line fault analysis techniques are presented in [10, 11].

Fault localization on a combined transmission line of overhead system and underground cable requires quite different approach as traveling wave velocity and characteristics impedance are different for an overhead line and underground cable. Phasor measurement techniques [12, 13] and fuzzy interface system [14] are applied for locating faults on a transmission line consisting of overhead conductors and underground cable. Phasor-based method introduces error since it uses only fundamental and harmonics components of fault voltage and current. In [15], SVM is utilized to classify and identify the fault section in a series compensated transmission line. DWT-based traveling wave method is proposed in [16] for localization of faults on a hybrid transmission line. But this method requires data recording at very high sampling rate for accuracy. All these techniques proposed in [12–16] need additional algorithm for fault section identification before localizing faults.

The present article has proposed a wavelet packet decomposition (WPD) and radial basis function neural network (RBFNN)-based fault localization method on a hybrid transmission line irrespective of fault section identification. The wavelet packet energy has been extracted from post-fault half cycle current signal recorded only at one end of the transmission line and fed to RBFNN for localizing faults on both overhead line and underground cable sections.

2 Wavelet Packet Energy

In wavelet packet decomposition (WPD), signal is passed through more filters as compare to DWT. In DWT, approximation coefficients are decomposed at each level by passing the signal through high- and low-pass filters. However, in WPD, both the detail and approximation coefficients are decomposed, and hence, it provides better resolution than DWT. A three-level wavelet packet decomposition tree is shown in Fig. 1.

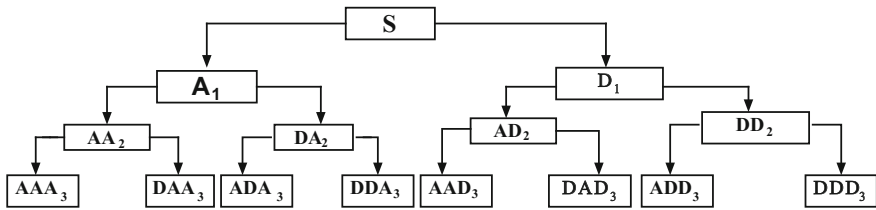


Fig. 1 Three-level wavelet packet decomposition tree

A wavelet packet function can be obtained from sequence functions satisfying the scaling function and the wavelet function [11] and is represented by

$$W_{j,n,k}(t) = 2^{-j/2} S_n(2^{-j}t - k) \tag{1}$$

where $k, j,$ and n are time localization parameter, scale parameter, and modulation parameter, respectively. The wavelet packet coefficients of a signal $f(t)$ are computed by taking the inner product of the signal and the particular wavelet packet function as

$$C_{j,n,k} = \langle f(t), W_{j,n,k}(t) \rangle = \int f(t)W_{j,n,k}(t)dt \tag{2}$$

The WPD coefficients are sorted out to wavelet packet nodes representing specific band of frequencies. Each coefficient of a wavelet packet represents the feature of the signal. The energy of a wavelet packet node is obtained by summing the square of coefficients in each frequency band corresponding to the node as

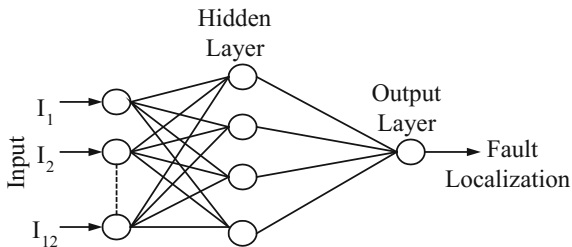
$$E_{j,n} = \sum_{k=1}^L C_{j,n,k}^2 \tag{3}$$

where $k = L$ is the number of WPD coefficients in each node for j -level wavelet packet decomposition with $n = 0, 1, 2, \dots, (2^j - 1)$.

3 Radial Basis Function Neural Network

Radial basis function neural networks (RBFNNs) are a feed-forward network consisting of three layers, i.e., input layer, hidden layer, and output layer. Input vectors are fed to the network via input layer, which communicate to one or more hidden layer where the actual processing is done. The hidden layer consisting of a set of radial basis functions calculates the Euclidean distance between the center and the input vector, and then, the result is passed to the radial basis function. RBFNN performs a nonlinear mapping from input layer to hidden layer and then

Fig. 2 Architecture of radial basis function neural network



linear mapping from hidden layer to output layer. For an input x , the output of the network can be represented as

$$d_i = w_{oi} + \sum_{j=1}^h \omega_{ji} \Phi(\|x - c_j\|, \beta_j) \tag{4}$$

where $i = 1, \dots, m$ and $j = 1, \dots, h$. w_{oi} is the biasing term, h is the number of hidden units, ω_{ji} is the weight between the j th hidden node and the i th output node, c_j is the center of the j th hidden node, β_j is the real constant known as spread factor, and $\Phi(\cdot)$ is the activation function. Here Gaussian radial basis function is used as activation function represented in (5) for the j th hidden unit.

$$\phi(z_j, \beta_j) = \exp\left(-z_j^2 / \beta_j^2\right), \quad z_j = \|x - c_j\| \tag{5}$$

In the present work, the normalized current energies of eight WPD frequency bands for each phase are fed to RBFNN for fault localization. Thus, input layer of this RBFNN has 24 inputs and the output layer has one output, i.e., fault location as shown in Fig. 2. One of the important features of this neural network is that it creates neurons in the hidden layer one by one until the error goal is achieved, leading to fast convergence irrespective of selection of neurons.

4 Transmission Network Under Consideration

In the present work, a 400 kV, three phase, 50 Hz power transmission network fed from both ends is simulated using ATP/EMTP software and the single-line diagram of the power system is shown in Fig. 3. The length of the transmission line is 140 km, of which overhead section is 100 km and underground section is 40 km. The transmission line is modeled using positive, negative, and zero sequence components of transmission line resistance, inductance, and capacitance. BCTRAN model of transformers (Tr1, Tr2, and Tr3) is used in EMTP simulation. Two three-phase balanced load of rating of 800 MVA, 0.92 lagging power factor (load 1) and 100 MVA, 0.87 lagging power factor (load 2) are connected at the Bus 2 of the transmission line. The voltages of the two alternators (Alt1 and Alt2) are

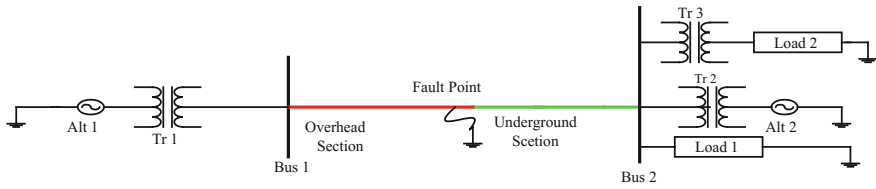


Fig. 3 Single-line diagram of the transmission system under consideration

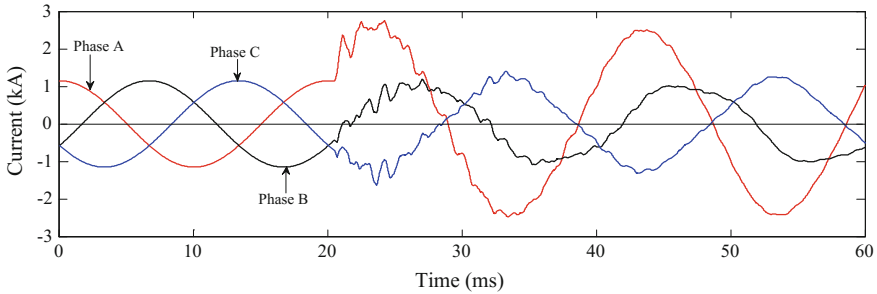


Fig. 4 Current waveform for SLG fault at 120 km, FIA 90° and fault resistance 0 Ω

considered as $V_1 = 21\angle 0^\circ$ kV and $V_2 = 21\angle(-10^\circ)$ kV. Single line to ground (SLG) and double-line fault (LL) with fault resistances (R_f) of 0, 20, and 150 Ω at different fault inception angles have been simulated. Faults have been initiated at nine locations with 10 km apart in overhead section and at seven locations with 5 km apart in underground cable section for training. The faults have also been created at 15 random locations, out of which nine locations are on the overhead section and six locations are on the underground section. The fault signals are recorded at Bus-1 for time duration of 60 ms with sampling frequency of 100 kHz. Current waveforms at Bus-1 for SLG fault at phase A at a distance 120 km away from Bus-1 with fault impedance 0 Ω and FIA = 90° are shown in the Fig. 4.

5 Feature Extraction and Fault Localization

The wavelet packet decomposition up to third-level decomposition with mother wavelet db1 has been used for feature extraction of fault currents recorded at Bus-1. Energies at each node of wavelet packet decomposition tree (Fig. 1) are calculated, and these are used as fault features for localization of faults on the transmission line. The extracted features are fed to RBF neural network designed in MATLAB for localization of faults on the hybrid transmission line. The efficacy of the proposed algorithm has been tested for different types of faults, fault resistances, and fault inception angles at different locations on both overhead line and underground cable sections. Sample results of fault localization are shown in Table 1. To obtain

Table 1 Results of fault localization

Actual fault location (km)	SLG fault for FIA = 0° and $R_f = 20 \Omega$		SLG fault for FIA = 0° and $R_f = 150 \Omega$		LL fault for FIA = 90° and $R_f = 0 \Omega$		LL fault for FIA = 0° and $R_f = 150 \Omega$	
	Estimated fault location (km)	%Error	Estimated fault location (km)	% Error	Estimated fault location (km)	%Error	Estimated fault location (km)	%Error
16	15.9659	-0.0243	16.028	0.0201	16.052	0.0372	15.973	-0.0195
23	22.9921	-0.0056	23.03	0.0212	22.963	-0.0264	22.978	-0.0157
36	36.0202	0.0145	35.999	-0.0005	36.033	0.0237	36.025	0.0176
43	43.0055	0.0039	42.983	-0.0118	43.008	0.0056	42.818	-0.1298
53	52.9858	-0.0101	52.974	-0.0186	53.059	0.0422	52.943	-0.0405
67	67.0057	0.0041	66.998	-0.0017	67.044	0.0314	66.98	-0.0144
76	76.0304	0.0217	76.028	0.0202	75.925	-0.0533	76.1	0.0715
87	87.0254	0.0181	87.034	0.0243	86.963	-0.0264	87.056	0.0401
92	91.9673	-0.0234	92.006	0.0046	92.004	0.0031	92.088	0.0626
107	107.0315	0.0225	106.98	-0.0137	106.98	-0.0127	106.9	-0.0705
113	113.0157	0.0112	113	0	112.7	-0.2142	112.96	-0.0259
119	118.9868	-0.0094	119.01	0.0058	119.31	0.2212	119.02	0.0135
122	121.9930	-0.0050	122.01	0.0075	121.85	-0.1085	122.01	0.0101
128	127.9922	-0.0056	128	0	128.14	0.1022	127.97	-0.0245
133	132.9988	-0.0008	133	0	132.75	-0.1793	133.04	0.0270

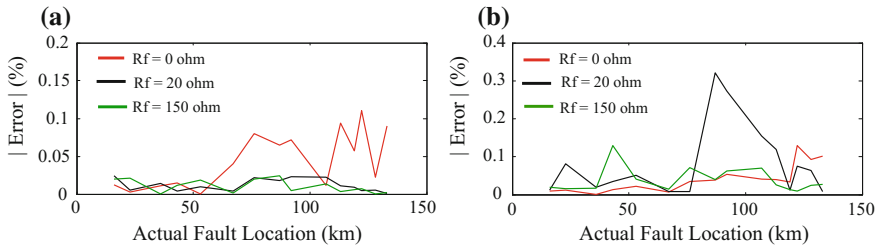


Fig. 5 Variation of absolute error of fault localization with fault resistances for **a** SLG fault with FIA 0° **b** LL fault with FIA 0°

uniform error for all fault locations, the error of fault localization is calculated with respect to total length of the line as given in (6).

$$\text{Error} = \frac{\text{Estimated fault location} - \text{Actual fault location}}{\text{Total length of transmission line}} \times 100\% \quad (6)$$

6 Result and Analysis

Faults on the transmission line cause power interruption to the consumers for long duration if these are not cleared quickly. Clearance of faults largely depends on fast and accurate localization of faults on the transmission line. The proposed algorithm clearly justifies this aspect as the accuracy of fault localization is very high as seen from Table 1. Fault conditions may vary depending on time of fault inception, numbers of phases involved, and geometrical location of fault points. This algorithm has been tested on a hybrid transmission line for SLG and LL faults with different fault resistances (0, 20, and 150 Ω) and fault inception angles (0° and 90°) at 15 different locations on both overhead and underground cable sections. The accuracy of fault localization is very high irrespective of types of faults, fault resistances, and fault inception angles. This proposed method is applicable for both low- and high-impedance faults, and the accuracy is even better for high fault resistance as shown in Fig. 5a, b.

7 Conclusion

This paper proposes a fault localization method using radial basis function neural network and wavelet packet decomposition for both end fed hybrid transmission line with an overhead line combined with an underground cable. The hybrid transmission line is modeled and simulated in EMTP software, and fault currents at

the local end of the line are recorded with sampling frequency 100 kHz. Wavelet packet decomposition up to third level with mother wavelet db1 is applied for feature extraction of the fault current signals. The normalized wavelet packet energies of fault currents are used as features and are fed to RBFNN for fault localization. The proposed algorithm performs with high degree of accuracy irrespective of fault resistance, FIA, and fault types. The major advantage of this algorithm is that this method is fast and independent of identification of fault section for locating faults on the transmission line.

References

1. Adly A. R., El Sehiemy R.A. and Abdelaziz A.Y.: A Novel Single End Measuring System Based Fast Identification Scheme for Transmission Line Faults. Measurement, (2017). doi: <http://dx.doi.org/10.1016/j.measurement.2017.02.041>.
2. Zin Abdullah Asuhaimi Mohd, Saini Makmur, Mustafa Mohd Wazir, Sultan Ahmad Rizal and Rahimuddin.: New Algorithm for Detection and Fault Classification on Parallel Transmission Line using DWT and BPNN based on Clarke's Transformation. Neurocomputing, (2015).
3. He Zhengyou, Lin Sheng, Deng Yujia, Li Xiaopeng and Qian Qingquan.: A rough membership neural network approach for fault classification in transmission lines. Electrical Power and Energy Systems, vol. 61, pp. 429–439, (2014).
4. Goli Ravi Kumar, Shaik Abdul Gafoor and Tulasi Ram S.S.: A transient current based double line transmission system protection using fuzzy-wavelet approach in the presence of UPFC. Electrical Power and Energy Systems, vol. 70, pp. 91–98, (2015).
5. Jafarian P. and Sanaye-Pasand M.: High Frequency Transients-Based Protection of Multiterminal Transmission Lines Using the SVM Technique. IEEE Trans. Power Del., vol. 28, pp. 188–196, (2013).
6. Ray Papia and Mishra Debani Prasad.: Support vector machine based fault classification and location of a long transmission line. Engineering Science and Technology, an International Journal, (MAY 2016).
7. Ye Lei, You Dahai, Yin Xianggen, Wang Ke and Wu Junchun.: An improved fault-location method for distribution system using wavelets and support vector regression. Electrical Power and Energy Systems, vol. 55, pp. 467–472, (2014).
8. Yusuff A. A., Jimoh A. A. and Munda J. L.: Fault location in transmission lines based on stationary wavelet transform, determinant function feature and support vector regression. Electric Power Systems Research, vol. 110, pp. 73–83, (2014).
9. Bharata Reddy M. Jaya, Gopakumar P. and Mohanta D.K.: A novel transmission line protection using DOST and SVM. Engineering Science and Technology, an International Journal, vol. 19, pp. 1027–1039, (2016).
10. Ekici Sami, Yildirim Selcuk and Poyraz Mustafa.: Energy and entropy-based feature extraction for locating fault on transmission lines by using neural network and wavelet Packet decomposition. Expert Systems with Applications, vol. 34, pp. 2937–2944, (2008).
11. Yusuff A. A., Fei C., Jimoh A. A. and Munda J. L.: Fault location in a series compensated transmission line based on wavelet packet decomposition and support vector regression. Electric Power Systems Research, Vol. 81, pp. 1258–1265, (2011).
12. El Din E. Sayed Tag, Aziz MM Abdel, Gilany M and Ibrahim DK.: Fault location scheme for combined overhead line with underground power cable. Electric Power System Research, vol. 76, no. 11, pp. 928–935, (Jul 2006).

13. Liu C. W., Lin T. C., Yu C. S. and Yang J. Z.: Fault location technique for two-terminal multi-section compound transmission lines using synchronized phasor measurements. *IEEE Trans. Smart Grid.*, vol. 3, no. 1, pp. 113–121, (Mar 2012).
14. Sadeh J. and Afradi H.: A new and accurate fault location algorithm for combined transmission lines using adaptive network-based fuzzy inference system. *Electric Power System Research*, vol. 79, no. 11, pp. 1538–1545, (Nov 2009).
15. Das P. K., Samantaray S. R. and Panda Ganapati.: Fault Classification and Section Identification of an Advanced Series-Compensated Transmission Line Using Support Vector Machine. *IEEE Trans. Power Del.*, vol. 22, no. 1, pp. 67–73, (Jan 2007).
16. Livani Hanif and Evrenosoglu Cansın Yaman.: A Machine Learning and Wavelet-Based Fault Location Method for Hybrid Transmission Lines. *IEEE TRANSACTIONS ON SMART GRID*, vol. 5, no. 1, (JANUARY 2014).

Design of an Adaptive Calibration Technique Using Data Fusion for Pressure Measurement

K. V. Santhosh and Bhagya R. Navada

Abstract This paper proposes design of adaptive calibration technique to eliminate the interference of noise in pressure measurement. Proposed paper objective is to design a signal-conditioning technique that measures the pressure accurately, even with variations in environmental parameters like humidity and temperature. Output of the capacitance pressure sensor is converted to voltage using the data conversion circuits. Distributed blackboard data fusion framework is used for creating an adaptive calibration technique to measure pressure accurately without interference of environmental parameters like temperature and humidity. Results of the proposed measurement technique are analyzed to evaluate the performance of proposed technique. Obtained results evidence the effective implementation of proposed calibration technique.

Keywords Calibration · Data · Fusion · Distributed black box framework
Pressure measurement

1 Introduction

Pressure sensors constitute more than 70% of sensor market. Most of the processes involve control of pressure as most of the hydraulic/pneumatic actuators are actuated by pressure. Controllers are used to control actuator pressure. For designing a stable controller, it is very essential to have knowledge of actual process variable. So, measurement of accurate pressure becomes a priority task for any process control application. Pressure measurement techniques are existing since a long time. Some of the techniques are surveyed and discussed to analyze the behavior, working, and characteristics.

K. V. Santhosh · B. R. Navada (✉)
Manipal Institute of Technology, Manipal University, Manipal, India
e-mail: kgbagya@gmail.com

K. V. Santhosh
e-mail: kv.santhu@gmail.com

In [1], pressure measurement by using micro-electrical mechanical systems (MEMSs)-based micro-nozzles. Paper [2] discusses the high-pressure measurement technique using piezoelectric sensors. Photonic crystal fiber sensors are used for measurement of pressure in [3], lookup table is used for calibration of sensor. Critically refracted longitudinal and Rayleigh waves and induced on the walls of vessels are analyzed to compute the pressure of vessel in [4]. Functional link artificial neural network-based calibration technique for capacitance pressure sensor is reported in [5]. In [6], calibration of pressure sensors is reported to compute the sit-to-stand timing. Multiplexed fiber Bragg gratings are used to measure pressure in a flexible superstructure in [7]. Design of fiber optic-based pressure sensor for residual pressure measurement is reported in [8]. In [9], high-pressure measurement is carried on by the principle of Faraday cup electrostatic discharge; applied pressure is measured by measuring the density of charge. Gas pressure is measured by finding the current load of a switched capacitor in [10]. In [11], discharge evaluation of flow process is measured by finding pressure drop across head-type flow sensor by neural network computation. In [12], calibration of CPS is achieved using ANN. Though a lot of techniques are reported for measurement of pressure, these concentrate only on pressure measurement with a certain range of measurement.

By analyzing the characteristics of pressure sensors in the following papers, it is found that [13] reports that CPS output varies with diaphragm properties. In [14], dielectric materials effect on output of CPS is discussed. In [15], temperature effect on CPS output is discussed. Analysis of pressure measurement sensor for variation in flow Reynolds number variation is reported in [16]. In [17], relation of pressure sensor output with variations in turbulent behavior of flow is reported. Analysis of pressure sensor behavior for step input, with changes in environment behavior, is discussed in [18]. From these papers, it is clear that the behavior of capacitance pressure sensor varies with changes in environmental parameters of measurement like humidity and temperature.

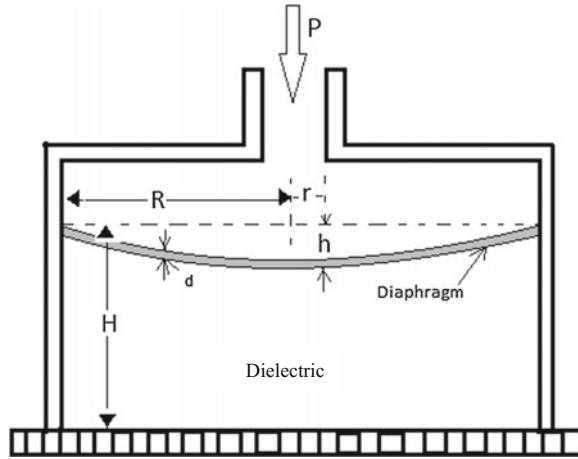
This paper makes an attempt to analyze the characteristics of pressure sensor behavior for variations in temperature and humidity. Also, the paper makes an attempt to measure pressure accurately and also makes the measurement technique independent to environmental parameters variations. The paper makes use of the concept of data fusion time wrapping techniques.

2 Available Technique

A. *Capacitance Pressure Sensor*

Capacitance pressure sensor consists of a thin diaphragm, made from elastic material. Process pressure is applied on one side of diaphragm, and other side is atmospheric pressure. Any change in applied pressure causes diaphragm to deflect and thus producing a change in capacitance. Schematic of CPS is shown in Fig. 1 [19–22].

Fig. 1 Capacitance pressure sensor



In the proposed work, a circular diaphragm is considered. A pressure of ‘P’ is applied to produce elasticity with a deflection ‘h’ at distance ‘r’ from diaphragm center. Deflection ‘h’ is given by

$$h = \frac{P\Psi(1 - q^2)^2}{\Phi} \text{ m} \tag{1}$$

where

- Ψ $3(1 - \rho^2)R^4$
- Φ $16 E d^3$
- q r/R
- ρ Poisson ratio
- E Young’s modulus
- ϵ_r Permittivity of dielectric material

The diaphragm movement causes a variation in capacitance to be formed across the plates of diaphragm, which is given by (2)

$$C = \int_0^R \frac{2\pi r}{H - h} dr F \tag{2}$$

On evaluating (2) and (1), we get

$$C = \frac{\pi R^2 \epsilon_o \epsilon_r}{H} \left(\sqrt{\frac{P\Psi}{\Phi H}} \right) \tanh^{-1} \left(\frac{P\Psi}{\Phi H} \right) F \tag{3}$$

The permittivity of dielectric used in capacitor is a function of relative humidity, which can be shown in relation (4)

$$\epsilon_{RH} = \epsilon. \left[1 + \frac{211}{t} \left(\frac{48.P}{t} .RH \right) .10^{-6} \right] \tag{4}$$

Young’s modulus of material is also a function of temperature which is given by (5)

Substitute in (1) and (3), we get

$$E(t) = E(t_0) * \left[1 + \left[\frac{t}{200 * \left[\ln \left(\frac{t}{1100} \right) \right]} \right] \right] \tag{5}$$

where

$E(t)$ E at t °C
 $E(t_0)$ E at t_0 °C

Capacitance function of temperature is given by (6)

$$C(t) = C(t_0) * \left(1 + \alpha(t - t_0) + \beta(t - t_0)^2 \right) F \tag{6}$$

where

$C(t)$ C at t °C
 $C(t_0)$ C at t_0 °C
 α, β constants

B. Data conversion circuit

555 IC is used to design a astable timer circuit to generate a train of pulses whose frequency

$$f = \frac{1}{\ln(2) * (R_1 + 2R_2) * C} \text{ Hz} \tag{7}$$

Derived frequency output from timer circuit is converted to voltage using a frequency to voltage converter (f - V)

$$V_{out} = (V_s * C_1 * R_1) * f V \tag{8}$$

3 Problem Statement

In this section, CPS is analyzed to know the effect of temperature and humidity on the characteristics. A simulation at different temperatures, like $t_1 = 25\text{ }^\circ\text{C}$, $t_2 = 50\text{ }^\circ\text{C}$, and $t_3 = 75\text{ }^\circ\text{C}$, and humidity of 10%RH, 40%RH, and 70%RH is carried out for finding the output capacitance of CPS. At each value of humidity and temperature, CPS is subjected to variation in input pressure and corresponding output capacitance is found.

Figures 2 and 3 show the variation of voltage considered at three different temperatures and humidity values with changes in input pressure. From the figures, it is clear that the output of CPS is a function of humidity and temperature. Now if the regular calibration technique is used, it produces erroneous reading as most calibration techniques use the mapping technique for computing pressure from the data conversion circuit output.

Fig. 2 CPS output voltage versus change in pressure at three different temperatures

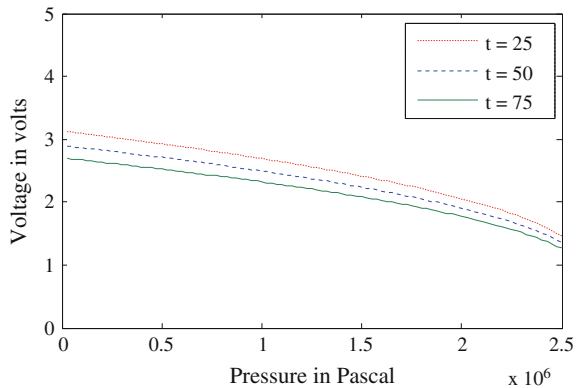
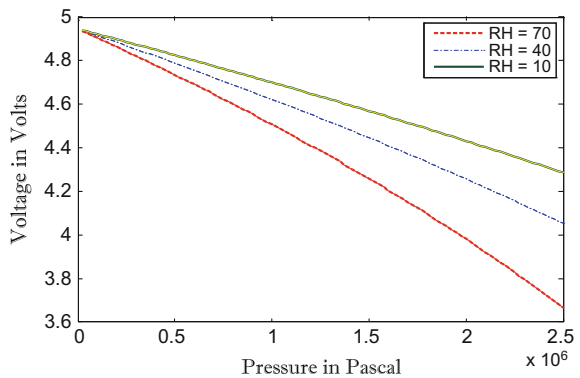


Fig. 3 CPS output voltage versus change in pressure at three different humidity values



4 Problem Solution

To overcome the drawback of interference of environmental parameters like humidity and temperature on pressure measurement, a technique is proposed using the technique of fusion. Data fusion performs combination of data collected from multiple sensors to offer completeness. Obtained data is fused in a form to obtain a quality output so that appropriate decision can be taken.

In the proposed technique, data fusion is achieved using distributed black box framework. Here, sensor data consisting of a number of transducers (T) are connected to sensor supervisor. Supervisor controls the handling of sensor measurements. Predefined confidence levels will be assigned for each sensor. The algorithm used for fusion produces a value F depending on the sensor values [23–25]. Figure 4 shows the block diagram of proposed data fusion framework.

The technique of data fusion consists of the following stages: In first stage, dynamic time wrapping is carried on to bring the sensor data to the equal weightage, further a parameter estimation using Bayesian curve fitting algorithm and extrapolation is used to find the mapping equation to make the output of calibration technique independent of parameter variations like humidity and temperature.

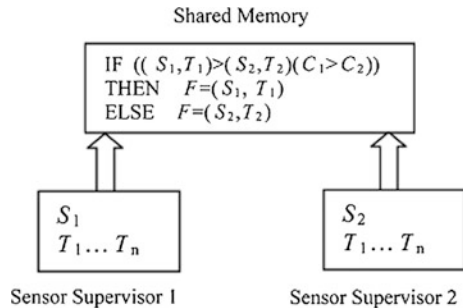
A. Dynamic time warping

Dynamic time warping (DTW) is a technique for finding any best alignment occurring among two sequences which are function of time under some constraints.

Primary purpose of DTW is to compare the data sequence from CPS for variations in humidity and temperature (time dependent) sequences $A := (a_1, a_2, \dots, a_Q)$ of length $Q \in N$ and $B := (b_1, b_2, \dots, b_P)$ of length $P \in N$. These sequence are signal is constrained over a period of time with equal intervals. In the following, the feature space is denoted by F . Then $a_q, b_p \in F$ for $p \in [1: N]$ and $q \in [1: N]$. To analyze features produced by CPS for temperature and humidity variations, $a, b \in F$, a cost function is defined relating to the output to compute the magnitude of dependencies of such function a, b on output of sensor.

$$c : F \times F \rightarrow R \geq 0. \tag{9}$$

Fig. 4 Block diagram of distributed black box framework



B. Polynomial interpolation

Polynomial interpolation of a given data is set by a polynomial. Interpolation polynomial is in the form

$$p(x) = a_n x^n + a_{n-1} x^{n-1} + \dots + a_1 x + a_0 \tag{10}$$

p interpolates the data points means that

$$p(x_i) = y_i, \quad \text{for all } i \in \{0, 1, \dots, n\} \tag{11}$$

C. Parameter estimation

Bayesian curve fitting is used to combine together multiple sensor observations. For a set of input measurement pairs (y_i, u_i) , $i \in \{1, 2, \dots, N\}$, an algebraic curve fitting the relation is computed.

D. Extrapolation

It is the process of estimating, beyond the original series, the value of the next state on the basis of its relationship with another variable.

5 Results and Conclusions

Once the data fusion technique is carried on using distributed black box framework, it is subjected to pressure measurement with variation in environmental parameters like humidity and temperature. For testing, the pressure is considered in the range of

Table 1 Shows the results of proposed technique for various input conditions

AP in 10 ⁶ Pa	RH	t in °C	MP in 10 ⁶ Pa	%error
0.5	10	25	0.486	2.80
0.72	20	30	0.718	0.28
0.85	25	35	0.851	-0.12
1.2	35	40	1.232	-2.67
1.4	45	45	1.386	1.00
1.6	50	50	1.577	1.44
1.9	55	55	1.879	1.11
2.2	60	60	2.234	-1.55
1.8	70	65	1.785	0.83
2.4	80	70	2.428	-1.17
1.7	90	75	1.745	-2.65
1.5	85	70	1.548	-3.20
1.3	75	65	1.268	2.46
0.9	65	60	0.841	6.56
0.6	30	55	0.631	-5.17

AP actual pressure
 MP measured pressure

0.5–2.5 Mpa, temperature between 0 and 75 °C, and humidity between 10 and 90% RH.

Response obtained from the proposed system is for variation in test input, and environmental parameters like humidity and temperature are shown in Table 1. Plot of input–output characteristics of proposed technique is plot in Fig. 5 and error graph in Fig. 6.

It is evident from Figs. 5 and 6, and Table 1, that the proposed measurement technique has output adaptive to variations in humidity and temperature. The percentage root mean square error obtained is 2.7%, which is considerable accurate.

Fig. 5 Response of the system for test inputs

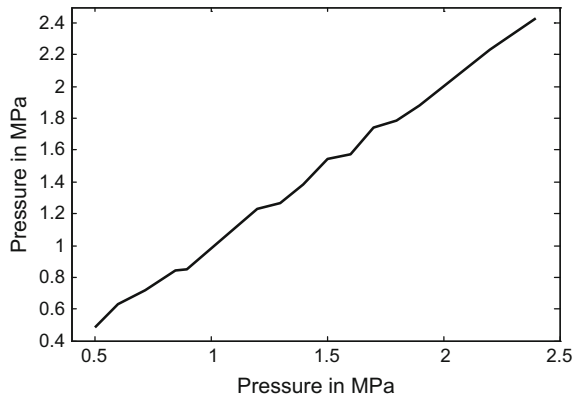
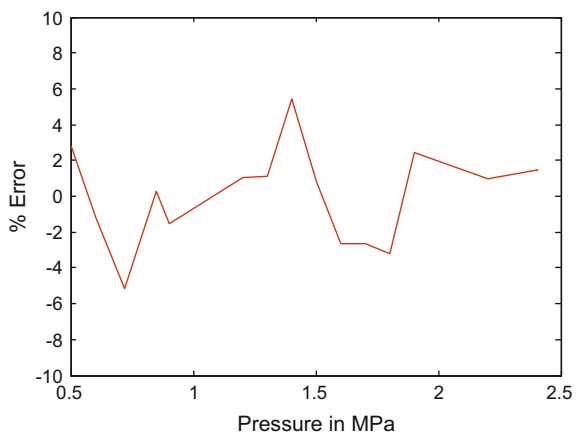


Fig. 6 Percentage error for variations in test inputs



References

1. C. Huang, J. W. Gregory, J. P. Sullivan, "Flow visualization and pressure measurements in micronozzles", *Journal of visualization*, vol. 10, no. 3, pp. 281–288, 2007.
2. S. B. Mishra, C. Nagaraj, V. Venkateswarlu, G. R. Adhikari, "Measurement and analysis of pore water pressure in large caverns and shafts in a hydro-electric project", *Journal of Geotech Geology Engineering*, vol. 26, pp. 367–374, 2008.
3. Wojtek J. Bock, Jiahua Chen, Tinko Eftimov, Waclaw Urbanczyk, "A photonic crystal fiber sensor for pressure measurements", *IEEE Transactions on instrumentation and measurement*, vol. 55, no. 4, pp. 1119–1124, 2006.
4. Zhangwei Ling, Hongliang Zhou, Hongjian Zhang, "Nondestructive pressure measurements in vessels using rayleigh waves and L_{CR} waves", *IEEE Transactions on instrumentation and measurement*, vol. 58, no. 5, pp. 1578–1584, 2009.
5. Jiaoying Huang, Haiwen Yuan, Yong Cui, Zhiqiang Zheng, "Nonintrusive pressure measurement with capacitance method based on FLANN", *IEEE Transactions on instrumentation and measurement*, vol. 59, no. 11, pp. 2914–2920, 2010.
6. Amaya Arcelus, Idana Veledar, Rafik Goubran, Frank Knoefel, Heidi Sveistrup, Martin Bilodeau, "Measurement of sit-to-stand timing and symmetry from bed pressure sensors", *IEEE Transactions on instrumentation and measurement*, vol. 60, no. 5, pp. 1732–1740, 2011.
7. David A Singlehurst, Christopher R Dennison, Peter M. Wild, "A distributed pressure measurement system comprising multiplexed in-fibre Bragg gratings within a flexible superstructure", *Journal of lightwave technology*, vol. 30, no. 1, pp. 123–129, 2012.
8. Jinde Yin, Tiegeng Liu, Junfeng Jiang, Kun Liu, Shuang Wang, Shengliang Zou, Zunqi Qin, Zhengyang Ding, "Self-Referenced residual pressure measurement method for fiber-optic pressure sensor chip", *IEEE photonics technology*, vol. 26, no. 10, pp. 957–960, 2014.
9. Di Song, Fawzi Salama, Johnny Matta, Poupak Mehrani, "Implementation of faraday cup electrostatic charge measurement technique in high-pressure gas-solid fluidized beds at pilot-scale", *Journal of powder technology*, vol. 290, pp. 21–26, 2016.
10. D. Smugala, P. Oramus, P. Krysztofiak, M. Bonk, P. Piekarski, T. Kaczmarczyk, "System for gas pressure measurements in the arc plasma environment", *Journal of Measurement*, vol. 90, pp. 199–207, 2016.
11. Georgiana Dunca, Diana Maria Bucur, Michel J Cervantes, Radu Popa, "Discharge evaluation from pressure measurements by a genetic algorithm based method", *Journal of flow measurement and instrumentation*, vol. 45, pp. 49–55, 2015.
12. Santhosh K V, B K Roy, "An Intelligent Pressure Measurement Technique Using Optimized ANN", *International Journal on Electrical and Power Engineering*, vol. 3, no. 4, pp. 16–21, Nov 2012.
13. Norhayati Soin, Burhanuddin Yeop Majids, "An Analytical Study on Diaphragm Behavior for Micro-Machined Capacitance Pressure Sensor", *Proc. International Conference on Semiconductor Electronics*, December, 2002, Penang, Malaysia.
14. Zongyang Zhang, Zhimin Wan, Chaojun Liu, Gang Cao, Yun Lu, Sheng Liu, "Effects of Adhesive Material on the Output Characteristics of Pressure Sensor", *Proc. 11th International Conference on Electronic Packaging Technology and High Density Packaging*, Shanghai, August 2011, China.
15. Cui Chun sheng, Ma Tie Hua, "The research of temperature compensation Technology and High-temperature Pressure Sensor", *Proc. International Conference on Electronic & Mechanical Engineering and Information Technology*, August 2011, Harbin, China.
16. Noriyuki Furuichi, Yoshiya Terao, "Static pressure measurement error at a wall tap of a flow nozzle for a wide range of Reynolds number", *Journal of flow measurement and instrumentation*, vol. 46, pp. 103–11, 2015.
17. Osamu Terashima, Yasuhiko Sakai, Kouji Nagata, Yasumasa Ito, Kazuhiro Onishi, Yuichi Shouji, "Simultaneous measurement of velocity of a planar turbulent jet", *Journal of Experimental thermal and fluid science*, vol. 75, pp. 137–146, 2016.

18. J. Y. Ferrandis, E. Rosenkrantz, G. Leveque, D. Baron, J. C. Segura, G. Cecilia, O. Provitina, "Full-scale hot cell test of an acoustic sensor dedicated to measurement of the internal gas pressure and composition of a LWR nuclear fuel rod", IEEE Transactions on nuclear science, vol. 60, no. 4, pp. 2894–2897, 2013.
19. Neubert, H. K. P, Instrument Transducers: an Introduction to their Performance and Design, Clarendon Press, Oxford 1975.
20. Lyons, J. L., The Designer's Handbook of PI-Pressure-Sensing Devices, Van Nostrand Reinhold, New York, 1980.
21. Bela G Liptak, Instrument Engineers' Handbook: Process Measurement and Analysis, 4th Edition, CRC Press, June 2003.
22. E.O. Doebelin, Measurement Systems - Application and Design, Tata McGraw Hill publishing company, 5th edition, 2003.
23. J. Llinas and E. Waltz, Multisensor Data Fusion. Boston, MA: Artech House, 1990.
24. D. Hall, Mathematical Techniques in Multisensor Data Fusion. Boston, MA: Artech House, 1992.
25. L. A. Klein, Sensor and Data Fusion Concepts and Applications, SPIE Opt. Engineering Press, Tutorial Texts, vol. 14, 1993.

Review on Internet of Things (IoT): Making the World Smart

Debajyoti Misra, Gautam Das and Debaprasad Das

Abstract Internet of things (IoT) is a network of objects linked to cyberspace. It increases rapidly and reaches all around, not only limited to smartphone or home appliances but employed in factories, business, and health care because it enhances efficiency, reduces cost, and saves lives. Think a world where billions of objects can feel, convey, and share information, and all interlinked over public or private Internet protocol (IP) networks. These interrelated things have data usually gathered, tested, and conformed to initiate an exercise, allowing a wealth of understanding for designing, managing, and judgment making. This is the world of the Internet of things (IoT). The Internet of things (IoT) is the upcoming trend of creation that assures to be better and makes our everyday life optimal, smarter, which is based on having intelligence devices and smart things operating at same time. Using Internet protocol (IP) facility, things can now be linked to the Internet, so permitting them to be understood, guided, and managed at every time and at every place. IoT is used in number of fields including designing smart city, connected vehicle, etc. This paper presents a review on IoT and depicts key challenges on the same field.

Keywords Internet of things (IoT) · IoT application · IoT architecture
IoT challenges · Radio frequency identification (RFID)

D. Misra (✉) · G. Das

Department of Electronics and Communication Engineering,
Siliguri Institute of Technology, Siliguri, India
e-mail: misra.debajyoti@gmail.com

G. Das

e-mail: gdas321@yahoo.co.in

D. Das

Department of Electronics and Communication Engineering,
Assam University, Silchar, India
e-mail: dasdebaprasad@yahoo.com

© Springer Nature Singapore Pte Ltd. 2018

R. Bera et al. (eds.), *Advances in Communication, Devices and Networking*,
Lecture Notes in Electrical Engineering 462,
https://doi.org/10.1007/978-981-10-7901-6_89

1 Introduction

Numbers of research communities are potently taking technical topics which add significantly updated content to the IoT. Nowadays, detecting, propulsion, exchanges of information, and control become very advanced and ubiquitous. This provides an opportunity to work in this field. The area of IoT is broad and provides many services, such as healthcare observation, transportation facility, and logistics department to find vehicles or packages or build the city smart. Generally, these things ask a platform that admits device monitoring, application development, and data management. It is apparent that the IoT comprises of vast number of objects being interconnected to the Internet. To provide novel and emerging technical improvement, the UK administration, in their 2015 budget, assigned £40,000,000 for research into the field of IoT [1]. IoT is the connection system between physical entities like various components, transportation system, constructions, and other things—fixed with electronics, software, detectors, and network connectivity that make capable of them together with the information and exchange data [2]. It also permits things to feel and operate remotely throughout present network framework, generating new opening for additional direct incorporation of the real world into automated systems and enhances perfection accurateness financial benefit. In the instance, Internet of things is raised with smart sensing devices and actuators; the technology develops an emerging Internet in the physical world, which also covers new technological innovation such as sophisticated grids, automated houses, and smart vehicle. Every object is separately identified through its particular calculating process but is capable to work within the present Internet architecture. Specialists on Internet of things make a calculation that the IoT will have of nearly 50 billion components by 2020 [3].

The IoT presents a new era of how various objects make our lives easier. Actually in IoT, the objects are having brain (they can take decision using sensors) and they can communicate to us (utilizing wireless networks) for taking better decisions. The Internet of things was first started its journey by the members of the radio frequency identification development (RFID) community in the year of 1999, and nowadays, IoT becomes compatible to the real world mostly due to the development of mobile devices, wireless transmission, remote server, and data analysis.

2 Application of IoT

Internet of things concerns with basic idea of things, specifically daily useable things which are able to be read, identifiable (able to identify location, addressable) and having ability to take command using the Internet, regardless of the communication means for example without using RFID, wireless LAN, wide area networks (WAN), or other means. IoT-based system not only limited to daily objects like the

electronic components or gadgets or the things made by higher technological advancement such as vehicles, heart monitoring electronic devices, injectable ID chip on livestock farming, automobiles having sensors, hi-tech DNA testing machine for environmental pathogen or food-borne pathogen observation or a particular operational objects which help fireman in search and saving operations but also things that we do not think of as electronic at all—for example, food and clothing [4] and other things like people, location of objects area, time information, and condition of objects (Fig. 1).

IoT provides anytime, anything, and anywhere (AAA) connectivity with real world. As per the report of Cisco Internet business solutions group, approximately 12.5 billion regular physical objects were connected to the Internet in the year 2010 and 25 billion in the year 2015 and will reach to 50 billion by 2020 (Fig. 2) because nowadays everyone using smart devices and which is increasing every day.

Popular technology research organization Gartner, Inc. made an assumption that there may be 20.8 billion of smart object on the IoT by 2020 [5]. Another technology market intelligence research organization named ABI Research made an approximation that there will be nearly more than 30 billion of smart objects connected to the IoT wirelessly by 2020 [6]. Technology experts and 83% of frequent Internet users agreed that the smart Web or Internet-based cloud of things,

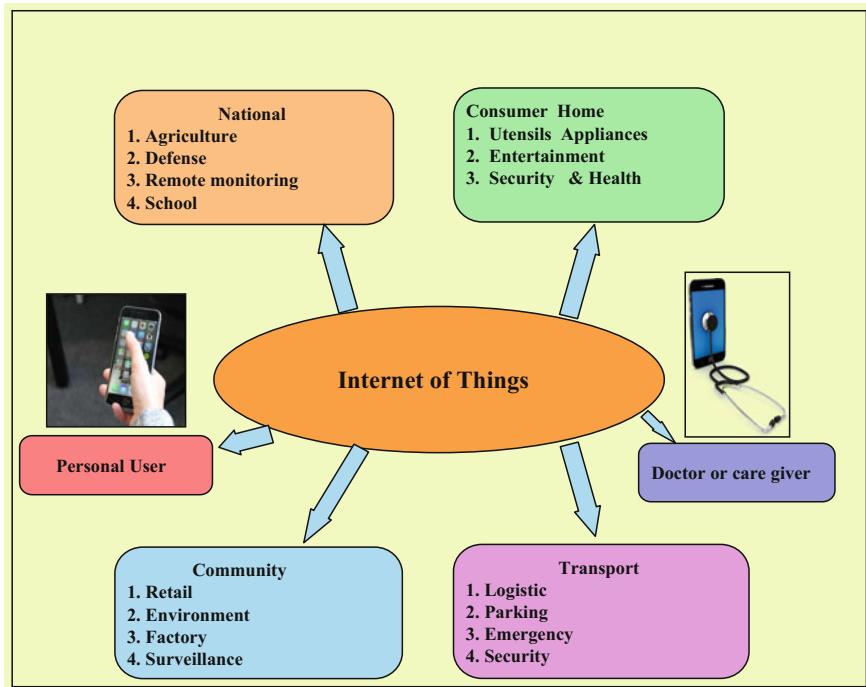
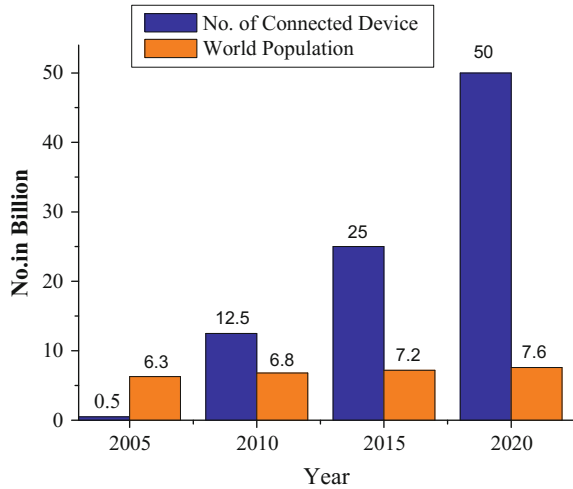


Fig. 1 Schematic of IoT application areas based on data caption

Fig. 2 Number of connected devices by 2020



wearable computer devices will become ubiquitous and favorable by 2025 (A research was done by Pew Research Internet Project [6]).

Basically, the domain of IoT is classified into five areas like body-borne smart things, IoT-based home automation, intelligent or smart city, smart surroundings, and smart or knowledge-based enterprise. Features or characteristics of all of these Internet of things' products and the corresponding solutions are different [7].

To obtain new opportunities, it requires a platform on which devices can connect directly. So, network of such a large number devices may face various problems related to their addressing, their privacy, security, and also adoptability with new technology, which is also a great challenge. Present research direction is moving ahead on this path.

3 Architecture of IoT

There is huge number of heterogeneous devices connected over the Internet; hence, there should be an optimal-layered architecture. IoT architecture supports several technologies. It helps to embellish in what way different technologies are associated with one another and provide the impact, modularity, and configuration of IoT arrangements in diversified situations. At least 30 billion objects in the Internet are expected in 2020. The existing TCP/IP protocol which is adopted in 1980 cannot handle such a big network of objects [8]. There is a need for open architecture that can provide proper security and quality of service (QoS) issues and work with existing network applications. Researchers also proposed multilayered protected architecture. Chen et al. [9] and Yang et al. [10] reported a three-key level architecture of IoT consists of application, network, and perception layer (top to down)

while Suo et al. [12] proposed a four-key level architecture having presentation, middleware, network, and physical layer. Wu et al. [11] suggested a five-layered architecture.

Xu Cheng et al. proposed a six-layered network hierarchical architecture [13]. A multilayered architecture has number of advantages such as complex systems can be broken down into apprehensible subsystem; each layer may be analyzed and tested independently. Such six-layer architecture is shown in Fig. 3.

A. Coding Layer

Coding layer is responsible for identification or recognition of the objects of interest. Every device is designated with a special ID which forms and differs from other objects [14].

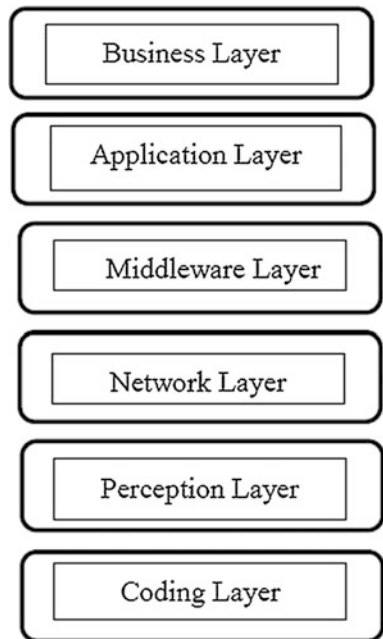
B. Perception Layer

Perception layer provides physical meaning to every object connected in IoT. It deals with data sensors network. Data sensors collect and process the information like RFID tags, IR sensors. Actuators also perform various operations such as acceptance of temperature, humidity, speed and location and convert into digital signal and pass them to network layer.

C. Network Layer

Network layer accepts the effective information (digital signals) from the lower perception layer and delivers these information to the integrated development

Fig. 3 Architecture of IOT



environment (IDE) of middleware layer using various technologies such as RFID, Wi-Fi, WiMax, Bluetooth, Zigbee, Global system for mobile communication, 3G using protocols like DDS, MQTT, IPv4, IPv6. This layer is also responsible for doing other jobs like cloud computing, data management process.

D. Middleware Layer

This layer enables services based on address and names. It provides flexibility to the individuals who write IoT application programs to act with smart devices without examining any definite hardware platform. Moreover, it also passes the necessary facilities to the network wire protocols [10, 11].

E. Application Layer

Application layer manages the overall facilities demanded by the customers. According to the customer requirement, it provides services. For example, applications like smart city, smart home, and it renders information of temperature, humidity to the customer who asks for it.

F. Business Layer

Business layer handles all the important features of IoT, its activity and services. The main activity of this layer is to create a plan for successful operation of business, diagrams, flowcharts, etc., on basis of the information taken from the application layer [15].

4 Literature Review (A Comparative Analysis)

During last decades, several researches have been done based on IoT. J. Belissent in 2010 gives an idea about the smart cities which provides new opportunities and creates new business models [16]. This paper suggests that information and communication technologies (ICTs) are an important subject for making the city smart. ICTs also help to make city services and 24×7 supervising more alertful, synergistic, and effective. It is reported that 70% of the world's population, above six billion people, will start to stay in cities and encompassing areas by 2050. So there is a demand that cities be smart, which offer platforms that enable adequate provisions of services and infrastructure to get economic growth, social, and environmental well-being to its residents, workers, and visitors [17–20].

Atzori et al. [20] proposed a city which runs technically by the arising of IoT. It is a revolutionary development of the recent Internet into a ubiquitous Web of interrelated smart devices which not only gleans data from the surrounds (sensing) and communicates with the real world but also usages present Internet protocols to allow facilities for conveying information, analytics, and applications.

Jin et al. [21] gave a model for making a smart city through Internet of things. In Spain, there is a smart city test bed at Santander, which is frequently used for researches and services.

Tinmaz E et al. presented an overall outline of existing solid waste management (SWM) system in Corlu town. Continuous investigation on the SWM practices is going on to develop present condition in various cities of Turkey [22].

IoT activities are achieving an impulse everywhere in the world. Europe is achieving the main place of IoT study with the formation of IoT European research cluster (IERC). An IoT center has formed in Shanghai to analyze technological improvement and its related trade standards. It reveals that the need for common information exchange, data storage, and processing infrastructure become very common today [9].

Pan et al. [18] shaped a smart energy building and its designs, prototype, and experiments using IoT. The paper represents IoT conceptual framework for energy efficiency and intelligence that can be incorporated into a building. Researchers first gather one-year information about building energy utilization data and then properly evaluate and analyze them.

Catarinucci et al. [23] proposed a framework for automated healthcare systems. In this work, they suggested IoT-based design for smart monitoring of patient health condition and a special system which tracks patients, personnel, and biomedical objects inside the hospitals and nursing institutes.

Lu et al. [24] proposed a cyber-physical system based on wireless technologies to provide vehicle-to-vehicle connectivity. In particular, it is related to challenges and evaluation of the modern connectionless system for automobile-to-smart sensing device, and also automobile-to-automobile, automobile-to-Internet, plus automobile-to-road infrastructure connectivity.

All these are few examples of previous work. These are having their advantages and disadvantages. It is a challenge to the researchers to design IoT-based system with an optimized result keeping the advantages of the existing designs.

5 Domain for Future Work

In this section, problems and anticipated areas of improvement are emphasized in seven topics, namely managing huge number smart devices, design and controlling, forming intelligence and big data, openness, toughness, safety, and privacy. These topics are discussed primarily to find difficulties which may grow in upcoming IoT.

1. Managing huge number smart devices

It is expected that billions of diversified smart devices are on the Internet. How to identify a particular one, authenticate access, maintain a proper environment, protect them, handle and care such huge number of devices on Internet are main problems. Whether Internet protocol version 6 efficiently tackles this type of situation? Whether agreements such as low-power wireless personal area networks (LoWPANs) version 6 combat such situation? Whether totally different standards and protocols come out? There should be some innovative idea or concept related to

the capability to introduce recent smart things, facilities, and functions for clients without hampering the class of existing facilities.

2. Design and controlling

This is important of having a proper framework which allows smooth connection, proper mechanism, and communications among billions or trillions of smart objects on Internet. There should be a proper mechanism of interaction of these objects with applications? In several occasions, objects, or group of objects necessarily remain separate, and these are saved from other objects. At other occasions, it forms an intelligence to share these smart objects and information. There should be effective planning for Internet of things to take help after smartphone platform. Smartphones provide a platform where a number of applications are readily obtainable from application store.

3. Forming Intelligence and Big Data

In the world of IoT, huge amount of raw data is collected on regular basis. There should be a proper mechanism which changes this unprocessed data into practical knowledge. It often occurs in the medical field that unprocessed values of smart sensors can be changed into relating significant actions or an individual such as eating, low respiration, or having any indication of depression. In many cases, it is also necessary that we have combined the sensor values with the recent past value of particular user activities to reach at exact data assignment. In future, further study is required to cope with such situation.

4. Openness

It can be seen that mostly sensor-based systems are closed-loop system. Nowadays, vehicles are sending sensor information to the manufacturers. Connected vehicles are also talking to each other to avoid collision. Similarly, physiological data of patient should be uploaded automatically in real time to prevent any miserable incidents. These systems ask for more openness to obtain this benefit. Remote access of the plants or else specific products is often very useful to industry. Though, security alarms arise, particularly whether there is some safety issue involved. More importance should also be given in this area.

5. Robustness

Robustness is very important and a challenging issue in the field of IoT because various kinds of networks are involved in this application. Basically, most of the IoT applications are based on a particular area of sensing, actuation, and communication platform. To improve robustness of the system, adaptive fast frequency hopping, forward error correction (FEC), and fast acknowledgment technology should work suitably. More investigation is required in this field also.

6. Security

Security is a major problem of IoT as most of the devices operate wirelessly. Generally, TCP/IP networks protect the confidentiality, integrity, and availability of

network data. As the number of Internet-enabled devices is increasing every day, a question arises, whether IPv6 and IPv4 are sufficient or need to be modified?

It is a challenge to protect these devices from security attacks. In order to do this, more importance should be given in secure data aggregation, secure routing, access control secure management, and on encryption.

7. Privacy

Trust security and privacy are the important parameters in the field of IoT. The omnipresence characteristics and flexible interactions related to IoT will give number opportunity and impotent facilities for individuals, however, also provide several scopes to break privacy. To figure out the privacy problem generated by IoT applications in future, the privacy strategies for every area must be defined and adopted to the individual IoT application and its infrastructure.

6 Conclusions

The main target of IoT is to enhance modern life by linking sophisticated equipment and new technologies. The article offers an outline of IoT concept, and its related technologies, application, and future scope of research of the field. This is helpful for new researcher who wants to gain new idea about Internet of things. At the end, it can be concluded that prescience of the IoT is to uplift erudition in detecting, controlling, communications, governing, and forming knowledge from huge volumes of information. New research problems are coming up due to huge amount sophisticated devices, the communication of the physical world of Internet, the insight information of the systems, and current difficulties of confidentiality and security. Further, cooperation between the researchers is expected to resolve the enormous difficulties sooner at the same time to stop recreating the wheel when a specific community cracks a problem.

References

1. Why the internet of things is the biggest thing yet [Online] Available at <http://softworx.co.za/why-the-internet-of-things-is-the-biggest-thing-yet>.
2. Shanzhi Chen, Hui Xu, Dake Liu, Bo Hu, and Hucheng Wang, "A vision of IoT: Application, challenges, opportunities with China perspective", IEEE Internet of things journal, vol. 1, no. 4, Aug 2014.
3. J. W. Dave Evans, "The internet of things: how the next evolution of the internet is changing everything", Cisco IBSG © 2011 Cisco and/or its affiliates, 2011.
4. "Budget 2015: some of the things we've announced" [Online] Available at <https://www.gov.uk/government/news/budget-2015-some-of-the-things-weve-announced>.
5. Gartner says 4.9 billion connected "Things will be in use in 2015", [Online] Available at <http://www.gartner.com/newsroom/id/2905717>.

6. More than 30 Billion Devices Will wirelessly Connect to the Internet of everything in 2020. [Online] Available at <https://www.abiresearch.com/press/more-than-30-billion-devices-will-wirelessly-conne/> London, May 09, 2013.
7. C. Perera, C. H. Liu, S. Jayawardena, "The Emerging Internet of Things Marketplace from an Industrial Perspective: A Survey," *IEEE Transactions on Emerging Topics in Computing*, vol. 3, no. 4, pp. 585–598, Dec. 2015.
8. Ronda Hauben, "From the ARPANET to the Internet", TCP Digest (UUCP), Available at http://www.columbia.edu/rh120/other/tcpdigest_paper.txt.
9. Wang Chen, "An IBE based security scheme on internet of things", 2012 IEEE International conference on Cloud Computing and Intelligent Systems 2012, pp. 1046,1049, Oct 2012.
10. Z. Yang et al., "Study and application on the architecture and key technologies for IOT", *Multimedia Technologies in International Conference (ICMT) 2011*, pp. 747–751, July 2011.
11. M. Wu, T. J. Lu, F. Y. Ling, J. Sun, and H. Y. Du, "Research on the architecture of Internet of Things", in *Proc. 3rd ICACTE*, 2010, pp. V5-484–V5-487, 2010.
12. Hui Suo, Jiafu Wan, Caifeng Zou, Jianqi Liu "Security in the internet of things: A Review," in *Computer Science and Electronics Engineering (ICCSEE)*, 2012, pp. 648–651, 2012.
13. Xu Cheng, Minghui Zhang, Fuquan Sun, "Architecture of internet of things internet and its key technology integration based on RFID," in *Fifth International Symposium on Computational Intelligence and Design*, pp. 294–297, 2012.
14. Debasis Bandyopadhyay, Jaydip Sen, "Internet of Things-Application and Challenges in Technology and Standardization" in *Wireless Personal Communications*, Vol. 58, pp. 49–69.
15. R. Khan, S. U. Khan, R. Zaheer, and S. Khan, "Future Internet: The Internet of Things architecture, possible applications and key challenges," in *Proc. 10th Int. Conf. FIT*, 2012, pp. 257–26, 2012.
16. J Belissent, Getting clever about smart cities: New opportunities require new business models, FORRESTER, Nov 2010.
17. Jayavardhana Gubbi, Slaven Marusic, Aravinda S. Rao, Yee Wei Law, Marimuthu Palaniswami, "A pilot study of urban noise monitoring architecture using wireless sensor network", *Advances in Computing communication and Informatics (ICACCI)*, 2013, Aug 22–25, 2013.
18. Jianli Pan, Raj Jain, Subharthi Paul, TamVu, Abusayeed Saifullah, Mo Sha, An Internet of Things Framework for Smart Energy in Buildings: Designs, Prototype, and Experiments, *IEEE internet of things journal*, vol. 2, no. 6, April 2015.
19. J. Jina, "An Information Framework of Creating a Smart city through Internet of Things", *IEEE Internet of Things Journal*, Vol I, No. 2, April 2014.
20. L. Atzori, A. Iera, and G. Morabito, "The internet of things: A survey," *Elsevier Computer Networking*, vol. 54, no. 15, pp. 2787–2805, 2010.
21. Jiong Jin, Jayavardhana Gubbi, Slaven Marusic, and Marimuthu Palaniswami, "An Information Framework for Creating a Smart City Through Internet of Things", *IEEE internet of things journal*, vol. 1, no. 2, April 2014.
22. Tinmaz E, Demir I, "Research on solid waste management system to improve existing situation in Çorlu town, Turkey", *PubMed Waste Manag.* 2006; 26(3):307–14, 2006.
23. Luca Catarinucci, Danilo de Donno, Luca Mainetti, Luca Palano, Luigi Patrono, Maria Laura Stefanizzi, and Luciano Tarricone, "An IoT aware architecture for smart healthcare system", *IEEE Internet of Things Journal*, Vol. 2, Issue: 6, pp 515–526, Mar 27, 2015.
24. Ning Lu, Nan Cheng, Ning Zhang, Xuemin Shen, and Jon W. Mark, "Connected vehicle: solution and challenges", *IEEE Internet of Things Journal*, Vol. 1, Issue: 4, pp 289–299, May 30, 2014.

Big Data and Data Science in Engineering Platform: A *Techno-educational Research Study in Indian Context*

P. K. Paul and Anubhav Kumar

Abstract *Big data management* is today treated as one of the important tools that deal large but related data sets. Complex data and traditional data processing are also very much important and valuable for solid and healthy big data management. Big data is useful, and today, it is implemented in most of the organizations as well as sectors. Healthcare, education, banking and finance, information foundations, business houses, etc., are most important and valuable place where big data is used. Due to the importance of Big Data and Analytics it is today treated as an important academic field international even in India also few universities have offered programs on the field. It is important and valuable for the creation of business and strategies of IT. In this paper, bachelors and masters engineering program details (*other than Science & Management Concentration*) are studied and provided which are available in Indian universities based on study. Paper is also highlighted regarding possible academic programs in Indian scenario based on Indian need and International degrees available.

Keywords Data science • Big data • India • Industrial program Universities • Data management • Analytics

1 Big Data and Its Current Uses

Today, most of the companies are also adopting big data systems for healthy and sophisticated transformation of raw data into required information. A Data scientist basically contributed in mixed of analytic, machine learning along with data mining skills [1, 2]. Big data and data science normally deal with the below-mentioned features and characteristics.

P. K. Paul (✉)
Raiganj University, Raiganj, West Bengal, India
e-mail: pkpaul.infotech@gmail.com

A. Kumar
Sri Sai College of Engineering and Technology, Pathankot, Punjab, India

- Big data analytics helps in industrial knowledge including contextual understanding for hidden solution to the business.
- It is useful in industry, government, research organizations, etc., Hence, many of these organizations and companies may adopt a basic training in quantitative analysis or computer programming. Big data technologies and systems today are in use of fields such as social, political, economic, legal, business, marketing [3, 4].

2 Objectives and Agendas

This is a conceptual paper and deals with the following aim and objectives (but not limited to the)—

- To learn about the core features as well as characteristics and features of data science and big data management.
- To dig out the latest and emerging educational programs on data science in international universities.
- To find out the latest of data science, big data management programs in Indian universities especially about engineering masters and bachelor programs.
- To find out the areas and modules which fall under the big data and data science running in Indian universities.
- To learn about the challenges, opportunities of Big Data Technologies in introducing in Universities and other Indian Higher Educational Institutes (HEIs).

3 Methodologies Undertaken

It is a conceptual and theoretical note, and thus, several research methodologies have been adopted. Different journals, handbook, encyclopedia, etc., in the areas of data science, big data, analytics also have been used as secondary and primary data. Websites, which are provided information about data science and big data, are also been utilized. Finally, to design this proposed research work, a search strategy has been used, i.e., ‘MTech Data Science’, ‘BTech Data Science’. Instead of data science, the keywords and terms of ‘big data management’ are also been used. Up to fifteen pages are used to study, and result is depicted and illustrated in next section/s.

4 Big Data and Data Science: What Is It and Where

As an interdisciplinary field, big data mainly deals with the processes and systems to extract knowledge of various kinds (*regardless of structured or unstructured*), and these are the persistence with few data analysis areas, viz. statistics, data mining, and predictive, similar to knowledge discovery in databases. Apart from these, few important are probability models, pattern recognition and learning, visualization, machine learning, signal processing, database, data engineering, statistical learning, data mining, predictive analytics. However, few other areas such as data warehousing, compression of data, computer programming, artificial intelligence high-performance computing are also important and valuable. Due to wider applicability of data science and big data, today, most of the organization and institutions adopted the data management benefits [5, 3]. Due to its need, many internal universities have started programs and degrees on big data and allied subjects. A few among them are listed as follows—

- MSc Data Science, Sheffield University, UK
- MSc Data Science, Goldsmith University of London, UK
- MSc Big Data, University of Stirling, Scotland
- MSc Data Engineering, University of Dundee, UK
- MSc Data Science, Edinburg Napier University, UK
- MSc Data Science, Kings College, London
- MSc Data Science, University of Southampton, England
- MSc Business Analytics, Imperial College, London

Due to wider job opportunities in most of the developed countries, *data analytics and related areas such as data science, big data, and analytics studies* have been started as an academic program. This study shows that UK ranks first in terms of offering data science-related program. Importantly, UK is dedicated currently also for doing well in healthy digital market creation in different sorts [6, 3]. A list of institutes with program, duration, etc., have been mentioned in the below-mentioned Table 1 availed by the prescribed and adopted research methods [3].

It is important to note that the area of Data Science is also related with and known as few others Data Analytics, Big Data Systems, Data Systems, Informatics Intelligence. Digital economy depends on cultivation and allied activities with knowledge; hence, big data management will help in manipulating large datasets, interpret and represent them into knowledge [7, 8]. In India, some of the universities offer data science in collaboration with the industrial giants (*mainly IBM, take a look on Table 2*).

Table 1 Data science-based engineering programs in Indian universities (according to the study adopted)

Programs	University	Duration	Core structures
Executive MTech Data Science	IIT, Hyderabad	2–4 years	Image and video analytics, topics in data mining, scaling to big data, data acquisition and productization, data security, data privacy, parallel and distributed systems, numerical linear algebra for data analytics, programming models for multicore and GPU architectures, information retrieval, Web databases and information systems, thick data analysis
MTech Data Science (Integrated and Lateral)	IIT Kanpur	5 years after 10 + 2 and 3 years after BTech second year	Data structure and algorithm, mathematics for CS, data science-tools and techniques, Seminar-data science, DBMS, OS, algorithms-II, inference-I, management decision analysis, inference-II, optimization, statistical analysis, management decision analysis, machine learning. with electives from the CSE, EE, economics, mathematics and statistics department, thesis
BTech Computer Science and Engineering (Big Data Analytics)	DIT University, Dehradun	4 years	Core subjects: theory of computation, computer organization, computer networks, Web technology, information management basics, Linux administration and shell programming, emerging big data, industrial tour, enterprise app development using IBM tools, AI, microprocessor, dot net, Hadoop and big data, OOAD, project-II, distributed computing, advance computer architecture, DW&DM, enterprise reporting using IBM Cognos BI tools, industrial training, RDBMS, BI,

(continued)

Table 1 (continued)

Programs	University	Duration	Core structures
			real-time systems, cyber law, big data analytics programming, project-III and various electives as per need
BTech Computer Science and Engineering (Big Data Analytics)	Modi University, Rajasthan	4 years	Focus on: big data which includes statistics, data mining, data warehousing and data visualization and major program as like DIT University, Dehradun
BTech Computer Science and Engineering (Big Analytics and Optimization)	University of Petroleum and Energy Studies Dehradun	4 years	DBMS, introduction to business analytics, advance DBMS, business process management, software engineering and project management, computer networks, statistical analysis, Java, Web with PHP, data mining and prediction modeling, DW and multidimensional modeling, automata theory, AI, BI, OR, embedded systems, industrial visit, minor project-I/II, network security, big data analytics, Web social analytics, major project, summer internship, BAO and cloud, enterprise information architecture, business strategy and analytics, mobile analytics, etc.
MTech CSE (Data Science and Analytics)	Ahmedabad University, Gujarat	2 years	Orientation to computing and data science program, data structure, data analysis, probability and statistical inference, technical communication, machine learning, big data analytics, numerical methods, high-performance computing, semester III and IV with many electives, research courses, projects
MTech CSE (Data Engineering)	Indraprastha Institute of Information	2 years	Data mining, database system implementation, information retrieval, data analytics, introduction to spatial

(continued)

Table 1 (continued)

Programs	University	Duration	Core structures
	Technology, Delhi		computing, machine learning, GPU computing, probabilistic graphical models, data warehousing, cloud computing and virtualization, collaborative filtering, privacy in location-based services, semantic Web, Web intelligence and big data analytics, business intelligence and data warehousing, financial data analytics, information integration and data analytics, distributed data mining, database methods in information retrieval (among these 16 credit for data analytics) apart from 30+ credit basic CSE courses and recommended internship
MTech Data Analytics	Jaypee Institute of Information Technology, Noida	2 years	Mathematics for data analytics, data warehousing and data mining, machine learning, data analytics laboratory, empirical research, big data technologies, large-scale graph analytics, advanced data analytics laboratory or industrial internship-I, and five electives third semester full internship 40 h/week, fourth semester full project or dissertation 50 h/week

5 Big Data Versus Indian Education: A Strategic Management

More than 40,000 higher educational institutes include colleges, universities, research and innovation centers, polytechnics serving India for creating manpower and its solid development. The institutions like *engineering colleges, management colleges, architecture colleges, polytechnic colleges* are basically governed and directed by the AICTE under the MHRD. Nation is producing large number of engineers. This study reveals that in India engineering colleges offer about 17 lakhs seats. Regarding computing field, it is important that this field is available in large

Table 2 Universities offering programs in collaboration with industrial unit/s

Universities	Mode and collaboration
IIT, Hyderabad	Regular degree but executive/flexible format
IIT Kanpur	Regular-traditional
DIT University, Dehradun	Regular in <i>collaboration with IBM</i>
Modi University, Rajasthan	Regular in <i>collaboration with IBM</i>
University of Petroleum and Energy Studies Dehradun	Regular in <i>collaboration with IBM</i>
Ahmedabad University, Gujarat	Regular-traditional
Indraprastha Institute of Information Technology, Delhi	Regular-traditional
Jaypee Institute of Information Technology, Noida	Regular-traditional

number with different nomenclature such as information technology, ICT, software engineering, information science, etc., in 4000+ engineering colleges. India holds about 30,000 affiliated colleges in which allied field is also offered with subject of computer science, information technology, computer applications, information science, ICT, software engineering, etc., with the degree of BSc, MSc, BCA, MCA, and so on. Though India has a solution for offering several programs on Bog Data etc. in India context (*Few possible programs have been proposed in Fig. 1*).

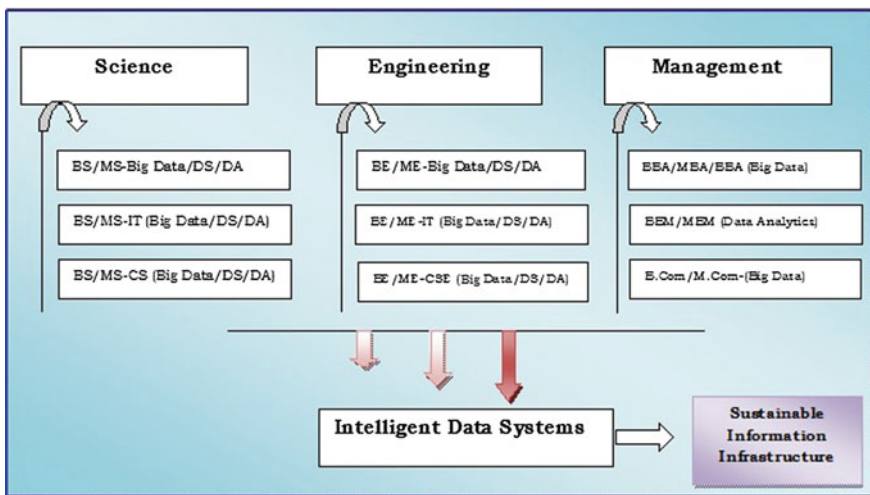


Fig. 1 Potential data science and big data program in Indian context

6 Findings

- Like Data Science, few popular and important fields include business intelligence, business analytics which are still treated as a practicing field or area.
- As it is a quantitative analysis of data and thus some of the methods and statistical learning model have been included classical statistical methods. Hence, economics and quantum analytics, mathematics students become main input criteria.
- UK offers most of the big data analytics and data science programs with not only MSc but also BSc program.
- In India, only a few institutes offer data science with BSc, MSc. Most of these are privately funded while few BTech and MTech are available in IITs.
- Analytics programs are mainly available in the private institutes, and there are huge potentialities for further development in governmental entities.

7 Concluding Suggestions

We are moving into a developed country, and thus, introducing new age programs are essential to provide skills and knowledge as per industrial and organizational demand. Another related nomenclature big data technologies are also gaining popularity in some extent. Due to wider acceptability and uses, many international universities have started programs on big data. Among the large number of institutes in India, only a few offers programs on data science and big data programs and most of these are listed in engineering colleges and few private universities with industry integrated way. Initially, universities may adopt specialization in the areas of data science and analytics, etc., in the allied degrees. With the degrees such as M.Com, MBA, MSc Mathematics, MSc Economics, MSc Actuarial Science, etc., big data analytics/data sciences specializations may be started. More importantly, in India, about 5000 colleges offer MCA degree (*with more than 1 lakh intake*) and in this data science major may be started. Naturally, in BCA also, same strategy may be adopted. Industrial collaboration is very essential for the creation of solid man power, and thus, like IBM, other potential industrial players may tied-up.

References

1. Bhattacharya, I., & Sharma, K. (2007) India in the knowledge economy-an electronic paradigm. *IJEM*, Vol. 21(6), pp. 543–568.
2. Chandhini, C., & Megana, L. P. (2013). Grid computing-a next level challenge with big data. *Int J Sci Eng Res*, 4(3).

3. Paul, P. K., A. Bhuimali, M.K. Ghose, R. Rajesh (2016) Health Data Science: Insight into the relevance of the domain with emerging and possible academic programs-A *Knowledge Survey*, *International Journal of Medical Research and Pharmaceutical Sciences*, 3 (10), Page-10–17.
4. https://en.wikipedia.org/wiki/Data_science (Accessed on 25-02-2017).
5. Buyya, R., Ranjan, R., & Calheiros, R. N. (2009, June). Modeling and simulation of scalable Cloud computing environments and the CloudSim toolkit: Challenges and opportunities. In *High Performance Computing & Simulation, 2009. HPCS'09. International Conference on* (pp. 1–11). IEEE.
6. Picciano, A. G. (2012). The Evolution of Big Data and Learning Analytics in American Higher Education. *Journal of Asynchronous Learning Networks*, 16(3), 9–20.
7. Wahi, A. K., Medury, Y., & Misra, R. K. (2015). Big data: enabler or challenge for Enterprise 2.0. *International Journal of Service Science, Management, Engineering, and Technology (IJSSMET)*, 6(2), 1–17.
8. https://en.wikipedia.org/wiki/Higher_education_in_India (Accessed on 25-02-2017).

Insight into the Cloud Computing Programs at Bachelors Levels: Emphasizing International Universities and Indian Potentialities

P. K. Paul and M. P. Pradhan

Abstract With the aid of Cloud Computing, virtualization for several devices has become possible. It is quite essential for its effective and efficient utilization. With connectedness through Internet and similar technologies, centralization of such information technology services has become possible to great extent. It is an important tool for development of environment having remote access to different domains of business, socio-economical and scientific initiatives. The attributes of service science provided are common in many contexts. Cloud Computing is available on different platforms, mainly private, public and hybrid. Cloud Computing is also related to the Big Data and Data Technologies. As an academic program, Cloud Computing is not so popular and available; but there is a potentiality to offer Cloud Computing and allied subjects in India and other developing countries.

Keywords Cloud Computing · Big Data · Universities · Emerging educational programs · India · MSc · MTech · BTech · Industry-integrated learning

1 Introduction

The virtualization of software, hardware, applications, systems and other information technology services is called as Cloud Computing. It is based on remote computing. Cloud Computing is responsible for the remote information technology and computing infrastructure available anytime and anywhere with adequate network and Internet facility. Companies and institutes are no longer using separate

P. K. Paul (✉)
Raiganj University, Raiganj, West Bengal, India
e-mail: pkpaul.infotech@gmail.com

M. P. Pradhan
Department of Computer Application, Sikkim University, Gangtok,
Sikkim, India

hardware, software, applications for managing their business. They are using common integrated systems either as public cloud, private cloud or hybrid Cloud Computing. Information transfer cycle becomes easy with the adoption of Cloud Computing [1, 2]. Large volume of data created by the business processes led to the evolution of data management tool which successively later was adapted as a field of study and research. Most the universities, Institute of National Importance, etc., do not have any full-fledged program in these fields. Though there are huge potentialities to offer the program including as a specializations, degrees, major, etc., in several disciplines.

2 Objectives and Agendas

As a conceptual paper, the paper is aimed at below-mentioned agenda and objectives. Few major agendas are as follows:

- Learn about Cloud Computing as well as virtualization with its basic principles and features.
- Find out main advantages of the Cloud Computing, virtualization in contemporary context.
- Learn about higher education systems including research in the academic and corporate houses.
- Find out some available and possible courses in Cloud Computing and virtualization in contemporary context.
- Know about the Cloud Computing and Cloud Science with emerging academic programs started in the universities, etc., as per the method followed.
- Emphasize on challenges as well issues of Cloud Computing programs in academia, especially in the developing countries.

3 Methodologies Undertaken

Data and sources in the areas of Cloud Computing, Big Data Management, etc., have been used for doing this work. The study is specially designed to find out the latest of Bachelors program in Cloud in International Universities. The search keyword 'BS/BSc Cloud Computing' has been used and up to 15 pages were considered for research purpose. Official Web site of UGC, *Government of India*, AICTE, *Government of India* and their link also played great role to know more about education systems in India. Related Journals of Cloud Computing, Big Data Management, Data Science, etc., also have been handled (national and international) to learn more about these areas and to design programs in Indian context.

4 Cloud Computing and Industries

Cloud Computing is a kind of virtualization for hardware, software, application and packages anytime and anywhere availability with remote-based services. Public cloud is come under the common and general Internet services, whereas private cloud depends on company's own server infrastructure. The combination of public Cloud Computing and private Cloud Computing is called hybrid Cloud Computing [3, 4]. In the areas of Defence, Bank and Commercial firms, hybrid services are useful, based on need. Cloud Computing and its popularity have increased during last few years because of its unparallel benefits. Moreover, international market of cloud products and services is also important. Some of the developed countries like USA, England and UK, Australia, Japan, Germany, Switzerland and many more were involved in design and implementation of Cloud Computing programs, initially [5, 6]. This study reveals that some European and US-based universities offer Bachelor and Master Degree with specialization of Cloud Computing and allied subjects with focus on technological and managerial aspects (with cloud integration) such as

- Cloud and database systems.
- Strategic management of the ICT.
- Infrastructure development and ICT.
- Network informatics.
- Converged networks and energy management.
- Internet sciences and clouds, etc.

5 Cloud Computing (CC) Programs: An Overview

Internationally many industries and universities offer programmes and research initiatives on Cloud Computing and allied areas. Among these, Microsoft Technologies have played an important role [2, 7]. An example is *MCSE-Private Cloud*. Cisco systems are another company which offers several programmed on fields related to Cloud

- Cisco Certified Network Associate (Cloud).
- Cisco Certified Network Professional (Data Centre).
- Cisco Certified Network Professional (Cloud).
- Cisco Certified Network Professional (Data Centre).

Similarly, Cloud and Big Data-related programs of Oracle Corporation, EC Council, etc., are also treated as important and valuable. In the developed countries, Cloud Computing programs are also available as Bachelor's level with Degree, Specialization, Major and Minors. The adopted study results that UK is leading territory to offer Cloud program at Bachelor level.

Programs, University (Duration)	Core structures
<i>BSc Cloud Computing</i> University of Wales, London (3 Year)	Computational Thinking, Computer Architecture, Information Engineering, Internet Protocols, IP Internetworking, Network Principles, Software Development, Cloud Computing Technologies, DBMS, LAN, Network OS, Web Development, Data Centre Technologies, Data Centre Virtualizations, WAN, Big Data
<i>BSc Cloud Computing</i> Staffordshire University, Staffordshire (4 Year)	Computer Networks, Hardware and Computer Systems, Data Storage and Software Systems, Virtualization, Network Security, Routing and Switching, Virtual Computing, Professional Skills for Networking, Converged Technologies, Communication Technologies, Project (Program map with CCNA, CCNP and CCNP Security Modules of CISCO Systems)
<i>BSc Cloud Computing</i> Cork Institute of Technology, Ireland (1 Year Full Time 1.5 Year PT)	Cloud Architecture, Business Intelligence, Cloud Computing with Python, IT Service Management, Converged Networks, Data Centre Virtualization, Cloud Application Development, Enterprise Storage Systems, Network Security, Internet and Network Services, Project, etc.
<i>BSc Cloud Computing</i> University of Wolverhampton, UK (3–6 Years)	NA
<i>BSc Software Design (Cloud Computing)</i> Athlone Institute of Technology, Ireland (4 Year)	Mathematics for Software Design, Software Development, Agile Methodologies, Software Development for Cloud, Databases, Web Development, Networks, Group Project, Web Development, Mobile Application Development, Operating Systems and Concurrency, Software Development, Software Engineering, Software Development for Cloud, Server-side Web Development, Web Development, Placement, Computer Graphics, Networks, Management and Organizational Behaviour, Databases, Data Mining and Machine Learning, The Engineer in Society, Security, Distributed Systems, Service Oriented Architecture
<i>BS CIS (Cloud Computing)</i> ECPI University, Virginia (4 Years)	Cloud Computing Concepts, Networking II, Routing and Switching, SAN and Disaster Recovery, Windows Client and Server, Network Security, Network Virtualization Fundamentals, Network Virtualization Administration, Enterprise Network Security

(continued)

(continued)

Programs, University (Duration)	Core structures
<i>BSc IT (Cloud Computing)</i> Asia Pacific University of Technology and Innovations, Malaysia (3 Years)	Introduction to Virtualization, Virtual Computing, Data Centre Infrastructure, System and Network Administration, Mobile and Wireless Technology, Web Applications, Integrated Business Processes with SAP ERP Systems, Computer Systems Security, Information Storage and Management, Internet of Things: Concepts and Applications, Enterprise Programming for Distributed Applications, Advanced Database Systems, Designing and Developing Applications on Cloud Computer Systems Management, Investigations in Cloud Computing, Cloud Computing Project

6 Indian Education Systems and Cloud Potentialities

India holds highest number (40,000+) of higher educational institutes including colleges and universities in the world. Among these universities, Engineering Colleges, Management and other technical colleges are important. India holds about 6375 Engineering Colleges, apart from Applied Art and Craft Colleges [2, 8, 9]. The Architecture and Designing is also fall-under of technical institutes and at present, total 177 (*as of 2015*) institutes are working nationwide. Cloud Computing and Systems may be offered in these institutes with specialization in Cloud Architecture, Cloud Systems Designing, etc. In its 29 States and 5 Union Territories, most popular nomenclatures are

- *Computer Science and Engineering (CSE).*
- *Information Technology (IT).*
- *Information Science and Engineering (offered mainly in Karnataka).*

Cloud Computing and similar program may be offered in large number of institutes and universities in India (*refer* Tables 1 and 2) with Cloud and allied domains.

Many of the colleges offer UG and PG degree with MA/MSc/MCom nomenclature. Few universities are also getting tied up with the foreign universities, thus healthy potentialities are awaiting. Institute of National Importance (INI) which is the most apex educational institutes may also offer Cloud Computing programs in different possible settings (*refer* Table 3), among the possible INI important institutes are Indian Institute of Technology (IIT), National Institute of Technology (NIT), Indian Institute of Management (IIM), Indian Institute of Information Technology (IIIT), Indian Institute of Engineering Science and Technology (IIEST) [2, 10].

Table 1 Universities and HEIs in India with numbers and possibilities [11, 12]

Universities	Numbers	Remarks
Central Universities	46	In about 15 Departments allied programs may be offered
State Universities	342	In most of the CS/CA Dept. Cloud and allied programs may be offered
State Private Universities	239	Almost, all these Universities offer professional programs and thus Cloud, etc., may be offered
Deemed Universities	125	Almost, all these Universities offer professional programs and thus Cloud, etc., may be offered
Colleges (HEIs)	33,000	In Engineering Colleges and few CS and CS Department, Cloud specialization may be offered

Table 2 Computing and related departments with vital statistics

Streams	Remarks
Computer Science and Engineering	Offered almost all 6375 Engineering Colleges in the nation with mostly double availability (IT + CSE) in a single institute. So it is higher than any other Engineering disciplines (with CA) in the nation. The domain has few Lakhs of total seats
Information Technology (IT)	
Information Science and Engineering (ISE)	
Computer Applications (CA)	Offered 1469 Colleges with MCA Degree with approximately 1 Lakh+ Seats
Computer Science (CS)	The CS is offered in Universities only and not under the Technical Fields. But close with HCI

7 Findings

- Cloud Computing is dedicated to provide the capacities of hardware and software systems with remote capabilities for all kinds of establishments.
- Big Data, Data Science, Big Data Management, Data Analytics, Business Analytics, etc., are related to the Cloud Computing and Virtualization.
- Cloud Computing, Big Data Management, etc., are offered in some leading International Universities with Bachelor's, Master's and Doctoral degree as full-fledged degree or specialization/Major.
- About 2.5 Lakh enrolments is every year offered as BSc/BTech/MTech/MSc level. Only a few are offered Cloud Computing and allied programs out of 40,000+ potential institutes. Few Private Institutes and Universities offer Cloud Computing Major. Some are also got tied up with leading venture like IBM.

8 Suggestions

Cloud Computing is an emerging discipline. It has the potentialities in form of its flexibility, cost saving, collaborative nature and adaptable in the areas of health, medical, education, government, business, etc. In India, Computing is available in practice and academia (i.e. degrees) but it is a fact that there are very minimum specializations in the field of Cloud *Computing* in the leading universities, etc.

Engineering	Engineering (Major)	Computing	Management
BE/BTech/ME/MTech—Cloud Computing and Systems	BE/BTech/ME/MTech—CS (Cloud Computing)	BCA/MCA (Cloud Computing)	BBA/MBA (Cloud System Management)
BE/BTech/ME/MTech—Big Data and Cloud Systems	BE/BTech/ME/MTech—IT (Cloud Computing)	BSc/MSc-IT (Cloud Computing)	BBM/MMA (Cloud Computing)
BE/BTech/ME/MTech—Virtualization Technology	BE/BTech/ME/MTech—ICT (Cloud Computing and Big Data)	BSc/MSc-CS (Cloud Computing and Virtualization)	PGDM/PGDBA (Cloud Computing)

Masters of Computer Application, Masters in the subjects of Information Technology, Computer Science, Software Engineering, ICT are available without any concentration of emerging Major *like Cloud*. Hence, there is a potentiality to offer Cloud Computing and allied programs in the available degrees and programs (*refer* Table 3).

9 Conclusion

In this rapidly changing society, Cloud Computing, Data Analytics, etc., play a crucial role for effective use of computation resources and efficiently managing cost of running business with a motive of increasing throughput and enhancing performance. Most of the organizations and institutions today are moving for healthy Information Technology implementation because of its benefits. Currently, few of the Indian universities, industries and engineering institutes are moving towards academic innovation with introduction of new programs. Though, it is a fact that many universities in the developed nations are moving more academic enhancement. Apart from Cloud Computing few popular and allied programs are also seen in program listing in some of the UK and USA-based universities which may be of great bright prospect to the Indian academic system.

Reference

1. Foster, I., Zhao, Y., Raicu, I., & Lu, S. (2008, November). Cloud computing and grid computing 360-degree compared. In *Grid Computing Environments Workshop, 2008. GCE'08* (pp. 1–10). IEEE.
2. Paul, P. K., & Chatterjee, D. (2015). I-Schools and the Present Worldwide Trend and the Indian Scenario. In *Encyclopedia of Information Science and Technology, Third Edition* (pp. 2525–2534). IGI Global.
3. Buyya, R., et.al.: Modeling and simulation of scalable Cloud computing environments and the CloudSim toolkit: Challenges and opportunities. In *HPCS-09. HPCS'09. International Conference*, Vol. 9, pp. 1–11, (2009).
4. McFarlane, D. C., & Latorella, K. A. The scope and importance of human interruption in HCI design. *HCI*, Vol. 17(1), pp. 1–61, (2002).
5. Dinh, H. T., Lee, C., Niyato, D., & Wang, P. (2013). A survey of mobile cloud computing: architecture, applications, and approaches. *Wireless communications and mobile computing*, 13(18), 1587–1611.
6. Subashini, S., & Kavitha, V.: A survey on security issues in service delivery models of cloud computing. *IJCA*, 34(1), pp. 1–11. (2011).
7. Zhang, Q., Cheng, L., & Boutaba, R. (2010). Cloud computing: state-of-the-art and research challenges. *Journal of internet services and applications*, 1(1), 7–18.
8. www.ugc.ac.in (Accessed several section on 10-03-2017).
9. www.mhrd.gov.in (Accessed several section on 10-03-2017).
10. www.en.wikipedia/Cloud_Computing (Accessed on 10-03-2017).
11. www.aicte-india.org (Accessed several section on 10-03-2017).
12. www.en.wikipedia/big_data (Accessed on 10-03-2017).

Approaches and Measures to Detect Wormhole Attack in Wireless Sensor Networks: A Survey

Diksha Giri, Samarjeet Borah and Ratika Pradhan

Abstract Wireless sensor networks (WSNs) contain a collection of sensor nodes. These nodes are linked with one another and have low computational power. Wireless sensor network is used for sending messages, data, and other important information over a wireless link for military purpose, environmental monitoring, Health checkups for patents, habitat monitoring, target tracking, and disaster management. Security is most important concept in WSN while sending such important message over wireless link. This permit attacker to penetrate the network and carried out various possible attacks with the purpose of stealing or editing actual data/information. In this paper, discussions are made on different techniques available to avoid and detect wormhole attack.

Keywords Wireless sensor network · Attack · Wormhole · Security Node

1 Introduction

Wireless sensor network (WSN) contains a set of sensor nodes. These nodes monitor large geographical areas for modelling and forecasting environmental applications and have characteristics such as minimum bandwidth, low energy, and low-power consumption which is used to. In WSN, sensor nodes are deployed in various regions where it collects data through its sensor nodes. Sensor nodes in WSN are to perform various tasks such as signal processing, transmitting the

D. Giri (✉) · S. Borah · R. Pradhan
Department of Computer Applications, Sikkim Manipal Institute
of Technology (SMIT), Majhitara, Rangpo 737136, Sikkim, India
e-mail: dikshamhs@gmail.com

S. Borah
e-mail: samarjeetborah@gmail.com

R. Pradhan
e-mail: cse_ratika@yahoo.co.in

collected information to the base station, and verifying routes with minimal energy. Wireless sensor networks are known to be useful in different environments such as environmental monitoring, military applications, security, application to robotics, and many more. This makes WSN vulnerable to many kinds of attacks. Among all these attacks, the threatening attack is said to be wormhole attack as it uses both in-band and out-of-band channel. Wormhole attack is categorized into denial-of-service attack, where attacker nodes/malicious nodes are linked with each other by high speed of channel link called wormhole link/tunnel. In wormhole attack, there may be minimum of two attackers' also known as malicious nodes present in the network. The attackers monitor the network and keep the track of wireless activities to get the information for itself. Security issues for mobile ad hoc networks are also very important requirement because in WSN nodes are fixed, but in MANETs [1–4], all mobile nodes are moveable. It is hard to provide security to such nodes while they are roaming. In MANET, nodes are mobile and they communicate directly without any base; here intermediate nodes also act as a communicator between the nodes. These intermediate nodes are like routers that use multi-hop radio channel which is linked by wireless links without any support of preexisting communication infrastructure. Routing protocol in WSN is divided into two main categories based on routing information update mechanism which are pro-active or table driven and re-active or on-demand routing protocol.

The following section of the paper is organized as follows: Sect. 2 presents security in wireless sensor network. Section 3 covers various issues related to wormhole attack. In Sect. 4, classification for wormhole attacks is discussed. Section 5 discusses various techniques which are used to mitigate wormhole attacks. Section 6 explains the analysis of various techniques, and conclusion is discussed in Sect. 7.

2 Security in Wireless Sensor Network

A WSN is a network with set of nodes which forms a temporal network without having any stable infrastructure or centralized management. In a WSN, sensor nodes set up routes dynamically among themselves on the basis of hop distance and shortest path; therefore, it is referred to as an infrastructureless network. In a WSN [5], sensor nodes which are in one another's wireless transmission range can directly communicate; however, nodes that are beyond the range of each other relies on other nodes to process the messages. The security mechanisms used must be encapsulated within routing protocols. The attacks get prevented, detected, and responded by these security mechanisms. There are five major security goals to maintain a reliable and secure network environment. They are mainly:

2.1 Categories of Security Attacks

External versus internal attacks: In case of external attacks [1], the attacker tries to cause congestion in the network. It either circulates fraudulent routing information or interferes with the working mechanism of the nodes. Internal attacks—here the attacking node wants to access the network normally like any other sensor nodes and involve it in the network activities to get access to the network. There are two major categories of security attacks in WSNs, which are called passive attacks and active attacks.

Passive Attacks: In case of passive attacks, the day-to-day activities of the network are generally not affected. In this case, the malicious nodes silently monitor the data exchanged within the network but does not alter it. Here the protocol of Security Council gets violated, and there is no secrecy. It is not that much easy to detect passive attack as network operations do not get affected. Passive attack is solved by using a powerful encryption method for the data packet being transmitted; therefore, the attacker finds it difficult to access the useful data.

Active Attacks: An active attack affects the whole normal working system of the network by altering or destroying the data which is transmitted in the network. An Active attacks can be internal or external. The nodes outside the network are responsible for external attacks. Compromised nodes within the network carry out internal attacks. The attacker already being within the network, internal attacks are difficult to detect and are more severe than external attacks. In active attacks, actions such as impersonation, modification, fabrication, and replication [6] are caused by an external node or compromised internal nodes.

Confidentiality: To secure information from being exposed by the third party. It is difficult to maintain confidentiality since the intermediate nodes receive the packets and the information to transmit by the nodes can be eavesdropped.

Availability: Availability to the service of the network should be open. Despite an attack, an assurance of availability on the network should be maintained. The routing protocol can be disrupted by the attacker on the network layer. Also, the attacker on higher layers could bring down high-level services.

Authentication: To identify the concerned entity in order to find the origin of the communication is what it claims to be or from. Without which an unauthorized node can attack the sensitive information and can have unauthorized access by interfering the operation of other nodes.

Integrity: Message in transmission cannot be altered.

Non-repudiation: Sending and receiving parties cannot deny for sending or receiving the message (Table 1).

Table 1 Various denial-of-service attacks on each layer

Layers	Attack	Defenses
Physical layer	Jamming	Spread-spectrum, priority messages, lower duty cycle, region mapping, mode change.
	Tampering	Tamperproofing, hiding
Data link layer	Collision	Error correction coder
	Exhaustion	Rate limitation
	Unfairness	Small frames
Network layer	Spoofed routing information and selective forwarding	Egress filtering, authentication, monitoring
	Sinkhole	Redundancy checking
	Sybil	Authentication, monitoring, redundancy
	Wormhole	Authentication, probing
	Hello flood	Authentication, packet leases by using geographic and temporal info
	Acknowledgment flooding	Authentication bidirectional link authentication verification
Transport layer	Flooding	Client puzzles
	De-synchronization	Authentication
Application layer	Path-based DoS	Authentication and anti-replay protection
	Re-programming attacks	

3 Wormhole Attack

In [7], wormhole attacks are explained which are categorized into two main categories as follows: one type of denial-of-service attack and one or more attackers are linked with each other by high speed of channel link also known as wormhole link or wormhole tunnel. In wormhole attack, data packets are received by malicious nodes at one point and get transferred to another attacker node (malicious node) which belongs to other part of the network through a wormhole link also called tunnel. Here the malicious nodes make the other neighbor nodes think that they are of single hop distance nodes so that the sender nodes can transfer data through them without hesitation.

The wormhole attack can be categorized in various ways such as in-band, out-of-band. In-band wormhole attack—a tunnel is built by the attacker over the previous wireless channel. This attack causes much damage as compared to the out-of-band attack; therefore, most attacker's launches in-band attack, whereas the out-of-band works outside the wireless channel and uses the different wireless networks. Other classifications are open wormhole attack [8] where both malicious nodes provide their identities, half-open wormhole attack, where only one attacker node provides its identity on the network, another one hides itself from the network, and closed wormhole attack where both nodes are hidden from the network (Fig. 1).

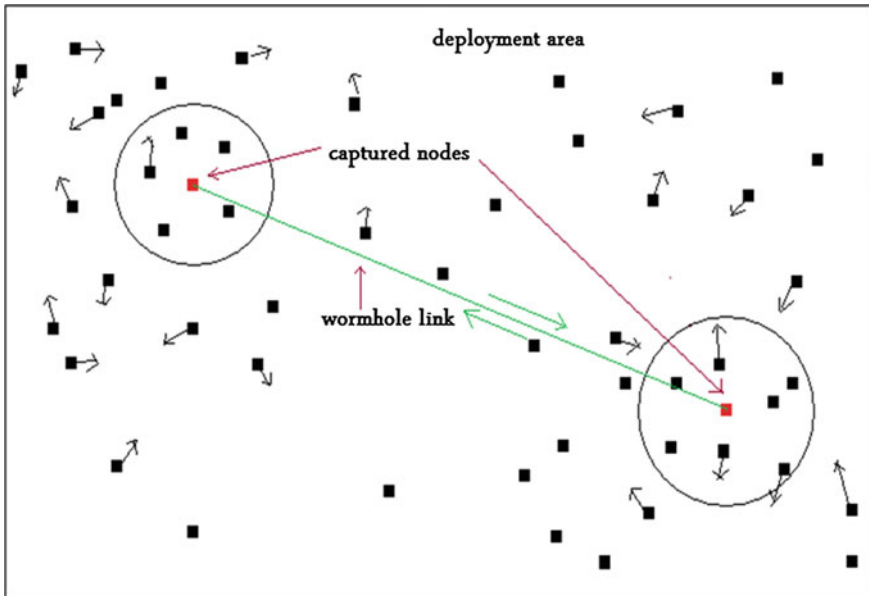


Fig. 1 Scenario of wormhole attack—This shows the wormhole scenario where nodes are deployed in a wireless network, and two malicious nodes (which are indicated by red color) are also present in the networks. Normally, it takes more than one hop for a packet near the attacker node to transmit packets, but with the false shortest path of the attacker node, the packets are transmitted. The wormhole link shown in the figure is the link through which malicious nodes tunnel the packets

4 Classification of Wormhole Attack

Wormhole attacks are classified into five main categories which are as follows:

- **Wormhole Using Packet Encapsulation:** Since data packets send between malicious nodes are encapsulated, the hop count is not affected here. Therefore, this type of attack is vulnerable using hop count.
- **Wormhole Using Out-of-band Channel:** The attacker nodes create out-of-band high bandwidth channel link also called tunnel between the attacker nodes to tunnel the packet.
- **Wormhole Using High-power Transmission:** One attacker node is placed with high-power transmission capability. When a broadcast route request packet is heard by this node, it rebroadcasts at a high-power level. With this, the attacker node establishes itself in the route path.
- **Wormhole Using Packet Relay:** The malicious nodes send the false information to its neighbor nodes that they are one hop distance nodes to them.
- **Wormhole Using Protocol Distortion:** In order to get the wormhole path to get selected, as a routing route, the malicious node tends to affect the network traffic by disturbing the routing protocol.

5 Techniques to Mitigate Wormhole Attack

The following is the survey of various techniques and approaches to detect wormhole attack in WSN.

5.1 Location and Time-Based Approaches

In this approach [9–12], nodes in the network are aware of the current position of its neighbor node before sending the packet, the receiver node then calculates the distance information about the source node and the total time required to traverse the path by the packet.

Hu et al. [13] proposed a mechanism, called to be packet leashes, types of leashes are: one is geographic leashes and other type of leashes is temporal leashes. In geographical leash, the receiver of the packet send by the source is nearby within a calculated distance from the source. Since the packets are traversed most at the speed of light, in temporal leash the packet is tagged with an upper bound, which controls the maximum travelling distance of the packet. The wormhole attack can be prevented by these leashes, as the travel distance of the packet can be calculated.

5.2 Cluster-Based Approach

The entire network is classified into clusters where each cluster network consists of its own cluster head (CH) and other nodes in the cluster as member nodes (non-CH). The member nodes only send the information to the cluster head, and the information is travelled among the nodes or outside the cluster network to the destination via or through this cluster head. The election of cluster head is done dynamically, and it has a job to maintain or update the routing information of the cluster nodes.

A cluster-based method is discussed in [14, 15]. It is based on the M-Leach protocol. Time is divided into parts of equal length called round. Each round is of four phases: setup phases, member's verification phase, cluster head routing phase, and steady-state phase.

5.3 Public Key Encapsulation-Based Approach

In [6], the proposed technique is based on public key encryption. In the said paper, all the nodes have its own public key. Message is broadcasted to all one hop neighbors who contain source address and its own public key. The reply message

from the receiver consists of the public key of the receiver encrypted with the public key of the sender and the destination address.

Now when the actual data is sent, the sender encrypts the data packet with the public key of the destination and the destination on receiving the packet decrypts the message with its private key. To check successful delivery, 2ACK scheme is proposed.

5.4 Moving Average (MA) Indicator-Based Approach

Chen et al. [16] proposed a method using a moving average (MA) indicator. The MA indicator utilizes the time series of price changes to decide on a transaction. The phenomenon of time series information changes corresponds to the change of the neighbor nodes in a WSN. However, it has drawbacks like time-consuming and high-cost project, which requires various combinations of the MA period be exhaustively examined. To eradicate these drawbacks, quantum-inspired tabu search (QTS) algorithm is used to search for the best combination of MA periods in each scenario in order to enhance the wormhole detection rate and network performance.

5.5 Hop-Count Technique

Ji et al. [17] proposed a method with hop count and response delay. Here every node calculates the average hop counts and the variance of the entire route in its routing table and updates continuously on arrival on new routes. Probability of current route under attack is calculated which only indicates the attack not the attacker node itself. The mechanism based on signature works for every node in the network that forwards the RREP which creates a signature at the end of the packet (for that the RREP packet format is modified to provide space for signature storage of 8 bits per node). Hence, when RREP is received by a node, firstly, it calculates the probability of attack, and on the basis of its value, it applies the signature testing.

5.6 Round-Trip Time (RTT) Mechanism

In [18], the method is based on round-trip time (RTT) where AOMDV is used which is an extension of the AODV protocol. When the source nodes broadcast RREQ packet, time is noted, and when reply is received, again time is noted. By using these values, RTT is calculated of the established route. Average RTT is

Table 2 Comparative study of various approaches

Method	Advantages	Research gaps
Khandare et al. 2013 [6]	Uses public key encryption technique. Secure communication with encryption technique is provided	Energy consumption is high; during 2ACK scheme, acknowledgment can be lost due to some link failure
Sharma et al. 2014 [8]	Location-based approach is used. Both hidden and exposed wormhole attack are detected	Energy consumption is high in case the failure of a link occurs, as it uses Euclidean distance formula to get the shortest path
Parmar Amish et al. 2016 [5]	Location-based approach—It has minimum overhead and has minimum end-to-end delay	Mobility of nodes is of great concern
Priya Maidamwar et al. 2013 [19]	Cluster-based approach—Threshold is computed for selection of cluster heads which changes for every round	Clusters are formed dynamically, also the selection of CHs are still random
Shahryar et al. 2015 [14]	Cluster-based approach—Before sending data, the detection and localization of wormhole attacks is done. Uses broadcasting packets instead of using complex encryption or heavy computation, and it is independent of network data	Overhead of cluster formation is high in some cases and increases the time of detection. The delay metric (sending and receiving packets) in the protocol is not optimal, especially in large networks
Singh et al. 2014 [8]	Hybrid approach—WRHT works against all categories of wormhole attacks	The network must operate on promiscuous mode; here each sensor node listens to the packets transferred by its own neighbor nodes

calculated by dividing the values with respective hop counts also called threshold round-trip time. After comparing the threshold value with each RTT, if the total round-trip time calculated is fewer than threshold RTT and hop count of that route is two or more, then wormhole link is suspected to be present in that route or no wormhole link is suspected. As the wormhole link is known to be present, the sender sends a dummy RREQ packet through that route so that malicious node is spotted (Table 2).

6 Analysis

Wireless sensor network is a network with big digits of sensor nodes placed in the area. In wormhole attack, malicious nodes can create a tunnel or wormhole link between each other, the malicious nodes can also deflect the route by sending false information that is the neighbor node. A wormhole tunnel in a network can be established in various ways by the attacker node to disturb the network. Placing a malicious node in the network with routes, an attacker can have control over the

routing protocol. If the data packet is transferred to the neighbor nodes in some specific modulating methods, then they are resistant to closed wormholes. To protect the packets from attack, packet encryption technique can be used. This encrypted data can be broadcasted or sent via multipath.

In a cluster-based network, clusters are selected dynamically. It may consist of one or more cluster heads. Generally, a cluster head (CH) is elected based on few parameters such as hop distance, reliability, trustworthiness. In the network, the nearest cluster is assigned to the nodes using any clustering algorithm. The member nodes are usually one hop distance to the cluster head, and the packets sent in a cluster network is sent via the cluster head to the base station. All nodes can be secured with a public key of their own, and when a packet is sent by the sender, it is sent to the cluster head, which can encrypt the packet with the key of the sender and send to the base station via a route or broadcasts the packet. If a wormhole node is present in the route, it cannot decrypt the message. This can provide a secured communication. The CH can also elect a substitute member based on parameters in case of the death of CH. With this, wormhole can be prevented and secured communication can be provided.

7 Conclusion

Wormhole attack is a challenging and difficult to detect; here two or more malicious nodes are placed in the network where attackers are linked with each other in the network and tunnel the packet through this link. This paper describes the details and gives a survey on wormhole attacks of various approaches with its classifications according to their underlying techniques. This paper includes efficient detection and prevention techniques for wormhole attacks proposed by various researchers along with the advantages and disadvantages. This survey gives a detailed idea about wormhole attack and its impacts on the network so that users can be aware and implement a proper detection and prevention algorithm to be on the safer side. There are various other detection and prevention techniques for wormhole attack. A secured communication can be assured using these detection techniques.

References

1. Pathak, S., & Jain, S. (2016). A novel weight based clustering algorithm for routing in MANET. *Wireless Networks*, 22(8), 2695–2704. <https://doi.org/10.1007/s11276-015-1124-82>.
2. Pathak, S., Dutta, N., & Jain, S. (2014). An improved cluster maintenance scheme for mobile AdHoc networks. In *IEEE 2014 international conference on advances in computing, communications and informatics*, pp. 2117–2121. <https://doi.org/10.1109/icacci.2014.6968281>.
3. Pathak, S., & Jain, S. (2017). An optimized stable clustering algorithm for mobile ad hoc networks, *EURASIP Journal on Wireless Communications and Networking*, Volume (2017), Number (1), pp. 1–11. <https://doi.org/10.1186/s13638-017-0832-4>.

4. Pathak S, Jain S: A novel weight based clustering algorithm for routing in MANET, *Wireless Networks-The Journal of Mobile Communication, Computation and Information*, Springer Link, Vol. 21, No. 8, pp 1–10 (2016).
5. Parmar Amish, V.B. Vaghela Detection and Prevention of Wormhole Attack in Wireless Sensor Network using AOMDV protocol, 7th International Conference on Communication, Computing and Virtualization 2016, ScienceDirect, *Procedia Computer Science* 79(2016) 700–707.
6. Pravin Khandare, Prof. N. P. Kulkarni, Public Key Encryption and 2Ack Based Approach to Defend Wormhole Attack, *International Journal of Computer Trends and Technology*-volume 4, Issue-3, pp. 247–252, 2013.
7. Saurabh Ughade, R.K. Kapoor, Ankur Pandey, An Overview on Wormhole Attack in Wireless Sensor Network: Challenges, Impacts, and Detection Approach, *International Journal of Recent Development in Engineering and Technology*, 2014.
8. Nishant Sharma, Upinderpal Singh, Various Approaches to Detect Wormhole Attack in Wireless Sensor Networks, A monthly journal of Computer Science and technology, *IJCSMC*, Vol. 3, Issue. 2, February 2014, pg. 29–33.
9. Nishant Sharma, Upinderpal Singh, A Location Based Approach to Prevent Wormhole Attack in Wireless Sensor Networks, *International Journal of Advanced Research in Computer Science and Software Engineering*, Volume 4, Issue 1, January 2014.
10. J. Kim, D. Sterne, R. Hardy, R. K. Thomas, and L. Tong, Timing based localization of in-band wormhole tunnels in manets, in *ACM WiSec*, 2010.
11. R. Poovendran and L. Lazos, A graph theoretic framework for preventing the wormhole attack in wireless ad hoc networks, *Wireless Network*, vol. 13, no. 1, 2007.
12. Honglong Chen, Wei Lou, Zhi Wang, On providing wormhole-attack-resistant localization using conflicting sets, *Wireless Communications and Mobile Computing*, vol. 15, pp. 1865, 2015, ISSN 15308669.
13. Y. C. Hu, A. Perrig and D. B. Johnson, Packet Leashes: A Defense against Wormhole Attacks in Wireless Networks, in 22nd Annual Joint Conference of the IEEE Computer and Communications Societies (INFOCOM), pp. 1976–1986, 2003.
14. Maliheh Shahryari, Hamid Reza Naj, A cluster based approach for wormhole attack detection in wireless sensor networks, *Journal of Advanced Computer Science & Technology*, 4 (1) (2015) 95–102.
15. Kehkasa Mirza, Vaidehi Shah, Using Cluster Based Approach Wormhole Attack Detection in Wireless Sensor Network: A Survey, *International Journal of Innovative Research in Science, Engineering and Technology*, Vol. 4, Issue 12, December 2015.
16. Honglong Chen, Wendong Chen, Zhibo Wang, Zhi Wang, Yanjun Li, Mobile Beacon Based Wormhole Attackers Detection and Positioning in Wireless Sensor Networks, *International Journal of Distributed Sensor Networks*, vol. 2014, pp. 1, 2014, ISSN 1550-1329.
17. Shiyu Ji, Tingting Chen, Sheng Zhong, Subhash Kak, DAWN: Defending against wormhole attacks in wireless network coding systems, *INFOCOM 2014 Proceedings IEEE*, pp. 664–672, 2014.
18. Saswati Mukherjee, Matangini Chattopadhyay, Samiran Chattopadhyay, Pragma Kar, Wormhole Detection Based on Ordinal MDS Using RTT in Wireless Sensor Network, *Journal of Computer Networks and Communications*, vol. 2016, pp. 1, 2016, ISSN 2090-7141.
19. Priya Maidamwar and Nekita Chavhan, Research on Qualitative Analysis of LEACH with Wormhole attack in Wireless Sensor Network, *International Journal of Advanced Computer Research (ISSN) Volume-3 Number-1 Issue-8 March-2013*, <https://doi.org/10.5121/ijns.2012.2404>.

Data Center Traffic Engineering: Multipath Routing with QoS Guarantee

Epherika Tariang and Nabajyoti Medhi

Abstract Traffic within a data center can sometime lead to congestion due to imbalance of distribution of traffic. In this paper, a software-defined networking (SDN) approach to traffic engineering within a data center is described. A video traffic distribution scheme is designed based on SDN, to improve network availability by means of multipath thus achieving load balancing. In this paper, queue bandwidth allocation (QBA) algorithm is proposed which allocates bandwidth to video traffic and other classes of traffic. QBA uses the concept of queue in OpenFlow (OF) 1.3 ([1] and McKeown et al. in ACM SIGCOMM Comput Commun Rev [2]) which guarantees quality of service (QoS) by reserving bandwidth on each queue for each class of traffic based on the priority of each class of traffic which is discussed in Sect. 3. Finally, simulations are performed to show that our proposal is significant in achieving load balancing to solve the queue congestion problem as well as allocate bandwidth to each queue using QBA.

Keywords Queue bandwidth allocation (QBA) · Software-defined networking (SDN) · OpenFlow (OF) · Quality of Service (QoS)

1 Introduction

Traffic delivered to end consumers is usually originated from a data center which could be from anywhere across the world. So as to ensure the communication quality, the QoS innovation has been created in conventional system which is the

E. Tariang
Department of Computer Science and Engineering, NIT Meghalaya,
Shillong, India
e-mail: mika.tariang.et@gmail.com

N. Medhi (✉)
Department of Computer Science and Engineering, Tezpur University,
Tezpur, India
e-mail: nmedhi@tezu.ernet.in

general execution of a system and is measured by error rates, bit rate, throughput, transmission delay, and so forth. QoS is especially imperative for the activity with extraordinary prerequisites, for example, Voice over Internet Protocol (VoIP) and video applications. For the improvement of end-to-end traffic delivery or to meet the delay requirements of interactive traffic (such as video traffic), over-provisioning of network links with two to three times more than the required bandwidth is usually adopted. However, despite the over-provisioning of the network links, their performance is usually poor. To overcome this problem, it is better to maintain the QoS of the traffic which will further improve the efficiency of the data center network. The data centers at present are inefficient and unable to scale, because of the difficulty of handling the QoS. With the emergence of SDN, some of the hurdles discussed above have been lifted. In order to overcome this inefficiency, solutions based on SDN have been provided which consist of a central control through which queues can be built dynamically and also bandwidth can be explicitly allocated to enable multipath routing. Taking this into consideration, the real issue in data center traffic management is the allocation of bandwidth to the queues in a scalable manner while maximizing the overall utilization of the network and also keeping in mind the important metrics like QoS requirements and load balancing.

In this paper, a fair bandwidth allocation algorithm QBA is proposed. The main contributions to this paper are summarized as follows. Firstly, traffic is classified into video and other types of traffic. Secondly, a QoS-guaranteed data center traffic management model which focuses on allocation of bandwidth to the video and other types of traffic is proposed. QoS ensures that the data is transferred in accordance with the priority which is based on the type of data it carries and reserves a constant network bandwidth for a particular application according to its requirement.

2 Background and Related Work

Several QoS architectures have been explored by the Internet Engineering Task Force (IETF) over the years. Based on these few architectures that are discussed in this section, a new algorithm QBA is proposed.

2.1 Integrated Services

Integrated services also known as IntServ is a QoS architecture in which every single router in the network implements IntServ, and also every application has to make its own reservation, which uses Resource Reservation Protocol (RSVP) as the underlying mechanism to signal it across the network. IntServ works well in small-scale network, but for a network as large as the Internet, it is hard for all

routers in the traffic path to support it and many states to be installed in each router. Hence, it is hard to keep track of all of the reservations.

2.2 *Differentiated Services*

The idea of differentiated services or DiffServ is that it classifies traffic on IP networks and also provides quality of service with low latency for critical network traffic such as voice or streaming media. DiffServ is a networking architecture that uses a 6-bit differentiated services code point (DSCP) field in the 8-bit differentiated services field (DS field) in the IP header. In contrast to IntServ, DiffServ requires no advance setup, no reservation, and no time-consuming end-to-end negotiation for each flow, but how individual router deals with the DS field of the specific configuration is not stipulated; therefore, it is difficult to predict end-to-end behavior. DiffServ provides QoS in each domain. It is complicated further if a packet crosses two or more DiffServ domains before reaching its destination. DiffServ alone does not guarantee QoS nor does it pertain to any SLA.

2.3 *OpenQoS*

Nowadays, SDN has been used to implement QoS. Egilmez et al. [3, 4] proposed an OpenFlow protocol-based controller, namely OpenQoS to achieve end-to-end QoS for multimedia-based applications. It is extended to a distributed architecture in [5]. OpenQoS classifies the traffic into data and multimedia flows. The multimedia flows are following the dynamic QoS-guaranteed routing algorithm, whereas the other data flows are following the shortest routing path algorithm. Unlike another OpenFlow-based QoS framework in [3], OpenQoS does not use the queue mechanisms that use OpenFlow to realize QoS guarantees for different service types. When the traffic of certain types exceeds the threshold, it can still cause link congestion.

2.4 *MCTEQ (Multiclass Traffic Engineering with QoS Guarantee)*

MCTEQ is another SDN model to traffic engineering for communication in inter-data center. It tries to optimize the joint-bandwidth allocation problem for multiple classes of traffic in inter-data center communication [6]. MCTEQ handles various classes of traffic according to their priority, keeping in mind the delay requirements of the interactive class which has the highest priority. It has been

discovered that MCTEQ is two times much faster than the existing proposed models and also has the maximum network utilization. It has also been discovered that MCTEQ handles the interactive flows much more efficiently than the existing approaches by carefully handling the end-to-end delay.

In this paper, the concept of differentiated services is used to classify video traffic and other data traffic and incorporated the OpenFlow queue mechanism so as to solve the queue congestion problem and also guarantee QoS. The main QoS parameter that is focused in this paper is bandwidth. Hence an algorithm is proposed, which will ensure fairness of allocation of bandwidth to the different classes of traffic.

3 Proposed Model

In this paper, the OpenFlow queue mechanism is introduced to solve the queue congestion problem and promote the reliability of data communication within the data center. The key function of traffic engineering is route optimization that improves network performance by searching optimized routing. But for a large-scale network with complicated structure and multipath among servers, it is hard to improve network performance according to traditional routing protocol to choose one route between the destination and the source; moreover, in this case it will waste network resources. For example, we consider a session with 2 Gb/s throughput requirement from source to destination in a network in which even the best path can achieve a throughput at most 1.5 Gb/s. To achieve better throughput, multiple paths can be used for packet delivery. Using another path with 0.5 Gb/s transmission rate simultaneously will achieve total throughput of 2 Gb/s. In this paper, the model proposed includes multipath routing which will help in load balancing along with QoS guarantee which uses the OpenFlow concept of queues. By this way, it is ensured that packets will be forwarded to multiple paths to avoid traffic congestion and at the same time, promote the network performance and reliability, to fully utilize the resources.

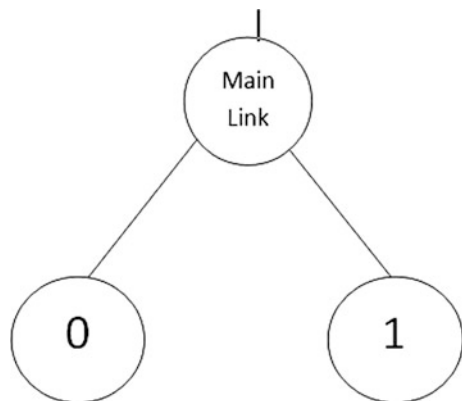
The controller used in this project is Ryu which is a Python-based controller. Multipath can be achieved on RYU via select group, in order to achieve traffic scheduling, which helps to achieve load balancing. In OpenFlow 1.3, group table is provided, which is used for load balancing. A group table has a number of group entries. Each flow entry points to a group which enables OpenFlow to indicate the forwarding methods. Groups were introduced in OpenFlow 1.1 which made complex operations on packets possible. Groups also enable flooding as well as more complex forwarding actions such as multipath, fast reroute, and link aggregation. In this paper, the following algorithm has been proposed for the allocation of bandwidth to each queue and also for handling bursty traffic and also forwarding traffic to two queues based on the nature of traffic. In this paper, video traffic has been chosen as one class of traffic and other traffic types are chosen as the second class of traffic.

For shaping the traffic, the standard Linux packet scheduling implementation of Hierarchical Token Bucket (HTB) [7] is used. HTB helps to control the use of the outgoing bandwidth of a link. It allows the use of a single link to simulate several other links to send different kinds of traffic. The division of the physical links into simulated links has to be done from our side which can be used to decide which class of traffic will go through which simulated link. HTB ensures that the amount of service provided to each class is at least the minimum of the amount it requests and the amount assigned to it. The simplest approach is shown in the picture at the bottom.

In Fig. 1, there are two queues 0 and 1 which share the main link. Queue 0 will be used to handle video traffic. Queue 1 on the other hand will be used to handle other classes of traffic. For this purpose, two queues are simulated for each link instead of a single queue. Classification of traffic can be done using DiffServ which differentiates the packets of different traffic classes by marking the packets with various DSCP values based on the type of traffic. With this idea in mind, traffic is shaped by prioritizing it using the differentiated services code point (DSCP) tags. The DSCP is a field in the IP header which has replaced the outdated 8-bit ToS field, six of which is used for DSCP marking, and the other two are ECN bits. DSCP is applied on per hop basis that allows each router in the path to prioritize the traffic based on the DSCP tag. The default DSCP is 0, and this could be modified to various DSCP values based on the traffic type.

The pseudocodes of QBA are shown in Algorithm 1. Initially, the topology is emulated using Mininet. B is the link bandwidth or link capacity. All the node disjoint paths of the topology are discovered by using a slight variation of the Dijkstra's algorithm. It is also used to store the number of paths n and the length of each of these i th paths l_i . Using the length of these paths, the bandwidth is allocated to each of the paths. The longer the path more is the bandwidth allocated to it. This is because traffic tends to take the shortest path available. Hence, with time the shortest path gets congested and could lead to link failure. As a result, shortest path gets lesser bandwidth than the longer paths.

Fig. 1 Link sharing using HTB



Algorithm 1: QBA (Queue bandwidth allocation algorithm)**Input:**

- network topology
- Link Bandwidth - B , b video/data rate,
- c is a constant = b/n ,
- $L(u,v)$ set of n tuples for n paths between u and v in the form (i, l_i) where
- i is the port number of i th path, l_i is the length of i th path between u and v .
- Q_{oi} bandwidth for other traffic, Q_{vi} bandwidth for video traffic.

Output: Allocation of bandwidth to Q_{vi} and Q_{oi}

```

1 Finding all possible node disjoint paths using slight variant of Dijkstra's
algorithm
2 Store number of paths -  $n$ 
3 Use the algorithm to find the length of paths
4 /* Allocate bandwidth to each path based on its length */
5/* Longer the path more is the bandwidth */
6 for  $i \in L(u,v)$ 
7 /* allocation of bandwidth to queue for other classes of traffic */
8  $Q_{oi} = B - c * l_i$ 
9 /*allocation of bandwidth to queue for video classes of traffic */
10  $Q_{vi} = B - Q_{oi}$ 
11 Mark incoming packets with DSCP values
12 if source is from video server:
13 mark with DSCP value 34
14 install matching action at switch to redirect to video traffic queue
15 else
16 mark with DSCP value 26
17 install matching action at switch to redirect to other traffic queue
18 end if
19 / * handling bursty traffic */
20 burst_limit =  $b$  /* (application traffic throughput) */
21 max_limit =  $Q_{vi}$ 
22 burst_threshold = max_limit/2 (recommended)
23burst_ratio = burst_threshold/burst_limit;
24 burst_time = clock_time /burst_ratio
25/* (clock time may be any constant duration for which we want to allow
burst traffic) */
26 set burst time, burst threshold and burst limit for each video traffic queue
of  $i$ th path
27end for
28 end

```

Table 1 is shown as an example of how DSCP marking can be implemented.

In Table 1, two queues are installed in one link. Queue 0 handles video traffic. Allocated bandwidth for video traffic is 1 Mbps. Whenever traffic arrives at a

Table 1 DSCP-based QoS using HTB

Queue id	QoS id	Allocated bandwidth (Mbps)	Class	DSCP
0	1	1	AF31	26
1	2	9	AF41	34

switch, the switch will perform matching actions and check if the packet is generated from a video server based on its source address. If a match is found, the packet will be marked with the DSCP value 26 which belongs to the class AF31 (Assured Forwarding with low drop probability) and directed to Queue 0. On the other hand, the packets which do not belong to video traffic will be marked with a DSCP value of 34 which belongs to the class AF41 (Assured Forwarding with low drop probability) and is redirected to the Queue 1. This way the traffic is shaped smoothly by separating the traversing queue of the video traffic from other traffic classes thus avoiding congestion. The real problem that could arise is how to handle traffic when it is bursty in nature. Since HTB is a hierarchical implementation of the Token Bucket Filter algorithm, it allows burstiness of traffic up to a certain limit called the burst limit within a stipulated time called the burst time. Hence, the problem of handling bursty traffic is solved by using the Token Bucket idea of limiting burstiness for a certain period of time as shown in Algorithm 1 from lines 19–26.

4 Implementation

The topology is setup using Mininet as shown in Fig. 2. For testing purpose, this simple topology with unequal paths is taken. The controller used here is Ryu.

In this experiment, multipath load balancing is implemented by creating three buckets in a SELECT group with different weights, which are selected in round

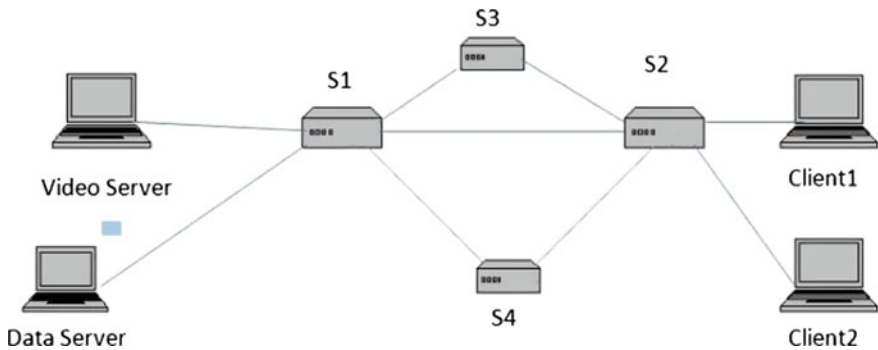


Fig. 2 A simple topology to demonstrate multipath with QoS guarantee

robin manner. The SELECT group is basically designed to achieve load balancing. Each bucket in a group has a weight assigned to it, and upon entry into the group each packet is sent to one bucket, depending on the selecting algorithm of the bucket which is usually weighted round robin. The bucket weight is assigned as a parameter to each bucket. Each bucket in the group consists of a list of actions. Also, the queue in OpenFlow is used, for ensuring a quality of service. In this case, two queues are created, queue 0 and queue 1, for each path each corresponding to port 1, port 2, port 3 simultaneously. The max rate and min rate for each queue is configured using OVS commands. For example, when switch 1 (dpid = 1) receives packets from host 1 (in port = 1), it will distribute the flow to out ports (port 1 = 3, port 2 = 2, and port 3 = 4) by SELECT group with a group ID 50 which is injected at switch 1, and also according to the max rate or min rate configured. This means that if the dpid is 1 (switch 1) and in port is 1 (from host 1), which means multipath has to be applied to the flow thus, achieving load balancing (multipath). Depending on the traffic class, the packets are marked with DSCP value 26 if it is coming from a video server based whose packet is matched based on its source address and marked with DSCP value 34 otherwise.

5 Result and Analysis

The simulation software is adopted for experiments for cost reason. The operating system used is Linux, SDN network is built with the Mininet emulator, and the controller Ryu is used. The experiment topology is illustrated in Fig. 1. The topology is built using Mininet, and the controller is started alongside. In this experiment, video traffic is used so as to achieve a more real-time result. Video traffic is streamed from video server to host 1 using VLC media player, and the following results were seen as shown in Fig. 3. It can be seen that traffic has been

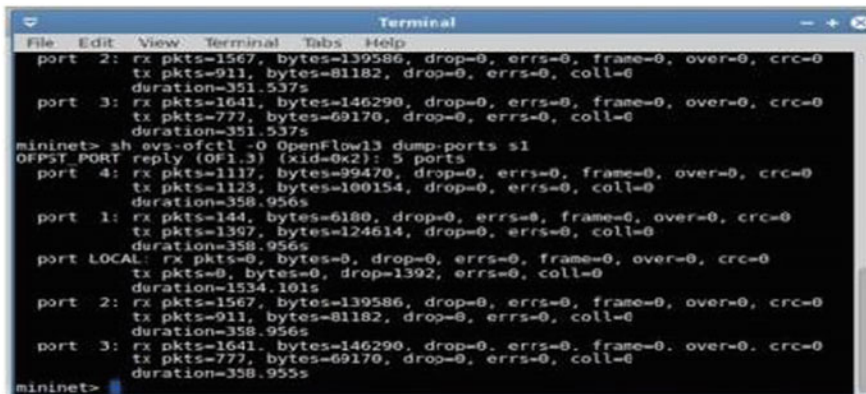


Fig. 3 Traffic is distributed across all three paths

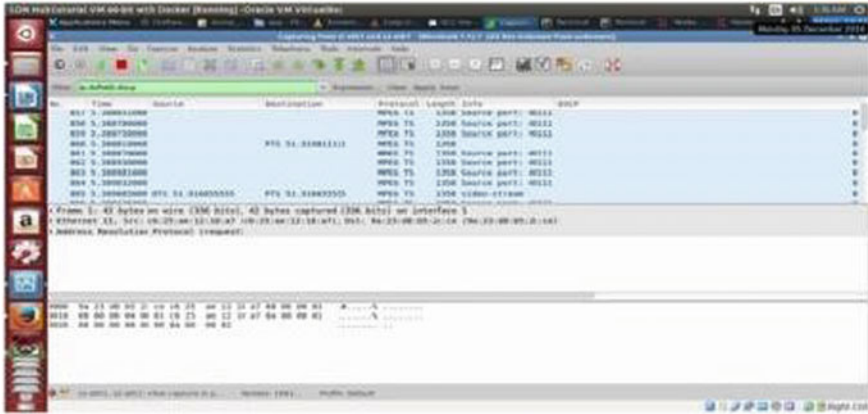


Fig. 4 Packets with default DSCP value 0

distributed across the three paths thus achieving load balancing. Another set of traffic was analyzed using Iperf which is a network testing tool that is used to generate TCP or UDP traffic and measures the throughput of the network that is carrying the traffic. These packets were analyzed using Wireshark which is commonly used for packet analyzing. The following results were obtained after successful classification of the packets by marking them with various DSCP values. Figure 4 shows packets before they were marked with a DSCP value.

The default DSCP value is 0. Figure 5 shows packets marked with DSCP value 26 (AF31) which indicates that it is video traffic. Figure 6 shows packets marked with DSCP value 34 (AF41). Figure 7 shows a video streamed from source to

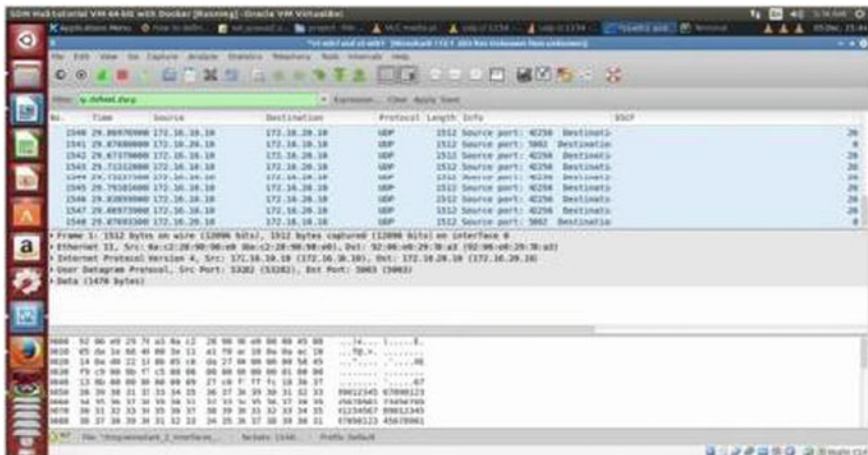


Fig. 5 Packets with DSCP value 26 (video traffic)

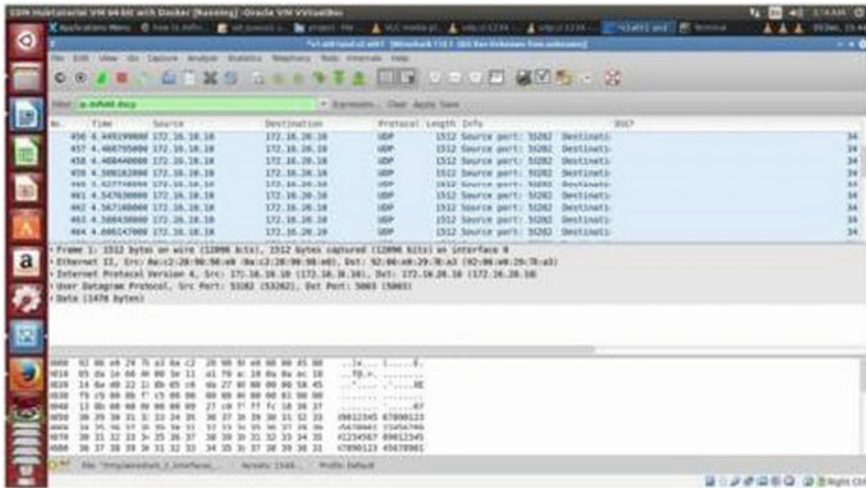


Fig. 6 Packets with DSCP value 34 (other traffic)

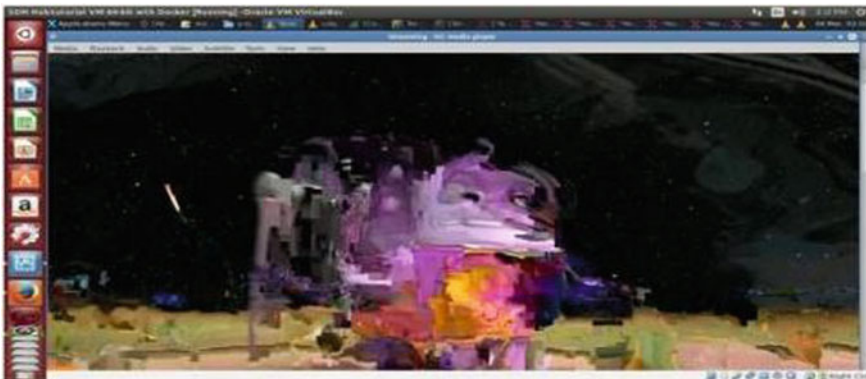


Fig. 7 Video streaming without queue implementation

destination without the queue implementation. It can be seen that the quality of the video is very poor. Figure 8 shows that video quality is much smoother using queue implementation with guaranteed bandwidth. Finally bursty traffic is generated using Iperf tool for a given period of burst time. Any traffic other than the video traffic which arrives at a rate of more than half of the video data rate is taken as bursty traffic, and it is allowed to burst for a stretch of calculated burst time up to a certain burst rate limit.



Fig. 8 Video streaming with queue implementation

6 Conclusion

Multipath load balancing of traffic within a data center is achieved using the SELECT group of Ryu controller. Also the concept of queues in OpenFlow has guaranteed QoS by configuring the max rate and min rate for each queue and also handling bursts within traffic. The queue congestion problem has been solved using the proposed model. As a result, fair allocation of bandwidth to video traffic class and other traffic classes is achieved using QBA.

References

1. Openflow1.3 Switch Specification, December 31, 2009, <http://www.openflow.org/documents/openflow-spec-v1.3.0.pdf>.
2. N. McKeown, T. Anderson, H. Balakrishnan, et al. OpenFlow: Enabling Innovation in Campus Networks. ACM SIGCOMM Computer Communication Review, (2008) April 2; New York, USA.
3. H. E. Egilmez, S. T. Dane, K. T. Bagci, et al. OpenQoS: An OpenFlow Controller Design for Multimedia Delivery with End-to-End Quality of Service over Software-Defined Networks. In Signal & Information Processing Association Annual Summit and Conference, (2012) December 3–6; Hollywood, USA.
4. H.E. Egilmez, S. Civanlar, A.M. Tekalp, An Optimization Framework for QoS-Enabled Adaptive Video Streaming over OpenFlow Networks, IEEE Trans. on Multimedia, 2013.
5. Egilmez, H.E. “Distributed QoS Architectures for Multimedia Streaming over Software Defined Networks,” Multimedia, IEEE Transactions on, vol. 16, no. 6, pp. 1597, 1609, Oct. 2014. 669.
6. Jason Wang, Ying Wang, Xiangming Dai, Brahim Benasou, “SDNbased Multi-Class QoS Guarantee in Inter-Data Center Communications”, IEEE Transactions on Cloud Computing, vol., no., pp. 1, 5555, <https://doi.org/10.1109/tcc.2015.2491930>.
7. HTB Linux queuing discipline manual - user guide, 5.5.2002, <http://luxik.cdi.cz/devik/qos/htb/manual/userg.htm>.

Two Identity-Based Aggregate Signature Schemes from Pairings

Subhas Chandra Sahana, Sourav Kumar Das, Sangeeta Mashahary and Bubu Bhuyan

Abstract An aggregate signature is a short digital signature which is the output of aggregation process. The signature aggregation is done on k signatures of k distinct messages from k distinct users. As the produced signature size is shorter, so it will be efficient to use the schemes in low-bandwidth communication environment. In this paper, we proposed two identity-based aggregate signature schemes from bilinear pairing operations. The proposed schemes are secure against existential forgery under adaptively chosen message and identity attack in the random oracle model based on the assumption of intractability of the computational Diffie–Hellman problem (CDHP). The efficiency analysis of the proposed identity-based aggregate signature schemes with other established identity-based aggregate signature schemes is also done in this paper.

Keywords Signature · Aggregate signature · Bilinear pairing · Computational Diffie–Hellman Problem (CDHP)

S. C. Sahana (✉) · S. K. Das · S. Mashahary · B. Bhuyan
Department of Information Technology, North Eastern
Hill University, Shillong 793022, India
e-mail: subhas.sahana@gmail.com

S. K. Das
e-mail: kumarsourav.it@gmail.com

S. Mashahary
e-mail: sangeetamashahary133@gmail.com

B. Bhuyan
e-mail: b.bhuyan@gmail.com

1 Introduction

In 2003, the first aggregate signature (BGLS), proposed by Boneh et al. [1] allows k members of a given group of potential signers to sign k different messages and all these signatures can be aggregated into a single signature. Actually, the aggregate signature [1] is based on the BLS [2] short signature.

As the size of aggregate signature is same as the individual signature, so we get a compact single signature of all individual signatures. This single signature can provide a proof to the verifier that the n players have indeed signed the original messages. Thus, aggregate signature provides non-repudiation security service on different messages signed by different users at the same time. Actually, there have been many practical application of aggregate signature scheme. As we are bounded by page limitation, only one example has been discussed. In public key infrastructure (PKI) of depth n , each user has been given a chain of certificate of length n . So, the chain contains n signatures by n certificate authorities (CAs) on n distinct certificate. If we use aggregate signature scheme, it is possible to obtain a compressed aggregated certificate [3]. Specifically, the main motivation is that X.509 certificates can be shortened into a single signature by compressing n signatures. It is also useful for compression where the signatures on many different messages are generated by many different users [4].

It is well known that that PKI-based cryptosystem has the biggest disadvantage related to certificate management activities. To avoid this problem, Shamir [5] introduced the concept of identity-based cryptosystem (IBC) in 1984. In IBC, the main advantage is that there is no need of public key distribution in the form of certificates as user can use his unique identity information such as name, email address by providing his own public key.

Due to various interesting practical applications and various advantages of IBC, discussed above, it is always a hot research area to achieve an efficient Id-based aggregate signature schemes. After the pioneering work [1, 2], many identity-based aggregate signature schemes have been proposed. In 2004, Cheon [6] presented first identity-based aggregate signature (IBAS). This scheme compresses the signatures into half, while the BGLS compresses multiple signatures into one. After that work, in 2006, Gentry and Ramzan proposed an efficient ID-based aggregate signature which is much faster than BGLS scheme as less number of operations are involved. In 2008, Wang [7] presented a new ID-based aggregate scheme which provides partial aggregation. It is also more efficient than BGLS scheme. At the same time, Wen [8] proposed a new aggregate signature with constant pairing operation (AS-CPO) scheme, which requires only two pairings in verification. This scheme is more efficient than BGLS as BGLS requires $O(n)$ pairing computation where n is the number of signers. However, many ID-based aggregate signature schemes [7, 9, 10] have been constructed from basic ID-based signature scheme.

The rest of the paper is organized as follows. In the next section, mathematical background of the proposed schemes has been explained. After that, the two proposed schemes have been presented in the next section. In Sect. 4, the efficiency analysis of the proposed ID-based aggregate signature schemes with other established ID-based aggregate signature schemes has been done.

2 Mathematical Background

Bilinear Pairing: Let G_1 be an additive cyclic group generated by P whose order is a prime q and G_2 be a multiplicative cyclic group of the same order q . A bilinear pairing is a map $e : G_1 \times G_1 \rightarrow G_2$ with the following properties:

- (a) Bilinearity: $e(aP, bQ) = e(P, Q)^{ab}$ for all $P, Q \in G_1$ and all $b \in \mathbb{Z}_q^*$.
- (b) Non-degenerate: There exists $P, Q \in G_1$ such that $e(P, Q) \neq 1$.
- (c) Computable: There is an efficient algorithm to compute (P, Q) , for all $P, Q \in G_1$.

Additionally, the security of these proposed schemes depends on the hardness of the following Diffie–Hellman problem.

Computational Diffie–Hellman Problem (CDHP): For $b \in_R \mathbb{Z}_q^*$, given P, aP, bP , to compute abP is known as computational Diffie–Hellman problem which is a hard problem.

3 Two Proposed ID-Based Aggregate Signature Schemes

An aggregate signature scheme consists of six algorithms. They are **Setup**, **Extract**, **Sign**, **Verify**, **AggSign**, and **AggVerify**. The first four algorithms are for an ordinary identity-based signature scheme, and last two algorithms are for signature aggregation and aggregate signature verification. It works as follows. The first proposed aggregate signature scheme is presented in Sect. 3.1, and other one is presented in Sect. 3.2.

3.1 A Proposed ID-Based Aggregate Signature Schemes (First One)

SETUP: Given a security parameter k , the private key generator (PKG) runs the setup algorithm and outputs two groups G_1 of prime order q and G_2 of same order. The bilinear pairing is given as $e : G_1 \times G_2 \rightarrow G_2$. PKG establishes the system parameters $q, G_1, G_2, P, Q, P_{\text{pub}}, P_{\text{pub}^2}, e, H_1, H_2$ where

1. P is the generator of group G_1 .
2. PKG picks master key $s \in Z_p^*$ and computes $P_{\text{pub}} = sP, P_{\text{pub}^2} = s^2P$.
3. PKG also chooses two cryptographic hash functions, $H_1 : \{0, 1\}^* \rightarrow G_1$ and $H_2 : \{0, 1\}^* \rightarrow Z_q^*$.

EXTRACT: Let P_1, P_2, \dots, P_n denote all the users to join the signing process. The identity of P_i is denoted as ID_i . For user's identity ID_i , its public key $Q_{ID_i} = H_2(ID_i)$ and private key $S_{ID_i} = sQ_{ID_i}$. The user makes Q_{ID_i} public and keeps S_{ID_i} secret.

SIGN: For a message m_i , user with identity ID_i follows the steps below:

1. Choose a random number $r_i \in Z_q^*$, and broadcasts $U_i = r_iP$.
2. Calculate the value $h_i = H_2(m_i, ID_i, U_i)$
3. Calculate the value $V_i = r_iP + h_iS_{ID_i}$
4. The signature σ_i is then the pair (U_i, V_i) .

VERIFY:

1. The designated player (DP) computes $U = \sum_{i=1}^n U_i$.
2. Compute $h_i = H_2(m_i, ID_i, U_i)$
3. Accept if $e(P_{\text{pub}}, V_i) = e(U_i, P_{\text{pub}})e(P_{\text{pub}^2}, h_iQ_{ID_i})$

AGGSIGN: DP computes $V = \sum_{i=1}^n V_i$. The aggregate signature on n different messages m_1, m_2, \dots, m_n given by n users P_1, P_2, \dots, P_n is $\sigma = (U, V)$.

AGGVERIFY: Given aggregate signature $\sigma = (U, V)$ by aggregating party and the list of $\langle ID, \text{message} \rangle$ pairs $\{ID_i, m_i\}$, the verifier verifies the aggregate signature compute

1.
$$h_i = H_2(ID_i, m_i, U_i).$$
2.
$$Q_{ID_i} = H_1(ID_i)$$
3. Accept the signature $\sigma = (U, V)$ if and only if

$$e(P_{\text{pub}}, V) = e(P_{\text{pub}}, U) \cdot e(P_{\text{pub}^2}, \sum_{i=1}^n h_iQ_{ID_i})$$

CORRECTNESS:

$$\begin{aligned}
e(P_{\text{pub}}, V) &= e\left(P_{\text{pub}}, \sum_{i=1}^n V_i\right) \\
&= \prod_{i=1}^n e(P_{\text{pub}}, V_i) = \prod_{i=1}^n e(P_{\text{pub}}, r_i P + h_i S_{ID_i}) \\
&= e\left(P_{\text{pub}}, \sum_{i=1}^n (r_i P + h_i S_{ID_i})\right) = e\left(P_{\text{pub}}, \sum_{i=1}^n \left(r_i P + \sum_{i=1}^n h_i S_{ID_i}\right)\right) \\
&= e\left(P_{\text{pub}}, U + \sum_{i=1}^n h_i S_{ID_i}\right) = e(P_{\text{pub}}, U) e\left(P_{\text{pub}}, \sum_{i=1}^n h_i S_{ID_i}\right) \\
&= e(P_{\text{pub}}, U) e\left(s \cdot P_{\text{pub}}, \sum_{i=1}^n h_i Q_{ID_i}\right) = e(P_{\text{pub}}, U) e\left(P_{\text{pub}^2}, \sum_{i=1}^n h_i Q_{ID_i}\right)
\end{aligned}$$

3.2 Another Proposed Improved Identity-Based Aggregate Signature Scheme (Second One)

SETUP: Given a security parameter k , the private key generator (PKG) runs the setup algorithm and outputs two group G_1 of prime order q and G_2 of same order. The bilinear pairing is given as $e : G_1 \times G_1 \rightarrow G_2$. PKG establishes the system parameters $q, G_1, G_2, P, Q, P_{\text{pub}}, P_{\text{pub}^2}, e, H_1, H_2$ where

1. P and Q are the random generators of group G_1 .
2. PKG picks master key $s \in Z_q^*$ and computes $P_{\text{pub}} = sP, P_{\text{pub}^2} = s^2P$.
3. PKG also chooses two cryptographic hash functions, $H_1 : \{0, 1\}^* \rightarrow G_1$ and $H_2 : \{0, 1\}^* \rightarrow Z_q^*$.

EXTRACT: Let P_1, P_2, \dots, P_n denote all the users to join the signing. The identity of P_i is denoted as ID_i . For user's identity ID_i , its public key $Q_{ID_i} = H_2(ID_i)$ and private key $s_{ID_i} = sQ_{ID_i}$. The user makes Q_{ID_i} public and keeps S_{ID_i} secret.

SIGN: For a message m_i , user with identity ID_i follows the steps below:

1. Choose a random number $r_i \in Z_q^*$ and broadcasts $U_i = r_i P_{\text{pub}}$
2. Calculate the value $h_i = H_2(m_i, ID_i, U_i)$
3. Calculate the value $V_i = r_i Q + h_i S_{ID_i}$
4. The signature σ_i is then the pair (U_i, V_i)

VERIFY:

1. The designated player computes $U = \sum_{i=1}^n$

2. Compute $h_i = H_2(m_i, ID_i, U_i)$
3. Accept if $e(P_{\text{pub}}, V_i) = e(U_i, Q)e(P_{\text{pub}}^2, h_i Q_{ID_i})$

AGGSIGN: DP computes $V = \sum_{i=1}^n V_i$. The aggregate signature on n different messages m_1, m_2, \dots, m_n given by n users P_1, P_2, \dots, P_n is $\sigma = (U, V)$

AGGVERIFY: Given aggregate signature $\sigma = (U, V)$ by aggregating party and the list of $\langle ID, \text{message} \rangle$ pairs $\{ID_i, m_i\}$, the verifier verifies the signature by computing the following:

1. $h_i = H_2(ID_i, m_i, U)$
2. Accept the signature $\sigma = (U, V)$ if and only if

$$e(P_{\text{pub}}, V) = e(Q, U) \cdot e\left(P_{\text{pub}}^2, \sum_{i=1}^n h_i Q_{ID_i}\right)$$

- **CORRECTNESS:**

$$\begin{aligned} e(P_{\text{pub}}, V) &= e\left(P_{\text{pub}}, \sum_{i=1}^n V_i\right) \\ &= \prod_{i=1}^n e(P_{\text{pub}}, V_i) \\ &= \prod_{i=1}^n e(P_{\text{pub}}, r_i Q + h_i S_{ID_i}) \\ &= \prod_{i=1}^n e(r_i P_{\text{pub}}, Q) e(s P_{\text{pub}}, h_i Q_{ID_i}) \\ &= \prod_{i=1}^n e(U_i, Q) e(P_{\text{pub}}^2, h_i Q_{ID_i}) \\ &= e\left(Q, \sum_{i=1}^n U_i\right) e\left(P_{\text{pub}}^2, \sum_{i=1}^n h_i Q_{ID_i}\right) \\ &= e(Q, U) e\left(P_{\text{pub}}^2, \sum_{i=1}^n h_i Q_{ID_i}\right) \end{aligned}$$

4 Efficiency Comparison

In this section, we will compare our schemes with the schemes in Refs. [7, 9, 10] as we have constructed these two schemes from the idea achieved from those papers. In general, the number of pairing computations of identity-based aggregate signature schemes (IBASs) is proportional to that of signers. But, our proposed IBAS schemes require constant number of pairing computations in aggregated signature

Table 1 Computational complexity of IBAS schemes in the number n of signers

IBAS scheme	Aggregated signature length	Individual sign	Individual signature verify	Aggregate sign	Aggregate signature verify
Ref. [9]	$2 \mathcal{G}_1 $	$3\Delta_{SM} + (n)\Delta_{PA} + 1\Delta_{Hash}$	$(n-1)\Delta_{PA} + 1\Delta_{Hash} + 3\Delta_{PO}$	$(n-1)\Delta_{PA}$	$2\Delta_{Hash} + 3\Delta_{PO} + n\Delta_{SM} + (n-1)\Delta_{PA}$
Ref. [7]	$(n+1) \mathcal{G}_1 $	$3\Delta_{SM} + 1\Delta_{PA} + 1\Delta_{Hash}$	$1\Delta_{Hash} + 3\Delta_{PO}$	$(n-1)\Delta_{PA}$	$2\Delta_{Hash} + 3\Delta_{PO} + n\Delta_{SM} + 2(n-1)\Delta_{PA}$
Ref [10]	$(n+1) \mathcal{G}_1 $	$3\Delta_{SM} + 1\Delta_{PA} + 1\Delta_{Hash}$	$1\Delta_{PA} + 1\Delta_{SM} + 2\Delta_{Hash} + 2\Delta_{PO}$	$(n-1)\Delta_{PA}$	$2\Delta_{Hash} + 2\Delta_{PO} + n\Delta_{SM} + \{n + (n-1)\}\Delta_{PA}$
First proposed scheme	$2 \mathcal{G}_1 $	$2\Delta_{SM} + 1\Delta_{PA} + 1\Delta_{Hash}$	$(n-1)\Delta_{PA} + 1\Delta_{Hash} + 3\Delta_{PO}$	$(n-1)\Delta_{PA}$	$2\Delta_{Hash} + 3\Delta_{PO} + n\Delta_{SM} + (n-1)\Delta_{PA}$
Second proposed scheme	$2 \mathcal{G}_1 $	$3\Delta_{SM} + 1\Delta_{PA} + 1\Delta_{Hash}$	$(n-1)\Delta_{PA} + 1\Delta_{Hash} + 3\Delta_{PO}$	$(n-1)\Delta_{PA}$	$2\Delta_{Hash} + 3\Delta_{PO} + n\Delta_{SM} + (n-1)\Delta_{PA}$

verification process and are independent of the number of signers. An efficiency comparison of our schemes with the existing established schemes is given in Table 1. Here, Δ_{PO} , Δ_{PA} , Δ_{Hash} , and Δ_{SM} denote the number of pairing operations, point addition in G_1 group, hash function, and scalar multiplications in G_1 group, respectively.

5 Conclusion

In this paper, we propose two ID-based aggregate signature schemes with constant pairings needed in signature verification process. We observe that the first scheme is as same efficient as the scheme [10] which assumed to be the most efficient IBAS scheme until now. The security of the scheme is purely based on difficulty of solving computational Diffie–Hellman problem in the random oracle model. Due to page limitation, the security proof is not given in the paper. Just like all other pairing-based cryptosystems, it is not only simple and efficient but also has a shorter signature size.

References

1. Boneh, Dan and Gentry, Craig and Lynn, Ben and Shacham, Hovav: Aggregate and verifiably encrypted signatures from bilinear maps, *Advances in cryptology EUROCRYPT*, Springer, 416–432 (2003).
2. Boneh, Dan and Lynn, Ben and Shacham, Hovav: Short signatures from the Weil pairing, *Journal of Cryptology*, Springer, 17, 297–319 (2004).
3. Meffert, Dennis: Bilinear pairings in cryptography, Masters thesis, Radboud Universiteit Nijmegen (2009).
4. Shakerian, Reza and Pour, Touraj Mohammad and Kamali, Seyed Hossein and Hedayati, Maysam: An identity based public key cryptography blind signature scheme from bilinear pairings, 3rd IEEE International Conference on Computer Science and Information Technology (ICCSIT), IEEE 7, 28–32 (2010).
5. Shamir, Adi: Identity-based cryptosystems and signature schemes, *Workshop on the Theory and Application of Cryptographic Techniques*, Springer, 47–53 (1984).
6. Cheon, Jung Hee and Kim, Yongdae and Yoon, HyoJin and others: A New ID-based Signature with Batch Verification, *IACR Cryptology ePrint Archive*, 131 (2004).
7. Wang, Zhu and Wu, Qian and Ye, Ding-feng and Chen, Hui-yan: Practical identity based aggregate signature from bilinear maps, *Journal of Shanghai Jiaotong University (Science)*, Springer 13, 684–687 (2008).
8. Wen, Yiling and Ma, Jianfeng: An aggregate signature scheme with constant pairing operations, *International Conference on Computer Science and Software Engineering IEEE*, 3, 830–833 (2008).
9. Yu, Yike and Zheng, Xuefeng and Sun, Hua: A new ID-based aggregate signature with constant pairing operations, *Second International Conference on Networks Security Wireless Communications and Trusted Computing (NSWCTC)*, IEEE 2, 188–191 (2010).
10. Shim, Kyung-Ah: An ID-based aggregate signature scheme with constant pairing computations, *Journal of Systems and Software*, Elsevier 83, 1873–1880 (2010).

Real-Time Hybrid Intrusion Detection System Using Machine Learning Techniques

**Inadyuti Dutt, Samarjeet Borah, Indra Kanta Maitra,
Kuharan Bhowmik, Ayindrilla Maity and Suvosmita Das**

Abstract Intrusion and intrusive activities have become a bottleneck for both Internet and Intranet users. An intrusion detection system tries to take care of such activities by constantly monitoring the user systems. Although there are two basic approaches in intrusion detection, i.e., misuse detection system and anomaly detection system, respectively, however, recent research works emphasize on hybrid approach which tries to gather the advantage of both misuse and anomaly-based systems. The proposed research work is based on such a hybrid system which uses misuse detection system for known types of intrusions and anomaly detection system for novel attacks. Frequency episode extraction method is specifically used for misuse-based detection and chi-square test is used for anomaly-based detection. Experiments show that the hybrid intrusion detection system is able to consider the real-time traffic of a network as well as the standard available data set for detecting the efficiency of the system. The proposed system learns and trains itself by detecting known attacks from misuse detection system and novel attacks from anomaly detection system, thereby improving the true positive rates and diminishing false negative rates consequently.

I. Dutt (✉) · I. K. Maitra · K. Bhowmik · A. Maity · S. Das
B. P. Poddar Institute of Management and Technology, Kolkata 700052, India
e-mail: inadyuti@gmail.com

I. K. Maitra
e-mail: ikm.1975@yahoo.com

K. Bhowmik
e-mail: kuharanbhowmik@gmail.com

A. Maity
e-mail: ayindrilla.maiti@gmail.com

S. Das
e-mail: suvosmita.chem@gmail.com

S. Borah
Sikkim Manipal Institute of Technology (SMIT), Majhitar, Rangpo 737136,
Sikkim, India
e-mail: samarjeetborah@gmail.com

Keywords Intrusion detection system · Hybrid system · Feature extraction
Frequency episode extraction · Chi-square test

1 Introduction

Security of computer and its networks is at persistent risk due to the increasing reliance on Internet and Intranet facilities. Novel solutions and techniques have been proposed to manage the security issues. Intrusion Detection System (IDS) has become essential software or applications which are employed to protect the network from malicious activities. Due to its inherent ability to detect an intrusion while it is actually happening, IDS has become increasingly popular in the last few decades. An IDS tries to collect and examine the information which arrives from both the Internet and Intranet so as to identify activities that could be ambiguous or maliciously corrupting the computer systems [1]. There are two variations in approaches in detecting intrusions, namely misuse detection and anomaly detection [2]. Another improved approach is referred to as hybrid system that usually combines the above two approaches to derive better results.

In misuse detection system, a set of specific signatures of well-known attacks are stored and then eventually being mapped with the real-time activities. In order to detect intrusion or intrusive activities, an IDS has to take into consideration a set of pre-defined models, or 'patterns', denoting the behavior of normal as well as anomalous activities. This is accomplished by monitoring the real-time network traffic and comparing the current traffic profile with the pre-defined, known set of anomalous and normal activities [3]. The solidity of this detection system becomes questionable when it is not able to detect attacks that have no pre-defined patterns.

Anomaly detection systems such as IDES [4] have eradicated the limitations of such systems that fail to notice the unknown attacks. According to anomaly detection system, intrusive activities do not occur in normal circumstances and therefore can be considered as anomalous. In order to detect such activities, there must be a constant vigilance on the day-to-day real-time traffic and any deviation from these daily activities can be referred to as anomalous. Both the normal and anomalous behaviors are considered to have patterns. While the normal behavior of the network traffic would not show the presence of any unknown, malicious file or a program that may infect other computer and its programs, whereas the anomalous behavior of the traffic would exhibit the presence of such malware. However, these systems may also find it difficult to detect unknown anomalies which remain unobserved within the day-to-day traffic. These systems may also fail to detect intrusions in a traffic which has been considered to be normal and intrusive activities have been overlooked or unexplored for that period.

In order to address the above issue, hybrid approach is used widely in recent times. According to this hybrid detection approach, the well-known attacks can be detected using misuse approach, whereas the novel attacks can be detected using

anomaly approach. The main advantage of such approach is the high detection rate of intrusions because the intrusion patterns that have not been noticed during the signature detection technique will be identified as novel attacks by the anomaly detection.

2 Related Works

Research works related to intrusion detection system using hybrid approach confirm the improvement in detection capabilities. In [4–6], misuse, as well as anomaly detection systems, has been used to utilize the merits of both the approaches. In [7], anomaly detection approach enlists the dubious activities and the misuse approach classifies them accordingly. Zhang et al. in [8] used random forest algorithm during misuse detection. The outlier detection produced from the misuse detection is then used for detecting unknown attacks. Similar to [8], Depren et al. in [9] used artificial neural network (ANN) techniques and decision tree algorithm for their hybrid model. The incremental results depicted that the system gave better performance in comparison with individual approaches. The paper by Xiang et al. [10] proposed tree classifiers for supervised learning and clustering techniques for unsupervised learning. In [11], hybrid approach was pronounced using Bayesian learning networks for supervised and ANN for unsupervised learning, respectively. Though their detection system was promising, it was mostly dependent on the type of training data being used. In [12], decision trees and support vector machine were used and had yielded a 100% accuracy using 1999KDD-CUP data set. Shon and Moon in [13] combined two existing SVM techniques to achieve low false alarm rate. In [14], the authors employed clustering techniques for classifying attacks. A hybrid IDS in [15] has two neural networks, one that acts as an anomaly-based detection for unknown attacks and the other acts as a misuse-based detection for known attacks. In [16], ANN is used to classify the exact type of the intrusion. The authors [17] have emphasized on SVM and combined with ant colony optimization techniques. In [18], the authors have concentrated on C4.5 and 1-class SVM techniques, respectively.

3 Theoretical Background

In order to build a hybrid intrusion detection system, both machine learning and statistical techniques can be utilized. An intrusion detection system considers each activity as a pattern and each such can be recognized through a statistical pattern recognition system. The statistical pattern recognition system first recognizes set of input patterns in order to extract and select them in training phase. The training phase has the feature extraction module that tries to look for the key features from

the input patterns. Then it classifies the patterns in classification phase by assigning the classified key patterns against the incoming test patterns [19].

3.1 Feature Construction and Feature Selection

Feature can be considered as an attribute that uniquely represents information from the raw input data set [19]. Features can be directly selected from the raw data set and have the ability to represent some patterns or behavior in the data set. Normally, the relationship between patterns and data is completely hidden. Feature extraction is the method of extracting and finding the most useful patterns from the data set.

Feature construction is first and foremost process of finding key features from the original data set. Though there are several algorithms for feature construction, the most commonly used approach is the manual approach of directly counting the number of occurrences of patterns. N-grams, association rule learning, and frequency episode extraction are used for constructing features automatically. In frequency episode extraction method, frequently occurring events are collected together to form episodes. The main intention of feature construction is to consider all possible informative features without increasing the dimensionality of data.

Feature selection is the next stage where the insignificant and repetitive features present, are removed. According to Isabelle Guyon et al. [20], the main objective of feature selection is to limit the storage requirement and increase the algorithmic speed. There are two ways of feature selection—manual and automatic. The automatic feature selection method includes filter methods, wrapper methods and embedded methods from machine learning.

Filter feature selection methods are commonly used to assign a scoring to each feature. Some examples of some filter methods include the chi-squared test, information gain, and correlation coefficient scores.

In this paper, frequency episode extraction is used during feature construction stage and chi-squared test is used during feature selection stage. Both these concepts would be discussed in the next section of proposed model in length.

4 Proposed Model

The primary objective of this proposed model is to design IDS which would constantly monitor the vulnerabilities of a system based on the files that arrive in the system through network. The proposed model utilizes machine learning and statistical techniques for building hybrid intrusion detection system. The model looks for virus definitions which consist of characters or string sequences obtained from viruses in files. A virus definition may be considered worth if it consists of sequences of text strings or bytecodes found commonly in the virus but infrequently in benign programs [21]. The proposed IDS would check specific areas in files or

system against the virus definitions that are stored in the database. Frequency episode extraction method is used to construct the patterns or signatures of the virus. According to this phenomenon, frequency episodes are collection of events occurring frequently together [19]. For example, the episode called ‘E’ is followed by ‘F’ several times in Fig. 1.

Episodes are partially ordered set of events [19]. The formal definition of frequent episodes as given in [19] is as follows: Let $I = \{i_1, i_2, \dots, i_n\}$ be a set of n features called items of a system audit data. Let $D = \{r_1, r_2, \dots, r_3\}$ be a set of records i this data set. Each record r_i contains a subset of features in I . A frequent episode is defined as an expression of the form:

$X, Y \Rightarrow (Z, w)$, where $X, Y, Z \dots I$ and w is the width of the considered time interval.

The proposed method has utilized the real-time data set for extracting episodes. The institutional server data for extracting the audit log reports have been used to prepare the episodes.

Chi-square test is widely used statistical method assessing the goodness of fit between a set of observed values and those expected theoretically. The chi-square test checks the null hypothesis. According to the null hypothesis, if there is no significant deviation between the expected and observed result then the virus code may be present. If there is no such significant deviation from the expected value, then the null hypothesis may be accepted or otherwise it would be rejected. Here, the tokens are taken as parameters for evaluating expected and observed values. These tokens are some repeated parts of virus codes that may be present in any of the files coming to the system. The occurrences of these virus code parts, i.e., tokens in specific frequencies, would identify the existence of a virus in that file. If there is a large deviation in observed value to that of the expected one, then the hypothesis of the existence of the virus code in the file is rejected. Otherwise, a small deviation would denote the hypothesis of the existence of the virus code in the file to be accepted.

The chi-square test is defined by the hypothesis:

H_0 The data has no significant deviation from the expected result

H_a The data has significant deviation from the expected result

Test Statistic:

For the chi-square goodness-of-fit computation, the test statistic is defined as

$$T = \sum ((O - E)/E^2)$$

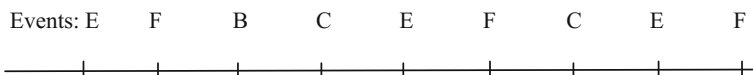


Fig. 1 A sequence of events

where

- O Observed value of virus token in file
- E Expected value of token in virus definition,
- T Observed chi-square value

4.1 Proposed Architecture of Hybrid Intrusion Detection System

The first and the foremost step is to compute the hash value for each file using some hash algorithm. SHA1 algorithm is used for finding the checksum integrity of a file as it is able to generate collision-free hash values. Once the file checksum integrity is checked, this hash value is compared to any of the file's hash value if being present in the already existing database table of files. If it matches to any of the old hash value, then it is assumed that the file already resides in the system. Otherwise, if it does not match with any of the old hash values, then the file is to be checked for malicious patterns with the help of frequency episode extraction method. The chi-square test is then used for feature selection after the features have been constructed from frequency episode extraction. The proposed architecture of IDS consists of two components (Fig. 2). The primary component consists of the

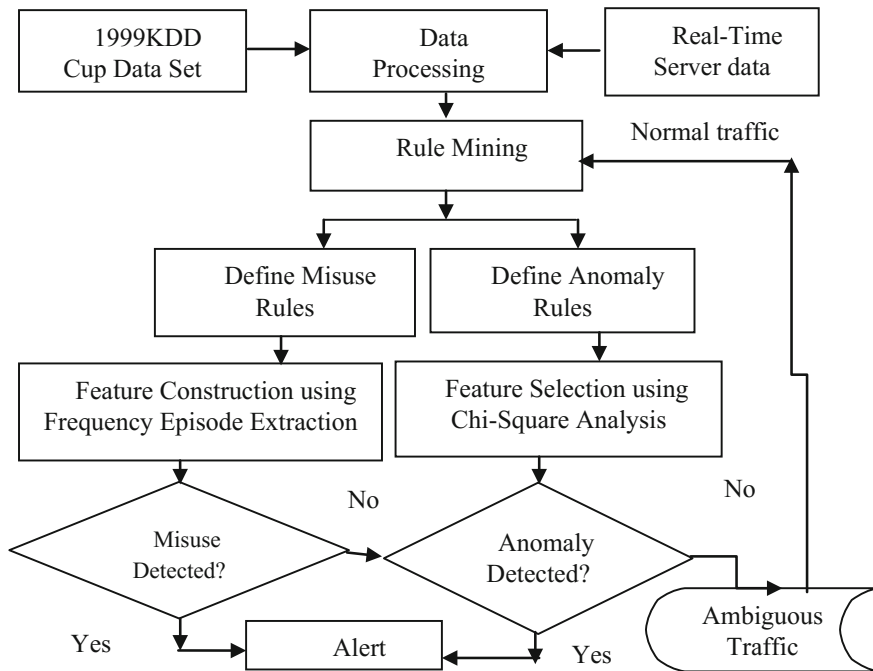


Fig. 2 Flow diagram of the proposed model

construction of the 15 features from the files that are extracted from the 1999KDDCup data set and real-time institutional server. Then, the next component uses rule mining technique by defining misuse and anomaly rules for further segregation of the features. The system learns and trains itself, thereby the performance of the proposed model gets enhanced each time and it detects a known or a novel attack.

4.2 Algorithm

```

Step 1: Accept User name and Password for a Login session
      While number of login attempts <=5
        Do
          Accept user name and password
          If (user name and password matches with the valid user name and
            password), then Start Session
          Else, Reject Session and increment number of login attempts
Step 2: Scan the System for new or unknown file
Step 3: Generate the Hash value using SHA1 and MD5 algorithms for the file.
Step 4: If (Hash value new) Go to Step 6
          Else if (Hash value of an already existing file), then
            Check value with that stored in table, file_hash1
Step 5: If (old Hash value = new value) then, File not changed
          Exit
          Else, Go to Step 6
Step 6: Extract the tokens of the file through Frequency Episode Extraction
Step 7: Using the Features perform Chi-Square test.
Step 8: Accept the values for O, E to compute T such that
          O = Observed value of virus token in file
          E = Expected value of token in virus definition.
          T = Observed Chi-square value,  $\sum ((O-E)/E^2)$ 
Step 9: Accept degrees of freedom (number of observations) as n
          Accept the level of significance, p as 0.05 (1-0.05 = 99.95% confidence
            level)
Step 10: If the  $\chi^2$  table (n, p) value > T (Observed Chi-square) value
          then Virus not present and Add to Database.
          Else Virus may be present.
          Send Alert Message for full System Scan.
Step 11: Send Alert Message for full System Scan
Step 12: Stop or End

```

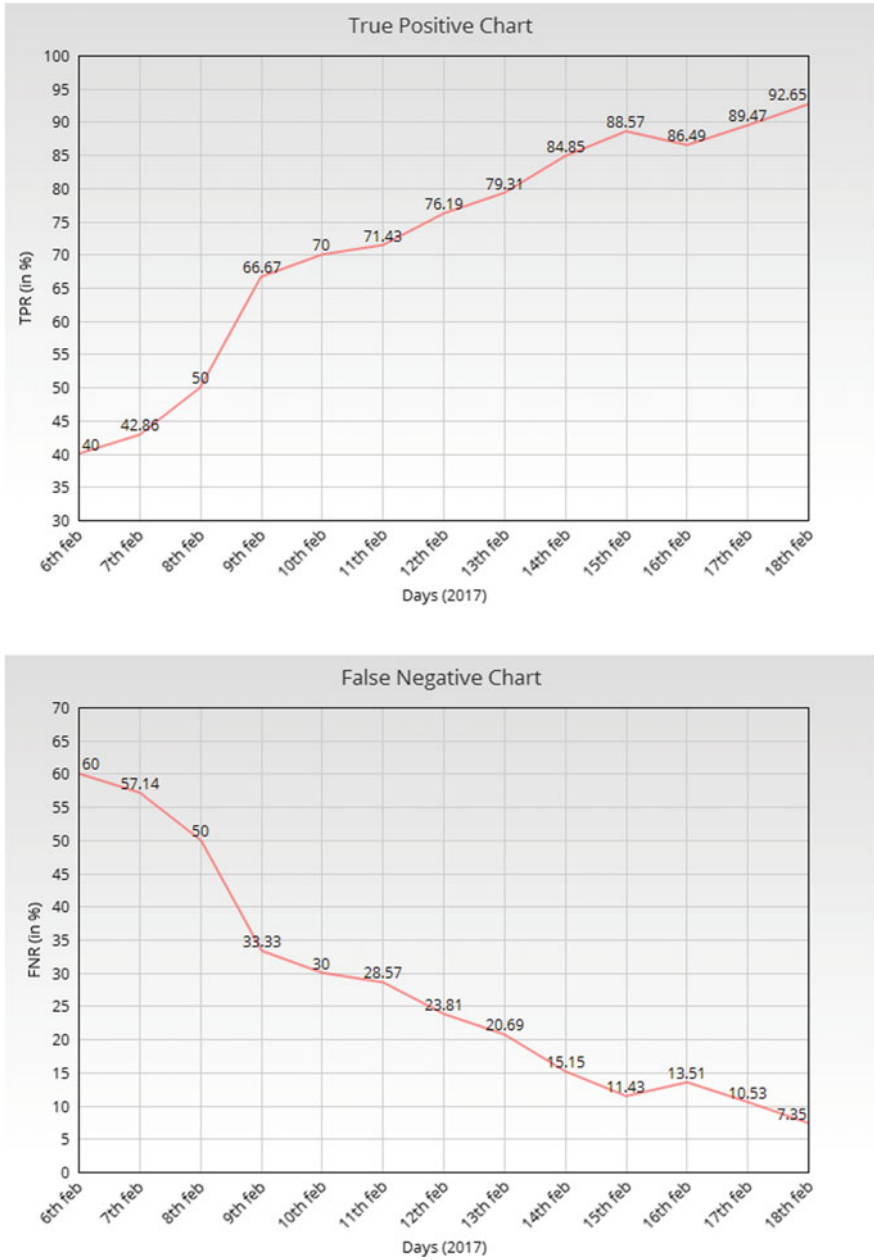


Fig. 3 Results of experiments depicting true positive and false negative charts

5 Conclusion

The proposed model is developed in C# and taken input as 32-bit operating system. Around two weeks, the experiment was conducted on all incoming files that were approximately more than 30,000 files. All files were a mixture of virus and clean files taken from Windows XP developer station. For training of the proposed model, 1999KDD Cup data set was considered. The results represent that the accuracy with respect to true positive rate has increased incrementally each day nearing to 92.65% on the last day of experimentation Fig. 3. Similarly, the proposed model shows a sharp fall in the false negative percentage to 7.35 as it learns and trains the system each day. Therefore, the proposed system learns and trains using machine learning techniques for detecting known attacks from misuse detection system and novel attacks from anomaly detection system, thereby improving the true positive rates and diminishing false negative rates consequently.

References

1. Masud M. M, Khan L., and Thuraisingham B.: A scalable multi-level feature extraction technique to detect malicious executables. Springer Science+Business Media, LLC 2007, Inf Syst Front 10:33–45, <https://doi.org/10.1007/s10796-007-9054-3>, (2008).
2. Denning D. E.: An intrusion-detection model. IEEE Journal on Software Engineering. Special Issue on Computer Issues and Privacy, vol. 13, Issue 2, pp. 222–232, (1987).
3. Mazzariello C., Romano S. P., and Sansone C.: Evaluating pattern recognition techniques in Intrusion Detection Systems. Conference: Pattern Recognition in Information Systems, Proceedings of the 5th International Workshop on Pattern Recognition in Information Systems, PRIS 2005, In conjunction with ICEIS 2005, Miami, FL, USA, pp. 144–153, (2005).
4. Lunt T. F., Tamaru A., Gilham F., Jagannathan R, Jalali C., Neumann P. G. Javitz H. S., Valdes A., and Garvey T. D.: A real time Intrusion Detection Expert System (IDES). Tech. report, SRI International, Menlo Park, CA, (1992).
5. Javitz H. S., Valdez A., Lunt T., and Tyson M.: Next generation Intrusion Detection Expert System (NIDES). Tech. Report SRI Technical Report A016, SRI International, (1993).
6. Porras A. Ph, and Neumann P. G.: Emerald: Event Monitoring Enabling Responses to Anomalous Live Disturbances. Proceedings of the National Information Systems Security Conference, pp. 353–365, (1997).
7. Tombini E, Debar H., Me L., Ducasse M., Telecom F., and Caen F.: A serial combination of anomaly and misuse IDSEs applied to HTTP traffic. Proceedings of the 20th Annual Computer Security Applications Conference (ACSAC'04), pp. 428–437, (2004).
8. Zhang J., and Zulkernine M.: A Hybrid Network Intrusion Detection Technique using Random Forests. The First International Conference on Availability, Reliability and Security (ARES'06), pp. 262–269, (2006).
9. Depren O., Topallar M, Anarim E., and Ciliz M.K.: An Intelligent Intrusion Detection System (IDS) for Anomaly and Misuse Detection in Computer Networks. Expert systems with Applications 29, no. 4, 713–722, (2005).
10. Xiang C. and Lim S.M.: Design of Multiple-level Hybrid Classifier for Intrusion Detection System. Proceedings of the 2005 IEEE Workshop on Machine Learning for Signal Processing, pp. 117–122, (2005).

11. Thames J.L, Abler R., and Saad A: Hybrid Intelligent Systems for Network Security. Proceedings of the 44th annual Southeast regional conference, ACM New York, NY, USA, pp. 286–289, (2006).
12. Peddabachigari S., Abraham A., Grosan C., and Thomas J.: Modeling Intrusion Detection System using Hybrid Intelligent Systems. *Journal of Network and Computer Applications*, no. 1, 114–132, (2007).
13. Shon T. and Moon J.: A Hybrid Machine Learning Approach to Network Anomaly Detection. *Information Sciences* 177, no. 18, 3799–3821.
14. Sabhnani M and Serpen G.: Application of Machine Learning Algorithms to KDD Intrusion Detection dataset within Misuse Detection Context. *International Conference on Machine Learning, Models, Technologies and Applications*, pp. 209–215, (2003).
15. Mylavarapu G., Thomas J., and Kumar TK A.: Real-Time Hybrid Intrusion Detection System Using Apache Storm, High Performance Computing and Communications (HPCC). 2015 IEEE 7th International Symposium on Cyberspace Safety and Security (CSS), 2015 IEEE 12th International Conference on Embedded Software and Systems (ICSS), (2015).
16. Demertzis K., Iliadis L., A Hybrid Network Anomaly and Intrusion Detection Approach Based on Evolving Spiking Neural Network Classification. *Springer International Publishing Switzerland 2014: International Conference on E-Democracy, CCIS 441*, pp. 11–23, 2014. https://doi.org/10.1007/978-3-319-11710-2_2, (2014).
17. Feng W., Zhang Q., Gongzhu H., and Huang J. X.: Mining Network Data for Intrusion Detection through combining SVMs with Ant Colony Networks. *Future Generation Computer Systems*, ELSEVIER, (2014).
18. Gisung K.: A Novel Hybrid Intrusion Detection Method Integrating Anomaly Detection with Misuse Detection. *Expert Systems with Applications*, ELSEVIER, (2013).
19. Thanh Nguyen H., Franke K., and Petrovic S.: Feature Extraction Methods for Intrusion Detection Systems. *Threats, Countermeasures, and Advances in Applied Information Security*, pp. 23–52, (2012).
20. Guyon I., and Elisseeff A.: An Introduction to Variable and Feature Selection. *Journal of Machine Learning Research* 3, pp. 1157–1182, (2003).
21. Wong W.: Analysis and Detection of Metamorphic, Computer Viruses. May, Thesis, Master of Science, San Jose State University, San Jose, CA, (2006).

IoT-Based Monitoring and Smart Planning of Urban Solid Waste Management

Krishangi Deka, Krishangi Goswami and Sagarika

Abstract The tremendous growth in the rate of urbanization in the past few decades has in turn increased the need for a stable and sustainable urban development plan. Solid waste collection is a very complex process that involves efficient management of the entire system, starting from the collection to the dumping of wastes, hygienically. This paper describes the real-time monitoring and management of waste collection system, thus, enabling us to be excused from collecting semi-empty bins. Furthermore, the incoming data can be effective to determine the minimum number of vehicles associated or bins to distribute. This paper hence gains insights into the status of waste in a city and therefore contributes to a cost-efficient, eco-friendly and more systematic way of waste collection.

Keywords Solid waste management · Internet of Things (IoT) · Smart bin · Urbanization · Sensors

1 Introduction

With the increase in population and urbanization, the state of cleanliness with respect to the management of waste is degrading enormously. The overflow of garbage in and around the bins and loitering of garbage create a very unruly and unhygienic condition in the surroundings nearby. It may invoke several serious diseases and ailments among the people nearby. It also most importantly deteriorates the judgment of the area. To avoid this and to enhance the cleaning, ‘smart waste management system’ is proposed in this paper. This will help to manage the garbage collection efficiently [1]. An efficient waste management system is a prerequisite for maintaining a safe and green environment. There are many technologies that are used for waste collection as well as for well-managed recycling

K. Deka (✉) · K. Goswami · Sagarika
Department of Electronics and Communication (ECE), Sikkim Manipal
Institute of Technology, Majitar, Rangpo, Sikkim 737136, India
e-mail: krishangi.d21@gmail.com

[2]. Moreover, the solid waste management involves many steps: generation, on-site handling, storage, selective sorting [3], collection, transfer, processing, and disposal. All of these subprocesses have to be implemented within existing legal and social regulations without harming the environment and public health. The complexity of the context of it and procedures involved are indeed a primary concern of local municipal authorities due to problems related to the collection, transportation, and processing of residential solid waste today. The garbage collection is manual which takes a lot of efforts and is time consuming. The type of waste collection may be either door-to-door or indirect collection. In both cases, the goal is to plan a system that would make smart the collection, in relation to the existing systems [2]. Hence to achieve this goal, we design a system to optimize this operation by reducing unnecessary cost and providing a higher-quality smart service to the citizens. This paper gives a comprehensive description of the application of sensors in urban environment to eradicate the existing problem.

This paper is focused on developing a smart system [4] which includes on-site handling, storage, and transfer process using cost-efficient and quality system. Considering all the factors, in the proposed system, the level of waste in the dustbins, i.e., the volume, is detected with the help of ultrasonic sensor. Pressure sensor is used to measure the weight of the dustbin. Red and green LEDs are used to indicate filled and empty level of dustbin, respectively. When the measured value of sensors exceeds a certain threshold value, this information with GPS location where the dustbin is located will be sent to local server through GSM system. Android device will fetch the information from server, about the area where dustbin is located, by comparing coordinates, update the location, and inform the respective vehicle to collect the waste. Microcontroller is used for interfacing the sensor system with GSM system. This will help to manage the garbage collection efficiently. Also, the concept behind this paper revolves around the Internet of Things (IoT), which is one of the fastest growing technologies that is being recognized and developed. IoT was initially developed as an application of mobile, home, and embedded systems. But now, it is a platform where any device that can send or receive data can be connected to the Internet. Once these devices are connected, they can store and share data on the cloud which can be used for data analytics and create meaningful solutions. Internet of Things has revolutionized the concept of smart cities making them more comfortable and able to give intelligent responses to different kinds of events or needs, by interactive sensing streets or active buildings which has been able to gather environment data about the city and measure the level of noise, traffic, crowds, temperature—literally everything [2].

As we aim at contributing toward a smart city, we have to keep in mind that the concept of a smart city varies from city to city, county to country. When it comes to India, for a person living in the city, the picture of a smart city contains a wish list of infrastructure and services that describes his or her level of aspiration. [5]. The research on smart cities has been a long ongoing survey which has already been conducted, and many applications have already been implemented. Some examples include: smart parking system which gives the position of a car park at any time [6]; smart agriculture system to improve agricultural and industrial production based on

weather conditions and environmental conditions [7]; smart transport system to find the best route considering the current traffic conditions [8]; and a lot more. These applications can be called a step toward realization of a complete smart city.

2 Block Diagram

Microcontroller (R5F100LEA): It is a Renesas RL78 series microcontroller of 16 bits with two modes of operation: high speed at 32 MHz and low speed at 32.768 kHz. Its ROM is 64 kBs and RAM of 4 kBs. It also has an additional data flash memory of 8 kBs. It has 32 general purpose registers of 8 bits. It has an on-chip interrupt function key, BCD adjustment key, and reset key (Fig. 1).

Ultrasonic sensor: Ultrasonic sensors of module HC-SR04 is used for the purpose of detecting the distance from an object (not being in direct contact with the object) with a very high accuracy. The sensor has a basically four pins, namely VCC, trigger (input), echo (output), and ground. Also, this module has a ranging distance of 2–400 cm.

Force-Sensitive Resistor: SENS-09375-ROHS is the force-sensitive resistor used in the prototype, with a 0.5" diameter sensing area. It is a sensor used to measure the physical pressure and weight. They are easy to use and are of low cost. The FSR is made of two layers. The more will be the pressure value when the pressure applied to the sensor surface is more. However, the harder the force on the sensor, the lower will be the resistance. When no force is being applied on the sensor surface, its resistance will be greater than 1 MΩ. It can sense the applied pressure in and around the range of 100 g to 10 kg.

Light-Emitting Diode (LED): An LED is a p-n junction semiconductor diode, which works when forward biased. It works on the principle of

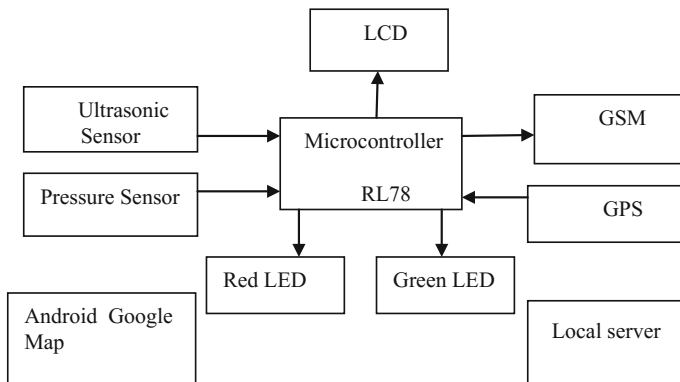


Fig. 1 Block diagram of the smart waste management system prototype

electroluminescence, where electrons and holes recombine to emit light in the form of energy of photons which is equal to or slightly less than the bandgap. LEDs can emit light of color red, yellow, orange, green, and blue. LEDs are usually small ($<1 \text{ mm}^2$).

Liquid Crystal Display (LCD): The liquid crystal display used in building this prototype is a 2X16(JHD-162A) flat panel display, which is a very basic module used in various devices and circuits. LCD utilizes the property of light modulation of crystals of liquid. In the type of LCD used in this paper, it can display 16 characters on each of the 2 lines.

Global System for Mobile Communications (GSM): GSM describes the protocols for second-generation (2G) digital mobile networks. It is a 2G network developed for the replacement of the first-generation (1G) analog cellular networks. The 2G network is a digital and circuit switch network for full duplex mode.

Global Positioning System (GPS): GPS is a universally used satellite navigation system that provides with the latitude and longitude, i.e., the geolocation of a place, and also provides with the time information to a receiver anywhere on the earth surface wherever there is an unobstructed and uninterrupted line of sight to the GPS satellites.

Android Google Maps: Developed by Google, Google Maps is a service that provides with the satellite imagery of a geographical region with personalized street maps, 360° view of streets, real-time traffic conditions and also gives the distance and source-to-destination planning of the route by foot, car, bicycle, bus, or any other means of transport.

Local Server: A server which is hosted locally on our own computer unlike a remote server, which is hosted elsewhere. Local server is preferred more for the purpose of testing such as testing out layouts, shopping cards, directory, memberships. Here, we have developed our local server (Apache Tomcat server 7.0) on Windows 10 platform.

3 Hardware Architecture

3.1 Components

See Table 1 and Fig. 2.

3.2 Circuit Diagram

In the circuit diagram of the proposed system of smart solid waste management, the microcontroller is interfaced with the ultrasonic sensor, the pressure sensor, the LED, LCD panel, GSM, and the GPS system. Alphanumeric LCD (ALCD) is used

Table 1 Hardware components and their specifications

Components	Specifications
Microcontroller	R5F-100LE (Renesas RL78)
Ultrasonic sensor	HCSR-04
Force-sensitive resistor/pressure sensor	SEN-09375 ROHS
GSM module	MGSM-900
LCD	16X2 (JHD-162A)
LED	Green and red
GPS	QUESTAR G702-001UB

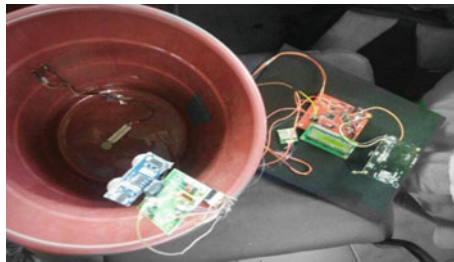


Fig. 2 Hardware components interfaced and mounted on a board. A green and a red LEDs, ultrasonic sensor, and force-resistive sensor have been mounted on the dustbin surface. The ultrasonic sensor measures the volume, whereas the force-resistive sensor measures the weight in the dustbin

to backlight the LED cathode display information about project. The LCD used is 16×2, 2 rows and 16 columns. So in each row, we can display 16 characters. The 1-byte data line of LCD is connected to the port 7.0 and port 7.7 of the microcontroller. The enable pin of LCD is connected to the port 0.5 of the microcontroller. The RS pin of the LCD is connected to port 0.6 of the microcontroller. Pin 1 of LCD is grounded, pin 2 is +5 V power supply, pin 3 is GND, pin 4 is for contrast adjustment, and pin 5 is usually for read or write operations. Since in this system of waste management, we are only doing write operation to the LCD, so pin 5 is GND. Pin 15 is the backlight LED anode terminal connected to +5 V, and pin 16 is grounded. For the GSM, its transmitter port is connected with the receiver port of microcontroller and receiver port of GSM is connected to the transmitter port of microcontroller. However, the receiver port of microcontroller is not being used. The ultrasonic sensor output port and pressure sensor output port are connected to port 5.0 and port 2.0 of the microcontroller, respectively. Also, the green and red LED output ports are connected to ports 5.2 and 5.3 of the microcontroller, respectively. Also, the GPS transmitter port is connected to that of the receiver port of the microcontroller. Since the GPS only transmits the location coordinates of the smart bin, its receiver ports are not made into any connection (Fig. 3).

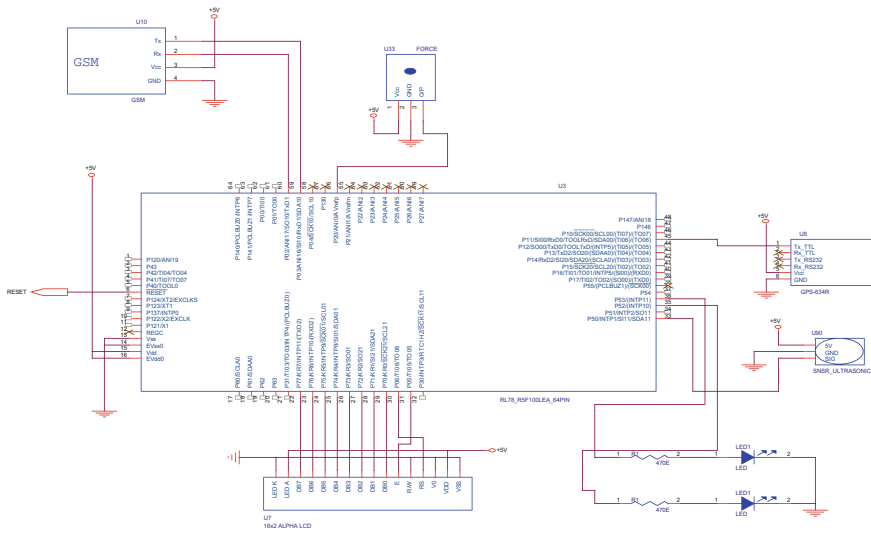


Fig. 3 Circuit diagram for the proposed system of smart waste management system

4 Software and Analysis

4.1 Real-Time Interface

The circuit for the smart waste management system, as mentioned in the previous section, has a smart bin equipped with sensors: an ultrasonic sensor, a pressure sensor, and a green and a red light-emitting diodes which measure the various parameters like volume and weight in the dustbin. The ultrasonic sensor measures the volume in the dustbin, and the pressure sensor measures the weight in the dustbin. Also, the system is interfaced with a GPS for determining the geographical coordinates of the smart bin. With the continuous use of the dustbin, it gets filled with time gradually. Every time the garbage level crosses the threshold and overflows after certain period of time, the sensors receive the details of the volume and weight of the dustbin, which is displayed through the LCD panel interfaced with the Renesas microcontroller. The interfacing of the microcontroller has been done using IDE Renesas CubeSuite+. The data is further saved on a MySQL database on local server and also sent as an instant message using the GSM module to the device with the phone number entered in the hyper terminal of GSM test kit. Every data received at real time is used and displayed by the android application interface for better viewing of the volume and weight of the filled bin, developed by using the IDE Eclipse. Also, the coordinates given by the GPS can be traced in and opened using Google Maps. This allows for an efficient location analyzing system which would allow to easily identify the details of every smart bin and hence would make the garbage collection system much easier. This will hence help the waste

management department to schedule and optimize the route for the collection of solid waste every time the garbage vehicle moves around the city for garbage collection. This helps in saving time, money, and resources of the municipality, and work is performed in a more efficient manner. This smart bin model can be applied to any of the smart cities around the world (Fig. 4).

4.2 Data Analysis

The smart bin system developed in this paper is designed to send the level of garbage in dustbins across an urban city. The data sent is used to gain a lot of insights like the volume, weight, and the location of the dustbin. The android app, developed by the IDE 'Eclipse,' has a login screen for the various users to log in through the window. In case of a new user, he can register through the registration page which can be accessed through the login page. After the user is logged in, he/she can access the main screen window where the details of the dustbin will be updated. Also, the user will be able to access the location through Google Maps using the button 'Map,' available below the main screen.

Moreover, the data sent by the smart bin system will also be saved in MySQL-Front database created in a local server (Apache Tomcat Server 7.0) developed in Windows 10. There will be two databases: one for the received data (receiveddata) and the other for the user information (userinfo). This data will be accessible to the concerned authorities of the garbage collection board, where they can find the updated status of the dustbin followed by the location coordinates provided and saved in the server. This updated status will then help them identify the filled dustbins and clear them out at the earliest, without causing inconvenience to the public and also reducing the number of vehicles associated with the collection of garbage (Fig. 5).

5 Advantages

The circuit is designed with the motive of making every dustbin handy at all times by using low-cost sensors attached in it. It, in a way, emphasizes on waste reduction and reutilization by providing a smart technique to the residents of an urban locality. The smart bin system can be a lot advantageous and beneficial to an urban locality as it will stop overflowing of bins along the roadsides and localities as smart bins can be managed at a real time. Filling and cleaning time of dustbin would be reduced, thus making fast availability of clean and empty dustbins to people. It would also find the shortest route by locations provided by Google Maps. Hence, it would reduce the workforce and number of garbage collecting vehicles across the

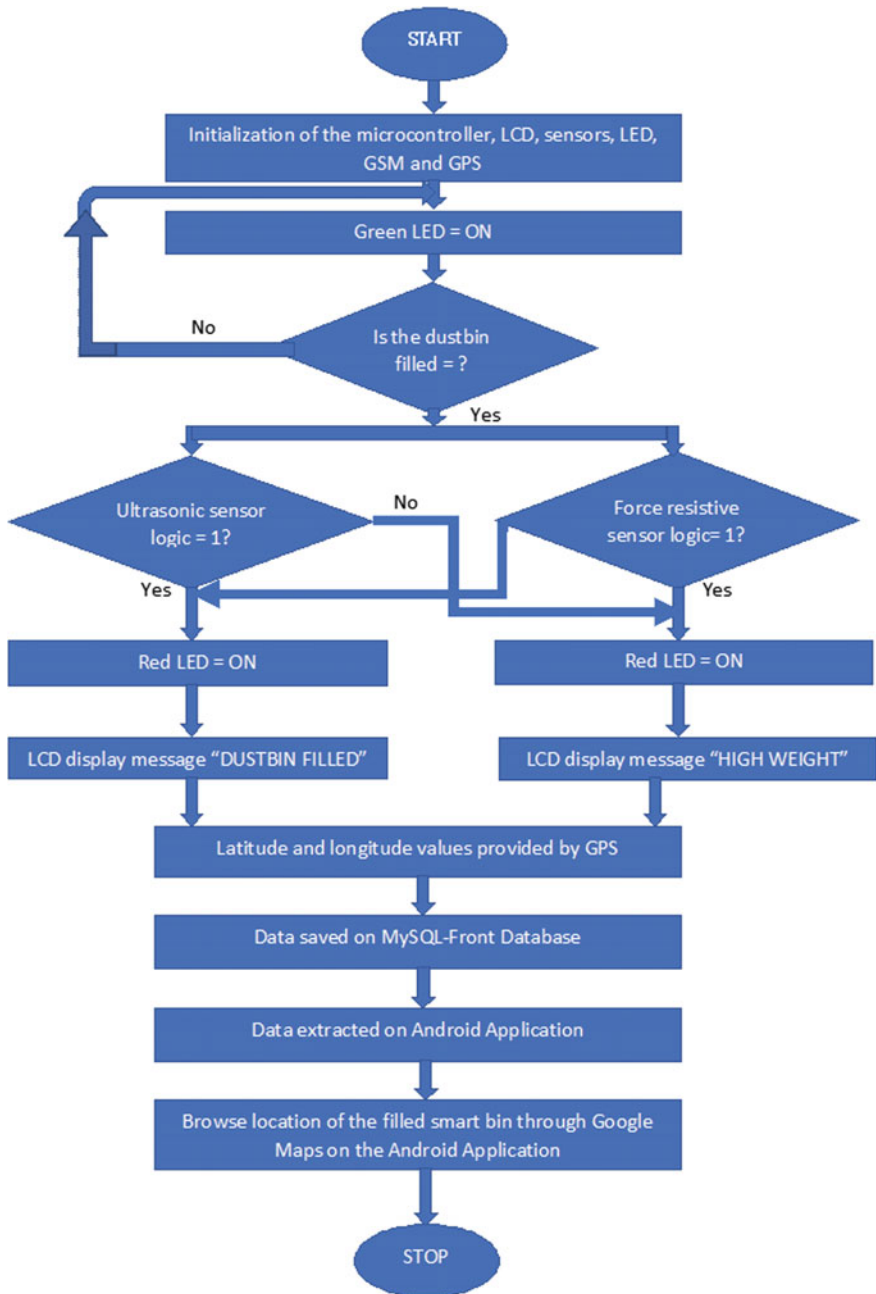


Fig. 4 Flowchart showing the overall design of the prototype of the smart solid waste management

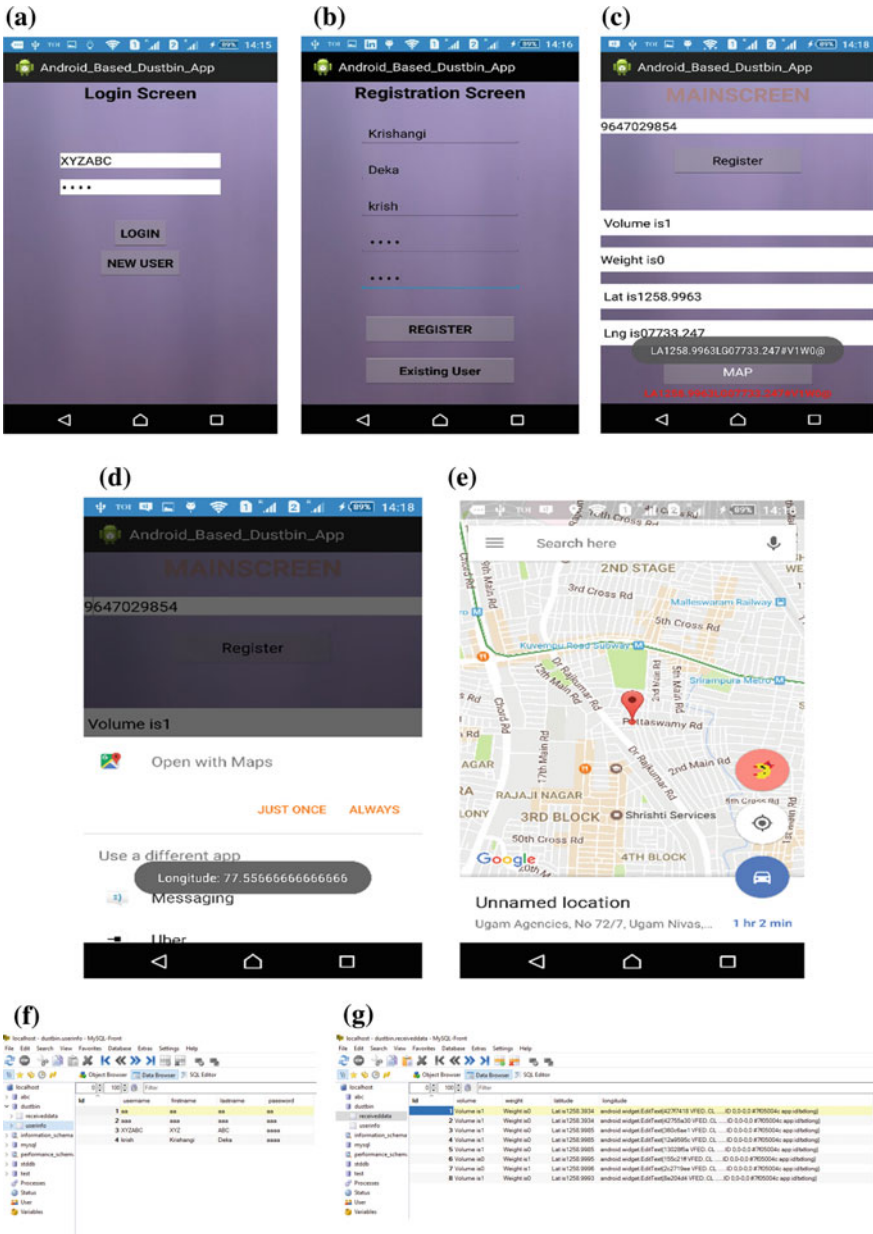


Fig. 5 Various screens of the android app and the MySQL database: **a** login screen, **b** registration screen, **c** main screen showing volume, weight, latitude, longitude, **d** the 'Map' option, **e** the coordinates shown in Google Maps, **f** user information database, and **g** received data database

region which can also be said to reduce the fuel consumption. This approach of smart bin aims to create a clean and green environment as it would reduce foul smell in urban areas, decrease fuel consumption, as already mentioned, and in turn reduce pollution in the air.

6 Conclusions

In this paper, we have basically examined the waste management system in an urban city and proposed an approach based on an Internet-of-Things platform using the RL78 series of microcontroller (R5F100LE), interfaced with other hardware components. This heterogeneous approach to contribute toward a smart city is made to achieve a higher level of flexibility. The smart system basically focuses on two aspects: Firstly, it is addressed to the government and private sectors to carry out and implement measures to utilize the resources for an efficient system of waste collection. Secondly, it is addressed to the public, so that they too can understand the environment and follow up with steps like reusing, recycling, and reducing wastes around them.

There can be numerous future works and improvements for this study. This paper basically is designed for a prototype of the actual waste management system. This has a scope of being developed on a much larger platform: implementing the IoT concept on the cloud and using Google Maps API for better visualization and a realistic approach. Also, this paper emphasizes on the cost and time factor by reducing the number of garbage vehicles associated with garbage collection and at the same time providing the best route for it. Therefore, future works and studies can be made in this regard that will offer the best results in every aspect.

References

1. Sharma Narayan, Singha Nirman, Dutta Tanmoy: Smart Bin Implementation for Smart Cities, *International Journal of Scientific & Engineering Research*, Volume 6, Issue 9, September-2015. ISSN 2229-5518.
2. Watson Brian J., Sharma Ratnesh K., Charles Susan K., Shah Amip J., Patel Chandrakant D., Marwah Manish, Hoover Christopher E., Christian Thomas W., and Bash Cullen E.: *Creating a Sustainable IT Ecosystem: Enabling Next-Generation Urban Infrastructures, Sustainable Systems and Technology*, 2009. ISSST '09. IEEE International Symposium on 18–20 May 2009, ISBN: 978-1-4244-4324-6.
3. Glouche Yann, Couderc Paul. A Smart Waste Management with Self Describing objects. Leister, Wolfgang and Jeung, Hoyoung and Koskelainen, Petri. *The Second International Conference on Smart Systems, Devices and Technologies (SMART'13)*, Jun 2013, Rome, Italy (Conference proceedings).
4. Qiu T., Xiao H., and Zhou P., "Framework and case studies of intelligence monitoring platform in facility agriculture ecosystem," in *AgroGeoinformatics (Agro-Geoinformatics)*, 2013 Second International Conference on, Aug 2013, pp. 522–525.

5. Bélissent Jennifer: Getting Clever About Smart Cities: New Opportunities Require New Business Models, For Vendor Strategy Professionals, November 2, 2010, Forrester Research, Inc., 400 Technology Square Cambridge, MA 02139 USA.
6. Srikanth. S. V, Pramod. P, Dileep K., Tapas S., Patil M., and Sarat C.: “Design and implementation of a prototype smart parking (spark) system using wireless sensor networks,” in Advanced Information Networking and Applications Workshops, 2009. WAINA '09. International Conference on, May 2009, pp. 401–406.
7. Wang. W. Q., Zhang X., Zhang J., and Lim H.: Smart traffic cloud: An infrastructure for traffic applications, in Parallel and Distributed Systems (ICPADS), 2012 IEEE 18th International Conference on, Dec 2012, pp. 822–827.
8. Huang. G. H and Chang. N.: Perspectives of Environmental Informatics and Systems Analysis, Journal of Environmental Informatics 1 (1) 1–6 (2003), 03JEI00001 1726-2135/1684-8799 © 2003 ISEIS.

Network Traffic Analysis and Packet Sniffing Using UDP

Md Ruhul Islam, Tawal K. Koirala and Ferdousi Khatun

Abstract The size of computer network is rapidly growing, and the new generation Internet needs more improvement to keep data transfer faster in the network. As the Internet users are increasing, the network traffic also parallelly increasing, so high attention is required to keep faster data transfer. For this reason, network monitoring secures the data and the management of network traffic is very essential task in the field of computer network. User data information is transferred through user datagram protocol (UDP) or transmission control protocol (TCP) via various nodes that present in the network. UDP is datagram-oriented protocol, i.e., it carries the datagram or packet from source node to destination node. To monitor the packet or datagram, packet sniffing is widely used; that is, a method of capturing the datagram to analyze the network log traffic occurs in a network during communication between various nodes that exist in the network. This paper provides a well-developed method to monitor and analyze the network traffic using UDP that removes the existing deficiency of traditional existing tool used for analyzing network traffic.

Keywords Packet sniffing · UDP · Packet capture · Wireshark · Network

Md. R. Islam (✉) · T. K. Koirala · F. Khatun
Department of Computer Science and Engineering, Sikkim Manipal Institute
of Technology (SMIT), Majhitar, Rangpo 737136, Sikkim, India
e-mail: ruhulislam786@gmail.com

T. K. Koirala
e-mail: koirala01@gmail.com

F. Khatun
e-mail: ferdousi9@yahoo.com

1 Introduction

Due to the advanced technology, the Internet user is growing rapidly. The main two transport layer protocols are TCP and UDP. UDP is connectionless datagram-oriented protocol that carries the datagram over the network between nodes [1]. As the Internet user increasing drastically, the size of network also increasing and the traffic is spreading over the network. Thus, analyzing network traffic is important concern in the field of computer network. For this, the packet sniffing is widely used to analyze the network traffic related and some other issues arise over the network [2]. Depending upon the analyzer, the network can be analyzed at a certain time interval. This paper analyses the network traffic in morning, afternoon, and evening sessions using Wireshark for UDP transport layer protocol. The UDP analysis is based on UDP data flow and UDP checksum.

2 Packet Sniffer and Wireshark

The network administrator used a device to monitor the data transmitted over the network is known as packet sniffer [3]. The packet sniffer is not only used for monitoring the network but also used for network management to detect log traffic, network security purposes, etc. Wireshark is tool used to analyze network packet. The libpcap library is used by Wireshark to capture packets at low-level work [4]. This Wireshark is captured the network packet transmitted over the network and tried to display that packet data in detail.

3 Analysis of Problem

One of the most serious and common network problems over the network is broadcast storms. A misconfigured network device or a defective node can flood in the network to create a network traffic. This storm amplifies itself until it completely shuts down the network. Another threat in computer network is malware-infected computer that can send a junk of e-mail or may attempt to replicate the computer on the LAN. An infected computer may slow down Internet traffic. And sometimes a single user can use so much bandwidth that it affects other users on the network [2]. So to find the cause of the problem, the network traffic has been analyzed using Wireshark and also compared the traffic and find out what is the reason for these problems in a network.

4 Proposed Solution Strategy

Figure 1 shows us how the data is being captured and filtered. First while installing this software, the data NIC will be automatically initialized. Every packet when received by NIC then the MAC address of the received packet is first compared to its own. If the MAC address is found same, the received packet is accepted; otherwise, it filters the packet [5]. The set filter in Fig. 1 denotes the types of filter for different protocols that are through from the NIC. Then after the protocols are captured and the captured packets will be processed which means only the selected packet will be shown. The UDP analysis is based on

- UDP data flow
- UDP checksum Graph.

5 Design Strategy for the Solution

Figure 2 shows the existing network topology of SMIT for academic block (A, B, C, D, E). The model that is being followed in this network is hierarchical network model.

6 Packet Counter Statistics

This shows statistics over IP, that is, all the HTTP packets. Table 1 provides us with the number of packets to each Web site. This will help us to identify how many requests and responses we have had. The rate in Table 1 denotes the rate on which the request and response are being processed in milli seconds. And the percent denotes the percentage of rate of data flow.

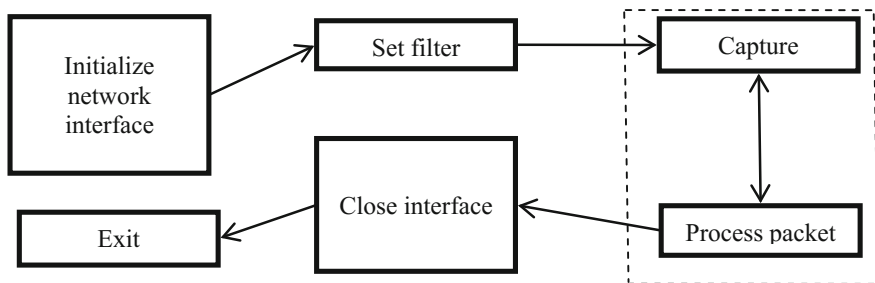


Fig. 1 How the data will be filtered and captured [2]

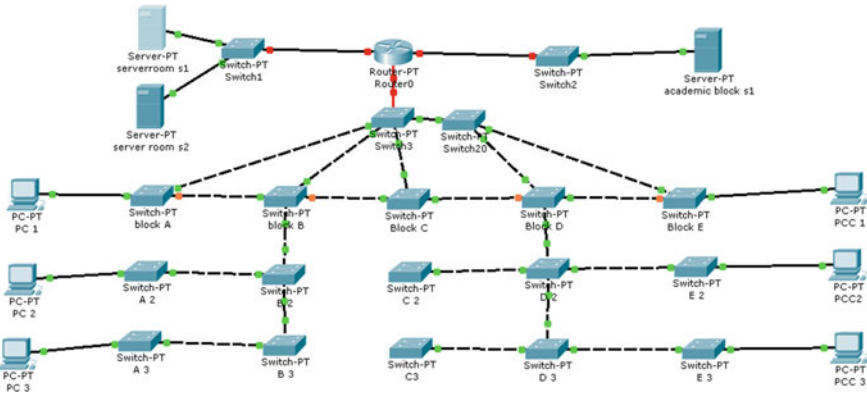


Fig. 2 Existing network topology of SMIT for academic blocks (A, B, C, D, E) [2]

Table 1 Number of packets to each Web site

HTTP/Packet Counter:	Count	Rate (ms)	Percent (%)
Total HTTP packets	5171	0.0016	100
HTTP request packets	4874	0.0015	94.26
NOTIFY	2466	0.008	50.59
GET	205	0.001	4.21
POST	6	0	0.12
HTTP response packets	297	0.001	5.74
1xx: informational	0	0	0.00
2xx: success	259	0.001	87.21
200 OK	259	0.001	100
3xx: redirection	1	0	0.34
302 found	1	0	100
4xx: client error	37	0	12.46
400 bad request	37	0	100
5xx: server error	0	0	0.00
???: broken	0	0	0
Other HTTP packets	0	0	0.00

Table 1 shows the filtered http request and responses in the captured data. Methods like NOTIFY, POST, GET are HTTP requests. HTTP response packet consists of the responses to those requests. Table 1 shows the responses are success, error, or broken, etc.

7 HTTP Request Statistics

Figure 3 shows the request distribution of Web sites and what kind of request that has been sent from which system and the number of times the request is being sent.

Figure 3 shows the number of url requests and the description of the url from the host IP.

8 Implementation and Result

Wireshark software is used to capture and analyze the packet over SMIT network. The packet sniffer makes the NIC card on the machine, and after that it enters in a promiscuous mode. As an Ethernet NIC is made with a “filter,” it always ignores the irrelevant traffic. If the destination MAC address differs with its own, then it refuses those frames or packet. The sniffer turns off this filter via NIC card driver, and NIC card goes to promiscuous mode. Generally, the NIC is used in workstations and the computer may be put into promiscuous mode. It is possible to change

Topic / Item	Count
HTTP Requests by HTTP Host	4874
239.255.255.250:1900	2891
[FF02::C]:1900	1772
172.16.0.55:52869	67
/picsdesc.xml	67
172.16.1.75:59231	16
ocsp.verisign.com	12
/	6
/MFewTzBNMEswSTAJBgUrDgMCgGUABBTsqZM65M8TA9rdzkbCnNwuMAd5VgQUz5mp6nsm9Evjjo%2FX8AUm7%2BP5p50CECYt7Y3oDVUUYNifYHelCLE%3D	3
/MFewTzBNMEswSTAJBgUrDgMCgGUABBS56bKHAoUD%2BOy%2B0LhPg9byQm4gQUf9Nlp8Ld7LwMAnzQzn6Aq2mTMCEFIAsolVwahuZWydRLM8c%3D	3
ctld.windowsupdate.com	12
172.16.2.11:2869	11
/upnphost/udhisapi.dll?content=uuid:dd4f6b42-e4ff-4552-8f90-a6e119cc209a	11
172.16.1.168:2869	11
172.16.0.55:52881	11
172.16.0.102:8200	11
www.msftncsi.com	6
172.16.3.2:2869	6
/upnphost/udhisapi.dll?content=uuid:476a9c18-f51e-49ec-8979-add27c964809	6
172.16.2.35:2869	5
/upnphost/udhisapi.dll?content=uuid:145ba3ea-3164-4d38-8c2f-2031b79712be	5
172.16.2.191:63989	4
/	4
csc3-2010-crl.verisign.com	3
crl.verisign.com	3
172.16.2.32:57325	3
/	3
172.16.0.53:36656	3
update.utorrent.li	2
update.utorrent.com	2

Fig. 3 Distribution of Web sites

the MAC address on NIC card. The equipment needs to observe all traffic and thus be promiscuous.

8.1 UDP-Based Analysis

A simple connectionless transmission protocol is user datagram protocol (UDP) with less protocol mechanism. It does not have the three-way handshaking mechanism used by TCP, thus it is unreliable. The UDP does not guarantee of duplicate protection or delivery ordering of packets. The UDP could potentially increase the stability and fairness in the Internet as it lacks congestion control over the network [6]. Data integrity is provided by UDP checksum, and port numbers are used to address different functions at sending and receiving nodes. The Ethernet and packet sniffer are used to monitor the network. The network adapter goes to promiscuous mode, and the communicated data over the network is received and recorded by the sniffer program [7].

Figure 4 shows the UDP data flow. The black line shows the overall broadcast, and the red one shows the UDP data flow. All non-TCP packet flows follow the same pattern as UDP packet flows. The rate of data flow for UDP is more which means in this the applications that use UDP is being used more.

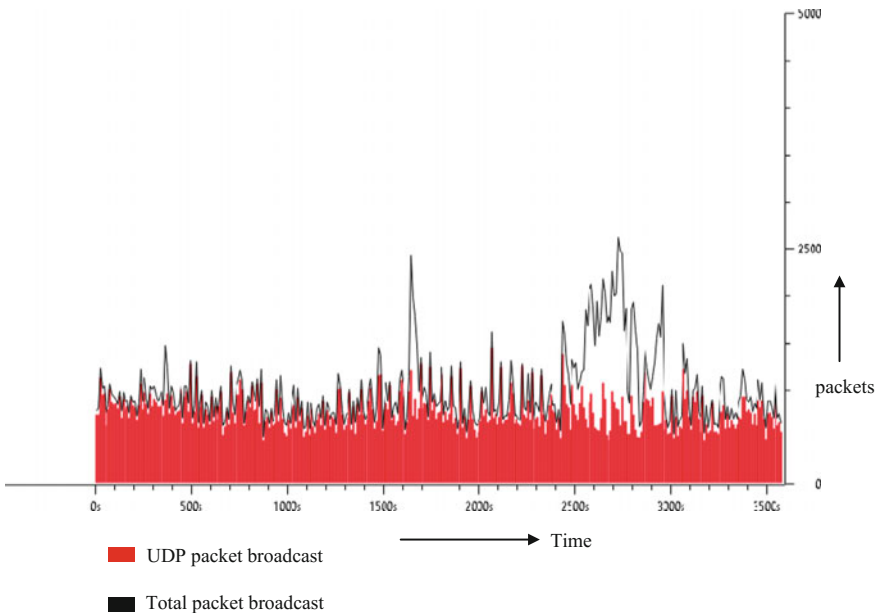


Fig. 4 UDP data flow (color online)

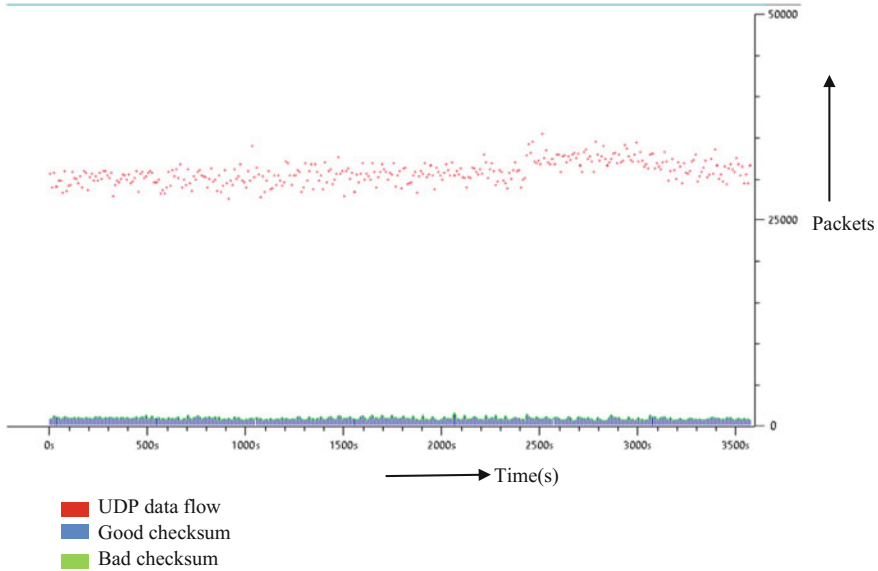


Fig. 5 UDP checksum

8.2 Filtering UDP Checksum

Checksum is the 16 bit 1’s complement of the 1’s complement sum of a pseudo-header of information from the IP header, the UDP header, and the data, padded with 0 octet at the end to make a multiple of two octets. If the checksum calculation results in the value zero, then it should be sent as the 1’s complement. The graph below shows the good and the bad checksum. Good checksum = 0 and bad checksum = 1.

Figure 5 shows how many good checksum and bad checksum are present in the UDP data flow. There is equal amount of bad checksum in one-second interval of time which means that the packets that is being captured are faulty in other words the packet that is captured is the packets that are not completely finalized before sending them out.

9 Conclusion

Packet analysis and network traffic monitoring are one of the most important concerns in the field of computer network. The monitoring is done based on UDP, connectionless datagram-oriented protocol. The UDP data flow and UDP checksum are analyzed. Packet sniffer is not just a hacker’s tool. It can be used for network traffic monitoring, traffic analysis, troubleshooting, and other useful purposes.

Packet sniffers can capture things like passwords and usernames or other sensitive information. Wireshark captured traffic from SMIT network. Packet sniffing is very useful tool to analyze network traffic over UDP protocol.

References

1. Pallavi Asrodia#1, Mr. Vishal Sharma*2, "Network Monitoring and Analysis by Packet Sniffing Method", International Journal of Engineering Trends and Technology (IJETT) – Volume 4 Issue 5- May 2013.
2. Aishwarya Bhandari, Samala Gautam, Tawal k Koirala, Md Ruhul Islam, "Packet Sniffing and Network traffic analysis using TCP –A New Approach", 2nd International Conference ON Emerging Trends and Advances in Electrical Engineering and Renewable Energy, Accepted on Oct 2016.
3. Yash Ketkar, Wasim Khan, "A Protocol Based Packet Sniffer", Yash Ketkar et al, International Journal of Computer Science and Mobile Computing, Vol. 4 Issue. 3, March- 2015, pg. 406–410.
4. A. Dabir, A. Matrawy, "Bottleneck Analysis of Traffic Monitoring Using Wireshark", 4th International Conference on Innovations in Information Technology, 2007, IEEE Innovations '07, 18–20 Nov. 2007, Page(s):158–162.
5. Qadeer M.A., Zahid M., Iqbal A., Siddiqui M.R "Network Traffic Analysis and Intrusion Detection Using Packet Sniffer" ICCSN '10 Second International Conference, 2010, Page(s): 313–317.
6. Min Zhang; Maurizio Dusi; Wolfgang John; Changjia Chen, "Analysis of UDP Traffic Usage on Internet Backbone Links", Applications and the Internet, 2009. SAINT '09. Ninth Annual International Symposium, 978-0-7695-3700-9/09, 2009 IEEE.
7. Bo Yu "Based on the network sniffer implement network monitoring", Computer Application and System Modeling (ICCASM), 2010 International Conference on Volume: 7, 2010, Page(s): V7-1–V7-3.

Strahler Order Classification and Analysis of Drainage Network by Satellite Image Processing

Ferdousi Khatun and Pratikshya Sharma

Abstract Drainage hydrographical network is one of the most salient features used for hydrological analysis, geomorphology, Earth science, terrain analysis and still is a research topic in the field of GIS. A drainage network generally extracted from toposheet processing, raster image processing, and the new advanced satellite image processing. The classification of the drainage network plays a very important role for geographers, geologists, hydrologists, biologist, and other scientists as it reveals the idea of the size and strength of specific stream within drainage networks. Recent freely available satellite images provide the digital elevation data over the earth surface is very important for faster extraction of drainage network.

Keywords DEM · Strahler order · Drainage network

1 Introduction

Water is the most important element that covers two-thirds of earth surface and drainage network is key feature for hydrologist, geomorphologist for various analyses [1]. A drainage or river network is pattern formed by river, lake, waterbodies, and streams in a river basin or watershed. This pattern is extracted from topographic sheet processing which is the traditional process, takes tedious time [2]. Nowadays, new generation advanced satellite provides accurate DEM data over the earth surface with various spatial resolution that are very useful and fastest way to extract the river network [3]. The streams can be extracted from raster image processing, toposheet processing, and satellite image processing. A stream network is classified for many purposes, and it may be based on water quality, stream order, etc.

F. Khatun (✉) · P. Sharma
Department of Computer Science and Engineering, Sikkim Manipal Institute
of Technology (SMIT), Majhitar, Rangpo 737136, Sikkim, India
e-mail: ferdousi9@yahoo.com

P. Sharma
e-mail: pratikshya2007@yahoo.co.in

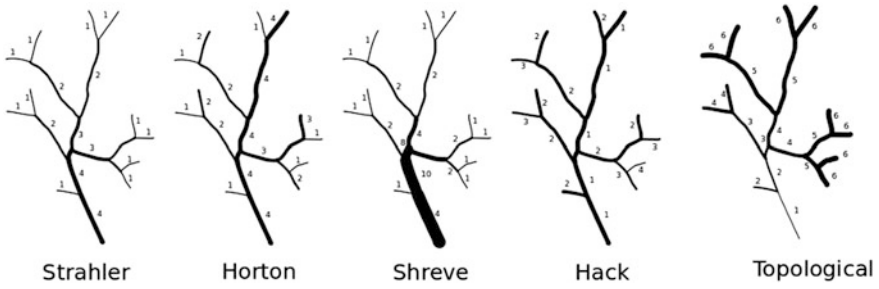


Fig. 1 Various stream ordering example [4]

Classification of stream network based on their order is very important to geologist, hydrologist, geographer, and many other scientists as it reveals the idea of the size of network and the strength of specific waterways within river network. A stream can be classified as Strahler order, Horton order, Shreve order, Hack order, Topological order (Fig. 1).

2 Working Procedure of Strahler Stream Order Classification

One of the most important river classifications is Strahler order where the ordering is based on the hierarchy of tributary instead the determination of the main channel. The ordering follows the below rule

1. Strahler order 1 implies the stream has no tributaries or no children.
2. If a node in the network has one and only one child or one tributary with Strahler greatest order i and the children or tributary have their order less than i , then it orders stick around i .
3. The Strahler order is $i + 1$ if the node has two or more children or tributaries with greatest order i .

Strahler's stream ordering starts in initial links that takes order one. From there, it proceeds downstream. While traversing, it checks every node with at least two equal tributaries with maximum order. If such conditions fail it continue with the greatest order, in this case if such node found, it increments the order by 1 and continue to downstream.

3 Methodology Used

See Fig. 2.

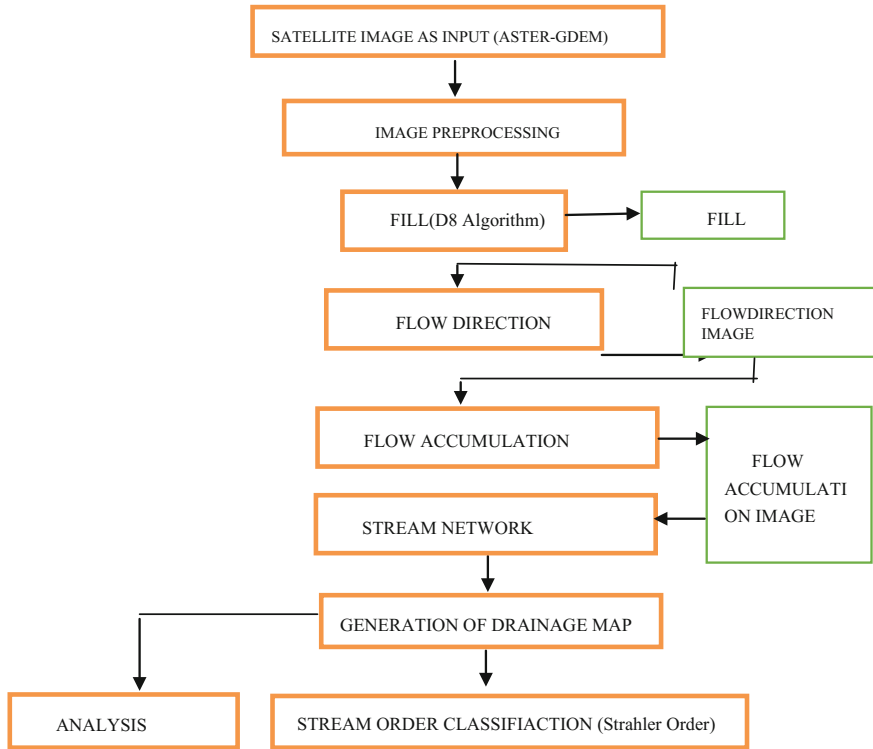


Fig. 2 Methodology used to extract drainage and classify stream

4 Study Area and Application of Used Methodology

The study area falls between 23°00'00.00"N SE lat to 24°00'00.00"N and 87°00'00.00"E long to 88°00'00.00"E long. The satellite image is downloaded from USGS site. This image is captured on September 23, 2014 and updated on January 2, 2015. The resolution of the image is 1-ARC second, i.e., 30 m. The study area covers the southwest part or West Bengal state where part of Damodar river flows (Fig. 3).

USGS ASTER GDEM is used. The main objective of this research is to extract the drainage pattern from DEM in MATLAB and classify it in MATLAB using Strahler order algorithm. To read the image in MATLAB, the ASTER DEM is converted into ASCII form. The ASCII image is read as grid form in MATLAB. As the satellite image contains artificial sink, it is better to remove the sink for accurate drainage network. The D8 algorithm is used to fill the image and make a depression-less DEM. Then flow direction is calculated and flow accumulation is generated from flow direction matrix. The stream network is generated from flow accumulation matrix by setting the threshold value 20,000. The extracted stream network is classified by Strahler order algorithm. The classified network is verified with the digitize map of that area (Figs. 4 and 5).

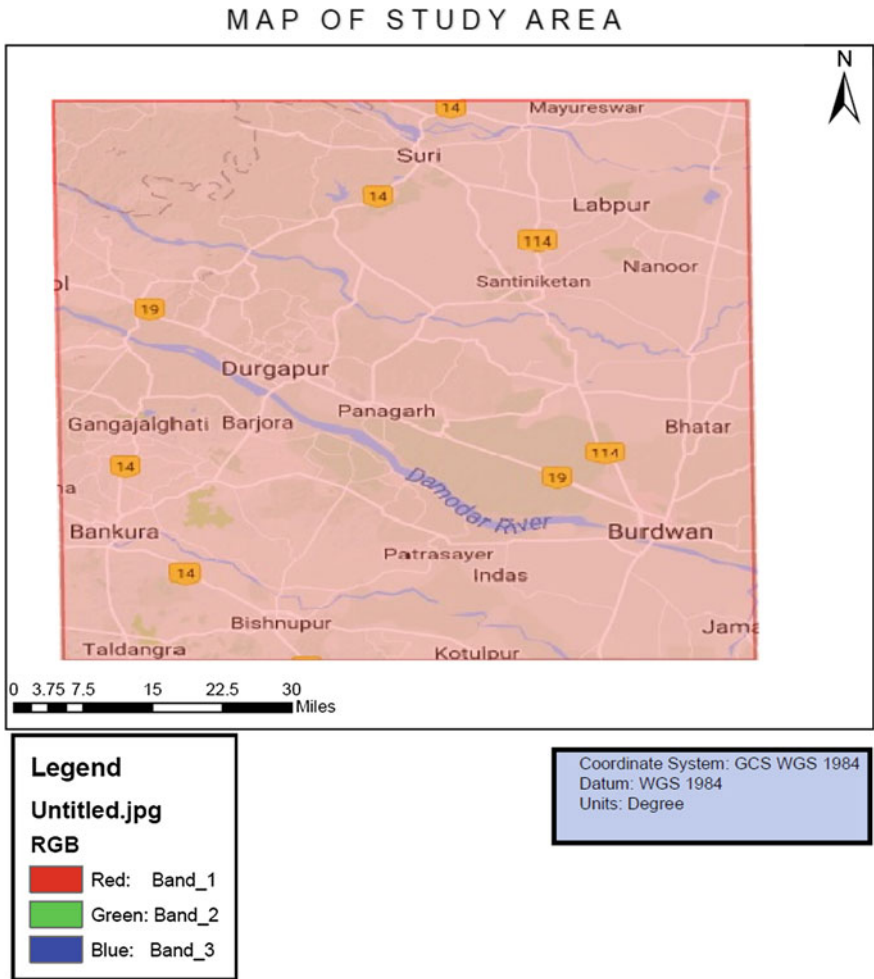


Fig. 3 Map of study area

5 Analysis

The classified stream order map of study area represents the extracted stream is of first to fourth order. From the above map, it is found that the maximum flow is in third- and fourth-order stream which is very useful for the agriculture, factory, and many other water resource planning departments. Only two parameters are extracted stream no and order of stream (Fig. 6).

The main application of above graph is in watershed analysis, morphological analysis, and water resource management department.

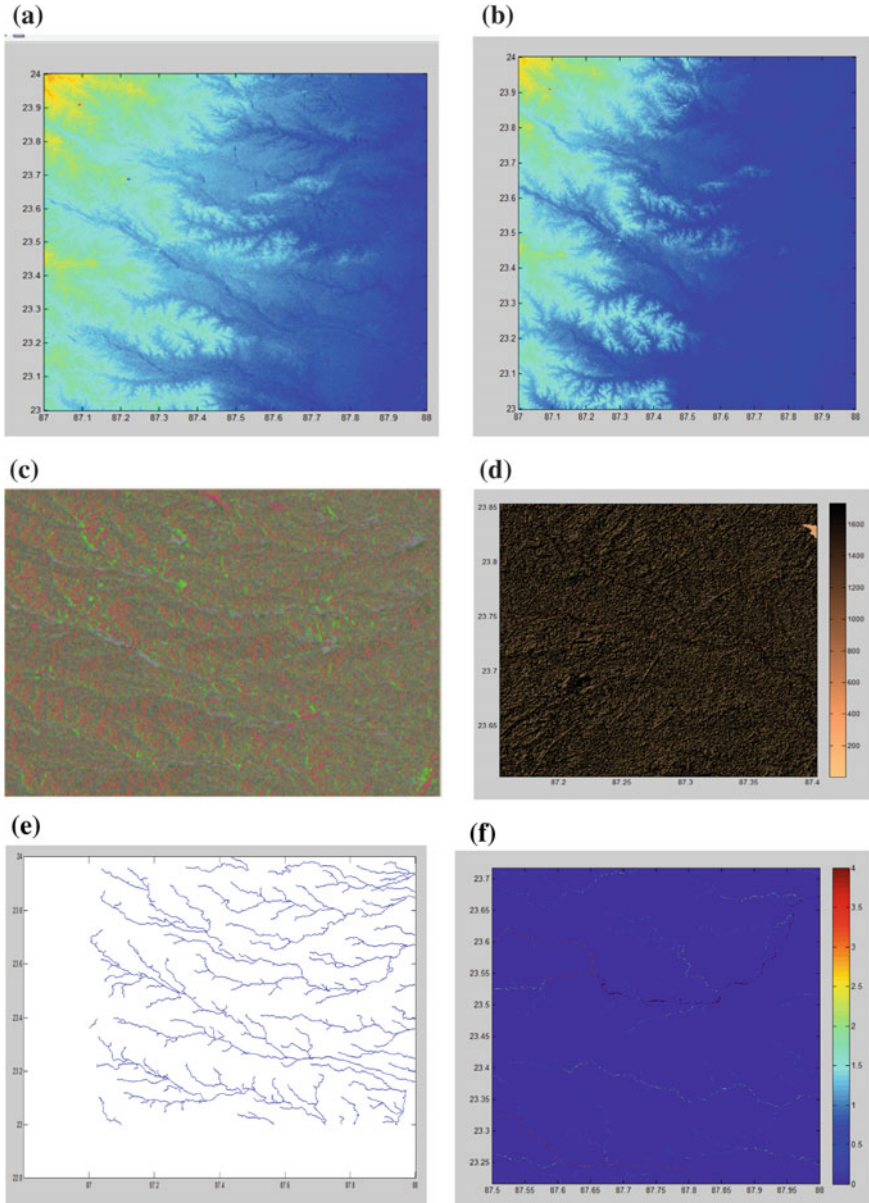


Fig. 4 Drainage extraction and classification, **a** ASTER GDEM of study area, **b** fill image, **c** flow direction image, **d** flow accumulation image, **e** stream network image, **f** classified stream network

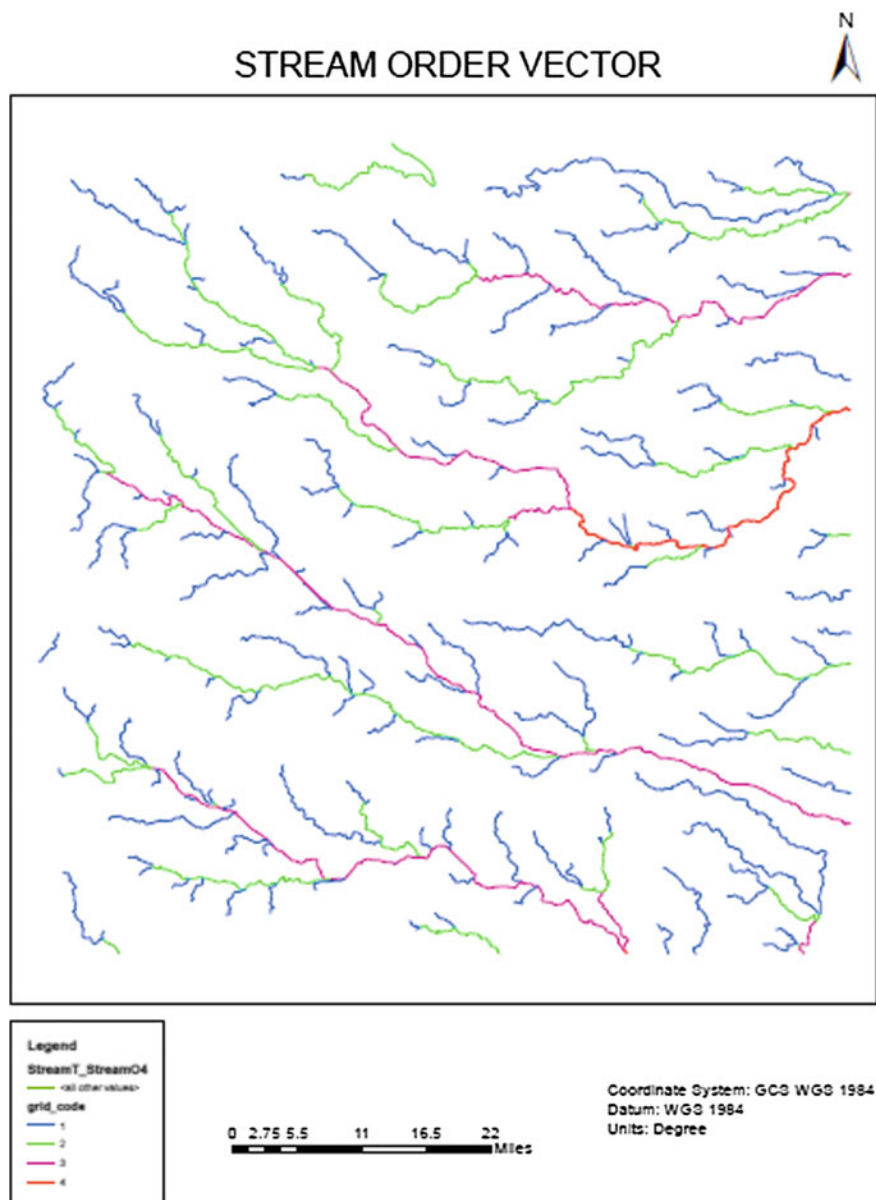


Fig. 5 Stream order vector map of study area

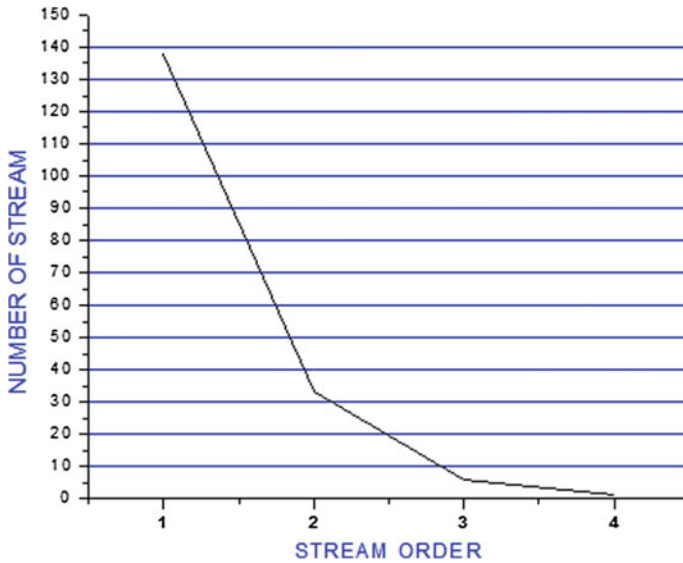


Fig. 6 Stream order versus number of stream graph of study area

6 Conclusion

The extraction of drainage networks can be done from contour map, raster map or DEMs. The satellite provided DEMs is very efficient to extract the drainage network in all terrain because the satellite gives the up-to-date changes happen on earth surface like change position of river network, new waterbody feature is capture via highly sensitive sensor present in satellite. Thus, less time required to extract the pattern from satellite provided DEM. Stream network classification is one of the main concern in the field of hydrology and geomorphological analysis. Strahler order classification is mostly used and has several application areas like water resource management department, irrigation department, geologist, biologist, and many other scientists. The classified map can be used by the earth science, geographer for further analysis as it reveals many information like size of stream, maximum and minimum flow in a stream, stream length.

References

1. Samih B. Al Rawashdeh, "Assessment of extraction drainage pattern from topographic maps based on photogrammetry", *Arabian Journal of Geosciences*, December 2013, Volume 6, Issue 12, pp 4873–4880.
2. Mohan P. Pradhan, M. K. Ghose, Yash R. Kharka, "Automatic Association of Strahler's Order and Attributes with the Drainage System", *International Journal of Advanced Computer Science and Applications*, Vol. 3, No. 8, 2012.

3. Sibila A. Genchi & Alejandro J. Vitale & Gerardo M. E. Perillo & María Cintia Piccolo “Geomorphometric assessment of drainage systems in a semi-arid region of Argentina using geospatial tools and multivariate statistics”, *Earth Science Informatics*, September 2016, Volume 9, Issue 3, pp 309–324.
4. Jarek Jasiewicz, <https://svn.osgeo.org/grass/grass-addons/grass7/raster/r.stream.order/r.stream.order.html>.

Digital Pen to Convert Handwritten Trajectory to Image for Digit Recognition

Debjoyti Ghosh, Sanchi Goyal and Rohit Kumar

Abstract In this paper, we present a digital pen for handwritten digits recognition based on acceleration in three-dimensional spaces. The digital pen consists of a triaxial accelerometer, an 8-bit microcontroller, and a RF transmission module. MATLAB GUI is used for signal preprocessing, noise rejection, and acceleration equivalent voltage to image conversion. Accelerometer generates signals due to the hand movement and transmits the data wirelessly to PC to detect the trajectory. Then, the trajectory is converted to image.

Keywords Triaxial · Graphical user interface · Accelerometer
Preprocessing · Neural network

1 Introduction

We have designed a pen which is based on human–computer interaction (HCI) techniques [1–3]. This pen is highly useful for blind people and it does not require any surface to write and can be operated without any external reference. It could sense the trajectory of hand gesture from variation in acceleration [4]. It is difficult to track the trajectory of hand gesture as different people have different speed and style [5, 6]. In order to overcome this problem, we have defined the writing style in Fig. 11 and we converted the trajectory into images. Our device is designed to convert digits from 0 to 9.

D. Ghosh (✉) · S. Goyal · R. Kumar
Department of Electronics and Communication Engineering,
Sikkim Manipal Institute of Technology, Majitar, Rangpo, Sikkim, India
e-mail: debjoyti.ghosh@gmail.com

S. Goyal
e-mail: sanchi_goyal@yahoo.in

R. Kumar
e-mail: rohitkumar1190@gmail.com

2 Hardware Design

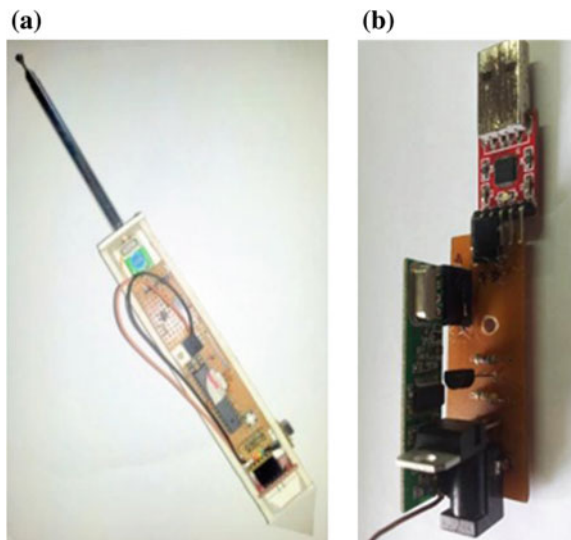
The designed pen has a triaxial accelerometer (MMA7260QT, Free-scale Semiconductor) [7], a microcontroller (AT mega 8 with a 10-bit A/D converter) [8], and a wireless ASK transmitter of 433 MHz. The user's hand movement generates acceleration signals which are detected by the triaxial accelerometer. The microcontroller converts the generated analog acceleration signals to digital value via A/D converter. The wireless transmitter transmits signals to a personal computer (PC) for further processing. The pen-type circuit board is of dimension $15\text{ cm} \times 2.5\text{ cm} \times 1.5\text{ cm}$ as shown in Fig. 1a. For better accuracy, we have used 1.5 g accelerometer.

The schematic diagram of digital pen's hardware is shown in Fig. 2. The accelerometer's sensitivity is set from -1.5 g to $+1.5\text{ g}$ and zero bias point is 1.65 V. The output of any axis is an analog voltage proportional to the acceleration in that axis.

The analog data from the three axes are given to the ADC of AT mega 8 (PC0-PC2). AVR ADC is a 10-bit ADC, i.e., it will give us a number between 0 and 1023 for voltage between 0 and 5 V, when we set the reference voltage at 5 V.

After ADC conversion, the data are serially sent to laptop for further processing. All the data sensed by the accelerometer are transmitted wirelessly to a PC by an RF transmitter at 433 MHz transmission band with 4800 bps transmission. The data obtained from the receiver are taken into the PC via a serial to USB convertor. The receiver at the computer end is shown in Fig. 1b. The complete circuit of transmitter and receiver is shown in Figs. 3 and 4, respectively.

Fig. 1 **a** Digital pen,
b Receiver



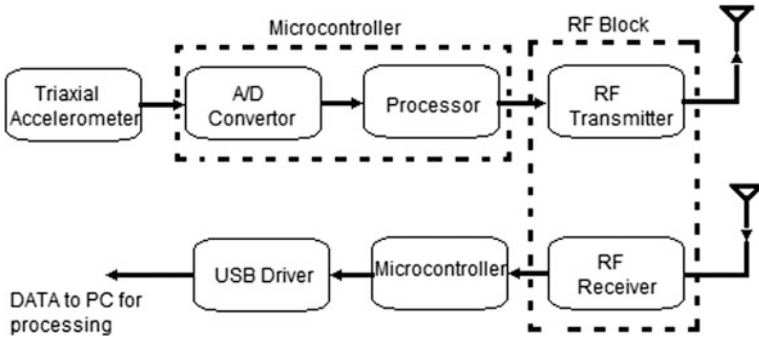


Fig. 2 Block diagram of the hardware of digital pen

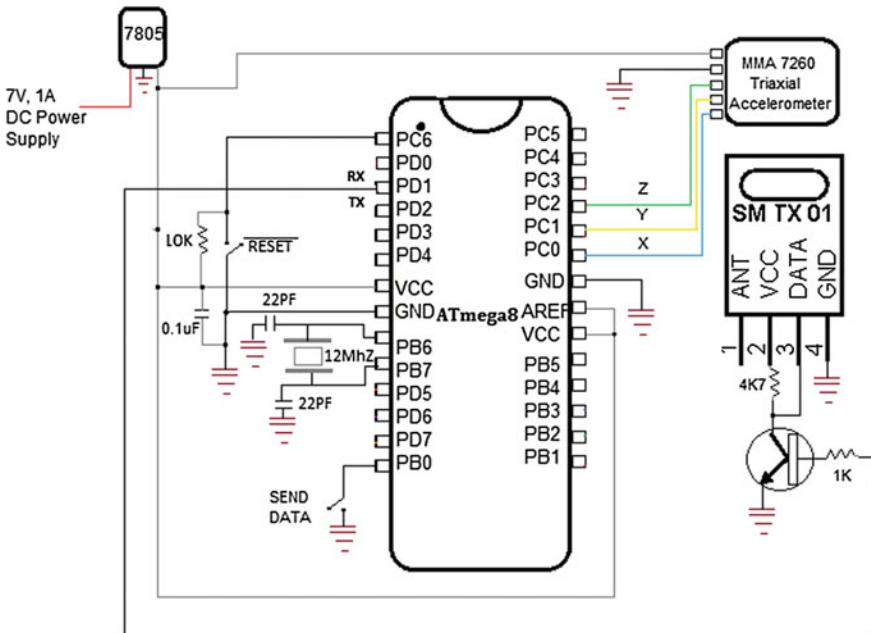


Fig. 3 Circuit diagram of digital pen

3 Trajectory Recognition Process

Acceleration acquisition, signal preprocessing, and image conversion are the main building blocks of our proposed trajectory recognition process. This paper includes recognition of hand gestures of digits from 0 to 9. The triaxial accelerometer detects the acceleration of the hand movement and then the generated signals are filtered by moving average filter for smoothness. The signals are further processed by

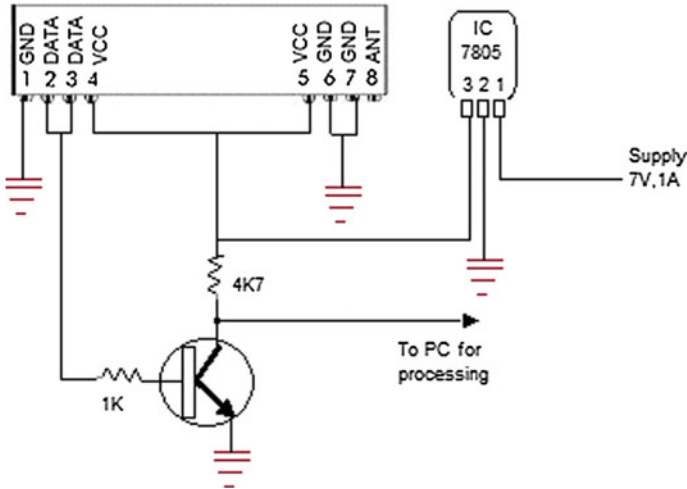


Fig. 4 Circuit diagram of receiver at computer end

polynomial curve-fitting technique. The plot is then saved as image. The saved image is cropped and resized to 7×5 dimensions.

3.1 Signal Preprocessing

The accelerometer generates hand movement acceleration signals which are being fed to the microcontroller. The data are then transmitted wirelessly to the personal computer (PC). Human hand slightly trembles while moving, which causes certain amount of noise as shown in Fig. 5. We can see that the trajectory of zero is not smooth but contains unwanted hand vibrations. The moving average filter and the polynomial curve fitting are the signal processing unit to remove noise. The moving average filter reduces the high-frequency noise of the raw data. The filter is expressed as

$$y[t] = \frac{1}{N} \sum_{i=1}^{N-1} x[t+i] \tag{1}$$

where $x[t]$ is the input signal, $y[t]$ is the output signal, and N is the number of points in the average filter. Figure 6 shows output response of filter with different orders $N = 4, 8, \text{ and } 10$. In this paper, we set $N = 8$. On increasing the order of filter, the high-frequency components are removed more precisely but there were more loss of data as compared to lower order ($N = 4$). So we optimized the order $N = 8$.

Curve fitting is then applied to the output of moving average filter. Here, we have used polynomial curve fitting of order 3. It further removes the unwanted

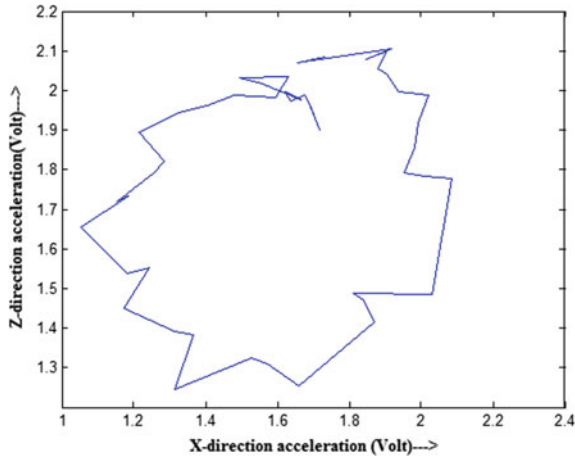


Fig. 5 x versus z plot for digit '0'

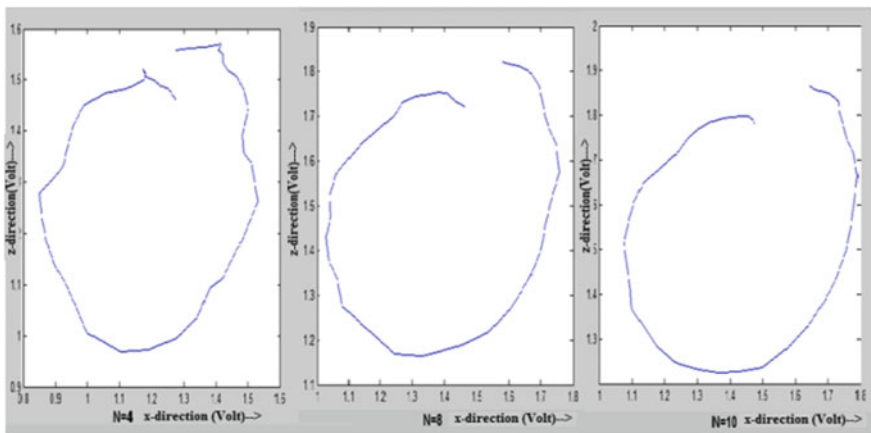


Fig. 6 x versus z plot for digit '0' using moving average filter for a $N = 4$, b $N = 8$, and c $N = 10$

glitches of the data obtained from the moving average filter and makes it suitable for the image conversion. We have seen that certain digits like 1, 4, and 7 requires polynomial curve fitting of lower order, i.e., order 1 or 2, and for certain digits like 0, 3, 8, and 9, we require higher order. So, we decided to set the order at 3 for a balanced output as shown in Fig. 7. The 'best' curve gives the minimum error between the data and the fit $f(x)$. The error is the sum of perpendicular distances of the data points. We get least squares error in Eq. (2).

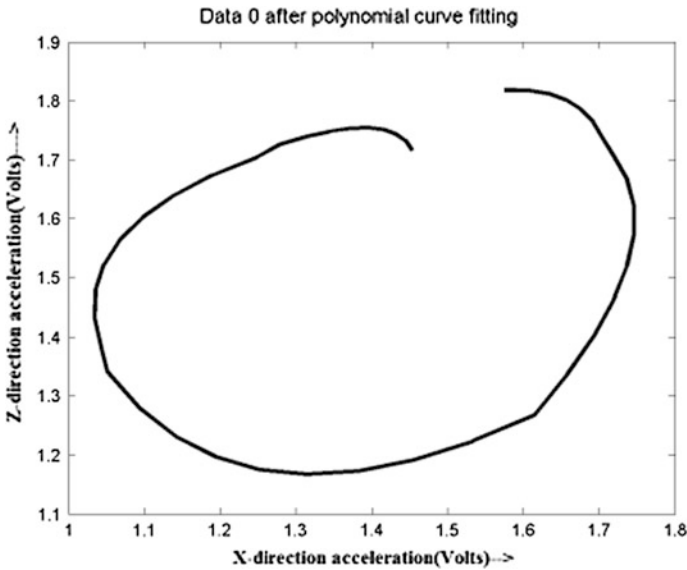


Fig. 7 x versus z plot of curve-fitted data ($N = 3$) for digit ‘0’

$$\text{err} = \sum_{i=1}^n \left(y_i - \left(a_0 + \sum_{k=1}^j a_k x^k \right) \right) \tag{2}$$

where ‘ n ’ is the number of data points given, ‘ i ’ is the index for current data point being summed, and the polynomial order is denoted by ‘ j ’. To minimize Eq. (2), the derivative with respect to each coefficient is set to zero.

$$\frac{\partial \text{err}}{\partial a_0} = -2 \sum_{i=1}^n \left(y_i - \left(a_0 + \sum_{k=1}^j a_k x^k \right) \right) = 0 \tag{3}$$

$$\frac{\partial \text{err}}{\partial a_1} = -2 \sum_{i=1}^n \left(y_i - \left(a_0 + \sum_{k=1}^j a_k x^k \right) \right) x = 0 \tag{4}$$

$$\frac{\partial \text{err}}{\partial a_2} = -2 \sum_{i=1}^n \left(y_i - \left(a_0 + \sum_{k=1}^j a_k x^k \right) \right) x^2 = 0 \tag{5}$$

⋮

$$\frac{\partial \text{err}}{\partial a_j} = -2 \sum_{i=1}^n \left(y_i - \left(a_0 + \sum_{k=1}^j a_k x_i^k \right) \right) x_i^j = 0 \tag{6}$$

Rewriting these $j + 1$ equations, and put into matrix form

$$\begin{bmatrix} n \sum x_i \sum x_i^2 & \dots & \sum x_i^j \\ \sum x_i \sum x_i^2 \sum x_i^3 & \dots & \sum x_i^{j+1} \\ \sum x_i^2 \sum x_i^3 \sum x_i^4 & \dots & \sum x_i^{j+2} \\ \vdots & & \vdots \\ \sum x_i^j \sum x_i^{j+1} \sum x_i^{j+2} & & \sum x_i^{j+j} \end{bmatrix} \begin{bmatrix} a_0 \\ a_1 \\ a_2 \\ a_3 \\ \vdots \\ a_j \end{bmatrix} = \begin{bmatrix} \sum y_i \\ \sum x_i y_i \\ \sum (x_i^2 y_i) \\ \vdots \\ \sum (x_i^j y_i) \end{bmatrix} \tag{7}$$

where all summations above are over $i = 1, \dots, n$. Now, we use the Gaussian elimination to find the coefficients.

$$A = \begin{bmatrix} n \sum x_i \sum x_i^2 & \dots & \sum x_i^j \\ \sum x_i \sum x_i^2 \sum x_i^3 & \dots & \sum x_i^{j+1} \\ \sum x_i^2 \sum x_i^3 \sum x_i^4 & \dots & \sum x_i^{j+2} \\ \vdots & & \vdots \\ \sum x_i^j \sum x_i^{j+1} \sum x_i^{j+2} & & \sum x_i^{j+j} \end{bmatrix}; \tag{8}$$

$$X = \begin{bmatrix} a_0 \\ a_1 \\ a_2 \\ a_3 \\ \vdots \\ a_j \end{bmatrix} \quad \text{and} \quad B = \begin{bmatrix} \sum y_i \\ \sum x_i y_i \\ \sum (x_i^2 y_i) \\ \vdots \\ \sum (x_i^j y_i) \end{bmatrix}$$

The above equations are linear with respect to the coefficients. So, we can express in the form of

$$AX = B \tag{9}$$

In order to find the coefficient matrix X, we use matrix inversion

$$X = A^{-1}B \tag{10}$$

The obtained smooth curve is shown in Fig. 7. To standardize the image, it has been cropped sharp to the border of the character. The cropped and resized image of digit ‘0’ is shown in Fig. 8. The image is then resized to 5 by 7 matrices, where all pixel values are assigned to 1 of all 10 by 10 boxes as shown in Fig. 9. Finally, data

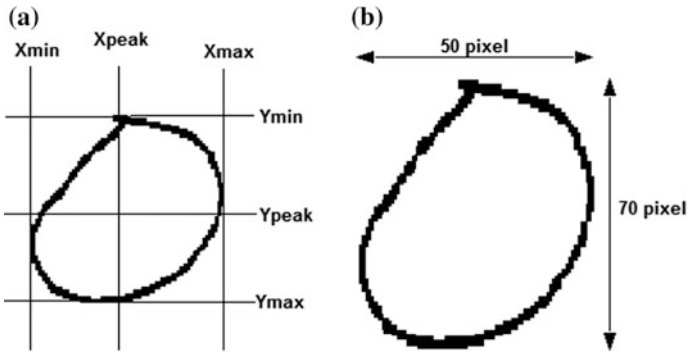
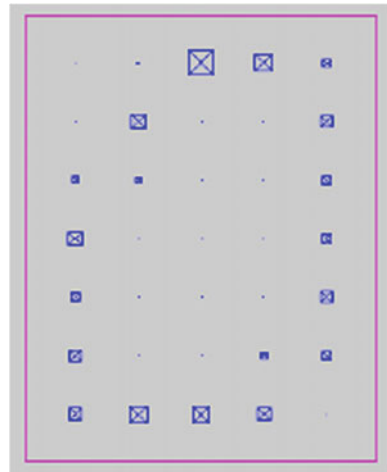


Fig. 8 a Crop limits for actual image, b Cropped and resized image for digit '0'

Fig. 9 Image resized to 7×5 to meet the network input requirement



stream is generated from 5 by 7 matrices to feed into neural network for further processing.

4 MATLAB GUI

A MATLAB GUI is created to understand the processing properly [9]. Figure 10 shows our MATLAB GUI. The functioning of MATLAB GUI starts by pressing START button which takes input from digital pen transmitting wirelessly to COM port. The status indicator in normal state remains red; it turns yellow on pressing START button and turns green when user transmits handwritten digits. When user stops writing, STOP button is pressed to start image processing.

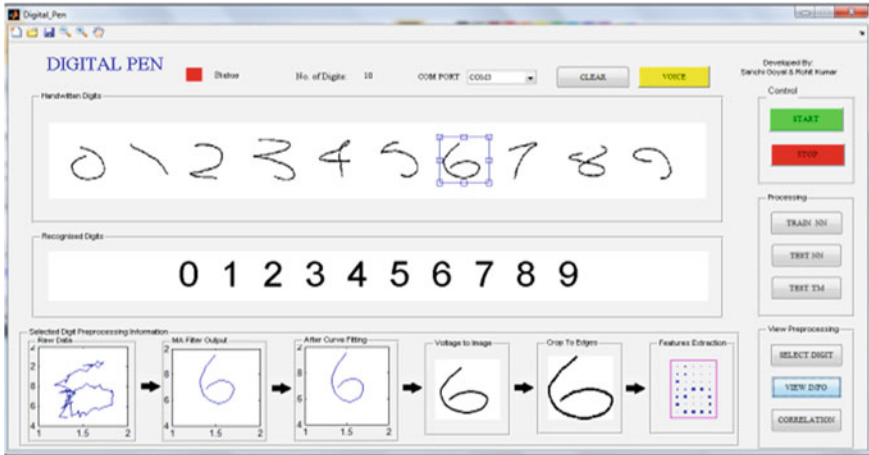


Fig. 10 MATLAB GUI for digital pen

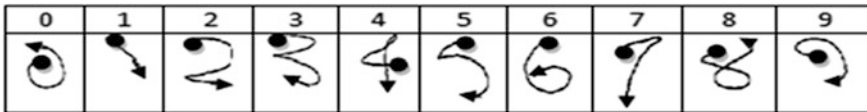


Fig. 11 Writing style for better recognition

5 Conclusion

The proposed handwritten digit recognition system consists of acceleration acquisition and image preprocessing. The result can be further extended to text conversion. The above result also motivates us to investigate the performance of the device for English alphabets and alphabets of other languages. The recognition will be even better if digits are written in the format defined in Fig. 11.

References

1. Sato, T. Yamaguchi, and F. Harashima: Natural interface using pointing behavior for human-robot gestural interaction, *IEEE Trans. Ind. Electron.*, 54, 2, pp. 1105–1112, Apr. 2007.
2. Y.S. Kim, B.S. Soh and S.G. Lee: A new wearable input device: SCURRY, *IEEE Trans. Ind. Electron.*, vol. 52, no. 6, pp. 1490–1499, Dec 2009.
3. A.D. Cheok, Y. Qiu, K. Xu, and K.G. Kumar: Combined wireless hardware and real-time computer vision interface for tangible mixed reality, *IEEE Trans. Ind. Electron.*, vol. 54, no. 4, pp. 2174–2189, Aug. 2007.

4. A. Akl: A Novel Accelerometer-based Gesture Recognition System, Department of Electrical and Computer Engineering, University of Toronto, 2010.
5. S.K. Devireddy, S.A. Rao: Hand written character Recognition Using Back Propagation Network, Journal of Theoretical and Applied Information Technology, pp. 1–13, 2005.
6. edge.rit.edu/edge/P10010/public/PDF/HME.pdf.
7. Datasheet of MMA7260QT 3 Axis Accelerometer Module, rhydolabz, Model #: SEN – 09041.
8. www.atmel.com/images/doc8159.pdf.
9. M. Stephens: Creating GUI's in Matlab, April 2, 2007.

Application of Particle Swarm Optimization-TVAC Algorithm in Power Flow Studies

Poulami Ghosh and Anand Kalwar

Abstract This paper presents a comparative study between particle swarm optimization and particle swarm optimization time-varying acceleration coefficients (TVAC) algorithm-based methodology for solving load flow in electrical power systems. Load flow study provides the system status in steady state and is required by several functions performed in power system control rooms.

Keywords Particle swarm optimization · Particle swarm optimization-TVAC Load flow · Electrical power system · Score

1 Introduction

Particle swarm optimization is the recent method in the era of artificial intelligence to improve the optimization level in different aspects. The novelty of the particle swarm optimization-TVAC includes acceleration factor to converge the power flow equations obtaining lesser amount of losses in the power system network. In the area of artificial intelligence, computational intelligence-based algorithm has been applied successfully to electrical power system-related problems, and particle swarm optimization (PSO) is pointed out among these techniques. PSO algorithms are applied for load flow study, and they are based on the behavior of birds' flocks searching for food [1]. PSO applications have provided good convergence properties, ease of implementation, and low computational time [2]. The novelty of this paper is to improve the convergence property of general PSO algorithm using the PSO-TVAC and to obtain the solution for power flow problem in power system network.

P. Ghosh (✉) · A. Kalwar
St. Thomas' College of Engineering & Technology, Kolkata 700023, India
e-mail: poulamighosh_stcet@yahoo.com

A. Kalwar
e-mail: anandkalwar98@gmail.com

2 Load Flow Study in Electrical Power Systems

Load flow or power flow study is done under steady-state condition of power system. The study is done to know the system bus voltages in order to determine later generation necessary to supply the adjustment in the generation buses and the power flow in system brunches. Therefore, it is possible to obtain the amount of power demand plus the power losses in the system branches. Besides, the voltage levels must comply with the predetermined boundaries, and overloaded operations added to those in the stability limit must be prevented [1].

3 Particle Swarm Optimization Approach for Load Flow Study

PSO is a meta-heuristic method, and it makes few or no assumptions initially for the problem to be optimized and searched over the solution space following a very effective algorithm. However, being meta-heuristic does not produce the optimal solution every time [3]. As it is not a tangent method, irrespective of the problem being convex or not, it can produce an optimal solution. PSO starts with a group of randomly generated population and fitness value to evaluate the population searching the optima with the random technique [4].

Position of the particle is influenced by velocity. Let $x_i(t)$ denote the position of particle i in the search space at time step t ; unless otherwise stated, t denotes discrete time steps. The position of the particle is changed by adding a velocity, $v_i(t)$, to the current position [1]:

$$x_i(t+1) = x_i(t) + v_i(t+1)$$

$$v_i(t) = v_i(t-1) + c_1 r_1 (\text{localbest}(t) - x_i(t-1))$$

$$+ c_2 r_2 (\text{globalbest}(t) - x_i(t-1))$$

where c_1 and c_2 , respectively, are learning rates for individual ability (cognitive) and social influence (group), and r_1 and r_1 uniformly random numbers are distributed in the intervals 0 and 1. So the parameters c_1 and c_2 represent weight of memory (position) of a particle toward memory (position) of the groups (swarm).

4 Particle Swarm Optimization-TVAC Approach for Load Flow Study

The inertia weight (w): The concept of inertia was developed in 1998 to better control the exploration and exploitation [5]. Inertia weight maintains the movement of a particle during evaluation. For very less a value of inertia, it is prone to

loss its knowledge of previous velocity and tend to quickly change direction. On the other hand if w is very high and c_1, c_2 is low then the exploitation part of the PSO algorithm is not so effective and thus lesser tendency of convergence. Thus, high inertia setting near 1 facilitates global search, and lower values [0.2, 0.5] facilitate local search. In this paper, a scheme where the inertia value decreases linearly from 0.7 to 0.2 over the iterations is applied.

Swarm size: An improvement in the optimal value with the increase in swarm size is possible, but a large swarm size increases the functions to be calculated, hence increasing the evaluation time. So we need to compromise between these two. In this methodology, the accepted swarm size is 30.

The acceleration coefficients: In the proposed method of PSO-TVAC, the c_1 and c_2 were adopted as follows:

$$C_1 = ((c1i - c1f) * iteration) / \text{maxiteration} + c1i,$$

$$C_2 = ((c2i - c2f) * iteration) / \text{maxiteration} + c2i$$

where $c1i, c2i, c1f,$ and $c2f$ are parameter constants, iteration is the current iteration number, maxiteration is the maximum allowable iteration [6].

The maximum velocity: It serves as a constraint to control the global exploration capability of the swarm. There has been set no maximum velocity which in turn helps in global search, i.e., exploration for the optima over a large space during the initial stage of iterations, and as with the iterations the acceleration factor and inertia are decreasing, it will encourage the particles to converge at the global optima at the end of search (Fig. 1).

5 Numerical Results

In this section, the proposed methodology for load flow computation is evaluated on the 14-bus case study. A computational procedure has been developed based on PSO methodology and on PSO-TVAC for solving the load flow. The selected results are best solutions over these ten runs. The obtained results of proposed methodology for case study are compared with those obtained using a conventional PSO-based computational method.

14-bus system case study.

Tables 1 and 2 show load flow results for 14-bus (Fig. 2) power system obtained through the application of a PSO-based method. Tables 3 and 4 present the results obtained with the proposed PSO-TVAC methodology.

Results:

See Figs. 3, 4, and 5.

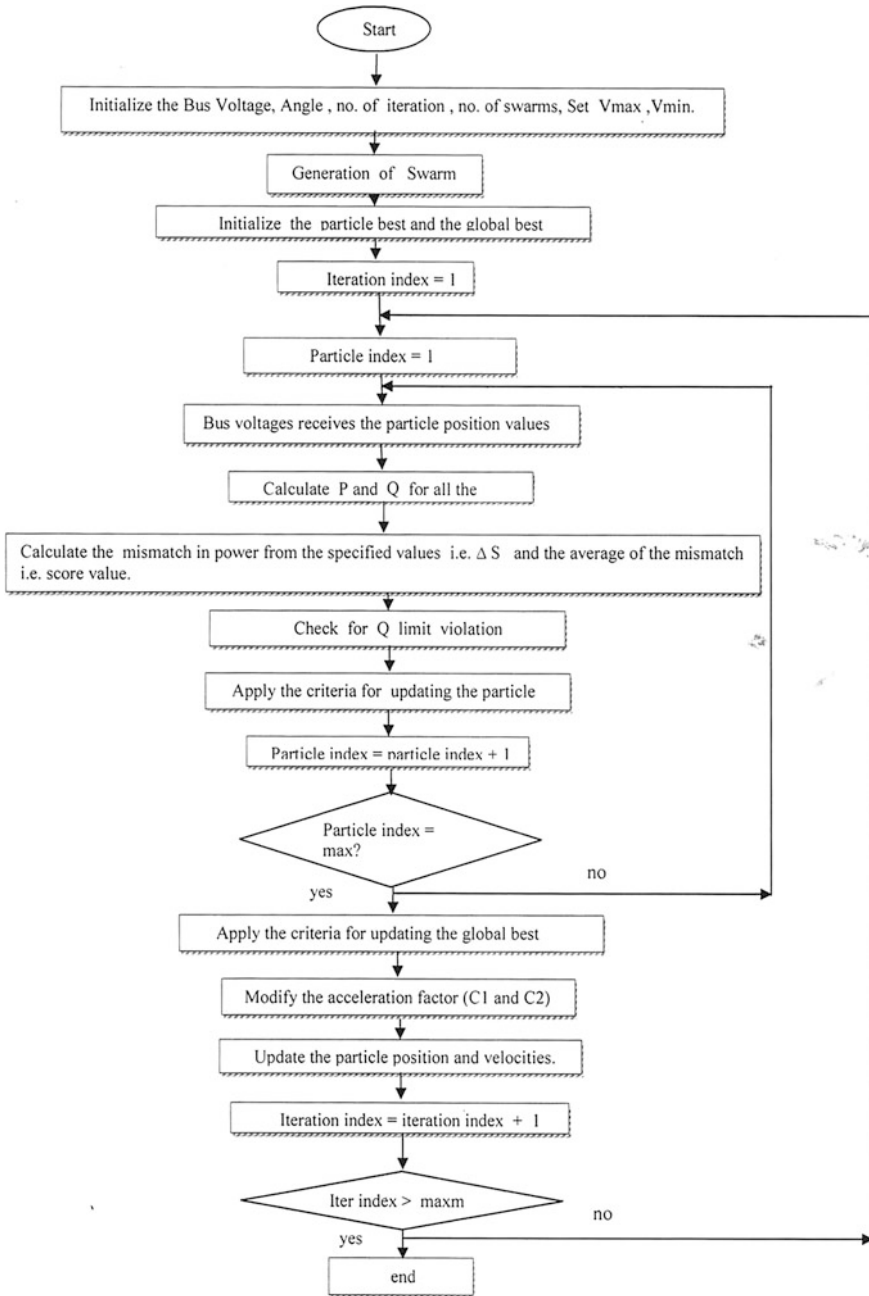


Fig. 1 Flowchart of the PSO-TVAC-based load flow

Table 1 Load flow analysis (particle swarm optimization)

Bus No.	V	Angle	Injection		Generation		LOAD	
	pu	Degree	MW	MVAR	MW	MVAR	MW	MVAR
1	1.0600	0.0000	226.971	-12.237	226.971	-12.237	0.000	0.000
2	1.0450	-4.9471	18.305	45.886	40.005	58.586	21.700	12.700
3	1.0100	-12.8762	-94.209	16.621	-0.009	35.621	94.200	19.000
4	1.0000	-10.1953	-89.541	-18.350	-41.741	-22.250	47.800	-3.900
5	1.0116	-8.2005	-0.636	-1.519	6.964	0.081	7.600	1.600
6	1.0700	-10.7161	-11.200	23.077	0.000	30.577	11.200	7.500
7	1.0314	-12.1938	-0.033	-0.025	-0.033	-0.025	0.000	0.000
8	1.0900	-12.1933	0.005	36.266	0.005	36.266	0.000	0.000
9	1.0000	-13.2668	-41.891	-42.740	-12.391	-26.140	29.500	16.600
10	1.0121	-12.7414	-9.004	-5.806	-0.004	-0.006	9.000	5.800
11	1.0600	-10.9930	19.737	13.141	23.237	14.941	3.500	1.800
12	1.0600	-9.0190	23.187	-13.276	29.287	-11.676	6.100	1.600
13	1.0407	-11.0463	-12.802	-5.879	0.698	-0.079	13.500	5.800
14	1.0000	-13.2565	-13.772	-4.697	1.128	0.303	14.900	5.000
Total			15.116	30.463	274.116	103.963	259.000	73.500

Table 2 Line flow and losses (PSO method)

From bus	To bus	P (MW)	Q (MVar)	From bus	To bus	P (MW)	Q (MVar)	Line loss	
								MW	MVar
1	2	155.809	-17.187	2	1	-151.571	30.126	4.238	12.940
1	5	71.162	10.680	5	1	-68.672	-0.402	2.490	10.279
2	3	74.919	5.789	3	2	-72.489	4.447	2.430	10.236
2	4	57.568	10.182	4	2	-55.750	-4.664	1.819	5.518
2	5	37.389	8.809	5	2	-63.619	-6.459	0.769	2.349
3	4	-21.720	15.062	4	3	22.179	-13.890	0.459	1.171
4	5	-83.498	0.385	5	4	84.429	2.551	0.931	2.936
4	7	17.586	-15.043	7	4	-17.586	16.138	0.000	1.095
4	9	9.924	0.267	9	4	-9.942	0.267	0.000	0.533
5	6	20.227	-24.709	6	5	-20.227	27.049	0.000	2.340
6	11	4.338	3.315	11	6	-4.314	-3.263	0.025	0.052
6	12	-8.959	8.682	12	6	9.126	-8.334	0.167	0.348
6	13	13.648	17.177	13	6	-13.370	-16.630	0.278	0.548
7	8	-0.005	-34.316	8	7	0.005	36.226	0.000	1.950
7	9	17.557	29.596	9	7	-17.557	28.371	0.000	1.225
9	10	-14.337	-8.908	10	9	14.428	9.149	0.091	0.241
9	14	-0.054	0.026	14	9	0.054	-0.026	0.000	0.000
10	11	-23.431	-14.955	11	10	24.050	16.404	0.619	1.449
12	13	14.060	-4.942	13	12	-13.623	5.337	0.437	0.395
13	14	14.191	5.413	14	13	-13.827	-4.672	0.364	0.741
Total loss								15.116	56.346

Table 3 Load flow analysis (PSO-TVAC method)

Bus No.	V	Angle	Injection		Generation		LOAD	
	pu	Degree	MW	MVAR	MW	MVAR	MW	MVAR
1	1.0600	0.0000	226.830	-14.417	226.830	-14.417	0.000	0.000
2	1.0450	-4.8853	18.253	35.288	39.953	47.988	21.700	12.700
3	1.0100	-12.6219	-94.229	9.604	-0.029	28.604	94.200	19.000
4	1.0118	-10.0547	-51.657	1.877	-3.857	-2.023	47.800	-3.900
5	1.0169	-8.4403	-7.896	-1.676	-0.296	-0.076	7.600	1.600
6	1.0700	-12.7462	3.094	15.173	14.294	22.673	11.200	7.500
7	1.0436	-13.2081	-2.708	4.702	-2.708	4.702	0.000	0.000
8	1.0800	-13.2081	-0.000	22.323	-0.000	22.323	0.000	0.000
9	1.0218	-14.7270	-38.428	-28.209	-8.928	-5.609	29.500	16.600
10	1.0223	-14.6607	-9.196	-5.798	-0.196	0.002	9.000	5.800
11	1.0418	-13.8188	-3.504	-1.791	-0.004	0.009	3.500	1.800
12	1.0564	-13.0722	1.291	-3.668	7.391	-2.068	6.100	1.600
13	1.0451	-13.6562	-13.500	-5.800	0.000	-0.000	13.500	5.800
14	1.0134	-15.2923	-14.900	-5.000	0.000	0.000	14.900	5.000
Total			13.450	28.607	272.450	102.107	259.000	73.500

Table 4 Line flow and losses (PSO-TVAC method)

From bus	To bus	P (MW)	Q (MVar)	From bus	To bus	P (MW)	Q (MVar)	Line loss	
								MW	MVar
1	2	153.942	-16.748	2	1	-149.806	29.375	4.136	12.627
1	5	72.888	8.061	5	1	-70.302	2.614	2.586	10.675
2	3	73.184	5.957	3	2	-70.864	3.817	2.320	9.774
2	4	55.308	3.871	4	2	-53.672	1.093	1.636	4.963
2	5	39.567	5.105	5	2	-38.737	-2.571	0.830	2.534
3	4	-23.365	8.674	4	3	23.773	-7.632	0.408	1.041
4	5	-65.785	9.643	5	4	66.362	-7.825	0.576	1.818
4	7	28.401	-14.932	7	4	-28.401	16.989	0.000	2.057
4	9	15.626	-1.237	9	4	-15.626	2.531	0.000	1.293
5	6	34.781	-21.682	6	5	-34.781	25.498	-0.000	3.816
6	11	14.478	8.350	11	6	-14.246	-7.864	0.232	0.485
6	12	4.263	3.640	12	6	-4.229	-3.569	0.034	0.070
6	13	19.134	10.832	13	6	-18.855	-10.282	0.279	0.550
7	8	0.000	-21.570	8	7	-0.000	22.323	0.000	0.753
7	9	25.693	20.999	9	7	-25.693	-29.886	0.000	1.112
9	10	-1.431	-0.004	10	9	1.432	0.005	0.001	0.002
9	14	4.322	1.156	14	9	-4.298	-1.104	0.024	0.052
10	11	-10.627	-5.803	11	10	10.742	6.073	0.115	0.269
12	13	5.521	-0.099	13	12	-5.460	0.153	0.060	0.055
13	14	10.815	4.328	14	13	-10.602	-3.896	0.212	0.432
Total loss								13.450	54.379

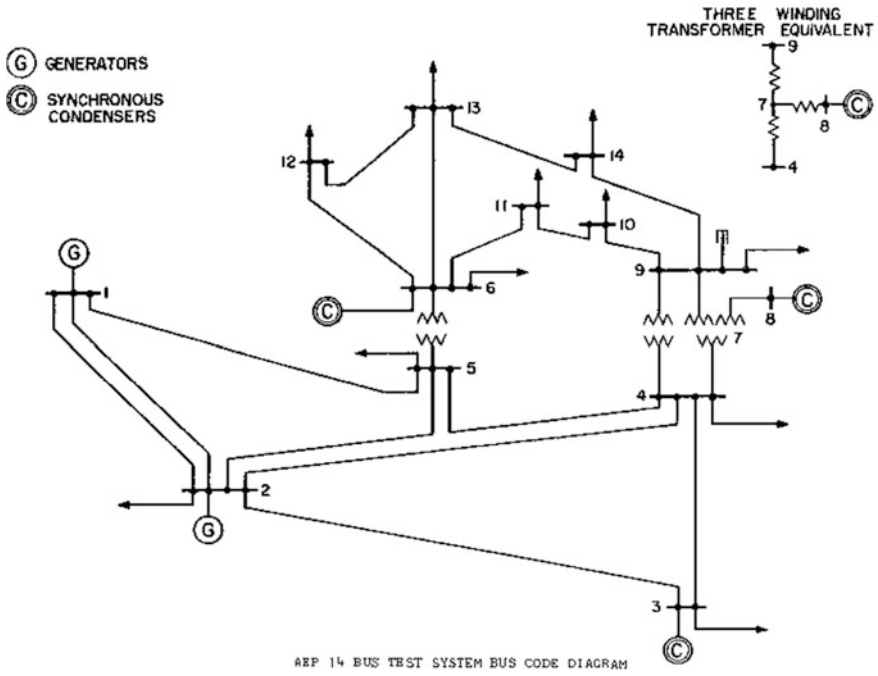


Fig. 2 IEEE 14-bus system

Fig. 3 Score versus iteration for PSO method

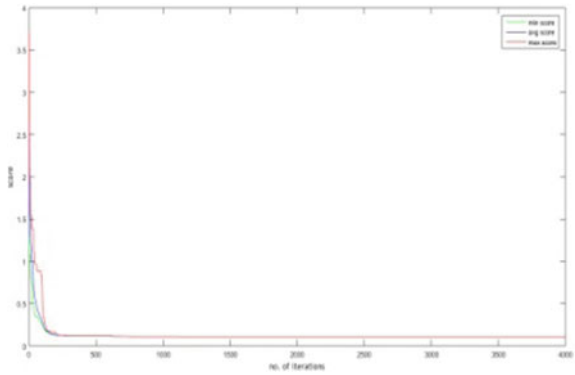


Fig. 4 Score versus iteration for PSO-TVAC method

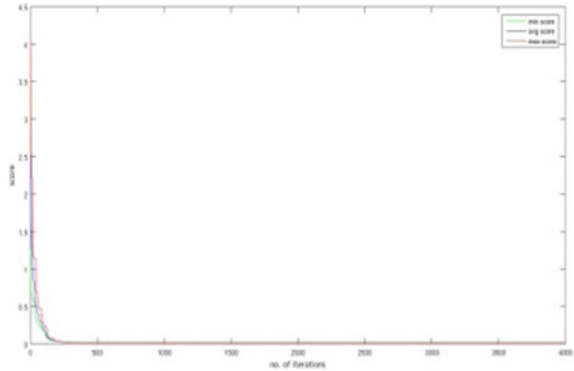
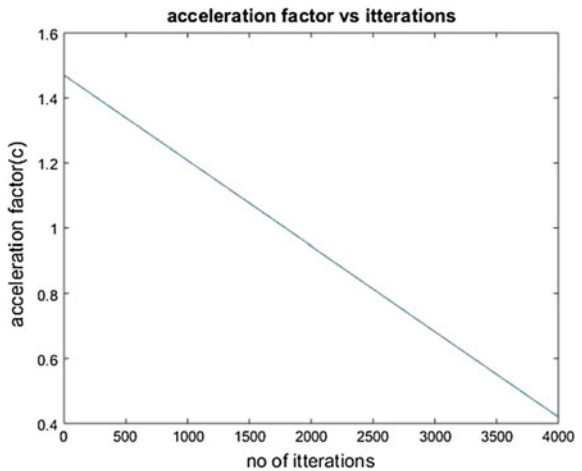


Fig. 5 Social cognitive factor versus no. of iteration in the PSO-TVAC method



6 Conclusion

This paper presents the solutions for load flow computations for 14 bus, and the proposed PSO-TVAC method has acceptability as score value; i.e., tolerance obtained is better than the conventional PSO method.

References

1. J. Kennedy and R. Eberhart, "Swarm Intelligence", Morgan Kaufmann Publishers, 2001.
2. K.S. Swarup, "Swarm intelligence approach to the solution of optimal power flow", J. Indian Inst. Sci., vol. 86, pp. 439–455, 2006.

3. X. Yan, Q. Wu, H. Liu, W. Huang "An Improved Particle Swarm Optimization and Its Application" *IJCSI International Journal of Computer Science Issues*, Vol. 10, Issue 1, No 1, January 2013.
4. C. P. Salomon, G. L.T.L. E. B. da Silva, M. P. Coutinho and C. H. V. de Moraes "A Hybrid Particle Swarm Optimization Approach For Load-Flow Computation" *International Journal of Innovative Computing, Information and Control* Volume 9, Number 11, November 2013.
5. J. C. Bansal, P. K. Singh, M. Saraswat, A. Verma, S. S. Jadon, A. Abraham "Inertia Weight Strategies in Particle Swarm Optimization" *Third World Congress on Nature and Biologically Inspired Computing IEEE* 2011.
6. S. Das, A. Abraham, and A. Konar "Particle Swarm Optimization and Differential Evolution Algorithms: Technical Analysis, Applications and Hybridization Perspectives" *Advances of computational intelligence in Springer* 2008.

Network-Based Digital Notice Board

Saikumar Valluru, Prachi and Arun Kumar Singh

Abstract In this project, we propose advanced hi-tech wireless notice board. Notice board is a primary thing in any institutions, organization, hospital, or public utility places. For passing any notice, we use papers. If we observe, lots of papers are being wasted due to this notices so we need to save papers in order to make an eco-friendly system. We are trying to develop a digital notice board which can overcome these problems. With this notice board, we can send our notice anytime without wasting any resource and can make our communication more efficient. We can handle proposed notice board with less errors and maintenance. We can replace normal notice board with digital notice board anywhere like institutions, organization, hospital, or public utility places and can update the notice anytime. For this, we used Raspberry Pi for wireless communication. Here we can change the news or notice or timetable which can be displayed on notice board. Raspberry Pi will act as server, and there will be multiple clients connected to the server, and these clients are connected with LCD. Here server and clients are connected via router for wireless communication. For displaying information, we need to approach server and from server, we can send our information to particular client or multiple clients and clients will be displaying that particular information. The goal of this paper is to provide the access to notices and articles quickly as compared to manual notice board. We can update text messages using centralized database anytime. The address is assigned to each receiver and information is displayed from the main server at the reception.

S. Valluru (✉) · Prachi · A. K. Singh
Department of Electronics and Communication,
Sikkim Manipal Institute of Technology, Majitar, Rangpo, India
e-mail: vallurusaikumar321@gmail.com

Prachi
e-mail: puja70631@gmail.com

1 Introduction

The project deals with displaying text messages sent by the user from a remote place. A server is fixed by setting up a local server on Raspberry Pi. LCD is attached to Raspberry Pi using GPIO pins, server will send the message to clients and clients will process the message and display the message on LCD display. If we want to access the particular client, then we have to give the IP address of particular client in the server; once connection is established between and server and clients, we can pass message to that particular client over TCP Sockets (Fig. 1).

2 Approach

- To establish a TCP/IP client–server wireless connection
- Configure server (Raspberry)
- Server: Stores the notices and replies to clients
- Configure client (Raspberry)

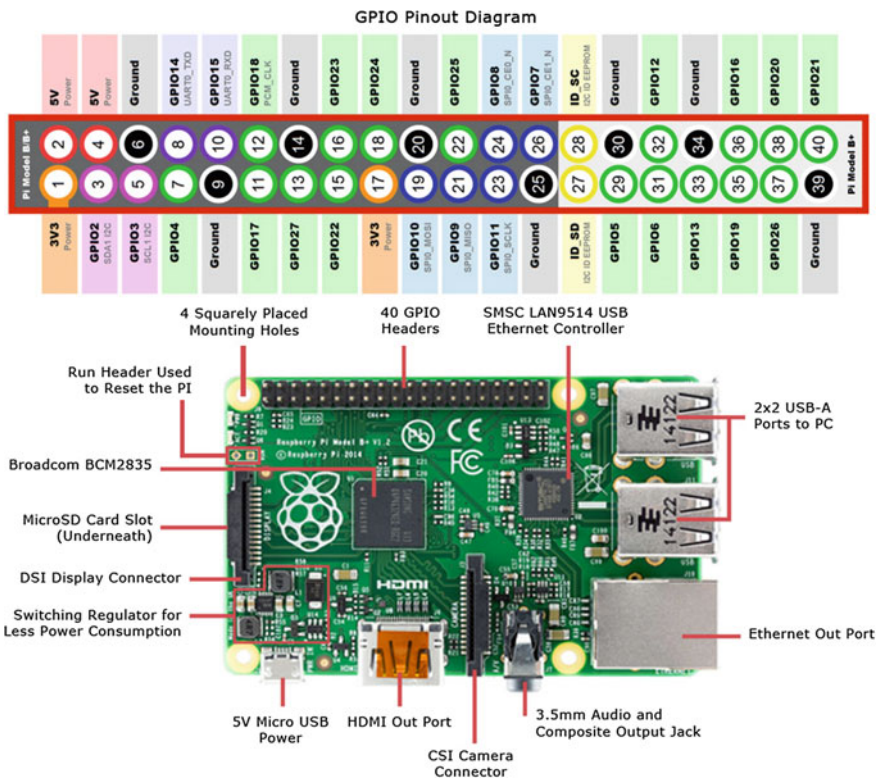


Fig. 1 Raspberry Pi board

- Client: It can receive information sent by the server
- Check the message to be sent wirelessly
- Check the message status
- Interface LCD with clients.

3 Literature Survey

There does not seem to be any previous work that is aimed at publicly displayed PowerPoint control. It seems that everyone relies solely on the fixed timers built into PowerPoint, normal PowerPoint presentations are usually conducted in person and can thus be controlled easily with remotes is thus no motivation for a motion-sensing controller in this context, as far as we know, there is no previous work that has the same our does.

- A. In paper [1], it works on LED scrolling message display system for that she uses GSM mobile phone. The system includes SMA antenna MAX 232 for communication purpose.
- B. In paper [2], the data can be sent directly to the digital monitor from an Android phone based on Raspberry Pi card and an Android application is used to send the information to the digital monitor.

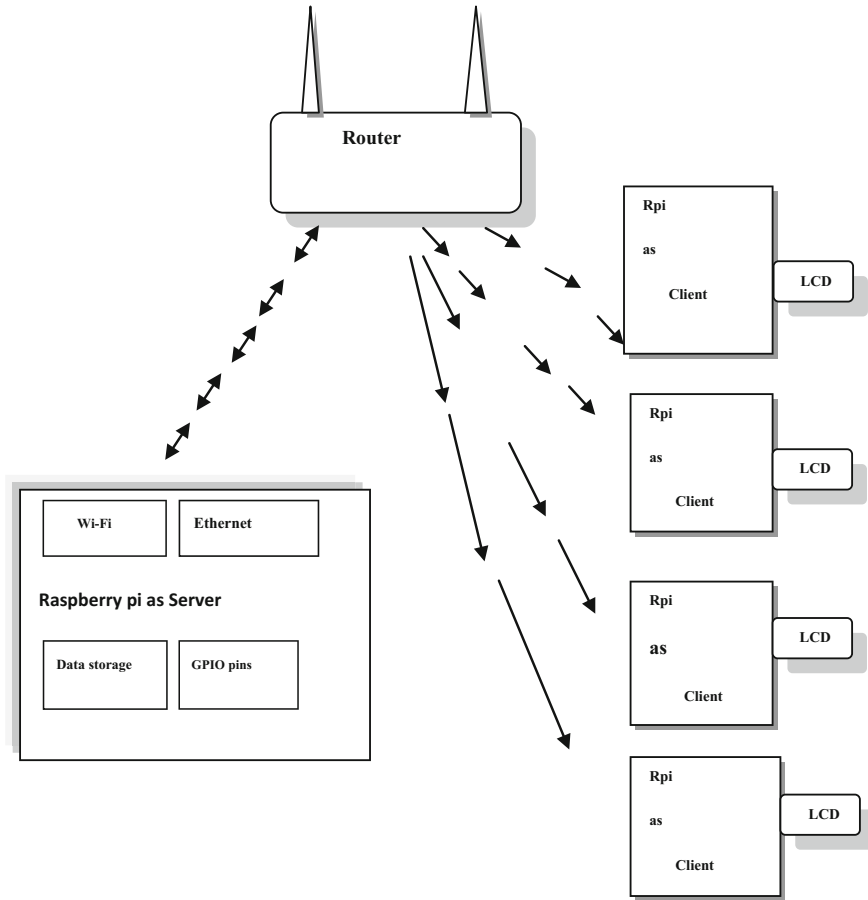
However, our proposed project does draw aspects from many other previous works that relate to SD card usage and wireless communication.

Our project using wireless communication provides very ideal solution for handling the digital notice board in educational institutions; the organization uses circulars and notice boards in order to convey the information to the students. So by using this type of display, we overcome the problem such as we can display all the information at time. This methodology will take added time for updating, and many students may not be aware of the information displayed on notice boards which are not eye-catching ones.

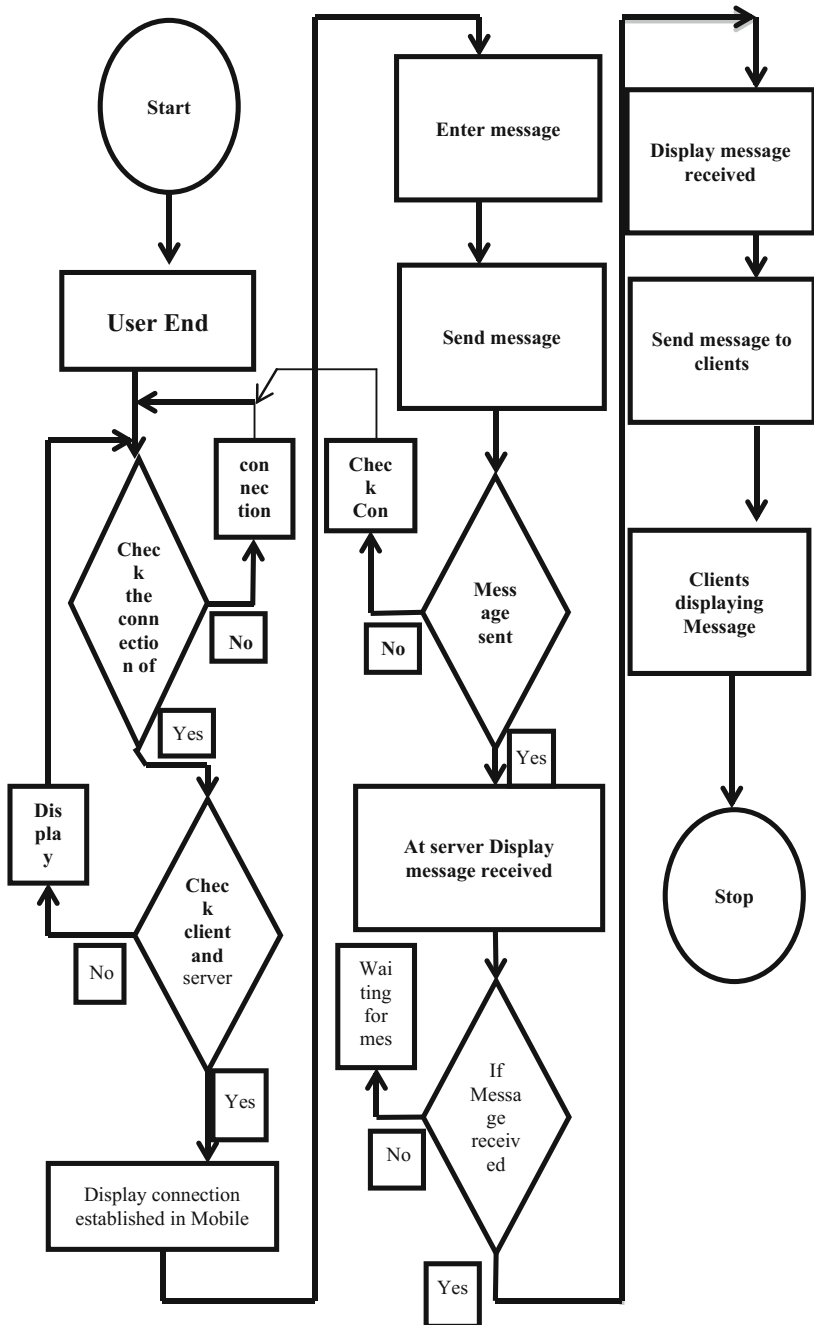
4 Planning

1. The literature review of digital notice board.
2. Introduction of Raspberry Pi in digital notice board.
3. Study about server and client connection.
4. Creating a network of server and client using Raspberry Pi.

5 Block Diagram



6 Flowchart



7 Result

The expected outcome of this project is we will try to display any notice wirelessly in multiple LCD screens, and we will try to access those particular LCD's individually and passing notice to that particular LCD.

8 Conclusion

Wireless operation provides fast transmission over long range of communication. It saves resources and time. Data can be sent from remote location provided user is authenticated. There is no limit of messages.

Text messages are stored in SD card and data can be seen whenever we want to see.

References

1. V.B Jadhav, T.S Nagwanshi, Y.P Patil, D.R Patil, "International Research Journal of Engineering and Technology", vol-03, pp: 2076–2078, 05 May 2016.
2. P U. Ketkarl, K P. kulkarni, R. M. Tunganyat, "GSM Mobile phone Based LED Scrolling message Display System". International Journal of scientific engineering and Technology (ISSN: 2277-1581), volume 2 issue 3, pp: 149–155, 2006, April 2013.

Author Index

A

Agarwal, Amit, 1, 679
Agarwal, Eshwar, 527, 539
Agrawal, Cherry, 527, 539
Ahmed, MdIrfan, 143
Amir, S.A., 625
Amitab, Khwairakpam, 295
Arun Kumar, G., 439
Asraful Sekh, Md., 29

B

Baidya, Dayarnab, 729
Banerjee, Chandan, 159
Banerjee, Pritha, 69
Baruah, Jayanta Kumar, 563
Barua, Sreeparna, 79
Basu, Banani, 183
Basumatary, Tenison, 419, 429
Bera, Parthasarathi, 509, 755, 777
Bera, Rabindranath, 107, 321, 329, 343, 563, 591, 599, 615, 633, 679
Bera, Soumyasree, 329, 679
Bezboruah, Tulshi, 419
Bhanja, Sukhendu, 9, 439
Bharti, 209
Bhaskar, Debasish, 591, 599, 679
Bhatia, D., 625
Bhattacharya, Susanta Kumar, 151
Bhoi, Akash Kumar, 287, 359, 369, 377, 385, 393
Bhowmik, Kuharan, 885
Bhuyan, Bubu, 877
Bhuyan, M., 789
Biswas, Amrita, 651
Borah, Samarjeet, 855, 885

Boro, M., 465, 789
Bose, Anindya, 641
Bose, Tanushree, 321, 351, 495, 503

C

Chahal, Jaspreet Singh, 133
Chakrabarti, Tapas, 125
Chakraborty, Biswajit, 797
Chakraborty, Debashis, 553
Chakraborty, M., 475
Chakraborty, Swastika, 679
Chatterjee, Basukinath, 767
Chatterjee, Indira, 509
Chatterjee, Sayan, 35
Chattopadhyay, Kalyan Kumar, 21
Chaudhury, Saurabh, 43, 57
Chauhan, Dinesh, 233
Chetia, Dipankar, 419, 429
Chettri, Preman, 591, 679
Chouhan, Sonali, 661

D

Das, Basudev, 641
Das, Debaprasad, 827
Das, Debmalya, 35
Das, Gautam, 827
Dash, Debashish, 57
Dash, Dinesh Kumar, 69, 97, 115
Das, Moumita, 35
Das, Saumya, 351, 495, 503
Das, Sourav Kumar, 877
Das, Suman, 51
Das, Suvosmita, 885
Datta, Asim, 151
Deka, Krishangi, 895

Dev Choudhury, B.K., 465
 Devi, Manju, 377
 Dey, Amit Baran, 183
 Dey, Anup, 79
 Dey, Chanchal, 797
 Dhar, Sourav, 447, 563
 Dhoundiyal, Sanya, 701
 Dixit, Abhishek, 409
 Dutt, Inadyuti, 885
 Dutta, L., 789
 Dutta, Sushanta Kabir, 169, 583

G

Garg, Sonali, 409
 Gayen, Amit, 797
 Ghoshal, Moinak, 159
 Ghoshal, Tanmay, 9
 Ghosh, Anindita, 553
 Ghosh, Debjyoti, 923
 Ghosh, Poulami, 933
 Ghosh, S.K., 313
 Ghosh, Sourav, 747
 Giri, Diksha, 855
 Goswami, Krishangi, 895
 Goswami, Suparna, 399
 Goyal, Sanchi, 923
 Gupta, Akhil, 209, 259
 Gupta, Avanti, 527, 539
 Gupta, Priya, 509
 Gurung, Riwas, 679

H

Handique, A., 625
 Haque, N., 199
 Hazarika, Anil, 465, 789
 Hegadi, Ravindra S., 689
 Hussain, Inamul, 43

I

Islam, Hashinur, 495, 503
 Islam, Md Ruhul, 907

J

Jain, Virander Kumar, 409
 Jhansi Rani, A., 87
 Jharia, Preeti, 661
 Joyprakash Singh, L., 459

K

Kalita, P., 465
 Kalwar, Anand, 933
 Kandar, Debdatta, 475, 737, 295
 Kaur, Inderpreet, 223, 247, 275
 Khanda, Ambar, 125

Khatun, Ferdousi, 907, 915
 Koirala, Tawal K., 907
 Kumar, Anubhav, 837
 Kumar, Ashish, 385
 Kumari, Rakhi, 107
 Kumar, Manish, 439
 Kumar, Rohit, 923
 Kumar, Sanjeet, 607
 Kumar, Susheel, 275

L

Lala, Archana, 385, 393
 Lalchhanhima, R., 737
 Laskar, Shakuntala, 669

M

Maiti, Soumen, 21
 Maitra, Indra Kanta, 885
 Maity, Ayindrilla, 885
 Maji, Bansibadan, 475, 701
 Majumder, Arijit, 9, 439
 Mandal, Sujoy, 641
 Manna, Shreema, 321
 Mashahary, Sangeeta, 877
 Medhi, Kishore, 295
 Medhi, Nabajyoti, 865
 Misra, Debajyoti, 827
 Mitra, A., 313
 Mitra, Esita, 115
 Mondal, Arnab Kumar, 755, 777
 Mostafa, Posiba, 35
 Mourya, G.K., 625
 Mukherjee, Amartya, 767
 Mukherjee, M., 199
 Mukherjee, Subra, 669

N

Nandi, Arnab, 183
 Nandy, Gourab, 767
 Nath, Rongan, 51
 Navada, Bhagya R., 817
 Nayan, Navneet, 607
 Neog, Pallavi, 615, 633

O

Olokede, Seyi Stephen, 177, 303

P

Pal, Antardipan, 35
 Palisetty, Rakesh, 485
 Pal, Shreyasi, 21
 Pal, T.K., 439
 Parihar, Anil Singh, 517
 Patel, Bikash, 807

Paul, Babu Sena, 177, 295, 303, 737
 Paul, P. K., 837, 847
 Paul, Rajat, 615, 633
 Paul, Sayak, 159
 Pittala, Suresh Kumar, 87
 Prachi, 943
 Pradhan, Arun, 719
 Pradhan, M.P., 847
 Pradhan, P. C., 1
 Pradhan, Ratika, 855
 Prakash, Om, 191
 Prasad, B.S.V., 439
 Pratiher, S., 199

R

Raha, S., 313
 Rahim, Mijanur, 29
 Rahman, Atiqur, 169
 Rahul, Singh, 191
 Rai, Kharka Bahadur, 591
 Rai, Prativa, 719
 Rajshri, 351
 Ramchurn, Geheshwar Sharma, 701
 Ray, Kailash Chandra, 485
 Reddy, N.S., 447
 Roy, Rupam Gupta, 729
 Roy, Shantanu, 615, 633
 Roy, Subhashis, 79
 Rynjah, Fairriky, 459

S

Sagarika, 895
 Saha, Malay, 125
 Saha, Priyanka, 97
 Saha, Tapas Kumar, 747
 Sahana, Subhas Chandra, 877
 Sahu, Sitanshu Sekhar, 607
 Saikia, Hemanta, 573
 Saini, J. P., 359, 369
 Saini, Rahul, 359, 369
 Saketh, M.S., 447
 Samanta, Koushik, 641
 Santhosh, K.V., 817
 Santra, Atanu, 641
 Sapkota, Kamal, 719
 Sarkar, Animesh, 807
 Sarkar, Anup, 69
 Sarkar, Mousumi, 9
 Sarkar, Pankaj, 169

Sarkar, Prasanta, 711
 Sarkar, Subir Kumar, 69, 79, 97, 115, 125
 Sarkar, Ujjaljyoti, 51
 Sarker, Rishiraj, 151
 Sarkhel, Saheli, 97
 Sarmah, A., 465
 Sarma, Kanak Chandra, 573
 Saurabh, Saket, 143
 Sawat, Dattatray D., 689
 Senapati, Suvam, 97
 Sen, Joy, 509
 Sen, Kausik, 797
 Sengupta, Debaparna, 151
 Sharma, Ganesh, 591, 679
 Sharma, Kamal Kant, 223, 247
 Sharma, Pratikshya, 915
 Sharma, Safal, 591, 599, 679
 Sharma, Sanjeev, 377
 Shome, S., 475
 Shukla, Priyanka, 107
 Singh, Additi Mrinal, 343
 Singh, Aheibam Dinamani, 399
 Singh, Amit Kumar, 719
 Singh, Arun Kumar, 679, 701, 943
 Singh, Balwinder, 223, 247
 Singh, Dhanprakash, 223
 Singh, Hidam Kumarjit, 419, 429
 Singh, Lairenlakpam Joyprakash, 583, 711
 Singh, Niharika, 359, 369
 Singh, Poornima, 393
 Singh, Soumendra, 313
 Singh, Vinod Kumar, 287, 359, 369, 377, 385, 393
 Sinha, Oindrila, 313
 Soni, Akash, 661
 Sur, Samarendra Nath, 329, 679
 Suting, Chiborhame, 777
 Swain, Bibhu P., 1
 Swarnakar, Jaydeep, 711
 Syiem, Bronson, 459

T

Tamang, Nima Donka, 329
 Tariang, Ephermika, 865
 Thakur, Gopal, 247
 Thakur, Sachin, 133
 Thakur, Subhashis, 21
 Tomar, Upendra, 287
 Tripathy, Susanta Kumar, 57

Tripati, Princi, [287](#)

V

Valluru, Saikumar, [943](#)

Verma, Kapil, [259](#)

Verma, O.P., [527](#)

Verma, Om Prakash, [517](#), [539](#)

Verma, Vinay Kumar, [183](#)

Vig, Sunny, [133](#), [233](#)

W

War, A., [625](#)

Warjri, S., [625](#)

Y

Yadav, Deepanshu, [517](#)

Yesmin, Sebina, [429](#)